AC ELECTRIC MOTORS CONTROL

AC ELECTRIC MOTORS CONTROL

ADVANCED DESIGN TECHNIQUES AND APPLICATIONS

Editor

Fouad Giri
University of Caen Basse-Normandie, France

WILEY
A John Wiley & Sons, Ltd., Publication

This edition first published 2013

Registered office
John Wiley & Sons Ltd, The Atrium, Southern Gate, Chichester, West Sussex, PO19 8SQ, United Kingdom

Library of Congress Cataloging-in-Publication Data

AC electric motors control : advanced design techniques and applications / [compiled by] Fouad Giri.
pages cm
Includes bibliographical references and index.
ISBN 978-1-118-33152-1 (hardback)
1. Electric motors, Alternating current–Automatic control. I. Giri, Fouad, editor of compilation.
TK2781.A33 2013
621.46–dc23

2012050753

A catalogue record for this book is available from the British Library

ISBN: 978-1-118-33152-1

Typeset in 10/12pt Times by Aptara Inc., New Delhi, India

Contents

List of Contributors

Haitham Abu-Rub
Department of Electrical & Computer Engineering, Texas A&M University at Qatar, Qatar

Tarek Ahmed-Ali
GREYC Lab, University of Caen Basse-Normandie, France

Vincent Van Assche
GREYC Lab, University of Caen Basse-Normandie, France

Giovanni Azzone
Dipartimento di Ingegneria "Enzo Ferrari", Università di Modena e Reggio Emilia, Italy

Gildas Besançon
Control System Department, GIPSA Lab, Grenoble Institute of Techology and Institut Universitaire de France, France

Marc Bodson
Electrical and Computer Engineering, University of Utah, USA

Robert Boisliveau
Ecole Centrale de Nantes, LUNAM, France

Ajit K. Chattopadhyay
Electrical Engineering Department, Bengal Engineering & Science University, India

Fatima-Zahra Chaoui
GREYC Lab, University of Caen Basse-Normandie, France

Maria Letizia Corradini
Scuola di Scienze e Tecnologie, Università di Camerino, Italy

Jesús De León
FIME, Universidad Autonoma de Nuevo Leon, Mexico

Marc Diguet
Alstom Transport, France

Philippe Dorléans
GREYC Lab, University of Caen Basse-Normandie, France

Rukmi Dutta
School of Electrical Engineering & Telecommunications, University of New South Wales, Australia

Abderrahim El Fadili
GREYC Lab, University of Caen Basse-Normandie, France

Abdelmounime El Magri
GREYC Lab, University of Caen Basse-Normandie, France

Gerardo Espinosa–Pérez
Facultad de Ingeniería, UNAM, México

Yong Feng
Department of Electrical Engineering, Harbin Institute of Technology, China

Malek Ghanes
ECS-Lab, ENSEA, France

Fouad Giri
GREYC Lab, University of Caen Basse-Normandie, France

Alain Glumineau
Ecole Centrale de Nantes, LUNAM, France

Jarosław Guziński
Faculty of Electrical and Control Engineering, Gdansk University of Technology, Poland

Fengling Han
School of Computer Science and Information Technology, RMIT University, Australia

Michaël Hilairet
LGEP, SUPELEC, CNRS, France

Gianluca Ippoliti
Dipartimento di Ingegneria dell'Informazione, Università Politecnica delle Marche, Italy

Hassan K. Khalil
Department of Electrical and Computer Engineering, Michigan State University, USA

Zbigniew Krzeminski
Faculty of Electrical and Control Engineering, Gdansk University of Technology, Poland

Arkadiusz Lewicki
Faculty of Electrical and Control Engineering, Gdansk University of Technology, Poland

Xuefang Lin Shi
Ampere Lab, INSA Lyon, France

Alberto Luviano-Juárez
UPIITA, IPN, México

Riccardo Marino
Dipartimento di Ingegneria Elettronica, Universitá di Roma "Tor Vergata," Italy

Jean-François Massieu
GREYC Lab, University of Caen Basse-Normandie, France

Felipe González Montañez
Departamento de Energía, Universidad Autónoma Metropolitana, México

Giuseppe Orlando
Dipartimento di Ingegneria dell'Informazione, Università Politecnica delle Marche, Italy

Romeo Ortega
LSS, SUPELEC, CNRS, France

Hamid Ouadi
FSAC, University of Casablanca, Morocco

Alessandro Pilloni
Deptartment of Electrical and Electronic Engineering (DIEE), University of Cagliari, Italy

Manuel Pineda-Sanchez
Deptartment of Electrical Engineering (DIE), Universidad Politécnica de Valencia, Spain

Alessandro Pisano
Deptartment of Electrical and Electronic Engineering (DIEE), University of Cagliari, Italy

Ruben Puche-Panadero
Deptartment of Electrical Engineering (DIE), Universidad Politécnica de Valencia, Spain

Faz Rahman
School of Electrical Engineering & Telecommunications, University of New South Wales, Australia

Hebertt Sira Ramírez
Department of Electrical Engineering, CINVESTAV-IPN, México

Martin Riera-Guasp
Deptartment of Electrical Engineering (DIE), Universidad Politécnica de Valencia, Spain

John Cortés Romero
Department of Electrical and Electronic Engineering, Universidad Nacional de Colombia, Colombia.

Dhruv Shah
LSS, SUPELEC, CNRS, France

Elias G. Strangas
Department of Electrical and Computer Engineering, Michigan State University, USA

Alexandru Ţiclea
Department of Control and System Engineering, Polytechnic University of Bucharest, Romania

Patrizio Tomei
Dipartimento di Ingegneria Elettronica, Universitá di Roma “Tor Vergata,” Italy

Dramane Traore
Ecole Centrale de Nantes, LUNAM, France

Cristiano Maria Verrelli
Dipartimento di Ingegneria Elettronica, Universitá di Roma “Tor Vergata,” Italy

Xinghuo Yu
School of Electrical and Computer Engineering, RMIT University, Australia

Roberto Zanasi
Dipartimento di Ingegneria “Enzo Ferrari”, Università di Modena e Reggio Emilia, Italy

Preface

The last two decades have witnessed spectacular developments in the technologies of power electronics and microprocessors. Due to these developments, sophisticated power converters and digital signal processors (DSP) have become available, making possible the use of high-performance AC drives in widespread applications. For this goal to be fully realized, one should get as much benefit as possible from the considerable progress made in the field of control theory. Three decades of intensive research activity has resulted in a proliferation of nonlinear control methods, published in hundreds of journal and conference papers. Of course, not all nonlinear control methods apply to AC motors, but a significant fraction does. The aim of this monograph is to make available to the scientific community a resource reflecting the wide variety of control problems posed by AC motors and drawing up the state of the art of the corresponding control methods for design, analysis, and implementation. In this respect, special focus is made on the topics of sensorless nonlinear observers, adaptive and robust nonlinear controllers, output-feedback controllers, fault detection and isolation algorithms, and fault-tolerant controllers. The most significant developments in these topics, and their applications to AC motor control, are described in this book, as well as some new research topics. Most of the concepts and methods are presented by their own inventors.

The book is intended for a wide variety of readers, including academia and industry researchers, graduate students and their professors, engineers, and practitioners. Although it includes many aspects of the theory, it is nonetheless beneficial to practitioners who will be able to use the methods without necessarily understanding every single detail of the theory. It will also be useful for newcomers to research in the field of AC motor control. For students and newcomers, the main prerequisites are undergraduate courses on linear and nonlinear system control, on electric machines, and on power electronics. Each chapter includes an introduction and an individual reference list, and the different chapters are written in a way that makes them readable independently from each other.

I am grateful to my colleagues from around the world who generously contributed to this work, bringing together considerable knowledge from a wide range of aspects of the research area. I feel particularly honored to offer this collective work originating from their contributions. Marc Bodson and Vincent van Assche not only directly contributed by co-authoring chapters, but also helped in other ways, with Marc reading and correcting parts of the manuscript, and Vincent retyping parts in Latex and compiling the whole manuscript. My sincere thanks go to Marc and Vincent for their contributions. Special and warm thanks go to Abderrahim El Fadili, Abdelmounim El Magri, and Hamid Ouadi, all three my former PhD students and current collaborators. The present book would certainly never have come

out without the innumerable and exciting exchanges we had along the past 10 years. I am particularly grateful to Abderrahim and Abdelmounim who kindly accepted to retype in Latex some chapters initially written in Word by the authors. Last, but not least, I would like to thank Peter Mitchell, Liz Wingett, and Richard Davies, all three from John Wiley & Sons, Ltd, UK, who provided numerous advice and material help during the editing stage of the book.

Fouad Giri
University Distinguished Professor
University of Caen Basse-Normandie
France

1

Introduction to AC Motor Control

Marc Bodson[1] and Fouad Giri[2]
[1]*Electrical and Computer Engineering, University of Utah, USA*
[2]*GREYC Lab, University of Caen Basse-Normandie, France*

1.1 AC Motor Features

The principles of operation of (AC) motors may be found in many books, including Hindmarsh (1985), Vas (1990), Leonard (2001) and Chiasson (2005). In this section, some basic facts are recalled, focusing on the features that contribute to the success of AC motors in motion control and to the continuing growth of their applications. "AC motors" refers to electric machines that convert AC electric energy into mechanical energy. There is a wide variety of such machines that differ by their operating principles, physical characteristics, and power level. Considering their operating principles, AC motors are classified in two main categories: induction and synchronous.

Induction motors exist in two main types, squirrel cage and wound rotor. In wound rotor machines, both the stator and the rotor windings are made of individually insulated coils. The rotor coils are made accessible on the stator side through slip rings. In squirrel-cage machines, the rotor windings are replaced by longitudinal bars placed in slots beneath the rotor's outer surface. The rotor bars are connected by circular conductors placed at the extremities. Operationally, a squirrel-cage motor is similar to a wound rotor motor with short-circuited windings.

For both types of motors, the stator windings generate a rotating magnetic field when supplied with polyphase AC. The speed of rotation of the field is given by the stator current frequency divided by the number of magnetic pole pairs created by the windings. By Faraday's and Lenz's laws, currents are induced in the rotor windings whenever the rotor speed differs from the speed of the magnetic field produced by the stator. This speed difference, called slip speed, must be kept small to guarantee high-energy conversion efficiency. Under this constraint, a change of rotational speed requires an adjustment of the stator electrical frequency.

AC Electric Motors Control: Advanced Design Techniques and Applications, First Edition. Edited by Fouad Giri.

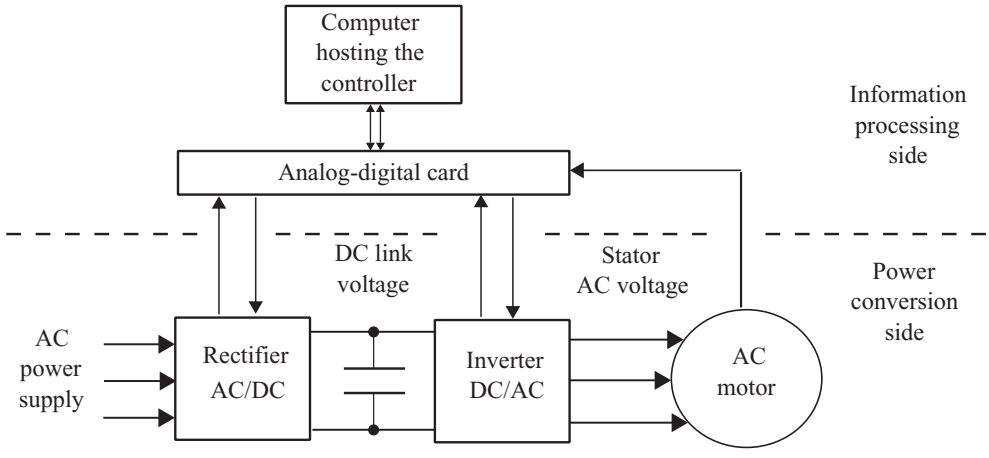

Figure 1.1 AC motor control architecture

Synchronous motors also exist in two versions, namely, permanent-magnet and wound rotor. Unlike induction motors, there are no induced rotor currents in synchronous motors in steady state, because the rotor rotates at the same speed as the rotating magnetic field. A motor torque is developed due to the interaction between the stator rotating field and a rotor field generated either by permanent magnets or by an injected rotor current.

For both induction and synchronous motors, variable speed operation is possible if the stator supply frequency is made variable. Until the development of modern power electronics, there was no simple and effective way to vary the frequency of the motors' supply voltages. Nowadays, reliable high-speed switching power converters are available that serve as actuators in AC motor control. Specifically, an AC motor is supplied with power through an association of two power converters, a rectifier and an inverter (Figure 1.1). The former, also called AC/DC converter, converts the AC power provided by the grid into DC power. Control of the rectifier is not always implemented, but is useful to regulate the DC voltage, or to enable regeneration of power to the grid. The inverter, also referred to as DC/AC converter, transforms the DC voltage into an AC voltage with a specified frequency. The result is achieved by chopping the DC voltage at a high rate, typically using a pulse-width modulation (PWM) technique. In this respect, it is worth emphasizing the considerable progress made in computer technology, which has resulted in fast multiprocessor computers and high-performance analog-digital interfaces. This progress has made possible the real-time implementation of sophisticated methods to control the power converters associated with AC machines.

DC motors require schemes similar to Figure 1.1, but with lower bandwidth requirements and fewer channels. However, ACs are produced in conductors through mechanical commutation, rather than electrical commutation. The commutators of DC motors are complex and vulnerable. As a result, AC motors offer a higher power/mass ratio, relatively low cost, and simple maintenance. AC motors exist with a variety of characteristics and in a large range of sizes, from a few watts to many thousands of kilowatts. For these reasons, AC drive systems have already replaced DC drives in several industrial fields and this widespread proliferation

is expected to continue. Nowadays, AC drives are used in almost all industrial applications, such as the following:

1. **Transport:** vehicle traction, marine propulsion
2. Milling in cement, steel, paper, and others industries
3. Pumping/compressing in oil and gas industry
4. Cranes and industrial vehicles
5. **Domestic machines:** lifts, washing machines, and others.

1.2 Control Issues

1.2.1 State-Feedback Speed Control

The prime objective in AC motor control is to make the rotor turn at a desired speed despite load variations. If the desired speed is constant, one talks of speed regulation, while tracking problems correspond to time-varying speeds. The desired speed, also called the speed reference signal, is often unknown a priori, making the control issue more difficult. Indeed, the achievement of a desired rotor speed profile necessitates a sufficient motor torque to overcome the load torque, but also to provide the required accelerations of the rotor during transient periods.

In AC induction motors, the generation of a given torque necessitates a sufficient level of rotor magnetization, that is, a sufficiently high flux magnitude in the rotor. Flux control is thus not independent from the problem of speed control and both are acted upon through the inverter control signals. These signals are binary signals commanding on and off conduction modes. The electromechanical nature of the motor entails nonlinearities associated with products of fluxes with currents and fluxes with speed. Furthermore, the three-phase nature of the motor means that the overall model is nonlinear, of high dimension, as well as controlled through binary signals. A common practice consists in reducing the model dimension by resorting to Park's transformation, which projects the three-phase variables (generally referred to as *abc*) on a two-phase rotating coordinate frame (generally referred to as *dq*) (see, e.g., Blaschke 1972; Leonard 2001). The binary nature of the inverter signals is generally coped with by averaging the signals over the PWM period and letting the control design be based on the corresponding averaged two-coordinate model (see, e.g., Sira-Ramirez and Silva-Ortigoza 2006). Model nonlinearity is handled using modern nonlinear control design techniques, including state- and output-feedback linearization, Lyapunov control, sliding-mode (SM) control, passivity-based control (Ortega *et al.* 1998; Isidori 1999; Sastry 1999; Vidyasagar 2002; Khalil 2003).

The basic ideas described so far lead to the control strategy depicted in Figure 1.2.

1.2.2 Adaptive Output-Feedback Speed Control

The basic state-feedback control strategy of Figure 1.2 assumes that all controlled system parameters are known. However, some system parameters are generally not known a priori, and may even be varying in normal operating conditions. In particular, the stator and the rotor resistances are sensitive to the magnitude of the currents, and thus undergo wide variations in the presence of speed reference and load torque changes. The rotor-load set inertia and rotor friction coefficient may also vary (e.g., in transportation applications). To maintain the control

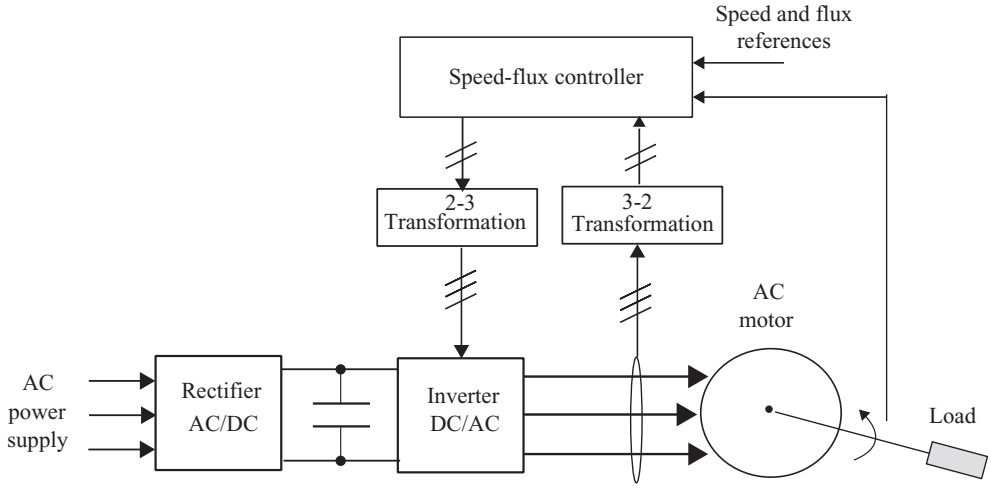

Figure 1.2 AC motor basic control strategy: state-feedback speed control

performance at the desired level despite changing operating conditions, the speed controller may need to be reinforced with a parameter adaptation capability (Krstic, Kanellakopoulos, and Kokotovic 1995; Astolfi, Karagiannis, and Ortega 2007).

Another limitation of the control strategy of Figure 1.2 is that all state variables are assumed to be accessible through measurements. However, reliable and cheap sensors are only available for stator currents and voltages. Flux sensors are generally not available on machines because of their high implementation cost and maintenance complexity. Mechanical sensors (for speed and, more rarely, torque measurements) are common, but also entail reliability issues and extra maintenance costs due to physical contact with rotor. Therefore, state observers are attractive to obtain online estimates of the states based only on electric measurements (Besançon 2007). Sensorless controllers involving online state estimation using observers are commonly referred to as output-feedback controllers. Modern control strategies, illustrated in Figure 1.3, combine both features: parameter adaptation and sensorless output-feedback.

1.2.3 Fault Detection and Isolation, Fault-Tolerant Control

Like any complex system, AC motors are facing faults in otherwise normal operating conditions. Faults may originate from the failure of certain system components, for example, sensors, inverter, rectifier, power supply, or even stator/rotor windings. Sensor failure may result in a loss of observability, while inverter, rectifier, or supply failure may cause a loss of controllability. Regardless, the controller designed on the basis of a faultless model may see its performance deteriorate drastically, sometimes causing unsafe operation of the whole system. To prevent unsafe running and continuously guaranteeing an acceptable level of performances, a fault-tolerant control (FTC) system is needed. The development of FTC systems has been an active research topic, especially over the past 15 years, and a review of relevant concepts and methods can be found in Blanke *et al.* (2000), Steinberg (2005), and Zhang and Jiang (2008), and Noura *et al.* (2009). Distinction is usually made between passive and active FTC

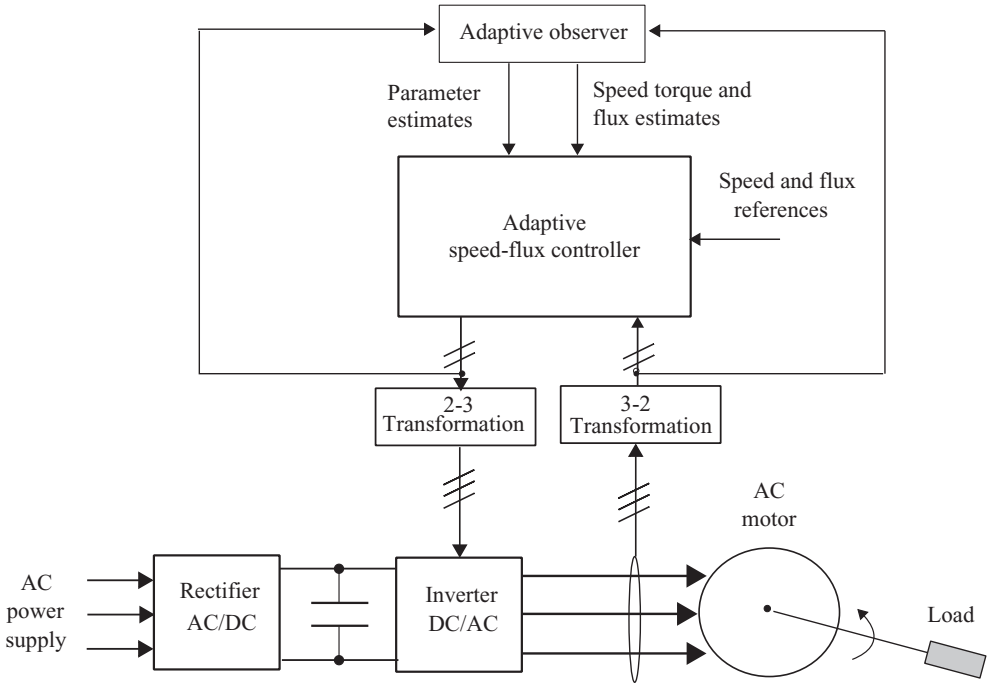

Figure 1.3 AC motor modern control strategy: adaptive output-feedback speed control

approaches. In the first case, component failures are considered as disturbances and a single control law is designed so that it is robust against the predefined set of disturbances. The active FTC approaches are those that dynamically react to fault occurrence by performing control reconfiguration. This is mainly done in two ways:

1. Selecting online (within a set of predesigned laws) the control law that best fits the detected fault type.
2. Redesigning online the control law to adapt it to the detected faulty situation.

Active FTC approaches require a fault detection and isolation (FDI) module. The role of the latter is twofold:

1. Making a binary decision, either that something has gone wrong or that everything is fine.
2. Determining the location as well as the nature of the fault.

FDI techniques are broadly classified as information-based, model-based (MB), and artificial-intelligence-based. An overview of MB techniques is provided by the survey papers Willsky (1976), Isermann (1984, 2005), Hwang *et al.* (2010). In this respect, observer-based FDI is particularly suitable to build up FTC in presence of mechanical sensors failure. This is illustrated in Figure 1.4.

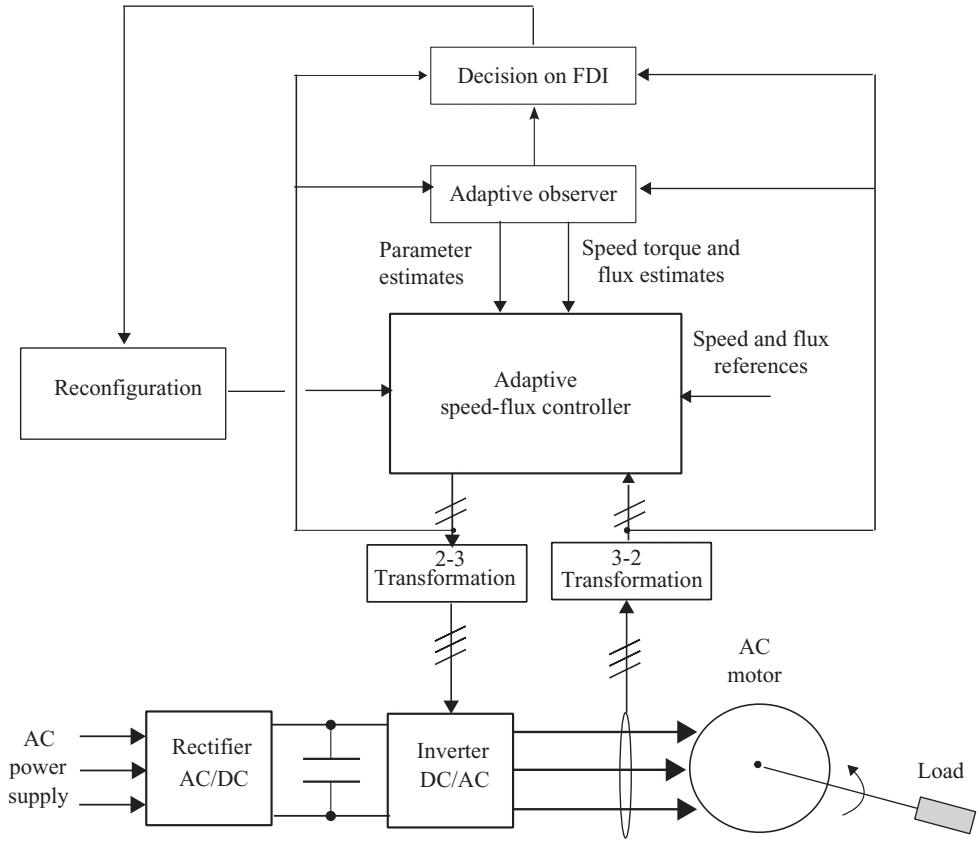

Figure 1.4 AC motor fault tolerant control strategy: failure mechanical sensors accommodation

1.2.4 Speed Control with Optimized Flux

It is common to set the flux reference to a constant value that generally equals the machine's nominal flux. However, energetic efficiency is only maximal when the motor operating conditions, essentially determined by the load torque, remain close to the nominal conditions. In practice, the torque may be subject to wide-range variations. Then, in presence of small loads (compared to nominal load), maintaining the nominal flux entails a waste of energy and a lower than optimal energetic efficiency. However, if the motor flux is given a small value, the achievable motor torque may not be sufficient to counteract large load torques. In general, speed-control strategies involving constant flux references do not guarantee optimal machine performance in the sense of maximal energetic efficiency and maximal torque. To remove the above shortcomings, it is necessary to let the flux reference be dependent on both the speed reference and the load torque. Thus, the flux reference must be state-dependent (Figure 1.5). Flux weakening is also used for both synchronous and induction machines to maximize the torque at high speeds in the presence of voltage constraints.

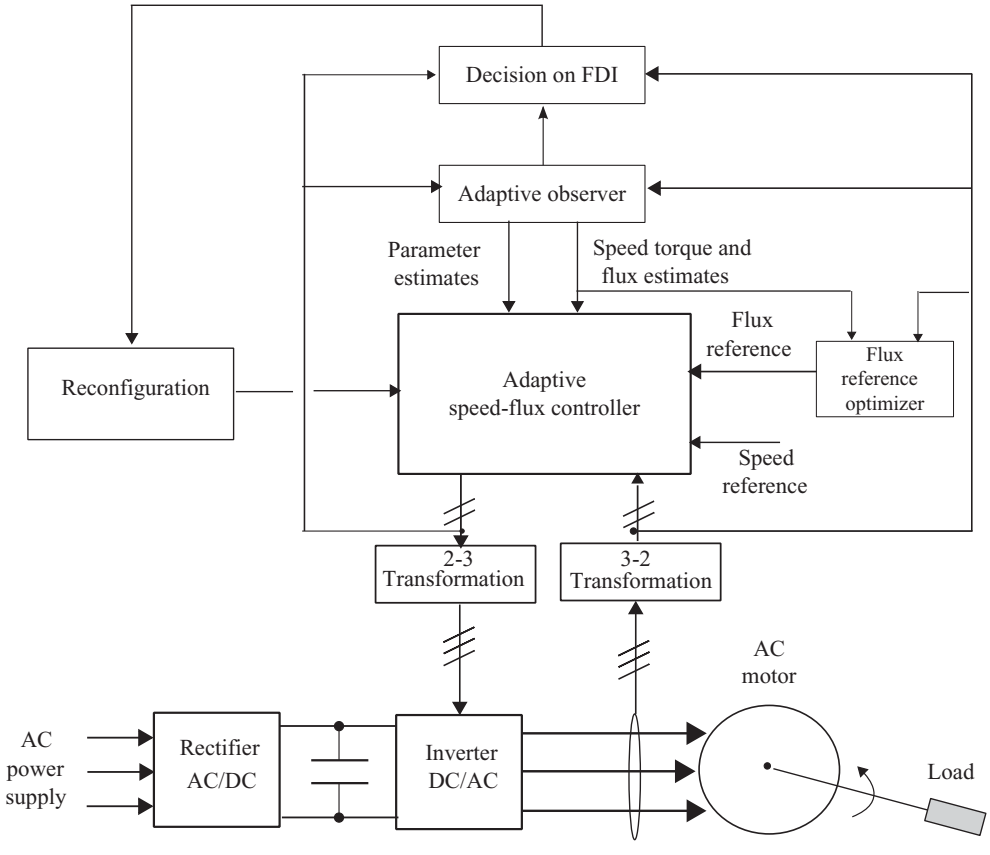

Figure 1.5 AC motor control strategy combining ftc and flux optimization

1.2.5 Power Factor Correction

The role of the rectifier in Figures 1.2, 1.3, 1.4, and 1.5 is to convert the supply AC power into DC power and transmit this power through a constant DC link voltage. Regulation of this voltage is desirable for the AC motor to operate effectively. Moreover, the rectifier-inverter-motor set strongly interacts with the AC power supply net as the power flow is bidirectional: the direction depends on the speed profile and on load variations. Then, undesirable current harmonics are likely to be generated in the AC line, due to the strongly nonlinear nature of the association "rectifier-inverter-motor." This harmonic pollution has several damaging effects on the quality of power distribution along the AC line, for example, electromagnetic compatibility issues, voltage distortion, larger power losses, and so on. In this respect, existing standards (e.g., IEEE519-1992 and IEC 61000-3-2/IEC 6100-3-4) indicate specific current harmonic limits, expressed in terms of power factor. Of course, the harmonics and power factor correction (PFC) can be improved using additional equipment and/or over-dimensioning the converter. However, this solution is costly and may not be sufficient.

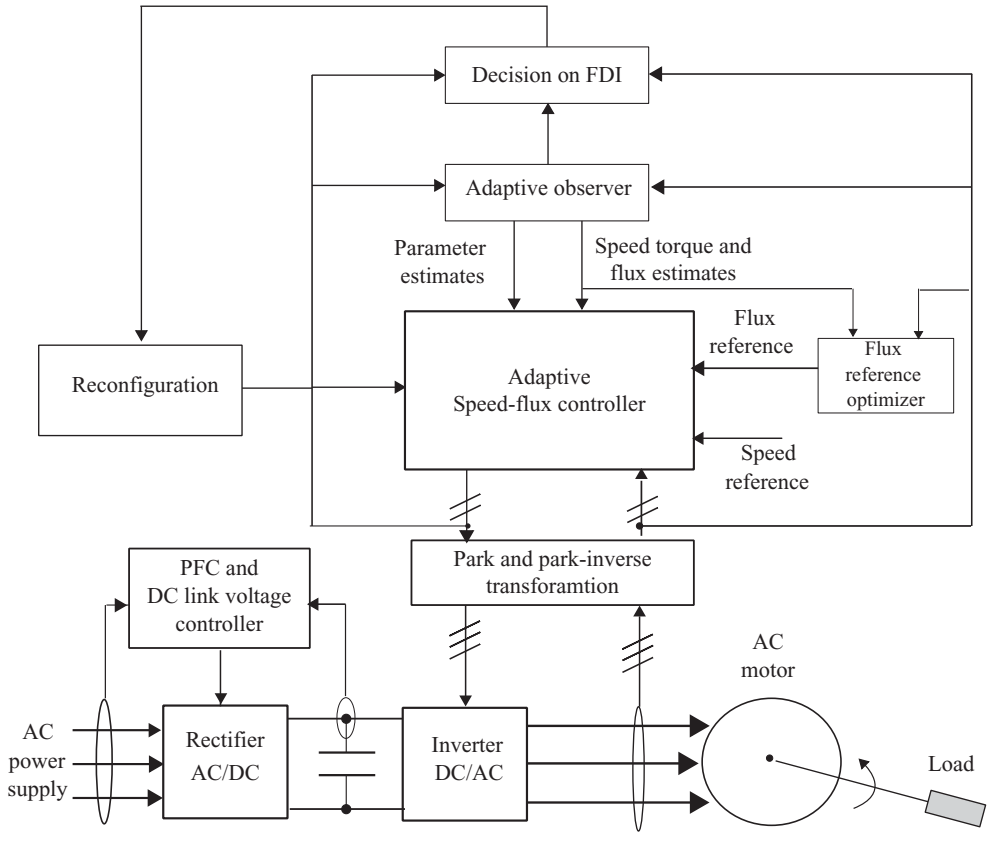

Figure 1.6 AC motor global control strategy combining ftc, flux optimization and PFC

In light of the above remarks, it becomes clear that a high-performance control strategy deals with the control problem for the whole "rectifier-inverter-motor" set, seeking simultaneous achievement of all relevant control objectives, namely, tight speed regulation for wide set-point variation range, FDI, flux optimization despite large load changes, and PFC. Figure 1.6 describes a global control strategy accounting for all requirements.

1.3 Book Overview

The main control problems relevant to AC motors have been briefly described in the previous section. The present book is not intended to be an encyclopedic survey of all existing solutions for all types of AC machines. It rather aims at showing how modern control methods involving sophisticated design and analysis techniques are beneficial to AC motors. The focus is on the most significant types of AC motors and a representative sample of application fields. The book gives an illustrative presentation of the motors and control methods, referring to specialized monographs for the required technical background in machine theory. In addition

to the present introduction, the book includes 22 other chapters organized in five parts, briefly overviewed in the following subsections.

1.3.1 Control Models for AC Motors

The first part of the book is about modeling of AC motors and their relevant power converters. It consists of Chapters 2 and 3, respectively, which are devoted to induction motors and synchronous motors. The physical principles of these machines and associated power converters are recalled. The corresponding three-phase models are established, and it is shown how simpler two-phase models can be obtained using specific coordinate transformations. Identification methods are presented for estimating the model parameters using experimental data. The established models will prove to be useful for control design in later chapters.

1.3.2 Observer Design Techniques for AC Motors

The second part of the book includes four chapters on observer design for AC motors. Chapter 4 is about the design and analysis of sensorless state observers for induction motors. Estimation issues and observability properties in induction motors are reviewed. The case of lack of speed measurement and unknown electrical parameters is considered. Then, a unifying observer approach is presented that includes sensorless observer design and its convergence analysis. The performance of the approach is evaluated, both by simulations and experiments.

Chapter 5 deals with state observers for active disturbance rejection in induction motor control. Generalized proportional integral (GPI) observers are proposed, in combination with linear output feedback controllers, for the direct field-oriented control and the classical field-oriented two-stage output feedback controller design. An observer-based active disturbance rejection scheme cancels the lumped effects of exogenous, time-varying, load torque disturbances, and of the endogenous state-dependent nonlinearities. The high-gain GPI observers estimate online the output phase variables and the lumped disturbance inputs affecting the underlying linear dynamics. Experimental results are presented for angular velocity and angular position trajectory tracking tasks, when the induction motor is subject to chaotic load torque profiles generated by an armature current programmed DC motor.

In Chapters 4 and 5, the nonlinear state observers are developed for induction motors assuming a continuous-time implementation. However, in modern control applications, continuous-time systems are only observed through sampled output signal measurements. Then, a classical solution consists of constructing a discrete-time approximation of the (continuous-time) observer. This solution is somewhat burdensome computationally, and does not necessarily preserve the convergence properties of the original continuous-time observer. Chapter 6 presents a different solution based on the hybrid continuous-discrete estimation principle. Hybrid observers are designed for induction motors taking into account communication constraints. They are formally shown to maintain satisfactory estimation accuracy when applied to the (continuous-time) system model, and the theoretical result is confirmed using experimental data.

Chapter 7 is on observer design for permanent-magnet synchronous motors (PMSM). A special emphasis is placed on the loss of observability arising at zero-speed without mechanical

sensors. This issue is dealt with by using an observer design method based on a high-order SM. The obtained observer turns out to be robust against disturbances and avoids the chattering phenomenon inherent to standard first order SMs. Stability and finite time convergence of the observer are analyzed and commented upon. Experimental results are carried out to highlight the technological interest of the proposed method. The constraints and issues of real-time computation are discussed.

1.3.3 Control Design Techniques for Induction Motors

The third part of the book includes seven chapters dealing with control design techniques for induction motors. Chapter 8 is about the use of high-gain observers in the control of induction motors with and without rotor position sensors, emphasizing closed-loop analysis of field-orientation schemes, and including the impact of orientation errors. The framework for studying field orientation in the presence of model uncertainty is used to design and analyze a nonlinear output feedback controller that requires only measurements of the rotor position and stator currents. The controller is designed to be robust to uncertainties in the rotor and stator resistances as well as to a bounded, time-varying load torque. A high-gain observer is used to estimate the rotor speed and acceleration from its position measurement. The same framework is extended to a case where only stator current measurements are available. In this case, a high-gain observer is used to estimate the speed from the field-oriented currents and voltages.

Chapter 9 is on adaptive output-feedback control of induction motors. It addresses the problem of adaptively controlling induction motors in order to achieve rotor speed and flux magnitude tracking, all without resorting to mechanical sensors. Uncertainties in the load torque and the rotor and stator resistances are accounted for. Adaptive output-feedback controllers are developed and formally shown to solve the control problem. The controller involves online estimation of the unknown parameters. The specific observability and identifiability conditions that allow for the exponential tracking and identification of the uncertain parameters are emphasized in terms of persistent excitation conditions. The key idea of the control and estimation design relies in adopting a two-time scale strategy by performing a sufficiently slow adaptation for the stator resistance estimate.

Chapter 10 is on nonlinear control of induction motors for speed regulation with maximal energetic efficiency. It is noticed that optimization cannot be properly coped with if the magnetic circuit nonlinearity is not accounted for. The controller includes an optimal flux reference generator (optimal in the sense of minimal stator current consumption) and a nonlinear regulator obtained using the backstepping design technique. It is shown that the controller regulates well the motor speed and the rotor flux in presence of wide-range variations of the machine speed reference and the load torque.

Chapter 11 presents an experimental evaluation of two robust control design techniques for induction motors, including a nonlinear backstepping technique with integral terms that improve robustness against parametric uncertainties, and a high-order SM technique designed for its intrinsic robustness quality. The two controllers are experimentally compared using an industrial benchmark setup.

Chapter 12 is on multiphase induction motor control. The motor is represented by a new complex dynamic model where the harmonic injection is considered and represented using

the power-oriented graphs graphical technique. Different field-oriented control strategies are designed in the multiphase and compared by investigating the trade-off between the different solutions that differ in required control degrees of freedom.

Chapter 13 is on the control of a wound rotor, or doubly-fed induction machine (DFIM) and associated AC/DC rectifier and DC/AC inverter. A multiloop nonlinear controller is developed using the backstepping design technique. It includes three regulators of rotor speed, DC link voltage, and PFC, respectively. The controller is formally shown to meet its objectives, that is, accurate motor speed-reference tracking, tight regulation of the DC Link voltage, and PFC.

Chapter 14 is on FDI in induction motors. Both MB and data-driven (DD) methods are developed. The MB approach involves SM observers based on residual evaluation and thresholding. DD methods, also referred to as "motor current signature analysis" (MCSA), are designed using processing techniques based on FFT, Hilbert transforms, and more advanced time/frequency combined analysis techniques.

1.3.4 Control Design Techniques for Synchronous Motors

The fourth part of the book includes six chapters on synchronous motor control. In Chapter 15, PMSMs are considered and the control problem is solved using a passivity-based output-feedback control. The structure of the main block of the controller comes from the application of the technique of interconnection and damping assignment passivity-based control. It involves different observers that estimate the mechanical coordinates (speed and load torque) and stator fluxes (which, in turn, are used to obtain information related to the mechanical position). Both simulation and experimental results are included.

Chapter 16 is on adaptive output-feedback control of PMSMs. Assuming that only stator currents and voltages are available for feedback, a novel sixth order nonlinear adaptive control algorithm is designed, which does not rely on nonrobust open-loop integration of motor dynamics and guarantees, under persistency of excitation, local exponential rotor speed tracking. Satisfactory performance is obtained even in the presence of inaccurate motor parameters, time-varying load torques, current sensing errors, and discrete-time controller implementation.

Chapter 17 is on robust fault detection and control of PMSMs. It proposes first a robust speed observer making use of currents measurements only. Next, a control law fed by speed observations is presented, and closed-loop stability of the overall system is proved robustly with respect to parameter variations of the dynamic model of the motor (inertia, friction, and load) with known bound. Finally, a residual-based detection approach is discussed for sensor faults affecting current measurements.

Chapter 18 is on digitization of variable structure control for PMSMs. SM controllers are designed to control the motor position and velocity and currents. The aim is to suppress mechanical resonance and reach high performances of PMSM servo systems, such as fast response, strong robustness, and high precision. In addition, an SM-based mechanical resonance suppressing method is proposed. An observer is applied to estimate the load speed and the shaft torsion angle. Finally, a high-order SM control is designed to guarantee the stability of the system. The digitization of the designed SM controllers is discussed for the purpose of practical implementation. The discretization behaviors of PMSM servo systems are analyzed, which helps obtain approximate boundary conditions for the sampling period.

Chapter 19 is on the control of interior permanent-magnet (IPM) synchronous motors. The control trajectories in terms of the current and voltage limit boundaries for optimum drive response is discussed. Techniques of sensorless control are proposed via direct torque control (DTC) in the stator *dq* flux estimation and in the rotor frame via stator flux and rotor position observers. Both open- and closed-loop operations are described. Techniques of sensorless control combining signal injection and observer methods at very low speed and covering a wide speed range are also included.

Chapter 20 is about nonlinear state-feedback controllers for three-phase wound-rotor synchronous motors. Considering the "converter-motor" set, the method makes it possible to provide motor speed regulation, in addition to other important control objectives such as PFC with respect to the grid supply and DC Link voltage regulation. To achieve these objectives, an adaptive control strategy is developed, based on a nonlinear model of the whole "converter-motor" set. The adaptation feature is motivated by the uncertain nature of some motor characteristics, for example, mechanical parameters. The closed-loop system stability and performance properties are formally analyzed using averaging theory.

1.3.5 Industrial Applications of AC Motors Control

The last part of the book consists of three chapters devoted to applications of AC motors in some industrial fields.

Chapter 21 is on AC motor control applications in vehicle traction. It describes the requirements of vehicle traction applications that AC drive systems must meet. The chapter reviews recent trends of vehicle traction drive architectures in the marketplace and in the available literature. It discusses suitable motor types, control requirements, energy storage and management issues between drive and regenerative braking modes of operation, and battery sizing. The battery management system with temperature compensation for charging and discharging current limits and for monitoring the state of charge (SOC) are discussed. The converter systems between batteries and the motor drive are designed for efficient management of bidirectional power flow. Examples of vehicle traction systems that use induction and IPM machines are included, as well as other types of machines in commercially available traction applications.

Chapter 22 is on induction motor control applications in high-speed train (HST) electric drives. It illustrates how state observers can be useful in fault diagnostic for modern high-speed electric traction applications. State observers are used for online estimation of motor speed and load torque. The analysis of speed and load torque signals makes it possible to assess the state of speed sensor and torque transmission systems in electric traction vehicle. When some malfunctioning is detected, for example, in the case of speed sensor faults, the motor control system can be switched to speed sensorless mode. The proposed diagnostic system is applied to a HST propelled by an induction squirrel-cage motor. Simulation and experimental results for a high-speed traction drive are presented.

Chapter 23 is on AC motor control applications in high-power industrial drives. The applications discussed include steel mills, cement and ore mills, ship drives, pumps and compressors for petrochemicals and electric power industry, paper mills, and so on. The brief features of the industrial AC drives developed by the leading manufacturers worldwide are presented together with new developments and trends for the future.

References

Astolfi A, Karagiannis D, and Ortega R (2007) *Nonlinear and Adaptive Control with Applications*. Springer.

Besançon G (2007) *Nonlinear Observers and Applications*. Springer.

Blanke M, Frei C, Kraus F, *et al*. (2000) What is fault-tolerant control? *IFAC Symposium on Fault Detection, Supervision and Safety for Technical Process*, pp. 40–51.

Blaschke F (1972) The principle of field orientation applied to the new trans-vector closed-loop control system for rotating field machine. *Siemens rev*, **93**, 217–220.

Chiasson JN (2005) *Modeling and High Performance Control of Electric Machines*. John Wiley & Sons.

Hindmarsh, J (1985) *Electrical Machines and their Applications 4th edn*. Oxford, Pergamon.

Hwang I, Kim S, Kim Y, and Seah CE (2010) A survey of fault detection, isolation, and reconfiguration methods. *IEEE Transactions on Control Systems Technology*, **18**, 636–653.

Isermann R (1984) Process fault detection based on modeling and estimation methods: a survey. *Automatica*, **20**, 387–304.

Isermann R (2005) Model-based fault-detection and diagnosis status and applications. *Annual. Reviews Control*, **29**, 71–85.

Isidori A (1999) *Nonlinear Control Systems: Part II*. Springer.

Khalil H (2003) *Nonlinear Systems*. Prentice Hall, Upper Saddle River NJ.

Krstic M, Kanellakopoulos I, and Kokotovic P (1995) *Nonlinear and Adaptive Control Design*. John Wiley & Sons.

Leonard W (2001) *Control of Electrical Drives*. Springer, New York.

Noura H, Theilliol D, Ponsart JC, and Chamseddine A (2009) *Fault-Tolerant Control Systems—Design and Practical Applications*. Springer.

Ortega R, Loria A, Nicklasson PJ, and Sira-Ramirez H (1998) *Passivity-Based Control of Euler-Lagrange Systems*. Springer, Berlin.

Vas P (1990) *Vector Control of AC Machines*. Clarendon Press, Oxford.

Sastry S (1999) *Nonlinear Systems; Analysis, Stability, and Control*. Springer Verlag.

Sira-Ramirez HJ, and Silva-Ortigoza R (2006) *Control Design Techniques in Power Electronics Devices*. Springer.

Steinberg M (2005) Historical overview of research in reconfigurable flight control. *Proceedings of Institution of Mechanical Engineers, Part G: Journal of Aerospace Engineering*, **219**, 263–275.

Vidyasagar M (2002) *Nonlinear Systems Analysis*. SIAM, PA.

Willsky AS (1976) A survey of design methods for failure detection in dynamic systems. *Automatica*, **12**, 601–611.

Zhang Y and Jiang J (2008) Bibliographical review on reconfigurable fault tolerant control systems. *Annual Reviews in Control*, **32**, 229–252.

Part One

Control Models for AC Motors

AC Electric Motors Control: Advanced Design Techniques and Applications, First Edition. Edited by Fouad Giri.

2

Control Models for Induction Motors

Abderrahim El Fadili, Fouad Giri, and Abdelmounime El Magri
GREYC Lab, University of Caen Basse-Normandie, France

2.1 Introduction

It is widely recognized that the induction motor has become one of the main actuators for industrial use. Indeed, as compared to the DC machine, it provides a better power/mass ratio, simpler maintenance (as it includes no mechanical commutators), and a relatively lower cost. It is largely agreed that these machines have promising perspectives in the industrial actuator field. This has motivated an intensive research activity on induction machine control, especially over the last 15 years.

However, the problem of controlling induction motors is not a simple issue due to the multivariable and highly nonlinear nature of these machines. Besides, some of their parameters are time varying and some of their state variables are not accessible to measurements. The problems of induction motor control and observation have been given a great deal of interest over the last decade (see, e.g., Lubineau *et al.* 2000; Montanan *et al.* 2006; Traore *et al.* 2008; El Fadili *et al.* 2012a). These problems are generally dealt with using model-based control approaches, that is, the controller or the observer design relies upon a given model that is supposed to accurately describe the machine of interest.

Control-oriented modeling of induction motors has first been accomplished by considering simplified assumptions, for example, linear magnetic characteristic and constant (or slowly varying) rotor speed (e.g., Lubineau *et al.* 2000). Then, the obtained models turn out to be linear and of quite limited use. More accurate nonlinear models, describing well the induction motor operating at nonconstant rotor speed, have been developed later (e.g., De Leon *et al.* 2001). Furthermore, these nonlinear models proved to be tractable and thus have been widely

AC Electric Motors Control: Advanced Design Techniques and Applications, First Edition. Edited by Fouad Giri.

used in control design. That is, most control designs presented in this book are based on the models that are by now standard. Therefore, the present chapter is mainly devoted to the development of these standard models. This will be accomplished by considering successively the cases of triphase motors and doubly-fed induction motors (DFIM).

This chapter is organized as follows: Section 2.2 is devoted to a brief description of triphase induction motor principles; the modeling of these motors is completed in Section 2.3 and the estimation of their unknown parameters, using experimental measurements, is dealt with in Section 2.4; the modeling of the DFIM machine is presented in Section 2.5; and concluding remarks and a list of references end the chapter.

2.2 Induction Motors—A Concise Description

As pointed out in Chapter 1, triphase induction motors are classified in two main categories: squirrel cage and wound rotor. In squirrel-cage induction motors (Figure 2.1), the stator is equipped with a winding directly connected to the power supply. The rotor winding is made of longitudinal bars in slots fixed just beneath the rotor outer surface. The bars are connected together at their extremities and short-circuited by rings. The rotor winding may be constituted of individual bars and rings made of conducting material connected together, or it may be a one-piece structure made by die casting together the rings and the bars. The rotor circuit is not externally accessible. This provides the motor with robustness but makes its control more complex.

The wound rotor induction motor is similar to the squirrel-cage motor except that the rotor winding is made of individually insulated coils. Connections from the coils are brought to collector rings. The rotor circuit is not short-circuited on itself as in the squirrel-cage motor. Rather, it is completed through external circuit (resistors, converters, etc.) connected to brushes that bear on the collector rings (Figure 2.2).

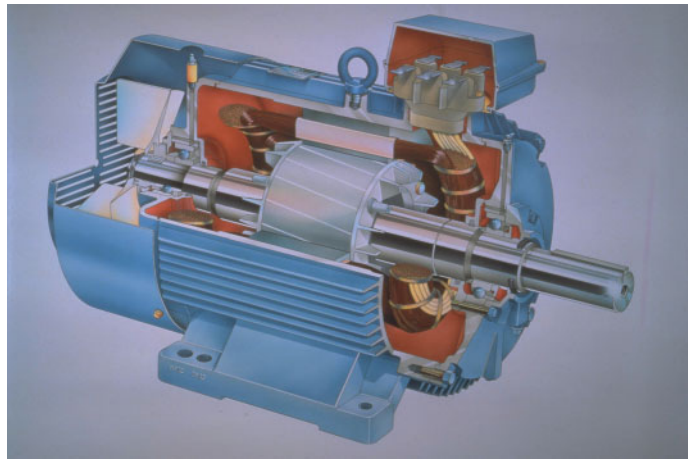

Figure 2.1 Squirrel-cage induction motor. Copyright granted, 2012, ABB; all rights reserved. (For a color version of this figure, please see color plates.)

Figure 2.2 Wound rotor of the DFIM. http://ewh.ieee.org; accessed December 21, 2012 © 1997 IEEE.

For both types of machine, a three-phase equivalent circuit is associated to the stator and to the rotor (Figure 2.3). By Faraday's and Lenz's Laws, the stator carrying a sinusoidal current of pulsation ω_s generates a rotating magnetic field. Then, induced currents are generated in the rotor bars. The induced currents tend to oppose the flux variation in the rotor coils resulting in a mechanical torque applied on the rotor. Then, the rotor starts turning at a speed ω_m and the rotor currents oscillating at the pulsation $\omega_r = \omega_s - p\omega_m$. The electromagnetic torque is proportional to the pulsation ω_r. It vanishes whenever the rotor current pulsation is zero. This is called synchronization. In normal operation, torque generation is necessarily accompanied by a difference ω_r between the stator pulsation ω_s and the rotor speed $p\omega_m$. This difference is called slip pulsation and constitutes an image of the torque.

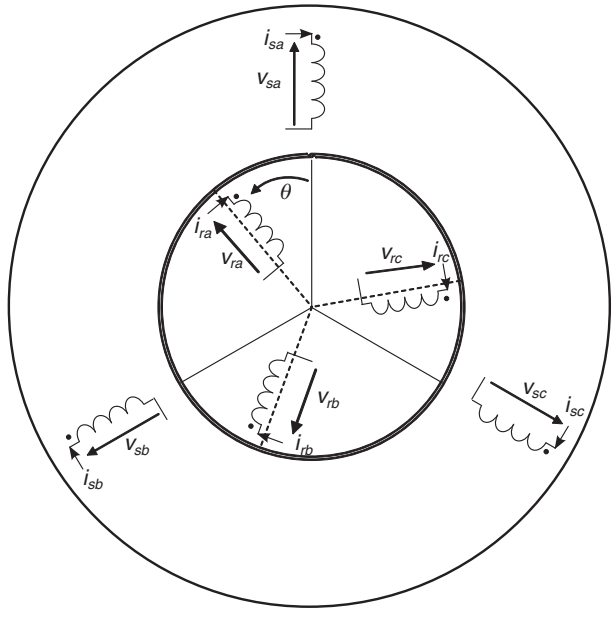

Figure 2.3 Induction motor structure equivalent

2.3 Triphase Induction Motor Modeling

2.3.1 Modeling Assumptions

1. **Linearity:** The fluxes and the corresponding induced currents are proportional, that is, all self- and mutual inductances are constant.
2. All iron losses are neglected.
3. The machine air gap is constant, smooth, and symmetric.
4. The stator and the rotor windings present a symmetrical structure providing the induction machine with a three-phase equivalent circuit (equation 2.3).

The machine triphase structure entails a sinusoidal spacial distribution of magnetomotive force (MMF) in the air gap and three-phase currents in the stator and rotor currents whenever the stator voltage is three-phase.

2.3.2 Triphase Induction Motor Modeling

The modeling process consists of applying the electromagnetic laws to the different windings and the motion equations to the rotor carrying the load (e.g., Leonard 2001). The application of the electromagnetic laws yields six voltage equations and six flux equations.

Voltages Equations

$$[v_{sabc}] = [R_s][i_{sabc}] + \frac{d}{dt}[\phi_{sabc}]. \tag{2.1}$$

$$[v_{rabc}] = [R_r][i_{rabc}] + \frac{d}{dt}[\phi_{rabc}]. \tag{2.2}$$

Flux Equations

$$[\phi_{sabc}] = [L_{os}][i_{sabc}] + [M_{osr}][i_{rabc}]. \tag{2.3}$$

$$[\phi_{rabc}] = [L_{or}][i_{rabc}] + [M_{osr}][i_{sabc}]. \tag{2.4}$$

In the above expressions, the following notations are used:

$$[v_{sabc}] = \begin{bmatrix} v_{sa} \\ v_{sb} \\ v_{sc} \end{bmatrix}; \quad [i_{sabc}] = \begin{bmatrix} i_{sa} \\ i_{sb} \\ i_{sc} \end{bmatrix}; \quad [\phi_{sabc}] = \begin{bmatrix} \phi_{sa} \\ \phi_{sb} \\ \phi_{sc} \end{bmatrix}. \tag{2.5}$$

$$[v_{rabc}] = \begin{bmatrix} v_{ra} \\ v_{rb} \\ v_{rc} \end{bmatrix}; \quad [i_{rabc}] = \begin{bmatrix} i_{ra} \\ i_{rb} \\ i_{rc} \end{bmatrix}; \quad [\phi_{rabc}] = \begin{bmatrix} \phi_{ra} \\ \phi_{rb} \\ \phi_{rc} \end{bmatrix}. \tag{2.6}$$

That is, the triphase quantities $[v_{sabc}]$, $[i_{sabc}]$, $[\phi_{sabc}]$, $[v_{rabc}]$, $[i_{rabc}]$, and $[\phi_{rabc}]$ denote the stator and the rotor voltages, currents, and fluxes. The subscripts s and r refer to the stator and the rotor, respectively. Similarly, the indices a, b, and c refer to the three phases.

A direct consequence of the machine perfect symmetry is that all resistance and inductance matrices are symmetric, that is,

$$[R_s] = \begin{bmatrix} R_s & 0 & 0 \\ 0 & R_s & 0 \\ 0 & 0 & R_s \end{bmatrix}, \qquad [R_r] = \begin{bmatrix} R_r & 0 & 0 \\ 0 & R_r & 0 \\ 0 & 0 & R_r \end{bmatrix}, \tag{2.7}$$

$$[L_{os}] = \begin{bmatrix} l_{os} & M_{os} & M_{os} \\ M_{os} & l_{os} & M_{os} \\ M_{os} & M_{os} & l_{os} \end{bmatrix}, \qquad [L_{or}] = \begin{bmatrix} l_{or} & M_{or} & M_{or} \\ M_{or} & l_{or} & M_{or} \\ M_{or} & M_{or} & l_{or} \end{bmatrix}, \tag{2.8}$$

where R_s and R_r are the stator and the rotor resistances, l_{os} and l_{or} are the self-inductances, M_{os} is the mutual inductance between two stator phases, and M_{or} is the mutual inductance between two rotor phases. Also, an immediate consequence of the working assumptions (Section 2.3.1), is that the various mutual inductances between the rotor and the stator are sinusoidal functions of the rotor position θ. Specifically, one has

$$[M_{osr}] = M_o \begin{bmatrix} \cos(p\theta) & \cos\left(p\theta + \frac{2\pi}{3}\right) & \cos\left(p\theta + \frac{4\pi}{3}\right) \\ \cos\left(p\theta + \frac{4\pi}{3}\right) & \cos(p\theta) & \cos\left(p\theta + \frac{2\pi}{3}\right) \\ \cos\left(p\theta + \frac{4\pi}{3}\right) & \cos\left(p\theta + \frac{2\pi}{3}\right) & \cos(p\theta) \end{bmatrix}, \tag{2.9}$$

where p designates the number of pole-pairs and M_o denotes the maximal mutual inductance between the stator phase and the rotor phase.

Mechanical Equations

The rotor motion undergoes the following usual second order differential equation:

$$J\frac{d\omega_m}{dt} = -F\omega_m + T_{em} - T_L - T_d, \tag{2.10}$$

where ω_m, T_L, T_{em}, and T_d are, respectively, the rotor speed, the load torque, the electromagnetic motor torque, and the dry torque. J designates the inertia of the rotor-load set, and F the viscous friction coefficient.

The expression of T_{em} is obtained from the energy balance. Specifically, one has

$$T_{em} = \frac{\partial W_{mag}}{\partial \theta} \quad \text{with} \quad W_{mag} = \frac{1}{2}\left([i_{sabc}]^T[\phi_{sabc}] + [i_{rabc}]^T[\phi_{rabc}]\right), \tag{2.11}$$

where W_{mag} denotes the magnetic energy. The induction motor model, including the seven equations (2.1), (2.2), and (2.10), entails two difficulties. On the one hand, the system order is relatively large and, one the other, the matrix (2.9) is a function of the rotor position θ, which is time varying. To overcome these difficulties, adequate coordinate transformations are available

that reduce the system order and eliminate the dependence on θ. The main transformations are presented in the following subsection.

2.3.3 Park Transformations

The key idea is that the MMF, created by a physical three-phase system, can be equivalently created by a fictive two-phase system involving two orthogonal windings (Figure 2.4).

The three-phase current system (i_a, i_b, i_c) traversing n_1 turns and two-phase current system (i_d, i_q), traversing n_2 turns are said to be equivalent if they produce the same air-gap MMF. The MMF created by (i_a, i_b, i_c) has the following components:

$$\varepsilon_a = n_1 i_a, \quad \varepsilon_b = n_1 i_b, \quad \varepsilon_c = n_1 i_c.$$

Similarly, the components of the MMF due to (i_d, i_q) are the following:

$$\varepsilon_d = n_2 i_d, \qquad \varepsilon_q = n_2 i_q.$$

Referring to Figure 2.4, the MMF due to (i_a, i_b, i_c) is represented by the vector $\vec{\varepsilon}$, which is a vector sum of the three MMF vectors ($\vec{\varepsilon_a}$, $\vec{\varepsilon_b}$, $\vec{\varepsilon_c}$). Figure 2.4 illustrates the projection of the vector $\vec{\varepsilon}$ along two orthogonal axes referred to direct axis d and quadrature axis q. The

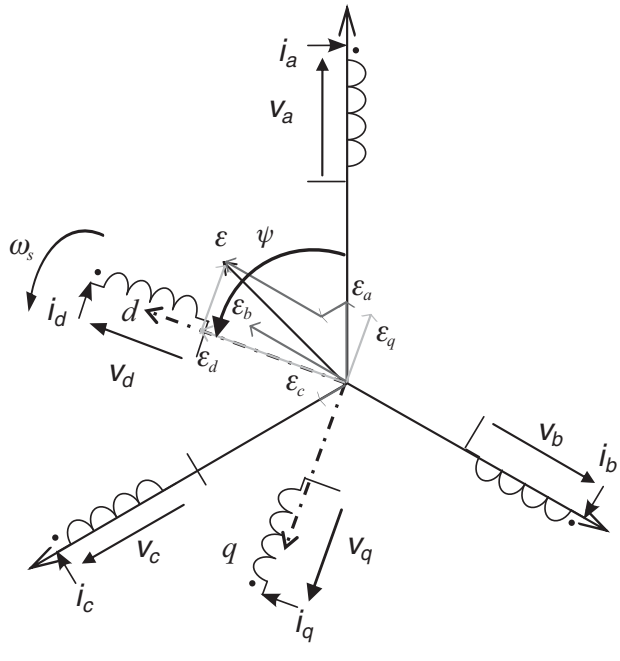

Figure 2.4 Triphase system (i_a, i_b, i_c) and its equivalent two-phase system (i_d, i_q). Both systems create the same MMF $\vec{\varepsilon}$

obtained components, $\vec{\varepsilon_d}$ and $\vec{\varepsilon_q}$, are given by the following expression:

$$\begin{bmatrix} \varepsilon_d \\ \varepsilon_q \end{bmatrix} = \begin{bmatrix} \cos(\psi) & \cos\left(\psi - \frac{2\pi}{3}\right) & \cos\left(\psi - \frac{4\pi}{3}\right) \\ -\sin(\psi) & -\sin\left(\psi - \frac{2\pi}{3}\right) & -\sin\left(\psi - \frac{4\pi}{3}\right) \end{bmatrix} \begin{bmatrix} \varepsilon_a \\ \varepsilon_b \\ \varepsilon_c \end{bmatrix}. \tag{2.12}$$

The system (2.12) is clearly noninvertible as it involves a nonsquare matrix. This is overcome by adding a third equation associated with a fictive MMF denoted ε_o. The new variable is defined to be proportional to the homopolar component of the triphase $(\varepsilon_a, \varepsilon_b, \varepsilon_c)$. Specifically, one has $\varepsilon_o = K_o(\varepsilon_a + \varepsilon_b + \varepsilon_c)$ for some proportional constant K_o to be defined later. To the fictive MMF ε_o is associated a fictive current, denoted i_o, referred to homopolar. Accordingly, one has $\varepsilon_o = n_2 i_o$.

Replacing in equation (2.12) the MMFs by the corresponding currents one gets the following relation between the three-phase current (i_a, i_b, i_c) (traversing n_1 turns) and the equivalent two-phase current (i_d, i_q) (traversing n_2 turns):

$$\begin{bmatrix} i_d \\ i_q \\ i_o \end{bmatrix} = \frac{n_1}{n_2} \begin{bmatrix} \cos(\psi) & \cos\left(\psi - \frac{2\pi}{3}\right) & \cos\left(\psi - \frac{4\pi}{3}\right) \\ -\sin(\psi) & -\sin\left(\psi - \frac{2\pi}{3}\right) & -\sin\left(\psi - \frac{4\pi}{3}\right) \\ K_o & K_o & K_o \end{bmatrix} \begin{bmatrix} i_a \\ i_b \\ i_c \end{bmatrix}. \tag{2.13}$$

As the fictive current i_o is not physically involved in the creation of the MMF, its orientation can be chosen arbitrarily. For convenience, the homopolar axis is let to be orthogonal to the plane dq. To complete the transformation (2.13), it remains to assign values to $\frac{n_1}{n_2}$ and K_o. Two options are discussed in the rest of this subsection leading to two variants of the Park transformation.

Park Transformation Preserving Amplitudes

The Park transformation goes back to 1929 (Blaschke 1972; (Vas 1990). The interest it has lately regained is mainly due to the considerable progress made in the digital computer technology and in the power electronic component technology. The spectacular advances achieved in these fields have made it possible to implement real-time applications involving the construction and manipulation of the Park transformation. The original Park transformation is defined by equation (2.13) letting the free parameters (i.e., $\frac{n_1}{n_2}$ and K_o) be chosen to meet the following requirements:

1. The homopolar current i_o coincides with the arithmetic mean value of the currents (i_a, i_b, i_c).
2. The components of the two-phase current (i_d, i_q) have the same amplitude as those of the triphase current (i_a, i_b, i_c), that is, current amplitude is preserved by the Park transformation.

The first requirement leads to the following double equality:

$$i_o = \frac{1}{3}(i_a + i_b + i_c) = \frac{n_1}{n_2} K_o(i_a + i_b + i_c).$$

This yields

$$\frac{n_1}{n_2}K_o = \frac{1}{3}. \tag{2.14}$$

The amplitude preservation requirement immediately entails the following expressions:

$$\begin{aligned} &i_a(t) = I_m\cos(\omega t), \quad i_b(t) = I_m\cos\left(\omega t - \frac{2\pi}{3}\right), \quad i_c(t) = I_m\cos\left(\omega t - \frac{4\pi}{3}\right), \\ &i_d(t) = I_m\cos(\omega t - \psi), \quad i_q(t) = I_m\sin(\omega t - \psi). \end{aligned} \tag{2.15}$$

On the other hand, one gets from equation (2.13) that

$$i_d(t) = \frac{n_1}{n_2}\frac{3}{2}I_m\cos(\omega t - \psi), \quad i_q(t) = \tfrac{n_1}{n_2}\tfrac{3}{2}I_m\sin(\omega t - \psi). \tag{2.16}$$

Comparing equations (2.15) and (2.16) gives, using (2.14):

$$\frac{n_1}{n_2} = \frac{2}{3} \quad \text{and} \quad K_o = \frac{1}{2}. \tag{2.17}$$

Using (2.17), it follows from (2.13) that the (amplitude preservation-based) Park transformation $[i_{dqo}] = [P(\psi)][i_{abc}]$ is entirely characterized by the following matrix:

$$[P(\psi)] = \frac{2}{3}\begin{bmatrix} \cos(\psi) & \cos\left(\psi - \frac{2\pi}{3}\right) & \cos\left(\psi - \frac{4\pi}{3}\right) \\ -\sin(\psi) & -\sin\left(\psi - \frac{2\pi}{3}\right) & -\sin\left(\psi - \frac{4\pi}{3}\right) \\ \frac{1}{2} & \frac{1}{2} & \frac{1}{2} \end{bmatrix}. \tag{2.18}$$

The inverse transformation, that is, $[i_{abc}] = [P(\psi)]^{-1}[i_{dqo}]$, is characterized by the inverse Park matrix

$$[P(\psi)]^{-1} = \begin{bmatrix} \cos(\psi) & -\sin(\psi) & 1 \\ \cos\left(\psi - \frac{2\pi}{3}\right) & -\sin\left(\psi - \frac{2\pi}{3}\right) & 1 \\ \cos\left(\psi - \frac{4\pi}{3}\right) & -\sin\left(\psi - \frac{4\pi}{3}\right) & 1 \end{bmatrix}. \tag{2.19}$$

The particular value, $\psi = 0$, yields the so-called Clarke matrices

$$[C] = \frac{2}{3}\begin{bmatrix} 1 & \frac{-1}{2} & \frac{-1}{2} \\ 0 & \frac{\sqrt{3}}{2} & -\frac{\sqrt{3}}{2} \\ \frac{1}{2} & \frac{1}{2} & \frac{1}{2} \end{bmatrix}, \quad [C]^{-1} = \frac{2}{3}\begin{bmatrix} 1 & 0 & \frac{1}{2} \\ \frac{-1}{2} & \frac{\sqrt{3}}{2} & \frac{1}{2} \\ \frac{-1}{2} & \frac{-\sqrt{3}}{2} & \frac{1}{2} \end{bmatrix}. \tag{2.20}$$

Park Transformation Preserving Energy

In this variant of (2.13), the free parameters, that is, the ratio n_1/n_2 and K_o, are chosen to ensure power conservation when passing from the triphase system to the two-phase system. Analytically, this means that the following equalities must hold:

$$v_a i_a + v_b i_b + v_c i_c = v_d i_d + v_q i_q + v_o i_o. \tag{2.21}$$

Equation (2.21) may be rewritten in the following more compact vector form:

$$[v_{abc}]^T [i_{abc}] = [v_{dqo}]^T [i_{dqo}]. \tag{2.22}$$

By (2.13), one has $[v_{dqo}] = [P(\psi)][v_{abc}]$ and $[i_{dqo}] = [P(\psi)][i_{abc}]$. Then, it follows from (2.22) that

$$[v_{dqo}]^T [i_{dqo}] = [[P(\psi)][v_{abc}]]^T [P(\psi)][i_{abc}] = [v_{abc}]^T [P(\psi)]^T [P(\psi][i_{abc}]. \tag{2.23}$$

Comparing with equation (2.22) yields

$$[P(\psi)]^T = [P(\psi)]^{-1} \tag{2.24}$$

and

$$\frac{n_1}{n_2} = \sqrt{\frac{2}{3}}, \qquad K_o = \tfrac{1}{\sqrt{2}}.$$

Then, the direct Park matrix conserving the power is

$$[P(\psi)] = \sqrt{\frac{2}{3}} \begin{bmatrix} \cos(\psi) & \cos\left(\psi - \frac{2\pi}{3}\right) & \cos\left(\psi - \frac{4\pi}{3}\right) \\ -\sin(\psi) & -\sin\left(\psi - \frac{2\pi}{3}\right) & -\sin\left(\psi - \frac{4\pi}{3}\right) \\ \frac{1}{\sqrt{2}} & \frac{1}{\sqrt{2}} & \frac{1}{\sqrt{2}} \end{bmatrix}, \tag{2.25}$$

and its inverse is

$$[P(\psi)]^{-1} = \sqrt{\frac{2}{3}} \begin{bmatrix} \cos(\psi) & -\sin(\psi) & \frac{1}{\sqrt{2}} \\ \cos\left(\psi - \frac{2\pi}{3}\right) & -\sin\left(\psi - \frac{2\pi}{3}\right) & \frac{1}{\sqrt{2}} \\ \cos\left(\psi - \frac{4\pi}{3}\right) & -\sin\left(\psi - \frac{4\pi}{3}\right) & \frac{1}{\sqrt{2}} \end{bmatrix}. \tag{2.26}$$

It is this transformation that is retained in the rest of this chapter, as well as in the next ones. Note that, the angle $\psi = 0$ is a free parameter in that transformation. One possible

choice is $\psi = 0$ and the corresponding Park matrix, commonly called Concordia matrix, is given by

$$[C] = \sqrt{\frac{2}{3}} \begin{bmatrix} 1 & -\frac{1}{2} & -\frac{1}{2} \\ 0 & \frac{\sqrt{3}}{2} & -\frac{\sqrt{3}}{2} \\ \frac{1}{\sqrt{2}} & \frac{1}{\sqrt{2}} & \frac{1}{\sqrt{2}} \end{bmatrix}. \tag{2.27}$$

Its inverse is

$$[C]^{-1} = \sqrt{\frac{2}{3}} \begin{bmatrix} 1 & 0 & \frac{1}{\sqrt{2}} \\ -\frac{1}{2} & \frac{\sqrt{3}}{2} & \frac{1}{\sqrt{2}} \\ -\frac{1}{2} & -\frac{\sqrt{3}}{2} & \frac{1}{\sqrt{2}} \end{bmatrix}. \tag{2.28}$$

2.3.4 Two-Phase Models of Induction Motors

Equations (2.1)–(2.4), and (2.10) get simplified by applying the Park transformation defined by the matrix (2.27). Roughly, all mathematical relationships initially expressed in terms of the triphase frame (a, b, c) are rewritten in terms of (d, q, o). The perfect symmetry of the induction motor implies that the sum of the currents carried by the rotor and the sum of those carried by the stator are both null. Then, the corresponding homopolar currents (i.e. the components along the axis o) are null (Blaschke 1972; Vas 1990; Leonard 2001). It turns out that, in the new frame (d, q), the initial electromagnetic system (2.1), and (2.2), consisting of six equations, boils down to a simpler system, consisting of only four equations. As mentioned earlier, the angle ψ in (2.27) is a free parameter assuming several possible choices. This entails several variants of the two-coordinate frame (d, q). The two most common in the literature are the following:

- The fixed reference frame (α, β), connected to the stator.
- The rotating reference frame (d, q), linked to, for example, the rotor flux or the stator current.

The passage from the triphase frame (a, b, c) to the fixed (α, β) frame is accomplished by choosing the transformation angle ψ, in the transformation matrix (2.25), as follows:

- Set $\psi = 0$, for the transformation of the stator variables.
- Set $\psi = \theta$, for the transformation of the rotor variables.

The passage from the triphase frame (a, b, c) to the rotating frame (d, q) is accomplished by choosing the transformation angle ψ as follows:

- Set $\psi = \theta_s$, for the transformation of stator variables.
- Set $\psi = \theta_r = \theta_s - \theta$, for the transformation of the rotor variables.

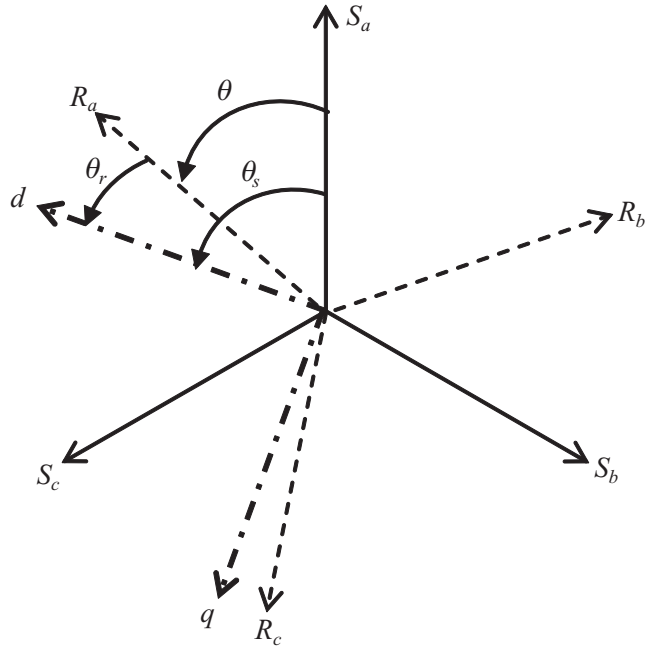

Figure 2.5 Angles between electric frames

Electric Equations in *dq* Coordinates

Following the above rules, the passage from the triphase frame (a, b, c) to the (d, q) frame necessitates the following transformations of the electric variables (Figure 2.5):

$$\begin{bmatrix} v_{sd} \\ v_{sq} \end{bmatrix} = [P(\theta_s)][v_{sabc}], \quad \begin{bmatrix} i_{sd} \\ i_{sq} \end{bmatrix} = [P(\theta_s)][i_{sabc}], \quad \begin{bmatrix} \phi_{sd} \\ \phi_{sq} \end{bmatrix} = [P(\theta_s)][\phi_{sabc}], \quad (2.29)$$

$$\begin{bmatrix} v_{rd} \\ v_{rq} \end{bmatrix} = [P(\theta_r)][v_{rabc}], \quad \begin{bmatrix} i_{rd} \\ i_{rq} \end{bmatrix} = [P(\theta_r)][i_{rabc}], \quad \begin{bmatrix} \phi_{rd} \\ \phi_{rq} \end{bmatrix} = [P(\theta_r)][\phi_{rabc}]. \quad (2.30)$$

Applying the transformations (2.29) and (2.30) to the induction machine equations (2.1) and (2.2), yields the following (d, q) equations:

$$v_{sd} = R_s i_{sd} + \frac{d\phi_{sd}}{dt} - \omega_s \phi_{sq}, \quad (2.31)$$

$$v_{sq} = R_s i_{sq} + \frac{d\phi_{sq}}{dt} + \omega_s \phi_{sd}, \quad (2.32)$$

$$v_{rd} = R_r i_{rd} + \frac{d\phi_{rd}}{dt} - (\omega_s - p\omega_m)\phi_{rq}, \quad (2.33)$$

$$v_{rq} = R_r i_{rq} + \frac{d\phi_{rq}}{dt} + (\omega_s - p\omega_m)\phi_{rd}, \quad (2.34)$$

where

$$\omega_s = \frac{d\theta_s}{dt}, \qquad \omega_m = \frac{d\theta}{dt}.$$

Flux Equations in *dq* Coordinates

Similarly, the passage from the triphase frame (a, b, c) to the (d, q) frame necessitates the following transformations of the fluxes:

$$[\phi_{sdq}] = [P(\theta_s][\phi_{sabc}]. \tag{2.35}$$

$$[\phi_{rdq}] = [P(\theta_r][\phi_{rabc}] \tag{2.36}$$

Using the flux-current expressions (2.3) and (2.4), the couple of equations (2.35) and (2.36) develops as follows:

At the stator:

$$[\phi_{sdq}] = [P(\theta_s][L_s][i_{sabc}] + [P(\theta_s][M_{sr}][i_{rabc}],$$

which implies, using (2.29)

$$[\phi_{sdq}] = [P(\theta_s][L_s][P(\theta_s]^{-1}[i_{sdq}] + [P(\theta_s][M_{sr}][P(\theta_r]^{-1}[i_{rdq}]. \tag{2.37}$$

At the rotor, one has

$$[\phi_{rdq}] = [P(\theta_r][L_r][i_{rabc}] + [P(\theta_r][M_{sr}][i_{sabc}],$$

which implies, due to (2.30)

$$[\phi_{rdq}] = [P(\theta_r][L_r][P(\theta_r]^{-1}[i_{rdq}] + [P(\theta_r][M_{sr}][P(\theta_s]^{-1}[i_{sdq}]. \tag{2.38}$$

The obtained flux equations in the (d, q) frame can be given the more compact forms

$$[\phi_{sdq}] = L_s[i_{sdq}] + M_{sr}[i_{rdq}], \quad [\phi_{rdq}] = L_r[i_{rdq}] + M_{sr}[i_{sdq}], \tag{2.39}$$

with

$$L_s = l_{so} - M_{os}, \text{ cyclical stator inductance;} \tag{2.40}$$

$$L_r = l_{ro} - M_{or}, \text{ cyclical rotor inductance;} \tag{2.41}$$

$$M_{sr} = \frac{3}{2}M_o, \text{ mutual inductance between the stator and rotor windings.} \tag{2.42}$$

Mechanical Equation in *dq* Coordinates

The mechanical equation of the induction motor describes the motion of the rotor carrying a load. It is readily checked that the motion undergoes the following dynamic equation:

$$\frac{d\omega_m}{dt} = -\frac{F}{J}\omega_m + \frac{T_{em}}{J} - \frac{T_L}{J} - \frac{T_d}{J}. \tag{2.43}$$

The electromagnetic torque is given by the expression

$$T_{em} = p\frac{p_m}{\omega_s}, \tag{2.44}$$

where p_m designates the mechanical power developed by the motor. The electric power absorbed by the motor is given by the expressions

$$\begin{aligned} p_a &= v_{sa}i_{sa} + v_{sb}i_{sb} + v_{sc}i_{sc} + v_{ra}i_{ra} + v_{rb}i_{rb} + v_{rc}i_{rc} \\ &= v_{sd}i_{sd} + v_{sq}i_{sq} + v_{rd}i_{rd} + v_{rq}i_{rq}, \end{aligned} \tag{2.45}$$

where the second equality is a direct consequence of the Park transformation preserving power when passing from the three- to the two-coordinate frame. Using equations (2.31), (2.32), (2.33), and (2.34) in the expression (2.45), it follows that that the power p_a can be decomposed into three parts:

1. The power dissipated by the Joule effect:

$$R_s\left(i_{sd}^2 + i_{sq}^2\right) + R_r\left(i_{rd}^2 + i_{rq}^2\right). \tag{2.46}$$

2. The power related to the electromagnetic exchange with sources:

$$i_{sd}\frac{d\phi_{sd}}{dt} + i_{sq}\frac{d\phi_{sq}}{dt} + i_{rd}\frac{d\phi_{rd}}{dt} + i_{rq}\frac{d\phi_{rq}}{dt}. \tag{2.47}$$

3. The mechanical power p_m, that produces the electromagnetic torque:

$$p_m = (\phi_{sd}i_{sq} - \phi_{sq}i_{sd})\frac{d\theta_s}{dt} + (\phi_{rd}i_{rq} - \phi_{rq}i_{rd})\frac{d\theta_r}{dt}. \tag{2.48}$$

Taking into account the flux equation (2.39), and replacing the rotor current components (d, q) by their equivalent expressions, one obtains from (2.48)

$$p_m = \frac{M_{sr}}{L_r}(\phi_{rd}i_{sq} - \phi_{rq}i_{sd})\frac{d(\theta_s - \theta_r)}{dt}. \tag{2.49}$$

Then, it follows from equation (2.44) that the torque rewrites as follows:

$$T_{em} = p\frac{M_{sr}}{L_r}(\phi_{rd}i_{sq} - \phi_{rq}i_{sd}). \tag{2.50}$$

The electromagnetic torque can also be expressed in the following two forms:

$$T_{em} = p(\phi_{sd} i_{sq} - \phi_{sq} i_{sd}), \qquad T_{em} = p\frac{M_{sr}}{L_s}(\phi_{sd} i_{rq} - \phi_{sq} i_{rd}). \tag{2.51}$$

Induction Motor Model in General *dq* Coordinate Frame

Eliminating the flux components (ϕ_{sd}, ϕ_{sq}) and the current components (i_{rd}, i_{rq}) in equations (2.31), (2.32), (2.33), and (2.34) and substituting equation (2.50) in equation (2.10), one gets the model of the induction machine expressed in the rotating frame (d, q):

$$\frac{d\omega_m}{dt} = p\frac{M_{sr}}{J L_r}(\phi_{rd} i_{sq} - \phi_{rq} i_{sd}) - \frac{T_L}{J} - \frac{T_d}{J} - \frac{F}{J}\omega_m, \tag{2.52}$$

$$\frac{di_{sd}}{dt} = -\gamma i_{sd} + \omega_s i_{sq} + \frac{M_{sr} R_r}{\sigma L_s L_r^2}\phi_{rd} + p\omega_m \frac{M_{sr}}{\sigma L_s L_r}\phi_{rq} + \frac{1}{\sigma L_s} v_{sd}, \tag{2.53}$$

$$\frac{di_{sq}}{dt} = -\gamma i_{sq} - \omega_s i_{sd} + \frac{M_{sr} R_r}{\sigma L_s L_r^2}\phi_{rq} - p\omega_m \frac{M_{sr}}{\sigma L_s L_r}\phi_{rd} + \frac{1}{\sigma L_s} v_{sq}, \tag{2.54}$$

$$\frac{d\phi_{rd}}{dt} = -\frac{R_r}{L_r}\phi_{rd} - (\omega_s - p\omega_m)\phi_{rq} + \frac{R_r M_{sr}}{L_r} i_{sd}, \tag{2.55}$$

$$\frac{d\phi_{rq}}{dt} = -\frac{R_r}{L_r}\phi_{rq} + (\omega_s - p\omega_m)\phi_{rd} + \frac{M_{sr} R_r}{L_r} i_{sq}, \tag{2.56}$$

with

$$\gamma = \frac{\left(L_r^2 R_s + M_{sr}^2 R_r\right)}{\sigma L_s L_r^2}, \qquad \sigma = 1 - \frac{M_{sr}^2}{L_s L_r},$$

where the following relations have been used:

$$i_{rd} = \frac{\phi_{rd} - M_{sr} i_{sd}}{L_r}, \qquad i_{rq} = \frac{\phi_{rq} - M_{sr} i_{sq}}{L_r}, \tag{2.57}$$

$$\phi_{sd} = \sigma L_s i_{sd} + \frac{M_{sr}}{L_r}\phi_{sd}, \qquad \phi_{sq} = \sigma L_s i_{sq} + \frac{M_{sr}}{L_r}\phi_{sq}. \tag{2.58}$$

Induction Motor Model in Fixed $\alpha\beta$ Coordinate Frame

The model of the induction motor in the fixed (α, β) frame is obtained by just letting $\omega_s = 0$ in the general model described by equation (2.54). Doing so, one gets the following model:

$$\frac{d\omega_m}{dt} = p\frac{M_{sr}}{J L_r}(\phi_{r\alpha} i_{s\beta} - \phi_{r\beta} i_{s\alpha}) - \frac{T_L}{J} - \frac{T_d}{J} - \frac{F}{J}\omega_m, \tag{2.59}$$

$$\frac{di_{s\alpha}}{dt} = -\gamma i_{s\alpha} + \frac{M_{sr} R_r}{\sigma L_s L_r^2}\phi_{r\alpha} + p\omega_m \frac{M_{sr}}{\sigma L_s L_r}\phi_{r\beta} + \frac{1}{\sigma L_s} v_{s\alpha}, \tag{2.60}$$

$$\frac{di_{s\beta}}{dt} = -\gamma i_{s\beta} + \frac{M_{sr}R_r}{\sigma L_s L_r^2}\phi_{r\beta} - p\omega_m \frac{M_{sr}}{\sigma L_s L_r}\phi_{r\alpha} + \frac{1}{\sigma L_s}v_{s\beta}, \tag{2.61}$$

$$\frac{d\phi_{r\alpha}}{dt} = -\frac{R_r}{L_r}\phi_{r\alpha} + p\omega_m\phi_{r\beta} + \frac{R_r M_{sr}}{L_r}i_{s\alpha}, \tag{2.62}$$

$$\frac{d\phi_{r\beta}}{dt} = -\frac{R_r}{L_r}\phi_{r\beta} - p\omega_m\phi_{r\alpha} + \frac{M_{sr}R_r}{L_r}i_{s\beta}. \tag{2.63}$$

Induction Motor Model in Oriented *d-q* Reference Frame

The rotor-flux-oriented model is obtained by considering as rotating reference frame the one whose d-axis coincides with the rotor flux Φ_r. Analytically, this amounts to letting $\phi_{rd} = \Phi_r$ and $\phi_{rq} = \dot{\phi}_{rq} = 0$. An immediate consequence is that the model becomes a fourth order (instead of fifth in the preceding model). Also, it readily follows from equation (2.54) that the pulsation ω_s takes the following value:

$$\omega_s = p\omega_m - \frac{M_{sr}R_r}{L_r}\frac{i_{sq}}{\Phi_r}.$$

This, together with equations (2.54) gives the-rotor-flux oriented model

$$\frac{d\omega_m}{dt} = p\frac{M_{sr}}{JL_r}\Phi_r i_{sq} - \frac{T_L}{J} - \frac{T_d}{J} - \frac{F}{J}\omega_m, \tag{2.64}$$

$$\frac{di_{sd}}{dt} = -\gamma i_{sd} + \omega_s i_{sq} + \frac{M_{sr}R_r}{\sigma L_s L_r^2}\Phi_r + \frac{1}{\sigma L_s}v_{sd}, \tag{2.65}$$

$$\frac{di_{sq}}{dt} = -\gamma i_{sq} - \omega_s i_{sd} - p\omega_m\frac{M_{sr}}{\sigma L_s L_r}\Phi_r + \frac{1}{\sigma L_s}v_{sq}, \tag{2.66}$$

$$\frac{d\Phi_r}{dt} = -\frac{R_r}{L_r}\Phi_r + \frac{R_r M_{sr}}{L_r}i_{sd}. \tag{2.67}$$

2.3.5 Doubly-Fed Induction Motor Model

In the case of a DFIM, the rotor coils are not short-circuited and, consequently, the voltages v_{rd} and v_{rq} are not null.

Considering the flux components, ϕ_{sd} and ϕ_{sq}, and the current components, i_{rd} and i_{rq}, as state variables and assuming that magnetic circuit is linear, the two-phase model of the DFIM, represented in a rotating reference frame (d, q), is as follows:

$$\frac{d\omega_m}{dt} = p\frac{M_{sr}}{JL_s}(\phi_{sq}i_{rd} - \phi_{sd}i_{rq}) - \frac{F}{J}\omega_m - \frac{T_L}{J} - \frac{T_d}{J}, \tag{2.68}$$

$$\frac{d\phi_{sd}}{dt} = -\frac{1}{\tau_s}\phi_{sd} + \omega_s\phi_{sq} + \frac{M_{sr}}{\tau_s}i_{rd} + v_{sd}, \tag{2.69}$$

$$\frac{d\phi_{sq}}{dt} = -\frac{1}{\tau_s}\phi_{sq} - \omega_s\phi_{sd} + \frac{M_{sr}}{\tau_s}i_{rq} + v_{sq}, \tag{2.70}$$

$$\frac{di_{rd}}{dt} = -\gamma_1 i_{rd} + (\omega_s - p\omega_m)i_{rq} + \frac{\gamma_2}{\tau_s}\phi_{sd} - p\omega_m\gamma_2\phi_{sq} - \gamma_2 v_{sd} + \gamma_3 v_{rd}, \tag{2.71}$$

$$\frac{di_{rq}}{dt} = -\gamma_1 i_{rq} - (\omega_s - p\omega_m)i_{rd} + \frac{\gamma_2}{\tau_s}\phi_{sq} + p\omega_m\gamma_2\phi_{sd} - \gamma_2 v_{sq} + \gamma_3 v_{rq}. \tag{2.72}$$

The parameters γ_1, γ_2, γ_3, σ, and τ_s are defined as follows:

$$\gamma_1 = \frac{R_r L_s^2 + R_s M_{sr}^2}{\sigma L_r L_s^2}, \quad \gamma_2 = \frac{M_{sr}}{\sigma L_s L_r}, \quad \gamma_3 = \frac{1}{\sigma L_r}, \quad \sigma = 1 - \frac{M_{sr}^2}{L_s L_r}, \quad \tau_s = \frac{L_s}{R_s}.$$

By choosing a reference frame linked to the stator voltage, the stator and grid currents are made directly related to the active and reactive powers. Then, the power exchanged between the motor and the grid can be controlled by controlling the currents. Letting the d-axis of the frame be oriented along the stator voltage entails $v_{sd} = V_s$ and $v_{sq} = 0$. Then, the model (2.68), (2.69), (2.70), (2.71), and (2.72) rewrites as follows (in the stator voltage linked dq frame):

$$\frac{d\omega_m}{dt} = p\frac{M_{sr}}{JL_s}(\phi_{sq}i_{rd} - \phi_{sd}i_{rq}) - \frac{F}{J}\omega_m - \frac{T_d}{J} - \frac{T_L}{J}, \tag{2.73}$$

$$\frac{d\phi_{sd}}{dt} = -\frac{1}{\tau_s}\phi_{sd} + \omega_s\phi_{sq} + \frac{M_{sr}}{\tau_s}i_{rd} + V_s, \tag{2.74}$$

$$\frac{d\phi_{sq}}{dt} = -\frac{1}{\tau_s}\phi_{sq} - \omega_s\phi_{sd} + \frac{M_{sr}}{\tau_s}i_{rq}, \tag{2.75}$$

$$\frac{di_{rd}}{dt} = -\gamma_1 i_{rd} + (\omega_s - p\omega_m)i_{rq} + \frac{\gamma_2}{\tau_s}\phi_{sd} - p\omega_m\gamma_2\phi_{sq} - \gamma_2 V_s + \gamma_3 v_{rd}, \tag{2.76}$$

$$\frac{di_{rq}}{dt} = -\gamma_1 i_{rq} - (\omega_s - p\omega_m)i_{rd} + \frac{\gamma_2}{\tau_s}\phi_{sq} + p\omega_m\gamma_2\phi_{sd} + \gamma_3 v_{rq}. \tag{2.77}$$

2.4 Identification of Induction Motor Parameters

In this section, an experimental procedure is described to get estimates of the mechanical and the electrical parameters of a squirrel-cage induction machine. The estimation procedure is illustrated using a machine of 2.2 kW power, whose characteristic are described in Table 2.1.

2.4.1 Identification of Mechanical Parameters

Deceleration Test

The present experiment consists, in first running the motor, being loadless ($T_L = 0$). Then, at some time the stator supply voltage is suddenly turned off. The time when the voltage is turned off is considered as $t = 0$, for the present experiment, and the motor speed at that moment is

Table 2.1 Rating plate of the used induction motor

Nominal power	P_n	2.2	kW
Nominal voltage	U_{sn}	380/420	V
Nominal current	I_{sn}	4.9	A
Frequency	f	50	Hz
Nominal speed	ω_{mn}	1430	rad/min
$\cos\psi$		0.81	

denoted ω_{mo}. As a consequence, the stator currents and the electromagnetic torque T_{em} vanish at $t = 0$ and the mechanical equation (2.52) simplifies to, for $t > 0$,

$$J\frac{d\omega_m}{dt} = -F\omega_m - T_d. \tag{2.78}$$

Clearly, equation (2.78) is linear in the quantities $(\frac{T_d}{J})$ and $(\frac{F}{J})$. Then, the least squares estimator can be resorted to get estimates of these quantities using a sufficiently large sample of measurements (t, ω_{mo}) (e.g., Ioannou and Fidan 2006). Presently, a quite simpler alternative necessitating only four speed measures is presented, getting benefit of the fact that speed measurements are weakly noisy. The key point is that the solution of the first order equation (2.78) is easily found. Specifically, one has

$$\omega_m(t) = \left(\omega_{mo} + \frac{T_d}{F}\right) e^{\frac{-t}{\tau_m}} - \frac{T_d}{F}, \tag{2.79}$$

using the fact that $\omega_m(0) = \omega_{mo}$, where $\tau_m = \frac{F}{J}$ is the mechanical constant time. The expression (2.79) shows that the rotor speed is exponentially decaying and vanishes at a finite stop time, say t_s. Figure 2.6 shows the decaying speed curve obtained when the motor of Table 2.1 is submitted to the deceleration test. From such a curve, let us get two arbitrary time-speed couples (t_1, ω_{m1}) and (t_2, ω_{m2}) with $t_2 = 2t_1$. Writing equation (2.79) for $t = t_1$ and $t = t_2$, one gets the following equations:

$$\omega_{m1} = \left(\omega_{mo} + \frac{T_d}{F}\right) e^{\frac{-t_1}{\tau_m}} - \frac{T_d}{F}, \tag{2.80}$$

$$\omega_{m2} = \left(\omega_{mo} + \frac{T_d}{F}\right) e^{\frac{-2t_1}{\tau_m}} - \frac{T_d}{F}. \tag{2.81}$$

Subtracting side-to-side equation (2.80) from equation (2.81), gives

$$\omega_{m2} - \omega_{m1} = \left(\omega_{mo} + \frac{T_d}{F}\right) e^{\frac{-t_1}{\tau_m}} \left(e^{\frac{-t_1}{\tau_m}} - 1\right). \tag{2.82}$$

Also, one immediately gets from (2.80)

$$\omega_{m1} - \omega_{mo} = \left(\omega_{mo} + \frac{T_d}{F}\right) \left(e^{\frac{-t_1}{\tau_m}} - 1\right). \tag{2.83}$$

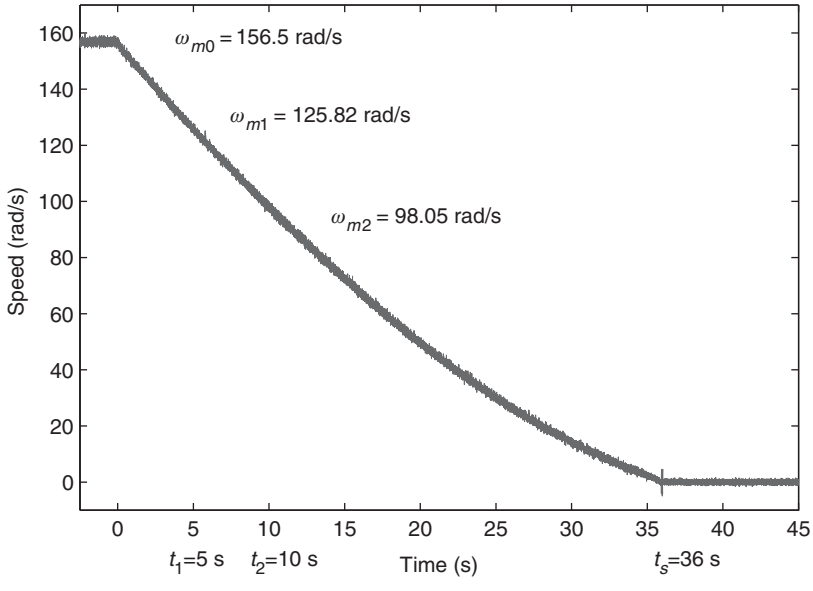

Figure 2.6 Speed evolution during deceleration test

Dividing side-to-side equations (2.82) and (2.83), one obtains an equation where the only unknown is τ_m. Solving that equation, one gets the following expression that determines $\tau_m = \frac{F}{J}$ from available informations

$$\tau_m = -\frac{t_1}{ln\left(\frac{\omega_m 2 - \omega_m 1}{\omega_m 1 - \omega_{mo}}\right)}. \tag{2.84}$$

A second useful expression is immediately obtained from equation (2.79) using the fact that the speed $\omega_m(t)$ vanishes (i.e., the motor stops turning) at $t = t_s$, which is a known time. Doing so, one gets an equation where the only unknown quantity is $\frac{T_d}{F}$. Solving that equation with respect to the unknown, one gets

$$\frac{T_d}{F} = \frac{\omega_{mo}}{e^{\frac{t_s}{\tau_m}} - 1}. \tag{2.85}$$

To illustrate the above procedure, consider again the deceleration test response of Figure 2.6. From that response one reads the numerical values of Table 2.2 concerning the quantities ω_{mo}, ω_{m1}, ω_{m2}, t_1, and t_s.

Table 2.2 The main results for the deceleration test

t_1	t_s	ω_{mo}	ω_{m1}	ω_{m2}
5 s	36 s	156, 5 rd/s	125, 82 rd/s	98.05 rd/s

Table 2.3 Measurements obtained during a progressive startup test

P_{as}	V_{as}	I_{as}
51.9 W	21.56 V	1.59 A

Then, applying equations (2.84) and (2.85), one obtains the following values of τ_m and $\frac{T_d}{F}$:

$$\tau_m = 50.17 \text{ s}, \qquad \frac{T_d}{F} = 149.22 \text{ rd/s} \tag{2.86}$$

where $\tau_m = \frac{F}{J}$. The point is that the two above equations involve three unknowns, namely F, J, and T_d. That is, a supplementary test is needed to determine the mechanical parameters.

Progressive Start Test

The dry torque T_d can be determined using a progressive start-up experiment. Accordingly, the stator voltage being initially null (stationary machine) is very slowly increased until the motor only just starts moving. At this time, the motor speed is still quasi null. Then, it follows from equation (2.43) that the dry torque T_d is quasi equal to the electromagnetic couple T_{em}, which we know is given by the expression (2.44). It follows the following expression of the dry torque:

$$T_d = p\frac{P_{as}}{\omega_s}, \tag{2.87}$$

where P_{as} is the power absorbed at the moment when the motor only just begins turning and ω_s is the grid voltage frequency. Note that all losses (copper, rotational) are null because the rotor speed is quasi zero and the stator voltage is very small. Table 2.3 describes the measurements obtained on the machine of Table 2.1.

From Table 2.1, one readily gets $\omega_s = 157$ rd/s and from Table 2.3 one has $P_{as} = 51.9$ W. These yield the value of the dry torque using the expression (2.87). This, together with the expressions in (2.86), gives the numerical values of all mechanical parameters (see Table 2.4).

2.4.2 Identification of Electrical Parameters

Traditionally, the steady-state model of a three-phase induction motor is represented by the per phase equivalent circuit. The steady state per phase equivalent circuit as viewed from the stator side is represented in Figure 2.7 (Leonard 2001).

Table 2.4 Mechanical parameters for induction motor

J	F	T_d
0.11 kgm^2	0.0022 Nms/rd	0.33 Nm

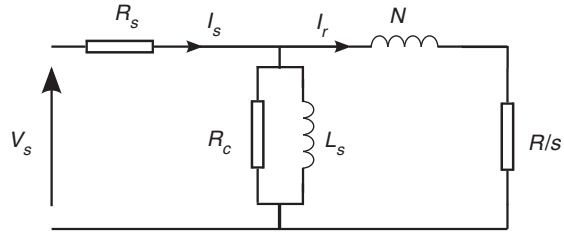

Figure 2.7 Per phase equivalent circuit, viewed from the stator, of a three-phase induction motors. V_s is the stator phase voltage; R_s is stator resistance and R is the rotor winding resistance brought to the stator side; N is the equivalent inductance of both stator and rotor leakage brought to the rotor side. L_s is the magnetizing and stator inductance; R_c is the equivalent resistance for core loss; and s is the slip.

The equivalent circuit parameters for an induction motor can be determined using specific tests on the motor. The tests are quite similar to those performed on transformers.

Stator Winding Resistance Measurement

The resistance of the stator winding is measured at DC, and the measurement is preferably performed after the motor temperature has reached its nominal value. This experimental test gives, for the induction motor characterized by Table 2.1, the following value:

$$R_s = 2.5\ \Omega, \tag{2.88}$$

Loadless Test

This experiment consists of applying a balanced three-phase voltage, at the rated frequency, to the stator terminals, while the rotor is carrying no mechanical load. Currents, voltages, and powers are measured at the motor input. As the slip of the loadless induction motor is very low, the value of the equivalent resistance in the rotor branch of the equivalent circuit is very high. The no-load rotor current is then negligible and the rotor branch of the equivalent circuit can also be negligible. The approximate equivalent circuit, in the loadless test, simplifies as it is shown in Figure 2.8.

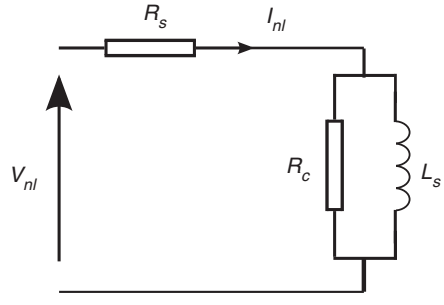

Figure 2.8 Induction machine equivalent circuit in loadless test

Table 2.5 The main results for the no-load test

V_{nl}	I_{nl}	P_{nl}	Q_{nl}	ω_{mnl}
220 V	1.6 A	140 W	1046.5 VAr	156.5 rad/s

In the loadless test, the losses are caused by the core, the stator copper, and the friction. It turns out that, the loadless test input power expresses as follows:

$$P_{nl} = P_{cop} + P_{rot} + P_{co}, \tag{2.89}$$

where the stator copper losses are given by

$$P_{cop} = 3R_s I_{nl}^2. \tag{2.90}$$

The friction losses are given by

$$P_{rot} = F\omega_{mnl}^2 + T_d\omega_{mnl}, \tag{2.91}$$

and the core losses are given by

$$P_{co} \simeq \frac{V_{nl}^2}{R_c} \tag{2.92}$$

where V_{nl}, I_{nl}, P_{nl}, Q_{nl}, and ω_{mnl} denote, respectively, the stator voltage, the stator current, the absorbed active power, the absorbed reactive power, and the rotor speed. The measurements performed, in loadless test on the induction motor of Table 2.1, yield the numerical values of Table 2.5.

The stator inductance L_s and the core resistance R_c are given by the following expressions:

$$L_s = \frac{3V_{nl}^2}{\omega_s Q_{nl}}, \quad R_c = \frac{3V_{nl}^2}{P_{nl} - 3R_s I_{nl}^2 - F\omega_{mnl}^2 + T_d * \omega_{mnl}}. \tag{2.93}$$

From equation (2.93) and Table 2.5, one gets the following values:

$$L_s = 441.6 \text{ mH}, \qquad R_c = 9500\ \Omega \tag{2.94}$$

Blocked Rotor Test

In this experiment the rotor is blocked, that is, prevented from turning. Then, a balanced three-phase voltage is applied to the stator terminals so that the resulting current equals the rated current. Again, all currents, voltages and powers are measured at the motor input. In the blocked rotor operation, the slip s is equal to 1. Then, the secondary impedance becomes much

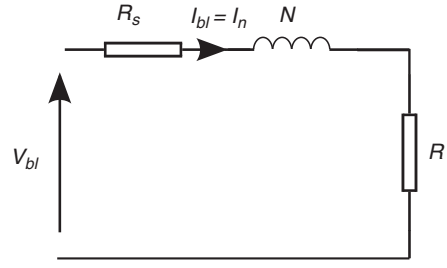

Figure 2.9 Induction machine equivalent circuit in blocked rotor test

smaller, compared to the magnetizing branch, so that the corresponding equivalent circuit boils down to the simpler configuration of Figure 2.9.

The measurements to be performed in this test are the following:

- The three-phase active power P_{bl}.
- The three-phase reactive power Q_{bl}.
- The line voltage V_{bl}.
- The line current I_{bl}.

R and N can be calculated from the following equations:

$$R = \frac{P_{bl}}{3I_{bl}^2} - R_s, \quad N = \frac{\sqrt{\left(\frac{V_{bl}}{I_{bl}}\right)^2 - (R+R_s)^2}}{\omega_s}. \tag{2.95}$$

As $N = \sigma L_r (\frac{L_s}{M_{sr}})^2$ and $R = R_r (\frac{L_s}{M_{sr}})^2$, the knowledge of R and N allows to calculate the rotor time constant and the parameter σ, using the expressions

$$T_r = \frac{L_s + N}{R}, \qquad \sigma = \frac{N}{N+L_s}. \tag{2.96}$$

The measurements made, in the blocked rotor test, on the induction machine of Table 2.1, are described in Table 2.6.

Table 2.6 Measurements made in blocked rotor test on the induction motor

V_{bl}	I_{bl}	P_{bl}	Q_{bl}
63.5 V	4.9 A	504 W	785 VAr

Table 2.7 Electrical parameter estimates of the induction motor

R_s	R_r	L_s	L_r	M_{sr}	T_r	σ
2.5 Ω	2.5 Ω	441.6 mH	441.6 mH	441.6 mH	100.6 ms	0.33

Then, using Table 2.6 and using the approximation that $L_r = M_{sr}$, one gets from equations (2.95) and (2.96) the electrical parameter estimates described in Table 2.7.

2.5 Conclusions

In this chapter, the problem of modeling induction motors has been concisely addressed. First, the triphase model is established applying electromagnetic and mechanical laws. This model is certainly the most physical as all variables it involves can be made accessible to measurements. However, it is hardly applicable in control design due to its high complexity. Then, simpler two-phase variants of that model are obtained by using the Park transformation. The simpler (two-phase) models are still nonlinear but will prove to be tractable in control design.

The modeling approach presented in this chapter is deliberately kept simple in the sense that the magnetic circuit has been supposed to be linear. As a matter of fact, in real-life machines, the magnetic circuit characteristic is nonlinear and linear approximations are only accurate if the machine operation does not entail wide-range rotor flux variation. Typically, the rotor flux must remain all the time close to its nominal value. The point is that a constant-flux operation cannot be optimal in the presence of varying load, when large speed variations are needed. In these situations, it is necessary to make the machine work with changing flux values to ensure high-efficiency operation. Models that account for the nonlinear nature of the machine magnetic characteristic have been presented in Levi (1995), Novotnak *et al.* (1999), Ouadi *et al.* (2011), and El Fadili *et al.* (2012b). An example of such models will be presented in Chapter 10 of this book.

References

Blaschke F (1972) The principle of field orientation applied to the new trans-vector closed-loop control system for rotating field machine. *Siemens Review*, **93**, 217–220.

De Leon J, Alvarez-Leal JG, Castro-Linares R, and Alvarez-Gallegos J (2001) Control of a flexible joint robot manipulator via a nonlinear control-observer scheme. *International Journal of Control*, **74**, 290–302.

El Fadili A, Giri F, Magri A, *et al.* (2012a) Adaptive nonlinear control of induction motors through AC/DC/AC converters. *Asian Journal of Control*, **14**, 1–14.

El Fadili A, Giri F, Magri A, *et al.* (2012b) Towards a global control strategy for induction motor. Speed regulation, flux optimization and power factor correction. *International Journal of Electrical Power and Energy Systems*, **43**, 230–244.

Ioannou PA and Fidan B (2006) *Adaptive Control Tutorial*. SIAM - Society for Industrial & Applied Mathematics.

Leonard W (2001) *Control of Electrical Drives*. Springer, New York.

Levi E (1995) A unified approach to main flux saturation modeling in D-Q axis models of induction machines. *IEEE Transactions on Energy Conversion*, **10**, 455–460.

Lubineau D, Dion JM, Dugard L, and Roye D (2000) Design of an advanced nonlinear controller for induction motor and experimental validation on an industrial benchmark. *EPJ Applied Physics*, **9**, 165–175.

Montanan M, Peresada S, and Tilli A (2006) A speed-sensorless indirect field-oriented control for induction motors based on high gain speed estimation. *Automatica*, **42**, 1637–1650.

Novotnak RT, Chiasson J, and Bodson M (1999) High performance motion control of an induction motor with magnetic saturation, *IEEE Transactions on Control Systems Technology*, **7**, 315–327.

Ouadi H, Giri F, and Dugard L (2011) Accounting for magnetic saturation in induction machines modeling. *International Journal of Modeling, Identification and Control*. **14**, 27–36.

Traore D, Plestan F, Glumineau A, and De Leon J (2008) Sensorless induction motor: high order sliding mode controller and adaptive interconnected observer. *IEEE Transactions on Industrial Electronics*, **55**, 3818–3827.

Vas P (1990) *Vector Control of AC Machines*. Clarendon Press, Oxford.

3

Control Models for Synchronous Machines

Abdelmounime El Magri, Fouad Giri, and Abderrahim El Fadili
GREYC Lab, University of Caen Basse-Normandie, France

3.1 Introduction

Compared to others, synchronous motors enjoy several features, for example, they are suitable for all applications necessitating important speed reversion and they are more efficient for drive applications where wide-range power variations are needed (from a few watts to several megawatts). Due to these features, the synchronous machine is nowadays widely used in various fields, for example, electric traction, high-speed machining, automotive, robotics, watches, computer peripherals, and energy production (Krause *et al*. 2002). Synchronous machines exist in two main variants: wound-rotor synchronous machines (WRSM) and permanent-magnet synchronous machines (PMSM). In WRSMs the rotor magnetic field is generated by a wound fixed on the rotor, while in PMSMs that field is generated by permanent magnets fixed on the rotor. Compared with induction motors, synchronous motors (especially PMSMs) are more suitable for electric traction as due to their better mass/power ratio, their higher power level, and their better efficiency. In effect, joule losses in PMSMs are much smaller (than in induction motors) due to the absence of rotor currents. WRSMs are quite suitable for high-power applications such as train driving (for instance, the French high-speed train *"Atlantic TGV"* is equipped with such type of machines) (El Magri *et al*. 2006). They also feature three control inputs (i.e., stator current amplitude, flux angle, and filed current), which makes them, just as their permanent-magnet cousins, able to ensure power optimization and high-power efficiency.

This chapter is about control-oriented mathematical modelling of synchronous motors. In the literature, three main modelling approaches have been developed for electrical machines in general. The first one is based on the finite element method (FEM) (Minnich *et al*. 1981;

AC Electric Motors Control: Advanced Design Techniques and Applications, First Edition. Edited by Fouad Giri.

Arkkio *et al*. 1990; Bangura and Arkadan 1999). This method provides a very accurate description of the electromagnetic field distribution in the machine. But, the proposed models are quite complex (large number of parameters) and computationally burdensome, which makes them of little interest for control design purpose. The second modelling method, referred to permeance network, consists of representing the machine magnetic circuit by an equivalent circuit diagram (Hecquet and Brochet 1998; Srairi *et al*. 2006). The obtained models are reasonably accurate but they suffer a large sensitivity to the air-gap permeance. The third modelling approach consists of applying to the machine the standard electromagnetic and mechanical laws (Blaschke 1972). The equations are made simpler by considering commonly admitted assumptions, for example, sinusoidal induction in the air gap, linearity of the magnetic circuit, negligence of iron losses, higher harmonics in slots, and spaces not account for. Furthermore, the size of the model is reduced thanks to the Park transformation, which projects the physical three-phase quantities onto two-coordinate frames. The models thus obtained prove to be reasonably accurate and tractable for control design.

This chapter is organized as follows: synchronous machine structures are briefly described in Section 3.2; in Section 3.3, the main modelling assumptions are described together with a new presentation of the Park transformation; the mathematical models of the PMSM and the WRSM are respectively established in Sections 3.4 and 3.5; and a conclusion and a reference list end the chapter.

3.2 Synchronous Machine Structures

Like all rotating electrical machines, the synchronous machine is an energy converter. It is reversible in the sense that it can operate either as a current generator (alternator) or as a motor. It is composed of two main parts, commonly referred to *armatures* (Figure 3.1). The stator is composed of three identical windings symmetrically distributed in space (120° between them). The windings are fixed in notches on the magnetic circuit. When the stator windings are current-fed by a balanced three-phase AC power supply, a turning field is generated along the air gap

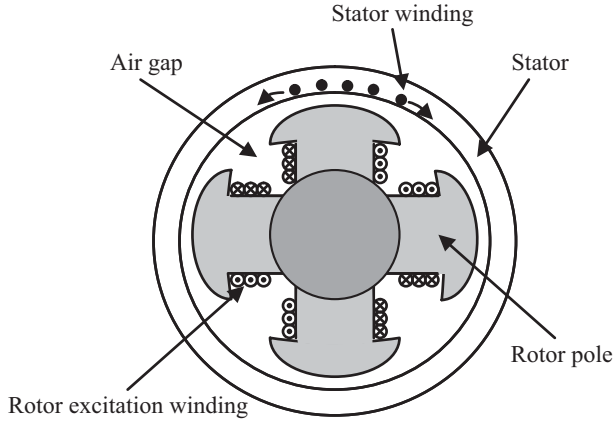

Figure 3.1 Electrical and magnetic structure of a wound-rotor synchronous machine with salient poles (number of poles $p = 2$)

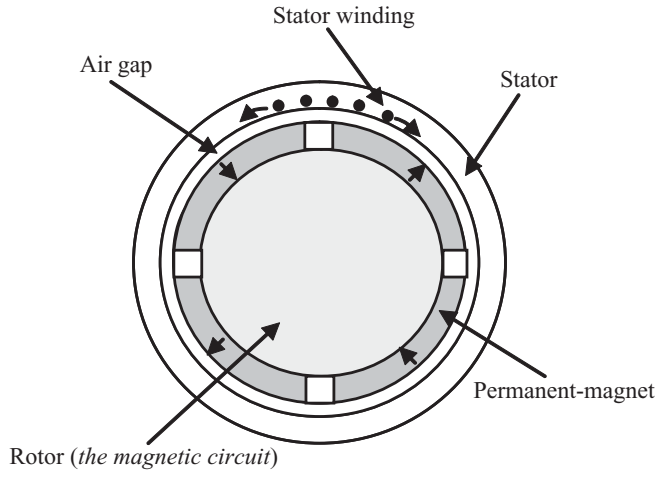

Figure 3.2 Structure of the permanent-magnet synchronous machine (number of poles $p = 2$)

(due to Ferraris's theorem (Kothari and Nagrath 2004)). The rotation speed of the turning field is proportional to both the number of poles of the machine and the pulsation of the stator currents (Krause *et al*. 2002; Multon *et al*. 2005). The second armature is the rotor (inductor) including, in the case of wound-rotor machines, a winding carrying a DC current, (Figure 3.1), or consisting of permanent magnets, in case of permanent-magnet machines (Figure 3.2). In the first case, the rotor consists of poles and windings wounded around. The windings carrying a DC current produce a magnetomotive force (MMF) along the air gap (Kothari and Nagrath 2004). In the second case, the MMF is generated by the permanent magnets. The inductor magnetic field interacts with the turning field created by the stator. This interaction results in an electromagnetic torque applied to the rotor entailing a rotation motion. In steady-state regime, the rotor velocity is identical to the speed of the turning field generated by the stator. This motivates the designation "synchronous machine" attributed to this type of machines.

3.3 Preliminaries

3.3.1 Modeling Assumptions

The following assumptions will prove to be useful in simplifying the machine modelling procedure, leading to tractable models:

A1: The induced electromagnetic force is assumed to be sinusoidal (with quasi-sinusoidally distributed stator winding).

A2: Iron permeability in the machine is assumed to be infinite. Therefore, the reluctance of the flux path is composed solely of the air gap and leakage reluctances. This amounts to supposition of the magnetic characteristic to be linear and ignore magnetic saturation.

A3: The Foucault current and the hysteresis losses are insignificant.

A direct consequence of the above assumptions is that the various mutual inductances between the stator and the rotor can be expressed as sinusoidal functions of the rotor position. The above assumptions are generally accepted as the resulting modelling errors are negligible in normal operation modes.

3.3.2 Three-Phase to Bi-Phase Transformations

A triplet (x_a, x_b, x_c) composed of sinusoidal variables is said to be a *balanced* three-phase system if the involved signals are of the form

$$x_a = A\cos(\omega t + \varphi), \tag{3.1a}$$

$$x_b = A\cos(\omega t + \varphi - 2\pi/3), \tag{3.2b}$$

$$x_c = A\cos(\omega t + \varphi + 2\pi/3). \tag{3.3c}$$

The variables may be currents, voltages, or magnetic fluxes. An inherent property to (balanced) three-phase systems is that their homopolar components, that is, $x_0 = x_a + x_b + x_c$, are null all the time. In the latter, this property will be systematically used because all involved three-phase systems will be balanced.

It was already emphasized in Chapter 2 that, a three-phase system like equation (3.1) is associated to a (fictive) three-coordinate frame, say *abc*. This frame is sometimes also said to be stationary or stator-related. Then, the Concordia transformation is resorted to project the *abc*-frame onto the fixed two-coordinate $\alpha\beta$-frame (Blaschke 1972). Accordingly, one has

$$\begin{pmatrix} x_a \\ x_b \\ x_c \end{pmatrix} = C_{32} \begin{pmatrix} x_\alpha \\ x_\beta \end{pmatrix} \tag{3.2}$$

and

$$\begin{pmatrix} x_\alpha \\ x_\beta \end{pmatrix} = C_{32}^T \begin{pmatrix} x_a \\ x_b \\ x_c \end{pmatrix}, \tag{3.3}$$

where C_{32} denotes the Concordia (3×2) matrix defined by

$$C_{32} = \sqrt{\frac{2}{3}} \begin{pmatrix} 1 & 0 \\ -1/2 & \sqrt{3}/2 \\ -1/2 & -\sqrt{3}/2 \end{pmatrix}. \tag{3.4}$$

It is easily checked that $C_{32}^T C_{32} = I_2$, where I_2 is the 2×2 identity matrix.

3.3.3 Concordia-Park Transformation ($\alpha\beta$ to dq)

The passage from the two-coordinate "α–β" frame to the rotating two-coordinate "d–q" is performed by multiplying the former by the following transformation matrix (Blaschke 1972)

$$P(\rho) = \begin{pmatrix} \cos(\rho) & -\sin(\rho) \\ \sin(\rho) & \cos(\rho) \end{pmatrix}, \tag{3.5}$$

where, ρ is the angular position of the rotating reference frame (dq). The latter is allowed to be rotating at any speed. Note that $P(\rho)^T P(\rho) = I_2$. Using equation (3.4), it turns out that the passage from a stationary three-phase system (a, b, c) to the corresponding bi-phase system expressed in the rotating dq-frame is performed as follows:

$$\begin{pmatrix} x_d \\ x_q \end{pmatrix} = P(\rho)^T C_{32}^T \begin{pmatrix} x_a \\ x_b \\ x_c \end{pmatrix}. \tag{3.6}$$

3.4 Dynamic Modeling of Wound-Rotor Synchronous Motors

The three-phase WRSM contains three identical armature windings, symmetrically distributed around the air gap, and one field winding (Figure 3.1).

From the electromagnetic viewpoint, the WRSM is described by a set of three stator circuits coupled through motion with a field winding (Figure 3.3). The stator and rotor circuits are

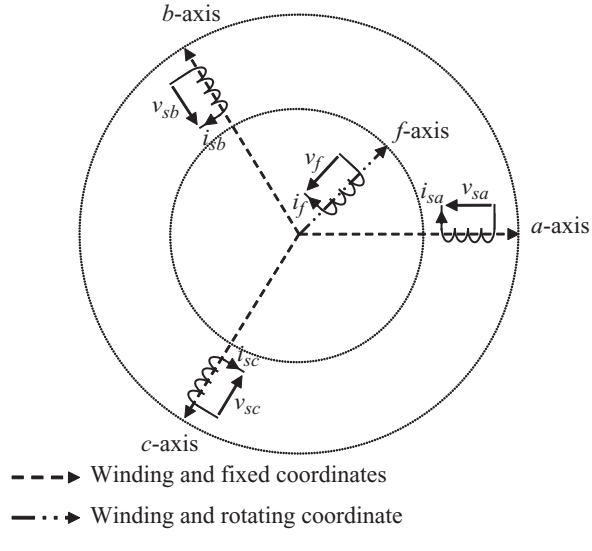

Figure 3.3 Electric structure of the wound-rotor synchronous machines

magnetically coupled with each other. Applying Faraday's and Ohm's laws, one gets the following equations describing the electrical dynamics of this machine:

$$\begin{pmatrix} v_{sa} \\ v_{sb} \\ v_{sc} \end{pmatrix} = \begin{pmatrix} R_s & 0 & 0 \\ 0 & R_s & 0 \\ 0 & 0 & R_s \end{pmatrix} \begin{pmatrix} i_{sa} \\ i_{sb} \\ i_{sc} \end{pmatrix} + \frac{d}{dt} \begin{pmatrix} \phi_{sa} \\ \phi_{sb} \\ \phi_{sc} \end{pmatrix} \tag{3.7}$$

and

$$v_f = R_f i_f + \frac{d\phi_f}{dt}, \tag{3.8}$$

where v_{sabc}, i_{sabc}, R_s, and ϕ_{sabc} are respectively the stator voltage, current, resistor, and flux, while v_f, i_f, R_f, and ϕ_f are the corresponding quantities of the rotor.

The fluxes of phase windings a, b, c, and f can be expressed in terms of the self- and mutual inductances

$$[\phi_{sabc}] = [L_{ss}][i_{sabc}] + [M_{sf}]i_f, \tag{3.9a}$$

$$[\phi_f] = [M_{fs}][i_{sabc}] + [L_f]i_f, \tag{3.9b}$$

with,

$$[i_{sabc}] = \begin{bmatrix} i_{sa} & i_{sb} & i_{sc} \end{bmatrix}^T; \quad [\phi_{sabc}] = \begin{bmatrix} \phi_{sa} & \phi_{sb} & \phi_{sc} \end{bmatrix}^T; \tag{3.10a}$$

$$[M_{fs}] = \begin{bmatrix} M_{fa} & M_{fb} & M_{fc} \end{bmatrix}^T; \quad [M_{sf}] = [M_{fs}]^T; \tag{3.10b}$$

$$[L_{ss}] = \begin{pmatrix} L_a & M_{ab} & M_{ac} \\ M_{ba} & L_b & M_{bc} \\ M_{ca} & M_{cb} & L_c \end{pmatrix}; \quad [R_s] = \begin{pmatrix} R_s & 0 & 0 \\ 0 & R_s & 0 \\ 0 & 0 & R_s \end{pmatrix}. \tag{3.10c}$$

In the above expressions, $[i_{sabc}]$ and $[\phi_{sabc}]$ are the stator current and flux, $[M_{fs}]$ is the mutual inductance between the rotor and the stator, $[L_{ss}]$ is the stator inductance matrix, and $[R_s]$ is the stator resistor.

The rotor saliency (compared to the stator) entails the variation of the magnetic circuit permeance. Accordingly, when the rotor makes a complete turn, the geometrical configuration is repeated $2p$ times with p being the number of pole pairs. It turns out that the period of the self- and the mutual inductances is $2p\theta$, with θ being the rotor position. The mutual inductance between the stator and the rotor windings also has a varying period, equal to $p\theta$. Analytically, the self-inductances of the (a, b, c) phase windings assume the following expressions:

$$L_a = L_{s0} + L_{sv}\cos(2p\theta), \tag{3.11a}$$

$$L_b = L_{s0} + L_{sv}\cos(2p\theta + 2\pi/3), \tag{3.11b}$$

$$L_c = L_{s0} + L_{sv}\cos(2p\theta - 2\pi/3). \tag{3.11c}$$

The mutual inductances between the stator phases are as follows:

$$M_{ab} = M_{s0} + L_{sv}\cos(2p\theta - 2\pi/3), \tag{3.12a}$$

$$M_{bc} = M_{s0} + L_{sv}\cos(2p\theta), \tag{3.12b}$$

$$M_{ac} = M_{s0} + L_{sv}\cos(2p\theta + 2\pi/3). \tag{3.12c}$$

The mutual inductances between the stator phases and the excitation winding are as follows:

$$M_{af} = M_{fs}\cos(p\theta), \tag{3.13a}$$

$$M_{bf} = M_{fs}\cos(p\theta - 2\pi/3), \tag{3.13b}$$

$$M_{cf} = M_{fs}\cos(p\theta + 2\pi/3), \tag{3.13c}$$

where L_{s0}, L_{sv}, M_{s0}, M_{sf}, and L_f are nonzero real constants depending on the machine structure.

Using equations (3.9a–b), it follows from equation (3.7) and (3.8) that the electrical equations of the three-phase model (a, b, c) can be rewritten as follows:

$$[v_{sabc}] = [R_s][i_{sabc}] + \frac{d}{dt}\{[L_{ss}][i_{sabc}] + [M_{sf}]i_f\}, \tag{3.14}$$

$$v_f = R_f i_f + \frac{d}{dt}\{[M_{fs}][i_{sabc}] + L_f i_f\}. \tag{3.15}$$

Owing to the mechanical equation, it follows applying the fundamental principle of dynamics to the rotor motion

$$T_{em} = T_L + F\omega + J\frac{d\omega}{dt}, \tag{3.16}$$

where T_L denotes the load torque, F is the viscous friction coefficient, and J the global rotor-load inertia. The electromagnetic torque developed by the machine depends on the inductance matrix and the current vector and can be given the following general expression:

$$T_{em} = \frac{1}{2}[i]^T \left\{\frac{dL}{d\theta}\right\}[i], \tag{3.17}$$

where $[L]$ includes all inductances and $[i]$ all currents. Specifically, one has

$$T_{em} = \frac{1}{2}\begin{bmatrix}[i_{sabc}] & i_f\end{bmatrix}^T \left[\frac{d}{d\theta}\begin{bmatrix}[L_{ss}] & [M_{sf}]\\ [M_{fs}] & L_f\end{bmatrix}\right]\begin{bmatrix}[i_{sabc}]^T & i_f\end{bmatrix}^T. \tag{3.18}$$

Note that L_f is independent on the rotor position θ and $[M_{sf}] = [M_{fs}]^T$. It immediately follows that

$$T_{em} = \frac{1}{2}[i_{sabc}]^T \left[\frac{d[L_{ss}]}{d\theta}\right][i_{sabc}] + [i_{sabc}]^T \left[\frac{d[M_{sf}]}{d\theta}\right] i_f. \tag{3.19}$$

The stator and the rotor voltages equations (3.14) and (3.15) constitute, together with the mechanical equation (3.19), the model of the WRSM in the fixed three-coordinate frame linked to the three stator windings. From expressions (3.10b–c), of the self-inductance $[L_{ss}]$ and the mutual $[M_{sf}]$, it is seen that the stator and the rotor flux depends on both the time and the rotor position. This makes this model difficult to be exploited in control design. Indeed, the inductance matrix contains 13 nonzero terms, including 12 depending on the rotor position θ. This entails burdensome real-time implementations especially in transient regimes. To overcome these difficulties, the the Park transformation is resorted to obtain a lower-size position-independent model. Analytically described by equation (3.6), this transformation allows the passage from the (stator-related frame) three-phase models (3.14), (3.15), (3.10b–c) to the corresponding rotating dq-frame two-phase model. In the dq-frame, all inductances turn out to be constant and all signals are steady-state sinusoidal and referred to dc-quantities along d-axis or q-axis.

3.4.1 Oriented dq-Frame Model of Salient Pole WRSM

As explained in Chapter 2, it is beneficial to let the dq-frame be rotating at the rotor speed and be oriented along the the rotor flux d-axis so that the rotor flux q-component can be set to zero, reducing the model size (Blaschke 1972).

Then, operating the transformation (3.6), on the (three-phase) current $[i_{sabc}]$, the voltage $[v_{sabc}]$, and the flux $[\phi_{sabc}]$, one obtains the two-phase system ($[i_{sdq}]$, $[v_{sdq}]$, and $[\phi_{sdq}]$). Following closely a similar procedure in Chapter 2, one gets the equations that govern the dq quantities. The obtained equations are listed in order.

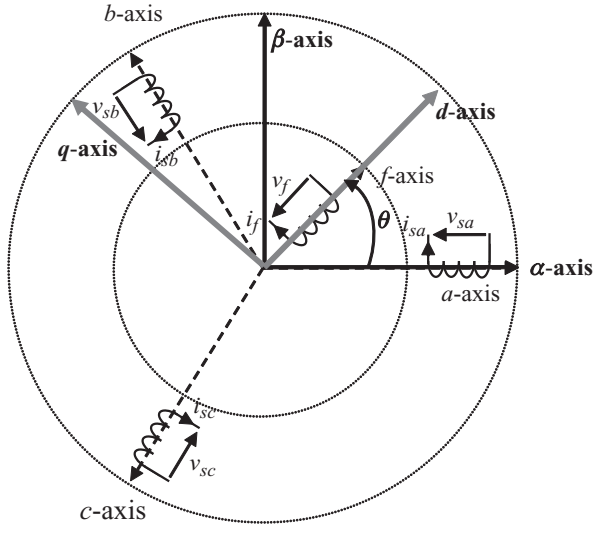

Figure 3.4 *abc*- and dq-coordinate frame in wound-rotor synchronous machines

Voltage Equations in dq Coordinates

$$[v_{sdq}] = [R_s][i_{sdq}] + \frac{\mathrm{d}[\phi_{sdq}]}{\mathrm{d}t} + p\omega Q[\phi_{sdq}], \tag{3.20}$$

$$v_f = R_f i_f + \frac{\mathrm{d}\phi_f}{\mathrm{d}t}. \tag{3.21}$$

Flux Equations in dq-Coordinates

$$\phi_{sd} = L_d i_{sd} + M i_f, \tag{3.22a}$$

$$\phi_{sq} = L_q i_{sq}, \tag{3.22b}$$

$$\phi_f = L_f i_f + M i_{sd}. \tag{3.22c}$$

Electromagnetic Torque Developed by the Machine

$$T_{em} = p\{\phi_{sd} i_{sq} - \phi_{sq} i_{sd}\} = p i_{sd} i_{sq}(L_d - L_q) + p M i_{sq} i_f, \tag{3.23}$$

where $L_d = 3(L_{s0} + L_{sv})/2$ is called d-axis inductance, $L_q = 3(L_{s0} - L_{sv})/2$ is the q-axis inductance, and $M = \sqrt{3/2} M_{fs}$ is the direct axis magnetizing inductance (mutual between the stator and rotor windings).

For convenience, equations (3.20), (3.21), (3.22), and (3.23) are put together

$$\frac{d\omega}{dt} = -\frac{F}{J}\omega + \frac{a_1}{J} i_{sd} i_{sq} + \frac{a_2}{J} i_f i_{sq} - \frac{1}{J} T_L, \tag{3.24a}$$

$$\frac{di_{sq}}{dt} = -b_1 i_{sq} - b_2 i_{sd}\omega - b_3 i_f \omega + b_4 v_{sq}, \tag{3.24b}$$

$$\frac{di_{sd}}{dt} = -c_1 i_{sd} + c_2 R_f i_f + c_3 i_{sq}\omega + c_4 v_{sd} - c_5 v_f, \tag{3.24c}$$

$$\frac{di_f}{dt} = -d_1 R_f i_f + d_2 i_{sd} - d_3 i_{sq}\omega - d_4 v_{sd} + d_5 v_f. \tag{3.24d}$$

The fourth order state-space representation (equations (3.24a-d) constitutes the model of the salient pole WRSM in the (rotor-flux-oriented) rotating dq-frame. This model is still nonlinear but it will prove to useful for control design purpose. It is acted on by v_{sd} and v_{sq}, the stator voltage in dq-coordinates, and v_f, the rotor excitation voltage. The model state vector includes the stator currents (i_{sd}, i_{sq}), the rotor excitation current i_f, and the rotor speed ω. The model enjoys the facts that all its parameters (see Table 3.1) are constant and all its state variables are measurable. Besides, the control of the instantaneous electromagnetic torque can be done easily through the currents (i_{sd}, i_{sq}, and i_f).

The model coefficients are described in Table 3.1.

Table 3.1 Notations used in wound-rotor synchronous machines (WRSM) model (equations 3.24a–d)

$a_1 = p(L_d - L_q)$	$a_2 = pM$			
$b_1 = \dfrac{R_s}{L_q}$	$b_2 = p\dfrac{L_d}{L_q}$	$b_3 = p\dfrac{M}{L_q}$	$b_4 = \dfrac{1}{L_q}$	
$c_1 = \dfrac{R_s L_f}{L_d L_f - M^2}$	$c_2 = \dfrac{M}{L_d L_f - M^2}$	$c_3 = \dfrac{pL_f L_q}{L_d L_f - M^2}$	$c_4 = \dfrac{L_f}{L_d L_f - M^2}$	$c_5 = \dfrac{M}{L_d L_f - M^2}$
$d_1 = \dfrac{L_d}{L_d L_f - M^2}$	$d_2 = \dfrac{R_s M}{L_d L_f - M^2}$	$d_3 = \dfrac{pML_q}{L_d L_f - M^2}$	$d_4 = \dfrac{M}{L_d L_f - M^2}$	$d_5 = \dfrac{L_d}{L_d L_f - M^2}$

R_s, stator resistor; R_f, rotor resistor; L_d, L_q, d- and q-axis stator inductances; L_f, rotor inductance; M, rotor and stator mutual inductance; p, number of pole pairs; F, combined rotor and load viscous friction; J, combined rotor and load inertia; T_L, machine load torque.

3.5 Permanent-Magnet Synchronous Machine Modeling

3.5.1 PMSM Modeling in abc-Coordinates

As already mentioned, PMSMs differ from WRSMs in that the excitation is provided by permanent magnets fixed on the rotor (Figure 3.5). Presently, the PMSM modelling is dealt with following the same approach as for the WRSM, using the same assumptions, conventions, and notations. Accordingly, the three fixed stator windings are labeled a, b, and c (just as for the WRSM). Then, the voltages between the three phases is given by the expression

$$[v_{sabc}] = [R_s][i_{sabc}] + \frac{\mathrm{d}[\phi_{sabc}]}{\mathrm{d}t} \tag{3.25}$$

where v_{sa}, v_{sb}, and v_{sc} denote the three-phase stator voltage in abc-coordinates; R_s the stator winding resistor; i_{sa}, i_{sb}, and i_{sc} are the currents in the three windings of the stator; and ϕ_{sa}, ϕ_{sb}, and ϕ_{sc} are the induced flux within the stator windings. In the rotor, a constant flux is

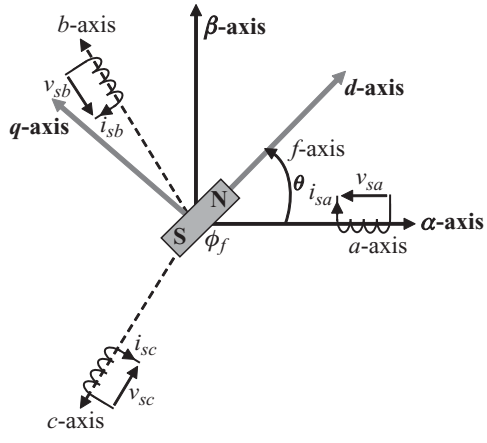

Figure 3.5 abc-coordinate frame and two-phase, stationary and rotating, frames in PMSMs

created by the magnets. The distribution of the excitation field in the air gap and the MMFs are assumed to be sinusoidal (by assumption A3). Consequently, the expressions of the mutual flux of the inductor phases assume the following expressions:

$$\phi_{ra} = \phi_r \cos(p\theta), \tag{3.26a}$$

$$\phi_{rb} = \phi_r \cos(p\theta - 2\pi/3), \tag{3.26b}$$

$$\phi_{rc} = \phi_r \cos(p\theta + 2\pi/3), \tag{3.26c}$$

where ϕ_r is the amplitude of the flux produced by the permanent magnets, assumed to be constant as the variation with temperature is insignificant. It turns out that the flux through each of the stator windings is the sum of the flux induced by the rotor magnets and the flux produced by the currents carried by the stator phases. Specifically, one has

$$[\phi_{sabc}] = [L_{ss}][i_{sabc}] + [\phi_{rabc}]. \tag{3.27}$$

Furthermore, the fact that the rotor flux (PMSMs) is generated by permanent magnets, equation (3.9a) is still valid provided that the quantity $[M_{sf}]i_f$ (flux produced by the inductor in the WRSM case) is replaced by its PMSM equivalent, that is, $[\phi_{rabc}]$. Now, using the flux expression (3.26a), the stator voltage expression (3.25) becomes

$$[v_{sabc}] = [R_s][i_{sabc}] + \frac{d}{dt}\{[L_{ss}][i_{sabc}]\} + \omega \frac{d}{d\theta}[\phi_{rabc}], \tag{3.28}$$

where we have used the rule $\frac{d}{dt}(\bullet) = \frac{d\theta}{dt}\frac{d}{d\theta}(\bullet) = \omega\frac{d}{d\theta}(\bullet)$.

The WRSM mechanical equation (3.19) remains valid for PMSMs again, provided the WRSM quantity $[M_{sf}]i_f$ is replaced by its PMSM equivalent $[\phi_{rabc}]$. Doing so, one gets

$$T_{em} = \frac{1}{2}[i_{sabc}]^T \left\{\frac{d[L_{ss}]}{d\theta}\right\}[i_{sabc}] + [i_{sabc}]^T \left\{\frac{d[\phi_{rabc}]}{d\theta}\right\}. \tag{3.29}$$

For convenience, the usual motion equation is rewritten

$$T_{em} = T_L + F\omega + J\frac{d\omega}{dt}. \tag{3.30}$$

3.5.2 PMSM Model in the Rotating dq-Frame

Electric Equations

The PMSM model in the rotating dq-frame, linked to the rotor (Figure 3.4), is derived from the abc-model, described by equation (3.28), by using the Concordia-Park transformation (3.6).

The dq-frame is made linked to the rotor by letting the angular position ρ (in equation (3.6)) be equal to the electrical position $\theta_e = p\theta$. Doing so, we get

$$C_{32}P(\theta_e)[v_{sdq}] = R_s C_{32}P(\theta_e)[i_{sdq}] + \frac{d}{dt}\left([L_{ss}]C_{32}P(\theta_e)[i_{sdq}]\right) + \omega\frac{d}{d\theta}\left(C_{32}P(\theta_e)[\phi_{rdq}]\right). \tag{3.31}$$

It can be checked that the matrix of inductances $[L_{ss}]$ can be given in the following form:

$$[L_{ss}] = L_{sv}I_3 + \frac{3}{2}L_{sv}C_{32}P(\theta_e)QP(\theta_e)^T C_{32}^T \tag{3.32}$$

with,

$$Q = \begin{pmatrix} 1 & 0 \\ 0 & -1 \end{pmatrix}; \quad I_3 = \begin{pmatrix} 1 & 0 & 0 \\ 0 & 1 & 0 \\ 0 & 0 & 1 \end{pmatrix}.$$

Then, multiplying both sides of equation (3.31) by $P(p\theta)^T C_{32}^T$ and replacing $[L_{ss}]$ by its expression (3.32), it follows that:

$$[v_{sdq}] = R_s[i_{sdq}] + \omega P(\theta_e)^T C_{32}^T \frac{\mathrm{d}}{\mathrm{d}\theta}\left(C_{32}P(\theta_e)[\phi_{rdq}]\right) + P(\theta_e)^T \frac{\mathrm{d}}{\mathrm{d}t}\left\{C_{32}^T\left(L_{sv}I_3 + \frac{3}{2}L_{sv}C_{32}P(\theta_e)QP(\theta_e)^T C_{32}^T\right)C_{32}P(\theta_e)[i_{sdq}]\right\}. \tag{3.33}$$

The following properties are readily checked:

$$\frac{\mathrm{d}}{\mathrm{d}t}(\bullet) = \omega\frac{\mathrm{d}}{\mathrm{d}\theta}(\bullet), \tag{3.34a}$$

$$\frac{\mathrm{d}}{\mathrm{d}\theta}\left(P(\theta_e)\right) = pP(\theta e)Q', \tag{3.34b}$$

$$P(\theta_e)Q'P(\theta_e)^T = Q', \tag{3.34c}$$

with,

$$Q' = \begin{pmatrix} 0 & -1 \\ 1 & 0 \end{pmatrix}.$$

Using equation (3.34a–c), the expression (3.33) is rewritten as follows:

$$[v_{sdq}] = R_s[i_{sdq}] + p\omega Q'[\phi_{rdq}] + \left(L_{sv}I_2 + \frac{3}{2}L_{sv}Q\right)\frac{\mathrm{d}[i_{sdq}]}{\mathrm{d}t} + p\omega P(\theta_e)^T\left(L_{sv}P(\theta_e)Q' + \frac{3}{2}L_{sv}P(\theta_e)Q'Q\right)[i_{sdq}] \tag{3.35}$$

The matrix of inductances in the dq-frame is defined as follows:

$$[L_{dq}] = \begin{pmatrix} L_d & 0 \\ 0 & L_q \end{pmatrix} = L_{cs} I_2 + \frac{3}{2} L_{sv} Q, \tag{3.36}$$

where the second equality is obtained using the definitions of the the direct axis inductance, $L_d = 3(L_{so} + L_{sv})/2$, of the quadratic inductance, $L_q = 3(L_{so} - L_{sv})/2$ and cylique inductance $L_{cs} = \frac{3}{2} L_{s0}$. Using equation (3.36), the stator voltage equation (3.35) takes the following final form:

$$[v_{sdq}] = R_s [i_{sdq}] + [L_{dq}] \frac{d[i_{sdq}]}{dt} + p\omega Q' [L_{dq}][i_{sdq}] + p\omega Q' [\phi_{rdq}]. \tag{3.37}$$

Mechanical Equation

The torque expression in the rotor-linked dq-frame is obtained from equation (3.29) using equation (3.32) and the properties (3.34a–c). Doing so, one obtains

$$\begin{aligned} T_{em} = {} & p \frac{1}{2} [i_{sdq}]^T P(\theta_e)^T C_{32}^T \frac{3}{2} p L_{sv} C_{32} P(\theta_e) \left(Q' Q + Q Q'^T \right) [i_{sdq}] \\ & + p [i_{sdq}]^T P(\theta_e)^T C_{32}^T C_{32} P(\theta_e) Q [\phi_{rdq}]. \end{aligned} \tag{3.38}$$

Note that $P(p\theta_e)^T C_{32}^T C_{32} P(p\theta_e) = I_2$ (properties of Park and Concordia transformations). It is also readily checked that

$$[i_{sdq}]^T Q' Q [i_{sdq}] = 2 i_{sd} i_{sq}; \quad L_{sv} = 3(L_d - L_q)/4; \quad \text{and} \quad Q' Q = Q Q'^T = I_2.$$

Then, the expression (3.38) rewrites

$$T_{em} = T_L + F\omega + J \frac{\mathrm{d}\omega}{\mathrm{d}t} = p \left(L_d - L_q \right) i_{sd} i_{sq} + [i_{sdq}]^T Q' [\phi_{rdq}]. \tag{3.39}$$

Recall that in the rotor-like dq-frame, the rotor flux is aligned with the d-axis. Consequently, the flux q-component ϕ_{rq} turns out to be null, while the d-component is determined by the equation $[i_{sdq}]^T Q' [\phi_{rdq}] = \sqrt{3/2}\, \phi_r i_{sq}$. Then, the electromagnetic torque rewrites

$$T_{em} = T_L + F\omega + J \frac{\mathrm{d}\omega}{\mathrm{d}t} = p \left(L_d - L_q \right) i_{sd} i_{sq} + p \sqrt{3/2} i_{sq} \phi_r. \tag{3.40}$$

From equations (3.37) and (3.40), replacing $[L_{dq}]$ and Q' by their expressions given by equation (3.36), one obtains the final form of the PMSM model in the rotor-flux-oriented, rotor-like dq-frame

$$\frac{\mathrm{d}\theta}{\mathrm{d}t} = \omega, \tag{3.41a}$$

$$\frac{\mathrm{d}\omega}{\mathrm{d}t} = -\frac{F}{J}\omega + p \frac{(L_d - L_q)}{J} i_{sd} i_{sq} + p \sqrt{\frac{3}{2}} \frac{\phi_r}{J} i_{sq} - \frac{1}{J} T_L, \tag{3.41b}$$

$$\frac{\mathrm{d}i_{sq}}{\mathrm{d}t} = -\frac{R_s}{L_q}i_{sq} - p\frac{L_d}{L_q}i_{sd}\omega - p\sqrt{\frac{3}{2}}\frac{\phi_r}{L_q}\omega + \frac{1}{L_q}v_{sq}, \tag{3.41c}$$

$$\frac{\mathrm{d}i_{sd}}{\mathrm{d}t} = -\frac{R_s}{L_d}i_{sd} + p\frac{L_q}{L_d}i_{sq}\omega + \frac{1}{L_d}v_{sd}. \tag{3.41d}$$

3.5.3 PMSM Model in the Fixed Bi-Phase αβ-Frame

Electric Equations

The model of the machine in the fixed $\alpha\beta$-frame is obtained from equations (3.37) and (3.39) by applying the Park-Concordia transformation defined in equations (3.2), (3.3), (3.4), (3.5), and (3.6). Accordingly, one has

$$\begin{aligned} P(\theta_e)^T[v_{s\alpha\beta}] = {} & R_s P(\theta_e)^T[i_{s\alpha\beta}] + [L_{dq}]\frac{\mathrm{d}}{\mathrm{d}t}\left(P(\theta_e)^T[i_{s\alpha\beta}]\right) \\ & + p\omega Q'[L_{dq}]P(\theta_e)^T[i_{s\alpha\beta}] + p\omega Q' P(\theta_e)^T[\phi_{r\alpha\beta}]. \end{aligned} \tag{3.42}$$

Multiplying both sides of equation (3.42) by $P(\theta_e)$, yields

$$\begin{aligned} [v_{s\alpha\beta}] = {} & R_s[i_{s\alpha\beta}] + P(\theta_e)[L_{dq}]\frac{\mathrm{d}}{\mathrm{d}t}\left(P(\theta_e)^T[i_{s\alpha\beta}]\right) \\ & + p\omega P(\theta_e)Q'[L_{dq}]P(\theta_e)^T[i_{s\alpha\beta}] + p\omega P(\theta_e)Q' P(\theta_e)^T[\phi_{r\alpha\beta}], \end{aligned} \tag{3.43}$$

where we have used the fact that $P(\theta_e)P(\theta_e)^T = I_2$. Using again the properties (3.34a–c), the above equation becomes

$$\begin{aligned} [v_{s\alpha\beta}] = {} & R_s[i_{s\alpha\beta}] + [L_{dq}]\frac{\mathrm{d}}{\mathrm{d}t}[i_{s\alpha\beta}] \\ & + p\omega P(\theta_e)\left(Q'[L_{dq}] + [L_{dq}]Q'^T\right)P(\theta_e)^T[i_{s\alpha\beta}] + p\omega Q'[\phi_{r\alpha\beta}]. \end{aligned} \tag{3.44}$$

It is easily checked that $p\omega P(\theta_e)\left(Q'[L_{dq}] + [L_{dq}]Q'^T\right)P(\theta_e)^T = p\omega(L_d - L_q)$. Accordingly, the stator voltage expression, in the fixed $\alpha\beta$-coordinate frame, takes the following form:

$$[v_{s\alpha\beta}] = R_s[i_{s\alpha\beta}] + [L_{dq}]\frac{\mathrm{d}}{\mathrm{d}t}[i_{s\alpha\beta}] + p\omega\left(L_d - L_q\right)[i_{s\alpha\beta}] + p\omega Q'[\phi_{r\alpha\beta}]. \tag{3.45}$$

Mechanical Equation

Again, applying the transformations (3.2), (3.3, (3.4), (3.5), and (3.6) to the torque expression (3.39), one obtains the corresponding $\alpha\beta$ form

$$T_{em} = p\frac{3}{2}L_{sv}[i_{s\alpha\beta}]^T P(\theta_e)Q'QP(\theta_e)^T[i_{s\alpha\beta}] + p[i_{s\alpha\beta}]^T P(\theta_e)Q' P(\theta_e)^T[\phi_{r\alpha\beta}]. \tag{3.46}$$

Introducing the notation $R(\theta_e) = P(\theta_e)Q'QP(\theta_e)^T$, the above expression rewrites

$$T_{em} = p\frac{3}{2}L_{sv}[i_{s\alpha\beta}]^T R(\theta_e)[i_{s\alpha\beta}] + p[i_{s\alpha\beta}]^T Q'[\phi_{r\alpha\beta}]. \tag{3.47}$$

It is easily checked that $[i_{s\alpha\beta}]^T Q'[\phi_{r\alpha\beta}] = (\phi_{r\alpha}i_{s\beta} - \phi_{r\beta}i_{s\alpha})$. Accordingly, the mechanical equation rewrites as follows:

$$T_{em} = T_L + F\omega + J\frac{\mathrm{d}\omega}{\mathrm{d}t} = p\frac{3}{2}L_{sv}[i_{s\alpha\beta}]^T R(\theta_e)[i_{s\alpha\beta}] + p(\phi_{r\alpha}i_{s\beta} - \phi_{r\beta}i_{s\alpha}) \tag{3.48}$$

On the other hand, operating the Park-Concordia transformation on the balanced three-phase flux system (3.26a–c) one obtains the corresponding two-phase system in the $\alpha\beta$-frame. It is checked that the obtained flux components, $\phi_{r\alpha}$ and $\phi_{r\beta}$, undergo the following equations:

$$\frac{\mathrm{d}\phi_{r\alpha}}{\mathrm{d}t} = -p\omega\phi_{r\beta}, \tag{3.49a}$$

$$\frac{\mathrm{d}\phi_{r\beta}}{\mathrm{d}t} = p\omega\phi_{r\alpha}. \tag{3.49b}$$

Writing together equations (3.45), (3.48), and (3.49a–b), yields the PMSM model in the fixed $\alpha\beta$-frame.

$$\frac{\mathrm{d}i_{s\alpha}}{\mathrm{d}t} = -\frac{R_s}{L_s}i_{s\alpha} + \frac{p}{L_s}\omega\phi_{r\beta} + \frac{1}{L_s}v_{s\alpha}, \tag{3.50a}$$

$$\frac{\mathrm{d}i_{s\beta}}{\mathrm{d}t} = -\frac{R_s}{L_s}i_{s\beta} - \frac{p}{L_s}\omega\phi_{r\alpha} + \frac{1}{L_s}v_{s\beta}, \tag{3.50b}$$

$$\frac{\mathrm{d}\phi_{r\alpha}}{\mathrm{d}t} = -p\omega\phi_{r\beta}, \tag{3.50c}$$

$$\frac{\mathrm{d}\phi_{r\beta}}{\mathrm{d}t} = p\omega\phi_{r\alpha}, \tag{3.50d}$$

$$\frac{\mathrm{d}\omega}{\mathrm{d}t} = \frac{2p}{3J}L_{sv}[i_{s\alpha\beta}]^T R(\theta_e)[i_{s\alpha\beta}] + \frac{p}{J}(\phi_{r\alpha}i_{s\beta} - \phi_{r\beta}i_{s\alpha}) - \frac{F}{J}\omega - \frac{1}{J}T_L. \tag{3.50e}$$

3.6 Conclusions

The modelling of smooth pole synchronous machines is identical to that of the salient pole machines. The air gap being uniform (constant thickness) entails $L_{sv} = 3(L_d - L_q)/4 = 0$ yielding $L_q = L_d = L_s$. Equations (3.24a–d), (3.41), and (3.50) remain all valid. The expression of electromagnetic torque simplifies to $T_{em} = p\sqrt{3/2}\phi_r i_{sq}$, because the variable reluctance torque is zero (no saliency).

The Park-Concordia transformations have proved to be major instruments in passing from the complex triphase machine model, expressed in the abc-frame, to the simpler fixed two-phase $\alpha\beta$-coordinate model and the rotating dq-coordinate model. The simpler models enjoy lower sizes and constant parameters that make them tractable in control design. The real-time

implementation of these models and the controllers based upon them has become possible in recent years due to the advances made in digital computer technology.

References

Arkkio A (1990) Finite element analysis of cage induction motors fed by static frequency converters. *IEEE Transactions on Magnetics*, **26**, 551–554.

Bangura JF and Arkadan AA (1999) A time-stepping coupled finite element-state space model for induction motor drives. I. Model formulation and machine parameter computation. *IEEE Transactions on Energy Conversion*, **14**, 1465–1471.

Blaschke F (1972) The principle of field orientation applied to the new trans-vector closed-loop control system for rotating field machine. *Siemens Reviews*, **93**, 217–220.

El Magri A, Giri F, Abouloifa A, and Haloua M (2006) Nonlinear control of wound-rotor synchronous-motor'. *IEEE International Conference on Control Applications*, pp. 3110–3115.

Hecquet M and Brochet P (1998) Simulations of synchronous machines using a electric-magnetic coupled network model. *IEEE Transactions on Magnetics*, **34**, 3656–3659.

Kothari DP and Nagrath IJ (2004) *Electric Machines*. McGraw-Hill Education.

Krause PC, Wasynczuk O, and Sudhoff SD (2002) *Analysis of Electric Machinery and Drive Systems*. Wiley-IEEE Press.

Minnich SH, Csendes ZJ, Berkery J, and Tandon SC (1981) Load characteristics of synchronous generators by the finite-element method. *IEEE Transactions on Power Apparatus and Systems*, **PAS-100**, 1–13.

Multon B, Ben Ahmed H, *et al*. (2005) Synchronous machines: general principles and structures. *Techniques de l'ingénieur. Génie électrique*, **D6**, Nř D3520.

Srairi S, Djerdir A, and Miraoui A (2006) Use of permeance network method in the demagnetization phenomenon modelling in a permanent magnet motor. *IEEE Transactions on Magnetics*, **42**, 1295–1298.

Part Two

Observer Design Techniques for AC Motors

AC Electric Motors Control: Advanced Design Techniques and Applications, First Edition. Edited by Fouad Giri.

4

State Observers for Estimation Problems in Induction Motors

Gildas Besançon[1] and Alexandru Ţiclea[2]

[1]*Control System Department, GIPSA Lab, Grenoble Institute of Techology and Institut Universitaire de France, France*

[2]*Department of Control and System Engineering, Polytechnic University of Bucharest, Romania*

4.1 Introduction

Induction motors are basically characterized by their dynamics in currents and fluxes under the effect of the applied voltages at the stator. Those electrical dynamics generate the mechanical torque and rotating speed of the machine. Estimation issues then arise from the fact that among all those quantities of interest, only stator currents can easily be measured online, while they are needed for control, or monitoring. From this, a lot of efforts have been dedicated to methods of reconstruction of the unmeasured variables, which amounts to a problem of *observer* design. The fact that a solution can exist is characterized by the so-called *observability* property, and in the case of induction motors, due to the nonlinear nature of the dynamics, this property depends on the operating conditions.

In addition, the problem is made even more difficult by the fact that model parameters themselves can change during operation, or just not be very well known. From this, the problem of state variable reconstruction extends to that of *parameter identification*.

The main point of this chapter is to review those three items: (1) observability, (2) state observer, state, and (3) parameter estimation, mostly in the spirit of former studies (Besançon 2001; Besançon *et al*. 2001; Besançon and Ţiclea 2003; Ţiclea 2006; Ţiclea and Besançcon 2006a, b, 2008). Those problems are also put in the perspective of some of the main studies that have been published in that respect over the last two decades.

Section 4.2 thus first recalls the problem(s) statement and some related references, while Section 4.3 focuses on some observer solutions and related conditions. Section 4.4 then

AC Electric Motors Control: Advanced Design Techniques and Applications, First Edition. Edited by Fouad Giri.

provides some illustrative simulation results accordingly, and some conclusions are finally given in Section 4.5.

4.2 Motor Representation and Estimation Issues

4.2.1 Problem Statement

The estimation issues and possible solutions will be settled for a model under the assumption of symmetric operation with uniform values of parameters over each phase.

Under those assumptions, electrical variables can be represented by two components, here chosen to be related to a frame rotating with the rotor, and denoted by α and β. Notations i and ϕ will be used to respectively refer to currents and fluxes, and subscripts s and r will respectively refer to the stator and the rotor. With the additional notation ω_m for the machine rotor speed, we can summarize state variables, for instance, by the following set:

$i_{s\alpha}, i_{s\beta}$ – the components of the stator current phasor i_s,
$\phi_{s\alpha}, \phi_{s\beta}$ – the components of the stator flux phasor ϕ_s,
ω_m – the mechanical speed,

while inputs correspond to the components $u_{s\alpha}$ and $u_{s\beta}$ of the stator voltage phasor u_s.

The corresponding state equations finally read as

$$\begin{aligned}
\tfrac{d}{dt} i_s &= \left[-\left(\tfrac{R_r}{\sigma L_r} + \tfrac{R_s}{\sigma L_s} \right) \mathcal{I} + p\omega_m \mathcal{J} \right] i_s + \left[\tfrac{R_r}{\sigma L_s L_r} \mathcal{I} - p \tfrac{1}{\sigma L_s} \omega_m \mathcal{J} \right] \phi_s + \tfrac{1}{\sigma L_s} u_s, \\
\tfrac{d}{dt} \phi_s &= -R_s i_s + u_s, \\
\tfrac{d}{dt} \omega_m &= -\tfrac{F}{J} \omega_m + p \tfrac{1}{J} (i_{s\beta} \phi_{s\alpha} - i_{s\alpha} \phi_{s\beta}) - \tfrac{1}{J} T_l,
\end{aligned} \tag{4.1}$$

where L stands for inductance, R stands for resistance (with indexes s and r still referring to the stator and the rotor, respectively), $\sigma = 1 - \frac{{L_M}^2}{L_s L_r}$ with L_M the maximum mutual inductance between one stator and one rotor winding, and

$$\mathcal{I} = \begin{pmatrix} 1 & 0 \\ 0 & 1 \end{pmatrix}, \quad \mathcal{J} = \begin{pmatrix} 0 & -1 \\ 1 & 0 \end{pmatrix}. \tag{4.2}$$

In addition, T_l denotes the load torque, J the total inertia momentum (rotor plus load), and F the friction coefficient. Finally, in both electrical and mechanical parts, p represents the number of pairs of poles.

On the basis of such a modelling, the estimation problems depend on the information we have on the model; for a classical state reconstruction problem, the model parameters are assumed to be pretty well known, and the problem is fully defined by the available measurement upon dynamical variables. In general, such a measurement, usually denoted by y, will be a vector at least corresponding to stator currents i_s. It often further includes ω_m, but the problem of avoiding the use of any rotor speed sensor has also motivated a lot of work.

In addition, the estimation problem can extend to the model parameters themselves, which may not be accurately known, or vary significantly under operation (typically under heating effect); a lot of work has been dedicated to the problem of rotor time constant estimation in that respect for instance.

A brief overview on existing results about estimation issues in induction motors is proposed in next subsection.

4.2.2 Short Literature Review

Complex instrumentation placed on an induction motor would only cancel the major strength of this device—simplicity. It is the reason why one can hardly, if ever, see flux transducers in induction-motor-driven variable speed industry applications. On the other hand, flux information is crucial for the control of the drive, so flux estimation is an inescapable part of any variable-speed control design. Moreover, speed sensors might also be undesirable, leaving the stator current as the only output information that can be used for state estimation. Notice then that "sensorless" in the context of induction motor usually means "speed-sensorless."

When the mechanical speed is available through measurement, the measured values can be injected into the differential equation (4.1) making the model linear time varying, which therefore allow for a possible *Kalman-like* observer (see Section 4.3). However, under measured speed conditions, it is possible to build effective reduced-order observers for flux only, which, as opposed to a Kalman solution, may employ a constant gain in the correction term (Verghese and Sanders 1988). Passivity can also be exploited in order to build flux observers when the speed is measured (Martin and Rouchon 2000).

When the rotor speed is not available through measurements, the observation problem becomes significantly complex. Not only the model is now nonlinear and requires some dedicated observer design, but studies such as Canudas de Wit *et al*. (2000) and Ibarra Rojas *et al*. (2004) show that under zero synchronous speed and constant mechanical speed the systems becomes unobservable (in fact, in this case there is no information from the rotor side contained in the stator currents). The locus of the unobservability points is a straight line in the speed-torque plane—called the *unobservability line* of the motor—that runs through the origin of the plane and lies in the quadrants that correspond to a generator operating mode of the motor. Notice that, under closed-loop operation with load torques falling in the range safely handled by the motor (acting as a brake), such observability losses usually happen at rather low mechanical speeds. Based on this idea, some authors claim speed-sensorless estimation results with respect to low mechanical speed situations, which is actually a rather long stretch from the precise unobservability conditions; in reality, at *any* constant speed, the synchronous speed is the one responsible for the presence of information exchange between rotor and stator.

Any effort to accurately observe the state of the induction motor is futile if the parameters of the system are not known with sufficient precision. Unfortunately, this is likely to be the case during operation; in particular, the parameters that are the most susceptible to be uncertain are the resistances, as they (significantly) change with the temperature. Therefore, a realistic induction motor observation problem would actually be a joint state and parameter estimation problem. It is worth noticing at this point that it is impossible to identify all five fundamental electrical parameters from the input-output data, even when using speed measurements. In reality, it is only possible to estimate variables that are in bijection with $\frac{L_r}{R_r}$, R_s, L_s, and σ (Besançon *et al*. 2001). Some potential sources of errors in simultaneous state and parameter estimation for induction motors with equations expressed in a stator-fixed reference

frame and with known stator resistance are pointed out in the sensitivity study performed by Alamir (2002).

The challenges raised by the induction motor observation problem motivated many research groups into efforts to design effective solutions, from both pure observation and observation in support of some particular control strategy perspectives. This generated in time an enormous body of literature on the subject of induction motor estimation and control, such that it is impossible to give a complete account of all existing solutions. We shall therefore limit ourselves here to mention the most relevant ideas that have been pursued in these efforts. Examples of references will be provided, which can be used as entry points for the interested reader to explore the literature.

Some factory values issued from equivalent circuit identification through some standard tests (Chapman 2005) are normally available for the parameters of electric machines. However, for improved accuracy, recursive output error identification methods (e.g., Børsting *et al*. 1994), linear least squares methods (e.g., de Souza Ribeiro *et al*. 2000; Zamora and García Cerrada 2000; Alonge *et al*. 2001) and nonlinear least squares methods (e.g., Wang *et al*. 2005; Oteafy *et al*. 2009) can also be applied, some without speed measurement, and with the advantage that they can be adapted to online operation for critical parameter monitoring.

Moving to simultaneous state and parameter estimation, the so-called extended Kalman filter (EKF) is a much employed solution that can accommodate a wide range of state and parameter combinations to be estimated, as the reader can discover by exploring the literature; this flexibility is however paid in rather low returned performance. Very popular in the 1990s, the EKF also captured the attention of researchers in recent years (Alonge and D'Ippolito 2010).

One of the major sources of problems with the EKF comes from the fact that the covariance of the estimation is propagated through a linear model, which leads to rather important inaccuracies. The unscented Kalman filter (UKF) adopts a superior technique to propagate this quantity, which leads to improved accuracy (although some empirical tuning is involved). See Akin *et al*. (2006) and Jafarzadeh *et al*. (2012) for its application to induction motor state estimation.

By exploiting the fact that the induction motor model is linear with respect to the current and flux, one class of methods considers the speed as an unknown parameter (constant or time varying) and focuses on building some *speed-adaptive* flux observers (Kubota *et al*. 1993). Efforts have also been made to include the adaptation of some parameters (resistances) along with the adaptation of the speed. Recent advances on these methods as well as a glimpse at the associated state-of-the-art can be found in Zaky 2012). A somewhat related class of methods uses reference models of flux or current dynamics in order to generate error signals that can be used to adapt the value of the mechanical speed. An overview on some of the methods that exploit this (model reference adaptive system (MRAS)) concept, as well as related recent advances, can be found in Orlowska-Kowalska and Dybkowski (2010).

Moving to nonlinear design techniques, the idea of adapting some parameters also appears in the design of sliding-mode observers for induction motors (e.g., Rao *et al*. 2010). For state estimation only, nonlinear interconnected observers are also reported (Ghanes *et al*. 2010). Efforts were also aimed at building nonlinear controllers that include adaptation mechanisms for the unmeasured states (speed, flux) and for some parameters (load torque, resistances). While solutions relied at first on open-loop integration of currents to compute an estimation of the flux (just like some of the early sliding-mode designs), results that did not employ

such integration started to emerge in recent years. For instance, speed-sensorless nonlinear controllers with local convergence have been designed with torque adaptation in Montanari *et al*. (2006) and torque and rotor resistance in Marino *et al*. (2008).

In the present chapter, we rather focus on a versatile solution to the construction of observation solutions for induction motors that can be adapted to the estimation of *any* combination of state variables and electrical parameters. This solution relies on the immersion of the induction motor model into an affine structure with respect to the unknowns; a Kalman-like observer can then be used for the observation of the system under this new (inherently redundant) representation.

This methodology is introduced in the sequel, after a review on possible observer approaches for estimation configurations of increasing complexity. Further details on the related observer tools can be found in Besançon (2007) and references therein.

4.3 Some Observer Approaches

4.3.1 Estimation under known and constant Speed and Parameters

In the case when the mechanical speed is known and assumed to be constant, or varying in a slow enough way, as well as all parameters, the motor modeling can be reduced to the current and flux dynamics, under the form of a classical linear time-invariant state-space representation

$$\begin{aligned} \dot{x}(t) &= Ax(t) + Bu(t), \\ y(t) &= Cx(t), \end{aligned} \tag{4.3}$$

where x gathers components of i_s, ϕ_s, and $y = i_s$, and matrices A, B, C directly follow from this fact and equation (4.1).

For such a model, the possibility to build a state observer is directly related to the observability property, which is classically characterized by the so-called Kalman rank condition

$$rank\mathcal{O} = n,$$

where n is the dimension of the state vector ($n = 4$ here), and $\mathcal{O} = \begin{pmatrix} C \\ CA \\ \vdots \\ CA^{n-1} \end{pmatrix}$ is the observability matrix.

This condition is clearly satisfied here whatever the operating conditions are (in particular the value of the speed), which means that an observer can be built under the classical form

$$\dot{\hat{x}}(t) = A\hat{x}(t) + Bu(t) - K[C\hat{x}(t) - y(t)], \tag{4.4}$$

where the observer gain K is designed either by pole placement (as in Luenberger approach) or by linear quadratic optimization (as in Kalman approach).

Using a forgetting factor for instance, Kalman equations can take the following form:

$$\begin{aligned} \dot{S}(t) &= -\lambda S(t) - A^T S(t) - S(t)A + C^T C;\ S(0) > 0; \\ K(t) &= S^{-1}(t)C^T; \end{aligned} \tag{4.5}$$

for a positive tuning parameter λ.

Notice that in any other situation, the estimation problem a priori becomes a *nonlinear problem*. It can in general be approached via a so-called *EKF* technique, namely the application of Kalman equations to a model linearized along the trajectories currently estimated by the observer, but with the limitations of the underlying *approximation* that is made via this linearization.

Depending on the specific situation under consideration however, some *exact* linear-like approaches can alternatively be applied, as described in next subsections.

4.3.2 Estimation under known Speed and Parameters

In the case when the speed variation may be significant, but remains measured, its measurement can be injected in the observer so as to keep a linear structure for the estimation error; in this situation, the speed variation is to satisfy some appropriate excitation condition so that the convergence of an observer based on Kalman equations is still guaranteed.

In that case, model (4.1) can again be reduced to state variables of i_s and ϕ_s as in equations (4.3), but now with a matrix $A = A(\omega_m)$ varying according to the rotor speed variations $\omega_m(t)$.

This means that the model structure is still linear, but now *time varying*, and consequently, Kalman equations (e.g., as in equation (4.5) can still provide the basis for an observer design, provided that the time-variation guarantees boundedness of $A(\omega_m)$, and *uniform complete observability* in the following sense:

$$\int_t^{t+T_0} \Phi_{\omega_m}^T(\tau, t) C^T C \Phi_{\omega_m}(\tau, t) d\tau \geq \alpha I, \tag{4.6}$$

for some $T_0, \alpha > 0$, any $t \geq t_0$ for some $t_0 \geq 0$, and Φ_{ω_m} the transition matrix of system $\dot{\zeta}(t) = A(\omega_m(t))\zeta(t)$.

Under this condition, an observer of the form (4.4) is again possible, where K is computed as in Kalman equations (4.5).

4.3.3 Estimation under unknown Speed and known Parameters

In the case when the speed is unknown and varying, then its dynamical equation is to be taken into account in the model for observer design (as in model (4.1). In this situation, the model becomes *nonlinear*, and the observer design is now subject to a *nonlinear observability condition*, corresponding to a rank condition based on the so-called *observation space* (Hermann and Krener 1977).

For the model rewritten as

$$\begin{aligned} \dot{x}(t) &= f(x(t)) + g(x(t))u(t) =: f_u(x(t)), \\ y(t) &= h(x(t)), \end{aligned} \tag{4.7}$$

where x now gathers i_s, ϕ_s, and ω_m, while $y = i_s$, and f, g, and h result from model (4.1), the observability rank condition (at x) reads

$$rank[d\mathcal{O}_h(x)] = n,$$

(with $n = 5$ now), where $\mathcal{O}_h$ denotes the *smallest real vector space containing the output function h and closed under Lie derivation*[1] *along* f_u for $u \in \mathbb{R}^m$ (*observation space*), and $d\mathcal{O}_h(x)$ the set of differential forms of functions of the observation space at x.

When applied to model (4.1), the inspection of this rank condition can lead to conditions for *structural* observability of the motor (Canudas de Wit *et al*. 2000). In particular, it results that observability can be lost under special conditions (see also Ibarra Rojas *et al*. 2004), when the speed is not measured (so-called *sensorless case*), corresponding to the notion of *unobservability* "at zero (low) speed" for instance, as it is commonly referred to in the literature. In fact, a condition for unobservability is typically given by the case of *zero synchronous speed and constant rotor speed*, yielding to a so-called *unobservability line* in the plane relating the electromechanical torque T_{em} to the rotor speed ω_m

$$\frac{R_r}{p\phi_r^T\phi_r} T_{em} + \omega_m = 0,$$

where $\phi_r = \frac{L_r}{L_m}\phi_s + \frac{L_s L_r}{L_m}\sigma i_s$ denotes the rotor flux, and

$$T_{em} = p i_s^T \mathcal{J} \phi_s, \tag{4.8}$$

with notations of equation (4.2).

In practice, this problem may be overcome by fluctuations, for instance due to the noise reinjected by feedback, or the inverter harmonic—omitted in the modeling considered here.

A possible observer solution for speed reconstruction is presented in the next subsection when the estimation problem is also extended to the case of possible unknown parameters.

[1]The Lie derivative of a function $h : \mathbb{R}^n \to \mathbb{R}$ along some $f : \mathbb{R}^n \to \mathbb{R}^n$ of components f_i, is defined for any $x \in \mathbb{R}^n$ of components x_i, by $L_f h(x) = \sum_{i=1}^{n} \frac{\partial h}{\partial x_i} f_i(x)$ (Isidori, 1995).

4.3.4 Estimation in the presence of unknown Speed and/or Parameters

Taking into account possible unknown—or slowly varying—parameters in model (4.1), and gathering them into a vector θ, the model becomes

$$\begin{aligned} \dot{x}(t) &= f_{un}(x(t), \theta) + g_{un}(x(t), \theta)u(t), \\ y(t) &= h(x(t)), \end{aligned} \tag{4.9}$$

for some uncertain f_{un} and g_{un} depending on vector θ.

This model can typically be rewritten in an extended form as

$$\begin{aligned} \dot{x}(t) &= f_{un}(x(t), \theta) + g_{un}(x(t), \theta)u(t), \\ \dot{\theta} &= 0, \\ y(t) &= h(x(t)), \end{aligned} \tag{4.10}$$

for which an EKF could be tried.

Alternatively, one can look for an appropriate transformation to rewrite this extended model again in a linear-like structure as follows:

$$\begin{aligned} \dot{X}(t) &= A(u(t), y(t))X(t) + B(u(t), y(t)), \\ y(t) &= CX(t), \end{aligned} \tag{4.11}$$

for which an *exact* Kalman Filter applies, and converges under an excitation condition similar to the one in inequality (4.6).

Remember that a formal study on the possibility to identify electrical parameters in the model can be found in Besançon *et al*. (2001), and that it appears that a set of four parameters, in bijection with

$$\frac{R_r}{L_r}, \quad R_s, \quad L_s, \quad \sigma$$

is indeed *structurally* identifiable, and that this result extends to the problem of simultaneous state estimation.

A significant study on appropriate transformation of model (4.1) into the form (4.11) (even including the load torque T_l in the parameters to be estimated) can be found in Ţiclea and Besançon (2006b), and is briefly recalled hereafter.

4.4 Some Illustration Results

This section presents some simulation results in order to illustrate the performance of the estimation method presented here. The main idea here is to summarize some appropriate transformations, and show that the necessary excitation level required by the observer can be available during normal operation within a closed-loop configuration that includes a voltage inverter. A

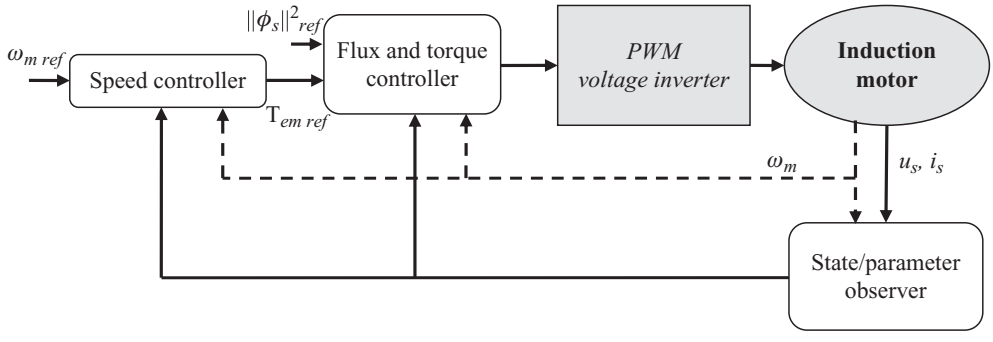

Figure 4.1 Setup for observer simulations. PWM, pulse-width modulation

typical configuration is given by the speed control scheme of Figure 4.1 hereafter, which is used as a test bench for our estimation method.

Within this setup, the behavior of the induction motor is implemented through equation (4.1) with parameters taken from an experimental platform available at GIPSA-lab, which is built around a two-pole induction motor with 7.5 kW rated power, 1450 rpm rated speed and 50 Nm rated torque. The values of the electrical parameters that the observer will try to estimate are as follows:

$$\begin{aligned} L_s &= 0.097\ \text{H}, \quad L_r = 0.091\ \text{H}, \quad M = 0.091\ \text{H}, \\ R_s &= 0.63\ \Omega, \quad R_r = 0.4\ \Omega. \end{aligned}$$

As far as the mechanical parameters are concerned, their values correspond to

$$J_m = 0.22\ \text{kg m}^2, \quad f_v = 0.001\ \text{N s/rad},$$

and are supposed to be known at all times.

The input of the induction motor is a PWM-like waveform generated through the model of a three-bridge voltage source inverter with ideal switch characteristics (e.g., no commutation delay) based on a vector control strategy. The reference vector for the inverter is in its turn generated by a torque and flux controller, designed by using available input-output (exact) linearization techniques applied to induction motors (von Raumer *et al*. 1994); the flux norm reference is set to 1 Wb, while the reference for electromechanical torque (as defined in equation (4.8) is provided by a (linear) PI speed regulator.

This strategy is proposed as an example of model-based control synthesis dependent on online estimations, that can illustrate the integration of the proposed observation solution into a closed-loop configuration. In fact, for all the variables involved in the control law that are not initially known, estimated values are used.

In the simulations, the measured signals fed to the observer and to the regulators are affected by measurement noise with sufficiently large spectrum so that it can be assimilated to white noise, with 10 mV peak value for stator voltages, 40 mA peak value for stator currents, and 0.01 rad/s for mechanical speed.

As far as the observer is concerned, note that the exponential forgetting factor recalled earlier admits both continuous-time and discrete-time formulations. In addition, both formulations can be specialized to simultaneous state and parameter estimation, yielding adaptive observers. We shall limit ourselves to present simulations involving the continuous-time exponential forgetting factor observer. See Ţiclea and Besançon (2008) for results with the continuous-time adaptive observer, Ţiclea and Besançon (2009) for the discrete-time exponential forgetting factor observer, and Ţiclea and Besançon (2012) for the discrete-time adaptive observer version.

For the transformation procedures summaries, the following notations will be used: y for stator currents of model (4.1) and z for stator fluxes, each of them being a vector of dimension 2, with components y_i and z_i, $i = 1, 2$, respectively.

In addition, let us define the following set of parameters (of a vector θ):

$$\begin{aligned} &\theta_1 := \tfrac{R_r}{\sigma L_r}, \quad \theta_2 := \tfrac{R_s}{\sigma L_s}, \quad \theta_3 := \tfrac{R_r R_s}{\sigma L_r L_s}, \\ &\theta_4 := \tfrac{1}{\sigma L_s}, \quad \theta_5 := \tfrac{R_r}{\sigma L_r L_s}, \quad \theta_6 := R_s, \quad \theta_7 := T_l. \end{aligned} \tag{4.12}$$

On this basis, the main transformations of interest can be recalled, and more details can be found in Ţiclea (2006) and Ţiclea and Besançon (2006b).

4.4.1 State and Parameter Estimation under known Speed

In the case when the rotor speed is known, but electrical parameters are to be estimated together with the state variables and the load torque, the following procedure can be used:

$$\text{Set} \quad Z_1 := \theta_5 z;\ Z_2 := \theta_4 z.$$

Then it can be checked that the extended vector

$$X_1 := \begin{pmatrix} y \\ z \\ Z_1 \\ Z_2 \\ \omega_m \\ \theta \end{pmatrix}$$

satisfies a new state representation of the form

$$\begin{aligned} \dot{X}_1 &= A_1(u, y, \omega_m) X_1 + B_1 u, \\ y &= C_1 X_1, \end{aligned}$$

for appropriate matrices A_1, B_1, and C_1.

An observer based on Kalman equations can then be designed. Some corresponding illustrative simulation results are presented in Figures 4.2, 4.3, and 4.4 where the speed tracking, torque estimation, and flux and parameter estimation errors can be seen, respectively. From those figures, it is clear that the speed indeed tracks its reference, while the torque as well as the flux components and the electrical parameters are well estimated.

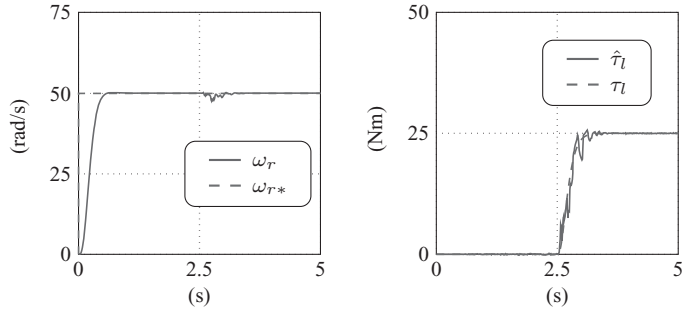

(a) Speed tracking

(b) Load torque evolution and estimation

Figure 4.2 Evolutions of mechanical variables under speed-sensed control with unknown parameters

4.4.2 State and Speed Estimation under known Parameters

In the case when the parameters are known, but only stator currents are measured, both the set of electrical state variables and the rotor speed can be estimated following a similar procedure as before. One can indeed check here that

$$X_2^T := \begin{pmatrix} y^T & z^T & \omega_m & \omega_m z^T & z_1^2 & z_2^2 & z_1 z_2 & T_l z^T & T_l \end{pmatrix}^T$$

now yields a state representation of the form

$$\begin{aligned} \dot{X}_2 &= A_2(u, y)X_2 + B_2 u, \\ y &= C_2 X_2, \end{aligned}$$

for new matrices A_2, B_2, and C_2.

Related estimation results are given as follows: the considered speed reference profile is presented in Figure 4.5 and the load torque evolution profile in Figure 4.6. Those figures also show the actual speed against the reference and the estimated load torque against the simulated one. The corresponding error evolution for all the estimated state variables can be seen in Figure 4.7.

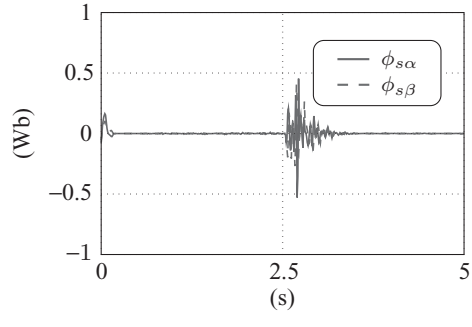

Figure 4.3 Evolution of flux estimation error under speed-sensed control with unknown parameters

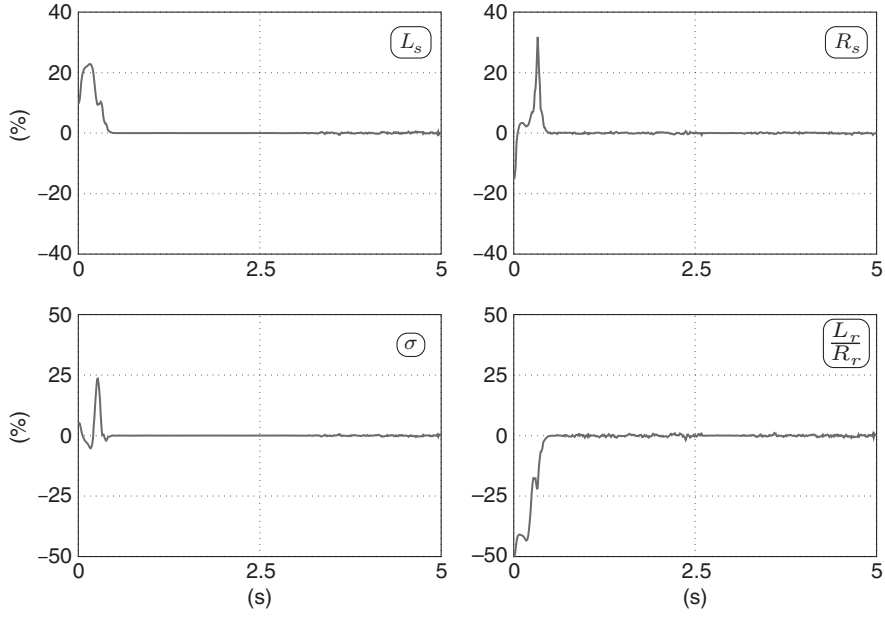

Figure 4.4 Relative parameter estimation errors under speed-sensed estimation

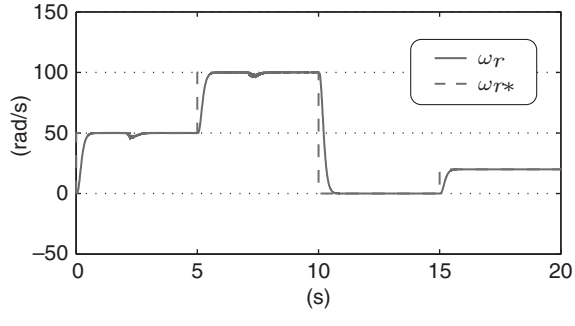

Figure 4.5 Speed tracking under speed-sensorless control with known parameters

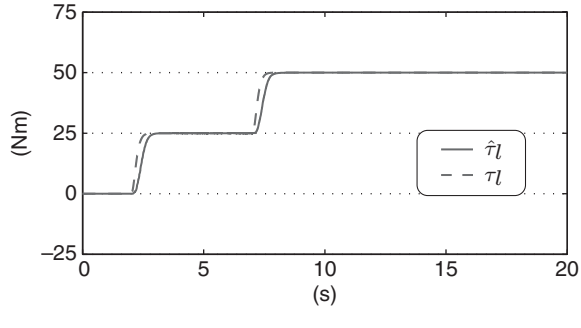

Figure 4.6 Speed-sensorless load torque estimation with known parameters

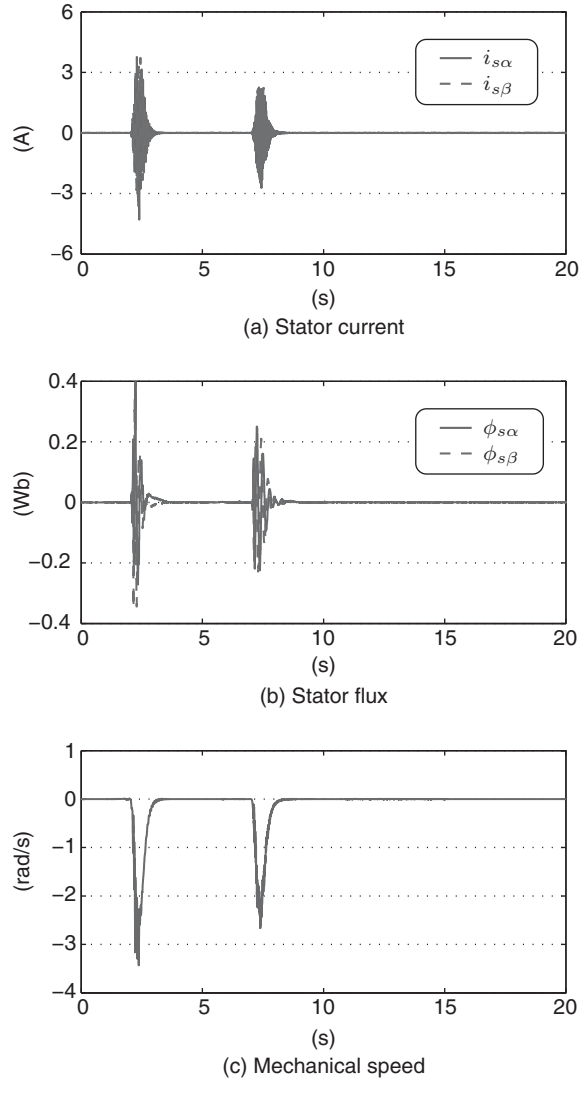

Figure 4.7 State estimation errors under sensorless-speed estimation with known parameters

4.4.3 State, Parameter, and Speed Estimation

In the case when both the rotor speed and the set of electrical parameters are not known, they can be estimated together with the remaining variables by now considering the following transformation:

$$X_3^T := \begin{pmatrix} y^T & z^T & Z^T & \omega_m Z_2^T & T_l Z_2^T & \xi^T & \bar{\theta}^T \end{pmatrix},$$

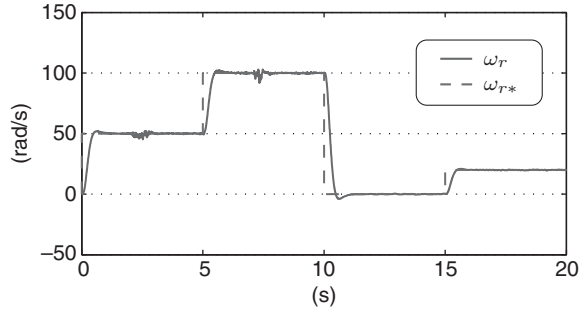

Figure 4.8 Speed tracking under speed-sensorless control with unknown parameters

with

$$Z := \begin{pmatrix} Z_1^T & Z_2^T & \theta_2 z^T \end{pmatrix}^T, \quad \xi := \begin{pmatrix} \omega_m & \theta_4 z_1^2 & \theta_4 z_2^2 & \theta_4 z_1 z_2 & \theta_2 \omega_m & \theta_4 \omega_m \end{pmatrix}^T,$$

and $\bar{\theta}$ made of θ together with $R_s\theta_2$, $T_l\theta_2$, and $T_l\theta_4$.

This new vector can indeed be checked to satisfy a new representation again of the form

$$\begin{aligned} \dot{X}_3 &= A_3(u, y)X_3 + B_3 u, \\ y &= C_3 X_3, \end{aligned}$$

for some matrices A_3, B_3, and C_3.

Some related simulation results can be found in Figures 4.8, 4.9, 4.10, and 4.11. In those simulations, one point is to show how the observer reacts to perturbations—it is therefore considered that the parameters are perfectly known at $t = 0$ (for instance, following preliminary open-loop tests with measured speed or not). The speed reference profile is now presented in Figure 4.8 along with the actual evolution of the speed. The associated load torque is presented in Figure 4.9 along with the estimated value of this quantity. Figure 4.10 presents the evolution

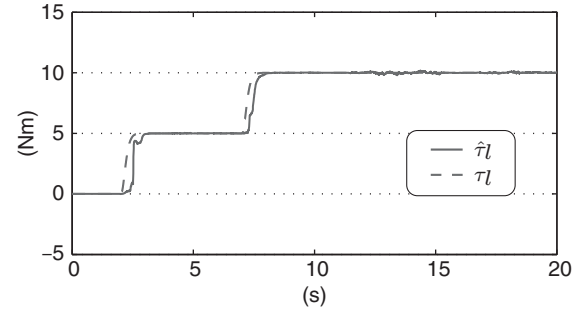

Figure 4.9 Speed-sensorless load torque estimation with unknown parameters

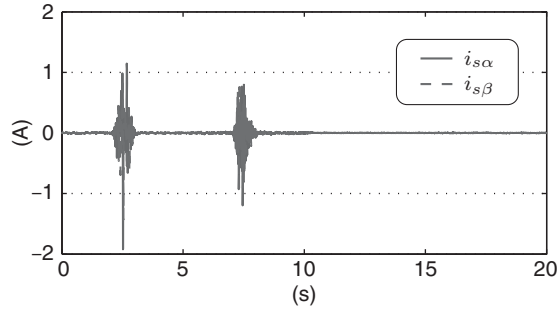

(a) Stator current

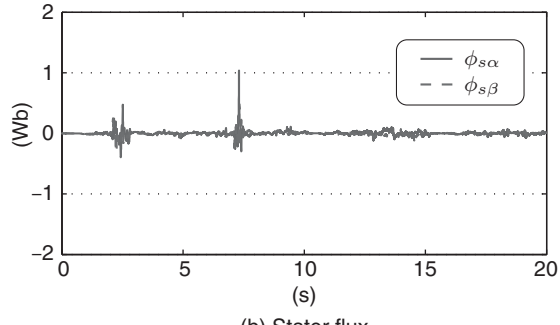

(b) Stator flux

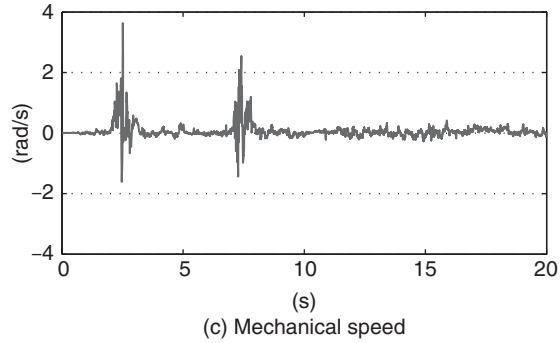

(c) Mechanical speed

Figure 4.10 State estimation errors under speed-sensorless estimation with unknown parameters

of the state estimation errors, while Figure 4.11 presents the relative errors in the estimations of the electrical parameters.

From these evolutions it appears that the reaction of the observer to perturbations is reflected to a significant degree into the estimations of the parameters before everything settles back to reasonable estimation errors. One possible remedy is to slow down the update actions with respect to the estimation of the parameters by employing an adaptive observer; see Ţiclea and Besançon (2008) for an exploration of this idea.

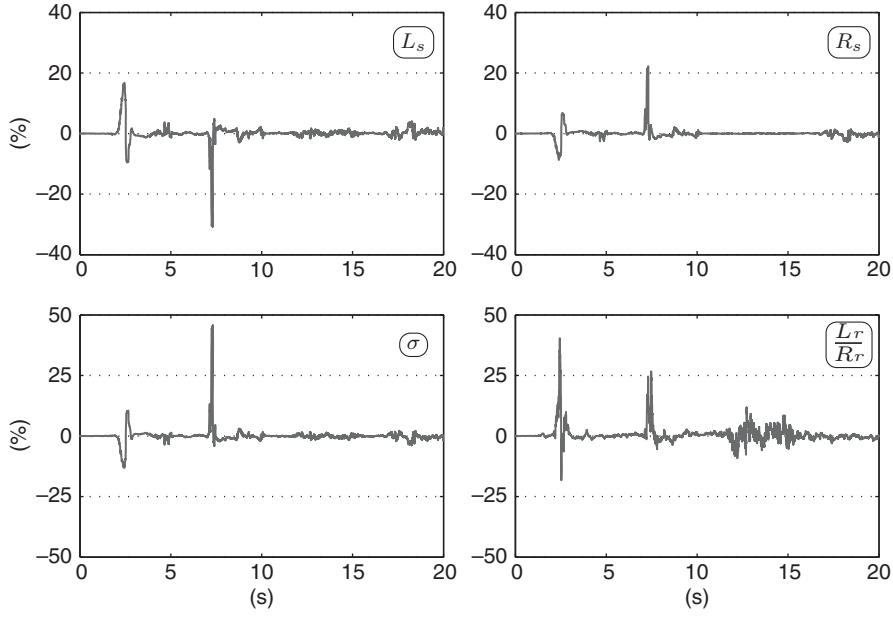

Figure 4.11 Relative parameter estimation errors under speed-sensorless estimation

4.4.4 Estimation close to Unobservability

As a last set of illustrative results, let us here consider the case of an operation close to this *unobservability line* mentioned in Section 4.3.3, with the requirement that the parameters need to be monitored (i.e., the preceding working configuration). Specifically, the mechanical speed is regulated to the value of 0.5 rad/s under the action of a driving torque that determines zero synchronous speed at steady state. For the values of parameters that are considered here, this gives a load torque of about −4.4 Nm.

The stator flux evolution obtained in those conditions is presented in Figure 4.12. In order to illustrate the behavior of the observer, we limit ourselves to the presentation of the evolution

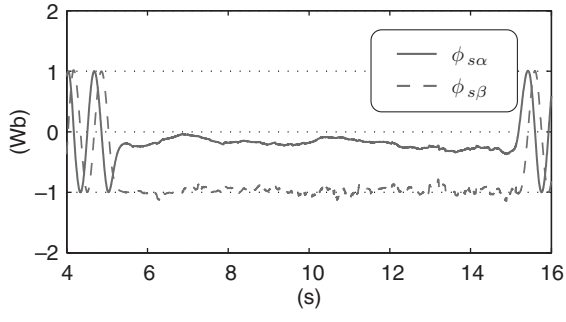

Figure 4.12 Stator flux evolution under speed-sensorless control close to the unobservability line

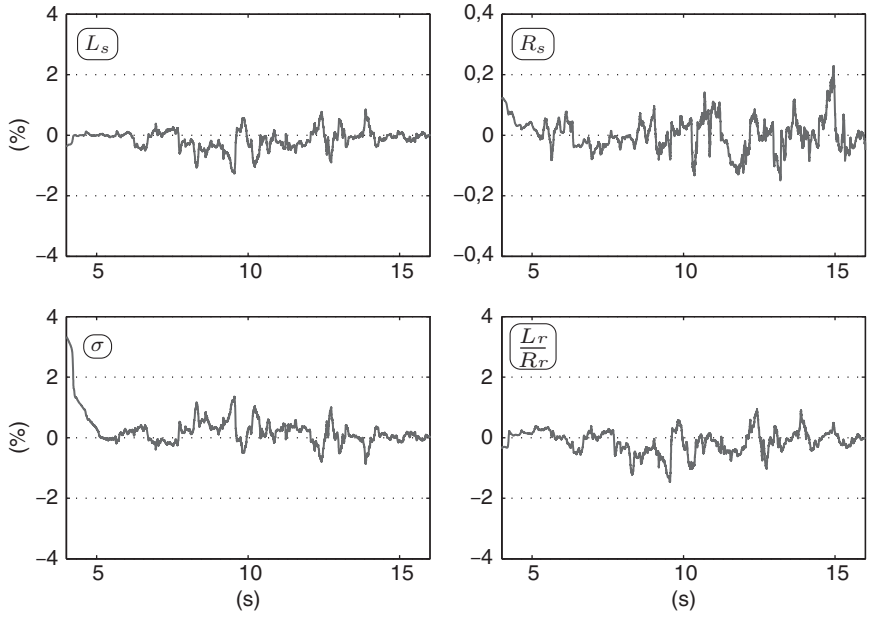

Figure 4.13 Relative estimation errors for the parameters under operation close to the inobservability line

of the relative estimation errors for the parameters in Figure 4.13. It is obvious that the unobservability condition is not rigorously fulfilled, as there are slight stator flux variations, mainly due to noise and errors propagating through the loop. It is nevertheless an operation close to the unobservability line and the results show that a sufficient excitation level can ensure observer stability even under conditions in which, theoretically, the system is on the verge of unobservability. It is worth remembering at this point that in the case of the exponential forgetting factor observer, the least singular value of S represents an indicator of the quantity of meaningful information that is present in the signals fed to the observer. This indicator can be monitored in real time in order to detect potentially critical situations for the observer.

4.5 Conclusions

In this chapter, various estimation problems related to the classical model of induction motors have been reviewed, at the light of (nonlinear) observer approaches for possible solutions. They include the basic problem of flux reconstruction, from stator currents and rotor speed measurements, as well as the analysis of the widely studied situation of estimation *without any speed sensor* (so-called sensorless configuration in the literature). The latter has also been extended to the case of possible unknown parameters, and various simulation results have been provided accordingly.

Although the formal analysis has been mostly provided on the basis of a continuous-time representation, some possible extensions to discrete-time have also been highlighted. Finally,

it should be emphasized that similar approaches can also be of interest for other machines, like synchronous ones for instance.

References

Akin B, Orguner U, Ersak A, and Ehsani M (2006) Simple derivative-free nonlinear state observer for sensorless AC drives. *IEEE/ASME Transactions on Mechatronics*, **11**(5), 634–643.

Alamir M (2002) Sensitivity analysis in simultaneous state/parameter estimation for induction motors. *International Journal of Control*, **75**(10), 753–758.

Alonge F and D'Ippolito F (2010) Robustness analysis of an extended Kalman filter for sensorless control of induction motors. *Proceedings of the 2010 IEEE Symposium on Industrial Electronics*, pp. 3257–3263.

Alonge F, D'Ippolito F, and Raimondi FM (2001) Least squares and genetic algorithms for parameter identification of induction motors. *Control Engineering Practice*, **9**(6), 647–657.

Besançon G (2001) On-line full state and parameter estimation in induction motors and application in control and monitoring. *Proceedings of the 2001 European Control Conference*.

Besançon G and Ţiclea A (2003) Simultaneous state and parameter estimation in asynchronous motors under sensorless speed control. *Proceedings of the 2003 European Control Conference*.

Besançon G, Besançon-Vodă A, and Bornard G (2001) A note on identifiability of induction motors. *Proceedings of the 2001 European Control Conference*.

Besançon G (2007) *Nonlinear Observers and Applications* Number 363. *Lecture Notes in Control and Information Sciences*. Springer.

Børsting H, Knudsen M, Rasnussen H, and Vadstrup P (1994) Estimation of physical parameters in induction motors. *Proceedings of the 10th IFAC Symposium on System Identification*, Vol. 2, pp. 553–558.

Canudas de Wit C, Youssef A, Barbot J, *et al.* (2000) Observability conditions of induction motors at low frequencies. *Proceedings of the 39th IEEE Conference on Decision and Control Sydney*, pp. 2044–2049.

Chapman SJ (2005) *Electric Machinery Fundamentals*, 4th edn. McGraw-Hill, New York.

de Souza Ribeiro LA, Brandão Jacobina C, Nogueira Lima AM, and Cunha Oliveira A (2000) Real-time estimation of the electric parameters of an induction machine using sinusoidal PWM voltage waveforms. *IEEE Transactions on Industry Applications*, **36**(3), 743–754.

Ghanes M, Barbot JB, de Leon-Morales J and Glumineau A (2010) A robust sensorless output feedback controller of the induction motor drives: new design and experimental validation. *International Journal of Control*, **83**(3), 484–497.

Hermann R and Krener AJ (1977) Nonlinear controllability and observability. *IEEE Transactions on Automatic Control*, **22**(5), 728–740.

Ibarra Rojas S, Moreno J, and Espinosa Pérez G (2004) Global observability analysis of sensorless induction motors. *Automatica*, **40**(6), 1079–1085.

Isidori A (1995) *Nonlinear Control Systems Communications and Control Engineering*, 3rd edn. Springer-Verlag.

Jafarzadeh S, Lascu C, and Fadali MS (2012) State estimation of induction motor drives using the unscented Kalman filter. *IEEE Transactions on Industrial Electronics*, **59**(11), 4207–4216.

Kubota H, Matsuse K, and Nakano T (1993) DSP based speed adaptive flux observer for induction motor applications. *IEEE Transactions on Industrial Applications*, **29**(2), 344–348.

Marino R, Tomei P, and Verrelli CM (2008) An adaptive tracking control from current measurements for induction motors with uncertain load torque and rotor resistance. *Automatica*, **44**(10), 2593–2599.

Martin P and Rouchon P (2000) Two simple flux observers for induction motors. *International Journal of Adaptive Control and Signal Processing*, **14**(2), 171–175.

Montanari M, Peresada S, and Tilli A (2006) A speed-sensorless indirect field-oriented control for induction motors based on high gain speed estimation. *Automatica*, **42**(10), 1637–1650.

Orlowska-Kowalska T and Dybkowski M (2010) Stator-current-based MRAS estimator for a wide range speed-sensorless induction-motor drive. *IEEE Transactions on Industrial Electronics*, **57**(4), 1296–1308.

Oteafy A, Chiasson J, and Bodson M (2009) Online identification of the rotor time constant of an induction machine *Proceedings of the 2009 American Control Conference*, pp. 4373–4378.

Rao S, Utkin V, and Buss M (2010) Design of first- and second-order sliding mode observers for induction motors using a stator-flux model. *International Journal of Control*, **83**(7), 1457–1464.

Ţiclea A (2006) *Techniques d'immersion pour l'estimation non linéaire. Application aux systèmes de puissance (In French).* PhD thesis. Institut National Polytechnique de Grenoble.

Ţiclea A and Besançon G (2006a) Observer design for state and parameter estimation in induction motors with simulation and experimental validation. *Proceedings of the 32nd Annual Conference of the IEEE Industrial Electronics Society*.

Ţiclea A and Besançon G (2006b) Observer scheme for state and parameter estimation in asynchronous motors with application to speed control. *European Journal of Control*, **12**(4), 400–412.

Ţiclea A and Besançon G (2008) On the state and parameter simultaneous estimation problem in induction motors. *Proceedings of the 17th IFAC World Congress*, pp. 11184–11189.

Ţiclea A and Besançon G (2009) State and parameter estimation via discrete-time exponential forgetting factor observer. *Proceedings of the 15th IFAC Symposium on System Identification*, pp. 1370–1374.

Ţiclea A and Besançon G (2012) Adaptive observer for discrete time state affine systems. *Proceedings of the 16th IFAC Symposium on System Identification*, pp. 1245–1250.

Verghese GC and Sanders SR (1988) Observers for flux estimation in induction machines. *IEEE Transactions on Industrial Electronics*, **35**(1), 85–94.

von Raumer T, Dion JM, Dugard L, and Thomas JL (1994) Applied nonlinear control of an induction motor using digital signal processing. *IEEE Transactions on Control Systems Technology*, **2**(4), 327–335.

Wang K, Chiasson J, Bodso M, and Tolbert LM (2005) A nonlinear least-squares approach for identification of the induction motor parameters. *IEEE Transactions on Automatic Control*, **50**(10), 1622–1628.

Zaky MS (2012) Stability analysis of speed and stator resistance estimators for sensorless induction motor drives. *IEEE Transactions on Industrial Electronics*, **59**(2), 858–870.

Zamora JL and García Cerrada A (2000) Online estimation of the stator parameters in an induction motor using only voltage and current measurements. *IEEE Transactions on Industry Applications*, **36**(3), 805–816.

5

State Observers for Active Disturbance Rejection in Induction Motor Control

Hebertt Sira Ramírez[1], Felipe González Montañez[2], John Cortés Romero[3], and Alberto Luviano-Juárez[4]

[1]*Department of Electrical Engineering, CINVESTAV-IPN, México*
[2]*Departamento de Energía, Universidad Autónoma Metropolitana, México.*
[3]*Department of Electrical and Electronic Engineering, Universidad Nacional de Colombia, Colombia*
[4]*UPIITA-IPN, México*

5.1 Introduction

Asymptotic estimation of perturbation inputs, with the aim of exactly, or approximately, canceling their influence on the system at the controller stage, has been treated in the existing literature under several headings: *disturbance accommodation control*, *active disturbance rejection control* (ADRC), and *intelligent Proportional–Integral–Derivative* (PID) *control*, also called, *model-free control*. In all these approaches, disturbances, whether state-dependent or not, are treated as a lumped single disturbance input that may be estimated online and then appropriately canceled by the controller. Roots of this line of work may be found in Shipanov (1939). Disturbance accommodation control is represented by the work of C.D. Johnson. Originally, the approach was cast in the context of linear systems (see Johnson 1971) and included a known linear model for the exogenous disturbances. The method, however, has been actively evolving, including extensions to discrete-time systems and to the decoupling of nonlinear systems (see Johnson (2008) for a survey). The ADRC method is represented by the works of the late Prof. Jingqing Han. The emphasis of this work lies on *nonlinear* observer-based disturbance estimation, for the canceling, and efficient time derivative calculations,

AC Electric Motors Control: Advanced Design Techniques and Applications, First Edition. Edited by Fouad Giri.

for the feedback (see, Han 2009). The original work of Han has been suitably extended and applied to various interesting technological fields by Z. Gao and his colleagues (see Gao 2001; Sun and Gao 2005; Gao 2006). The third methodology: model-free control, was developed by Fliess and Join (2008). This technique proposes controller design on the basis of one-dimensional, or at most two-dimensional, local phenomenological models (called *local ultra-models*) of the nonlinear plant. These models are online adapted to the actual plant via fast algebraic estimation and identification techniques characterized by frequent resettings. The theoretical support of this methodology stems from the differential algebraic viewpoint in linear and nonlinear systems (see Fliess *et al.* 2008). In recent years, the authors of this chapter have been involved in developing illustrative laboratory applications of the ADRC method for nonlinear systems using only linear feedback and linear observers, known as generalized proportional integral (GPI) observers, for simultaneous estimation of states and of nonlinear disturbances. The disturbances are viewed as an aggregation of exogenous and endogenous disturbances into a single time signal with no additional structure. The method thus proposes *global ultra-models* of the perturbed plant that require no online resettings. The approach is systematically used in the context of an input-output system description, regardless of the complexities of the nonlinear system. The method is circumscribed to either differentially flat systems, or to minimum phase systems (see Luviano-Juárez *et al.* 2010; Sira-Ramírez *et al.* 2009; Sira-Ramírez *et al.* 2012a; Sira-Ramírez *et al.* 2012b; Sira-Ramírez *et al.* 2012c).

GPI observers, a dual counterpart of GPI controllers (see Fliess *et al.* 1991), were introduced in Sira-Ramírez and Feliu-Battle (2011) in the context of sliding-mode observers for flexible robotics systems. The nonsliding version appears in Luviano-Juárez *et al.* (2010), as applied to chaotic systems synchronization. The linear GPI observer naturally incorporates a self-updating polynomial model of the overall disturbance effects as well as iterated output error integral injections aimed at attenuating the effects, on the estimation error dynamics, of lumped exogenous and state-dependent perturbation input signals present in the input-output model of the plant. GPI observers are capable of accurate online estimations of: (a) the output-related phase variables of the underlying pure integration input-output system obtained after disturbance cancelation, (b) the, nonlinear state-dependent, additive perturbation input signal itself, and (c) the estimation of a certain number of the perturbation input time derivatives (this allows a natural extension to the control of nonlinear input-delayed systems; Sira-Ramírez *et al.* 2010a).

This chapter is devoted to the GPI observer-based ADRC approach for trajectory tracking in induction motors subject to, both, external disturbance inputs and endogenous nonlinearities treated also as unknown disturbances. Two traditional control design techniques are cast into this context. Namely, the two stage (inner loop–outer loop) controller design and the direct armature voltage field-oriented controller. The fundamental advantage of this proposal lies in the single-handed cancelation of the effects of time-varying torques, and of unmodeled frictions and nonlinearities containing possibly uncertain parameters. For detailed background on induction motor control, we refer the readers to the excellent books by Trzynadlowski (1994), Leonhard (2001), Ortega *et al.* (1998), Chiasson (2005), and Marino *et al.* (2010). The chapter is organized as follows: Section 5.2 deals with the problem of controlling an induction motors using two observer-based ADRC loops, one for the current tracking task and a second one for the angular velocity regulation. Section 5.3 presents the armature voltage field-oriented controller for the decoupled regulation of the angular velocity and the flux magnitude. Both schemes present experimental results and comparisons with existing control strategies. Finally,

the Appendix contains some theoretical generalities about the active disturbance rejection (ADR) scheme and its relation to global ultra-models.

5.2 A Two-Stage ADR Controller Design for the Induction Motor

Consider the following model of the induction motor in a fixed stator frame:

$$J\frac{d\omega_m}{dt} = \frac{pM_{sr}}{L_r}\mathrm{Im}\left(i_s\overline{\phi_r}\right) - B\omega_m - T_L(t), \tag{5.1}$$

$$L_r\frac{d\phi_r}{dt} = -\left(R_r - jpL_r\omega_m\right)\phi_r + R_rM_{sr}i_s, \tag{5.2}$$

$$L_s\sigma\frac{di_s}{dt} = \frac{M_{sr}}{L_r^2}\left(R_r - jpL_r\omega_m\right)\phi_r - \gamma L_s\sigma i_s + v_s, \tag{5.3}$$

where ω_m is the shaft's angular velocity, i_s is the complex armature current, ϕ_r is the complex flux, v_s is the complex input voltage, and the variable $T_L(t)$ is the unknown, time-varying, load torque perturbation input. Also, the following auxiliary parameters are defined in terms of the machine parameters: $\sigma := 1 - M_{sr}^2/(L_sL_r)$; $\gamma := R_sL_r^2 + R_rM_{sr}^2/(L_s\sigma L_r^2)$. The following complex variable notation is used: $i_s = i_{s\alpha} + ji_{s\beta}$; $\phi_r = \phi_{r\alpha} + j\phi_{r\beta} = \psi_r e^{j\theta_\psi}$; and $v_s = v_{s\alpha} + jv_{s\beta}$, where $j = \sqrt{-1}$ is the imaginary unit, and $\overline{z}$ is the conjugate of z.

5.2.1 The Flux Simulator

Of all variables in the induction motor model, the rotor flux variable, ϕ_r, cannot be easily measured. For this reason, an observer is usually devised for the flux dynamics given in equation (5.2). In this case, the observer is simply given by a replica of the system itself (see Verghese and Sanders 1988; Martin and Rouchon 2000; Chiasson 2005). If the observer is proposed as

$$L_r\frac{d\hat{\phi}_r}{dt} = -\left(R_r - jpL_r\omega_m\right)\hat{\phi}_r + R_rM_{sr}i_s, \tag{5.4}$$

the estimation error, defined as $e_{\phi_r} := \phi_r - \hat{\phi}_r$, satisfies

$$L_r\frac{de_{\phi_r}}{dt} = -\left(R_r - jpL_r\omega_m\right)e_{\phi_r} \tag{5.5}$$

Consider the Lyapunov function candidate, $V(e_{\phi_r}) = \frac{1}{2}L_r|e_{\phi_r}|^2$. Then, along solutions of equation (5.5), $\dot{V}(e_{\phi_r}) = -R_r|e_{\phi_r}|^2 = -2\frac{R_r}{L_r}V(e_{\phi_r})$. Hence, the origin of the complex simulation error space, $e_{\phi_r} = 0$, is a globally asymptotic exponential equilibrium point for equation (5.5). The flux simulator variable, $\hat{\phi}_r$, will be used, henceforth, in place of the actual flux without further considerations. The stability theoretical issues of its presence in a stabilizing feedback loop has been thoroughly analyzed in the existing literature (see Hinkkanen (2004) and the references therein).

5.2.2 Formulation of the Problem and Background Results

The compact model in complex variables (5.1), (5.2), and (5.3) may be expanded to be written in the following form:

$$\begin{aligned} J\frac{d\omega_m}{dt} &= \tfrac{pM_{sr}}{L_r}\mathrm{Im}\left(i_s\psi_r e^{-j\theta_\psi}\right) - B\omega_m - T_L, \\ \frac{d}{dt}\psi_r^2 &= -2\frac{R_r}{L_r}\psi_r^2 + 2\frac{R_r M_{sr}}{L_r}\mathrm{Re}\left(i_s\psi_r e^{-j\theta_\psi}\right), \\ L_r\frac{d}{dt}\theta_\psi &= pL_r\omega_m + \frac{1}{\psi_r^2}R_r M_{sr}\mathrm{Im}\left(i_s\psi_r e^{-j\theta_\psi}\right), \\ L_s\sigma\frac{di_s}{dt} &= \frac{M_{sr}}{L_r^2}\left(R_r - jpL_r\omega_m\right)\psi_r e^{j\theta_\psi} - \gamma L_s\sigma i_s + v_s. \end{aligned} \tag{5.6}$$

The first two equations in (5.6) reveal an interesting indirect control decoupling property. The mechanical part of the system, represented by the angular velocity equation, is ruled by $\mathrm{Im}\left(i_s\psi_r e^{-j\theta_\psi}\right) = \mathrm{Im}\left(i_s\overline{\phi}_r\right)$, while the electromagnetic part, represented by the squared flux magnitude equation, is governed by $\mathrm{Re}\left(i_s\psi_r e^{-j\theta_\psi}\right) = \mathrm{Re}\left(i_s\overline{\phi}_r\right)$. Therefore, viewing the complex current i_s as auxiliary control inputs, both constitutive parts of the system can, in principle, be controlled independently of each other. This representation also establishes that the complex flux phase angle θ_ψ is largely determined by the manner in which the angular velocity is controlled via the stator currents.

5.2.3 Assumptions

- It is assumed that only the shaft's angular position θ_m is measured. The angular velocity ω_m and the angular acceleration $\dot{\omega}_m$ are either online estimated by the GPI observer, or else, they are obtained via the "dirty derivative" method.
- The gain parameters pM_{sr}/JL_r and $1/\sigma L_s$ are assumed to be known. The viscous friction coefficient B is assumed to be unknown.
- The load torque $T_L(t)$ is assumed to be, time varying but unknown. However, a finite number of its time derivatives are assumed to be uniformly absolutely bounded almost everywhere.

The trajectory tracking problem will be formulated in terms of the angular velocity. The disturbance observer, however, will be treated in terms of the angular position second order dynamics. This allows an alternative estimation of the angular velocity.

5.2.4 Problem Formulation

Consider the induction motor dynamics equations (5.1), (5.2), and (5.3). Given a desired constant reference level for the square of the rotor flux magnitude, ψ_r^{*2}, and given a smooth reference trajectory, $\omega_m^*(t)$, for the angular velocity of the motor shaft, find a feedback control law for the voltage v_s such that ω_m is forced to track the given reference trajectory, $\omega_m^*(t)$, while the square of the rotor flux magnitude ψ_r^2 is set to stabilize itself around the

desired constant value, ψ_r^{*2}. These objectives are to be achieved regardless of the presence of unknown but bounded perturbation inputs represented by (1) the load input torque, $T_L(t)$, (2) unmodeled torques due to friction terms in the rotor shaft dynamics, and (3) the effects of all additive, flux- and current-dependent, nonlinear terms acting on the (complex) stator current dynamics.

5.2.5 *Control Strategy*

The proposed control scheme consists of a two-stage feedback controller design led by the ADRC methodology. The first design stage controls the angular velocity of the motor shaft to track the reference signal $\omega_m^*(t)$ by means of the stator currents i_s taken as auxiliary control inputs. As a simultaneous, decoupled objective, it is desired to have the square of the flux magnitude ψ_r^2 converging towards a given constant value ψ_r^{*2}.

As a result of the first design stage, a set of desirable current trajectories is synthesized. The obtained currents are thus taken as output references for the second design stage where the control inputs are now represented by the stator voltages. The second stage designs a feedback controller to force, in a robust fashion, the actual currents to track the current references obtained in the first stage.

Outer Loop Controller Design Stage

Consider the perturbed rotor dynamics in equation (5.1). Taking the complex stator current, i_s, as a control input vector, the following partial complex feedback controller is obtained:

$$i_s = \frac{\phi_r}{\psi_r^2}\left[\frac{\psi_r^{*2}}{M_{sr}} + j v_{aux}\right], \tag{5.7}$$

with ψ_r^* being a constant desired flux magnitude reference value and v_{aux} is a yet to be specified auxiliary control input that does not affect the flux magnitude dynamics.

Indeed, in closed loop, the square modulus of the rotor flux satisfies

$$\frac{d\psi_r^2}{dt} = -2\frac{R_r}{L_r}\left[\psi_r^2 - \psi_r^{*2}\right],$$

and then, clearly, ψ_r tends to ψ_r^* in an exponential asymptotic manner. Notice, that the partial feedback equation (5.7) requires no cancelations of exogenous or endogenous disturbances.

On the other hand, the partially controlled angular position dynamics satisfies the following perturbed set of differential equations:

$$\begin{aligned}\frac{d\theta_m}{dt} &= \omega_m,\\ \frac{d\omega_m}{dt} &= \frac{pM_{sr}}{JL_r} v_{aux} - B\omega_m - \frac{T_L(t)}{J}.\end{aligned} \tag{5.8}$$

Considerations are shifted towards the following global ultra-model (see the Appendix for definitions and properties):

$$\begin{aligned}\frac{d\theta_m}{dt} &= \omega_m,\\ \frac{d\omega_m}{dt} &= \frac{pM_{sr}}{JL_r}v_{aux} + \xi_1(t).\end{aligned} \tag{5.9}$$

where $\xi_1(t) = -B\omega_m(t) - T_L(t)/J$ is regarded as a pure time-varying unknown but uniformly absolutely bounded signal with a finite number of equally unknown but bounded time derivatives, directly related to the load torque and of the effects of the possibly unknown viscous friction term. Note that $\xi_1(t)$ is observable according to the differential algebraic definition in Diop and Fliess (1991). The control input v_{aux} is the auxiliary control input appearing in equation (5.7), specified by the next theorem.

Theorem 5.2.1 *Consider the global ultra-model in equation (5.9) describing the partially closed-loop angular position dynamics in equation (5.8). Assume that $\xi_1(t)$ is uniformly absolutely bounded with uniformly absolutely bounded time derivatives up to some given finite order p. The observer-based control input v_{aux},*

$$v_{aux} = \frac{JL_r}{pM_{sr}}\left[\dot{\omega}_m^*(t) - k_{\omega_m}\left(\hat{\omega}_m - \omega_m^*(t)\right) - \hat{\xi}_1(t)\right], \tag{5.10}$$

forces the angular velocity tracking error to evolve in a small vicinity of zero in spite of the effects of the lumped disturbance input $\xi_1(t)$.

The variables $\hat{\xi}_1$ and $\hat{\omega}_m$, are given, respectively, by $\rho_{1\theta_m}$ and $\hat{\omega}_m$, which, in turn, are generated via the following linear GPI observer:

$$\begin{aligned}\frac{d\hat{\theta}_m}{dt} &= \hat{\omega}_m + \lambda_{(p+1)1}(\theta_m - \hat{\theta}_m),\\ \frac{d\hat{\omega}_m}{dt} &= \frac{pM_{sr}}{JL_r}v_{aux} + \rho_{1\theta_m} + \lambda_{p1}(\theta_m - \hat{\theta}_m),\\ \dot{\rho}_{1\theta_m} &= \rho_{2\theta_m} + \lambda_{(p-1)1}(\theta_m - \hat{\theta}_m),\\ &\vdots\\ \dot{\rho}_{p\theta_m} &= \lambda_{01}(\theta_m - \hat{\theta}_m),\end{aligned}$$

with appropriately chosen gain parameters $\lambda_{(p+1)1}, \ldots, \lambda_{01}$, and $k_{\omega_m} > 0$, so that the dominant characteristic polynomials, respectively, governing the tracking error $e_{\omega_m} = \omega - \omega^*(t)$ and the estimation errors $\tilde{e}_{\theta_m} = \theta_m - \hat{\theta}_m$, $\tilde{e}_{\omega_m} = \dot{\tilde{e}}_{\theta_m} + \lambda_{(p+1)1}\tilde{e}_{\theta_m}$

$$\begin{aligned}p_{c,\omega}(s) &= s + k_{\omega_m},\\ p_{o,\theta}(s) &= s^{p+2} + \lambda_{(p+1)1}s^{p+1} + \cdots + \lambda_{11}s + \lambda_{01},\end{aligned} \tag{5.11}$$

are Hurwitz polynomials with roots sufficiently far into the left half of the complex plane. While the position estimation error characteristic polynomial is Hurwitz, the angular velocity estimation error remains bounded. The further away from the imaginary axis the location of such roots, the smaller the neighborhoods uniformly bounding, respectively, in the reconstruction error phase space and the tracking error phase space, the angular position estimation error phase vector $\chi = (\tilde{e}_{\theta_m}, \dot{\tilde{e}}_{\theta_m}, \ldots, \tilde{e}_{\theta_m}^{(p+1)})^T$ *and the tracking error* e_{ω_m}.

Proof: The angular position estimation error, defined as $\tilde{e}_{\theta_m} := \theta_m - \hat{\theta}_m$, satisfies the following perturbed injected dynamics:

$$\tilde{e}_{\theta_m}^{(p+2)} + \lambda_{(p+1)1}\tilde{e}_{\theta_m}^{(p+1)} + \cdots + \lambda_{11}\dot{\tilde{e}}_{\theta_m} + \lambda_{01}\tilde{e}_{\theta_m} = \xi_1^{(p)}(t).$$

By an appropriate choice of the coefficients, λ_i; $i = 0, 1, \ldots, p+1$; the characteristic polynomial corresponding to the linear part of the above dynamics can be selected to be a Hurwitz polynomial. The estimation error is assured to be ultimately uniformly bounded by a small disk around the origin of the estimation error state space as the observer gains are set to produce eigenvalues sufficiently far at the left half of the complex plane (for more details, see the Appendix at the end of this chapter.).

The first order tracking error dynamics for the angular velocity, ω_m, is given by

$$\dot{e}_{\omega_m} + k_{\omega_m} e_{\omega_m} = \xi_1(t) - \hat{\xi}_1(t) - k_{\omega_m}(\omega_m - \hat{\omega}_m). \tag{5.12}$$

According to the dynamics induced by the GPI observer, the estimation errors $\xi_1(t) - \hat{\xi}_1(t)$ and $\omega_m - \hat{\omega}_m = \dot{\tilde{e}}_{\theta_m} + \lambda_{p+1}\tilde{e}_{\theta_m}$ converge towards an arbitrarily small vicinity of zero and, consequently, the right-hand side term of equation (5.12) remains uniformly ultimately bounded. The tracking error, $e_{\omega_m} = \omega_m - \omega_m^*(t)$, uniformly absolutely converges towards a small as desired vicinity of zero for an appropriately chosen gain, k_{ω_m}, so that the corresponding root of the dominant characteristic polynomial in the complex variable s, $p_{c,\omega_m}(s) = s + k_{\omega_m}$, is located, on the real line, sufficiently far into the left half of the complex plane. □

Inner Loop Controller Design Stage

Consider now the perturbed stator currents dynamics

$$\frac{di_s}{dt} = \frac{M_{sr}}{\sigma L_s L_r}\left(\frac{R_r}{L_r} - jp\omega_m\right)\phi_r - \gamma i_s + \frac{1}{\sigma L_s} v_s.$$

Let $i_s^*(t)$ be the desired stator current vector reference trajectory as represented by equation (5.7).

The stator current tracking error, $e_{i_s} := i_s - i_s^*(t)$, satisfies

$$\frac{de_{i_s}}{dt} = \frac{1}{\sigma L_s} v_s + \xi_2(t), \tag{5.13}$$

with $\xi_2(t)$ given by

$$\xi_2(t) = \frac{M_{sr}}{\sigma L_s L_r}\left(\frac{R_r}{L_r} - jp\omega_m\right)\phi_r - \gamma i_s - \frac{di_s^*(t)}{dt}.$$

It is assumed that $\xi_2(t)$ and a sufficiently large number, q, of its time derivatives are uniformly absolutely bounded. In a more general context this condition has been found to be, both, a necessary and sufficient condition for the existence of solutions of nonlinear differential equations with state-dependent perturbation inputs (see Gliklikh 2006).

Theorem 5.2.2 *The observer-based controller specified by*

$$v_s = -\sigma L_s\left[k_{i_s} e_{i_s} + \hat{\xi}_2(t)\right],$$

with $\hat{\xi}_2(t)$, generated by the GPI observer,

$$\begin{aligned}
\frac{d\hat{e}_{i_s}}{dt} &= \frac{1}{\sigma L_s} v_s + \vartheta_{1e_I} + \lambda_{q2}(e_{i_s} - \hat{e}_{i_s}),\\
\dot{\vartheta}_{1e_I} &= \vartheta_{2e_I} + \lambda_{(q-1)2}(e_{i_s} - \hat{e}_{is}),\\
&\vdots\\
\dot{\vartheta}_{(q-1)e_I} &= \vartheta_{qe_I} + \lambda_{12}(e_{i_s} - \hat{e}_{i_s}),\\
\dot{\vartheta}_{qe_I} &= \lambda_{02}(e_{i_s} - \hat{e}_{i_s}),\\
\hat{\xi}_2 &= \vartheta_{1e_I},
\end{aligned} \tag{5.14}$$

globally asymptotically stabilizes the tracking error e_{i_s} to a small as desired vicinity of zero, while $\hat{\xi}_2(t)$ arbitrarily closely reconstructs the unknown (state-dependent) disturbance $\xi_2(t)$, provided the constant coefficients, $\{\lambda_{q2}, \lambda_{(q-1)2}, \ldots, \lambda_{02}\}$ and k_{i_s} are chosen so that the polynomials in the complex variables s,

$$\begin{aligned}
p_\xi(s) &= s^{q+1} + \lambda_{q2}s^q + \lambda_{(q-1)2}s^{q-1} + \cdots + \lambda_{12}s + \lambda_{02},\\
p_{i_s}(s) &= s + k_{i_s},
\end{aligned}$$

are Hurwitz polynomials with roots located sufficiently far from the imaginary axis in the complex plane.

Proof: The proof is similar to that of the previous theorem. □

A scheme of the proposed strategy is depicted in Figure 5.1.

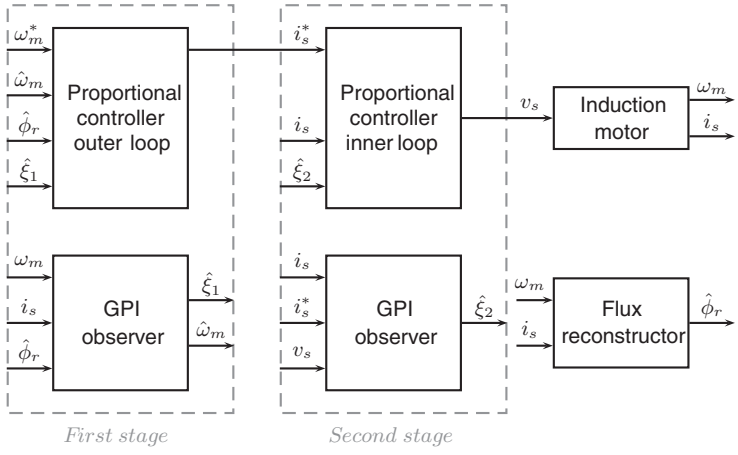

Figure 5.1 Control scheme. GPI, generalized proportional integral

5.2.6 Experimental Results

An induction motor coupled with a DC motor generating a time-varying load torque input, was used for the experimental tests (see Figure 5.2). The induction motor, manufactured by WEG, has the following nominal parameters: rated power, 0.75 HP, $J = 2 \times 10^{-3}$ kg m^2, $p = 1$, $M_{sr} = 0.2374$ H, $L_r = 0.2505$ H, $L_s = 0.2505$ H, $R_s = 4.32\,\Omega$, and $R_r = 2.8807\,\Omega$. The position measurement was carried out by a 10 000 PPR optical encoder, directly coupled to the rotor shaft, and the induction motor current signals and the armature current of the load DC motor were measured by Hall Effect current sensors (LEM LA-55P). The torque load was measured indirectly through the DC motor current, given that $T_L(t) = k_m i_L$, with $k_m = 1.4285$ Nm/A. The reference value for the flux magnitude was chosen so as to maximize the induced torque when subject to nominal currents. It was set $\psi_r^* = Mi_{nom}/\sqrt{2} = 0.5036$ Wb, where $i_{nom} = 3$A.

The GPI observer-based controller was synthesized on a MATLAB - xPC Target environment using a sampling period of 0.125 ms. The communication between the plant and the controller was performed by two data acquisition devices. Analog data was channeled through a National Instruments PCI-6025E data acquisition card. The digital outputs and the position encoder readings were gathered in a National Instruments PCI-6602 data acquisition card.

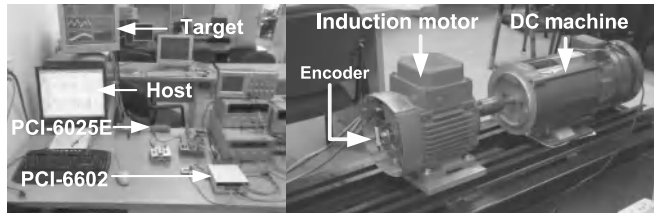

Figure 5.2 Experimental setup

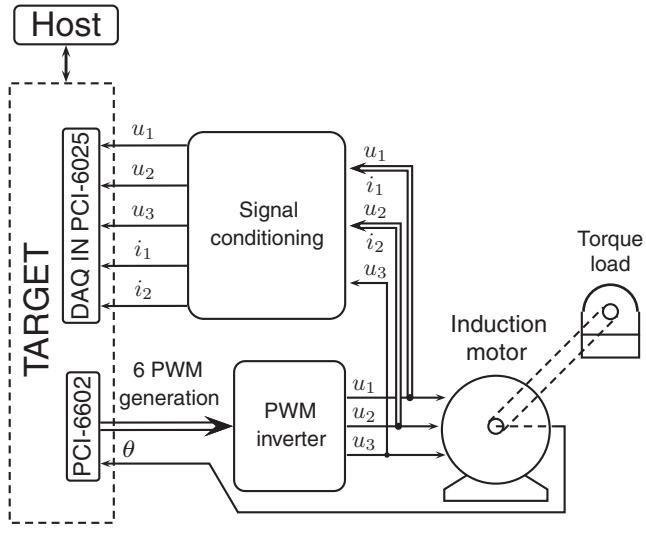

Figure 5.3 Block diagram of the control system. PWM, pulse-width modulation

The voltage and current signals were low pass filtered with a cut-off frequency of 1.0 kHz. A schematic diagram of the control system is depicted in Figure 5.3.

The angular velocity reference trajectory to be tracked $\omega^*(t)$ was set to be a rest-to-rest smooth trajectory rising from 0 to 15 s^{-1}, in 5 s. The characteristic polynomial associated with the velocity control loop was set to be $s + k_{\omega_m}$, with $k_{\omega_m} = 85$ (the associated approximation coefficient of Theorem 5.2.1, p, was 5). The characteristic polynomial associated to the current-control loop was set to be $s + k_{i_s}$, with $k_{i_s} = 400$. The characteristic polynomial associated with the velocity-control loop disturbance observer was specified by $(s^2 + 2\zeta_{o,\omega}\omega_{o,\omega}s + \omega_{o,\omega}^2)^3(s + p_{o,\omega})$, with $\zeta_{o,\omega} = 4.5$, $\omega_{o,\omega} = 4$, and $p_{o,\omega} = 4$. The characteristic polynomial associated with the current-control loop disturbance observer was given by $(s^2 + 2\zeta_{o,sc}\omega_{o,sc}s + \omega_{o,sc}^2)^3(s + p_{o,sc})$, with $\zeta_{o,sc} = 6.2$, $\omega_{o,sc} = 80$, and $p_{o,sc} = 80$ (the approximation parameter q given in Theorem 5.2.2 was also 5).

Figure 5.4 shows an accurate velocity tracking with respect to the desired trajectory. Figure 5.5 shows that the flux magnitude is regulated within an absolute error below 2×10^{-4} Wb. Figure 5.6 depicts the actual current variables perfectly tracking the desired reference currents in both phases. Finally, to illustrate the robustness of the strategy, a load torque was applied via a DC motor, in generator configuration, whose armature current tracked a state variable of a Chua's circuit. The load is switched in at the instant $t = 5$ s. The disturbance estimation, as well as the applied load torque are shown in Figure 5.7.

We carried out experiments under the same trajectory tracking task using two other effective approaches. One tried method consisted in the passivity-based control, reported in Karagiannis *et al.* (2009), where a load torque estimator is proposed to solve the problem of controlling the velocity of an induction motor in the presence of unknown mechanical torque inputs. The proposed parameters for this scheme were set as follows: $k = 10$, $c = 0.4$, $\delta = 0.001$, $\epsilon = 2273$, and $\gamma = 30$. The other methods used for comparisons included the classic observer-based PI control scheme in a field-oriented control scheme, obtained from Bodson

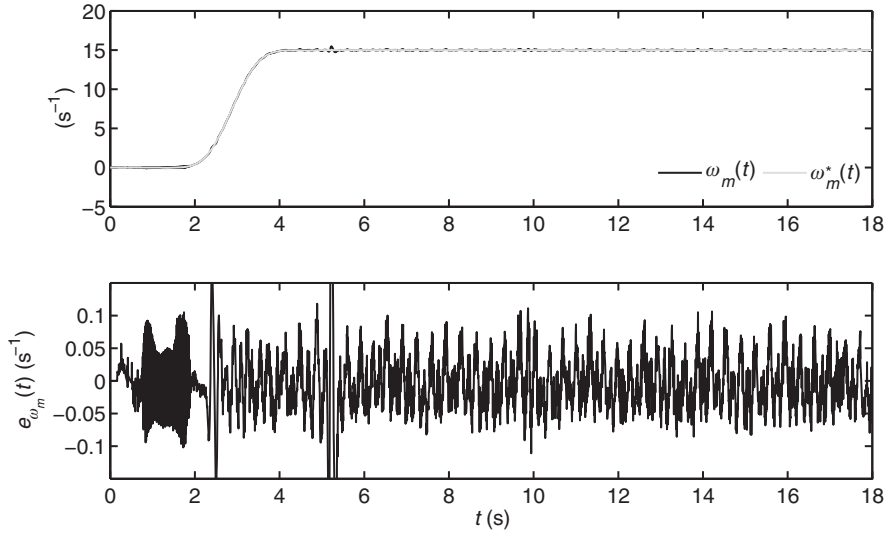

Figure 5.4 Velocity trajectory tracking

et al. (1995). The controller parameters were determined as follows: the closed-loop characteristic polynomial for the velocity was given by $s^2 + 2\zeta_1\omega_1 s + \omega_1^2$, with $\zeta_1 = 1$ and $\omega_1 = 50$. The closed-loop characteristic polynomial for the flux regulation was $s^2 + 2\zeta_2\omega_2 s + \omega_2^2$, with $\zeta_2 = 1$ and $\omega_2 = 8$. Finally, the closed-loop characteristic polynomial for the current variables was given by $s^2 + 2\zeta_3\omega_3 s + \omega_3^2$, with $\zeta_3 = 1$ and $\omega_3 = 45$.

Figure 5.8 shows that the three control strategies achieve efficient angular velocity tracking results. However, in the flux regulation task, the passivity-based approach did not achieve

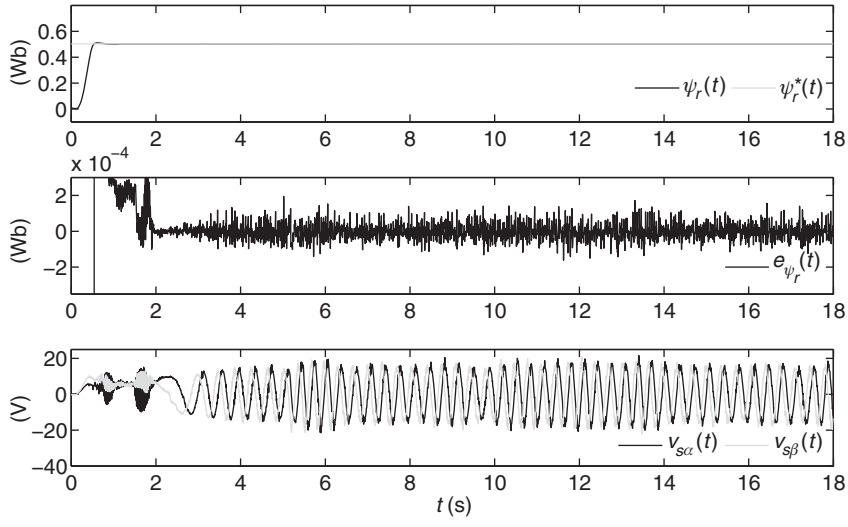

Figure 5.5 Flux magnitude regulation and control input

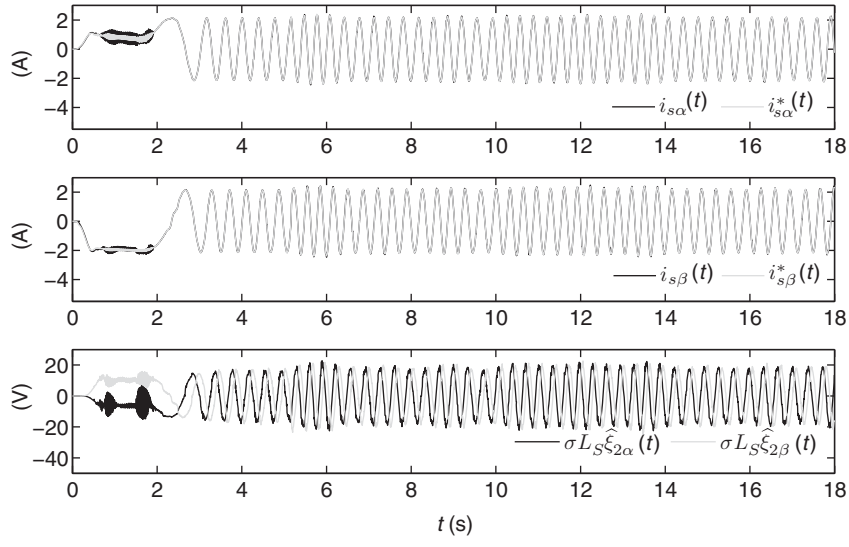

Figure 5.6 Current tracking and disturbance electric variables

an accurate regulation, while the observer-based PI controller and the GPI observer-based control scheme exhibited good results. Finally, since the observer-based PI control scheme is not capable of estimating the disturbance input, the disturbance estimations were reported for the passivity-based scheme and the GPI scheme (Figure 5.9). Both methodologies achieved good performances in spite of abrupt load variations.

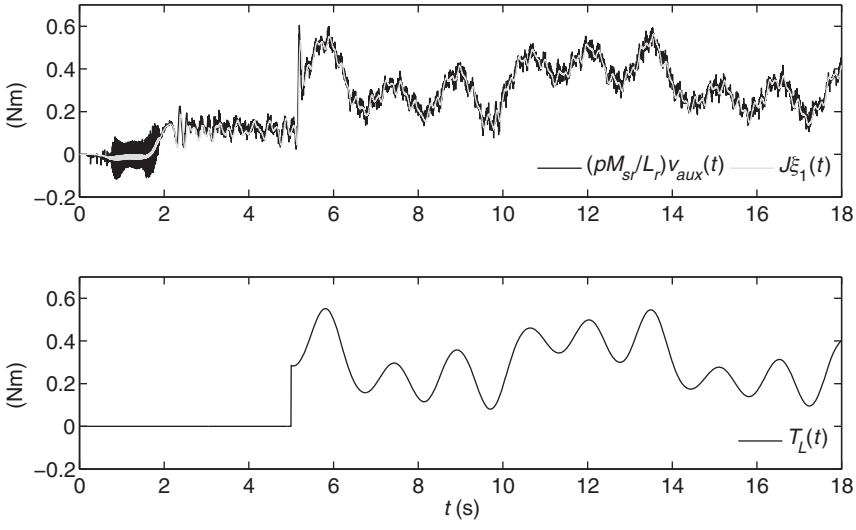

Figure 5.7 Lumped mechanical disturbances estimation

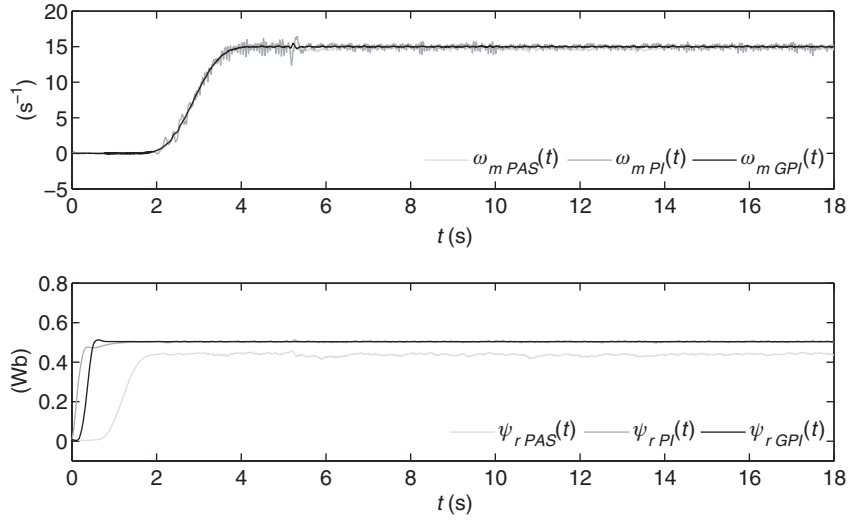

Figure 5.8 Behavior of different approaches in performance comparison

5.3 Field-Oriented ADR Armature Voltage Control

The classical indirect control decoupling property, exploited in the preceding paragraphs for the two-stage controller design, is seen to be inherited in the form of a direct control decoupling property, by the field-oriented voltage-control approach here explored. This direct approach has been used in feedback linearization control schemes for the induction motor in Kim *et al.* (1990) and Bodson *et al.* (1994).

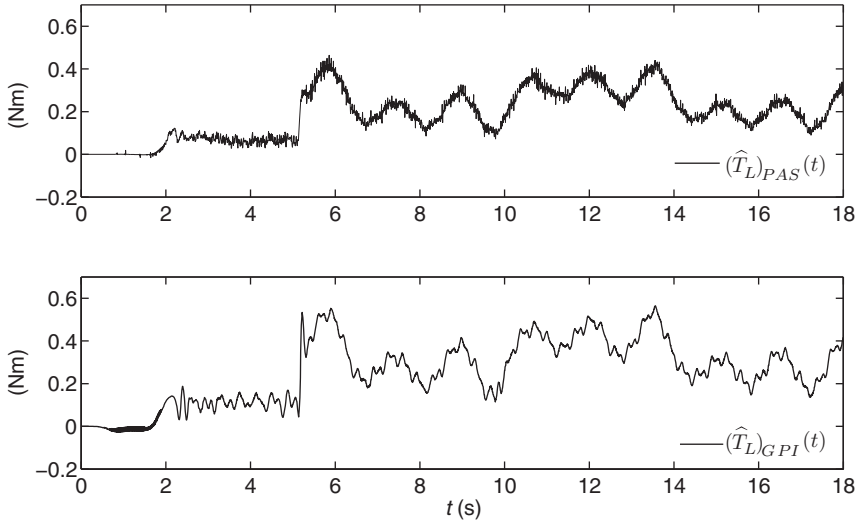

Figure 5.9 Behavior of different approaches in mechanical disturbance estimation

5.3.1 Control Decoupling Property of the Induction Motor System

It is not difficult to see that the variables ω_m and ψ_r^2 are, both, relative degree 2 outputs with respect to the complex control input v_s and that, moreover, these variables satisfy the following set of real, nonlinear, second order controlled differential equations:

$$\begin{aligned}\frac{d^2\omega_m}{dt^2} &= \frac{pM_{sr}}{JL_rL_s\sigma}\mathrm{Im}\left(v_s\overline{\phi_r}\right) + \xi_\omega\left(\omega_m, \dot{\omega}_m, \psi_r^2, \frac{d\psi_r^2}{dt}, T_L, \dot{T}_L\right),\\ \frac{d^2}{dt^2}\psi_r^2 &= \frac{2R_rM_{sr}}{L_rL_s\sigma}\mathrm{Re}\left(v_s\overline{\phi_r}\right) + \xi_\psi\left(\omega_m, \dot{\omega}_m, \psi_r^2, \frac{d\psi_r^2}{dt}, T_L\right),\end{aligned} \tag{5.15}$$

where

$$\begin{aligned}\xi_\omega(\cdot) &= \frac{pM_{sr}}{L_r}\left[\left(\frac{R_r}{L_r}-\sigma\right)\mathrm{Im}\left(i_s\overline{\phi_r}\right) - p\omega_m\mathrm{Re}\left(i_s\overline{\phi_r}\right) - \frac{p}{L_sL_r\sigma}\omega_m\psi_r^2\right] - B\dot{\omega}_m - \dot{T}_L,\\ \xi_\psi(\cdot) &= \left(\frac{4R_r^2}{L_r^2} + \frac{2R_r^2M_{sr}^2}{L_s\sigma L_r^3}\right)\psi_r^2 + \left(\frac{-6R_r^2M_{sr}}{L_r^2} - \frac{2R_r\gamma M_{sr}}{L_r}\right)\mathrm{Re}\left(i_s\overline{\phi_r}\right)\\ &\quad + \left(\frac{2R_rM_{sr}p}{L_r}\right)\omega_m\mathrm{Im}\left(i_s\overline{\phi_r}\right) + \left(\frac{2R_r^2M_{sr}^2}{L_r^2}\right)i_s^2.\end{aligned} \tag{5.16}$$

As it can be easily seen, the nature of the nonlinear terms $\xi_\omega(\cdot)$ and $\xi_\psi(\cdot)$ is quite involved. As it was shown in the last section, the key observation in the GPI observer-based control approach is that such time-varying perturbation inputs can be approximately estimated (and then canceled at the controller stage) using linear high-gain observers equipped with sufficient output estimation error iterated integral injections. This procedure is, incidentally, in the very same spirit of *total* ADR (see Gao 2006; Tian and Gao 2009) and nonlinear *model-free control* (see Fliess *et al.* 2008). The armature input voltage v_s can be directly used to robustly control, in a naturally decoupled fashion, both the angular velocity of the motor shaft and the squared magnitude of the flux via extended, second order, controlled equations. For this, we propose to consider the observer construction problem in the context of the the angular velocity dynamics and the squared flux magnitude extended dynamics viewed as simplified global ultra-models with purely time-varying additive disturbance inputs. Denote by $\xi_\omega(t)$ the quantity $\xi_\omega(\omega_m(t), \dot{\omega}_m(t), \psi_r(t), \frac{d\psi_r(t)^2}{dt}, T_L(t), \dot{T}_L(t))$ and by $\xi_\psi(t)$, the function $\xi_\psi(\omega_m(t), \dot{\omega_m}(t), \psi_r(t), \frac{d\psi_r(t)^2}{dt}, T_L(t))$

$$\begin{aligned}\frac{d^2\omega_m}{dt^2} &= \frac{pM_{sr}}{JL_rL_s\sigma}\mathrm{Im}\left(v_s\overline{\phi_r}\right) + \xi_\omega(t)\\ \frac{d^2}{dt^2}\psi_r^2 &= \frac{2R_rM_{sr}}{L_rL_s\sigma}\mathrm{Re}\left(v_s\overline{\phi_r}\right) + \xi_\psi(t)\end{aligned} \tag{5.17}$$

The above fourth order dynamics is complemented with the following perturbed dynamics for the complex flux argument, θ_ψ:

$$\frac{d}{dt}\theta_\psi = p\omega_m + \frac{R_r}{p\psi_r^2}\left(J\dot{\omega}_m + B\omega_m + T_L(t)\right). \tag{5.18}$$

This last equation will play the role of the *zero dynamics* corresponding to the controlled fourth order system described above. Note that $\dot{\omega}_m$ is just a state of the extended angular velocity dynamics written in equation (5.17).

5.3.2 Problem Formulation

It is desired to have the rotor angular velocity ω_m track, even if in an arbitrarily closed manner, a given, desired angular velocity reference trajectory $\omega^*(t)$, while the squared magnitude of the complex flux is independently controlled, as closely as desired, towards a given constant reference value, ψ_r^{*2}. Besides, the tracking process must be carried out regardless of the unknown time-varying load input torque $T_L(t)$, the presence of both viscous and Coulomb friction terms in the rotor dynamics, and the rather complex nonlinearities represented by the functions $\xi_\omega(\omega_m, \dot{\omega}_m, \psi_r^2, \frac{d\psi_r^2}{dt}, T_L(t), \frac{dT_L(t)}{dt})$ and $\xi_\psi(\omega_m, \dot{\omega}_m, \psi_r^2, \frac{d\psi_r^2}{dt}, T_L(t))$, respectively affecting the extended second order dynamics of the angular velocity and of the squared magnitude of the flux.

5.3.3 Control Strategy

Suppose, for a moment, that the complex flux, ϕ_r, is perfectly known. Then, it is possible to set, with the help of the auxiliary complex control input variable: $v = v_a + jv_b$, the following input voltage field-oriented controller:

$$v_s = \left(\frac{\phi_r}{\psi_r^2}\right) v, \tag{5.19}$$

yielding the following set of control-decoupled linear disturbed systems,

$$\begin{aligned} \frac{d^2\omega_m}{dt^2} &= \left(\frac{pM_{sr}}{JL_rL_s\sigma}\right) v_b + \xi_\omega(t), \\ \frac{d^2}{dt^2}\psi_r^2 &= \left(\frac{2R_rM_{sr}}{L_rL_s\sigma}\right) v_a + \xi_\psi(t). \end{aligned} \tag{5.20}$$

Naturally, the lack of measurability of ϕ_r prompts us to rely on the asymptotic complex flux estimate, $\hat{\phi}_r$. For a discussion on how the "nonlinear separation principle" has been traditionally used in induction motor control see pp. 359–360 in Ortega *et al.* (1998), and for its justification in feedback linearization, see Maggiore and Passino (2005). For a justification in rather general terms, see Hinkkanen (2004), and the many references therein.

For the theorem below, let the set of parameters, $\{\kappa_1^{\psi}, \kappa_0^{\psi}\}$, $\{\kappa_1^{\omega}, \kappa_0^{\omega}\}$, be such that the polynomials in the complex variable s, given by

$$p_{\psi,c}(s) = s^2 + \kappa_1^{\psi} s + \kappa_0^{\psi}, \quad p_{\omega,c}(s) = s^2 + \kappa_1^{\omega} s + \kappa_0^{\omega}, \tag{5.21}$$

are Hurwitz polynomials. Similarly, let the set of parameters, for some given integers n and m[1], $\{\gamma_{m+1}^{\psi}, \gamma_m^{\psi}, \ldots, \gamma_0^{\psi}\}$, $\{\pi_{n+1}^{\omega}, \pi_n^{\omega}, \ldots, \pi_0^{\omega}\}$, be such that the polynomials in the complex variable s, given by

$$\begin{aligned} p_{\psi,o}(s) &= s^{m+2} + \gamma_{m+1}^{\psi} s^{m+1} + \gamma_m^{\psi} s^m + \cdots + \gamma_0^{\psi}, \\ p_{\omega,o}(s) &= s^{n+2} + \pi_{n+1}^{\omega} s^{n+1} + \pi_n^{\omega} s^n + \cdots + \pi_0^{\omega}, \end{aligned} \tag{5.22}$$

are also Hurwitz polynomials, with roots located sufficiently far into the left half of the complex plane. Furthermore, let $\xi_{\psi}^{(m)}(t)$ and $\xi_{\omega}^{(n)}(t)$, be functions of time uniformly absolutely bounded by finite constants.

Theorem 5.3.1 *The armature voltage field-oriented controller,*

$$\begin{aligned} v_s &= v_{s\alpha} + j v_{s\beta} = \left(\frac{\hat{\phi}_r}{\hat{\psi}_r{}^2} \right) v, \quad v = v_a + j v_b, \\ v_a &= -\frac{L_r L_s \sigma}{2 R_r M_{sr}} \left[\widehat{\xi_{\psi}} + \kappa_1^{\psi} \left(\widehat{\frac{d\psi_r^2}{dt}} \right) + \kappa_0^{\psi} \left(\hat{\psi}_r{}^2 - (\psi_r^*)^2 \right) \right], \\ v_b &= -\frac{J L_r L_s \sigma}{p M_{sr}} \left[\widehat{\xi_{\omega}} - \ddot{\omega}^*(t) + \kappa_1^{\omega} (\widehat{\omega}_m - \dot{\omega}^*(t)) + \kappa_0^{\omega} \left(\omega_m - \omega^*(t) \right) \right], \end{aligned} \tag{5.23}$$

with $\widehat{\xi_{\psi}}$ *and* $\widehat{\left(\frac{d\psi_r^2}{dt} \right)}$ *given, respectively, by the variables* ϑ_1^{ψ} *and* ζ_2^{ψ} *generated by the following linear high-gain GPI observer:*

$$\begin{aligned} \dot{\zeta}_1^{\psi} &= \zeta_2^{\psi} + \gamma_{m+1}^{\psi} (\hat{\psi}_r{}^2 - \zeta_1^{\psi}), \\ \dot{\zeta}_2^{\psi} &= \vartheta_1^{\psi} + \left(\frac{2 R_r M_{sr}}{L_r L_s \sigma} \right) v_a + \gamma_m^{\psi} (\hat{\psi}_r{}^2 - \zeta_1^{\psi}), \\ \dot{\vartheta}_1^{\psi} &= \vartheta_2^{\psi} + \gamma_{m-1}^{\psi} (\hat{\psi}_r{}^2 - \zeta_1^{\psi}), \\ \dot{\vartheta}_2^{\psi} &= \vartheta_3^{\psi} + \gamma_{m-2}^{\psi} (\hat{\psi}_r{}^2 - \zeta_1^{\psi}), \\ &\vdots \\ \dot{\vartheta}_{m-1}^{\psi} &= \vartheta_m^{\psi} + \gamma_1^{\psi} (\hat{\psi}_r{}^2 - \zeta_1^{\psi}), \\ \dot{\vartheta}_m^{\psi} &= \gamma_0^{\psi} (\hat{\psi}_r{}^2 - \zeta_1^{\psi}), \end{aligned} \tag{5.24}$$

[1]The integers n and m are, in principle, sufficiently large, indicating the number of iterated output estimation error integral injections needed to attenuate the effect of unmodeled plant nonlinearities in the GPI observation error dynamics. In practice, however, they are small and chosen within the range of 3–5. We recall here a quote by J. von Neumann: "With four parameters I can fit an elephant, and with five I can make him wiggle his trunk!"

and with $\widehat{\xi_\omega}$ and $\widehat{\dot{\omega}_m}$ given, respectively, by the variables ϑ_1^ω and ζ_2^ω, generated by the following linear high-gain GPI observer:

$$\begin{aligned}
\dot{\zeta}_1^\omega &= \zeta_2^\omega + \pi_{n+1}^\omega(\omega_m - \zeta_1^\omega),\\
\dot{\zeta}_2^\omega &= \vartheta_1^\omega + \left(\frac{pM_{sr}}{JL_rL_s\sigma}\right)v_b + \pi_n^{\omega_m}(\omega_m - \zeta_1^\omega),\\
\dot{\vartheta}_1^\omega &= \vartheta_2^\omega + \pi_{n-1}^\omega(\omega_m - \zeta_1^\omega),\\
\dot{\vartheta}_2^\omega &= \vartheta_3^\omega + \pi_{n-2}^\omega(\omega_m - \zeta_1^\omega),\\
&\vdots\\
\dot{\vartheta}_{n-1}^\omega &= \vartheta_n^\omega + \pi_1^\omega(\omega_m - \zeta_1^\omega),\\
\dot{\vartheta}_n^\omega &= \pi_0^\omega(\omega_m - \zeta_1^\omega),
\end{aligned} \tag{5.25}$$

globally ultimately drives the angular velocity $\omega_m(t)$ and the squared magnitude of the flux, ψ_r^2, towards vicinities of the reference trajectories $\omega^*(t)$ and $(\psi_r)^2$, which can be uniformly made as small as desired, regardless of the nonlinearities present in the functions, $\xi_\psi(\omega_m, \phi, i_s, \phi_r, d\psi_r^2/dt)$ and, $\xi_\omega(\omega_m, \dot{\omega}_m, \phi_r, i_s, T_L, \dot{T}_L)$, defined above.

Proof: Define the tracking error: $e_\omega := \omega_m - \omega_m^*(t)$, and the stabilization error: $e_\psi := \psi_r^2 - (\psi_r^*)^2$. Likewise, let $\tilde{e}_\omega := \omega_m - \zeta_1^\omega$ and $\tilde{e}_\psi := \psi_r^2 - \zeta_1^\psi$ denote, respectively, the estimation errors associated with the angular velocity and the squared flux magnitude. The estimation errors are easily seen to satisfy the following linear perturbed equations:

$$\begin{aligned}
\tilde{e}_\omega^{(n+2)} + \gamma_{n+1}^\omega \tilde{e}_\omega^{(n+1)} + \cdots + \gamma_0^\omega \tilde{e}_\omega &= \xi_\omega^{(n)}(t),\\
\tilde{e}_\psi^{(m+2)} + \pi_{m+1}^\psi \tilde{e}_\psi^{(m+1)} + \cdots + \pi_0^\psi \tilde{e}_\psi &= \xi_\psi^{(m)}(t).
\end{aligned} \tag{5.26}$$

In the Appendix, it is proven in general terms that under all the assumptions specified above, the GPI observer estimation error trajectories, and those of its various time derivatives, converge towards arbitrarily small neighborhoods of the estimation error phase space where they remain ultimately bounded. As for the control part, the closed-loop dynamics of the second order tracking error dynamics for the angular velocity, ω_m, and the closed-loop dynamics of the squared flux magnitude, ${\psi_r}^2$ (given that $\hat{\psi}_r \to \psi_r$, exponentially), are given by

$$\begin{aligned}
\ddot{e}_\omega + \kappa_1^\omega \dot{e}_\omega + \kappa_0^\omega e_\omega &= \xi_\omega(t) - \widehat{\xi_\omega}(t) + \kappa_1^\omega \dot{\tilde{e}}_\omega,\\
\ddot{e}_\psi + \kappa_1^\psi \dot{e}_\psi + \kappa_0^\psi e_\psi &= \xi_\psi(t) - \widehat{\xi_\psi}(t) + \kappa_1^\psi \dot{\tilde{e}}_\psi.
\end{aligned} \tag{5.27}$$

The convergence of $\widehat{\xi_\omega}(t)$ towards an arbitrarily small vicinity of $\xi_\omega(t)$ and that of $\dot{\tilde{e}}_\omega$ towards a small vicinity of zero establishes that the tracking errors e_ω and $\dot{e}_\omega$ ultimately absolutely converge towards a small as desired vicinity of the origin for gains, κ_1^ω and κ_0^ω, appropriately chosen so that the roots of the dominant characteristic polynomial in the complex variable s,

$p_{c,\omega}(s) = s^2 + \kappa_1^\omega s + \kappa_0^\omega$ are located sufficiently far into the left half of the complex plane. A corresponding statement can be made for $\widehat{\xi_\psi}(t)$ and $\dot{\tilde{e}}_\psi$ with the same implications on e_ψ and $\dot{e}_\psi$.

The "steady state" of the load torque perturbed complex flux argument dynamics, corresponding to the previously defined controller, is described by

$$\frac{d}{dt}\theta_\psi = p\omega_m^*(t) + \frac{R_r}{p(\psi_r^*)^2}\left(J\dot{\omega}_m^*(t) + B\omega_m^*(t) + T_L(t)\right).$$

Instability of the complex flux argument θ_ψ is of no concern whatsoever, much as it is of no concern the "instability" of the unbounded uniformly growing angular position of the rotor, for any ultimately constant angular velocity reference trajectory. Moreover, it has been seen that θ_ψ has absolutely no influence on the closed-loop dynamics of ω_m and ψ_r^2. □

5.3.4 Experimental Results

Experimental tests were carried out to illustrate the effectiveness of the proposed control scheme in an angular velocity tracking task, using the same test bed as used in the two-stage controller design case. For the control scheme of Section 5.3, the angular velocity was estimated through the discrete measurement of the position, by taking the filtered difference between consecutive encoder records, where the filter proposed was a first order low pass filter with cut frequency of 67 Hz. The angular velocity output reference trajectory $\omega^*(t)$ was defined as a series of ramps, which takes values of 0 to 35, 35 to -5, -5 to 15, 15 to -5, and -5 to 20 rad $-$ s^{-1}, during time intervals of 2.0 s. The characteristic polynomial associated with the velocity control loop was set to be of the form: $s^2 + \kappa_1^\omega s + \kappa_0^\omega$, with $\kappa_1^\omega = 208$ and $\kappa_0^\omega = 6400$. The characteristic polynomial for the flux control loop was set to be of a similar form, with $\kappa_1^\psi = 20$ and $\kappa_0^\psi = 100$. The characteristic polynomial associated with the angular velocity control loop disturbance observer (setting $p = 5$) was chosen of the form: $(s^2 + 2\zeta_{o,\omega}\omega_{o,\omega}s + \omega_{o,\omega}^2)^3(s + p_{o,\omega})$, with $\zeta_{o,\omega} = 11$, $\omega_{o,\omega} = 60$, and $p_{o,\omega} = 60$, while the characteristic polynomial associated with the flux control loop disturbance observer (setting $m = 5$) was set to be: $(s^2 + 2\zeta_{\psi,\omega}\omega_{\psi,\omega}s + \omega_{\psi,\omega}^2)^3(s + p_{\psi,\omega})$, with $\zeta_{\psi,\omega} = 1$, $\omega_{\psi,\omega} = 200$, and $p_{\psi,\omega} = 200$.

Figure 5.10 depicts a rather accurate angular velocity tracking of the desired reference trajectory. Figure 5.11 depicts the remarkable quality of the flux magnitude stabilization. In Figure 5.12, the armature control input voltage and armature currents are shown in the reference frame: α, β. The chaotic nature of the DC motor generated mechanical load torque is depicted in Figure 5.13. Figure 5.14 shows the disturbance estimations, associated with the flux and velocity control loops. The chaotic load torque was synthesized using the evolution of a Chua's circuit state variable trajectory acting as a reference signal for the armature current in the DC motor.

The performance of our proposed control scheme was compared with other two armature voltage field-oriented control strategies, differing only in the linear part of the design while excluding the GPI observer. A PD controller and a PID control scheme with well-tuned gains were chosen for the comparison. The experimental comparison results are depicted in Figures 5.15, 5.16, 5.17, and 5.18, where the GPI observer significantly improves the

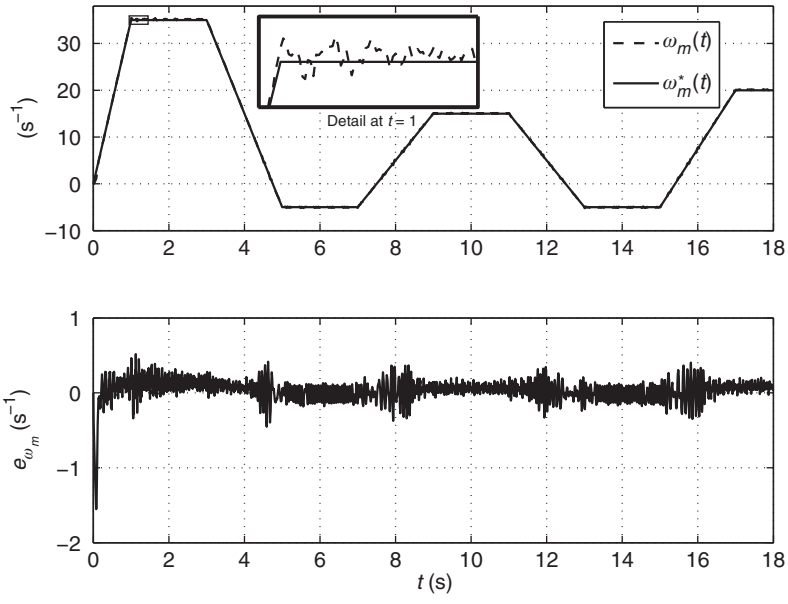

Figure 5.10 Angular velocity reference trajectory tracking and tracking error

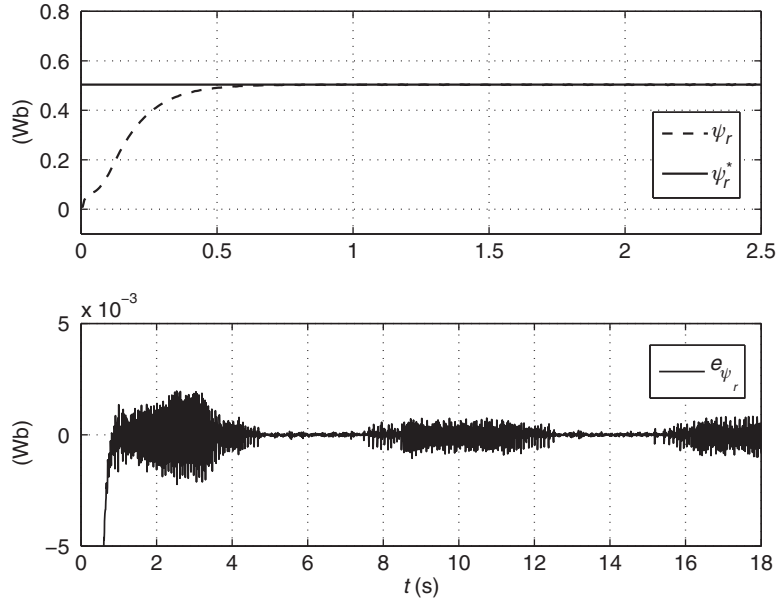

Figure 5.11 Flux magnitude regulation and its stabilization error

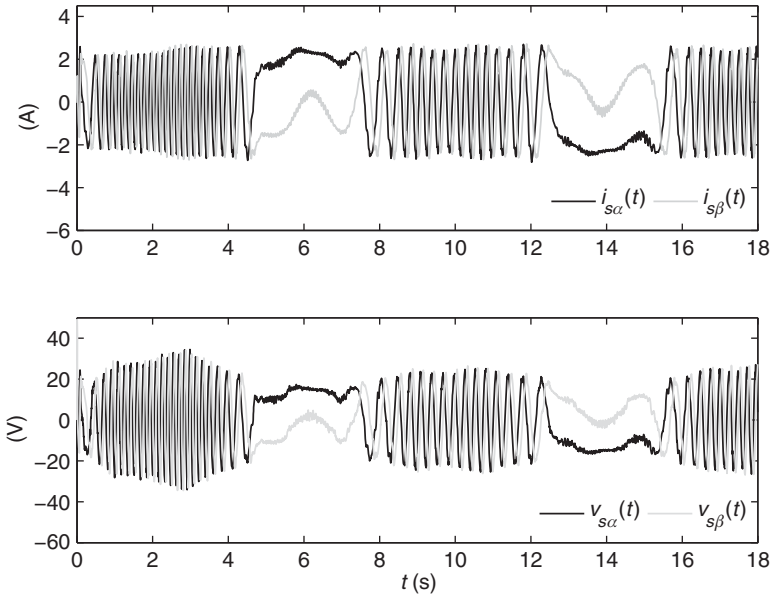

Figure 5.12 Armature voltages and currents in the a, b reference frame

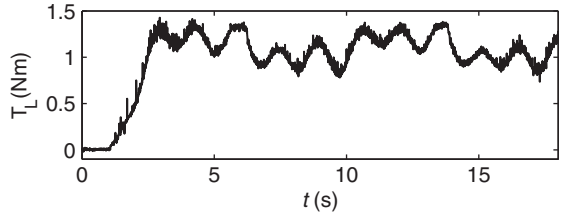

Figure 5.13 Direct-current (DC) motor generated chaotic disturbance torque input, $\tau_L(t)$

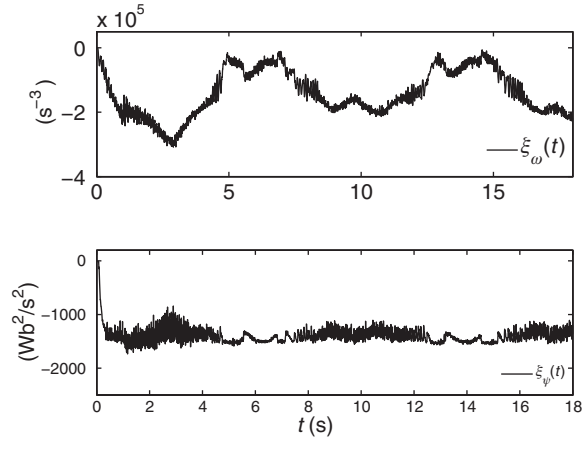

Figure 5.14 Estimated disturbance inputs, $\xi_\omega(t)$, $\xi_\psi(t)$

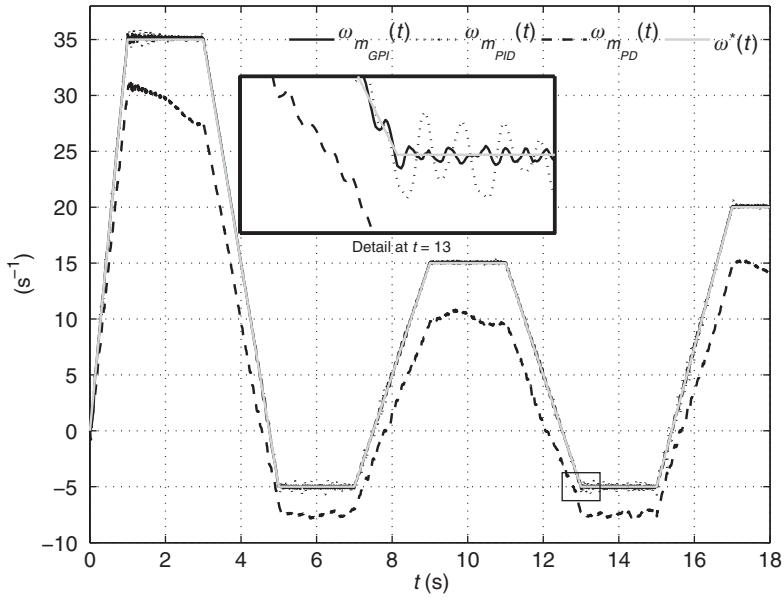

Figure 5.15 Performance comparison with PD and PID control schemes

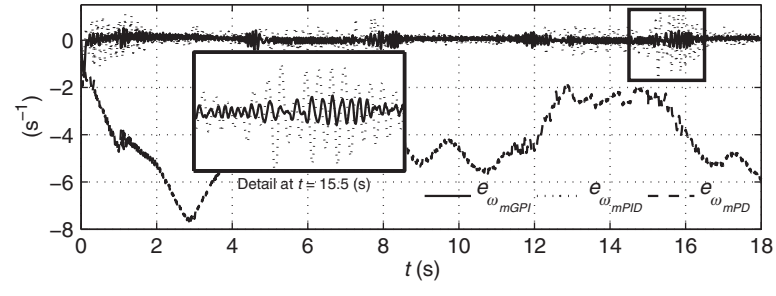

Figure 5.16 Performance comparison with PD and PID control schemes

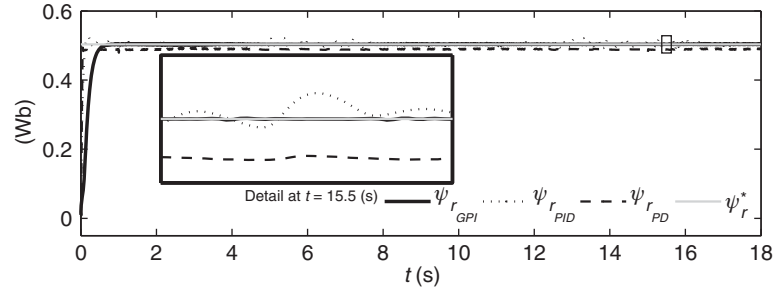

Figure 5.17 Performance comparison with PD and PID control schemes

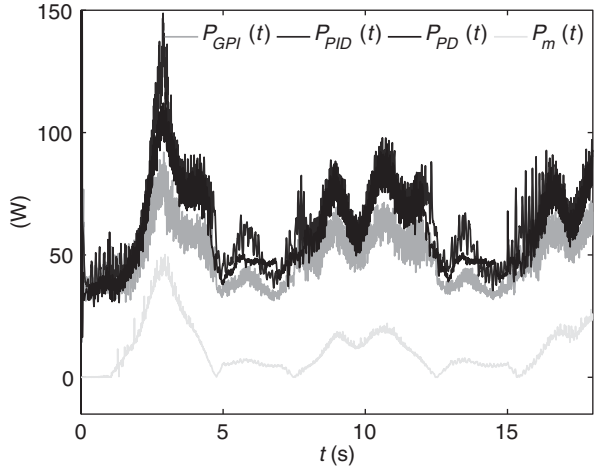

Figure 5.18 Performance comparison, power consumption

performance of the single PD control loop (the control gains were even larger than the ones used in the GPI observer-based control). The PD control scheme exhibits poor tracking results. On the other hand, the PID controller shows a quite satisfactory performance in, both, the velocity and flux control. However, its behavior in the presence of the applied torque input is slightly affected by the time-varying disturbance. The proposed GPI observer-based controller achieved the most accurate results in steady state. In Figure 5.18, the power consumption analysis is shown for a mechanical torque generation P_m. In this case, even though all strategies had a similar power consumption, the GPI control exhibited the lowest results.

5.A Appendix

5.A.1 Generalities on Ultra-Models and Observer-Based Active Disturbance Rejection Control

Consider the following problem: it is desired to asymptotically stabilize to the origin the set of phase variables of the scalar, nth order, nonlinear controlled system

$$y^{(n)} = \phi(t, y, \dot{y}, \ldots, y^{(n-1)}) + \mu(t, y)u, \tag{5.A.1}$$

on the basis of knowledge of the output function, $y(t)$, alone.

5.A.2 Assumptions

- It is assumed that for every given set of initial conditions: $Y_0 = \{y_0, \dot{y}_0, \ldots, y_0^{(n-1)}\}$, specified at time $t = 0$, and any given smooth bounded scalar control input function, $u(t)$, a bounded solution, $y(t)$, exists for equation (5.A.1).

- Assume that the scalar function $\phi(t, y, \dot{y}, \ldots, y^{(n-1)})$ is completely unknown while the control input gain function, $\mu(t, y(t))$, is perfectly known. Notice that for a given $u(t)$, the solution $y(t)$ of the above differential equation trivially satisfies: $y^{(n)}(t) = \phi(t, y(t), \dot{y}(t), \ldots, y^{(n-1)}(t)) + \mu(t, y(t))u(t)$.
- It is assumed, based on the last fact, that as a time function, the first time derivatives $\phi^{(j)}(t, y, \dot{y}, \ldots, y^{(n-1)})$, up to a given finite order m, are all uniformly absolutely bounded. In other words, there exists constants K_j such that,[2]

$$\sup_t |\phi^{(j)}(t, y(t), \dot{y}(t), \ldots, y^{(n-1)}(t))| \leq K_j, \;\; j = 0, 1, 2, \ldots, m. \tag{5.A.2}$$

- The scalar control input gain $\mu(t, y(t))$ is bounded and uniformly absolutely bounded away from zero, that is, there exists a constant $M > 0$, such that $\inf_t |\mu(t, y(t))| \geq M$

Definition A.2.1 *The scalar perturbed system*

$$z^{(n)} = \mu(t, z)u + \xi(t), \tag{5.A.3}$$

with initial conditions $\{z_0, \dot{z}_0, \ldots, z_0^{(n-1)}\} = Y_0$, *is a* global ultra-model *of equation (5.A.1)*, if *for every u and for all* $t \geq 0$

$$\xi(t) = \phi(t, y(t), \dot{y}(t), \ldots, y^{(n-1)}(t)). \tag{5.A.4}$$

Definition A.2.2 *Two systems:* $y^{(n)} = A(t, y, \dot{y}, \ldots, y^{(n-1)})$ *and* $z^{(n)} = B(t, z, \dot{z}, \ldots, z^{(n-1)})$ *with identical corresponding sets of initial conditions,* Y_0 and Z_0, *are trajectory equivalent if* $y(t) = z(t)$ *for all* $t \geq 0$.

Theorem A.2.3 *The system (A.3), with initial conditions:* $Z_0 = Y_0$, *and satisfying equation (A.4), is trajectory equivalent to the system (A.1).*

Proof: The error, $e(t) = y(t) - z(t)$, clearly satisfies

$$e^{(n)}(t) = [\mu(t, e(t) + z(t)) - \mu(t, z(t))]\, u(t),$$

with $e_0 = \dot{e}_0 = \cdots = e_0^{(n-1)} = 0$. It follows that $e_0^{(n)} = e_0^{(n+1)} = \cdots = e_0^{(n+j)} = 0$ for all j. Hence, $e(t) = 0$ for all t. The systems are trajectory equivalent. □

[2]This assumption cannot be verified a priori when $\phi(\cdot)$ is completely unknown. However, in cases where the nonlinearity is known except for some of its parameters, as it is the case of our motor system, its validity can be assessed with some work. As pointed out earlier, these conditions constitute a necessary and sufficient condition for the existence of solutions of the perturbed system for any given smooth and bounded control input u (see Gliklikh, 2006)

The systems (5.A.1), (A.3), and (5.A.4), are *identical* in the precise sense that their trajectories are *the same*, over any time interval, for a sheared control input function and with the same initial conditions. Consequently, *the distinction between z and y becomes irrelevant*. Any pertinent consideration on the system (5.A.1) may be examined on the linear trajectory equivalent system (5.A.3), viewed now without any ambiguity as

$$y^{(n)} = \mu(t, y)u + \xi(t), \tag{5.A.5}$$

which is devoid of the phase variables-dependent nonlinear structure. In practise, the time-valued nonlinearities, lumped in $\xi(t)$, constitutes an unknown term, thus acting as a proper disturbance to the system that needs to be estimated for ADRC.

5.A.3 Observing the uncertain System through the Ultra-Model

Setting $y_1 = y$, $y_2 = \dot{y}, \ldots, y_n = y^{(n-1)}$, a state space model for such an uncertain system is given by

$$\begin{aligned} \dot{y}_j &= y_{j+1}, \quad j = 1, \ldots, n-1, \\ \dot{y}_n &= \phi(t, y_1, y_2, \ldots, y_n) + \mu(t, y_1)u. \end{aligned} \tag{5.A.6}$$

Propose the following observer for the phase variables, $\{y_1, y_2, \ldots, y_n\}$, associated with y, characterized by the states $\hat{y}_1, \ldots, \hat{y}_n$, and complemented by m output estimation error iterated integral injections, characterized by the variable, ζ_1. We have

$$\begin{aligned} \dot{\hat{y}}_j &= \hat{y}_{j+1} + \lambda_{n+m-j}(y_1 - \hat{y}_1), \quad j = 1, \ldots, n-1, \\ \dot{\hat{y}}_n &= \mu(t, y_1)u + \zeta_1 + \lambda_m(y_1 - \hat{y}_1), \\ \dot{\zeta}_i &= \zeta_{i+1} + \lambda_{m-i}(y_1 - \hat{y}_1), \quad i = 1, \ldots, m-1, \\ \dot{\zeta}_m &= \lambda_0(y_1 - \hat{y}_1). \end{aligned} \tag{5.A.7}$$

Let the estimation error, $\tilde{e}_y$, in reference to the ultra-model system, be defined as $\tilde{e}_y = \tilde{e}_1 := y_1 - \hat{y}_1 = y - \hat{y}_1$ with $\tilde{e}_2 = y_2 - \hat{y}_2$, etc.,

$$\begin{aligned} \dot{\tilde{e}}_j &= \tilde{e}_{j+1} - \lambda_{n+m-j}\tilde{e}_1, \quad j = 1, \ldots, n-1, \\ \dot{\tilde{e}}_n &= \xi(t) - \zeta_1 - \lambda_m\tilde{e}_1, \\ \dot{\zeta}_i &= \zeta_{i+1} + \lambda_{m-i}\tilde{e}_1, \quad i = 1, \ldots, m-1, \\ \dot{\zeta}_m &= \lambda_0\tilde{e}_1. \end{aligned} \tag{5.A.8}$$

It is not difficult to see that the estimation error, $\tilde{e}_y = \tilde{e}_1$, satisfies, after elimination of all variables ζ, the following $n + m$th order perturbed linear differential equation:

$$\tilde{e}_y^{(n+m)} + \lambda_{n+m-1}\tilde{e}_y^{(n+m-1)} + \cdots + \lambda_1\dot{\tilde{e}}_y + \lambda_0\tilde{e}_y = \xi^{(m)}(t). \tag{5.A.9}$$

Clearly, if $\xi^{(m)}(t)$ is uniformly absolutely bounded, then choosing the gain coefficients, λ_j, $j = 0, 1, \ldots, n+m-1$, so that the characteristic polynomial in the complex variable s,

$$p_o(s) = s^{n+m} + \lambda_{n+m-1}s^{n+m-1} + \cdots + \lambda_1 s + \lambda_0, \tag{5.A.10}$$

exhibits all its roots sufficiently far from the imaginary axis, in the left half of the complex plane, then the trajectories for e_y and for its time derivatives ultimately absolutely converge, in an exponentially dominated manner, towards a small as desired vicinity of the origin of the estimation error phase space, $\{\tilde{e}_y, \dot{\tilde{e}}_y, \ldots, \tilde{e}_y^{(n+m-1)}\}$, where they remain ultimately bounded. The further away the roots are located in the left half of the complex plane the smaller the vicinity of ultimate boundedness around the origin of the estimation error phase space. To prove this result we proceed as follows: let $\chi = (\tilde{e}_1, \ldots, \tilde{e}_{n+m})^T$ denote the phase variables of equation (5.A.9). The perturbed linear system (5.A.9) is of the form $\dot{\chi} = A\chi + b\xi^{(m)}(t)$, with A being a Hurwitz matrix written in companion form and b is a vector of zeroes except for the last component being equal to 1. The Hurwitz character of A implies that, given a positive definite matrix Q, there exists a positive definite matrix P, such that $-Q = A^T P + PA$. The largest (real negative) eigenvalue of $-Q$ denoted by $\sigma_{max}(-Q) < 0$ satisfies $|\sigma_{max}(-Q)| \leq 2\|P\||\rho_{max}(A)|$ with $|\rho_{max}(A)|$ being the absolute value of the largest negative real part of the eigenvalues of A. The Lyapunov function candidate, $V(\chi) = \frac{1}{2}\chi^T P\chi$, exhibits, along the solutions of the linear perturbed system, a time derivative of the form $\dot{V}(\chi, t) = \frac{1}{2}\chi^T(A^T P + PA)\chi + b^T P\chi\phi^{(m)}(t)$. It follows, using the form of b, the uniform bound on $\xi^{(m)}(t)$ and the just established matrix inequalities, that everywhere outside the sphere: $\mathcal{S} = \{\chi \in R^{n+m} \mid \|\chi\|^2 \leq K^2/(|\rho_{max}(A)|)^2\}$, the time derivative $\dot{V}(\chi, t)$ is strictly negative, while inside the sphere $\mathcal{S}$ its sign is undefined. Hence, all trajectories, $x(t)$, starting outside this sphere, defined in the estimation error phase space, converge towards its interior, and all those trajectories starting inside $\mathcal{S}$ will never abandon it. The more negative the real parts of all the eigenvalues of A, the larger $(\rho_{max}(A))^2$, and smaller the radius of the ultimate bounding sphere $\mathcal{S}$ in the x space. From equation (5.A.8) it follows that

$$\zeta_1 = \xi(t) - \lambda_m\tilde{e}_1 - \dot{\tilde{e}}_n. \tag{5.A.11}$$

Hence, as $\tilde{e}_1$ and $\tilde{e}_n$ evolve towards the small bounding sphere in the estimation error phase space, the trajectory of ζ_1 tracks arbitrarily close the unknown function, $\xi(t)$. This fact demonstrates the *self-updating* character of the polynomial disturbance model, as an internal model in the GPI observer. Clearly, ζ_i converges towards a vicinity of $\xi^{(i-1)}(t)$, $i = 1, \ldots, m$. From the definition of the estimation errors for y, and its time derivatives, it follows that $\hat{y}_j$, $j = 1, \ldots, n$, reconstruct, in an arbitrarily close fashion, the time derivatives of y.

5.A.4 The Observer-Based Active Disturbance Rejection Controller

The stabilizing controller is given by

$$u = -\frac{1}{\mu(t, y)}\left[\sum_{k=0}^{n-1}\kappa_k\hat{y}_{k+1} + \zeta_1\right], \tag{5.A.12}$$

with the set of coefficients, $\{\kappa_0, \ldots, \kappa_{n-1}\}$, chosen so that $p_c(s) = s^n + \kappa_{n-1}s^{n-1} + \cdots + \kappa_0$ exhibits all its roots in the left half of the complex plane $\mathbb{C}$. The closed-loop output $e = y - 0 = y$ is governed by

$$e^{(n)} + \kappa_{n-1}e^{(n-1)} + \cdots + \kappa_0 e = (\xi(t) - \zeta_1) + \sum_{k=1}^{n-1} \kappa_k \tilde{e}_y^{(k)}. \tag{5.A.13}$$

Theorem A.4.1 *The disturbance rejection output feedback controller in equation (A.12) drives the trajectory of the controlled system output, $y(t)$, towards a small as desired vicinity of the origin of the output phase space, $(y, \dot{y}, \ldots, y^{(n-1)})$, provided the set of coefficients $\{\kappa_0, \ldots, \kappa_{n-1}\}$, are chosen so that $p_c(s) = s^n + \kappa_{n-1}s^{n-1} + \cdots + \kappa_0$ is a Hurwitz polynomial with roots sufficiently far from the imaginary axis in $\mathbb{C}$.*

Proof: According to the previous theorem, the term $\xi(t) - \zeta_1$ and the terms $\tilde{e}_y^{(k)}$, $k = 1, 2, \ldots, n-1$, evolve toward a small as desired neighborhood of the origin. It follows that the right-hand side of the linear system (5.A.13) evolves, in an uniformly ultimately bounded fashion, within a sufficiently small neighborhood of the origin of the output tracking error phase space. Using the same arguments as in the proof of the previous theorem, it follows that the error, $e = y - 0$, and its time derivatives, converge towards a small as desired vicinity of the tracking error phase space coordinates: $\eta = (e, \dot{e}, \ldots, e^{(n-1)})$, provided the roots of $p_c(s)$ are located sufficiently to the left of the imaginary axis in $\mathbb{C}$. □

Implementation of the GPI observer-based ADRC algorithm requires low pass filtering, along with "clutching" of the high-gain observer output signals. Real life noises do not preclude the application of high-gain observers, as it can be inferred from the experimental results here presented. The integer m, depicting the order of approximation of the lumped disturbance signal $\xi(t)$, is typically chosen as $m = 3$ or, at most, $m = 5$ (see Sira-Ramírez *et al.* (2010b) for experimental details on other types of systems).

References

Bodson M, Chiasson J, and Novotnak R (1994) High-performance induction motor control via input-output linearization. *Control Systems Magazine, IEEE*, **14**(4), 25–33.

Bodson M, Chiasson J, and Novotnak R (1995) Nonlinear speed observer for high-performance induction motor control. *IEEE Transactions on Industrial Electronics*, **42**(4), 337–343.

Chiasson J (2005) *Modeling and High-Performance Control of Electric Machines*. Wiley-IEEE Press, Hoboken, NJ.

Diop S, and Fliess M (1991) Nonlinear observability, identifiability and persistent trajectories. *36th IEEE Conference on Decision and Control,* Brighton, England, pp. 714–719.

Fliess M, Marquez R, Delaleau E, and Sira-Ramírez H (2002) Correcteurs Proportionnels-Intègraux Généralisés. *ESAIM: Control, Optimization and Calculus of Variations*, **7**(2), 23-41.

Fliess M, Join C, and Sira-Ramírez H (2008) Non-linear estimation is easy. *International Journal of Modeling, Identification and Control*, **4**(1), 12–27.

Fliess M and Join C (2008) Intelligent PID controller. *16th Mediterranean Conference on Control and Automation,* Ajaccio, France, pp. 326–331.

Gao Z, Huang Y, and Han J (2001) An alternative paradigm for control system design. *40th IEEE Conference on Decision and Control 2001*, 4578–4585.

Gao Z (2006) Active disturbance rejection control: a paradigm shift in feedback control system design. *American Control Conference,* Minneapolis, MN. pp. 2399–2405.

Gliklikh YE (2006) Necessary and sufficient conditions for global -in-time existence of solutions of ordinary, stochastic and parabolic differential equations. *Abstract and Applied Analysis*, **2006**, 1–17.

Han J (2009) From pid to active disturbance rejection control. *IEEE Transactions on Industrial Electronics*, **56**, 900–906.

Hinkkanen M (2004) Flux estimators for speed sensorless induction motor drives. *PhD Thesis. Helsinki University of Technology* Institute of Intelligent Power Electronics Publications, Publication 9.

Johnson CD (1971) Accommodation of external disturbances in linear regulator and servomechanism problems. *IEEE Transactions on Automatic Control*, **AC-16**, 635–644.

Johnson CD (2008) Real-time disturbance-observers; origin and evolution of the idea. Part 1: the early years. *40th Southeastern Symposium on System Theory.* New Orleans, LA 88–91.

Karagiannis D, Astolfi A, Ortega R, and Hilairet M (2009) A nonlinear tracking controller for voltage–fed induction motors with uncertain load torque. *IEEE Transactions on Control Systems Technology*, **17**(3), 608–619.

Kim D, Ha I, and Ko M (1990) Control of induction motors via feedback linearization with input-output decoupling. *International Journal of Control*, **51**(4), 863–883.

Leonhard W (2001) *Control of Electrical Drives* Power Systems, edn. Springer, Berlin.

Luviano-Juárez A, Cortés-Romero J, and Sira-Ramírez H (2010) Synchronization of chaotic oscilators by means of proportional integral observers. *International Journal of Bifurcation and Chaos*, **20**(5), 1509–1517.

Maggiore M, and Passino K (2005) Output feedback tracking: a separation principle approach. *Automatic Control, IEEE Transactions,* **50**(1), 111–117.

Marino R, Tomei P, and Verrelli C (2010) *Induction Motor Control Design Advances in Industrial Control*. Springer-Verlag, London.

Martin P and Rouchon P (2000) Two simple flux observers for induction motors. *International Journal of Adaptive Control and Signal Processing*, **14**, 171–175. doi: 10.1002/(SICI)1099-1115(200003/05)14:2/3<171::AID-ACS583>3.0.CO;2-0.

Ortega R, Loría-Perez J, Nicklasson P, and Sira-Ramirez H (1998) *Passivity-Based Control of Euler-Lagrange Systems Mechanical, Electrical and Electromechanical Applications Communications and Control Engineering*. Springer-Verlag, London.

Shipanov AG (1939) Theory and methods of designing automatic regulators. *Automatika in Telemekhanika*, **4**, 49–66.

Sira-Ramírez H, Luviano-Juárez A, and Cortés-Romero J (2012) Flatness-based linear output feedback control for disturbance rejection and tracking tasks on a Chua's Circuit. *International J. of Control*, **85** (accepted for publication, to appear).

Sira-Ramírez H, Núñez C, and Visairo N (2009) Robust sigma-delta generalised proportional integral observer based control of a 'buck' converter with uncertain loads. *International Journal of Control*, **83**(8), 1631–1640.

Sira-Ramírez H, Velasco-Villa M, and Rodríguez-Angeles A (2010) Trajectory tracking control of an input delayed monocycle. *American Control Conference 2009*, Baltimore USA.

Sira-Ramírez H, López-Uribe C, and Velasco-Villa M (2012a) Linear observer-based active disturbance rejection control of the omnidirectional mobile robot. *Asian Journal of Control*, (accepted for publication, to appear).

Sira-Ramírez H, Feliu-Batlle V (2011) Robust Σ - Δ modulation based sliding mode observers for linear systems subject to time polynomial inputs. *International Journal of Systems Science*, **42**(4), 621–631.

Sira-Ramírez H, Luviano-Juárez A, and Cortés-Romero J (2012b) Robust input-output sliding mode control of the buck converter. *Control Engineering Practice* (accepted for publication, to appear).

Sira-Ramírez H, Luviano-Juárez A, and Cortés-Romero J (2012c) Flatness-based linear output feedback control for disturbance rejection and tracking tasks on a Chua's Circuit. *International J. of Control*, **85**(5), 594–602.

Sira-Ramírez H, Ramírez-Neria M, and Rodríguez-Angeles A (2010b) On the linear control of nonlinear mechanical systems. *49th IEEE Conference on Decision and Control*, Atlanta, 1999–2004.

Sun B, and Gao Z (2005) A DSP-based active disturbance rejection control design for a 1-kW H-bridge DC–DC power converter. *IEEE Transactions on Industrial Electronics*, **52**(5), 1271–1277.

Tian G and Gao Z (2009) From Poncelet's invariance principle to active disturbance rejection. *American Control Conference, 2009. ACC '09.*, pp. 2451–2457, St. Louis, MO.

Trzynadlowski A (1994) *The Field Orientation Principle in Control of Induction Motors*. Kluwer Academic Publishers, Norwell, MA.

Verghese G and Sanders S (1988) Observers for flux estimation in induction machines. *IEEE Transactions on Industrial Electronics*, **35**(1), 85–94.

6

Observers Design for Systems with Sampled Measurements, Application to AC Motors

Vincent Van Assche, Philippe Dorléans, Jean-François Massieu, and Tarek Ahmed-Ali
GREYC Lab, University of Caen Basse-Normandie, France

6.1 Introduction

This work is devoted to observer design for a class of uniformly observable systems with sampled and delayed measurements. In the last decades, the design of nonlinear observers for continuous systems with sampled measurements has received a great attention. This interest is motivated by many engineering applications, such as network control systems (NCSs) in which the output is transmitted over a shared digital communication network, and is only available at discrete-time instants. For linear systems, it is usually possible to design observers by using the discrete-time model of the continuous-time system. This is not always possible for nonlinear systems because the exact discrete-time model is generally not available. In this case, there exist two main approaches for dealing with this problem. The first one is based on the design of a discrete observer by using a consistent approximation of the exact discretized model. This approach provides a semi-global practical stability of the observation error. More details on this method can be founded in the work from Arcak and Nešić (2004) and its references. The second one is based on a mixed continuous and discrete design. This approach has been inspired by Jazwinski (1970) who introduced the continuous-discrete Kalman filter to solve a filtering problem for stochastic continuous-discrete time systems. It consists of two steps. In the first one (which is called the prediction step), the observer is a copy of the model system,

AC Electric Motors Control: Advanced Design Techniques and Applications, First Edition. Edited by Fouad Giri.

whereas in the second step, the value of the state estimate is updated using the newly available sampled measure. The exponential convergence of the observation error is then ensured under some sufficient conditions on the sampling period through the stability analysis of impulsive systems. Deza *et al*. (1992) use this approach to write a discrete-continuous version of the well-known high-gain observer (Gauthier *et al*. 1992). Nadri and Hammouri (2003) have designed observers for a MIMO class of state affine systems where the dynamical matrix depends on the inputs when those inputs are regularly persistent. This work was extended to adaptive observers by Ahmed-Ali *et al*. (2009). Astorga *et al*. (2002) used a similar method for a larger class of systems and applied it to the observation of an emulsion copolymerization process. The observation of a class of systems with output injection has been treated by Nadri *et al*. (2004) and recently, Hammouri *et al*. (2006) developed a high-gain continuous-discrete observer by using constant observation gains. Andrieu and Nadri (2010) extend the work from Zemouche *et al*. (2008) to the discrete-time measurements case. Recently, a hybrid sampled-data observer dedicated of a class of nonlinear systems has been presented by Karafyllis and Kravaris (2009). This scheme is based on an inter-sample time predictor that estimates the output between two sampling instants: the estimates remain continuous and only the predictor is re-initialized at each sampling instant. This algorithm has been extended to some networked control systems by Ahmed-Ali and Lamnabhi-Lagarrigue (2012) by using a *Lyapunov Krasovskii* approach. The design of observers for linear detectable systems with sampled and delayed measurements was also treated by Hespanha *et al*. (2007b) by using a descriptor system approach and a *Lyapunov Krasovskii* functional. The authors have proposed a hybrid observer for a class of linear systems and derive sufficient conditions based on *linear matrix inequalities* to guarantee exponential convergence of the observation error. This idea has also been used by Raff *et al*. (2008) and Van Assche *et al*. (2011) for some classes of nonlinear systems with nonuniformly sampled measurements.

In this chapter, we present two classes of observers. The first one is an extension to delayed measurements of the continuous-discrete observer developed by Nadri and Hammouri (2003). The second one is based on the introduction of an estimator of the delayed output between two updating instants. It can be viewed as an extension of the work by Ahmed-Ali *et al*. (2012) to the sampled-data case by using the idea that consists the predicting of the output between two sampling instants developed by Karafyllis and Kravaris (2009).

The chapter is structured as follows: first, two observer designs are presented, then the application of those designs to the case of an induction motor without speed sensor is explained, and eventually, some simulations results are given to illustrate this application.

6.2 Nomenclature

The following notation will be used throughout this chapter. $\mathbb{R}$ denotes the field of real numbers, $\mathbb{R}^+$ the set of strictly positive real numbers and $\mathbb{R}_0^+ = \mathbb{R}^+ \cup \{0\}$. I_p is the identity matrix of dimension $p \times p$ and 0_p represents the zero matrix of dimensions $p \times p$. The transpose of a matrix M will be noted M'. The Euclidean norm of a vector a will be noted $\|a\|$ and the $\mathcal{L}_2$ norm of a matrix A will be noted $\|A\|$. The time dependency of the signals will be omitted for signals taken at time t, that is, the system state $x(t)$ will be written x and its derivative will be written $\dot{x}$.

6.3 Observer Design

6.3.1 Nonlinear System Model

In this chapter, two observer designs are presented to be applied to the case of an AC motor with sampled measurements. Those designs can be applied to a larger class of nonlinear models and are first presented within the framework of this class of systems. Then, their application to the case of an AC motor is explained.

The value of the output of the system is known only at the sampling instants noted t_k where $(t_k)_{k\in\mathbb{N}}$ is an increasing sequence with $\lim_{k\to+\infty} t_k = +\infty$. It is assumed that an upper bound T_e is known for the size of the sampling intervals

$$T_e \geq t_{k+1} - t_k, \ \forall k \in \mathbb{N}. \tag{6.1}$$

A general nonlinear system with sampled output can be written

$$\begin{cases} \dot{x} = f(x,u), \\ y(t_k) = h(x(t_k)). \end{cases} \tag{6.2}$$

The observer design presented in the sequel applies to the following class of uniformly observable nonlinear systems:

$$\begin{cases} \dot{x} = Ax + \phi(x,u), \\ y(t_k) = Cx(t_k), \end{cases} \tag{6.3}$$

with the following hypothesis:

H1: The state vector $x \in \mathbb{R}^n$ is composed of q subvectors, $x_1, \ldots, x_q$, that is,

$$x = \left(x_1' \cdots x_q'\right)' \tag{6.4}$$

with $\forall i = 1, \ldots, q, x_i \in \mathbb{R}^p$, with, obviously, $n = pq$.

H2: $A \in \mathbb{R}^{n\times n}$ is a block diagonal matrix

$$A = \begin{pmatrix} 0 & I_p & 0 & \cdots & 0 \\ \vdots & \ddots & I_p & \ddots & \vdots \\ \vdots & & \ddots & \ddots & 0 \\ \vdots & & & \ddots & I_p \\ 0 & \cdots & \cdots & \cdots & 0 \end{pmatrix} \tag{6.5}$$

H3: ϕ is a $n \times 1$ matrix of mappings, block-triangular in x, that is,

$$\phi(x,u) = \begin{pmatrix} \phi_1(x_1,u) \\ \phi_2(x_1,x_2,u) \\ \cdots \\ \phi_q(x_1,\ldots,x_q,u) \end{pmatrix}. \tag{6.6}$$

H4: The functions ϕ_i are globally Lipschitz with respect to x, uniformly in u, that is, $\exists \beta > 0$ such that $\forall (x_a, x_b) \in \mathbb{R}^n \times \mathbb{R}^n$ and $\forall u \in \mathbb{R}^p$

$$\left\| \phi_i(x_{a,1},\ldots,x_{a,i},u) - \phi_i(x_{b,1},\ldots,x_{b,i},u) \right\| \leq \beta \left\| x_a^i - x_b^i \right\|, \tag{6.7}$$

where x_a^i and x_b^i are the vectors $(x_{a,1},\ldots,x_{a,i})'$ and $(x_{b,1},\ldots,x_{b,i})'$, respectively.

H5: $C \in \mathbb{R}^{p\times n}$ with $C = \begin{pmatrix} I_p & 0_p & \cdots & 0_p \end{pmatrix}$.

6.3.2 Observer Design with a Time-Delay Approach

The first observer design we present handles the sample mechanism as a variable time-delay. This observer is an extension to the multiple output case of the observer proposed by Van Assche *et al*. (2011), based on the high-gain approach from Gauthier *et al*. (1992), to handle a class of nonlinear systems with variable measurements delays, without imposing a bound on the variation rate of the delay.

The sampling mechanism is transformed into a time-variable delay by defining the following delay function:

$$\tau(t) = t - t_k, \quad \forall t \in [t_k, t_{k+1}), \tag{6.8}$$

with $\dot{\tau} = 1$ in the intervals $[t_k, t_{k+1})$, such that at any time $t \in [t_k, t_{k+1})$, system (6.3) is equivalent to

$$\begin{cases} \dot{x} = Ax + \phi(x,u), \\ y(t_k) = Cx(t-\tau(t)). \end{cases} \tag{6.9}$$

The following theorem applies to any variable time delay system of the form (6.9). In the sequel, it will be applied to the particular case where the delay is of the form (6.8) to model the sampling mechanism.

Theorem 6.3.1 *Consider the observer*

$$\dot{\hat{x}} = A\hat{x} + \phi(\hat{x},u) - \theta\Delta^{-1}S^{-1}C^T\left[C\hat{x}(t-\tau) - y(t-\tau)\right], \tag{6.10}$$

where θ is a positive constant satisfying $\theta > 1$, S is a symmetric positive definite matrix solution of the equation

$$SA + A^TS - C^TC = -S, \tag{6.11}$$

and Δ *is the following block-diagonal matrix:*

$$\Delta = \text{Diag}\left(I_p, \frac{1}{\theta} I_p, \frac{1}{\theta^2} I_p, \ldots, \frac{1}{\theta^{q-1}} I_p\right). \tag{6.12}$$

For sufficiently large positive value of θ*, there exists a positive constant* T *such that, for any* $\tau(t) < T$ *and any initial condition* $x(0) = x_0$ *and* $\hat{x}(0) = \hat{x}_0$*,*

$$\lim_{t \to +\infty} \|\hat{x} - x\| = 0. \tag{6.13}$$

Proof: Let the observation error be noted

$$\tilde{x} = \hat{x} - x. \tag{6.14}$$

Using equations (6.3) and (6.10), one can write the dynamic equation of this error

$$\dot{\tilde{x}} = A\tilde{x} + \phi(\hat{x}, u) - \phi(x, u) - \theta \Delta^{-1} S^{-1} C' C \tilde{x}(t - \tau(t)). \tag{6.15}$$

Using the change of coordinates

$$\bar{x} = \Delta \tilde{x} \tag{6.16}$$

and the Newton-Leibniz formula

$$\bar{x}(t - \tau(t)) = \bar{x} - \int_{t-\tau(t)}^{t} \dot{\bar{x}}(\sigma) \mathrm{d}\sigma,$$

together with the property $C\Delta = C\Delta^{-1} = C$, one can rewrite equation (6.15) in the following form:

$$\dot{\bar{x}} = \theta\left[A - S^{-1} C' C\right]\bar{x} + \Delta\left[\phi(\hat{x}, u) - \phi(x, u)\right] + \theta S^{-1} C' C \int_{t-\tau(t)}^{t} \dot{\bar{x}}(\sigma) \mathrm{d}\sigma. \tag{6.17}$$

In order to derive an upper bound on the delay ensuring the asymptotic convergence of the observation error, we use a *Lyapunov-Krasovskii* functional proposed by Fridman *et al.* (2008).

$$W = \bar{x}' S \bar{x} + \int_{t-T}^{t} \int_{\sigma}^{t} \left\|\dot{\bar{x}}(\xi)\right\|^2 \mathrm{d}\xi \, \mathrm{d}\sigma. \tag{6.18}$$

After some straightforward computations, the functional (6.18) can be rewritten as

$$W = \bar{x}' S \bar{x} + \int_{t-T}^{t} (\sigma - t - T) \left\|\dot{\bar{x}}(\sigma)\right\|^2 \mathrm{d}\sigma.$$

Its derivative satisfies the following inequality:

$$\dot{W} \leq \theta \bar{x}' \left(A'S + SA - 2C'C\right) \bar{x} + 2\bar{x}' S \Delta\left(\phi(\hat{x}, u) - \phi(x, u)\right) + 2\theta \bar{x}' C'C I + T \left\|\dot{\bar{x}}\right\|^2 - \int_{t-T}^{t} \left\|\dot{\bar{x}}(\sigma)\right\|^2 \mathrm{d}\sigma, \tag{6.19}$$

with

$$I = \int_{t-\tau(t)}^{t} \dot{\bar{x}}(\sigma) \mathrm{d}\sigma. \tag{6.20}$$

We will now bound the different terms of the right-hand side of this equation to express a sufficient condition on T ensuring that this derivative is negative.

Using equation (6.11) in the first term of (5.19) leads to

$$\dot{W} \leq \theta V - \theta \bar{x}' C'C \bar{x} + 2\bar{x}' S \Delta\left(\phi(\hat{x}, u) - \phi(x, u)\right) + 2\theta \bar{x}' C'C I + T \left\|\dot{\bar{x}}\right\|^2 - \int_{t-T}^{t} \left\|\dot{\bar{x}}(\sigma)\right\|^2 \mathrm{d}\sigma, \tag{6.21}$$

where $V = \bar{x}' S \bar{x}$.

Using the triangular structure and the Lipschitz property of the function ϕ, if $\theta > 1$, Gauthier *et al.* (1992) proved that

$$\left\|\Delta\left(\phi(\hat{x}, u) - \phi(x, u)\right)\right\| \leq \sqrt{q}\beta \left\|\bar{x}\right\|. \tag{6.22}$$

This implies the existence of a constant

$$k_1 = 2\frac{\lambda_{\max}(S)}{\lambda_{\min}(S)}\sqrt{q}\beta, \tag{6.23}$$

such that

$$\left\|2\bar{x}' S \Delta\left(\phi(\hat{x}, u) - \phi(x, u)\right)\right\| \leq k_1 V, \tag{6.24}$$

where $\lambda_{\max}(S)$ and $\lambda_{\min}(S)$ are the largest and smallest eigenvalues of S, respectively. Thus, equation (6.21) becomes

$$\dot{W} \leq -\theta V + k_1 V - \theta \bar{x}' C'C \bar{x} + 2\theta \bar{x}' C'C I + T \left\|\dot{\bar{x}}\right\|^2 - \int_{t-T}^{t} \left\|\dot{\bar{x}}(\sigma)\right\|^2 \mathrm{d}\sigma. \tag{6.25}$$

Now, remark that

$$2\theta \bar{x}' C'C I - \theta \bar{x}' C'C \bar{x} = \theta I' C'C I - \theta \left(C\bar{x} - I\right)' \left(C\bar{x} - I\right) \leq \theta I C'C I,$$

therefore,

$$\dot{W} \leq -\theta V + k_1 V + \theta I' C' C I + T \left\| \dot{\hat{x}}(t) \right\|^2 - \int_{t-\tau(t)}^{t} \left\| \dot{\hat{x}}(\sigma) \right\|^2 \mathrm{d}\sigma. \tag{6.26}$$

From equation (6.17) comes

$$\left\| \dot{\hat{x}} \right\| \leq \theta\alpha \left\| \bar{x} \right\| + \left\| \Delta \left(\phi(\hat{x}, u) - \phi(x, u) \right) \right\| + \theta \lambda_{\max} \left(S^{-1} \right) \left\| I \right\|,$$

where $\alpha = \left\| A - S^{-1} C' C \right\|$. Using equation (6.22) once again leads to

$$\left\| \dot{\hat{x}} \right\| \leq \theta \left(\alpha + \sqrt{q}\beta \right) \left\| \bar{x} \right\| + \theta \lambda_{\max}(S^{-1}) \left\| I \right\|,$$

and consequently, through the Young inequality, to

$$\left\| \dot{\hat{x}} \right\|^2 \leq \theta^2 k_2 \left(V - \left\| I \right\|^2 \right),$$

where

$$k_2 = 2 \sup \left\{ \left(\frac{\alpha + \sqrt{q}\beta}{\lambda_{\min}(S)} \right)^2, \lambda_{\max}^2(S^{-1}), 1 \right\}. \tag{6.27}$$

With the Jensen's inequality

$$\left\| I \right\|^2 \leq T \int_{t-\tau(t)}^{t} \left\| \dot{\hat{x}}(\sigma) \right\|^2 \mathrm{d}\sigma, \tag{6.28}$$

we get

$$\left\| \dot{\hat{x}} \right\|^2 \leq \theta^2 k_2 \left(V + T \int_{t-\tau(t)}^{t} \left\| \dot{\hat{x}}(\sigma) \right\|^2 \mathrm{d}\sigma \right).$$

Using this into equation (6.26) gives

$$\dot{W} \leq -(\theta - k_1 - T\theta^2 k_2) V - (1 - \theta T - T^2 \theta^2 k_2) \int_{t-\tau(t)}^{t} \left\| \dot{\hat{x}}(\sigma) \right\|^2 \mathrm{d}\sigma. \tag{6.29}$$

Let us set $T = \frac{1}{2k_2\theta}$, so that equation (6.29) becomes

$$\dot{W} \leq -\left(\frac{\theta}{2} - k_1 \right) V - \left(1 - \frac{3}{8k_2} \right) \int_{t-\tau(t)}^{t} \left\| \dot{\hat{x}}(\sigma) \right\|^2 \mathrm{d}\sigma. \tag{6.30}$$

Since $k_2 \geq 1$, we always have $\left(1 - \frac{3}{8k_2}\right) \geq 0$. Hence, with this value of T, if $\left(\frac{\theta}{2} - k_1\right) > 0$, then $\dot{W}$ is negative and equation (6.30) becomes

$$\dot{W} \leq -\left(\frac{\theta}{2} - k_1\right) V < 0. \tag{6.31}$$

Integrating this equation and applying Barbalat's lemma proves that if the two following conditions are met:

$$\theta > \sup\{1, 2k_1\}, \tag{6.32a}$$

$$\tau(t) \in \left[0, \frac{1}{2k_2\theta}\right), \tag{6.32b}$$

then

$$\lim_{t \to +\infty} \|\tilde{x}\| = 0, \tag{6.33}$$

which proves the theorem. □

Theorem 6.3.1 proves that if the variable delay $\tau(t)$ is bounded with a sufficiently small bound in system (6.3), equation (6.10) gives an asymptotically convergent observer. Furthermore, equation (6.32) gives computable conditions on the delay bound T and the observer gain θ such that the convergence of the observation error is ensured. Obviously, this result can be directly applied to the sampled measurements case, as in the following result.

Corollary 6.3.2 *Consider a system with sampled measurements*

$$\begin{cases} \dot{x} = Ax + \phi(x, u), \\ y(t_k) = Cx(t_k), \end{cases} \tag{6.34}$$

for which the hypotheses H1–H5 apply. In this case, the observer can be written

$$\dot{\hat{x}} = A\hat{x} + \phi(\hat{x}, u) - \theta\Delta^{-1}S^{-1}C^T\left[C\hat{x}(t_k) - y(t_k)\right] \quad \text{for } t \in [t_k, t_{k+1}). \tag{6.35}$$

Assuming that the following conditions are fulfilled:

$$\theta > \sup\{1, 2k_1\}, \tag{6.36a}$$

$$T_e < \frac{1}{2k_2\theta}, \tag{6.36b}$$

where k_1 and k_2 are defined by equations (6.23) and (6.27), respectively, then (6.35) is a global asymptotic observer for system (6.34).

Proof: This corollary is a straightforward application of Theorem 6.3.1: taking $\tau(t) = t - t_k$, with k such that $t_k \leq t < t_{k+1}$, system (6.34) can be rewritten as system (6.3). □

Note that in this case, $\dot{\tau} = 1$ and the demonstration of theorem 6.3.1 still holds thanks to the Lyapunov-Krasovskii functional used.

Remark 6.3.3 *In the case where the measurements are acquired through a numerical network inducing a further transmission delay δ, it is easy to adapt this scheme with the variable delay $\tau = t - t_k$ by taking k such that $t \in [t_k + \delta, t_{k+1} + \delta)$, that is, the total delay minimum value equals δ and it is reset to this minimum value at each instant $t_k + \delta, k \in \mathbb{R}$. The observer converges asymptotically if $\forall k, t_{k+1} - t_k + \delta < T_e$ and conditions (6.36) are respected.*

6.3.3 Observer Design with an Output Predictor

In the observer presented above, the error between the system output y and the observer output $C\hat{x}$ is used at each sampled instant. Although this observer converges when the sampling intervals are sufficiently small, its performance degrades rapidly as the sampling intervals increase. To allow larger sampling interval, we follow Karafyllis and Kravaris (2009) and add an inter-sample output prediction equation to the observer.

In this case, the output delay δ, which comes in addition to the sampling of the measurements, has to be explicitly taken into account. Hence, the system we handle now is similar to (6.34) but it is assumed that the measure $y(t_k)$ is not available to the observer before instant $t_k + \delta$, where δ represents the transmission delay.

Corollary 6.3.4 *Consider system (6.34) with hypotheses H1–H5. For sufficiently large values of θ, there exist two positive reals T_δ and T_e such that if $\delta \leq T_\delta$ and, $\forall k \in \mathbb{N}, t_{k+1} - t_k < T_e$ then*

$$\begin{cases} \dot{\hat{x}} = A\hat{x} + \phi(\hat{x}, u) - \theta\Delta^{-1}S^{-1}C'(C\hat{x}(t-\delta) - w), \\ \dot{w} = CA\hat{x}(t-\delta) + C\phi(\hat{x}(t-\delta), u(t-\delta)), \text{ for } t \in [t_k + \delta, t_{k+1} + \delta), \\ w(t_k + \delta) = y(t_k), \end{cases} \tag{6.37}$$

is a global exponential observer.

The variable w represents the prediction of the output of the system when the current measured output is not available: at each delayed sampling instant $t_k + \delta$, w takes the value of the measured output $y(t_k)$ and between two sampling instants, the evolution of w is computed continuously using the estimated state $\hat{x}$. The observation equation itself is the classical continuous-time high-gain observer equation, using the predictor output w instead of the unavailable system output y.

Sketch of the proof: To prove this corollary, two error terms are needed, the usual state estimation error and the error due to the delay δ between the predictor and the system output

$$\tilde{x} = \hat{x} - x, \tag{6.38}$$

$$\tilde{w} = w - y(t - \delta). \tag{6.39}$$

The equations of the evolution of those errors are deduced from equations (6.34) and (6.37),

$$\dot{\tilde{x}} = A\tilde{x} + \phi(\hat{x}, u) - \phi(x, u) - \theta\Delta^{-1}S^{-1}C^T\left(C\hat{x} - w\right), \tag{6.40}$$

$$\widetilde{w} = CA\tilde{x}(t-\delta) + C\phi(\hat{x}(t-\delta), u(t-\delta)) - C\phi(x(t-\delta), u(t-\delta)) \quad \forall t \in [t_k + \delta, t_{k+1} + \delta), \tag{6.41}$$

$$\widetilde{w}(t_k + \delta) = 0. \tag{6.42}$$

To prove the convergence of the error $\tilde{x}$ towards 0, the following Lyapunov candidate is used, based on the work from Hespanha *et al*. (2007b):

$$U = \bar{x}'S\bar{x} + \int_{t-\tau}^{t}\int_{\zeta}^{t}\left\|\dot{\tilde{x}}(\sigma)\right\| \mathrm{d}\sigma\,\mathrm{d}\zeta + \gamma\psi(t)\left\|\widetilde{w}\right\|^2, \tag{6.43}$$

where $\bar{x} = \Delta\tilde{x}$, as in (6.16), γ is a positive design parameter and $\psi(t)$ is a piecewise differentiable function such that

$$\begin{cases} \psi(t) > 0, \quad \forall t > 0, \\ \psi(t_k) = \psi_{\max} \in \mathbb{R}^+, \quad \forall k \in \mathbb{N}, \\ \dot{\psi}(t) < 0, \quad \forall k \in \mathbb{N},\ \forall t \in [t_k, t_{k+1}). \end{cases} \tag{6.44}$$

Since, $\widetilde{w}(t_k) = 0$ for all $k \in \mathbb{N}$,

$$U(t_k) \leq \lim_{t \to t_k^-} U(t). \tag{6.45}$$

The functional U is differentiable on the intervals $[t_k, t_{k+1})$. Equation (6.43) is differentiated and, for each term of its differentiation, a suitable bound depending on either $\|\bar{x}\|^2$, $\int_{t-\delta}^{t}\left\|\dot{\tilde{x}}(\sigma)\right\|^2 \mathrm{d}\sigma$, or $\|\tilde{w}\|^2$ can be found, such that one can find three constants k_1, k_2, and k_3 with, $\forall k \in \mathbb{N}$, $\forall t \in [t_k, t_{k+1})$,

$$\dot{U} \leq -k_1\|\bar{x}\|^2 - k_2\int_{t-\delta}^{t}\left\|\dot{\tilde{x}}(\sigma)\right\|^2 \mathrm{d}\sigma - k_3\left\|\widetilde{w}\right\|^2 \leq -\epsilon U, \tag{6.46}$$

for some real $\epsilon > 0$. Equations (6.45) and (6.46) imply that U decreases inside each sampling interval and does not increase at the sampling instants thus proving the corollary.

6.4 Application to the AC Motor

6.4.1 Model of the AC Motor

This section presents the application of the above observer designs to a model of induction motor in the (α, β) reference frame. The machine is controlled through the stator voltage

$v_{s\alpha}$ and $v_{s\beta}$ and the stator current $i_{s\alpha}$ and $i_{s\beta}$ are the measured and sampled outputs, and we note

$$v = \begin{pmatrix} v_{s\alpha} \\ v_{s\beta} \end{pmatrix} \quad \text{and} \quad i = \begin{pmatrix} i_{s\alpha} \\ i_{s\beta} \end{pmatrix}.$$

It is also assumed that the load torque T_L may vary with time, hence an unknown and bounded input signal is added: u_L, which represents the variation of the load torque.

The state of the system is a dimension 6 vector that will be subdivided into 3 subvectors of dimension 2 for the design of the observer

$$x = \begin{pmatrix} i_{s\alpha} \\ i_{s\beta} \\ \phi_{r\alpha} \\ \phi_{r\beta} \\ \omega_m \\ T_L \end{pmatrix} = \begin{pmatrix} i, \\ \Phi \\ x_3 \end{pmatrix}, \tag{6.47}$$

where the subvector $\Phi = \begin{pmatrix} \phi_{r\alpha} \\ \phi_{r\beta} \end{pmatrix}$ is the instantaneous rotor flux vector and the components of the third subvector x_3 are the rotor speed ω_m and the load torque T_L: $x_3 = \begin{pmatrix} \omega_m \\ T_L \end{pmatrix}$. The output vector y is measured at each sampling instant: $y(t_k) = i(t_k) = Cx(t_k)$, with k such that $t_k \leq t < t_{k+1}$ and $C = \begin{pmatrix} I_2 & 0_2 & 0_2 \end{pmatrix}$.

The model of the induction machine is then

$$\begin{cases} \dfrac{\mathrm{d}i}{\mathrm{d}t} = -\gamma i + kF(\omega_m)\Phi + \dfrac{1}{\sigma L_s} v, \\ \dot{\Phi} = \dfrac{L_m}{\tau_r} i - F(\omega_m)\Phi, \\ \dot{\omega}_m = \dfrac{pL_m}{JL_r}\left(\phi_{r\alpha} i_{s\beta} - \phi_{r\beta} i_{s\alpha}\right) - \dfrac{1}{J} T_L, \\ \dot{T}_L = u_L, \\ y = i(t_k), \quad \text{with } k \text{ such that } t_k \leq t < t_{k+1}, \end{cases} \tag{6.48}$$

with

$$\begin{aligned} \gamma &= \frac{R_s}{\sigma L_s} + \frac{R_r {L_m}^2}{\sigma L_s {L_r}^2}, & k &= \frac{L_m}{\sigma L_r L_s}, \\ \sigma &= 1 - \frac{{L_m}^2}{L_r L_s}, & \tau_r &= \frac{L_r}{R_r}, \\ F(\omega_m) &= \frac{1}{\tau_r} I_2 - p\omega_m J_2, & J_2 &= \begin{pmatrix} 0 & 1 \\ -1 & 0 \end{pmatrix}. \end{aligned}$$

The definition of the parameters in this model are given in Table 6.1.

Table 6.1 AC machine parameters

Parameter	Definition
L_s	Stator self-inductance
L_r	Rotor self-inductance
L_m	Mutual inductance between stator and rotor windings
R_r	Rotor resistance
R_s	Stator resistance
τ_r	Rotor time constant

This model will also be noted in a shorter form,

$$\begin{cases} \dot{x} = f(x, v) + h(u_L), \\ y = Cx(t_k). \end{cases} \tag{6.49}$$

To be able to design a high-gain observer as in Corollary 6.3.2, we follow the method proposed by Dib *et al*. (2011) for the continuous-time case. The following change of variable is used:

$$z = \begin{pmatrix} z_1 \\ z_2 \\ z_3 \end{pmatrix} = g(x), \tag{6.50}$$

where z_1, z_2, and z_3 belong to $\mathbb{R}^2$, with

$$z_1 = g_1(x) = i, \tag{6.51}$$

$$z_2 = g_2(x) = kF(\omega_m)\Phi, \tag{6.52}$$

$$z_3 = g_3(x) = p\omega_m J_2 \left(-\frac{kL_m}{\tau_r} i + kF(\omega_m)\Phi \right) + kp \left(\frac{kL_m}{JL_r} \Phi J_2 i + \frac{T_L}{J} \right) J_2 \Phi. \tag{6.53}$$

We assume that the Jacobian of $g(x)$

$$\frac{\partial g}{\partial x} = \begin{pmatrix} I_2 & 0_2 & 0_2 \\ 0_2 & \dfrac{\partial g_2}{\partial \Phi} & \dfrac{\partial g_2}{\partial x_3} \\ \dfrac{\partial g_3}{\partial i} & \dfrac{\partial g_3}{\partial \Phi} & \dfrac{\partial g_3}{\partial x_3} \end{pmatrix} \tag{6.54}$$

is regular almost everywhere, which is true provided that $\Phi \neq 0$ and

$$\arctan\left(\frac{\Phi_\beta}{\Phi_\alpha}\right) - \arctan\left(p\tau_r\omega_m\right)$$

is not constant almost everywhere (Dib *et al*. 2011). This implies that the AC Motor model used is weakly observable in the sense of Hermann and Krener (1977).

Using z as state variable, the machine model (6.48) becomes

$$\begin{cases} \dot{z}_1 = z_2 + \psi_1(z_1, v), \\ \dot{z}_2 = z_3 + \psi_2(z_1, z_2), \\ \dot{z}_3 = \psi_3(x, u_L), \\ y = z_1(t_k), \quad \text{with } k \text{ such that } t_k \leq t < t_{k+1}, \end{cases} \tag{6.55}$$

where

$$\begin{aligned} \psi_1(z_1, u) &= -\gamma z_1 + \frac{1}{\sigma L_s} v, \\ \psi_2(z_1, z_2) &= \frac{1}{\tau_r}\left(\frac{L_m}{\tau_r} z_1 - z_2\right), \\ \psi_3(x, u_L) &= \frac{\partial g_3}{\partial i}\frac{\mathrm{d}i}{\mathrm{d}t} + \frac{\partial g_3}{\partial \Phi}\dot{\Phi} + \frac{\partial g_3}{\partial \omega_m}\dot{\omega}_m + \frac{\partial g_3}{\partial T_L} u_L. \end{aligned}$$

This system can be rewritten

$$\begin{cases} \dot{z} = Az + \psi(z, u), \\ y = Cz(t_k), \end{cases} \tag{6.56}$$

with

$$A = \begin{pmatrix} 0_2 & I_2 & 0_2, \\ 0_2 & 0_2 & I_2 \\ 0_2 & 0_2 & 0_2 \end{pmatrix}, \quad \psi(z, u) = \begin{pmatrix} \psi_1(z_1, v) \\ \psi_2(z_1, z_2) \\ \psi_3(x, u_L) \end{pmatrix}.$$

The AC machine model in z is of the form (6.3), hence we can present two observer designs whose convergences are ensured by Corollaries 6.3.3 and 6.3.3, respectively.

6.4.2 *Observer for AC Machine with Sampled and Held Measurements*

The first observer, as written in Corollary 6.3.3, is a direct adaptation to the sampled measures case of the one proposed by Dib *et al*. (2011):

$$\dot{\hat{x}} = f(\hat{x}, v) + \theta \Delta^{-1} \left(\frac{\partial g}{\partial x}\right)^{-1} S^{-1} C^T \left[C\hat{x}(t_k) - y(t_k)\right], \quad \forall t \in [t_k, t_{k+1}) \tag{6.57}$$

Applying the change of variables (6.50) to the state estimation, we define

$$\hat{z} = g(\hat{x}). \tag{6.58}$$

From equations (6.48) and (6.56), we have

$$\frac{\partial g}{\partial x} f(x, v) = Az + \psi(z, u), \tag{6.59}$$

and, obviously, by replacing x with $\hat{x}$,

$$\frac{\partial g}{\partial \hat{x}} f(\hat{x}, v) = A\hat{z} + \psi(\hat{z}, u). \tag{6.60}$$

Multiplying equation (6.57) by the Jacobian of g, using equation (6.60), and remarking that $C\hat{x} = C\hat{z}$, leads to

$$\dot{\hat{z}} = A\hat{z} + \psi(\hat{z}, u) + \theta \Delta^{-1} C^T \left[C\hat{z}(t_k) - y(t_k) \right]. \tag{6.61}$$

This is indeed the form of the observer from Corollary 6.3.2. Hence,

$$\lim_{t \to \infty} \|\hat{z} - z\| = 0 \tag{6.62}$$

provided that the gain θ and the sampling period T_e are set such that conditions (6.36) are fulfilled.

6.4.3 *Observer for the AC Machine with Predictor*

The second observer design adds an output-predictor

$$\begin{cases} \dot{\hat{x}} = f(\hat{x}, u) - \theta \Delta^{-1} \left(\dfrac{\partial g}{\partial x} \right)^{-1} S^{-1} C^T \left[C\hat{x}(t - \delta) - w \right], \\ \dot{w} = Cf\big(\hat{x}(t - \delta), v(t - \delta)\big), \quad t \in [t_k + \delta, t_{k+1} + \delta), \\ w(t_k + \delta) = y(t_k). \end{cases} \tag{6.63}$$

In the same way as in Section 6.4.2, we apply the change of variable (6.58) to this observer to rewrite it in the form used in Corollary 6.3.3. The first equation from (6.63) is treated in the same way as the observer equation (6.57) in Section 6.4.2 (except that w replaces y). For the second equation from (6.63), one can remark, from (6.54), that

$$C \left(\frac{\partial g}{\partial x} \right) f(\hat{x}, u) = Cf(\hat{x}, u). \tag{6.64}$$

Table 6.2 Simulation parameters

Parameter	Value	Definition
L_s	140 mH	Stator self-inductance
L_r	25 mH	Rotor self-inductance
L_m	50 mH	Mutual inductance between stator and rotor windings
R_r	0.5 Ω	Rotor resistance
R_s	1.67 Ω	Stator resistance
T_s	2e-04 s	Simulation step time
T	$60 \times T_s = 0.012$ s	Sample time
θ	42	Observer gain

Hence, we have, for $t \in [t_k + \delta, t_{k+1} + \delta)$,

$$\dot{w} = C\left(\frac{\partial g}{\partial x}\right) f(\hat{x}, u) = CA\hat{z}(t-\delta) + C\psi\left(\hat{z}(t-\delta), u(t-\delta)\right). \tag{6.65}$$

Hence, observer (6.63) can be rewritten in the form used in Corollary 6.3.3

$$\begin{cases} \dot{\hat{z}} = A\hat{z} + \psi(\hat{z}, u) - \theta\Delta^{-1}S^{-1}C^T\left[C\hat{z}(t-\delta) - w\right], \\ \dot{w} = CA\hat{z}(t-\delta) + C\psi\left(\hat{z}(t-\delta), u(t-\delta)\right), \quad t \in [t_k + \delta, t_{k+1} + \delta), \\ w(t_k + \delta) = y(t_k), \end{cases} \tag{6.66}$$

and converges for small enough values of the maximal sample interval T_e and the delay δ.

6.4.4 Simulation

Both observers introduced in Sections 6.4.2 and 6.4.3 have been applied to the same simulation model of an AC machine of the form (6.48) with sampled output. The parameters values used in the simulation are presented in Table 6.2. The physical values have been measured on a real AC Motor bench at the GREYC Laboratory by Dorléans and Massieu (2012).

The results of the simulation of the motor model and both observer schemes are shown in Figure 6.1. The control input of the motor is the square wave function seen in Figure 6.1a. To test the observers, a perturbation is introduced: the load torque T_L is also a square wave, with a phase shift of one-fourth of a period compared to the input signal (as seen in Figures 6.1c and 6.1e). The effect on the motor speed is visible in the bumps seen on the curve of the actual speed in Figure 6.1a. For both observers, the speed estimation (Figures 6.1b and 6.1d) and torque estimation (Figures 6.1c and 6.1e) are drawn.

As shown in Figure 6.1b–c, with those parameters, the observer with sample and hold equation (6.57) does not converge. Note that we were able to make this observer converge by reducing the sample interval T_e. With the parameters from Table 6.2, the observer with predictor (6.63) does converge (see Figures 6.1d,e. The added complexity and increased computation involved by the inclusion of the predictor in the observer scheme is counterbalanced by the larger sample intervals it allows.

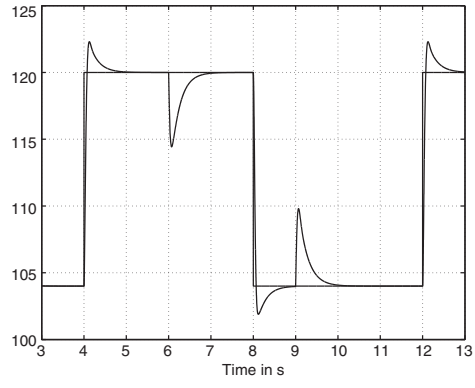

(a) Reference speed (square wave) and actual speed of system (6.48)

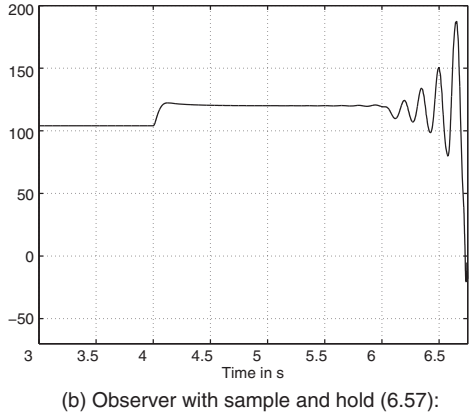

(b) Observer with sample and hold (6.57): speed estimation

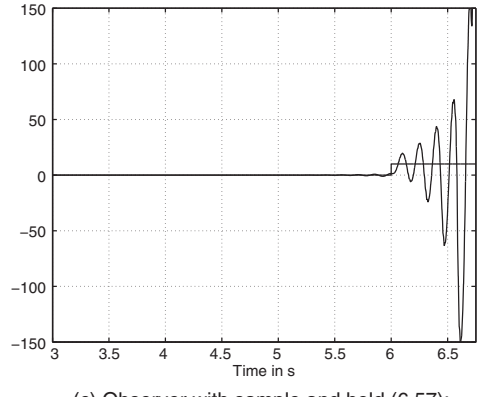

(c) Observer with sample and hold (6.57): torque estimation

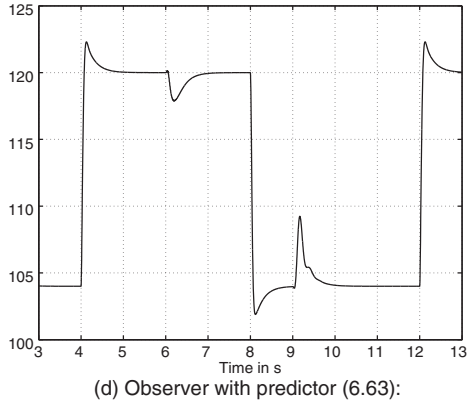

(d) Observer with predictor (6.63): speed estimation

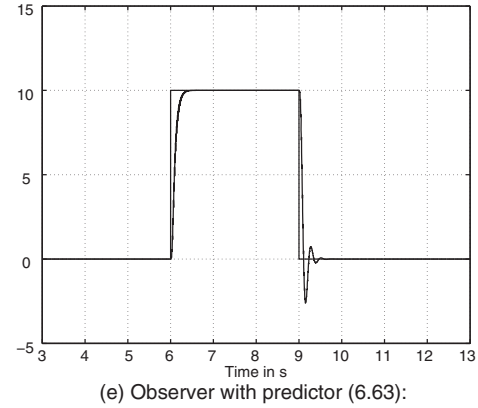

(e) Observer with predictor (6.63): torque estimation

Figure 6.1 Simulation results

6.5 Conclusions

This chapter presents two observer designs for nonlinear systems with sampled measurements and their application to an induction motor. The first design is a direct adaptation of the continuous high gain observer proposed by Dib *et al*. (2011). The output is sampled and its value is held, thus the correction term in the observer equation is constant between sampling instants. The second observer scheme includes a predictor based on the work by Karafyllis and Kravaris (2009) to estimate the output between two sampling instants. At each sampling instant, the predictor is reset to the actual value of the output. The output estimation is fed to the correction term of the observer.

The Matlab/Simulink was used to test the implementation of those observer on a simulation model of the induction machine. The model of the induction machine was adapted to the high gain framework through a change of variable. Simulations were done with different values of sampling period and observer gain and the introduction of the predictor allows for larger sampling intervals, as in the case shown on Figure 6.1.

Further work involves the implementation of the observer with predictor on a real induction machine. The real-time numerical implementation of the predictor scheme is not trivial, not only because of the predictor itself but also because of the change of variable used to adapt the motor model as it involves the computation of the inverse of the Jacobian of the transformation.

References

Ahmed-Ali T and Lamnabhi-Lagarrigue F (2012) High gain observer design for some networked control systems. *IEEE Transaction on Automatic Control,* **57**, 995–1000.

Ahmed-Ali T, Cherrier E, and Lamnabhi-Lagarrigue F (2012) Cascade high predictors for a class of nonlinear systems. *IEEE Transaction on Automatic Control,* **57**, 224–229.

Ahmed-Ali T, Postoyan R, and Lamnabhi-Lagarrigue F (2009) Continuous-discrete adaptive observers for state affine systems. *Automatica,* **45**, 2986–2990.

Andrieu V and Nadri M (2010) Observer design fot Lipschitz systems with discrete-time measurements. *CDC'10 Conference on Decision and Control*, **45**, Atlanta, GA.

Arcak M and Nešić D (2004) A framework for nonlinear sampled-data observer design via approximate discrete-time models and emulation. *Automatica,* **40**, 1931–1938.

Astorga CM, Othman N, Othman S, *et al*. (2002) Nonlinear continuous-discrete observers: applications to emulsion polymerization reactors. *Control Engineering Practice,* **10**, 3–13.

Deza F, Busvelle E, Gauthier J, and Rakotopora D (1992) High gain estimation for nonlinear systems. *Systems & Control Letters,* **18**, 295–299.

Dib A, Farza M, M'Saad M, *et al*. (2011) High gain observer for sensorless induction motor. *18th IFAC World Congress*, Milan, Italy.

Dorléans P and Massieu JF (2012) Plate-forme machine asynchrone et carte DSP DS1103. Internal report, AUTO Team, GREYC Lab.

Fridman E, Dambrine M, and Yeganefar N (2008) On input-to-state stability of systems with time-delay: a matrix inequalities approach. *Automatica,* **44**, 2364–2369.

Gauthier J, Hammouri H, and Othman S (1992) A simple obsever for nonlinear systems: application to bioreactors. *IEEE Transactions Automatic Control*, **37**(6), 875–880.

Hammouri H, Nadri M, and Mota R (2006) Constant gain observer for continuous-discrete time uniformly observable systems *Proceeding of the 45th IEEE on & Control*, San Diego, CA, pp. 6240–6244.

Hermann R and Krener AJ (1977) Nonlinear controllability and observability. *IEEE Transactions on Automatic Control,* **AC-26**, 1–34.

Hespanha J, Naghshtabrizi P, and Xu Y (2007b) A survey of recent results in networked control systems. *IEEE Special Issue on Technology of Networked Control Systems*, **95**(1), 138–162.

Jazwinski A (1970) *Stochastic processes and Filtering Theory. Mathematics in Science and Engineering*. Academic Press.

Karafyllis I and Kravaris C (2009) From continuous-time design to sampled-data design of nonlinear observers. *IEEE Control*, **54**, 2169–2174.

Nadri M and Hammouri H (2003) Design of a continuous-discrete observer for state affine systems. *Applied Mathematics*, **16**, 967–974.

Nadri M, Hammouri H, and Astorga CM (2004) Observer design for continuous-discrete time state affine systems up to output injection. *European Journal of Control*, **10**, 252–263.

Raff T, Kögel M, and Allgöwer F (2008) Observer with sample-and-hold updating for Lipschitz nonlinear systems with nonuniformly sampled measurements. *ACC'08, American Control Conference*, Seattle, WA.

Van Assche V, Ahmed-Ali T, Hann C, and Lamnabhi-Lagarrigue F (2011) High gain observer design for nonlinear systems with time varying delayed measurements. *18th IFAC World Congress*, Milan, Italy.

Zemouche A, Boutayeb M, and Bara GI (2008) Observers for a class of Lipschitz systems with extension to $\mathcal{H}_\infty$ performance analysis. *Systems & Control Letters*, **57**(1), 18–27.

7

Experimental Evaluation of Observer Design Technique for Synchronous Motor

Malek Ghanes[1] and Xuefang Lin Shi[2]
[1]*ECS-Lab, ENSEA, France*
[2]*Ampere Lab, INSA Lyon, France*

7.1 Introduction

7.1.1 Problem Statement

Permanent-magnet synchronous motors (PMSM) drives are replacing classic DC and induction motors drives, such as industrial robots and machine tools (Yang *et al.* 2009). Advantages of PMSMs include high efficiency, compactness, high torque to inertia ratio, rapid dynamic response, and simple modeling and control (Changsheng and Elbuluk 2001); (Peng *et al.* 2010). In the last years the price of rare-earth magnet material decreased significantly. For this reason PM-Machines are available for standard drives up to 300 kW (Montesinos *et al.* 2005).

PMSMs can be divided in two categories, which are based on the assembly of the permanent-magnets. The permanent magnets can be mounted on the surface of the rotor (surface permanent magnet synchronous motor—SPMSM) or inside of the rotor (interior permanent-magnet synchronous motor—IPMSM). These two configurations have an influence on the shape of the back electromotive force (BEMF) and on the inductance variation (Benjak and Gerling 2010). This chapter is devoted to the first configuration, that is, SPMSM. Industries concerned by SPMSM are continuously seeking for cost reductions in their products. The main drawback of a SPMSM is the position sensor. The use of such direct position/speed sensors induces additional electronics, extra wiring, extra space, frequent maintenance, careful mounting, and default probability. Moreover, the sensor is vulnerable for electromagnetic noise in hostile

AC Electric Motors Control: Advanced Design Techniques and Applications, First Edition. Edited by Fouad Giri.

environments and has a limited temperature range. In addition, the inertia of the rotor is increased by the attachment of the sensor to the rotor axis (Chi *et al.* 2009). For PMSM rated up to 10 kW the cost of an encoder is below 10% (Benjak and Gerling 2010), but for applications in the automotive industry with the high number of produced units the elimination of the position sensor is desirable.

For these reasons, PMSM drive research have been concentrated on the elimination of the mechanical sensors at the motor shaft (encoder, resolver, etc.) without deteriorating the dynamic performances of the drive.

7.1.2 State of the Art and Objectives

State of the Art

In order to avoid sensor position of SPMSM, several approaches for the so-called sensorless control have attracted a great deal of attention recently (see, Bolognani *et al.* 2001; Gumus *et al.* 2007; Yu and Kaynak 2009; Arellano-Padilla *et al.* 2010; Benjak and Gerling 2010; Halder *et al.* 2010; Lee and Lee 2013). These methods can be classified into three main categories. The first category is based on fundamental excitation methods, which are divided into two main groups; nonadaptive (Benjak and Gerling 2010) or adaptive methods (Bolognani *et al.* 2001; Yu and Kaynak 2009; Benjak and Gerling 2010; Lee and Lee 2013). The second category is based on saliency and signal injection methods (Arellano-Padilla *et al.* 2010). The third one is based on artificial intelligence methods (Gumus *et al.* 2007; Halder *et al.* 2010). This chapter is devoted to the first category with adaptive methods, that is, using mainly observer methods. To our best knowledge, the methods proposed in the literature to estimate the position and speed of SPMSM motor are usually tested and evaluated experimentally at high speed whereas as shown in Zaltni and Ghanes (2010) the main difficulties are primarily at very low speed of the SPMSM unobservability.

Objectives

The aim of this chapter is to provide an experimental evaluation of a model reference adaptive system (MRAS) observer based on super twisting observer (STO) without a position sensor of SPMSM. The observer is implemented and tested on experimental setup, with the aim to compare its speed and position tracking capability on high speeds and low speeds where particularly the motor state of SPMSM is unobservable.

Organization

This chapter is organized as follows:

- In Section 7.2, SPMSM model and a brief review of its observability analysis are presented.
- In Section 7.3, MRAS observer for SPMSM is described.
- In Section 7.4, experimental results of MRAS observer are illustrated on SPMSM high- and low-speed benchmark.
- In Section 7.5, some conclusions are drawn.

7.2 SPMSM Modeling and its Observability

7.2.1 SPMSM Model

In the $(\alpha - \beta)$ fixed reference frame, the dynamic model of the SPMSM reads (Zaltni and Ghanes 2010; Lee and Lee 2013)

$$\begin{pmatrix} \dot{i}_\alpha \\ \dot{i}_\beta \\ \dot{\omega} \end{pmatrix} = \begin{pmatrix} -\frac{R_s}{L_s} i_\alpha + \frac{\phi_m}{L_s} e_\alpha \\ -\frac{R_s}{L_s} i_\beta + \frac{\phi_m}{L_s} e_\beta \\ \frac{P}{J}\phi_m(-\sin(\theta_e) i_\alpha + \cos(\theta_e) i_\beta) - \frac{f_v}{J}\omega \end{pmatrix} + \begin{pmatrix} \frac{1}{L_s} & 0 & 0 \\ 0 & \frac{1}{L_s} & 0 \\ 0 & 0 & -\frac{1}{J} \end{pmatrix} \begin{pmatrix} u_\alpha \\ u_\beta \\ T_l \end{pmatrix}, \quad (7.1)$$

where

$$\begin{cases} e_\alpha = -\omega_e \sin(\theta_e), \\ e_\beta = \omega_e \cos(\theta_e) \end{cases}, \quad (7.2)$$

refer respectively to BEMF and ω is the rotor speed; $\omega_e = P.\omega$ is the electric rotor speed; $[i_\alpha \quad i_\beta]^T$ $[u_\alpha \quad u_\beta]^T$ are the $(\alpha - \beta)$ stator current and voltage vector, respectively; R_s is the stator resistance; L_s is the stator inductance; P is the pair pole number; J is the moment of inertia; ϕ_m is the magnetic flux; f_v is the viscous friction; T_l is the load torque.

7.2.2 Quick Review on the Observability of SPMSM

The observability phenomena of SPMSM has been studied by several authors (see, for instance, Junfeng *et al.* 2004; Vaclavec and Blaha 2008; Zaltni and Ghanes 2010). In Zaltni and Ghanes (2010) we have presented sufficient and necessary conditions under which the PMSM is observable and unobservable. The problem was to characterize the conditions under which the state x of the sensorless PMSM can be observed from measures (currents) and its derivatives at any order. The result is that the SPMSM observability cannot be established in the particular case of zero speed and zero acceleration even if we use the higher derivatives of currents. This is a sufficient and necessary condition for loss of observability.

7.3 Robust MRAS Observer

The structure of the proposed MRAS speed observer based on STO for SPMSM is shown in Figure 7.1. This structure is made up of a reference model (STO), an adjustable model, and an adaptation mechanism.

7.3.1 Reference Model

The reference model consists of designing a second order sliding-mode observer (STO), which computes the reference BEMFs $\hat{e}_{\alpha,\beta} = [\hat{e}_\alpha \quad \hat{e}_\beta]^T$ using only measured stator currents and voltages. This reference model does not depend on the velocity.

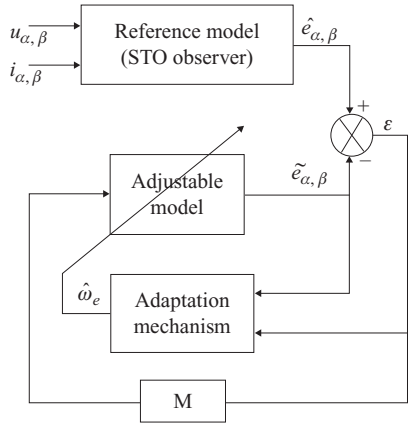

Figure 7.1 Structure of the MRAS speed-observer-based STO

The general form of the STO is defined as follows (Levant 1998):

$$\begin{cases} v(e_1) = v_1 + \lambda |e_1|^{\frac{1}{2}} sgn(e_1), \\ \dot{v}_1 = \alpha sgn(e_1), \end{cases} \tag{7.3}$$

with $e_1 = x_1 - \hat{x}_1$, λ, $\alpha > 0$ are the observer parameters, v_1 is the output of the differentiator, x_1 is the estimated variable and

$$sgn(e_1), = \begin{cases} 1, & if \quad e_1 > 0; \\ -1, & if \quad e_1 < 0; \\ \in [-1 \quad 1], & if \quad e_1 = 0. \end{cases}$$

Let $x = [i_\alpha \quad i_\beta]$. Consider only current dynamic equations of model (7.1), we can write

$$\begin{cases} \dot{x}_1 = ax_1 - be_\alpha + cu_\alpha, \\ \dot{x}_2 = ax_2 - be_\beta + cu_\beta, \end{cases} \tag{7.4}$$

where $a = -\frac{R_s}{L_s}$, $b = \frac{\phi_m}{L_s}$, and $c = \frac{1}{L_s}$. Let

$$[x_a \quad x_b] = -b[e_\alpha \quad e_\beta] \tag{7.5}$$

be the vector of unknown variables. System (7.4) becomes

$$\begin{cases} \dot{x}_1 = ax_1 + x_a + cu_\alpha, \\ \dot{x}_2 = ax_2 + x_b + cu_\beta \end{cases}. \tag{7.6}$$

Currents and voltages are assumed to be measurable. Applying the STO (7.3) to system (7.6), we obtain

$$\begin{aligned}
\dot{\hat{x}}_1 &= \tilde{x}_a + a\hat{x}_1 + cu_\alpha + \lambda_1|e_1|^{\frac{1}{2}}sgn(e_1),\\
\dot{\tilde{x}}_a &= \alpha_1 sgn(e_1),\\
\dot{\hat{x}}_2 &= \tilde{x}_b + a\hat{x}_2 + cu_\beta + \lambda_2|e_2|^{\frac{1}{2}}sgn(e_2),\\
\dot{\tilde{x}}_b &= \alpha_2 sgn(e_2),
\end{aligned} \tag{7.7}$$

where $e_1 = x_1 - \hat{x}_1$, $e_2 = x_2 - \hat{x}_2$, and $\lambda_1, \quad \lambda_2, \quad \alpha_1, \quad \alpha_2 > 0$.

Error dynamics of the observer are given by

$$\begin{aligned}
\dot{e}_1 &= (x_a - \tilde{x}_a) + a(x_1 - \hat{x}_1) - \lambda_1|e_1|^{\frac{1}{2}}sgn(e_1),\\
\dot{e}_a &= f_1(x_b) - \alpha_1 sgn(e_1),\\
\dot{e}_2 &= (x_b - \tilde{x}_b) + a(x_2 - \hat{x}_2) - \lambda_2|e_2|^{\frac{1}{2}}sgn(e_2),\\
\dot{e}_b &= f_2(x_a) - \alpha_2 sgn(e_2),
\end{aligned} \tag{7.8}$$

with $f_1(x_b) = \omega_e x_b$ and $f_2(x_a) = -\omega_e x_a$

Corollary 7.3.1 *Taking into account the result proposed in Levant (1998) with respect to the STO (7.3) dedicated to the observer design (7.7). For any initial conditions $x(0)$, $\hat{x}(0)$, there exists a choice of λ_i and α_i such that the observer state $\hat{x}$ converges in finite time to x, that is, $\hat{x}_1 \longmapsto x_1$ and $\hat{x}_2 \longmapsto x_2$, then e_1, e_2, $\dot{e}_1$, and $\dot{e}_2$ converges to zero and by consequence $\tilde{x}_a \longmapsto x_a$ and $\tilde{x}_b \longmapsto x_b$.*

The observer parameters $\alpha_1, \alpha_2, \lambda_1$, and λ_2 have respectively the following expressions (Levant 1998):

$$\begin{aligned}
&\alpha_1 > f_1^+ \quad \text{and} \quad \lambda_1 > (f_1^+ + \alpha_1)\sqrt{\frac{2}{\alpha_1 - f_1^+}},\\
&\alpha_2 > f_2^+ \quad \text{and} \quad \lambda_2 > (f_2^+ + \alpha_2)\sqrt{\frac{2}{\alpha_2 - f_2^+}},
\end{aligned} \tag{7.9}$$

where $f_1^+ = max(f_1(x_b)) \quad \text{and} \quad f_2^+ = max(f_2(x_a))$.

Having $\tilde{x}_a$ and $\tilde{x}_b$ we can easily deduce the estimated BEMFs $\hat{e}_{\alpha,\beta}$ from equation (7.5).

7.3.2 Adjustable Model

The adjustable model is tunable by the estimated velocity and it computes the estimated BEMFs $\tilde{e}_{\alpha,\beta} = [\tilde{e}_\alpha \quad \tilde{e}_\beta]^T$ from the following equation:

$$\dot{\tilde{e}}_{\alpha,\beta} = \hat{\omega}_e J\tilde{e}_{\alpha,\beta} + M(\tilde{e}_{\alpha,\beta} - \hat{e}_{\alpha,\beta}), \tag{7.10}$$

where $\hat{\omega}_e$ is the estimated velocity and

$$J = \begin{pmatrix} 0 & -1 \\ 1 & 0 \end{pmatrix}.$$

For convergence, a feedback loop is introduced and the feedback gain

$$M = m \begin{pmatrix} 1 & 0 \\ 0 & 1 \end{pmatrix},$$

where m is a positive constant.

7.3.3 Adaptation Mechanism

If the velocity estimation error exist, it will lead to the observed BEMFs estimation errors

$$\varepsilon = \tilde{e}_{\alpha,\beta} - \hat{e}_{\alpha,\beta}. \tag{7.11}$$

Then, these errors together with the estimation model's output $\tilde{e}_{\alpha,\beta}$ are used to construct the manifold S as

$$S = \varepsilon^T J \tilde{e}_{\alpha,\beta}. \tag{7.12}$$

The estimated velocity is

$$\hat{\omega}_e = K sgn(S). \tag{7.13}$$

Note that the speed estimate is a discontinuous function of the manifold and K is a positive constant.

The BEMFs used in the reference model also satisfy the following equation

$$\dot{\hat{e}}_{\alpha,\beta} = \omega_e J \hat{e}_{\alpha,\beta}. \tag{7.14}$$

To show that the sliding mode can be enforced in the manifold $S = 0$, we need to show that there exists M sufficiently high such that the manifold is attractive

$$S\dot{S} < 0. \tag{7.15}$$

After differentiating (7.12) and replacing the derivative of the BEMFs from (7.10) and (7.14), the following expression is obtained:

$$\dot{S} = f(\omega_e, \hat{e}_{\alpha,\beta}, \tilde{e}_{\alpha,\beta}) - K(\tilde{e}^T_{\alpha,\beta}\hat{e}_{\alpha,\beta}) sgn(S), \tag{7.16}$$

where f is a function of the reference and estimated BEMFs and speed. Since this term is greater than zero when the motor is exited and f has a positive upper value, it's clear from

(7.16) that sufficiently high K can be selected such that condition (7.15) is fulfilled. Thus, sliding mode is enforced in the manifold S and after sliding mode begins, we have S = 0.

The boundary layer method described in Utkin *et al.* (1999) is used to find the equivalent control $\omega_{e,eq}$. Once sliding mode occurs, we can also assume $\dot{S} = 0$ along with $S = 0$. The expression of the equivalent control becomes

$$\omega_{e,eq} = \omega_e + m\frac{\varepsilon^T J\tilde{e}_{\alpha,\beta}}{\tilde{e}^T_{\alpha,\beta}\hat{e}_{\alpha,\beta}}. \tag{7.17}$$

From equation (7.17), when the manifold converge to zero ($S = \varepsilon^T J\tilde{e}_{\alpha,\beta} = 0$), the equivalent speed tends to the real speed. The equivalent speed represents the low-frequency component of the discontinuous term (7.13). Thus, while the high-frequency switching function is fed into the observer, its low-frequency component can be obtained by low-pass filtering (LPF) and represents the speed estimate.

7.3.4 Rotor Position Observer

The observed rotor position is obtained simply from the phase of the estimated BEMFs coming from equation (7.7) and (7.5) as follows:

$$\hat{\theta}_e = \arctan\left(\frac{-\hat{e}_\alpha}{\hat{e}_\beta}\right). \tag{7.18}$$

However, it is shown in Zaltni and Ghanes (2010) that the SPMSM is not observable at very low speed. To overcome this problem, an estimator/observer swapping system is proposed to ensure position estimation in all speed range and to overcome position observability problems at very low frequencies (see Section 7.2.2). The estimator is obtained by integrating the estimated speed in equation (7.17). So it does not depend directly on the BEMFs. Thus, since the speed is always observable, there is no problem of observability using this position estimator. However, it is evident that the estimator is sensible to parameter variation. The position is equal to the observer when the motor operate at high frequencies and swap to the estimator since the speed become less than 5 rad/s.

7.4 Experimental Results

The observer is tested on a significant benchmark where high- and very low-speed operation modes of SPMSM are considered (Figure 7.3). It is tested in an open-loop control as showed in Figure 7.2.

The experimental testing is composed of an SPMSM with a 4096-pulse incremental encoder to validate the observer. Another identical SPMSM is used as load torque generation. A commercial 15 kW inverter is supplied with a DC voltage source Xantrex. Three LEM current sensors (LEM LA 100P) are used. A real-time controller board of dSPACE DS1104 and interfaces are used to implement the speed, current control, and the proposed observer. The experimental results (measurements and state estimation) are obtained with ControlDesk. The experimental sampling time T_e is equal to 200 μs.

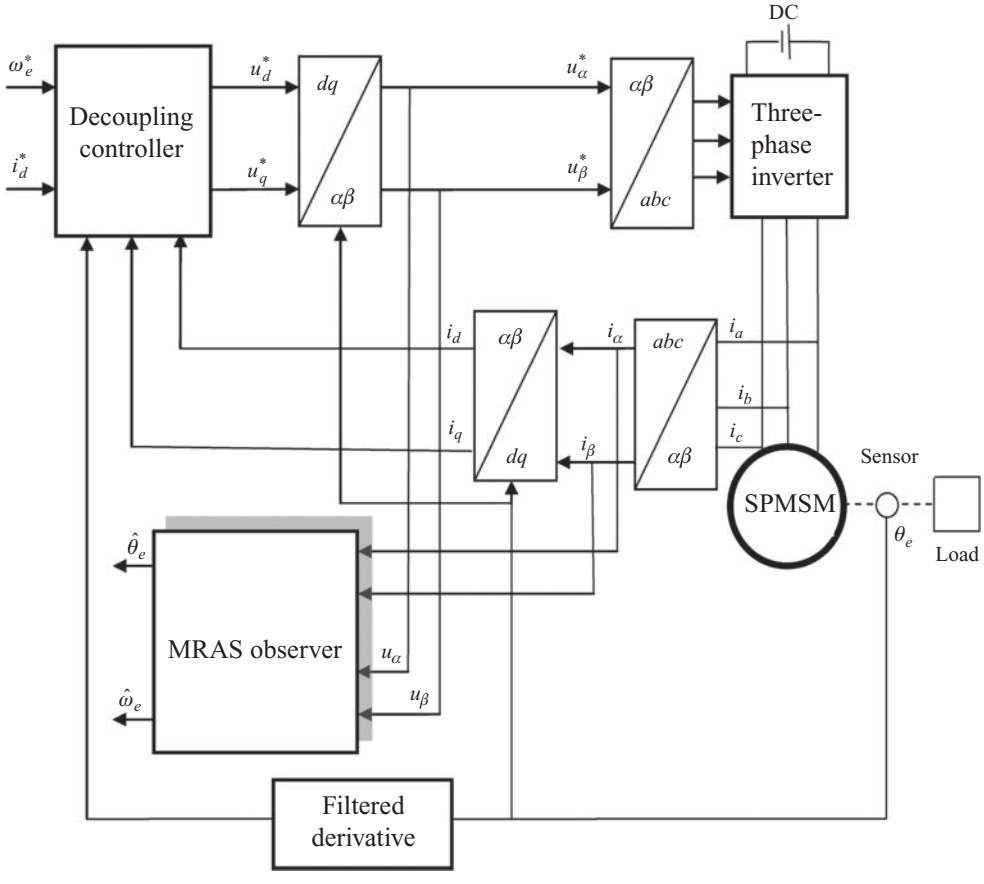

Figure 7.2 Block diagram scheme

The specifications and parameters of SPMSM and MRAS observer are listed in Table 7.1.

7.4.1 Nominal Conditions

Using the identified parameters of SPMSM (Table 7.1), the proposed MRAS observer is designed. It's clear that due to experimental conditions, the identified parameters are not exactly the real parameters of SPMSM. The control experimental conditions are nearly different, taking into account the identification conditions. Furthermore, the identification methodology introduces a certain uncertainty in its results. Thus, this case is by oneself a robustness test. From now this case is called the nominal condition test.

Rotor Speed Observation Results

The experimental results of rotor speed are given in Figure 7.3. It can be noted that the observed speed (Figure 7.3 (dash-dot line)) coming from equation (7.17), tracks correctly the

Table 7.1 Parameters specification of SPMSM and MRAS observer

SPMSM parameters	value	MRAS observer parameters	value
P_n	1.6 kW	α_1	80 000
ω_n	3000 rpm	α_2	80 000
U_n	540 V	λ_1	100
I_n	5.8 A	λ_2	100
R_s	2.06 Ω	K	700
L_s	9.15 mH	m	100
P	3		
ϕ_m	0.29 Wb		
J	0.0249 kgm^2		
f_v	0.0075 kgm^{2}s^{-1}		
T_l	5.1 Nm		

SPMSM, surface permanent-magnet synchronous motor; MRAS, model reference adaptive system.

motor speed (Figure 7.3 (dashed line)) when the synchronous motor operates at high and very low speeds.

Rotor Position Observation Results

For rotor position observation, the experimental results are displayed in Figure 7.4. The observed position (Figure 7.4 (solid line)) is obtained at high and very low frequencies according to Section 7.3.4 and tracks well the measured position (Figure 7.4 (dashed line)).

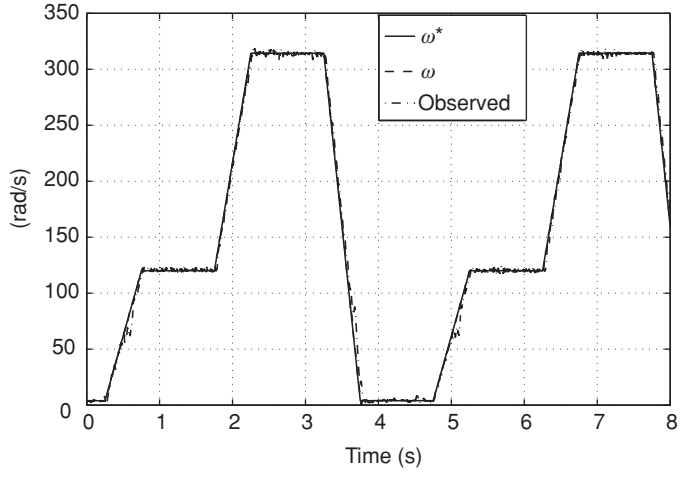

Figure 7.3 Rotor speed

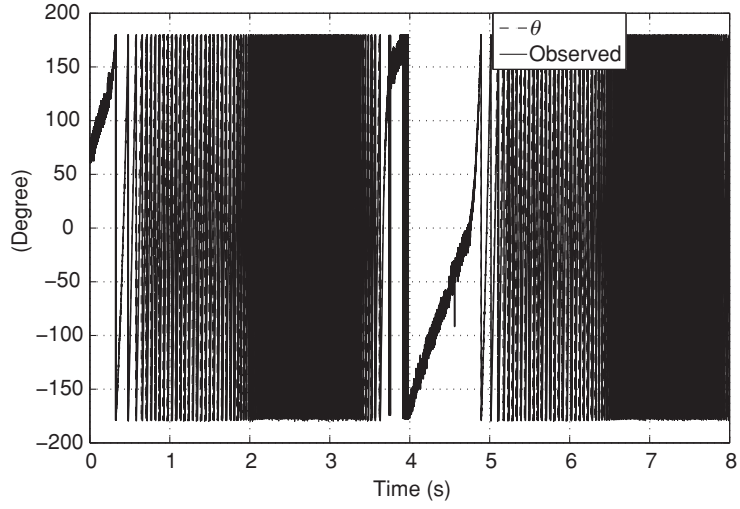

Figure 7.4 Rotor position

However, at very low speeds ($t = 4$ s to $t = 5$ s) the estimated position (Figure 7.4 (solid line)) is affected by chattering phenomena due to significant current measurement noises.

The applied stator voltages u_α-u_β and measured stator currents i_α-i_β are shown in Figure 7.5.

7.4.2 Parameter Variation Effect

The robustness to internal disturbance of the proposed observer is tested by variation of $+100\%$ of stator resistance R_s. Experimental results of rotor speed and position observation

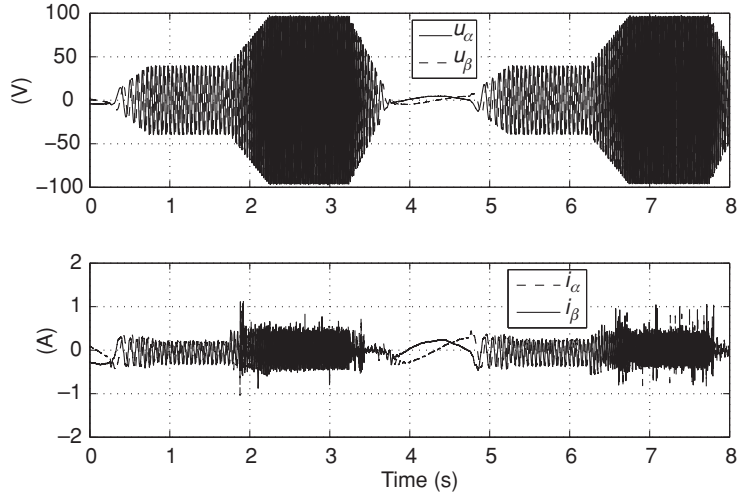

Figure 7.5 Stator voltages and currents

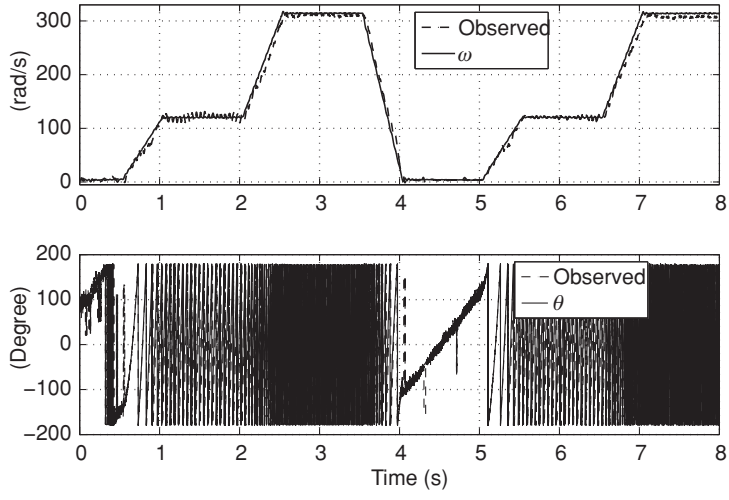

Figure 7.6 Rotor speed and position with $+100\%$ of R_s

are depicted in Figure. 7.6. Compared to the results of nominal condition (Figures 7.3 and 7.4), it can be remarked that the proposed observer is very robust to this variation. However, the observed speed is a little sensible at high speeds, while the observed position is sensitive only at very low speeds.

7.4.3 Load Torque Effect

The robustness to external disturbance of the proposed observer is tested by applying to the motor a constant load torque T_l at high and low speeds. At same time, a variation of $+100\%$ of stator resistance R_s is carried out. The experimental results (Figure 7.7a-b) show that the observed speed is well estimated when the load torque is applied at high speed (Figure. 7.7a). However, at very low speeds the observed speed (Figure 7.7b) is very sensitive.

7.5 Conclusions

A robust MRAS observer based on super twisting algorithm is proposed for acceptable accuracy and robustness rotor speed observation. This observer is designed to achieve sensor-less control scheme for SPMSM. The stability of the proposed MRAS observer has been studied using Lyapunov arguments. To overcome the problem of observability at very low speed, the rotor position has been obtained using an estimator/observer swapping system when the speed becomes less than 5 rad/s. An experimental evaluation has been presented to illustrate the performance and the robustness of the proposed speed and position observation design.

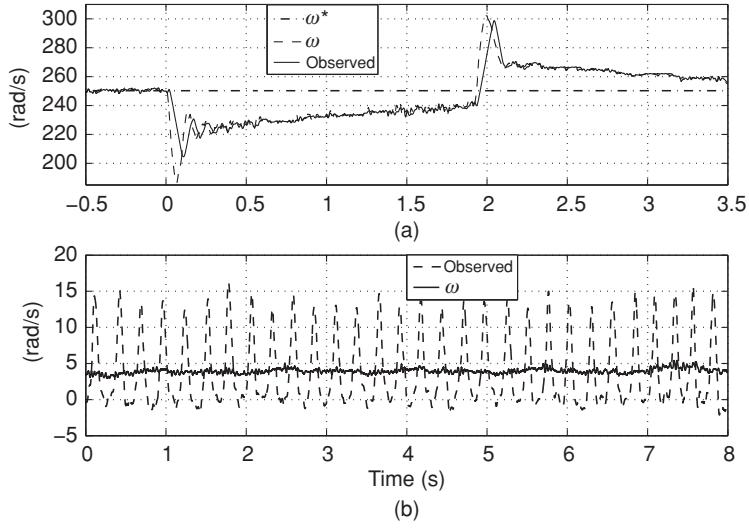

Figure 7.7 Rotor speed with +100% of R_s and load torque

References

Arellano-Padilla J, Gerada C, Asher G, and Sumner M (2010) Inductance characteristics of PMSMs and their impact on saliency-based sensorless control. *International Power Electronics and Motion Control Conference EPE-PEMC*, 1–9.

Bolognani S, Zigliotto M, and Zordan M (2001) Extended-range PMSM sensorless speed drive based on stochastic filtering. *IEEE Transactions on Power Electronics*, **16**, 110–117.

Benjak O and Gerling D (2010) Review of position estimation methods for IPMSM drives without a position sensor. Part I: nonadaptive methods. *International Conference on Electrical Machines - ICEM*.

Changsheng Li and Elbuluk M (2001) A Sliding mode observer for sensorless control of permanent magnet synchronous motors. *IEEE IAS Annual Meeting*, **2**, 1273–1278.

Chi S, Zheng Z, and Xu L (2009) Sliding-mode sensorless control of direct-drive PM synchronous motors for washing machine applications. *IEEE Transaction on Industry Applications*, **45**, 582–590.

Gumus B, Ozerdem, MS, and Ozdemir M (2007) Permanent magnet synchronous motor's sensorless vector control with artificial neural network observer. *International Aegean Conference on Electrical Machines and Power Electronics.*

Halder KK, Roy NK, and Ghosh BC (2010) A high performance position sensorless surface permanent magnet synchronous motor drive based on flux angle. *IEEE-ICECE*, 78–81.

Junfeng X, Fengyan W, Shaofeng X, *et al*. (2004) A new control method for permanent magnet synchronous machines with observer. *IEEE Power Electronics Specialists Conference*, 1004–1408.

Lee H and Lee J (2013) Design of an iterative sliding mode observer for sensorless PMSM control. *IEEE Transactions on Control Systems Technology* (to appear).

Levant A (1998) Robust exact differentiation via sliding mode technique. *Automatica*, **12**, 379–384.

Montesinos D, Galceran S, Sudria A, and Gomis O (2005) Low cost sensorless control of permanent magnet motors, an overview and evaluation. *International Conference on Electric Machines and Drives, ICEMS*, 1681–1688.

Peng H, Lei H, and Chang-yun M (2010) Research on speed sensorless backstepping control of permanent magnet synchronous motor. *IEEE-ICCASM*, 609–612.

Utkin U, Guldner J, and Shi J (1999) Sliding mode control in electromechanical systems, 1st edn. Taylor and Francis, London.

Vaclavec and Blaha P (2008) A new control method for permanent magnet synchronous machines with observer. *IEEE International Conference on Power and Energy*, pp. 265–270.

Yang Z, Hara S, Kanae S, *et al*. (2009) An Adaptive robust nonlinear motion controller combined with disturbance observer. *IEEE transactions on Control Systems Technology*, **18**, 454–462.

Yu X and Kaynak O (2009) Sliding-mode control with soft computing: a survey. *IEEE Transaction on Indusustrial Electronics*, **56**, 3275–3283.

Zaltni D and Ghanes M (2010) Synchronous motor observability study and an improved zero-speed position estimation design. *IEEE CDC*.

Part Three

Control Design Techniques for Induction Motors

AC Electric Motors Control: Advanced Design Techniques and Applications, First Edition. Edited by Fouad Giri.

8

High-Gain Observers in Robust Feedback Control of Induction Motors

Hassan K. Khalil and Elias G. Strangas
Department of Electrical and Computer Engineering, Michigan State University, USA

8.1 Chapter Overview

In this chapter, a nonlinear control approach to the speed tracking problem of induction motors is discussed. In this approach, no speed measurement is used, but instead either reliable position measurement by optical encoders or resolvers or no position measurement at all is utilized. For this task, no rotor flux measurement is needed; a second order observer is used to estimate the flux.

Classic field orientation requires the transformation of variables, to either the stator, or, most commonly, the rotor flux frame of reference. Here the field orientation change of variables is performed using the flux estimate rather than the flux itself. This makes all the new variables available for feedback.

To estimate speed, and acceleration when it is needed, a special design of the observer gain is used that makes the observer robust to uncertainties in modeling nonlinear functions. The technique, known as high-gain observers, works for a wide class of nonlinear systems and guarantees that the output feedback controller recovers the performance of the state feedback controller when the observer gain is sufficiently high. A separation principle allows us to separate the controller design into two tasks. First, to design a state feedback controller that stabilizes the system and meets other design specifications. Then, an output feedback controller is obtained by replacing the state by its estimate, provided by the high-gain observer.

AC Electric Motors Control: Advanced Design Techniques and Applications, First Edition. Edited by Fouad Giri.

Uncertainty in the rotor resistance and the load torque is allowed. Robust control techniques are used to overcome the effect of this uncertainty on the tracking accuracy. The flux controller is designed using either the traditional method with two PI controllers or a continuous approximation of variable structure control. For speed control, in the case when position measurement is available, the use of robust control is presented for current-control and voltage-control schemes. In the current-control scheme, a PI controller is used to regulate the current to a desired value that is designed using sliding-mode control. The voltage-control scheme uses another change of variables that brings the acceleration as one of the state variables. This change of variables, which is dependent on the uncertain quantities, results in a state equation where the uncertain terms satisfy the matching condition. The uncertain change of variables is not used in the implementation of the controller, as both the speed and acceleration are estimated from the position using a robust high-gain observer. The control design is a continuous approximation of sliding-mode control. We show that the speed tracking error will be asymptotically bounded by a bound that can be made arbitrarily small by choice of certain design parameters. We also show that in the special case when the speed reference and load torque are constant, the speed tracking error tends to zero asymptotically as time approaches infinity.

When position measurement is not available, the speed control is a current-control scheme in which a PI controller is used to regulate the current, as in the previous case. We derive a third order nonlinear model that captures the essence of the speed control problem. The model has the speed and two flux estimation errors as state variables, the q-axis current as the control input, and a virtual speed, provided by the high-gain observer, as the measured output. We show how the model can be used to investigate the design of a feedback controller with integral action.

8.2 Field Orientation

The squirrel-cage induction machine can be described by the fundamental equations that result from electromagnetic considerations. These relate stator and rotor flux linkages and terminal voltages and currents, as well as the developed torque and speed. We start with these equations describing a linear model, neglecting saturation and nonuniform current distribution in the rotor bars. We use variables in complex form, in the natural frames of reference of the stator and rotor. The angle θ is the relative position of the rotor (axis of phase a with respect to the stator),

$$R_r \mathbf{i}_r + \frac{d\boldsymbol{\lambda}_r}{dt} = 0, \tag{8.1}$$

$$R_s \mathbf{i}_s + \frac{d\boldsymbol{\lambda}_s}{dt} = \mathbf{u}_s, \tag{8.2}$$

with the flux linkages $\boldsymbol{\lambda}_r$ and $\boldsymbol{\lambda}_s$ in their corresponding natural stator and rotor frames of reference,

$$\boldsymbol{\lambda}_r = M\left[(1+\sigma_r)\mathbf{i}_r + \mathbf{i}_s e^{-\mathbf{i}p\theta}\right], \tag{8.3}$$

$$\boldsymbol{\lambda}_s = M\left[(1+\sigma_s)\mathbf{i}_s + \mathbf{i}_r e^{\mathbf{i}p\theta}\right]. \tag{8.4}$$

These result in

$$R_r \mathbf{i}_r + L_r \frac{d\mathbf{i}_r}{dt} + M \frac{d}{dt}\left(\mathbf{i}_s e^{-\mathrm{i}p\theta}\right) = 0, \tag{8.5}$$

$$R_s \mathbf{i}_s + L_s \frac{d\mathbf{i}_s}{dt} + M \frac{d}{dt}\left(\mathbf{i}_r e^{\mathrm{i}p\theta}\right) = \mathbf{u}_s, \tag{8.6}$$

with $L_s = (1+\sigma_s)M$ and $L_r = (1+\sigma_r)M$. The torque, resulting from the interaction of currents and fluxes, can be written in a variety of ways. Using stator currents and rotor flux linkages we obtain

$$T_d = \frac{pM}{L_r} \Im\left[\left(\boldsymbol{\lambda}_r e^{\mathrm{i}p\theta}\right)^* \mathbf{i}_s\right], \tag{8.7}$$

The equation of motion is

$$\frac{d^2\theta}{dt^2} = \dot{\omega} = \frac{1}{J}\left[T_d - T_L\right], \tag{8.8}$$

with J as the system moment of inertia and T_L the load torque.

This system of equations can be rewritten with all variables transformed in any common frame of reference. Of the possible frames of reference, the most often used are the stator, stator voltages, stator flux, and rotor flux; see, for example, Leonhard (1996), Krishnan (2001), and Novotony *et al.* (2010). Although the motor is often driven by stator currents, we keep the stator voltage equation so that we can use it to estimate rotor position.

In the reference system of the stator, and using matrix notation, the equations become

$$\dot{\theta} = \omega, \tag{8.9}$$

$$\dot{\omega} = -\mu \lambda_r^T E i_s - T_L/J, \tag{8.10}$$

$$\dot{\lambda}_r = (-\alpha_r I + p\omega E)\lambda_r + \alpha_r M i_s, \tag{8.11}$$

$$\dot{i}_s = (\beta\alpha_r I - p\ \beta\omega E)\lambda_r - (a_s\eta + \alpha_r\beta M) i_s + \gamma u_s, \tag{8.12}$$

where $\alpha_r = R_r/L_r$, $\alpha_s = R_s/L_s$, $\beta = M/\sigma L_r L_s$, $\gamma = 1/\sigma L_s$, $\eta = 1/\sigma$, $\mu = pM/JL_r$, $\sigma = 1 - M^2/L_s L_r$, and

$$I = \begin{bmatrix} 1 & 0 \\ 0 & 1 \end{bmatrix}, \quad E = \begin{bmatrix} 0 & -1 \\ 1 & 0 \end{bmatrix}.$$

The rotor flux, stator current, and stator voltage in the stator frame of reference are

$$\lambda_r = [\lambda_a, \lambda_b]^T, \quad i_s = [i_a, i_b]^T, \quad u_s = [u_a, u_b]^T. \tag{8.13}$$

The angle between the stator and the rotor flux is:

$$\rho = \tan^{-1}(\lambda_a, \lambda_b). \tag{8.14}$$

The rotor flux, stator current, and stator voltage in the rotor flux frame of reference are

$$\lambda_r = [\lambda_d, 0]^T, \quad i_s = \left[i_d, i_q\right]^T, \quad u_s = \left[u_d, u_q\right]^T, \tag{8.15}$$

and the transformation matrix is

$$F(\rho) = \begin{bmatrix} \cos\rho & \sin\rho \\ -\sin\rho & \cos\rho \end{bmatrix}. \tag{8.16}$$

In particular,

$$\begin{bmatrix} i_d \\ i_q \end{bmatrix} = F(\rho) \begin{bmatrix} i_a \\ i_b \end{bmatrix}, \quad \begin{bmatrix} u_d \\ u_q \end{bmatrix} = F(\rho) \begin{bmatrix} u_a \\ u_b \end{bmatrix}, \quad \begin{bmatrix} \lambda_d \\ 0 \end{bmatrix} = F(\rho) \begin{bmatrix} \lambda_a \\ \lambda_b \end{bmatrix}. \tag{8.17}$$

The torque equation in the rotor flux frame of reference becomes

$$T_d = \frac{pM}{L_r} \lambda_d i_q, \tag{8.18}$$

and the rotor flux λ_d can be estimated through an open-loop observer using equation (8.11), while the angle of this flux, ρ, can be calculated from the stator currents and speed

$$\dot{\lambda}_d = -\alpha_r \lambda_d + \alpha_r M i_d, \tag{8.19}$$

$$\dot{\rho} = \omega + \frac{\alpha_r M i_q}{\lambda_d}. \tag{8.20}$$

Equations (8.18) and (8.19) show decoupling of the rotor flux from the q-axis current and suggest a simple controller for the torque, while the open-loop observer from equations (8.19) and (8.20) is the classic rotor field orientation method. Finally, the stator current satisfies

$$\dot{i}_d = p\,\omega i_q + \alpha_r \beta \lambda_d - (\alpha_s \eta + \alpha_r \beta M) i_d + \alpha_r M i_q^2 / \lambda_d + \gamma u_d, \tag{8.21}$$

$$\dot{i}_q = -p\,\omega i_d - p\,\omega \beta \lambda_d - (\alpha_s \eta + \alpha_r \beta M) i_q - \alpha_r M i_d i_q / \lambda_d + \gamma u_q. \tag{8.22}$$

The estimates of ρ and λ_d depend on the parameters of the system and are subject to errors. Of those, errors in the rotor resistance, R_r, and the corresponding rotor time constant, $1/\alpha_r$, cause inaccuracies in the estimates of both flux magnitude and angle. Moreover, an open-loop observer based on equation (8.11) requires the speed ω. The underlying assumption in this chapter is that the speed is not directly measured. It is estimated from the position θ when a mechanical sensor is used or from the stator current and voltage when θ is not measured. Therefore, the implemented open-loop flux observer takes the form

$$\dot{\hat{\lambda}}_r = (-\alpha_{r0} I + p\,\omega_0 E)\hat{\lambda}_r + \alpha_{r0} M i_s, \tag{8.23}$$

where α_{r0} is a nominal value of α_r and ω_0 is a replacement for ω, with the most common choices are a speed estimate $\hat{\omega}$ or the speed reference ω^*. The estimated rotor flux and its

angle, $\tan^{-1}(\hat{\lambda}_a, \hat{\lambda}_b)$, which are obtained from the flux observer (8.23), are different from the ones obtained when $\alpha_r = \alpha_{r0}$ and $\omega_0 = \omega$. However, for convenience, we continue to denote them by λ_d and ρ, which are now given by

$$\dot{\lambda}_d = -\alpha_{r0}\lambda_d + \alpha_{r0} M i_d, \tag{8.24}$$

$$\dot{\rho} = p\omega_0 + \frac{\alpha_{r0} M i_q}{\lambda_d}. \tag{8.25}$$

The stator current and voltage transformed to this estimated frame of reference are given by equation (8.17), with the newly calculated ρ. To calculate the developed torque in this estimated frame of reference we start again from equation (8.7)

$$T_d = \frac{pM}{L_r}(i_b\lambda_a - i_a\lambda_b). \tag{8.26}$$

Defining rotor flux errors in the stator frame of reference

$$e_a = \lambda_a - \hat{\lambda}_a, \quad e_b = \lambda_b - \hat{\lambda}_b, \quad \big[\, e_a, e_b \,\big]^T = F(-\rho)\big[\, e_d, e_q \,\big]^T, \tag{8.27}$$

and transforming the variables for the torque to the estimated frame of reference

$$\begin{bmatrix} i_a \\ i_b \end{bmatrix} = F(-\rho)\begin{bmatrix} i_d \\ i_q \end{bmatrix}, \qquad \begin{bmatrix} \lambda_a \\ \lambda_b \end{bmatrix} = F(-\rho)\begin{bmatrix} \lambda_d \\ \lambda_q \end{bmatrix}, \tag{8.28}$$

and since $\lambda_q = 0$, we obtain

$$\begin{bmatrix} \lambda_a \\ \lambda_b \end{bmatrix} = F(-\rho)\left\{\begin{bmatrix} \lambda_d \\ 0 \end{bmatrix} + \begin{bmatrix} e_d \\ e_q \end{bmatrix}\right\}, \tag{8.29}$$

giving the torque equation using variables in the estimated frame of reference

$$T_d = \frac{pM}{L_r}\left[i_q\lambda_d + (i_q e_d - i_d e_q)\right]. \tag{8.30}$$

The stator currents i_d and i_q satisfy the equations

$$\dot{i}_d = p\,\omega_0 i_q + \alpha_r\beta\lambda_d - (\alpha_s\eta + \alpha_r\beta M)i_d + \alpha_{r0} M i_q^2/\lambda_d + \gamma u_d + \alpha_r\beta e_d + p\,\beta\omega e_q, \tag{8.31}$$

$$\dot{i}_q = -p\,\omega_0 i_d - p\,\omega\beta\lambda_d - (\alpha_s\eta + \alpha_r\beta M)i_q - \alpha_{r0} M i_d i_q/\lambda_d + \gamma u_q - p\,\beta\omega e_d + \alpha_r\beta e_q, \tag{8.32}$$

while the rotor flux errors e_d and e_q satisfy the equations

$$\dot{e}_d = -\alpha_r e_d + (p\,\omega_0 - p\,\omega + \alpha_{r0} M i_q/\lambda_d)e_q + (\alpha_r - \alpha_{r0})(M i_d - \lambda_d), \tag{8.33}$$

$$\dot{e}_q = -(p\,\omega_0 - p\,\omega + \alpha_{r0} M i_q/\lambda_d)e_d - \alpha_r e_q + (\alpha_r - \alpha_{r0}) M i_q + p(\omega - \omega_0)\lambda_d. \tag{8.34}$$

8.3 High-Gain Observers

To motivate the design of high-gain observers, consider the second order nonlinear system

$$\dot{x}_1 = x_2, \tag{8.35}$$

$$\dot{x}_2 = \phi(x, u, w, d), \tag{8.36}$$

$$y = x_1, \tag{8.37}$$

where $x = [x_1, x_2]^T$ is the state vector, u is the control input, y is the measured output, d is a vector of disturbance inputs, and w is a vector of known exogenous signals. The function ϕ is locally Lipschitz in (x, u) and continuous in (d, w). We assume that $d(t)$ and $w(t)$ are bounded piecewise continuous functions of time. Suppose the state feedback control $u = \gamma(x, w)$ stabilizes the origin $x = 0$ of the closed-loop system

$$\dot{x}_1 = x_2, \tag{8.38}$$

$$\dot{x}_2 = \phi(x, \gamma(x, w), w, d), \tag{8.39}$$

uniformly in (w, d), where $\gamma(x, w)$ is locally Lipschitz in x and continuous in w. To implement this feedback control using only measurements of the output y, we use the observer

$$\dot{\hat{x}}_1 = \hat{x}_2 + h_1(y - \hat{x}_1), \tag{8.40}$$

$$\dot{\hat{x}}_2 = \hat{\phi}(\hat{x}, u, w) + h_2(y - \hat{x}_1), \tag{8.41}$$

where $\hat{\phi}(x, u, w)$ is a nominal model of $\phi(x, u, w, d)$. The estimation error

$$\tilde{x} = \begin{bmatrix} \tilde{x}_1 \\ \tilde{x}_2 \end{bmatrix} = \begin{bmatrix} x_1 - \hat{x}_1 \\ x_2 - \hat{x}_2 \end{bmatrix}$$

satisfies the equation

$$\dot{\tilde{x}}_1 = -h_1\tilde{x}_1 + \tilde{x}_2, \tag{8.42}$$

$$\dot{\tilde{x}}_2 = -h_2\tilde{x}_1 + \delta(x, \tilde{x}, w, d), \tag{8.43}$$

where

$$\delta(x, \tilde{x}, w, d) = \phi(x, \gamma(\hat{x}, w), w, d) - \hat{\phi}(\hat{x}, \gamma(\hat{x}, w), w).$$

In the absence of δ, asymptotic error convergence is achieved when the eigenvalues of the matrix

$$\begin{bmatrix} -h_1 & 1 \\ -h_2 & 0 \end{bmatrix}$$

have negative real parts, which is the case for any positive constants h_1 and h_2. In the presence of δ, we design h_1 and h_2 with the additional goal of rejecting the effect of δ on $\tilde{x}$. This is

ideally achieved if the transfer function

$$G_o(s) = \frac{1}{s^2 + h_1 s + h_2} \begin{bmatrix} 1 \\ s + h_1 \end{bmatrix}$$

from δ to $\tilde{x}$ is identically zero. While this is not possible, we can make $\sup_{\omega \in R} \|G_o(j\omega)\|$ arbitrarily small by choosing $h_2 \gg h_1 \gg 1$. In particular, taking

$$h_1 = \frac{\alpha_1}{\varepsilon}, \qquad h_2 = \frac{\alpha_2}{\varepsilon^2}, \tag{8.44}$$

for some positive constants α_1, α_2, and ε, with $\varepsilon \ll 1$, it can be shown that

$$G_o(s) = \frac{\varepsilon}{(\varepsilon s)^2 + \alpha_1 \varepsilon s + \alpha_2} \begin{bmatrix} \varepsilon \\ \varepsilon s + \alpha_1 \end{bmatrix}.$$

Hence, $\lim_{\varepsilon \to 0} G_o(s) = 0$. The disturbance rejection property of the high-gain observer can also be seen in the time domain by using the scaled estimation errors

$$\xi_1 = \frac{\tilde{x}_1}{\varepsilon}, \qquad \xi_2 = \tilde{x}_2, \tag{8.45}$$

which satisfy the singularly perturbed equation

$$\varepsilon \dot{\xi}_1 = -\alpha_1 \xi_1 + \xi_2, \tag{8.46}$$

$$\varepsilon \dot{\xi}_2 = -\alpha_2 \xi_1 + \varepsilon \delta(x, \tilde{x}, w, d). \tag{8.47}$$

This equation shows that reducing ε diminishes the effect of δ. However, the transient response suffers from the *peaking phenomenon*. The initial condition $\xi_1(0)$ could be $O(1/\varepsilon)$ when $x_1(0) \neq \hat{x}_1(0)$. Consequently, the transient response of equation (8.46) could contain a term of the form $(1/\varepsilon)e^{-at/\varepsilon}$ for some $a > 0$. While this exponential mode decays rapidly, it exhibits an impulsive-like behavior where the transient peaks to $O(1/\varepsilon)$ values before it decays rapidly towards zero. In fact, the function $(1/\varepsilon)e^{-at/\varepsilon}$ approaches an impulse function as ε tends to zero. In addition to inducing unacceptable transient response, the peaking phenomenon could destabilize the closed-loop nonlinear system (see Khalil 2002, Section 14.5). A key idea to overcome the peaking phenomenon is to design the control law $\gamma(\hat{x}, w)$ and the nominal function $\hat{\phi}(\hat{x}, u, w)$ to be globally bounded in $\hat{x}$, that is, bounded for all $\hat{x}$ when w is bounded. This property can be always achieved by saturating u and/or $\hat{x}$ outside compact sets of interest. A typical way to determine the saturation levels is to simulate the closed-loop system under state feedback and determine a compact set of operation; that is, a set Ω such that $x(t) \in \Omega$ for all $t \geq 0$. Then we determine bounds M_1 and M_2 such that $|x_1(t)| < M_1$ and $|x_2(t)| < M_2$ over Ω. The estimates $\hat{x}_1$ and $\hat{x}_2$ are saturated at $\pm M_1$ and $\pm M_2$, respectively. The global boundedness of γ and $\hat{\phi}$ in $\hat{x}$ provides a buffer that protects the plant from peaking because during the peaking period the control $\gamma(\hat{x}, w)$ saturates. Since the peaking period shrinks to zero as ε tends to zero, for sufficiently small ε the peaking period is so small that the state of the plant x remains close to its initial value. After the peaking period, the estimation

error becomes of the order $O(\varepsilon)$ and the feedback control $\gamma(\hat{x}, w)$ becomes $O(\varepsilon)$ close to $\gamma(x, w)$. Consequently, the trajectories of the closed-loop system under the output feedback controller asymptotically approach the trajectories under the state feedback controller as ε tends to zero. Thus, the performance achieved under state feedback can be recovered by output feedback by choosing ε small enough. This allows us to separate the observer design from the feedback control design. For the purpose of feedback control, we act as if both x_1 and x_2 were measured. Then, a high-gain observer is implemented, x_1 and x_2 are replaced by their saturated estimates, and ε is tuned, by gradually decreasing it, until the performance under output feedback is sufficiently close to the performance under state feedback.

The high-gain observer design can be extended to higher order systems of the form

$$\dot{x}_i = x_{i+1}, \quad \text{for } 1 \leq i \leq r-1; \tag{8.48}$$

$$\dot{x}_r = \phi(x, z, u, w, d); \tag{8.49}$$

$$\dot{z} = \psi(x, z, u, w, d); \tag{8.50}$$

$$y = x_1; \tag{8.51}$$

where x and z constitute the state vector. The vector x represents a chain of r integrators with the state of the first integrator x_1 being the measured output y. The vector z represents the state of the internal dynamics, which are not estimated by the high-gain observer. The r-dimensional high-gain observer takes the form

$$\dot{\hat{x}}_i = \hat{x}_{i+1} + (\alpha_i/\varepsilon^i)(y - \hat{x}_1), \quad \text{for } 1 \leq i \leq r-1; \tag{8.52}$$

$$\dot{\hat{x}}_r = \hat{\phi}(\hat{x}, u, w) + (\alpha_r/\varepsilon^r)(y - \hat{x}_1); \tag{8.53}$$

where ε is a small positive constant and the positive constants α_1 to α_r are chosen such that the roots of the polynomial

$$s^r + \alpha_1 s^{r-1} + \cdots + \alpha_{r-1} s + \alpha_r$$

have negative real parts. In feedback control, we first design a state feedback controller as if the vector x was measured; then we replace x by its estimate $\hat{x}$ provided by the high-gain observer. By tuning ε to be small enough we recover the performance achieved under state feedback.

8.4 Speed and Acceleration Estimation using High-Gain Observers

8.4.1 Speed Estimation using a Mechanical Sensor

When measurement of θ is available using a mechanical sensor, such as an optical encoder, the estimation of speed is based on the model

$$\dot{\theta} = \omega, \tag{8.54}$$

$$\dot{\omega} = \mu \left[i_q \lambda_d + (i_q e_d - i_d e_q) \right] - \frac{T_L}{J}. \tag{8.55}$$

A high-gain speed observer is taken as

$$\dot{\hat{\theta}} = \hat{\omega} + (\alpha_1/\varepsilon)(\theta - \hat{\theta}), \tag{8.56}$$

$$\dot{\hat{\omega}} = \mu i_q \lambda_d + (\alpha_2/\varepsilon^2)(\theta - \hat{\theta}), \tag{8.57}$$

where α_1 and α_2 are positive constants that assign the roots of $s^2 + \alpha_1 s + \alpha_2$ at desired locations in the left-half plane and ε is a small positive parameter, which is tuned to achieve the desired performance.

8.4.2 Speed and Acceleration Estimation using a Mechanical Sensor

In one of the control schemes of Section 8.6, the feedback controller uses the speed ω and the acceleration $a = \dot{\omega}$. When θ is measured, we can build a high-gain observer to estimate ω and a using the model

$$\dot{\theta} = \omega, \tag{8.58}$$

$$\dot{\omega} = a, \tag{8.59}$$

$$\dot{a} = F(\omega, \omega_0, \lambda_d, i_d, i_q) + \mu\gamma\lambda_d u_q + \delta_2(\cdot), \tag{8.60}$$

where F is given by

$$F = \mu\lambda_d \left[-p\ \beta\omega\lambda_d - p\ \omega_0 i_d - (\alpha_{r0} + \alpha_s \eta + \alpha_{r0}\beta M) i_q \right],$$

and δ_2 is an uncertain function whose components are proportional to e_d, e_q, or $(\alpha_r - \alpha_{r0})$. A high-gain observer to estimate ω and a is given by

$$\dot{\hat{\theta}} = \hat{\omega} + (\alpha_1/\varepsilon)(\theta - \hat{\theta}), \tag{8.61}$$

$$\dot{\hat{\omega}} = \hat{a} + (\alpha_2/\varepsilon^2)(\theta - \hat{\theta}), \tag{8.62}$$

$$\dot{\hat{a}} = F(\hat{\omega}, \omega_0, \lambda_d, i_d, i_q) + \mu\gamma\lambda_d u_q + (\alpha_3/\varepsilon^3)(\theta - \hat{\theta}), \tag{8.63}$$

where the constants α_1, α_2 and α_3 assign the roots of $s^3 + \alpha_1 s^2 + \alpha_2 s + \alpha_3$ in the left-half plane and $\varepsilon > 0$ is chosen sufficiently small. It is typical to implement the the flux observer (8.23) with $\omega_0 = \hat{\omega}$, in which case ω_0 in (8.63) is taken as $\hat{\omega}$.

8.4.3 Speed Estimation without a Mechanical Sensor

Information about ω is contained in the derivative of i_q, as seen from the term $p\omega\beta\lambda_d$ on the right-hand side of (8.32). Rewrite equation (8.32) together with the $\dot{\omega}$-equation

$$\dot{i}_q = -p\ \beta\ \lambda_d \omega - f_1(\lambda_d, i_d, i_q, u_q, \omega_0) + \delta_3, \tag{8.64}$$

$$\dot{\omega} = \mu i_q \lambda_d + \delta_4, \tag{8.65}$$

where

$$f_1(\lambda_d, i_d, i_q, u_q, \omega_0) = p\ \omega_0 i_d + (\alpha_s \eta + \alpha_{r0}\beta M) i_q + \alpha_{r0} M i_d i_q/\lambda_d - \gamma u_q$$

is available online, and δ_3 and δ_4 are uncertain terms given by

$$\begin{aligned}\delta_3 &= -(\alpha_r - \alpha_{r0})\beta M i_q - p\ \beta\ \omega e_d + \alpha_r \beta e_q,\\ \delta_4 &= \mu(i_q e_d - i_d e_q) - T_L/J.\end{aligned}$$

We view i_q as the measured output and use it, together with the models (8.64) and (8.65), to build an observer to estimate ω. The high-gain observer of Section 8.3 can be designed if the uncertain terms appear only on the right-hand side of (8.65). The presence of δ_3 in (8.64) violates this condition. The change of variables

$$\begin{aligned}\Omega &= \omega - \frac{\delta_3}{p\ \beta\ \lambda_d}\\ &= \left(\frac{\lambda_d + e_d}{\lambda_d}\right)\omega + \frac{1}{p\ \beta\ \lambda_d}[(\alpha_r - \alpha_{r0})\beta M i_q - \alpha_r \beta e_q]\end{aligned} \tag{8.66}$$

brings equations (8.64) and (8.65) into the form

$$\dot{i}_q = -p\ \beta\ \lambda_d \Omega - f_1(\lambda_d, i_d, i_q, u_q, \omega_0), \tag{8.67}$$

$$\dot{\Omega} = \mu i_q \lambda_d + \delta_5, \tag{8.68}$$

which is suitable for high-gain observer design, where

$$\begin{aligned}\delta_5 &= \delta_4 - \frac{d}{dt}\left(\frac{\delta_3}{p\ \beta\lambda_d}\right)\\ &\stackrel{\text{def}}{=} f_2(\lambda_d, i_d, i_q, \omega, u_q, e_d, e_q, T_L, \omega_0),\end{aligned}$$

and f_2 is a continuous function of its arguments. The change of variables (8.66) is invertible, provided $\lambda_d + e_d \neq 0$. We use the high-gain observer

$$\dot{\hat{i}}_q = -p\ \beta\lambda_d \hat{\Omega} - f_1(\lambda_d, i_d, i_q, u_q, \omega_0) + \left(\frac{\alpha_1}{\varepsilon}\right)(i_q - \hat{i}_q), \tag{8.69}$$

$$\dot{\hat{\Omega}} = \mu i_q \lambda_d - \left(\frac{\alpha_2}{\varepsilon^2 p\ \beta\lambda_d}\right)(i_q - \hat{i}_q), \tag{8.70}$$

where ε is a small positive parameter and α_1 and α_2 are positive constants that assign the roots of $s^2 + \alpha_1 s + \alpha_2 = 0$ at desired locations in the left-half plane. The scaled estimation errors

$$\xi_1 = \frac{i_q - \hat{i}_q}{\varepsilon}, \qquad \xi_2 = \Omega - \hat{\Omega}$$

satisfy the equations

$$\varepsilon\dot{\xi}_1 = -\alpha_1\xi_1 - p\,\beta\lambda_d\xi_2, \tag{8.71}$$

$$\varepsilon\dot{\xi}_2 = \left(\frac{\alpha_2}{p\,\beta\lambda_d}\right)\xi_1 + \varepsilon\delta_5. \tag{8.72}$$

For small ε, the closed-loop system will be a singularly perturbed one, with ξ_1 and ξ_2 as the fast variables. According to singular perturbation theory (Kokotović *et al.* 1999), the stability of the fast dynamics is determined by the matrix

$$\begin{bmatrix} -\alpha_1 & -p\,\beta\lambda_d \\ \dfrac{\alpha_2}{p\,\beta\lambda_d} & 0 \end{bmatrix}$$

in which $\lambda_d > 0$ is treated as a constant. By design, the roots of the characteristic equation $s^2 + \alpha_1 s + \alpha_2 = 0$ have negative real parts. From the high-gain observer theory (Atassi and Khalil 1999), we know that if the control input u_s is bounded uniformly in ε, then the estimation error $\Omega - \hat{\Omega}$ will be $O(\varepsilon)$ after a short transient period $[0, T(\varepsilon)]$, where $\lim_{\varepsilon\to 0} T(\varepsilon) = 0$. Moreover, the closed-loop system with feedback from $\hat{\Omega}$ recovers the performance of the closed-loop system with feedback from Ω as ε tends to zero. Hence, we can design the feedback controller with feedback signals from λ_d, i_d, i_q, and the virtual speed Ω, defined by (8.66). In implementation, Ω is replaced $\hat{\Omega}$, which is provided by the speed observers (8.69) and (8.70). The boundedness of u_s uniformly in ε is ensured by saturating $\hat{\Omega}$ outside a compact set of interest.

8.5 Flux Control

In the traditional field-oriented control, the estimated flux λ_d is regulated to a reference flux $\lambda^* > 0$, which is taken here as a constant or a time-varying function that approaches a constant at steady state. This is achieved by the design of a state feedback control law for u_d using the second order model

$$\dot{\lambda}_d = -\alpha_{r0}\lambda_d + \alpha_{r0}Mi_d, \tag{8.73}$$

$$\begin{aligned}\dot{i}_d = {} & p\,\omega_0 i_q + \alpha_r\beta\lambda_d - (\alpha_s\eta + \alpha_r\beta M)i_d + \alpha_{r0}Mi_q^2/\lambda_d + \gamma u_d \\ & + \alpha_r\beta e_d + p\,\beta\omega e_q.\end{aligned} \tag{8.74}$$

This is a simple control problem and there are several methods to design such a controller. The traditional approach uses two PI controllers (Leonhard 1996), which are derived as follows. First, we view i_d as a control input to equation (8.73) and design the PI flux controller

$$\dot{\phi}_\lambda = \lambda_d - \lambda^* \stackrel{\text{def}}{=} \tilde{\lambda}_d, \qquad i_D = -K_f(\tau_f\tilde{\lambda}_d + \phi_\lambda), \tag{8.75}$$

to regulate λ_d to λ^*. Then, we design the PI current controller

$$\dot{\phi}_d = i_d - i_D \stackrel{\text{def}}{=} \tilde{i}_d, \qquad u_d = -K_d(\tau_d \tilde{i}_d + \phi_d), \tag{8.76}$$

for equation (8.74) to regulate i_d to i_D. With tight feedback loops, we can ensure the regulation of λ_d to λ^* for a wide range of variation of the variables (i_q, e_d, e_q) and the parameter α_r. The design should ensure that λ_d starts at a positive value and approaches λ^* monotonically so that λ_d is always positive. The initial condition of λ_d is determined by the initial condition of the observer (8.23), which is at our disposal.

Alternatively, we can approach the design of u_d as a nonlinear control problem for which a number of techniques are available to robustly regulate λ_d to λ^*. As an example, we describe a continuously implemented sliding-mode controller. Taking the sliding surface as

$$s_1 = Mi_d - \lambda^*, \tag{8.77}$$

we can rewrite equations (8.73) and (8.74) as

$$\dot{\lambda}_d = -\alpha_{r0}\lambda_d + \alpha_{r0}\lambda^* + \alpha_{r0}s_1, \tag{8.78}$$

$$\begin{aligned}\dot{s}_1 = M[&p\ \omega_0 i_q + \alpha_r\beta\lambda_d - (\alpha_s\eta + \alpha_r\beta M)i_d + \alpha_{r0}Mi_q^2/\lambda_d + \gamma u_d \\ &+ \alpha_r\beta e_d + p\ \beta\omega e_q] - \dot{\lambda}^*.\end{aligned} \tag{8.79}$$

Taking

$$u_d = \frac{1}{\gamma}[-p\ \omega_0 i_q - \alpha_{r0}\beta\lambda_d + (\alpha_s\eta + \alpha_{r0}\beta M)i_d - \alpha_{r0}Mi_q^2/\lambda_d + \dot{\lambda}^*/M + v_d],$$

reduces the $\dot{s}_1$-equation to

$$\dot{s}_1 = M[v_d + \alpha_r\beta e_d + p\ \beta\omega e_q - (\alpha_r - \alpha_{ro})\beta M i_d].$$

The choice

$$v_d = -k_1 \text{sat}(s_1/\mu_1),$$

with

$$k_1 \geq k_0 + |\alpha_r\beta e_d + p\ \beta\omega e_q - (\alpha_r - \alpha_{ro})\beta M i_d|,$$

for some positive constants k_1 and k_0 and a small positive constant μ_1, ensures that

$$s_1\dot{s}_1 \leq -k_0 M|s_1|, \qquad \text{for } |s_1| \geq \mu_1,$$

which shows that, within finite time, s_1 and $|\lambda_d - \lambda^*|$ will be of the order $O(\mu_1)$. By choosing λ^* and the initial condition $\lambda_d(0)$, it can be ensured that λ_d will be always positive.

8.6 Speed Control with Mechanical Sensor

The goal is to design a feedback controller to regulate the speed ω to the speed reference ω^* with measurement of the angle θ. We describe two designs. The first design is a current-control scheme where the current i_q is treated as the control input, while v_q is determined by a PI controller that regulates the current i_q to its desired value. The second design is a voltage-control scheme where the voltage u_q is treated as the control input.

In the current-control scheme, we assume that the flux observer (8.23) is implemented using the speed estimate $\hat{\omega}$ provided by the high-gain observer of Section 8.4.1. Because of the performance recovery property of the high-gain observer, we proceed with the design as if ω was available for feedback. Therefore, the current i_q is designed using the model

$$\dot{\theta} = \omega, \tag{8.80}$$

$$\dot{\omega} = \mu \left[i_q \lambda_d + (i_q e_d - i_d e_q) \right] - T_L/J, \tag{8.81}$$

$$\dot{e}_d = -\alpha_r e_d + \alpha_{r0} M i_q e_q/\lambda_d + (\alpha_r - \alpha_{r0})(M i_d - \lambda_d), \tag{8.82}$$

$$\dot{e}_q = -\alpha_{r0} M i_q e_d/\lambda_d - \alpha_r e_q + (\alpha_r - \alpha_{r0}) M i_q, \tag{8.83}$$

where equations (8.82) and (8.83) are obtained from equations (8.33) and (8.34), respectively, by setting $\omega_0 = \omega$. To study the regulation of ω to ω^*, we set

$$x_1 = \theta - \int \omega^*, \qquad x_2 = \omega - \omega^*.$$

Assuming that the flux λ_d has been regulated to a constant value λ^*, the term $(M i_d - \lambda_d)$ on the right-hand side of equation (8.82) is set equal to zero and equations (8.80), (8.81), (8.82), and (8.83) simplify to

$$\dot{x}_1 = x_2, \tag{8.84}$$

$$\dot{x}_2 = \mu(\lambda^* + e_d) i_q - \mu \lambda^* e_q/M - \dot{\omega}^* - T_L/J, \tag{8.85}$$

$$\dot{e}_d = -\alpha_r e_d + \alpha_{r0} M i_q e_q/\lambda^*, \tag{8.86}$$

$$\dot{e}_q = -\alpha_{r0} M i_q e_d/\lambda^* - \alpha_r e_q + (\alpha_r - \alpha_{r0}) M i_q. \tag{8.87}$$

The function

$$V = e_d^2 + e_q^2$$

satisfies the equation

$$\dot{V} = -2\alpha_r V + 2(\alpha_r - \alpha_{r0}) M i_q e_q,$$

which shows that for any bounded i_q the flux errors e_d and e_q will be bounded and, after some finite time, their ultimate bounds will be proportional to $\sqrt{|\alpha_r - \alpha_{r0}|}$. Therefore, the design of the control i_q can be carried out using equations (8.84) and (8.85) provided it is made

robust with respect to the bounded uncertainties e_d, e_q, and T_L. Consider the continuously implemented sliding-mode control

$$i_q = I_q \, \text{sat}(s_2/\mu_2),$$

where

$$s_2 = ax_1 + x_2, \qquad a > 0,$$

I_q is the maximum value of i_q, and μ_2 is a small positive constant. Let Ω be a compact set defined by

$$\Omega = \{|x_1| \le b/a, \ |s_2| \le b, \ V \le c^2\},$$

where $b > \mu_2$ and $c > (\alpha_r - \alpha_{r0})MI_q/2$. If the inequalities

$$\lambda^* + e_d \ge k_1 \quad \text{and} \quad I_q \ge k_2 + \frac{ax_2 - \mu\lambda^* e_q/M - \omega^* - Y_L/J}{\mu(\lambda^* + e_d)}$$

are satisfied in Ω for some positive constants k_1 and k_2, then it a positively invariant set, because on the boundaries $|x_1| = b/a$, $|s_2| = b$ and $V = c^2$, we have $x_1\dot{x}_1 \le 0$, $s_2\dot{s}_2 \le 0$, and $\dot{V} \le 0$, respectively. All trajectories starting in Ω will reach the set

$$\{|x_1| \le h\mu_2/a, \ |s_2| \le \mu_2\}, \qquad h > 1,$$

in finite time, which shows that the regulation error $x_2 = \omega - \omega^*$ will ultimately be of the order of μ_2; hence, it can be reduced by decreasing μ_2. Furthermore, if ω^* and T_L are constant and $(\alpha_r - \alpha_{r0})$ is sufficiently small, it can be shown that the trajectories converge to an equilibrium point where $\omega = \omega^*$.

In the voltage-controlled scheme, the voltage u_q is treated as the control input while i_q is a state variable that satisfies equation (8.32). Under assumptions similar to the current-control scheme, and with the definitions

$$x_1 = \theta - \int \omega^*, \quad x_2 = \omega - \omega^*, \quad x_3 = \dot{\omega} - \dot{\omega}^*,$$

we arrive at the model

$$\dot{x}_1 = x_2, \tag{8.88}$$

$$\dot{x}_2 = x_3, \tag{8.89}$$

$$\dot{x}_3 = \mu\lambda^*[-p\,\beta\omega\lambda^* - p\,\omega\lambda^*/M - (\alpha_{r0} + \alpha_s\eta + \alpha_{r0}\beta M)i_q)] - \dot{\omega}^* + \mu\gamma\lambda^* u_d + \delta_6, \tag{8.90}$$

$$\dot{e}_d = -\alpha_r e_d + \alpha_{r0} M i_q e_q/\lambda^*, \tag{8.91}$$

$$\dot{e}_q = -\alpha_{r0} M i_q e_d/\lambda^* - \alpha_r e_q + (\alpha_r - \alpha_{r0})M i_q, \tag{8.92}$$

where δ_6 is an uncertain term whose components are proportional to e_d, e_q, or $(\alpha_r - \alpha_{r0})$. Once again, for any bounded i_q the flux errors e_d and e_q will be bounded and, after some finite time, their ultimate bounds will be proportional to $\sqrt{|\alpha_r - \alpha_{r0}|}$. Thus, the design of u_q is a robust control problem for the equations (8.88), (8.89), and (8.90). Using the high-gain observer of Section 8.4.2 to estimate ω and $\dot{\omega}$, and relying on the performance recovery property of high-gain observers, we can proceed to design a state feedback control in terms of x_1, x_2, and x_3. A continuously implemented sliding-mode controller can be designed similar to the current-control scheme and with similar results. The details can be found in Khalil *et al.* (1996).

8.7 Speed Control without Mechanical Sensor

The goal is to design a feedback controller to regulate the speed ω to the speed reference ω^*. This time, however, we do not have measurements of θ and we use the high-gain observer of Section 8.4.3 to estimate the speed. The flux observer (8.23) is implemented with $\omega_0 = \omega^*$ and we assume that flux λ_d has been regulated to a constant value λ^*. We rewrite equation (8.32) as

$$\dot{i}_q = -(\alpha_s \eta + \alpha_r \beta M) i_q - \alpha_{r0} i_q + \gamma u_q + d_2, \tag{8.93}$$

where

$$d_2 = -p\ \beta\omega\lambda^* - p\omega^*\lambda^*/M - -p\ \beta\omega e_d + \alpha_r \beta e_q$$

acts as a disturbance input. For any current command i_Q, we can design a state feedback controller for u_q, with sufficiently large gains, to regulate i_q to i_Q. Once again, the traditional approach (Leonhard 1996) uses the PI current controller

$$\dot{\phi}_q = i_q - i_Q \stackrel{\text{def}}{=} \tilde{i}_q, \qquad u_q = -K_q(\tau_q \tilde{i}_q + \phi_q). \tag{8.94}$$

This allows us to view i_Q as the control input. Thus, the motor dynamics can be described by the third order model

$$\dot{e}_d = -\alpha_r e_d + (p\omega^* - p\omega + \alpha_{r0} M i_Q/\lambda^*) e_q, \tag{8.95}$$

$$\dot{e}_q = -(p\omega^* - p\omega + \alpha_{r0} M i_Q/\lambda^*) e_d - \alpha_r e_q + (\alpha_r - \alpha_{r0}) M i_Q + p(\omega - \omega^*)\lambda^*, \tag{8.96}$$

$$\dot{\omega} = \mu[i_Q(\lambda^* + e_d) - e_q\lambda^*/M] - T_L/J, \tag{8.97}$$

$$\Omega = \left(\frac{\lambda^* + e_d}{\lambda^*}\right)\omega - \frac{\alpha_r e_q}{p\lambda^*} + a i_Q, \tag{8.98}$$

where Ω is viewed as the measured output and $a = (\eta - \hat{\eta})/(p\ \beta\lambda^*)$. In Khalil *et al.* (2009) it is shown how to apply the singular perturbation theory (Kokotović *et al.* 1999), to justify the model (8.95), (8.96), (8.97), and (8.98) when the gain K_q is sufficiently large.

The model (8.95), (8.96), (8.97), and (8.98) enables us to design the current i_Q as a feedback function of Ω to regulate ω to ω^*, and perform rigorous analysis of the nonlinear closed-loop

system. When ω^* and T_L are constant, or approach constant limits at steady state, it is natural to use integral action to ensure zero steady-state error (Khalil 2002). Under the condition $\Omega = \omega^*$, the equilibrium equations are

$$0 = -\alpha_r \bar{e}_d + (p\omega^* - p\bar{\omega} + \alpha_{r0} M \bar{i}_Q/\lambda^*)\bar{e}_q, \tag{8.99}$$

$$0 = -(p\omega^* - p\bar{\omega} + \alpha_{r0} M \bar{i}_Q/\lambda^*)\bar{e}_d - \alpha_r \bar{e}_q + (\alpha_r - \alpha_{r0}) M \bar{i}_Q + p(\bar{\omega} - \omega^*)\lambda^*, \tag{8.100}$$

$$0 = \mu[\bar{i}_Q(\lambda^* + \bar{e}_d) - \bar{e}_q \lambda^*/M] - T_L/J, \tag{8.101}$$

$$\omega^* = \left(\frac{\lambda^* + \bar{e}_d}{\lambda^*}\right)\bar{\omega} - \frac{\alpha_r \bar{e}_q}{p\lambda^*} + a\bar{i}_Q. \tag{8.102}$$

Solving equations (8.99) and (8.100) for $\bar{e}_d$ and $\bar{e}_q$ in terms of $\bar{i}_Q$ and $\tilde{\omega} \stackrel{\text{def}}{=} \bar{\omega} - \omega^*$ and substituting in equation (8.102), it can be shown that

$$\left(-p\tilde{\omega} + \frac{\alpha_{r0} M \bar{i}_Q}{\lambda^*}\right)\left(p\tilde{\omega} + \frac{(\alpha_r - \alpha_{r0}) M \bar{i}_Q}{\lambda^*}\right)\omega_c = 0, \tag{8.103}$$

where

$$\omega_c = p\omega^* + \frac{\alpha_{r0} M \bar{i}_Q}{\lambda^*}.$$

Assuming that $\omega_c \neq 0$, the equation has two solutions:

$$\tilde{\omega} = \frac{-(\alpha_r - \alpha_{r0}) M \bar{i}_Q}{p\lambda^*} \quad \text{or} \quad \tilde{\omega} = \frac{\alpha_{r0} M \bar{i}_Q}{p\lambda^*}.$$

It is clear that the first solution is the one we should be interested in because it yields zero steady-state speed error in the nominal case $\alpha_{r0} = \alpha_r$. The equilibrium point corresponding to this solution is

$$\bar{e}_d = \bar{e}_q = 0, \tag{8.104}$$

$$\bar{i}_Q = \frac{b\omega^* + T_L/J}{\mu\lambda^*},$$

$$\bar{\omega} = \omega^* - \frac{(\alpha_r - \alpha_{r0}) M \bar{i}_Q}{p\lambda^*}. \tag{8.105}$$

Can we stabilize this equilibrium point while using integral action? To answer this question, we linearize equations (8.95), (8.96), (8.97), and (8.98) at the equilibrium point (8.105) to obtain the linear model

$$\dot{x} = Ax + B(i_Q - \bar{i}_Q),$$

$$\Omega - \omega^* = Cx + D(i_Q - \bar{i}_Q),$$

where

$$A = \begin{bmatrix} -\alpha_r & \frac{\alpha_r M \bar{i}_Q}{\lambda^*} & 0 \\ -\frac{\alpha_r M \bar{i}_Q}{\lambda^*} & -\alpha_r & p\lambda^* \\ \mu \bar{i}_Q & -\frac{\mu\lambda^*}{M} & -0 \end{bmatrix},$$

$$B = \begin{bmatrix} 0 \\ (\alpha_r - \alpha_{r0})M \\ \mu\lambda^* \end{bmatrix},$$

$$C = \begin{bmatrix} \frac{\bar{\omega}}{\lambda^*} & -\frac{\alpha_r}{p\lambda^*} & 1 \end{bmatrix}, \qquad D = \frac{(\alpha_r - \alpha_{r0})M}{p\lambda^*},$$

with the transfer function

$$G(s) = C(sI - A)^{-1}B + D = \frac{n(s)}{d(s)},$$

in which

$$n(s) = \mu\lambda^* \left[s^2 + \alpha_r s + \frac{\omega_c \alpha_r M \bar{i}_Q}{\lambda^*} \right] \times \left[1 + \frac{(\alpha_r - \alpha_{r0})M}{\mu p \lambda^{*2}} s \right],$$

$$d(s) = s \left[(s + \alpha_r)^2 + \left(\frac{\alpha_r M \bar{i}_Q}{\lambda^*} \right)^2 \right] + \frac{p\mu\lambda^{*2}}{M} \left(s + \alpha_r - \frac{\alpha_r M^2 \bar{i}_Q^2}{\lambda^{*2}} \right).$$

Let us note the important role played by $\omega_c \bar{i}_Q$ in the control design. When $\omega_c \bar{i}_Q = 0$, $G(s)$ has a zero at the origin. Hence, it is impossible to design any linear controller with integral action. This follows from the theory of servomechanisms (Davison 1976). When $\omega_c \bar{i}_Q < 0$, $G(s)$ has a real zero in the right-half plane; hence, it is nonminimum phase. It is possible to design a controller with integral action to stabilize the system, but such a controller cannot be a simple PI controller. This fact can be seen by sketching the root locus of the system for the different possible pole-zero patterns. For a PI controller, the root locus will always have a branch that

lies entirely on the positive real axis. This leaves us with the case when $\omega_c \bar{i}_Q$ is positive. In this case the transfer function $G(s)$ is minimum phase and we can design a PI controller with high-gain feedback, of the form

$$\dot{\phi}_\omega = \Omega - \omega^*, \quad i_Q = -K[(\Omega - \omega^*)\phi_\omega],$$

to stabilize the closed-loop system and achieve good tracking properties. The condition

$$\omega_c \bar{i}_Q = \bar{i}_Q \left[p\omega^* + \frac{\alpha_{r0} M \bar{i}_Q}{\lambda^*} \right] > 0$$

is satisfied when the motor is operated in the motoring mode, but not in the generating mode.

The condition $\omega_c \bar{i}_Q = 0$ is satisfied if $\bar{i}_Q = 0$ or $\omega_c = 0$. The case $\omega_c = 0$ indicates operation at zero frequency. It is well known in the induction motor literature that operating the motor at zero (or low) frequency is challenging, and that a design for such case will have to exploit secondary phenomena of the machine, which are not conveyed in our model (see, e.g., Ferrah *et al.* 1992). The case $\bar{i}_Q = 0$ indicates that the motor is running at constant speed without producing electromagnetic torque, which is unrealistic because balancing the motor's friction alone would require production of electromagnetic torque.

8.8 Simulation and Experimental Results

In Khalil and Strangas (1996), Aloliwi *et al.* (2000), and Aloliwi *et al.* (1997), the speed tracking problem is discussed and a controller is developed using rotor position sensors and under uncertainty of the stator and rotor resistance and the load torque. Simulation results are presented in Khalil *et al.* (1996) and Aloliwi *et al.* (2000), while Aloliwi *et al.* (1997) presents experimental results. The change of variables presented earlier is utilized and a third order high-gain observer is used to estimate the rotor speed and acceleration from its position. In the experimental results of Aloliwi *et al.* (1997), the rotor resistance was varied up to 200%, and the controller was shown to track the speed reference even after the application of a step load. The actual and estimated speed and flux for rotor resistance at 200% of its nominal value showed good performance.

In Strangas *et al.* (1999), a torque controller is presented. Neither the terminal voltages nor the speed is measured, and the rotor resistance and torque are unknown, although the stator resistance is considered to be known accurately. The speed of the rotor is estimated from the stator currents using a high-gain observer. Simulation and experimental results verify the analysis results that the system is locally stable at zero torque and flux errors at low speeds as long as the torque command is adequate, and remains at the original stable point during short torque transients. This was demonstrated for speed reversal where the load was only inertia and for torque command reversal. Also, although there could be a significant error in speed estimate, the torque tracking was appreciably better.

In Khalil *et al.* (2009), the problem of tracking a speed command without a position measurement is addressed. The discussion is centered on the development of a high-gain speed observer to estimate the speed from field-oriented currents and voltages. It is independent of the feedback controller design, and uses the change of variables discussed earlier. It allows for

errors in both rotor and stator resistance. Simulation and experiments on a 2HP squirrel-cage induction motor showed closeness between the results of a full and reduced model, made possible by the use of high-gain feedback. These were compared for 10% increase in R_s and R_r. The inability to maintain stability at steady state when $\omega_c \bar{i}_Q < 0$ as discussed earlier was demonstrated.

8.9 Conclusions

This chapter summarized the research conducted at Michigan State University to use high-gain observers and robust nonlinear techniques for the control of electric drives. The work has focused on field-oriented control of induction motors, but the same tools can be applied to other machines and different control strategies. One outcome of the experimental testing of the proposed control strategies is the confirmation that high-gain observers can be successfully implemented in electric drives with a sampling frequency in the range 10–20 kHz and with the typical measurement noise that results from using optical encoders.

References

Aloliwi B, Khalil HK, and Strangas EG (1997) Robust speed control of induction motors. *Proceedings of American Control Conference*, Albuquerque, NM WP16:4.

Aloliwi B, Khalil HK, and Strangas EG (2000) Robust speed control of induction motors: application to a benchmark example. *International Journal Adaptive Control and Signal Processing*, **14**, 157–170.

Atassi AN and Khalil HK (1999) A separation principle for the stabilization of a class of nonlinear systems. *IEEE Transactions on Automatic Control*, **44**, 1672–1687.

Davison EJ (1976) The robust control of a servomechanism problem for linear time-invariant multivariable systems. *IEEE Trans. Automat. Contr.*, **AC-21**(1), 25–34.

Khalil HK (2002) *Nonlinear Systems* 3rd edn. Prentice Hall, Upper Saddle River, NJ.

Khalil HK and Strangas EG (1996) Robust speed control of induction motors using position and current measurement. *IEEE Transactions on Automatic Control*, **41**, 1216–1220.

Khalil HK, Strangas EG, and Jurkovic S (2009) Speed observer and reduced nonlinear model for sensorless control of induction motors. *IEEE Transactions on Control Systems Technology*, **17**, pp. 327–339.

Ferrah A, Bradley KJ, and Asher GM (1992) Sensorless speed detection of inverter fed induction motors using slot harmonics and fast fourier transform. *Power Electronics Specialists Conference*, 279–286.

Kokotović PV, Khalil HK, and O'Reilly J (1999) *Singular Perturbations Methods in Control: Analysis and Design*. SIAM.

Leonhard W (1996) *Control of Electrical Drives* 2nd edn. Springer.

Novotony DW, Lipo TA, and Jahns TM (2010) *Introduction to Electric Machines and Drives*. University of Wisconsin.

Krishnan R (2001) *Electric Motor Drives*. Prentice Hall, Upper Saddle River, NJ.

Strangas EG, Khalil HK, Aloliwi B, *et al.* (1999). Robust tracking controllers for induction motors without rotor position sensor: analysis and experimental results. *IEEE Transactions on Energy Conversion*, **14**, 1448–1458.

9

Adaptive Output Feedback Control of Induction Motors

Riccardo Marino, Patrizio Tomei, and Cristiano Maria Verrelli
Dipartimento di Ingegneria Elettronica, Universitá di Roma "Tor Vergata", Italy

9.1 Introduction

Induction motors have definite advantages with respect to more expensive and less reliable electric motors such as direct-current ones: no commutator, no brushes, no rotor windings in squirrel-cage motors, capability of producing higher torques with lower weights, smaller size, and lower rotating masses. The availability of low-cost powerful digital signal processors and significant advances on power electronics allow for the design of complex induction motor (IM) controllers with the aim of achieving high performance on speed tracking and power efficiency. Flux sensors are typically not available so that an output feedback control problem is to be addressed, in which only the rotor speed and the stator currents are available from measurements. On the other hand, speed sensors may fail or be eliminated on purpose to increase reliability and noise immunity as well as to reduce cost and maintenance: in this case, the estimation and tracking control problem is called "sensorless" since only stator currents are assumed to be measured and available for feedback. Several difficulties naturally arise: motor dynamics are nonlinear and multivariable; measured outputs (stator currents for the sensorless case and stator currents/rotor speed for the output feedback case) do not coincide with the controlled outputs (rotor speed and flux modulus) that are required to track smooth bounded reference signals; three critical parameters, namely rotor and stator resistances (which vary during operations due to motor heating) and load torque (which depends on applications), are typically uncertain and are to be estimated online.

The sensorless estimation and tracking control problem with no use of nonrobust open-loop integration of flux dynamics (or equivalently rotor flux measurements) has been recently

AC Electric Motors Control: Advanced Design Techniques and Applications, First Edition. Edited by Fouad Giri.

addressed. Even though significant contributions can be found in Khalil *et al.* (2009), Lin *et al.* (2000), Marino *et al.* (2005, 2008), Montanari *et al.* (2006, 2007), (see also Zaky 2012; Traoré *et al.* 2012), the problem of designing an estimation and tracking control algorithm and of proving its closed-loop stability for sensorless IMs with uncertainties in load torque and stator and rotor resistances still remains open to the best of our knowledge. This constitutes an important problem in real applications since, as experimentally demonstrated in Montanari *et al.* (2006) (see also Mitronikas *et al.* 2001; Karanayil *et al.* 2007; Jadot *et al.* 2009; Hinkkanen *et al.* 2010), errors in estimating the stator resistance may lead to steady-state rotor speed and flux modulus tracking errors and even to instability, especially at low speeds.

Even when the rotor speed measurement is available for feedback (output feedback case) the corresponding theoretical estimation and tracking control problem can be still considered open: the available results in Behal *et al*. (2003), Fattah and Loparo (2001), Feemster *et al.* (2000), Jadot *et al.* (2009), Karagiannis *et al.* (2009), Marino *et al.* (1999), Peresada and Tonielli (2000), Peresada *et al.* (1999), and Vedagarbha *et al.* (1997) do not solve, via a priori verifiable persistency of excitation conditions, the critical case of output tracking in the presence of uncertain load torque, rotor and stator resistances. In particular: (1) only the case of known stator resistance is solved in Marino *et al.* (1999), in the presence, however, of not a priori verifiable persistency of excitation conditions; (2) only a qualitative sensitivity analysis of the persistency of excitation conditions is provided by Jadot *et al.* (2009) for the speed regulation (and not tracking) problem.

The aim of this chapter is to show that, under specific observability and identifiability conditions, solutions to the above sensorless and output feedback estimation and tracking control problems exist. They are constituted by dynamic nonlinear adaptive control algorithms that incorporate closed-loop observers for the unmeasured motor variables and closed-loop identifiers for the uncertain parameters (load torque and motor resistances). In particular, owing to the use of a sufficiently slow adaptation for the stator resistance estimate (see Montanari and Tilli (2006) and Jadot *et al.* (2009) for a similar approach to parameter estimation in IMs (Ha and Lee 2000) and for the identification of stator resistance from the generated torque at steady state, the closed-loop error system is guaranteed to be locally exponentially stable under: (1) persistency of excitation conditions, which may be interpreted in terms of rotor speed and flux observability and rotor resistance identifiability, and involve the rotor speed and flux modulus reference signals only; (2) conditions for the identifiability in first approximation of the stator resistance at steady state. Exponential rotor speed and flux modulus tracking is thus, in both cases, achieved along with exponential estimation of the unmeasured state variables and uncertain parameters.

Theoretical and simulative comparisons between the two presented controllers (sensorless control and output feedback one) are finally carried out in terms of persistency of excitation requirements and closed-loop performances: a time-varying rotor flux reference signal is no longer needed in the output feedback case (leading to the possibility of minimizing the power losses at steady state), while, as expected, transient performance are largely improved when the rotor speed signal is available for feedback.

9.2 Problem Statement

Assuming linear magnetic circuits, the dynamics of a balanced nonsaturated IM with one pole pair in a fixed reference frame attached to the stator are given by the well-known fifth order

model (see, for instance, Krause 1986; Leonhard 2001; Marino *et al.* 2010)

$$\begin{aligned}
\frac{\mathrm{d}\omega_m}{\mathrm{d}t} &= \mu(\phi_{ra} i_{sb} - \phi_{rb} i_{sa}) - \frac{T_L}{J},\\
\frac{\mathrm{d}\phi_{ra}}{\mathrm{d}t} &= -\alpha\phi_{ra} - \omega_m \phi_{rb} + \alpha L_m i_{sa},\\
\frac{\mathrm{d}\phi_{rb}}{\mathrm{d}t} &= -\alpha\phi_{rb} + \omega_m \phi_{ra} + \alpha L_m i_{sb},\\
\frac{\mathrm{d}i_{sa}}{\mathrm{d}t} &= -\Big(\frac{R_s}{\sigma} + \beta\alpha L_m\Big) i_{sa} + \frac{1}{\sigma} v_{sa} + \beta\alpha\phi_{ra} + \beta\omega_m\phi_{rb},\\
\frac{\mathrm{d}i_{sb}}{\mathrm{d}t} &= -\Big(\frac{R_s}{\sigma} + \beta\alpha L_m\Big) i_{sb} + \frac{1}{\sigma} v_{sb} + \beta\alpha\phi_{rb} - \beta\omega_m\phi_{ra},
\end{aligned} \tag{9.1}$$

in which ω_m is the rotor speed, ϕ_{ra} and ϕ_{rb} are the rotor fluxes, i_{sa} and i_{sb} are the stator currents, $\omega_m, \phi_{ra}, \phi_{rb}, i_{sa}$, and i_{sb} constitute the state variables, v_{sa}, and v_{sb} are the stator voltages (which constitute the control inputs) in a fixed reference attached to the stator; the outputs to be controlled are the rotor speed ω_m and the rotor flux modulus $\sqrt{\phi_{ra}^2 + \phi_{rb}^2}$. The model parameters are: load torque $T_L = T_{Ln} + \theta$, where $\theta \in [-\theta_m, \theta_m]$ denotes the constant uncertain variation from the constant nominal value T_{Ln} (T_L is typically uncertain since it depends on applications); (known) motor moment of inertia J; rotor and stator windings resistances R_r and R_s and (known) inductances L_r and L_s; and (known) mutual inductance L_m. To simplify notations we use the reparametrization: $\alpha = \frac{1}{\tau_r} = \frac{R_r}{L_r}$, $\beta = \frac{L_m}{\sigma L_r}$, $\mu = \frac{L_m}{JL_r}$, $\sigma = L_s(1 - \frac{L_m^2}{L_s Lr})$. Besides the load torque T_L, the parameters α and R_s are also assumed to be uncertain taking into account resistance variations during operations due to motor heating. If we introduce, as in Marino *et al.* (1999), an angle $\varepsilon_0(t)$, whose dynamics $\frac{d\varepsilon_0(t)}{dt} = \omega_0(t)$ will be later defined ($\varepsilon_0(0)$ is an arbitrary initial condition), we can equivalently consider the vectors $[\phi_{rd}, \phi_{rq}]^T$, $[i_{sd}, i_{sq}]^T$, and $[v_{sd}, v_{sq}]^T$, which are obtained by multiplying the corresponding (a, b) vectors $[\phi_{ra}, \phi_{rb}]^T$, $[i_{sa}, i_{sb}]^T$, and $[v_{sa}, v_{sb}]^T$ by the matrix $\mathcal{R}(\varepsilon_0) = \begin{bmatrix} \cos\varepsilon_0 & \sin\varepsilon_0 \\ -\sin\varepsilon_0 & \cos\varepsilon_0 \end{bmatrix}$. Such vectors contain the direct and quadrature components of rotor flux, stator current, and stator voltage vectors, respectively, with respect to a time-varying (d, q) reference frame rotating at speed $\omega_0(t)$ and identified by the angle $\varepsilon_0(t)$ in the fixed (a, b) reference frame. Using the state coordinates ($\omega_m, \phi_{rd}, \phi_{rq}, i_{sd}$ and i_{sq}) and the control variables (v_{sd} and v_{sq}) the motor dynamics (9.1) become (see, for instance, Krause 1986)

$$\begin{aligned}
\frac{\mathrm{d}\omega_m}{\mathrm{d}t} &= \mu(\phi_{rd} i_{sq} - \phi_{rq} i_{sd}) - \frac{T_L}{J},\\
\frac{\mathrm{d}\phi_{rd}}{\mathrm{d}t} &= -\alpha\phi_{rd} + (\omega_0 - \omega_m)\phi_{rq} + \alpha L_m i_{sd},\\
\frac{\mathrm{d}\phi_{rq}}{\mathrm{d}t} &= -\alpha\phi_{rq} - (\omega_0 - \omega_m)\phi_{rd} + \alpha L_m i_{sq},\\
\frac{\mathrm{d}i_{sd}}{\mathrm{d}t} &= -\Big(\frac{R_s}{\sigma} + \beta\alpha L_m\Big) i_{sd} + \frac{1}{\sigma} v_{sd} + \omega_0 i_{sq} + \beta\alpha\phi_{rd} + \beta\omega_m\phi_{rq},\\
\frac{\mathrm{d}i_{sq}}{\mathrm{d}t} &= -\Big(\frac{R_s}{\sigma} + \beta\alpha L_m\Big) i_{sq} + \frac{1}{\sigma} v_{sq} - \omega_0 i_{sd} + \beta\alpha\phi_{rq} - \beta\omega_m\phi_{rd}.
\end{aligned} \tag{9.2}$$

Let us denote by $\omega_m^*(t)$ and $\phi^*(t) \geq c_\phi > 0$ the smooth bounded reference signals with bounded time derivatives for the output variables to be controlled, which are the rotor speed ω_m and the rotor flux modulus $\sqrt{\phi_{ra}^2 + \phi_{rb}^2} = \sqrt{\phi_{rd}^2 + \phi_{rq}^2}$, respectively. Following the field-oriented control strategy in Blaschke (1972), our goal is to design dynamic sensorless and output feedback compensators of the form

$$\begin{aligned} \frac{\mathrm{d}\varepsilon_0(t)}{\mathrm{d}t} &= \omega_0(t), \\ \begin{bmatrix} v_{sa}(t) \\ v_{sb}(t) \end{bmatrix} &= \begin{bmatrix} \cos\varepsilon_0(t) & -\sin\varepsilon_0(t) \\ \sin\varepsilon_0(t) & \cos\varepsilon_0(t) \end{bmatrix} \begin{bmatrix} v_{sd}(t) \\ v_{sq}(t) \end{bmatrix}, \end{aligned} \tag{9.3}$$

by choosing $\omega_0(t)$, $v_{sd}(t)$, and $v_{sq}(t)$ so that, for any initial condition $(\omega_m(0), \phi_{ra}(0), \phi_{rb}(0), i_{sa}(0), i_{sb}(0),$ or $\varepsilon_0(0))$ in a suitable domain $\mathcal{D}$ and for any uncertainty $[\theta, \alpha, R_s]^T$ in the known region $[-\theta_m, \theta_m] \times [\alpha_m, \alpha_M] \times [R_{sm}, R_{sM}]$, $(\theta_m \geq 0, 0 < \alpha_m \leq \alpha_M, 0 < R_{sm} \leq R_{sM})$, we have

$$\lim_{t\to\infty} \left[\omega_m(t) - \omega_m^*(t)\right] = 0, \tag{9.4}$$

and

$$\lim_{t\to\infty} \left[\phi_{rd}(t) - \phi^*(t)\right] = 0, \tag{9.5}$$

$$\lim_{t\to\infty} \left[\phi_{rq}(t)\right] = 0, \tag{9.6}$$

which imply that

$$\lim_{t\to\infty} \left[\sqrt{\phi_{ra}^2(t) + \phi_{rb}^2(t)} - \phi^*(t)\right] = 0.$$

Equations (9.5) and (9.6) imply that the flux vector ($\phi_{ra}(t)$ and $\phi_{rb}(t)$) asymptotically rotates at speed $\omega_0(t)$ and that the (d, q) frame rotating at speed $\omega_0(t)$ tends to have the d-axis coincident with the rotating flux vector as t goes to infinity, that is, field orientation is achieved.

9.3 Nonlinear Estimation and Tracking Control for Sensorless Induction Motors

Sensorless control for rotor speed and flux modulus tracking in IMs is typically based on the feedforward control, which depends on all system parameters, including load torque and resistances. The simplest feedback action is to add PI controls on the direct and quadrature stator voltage vector components on the basis of the direct and quadrature stator currents errors

(see, Marino *et al.* 2004 2010). Field orientation is not attained in the presence of parameter errors (especially in load torque and rotor resistance) and steady-state errors may appear: they cannot be arbitrarily reduced by increasing the PI gains in the current loop. Steady-state speed tracking errors may not be acceptable in high-performance traction applications such as driverless subways or trains. Field orientation and consequently vanishing speed tracking errors can be achieved by online estimation of the critical parameters load torque and rotor resistance: this estimation is inherently linked with the estimation of rotor speed and fluxes and of stator resistance. This is a difficult problem since there are identifiability and observability issues when only stator currents are measured: it is well established that a time-varying flux modulus is required for the simultaneous estimation of rotor speed and rotor resistance (see Ha and Lee 2000; Marino *et al.* 2010, and references therein). Hence the estimation and tracking control problems are strictly related for sensorless IMs: a controller with parameters errors may give steady-state errors or even instability, while parameter estimation cannot be achieved if the sensorless motor is not kept in persistently exciting operating conditions. In this section we present a sensorless solution to the estimation and tracking control problem for IMs with uncertain load torque and rotor and stator resistances, which relies on: (1) persistency of excitation conditions, which may be interpreted in terms of rotor speed and flux observability and rotor resistance identifiability and involve the rotor speed and flux modulus reference signals only; (2) conditions for the identifiability in first approximation of the stator resistance at steady state.

9.3.1 Estimation and Tracking Control Algorithm

We propose the following estimation and tracking control algorithm, which is based on a stator current-control loop containing feedforward actions and stabilizing feedback terms:

$$
\begin{aligned}
&\begin{bmatrix} v_{sa} \\ v_{sb} \end{bmatrix} = \begin{bmatrix} \cos\varepsilon_0 & -\sin\varepsilon_0 \\ \sin\varepsilon_0 & \cos\varepsilon_0 \end{bmatrix} \begin{bmatrix} v_{sd} \\ v_{sq} \end{bmatrix},\\
&v_{sd} = \sigma\Big[\Big(\frac{\hat{R}_s}{\sigma} + \hat{\alpha}\beta L_m\Big) i_{sd} - \omega_0 i_{sq} - \beta\hat{\alpha}\hat{\phi}_{rd} - \beta\omega_m^*\hat{\phi}_{rq} - k_e(i_{sd} - i_{sd}^*) + \frac{\mathrm{d}}{\mathrm{d}t} i_{sd}^*(t)\\
&\qquad -\frac{k}{4}(i_{sd} - i_{sd}^*)\beta^2\Big(3 + \alpha_M^2 + \omega_m^{*2} + \frac{\dot{\phi}^{*2}}{\hat{\alpha}^2} + L_m^2(i_{sd} - i_{sd}^*)^2\Big)\Big],\\
&v_{sq} = \sigma\Big[\Big(\frac{\hat{R}_s}{\sigma} + \hat{\alpha}\beta L_m\Big) i_{sq} + \omega_0 i_{sd} - \beta\hat{\alpha}\hat{\phi}_{rq} + \beta\hat{\omega}_m\hat{\phi}_{rd} - k_e(i_{sq} - i_{sq}^*) + \frac{\mathrm{d}}{\mathrm{d}t} i_{sq}^*(t)\\
&\qquad -\frac{k}{4}(i_{sq} - i_{sq}^*)\beta^2\Big(L_m^2[i_{sq}^{*2} + (i_{sq} - i_{sq}^*)^2] + \omega_m^{*2} + 5 + \alpha_M^2 + \phi^{*2}\Big)\Big], \qquad (9.7)\\
&\begin{bmatrix} i_{sd} \\ i_{sq} \end{bmatrix} = \begin{bmatrix} \cos\varepsilon_0 & \sin\varepsilon_0 \\ -\sin\varepsilon_0 & \cos\varepsilon_0 \end{bmatrix} \begin{bmatrix} i_{sa} \\ i_{sb} \end{bmatrix},
\end{aligned}
$$

in which: the reference signals i_{sd}^* and i_{sq}^* for i_{sd} and i_{sq} and the speed ω_0 of the (d, q) rotating frame, which, as in field-oriented control, are responsible for rotor speed and flux modulus

tracking, are chosen as

$$
\begin{aligned}
i_{sd}^* &= \frac{\phi^*}{L_m} + \frac{\dot{\phi}^*}{\hat{\alpha} L_m}, \\
i_{sq}^* &= \frac{1}{\mu \phi^*}\Big[-k_\omega(\hat{\omega}_m - \omega_m^*) + \frac{T_{Ln}}{J} + \frac{\mathrm{sat}(\hat{\theta})}{J} + \dot{\omega}_m^*\Big], \\
\dot{\varepsilon}_0 &= \omega_0 = \hat{\omega}_m + \frac{\hat{\alpha} L_m i_{sq}^*}{\phi^*};
\end{aligned}
\tag{9.8}
$$

the estimates ($\hat{\omega}_m, \hat{\phi}_{rd}, \hat{\phi}_{rq}, \hat{\theta}, \hat{\alpha}$, and $\hat{R}_s$) for the unmeasured state variables (ω_m, ϕ_{rd}, and ϕ_{rq}) and for the uncertain constant parameters (θ, α, and R_s) appearing in equations (9.7) and (9.8) are provided by the eighth order dynamic closed-loop adaptive observer, which includes four auxiliary internal variables ($\hat{i}_{sd}, \hat{i}_{sq}, \hat{z}_d$, and $\hat{z}_q$)

$$
\begin{aligned}
\hat{\phi}_{rd} &= -\frac{1}{\beta}(i_{sd} - \hat{z}_d), \quad \hat{\phi}_{rq} = -\frac{1}{\beta}(i_{sq} - \hat{z}_q), \\
\dot{\hat{i}}_{sq} &= -\Big(\frac{\hat{R}_s}{\sigma} + \beta\hat{\alpha} L_m\Big) i_{sq} + \frac{1}{\sigma} v_{sq} - \omega_0 i_{sd} - \beta\hat{\omega}_m \phi^* + (\lambda_1 + \lambda_2 + \lambda_3)(i_{sq} - \hat{i}_{sq}) \\
&\quad - \frac{\dot{\phi}^*}{\phi^*}(i_{sq} - \hat{i}_{sq}) - \beta[\omega_m^*(\hat{\phi}_{rd} - \phi^*) - \hat{\alpha}\hat{\phi}_{rq}], \\
\dot{\hat{\omega}}_m &= \mu\phi^* i_{sq} - \frac{(\lambda_1\lambda_3 + \lambda_1\lambda_2 + \lambda_2\lambda_3)}{\beta\phi^*}(i_{sq} - \hat{i}_{sq}) \\
&\quad - \frac{T_{Ln}}{J} - \frac{\hat{\theta}}{J} + \frac{1}{\phi^*}\Big[\frac{T_{Ln}}{J} + \frac{\mathrm{sat}(\hat{\theta})}{J} + \dot{\omega}_m^*\Big][\hat{\phi}_{rd} - \phi^*] \\
&\quad - \mu\Big[\frac{\phi^*}{L_m} + \frac{\dot{\phi}^*}{\hat{\alpha} L_m}\Big]\hat{\phi}_{rq}, \\
\dot{\hat{\theta}} &= \frac{J\lambda_1\lambda_2\lambda_3}{\beta\phi^*}(i_{sq} - \hat{i}_{sq}), \\
\dot{\hat{i}}_{sd} &= -\Big(\frac{\hat{R}_s}{\sigma} + \beta\hat{\alpha} L_m\Big) i_{sd} + \frac{1}{\sigma} v_{sd} + \omega_0 i_{sq} - \omega_m^*(i_{sq} - \hat{z}_q) - \hat{\alpha}(i_{sd} - \hat{z}_d) + k_i(i_{sd} - \hat{i}_{sd}), \\
\dot{\hat{z}}_d &= -\frac{\hat{R}_s}{\sigma} i_{sd} + \frac{1}{\sigma} v_{sd} + \omega_0 \hat{z}_q + \frac{\hat{\alpha}}{\gamma_1}(i_{sd} - \hat{i}_{sd}), \\
\dot{\hat{z}}_q &= -\frac{\hat{R}_s}{\sigma} i_{sq} + \frac{1}{\sigma} v_{sq} - \omega_0 \hat{z}_d + \frac{\omega_m^*}{\gamma_1}(i_{sd} - \hat{i}_{sd}), \\
\dot{\hat{\alpha}} &= \mathrm{Proj}\left[-\frac{\beta\dot{\phi}^*}{\gamma_2\hat{\alpha}}(i_{sd} - \hat{i}_{sd}), \hat{\alpha}\right], \\
\hat{\alpha}(0) &\in [\alpha_m, \alpha_M], \quad 0 < \alpha_m - \varepsilon_\alpha, \\
\dot{\hat{R}}_s &= -\varepsilon_R\left[\frac{(\omega_m^* i_{sq} + \hat{\alpha} i_{sd})}{\sigma\gamma_1}(i_{sd} - \hat{i}_{sd})\right], \\
\hat{R}_s(0) &\in [R_{sm}, R_{sM}],
\end{aligned}
\tag{9.9}
$$

where Proj$[\zeta, \hat{\alpha}]$ is the projection algorithm (see, Marino *et al.* 2008) defined by

$$\text{Proj}[\zeta, \hat{\alpha}] = \begin{cases} \zeta, & \text{if } \alpha_m \leq \hat{\alpha} \leq \alpha_M; \\ \zeta, & \text{if } \hat{\alpha} < \alpha_m \text{ and } \zeta \geq 0; \\ \zeta, & \text{if } \hat{\alpha} > \alpha_M \text{ and } \zeta \leq 0; \\ \xi_{\zeta 1}\zeta, & \text{if } \hat{\alpha} < \alpha_m \text{ and } \zeta < 0; \\ \xi_{\zeta 2}\zeta, & \text{if } \hat{\alpha} > \alpha_M \text{ and } \zeta > 0; \end{cases}$$

$$\xi_{\zeta 1} = 1 - \frac{{\alpha_m}^2 - \hat{\alpha}^2}{{\alpha_m}^2 - (\alpha_m - \varepsilon_\alpha)^2},$$

$$\xi_{\zeta 2} = 1 - \frac{\hat{\alpha}^2 - {\alpha_M}^2}{(\alpha_M + \varepsilon_\alpha)^2 - {\alpha_M}^2}.$$

The load torque uncertainty saturated estimate appearing in equations (9.8) and (9.9) is defined as

$$\text{sat}(\hat{\theta}) = \begin{cases} \hat{\theta}, & \text{if } 0 \leq \hat{\theta} \leq \theta_m; \\ \sum_{i=0}^{3} l_i \hat{\theta}^i, & \text{if } \theta_m < \hat{\theta} < \theta_m + \varepsilon; \\ \theta_m + \varepsilon, & \text{if } \hat{\theta} \geq \theta_m + \varepsilon; \end{cases}$$

$$l_0 = \frac{\theta_m^2(\theta_m + \varepsilon)}{\varepsilon^2}, \qquad l_1 = \frac{-2\theta_m\varepsilon - 3\theta_m^2 + \varepsilon^2}{\varepsilon^2},$$

$$l_2 = \frac{\varepsilon + 3\theta_m}{\varepsilon^2}, \qquad l_3 = -\frac{1}{\varepsilon^2},$$

in which sat(x) is a class $\mathcal{C}^1$ odd function that is linear in the closed set $[-\theta_m, \theta_m]$ and satisfies $|\text{sat}(x)| \leq \theta_m + \varepsilon$ for all $x \in \Re$. The overall estimation and tracking control algorithm (9.7), (9.8), and (9.9) depends on: the available i_{sa} and i_{sb} measurements; the smooth bounded reference signals (ω_m^* and ϕ^*) and their bounded first and second order time derivatives; the known motor parameters J, L_r, L_s, and L_m; the known bounds θ_m, α_m, α_M, R_{sm}, and R_{sM}; the positive control parameters k_ω, k_e, k, k_i, $\lambda_1 \neq \lambda_2 \neq \lambda_3$, γ_1, γ_2, ε_α, ε_R, and ε.

9.3.2 Stability Analysis

As in Marino *et al.* (2008), introduce the angle ε_0^* that satisfies

$$\dot{\varepsilon}_0^*(t) = \omega_m^*(t) + \frac{\alpha L_m}{\mu\phi^{*2}(t)}\Big[\frac{T_L}{J} + \dot{\omega}_m^*(t)\Big],$$

$$\varepsilon_0^*(0) = \varepsilon_0(0),$$

depending on the uncertain parameters α and T_L; define the tracking and estimation errors: $\tilde{\omega}_m = \omega_m - \omega_m^*$, $\tilde{\phi}_{rd} = \phi_{rd} - \phi^*$, $\tilde{\phi}_{rq} = \phi_{rq}$, $e_d = i_{sd} - i_{sd}^*$, $e_q = i_{sq} - i_{sq}^*$, $\tilde{i}_{sd} = i_{sd}$

$-\hat{i}_{sd}, \tilde{i}_{sq} = i_{sq} - \hat{i}_{sq}, e_\omega = \hat{\omega}_m - \omega_m, e_{\phi d} = \phi_{rd} - \hat{\phi}_{rd}, e_{\phi q} = \phi_{rq} - \hat{\phi}_{rq}, \tilde{\theta} = \theta - \hat{\theta}, \tilde{\alpha} = \alpha - \hat{\alpha}, \tilde{R}_s = R_s - \hat{R}_s$. Consider the changes of variables

$$\begin{bmatrix} \tilde{z}_a \\ \tilde{z}_b \end{bmatrix} = \begin{bmatrix} \cos\varepsilon_0^* & -\sin\varepsilon_0^* \\ \sin\varepsilon_0^* & \cos\varepsilon_0^* \end{bmatrix} \begin{bmatrix} \beta e_{\phi d} \\ \beta e_{\phi q} \end{bmatrix},$$

$$\tilde{x}_1 = \frac{\tilde{i}_{sq}}{\beta^2 \phi^{*2}}, \quad \tilde{x}_2 = \frac{e_\omega}{\beta\phi^*}, \quad \tilde{x}_3 = \frac{\tilde{\theta}}{J\beta\phi^*},$$

$$e = \begin{bmatrix} 1 & 1 & 1 \\ \lambda_2+\lambda_3 & \lambda_1+\lambda_3 & \lambda_1+\lambda_2 \\ \lambda_2\lambda_3 & \lambda_1\lambda_3 & \lambda_1\lambda_2 \end{bmatrix}^{-1} \begin{bmatrix} \tilde{x}_1 \\ \tilde{x}_2 \\ \tilde{x}_3 \end{bmatrix},$$

let $y = [\tilde{\omega}_m, \tilde{\phi}_{rd}, \tilde{\phi}_{rq}, e_d, e_q, e^T, \tilde{i}_{sd}, \tilde{z}_a, \tilde{z}_b, \tilde{\alpha}]^T \in \Re^{12}$, and choose the positive control parameters k_e, λ_1, λ_2, and λ_3 such that

$$k_e > \alpha_M L_m^2,$$

$$\min\{\lambda_1, \lambda_2, \lambda_3\} + \inf_{t\geq 0}\left\{\frac{\dot{\phi}^*(t)}{\phi^*(t)}\right\} \geq \tilde{c}_\phi > 0.$$

Assume, as in Marino *et al.* (2008), that there exist two positive reals t_p and k_p such that the persistency of excitation condition (I_3 is the 3×3 identity matrix)

$$\int_t^{t+t_p} \Gamma^T(\tau)\Gamma(\tau)d\tau \geq k_p I_3, \quad \forall\, t \geq 0, \tag{9.10}$$

which may be physically interpreted in terms of motor observability and rotor resistance identifiability (see Marino *et al.* 2008, and related references therein), holds with

$$\Gamma^T(t) = \begin{bmatrix} \alpha\cos\varepsilon_0^*(t) - \omega_m^*(t)\sin\varepsilon_0^*(t) \\ \alpha\sin\varepsilon_0^*(t) + \omega_m^*(t)\cos\varepsilon_0^*(t) \\ -\frac{\beta\dot{\phi}^*(t)}{\alpha} \end{bmatrix}.$$

Note that ε_0^* (and consequently (9.10)) only depends on the exogenous reference signals ω_m^* and ϕ^*.

Remark 9.3.1 *The proposed estimation and tracking control algorithm is obtained by replacing the uncertain stator resistance R_s by its estimate $\hat{R}_s$ in the estimation and tracking control law presented in Marino et al. (2008), which assumes the knowledge of the stator resistance and relies on backstepping and robust adaptive techniques involving the Lyapunov function*

$$W = \frac{1}{2}\Big[\tilde{\omega}_m^2 + s_\alpha(\tilde{\phi}_{rd}^2 + \tilde{\phi}_{rq}^2 + e_d^2 + e_q^2) + s_\beta\|e\|^2 + s_\gamma\Big(\tilde{i}_{sd}^2 + \gamma_1\tilde{z}_a^2 + \gamma_1\tilde{z}_b^2 + \gamma_2\tilde{\alpha}^2 + 2p\big\|Q_p(t)[\tilde{z}_a, \tilde{z}_b, \tilde{\alpha}]^T - \Gamma^T(t)\tilde{i}_{sd}\big\|^2\Big)\Big],$$

where $s_\alpha, s_\beta, s_\gamma, p \in \Re^+$ *and the matrix* $Q_p(t)$ *is the solution of the linear matrix differential equation*

$$\dot{Q}_p(t) = -Q_p(t) + \Gamma^T(t)\Gamma(t),$$
$$Q_p(0) = \mathrm{e}^{-t_p} k_p I.$$

The fluxes are estimated through the estimates $\hat{z}_d$ *and* $\hat{z}_q$ *of the auxiliary variables* $z_d = i_{sd} + \beta\phi_{rd}$ *and* $z_q = i_{sq} + \beta\phi_{rq}$ *whose dynamics*

$$\dot{z}_d = -\frac{R_s}{\sigma} i_{sd} + \frac{1}{\sigma} v_{sd} + \omega_0 z_q,$$
$$\dot{z}_q = -\frac{R_s}{\sigma} i_{sq} + \frac{1}{\sigma} v_{sq} - \omega_0 z_d$$

depend on neither the unmeasured rotor speed ω_m *nor the uncertain parameter* α.

The design of the estimation law for $\hat{R}_s$ is based on the following stability analysis. The closed-loop error system can be written as

$$\begin{aligned}\dot{y} &= Q_1(y,t) + Q_2(y,t)\tilde{R}_s \\ &\doteq A_y(t)y + B_y(y,t)y + A_R(t)\tilde{R}_s + B_R(y,t)\tilde{R}_s,\end{aligned}$$

where

$$\lim_{\|y\|\to 0} \sup_{t\geq 0} \frac{\|B_y(y,t)y\|}{\|y\|} = 0,$$
$$\lim_{\|[y,\tilde{R}_s]\|\to 0} \sup_{t\geq 0} \frac{\|B_R(y,t)\tilde{R}_s\|}{\|[y,\tilde{R}_s]\|} = 0.$$

Since, according to Marino *et al.* (2008), the origin of the unperturbed system (i.e., when $\tilde{R}_s = 0$)

$$\dot{y} = A_y(t)y + B_y(y,t)y$$

is locally exponentially stable, the origin of the linearized unperturbed system

$$\dot{\zeta} = A_y(t)\zeta$$

is exponentially stable (see Khalil 1996) so that there exists a function V_ζ such that

$$\begin{aligned} c_1\|\zeta\|^2 \le V_\zeta(\zeta,t) \le c_2\|\zeta\|^2,\\ \frac{\partial V(\zeta,t)}{\partial t} + \frac{\partial V(\zeta,t)}{\partial \zeta} A_y(t)\zeta \le -c_3\|\zeta\|^2,\\ \left\| \frac{\partial V(\zeta,t)}{\partial \zeta} \right\| \le c_4\|\zeta\|, \end{aligned}$$

in terms of certain positive reals c_i, $1 \le i \le 4$.

As in Jadot *et al.* (2009) and Montanari and Tilli (2006) and in accordance with our simulation results, we assume that there exists, for any $\tilde{R}_s$ in a sufficiently small compact set (containing the origin), a steady-state solution $h(\tilde{R}_s, t)$ to the closed-loop error system. In particular, let $\overline{B_r(0)}$ be the closed ball centered at the origin with sufficiently small radius r and assume that for all $(\tilde{R}_s, t) \in \overline{B_r(0)} \times [0, +\infty)$ the following condition holds:

$\mathcal{A}$) there exists a smooth solution $h(\tilde{R}_s, t)$ to the nonlinear partial differential equation

$$\frac{\partial h(\tilde{R}_s,t)}{\partial t} = Q_1(h(\tilde{R}_s,t),t) + Q_2(h(\tilde{R}_s,t),t)\tilde{R}_s$$

with $h = [h_{\tilde{\omega}_m}, h_{\tilde{\phi}_{rd}}, h_{\tilde{\phi}_{rq}}, h_{e_d}, h_{e_q}, h_{e_1}, h_{e_2}, h_{e_3}, h_{\tilde{i}_{sd}}, h_{\tilde{z}_a}, h_{\tilde{z}_b}, h_{\tilde{\alpha}}]^T$ ($h(\tilde{R}_s, t)$ being bounded on $\overline{B_r(0)} \times [0, +\infty)$ along with its first order partial derivatives) and satisfying

$$h(0,t) = 0, \qquad \forall\, t \ge 0.$$

We will look for a measurable steady-state solution component from which $\tilde{R}_s$ can be in first approximation identified. To this purpose, we first recall that $\beta e_{\phi d} = z_d - \hat{z}_d = \tilde{z}_d$, and $\beta e_{\phi q} = z_q - \hat{z}_q = \tilde{z}_q$, so that

$$\begin{bmatrix} \tilde{z}_a \\ \tilde{z}_b \end{bmatrix} = \begin{bmatrix} \cos\varepsilon_0^* & -\sin\varepsilon_0^* \\ \sin\varepsilon_0^* & \cos\varepsilon_0^* \end{bmatrix} \begin{bmatrix} \tilde{z}_d \\ \tilde{z}_q \end{bmatrix},$$

and we then consider the dynamics of $\tilde{z}_a$ and $\tilde{z}_b$. They only depend, in first approximation, on the measurable $\tilde{i}_{sd}$ and on the uncertain $\tilde{R}_s$, and they can be written as

$$\begin{aligned} \dot{\tilde{z}}_a &= \tilde{\omega}_0\tilde{z}_b - \frac{1}{\gamma_1}[\hat{\alpha}\cos\varepsilon_0^* - \omega_m^*\sin\varepsilon_0^*]\tilde{i}_{sd} - \frac{\tilde{R}_s}{\sigma}[i_{sd}\cos\varepsilon_0^* - i_{sq}\sin\varepsilon_0^*]\\ &\doteq p_a(y,t) - A_{za}(y,t)\tilde{R}_s - B_{za}(y,t)p(y),\\ \dot{\tilde{z}}_b &= -\tilde{\omega}_0\tilde{z}_a - \frac{1}{\gamma_1}[\hat{\alpha}\sin\varepsilon_0^* + \omega_m^*\cos\varepsilon_0^*]\tilde{i}_{sd} - \frac{\tilde{R}_s}{\sigma}[i_{sd}\sin\varepsilon_0^* + i_{sq}\cos\varepsilon_0^*]\\ &\doteq p_b(y,t) - A_{zb}(y,t)\tilde{R}_s - B_{zb}(y,t)p(y), \end{aligned}$$

where

$$\tilde{\omega}_0 = \tilde{\omega}_m + e_\omega - \frac{L_m}{\mu\phi^{*2}}\Big[\frac{T_L}{J} + \dot{\omega}_m^*\Big]\tilde{\alpha} + \frac{L_m}{\mu\phi^{*2}}(\alpha - \tilde{\alpha})\Big[-k_\omega(\tilde{\omega}_m + e_\omega) - \frac{(\theta - \text{sat}(\hat{\theta}))}{J}\Big],$$

and

$$\begin{aligned}
A_{za} &= \frac{1}{\sigma}[i_{sd}\cos\varepsilon_0^* - i_{sq}\sin\varepsilon_0^*],\\
B_{za} &= \frac{1}{\gamma_1}[\hat{\alpha}\cos\varepsilon_0^* - \omega_m^*\sin\varepsilon_0^*],\\
A_{zb} &= \frac{1}{\sigma}[i_{sd}\sin\varepsilon_0^* + i_{sq}\cos\varepsilon_0^*],\\
B_{zb} &= \frac{1}{\gamma_1}[\hat{\alpha}\sin\varepsilon_0^* + \omega_m^*\cos\varepsilon_0^*],\\
p_a &= \tilde{\omega}_0\tilde{z}_b, \quad p_b = -\tilde{\omega}_0\tilde{z}_a, \quad p = \tilde{i}_{sd}.
\end{aligned}$$

From the $(\tilde{z}_a, \tilde{z}_b)$-dynamics we obtain at steady state

$$\begin{aligned}
f_a(\tilde{R}_s, t) &\doteq \frac{\partial h_{\tilde{z}_a}(\tilde{R}_s, t)}{\partial t}\\
&= p_a(h(\tilde{R}_s, t), t) - A_{za}(h(\tilde{R}_s, t), t)\tilde{R}_s\\
&\quad - B_{za}(h(\tilde{R}_s, t), t)p(h(\tilde{R}_s, t)),\\
f_b(\tilde{R}_s, t) &\doteq \frac{\partial h_{\tilde{z}_b}(\tilde{R}_s, t)}{\partial t}\\
&= p_b(h(\tilde{R}_s, t), t) - A_{zb}(h(\tilde{R}_s, t), t)\tilde{R}_s\\
&\quad - B_{zb}(h(\tilde{R}_s, t), t)p(h(\tilde{R}_s, t)).
\end{aligned} \tag{9.11}$$

Even though the signals B_{za} and B_{zb} are not measurable owing to their dependence on the unmeasurable ε_0^*, the variable (we omit, for the sake of brevity, the dependence on y and t)

$$s_\pi = [A_{za}B_{za} + A_{zb}B_{zb}]p = \frac{\big(\hat{\alpha}i_{sd} + \omega_m^* i_{sq}\big)}{\sigma\gamma_1}\tilde{i}_{sd}$$

is available for feedback and shows the following useful property: at steady state for $\tilde{R}_s \in \overline{B_r(0)}$ (we omit, for the sake of brevity, the dependence on $\tilde{R}_s$, $h(\tilde{R}_s, t)$, and t), it satisfies

$$\begin{aligned}
s_\pi &= -A_{za}f_a - A_{za}^2\tilde{R}_s + A_{za}p_a\\
&\quad - A_{zb}f_b - A_{zb}^2\tilde{R}_s + A_{zb}p_b,
\end{aligned} \tag{9.12}$$

which, according to Hadamard's Lemma in Arnold (1992), becomes ($\bar{f}_a(\tilde{R}_s, t)$ and $\bar{f}_b(\tilde{R}_s, t)$, are suitable functions, and $\tilde{R}_s \in \overline{B_r(0)}$)

$$\begin{aligned} s_\pi &= -[A_{za}\bar{f}_a + A_{za}^2 + A_{zb}\bar{f}_b + A_{zb}^2]\tilde{R}_s + A_{za}p_a + A_{zb}p_b \\ &= -[A_{za}\bar{f}_{a,0} + A_{za}^2 + A_{zb}\bar{f}_{b,0} + A_{zb}^2]\tilde{R}_s + A_{za}p_a \\ &\quad + A_{zb}p_b - [A_{za}(\bar{f}_a - \bar{f}_{a,0}) + A_{zb}(\bar{f}_b - \bar{f}_{b,0})]\tilde{R}_s, \end{aligned} \tag{9.13}$$

where $\bar{f}_{a,0} = \bar{f}_a(0, t)$, and $\bar{f}_{b,0} = \bar{f}_b(0, t)$. By neglecting, in the right- hand side of the previous equation, the higher order terms[1] in $\tilde{R}_s$ (in accordance with our local results) we obtain for $\tilde{R}_s \in \overline{B_r(0)}$

$$s_\pi = -\lambda \tilde{R}_s, \tag{9.14}$$

with

$$\begin{aligned} \lambda &= \frac{i_{dr}^2}{\sigma^2} + \frac{i_{qr}^2}{\sigma^2} + \frac{\bar{f}_{a,0}}{\sigma}[i_{dr}\cos\varepsilon_0^* - i_{qr}\sin\varepsilon_0^*] + \frac{\bar{f}_{b,0}}{\sigma}[i_{dr}\sin\varepsilon_0^* + i_{qr}\cos\varepsilon_0^*], \\ i_{dr} &= \frac{\phi^*}{L_m} + \frac{\dot{\phi}^*}{\alpha L_m}, \\ i_{qr} &= \frac{1}{\mu\phi^*}\Big[\frac{T_L}{J} + \dot{\omega}_m^*\Big]. \end{aligned}$$

We now assume that in first approximation, $\tilde{R}_s$ is identifiable at steady-state from s_π. In analytical terms, according to (9.14), we thus introduce the following condition ($b = 1$ or $b = -1$; $\tilde{R}_s \in \overline{B_r(0)}$)

$\mathcal{B}$) $b\lambda(t) \geq c_R$ for all $t \geq 0$ with c_R a positive real.

The remainder of the section is devoted to show that, if $\mathcal{B}$ is satisfied, designing the stator resistance estimation law as

$$\dot{\hat{R}}_s(t) = -b\varepsilon_R s_\pi(y(t), t)$$

solves the problem stated in the previous section. Without loss of generality we will consider $b = 1$, which is in accordance with our simulation results and with the following remark.

Remark 9.3.2 *If $\bar{f}_{a,0} = \bar{f}_{b,0} = 0$, then $\lambda = \frac{i_{dr}^2}{\sigma^2} + \frac{i_{qr}^2}{\sigma^2}$, whose positiveness is clearly related to stator resistance identifiability conditions. The above design may be thus interpreted as a modification of the design proposed in Marino et al. (2010) for the case of constant rotor speed and flux modulus and zero load torque, which led to the stator resistance estimator*

[1]Recall that, by Hadamard's Lemma in Arnold (1992), $h(\tilde{R}_s, t) = h_*(\tilde{R}_s, t)\tilde{R}_s$ with $h_*(\tilde{R}_s, t)$ a suitable bounded function on $\overline{B_r(0)} \times [0, +\infty)$.

[k_R is a positive control parameter]

$$\hat{R}_s = \xi_s - \frac{k_R}{2}\left(i_{sa}^2 + i_{sb}^2\right),$$
$$\dot{\xi}_s = -\frac{k_R}{\sigma}\left(i_{sa}^2 + i_{sb}^2\right)\hat{R}_s + \frac{k_R}{\sigma}\left(v_{sa}i_{sa} + v_{sb}i_{sb}\right),$$

with a resulting stator resistance estimation error dynamics of the form

$$\dot{\tilde{R}}_s = -\frac{k_R}{\sigma}\left(i_{sa}^2 + i_{sb}^2\right)\tilde{R}_s$$
$$= -\frac{k_R}{\sigma}\left(i_{sd}^2 + i_{sq}^2\right)\tilde{R}_s.$$

Define

$$y_*(t) = h(\tilde{R}_s(t), t),$$

so that we can write for $\tilde{R}_s \in \overline{B_r(0)}$

$$\begin{aligned}\dot{y}_*(t) &= g_t(\tilde{R}_s(t), t) + g_R(\tilde{R}_s(t), t)\dot{\tilde{R}}_s(t)\\ &= Q_1(h(\tilde{R}_s(t), t), t) + Q_2(h(\tilde{R}_s(t), t), t)\tilde{R}_s(t) + g_R(\tilde{R}_s(t), t)\dot{\tilde{R}}_s(t)\\ &= A_y(t)y_*(t) + B_y(y_*(t), t)y_*(t) + A_R(t)\tilde{R}_s(t) + B_R(y_*(t), t)\tilde{R}_s(t)\\ &\quad +\varepsilon_R g_R(\tilde{R}_s(t), t)[A_{za}(y(t), t)B_{za}(y(t), t)\\ &\quad +A_{zb}(y(t), t)B_{zb}(y(t), t)]p(y(t)),\end{aligned}$$

with

$$g_t(\tilde{R}_s, t) = \frac{\partial h(\tilde{R}_s, t)}{\partial t},$$
$$g_R(\tilde{R}_s, t) = \frac{\partial h(\tilde{R}_s, t)}{\partial \tilde{R}_s}.$$

Introduce the tracking error

$$\begin{aligned}\xi(t) &= y(t) - y_*(t) = y(t) - h(\tilde{R}_s(t), t)\\ &= [\xi_{\tilde{\omega}_m}(t), \xi_{\tilde{\phi}_{rd}}(t), \xi_{\tilde{\phi}_{rq}}(t), \xi_{e_d}(t), \xi_{e_q}(t), \xi_{e_1}(t),\\ &\quad \xi_{e_2}(t), \xi_{e_3}(t), \xi_{\tilde{i}_{sd}}(t), \xi_{\tilde{z}_a}(t), \xi_{\tilde{z}_b}(t), \xi_{\tilde{\alpha}}(t)]^T,\end{aligned}$$

so that we have for $\tilde{R}_s \in \overline{B_r(0)}$

$$\begin{aligned}\dot{\xi}(t) = {} & A_y(t)\xi(t) + B_y(y(t), t)y(t) - B_y(y_*(t), t)y_*(t) \\ & + B_R(y(t), t)\tilde{R}_s(t) - B_R(y_*(t), t)\tilde{R}_s(t) \\ & - \varepsilon_R g_R(\tilde{R}_s(t), t)[A_{za}(y(t), t)B_{za}(y(t), t) \\ & + A_{zb}(y(t), t)B_{zb}(y(t), t)]h_{\tilde{i}_{sd}}(\tilde{R}_s(t), t) \\ & - \varepsilon_R g_R(\tilde{R}_s(t), t)[A_{za}(y(t), t)B_{za}(y(t), t) \\ & - A_{zb}(y(t), t)B_{zb}(y(t), t)]\xi_{\tilde{i}_{sd}}(t). \end{aligned} \tag{9.15}$$

We will show that the origin of the closed-loop error system with state variables (ξ and $\tilde{R}_s$) is locally exponentially stable provided that the design parameter ε_R is chosen sufficiently small: exponential convergence to zero of $\tilde{R}_s(t)$ will guarantee exponential convergence to zero of $y_*(t)$ (and therefore of $y(t)$). To this purpose, from equation (9.11) we write for $\tilde{R}_s \in \overline{B_r(0)}$

$$\begin{aligned} f_a(\tilde{R}_s(t), t) = {} & p_a(y_*(t), t) - A_{za}(y(t), t)\tilde{R}_s(t) - B_{za}(y(t), t)p(y_*(t)) \\ & - [A_{za}(y_*(t), t) - A_{za}(y(t), t)]\tilde{R}_s(t) \\ & - [B_{za}(y_*(t), t) - B_{za}(y(t), t)]p(y_*(t)), \\ f_b(\tilde{R}_s(t), t) = {} & p_b(y_*(t), t) - A_{zb}(y(t), t)\tilde{R}_s(t) - B_{zb}(y(t), t)p(y_*(t)) \\ & - [A_{zb}(y_*(t), t) - A_{zb}(y(t), t)]\tilde{R}_s(t) \\ & - [B_{zb}(y_*(t), t) - B_{zb}(y(t), t)]p(y_*(t)), \end{aligned}$$

so that

$$\begin{aligned} m_a(y(t), y_*(t), t) = {} & -A_{za}(y(t), t)\tilde{R}_s(t) - f_a(\tilde{R}_s(t), t) \\ & + p_a(y_*(t), t) - [A_{za}(y_*(t), t) - A_{za}(y(t), t)]\tilde{R}_s(t) \\ & - [B_{za}(y_*(t), t) - B_{za}(y(t), t)]p(y_*(t)) \\ \doteq {} & -A_{za}(y(t), t)\tilde{R}_s(t) - f_a(\tilde{R}_s(t), t) + N_a(y(t), y_*(t), t), \\ m_b(y(t), y_*(t), t) = {} & -A_{zb}(y(t), t)\tilde{R}_s(t) - f_b(\tilde{R}_s(t), t) \\ & + p_b(y_*(t), t) - [A_{zb}(y_*(t), t) - A_{zb}(y(t), t)]\tilde{R}_s(t) \\ & - [B_{zb}(y_*(t), t) - B_{zb}(y(t), t)]p(y_*(t)) \\ \doteq {} & -A_{zb}(y(t), t)\tilde{R}_s(t) - f_b(\tilde{R}_s(t), t) + N_b(y(t), y_*(t), t), \end{aligned} \tag{9.16}$$

with

$$\begin{aligned} m_a(y(t), y_*(t), t) = {} & B_{za}(y(t), t)p(y_*(t)), \\ m_b(y(t), y_*(t), t) = {} & B_{zb}(y(t), t)p(y_*(t)). \end{aligned}$$

The stator resistance estimation error dynamics can be rewritten as ($\tilde{R}_s \in \overline{B_r(0)}$)

$$\begin{aligned}\dot{\tilde{R}}_s(t) = \varepsilon_R[&A_{za}(y(t),t)B_{za}(y(t),t)\\ &+A_{zb}(y(t),t)B_{zb}(y(t),t)]p(y_*(t))\\ &+\varepsilon_R[A_{za}(y(t),t)B_{za}(y(t),t)\\ &+A_{zb}(y(t),t)B_{zb}(y(t),t)]\xi_{\tilde{i}_{sd}}(t),\end{aligned}$$

since, by definition, $p(y_*(t)) = h_{\tilde{i}_{sd}}(\tilde{R}_s(t),t)$ and $\xi_{\tilde{i}_{sd}}(t) = \tilde{i}_{sd}(t) - h_{\tilde{i}_{sd}}(\tilde{R}_s(t),t)$. Thus we have ($\tilde{R}_s \in \overline{B_r(0)}$)

$$\begin{aligned}\dot{\tilde{R}}_s(t) = \varepsilon_R[&A_{za}(y(t),t)m_a(y(t),y_*(t),t)\\ &+A_{zb}(y(t),t)m_b(y(t),y_*(t),t)]\\ &+\varepsilon_R[A_{za}(y(t),t)B_{za}(y(t),t)\\ &+A_{zb}(y(t),t)B_{zb}(y(t),t)]\xi_{\tilde{i}_{sd}}(t).\end{aligned} \tag{9.17}$$

Recalling that for $\tilde{R}_s \in \overline{B_r(0)}$ (a_1 and a_2 are suitable positive reals that do not depend on ε_R and t)

$$\begin{aligned}\|y_*\| &\le a_1|\tilde{R}_s|,\\ \|g_R(\tilde{R}_s,t)\| &= \left\|\frac{\partial h(\tilde{R}_s,t)}{\partial \tilde{R}_s}\right\| \le a_2,\\ \|y\| &\le \|y_*\| + \|\xi\|,\end{aligned} \tag{9.18}$$

on the basis of the quadratic function

$$V(\xi,\tilde{R}_s,t) = V_\zeta(\xi,t) + \frac{\tilde{R}_s^2}{2}$$

and its time derivative along the trajectories of the closed-loop system we can establish, according to $\mathcal{B}$, that the origin of the closed-loop error system (recall equations (9.12), (9.13), (9.14), (9.15), (9.16), (9.17), and (9.18)) with state variables (ξ and $\tilde{R}_s$) is locally exponentially stable[2] provided that a sufficiently small design parameter ε_R is chosen. Since exponential convergence to zero of $\tilde{R}_s(t)$ implies exponential convergence to zero of $y_*(t)$, we can establish that $y(t)$ converges exponentially to zero. Therefore exponential convergence to zero of all tracking and estimation errors is achieved[3].

[2]Due to the conservative nature of the Lyapunov analysis, the computable attraction domain of the origin of the closed-loop error system may be much smaller than the effective one and, in any case, its determination depends on the knowledge of the positive real c_R appearing in $\mathcal{B}$.

[3]Note that, since the origin of the closed-loop error system is locally exponentially stable, sufficiently small initial tracking and estimation errors guarantee that $\tilde{R}_s(t) \in \overline{B_r(0)}$ for all $t \ge 0$.

Remark 9.3.3 *The conditions $\mathcal{A}$ and $\mathcal{B}$ required by the above control design can be interpreted as follows. Assume that: (1) the motor is controlled, under persistency of excitation (9.10), by the algorithm proposed in Marino et al. (2008), which is not adaptive with respect to the stator resistance; (2) the stator resistance is slightly different from its nominal value used by the controller so that a sufficiently small stator resistance estimation error $\tilde{R}_s$ appears. A sufficient condition for successfully applying the above estimation and tracking control design is the existence, for any $\tilde{R}_s$ in a sufficiently small compact set (containing the origin), of a steady-state solution $h(\tilde{R}_s, t)$ to the closed-loop error system with the suitable measurable component s_π from which $\tilde{R}_s$ can be in first approximation identified (in the sense of $\mathcal{B}$). The gist of the control and estimation design can be alternatively explained in the following simplified terms: if the controller in Marino et al. (2008) is used with a constant value of the stator resistance, which is slightly different from its actual value, then a steady-state solution appears that causes the output function s_π to be, in first approximation, monotone with respect to the R_s-estimation error $\tilde{R}_s$; thus, by adjusting the R_s-estimate $\hat{R}_s$ on the basis of this output function (slowly in order not to deviate too much from the steady-state solution) one can obtain correct estimation of R_s and consequent convergence to zero of all tracking and estimation errors.*

Remark 9.3.4 *The ninth order estimation and tracking control algorithm (9.7), (9.8), and (9.9) contains twelve control parameters $k_\omega, k_e, k, k_i, \lambda_1, \lambda_2, \lambda_3, \gamma_1, \gamma_2, \varepsilon_\alpha, \varepsilon_R$ and ε whose role may be evaluated by examining both the closed loop error equations and the corresponding stability analysis. The parameters $k_\omega, k_e, k_i, (\lambda_1, \lambda_2, \lambda_3)$ directly affect the dynamics of the tracking and estimation errors $\tilde{\omega}_m, (e_d, e_q), \tilde{i}_{sd}, (\tilde{x}_1, \tilde{x}_2, \tilde{x}_3)$, respectively, while the parameter γ_1 determines the influence of the estimation error $\tilde{i}_{sd}$ on the dynamics of the error variables $(\tilde{z}_a, \tilde{z}_b)$; the parameter γ_2^{-1} and ε_R are the adaptation gains for $\hat{\alpha}$ and $\hat{R}_s$, respectively, while the parameters k, ε_α and ε characterize the robustifying terms in v_{sd} and v_{sq}, the projection algorithm* $\mathrm{Proj}[\cdot, \cdot]$, *and the saturation function* $\mathrm{sat}(\cdot)$, *respectively.*

Remark 9.3.5 *As in Marino et al. (2008), the rotor flux modulus reference signal is required to be time varying: if $\|[\dot{\phi}^*(t), \ddot{\omega}_m^*(t)]\| = 0$ for all $t \geq 0$, then all the points $(\tilde{\omega}_m, \tilde{\phi}_{rd}, \tilde{\phi}_{rq}, e_d, e_q, \tilde{x}_1, \tilde{x}_2, \tilde{x}_3, \tilde{i}_{sd}, \tilde{z}_a, \tilde{z}_b, \tilde{\alpha}, \tilde{R}_s) = (-\mathcal{G}\tilde{\alpha}, 0, 0, 0, 0, 0, \frac{\mathcal{G}}{\beta\phi^*}\tilde{\alpha}, 0, 0, 0, 0, \tilde{\alpha}, 0)$, with $\mathcal{G} = \frac{L_r}{\phi^{*2}}(T_L + J\dot{\omega}_m^*)$, are equilibrium points for the closed-loop system so that, when both rotor speed and flux modulus reference signals are constant, local exponential rotor speed tracking may not be guaranteed by the sensorless estimation and tracking control algorithm (9.7), (9.8), and (9.9). This is strictly related to the fact that when rotor speed and (nonzero) flux modulus are constant so that $L_m i_{sa} - \phi_{ra} = -c\phi_{rb}$, $L_m i_{sb} - \phi_{rb} = c\phi_{ra}$ with $c = \frac{T_L L_r}{(\phi_{ra}^2 + \phi_{rb}^2)}$ model (9.1) becomes*

$$
\begin{aligned}
0 &= \mu(\phi_{ra} i_{sb} - \phi_{rb} i_{sa}) - \frac{T_L}{J}, \\
\frac{\mathrm{d}\phi_{ra}}{\mathrm{d}t} &= -\alpha_e \phi_{rb}, \\
\frac{\mathrm{d}\phi_{rb}}{\mathrm{d}t} &= \alpha_e \phi_{ra},
\end{aligned}
$$

$$\frac{\mathrm{d}i_{sa}}{\mathrm{d}t} = -\frac{R_s}{\sigma} i_{sa} + \frac{1}{\sigma} v_{sa} + \beta \alpha_e \phi_{rb},$$
$$\frac{\mathrm{d}i_{sb}}{\mathrm{d}t} = -\frac{R_s}{\sigma} i_{sb} + \frac{1}{\sigma} v_{sb} - \beta \alpha_e \phi_{ra},$$

in which the lumped parameter $\alpha_e = \alpha c + \omega_m$ replaces the separate α and ω_m in (9.1). Recall that necessary conditions for equation (9.10) to be satisfied (see Marino et al. (2008) accordingly are ($\tau \in [t, t + t_p]$): i) $\dot{\varepsilon}_0^*(\tau) \neq 0$, in the case of constant rotor speed reference signal $\omega_m^*(\tau)$; ii) $\dot{\phi}^*(\tau) \neq 0$. A sufficient condition for inequality (9.10) to be satisfied (with $t_p = \frac{2\pi}{|\omega_{0c}|}$) is to choose a time-varying rotor flux modulus reference signal $\phi^*(t)$ and a constant rotor speed reference value ω_m^* such that ($t \geq 0$)

$$\frac{1}{\phi^{*2}(t)} = \phi_c^{*2} + \varepsilon_* \cos\left(\frac{t}{\varepsilon_*}\right),$$
$$0 \neq \omega_{0c} = \omega_m^* + \frac{\alpha L_m T_L \phi_c^{*2}}{\mu J},$$

in which ϕ_c^* is a positive constant and ε_* is a sufficiently small positive real. Note that the smaller the ω_m^* is, the larger t_p results: roughly speaking, the convergence to zero of the tracking and estimation errors is faster at higher speeds.

Remark 9.3.6 *The estimation and tracking control algorithm (9.7), (9.8), and (9.9) for sensorless IMs exhibits the following interesting similarities with the estimation and tracking control algorithm for sensorless permanent-magnet synchronous motors (PMSMs) rigorously derived in Tomei and Verrelli (2011): (1) both estimation and tracking control algorithms are straightforward modifications of the field-oriented controls for IMs and PMSMs, which incorporate closed-loop observers for the unmeasured variables (rotor speed ω_m, rotor fluxes ϕ_{ra} and ϕ_{rb} for IMs—rotor speed ω_m, sine and cosine functions of electrical angle* $\sin(\theta_e)$ *and* $\cos(\theta_e)$ *for PMSMs) and the uncertain parameters (load torque T_L and motor resistances R_r and R_s for IMs—load torque T_L for PMSMs); (2) both estimation and tracking control algorithms use estimates of stator currents (as auxiliary variables) and estimates of advantageous variables whose dynamics do not depend on unmeasured variables and uncertain parameters*[4]*; (3) the closed-loop observers incorporated by both the estimation and tracking control algorithms rely on persistency of excitation conditions, which can be physically interpreted in terms of motor observability and parameter identifiability and only restrict the family of reference signals*[5].

[4]The role played by z_d and z_q for IMs is played by ξ_a and ξ_b for PSMSs where $\xi_a = a\cos(\theta_e) + b i_{sa}$ and $\xi_b = a\cos(\theta_e) + b i_{sb}$ with a, b positive parameters.

[5]The role played by $\dot{\varepsilon}_0^*$ and $\dot{\phi}^*$ for the IMs case is played by ω_m^* for the PMSMs case.

9.4 Nonlinear Estimation and Tracking Control for the Output Feedback Case

The intuitive steps of the estimation and tracking control design presented in the previous section allow for a straightforward simplification when the rotor speed is measured. This leads to a novel output feedback estimation and tracking control algorithm for IMs, which is itself a specific contribution of this chapter.

9.4.1 Estimation and Tracking Control Algorithm

When rotor speed is measured and available for feedback, an estimation and tracking control design similar to the one presented in the previous section leads to the following slight modifications to the adaptive observer (9.9) ($\lambda_1 \neq \lambda_2$):

$$
\begin{aligned}
\dot{\hat{\omega}}_m &= \mu\phi^* i_{sq} + (\lambda_1+\lambda_2)(\omega_m - \hat{\omega}_m) - \frac{T_{Ln}}{J} - \frac{\hat{\theta}}{J} \\
&\quad + \frac{1}{\phi^*}\Big[\frac{T_{Ln}}{J} + \frac{\mathrm{sat}(\hat{\theta})}{J} + \dot{\omega}_m^*\Big][\hat{\phi}_{rd} - \phi^*] - \mu\Big[\frac{\phi^*}{L_m} + \frac{\dot{\phi}^*}{\hat{\alpha}L_m}\Big]\hat{\phi}_{rq}, \\
\dot{\hat{\theta}} &= -J\lambda_1\lambda_2(\omega_m - \hat{\omega}_m), \\
\dot{\hat{i}}_{sq} &= -\Big(\frac{\hat{R}_s}{\sigma} + \beta\hat{\alpha}L_m\Big)i_{sq} + \frac{1}{\sigma}v_{sq} - \omega_0 i_{sd} - \beta\omega_m\phi^* \\
&\quad + k_i(i_{sq} - \hat{i}_{sq}) - \beta[\omega_m^*(\hat{\phi}_{rd} - \phi^*) - \hat{\alpha}\hat{\phi}_{rq}], \\
\dot{\hat{z}}_d &= -\frac{\hat{R}_s}{\sigma}i_{sd} + \frac{1}{\sigma}v_{sd} + \omega_0\hat{z}_q + \frac{\hat{\alpha}}{\gamma_1}(i_{sd} - \hat{i}_{sd}) - \frac{\omega_m^*}{\gamma_1}(i_{sq} - \hat{i}_{sq}), \\
\dot{\hat{z}}_q &= -\frac{\hat{R}_s}{\sigma}i_{sq} + \frac{1}{\sigma}v_{sq} - \omega_0\hat{z}_d + \frac{\omega_m^*}{\gamma_1}(i_{sd} - \hat{i}_{sd}) + \frac{\hat{\alpha}}{\gamma_1}(i_{sq} - \hat{i}_{sq}), \\
\dot{\hat{\alpha}} &= \mathrm{Proj}\Big[-\frac{\beta}{\gamma_2}\Big[\frac{\dot{\phi}^*}{\hat{\alpha}}(i_{sd} - \hat{i}_{sd}) + L_m i_{sq}^*(i_{sq} - \hat{i}_{sq})\Big], \hat{\alpha}\Big], \\
\hat{\alpha}(0) &\in [\alpha_m, \alpha_M], \quad 0 < \alpha_m - \varepsilon_\alpha, \\
\dot{\hat{R}}_s &= -\varepsilon_R\Big[\frac{(\omega_m^* i_{sq} + \hat{\alpha} i_{sd})}{\sigma\gamma_1}(i_{sd} - \hat{i}_{sd}) + \frac{(-\omega_m^* i_{sd} + \hat{\alpha} i_{sq})}{\sigma\gamma_1}(i_{sq} - \hat{i}_{sq})\Big], \\
\hat{R}_s(0) &\in [R_{sm}, R_{sM}].
\end{aligned}
\tag{9.19}
$$

9.4.2 Stability Proof

Local exponential rotor speed and flux modulus tracking along with uncertain parameters estimation can be proved by using arguments similar to those used in the previous section. This simplified algorithm (locally) extends the result presented in Marino *et al.* (1999) to

the case of uncertain stator resistance[6], while providing, in contrast to Jadot *et al.* (2009), the following, a priori verifiable, persistency of excitation conditions depending on reference signals only:

$\mathcal{P}$) there exist two positive reals t_p and k_p such that

$$\int_t^{t+t_p} \bar{\Gamma}^T(\tau)\bar{\Gamma}(\tau)d\tau \geq k_p I_3, \quad \forall\, t \geq 0 \tag{9.20}$$

holds with

$$\bar{\Gamma}(t) = \begin{bmatrix} l_{11}(t), l_{12}(t), -\frac{\beta\dot{\phi}^*(t)}{\alpha} \\ -l_{12}(t), l_{11}(t), -\beta L_m i_{qr}(t) \end{bmatrix},$$
$$l_{11}(t) = \alpha\cos\varepsilon_0^*(t) - \omega_m^*(t)\sin\varepsilon_0^*(t)$$
$$l_{12}(t) = \alpha\sin\varepsilon_0^*(t) + \omega_m^*(t)\cos\varepsilon_0^*(t).$$

In particular, in contrast to the sensorless case, constant rotor speed and flux modulus references and nonzero load torques suffice to satisfy equation (9.20) (with $t_p = \frac{2\pi}{|\varepsilon_0^*|}$). On the other hand, equation (9.20) cannot be satisfied when rotor speed and flux modulus reference signals are constant and the load torque is zero: when rotor speed and flux modulus are constant and the load torque is zero (so that no rotor currents are induced), the rotor resistance is not identifiable from rotor speed and stator current measurements.

Remark 9.4.1 *Even though the structure of both estimation and tracking control algorithms (sensorless case and output feedback case) is similar*[7]*, the observation and adaptation strategies are substantially different: while in the sensorless case the information about* (ω_m, T_L) *and* $(\phi_{rd}, \phi_{rq}, \alpha)$ *is taken from* i_{sq} *and* i_{sd} *respectively, in the output feedback case the information about* T_L *is directly extracted from* ω_m *and the remaining information about* $(\phi_{rd}, \phi_{rq}, \alpha)$ *is taken from* (i_{sd}, i_{sq})*.*

9.5 Simulation Results

We perform simulations for the two controllers designed in the previous sections. The aim is to confirm the analytical results presented in the chapter while enlightening the reader about the theoretical role of the speed sensor in the considered scenario. The simulations are carried out with reference to the three-phase single pole pair 0.6 kW IM (OEMER 7-80/C), whose model has been experimentally validated in Marino *et al.* (2010) and whose parameters are: $J = 0.0075\,\text{Kgm}^2$, $R_s = 5.3\,\Omega$, $R_r = 3.3\,\Omega$, $L_s = 0.365\,\text{H}$, $L_r = 0.375\,\text{H}$, and $L_m = 0.34\,\text{H}$

[6]Note that the simplified controller is apparently much simpler than the one presented in Marino *et al.* (1999) and it exhibits definite implementation advantages.

[7]Note that, even though the measured speed ω_m is available, no modification of i_{sq}^* and ω_0, as well as of v_{sd} and v_{sq}, is introduced: from a practical point of view, this allows the filtered estimate $\hat{\omega}_m$ to appear in crucial parts of the controller instead of the possibly noisy signal ω_m.

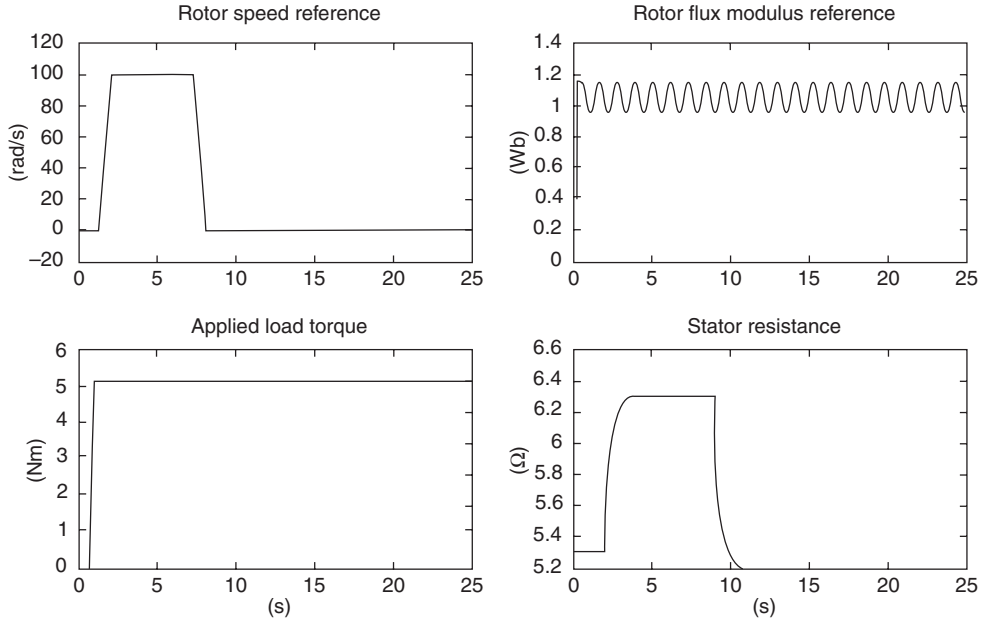

Figure 9.1 Sensorless case: rotor speed and flux modulus reference signals, applied load torque, and stator resistance

(see Section 1.8 of Marino *et al.* (2010) for the complete set of data provided by the manufacturer). All initial conditions of the motor and of the estimation and tracking control algorithms are set to zero except for $\phi_{ra}(0) = 0.1$ Wb, $\hat{\alpha}(0) = 11.1\ \text{s}^{-1}$ (the value of the parameter α is $8.8\ \text{s}^{-1}$), and $\hat{R}_s(0) = 5.39\,\Omega$.

9.5.1 Sensorless Case

We test the sensorless estimation and tracking control algorithm (9.7), (9.8), and (9.9) by simulation with parameters (the values are in SI units) $k_\omega = 120$, $k_e = 900$, $k = 0.01$, $k_i = 900$, $\lambda_1 = 120$, $\lambda_2 = 150$, $\lambda_3 = 180$, $\gamma_1 = 120^{-1}$, $\gamma_2 = 900^{-1}$, $\alpha_m = 4.5$, $\alpha_M = 13.5$, $\varepsilon_\alpha = 0.9$, and $\varepsilon_R = 0.001$. The references for rotor speed and flux modulus along with the applied torque and the stator resistance are reported in Figure 9.1. The rotor flux modulus reference is time varying according to the persistency of excitation condition (9.10). The rotor speed reference goes from 0 to 100 rad/s and back to zero, which is a critical theoretical situation for stator resistance uncertainty. The stator resistance increases its nominal value from $5.3\,\Omega$ to $6.3\,\Omega$ as rotor speed increases and then decreases to $5.2\,\Omega$ as rotor speed decreases. The load torque T_L (5.104 Nm) is applied at $t = 0.9$ s (before that the rotor speed reference signal grows up to the value 100 rad/s); the uncertainty θ is -12% of the load torque nominal value T_{Ln}. Figures 9.2 and 9.3 show the time histories of the rotor speed and flux modulus and the corresponding tracking errors, Figures 9.4, 9.5, and 9.6 show the convergence to zero of the uncertain parameters estimation errors, while the a and b components of the stator voltage

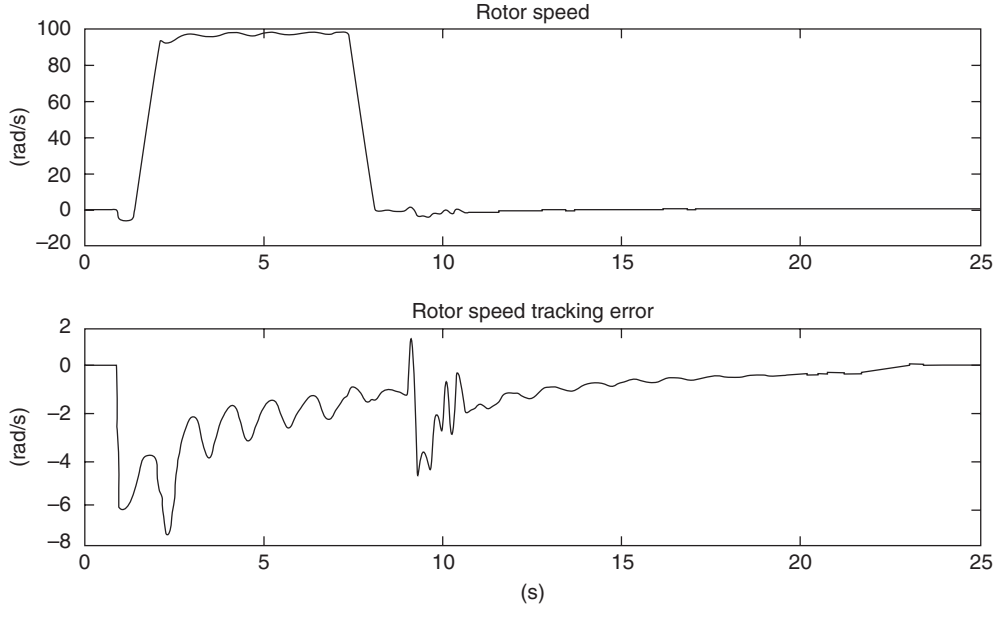

Figure 9.2 Sensorless case: rotor speed and corresponding tracking error

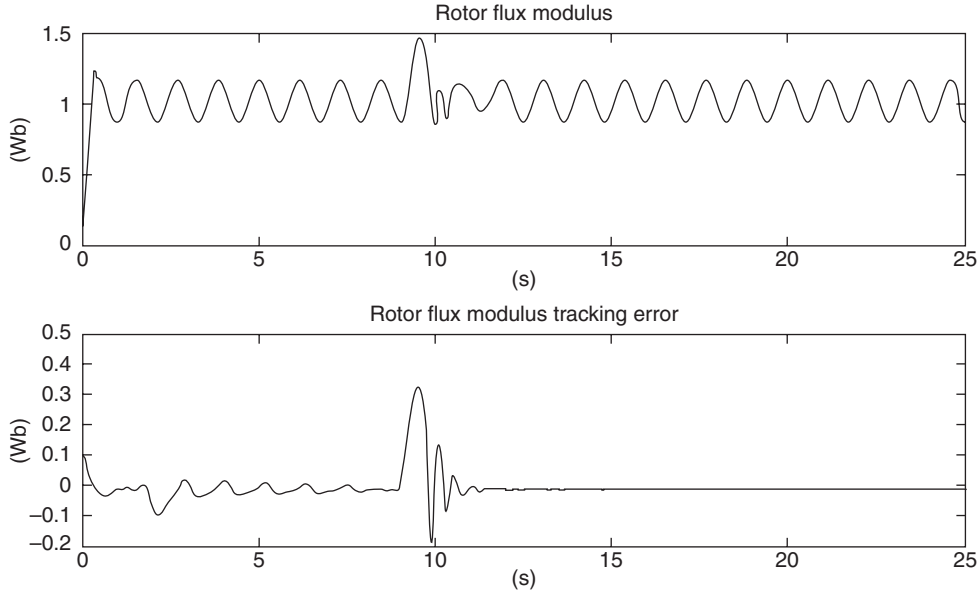

Figure 9.3 Sensorless case: rotor flux modulus and corresponding tracking error

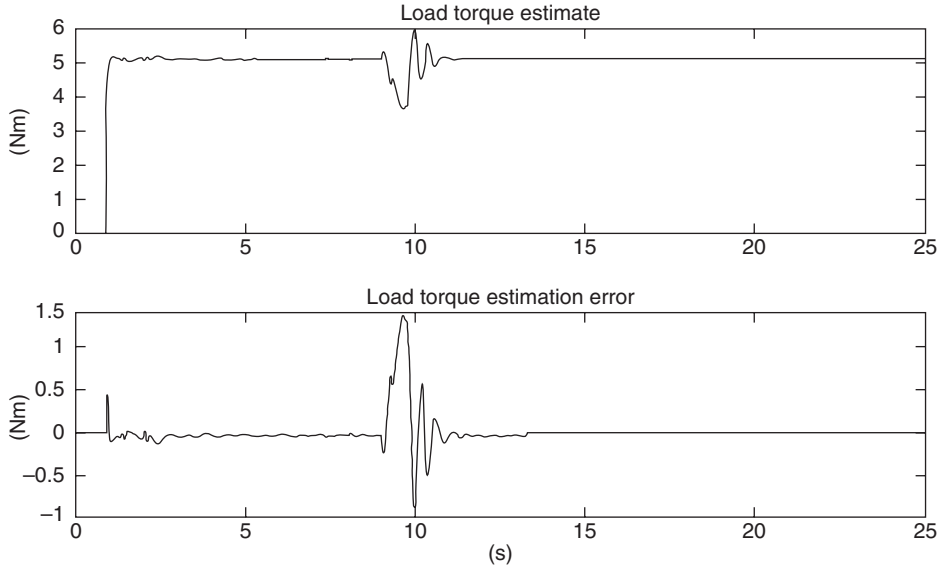

Figure 9.4 Sensorless case: load torque estimate and estimation error

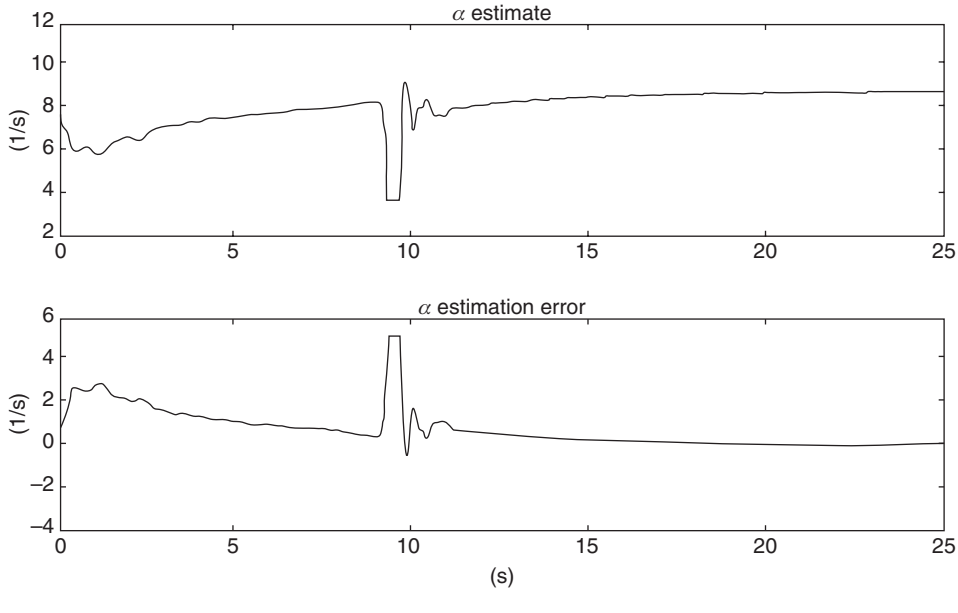

Figure 9.5 Sensorless case: α estimate and estimation error

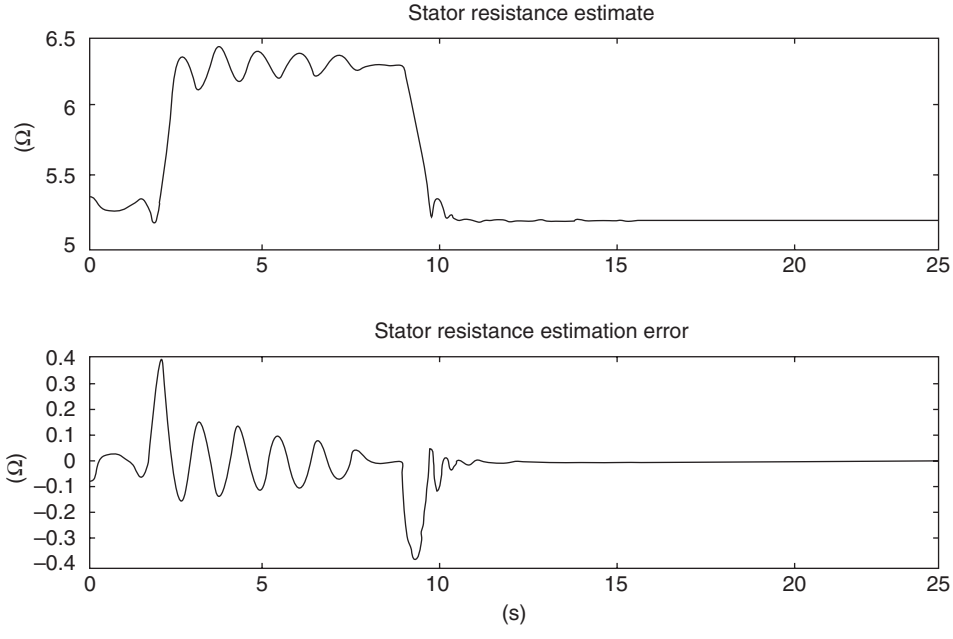

Figure 9.6 Sensorless case: stator resistance estimate and estimation error

vector are reported in Figure 9.7. Rather satisfactory dynamic performances, in the presence of parameter uncertainties, are achieved by only measuring the stator currents.

9.5.2 Output Feedback Case

We test the output feedback control by simulation with the same control parameter values (λ_3 is not needed here). Since no constraint concerning the time-varying nature of the rotor flux modulus reference is required, we are able to illustrate the benefits of choosing a definitely constant rotor flux modulus reference signal that asymptotically minimizes the power losses depending on the uncertain parameters estimates. The references for rotor speed and flux modulus along with the applied torque and the stator resistance are reported in Figure 9.8. The first and the last two profiles are the same of the previous subsection (rotor speed reference signal, load torque[8], and stator resistance), while the availability of estimates for the critical uncertain parameters T_L, R_s, and α involved in the expression of the rotor flux modulus

$$\phi_{pl}^{*}(T_L, R_s, \alpha) = \sqrt[4]{\left(\frac{L_m^2 L_r \alpha}{R_s} + L_r^2\right) T_L^2}, \tag{9.21}$$

minimizing the power losses at steady state (see, Vedagarbha *et al.* 1997), allows for online adjustment of the rotor flux modulus reference. In particular, after a flux excitation phase (of

[8] As in the previous subsection the uncertainty θ is -12% of the load torque nominal value T_{Ln}.

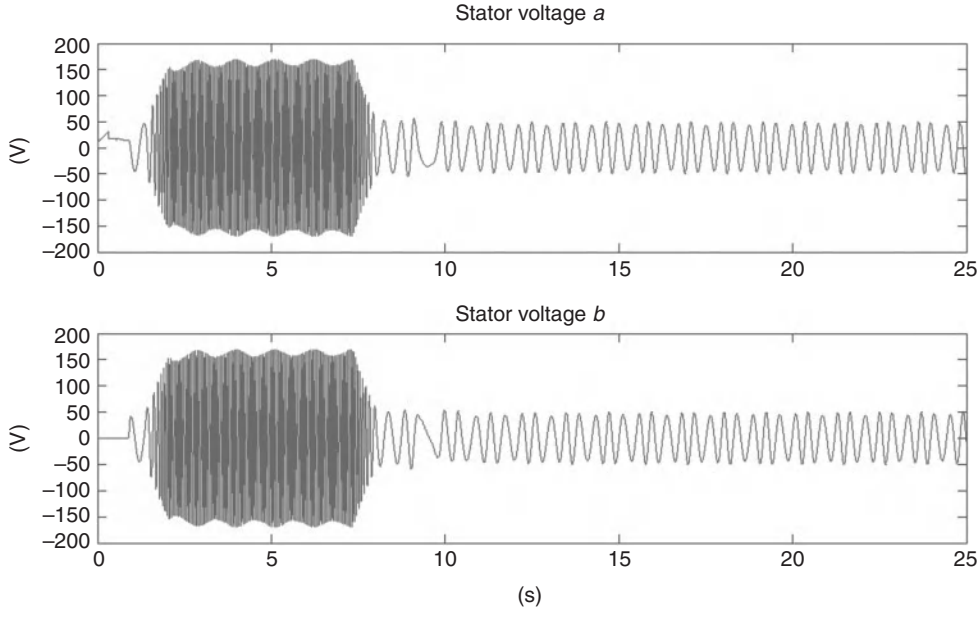

Figure 9.7 Sensorless case: stator voltage vector (a, b) components

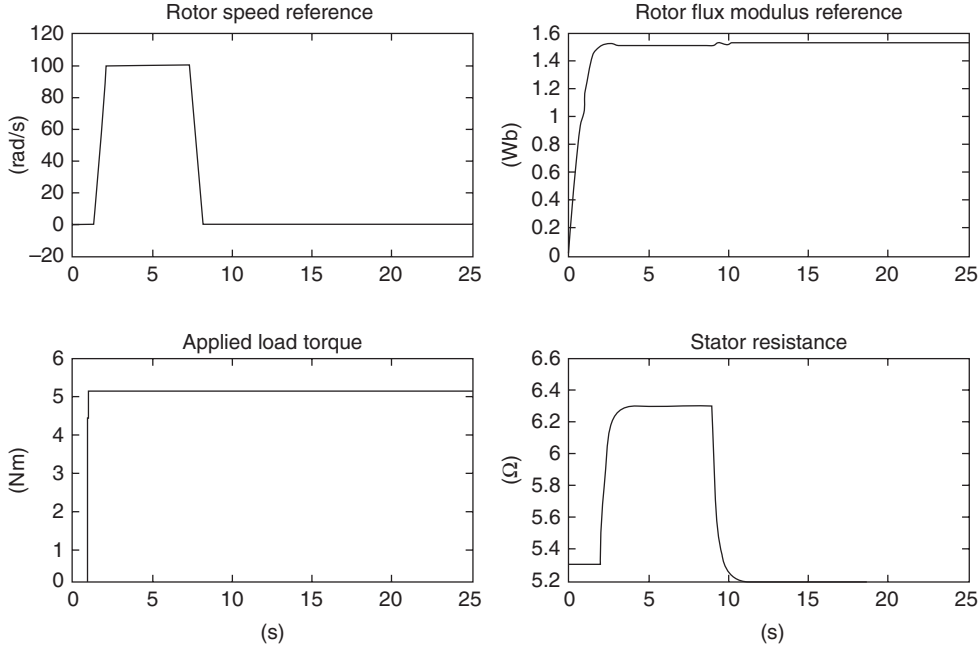

Figure 9.8 Output feedback case: rotor speed and flux modulus reference signals, applied load torque and stator resistance

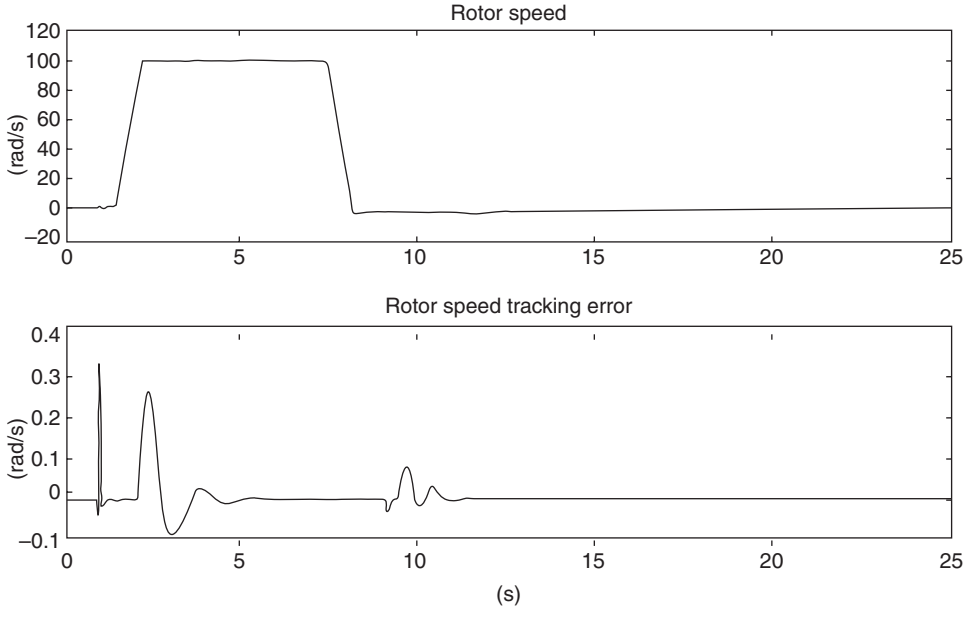

Figure 9.9 Output feedback case: rotor speed and corresponding tracking error

about 1 s), the rotor flux modulus reference is chosen as the output of a unitary gain third order filter with input $\phi^*_{pl}(q_1, q_2, q_3)$, which depends on the saturated estimates (provided by the adaptive controller)

$$
\begin{aligned}
q_1 &= \mathrm{sat}_{(\mathrm{T_{Ln}}-\theta_{\mathrm{m}},\mathrm{T_{Ln}}+\theta_{\mathrm{m}})}(\hat{T}_L),\\
q_2 &= \mathrm{sat}_{(R_{sm},R_{sM})}(\hat{R}_s),\\
q_3 &= \mathrm{sat}_{(\alpha_m,\alpha_M)}(\hat{\alpha}),
\end{aligned}
$$

of the uncertain load torque, stator resistance, and parameter α. The saturation function $\mathrm{sat}_{(l_1,l_2)}(x)$ is a continuous odd function, which is linear in the closed set $[l_1, l_2]$ and satisfies $\mathrm{sat}_{(l_1,l_2)}(x) = l_1$ for all $x \leq l_1$ and $\mathrm{sat}_{(l_1,l_2)}(x) = l_2$ for all $x \geq l_2$. Figures 9.9 and 9.10 show the time histories of the rotor speed and flux modulus and the corresponding tracking errors, Figures 9.11, 9.12, and 9.13 show the convergence to zero of the uncertain parameters estimation errors, while the absorbed power and the power losses are reported in Figure 9.14. Satisfactory dynamic performances are achieved in the presence of parameter uncertainties, while stator currents and voltages are within physical limits: transient tracking and estimation behaviors are, as expected, largely improved when the rotor speed signal is available for feedback (compare Figures 9.9 and 9.10 with Figures 9.2 and 9.3).

Finally, the same simulation is performed by maintaining the nominal value (1.16 Wb) of the rotor flux modulus reference[9] instead of suitably adjusting it via the converging estimates of

[9]Note that 1.16 Wb is the value to which a sinusoidal component has been previously added in order to obtain rotor resistance identifiability.

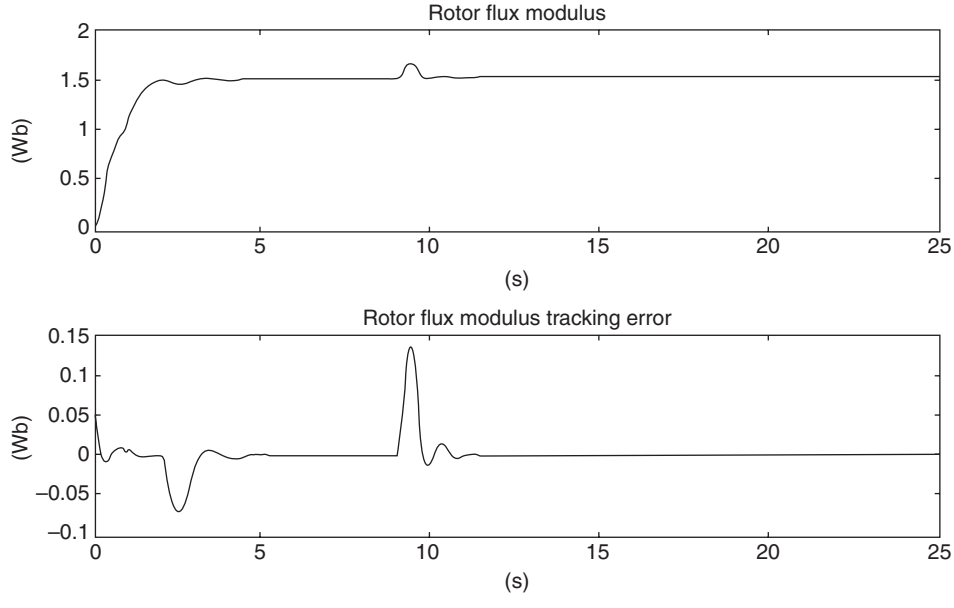

Figure 9.10 Output feedback case: rotor flux modulus and corresponding tracking error

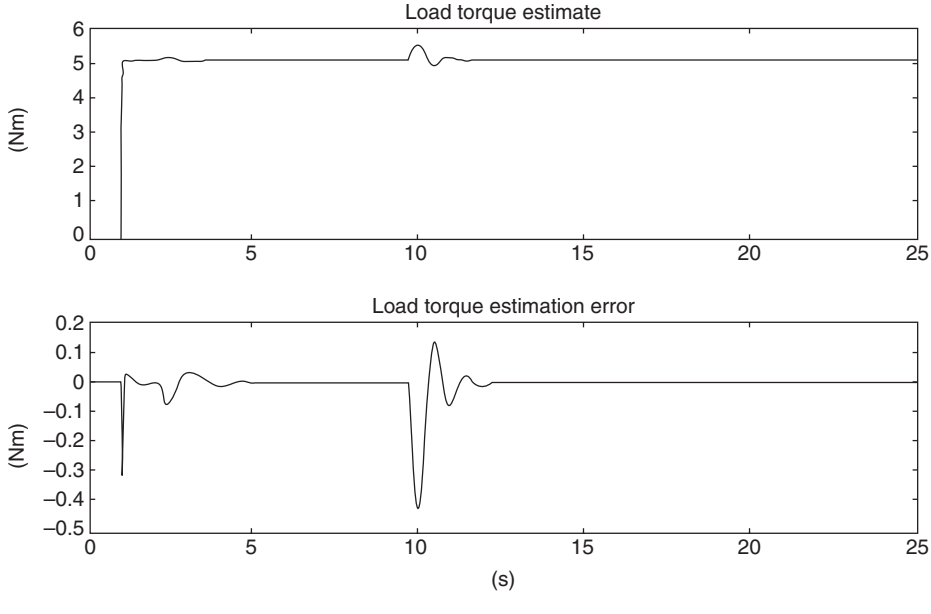

Figure 9.11 Output feedback case: load torque estimate and estimation error

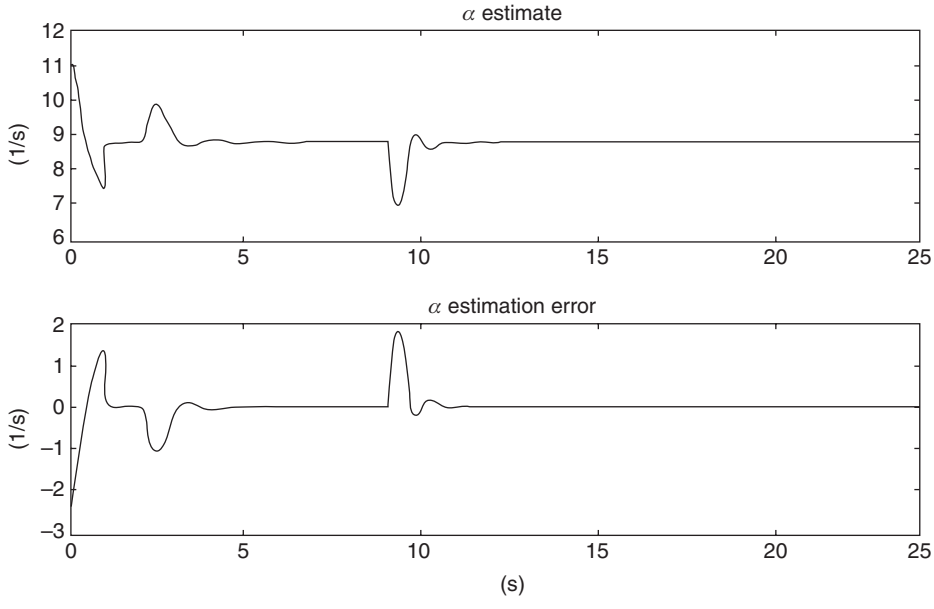

Figure 9.12 Output feedback case: α estimate and estimation error

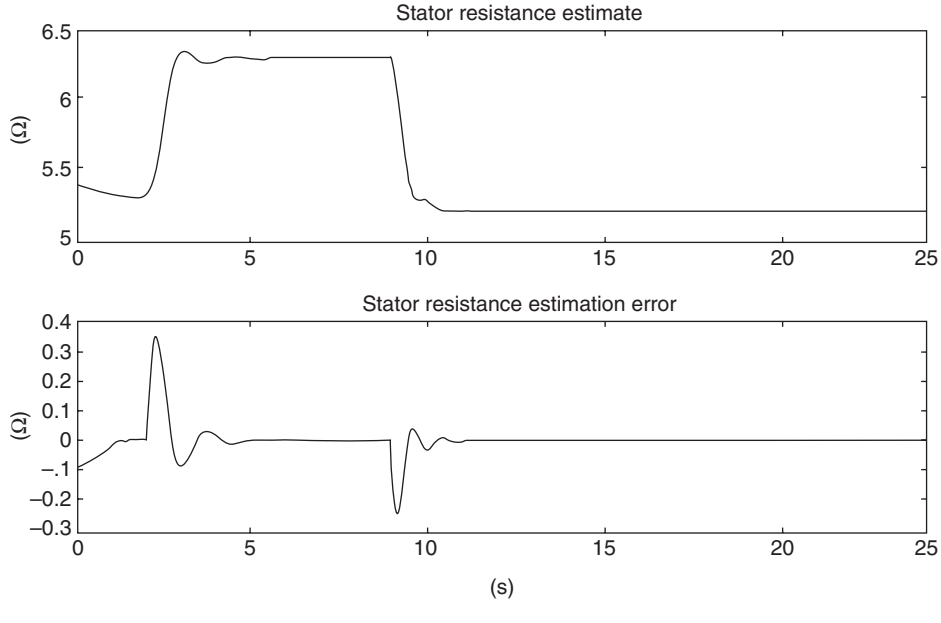

Figure 9.13 Output feedback case: stator resistance estimate and estimation error

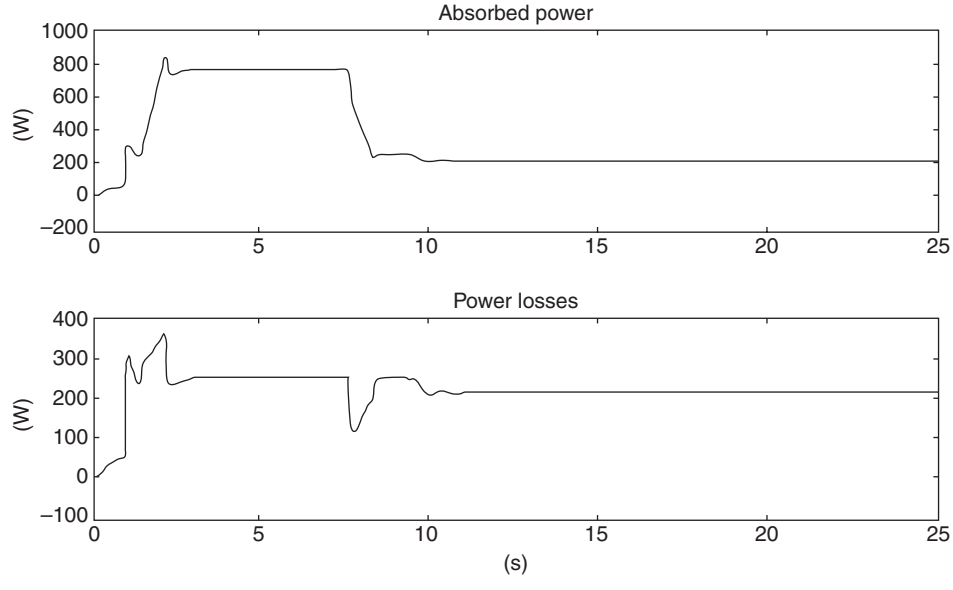

Figure 9.14 Output feedback case: absorbed power and power losses

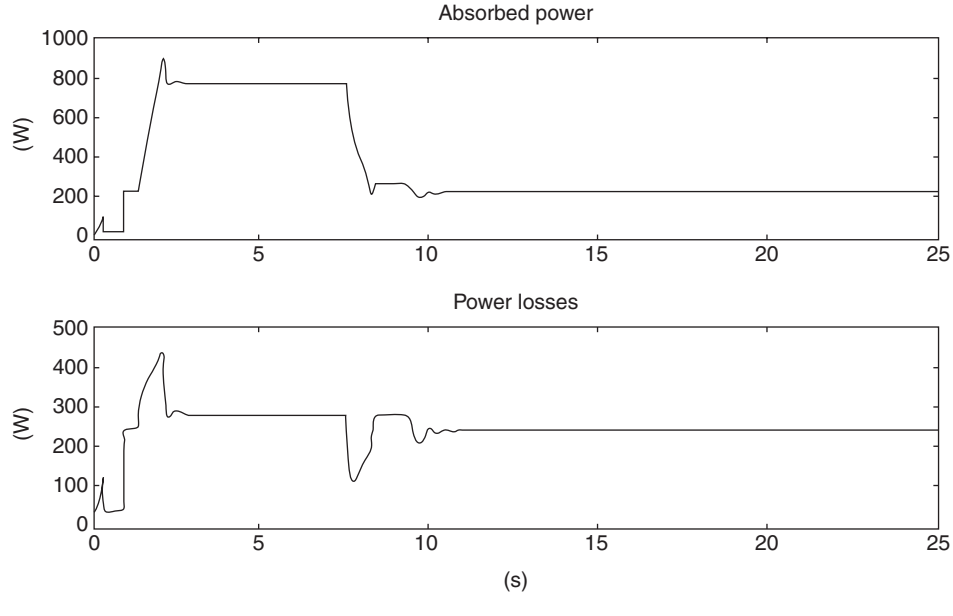

Figure 9.15 Output feedback case (control with nominal flux reference): absorbed power and power losses

the uncertain parameters: Figure 9.15 (recall Figure 9.14) apparently illustrates the corresponding benefits, since an increase of the absorbed power results.

9.6 Conclusions

In this chapter, the existence of solutions to both the sensorless and output feedback estimation and tracking problems for sensorless IMs (9.1) with uncertain load torque and resistances has been demonstrated. Exponential rotor speed and flux modulus tracking is guaranteed along with unmeasured states and uncertain parameters estimation provided that persistency of excitation conditions restricting the reference signals ω_m^* and ϕ^* are satisfied along with conditions for the identifiability in first approximation of the stator resistance at steady state. Specific contributions of the chapter are: (1) a proof for the the exponential estimation of both rotor and stator resistances in the presence of uncertain load torque for IMs with no speed sensors; (2) a novel estimation and tracking control algorithm when the rotor speed is measured; (3) a clear interpretation, in terms of parameter identifiability and power loss minimization, of the theoretical potentialities of feeding back speed measurements in the presented scenario of uncertain load torque and motor resistances.

References

Arnold VI (1992) *Ordinary Differential Equations*. Springer, Berlin.

Behal A, Feemster M, and Dawson DM (2003) An improved indirect field-oriented controller for the induction motor. *IEEE Transactions on Control Systems Technology*, **11**, 248–252.

Blaschke F (1972) The principle of field orientation applied to the new transvector closed-loop control system for rotating field machines. *Siemens-Review*, **39**, 217–220.

Fattah HAA and Loparo KA (2001) Speed control of electrical machines: unknown load torque case. *IEEE Transactions on Automatic Control*, **46**, 1979–1983.

Feemster M, Vedagarbha P, Haste D, and Dawson DM (2000) Adaptive output-feedback control of induction motors. *International Journal of Systems Science*, **31**, 1195–1208.

Ha IJ and Lee SH (2000) An online identification method for both stator and rotor resistances of induction motors without rotational transducers. *IEEE Transactions on Industrial Electronics*, **47**, 842–853.

Hinkkanen M, Harnefors L, and Luomi J (2010) Reduced-order flux observers with stator-resistance adaptation for speed-sensorless induction motor drives. *IEEE Transactions on Power Electronics*, **25**, 1173–1183.

Jadot F, Moreno-Valenzuela, J, and Sepulchre R (2009) Adaptive regulation of vector-controlled induction motors. *IEEE Transactions on Control Systems Technology*, **17**, 646–657.

Karagiannis D, Astolfi A, Ortega R, and Hilairet M (2009) A nonlinear tracking controller for voltage-fed induction motors with uncertain load torque. *IEEE Transactions on Control Systems Technology*, **17**, 608–619.

Karanayil B, Rahman MF, and Grantham C (2007) Online stator and rotor resistance estimation scheme using artificial neural networks for vector controlled speed sensorless induction motor drive. *IEEE Transactions on Industrial Electronics*, **54**, 167–176.

Khalil HK (1996) *Nonlinear Systems*. Prentice-Hall, Upper Saddle River, NJ.

Khalil HK, Strangas EG, and Jurkovic S (2009) Speed observer and reduced nonlinear model for sensorless control of induction motors. *IEEE Transactions on Control Systems Technology*, **17**, 327–339.

Krause PC (1986) *Analysis of Electric Machinery*. McGraw-Hill, New York.

Leonhard W (2001) *Control of Electrical Drives*. Springer-Verlag, Berlin.

Lin YC, Fu LC, and Tsai CY (2000) Non-linear sensorless indirect adaptive speed control of induction motor with unknown rotor resistance and load. *International Journal of Adaptive Control and Signal Processing*, **14**, 109–140.

Marino R, Peresada S, and Tomei P (1999) Global adaptive output feedback control of induction motors with uncertain rotor resistance. *IEEE Transactions on Automatic Control*, **44**, 967–983.

Marino R, Tomei P, and Verrelli CM (2004) A global tracking control for speed-sensorless induction motors. *Automatica*, **40**, 1071–1077.

Marino R, Tomei P, and Verrelli CM (2005) A nonlinear tracking control for sensorless induction motors. *Automatica*, **41**, 1071–1077.

Marino R, Tomei P, and Verrelli CM (2008) An adaptive tracking control from current measurements for induction motors with uncertain load torque and rotor resistance. *Automatica*, **44**, 2593–2599.

Marino R, Tomei P, and Verrelli CM (2010) *Induction Motor Control Design*. Springer, London.

Mitronikas ED, Safacas AN, and Tatakis EC (2001) A new stator resistance tuning method for stator-flux-oriented vector-controlled induction motor drive. *IEEE Transactions on Industrial Electronics*, **48**, 1148–1157.

Montanari M, Peresada S, Rossi C, and Tilli A (2007) Speed sensorless control of induction motors based on a reduced-order adaptive observer. *IEEE Transactions on Control Systems Technology*, **15**, 1049–1064.

Montanari M, Peresada S, and Tilli A (2006) A speed-sensorless indirect field-oriented control for induction motors based on high gain speed estimation. *Automatica*, **42**, 1637–1650.

Montanari M and Tilli A (2006) Sensorless control of induction motors based on high-gain speed estimation and online stator resistance adaptation. *32nd IEEE Annual Conference on Industrial Electronics, IECON*, pp. 1263–1268.

Peresada S and Tonielli A (2000) High-performance robust speed-flux tracking controller for induction motor. *International Journal of Adaptive Control and Signal Processing*, **14**, 177–200.

Peresada S, Tonielli A, and Morici R (1999) High-performance indirect field-oriented output-feedback control of induction motors. *Automatica*, **35**, 1033–1047.

Tomei P and Verrelli CM (2011) Observer-based speed tracking control for sensorless permanent magnet synchronous motors with unknown load torque. *IEEE Transactions on Automatic Control*, **56**, 1484–1488.

Traoré D, De Leon J, and Glumineau A (2012) Adaptive interconnected observer-based backstepping control design for sensorless induction motor. *Automatica*, **48**, 682–687.

Vedagarbha P, Dawson DM, and Burg T (1997) Rotor velocity/flux control of induction motors with improved efficiency. *Mechatronics*, **7**, 105–127.

Zaky MS (2012) Stability analysis of speed and stator resistance estimators for sensorless induction motor drives. *IEEE Transactions on Industrial Electronics*, **59**, 858–870.

10

Nonlinear Control for Speed Regulation of Induction Motor with Optimal Energetic Efficiency

Abderrahim El Fadili[1], Abdelmounime El Magri[1], Hamid Ouadi[2], and Fouad Giri[1]
[1]*GREYC Lab, University of Caen Basse-Normandie, France*
[2]*FSAC, University of Casablanca, Morocco*

10.1 Introduction

A great deal of interest has been paid to induction machine control over the last years. However, most works have focused on the speed/flux/torque regulation supposing the machine magnetic circuit to be linear. The point is that speed regulation cannot be ensured in optimal efficiency conditions, for a wide range of speed and load torque variations, unless the magnetic circuit nonlinearity is explicitly accounted for in the motor model. Several studies have dealt with speed/flux regulation (with constant flux reference (CFR)) following several control strategies ranging from simple techniques, for example, field-oriented control (Montanan *et al.* 2006; Ouadi and Giri 2002), to more sophisticated nonlinear approaches, e.g. feedback linearization (Abdelaziz and Ghedjati 2007), direct torque control (Jasinski *et al.* 2006; Singh *et al.* 2006), or sliding-mode control (Traore *et al.* 2008). A common point of these works is that the control design relies on a relatively simple model, called standard in Chapter 2. This model assumes a linear representation of the magnetic circuit and this assumption is not true in real-life machines. Accordingly, the control objective concerning the flux is limited, in most available solutions, to regulation around constant values (Figure 10.1). Specifically, the CFR is equal

AC Electric Motors Control: Advanced Design Techniques and Applications, First Edition. Edited by Fouad Giri.

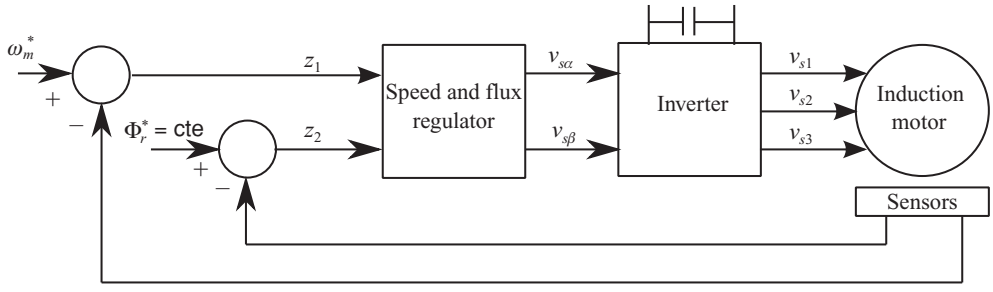

Figure 10.1 Control strategy involving constant flux reference (the controller is obtained from the standard model)

to its nominal value generally located at the elbow of the machine magnetic characteristic (Moreno-Eguilaz and Peracaula 1999; Canudas *et al.* 2000). Doing so, energetic efficiency is only maximal when the machine operates all the time in the neighborhood of its nominal point. But, this is not the case in all practical applications because the machine load is generally varying online or may depend on system states such as position or velocity (Leonard 2001). Indeed, in presence of small loads, the operation point is below the nominal value causing useless energy stored in stator inductances, which reduces the machine efficiency. Also, in the case of overloaded machine, the operation point is placed in the saturation zone of the magnetic characteristic. Then, the standard model is no longer valid and, consequently, the control performances are no longer guaranteed. To overcome the above shortcomings, it is necessary in speed control to let the flux reference be dependent on both the speed reference and load torque, that is, the flux reference must be state-dependent (Figure 10.2). Examples of speed/flux controllers involving state-dependent flux reference have been developed in Novotnak *et al.* (1999), Elfadili *et al.* (2009), Ouadi *et al.* (2010), El Fadili *et al.* (2012). The proposed controllers include flux reference optimizers, the design of which relies on a machine model that takes into account the nonlinearity of the magnetic characteristic.

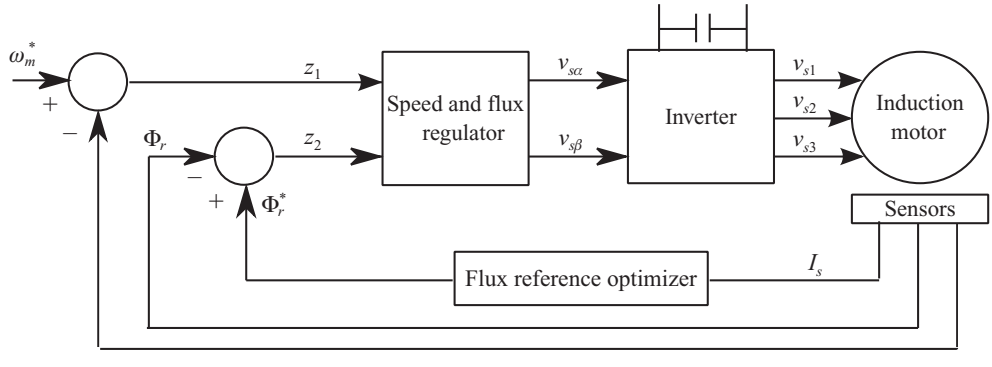

Figure 10.2 Control strategy involving state-dependent optimal flux (SDOF) reference

The control strategy presented in this chapter enjoys the following features:

System modeling: The induction machine is represented by an experimentally validated model that accounts for the nonlinearity of the magnetic characteristic (Ouadi *et al.* 2011).

Control design: A multivariable controller is built up on the basis of the preceding model, using a nonlinear design technique. Specifically, the controller consists of two main components: (1) A nonlinear regulator that makes the motor velocity match its varying reference value and enforces the rotor flux norm track its optimal state-dependent reference. (2) An online flux reference optimizer that provides the preceding speed/flux regulator with the optimal flux reference (OFR) trajectory. Optimality is intended in the sense that the developed motor torque is not oversized, reducing thus the stator current consumption. The flux optimizer design relies on the above motor model and expresses in function of state variables, especially the stator currents.

Control performance analysis: The performances of the whole nonlinear controller are formally analyzed making adequate use of relevant tools from Lyapunov stability.

The chapter is organized as follows: in Section 10.2, the induction motor is modeled taking into account magnetic saturation; the multi-objective controller is designed and analyzed in Section 10.3; the control performances are illustrated through numerical simulations in Section 10.4.

10.2 Induction Motor Modeling with Saturation Effect Inclusion

As mentioned in Section 10.1, the achievement of speed regulation and flux optimization in presence of wide-range load variation necessitates that the control design is based on a model that takes into consideration the nonlinear nature of the machine magnetic circuit. Several modeling methods have been proposed to account for such saturation effect (Faiz and Seifi 1995; Levi 1995; Thiringer 1996; Abdel Fattah and Loparo 2003; Pedra *et al.* 2009). However, the obtained models have usually proved not to be useful for control design purpose. Alternative modeling methods that provide control-oriented models are still very few, for example, Novotnak *et al.* (1999) and Ouadi *et al.* (2011). Presently, the focus is put on the approach of Ouadi *et al.* (2011).

Inductances Saturation

In this section, we emphasize the effect of magnetic saturation on the self- and mutual inductances at, and between, the stator and the rotor. The magnetic fluxes for the stator and rotor phases are given by Leonard (2001)

$$\phi_s = \phi_{ls} + \phi_\mu = l_s i_s + \phi_\mu, \tag{10.1}$$

$$\phi_r = \phi_{lr} + \phi_{\mu r} = l_r i_r + \phi_{\mu r}, \tag{10.2}$$

where ϕ_μ and $\phi_{\mu r}$ designate the magnetizing air-gap fluxes along one phase of the stator and rotor, respectively; ϕ_{ls} and ϕ_{lr} are the leakage fluxes at the stator and the rotor, respectively.

The expressions (10.1)-(10.2) mean that ϕ_{ls} and ϕ_{lr} are proportional, respectively, to the stator and the rotor current. This is valid in real-life machines because the large leakage flux is circulating in air, not in iron. Letting k denote the machine transformation ratio, the flux equations (10.1) and (10.2) are rewritten as, in the *dq*-coordinates:

$$\phi_{sd} = l_s i_{sd} + \phi_{\mu d}, \qquad \phi_{sq} = l_s i_{sq} + \phi_{\mu q}, \tag{10.3}$$

$$\phi_{rd} = l_r i_{rd} + k\phi_{\mu d}, \qquad \phi_{rq} = l_r i_{rq} + k\phi_{\mu q}. \tag{10.4}$$

The contribution of the stator and the rotor to the air-gap flux generation is expressed in term of the magnetizing current, denoted by i_μ (Ouadi *et al.* 2011; Thiringer 1996; Faiz and Seifi 1995). Then, the (d, q) components of the system are given by the expressions

$$i_{\mu d} = i_{sd} + k i_{rd}, \qquad i_{\mu q} = i_{sq} + k i_{rq}. \tag{10.5}$$

For squirrel-cage motors, the transformation ratio can be chosen equal to unity, that is, $k = 1$.

Assuming that the magnetizing flux saturates only in amplitude (its direction remains unchanged), it follows that the instantaneous quantities ϕ_μ and i_μ are in phase. On the other hand, the norms Φ_μ and I_μ are related to each other by the magnetic characteristic $\Phi_\mu = \lambda(I_\mu)$, depicted by Figure 10.3a. Using these observations, it follows that the instantaneous values ϕ_μ and i_μ are related by

$$\phi_\mu = \frac{\Phi_\mu}{I_\mu} i_\mu. \tag{10.6}$$

The forthcoming development involves the static magnetizing parameter L_m, defined as follows (Ouadi *et al.* 2011):

$$L_m = \frac{\Phi_\mu}{I_\mu} = \frac{\Phi_\mu}{\lambda^{-1}(\Phi_\mu)}. \tag{10.7}$$

Clearly, the magnetizing inductance L_m is dependent on the (varying) magnetizing flux Φ_μ. In Ouadi *et al.* (2011), it is shown that this dependence can be captured by a polynomial function of the form

$$\frac{1}{L_m} = \kappa(\Phi_\mu) = q_0 + q_1 \Phi_\mu + q_2 \Phi_\mu^2 + \cdots + q_n \Phi_\mu^n. \tag{10.8}$$

Figure 10.3b illustrates the polynomial approximation for a (loadless) 7.5 kW induction machine. In view of equation (10.7), the (d, q)-components of the magnetizing flux can be expressed as follows:

$$\phi_{\mu d} = L_m i_{\mu d}, \qquad \phi_{\mu q} = L_m i_{\mu q}. \tag{10.9}$$

From equations (10.3), (10.4), (10.5), and (10.9), the inductances L_s and L_r can be written as the sum of the leakage and the magnetizing inductances

$$L_s = l_s + L_m, \qquad L_r = l_r + L_m. \tag{10.10}$$

In induction motor analysis, the leakage inductances are usually grouped together either in the stator side or on the rotor side. Considering the first option, amounts to let $l_r = 0$ and $l_s = l_{seq}$. Then, equation (10.10) becomes

$$L_s = l_{seq} + L_m, \quad L_r = L_m, \quad \phi_r = \phi_\mu, \tag{10.11}$$

where l_{seq} is the equivalent inductance of both the stator and the rotor leakage brought to the stator side.

Induction Motor Model

Using the previous inductance expressions, it is shown in Ouadi *et al.* (2011) that, the induction machine dynamics are described in the α-β frame by the following model that accounts for magnetic saturation:

$$\frac{d\omega_m}{dt} = p\frac{L_m}{JL_r}(\phi_{r\alpha} i_{s\beta} - \phi_{r\beta} i_{s\alpha}) - \frac{T_L}{J} - \frac{F}{J}\omega_m, \tag{10.12}$$

$$\frac{di_{s\alpha}}{dt} = -\gamma i_{s\alpha} + \frac{L_m R_r}{\sigma L_s L_r^2}\phi_{r\alpha} + p\omega_m \frac{L_m}{\sigma L_s L_r}\phi_{r\beta} + \frac{1}{\sigma L_s} v_{s\alpha}, \tag{10.13}$$

$$\frac{di_{s\beta}}{dt} = -\gamma i_{s\beta} + \frac{L_m R_r}{\sigma L_s L_r^2}\phi_{r\beta} - p\omega_m \frac{L_m}{\sigma L_s L_r}\phi_{r\alpha} + \frac{1}{\sigma L_s} v_{s\beta}, \tag{10.14}$$

$$\frac{d\phi_{r\alpha}}{dt} = -\frac{R_r}{L_r}\phi_{r\alpha} + p\omega_m \phi_{r\beta} + \frac{R_r L_m}{L_r} i_{s\alpha}, \tag{10.15}$$

$$\frac{d\phi_{r\beta}}{dt} = -\frac{R_r}{L_r}\phi_{r\beta} - p\omega_m \phi_{r\alpha} + \frac{L_m R_r}{L_r} i_{s\beta}. \tag{10.16}$$

Replacing the stator, the rotor and the mutual inductances (L_s, L_r, and L_m) by their equivalent expressions given by equation (10.11), the above model simplifies to

$$\frac{d\omega_m}{dt} = \frac{p}{J}(\phi_{r\alpha} i_{s\beta} - \phi_{r\beta} i_{s\alpha}) - \frac{T_L}{J} - \frac{F}{J}\omega_m, \tag{10.17}$$

$$\frac{di_{s\alpha}}{dt} = -\gamma i_{s\alpha} + \frac{R_r}{l_{seq}}\kappa(\Phi_r)\phi_{r\alpha} + p\frac{1}{l_{seq}}\omega_m \phi_{r\beta} + \frac{1}{l_{seq}} v_{s\alpha}, \tag{10.18}$$

$$\frac{di_{s\beta}}{dt} = -\gamma i_{s\beta} + \frac{R_r}{l_{seq}}\kappa(\Phi_r)\phi_{r\beta} - p\frac{1}{l_{seq}}\omega_m \phi_{r\alpha} + \frac{1}{l_{seq}} v_{s\beta}, \tag{10.19}$$

$$\frac{d\phi_{r\alpha}}{dt} = -R_r\kappa(\Phi_r)\phi_{r\alpha} + p\omega_m \phi_{r\beta} + R_r i_{s\alpha}, \tag{10.20}$$

$$\frac{d\phi_{r\beta}}{dt} = -R_r\kappa(\Phi_r)\phi_{r\beta} - p\omega_m \phi_{r\alpha} + R_r i_{s\beta}, \tag{10.21}$$

where l_{seq} is the equivalent inductance of both stator and rotor leakage brought on the stator side. In this case, the parameter $\sigma = 1 - \frac{L_m^2}{L_s L_r}$ becomes $\sigma = \frac{L_s - L_m}{L_s} = \frac{l_{seq}}{L_s}$. The corresponding model in the rotating dq-coordinate frame is described by the following equations:

$$\frac{d\omega_m}{dt} = \frac{p}{J}(\phi_{rd} i_{sq} - \phi_{rq} i_{sd}) - \frac{T_L}{J} - \frac{F}{J}\omega_m, \tag{10.22}$$

$$\frac{di_{sd}}{dt} = -\gamma i_{sd} + \omega_s i_{sq} + \frac{R_r}{l_{seq}}\kappa(\Phi_r)\phi_{rd} + p\frac{1}{l_{seq}}\omega_m \phi_{rq} + \frac{1}{l_{seq}} v_{sd}, \tag{10.23}$$

$$\frac{di_{sq}}{dt} = -\gamma i_{sq} - \omega_s i_{sd} + \frac{R_r}{l_{seq}}\kappa(\Phi_r)\phi_{rq} - p\frac{1}{l_{seq}}\omega_m \phi_{rd} + \frac{1}{l_{seq}} v_{sq}, \tag{10.24}$$

$$\frac{d\phi_{rd}}{dt} = -R_r \kappa(\Phi_r)\phi_{rd} - (\omega_s - p\omega_m)\phi_{rq} + R_r i_{sd}, \tag{10.25}$$

$$\frac{d\phi_{rq}}{dt} = -R_r \kappa(\Phi_r)\phi_{rq} + (\omega_s - p\omega_m)\phi_{rd} + R_r i_{sq}, \tag{10.26}$$

where the various notations are defined as follows:

- $\kappa(\Phi_r)$ is the only varying parameter depending on the machine magnetic state as shown by Figure 10.3b; this dependence has been given a polynomial approximation in Ouadi *et al.* (2011)

$$\kappa(\Phi_r) = q_0 + q_1 \Phi_r + q_2 \Phi_r^2 + \cdots + q_n \Phi_r^n, \tag{10.27}$$

  and the involved coefficients have been identified (based on spline approximation) using the experimental magnetic characteristic of Figure 10.3a.

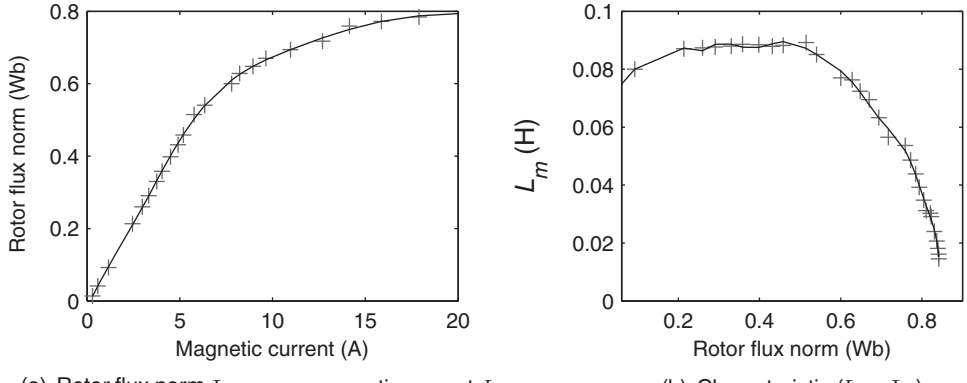

(a) Rotor flux norm Φ_r versus magnetic current I_μ (b) Characteristic (L_m, Φ_r)

Figure 10.3 Magnetic characteristic experimentally obtained in (Ouadi *et al.* 2011) for a 7.5 kW induction motor. The crosses (+++) indicate experimental points, the solid line the corresponding polynomial interpolation

- Φ_r denotes the amplitude of the (instantaneous) rotor flux, denoted as ϕ_r. Accordingly, one has

$$\Phi_r = \sqrt{\phi_{r\alpha}^2 + \phi_{r\beta}^2} \tag{10.28}$$

  where $(\phi_{r\alpha}, \phi_{r\beta})$ (resp. (ϕ_{rd}, ϕ_{rq})) denote the rotor flux α, β (resp. d, q) components.
- $(i_{s\alpha}, i_{s\beta})$ (resp. (i_{sd}, i_{sq})) are the α, β (resp. d, q) components of the stator current.
- $(v_{s\alpha}, v_{s\beta})$, (resp. v_{sd}, v_{sq}) denote the stator voltage in α, β (resp. d, q) coordinate (obtained after Park transformation) of the three-phase stator voltages.
- ω_m represents the motor speed.
- R_s and R_r are the stator and rotor resistances.
- F, J, and T_L are respectively the friction coefficient, rotor inertia, and load torque.
- p is the number of pole pairs.
- $l_{seq} = \sigma L_s$ is the equivalent inductance of both stator and rotor leakage brought to the stator side.
- $\gamma = \frac{R_s + R_r}{l_{seq}}$

Numerical values of the model parameters are given by Table 10.1, they correspond to an induction motor of 7.5 kW.

10.3 Controller Design

10.3.1 Control Objective

The aim is to develop a controller able to achieve the two following objectives:

1. **Speed regulation:** the machine speed ω_m must track, as closely as possible, a given time-varying reference signal ω_m^*.
2. **Flux optimization:** the rotor flux norm Φ_r must track as accurately as possible a state-dependent flux reference $\Phi_r^* = F(I_s)$, where I_s denotes the stator current norm and the function $F(.)$ has yet to be determined so that $\Phi_r = \Phi_r^*$ entails the minimization of the stator current consumed by the machine.

10.3.2 Rotor Flux Reference Optimization

It was already mentioned that, most existing induction machine speed controllers involve a flux regulation loop (Figure 10.1). Furthermore, this loop is generally designed based upon standard models that ignore the machine magnetic saturation. Then, for coherency, the flux reference signal is generally given a constant value coinciding with the machine nominal flux value (Ouadi and Giri 2002; Jasinski *et al.* 2006; Montanan *et al.* 2006; Singh *et al.* 2006; Abdelaziz and Ghedjati 2007; Traore *et al.* 2008). As a result, such controllers are unable to achieve optimal machine performances (high energetic efficiency, unitary power factor, optimized motor torque) in presence of small loads. In El Fadili *et al.* (2012) and Ouadi *et al.* (2010), new controllers have been proposed that include flux reference optimizers. Optimality was intended in the sense of minimal stator current consumption and the optimizers were

designed using models that account for the magnetic circuit saturation. The approach of El Fadili *et al.* (2012) is revisited in the following text.

The first step is to find a relationship between the rotor flux norm and the stator current norm. In this respect, recall that the norms of all electrical quantities are invariant when passing from the $\alpha\beta$-coordinates to the dq-coordinates. Then, it makes sense for simplicity to conduct the present development within the oriented dq-coordinates frame. Indeed, within this reference frame, the flux q-component is null and all state variables are constant in steady state. That is, the dq-coordinate model described by equations (10.22), (10.23), (10.24), (10.25), and (10.26) is based upon. It turns out that, the machine electromagnetic torque T_{em} is simply expressed as follows:

$$T_{em} = p\phi_{rd} i_{sq} = p\Phi_r i_{sq}. \tag{10.29}$$

On the other hand, equation (10.25) simplifies to

$$\frac{\mathrm{d}\Phi_r}{\mathrm{d}t} = R_r i_{sd} - R_r \kappa(\Phi_r)\Phi_r, \tag{10.30}$$

yielding the steady-state current i_{sd},

$$i_{sd} = \kappa(\Phi_r)\Phi_r. \tag{10.31}$$

In turn, the stator current norm expression simplifies to

$$I_s = \sqrt{i_{sd}^2 + i_{sq}^2}. \tag{10.32}$$

Then, using equations (10.29), (10.30), (10.31), and (10.32), one gets the following expression of the electromagnetic torque:

$$T_{em} = p\Phi_r \sqrt{I_s^2 - (\kappa(\Phi_r)\Phi_r)^2}. \tag{10.33}$$

Figure 10.4 shows the curves representing the electromagnetic torque T_{em} versus the flux Φ_r, for various values of the stator current I_s. It is clearly seen that, to a given torque it corresponds a multitude of operation points differing by the value of the flux Φ_r and the current I_s. For instance, a torque $T_{em} = 20$ Nm can be produced, for the machine of Table 10.1, with

- a flux $\Phi_r = 0.5$ Wb and a current $I_s = 8.5$ A;
- a flux $\Phi_r = 0.37$ Wb and a current $I_s = 10$ A;
- a flux $\Phi_r = 0.21$ Wb and a current $I_s = 16$ A.

From an energetic viewpoint, the best operation point is one that involves the least current consumption. Let $T_{ei} (i = 1, \ldots, r)$ be a sufficiently large sample of relevant torque values. It is readily seen from Figure 10.4 that for any T_{ei}, there is a unique couple (Φ_{ri}, I_{si}) that involves the least possible stator current. That is, a set of couples (Φ_{ri}, I_{si}) can be obtained using

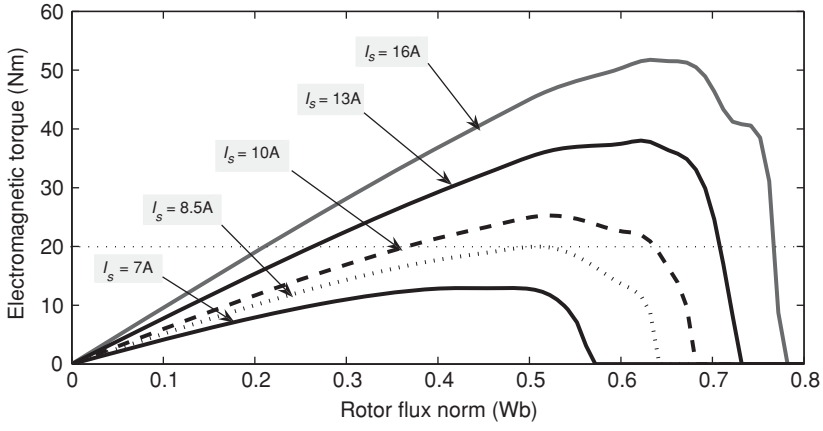

Figure 10.4 Electromagnetic torque T_{em} in function of rotor flux ϕ_r, for different stator currents norm I_s

equation (10.33) and interpolated to get a polynomial function $F(.)$ such that $\Phi_{ri} = F(I_{si})$. The polynomial interpolation thus obtained, referred to flux reference optimizer, is denoted as

$$\Phi_r^* = F(I_s) = h_0 + h_1 I_s + h_2 I_s^2 + \cdots + h_n I_s^n. \tag{10.34}$$

Note that this polynomial flux optimizer is nothing other than the optimal current flux (OCF) characteristic. The optimizer associated to the machine defined by the numerical characteristics of Table 10.1 is shown in Figure 10.5. Recall that optimality is understood in the sense of minimal absorbed stator current I_s for a given torque T_{em}.

Remark 10.3.1 *The polynomial interpolation yielding the function $F(.)$ can be performed using, for example, the Matlab functions POLYDER, POLYVAL, SPLINE, and POLYFIT.*

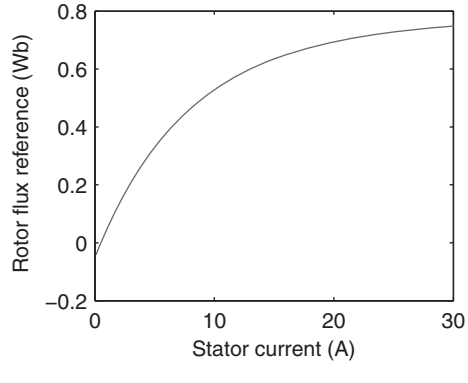

Figure 10.5 Optimal current-flux characteristic obtained, for the induction machine with physical characteristics of Table 10.1

10.3.3 Speed and Flux Control Design and Analysis

In this section, a speed and a flux regulator is designed for the saturated induction machine described by equations (10.17), (10.18), (10.19), (10.20), and (10.21). The speed reference ω_m^* and its two first derivatives are bounded. These requirements can always be met by filtering the original reference through second order linear filters. The flux reference Φ_r^* is provided online by the optimizer (10.34). Recall that if Φ_r (with $\Phi_r = \sqrt{\phi_{r\alpha}^2 + \phi_{r\beta}^2}$) equals Φ_r^*, the machine will operate in optimal conditions (i.e., with minimal absorbed stator current I_s).

The speed/flux controller design will now be performed in two steps using the backstepping technique (Krstic *et al.* 1995). First, introduce the tracking errors

$$z_1 = \omega_m^* - \omega_m, \tag{10.35}$$

$$z_2 = \Phi_r^{*2} - (\phi_{r\alpha}^2 + \phi_{r\beta}^2), \tag{10.36}$$

from the polynomial interpolation of the experimental points $(\Phi_{T_{ej}}^*, I_{T_{ej}}^*)$. This characteristic defines the flux reference optimizer

Step 1. It follows from equation (10.17), (10.20), and (10.21) that the errors z_1 and z_2 undergo the differential equations

$$\dot{z}_1 = \dot{\omega}_m^* - \frac{p}{J}(\phi_{r\alpha} i_{s\beta} - \phi_{r\beta} i_{s\alpha}) + \frac{T_L}{J} + \frac{F}{J}\omega_m, \tag{10.37}$$

$$\begin{aligned} \dot{z}_2 &= 2\dot{\Phi}_r^* \Phi_r^* - 2(\dot{\phi}_{r\alpha}\phi_{r\alpha} + \dot{\phi}_{r\beta}\phi_{r\beta}), \\ \dot{z}_2 &= 2\dot{\Phi}_r^* \Phi_r^* + 2R_r\kappa(\Phi_r)\Phi_r + R_r(i_{s\alpha}\phi_{r\alpha} + i_{s\beta}\phi_{r\beta}). \end{aligned} \tag{10.38}$$

In equations (10.37) and (10.38), the quantities $\frac{p}{J}(\phi_{r\alpha} i_{s\beta} - \phi_{r\beta} i_{s\alpha})$ and $R_r(i_{s\alpha}\phi_{r\alpha} + i_{s\beta}\phi_{r\beta})$ stand up as virtual control signals. Let us temporarily suppose these to be the actual control signals and consider the Lyapunov function candidate

$$V_1 = \frac{1}{2}(z_1^2 + z_2^2). \tag{10.39}$$

It can be easily checked that the time derivative of equation (10.39) can be made negative definite function of (z_1, z_2), that is,

$$\dot{V}_1 = -c_1 z_1^2 - c_2 z_2^2, \tag{10.40}$$

by letting $\frac{p}{J}(\phi_{r\alpha} i_{s\beta} - \phi_{r\beta} i_{s\alpha}) = \mu_1$ and $R_r(i_{s\alpha}\phi_{r\alpha} + i_{s\beta}\phi_{r\beta}) = \nu_1$ with

$$\mu_1 = c_1 z_1 + \dot{\omega}_m^* + \frac{T_L}{J} + \frac{F}{J}(\omega_m^* - z_1), \tag{10.41}$$

and

$$\nu_1 = c_2 z_2 + 2\dot{\Phi}_r^* \Phi_r^* + 2R_r\kappa(\Phi_r)\Phi_r, \tag{10.42}$$

where c_1 and c_2 are any positive design parameters.

As the quantities $\frac{p}{J}(\phi_{r\alpha}i_{s\beta} - \phi_{r\beta}i_{s\alpha})$ and $R_r(i_{s\alpha}\phi_{r\alpha} + i_{s\beta}\phi_{r\beta})$ are not the actual control signals, they cannot be let equal to μ_1 and ν_1, respectively. Nevertheless, we retain the expressions of μ_1 and ν_1 as the first stabilizing functions and introduce the new errors

$$z_3 = \mu_1 - \frac{p}{J}(\phi_{r\alpha}i_{s\beta} - \phi_{r\beta}i_{s\alpha}), \tag{10.43}$$

$$z_4 = \nu_1 - R_r(i_{s\alpha}\phi_{r\alpha} + i_{s\beta}\phi_{r\beta}). \tag{10.44}$$

Then, using the notations (10.41), (10.42), (10.43), and (10.44), the dynamics of the errors z_1 and z_2, initially described by equations (10.37) and (10.38), can be rewritten as follows:

$$\begin{aligned} \dot{z}_1 &= \omega_m^* - (\mu_1 - z_1) + T_L + F\omega_m, \\ \dot{z}_1 &= -c_1 z_1 + z_3, \end{aligned} \tag{10.45}$$

$$\dot{z}_2 = -c_2 z_2 + z_4. \tag{10.46}$$

Similarly, the time derivative of V_1 can be expressed in function of the new errors as follows:

$$\dot{V}_1 = -c_1 z_1^2 - c_2 z_2^2 + z_1 z_3 + z_2 z_4. \tag{10.47}$$

Step 2: The second design step consists of choosing the actual control signals, $v_{s\alpha}$ and $v_{s\beta}$, so that all errors (z_1, z_2, z_3, and z_4) converge to zero. To this end, it must be made clear how these errors depend on the actual control signals ($v_{s\alpha}$ and $v_{s\beta}$). First, focusing on z_3, it follows from equation (10.43) that

$$\dot{z}_3 = \dot{\mu}_1 - \frac{p}{J}(\dot{\phi}_{r\alpha}i_{s\beta} + \phi_{r\alpha}\dot{i}_{s\beta} - \dot{\phi}_{r\beta}i_{s\alpha} - \phi_{r\beta}\dot{i}_{s\alpha}). \tag{10.48}$$

Using equations (10.18), (10.19), (10.20), (10.21), and (10.41), one gets from equation (10.48)

$$\begin{aligned} \dot{z}_3 = {} & c_1\dot{z}_1 + \ddot{\omega}_m^* + \frac{\dot{T}_L}{J} + \frac{F}{J}(\dot{\omega}_m^* - \dot{z}_1) - \frac{p}{J}((-R_r\kappa(\Phi_r)\phi_{r\alpha} + p\omega_m\phi_{r\beta} + R_r i_{s\alpha})i_{s\beta} \\ & + \phi_{r\alpha}\left(-\gamma i_{s\beta} + \frac{1}{l_{seq}}R_r\kappa(\Phi_r)\phi_{r\beta} - p\frac{1}{l_{seq}}\omega_m\phi_{r\alpha} + \frac{1}{l_{seq}}v_{s\beta}\right) \\ & - (-R_r\kappa(\Phi_r)\phi_{r\beta} - p\omega_m\phi_{r\alpha} + R_r i_{s\beta})i_{s\alpha} \\ & - \phi_{r\beta}\left(-\gamma i_{s\alpha} + \frac{R_r}{l_{seq}}\kappa(\Phi_r)\phi_{r\alpha} + p\frac{1}{l_{seq}}\omega_m\phi_{r\beta} + \frac{1}{l_{seq}}v_{s\alpha})\right). \end{aligned} \tag{10.49}$$

For convenience, the above equation is given the following compact form:

$$\dot{z}_3 = \mu_2 + \frac{p}{J}\frac{1}{l_{seq}}(\phi_{r\alpha}v_{s\beta} - \phi_{r\beta}v_{s\alpha}), \tag{10.50}$$

with

$$\begin{aligned}\mu_2 = {} & c_1(-c_1z_1 + z_3) + \ddot{\omega}_m^* + \frac{\dot{T}_L}{J} + \frac{F}{J}(\dot{\omega}_m^* - (-c_1z_1 + z_3)) \\ & - \frac{p}{J}((-R_r\kappa(\Phi_r)\phi_{r\alpha} + p\omega_m\phi_{r\beta} + R_r i_{s\alpha})i_{s\beta} \\ & + \phi_{r\alpha}\left(-\gamma i_{s\beta} + \frac{R_r}{l_{seq}}\kappa(\Phi_r)\phi_{r\beta} - p\frac{1}{l_{seq}}\omega_m\phi_{r\alpha}\right) \\ & - (-R_r\kappa(\Phi_r)\phi_{r\beta} - p\omega_m\phi_{r\alpha} + R_r i_{s\beta})i_{s\alpha} \\ & - \phi_{r\beta}\left(-\gamma i_{s\alpha} + \frac{R_r}{l_{seq}}\kappa(\Phi_r)\phi_{r\alpha} + p\frac{1}{l_{seq}}\omega_m\phi_{r\beta})\right). \end{aligned} \tag{10.51}$$

Similarly, it follows from equation (10.44) that z_4 undergoes the following differential equation:

$$\dot{z}_4 = \dot{\nu}_1 - R_r(\dot{i}_{s\alpha}\phi_{r\alpha} + i_{s\alpha}\dot{\phi}_{r\alpha} + \dot{i}_{s\beta}\phi_{r\beta} + i_{s\beta}\dot{\phi}_{r\beta}). \tag{10.52}$$

Using equations (10.17), (10.18), (10.19), (10.20), (10.21), and (10.42), it follows from equation (10.52):

$$\begin{aligned}\dot{z}_4 = {} & (c_2\dot{z}_2 + 2\ddot{\Phi}_r^*\Phi_r^* + 2R_r\dot{\kappa}(\Phi_r)\Phi_r + 2R_r\kappa(\Phi_r)\dot{\Phi}_r) + 2\dot{\Phi}_r^{*^2} \\ & - R_r\left(-\gamma i_{s\alpha} + \frac{R_r}{l_{seq}}\kappa(\Phi_r)\phi_{r\alpha} + p\frac{1}{l_{seq}}\omega_m\phi_{r\beta} + \frac{1}{l_{seq}}v_{s\alpha}\right)\phi_{r\alpha} \\ & + i_{s\alpha}((-R_r\kappa(\Phi_r)\phi_{r\alpha} + p\omega_m\phi_{r\beta} + R_r i_{s\alpha}) \\ & + \left(-\gamma i_{s\beta} + \frac{R_r}{l_{seq}}\kappa(\Phi_r)\phi_{r\beta} - p\frac{1}{l_{seq}}\omega_m\phi_{r\alpha} + \frac{1}{l_{seq}}v_{s\beta}\right)\phi_{r\beta} \\ & + i_{s\beta}(-R_r\kappa(\Phi_r)\phi_{r\beta} - p\omega_m\phi_{r\alpha} + R_r i_{s\beta})), \end{aligned} \tag{10.53}$$

where the derivative $\dot{\kappa}(\Phi_r)$ is obtained from (10.27):

$$\dot{\kappa}(\Phi_r) = \frac{d\kappa}{d\Phi_r}\frac{\Phi_r}{dt} = \frac{d\kappa}{d\Phi_r}\left(\frac{\dot{\phi}_{r\alpha}}{\Phi_r}\phi_{r\alpha} + \frac{\dot{\phi}_{r\beta}}{\Phi_r}\phi_{r\beta}\right). \tag{10.54}$$

In turn, equation (10.53) is given the following compact form:

$$\dot{z}_4 = \nu_2 - \frac{R_r}{l_{seq}}(v_{s\alpha}\phi_{r\alpha} + v_{s\beta}\phi_{r\beta}), \tag{10.55}$$

with

$$\begin{aligned}\nu_2 = {} & (c_2(-c_2z_2 + z_2) + 2\ddot{\Phi}_r^*\Phi_r^* + 2R_r\dot{\kappa}(\Phi_r)\Phi_r + 2R_r\kappa(\Phi_r)\dot{\Phi}_r) + 2\dot{\Phi}_r^{*^2} \\ & - R_r\left(-\gamma i_{s\alpha} + \frac{R_r}{l_{seq}}\kappa(\Phi_r)\phi_{r\alpha} + p\frac{1}{l_{seq}}\omega_m\phi_{r\beta}\right)\phi_{r\alpha} \end{aligned}$$

$$
\begin{aligned}
&+ i_{s\alpha}((-R_r\kappa(\Phi_r)\phi_{r\alpha} + p\omega_m\phi_{r\beta} + R_r i_{s\alpha}) \\
&+ \left(-\gamma i_{s\beta} + \frac{R_r}{l_{seq}}\kappa(\Phi_r)\phi_{r\beta} - p\frac{1}{l_{seq}}\omega_m\phi_{r\alpha} + \frac{1}{l_{seq}}v_{s\beta}\right)\phi_{r\beta} \\
&+ i_{s\beta}(-R_r\kappa(\Phi_r)\phi_{r\beta} - p\omega_m\phi_{r\alpha} + R_r i_{s\beta})).
\end{aligned} \tag{10.56}
$$

To analyze the stability of the error system, composed of equations (10.45), (10.46), (10.50), and (10.55), consider the following augmented Lyapunov function candidate:

$$
V_2 = \frac{1}{2}z_1^2 + \frac{1}{2}z_2^2 + \frac{1}{2}z_3^2 + \frac{1}{2}z_4^2. \tag{10.57}
$$

Its time derivative along the trajectory of the state vector (z_1, z_2, z_3, z_4) is

$$
\dot{V}_2 = z_1\dot{z}_1 + z_2\dot{z}_2 + z_3\dot{z}_3 + z_4\dot{z}_4. \tag{10.58}
$$

Using equation (10.47), (10.48), and (10.55), equation (10.58) gives

$$
\begin{aligned}
\dot{V}_2 = &-c_1z_1^2 - c_2z_2^2 + z_1z_3 + z_2z_4 + z_4\left(\nu_2 - \frac{R_r}{l_{seq}}(v_{s\alpha}\phi_{r\alpha} + v_{s\beta}\phi_{r\beta})\right) \\
&+ z_3\left(\mu_2 + \frac{p}{J}\frac{1}{l_{seq}}(\phi_{r\alpha}v_{s\beta} - \phi_{r\beta}v_{s\alpha})\right).
\end{aligned} \tag{10.59}
$$

Adding $-c_1z_1^2 - c_2z_2^2 - c_3z_3^2 - c_4z_4^2$ to the right-hand side of equation (10.59) and rearranging terms, yields

$$
\begin{aligned}
\dot{V}_2 = &-c_1z_1^2 - c_2z_2^2 - c_3z_3^2 - c_4z_4^2 + z_4\left(\nu_2 + z_2 + c_4z_4 - \frac{R_r}{l_{seq}}(v_{s\alpha}\phi_{r\alpha} + v_{s\beta}\phi_{r\beta})\right) \\
&+ z_3\left(\mu_2 + z_1 + c_3z_3 + \frac{p}{J}\frac{1}{l_{seq}}(\phi_{r\alpha}v_{s\beta} - \phi_{r\beta}v_{s\alpha})\right),
\end{aligned} \tag{10.60}
$$

where c_3 and c_4 are new arbitrary positive real design parameters. Equation (10.60) suggests that the control signals $v_{s\alpha}$ and $v_{s\beta}$ should be chosen in order to set to zero the two quantities between curly brackets (on the right-hand side of equation (10.60)). Letting these quantities equal to zero and solving the resulting second order linear equation system with respect to $v_{s\alpha}$ and $v_{s\beta}$ gives the following control law:

$$
\begin{bmatrix} v_{s\alpha} \\ v_{s\alpha} \end{bmatrix} = \begin{bmatrix} \lambda_0 & \lambda_1 \\ \lambda_2 & \lambda_3 \end{bmatrix}^{-1} \begin{bmatrix} -\mu_2 - z_1 - c_3z_3 \\ -\nu_2 - z_2 - c_4z_4 \end{bmatrix}, \tag{10.61}
$$

with

$$
\begin{aligned}
\lambda_0 &= -\frac{p}{Jl_{seq}}\phi_{r\beta}, \qquad \lambda_1 = \frac{p}{Jl_{seq}}\phi_{r\alpha}, \\
\lambda_2 &= -\frac{R_r}{l_{seq}}\phi_{r\alpha}, \qquad \lambda_3 = -\frac{R_r}{l_{seq}}\phi_{r\beta}.
\end{aligned} \tag{10.62}
$$

Note that inversed matrix in equation (10.61) is nonsingular in practice because its determinant is given by $D = \lambda_0\lambda_3 - \lambda_2\lambda_4 = -\frac{R_r}{l_{seq}^2}\frac{p}{J}(\phi_{r\alpha}^2 + \phi_{r\beta}^2)$ and $\Phi_r = \sqrt{\phi_{r\alpha}^2 + \phi_{r\beta}^2}$ never vanish in practice because of the machine nonzero remnant flux.

The properties of the speed/flux regulator thus designed are described in the following theorem:

Theorem 10.3.2 *(Speed/flux regulator). Consider the closed-loop system composed of:*

- *the induction machine, described by model (10.17–10.21),*
- *and the nonlinear regulator defined by the control law (10.61) and the flux optimizer (10.34). Then, one has the following properties:*

1. *The closed-loop error system undergoes, in the (z_1, z_2, z_3, z_4) coordinates, the following equations:*

$$\dot{z}_1 = -c_1 z_1 + z_3, \tag{10.63}$$

$$\dot{z}_2 = -c_2 z_2 + z_4, \tag{10.64}$$

$$\dot{z}_3 = -c_3 z_3 - z_1, \tag{10.65}$$

$$\dot{z}_4 = -c_4 z_4 - z_2. \tag{10.66}$$

2. *The above linear system is globally asymptotically stable with respect to the Lyapunov function $V_2 = \frac{1}{2}z_1^2 + \frac{1}{2}z_2^2 + \frac{1}{2}z_3^2 + \frac{1}{2}z_4^2$. Consequently, all errors vanish exponentially fast, whatever their initial conditions.*

Proof: Part 1. Equations (10.63) and (10.64) are immediately obtained from equation (10.45) and (10.46). Equation (10.65) is obtained by substituting the control law (10.61) to $(v_{s\alpha}, v_{s\beta})$ on the right-hand side of equation (10.50). Equation (10.66) is obtained by substituting the control law (10.61) to $(v_{s\alpha}, v_{s\beta})$ on the right-hand side of equation (10.55). This proves Part 1.

Part 2. On the other hand, it is readily seen from equation (10.57) that V_2 is a Lyapunov function of the error system (10.63), (10.64), (10.65), and (10.66). Substituting the control law (10.61) to $(v_{s\alpha}, v_{s\beta})$ on the right-hand side of equation (10.60) yields:

$$\dot{V}_2 = -c_1 z_1^2 - c_2 z_2^2 - c_3 z_3^2 - c_4 z_4^2. \tag{10.67}$$

As $\dot{V}_2$ is a negative definite function of the state vector (z_1, z_2, z_3, z_4), the error system is globally asymptotically stable. But asymptotic stability implies exponential stability due to system linearity (Khalil 2003). Theorem 10.3.1 is established. □

Remark 10.3.3 *The derivatives $\dot{\Phi}_r^*$ and $\ddot{\Phi}_r^*$ are obtained using the relation*

$$\Phi_r = F(I_s) = h_0 + h_1 I_s + h_2 I_s^2 + \cdots + h_n I_s^n. \tag{10.68}$$

Specifically, one has:

$$\begin{aligned}\dot{\Phi}_r^* &= \frac{dF(I_s)}{dI_s}\frac{dI_s}{dt} \\ &= \frac{dF(I_s)}{dI_s}\left(\frac{\dot{i}_{s\alpha}i_{s\alpha}+\dot{i}_{s\beta}i_{s\beta}}{I_s}\right). \qquad (10.69)\end{aligned}$$

$$\begin{aligned}\ddot{\Phi}_r^* &= \frac{d^2F(I_s)}{dI_s^2}\left(\frac{\dot{i}_{s\alpha}i_{s\alpha}+\dot{i}_{s\beta}i_{s\beta}}{I_s}\right)^2 \\ &+\frac{dF(I_s)}{dI_s}\left(\frac{\ddot{i}_{s\alpha}i_{s\alpha}+\dot{i}_{s\alpha}^2+\ddot{i}_{s\beta}i_{s\beta}+\dot{i}_{s\beta}^2}{I_s}\right)-\frac{\mathrm{d}F(I_s)}{\mathrm{d}I_s}\left(\frac{(\dot{i}_{s\alpha}i_{s\alpha}+\dot{i}_{s\beta}i_{s\beta})^2}{I_s^3}\right). \qquad (10.70)\end{aligned}$$

Note that the derivatives $\frac{\mathrm{d}F(I_s)}{\mathrm{d}I_s}$ *and* $\frac{\mathrm{d}^2F(I_s)}{\mathrm{d}I_s^2}$ *are easily obtained due to the polynomial nature of equation (10.34).*

10.4 Simulation

This section illustrates the supremacy of the control strategy, involving the OFR optimizer, over control strategies with a CFR. The comparison is performed using a 7.5 kW induction machine whose characteristics are summarized in Table 10.1. The experimental protocol is described by Figures 10.6, 10.7, 10.8, and 10.9e. The applied load torque T_L (Figure 10.6) and rotor speed reference ω_m^* (Figure 10.7) are chosen so that the induction machine works in two very different zones of its magnetic characteristic. Recall that the nonlinear controller to be illustrated is described by: (1) the control laws (10.61); and (2) the flux reference optimizer (10.34). The following values of the controller design parameters proved to be suitable: $c_1 = 100$, $c_2 = 400$, $c_3 = 500$, and $c_4 = 1000$. The above controller will be compared with its simplified CFR version obtained keeping the flux reference constant equal to its nominal value, that is, $\Phi_r^* = 0.56$ Wb. To avoid confusion, the two controllers will be referred to OFR controller and CFR controller. The performances of both controllers are illustrated by Figures 10.7, 10.8, and 10.9. It is seen in Figure 10.7 that both controllers ensure a perfect asymptotic speed reference tracking despite the changes of load torque T_L. Figure 10.8 shows the resulting (state-dependent) OFR (for the OFR controller) and the CFR (for the simplified

Table 10.1 Numerical values of considered motor characteristics

Characteristic	Symbol	Value	Unity
Nominal power	P_N	7.5	kW
Nominal voltage	U_{sn}	380	V
Nominal flux	Φ_{rn}	0.56	Wb
Stator resistance	R_s	0.63	Ω
Rotor resistance	R_r	0.52	Ω
Inertia moment	J	0.22	Kgm^2
Friction coefficient	F	0.001	$\mathrm{Nm\ s\ rad}^{-1}$
Number of pole pairs	p	2	
Leakage equivalent inductance	l_{seq}	7	mH

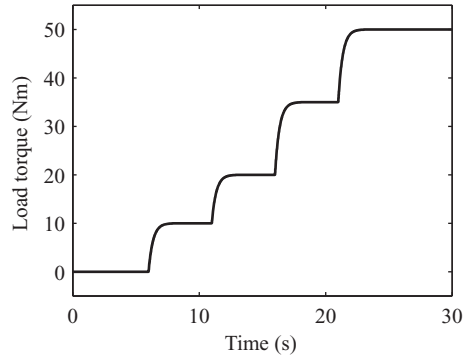

Figure 10.6 Applied load torque T_L (Nm)

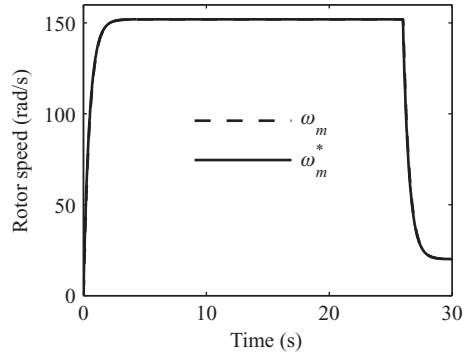

Figure 10.7 Rotor speed ω_m (rad/s) response: the identical speed responses obtained by the OFR controller and the constant flux controller

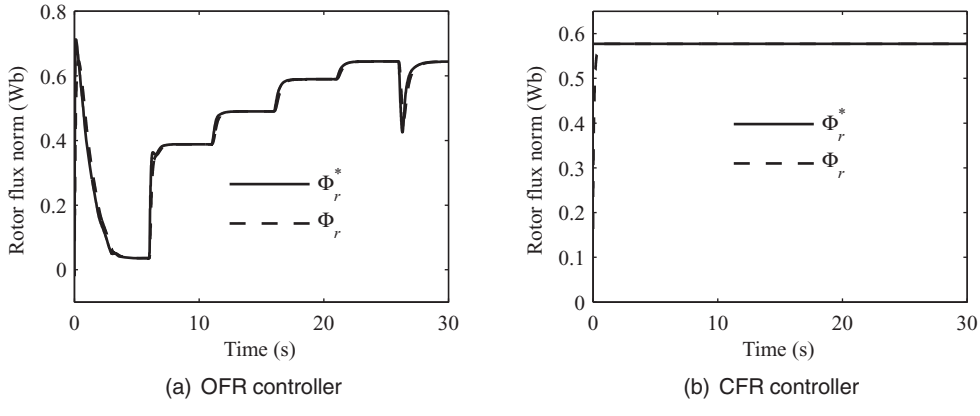

Figure 10.8 Flux tracking. Dashed, rotor flux reference; solid, measured flux response

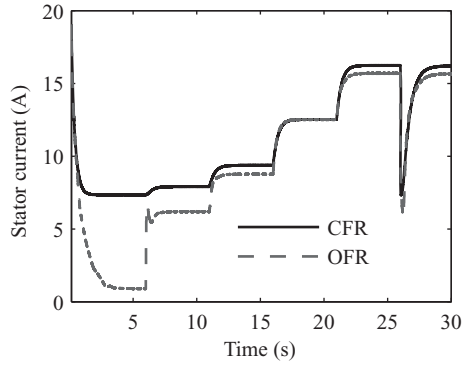

(a) Absorbed stator current (A) (Solid: constant flux controller, Dashed : flux-optimize-based controller)

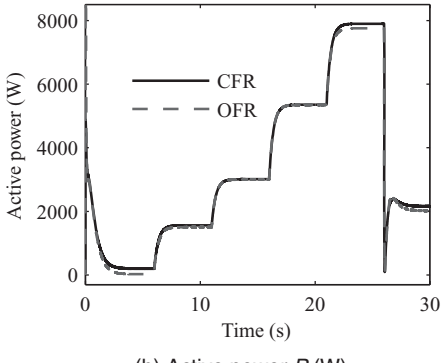

(b) Active power *P* (W)

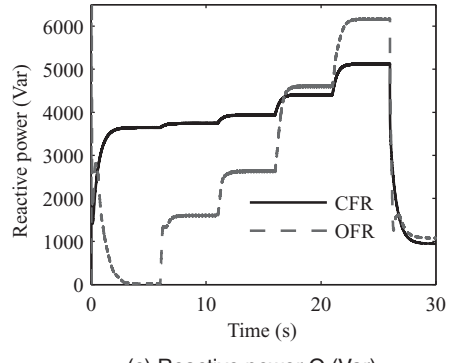

(c) Reactive power Q (Var)

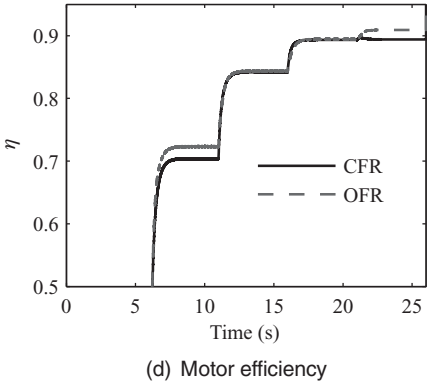

(d) Motor efficiency

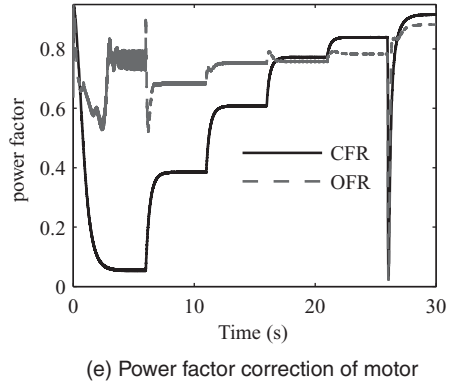

(e) Power factor correction of motor

Figure 10.9 Supremacy of the OFR controller (containing flux reference optimizer) over the CFR regulator (involving constant flux reference)

CFR controller). Clearly, the state-dependent flux reference varies significantly in function of the load torque and the speed.

Figures 10.9a–e show a substantial supremacy of the OFR regulator over the CFR regulator. First, let us focus on Figure 10.9a, which shows the absorbed stator currents for both controllers, in various operation conditions. It is seen that the OFR controller requires a smaller current than the constant flux controller. This difference is more significant in presence of low load torques, because in this situation the OFR is most different from the CFR. The reduction of the absorbed stator current entails the reduction of the consumed reactive power Q (Figure 10.9c). The absorbed active power P, which is mainly determined by the speed and load torque, remains quasi the same with both regulators (Figure 10.9b). Let us evaluate the consequence of these observation in terms of energetic efficiency and of power factor correction. These are analytically defined by

$$\eta = \frac{T_L \omega_m}{P}, \qquad p_f = \frac{P}{\sqrt{P^2 + Q^2}}, \tag{10.71}$$

where the active and reactive powers are given by the following expressions, respectively:

$$P = v_{s\alpha} i_{s\alpha} + v_{s\beta} i_{s\beta}, \qquad Q = v_{s\beta} i_{s\alpha} - v_{s\alpha} i_{s\beta}. \tag{10.72}$$

Figures 10.9d–e show that the machine efficiency η and power factor p_f are much better with the OFR control strategy, thanks to the flux reference optimizer.

10.5 Conclusions

The problem of induction machine control has been addressed in presence of magnetic circuit saturation. A speed-flux controller described by equation (10.61) is designed using the backstepping technique based on model (10.17), (10.18), (10.19), (10.20), and (10.21). The proposed controller involves a (state-dependent) flux reference optimizer. The latter performs an online tuning of the flux reference so that the absorbed stator current is minimized. It is formally shown (Theorem 10.3.2) that the proposed controller guarantees the global convergence of the errors $z_1 = \omega_m^* - \omega_m$, and $z_2 = \Phi_r^{*2} - \Phi_r^2$ to zero (with $\Phi_r^2 = \phi_{r\alpha}^2 + \phi_{r\beta}^2$). That is, the tracking objective is perfectly achieved both for the rotor speed and flux. Furthermore, it is shown by simulation that, in all operation conditions, the absorbed stator current is actually smaller with the proposed OFR controller, compared to standard CFR controllers.

References

Abdel Fattah HA and Loparo KA (2003) Passivity-based torque and flux tracking for induction motors with magnetic saturation. *Automatica*, **39**, 2123–2130.

Abdelaziz M and Ghedjati K (2007) Control by feedback linearization of the torque and the flux of the induction motor. *7th WSEAS International Conference on Systems Theory and Scientific Computation*, Vol. VII, pp. 84–90.

Canudas de Wit C and Ramirez J (2000) *Optimization, Discretization, Observers and Control of Inductions Motors*. Hermes Science Europe Ltd, Paris.

El Fadili A, Giri F, Magri A, *et al.* (2012) Towards a global control strategy for induction motor. Speed regulation, flux optimization and power factor correction. *International Journal of Electrical Power and Energy Systems*, **43**, 230–244.

El Fadili A, Giri F, Ouadi H, *et al.* (2009) Induction machine control in presence of magnetic saturation speed regulation with optimized flux reference. *European Control Conference*, Budapest, Vol. VII, pp. 2542–2547.

Faiz J and Seifi AR (1995) Dynamic analysis of induction motors with saturable inductances. *Electric Power Systems Research*, **34**, 205–210.

Jasinski M, Cichowlas M, and Kazmierkowski MP (2006) Direct control for AC/DC/AC converter-fed induction motor with active filtering function. *International Journal for Computation and Mathematics in Electrical and Electronic Engineering*, **25**, 235–242.

Khalil H (2003) *Nonlinear Systems*. Prentice Hall, Upper Saddle River NJ.

Krstic M, Kanellakopoulos I, and Kokotovic P (1995) *Nonlinear and Adaptive Control Design*. John Wiley & Sons.

Leonard W (2001) *Control of Electrical Drives* Springer, New York.

Levi E (1995) A unified approach to main flux saturation modelling in D-Q axis models of induction machines. *IEEE Transactions on Energy Conversion*, **10**, 455–460.

Montanan M, Peresada S, and Tilli A (2006) A speed-sensorless indirect field-oriented control for induction motors based on high gain speed estimation. *Automatica*, **42**, 1637–1650.

Moreno-Eguilaz JM and Peracaula J (1999) Efficiency optimization for induction motor drives: past, present and future. *Electrimacs 99: Modelling and Simulation of Electric Machines Converters and Systems, IMACS, Lisboa, Potugal*, pp. 187–191.

Novotnak RT, Chiasson J, and Bodson M (1999) High performance motion control of an induction motor with magnetic saturation. *IEEE Transactions on Control Systems Technology*, **7**, 315–327.

Ouadi H and Giri F (2002) Induction motor robust adaptive control. *Mediterranean conference on control and Automation-MED 2002, Lisbon Portugal*.

Ouadi H, Giri F, Elfadili A, and Dugard L (2010) Induction machine speed control with flux optimization. *Control Engineering Practice*, **18**, 55–66.

Ouadi H, Giri F, and Dugard L (2011) Accounting for magnetic saturation in induction machines modelling. *International Journal of Modelling, Identification and Control*, **14**, 27–36.

Pedra J, Candela I, and Barrera A (2009) Saturation model for squirrel-cage induction motors. *Electric Power Systems Research*, **79**, 1054–1061.

Singh B, Bhuvaneswari G, and Garg V (2006) Improved power quality AC-DC converter for electric multiple units in electric traction. *Power India Conference*, pp. 21–26.

Thiringer T (1996) Measurements and modelling of low-frequency disturbances in induction machines. Chalmers University of Technology Dissertation, Goteborg.

Traore D, Plestan F, Glumineau A, and De Leon J (2008) Sensorless induction motor: high order sliding mode controller and adaptive interconnected observer. *IEEE Transactions on Industrial Electronics*, **55**, 3818–3827.

11

Experimental Evaluation of Nonlinear Control Design Techniques for Sensorless Induction Motor

Jesús De León[1], Alain Glumineau[2], Dramane Traore[2], and Robert Boisliveau[2]
[1]*FIME, Universidad Autonoma de Nuevo Leon, France*
[2]*Ecole Centrale de Nantes, LUNAM, France*

11.1 Introduction

The induction motor (IM) is one of the most widely used actuator for industrial applications, due to its reliability, ruggedness, and relatively low cost. Unlike DC motors, the IM is difficult to control due to the coupling nonlinear dynamics. However, thanks to the new developments in power electronics, several methodologies have been proposed to solve such control problem. To facilitate the design and implementation of the IM controller, it is necessary to introduce sensors to measure the electrical currents, the rotor position, and velocity. A load torque sensor is very rare. A reduction in the number of sensors reduces the cost and the maintenance of the overall control system and becomes attractive economically. It is a challenge for a scientific point of view. For these reasons the IM drive without mechanical sensor has had a considerable interest in the last years. In controlling an IM, several difficulties are found, for instance, the estimation of the state variables at low frequencies and ensuring the robustness of the controller against parameter variations, where the most critical parameter affecting performance at low speed is stator resistance (see Holtz 2002).

Several efforts have focused on sensorless schemes in order to solve the IM control problem, taking into account the robustness with respect to parametric uncertainties and their

AC Electric Motors Control: Advanced Design Techniques and Applications, First Edition. Edited by Fouad Giri.

performance under different operation conditions. This drawback is mainly due to the IM observability property that can be lost under some operation conditions. For instance, in Ibarra-Rojas *et al*. (2004), the authors have demonstrated that the main conditions to lose the observability of IM are: the excitation voltages frequency is zero and the rotor speed is constant.

In this chapter, a comparative experimental study between nonlinear robust sensorless IM controllers, taking into account different operation conditions and under parametric uncertainties, is presented. The nonlinear controllers considered in the chapter are (a) a integral backstepping control (IBC) (Traore *et al*. 2012) and (b) a high-order sliding-mode control (HOSMC) (Traore *et al*. 2008). These control schemes are designed to improve the performance of the sensorless IM, at different operation conditions, in particular at low frequencies and in presence of unknown load torque.

Furthermore, to improve the performance of the backstepping control method, additional integral terms are introduced to improve the robustness properties of the controller in spite of uncertainties and perturbations.

Regarding the high-order sliding-mode (HOSM) speed-flux controller, a sliding manifold is designed in order to ensure finite-time convergence of sliding variable and its high-order time derivatives to zero in spite of uncertainties and disturbances.

For implementing such controllers and to reduce the number of sensors, an adaptive interconnected observer is designed for estimating of the fluxes, the speed, the load torque, and, moreover, the stator resistance.

Furthermore, experimental results comparing the performance of both control schemes are obtained on the framework of a specific sensorless IM benchmark (Benchmark 2005).

This chapter is organized as follows. Section 11.2 is devoted to the description of the IM model and the problem formulation. The robust integral backstepping is developed in Section 11.3. The HOSMC is presented in Section 11.4. To implement the proposed controller and to estimate the nonmeasured variables in Section 11.5, an adaptive interconnected observer design is introduced. Furthermore, experimental results are given and discussed related with the performance of the control schemes in Section 11.6. Finally, conclusions are drawn in Section 11.7.

11.2 Problem Formulation

In a rotating frame d- and q-axes (Chiasson 2005), the IM is described by

$$\begin{pmatrix} \dot{i}_{sd} \\ \dot{i}_{sq} \\ \dot{\phi}_{rd} \\ \dot{\phi}_{rq} \\ \dot{\omega}_m \end{pmatrix} = \begin{pmatrix} ba\phi_{rd} + bp\omega_m\phi_{rq} - \gamma i_{sd} + \omega_s i_{sq} + m_1 v_{sd} \\ ba\phi_{rq} - bp\omega_m\phi_{rd} - \gamma i_{sq} - \omega_s i_{sd} + m_1 v_{sq} \\ -a\phi_{rd} + (\omega_s - p\omega_m)\phi_{rq} + aL_m i_{sd} \\ -a\phi_{rq} - (\omega_s - p\omega_m)\phi_{rd} + aL_m i_{sq} \\ m(\phi_{rd} i_{sq} - \phi_{rq} i_{sd}) - c\omega_m - \frac{1}{J} T_l \end{pmatrix}, \tag{11.1}$$

where $i_{sd}, i_{sq}, \phi_{rd}, \phi_{rq}, v_{sd}, v_{sq}, \omega_m, T_l$, and ω_s, respectively, denote the stator currents, the rotor fluxes, the stator voltage inputs, the angular speed, the load torque, and the stator frequency. The subscripts s and r refer to the stator and rotor. The parameters $a = R_r/L_r, b = L_m/\sigma L_s L_r, c = F_v/J, \gamma = \frac{L_r^2 R_s + L_m^2 R_r}{\sigma L_s L_r^2}, \sigma = 1 - (L_m^2/L_s L_r), m = pL_m/JL_r, m_1 = 1/\sigma L_s,$

and $\gamma_1 = \frac{L_m^2 R_r}{\sigma L_s L_r^2}$. We denote R_s and R_r as the resistances, L_s and L_r as the inductances, L_m as the mutual inductance between the stator and rotor windings, p as the number of pole pair, J as the inertia of the system (motor and load), and F_v as the viscous damping coefficient.

The following assumptions are introduced:

1. The stator currents are available for measurement and they represent the measurable outputs of the system; on the contrary, the speed and the fluxes are not available for measurement,
2. The load torque is unknown and is considered as a disturbance modeled by a piecewise function.
3. The stator resistance is considered as a bounded parameter slowly varying with the temperature.
4. The other parameters are constant and given by offline identification with bounded uncertainties.

11.2.1 Control and Observation Problem

The IM control problem is solved by combining the advantages of the field-oriented controller (FOC) design with the robustness properties of nonlinear controllers.

The IM observation problem can be established as follows: to estimate the speed and flux, and, moreover, to identify the load torque and the stator resistance simultaneously, from the measurement of the stator currents and the stator voltages under different operation conditions (at low and high speed: Ghanes *et al*. 2006b).

11.3 Robust Integral Backstepping

By using the same reference frame as the FOC design (Blaschke 1972), a nonlinear backstepping control is robustly designed by introducing additional integral terms. Denote ω_m^* and ϕ^* as the smooth bounded reference signals of the speed ω_m and the rotor flux modulus $\sqrt{\phi_{rd}^2 + \phi_{rq}^2}$, respectively. Following the strategy of FOC ($\|\phi_{rd}\| = \sqrt{\phi_{rd}^2 + \phi_{rq}^2}$, $\phi_{rq} = 0$) (see Blaschke 1972) and the fact that the stator frequency is given by $\omega_s = p\omega_m + a\frac{L_m}{\phi_{rd}} i_{sq}$, a control strategy based on an integral backstepping method is designed.

11.3.1 Controller Design using an Integral Backstepping Method

Following the classical backstepping method (Krstic *et al*. 1995) completed by an integral action to reject some class of uncertainties (see Traore *et al*. 2012), the controller design is done in two steps:

1. The control problem is to choose i_{sd}^* and i_{sq}^* in such a way as to force ω_m and ϕ_{rd} to track their desired reference signals ω_m^* and ϕ_{rd}^*, that is, $(\omega_m \to \omega_m^*)$ and $(\phi_{rd} \to \phi_{rd}^*)$.
2. *Current loops design*: Find the controls v_{sd} and v_{sq} such that the currents i_{sd} and i_{sq} converge fast to desired references i_{sd}^* and i_{sq}^*, respectively.

It is well known that the control performances of IM is still affected by the uncertainties of the plant, such as mechanical parameter uncertainties, external load disturbance, no ideal field orientation in a transient state, and unmodeled dynamics in practical applications. As introduced before, the backstepping control robustness of speed/flux and currents controllers can be increased by the introduction of new integral terms. This design is detailed in the following text.

Speed and Flux Loops

Let us consider the reduced model of IM given by

$$\begin{pmatrix} \dot{\omega_m} \\ \dot{\phi}_{rd} \end{pmatrix} = \begin{pmatrix} m\phi_{rd} i_{sq} - c\omega_m - \frac{T_l}{J} + \Delta\Gamma_{\omega_m}\left(m, c, \frac{T_l}{J}\right) \\ -a\phi_{rd} + aL_m i_{sd} + \Delta\Gamma_{\phi_{rd}}(a, L_m) \end{pmatrix}, \tag{11.2}$$

where $\Delta\Gamma_{\omega_m}(m, c, \frac{T_l}{J})$ and $\Delta\Gamma_{\phi_{rd}}(a, L_m)$ are the parametric uncertain terms satisfying $|\Delta\Gamma_\sigma| \leq \eta_\sigma$, for $\sigma = \omega_m, \phi_{rd}$.

The reduced model is obtained using current controls v_{sd} and v_{sq} (defined later), which are designed and tuned to force i_{sd} and i_{sq} to track their corresponding references i_{sd}^* and i_{sq}^* sufficiently fast. Consequently, references i_{sd}^* and i_{sq}^* can then be considered as *virtual inputs* of the reduced model (11.2).

To solve speed and flux tracking problem, let us define the tracking errors as

$$z_\sigma = \sigma^* - \sigma + K'_\sigma \int_0^t (\sigma^* - \sigma)dt, \quad for \quad \sigma = \omega_m, \phi_{rd},$$

where a supplementary integral term is introduced with respect to the classical backstepping algorithm.

Next, replacing i_{sq} by i_{sq}^* and i_{sd} by i_{sd}^* in equation (11.2), it follows that the dynamics of z_{ω_m} and $z_{\phi_{rd}}$ are expressed as

$$\begin{cases} \dot{z}_{\omega_m} = \dot{\omega_m}^* - m\phi_{rd} i_{sq}^* + c\omega_m + \frac{T_l}{J} + K'_{\omega_m}(\omega_m^* - \omega_m) - \Delta\Gamma_{\omega_m}, \\ \dot{z}_{\phi_{rd}} = \dot{\phi}_{rd}^* + a\phi_{rd} - aL_m i_{sd}^* + K'_\phi(\phi_{rd}^* - \phi_{rd}) - \Delta\Gamma_{\phi_{rd}}. \end{cases} \tag{11.3}$$

Choosing the following candidate Lyapunov function $V_{z_{\omega m}} = \frac{1}{2} z_{\omega_m}^2$ and by taking the derivative along the trajectories of equation (11.3) yields

$$\dot{V}_{z_{\omega m}} = -K_{\omega_m} z_{\omega_m} \left\{ \dot{\omega_m}^* - m\phi_{rd} i_{sq}^* + c\omega_m + \frac{T_l}{J} + K'_{\omega_m}(\omega_m^* - \omega_m) - \Delta\Gamma_{\omega_m} \right\}.$$

Following the backstepping methodology, by choosing the virtual control inputs i_{sq}^* as

$$i_{sq}^* = \frac{1}{m\phi_{rd}} [\dot{\omega_m}^* + c\omega_m + \frac{T_l}{J} + K z_{\omega_m} + K'_{\omega_m}(\omega_m^* - \omega_m)], \tag{11.4}$$

it follows that

$$\dot{V}_{z_{\omega_m}} = -K_{\omega_m} z_{\omega_m}^2 - z_{\omega_m} \Delta\Gamma_{\omega_m}, \qquad K_{\omega_m} > 0.$$

Following the same procedure as above, consider the Lyapunov function $V_{z_{\phi_{rd}}} = \frac{1}{2} z_{\phi_{rd}}^2$. Then,

$$\dot{V}_{z_{\phi_{rd}}} = z_{\phi_{rd}} \{\dot{\phi}_{rd}^* + a\phi_{rd} - aL_m i_{sd}^* + K_\phi'(\phi_{rd}^* - \phi_{rd}) - \Delta\Gamma_{\phi_{rd}}\}.$$

Choosing the virtual control inputs i_{sd}^* as follows:

$$i_{sd}^* = \tfrac{1}{aL_m}[\dot{\phi}_{rd}^* + a\phi_{rd} + K_\phi z_{\phi_{rd}} + K_\phi'(\phi_{rd}^* - \phi_{rd})]. \tag{11.5}$$

Finally, we get

$$\dot{V}_{z_{\phi_{rd}}} = -K_\phi z_{\phi_{rd}}^2 - z_{\phi_{rd}} \Delta\Gamma_{\phi_{rd}}, \qquad K_{\phi_{rd}} > 0.$$

Current Loops

Now to design the control laws for the complete model (11.1), one introduces the following tracking errors:

$$z_{i\sigma} = i_{s\sigma}^* - i_{s\sigma} + z_{i\sigma}', \quad \text{with} \quad z_{i\sigma}' = K_{i\sigma}'' \int_0^t (i_{s\sigma}^* - i_{s\sigma}) dt, \tag{11.6}$$

for $\sigma = d, q$. K_{iq}'' and K_{id}'' are positive constants. Next, consider the following candidate Lyapunov functions:

$$V_{z_{iq}} = V_{z_{\omega_m}} + \tfrac{1}{2} z_{iq}^2 + \tfrac{1}{2} z_{iq}'^2, \qquad V_{z_{id}} = V_{z_{\phi_{rd}}} + \tfrac{1}{2} z_{id}^2 + \tfrac{1}{2} z_{id}'^2. \tag{11.7}$$

Taking the time derivative of $V_{z_{iq}}$ along the trajectories of equation (11.3) and by replacing equation (11.4), it follows that

$$\begin{aligned} \dot{V}_{z_{iq}} = &-K_{\omega_m} z_{\omega_m}^2 + z_{iq} \left\{ \frac{di_{sq}^*}{dt} - \frac{di_{sq}}{dt} + K_{iq}''(i_{sq}^* - i_{sq}) \right\} \\ &+ z_{iq}' K_{iq}''(i_{sq}^* - i_{sq}) - z_{\omega_m} \Delta\Gamma_{\omega_m}. \end{aligned} \tag{11.8}$$

From equation (11.1), $\frac{di_{sq}}{dt} = ba\phi_{rq} - bp\omega_m \phi_{rd} - \gamma i_{sq} - \omega_s i_{sd} + m_1 v_{sq}$ and by choosing the control v_{sq} as

$$v_{sq} = \frac{1}{m_1} \left[K_{iq} z_{iq} + bp\omega_m \phi_{rd} - ab\phi_{rq} + \gamma i_{sq} + \omega_s i_{sd} + \frac{di_{sq}^*}{dt} \right], \tag{11.9}$$

it follows that

$$\begin{aligned} \dot{V}_{z_{iq}} &= -K_{\omega_m} z_{\omega_m}^2 - K_{iq} z_{iq}^2 + \{z_{iq} + z_{iq}'\} K_{iq}''(i_{sq}^* - i_{sq})\} - z_{\omega_m} \Delta\Gamma_{\omega_m} \\ &= -K_{\omega_m} z_{\omega_m}^2 - \{K_{iq} - K_{iq}''\} z_{iq}^2 - K_{iq}'' z_{iq}'^2 - z_{\omega_m} \Delta\Gamma_{\omega_m} \\ &\leq -K_1 V_{z_{id}} - z_{\omega_m} \Delta\Gamma_{\omega_m}, \end{aligned} \tag{11.10}$$

where K_{iq} and K''_{iq} are positive constants with $K_{iq} > K''_{iq}$ and $K_1 = min\{K_{\omega_m}, K_{idq} - K''_{iq}, K''_{iq}\}$.

Now, taking the time derivative of $V_{z_{id}}$ along the trajectories of equation (11.3) and replacing equation (11.5), it follows that

$$\dot{V}_{z_{id}} = -K_\phi z_{\phi_{rd}}^2 + z_{\phi_{rd}} \left\{ \frac{di^*_{sd}}{dt} - \frac{di_{sd}}{dt} + K''_{id}(i^*_{sd} - i_{sd}) \right\} - z_{\phi_{rd}} \Delta\Gamma_{\phi_{rd}}. \tag{11.11}$$

From equation (11.1), $\frac{di_{sd}}{dt} = ba\phi_{rd} + bp\omega_m\phi_{rq} - \gamma i_{sd} + \omega_s i_{sq} + m_1 v_{sd}$ and by working out the control v_{sd}

$$v_{sd} = \frac{1}{m_1}\left[K_{id} z_{id} - ba\phi_{rd} - bp\omega_m\phi_{rd} + \gamma i_{sd} - \omega_s i_{sq} + \frac{di^*_{sd}}{dt} \right], \tag{11.12}$$

equation (11.11) can be rewritten as

$$\begin{aligned} \dot{V}_{z_{id}} &= -K_\phi z_{\phi_{rd}}^2 - \{K_{id} - K''_{id}\} z_{id}^2 - K''_{id} z'^2_{id} - z_{\phi_{rd}} \Delta\Gamma_{\phi_{rd}} \\ &= -K_2 V_{z_{id}} - z_{\phi_{rd}} \Delta\Gamma_{\phi_{rd}} \end{aligned} \tag{11.13}$$

where K_{id} and K''_{id} are positive constants with $K_{id} > K''_{id}$ and $K_2 = min\{K_\phi, K_{id} - K''_{id}, K''_{id}\}$.

Proposition 11.3.1 *Consider the reduced order model of IM drive system represented by equation (11.2) with the reference signals ω^*_m and ϕ^*_{rd}, and assume that they are differentiable and bounded. Then, system (11.2) in closed loop with speed, flux, and current tracking laws (11.4), (11.5), (11.9), and (11.12) is strongly uniformly practically stable.*

Proof: Consider the following candidate Lyapunov function

$$\begin{aligned} V_c &= V_{z_{iq}} + V_{z_{id}} \\ &= \frac{1}{2} z_{\omega_m}^2 + \frac{1}{2} z_{iq}^2 + \frac{1}{2} z'^2_{iq} + \frac{1}{2} z_{\phi_{rd}}^2 + \frac{1}{2} z_{id}^2 + \frac{1}{2} z'^2_{id}. \end{aligned} \tag{11.14}$$

Taking its time derivative and replacing the suitable terms, after straightforward computations, one has

$$\dot{V}_c = -\kappa V_c + \Upsilon, \tag{11.15}$$

where $\kappa = min\{K_{\omega_m} - \frac{1}{2\widetilde{\xi}_1^2}, K_\phi - \frac{1}{2\widetilde{\xi}_2^2}, K_{iq}, K_{iq} - K''_{iq}, K_{id}, K_{id} - K''_{id}, K''_{id}\}$ and $\Upsilon = \frac{\widetilde{\xi}_1^2 \eta^2_{\omega_m}}{2} + \frac{\widetilde{\xi}_2^2 \eta^2_{\phi_{rd}}}{2}$, $\forall\ \widetilde{\xi}_i \in (0, 1)\ i = 1, 2$.

It follows that the tracking dynamics is strongly uniformly practically stable (Lakshmikantham *et al*. 1990). The tracking errors converge to the ball of radius $\frac{\Upsilon}{\kappa}$, which can be reduce by the tuning of the controller gains. □

11.4 High-Order Sliding-Mode Control

The success of sliding-mode (SM) control for electric drives is mainly due to its disturbance rejection property, strong robustness and simple implementation, as shown by the large number

of papers on sensorless IM drive (see e.g., Zhang *et al*. 2000; Lascu *et al*. 2005), that use the standard approach of SM control. In Utkin (1993), the concepts and principles of SM control applied to electrical motors has been introduced. However, one of the disadvantages associated with SM control is the chattering phenomenon that may occur on the neighbor of the sliding surface.

Several approaches have been proposed in order to reduce or eliminate the undesirable effects of chattering. In order to overcome this drawback and to improve the controller performances, an approach called HOSM algorithm has been proposed to keep the main advantages of the standard SM control, the chattering effect being attenuated and high-order precision provided (Levant 2001).

A rth order SM controller with finite-time convergence has been proposed in Plestan *et al*. (2008), Levant (2001), and Laghrouche *et al*. (2006). In the sequel, the HOSM speed-flux control is based on Plestan *et al*. (2008) and Traore *et al*. (2008) where it is proposed an easy implementation, an a priori well-known convergence time with robustness with respect to uncertainties and disturbance.

Then, in this section, the goal is to design a robust (with respect to uncertainties/disturbances) flux and speed controller. Define σ_ϕ and σ_{ω_m}, the sliding variables as $\sigma_\phi = \phi_{rd} - \phi_{rd}^*$ and $\sigma_{\omega_m} = \omega_m - \omega_m^*$. From equations (11.26) and (11.27), the relative degree of σ_ϕ and σ_{ω_m} with respect to u are equal to (2, 2), which implies that at least a second order SM controller is respectively designed for the flux and speed.

Furthermore, to reduce or eliminate the chattering effect and to improve the robustness of the controller, third order HOSM controllers are designed for the two outputs, which means that the discontinuous term is applied to $\sigma_\phi^{(3)}$ and $\sigma_{\omega_m}^{(3)}$ through $\dot{u}$.

It follows that

$$\begin{pmatrix} \phi_{rd}^{(2)} \\ \omega_m^{(2)} \end{pmatrix} = \begin{pmatrix} \varphi_{\alpha_1}(\cdot) \\ \varphi_{\alpha_2}(\cdot) \end{pmatrix} + \varphi_\beta(\cdot) \begin{pmatrix} v_{sd} \\ v_{sq} \end{pmatrix}. \tag{11.16}$$

For flux-oriented control $\phi_{rq} = 0$, φ_{α_1}, φ_{α_2}, and φ_β read as

$$\varphi_{\alpha_1} = -a\dot{\phi}_{rd} + aL_m(ba\phi_{rd} - \gamma i_{sd} + \omega_s i_{sq}), \tag{11.17}$$

$$\varphi_{\alpha_2} = m[\dot{\phi}_{rd} i_{sq} + \phi_{rd}(-bp\omega_m \phi_{rd} - \gamma i_{sq} - \omega_s i_{sd})] - c\dot{\omega}_m - \frac{\dot{T}_l}{J}, \tag{11.18}$$

$$\varphi_\beta = \begin{bmatrix} aL_m m_1 & 0 \\ 0 & mm_1\phi_{rd} \end{bmatrix}. \tag{11.19}$$

As there are uncertainties on several parameters, one supposes that the previous terms read as

$$\begin{aligned} \varphi_{\alpha 1} &= \varphi_{\alpha 1}^{Nom} + \Delta\varphi_{\alpha 1}, \quad \varphi_{\alpha 2} = \varphi_{\alpha 2}^{Nom} + \Delta\varphi_{\alpha 2}, \\ \varphi_\beta &= \varphi_\beta^{Nom} + \Delta\varphi_\beta, \end{aligned} \tag{11.20}$$

such that $\varphi_{\alpha 1}^{Nom}$, $\varphi_{\alpha 2}^{Nom}$, and φ_β^{Nom} are the well-known nominal terms whereas $\Delta\varphi_{\alpha 1}$, $\Delta\varphi_{\alpha 2}$, and $\Delta\varphi_\beta$ contain all the uncertainties due to parameters variations and disturbance. Suppose

that these uncertainties are bounded. The control input u reads as (note that matrix φ_β^{Nom} is invertible on the work domain $(\phi_{rd} \neq 0)$)[1]

$$\begin{pmatrix} v_{sd} \\ v_{sq} \end{pmatrix} = \varphi_\beta^{Nom\,-1} \left\{ - \begin{pmatrix} \varphi_{\alpha_1}^{Nom} \\ \varphi_{\alpha_2}^{Nom} \end{pmatrix} + \begin{pmatrix} \nu_{sd} \\ \nu_{sq} \end{pmatrix} \right\}. \tag{11.21}$$

From equations (11.16), (11.17), (11.18), (11.19), (11.20), and (11.21), switching variables dynamics read as

$$\begin{pmatrix} \phi_{rd}^{(2)} & \omega_m^{(2)} \end{pmatrix}^T = \Psi_\alpha + \Psi_\beta \begin{pmatrix} \nu_{sd} & \nu_{sq} \end{pmatrix}^T. \tag{11.22}$$

$\varphi_{\alpha_1}^{Nom}$, $\varphi_{\alpha_1}^{Nom}$, and φ_β^{Nom} are bounded C^1-functions in the operation domain D of IM, which implies that Ψ_α and Ψ_β are uncertain bounded C^1-functions. Then, one gets

$$\begin{pmatrix} \sigma_\phi^{(3)} \\ \sigma_{\omega_m}^{(3)} \end{pmatrix} = \underbrace{\dot{\Psi}_\alpha + \dot{\Psi}_\beta \begin{pmatrix} \nu_{sd} \\ \nu_{sq} \end{pmatrix} - \begin{pmatrix} \phi_{rd^*}^{(3)} \\ \omega_m^{*\,(3)} \end{pmatrix}}_{\varphi_1} + \underbrace{\Psi_\beta}_{\varphi_2} \begin{pmatrix} \dot{\nu}_{sd} \\ \dot{\nu}_{sq} \end{pmatrix}.$$

The control law synthesis is made in two steps: the design of the switching variable and the discontinuous input.

11.4.1 Switching Vector

From equation (29) and Theorem 3 in Traore *et al*. (2008), the switching vector reads as

- *For* $t \leq t_F$. $S_\phi = \sigma_\phi^{(2)} - \chi_\phi$, and $S_{\omega_m} = \sigma_{\omega_m}^{(2)} - \chi_{\omega_m}$ with

$$\begin{aligned} \chi_\phi &= K_\phi F^2 e^{Ft} T \sigma_\phi(0) - 2\zeta_\phi \omega_{n\phi}(\dot{\sigma}_\phi - K_\phi F e^{Ft} T \sigma_\phi(0)) - \omega_{n\phi}^2(\sigma_\phi - K_\phi e^{Ft} T \sigma_\phi(0)), \\ \chi_{\omega_m} &= K_{\omega_m} F^2 e^{Ft} T \sigma_{\omega_m}(0) - 2\zeta_{\omega_m} \omega_{n\omega_m}(\dot{\sigma}_{\omega_m} - K_{\omega_m} F e^{Ft} T \sigma_{\omega_m}(0)) \\ &\quad - \omega_{n\omega_m}^2(\sigma_{\omega_m} - K_{\omega_m} e^{Ft} T \sigma_{\omega_m}(0)). \end{aligned}$$

- *For* $t > t_F$. $S_\phi = \sigma_\phi^{(2)} + 2\zeta_\phi \omega_{n\phi} \dot{\sigma}_\phi + \omega_{n\phi}^2 \sigma_\phi$ and $S_{\omega_m} = \sigma_{\omega_m}^{(2)} + 2\zeta_{\omega_m} \omega_{n\omega_m} \dot{\sigma}_{\omega_m} + \omega_{n\omega_m}^2 \sigma_{\omega_m}$,

with

$$\begin{aligned} K_\phi &= \left[\sigma_\phi^{(2)}(0) 0 \dot{\sigma}_\phi(0) 0 \sigma_\phi(0) 0 \right] \cdot K_\phi^{-1}, \\ K_{\omega_m} &= \left[\sigma_{\omega_m}^{(2)}(0) 0 \dot{\sigma}_{\omega_m}(0) 0 \sigma_{\omega_m}(0) 0 \right] \cdot K_{\omega_m}^{-1}, \end{aligned}$$

[1]The interest of a such feedback is that it allows to minimize gain values of the control discontinuous function.

with F being a $2r \times 2r$-dimensional stable matrix (strictly negative eigenvalues), T being a $2r \times 1$-dimensional vector and

$$\mathcal{K}_c = \begin{bmatrix} F^{r-1}T\sigma_c^{(r-j)}(0) & F^{r-1}e^{Ft_f}T & F^{r-2}T\sigma_c^{(r-j)}(0) \\ F^{r-2}e^{Ft_f}T \cdots T\sigma_c^{(r-j)}(0) & e^{Ft_f}T \end{bmatrix}, \tag{11.23}$$

with $c := \phi, \omega_m$.

11.4.2 Discontinuous Input

The control discontinuous input reads as

$$\begin{pmatrix} \dot{v}_{sd} & \dot{v}_{sq} \end{pmatrix}^T = \begin{pmatrix} -\alpha_\phi.\text{sign}(S_\phi) & -\alpha_{\omega_m}.\text{sign}(S_{\omega_m}) \end{pmatrix}^T. \tag{11.24}$$

From equation (11.23), it yields

$$\begin{pmatrix} \dot{S}_\phi & \dot{S}_{\omega_m} \end{pmatrix}^T = \varphi_1 + \varphi_2 \cdot \dot{v} - \begin{pmatrix} \chi_\phi & \chi_{\omega_m} \end{pmatrix}^T. \tag{11.25}$$

By using the same method as Theorem 3 in Traore *et al*. (2008), it yields that there exist gains α_ϕ and α_{ω_m} such that

$$\dot{S}_\phi S_\phi \leq -\eta_\phi |S_\phi|, \quad \dot{S}_{\omega_m} S_{\omega_m} \leq -\eta_{\omega_m} |S_{\omega_m}|,$$

to obtain the convergence to the sliding surfaces.

11.5 Adaptive Interconnected Observers Design

In this section, an observer is designed to estimate the unmeasurable variables of the IM. However, under different operation conditions of the IM some difficulties are present. One the most important difficulties is the observability problem at low speed. However, few studies have highlighted this problem of unobservability. In Canudas *et al*. (2000), Ibarra-Rojas *et al*. (2004), Ghanes *et al*. (2006b), it is shown that there is observability lost when excitation voltages frequency is zero and rotor speed is constant. Nevertheless, in the literature, some sensorless algorithms are tested and evaluated at high and low speed (Ghanes *et al*. 2006a; Montanari and Tilli 2006).

Then, taking into account the observation problem, an adaptive interconnected observer is designed for the sensorless IM to estimate speed, flux, load torque, and stator resistance.

Now, considering system (11.1) and from the previous assumptions, the model can be extended by the equations

$$\dot{T}_l = 0, \qquad \dot{R}_s = 0.$$

Then, the extended IM model can be represented as the interconnection between subsystems (11.26) and (11.27).

$$\Sigma_1 : \left\{ \dot{X}_1 = A_1(X_2, y)X_1 + g_1(u, y, X_2, X_1) + \Phi T_l \ , \right. \tag{11.26}$$

$$\Sigma_2 : \left\{ \dot{X}_2 = A_2(X_1)X_2 + g_2(u, y, X_1, X_2) \ . \right. \tag{11.27}$$

$y_1 = C_1X_1$, $y_2 = C_2X_2$, $X_1 = (i_{sd}\omega_m R_s)^T$, $X_2 = (i_{sq}\phi_{rd}\phi_{rq})^T$ are the states, $u = (v_{sd}v_{sq})^T$ is the input, and $y = (i_{sd}i_{sq})^T$ is the output of the IM model, T_l is considered as a parameter to be identified by the adaptive part of the observer.

Remark 11.5.1 *Furthermore, the IM physical operation domain $\mathcal{D}$ is defined by the set of values*

$$\mathcal{D} = \{X \in R^6 \mid |\phi_{rd}| \leq {\Phi_d}^{max}, |\phi_{rq}| \leq {\Phi_q}^{max}, |i_{sd}| \leq {I_d}^{max}, |i_{sq}| \leq {I_q}^{max}, \\ |\omega_m| \leq \omega_m^{max}, |R_s| \leq {R_s}^{max}\},$$

where $X = (\phi_{rd}, \phi_{rq}, i_{sd}, i_{sq}, \omega_m, T_l, R_s)$, and ${\Phi_d}^{max}$, ${\Phi_q}^{max}$, ${I_d}^{max}$, ${I_q}^{max}$, ω_m^{max}, ${T_l}^{max}$, and ${R_s}^{max}$ are respectively the actual maximum values for the fluxes, currents, speed, torque load, and stator resistance determined from the motor specification sheet. This domain is important because it allows to determine the domain of the realistic initial conditions for the observer-controller scheme. Moreover, the bounds of the motor parameters uncertainties are known.

From equations (11.26) and (11.27), we can easily verify that the matrix $A_1(X_2, y)$ is globally Lipschitz with respect to X_2, and matrix $A_2(X_1)$ is globally Lipschitz with respect to X_1. The terms $g_1(u, y, X_2, X_1)$ and $g_2(u, y, X_2, X_1)$ are globally Lipschitz with respect to X_2, X_1 and uniformly with respect to (u, y), as long as the *IM* state remains in $\mathcal{D}$. Then, the nominal adaptive interconnected observers for equations (11.26) and (11.27) are given by equations (11.28) and (11.29):

$$O_1 : \begin{cases} \dot{\widehat{X}}_1 = A_1(\widehat{X}_2, y)\widehat{X}_1 + g_1(u, y, \widehat{X}_2, \widehat{X}_1) + \Phi\hat{T}_l \\ \qquad\quad + \left(\varpi\Lambda S_3^{-1}\Lambda^T + \Gamma S_1^{-1}\right) C_1^T(y_1 - \hat{y}_1) + KC_2^T(y_2 - \hat{y}_2), \\ \dot{\hat{T}}_l = \varpi S_3^{-1}\Lambda^T C_1^T(y_1 - \hat{y}_1) + B_1(\widehat{X}_2)(y_2 - \hat{y}_2) + B_2(\widehat{X}_2)(y_1 - \hat{y}_1), \\ \dot{S}_1 = -\theta_1 S_1 - A_1^T(\widehat{X}_2, y)S_1 - S_1A_1(\widehat{X}_2, y) + C_1^T C_1, \\ \dot{S}_3 = -\theta_3 S_3 + \Lambda^T C_1^T C_1\Lambda, \\ \dot{\Lambda} = \left(A_1(\widehat{X}_2, y) - \Gamma S_1^{-1}C_1^T C_1\right)\Lambda + \Phi, \end{cases} \tag{11.28}$$

$$O_2 : \begin{cases} \dot{\widehat{X}}_2 = A_2(\widehat{X}_1)\widehat{X}_2 + g_2(u, y, \widehat{X}_1, \widehat{X}_2) + S_2^{-1}C_2^T(y_2 - \hat{y}_2), \\ \dot{S}_2 = -\theta_2 S_2 - A_2^T(\widehat{X}_1)S_2 - S_2A_2(\widehat{X}_1) + C_2^T C_2, \end{cases} \tag{11.29}$$

with $\hat{y}_1 = C_1\widehat{X}_1$, $\hat{y}_2 = C_1\widehat{X}_2$, $\widehat{X}_2 = (\hat{\imath}_{sd}\hat{\omega}_m\hat{R}_s)^T$, and $\widehat{X}_2 = (\hat{\imath}_{sq}\hat{\phi}_{rd}\hat{\phi}_{rq})^T$ are the estimated state variables, respectively, of X_1 and X_2. θ_1, θ_2, and θ_3 are positive constants, S_1 and S_2 are symmetric positive definite matrices, with $S_3(0) > 0$, $B_1(\widehat{X}_2) = km\hat{\phi}_{rd}$, $B_2(\widehat{X}_2) = -km\hat{\phi}_{rq}$, $\Gamma = diag(1, 1, \alpha)$, $KC_2^T = (-k_{c1}, -k_{c1}, 0)^T$, where $k, k_{c1}, k_{c2}, \alpha$, and ϖ are positive constants. Note that $(\varpi\Lambda S_3^{-1}\Lambda^T C_1^T + \Gamma S_1^{-1}C_1^T)$ and KC_2^T are the gains of observer (11.28) and $S_2^{-1}C_2^T$ is the gain of observer (11.29).

Following Remark 11.5.1, one now assumes that all parameters of IM are uncertain and bounded with well-known values. In order to analyze the robustness of the observer under parametric uncertainties, systems (11.26) and (11.27) are now written in the following form:

$$\Sigma_{1,\Delta} : \begin{cases} \dot{X}_1 = A_1(X_2, y)X_1 + g_1(u, y, X_2, X_1) + \Phi T_l + \Delta A_1(X_2, y) \\ \qquad\quad +\Delta g_1(u, y, X_2, X_1), \end{cases} \tag{11.30}$$

$$\Sigma_{2,\Delta} : \left\{ \dot{X}_2 = A_2(X_1)X_2 + g_2(u, y, X_1, X_2) + \Delta A_2(X_1) + \Delta g_2(u, y, X_1, X_2) \right., \tag{11.31}$$

with $y_1 = C_1X_1$, $y_2 = C_2X_2$, where $\Delta A_1(X_2, y)$, $\Delta A_2(X_1)$, $\Delta g_1(u, y, X_2, X_1)$, and $\Delta g_2(u, y, X_1, X_2)$ are, respectively, the uncertain terms of $A_1(X_2, y)$, $A_2(X_1)$, $g_1(u, y, X_2, X_1)$, and $g_2(u, y, X_1, X_2)$.

Let us define the estimation errors as

$$\epsilon_1' = X_1 - \widehat{X}_1, \quad \epsilon_2 = X_2 - \widehat{X}_2, \quad \epsilon_3 = T_l - \hat{T}_l.$$

From equations (11.30), (11.31) and (11.28), (11.29) and applying the transformation $\epsilon_1 = \epsilon_1' - \Lambda\epsilon_3$, the dynamics of the estimation errors are given by

$$\begin{aligned} \dot{\epsilon}_1 &= \left[A_1(\widehat{X}_2, y) - \Gamma S_1^{-1}C_1^T C_1 + \Lambda\Psi_2\right]\epsilon_1 + [A_1(X_2, y) \\ &\quad +\Delta A_1(X_2, y) - A_1(\widehat{X}_2, y)]X_1 + g_1(u, y, X_2, X_1) + \Lambda\Psi_2\Lambda\epsilon_3 \\ &\quad +\Delta g_1(u, y, X_2, X_1) - g_1(u, y, \widehat{X}_2, \widehat{X}_1) + (\Psi_2\Lambda - K')\epsilon_2, \\ \dot{\epsilon}_2 &= \left[A_2(\widehat{X}_1) - S_2^{-1}C_2^T C_2\right]\epsilon_2 + [A_2(X_1) + \Delta A_2(X_1) - A_2(\widehat{X}_1)]X_2 \\ &\quad +g_2(u, y, X_1, X_2) - g_2(u, y, \widehat{X}_1, \widehat{X}_2) + \Delta g_2(u, y, X_1, X_2), \\ \dot{\epsilon}_3 &= -\left[\varpi S_3^{-1}\Lambda^T C_1^T C_1\Lambda + \Psi_2\Lambda\right]\epsilon_3 - \left[\varpi S_3^{-1}\Lambda^T C_1^T C_1 + \Psi_2\right]\epsilon_1 - \Lambda\Psi_1\epsilon_2, \end{aligned} \tag{11.32}$$

where $\Psi_1 = B_1(\widehat{X}_2)C_2$, $\Psi_2 = B_2(\widehat{X}_2)C_1$, and $K' = KC_2^T C_2$.

Consider the following candidate Lyapunov function $\sum_{i=1}^{3} V_i$, where $V_i = \epsilon_i^T S_i\epsilon_i$. Taking the time derivative of V_o and by using equation (11.32), and by developing some computations, implies

$$\dot{V}_o \leq -\delta V_o + \mu\psi\sqrt{V_o}, \tag{11.33}$$

where μ is a constant associated with the nonlinear terms that are Lipschitz and $\psi > 0$ (see Traore *et al*. (2008) for the computations details). Then, using practical stability results, it follows that the observation error is uniformly practically stable.

Remark 11.5.2 *For the FOC, by definition it is necessary to have $\phi_{rq} \equiv 0$. The d-axis angle θ_m can be computed from the stator frequency (ω_s):*

$$\dot{\theta}_m = \omega_s = p\omega_m + a\frac{L_m}{\phi_{rd}} i_{sq}. \tag{11.34}$$

The estimation $\hat{\theta}_m$ of the d-axis angle is then computed by

$$\dot{\hat{\theta}}_m = \hat{\omega}_s = p\hat{\omega_m} + a\frac{L_m}{\hat{\phi}_{rd}} i_{sq} - \frac{(i_{sq} - \hat{i}_{sq})}{\beta_1 \hat{\phi}_{rd}} k_{\omega_s}. \tag{11.35}$$

Then, the error dynamic of the estimation is given by

$$\dot{\epsilon}_{\theta_m} = p\epsilon_{\omega_m} - \frac{aL_m i_{sq}}{\phi_{rd}\hat{\phi}_{rd}} \epsilon_{\phi_{rd}} + \frac{k_{\omega_s}}{\beta_1 \hat{\phi}_{rd}} \epsilon_{i_{sq}}, \tag{11.36}$$

with $\epsilon_{\theta_m} = \theta_m - \hat{\theta}_m$, $\epsilon_{\omega_m} = \omega_m - \hat{\omega_m}$, $\epsilon_{\phi_{rd}} = \phi_{rd} - \hat{\phi}_{rd}$, and $\epsilon_{i_{sq}} = i_{sq} - \hat{i}_{sq}$. The gain k_{ω_s} can be tuned to ensure the convergence to zero for the nominal case or to a small ball for the uncertain case for which the radius can be balanced by the gain tuning.

Remark 11.5.3 *Since the observability properties are lost at very low speed, it is well known that it is impossible to reconstruct the state of the IM that asymptotically converges to indistinguishable trajectories (Ibarra-Rojas et al. 2004). However, under these trajectories, it is possible to design an observer whose, performances are acceptable even if the asymptotic stability can not be guaranteed. Thus, it is necessary to use a notion of stability that is more suitable than asymptotic stability, this is the practical stability (Lakshmikantham et al. 1990).*

Then, using Lyapunov-like arguments, an analysis of stability has been presented in Traore et al. (2012), where sufficient conditions have been obtained in order to ensure the practical stability of the closed-loop system.

11.6 Experimental Results

The experimental results are obtained using an experimental setup described in Benchmark (2005) and shown in Figure 11.1. The experimental setup and observer-controller scheme is given in Figure 11.2.

IM characteristics

The motor parameters values are: nominal rate power 1.5 kW, nominal angular speed 1430 rpm, number of pole pairs 2, nominal voltage 220 V, nominal current 7.5 A.

The identified parameters values are $R_s = 1.633\ \Omega$, $L_m = 0.099$ H, $R_r = 0.93\ \Omega$, $J = 0.0111\ \text{Nms}^2/\text{rad}$, $L_s = 0.142$ H, $F_v = 0.0018$ Nms/rad, $L_r = 0.076$ H.

Figure 11.1 Experimental setup. (For a color version of this figure, please see color plates.)

Hardware characteristics
To implement the controllers and observer, the setup hardware consists in the following components:

1. Three-phase inverter operated with a symmetrical pulse-width modulation (PWM) technique with 5 kHz switching frequency.
2. A permanent-magnet synchronous motor controlled by an industrial drive to provide a desired load torque.

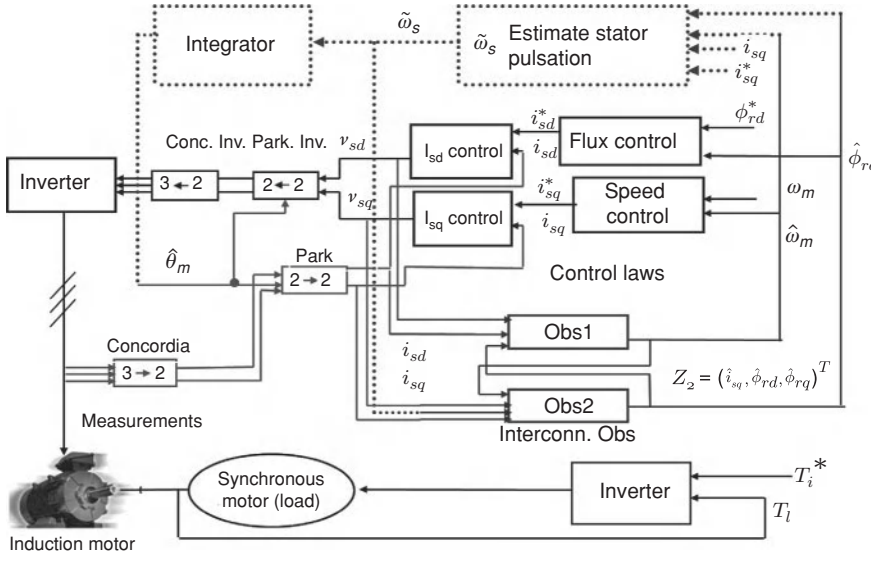

Figure 11.2 Experimental setup and observer-control scheme. (For a color version of this figure, please see color plates.)

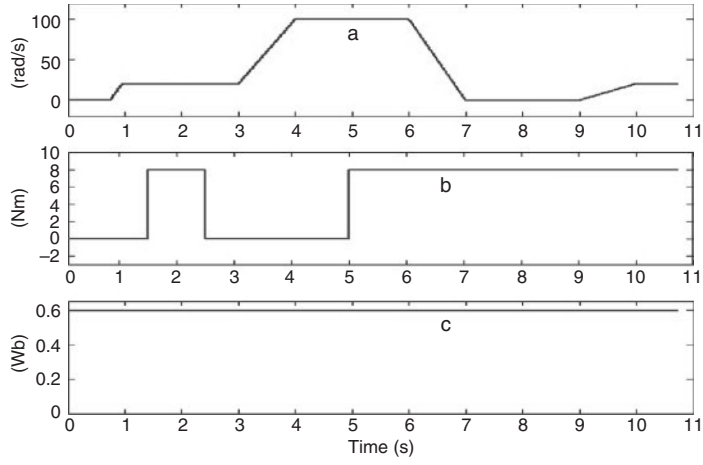

Figure 11.3 Benchmark trajectories. a, reference speed ω_m (rad/s); b, load torque disturbance T_l (Nm); c, reference flux ϕ^*_{rd} (Wb)

3. A custom floating-point digital signal processor dSPACE (DS1103) board, and its interface. The dSPACE board performs data acquisition (two stator currents, DC-link voltage, load torque and rotor speed, by means of a 512 ppr incremental encoder (only for monitoring purposes), computes the control algorithm and generates the PWM signals for the inverter.

Software characteristics
The software associated with the data acquisition and control system are:

1. Matlab/Simulink,
2. a user-developed interface between the Simulink program and the dSPACE system board.

Benchmark trajectories
The sensorless trajectories of the benchmark are such that (see Figure 11.3): after the reference speed is carried to 20 rad/s and from 1.5 to 2.5 s the load torque is applied. This first step allows to test the performances and the robustness of the controller without mechanical sensors at low speed but under observable conditions. From 3 to 4 s, the speed is carried to its nominal value (100 rad/s) and remains constant until $t = 6$ s. Again the load torque is applied from 5 s. This second step is defined to test the controller behavior during a great transient speed. Then, the motor is driven to reach a negative constant low-speed value from 7 to 9 s. This speed is chosen to obtain a stator pulsation equal to zero. This last step allows to illustrate the IM unobservability phenomena (from $t = 7$ s to $t = 9$ s). Finally, the IM is driven in order to leave the unobservability conditions.

All control and observer algorithms are computed with a sampling rate of 200 μs.

Interconnected adaptive observer Tuning
The Interconnected Adaptive observer is implemented to estimate the flux and the rotor speed and to identify the load torque and the stator resistance.

For the observer design, the gains are chosen as follows: $\alpha = 50$, $\varpi = 10$, $k = 0.16$, $k_{c1} = 450$, $K_{c2} = 0.5$, $\theta_1 = 5000$, $\theta_2 = 7000$, and $\theta_3 = 10^{-9}$.

Rotor speed and flux amplitude are provided by observer (11.28) and (11.29). Stator resistance observer is initialized as $R_{s0} = 1.9\ \Omega$. The initial value of ϕ_{rd} in the observer is $\phi_{rd0} = 0.1$ Wb.

Now, experimental results for the two proposed-observer schemes are given for nominal conditions and robustness test cases, then compared.

11.6.1 Integral Backstepping Control and Adaptive Observer

To implement the integral backstepping controller the following gains of the controller were chosen as follows: $K_{\omega_m} = 200\ \text{s}^{-1}$, $K_\phi = 1100\ \text{s}^{-1}$, $K_{id} = 550\ \text{s}^{-1}$, $K'_{id} = 20\ \text{s}^{-1}$, $K''_{id} = 34\ \text{s}^{-1}$, $K_{iq} = 1200\ \text{s}^{-1}$, $K'_{iq} = 10\ \text{s}^{-1}$, $K''_{iq} = 35\ \text{s}^{-1}$, and $k_{\omega_s} = 90$ rad s Ω^2.

Nominal case

The experimental responses obtained by considering the nominal case with identified parameters are shown on Figure 11.4. Notice the good performance of the proposed scheme that maintains the speed close to the desired reference even though the presence of disturbance (load torque). Notice that on the experimental setup, the load torque is measured to compare it with the value provided by the observer.

Note that, for experimental test, "nominal case" means with the use of the identified parameters (thus with already errors on parameters). The estimated load torque (Figure 11.4d) converges to the measured load torque (Figure 11.4c) under conditions of observability and at

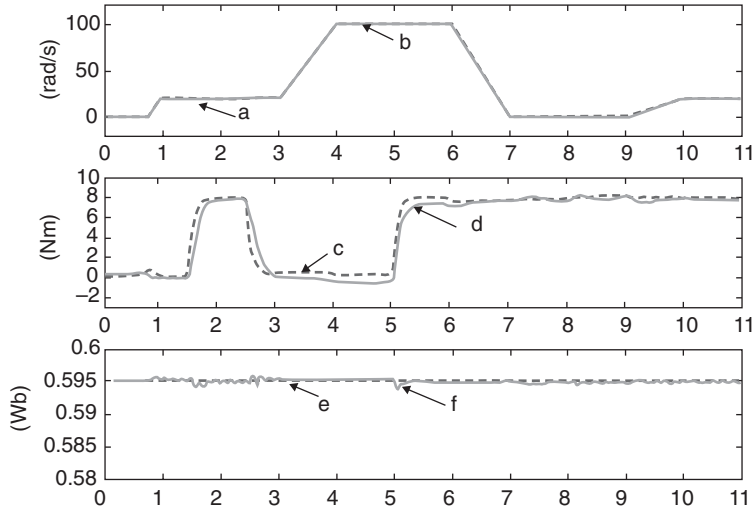

Figure 11.4 Integral backstepping control (IBC), experimental results for nominal case versus time (s); a, c, measured speed and torque; b, d, f, estimated speed, torque and flux; e, reference flux

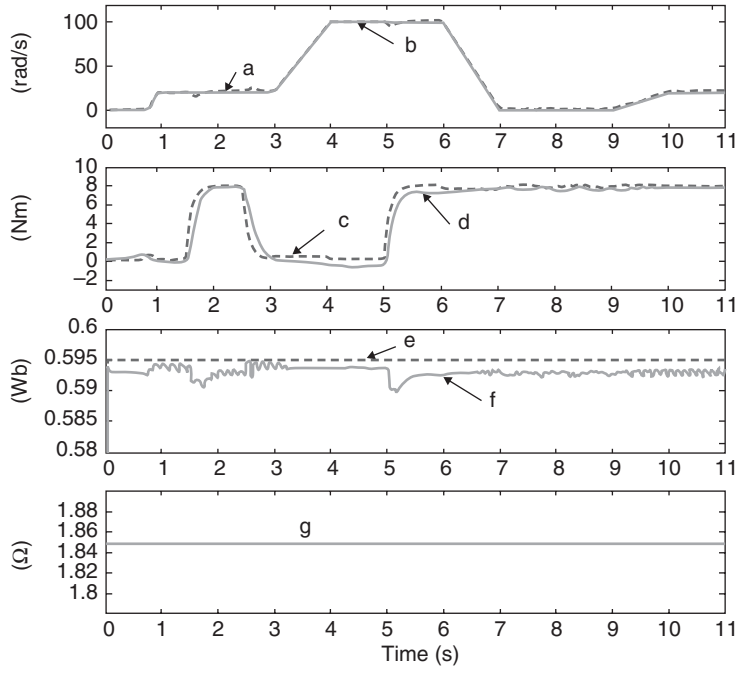

Figure 11.5 Integral backstepping control (IBC) +50% for R_r; a, c, measured speed and load torque; e, reference flux; b, d, f, g, observed speed, load torque, flux(ϕ_{rd}), and stator resistance

very low frequency (conditions of unobservability between 7 and 9 s). Nevertheless, it shows a small static error when the motor speed increases (between 4 and 6 s).

The following cases are experimented under parameters variations for robustness tests:

+50% rotor resistance variation (R_r)

In Figures 11.5 and 11.6 the results for a +50% variation of R_r that are included in the observer-controller parameters are shown. These results are similar to those obtained for the nominal case (Figure 11.4). following can be noted:

- the estimated speed (Figure 11.5b) converges to the measured one (Figure 11.5a),
- a good tracking for the flux (Figures 11.5e and f) and a good estimation of the load torque (Figures 11.5c and d),
- the estimation error for the flux angle (ϕ_{rq}) is almost zero (Figure 11.6d),
- the estimation of the stator resistance is always good (Figure 11.5g).

+10% rotor inductance variation (L_r)

Figures 11.7 and 11.8 display the good performances for the case of a +10% rotor inductance variation applied at the same time for the observer and the controller parameters. A good

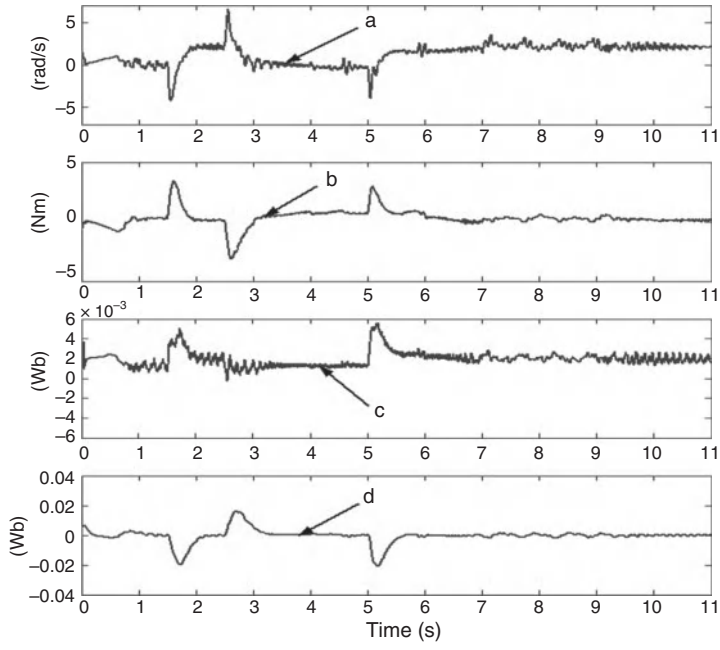

Figure 11.6 Integral backstepping control (IBC) +50% for R_r; a, b, speed and load torque estimation errors; c, d, flux tracking error (ϕ_{rd}) and flux angle error (ϕ_{rq}) du flux

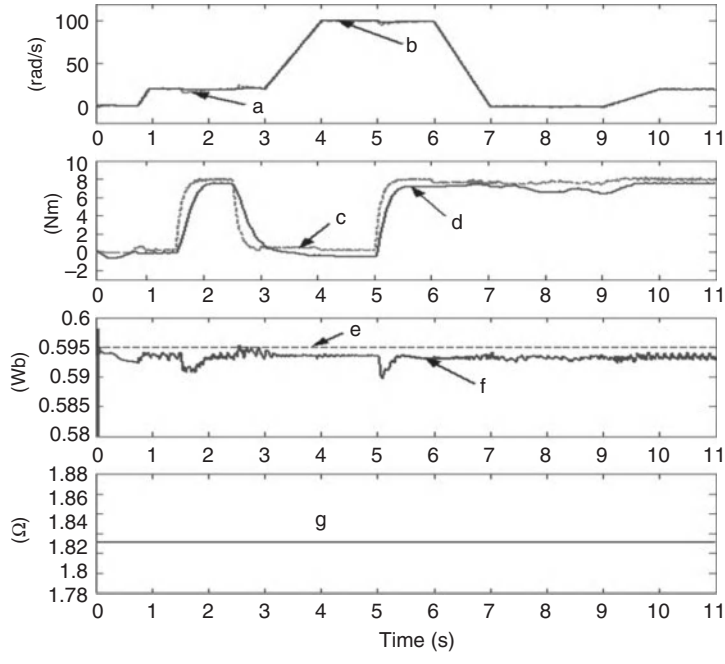

Figure 11.7 Integral backstepping control (IBC), +10% of L_r; a, c, measured speed and load torque; e, reference flux; b, d, f, g, observed speed, load torque, flux(ϕ_{rd}), and stator resistance

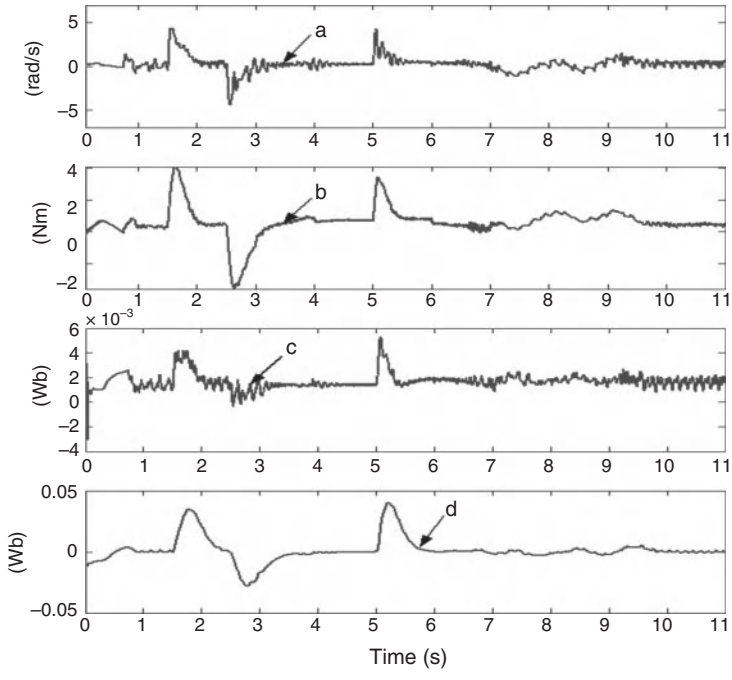

Figure 11.8 Integral backstepping control (IBC), +10% of L_r; a, b, speed and load torque estimation errors; c, d, flux tracking error (ϕ_{rd}) and flux angle error(ϕ_{rq})

tracking is obtained with disturbance rejection. The flux angle is well oriented Figure 11.8d even when the load torque is applied.

+10% stator inductance variation (L_s)
A robustness test is given by a +10% variation on the stator inductance for the controller and the observer parameters (Figures 11.9 and 11.10). The estimated load torque converges even for the unobservable areas (Figure 11.9c) to the measured load torque (Figure 11.9d). In addition, there are not many oscillations of the IM speed for the high speed (Figure 11.10a for $t = 5$ s) and a good flux angle (Figure 11.10d). Nevertheless oscillations appear on the speed and the flux when the load torque is canceled for slow speed (Figures 11.9a–f for $t = 2.5$ s). A good stator resistance estimation is obtained (Figure 11.9g). It is clear that the IBC has good robutness performances when associated to the adaptive interconnected observer.

> The conclusion is that, in all cases, the speed and the flux track the desired references, which shows the robustness of the proposed scheme under parametric uncertainties and unknown load torque disturbance even in the unobservable case.

11.6.2 High-Order Sliding-Mode Control and Adaptive Observer

To optimize the behavior and the performances of the motor, two parameters tuning have been chosen: the first one to induce the reaching of the motor flux, the second one to reject

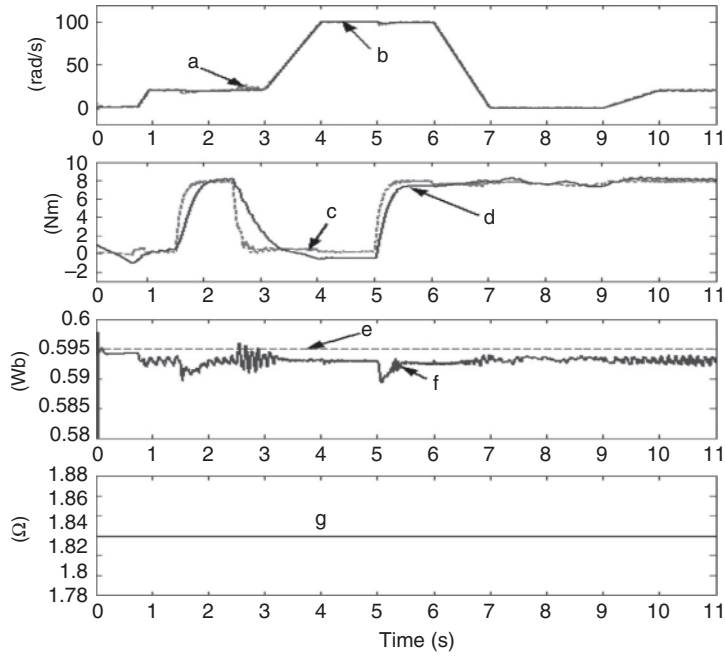

Figure 11.9 Integral backstepping control (IBC), +10% of L_s; a, c, measured speed and load torque; e, reference flux; b, d, f, g, observed speed, torque, flux (ϕ_{rd}), and stator resistance

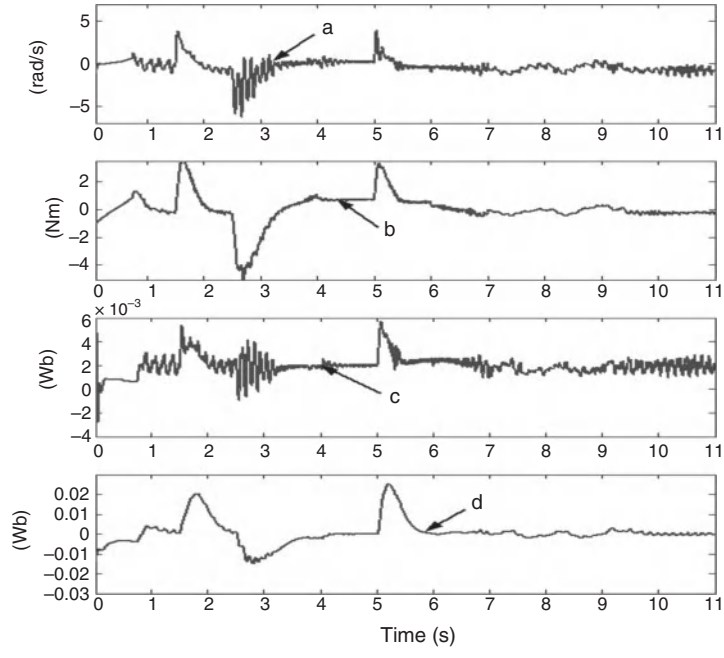

Figure 11.10 Integral backstepping control (IBC), +10% of L_s; a, b, speed and load torque estimation errors; c, d, flux tracking error (ϕ_{rd}) and flux angle error (ϕ_{rq})

disturbance (such as load torque) and to ensure high-level accuracy for the trajectory tracking. Then, the HOSM controller parameters are chosen such that $t_F = 0.3$ s and

- $t \leq 5$ s. $\zeta_\phi = 0.35$, $\omega_{n\phi} = 316$ rad/s, $\alpha_\phi = 6.10^4$, $\zeta_{\omega_m} = 1.56$, $\omega_{n\omega_m} = 32$ rad/s, $\alpha_{\omega_m} = 8.10^4$,
- $t > 5$ s. $\zeta_\phi = 0.35$, $\omega_{n\phi} = 447$ rad/s, $\alpha_\phi = 15.10^4$, $\zeta_{\omega_m} = 0.7$, $\omega_{n\omega_m} = 200$ rad/s, $\alpha_{\omega_m} = 8.10^6$

Nominal Case

The experimental results of the nominal case with identified parameters (except stator resistance) are shown in Figure 11.11. These figures show the good performance of the complete system observer-controller in trajectory tracking and disturbance rejection. The estimated motor speed (Figure 11.11b) converges to the measured speed (Figure 11.11a) near and under conditions of unobservability. It is the same conclusion for estimated flux (Figure 11.11f) with respect to reference flux (Figure 11.11e). The estimated load torque (Figure 11.11d) converges to the measured load torque (Figure 11.11c), under conditions of observability and at very low frequency (conditions of unobservability) (between 7 and 9 s). Nevertheless, it shows a small static error when the motor speed increases (between 4 and 6 s). The load torque is well

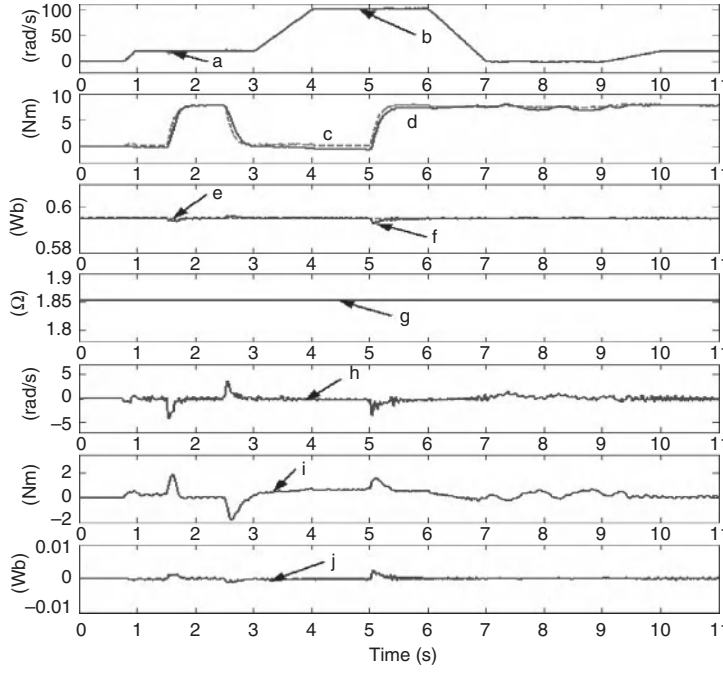

Figure 11.11 HOSM, nominal case; a, b, estimated and measured speeds; c, d, measured and estimated load torques; e, f, reference and estimated fluxes; g, estimated stator resistance; h, speed error; i, torque error; j, flux error versus time

rejected excepted at the time when it is applied (Figure 11.11h and j at time 1.5 s and 5 s) and when it is removed (Figure 11.11h, j at time 2.5 s). In Figure 11.11g, it can be viewed that the stator resistance estimation remains almost constant despite noise and transient dynamics of speed and load torque. This test shows the capability of the proposed controller to guarantee flux and speed tracking of slowly varying speed reference with excitation frequency close to zero (between 7 and 9 s).

Robustness Tests

+50% *rotor resistance variation (R_r):* The robustness of the observer-controller scheme is confirmed by the result obtained with rotor resistance variation (+50%) applied to the observer and controller parameters Figure 11.12 (evaluation of robustness with respect to inductances variations has also been successfully made). The increase of the rotor resistance value does not affect the performance of the speed trajectories tracking, when the observability conditions of are verified. It shows a static error when the motor is under unobservable condition (between 7 and 9 s) (Figure 11.12a, b). The static error transitory increases when the load torque is applied at time 1.5 s and 5 s (Figure 11.12h, j).

+10% *rotor inductance variation (L_r):* Robustness tests are made with variation of rotor inductance (+10%). The results of these tests are shown on Figure 11.13. The rotor inductance

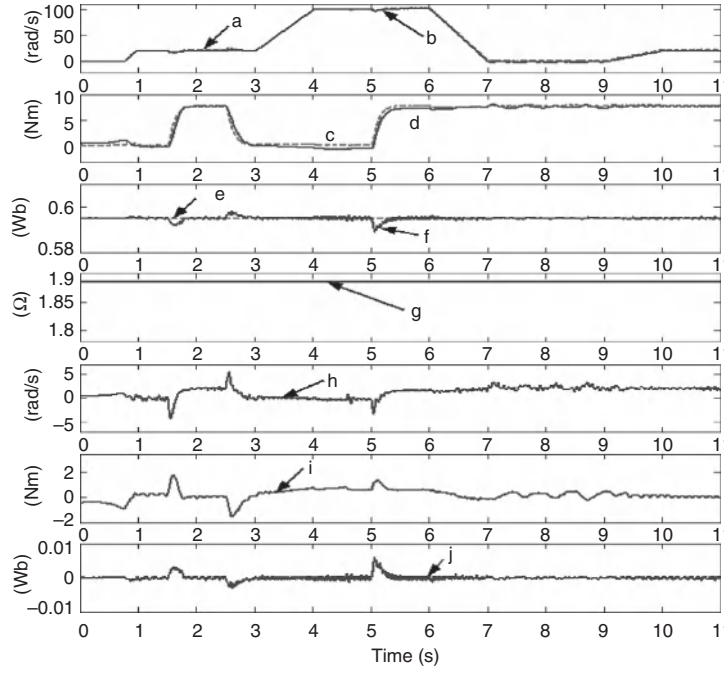

Figure 11.12 HOSM, rotor resistance variation (+50%); a, b, estimated and measured speeds; c, d, measured and estimated load torques; e, f, reference and estimated fluxes; g, estimated stator resistance; h, speed error; i, torque error; j, flux error versus time

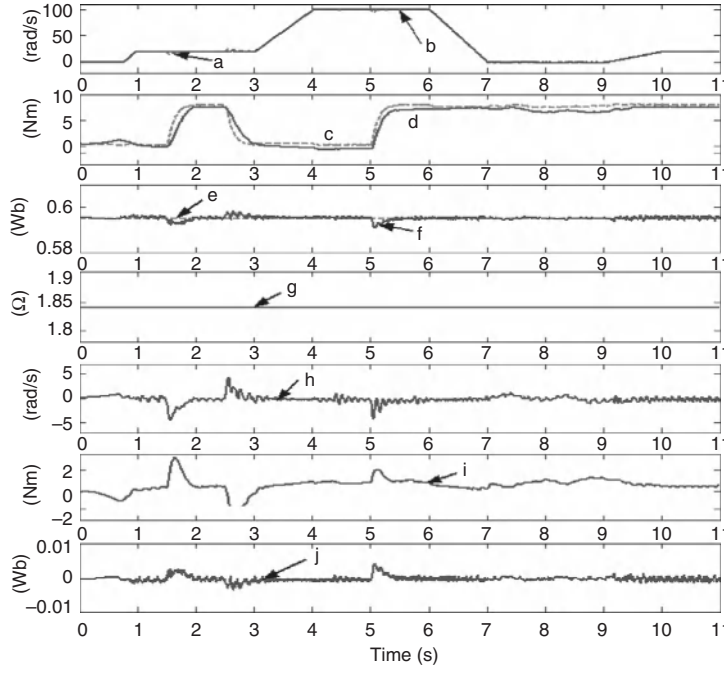

Figure 11.13 HOSM, rotor inductance variation (+10%); a, b, estimated and measured speeds; c, d, measured and estimated load torques; e, f, reference and estimated fluxes; g, estimated stator resistance; h, speed error; i, torque error; j, flux error versus time

does not affect the performances of both observer-controller schemes. It appears a small oscillation at the time when the load torque is applied (Figure 11.13a, b) at time 5 s.

+10% *stator inductance variation (L_s):* Last robustness tests are made with variation of stator inductance (+10%). The results of these tests are shown on Figure 11.14. By analyzing this figure, we can see that the stator inductance variation does not affect the performances of both observer-controller schemes. Nevertheless, it shows a small oscillation at the time when the load torque is applied (Figure 11.14a and b) at time 5 s.

11.7 Robust Nonlinear Controllers Comparison

In this section, we compare the performance of the two proposed control approaches. To validate the performance of such controllers, we take into account the following criterions:

- Practical implementation
- Robustness under uncertainties
- Computational effort
- Simplicity to tune
- Transient performances
- Structural properties and knowledge of the process control.

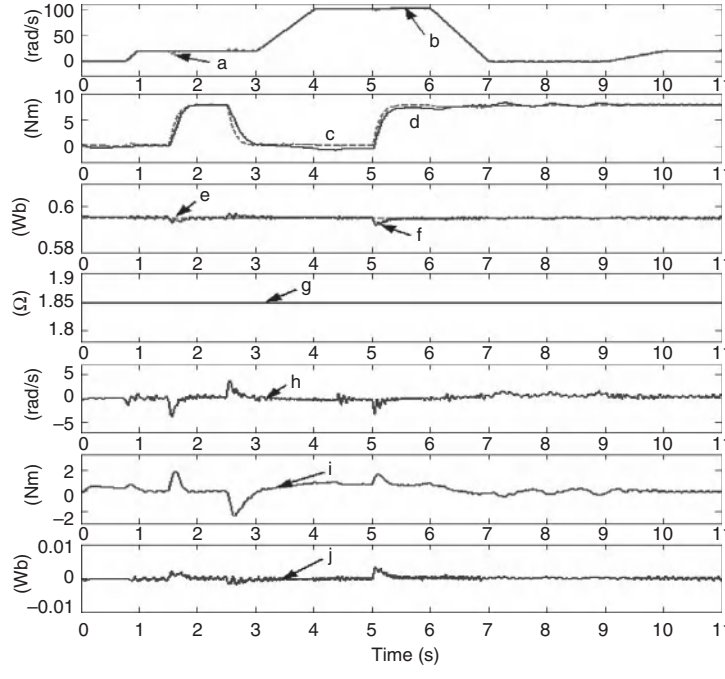

Figure 11.14 HOSM; stator inductance variation (+10%); a, b, estimated and measured speeds; c, d, measured and estimated load torques; e, f, reference and estimated fluxes; g, estimated stator resistance; h, speed error; i, torque error; j, flux error versus time

The HOSM and the IBCs are implemented and validated experimentally on the same IM setup and use the same electromechanical model for the control design.

11.7.1 High-Order Sliding-Mode Control

It is well known that the success of the SM control applied to IM drives is due to its disturbance rejection and robustness. The HOSM control introduced in Section 11.4 is characterized by:

Advantages

1. *Convergence properties:* Finite-time convergence is achieved. The time of convergence can be fixed a priori.
2. Stability and robustness despite uncertainties.

Limitations

1. Tuning difficulty.
2. *Computational effort:* The control design requires a mayor computational effort and difficulties for the experimental implementation.
3. *Transient performance:* High-frequency signal components.

11.7.2 Integral Backstepping Control

The proposed IBC design is a robust recursive design methodology. The construction of the control laws and Lyapunov functions is easy and systematic.

Advantages

1. *Recursive design procedure:* Its flexibility to avoid cancelations of useful nonlinearities and to pursue the objectives of stabilization and tracking.
2. *Convergence properties:* Asymptotic convergence is achieved.
3. *Stability with uncertainties:* Lyapunov arguments are used to prove stability and it is easy to built.
4. *Computational effort:* The control design is simple and easy to implement experimentally.
5. *Structural properties:* The integral term increases the robustness of the control.
6. *Transient performance:* Easy to tune.

Limitations

The backstepping methodology (with integral term or not) needs the knowledge of a sufficiently precise model.

11.7.3 Experimental Results: Comparison

From experimental results, the following observations can be made:

1. The same hardware and software are used to implement the different control laws on the same setup.
2. The transient performance is improved by using IBC.
3. Even if attenuated with respect to SM of order one, the HOSM controller leads to significative high-frequency content in the control signals.
4. The behavior of the IBC is more desirable since the chattering voltages and currents can damage the motor and hence shorten the longevity.
5. The price to pay for the elimination of the chattering is an important computation effort to achieve the tracking performance.

In Table 11.1, a computation time comparison is reported for the two controllers and the observer presented in this paper. Two other observers-controllers computation times are also

Table 11.1 Time computation comparison

Controller	Control time (μs)	Observation time (μs)
PI	10	20[a]
SM order 1	11	20[a]
Backstepping	12	34[b]
HOSM	35	34[b]

SM, sliding mode; HOSM, high-order sliding mode.
[a] Interconnected observer, [b] Adaptive interconnected observer.

given: an FOC-PI controller (Traore *et al*. 2007b) and a SM controller of order 1 (Traore *et al*. 2007a) associated to an interconnected oberver. Even though their computation times are lower for these observer-controller schemes, the global performances of these two controllers are weaker than the two controllers presented in this paper.

11.8 Conclusions

This study investigates two observer-control schemes based on two approaches: an HOSMC and an IBC, which are applied to the control of an IM without using mechanical sensors (position sensor, speed sensor, load torque sensor).

The major contributions of this study are summarized as follows:

1. An adaptive interconnected observer to estimate the rotor speed, the rotor fluxes, and the load torque even when nominal value of the external load disturbance is applied.
2. A comparative study to investigate the performances of the proposed control schemes in order to achieve good speed and flux trackings for IM without mechanical sensor under conditions of observability and unobservability. The advantages and limitations are analyzed in terms of: (a) practical implementation, (b) robustness under uncertainties, (c) computational effort, (d) simplicity to tune, (e) transient performances, (f) structural properties.
3. The implementation of the proposed control schemes on experimental setup with a significant sensorless control benchmark, has been presented. Finally, the robustness of the observer and controller have been tested under significant parameter variations.

This research has been partially supported by CONACYT Ciencia Basica No. 105799. CONACYT Estancias Sabaticas. SEP CASEP-CA-232 UANL.

References

Benchmark (2005) Lunam Université, Ecole Centrale de Nantes, IRCcyN www2.irccyn.ec-nantes.fr/BancEssai/

Blaschke F (1972) The principle of field orientation applied to the new trans-vector closed-loop control system for rotating field machine. *Siemens Review*, **93**, 217–220.

Canudas C, Youssef A, Barbot J, *et al.* (2000) Observability conditions of induction motors at low frequencies *IEEE Conference on Decision and Control*, Sydney, Australia.

Ghanes M, De Leon J, and Glumineau A (2006a) Novel controller for induction motor without mechanical sensor and experimental validation. *Proceedings of the 45th IEEE CDC*, Manchester Grand Hyatt Hotel San Diego USA, December 13–15, pp. 4008–4013.

Ghanes M, De Leon J, and Glumineau A (2006b) Observability study and observer-based interconnected form for sensorless induction motor. *Proceedings of the 45th IEEE CDC*, Manchester Grand Hyatt Hotel San DiegoUSA, December 13–15, pp. 1240–1245.

Holtz J (2002) Sensorless control induction motor drive. *Proceedings of the IEEE*, **90**, 1359–1394.

Ibarra-Rojas S, Moreno J, and Espinosa G (2004) Global observability analysis of sensorless induction motor. *Automatica*, **40**, 1079–1085.

Chiasson J (2005) *Modeling and High-Performance Control of Electrical Machines*. IEEE Press Series, Power Engineering. John Wiley & Sons.

Krstic M, Kanellakopoulos I, and Kolotovic P (1995) *Nonlinear and Adaptive Control Design*. John Wiley & Sons.

Laghrouche S, Plestan F, and Glumineau A (2006) *Practical Higher Order Sliding Mode Control: Optimal Control Based Approach and Application to Electromechanical Systems*. *Lecture Notes in Control and Information Science*, Vol. 334, pp. 169–191. Springer-Verlag.

Lakshmikantham V, Leela S, and Martynyuk A (1990) *Practical Stability of Nonlinear Systems*. World Scientific Publishing. ISBN 981020356X.

Lascu C, Boldea I, and Blaabbjerg F (2005) Very-low-speed variable-structure control of sensorless induction machine drives without signal injection. *IEEE Transactions on Industry Applications*, **41**(2), 591–598.

Levant A (2001) Universal siso sliding-mode controllers with finite-time convergence. *IEEE Transactions on Automatic Control*, **49-9**, 1447–1451.

Montanari M and Tilli A (2006) Sensorless control of induction motors based on high-gain speed estimation and on-line stator resistance adaptation. *Annual Conference of the IEEE Industrial Electronics Society*.

Plestan F, Glumineau A, and Laghrouche S (2008) A new algorithm for high order sliding mode control. *International Journal of Robust and Nonlinear Control, Special Issue*, **18**, 531–537.

Traore D, De Leon J, and Glumineau A (2012) Adaptive interconnected observer-based backstepping control design for sensorless induction motor. *Automatica*, **48**, 682–687.

Traore D, De Leon J, Glumineau A, and Loron L (2007a) Sliding mode controller design for sensorless induction motor: experimental test on low frequencies benchmark. *Proceeding of 7th IFAC Symposium on Nonlinear Control Systems*.

Traore D, De Leon J, Glumineau A, and Loron L (2007b) Speed sensorless field-oriented control of induction motor with interconnected observers: experimental tests on low frequencies benchmark. *IET Control Theory Applications*, **1-6** (10), 1681–1692.

Traore D, Plestan F, Glumineau A, and De Leon J (2008) Sensorless induction motor: high-order sliding-mode controller and adaptive interconnected observer. *IEEE Transactions on Industrial Electronics*, **55**(11), 3818–3827.

Utkin V (1993) Sliding mode control design principles and applications to electrical drives. *IEEE Transactions on Industry Electronics*, **40-1** (1), 23–36.

Zhang Y, Changxi J, and Utkin V (2000) Sensorless sliding-mode control of induction motors. *IEEE Transactions on Industrial Electronics*, **47-6**, 1286–1297.

12

Multiphase Induction Motor Control

Roberto Zanasi and Giovanni Azzone
Dipartimento di Ingegneria "Enzo Ferrari", Università di Modena e Reggio Emilia, Italy

12.1 Introduction

The interest in multiphase variable-speed induction machines is considerably increased during the last few years (see Jones and Levi 2002; Levi *et al.* 2007), especially in the last two decades when the multiphase machines started to be considered as potential alternative to the conventional three-phase machines. The reasons can be easily pointed out considering the advantages and benefits of the multiphase motors with respect to the conventional three-phase ones, such as reduction of the torque pulsations, improved reliability, and higher power in terms of provided mechanical torque. Combining all these enhancements with the intrinsic induction motors robustness and versatility, it is quite clear that their use in industrial applications has seen a substantial growth worldwide. Nowadays there are several applications where the use of these kinds of machines is considerably growing: electrical and hybrid vehicles, aerospace applications, electrical ship propulsion, locomotive traction, high-power industrial applications, and in general applications where high reliability is demanded. Moreover, the advantages of the odd order harmonic injection, existing in concentrated-winding multiphase machines (see Toliyat *et al.* 1991a, 1991b), are well known in literature for providing a higher torque density and adding additional degrees of freedom especially in terms of motor control. In literature, different field-oriented control strategies addressed to induction motors with a specific number of stator and rotor phases have been discussed, especially for five-phase machines (see, for instance, Xu *et al.* 2001, 2002, Pereira *et al.* 2006; Duran *et al.* 2008).

This chapter presents a new complex dynamic model of a multiphase induction motor considering an arbitrary number of stator and rotor phases and including the odd order harmonic injection. Starting from the machine equations, the indirect rotor field-oriented

AC Electric Motors Control: Advanced Design Techniques and Applications, First Edition. Edited by Fouad Giri.

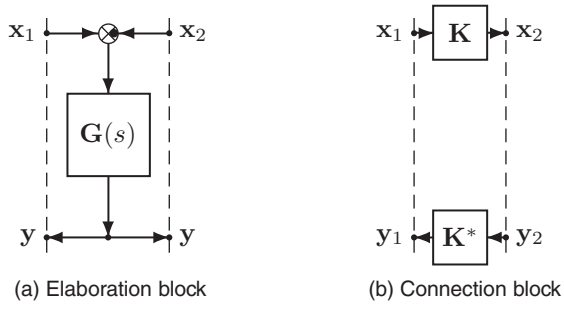

Figure 12.1 POG main blocks

control (IRFOC) is extended to the multiphase general case. Finally, some simulation results are presented in the specific case of a five-phase induction motor.

12.2 Power-Oriented Graphs

The power-oriented graphs technique (hereafter called POG) (see Zanasi 1991; Morselli and Zanasi 2006; Zanasi 2010), is a graphical energy-based technique particularly suitable for modeling dynamic physical systems. The POG block schemes are normal block diagrams combined with a particular modular structure essentially based on the use of the two blocks shown in Figure 12.1: the *elaboration block* stores and/or dissipates energy (i.e., springs, masses, dampers, capacities, inductances, resistances, etc.); the *connection block* redistributes the power within the system without storing nor dissipating energy (i.e., any type of gear reduction, transformers, etc.). The POG schemes can be used for both scalar and vectorial systems, described by both real and complex variables. In the vectorial case, $\mathbf{G}(s)$ and $\mathbf{K}$ are matrices: $\mathbf{G}(s)$ is always a square matrix of positive real transfer functions; matrix $\mathbf{K}$ can also be rectangular, time varying, and function of other state variables. The circle present in the elaboration block is a summation element where the black spot represents a minus sign that multiplies the entering variable. The connection block transforms the power variables imposing the constraint $\mathbf{x}_1^* \mathbf{y}_1 = \mathbf{x}_2^* \mathbf{y}_2$. The main feature of the POGs is to keep a direct correspondence between the dashed sections of the graphs and real power sections of the modeled systems: the real part of the scalar product $\mathbf{x}^* \mathbf{y}$ of the two *power vectors* $\mathbf{x}$ and $\mathbf{y}$ involved in each dashed line of a POG (see Figure 12.1) has the physical meaning of *the power flowing through that particular section*. From the POG schemes one can directly obtain the state space equations of the system: $\mathbf{L}\,\dot{\mathbf{x}} = -\mathbf{A}\mathbf{x} + \mathbf{B}\mathbf{u}$, $\mathbf{y} = \mathbf{B}^* \mathbf{x}$. This correspondence is shown in Figure 12.2. The *energy matrix* $\mathbf{L}$ is always symmetric and positive definite: $\mathbf{L} = \mathbf{L}^* > 0$. When an eigenvalue of matrix $\mathbf{L}$ tends to zero (or to infinity) the system degenerates towards a smaller dynamic system. The dynamic equations $\overline{\mathbf{L}}\dot{\mathbf{z}} = -\overline{\mathbf{A}}\mathbf{z} + \overline{\mathbf{B}}\mathbf{u}$ and $\mathbf{y} = \overline{\mathbf{B}}^* \mathbf{z}$ of the "reduced" system can be obtained from the original one using a "congruent" transformation $\mathbf{x} = \mathbf{T}\mathbf{z}$ (matrix $\mathbf{T}$ can also be complex and/or rectangular) where $\overline{\mathbf{L}} = \mathbf{T}^* \mathbf{L} \mathbf{T}$, $\overline{\mathbf{A}} = \mathbf{T}^* \mathbf{A} \mathbf{T} - \mathbf{T}^* \mathbf{L} \dot{\mathbf{T}}$, and $\overline{\mathbf{B}} = \mathbf{T}^* \mathbf{B}$. When matrix $\mathbf{T}$ is rectangular, the system is transformed and reduced at the same time. The POG schemes maintain their physical meaning even when the dynamic system is described using complex variables.

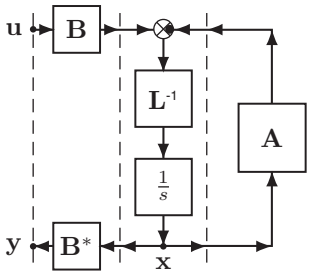

$$\begin{cases} \mathbf{L}\dot{\mathbf{x}} = -\mathbf{A}\mathbf{x} + \mathbf{B}\mathbf{u} \\ \mathbf{y} = \mathbf{B}^*\mathbf{x} \end{cases} \tag{12.1}$$

$$\Downarrow (\mathbf{x} = \mathbf{T}\mathbf{z})$$

$$\begin{cases} \overline{\mathbf{L}}\dot{\mathbf{z}} = -\mathbf{A}\mathbf{z} + \overline{\mathbf{B}}\mathbf{u} \\ \mathbf{y} = \overline{\mathbf{B}}^*\mathbf{z} \end{cases} \tag{12.2}$$

Figure 12.2 POG block scheme of a generic dynamic system

An example of POG modeling of an electrical *RC* circuit is shown in Figure 12.3. The *C* and *R* physical elements are described by two POG elaboration blocks. There is a direct correspondence between physical power sections and dashed sections in the POG model. The summation elements present in the elaboration blocks are a mathematical description of the current and voltage Kirchhoff's laws applied to the considered electrical system.

12.2.1 Notations

In this chapter the following notations are used to denote, respectively, full, diagonal, column, and row matrices:

$$\left[\!\!\left[\overset{i}{R}_{i,j} \right]\!\!\right]_{1:n}^{j}{}_{1:m} = \begin{bmatrix} R_{11} & R_{12} & \cdots & R_{1m} \\ R_{21} & R_{22} & \cdots & R_{2m} \\ \vdots & \vdots & \ddots & \vdots \\ R_{n1} & R_{n2} & \cdots & R_{nm} \end{bmatrix}, \qquad \left[\!\!\left[\overset{i}{R}_{i} \right]\!\!\right]_{1:n} = \begin{bmatrix} R_1 & & \\ & \ddots & \\ & & R_n \end{bmatrix},$$

$$\left[\!\!\left[\overset{i}{R}_{i} \right]\!\!\right]_{1:n} = \begin{bmatrix} R_1 & R_2 & \cdots & R_n \end{bmatrix}^{\mathrm{T}}, \qquad \left[\!\!\left[\overset{j}{R}_{j} \right]\!\!\right]_{1:m} = \begin{bmatrix} R_1 & R_2 & \cdots & R_m \end{bmatrix}.$$

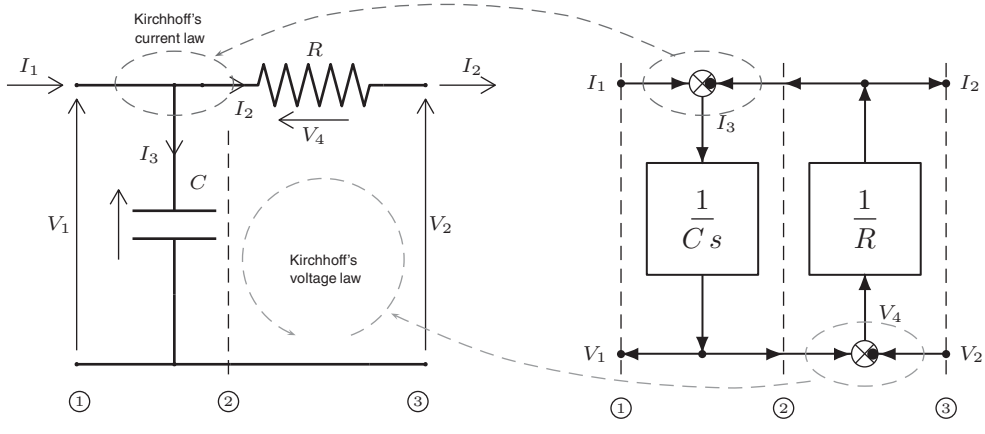

Figure 12.3 POG modeling of an electrical *RC* circuit

The symbol $\delta(n)|_k^m$ denote the following function:

$$\delta(n)|_k^m = \begin{cases} 1, & \text{if } n \in [k,\ k \pm m,\ k \pm 2m, \ldots]; \\ 0, & \text{in the other cases ;} \end{cases}$$

where $n, k, m \in \mathbb{Z}$. The symbol $\mathbf{I}_m$ denotes an identity matrix of order m.

12.3 Multiphase Induction Motor Complex Dynamic Modeling

The basic structure of a multiphase star-connected induction motor is shown in Figure 12.4. The electrical and mechanical parameters of the motor are shown in Table 12.1. All the electrical parameters of the motor have been obtained connecting in series the p polar couples of the motor.

12.3.1 Hypothesis for the Induction Motor Modeling

H1: The stator and rotor phases are considered star-connected, therefore the following relations hold:

$$\sum_{h=1}^{m_s} I_{sh} = I_{s1}+I_{s2}+\ldots+I_{sm_s} = 0\,, \qquad \sum_{h=1}^{m_r} I_{rh} = I_{r1}+I_{r2}+\ldots+I_{rm_r} = 0. \quad (12.3)$$

H2: The stator and rotor phases have a *concentrated-winding* structure in order to provide the harmonic injection: this means that the self- and mutual inductances are described by odd order Fourier series decompositions, and therefore their resultant shapes depend on the assigned

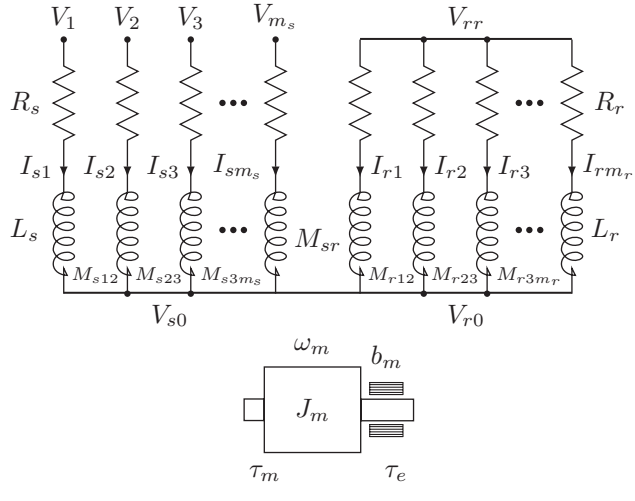

Figure 12.4 Structure of a multiphase induction motor

Table 12.1 Electrical and mechanical parameters of a multiphase induction motor

m_s, m_r	Number of stator and rotor phases
p	Number of rotor and stator polar expansions
γ_s, γ_r	Stator and rotor angular phase displacement ($\gamma_s = \frac{2\pi}{m_s}$, $\gamma_r = \frac{2\pi}{m_r}$)
θ_m, ω_m	Angular position and angular velocity of the rotor
θ_s, ω_s	Angular position and frequency of the stator voltages
θ	Electric angle ($\theta = p\,\theta_m$)
R_s, L_s	Resistance and self-inductance coefficient of the stator phases
R_r, L_r	Resistance and self-inductance coefficient of the rotor phases
M_{s0}, M_{r0}	Maximum mutual inductance coefficients of the stator and rotor phases
M_{sr0}	Maximum mutual inductance coefficient between stator and rotor phases
I_{si}, I_{ri}	Stator and rotor currents of the ith phase
V_i	Line voltage of the ith stator phase
V_{s0}, V_{r0}	Stator and rotor voltages of the star centers
J_m, b_m	Inertia momentum and linear friction coefficient of the rotor
τ_m, τ_e	Electromotive torque and external load torque acting on the rotor

Fourier coefficients and on the number of injected harmonics. This can be mathematically expressed defining the self- and mutual inductance coefficients L_{si}, L_{ri}, M_{sij}, and M_{rij} as follows:

$$\begin{cases} M_{sij} = M_{s0} \sum_{n=1:2}^{m_s-2} a_n^s \cos(n\,(i-j)\gamma_s) \\ L_{s0} = L_s - M_{s0} > 0 \end{cases}, \qquad \begin{cases} M_{rij} = M_{r0} \sum_{n=1:2}^{m_r-2} a_n^r \cos(n\,(i-j)\gamma_r) \\ L_{r0} = L_r - M_{r0} > 0 \end{cases} \tag{12.4}$$

with $i, j \in \{1, 2, \ldots, m_s\}$ for the stator and $i, j \in \{1, 2, \ldots, m_r\}$ for the rotor. Parameters a_n^s and a_n^r are the stator and rotor Fourier coefficients. The coefficients L_{s0} and L_{r0} describe the part of the self-inducted flux that does not concatenate with the other stator and rotor phases.

H3: The rotor phases are short-circuited: $V_{rr} = V_{r0}$ (see Figure 12.4).

H4: The input stator voltages V_i are supposed to be balanced: $\sum_{i=0}^{m_s} V_i = 0$.

12.3.2 Complex Dynamic Modeling of the Induction Motor

Let now ${}^t\mathbf{V}_s$, ${}^t\mathbf{I}_s$, ${}^t\mathbf{V}_r$, and ${}^t\mathbf{I}_r$ denote the stator phase and rotor phase voltage and current vectors in the external reference frame Σ_t (see Figure 12.4):

$${}^t\mathbf{V}_s = \begin{bmatrix} V_{s1} \\ V_{s2} \\ \vdots \\ V_{sm_s} \end{bmatrix}, \quad {}^t\mathbf{I}_s = \begin{bmatrix} I_{s1} \\ I_{s2} \\ \vdots \\ I_{sm_s} \end{bmatrix}, \quad {}^t\mathbf{V}_r = \begin{bmatrix} V_{r1} \\ V_{r2} \\ \vdots \\ V_{rm_r} \end{bmatrix}, \quad {}^t\mathbf{I}_r = \begin{bmatrix} I_{r1} \\ I_{r2} \\ \vdots \\ I_{rm_r} \end{bmatrix}$$

where $V_{si} = V_i - V_{s0}$ for $i \in \{1, 2, \ldots, m_s\}$, and $V_{ri} = V_{rr} - V_{r0} = 0$ for $i \in \{1, 2, \ldots, m_r\}$. Using the following generalized state vector ${}^t\dot{\mathbf{q}}$ and extended input vector ${}^t\mathbf{V}$:

$$ {}^t\dot{\mathbf{q}} = \left[\begin{array}{c} {}^t\mathbf{I}_s \\ {}^t\mathbf{I}_r \\ \hline \omega_m \end{array}\right] = \left[\begin{array}{c} {}^t\mathbf{I}_e \\ \hline \omega_m \end{array}\right], \qquad {}^t\mathbf{V} = \left[\begin{array}{c} {}^t\mathbf{V}_s \\ {}^t\mathbf{V}_r \\ \hline -\tau_e \end{array}\right] = \left[\begin{array}{c} {}^t\mathbf{V}_e \\ \hline -\tau_e \end{array}\right] $$

and applying the "Lagrangian" approach discussed in Zanasi *et al.* (2009) and Zanasi and Azzone (2010), one obtains the following dynamic equations of the multiphase induction motors:

$$ \frac{d}{dt}\left(\underbrace{\left[\begin{array}{c|c} {}^t\mathbf{L}_e & 0 \\ \hline 0 & J_m \end{array}\right]}_{{}^t\mathbf{L}({}^t\mathbf{q})} \underbrace{\left[\begin{array}{c} {}^t\mathbf{I}_e \\ \hline \omega_m \end{array}\right]}_{{}^t\dot{\mathbf{q}}} \right) = - \underbrace{\left[\begin{array}{c|c} {}^t\mathbb{R}_e + {}^t\mathbf{F}_e & {}^t\mathbf{K}_e \\ \hline -{}^t\mathbf{K}_e^{\mathrm{T}} & b_m \end{array}\right]}_{{}^t\mathbf{R} + {}^t\mathbf{W}} \underbrace{\left[\begin{array}{c} {}^t\mathbf{I}_e \\ \hline \omega_m \end{array}\right]}_{{}^t\dot{\mathbf{q}}} + \underbrace{\left[\begin{array}{c} {}^t\mathbf{V}_e \\ \hline -\tau_e \end{array}\right]}_{{}^t\mathbf{V}}. \tag{12.5} $$

The structures of the energy matrix ${}^t\mathbf{L}({}^t\mathbf{q})$, the dissipating matrix ${}^t\mathbf{R}$, and the energy redistribution matrix ${}^t\mathbf{W}$ are the following:

$$ {}^t\mathbf{L}({}^t\mathbf{q}) = \left[\begin{array}{cc|c} {}^t\mathbf{L}_s & {}^t\mathbf{M}_{sr}^{\mathrm{T}}(\theta_m) & 0 \\ {}^t\mathbf{M}_{sr}(\theta_m) & {}^t\mathbf{L}_r & 0 \\ \hline 0 & 0 & J_m \end{array}\right] = \left[\begin{array}{c|c} {}^t\mathbf{L}_e & 0 \\ \hline 0 & J_m \end{array}\right], $$

$$ {}^t\mathbf{R} = \left[\begin{array}{cc|c} {}^t\mathbb{R}_s & 0 & 0 \\ 0 & {}^t\mathbb{R}_r & 0 \\ \hline 0 & 0 & b_m \end{array}\right] = \left[\begin{array}{cc|c} R_s\,\mathbf{I}_{m_s} & 0 & 0 \\ 0 & R_r\,\mathbf{I}_{m_r} & 0 \\ \hline 0 & 0 & b_m \end{array}\right] = \left[\begin{array}{c|c} {}^t\mathbb{R}_e & 0 \\ \hline 0 & b_m \end{array}\right], $$

$$ {}^t\mathbf{W} = \left[\begin{array}{cc|c} 0 & -\frac{1}{2}\,{}^t\dot{\mathbf{M}}_{sr}^{\mathrm{T}} & \frac{1}{2}\frac{\partial\,{}^t\mathbf{M}_{sr}^{\mathrm{T}}}{\partial\theta_m}\,{}^t\mathbf{I}_r \\ -\frac{1}{2}\,{}^t\dot{\mathbf{M}}_{sr} & 0 & \frac{1}{2}\frac{\partial\,{}^t\mathbf{M}_{sr}}{\partial\theta_m}\,{}^t\mathbf{I}_s \\ \hline -\frac{1}{2}\,{}^t\mathbf{I}_r^{\mathrm{T}}\frac{\partial\,{}^t\mathbf{M}_{sr}}{\partial\theta_m} & -\frac{1}{2}\,{}^t\mathbf{I}_s^{\mathrm{T}}\frac{\partial\,{}^t\mathbf{M}_{sr}^{\mathrm{t}}}{\partial\theta_m} & 0 \end{array}\right]. $$

In order to take into account the odd order harmonic injection of the motor, see equations (12.4) of Hypothesis H2, the self- and mutual inductance matrices ${}^t\mathbf{L}_s$, ${}^t\mathbf{L}_r$, and ${}^t\mathbf{M}_{sr}$ are

supposed to have the following structure:

$$
{}^{t}\mathbf{L}_s = L_{s0}\,\mathbf{I}_{m_s} + M_{s0}\left\|\left[\sum_{n=1:2}^{m_s-2} a_n^s\,\cos(n\,(i-j)\gamma_s)\right]\right\|_{1:m_s}^{i\;\;j}
$$

$$
{}^{t}\mathbf{L}_r = L_{r0}\,\mathbf{I}_{m_r} + M_{r0}\left\|\left[\sum_{n=1:2}^{m_r-2} a_n^r\,\cos(n\,(i-j)\gamma_r)\right]\right\|_{1:m_r}^{i\;\;j}
$$

$$
{}^{t}\mathbf{M}_{sr}(\theta) = M_{sr0}\left\|\left[\sum_{n=1:2}^{m_{sr}-2} a_n^{sr}\,\cos(n(\theta + i\gamma_r - j\gamma_s))\right]\right\|_{0:m_r-1}^{i\;\;j}
$$

where $m_{sr} = \min\{m_s, m_r\}$, $L_{s0} = L_s - M_{s0}$, and $L_{r0} = L_r - M_{r0}$, that means the stator and rotor phases have a concentrated-winding structure. The coefficients a_n^s, a_n^r, and a_n^{sr} of the Fourier series are supposed to satisfy the following constraints:

$$
\sum_{n=1:2}^{m_s-2} |a_n^s| \le 1, \quad \sum_{n=1:2}^{m_r-2} |a_n^r| \le 1, \quad \sum_{n=1:2}^{m_{sr}-2} |a_n^{sr}| \le 1.
$$

Once the motor dynamic equations have been obtained, a state space transformation has to be performed in order to project them onto a new rotating reference frame. Let ${}^{t}\tilde{T}_{\underline{\omega}N} \in \mathbb{C}^{m\times(m+1)/2}$ denote the following composed matrix:

$$
{}^{t}\tilde{T}_{\underline{\omega}N}(m,\theta) = {}^{t}\tilde{T}_{\underline{\omega}}(m,\theta)\,\mathbf{N}_m = \left[\,{}^{t}\tilde{T}_{\omega} \quad \mathbf{z}_m\,\right]\mathbf{N}_m, \tag{12.6}
$$

where ${}^{t}\tilde{T}_{\omega}(m,\theta) \in \mathbb{C}^{m\times(m-1)/2}$ is a complex orthonormal matrix defined as

$$
{}^{t}\tilde{T}_{\omega}(m,\theta) = \sqrt{\frac{1}{m}}\;\left\|\left[\,e^{j\,k(\theta - h\gamma_m)}\,\right]\right\|_{0:m-1\quad 1:2:m-2}^{h\qquad k}, \qquad \gamma_m = \frac{2\pi}{m},
$$

and vector $\mathbf{z}_m \in \mathbb{R}^m$ and matrix $\mathbf{N}_m \in \mathbb{R}^{(m+1)/2\times(m+1)/2}$ are defined as follows:

$$
\mathbf{z}_m = \left\|\left[\,\sqrt{\tfrac{1}{m}}\,\right]\right\|_{0:m-1}^{h}, \qquad \mathbf{N}_m = \begin{bmatrix} \sqrt{2}\,\mathbf{I}_{\frac{m-1}{2}} & 0 \\ 0 & 1 \end{bmatrix}.
$$

Based on matrix (12.6), the following transformation matrix

$$
{}^{t}\mathbf{T}_{\omega} \in \mathbb{C}^{(m_s+m_r+1)\times(m_s+m_r)/2+2}
$$

can be defined as

$$
{}^{t}\mathbf{T}_{\omega} = \left[\begin{array}{cc|c} {}^{t}\tilde{T}_{\underline{\omega}N}(m_s,\theta_s) & 0 & 0 \\ 0 & {}^{t}\tilde{T}_{\underline{\omega}N}(m_r,\theta_p) & 0 \\ \hline 0 & 0 & 1 \end{array}\right] = \left[\begin{array}{c|c} {}^{t}\overline{\mathbf{T}}_{\underline{\omega}N} & 0 \\ \hline 0 & 1 \end{array}\right] \tag{12.7}
$$

$$
= \left[\begin{array}{cc|c} {}^{t}\tilde{T}_{\underline{\omega}}(m_s,\theta_s) & 0 & 0 \\ 0 & {}^{t}\tilde{T}_{\underline{\omega}}(m_r,\theta_p) & 0 \\ \hline 0 & 0 & 1 \end{array}\right] \left[\begin{array}{cc|c} \mathbf{N}_{\mathbf{m_s}} & 0 & 0 \\ 0 & \mathbf{N}_{m_r} & 0 \\ \hline 0 & 0 & 1 \end{array}\right] \tag{12.8}
$$

$$
= \left[\begin{array}{c|c} {}^{t}\overline{\mathbf{T}}_{\underline{\omega}} & 0 \\ \hline 0 & 1 \end{array}\right] \left[\begin{array}{c|c} \overline{\mathbf{N}} & 0 \\ \hline 0 & 1 \end{array}\right] = {}^{t}\overline{\mathbf{T}}_{\omega}\,\mathbf{N}, \tag{12.9}
$$

where $\theta_p = \theta_s - \theta$. The complex matrix ${}^{t}\mathbf{T}_{\omega}$, whose columns are orthogonal vectors, is used to perform a "pseudo" state space transformation ${}^{t}\dot{\mathbf{q}} = {}^{t}\mathbf{T}_{\omega}\,{}^{\omega}\dot{\mathbf{q}}$ from the original external reference frame Σ_t to a new complex rotating one $\bar{\Sigma}_{\omega}$. The new dynamic equations of the transformed system assume the following structure:

$$
\underbrace{\left[\begin{array}{c|c} {}^{\omega}\bar{\mathbf{L}}_e & 0 \\ \hline 0 & J_m \end{array}\right]}_{{}^{\omega}\mathbf{L}} \underbrace{\left[\begin{array}{c} {}^{\omega}\dot{\bar{\mathbf{I}}}_e \\ \hline \dot{\omega}_m \end{array}\right]}_{{}^{\omega}\ddot{\mathbf{q}}} = -\underbrace{\left[\begin{array}{c|c} {}^{\omega}\bar{\mathbb{R}}_e + {}^{\omega}\bar{\mathbf{F}}_e + {}^{\omega}\bar{\Omega}_e & {}^{\omega}\bar{\mathbf{K}}_e \\ \hline -{}^{\omega}\mathbf{K}_e^{*} & b_m \end{array}\right]}_{{}^{\omega}\mathbf{R} + {}^{\omega}\mathbf{W}} \underbrace{\left[\begin{array}{c} {}^{\omega}\bar{\mathbf{I}}_e \\ \hline \omega_m \end{array}\right]}_{{}^{\omega}\dot{\mathbf{q}}} + \underbrace{\left[\begin{array}{c} {}^{\omega}\bar{\mathbf{V}}_e \\ \hline -\tau_e \end{array}\right]}_{{}^{\omega}\mathbf{V}}. \tag{12.10}
$$

The reason why the considered state space transformation is called "pseudo" is because the complex vectors ${}^{\omega}\dot{\mathbf{q}}$ and ${}^{\omega}\mathbf{V}$ are obtained using matrix ${}^{t}\mathbf{T}_{\omega}$ (see equation (12.7)):

$$
{}^{\omega}\dot{\mathbf{q}} = {}^{t}\mathbf{T}_{\omega}^{*}\,{}^{t}\dot{\mathbf{q}} = \left[\begin{array}{c} {}^{\omega}\bar{\mathbf{I}}_s \\ {}^{\omega}\bar{\mathbf{I}}_r \\ \hline \omega_m \end{array}\right] = \left[\begin{array}{c} {}^{\omega}\bar{\mathbf{I}}_e \\ \hline \omega_m \end{array}\right], \qquad {}^{\omega}\mathbf{V} = {}^{t}\mathbf{T}_{\omega}^{*}\,{}^{t}\mathbf{V} = \left[\begin{array}{c} {}^{\omega}\bar{\mathbf{V}}_s \\ {}^{\omega}\bar{\mathbf{V}}_r \\ \hline -\tau_e \end{array}\right] = \left[\begin{array}{c} {}^{\omega}\bar{\mathbf{V}}_e \\ \hline -\tau_e \end{array}\right]
$$

while the transformed matrices ${}^{\omega}\mathbf{L}$, ${}^{\omega}\mathbf{R}$, and ${}^{\omega}\mathbf{W}$ are obtained using matrix ${}^{t}\overline{\mathbf{T}}_{\omega}$ (see equation (12.9)):

$$
{}^{\omega}\mathbf{L} = {}^{t}\overline{\mathbf{T}}_{\omega}^{*}\,{}^{t}\mathbf{L}\,{}^{t}\overline{\mathbf{T}}_{\omega}, \qquad {}^{\omega}\mathbf{R} = {}^{t}\overline{\mathbf{T}}_{\omega}^{*}\,{}^{t}\mathbf{R}\,{}^{t}\overline{\mathbf{T}}_{\omega}, \qquad {}^{\omega}\mathbf{W} = {}^{t}\overline{\mathbf{T}}_{\omega}^{*}\,{}^{t}\mathbf{W}\,{}^{t}\overline{\mathbf{T}}_{\omega}.
$$

Note that the transformation matrix ${}^{t}\overline{\mathbf{T}}_{\omega}$ does not change the diagonal structure of the transformed matrix ${}^{\omega}\mathbf{R}$ with respect to ${}^{t}\mathbf{R}$, it only reduces its dimension:

$$
{}^{\omega}\mathbf{R} = {}^{t}\overline{\mathbf{T}}_{\omega}^{*}\,{}^{t}\mathbf{R}\,{}^{t}\overline{\mathbf{T}}_{\omega} = \left[\begin{array}{cc|c} {}^{\omega}\bar{\mathbb{R}}_s & 0 & 0 \\ 0 & {}^{\omega}\bar{\mathbb{R}}_r & 0 \\ \hline 0 & 0 & b_m \end{array}\right] = \left[\begin{array}{cc|c} R_s\,\mathbf{I}_{\frac{m_s-1}{2}} & 0 & 0 \\ 0 & R_r\,\mathbf{I}_{\frac{m_r-1}{2}} & 0 \\ \hline 0 & 0 & b_m \end{array}\right] = \left[\begin{array}{cc} {}^{\omega}\bar{\mathbb{R}}_e & 0 \\ 0 & b_m \end{array}\right].
$$

On the contrary, it can be easily proved that the energy matrix ${}^{\omega}\mathbf{L}$ in the new transformed reference frame $\bar{\Sigma}_{\omega}$ has the following symmetric constant structure:

$$
{}^{\omega}\mathbf{L} = \left[\begin{array}{cc|c}
L_{s0} + \frac{m_s}{2} M_{s0}\, \mathbf{a}_s & M_{sre}\, \mathbf{a}_{sr}^{\mathrm{T}} & 0 \\
M_{sre}\, \mathbf{a}_{sr} & L_{r0} + \frac{m_r}{2} M_{r0}\, \mathbf{a}_r & 0 \\
\hline
0 & 0 & J_m
\end{array}\right],
$$

and the energy redistribution matrix ${}^{\omega}\mathbf{W}$ has the following skew-symmetric structure:

$$
{}^{\omega}\mathbf{W} = \left[\begin{array}{cc|c}
j\,\omega_s\, \mathbf{k}_{m_s}(L_{s0} + \frac{m_s}{2} M_{s0}\, \mathbf{a}_s) & j\,(\omega_s - \frac{\omega}{2})\, M_{sre}\, \mathbf{k}_{m_s}\, \mathbf{a}_{sr}^{\mathrm{T}} & {}^{\omega}\bar{\mathbf{K}}_s \\
j\,(\omega_s - \frac{\omega}{2})\, M_{sre}\, \mathbf{k}_{m_r}\, \mathbf{a}_{sr} & j\,\omega_p\, \mathbf{k}_{m_r}(L_{r0} + \frac{m_r}{2} M_{r0}\, \mathbf{a}_r) & {}^{\omega}\bar{\mathbf{K}}_r \\
\hline
-{}^{\omega}\mathbf{K}_s^* & -{}^{\omega}\mathbf{K}_r^* & 0
\end{array}\right],
$$

where

$$
\mathbf{k}_m = \overset{k}{\underset{1:2:m-2}{[\![\ k\ ]\!]}}, \qquad M_{sre} = \frac{M_{sr0}\sqrt{m_s m_r}}{2}, \qquad \omega_p = \omega_s - \omega.
$$

Note that ω_p is the slip velocity of the motor. Moreover $\mathbf{a}_s$, $\mathbf{a}_r$, and $\mathbf{a}_{sr}$ are real, constant matrices (function of the Fourier series coefficients) defined as follows:

$$
\mathbf{a}_s = \overset{k}{\underset{1:2:m_s-2}{[\![\ a_k^s\ ]\!]}}, \qquad \mathbf{a}_r = \overset{k}{\underset{1:2:m_r-2}{[\![\ a_k^r\ ]\!]}}, \qquad \mathbf{a}_{sr} = \overset{k}{\underset{1:2:m_r-2}{\overset{l}{\underset{1:2:m_s-2}{[\![\ a_k^{sr}\ \delta(k)|_l^{\infty}\ ]\!]}}}}.
$$

The transformed complex conjugate stator and rotor torque vectors are defined as

$$
{}^{\omega}\bar{\mathbf{K}}_s^* = -j\,\frac{p}{2}\, M_{sre}^{\omega}\, \bar{\mathbf{I}}_r^*\, \mathbf{k}_{m_r}\, \mathbf{a}_{sr}\,, \qquad {}^{\omega}\bar{\mathbf{K}}_r^* = j\,\frac{p}{2}\, M_{sre}\, {}^{\omega}\bar{\mathbf{I}}_s^*\, \mathbf{k}_{m_s}\, \mathbf{a}_{sr}^{\mathrm{T}}\,.
$$

The transformed vectors ${}^{\omega}\bar{\mathbf{I}}_e$ and ${}^{\omega}\bar{\mathbf{V}}_e$ have the following structure:

$$
\begin{aligned}
{}^{\omega}\bar{\mathbf{I}}_e &= {}^{t}\overline{\mathbf{T}}_{\underline{\omega}N}^{*}\, {}^{t}\mathbf{I}_e = \left[\begin{array}{c} {}^{t}\tilde{T}_{\underline{\omega}N}^{*}(m_s, \theta_s)\, {}^{t}\mathbf{I}_s \\ \hline {}^{t}\tilde{T}_{\underline{\omega}N}^{*}(m_r, \theta_p)\, {}^{t}\mathbf{I}_r \end{array}\right] = \left[\begin{array}{c} {}^{\omega}\bar{\mathbf{I}}_s \\ {}^{\omega}I_{sm_s} \\ \hline {}^{\omega}\mathbf{I}_r \\ {}^{\omega}I_{rm_r} \end{array}\right], \\
{}^{\omega}\bar{\mathbf{V}}_e &= {}^{t}\overline{\mathbf{T}}_{\underline{\omega}N}^{*}\, {}^{t}\mathbf{V}_e = \left[\begin{array}{c} {}^{t}\tilde{T}_{\underline{\omega}N}^{*}(m_s, \theta_s)\, {}^{t}\mathbf{V}_s \\ \hline {}^{t}\tilde{T}_{\underline{\omega}N}^{*}(m_r, \theta_p)\, {}^{t}\mathbf{V}_r \end{array}\right] = \left[\begin{array}{c} {}^{\omega}\bar{\mathbf{V}}_s \\ {}^{\omega}V_{sm_s} \\ \hline 0 \end{array}\right],
\end{aligned}
\tag{12.11}
$$

where ${}^{\omega}\bar{\mathbf{V}}_r = 0$ because the rotor phases are short-circuited. The components ${}^{\omega}I_{sm_s}$, ${}^{\omega}I_{rm_r}$, and ${}^{\omega}V_{sm_s}$ in (12.11) are defined as follows:

$$
{}^{\omega}I_{sm_s} = \frac{1}{\sqrt{m_s}} \sum_{i=1}^{m_s} I_{si}, \qquad {}^{\omega}I_{rm_s} = \frac{1}{\sqrt{m_r}} \sum_{i=1}^{m_r} I_{ri}, \qquad {}^{\omega}V_{sm_s} = \frac{1}{\sqrt{m_s}} \sum_{i=1}^{m_r} V_{si}.
$$

Considering that the stator and rotor phases are star-connected (see equation (12.3)), it results that ${}^{\omega}I_{sm_s} = 0$ and ${}^{\omega}I_{rm_r} = 0$. Moreover, ${}^{\omega}V_{sm_s} = 0$ because the input stator voltages are supposed to be balanced. The vectors ${}^{\omega}\bar{\mathbf{I}}_s$, ${}^{\omega}\bar{\mathbf{I}}_r$, and ${}^{\omega}\bar{\mathbf{V}}_s$ in (12.11) have the following structure:

$$
{}^{\omega}\bar{\mathbf{I}}_s = \Big\|\Big[\ {}^{\omega}\bar{I}_{sk}\ \Big]\Big\|_{1:2:m_s-2}^{k} = \Big\|\Big[\ I_{dsk} + j\, I_{qsk}\ \Big]\Big\|_{1:2:m_s-2}^{k}, \qquad
{}^{\omega}\bar{\mathbf{I}}_r = \Big\|\Big[\ {}^{\omega}\bar{I}_{rk}\ \Big]\Big\|_{1:2:m_r-2}^{k} = \Big\|\Big[\ I_{drk} + j\, I_{qrk}\ \Big]\Big\|_{1:2:m_r-2}^{k},
$$

$$
{}^{\omega}\bar{\mathbf{V}}_s = \Big\|\Big[\ {}^{\omega}\bar{V}_{sk}\ \Big]\Big\|_{1:2:m_s-2}^{k} = \Big\|\Big[\ V_{dsk} + j\, V_{qsk}\ \Big]\Big\|_{1:2:m_s-2}^{k}.
$$

Finally, the mechanical torque τ_m in the reference frame $\bar{\Sigma}_{\omega}$ can be expressed as follows:

$$
\begin{aligned}
\tau_m &= \mathrm{Re}\,({}^{\omega}\bar{\mathbf{K}}_e^{*}\,{}^{\omega}\bar{\mathbf{I}}_e) = \mathrm{Re}\left(\begin{bmatrix} {}^{\omega}\bar{\mathbf{K}}_s^{*} & {}^{\omega}\bar{\mathbf{K}}_r^{*} \end{bmatrix}\begin{bmatrix} {}^{\omega}\bar{\mathbf{I}}_s \\ {}^{\omega}\bar{\mathbf{I}}_r \end{bmatrix}\right) \\
&= \frac{p}{2}\, M_{sre}\, \mathrm{Re}\left(\begin{bmatrix} -j\,{}^{\omega}\bar{\mathbf{I}}_r^{*}\,\mathbf{k}_{m_r}\,\mathbf{a}_{sr} \ \Big|\ j\,{}^{\omega}\bar{\mathbf{I}}_s^{*}\,\mathbf{k}_{m_s}\,\mathbf{a}_{sr}^{\mathrm{T}} \end{bmatrix}\begin{bmatrix} {}^{\omega}\bar{\mathbf{I}}_s \\ {}^{\omega}\bar{\mathbf{I}}_r \end{bmatrix}\right) \\
&= p\, M_{sre} \sum_{k=1:2}^{m_{sr}-2} k\, a_k^{sr}(I_{drk}\, I_{qsk} - I_{dsk}\, I_{qrk}).
\end{aligned} \tag{12.12}
$$

A POG graphical representation of system (12.10) is shown in Figure 12.5. Section ①–③ represents the state space transformation $\Sigma_t \leftrightarrow \bar{\Sigma}_{\omega}$. Function "Re(·)" denotes the "complex to real conversion" of the input. Section ③–④, that is, the lightly shaded section of Figure 12.5, represents the *electrical part* of the system: note that this part is described only by complex matrices and complex variables. The *mechanical part* of the motor is described by section ⑥–⑦: this part is characterized only by real values and real variables. Section ④–⑥ represents the energy and power conversion (without accumulation or dissipation) between the electrical and mechanical parts.

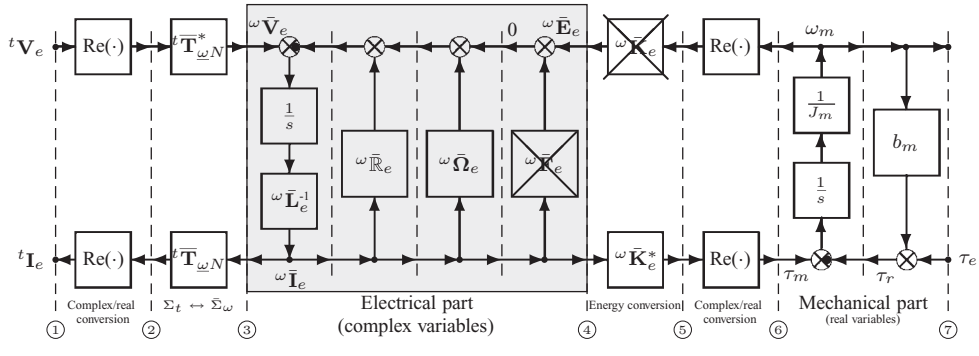

Figure 12.5 POG graphical representation of a multiphase induction motor in the frame $\bar{\Sigma}_{\omega}$

It can be easily proved that in (12.10), the term ${}^{\omega}\overline{\mathbf{K}}_e\,\omega_m$ is simplified by the term ${}^{\omega}\bar{\mathbf{F}}_e\,{}^{\omega}\bar{\mathbf{I}}_e$, so the dynamics of the system can be rewritten in the following simplified form:

$$\underbrace{\left[\begin{array}{c|c} {}^{\omega}\bar{\mathbf{L}}_e & 0 \\ \hline 0 & J_m \end{array}\right]}_{{}^{\omega}\mathbf{L}} \underbrace{\left[\begin{array}{c} {}^{\omega}\dot{\bar{\mathbf{I}}}_e \\ \hline \dot{\omega}_m \end{array}\right]}_{{}^{\omega}\ddot{\mathbf{q}}} = -\underbrace{\left[\begin{array}{c|c} {}^{\omega}\bar{\mathbb{R}}_e + {}^{\omega}\bar{\Omega}_e & 0 \\ \hline -{}^{\omega}\mathbf{K}_e^* & b_m \end{array}\right]}_{{}^{\omega}\mathbf{R}+{}^{\omega}\mathbf{W}} \underbrace{\left[\begin{array}{c} {}^{\omega}\bar{\mathbf{I}}_e \\ \hline \omega_m \end{array}\right]}_{{}^{\omega}\dot{\mathbf{q}}} + \underbrace{\left[\begin{array}{c} {}^{\omega}\bar{\mathbf{V}}_e \\ \hline -\tau_e \end{array}\right]}_{{}^{\omega}\mathbf{V}}. \tag{12.13}$$

12.4 Multiphase Indirect Field-Oriented Control with Harmonic Injection

The field-oriented control in the multiphase case can be now investigated starting from equation (12.13). Let us now consider the case $m_s = m_r = m_{sr}$ and let $\mathbf{P}_\pi$ denote the following permutation matrix:

$$\mathbf{P}_\pi = \underset{1:\frac{m_{sr}-1}{2}}{\overset{h}{\left\| \mathbf{e}_h \quad \mathbf{e}_{m_s+h} \right\|}}, \tag{12.14}$$

where $\mathbf{e}_h$ denotes a column vector of length $m_{sr}-1$ with 1 in the hth position and 0 in all the other positions. Applying the transformation ${}^{\omega}\bar{\mathbf{I}}_e = \mathbf{P}_\pi\,{}^{\omega}\bar{\mathbf{I}}_{e_k}$ to the electrical part of system (12.13), the following reordered system referred to the new reference frame $\bar{\Sigma}_{\omega_k}$ is obtained:

$$\underbrace{\left[\begin{array}{c|c} {}^{\omega}\bar{\mathbf{L}}_{e_k} & 0 \\ \hline 0 & J_m \end{array}\right]}_{{}^{\omega}\mathbf{L}_k} \underbrace{\left[\begin{array}{c} {}^{\omega}\dot{\bar{\mathbf{I}}}_{e_k} \\ \hline \dot{\omega}_m \end{array}\right]}_{{}^{\omega}\ddot{\mathbf{q}}_k} = -\underbrace{\left[\begin{array}{c|c} {}^{\omega}\bar{\mathbb{R}}_{e_k} + {}^{\omega}\bar{\Omega}_{e_k} & 0 \\ \hline -{}^{\omega}\mathbf{K}_{e_k}^* & b_m \end{array}\right]}_{{}^{\omega}\mathbb{R}_k+{}^{\omega}\mathbf{W}_k} \underbrace{\left[\begin{array}{c} {}^{\omega}\bar{\mathbf{I}}_{e_k} \\ \hline \omega_m \end{array}\right]}_{{}^{\omega}\dot{\mathbf{q}}_k} + \underbrace{\left[\begin{array}{c} {}^{\omega}\bar{\mathbf{V}}_{e_k} \\ \hline -\tau_e \end{array}\right]}_{{}^{\omega}\mathbf{V}_k}, \tag{12.15}$$

where matrices and vectors ${}^{\omega}\bar{\mathbf{L}}_{e_k} = \mathbf{P}_\pi^{\mathrm{T}}\,{}^{\omega}\bar{\mathbf{L}}_e\,\mathbf{P}_\pi$, ${}^{\omega}\bar{\mathbb{R}}_{e_k} = \mathbf{P}_\pi^{\mathrm{T}}\,{}^{\omega}\bar{\mathbb{R}}_e\,\mathbf{P}_\pi$, ${}^{\omega}\bar{\Omega}_{e_k} = \mathbf{P}_\pi^{\mathrm{T}}\,{}^{\omega}\bar{\Omega}_e\,\mathbf{P}_\pi$, ${}^{\omega}\bar{\mathbf{I}}_{e_k} = \mathbf{P}_\pi^{\mathrm{T}}\,{}^{\omega}\bar{\mathbf{I}}_e$, ${}^{\omega}\bar{\mathbf{V}}_{e_k} = \mathbf{P}_\pi^{\mathrm{T}}\,{}^{\omega}\bar{\mathbf{V}}_e$, and ${}^{\omega}\bar{\mathbf{K}}_{e_k}^* = {}^{\omega}\bar{\mathbf{K}}_e^*\,\mathbf{P}_\pi$ are expressed as follows:

$${}^{\omega}\bar{\mathbf{L}}_{e_k} = \underset{1:2:m_{sr}-2}{\overset{k}{\left\| \begin{bmatrix} L_{se_k} & M_{sre_k} \\ M_{sre_k} & L_{re_k} \end{bmatrix} \right\|}}, \quad {}^{\omega}\bar{\mathbf{I}}_{e_k} = \underset{1:2:m_{sr}-2}{\overset{k}{\left\| \begin{bmatrix} {}^{\omega}\bar{I}_{sk} \\ {}^{\omega}\bar{I}_{rk} \end{bmatrix} \right\|}}, \quad {}^{\omega}\bar{\mathbf{V}}_{e_k} = \underset{1:2:m_{sr}-2}{\overset{k}{\left\| \begin{bmatrix} {}^{\omega}\bar{V}_{sk} \\ 0 \end{bmatrix} \right\|}},$$

$${}^{\omega}\bar{\mathbb{R}}_{e_k} = \underset{1:2:m_{sr}-2}{\overset{k}{\left\| \begin{bmatrix} R_s & 0 \\ 0 & R_r \end{bmatrix} \right\|}}, \quad {}^{\omega}\bar{\Omega}_{e_k} = \underset{1:2:m_{sr}-2}{\overset{k}{\left\| \begin{bmatrix} j\,\omega_s\,k\,L_{se_k} & j\,\omega_s\,k\,M_{sre_k} \\ j\,\omega_p\,k\,M_{sre_k} & j\,\omega_p\,k\,L_{re_k} \end{bmatrix} \right\|}},$$

$${}^{\omega}\bar{\mathbf{K}}_{e_k}^* = \underset{1:2:m_{sr}-2}{\overset{k}{\left\| \; j\,\tfrac{p}{2}\,k\,M_{sre_k}\,{}^{\omega}\bar{I}_{rk}^* \;\middle|\; -j\,\tfrac{p}{2}\,k\,M_{sre_k}\,{}^{\omega}\bar{I}_{sk}^* \; \right\|}},$$

with $L_{se_k} = L_{s0} + \frac{m_s}{2}\,a_k^s\,M_{s0}$, $L_{re_k} = L_{r0} + \frac{m_r}{2}\,a_k^r\,M_{r0}$, and $M_{sre_k} = M_{sre}\,a_k^{sr}$. From (12.15) it clearly follows that a multiphase induction motor with an odd order harmonic injection can

be mathematically described by $\frac{m_{sr}-1}{2}$ sets of decoupled equations in the frame $\bar{\Sigma}_{\omega_k}$: in other words, the system can be seen as the set of $\frac{m_{sr}-1}{2}$ three-phase induction motors whose dynamic equations are the projection of system (12.10) in the kth subspace and supplied by balanced voltages at frequencies $k\,\omega_s$. In addition, the overall mechanical torque of the motor τ_m is the sum of the torques generated by the $\frac{m_{sr}-1}{2}$ internal decoupled motors:

$$\begin{aligned}\tau_m &= \sum_{k=1:2}^{m_{sr}-2} \tau_{m_k} = \sum_{k=1:2}^{m_{sr}-2} \mathrm{Re}\,({}^{\omega}\bar{\mathbf{K}}^{*}_{e_k}\,{}^{\omega}\bar{\mathbf{I}}_{e_k}) \\ &= \mathrm{Re}\left(\sum_{k=1:2}^{m_{sr}-2} \left\| \left[-j\,\frac{p}{2}\,k\,M_{sre_k}\,{}^{\omega}\bar{I}^{*}_{rk} \;\middle|\; j\,\frac{p}{2}\,k\,M_{sre_k}\,{}^{\omega}\bar{I}^{*}_{sk} \right] \right\|_{1:2:m_{sr}-2}^{k} \left\| \begin{bmatrix} {}^{\omega}\bar{I}_{sk} \\ {}^{\omega}\bar{I}_{rk} \end{bmatrix} \right\|_{1:2:m_{sr}-2}^{k} \right) \\ &= p\,M_{sre} \sum_{k=1:2}^{m_{sr}-2} k\,a^{sr}_{k}(I_{drk}\,I_{qsk} - I_{dsk}\,I_{qrk}).\end{aligned}$$

Clearly, this expression coincides with the one given in (12.12). The same concept can be applied to the field-oriented control theory: the basic idea is to define the global control equations in the multiphase case as a set of $\frac{m_{sr}-1}{2}$ independent control equations, respectively referred to each odd harmonic subspace. For this purpose the multiphase IRFOC is considered. This type of control, in the three-phase case, is widely described in Vas (1990) and Leonard (2001). Let ${}^{\omega}\bar{\Phi}_{e_k} = {}^{\omega}\bar{\mathbf{L}}_{e_k}\,{}^{\omega}\bar{\mathbf{I}}_{e_k}$ denote the flux vector in the frame $\bar{\Sigma}_{\omega_k}$. Substituting ${}^{\omega}\bar{\Phi}_{e_k}$ in equations (12.15) one obtains the following reordered motor dynamic equations as function of the flux:

$$\left\| \begin{bmatrix} {}^{\omega}\bar{V}_{sk} \\ 0 \end{bmatrix} \right\|_{1:2:m_{sr}-2}^{k} = \left\| \begin{bmatrix} R_s & 0 \\ 0 & R_r \end{bmatrix} \right\|_{1:2:m_{sr}-2}^{k} \left\| \begin{bmatrix} {}^{\omega}\bar{I}_{sk} \\ {}^{\omega}\bar{I}_{rk} \end{bmatrix} \right\|_{1:2:m_{sr}-2}^{k} + \left\| \begin{bmatrix} j\,\omega_s\,k & 0 \\ 0 & j\,\omega_p\,k \end{bmatrix} \right\|_{1:2:m_{sr}-2}^{k} \left\| \begin{bmatrix} {}^{\omega}\bar{\Phi}_{sk} \\ {}^{\omega}\bar{\Phi}_{rk} \end{bmatrix} \right\|_{1:2:m_{sr}-2}^{k} + \left\| \begin{bmatrix} {}^{\omega}\dot{\bar{\Phi}}_{sk} \\ {}^{\omega}\dot{\bar{\Phi}}_{rk} \end{bmatrix} \right\|_{1:2:m_{sr}-2}^{k}.$$

where

$${}^{\omega}\bar{\Phi}_{sk} = \Phi_{dsk} + j\,\Phi_{qsk}, \qquad {}^{\omega}\bar{\Phi}_{rk} = \Phi_{drk} + j\,\Phi_{qrk}.$$

Imposing the field orientation condition, that is the rotor flux is supposed to be aligned with the direct axis ensuring null quadrature components of the rotor flux, one can write the IRFOC main equations in the frame $\bar{\Sigma}_{\omega_k}$ as follows:

$$\tau_m = \sum_{k=1:2}^{m_{sr}-2} \tau_{m_k} = p \sum_{k=1:2}^{m_{sr}-2} k\,\frac{M_{sre_k}}{L_{re_k}}\,\Phi_{drk}\,I_{qsk}, \tag{12.16}$$

$$\Phi_r = \sum_{k=1:2}^{m_{sr}-2} \Phi_{drk} = \sum_{k=1:2}^{m_{sr}-2} M_{sre_k}\,I_{dsk}, \tag{12.17}$$

$$\omega_{pk} = k\,\frac{I_{qsk}}{T_{rk}\,I_{dsk}}, \qquad k \in \{1:2:m_{sr}-2\}, \tag{12.18}$$

where $\Phi_{drk} = \mathrm{Re}({}^{\omega}\bar{\Phi}_{rk})$, $I_{dsk} = \mathrm{Re}({}^{\omega}\bar{I}_{sk})$, $I_{qsk} = \mathrm{Im}({}^{\omega}\bar{I}_{sk})$, and $T_{rk} = L_{re_k}/R_r$ is the rotor constant of the kth harmonic subspace. Note that each subspace is characterized by the respective ω_{pk} slip velocity. Concluding, the multiphase induction motor with harmonic injection can be described and modeled as a set of $k = \frac{m_{sr}-1}{2}$ three-phase decoupled machines that can be independently controlled performing the decoupling between the torque and flux in each harmonic subspace, as described by equations (12.16), (12.17), and (12.18).

12.4.1 Five-Phase Indirect Rotor Field-Oriented Control

Let us now consider the case of a five-phase induction motor characterized by the combined action of the fundamental and third harmonic currents. The IRFOC equations can be obtained from equations (12.16), (12.17), and (12.18) imposing $m_s = m_r = m_{sr} = 5$:

$$\tau_1 = p\,\frac{M_{sre_1}}{L_{re_1}}\,\Phi_{dr1}\,I_{qs1}, \qquad \tau_3 = 3\,p\,\frac{M_{sre_3}}{L_{re_3}}\,\Phi_{dr3}\,I_{qs3}, \tag{12.19}$$

$$\Phi_{dr1} = M_{sre_1}\,I_{ds1}, \qquad \Phi_{dr3} = M_{sre_3}\,I_{ds3}, \tag{12.20}$$

$$\omega_{p1} = \frac{I_{qs1}}{T_{r1}\,I_{ds1}}, \qquad \omega_{p3} = 3\,\frac{I_{qs3}}{T_{r3}\,I_{ds3}}. \tag{12.21}$$

Note that $\tau_m = \tau_1 + \tau_3$ and $\Phi_r = \Phi_{dr1} + \Phi_{dr3}$. In this case it is clear that the field-oriented control of the two subspaces is totally decoupled: the stator direct-current components I_{ds1} and I_{ds3} directly control the rotor direct flux components Φ_{dr1} and Φ_{dr3}, while the stator quadrature current components I_{qs1} and I_{qs3} independently control the torque components τ_1 and τ_3, assuming that the rotor flux components remain constant. Let us now suppose that the third harmonic component is a k_3 fraction of the fundamental component:

$$I_{ds3} = k_3\,I_{ds1}, \qquad I_{qs3} = k_3\,I_{qs1}. \tag{12.22}$$

In this case, it has been chosen $k_3 = 0.15$ in order to avoid saturation effects ensuring a more flattened flux (see Xu *et al.* 2001, 2002). Substituting the expressions of the direct and quadrature third harmonic stator current components I_{ds3} and I_{qs3} defined in equation (12.22) into equations (12.19), (12.20), and (12.21), one obtains the following direct and quadrature fundamental stator current components I_{ds1} and I_{qs1} and slip velocity:

$$I_{qs1} = \frac{\tau_m}{p\,\Phi_r}\,\frac{\left(\dfrac{M_{sre_1}}{M_{sre_1} + k_3\,M_{sre_3}}\right)}{\left(\dfrac{M_{sre_1}}{L_{re_1}} + 3\,k_3^2\,\dfrac{M_{sre_3}^2}{L_{re_3}\,M_{sre_1}}\right)}, \tag{12.23}$$

$$I_{ds1} = \frac{\Phi_r}{M_{sre_1} + k_3\,M_{sre_3}}, \tag{12.24}$$

$$\omega_{p1} = \frac{I_{qs1}}{T_{r1}\,I_{ds1}}. \tag{12.25}$$

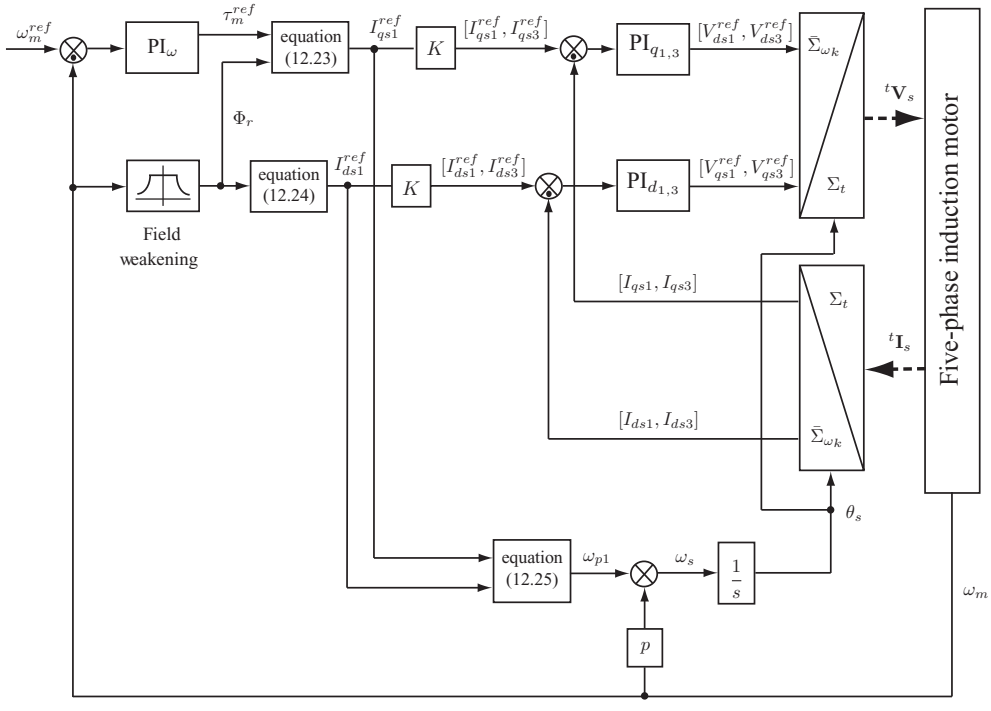

Figure 12.6 IRFOC of a five-phase induction motor: fundamental plus third harmonic injection

These variables are used to implement the IRFOC control of a five-phase induction motor as shown in Figure 12.6: the outer PI$_\omega$ regulator controls the motor angular velocity ω_m by tracking the defined velocity reference ω_m^{ref} and generates the torque reference τ_m^{ref}. The inner PI$_{d_k}$ and PI$_{q_k}$ controllers respectively regulate the stator direct-current components I_{ds1} and I_{ds3}, directly controlling the rotor flux Φ_r, and the stator quadrature current components I_{qs1} and I_{qs3}, directly controlling the mechanical torque τ_m. In such a way, the decoupling between the fundamental and the third harmonic has been achieved and the voltage references V_{ds1}^{ref}, V_{ds3}^{ref}, V_{qs1}^{ref}, and V_{qs3}^{ref} are then transformed to generate the balanced motor input voltage vector $^t\mathbf{V}_s$. Note that $K = [1 \;\; k_3]$ according to equation (12.22).

An alternative strategy that can be considered is to control the first subspace only, that corresponds to the fundamental harmonic, and generate the voltage references V_{ds1}^{ref} and V_{qs1}^{ref}, while the third harmonic injection contributions can be obtained using an appropriate scaling coefficient $k_{V3} = f(k_3)$ in order to calculate the voltage references $V_{ds3}^{ref} = k_{V3}\, V_{ds1}^{ref}$ and $V_{qs3}^{ref} = k_{V3}\, V_{qs1}^{ref}$ that act in the third subspace. The first solution (see Figure 12.6) is more flexible because a custom control for each harmonic subspace can be designed, but its implementation has a higher cost in terms of number of used controllers and tuning. On the other side, the second solution (see Figure 12.7) has a simpler structure but it is limited to the first subspace only, so the control is focused only on the subspace of the fundamental. The trade-off that has to be considered is between the control degrees of freedom and the control computational and implementation costs.

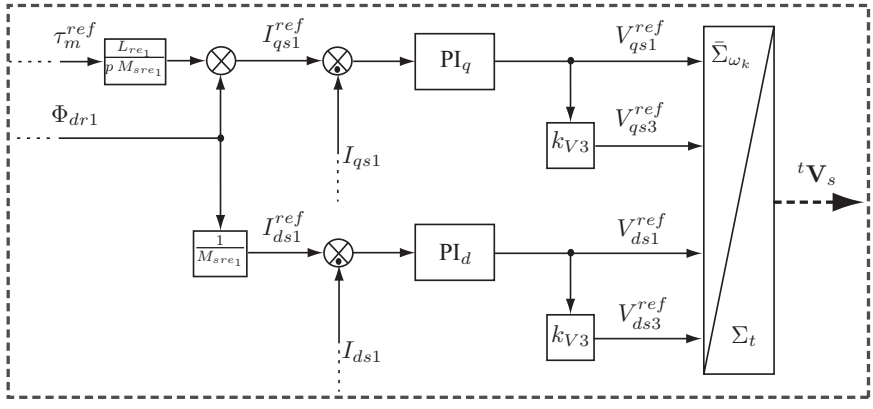

Figure 12.7 IRFOC of a five-phase induction motor: control of the fundamental and scaling of the third harmonic (see Figure 12.6 for the remaining scheme)

12.4.2 Five-Phase IRFOC Simulation Results

The simulation results presented in this section have been obtained in Matlab/Simulink by implementing the complex and reduced order model of a five-phase induction motor considering the third harmonic injection and using the IRFOC strategy described in Figure 12.6. The electrical and mechanical parameters of the considered motor are listed in Table 12.2. Note that this motor is supposed to have a concentrated winding phase structure in order to take into account the third harmonic injection. In this case the balanced voltage input vector has the following structure:

$$^t\mathbf{V}_s = \left\| \left[V_{sh} \right] \right\|_{1:5}^{h} = \sum_{k=1:2}^{3} \left\| \left[V_{mk} \cos(k\,(\theta_s - (h-1)\,\gamma_s)) \right] \right\|_{1:5}^{h},$$

Table 12.2 Electrical and mechanical parameters of the considered five-phase induction motor

Stator parameters		Rotor parameters	
m_s	5	m_r	5
L_s	115.5 mH	L_r	43.2 mH
R_s	2.7 Ω	R_r	0.85 Ω
M_{s0}	114 mH	M_{r0}	42.9 mH
Motor parameters			
p	2	M_{sr0}	66.2 mH
V_{s_Δ}	220 V	f_n	50 Hz
J_m	0.002 Kg m^2	ω_n	1390 rpm
P_n	0.75 kW	Φ_{r_n}	0.58 Wb

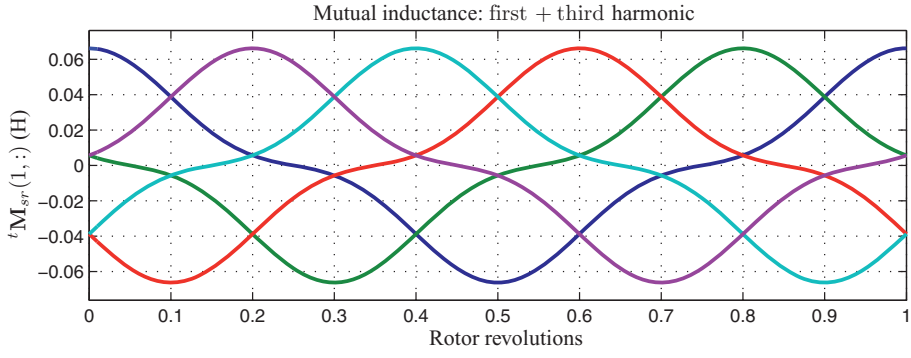

Figure 12.8 Mutual inductance between the first stator phase and the rotor phases (for a color version of this figure, please see color plates.)

where k indicates the injected harmonic order and h the number of stator phases. The following Fourier coefficient matrices have been used:

$$\mathbf{a}_s = \mathbf{a}_r = \mathbf{a}_{sr} = \begin{bmatrix} 0.8 & 0 \\ 0 & 0.2 \end{bmatrix}.$$

These coefficient matrices define the shape of the mutual inductance $^t\mathbf{M}_{sr}$. The behavior of the mutual inductance $^t\mathbf{M}_{sr}$ between the first stator phase and the rotor phases as function of the rotor revolutions is shown in Figure 12.8.

The outer velocity tracking is shown in Figure 12.9: the dashed line represents the trapezoidal profile reference ω_m^{ref} (see Figure 12.6) while the solid line represents the motor angular velocity ω_m. The tracking error is quite small and it increases only during the rising and falling edges. On the other hand, the inner current loops separately control the fundamental

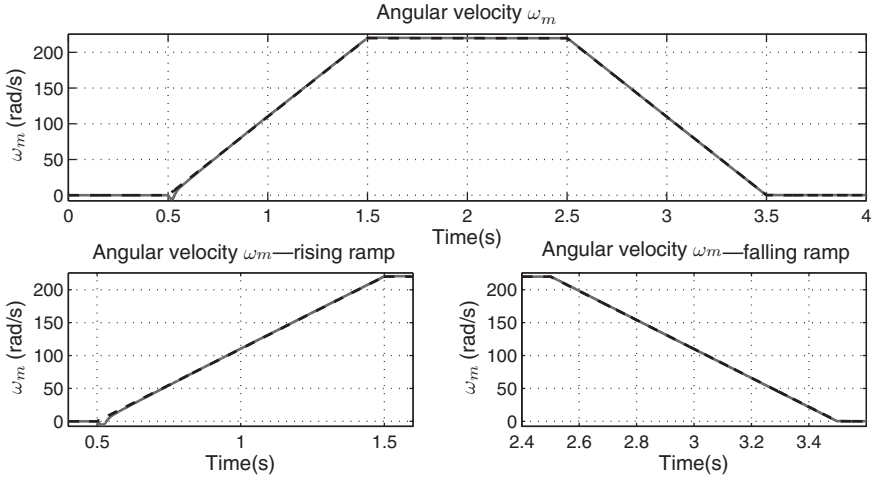

Figure 12.9 Angular velocity ω_m: actual values (solid) and reference values (dashed)

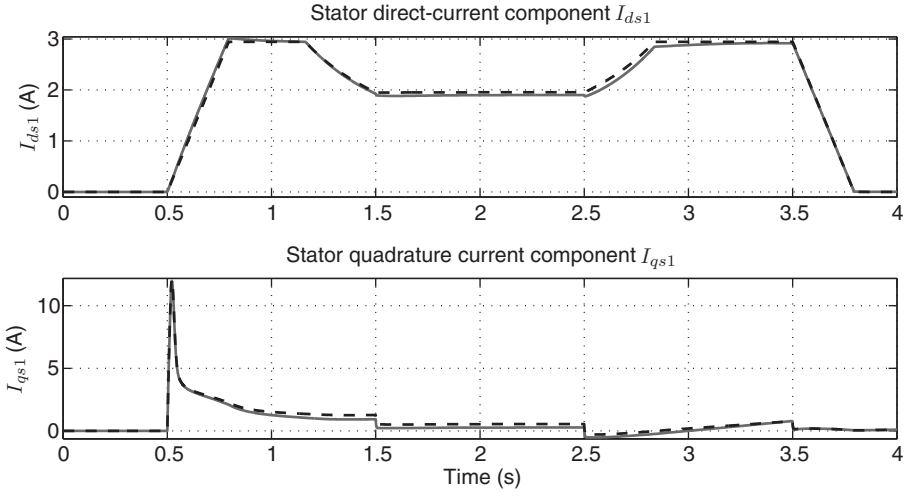

Figure 12.10 Controlled stator current components I_{ds1} and I_{qs1} in the fundamental subspace: actual values (solid) and reference values (dashed)

and the third harmonic subspaces: in each subspace the stator direct and quadrature current components are controlled, as depicted in Figures 12.10 and 12.11, in order to perform the flux and torque control. The time behavior of the stator voltage and current vectors ${}^t\mathbf{V}_s$ and ${}^t\mathbf{I}_s$ in the original reference frame Σ_t during the rising ramp of the velocity tracking are respectively shown in Figures 12.12 and 12.13: from their detailed zooms one can note that the shape of the phase voltages and currents is the sum of the fundamental and the third harmonic

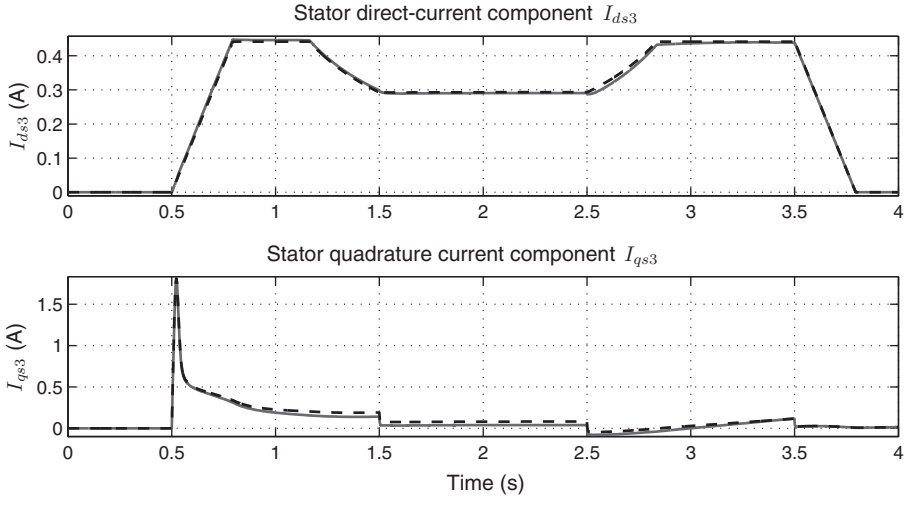

Figure 12.11 Controlled stator current components I_{ds3} and I_{qs3} in the third harmonic subspace: actual values (solid) and reference values (dashed)

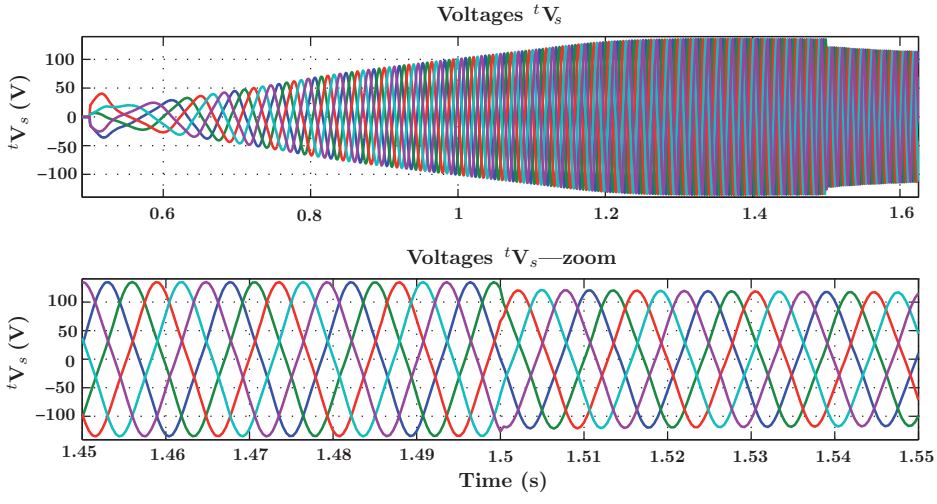

Figure 12.12 Stator voltages in the original reference frame Σ_t during the velocity rising ramp (for a color version of this figure, please see color plates.)

contributions. The generated mechanical torque τ_m and the applied load torque profile τ_e are shown in Figure 12.14: for $t \in [0, 0.5]$ and $t \in [3.5, 4]$ the torque τ_m is null because no load torque τ_e is applied and no velocity is tracked, while for $t \in [0.5, 1.5]$ and $t \in [2.5, 3.5]$ the torque τ_m evolves according to the load torque profile τ_e and to the velocity rising and falling transients (see Figure 12.9).

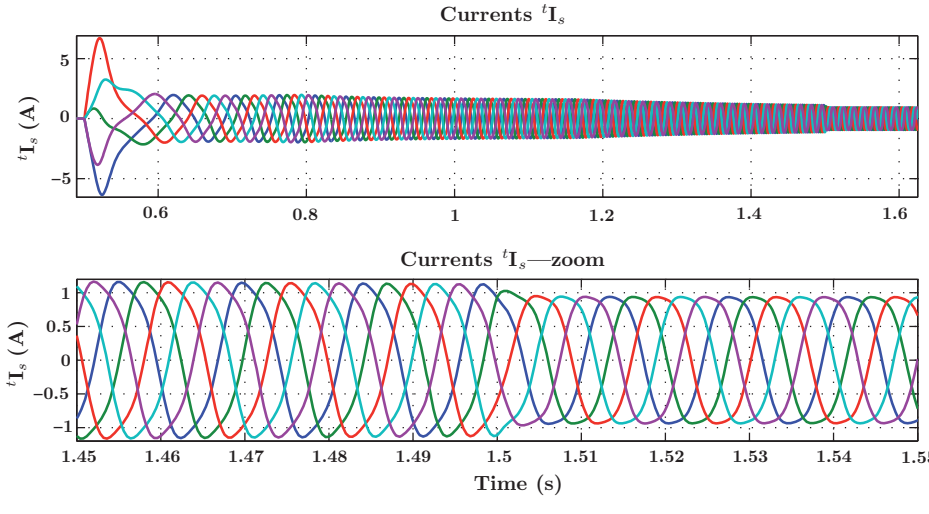

Figure 12.13 Stator currents in the original reference frame Σ_t during the velocity rising ramp (for a color version of this figure, please see color plates.)

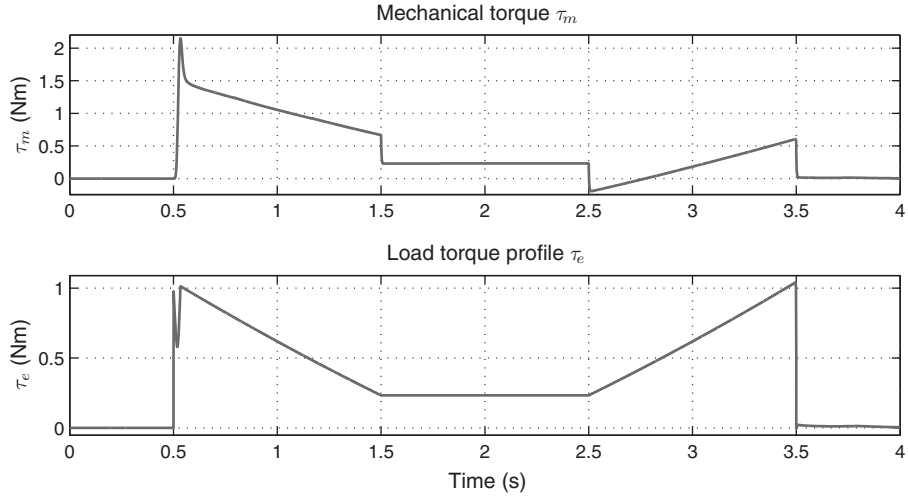

Figure 12.14 Mechanical torque τ_m and load torque τ_e

12.5 Conclusions

In this chapter the modeling and control of a multiphase induction motor with harmonic injection has been addressed. First of all the motor dynamic equations in the complex rotating reference frame have been obtained considering a generic number of stator and rotor phases and the corresponding odd order harmonic injection. Starting from this equations, the multiphase field-oriented control has been investigated and the main multiphase IRFOC relations have been given. Finally, a five-phase induction motor has been considered and the control decoupling between the fundamental and the third harmonic subspaces has been presented. The five-phase model together with the decoupled IRFOC have then been implemented in Matlab/Simulink and the obtained simulation results have been shown.

References

Duran MJ, Salas F, and Arahal MR (2008) Bifurcation analysis of five-phase induction motor drives with third harmonic injection. *IEEE Transactions on Industrial Electronics*, **55**(5), 2006–2014.

Jones M and Levi E (2002) A literature survey of state-of-the-art in multiphase AC drives. *37th International Universities Power Engineering Conference, UPEC*, Stafford, pp. 505–510.

Leonhard W (2001) *Control of Electrical Drives*. Springer-Verlag, 3rd edn, Berlin. ISBN 3-540-41820-2.

Levi E, Bojoi R, Profumo F, *et al*. (2007) Multiphase induction motor drives - A technology status review. *IET Electric Power Applications*, **1**(4) 489–516.

Morselli R and Zanasi R (2006) Modeling of automotive control systems using power oriented graphs. *32nd Annual Conference of the IEEE Industrial Electronics Society, IECON*, Paris, pp. 5295–5300.

Pereira LA, Scharlau CC, Pereira LFA, and Haffner JF (2006) General model of a five-phase induction machine allowing for harmonics in the air gap field. *IEEE Transactions on Energy Conversion*, **21**(4), 891.

Toliyat HA, Lipo TA, and White JC (1991) Analysis of a concentrated winding induction machine for adjustable speed drive applications. I. Motor analysis. *IEEE Transactions on Energy Conversion*, **6**(4), 679–683.

Toliyat HA, Lipo TA, and White JC (1991) Analysis of a concentrated winding induction machine for adjustable speed drive applications. II. Motor design and performance. *IEEE Transactions on Energy Conversion*, **6**(4), 684–692.

Vas P (1990) *Vector Control of AC Machines.* Clarendon Press, Oxford, 1st edn. ISBN 0-19-859370-8.

Xu H, Toliyat HA, and Petersen LJ (2001) Rotor field oriented control of five-phase induction motor with the combined fundamental and third harmonic currents. *IEEE APEC*, **1**, pp. 392–398.

Xu H, Toliyat HA, and Petersen LJ (2002) Five-phase induction motor drives with DSP-based control system. *IEEE Transactions on Power Electronics*, **17**(4), 524–533.

Zanasi R (1991) Power Oriented modeling of dynamical system for simulation. *Proceedings of IMACS Symposium on Modeling and Control of Technological Systems, MCTS*, Lille, Vol. 2, pp. 31–35.

Zanasi R, Grossi F, and Azzone G (2009) The POG technique for modeling multiphase asynchronous motors. *Proceding of 5th IEEE International Conference on Mechatronics*, Málaga, pp. 14–17.

Zanasi R (2010) The power-oriented graphs technique: system modeling and basic properties. *Proceding of Vehicle Power and Propulsion Conference, VPPC*, Lille, France, pp. 1–6.

Zanasi R and Azzone G (2010) Complex dynamic model of a multiphase asynchronous motor. *Proceeding of International Conference on Eletrical Machines, ICEM*, September 6, Rome, Italy.

Zanasi R and Azzone G (2011) Field oriented control of a multiphase asynchronous motor with harmonic injection. *Proceeding of 18th IFAC World Congress*, August 28–September 2, 2011, Milan, Italy.

13

Backstepping Controller for DFIM with Bidirectional AC/DC/AC Converter

Abderrahim El Fadili, Vincent Van Assche,
Abdelmounime El Magri, and Fouad Giri
GREYC Lab, University of Caen Basse-Normandie, France

13.1 Introduction

The doubly-fed induction motor (DFIM) enjoys several features, for example, high-power handling capability (without necessitating power rating increase of the converters), good stability performances both at low- and high-speed operations (Khojet El Khil *et al.* 2006). These features explain why this type of machine is getting spread in different fields of industry. It has proved to be quite suitable both as a motor in various applications (Metwally *et al.* 2002; Peresadaa *et al.* 2004; Bonnet *et al.* 2007; Salloum *et al.* 2007; Vidal *et al.* 2008; Xiying and Jian 2010) as well as a generator, especially in wind–energy conversion (Boukhezzar and Siguerdidjane 2009; Poitiers *et al.* 2009; Abo-Khalil 2012; Song *et al.* 2012). It also turns out to be a possible alternative to the synchronous machine in high-power applications, for example, railway traction, marine propulsion, metallurgy, rolling mills, or hydroelectric stations, and in very low-speed applications, for example, coiler-uncoiler.

The DFIM is a wound-rotor AC induction motor that can be controlled from the stator and/or from the rotor, thus offering various combinations. The first option is one where the DFIM is (doubly) acted upon, that is, both from the stator and the rotor (Figure 13.1). This configuration necessitates two converters, powering respectively the stator and the rotor. Of course, this has a price but this is largely compensated by the flexibility offered by the numerous

AC Electric Motors Control: Advanced Design Techniques and Applications, First Edition. Edited by Fouad Giri.

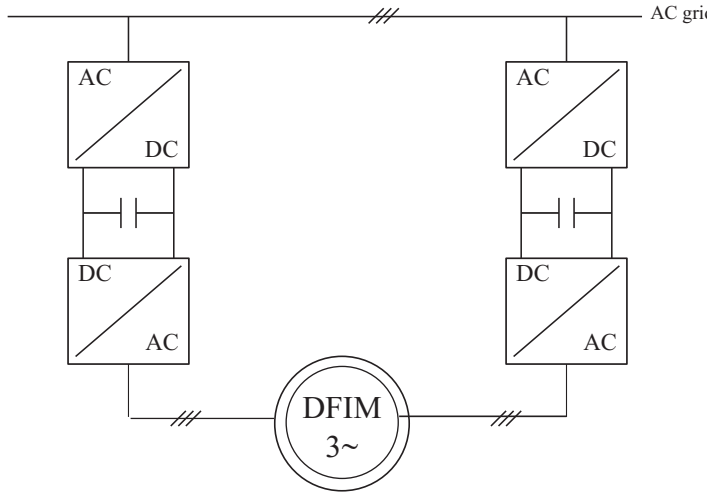

Figure 13.1 DFIM supplied by tow inverters in stator and rotor

control inputs, yielding four freedom degrees (Ourici 2012). The second configuration is one where the DFIM is controlled from the rotor (Figure 13.2). Then, a single bidirectional pulse-width modulation (PWM) power converter is implemented on the rotor, while the stator side is directly connected to the power grid (Verna *et al*. 2010). This configuration is suitable for applications involving limited rotor speed variation around the synchronous speed value. Indeed, as the power supplied from the rotor (slip power) is proportional to the slip, only a small fraction of the overall system power can be handled by means of the rotor-side power

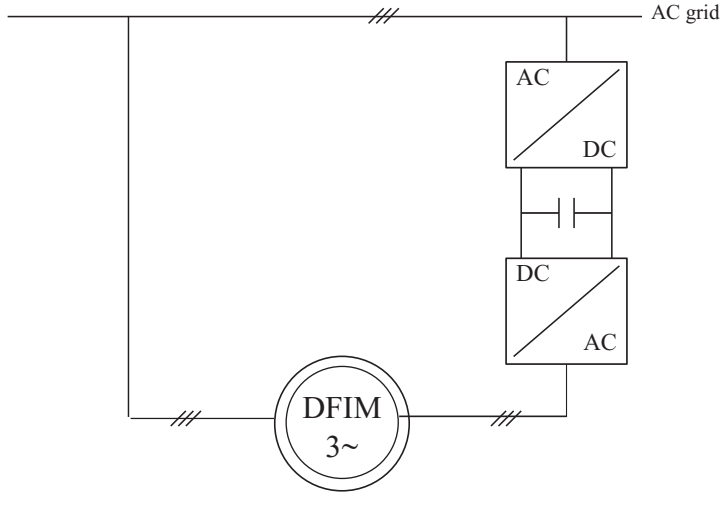

Figure 13.2 DFIM supplied by the rotor (inverter in rotor only)

converter. Moreover, in varying-speed drive applications, the slip power regenerated by the rotor-side converter, during motor operation stages, is released to the line grid resulting in highly efficient energy conversion (Peresadaa *et al.* 2004).

The problem of controlling DFIMs has been dealt with following different approaches. In Hopfensperger *et al.* (2000), a field-oriented controller without position sensor has been proposed for DFIMs in motor applications with one converter on the rotor side whereas the stator side is connected to the network. Field-oriented control of DFIMs with tow inverters, with and without speed sensor, was presented in Metwally *et al.* (2002) and Khojet El Khil *et al.* (2004). In Gritli *et al.* (2011), fault-tolerant control of DFIMs has been studied under time-varying conditions. Other control strategies have been proposed including direct torque control (Bonnet *et al.* 2007), sliding-mode control (Vidal *et al.* 2008), output-feedback control (Peresadaa *et al.* 2004), and loop-shaping H_∞ control (Salloum *et al.* 2007).

This chapter presents a theoretical framework for designing a global control strategy of the DFIM and related power equipments. The DFIM stator windings are directly connected to the line grid, while the rotor windings are controlled via a bidirectional power converter. The control objective is twofold: (1) tight speed regulation over wide-range speed-reference variation, despite the load torque uncertainly; (2) power factor correction (PFC) for the overall controlled system including the DFIM and related converters. A multiloop nonlinear adaptive controller is designed, on the basis of the DFIM nonlinear model, using the backstepping technique. The achieved control performances are formally described using tools from the averaging theory.

The chapter is organized as follows: in Section 13.2, the whole association including the AC/DC/AC power converters and the DFIM is modeled; the multiloop adaptive controller is designed and analyzed in Section 13.3; the control performances are illustrated through numerical simulations in Section 13.4.

13.2 Modeling "AC/DC/AC Converter—Doubly-Fed Induction Motor" Association

The controlled system is illustrated by Figure 13.3. It includes two parts: (1) a "DFIM-inverter" association; (2) a triphase AC/DC rectifier. The rectifier is an AC/DC converter operating, just as the DC/AC inverter, according to the well-known PWM principle.

13.2.1 Doubly-Fed Induction Motor Model

The model of DFIM, expressed in the oriented stator-voltage-linked dq-frame, has already been presented in Chapter 2. It was obtained by operating the (energy preserving) Park transformation on the three-phase electrical quantities. This choice is suitable as it facilitates the control of the active and the reactive powers exchanged between the motor and the grid.

Considering as state variables the flux components (ϕ_{sd} and ϕ_{sq}) and the current components (i_{rd} and i_{rq}), the DFIM two-phase model has been shown to be defined by the following state-space representation:

$$\frac{d\omega_m}{dt} = p\frac{M_{sr}}{JL_s}(\phi_{sq}i_{rd} - \phi_{sd}i_{rq}) - \frac{T_L}{J} - \frac{F}{J}\omega_m, \tag{13.1}$$

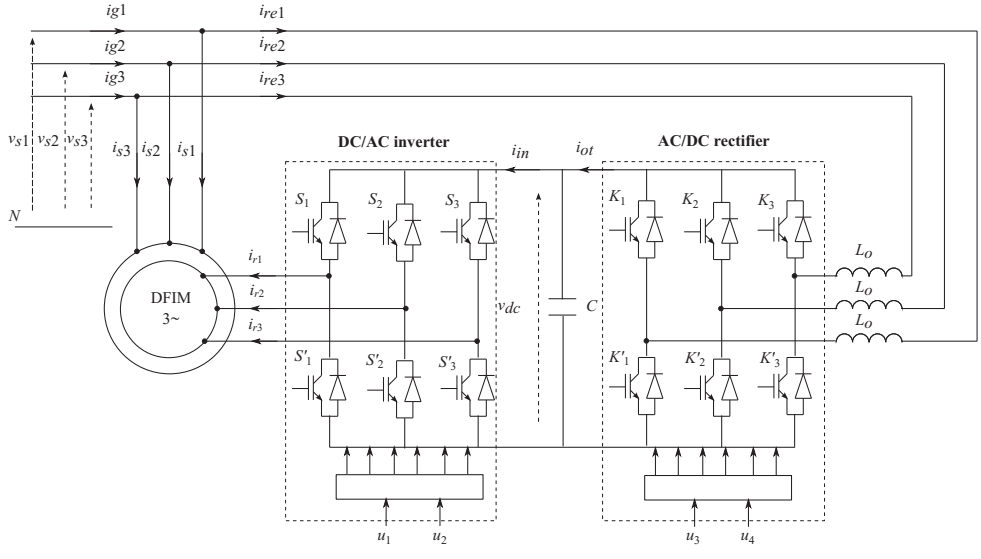

Figure 13.3 Controlled system including a DFIM and associated AC/DC/AC converters

$$\frac{d\phi_{sd}}{dt} = -\frac{1}{\tau_s}\phi_{sd} + \omega_s\phi_{sq} + \frac{M_{sr}}{\tau_s}i_{rd} + V_s, \tag{13.2}$$

$$\frac{d\phi_{sq}}{dt} = -\frac{1}{\tau_s}\phi_{sq} - \omega_s\phi_{sd} + \frac{M_{sr}}{\tau_s}i_{rq}, \tag{13.3}$$

$$\frac{di_{rd}}{dt} = -\gamma_1 i_{rd} + (\omega_s - p\omega_m)i_{rq} + \frac{\gamma_2}{\tau_s}\phi_{sd} - p\omega_m\gamma_2\phi_{sq} - \gamma_2 V_s + \gamma_3 v_{rd}, \tag{13.4}$$

$$\frac{di_{rq}}{dt} = -\gamma_1 i_{rq} - (\omega_s - p\omega_m)i_{rd} + \frac{\gamma_2}{\tau_s}\phi_{sq} + p\omega_m\gamma_2\phi_{sd} + \gamma_3 v_{rq}, \tag{13.5}$$

where ϕ_{sd} and ϕ_{sq} are stator flux dq-components; i_{rd} and i_{rq} are rotor current dq-components; V_s is the stator voltage norm; v_{rd} and v_{rq} are rotor voltage dq-components; ω_m is the motor speed; ω_s is the dq-frame speed; R_s and R_r are stator and rotor resistances; L_s and L_r are stator and rotor self-inductances; M_{sr} is the mutual inductance between the stator and the rotor; F, J, and T_L are friction coefficient, rotor inertia, and load torque, respectively; and p is the number of pole pairs and rotor windings.

The remaining parameters are defined as follows:

$$\gamma_1 = \frac{R_r L_s^2 + R_s M_{sr}^2}{\sigma L_r L_s^2}, \quad \sigma = 1 - \frac{M_{sr}^2}{L_s L_r}, \quad \tau_s = \frac{L_s}{R_s}, \quad \gamma_2 = \frac{M_{sr}}{\sigma L_s L_r}, \quad \gamma_3 = \frac{1}{\sigma L_r}.$$

13.2.2 Modeling of the System "DC/AC Inverter–DFIM"

The inverter is featured by the fact that the rotor voltage d and q components are independently controlled. To this end, these voltages are expressed in function of the corresponding control inputs (see, e.g., Michael *et al.* 1998):

$$v_{rd} = v_{dc}u_1, \quad v_{rq} = v_{dc}u_2, \quad i_{in} = u_1 i_{rd} + u_2 i_{rq}, \tag{13.6}$$

where u_1 and u_2 are (averaged versions) of the dq-components of the triphase duty ratio system (s_1, s_2, s_3). Specifically, the former are obtained by operating the Park transformation on the latter and averaging the result over the PWM periods; i_{in} designates the input current inverter; v_{dc} denotes the voltage in capacitor C; and s_1, s_2, and s_3 are binary input signals, defined as follows:

$$s_i = \begin{cases} 1, & \text{if } S_i \text{ On } \textit{and } S_i' \text{ Off;} \\ 0, & \text{if } S_i \text{ Off } \textit{and } S_i' \text{ On;} \end{cases} \quad i = 1, 2, 3. \tag{13.7}$$

Now, let us define the averaged state variables:

$$\overline{\omega}_m = x_1, \overline{\phi}_{sd} = x_2, \overline{\phi}_{sq} = x_3, \overline{i}_{rd} = x_4, \overline{i}_{rq} = x_5, \overline{v}_{dc} = x_6, \overline{v}_{rd} = u_1 x_6, \overline{v}_{rq} = u_2 x_6.$$

As is clear from the context, the notation $\overline{\bullet}$ refers to averaging over the PWM periods. Then, it is proved in many places that instantaneous "DFIM-inverter" representation (equations (13.1), (13.2), (13.3), (13.4), and (13.5) assumes the following averaged form, involving the averaged variables (13.6):

$$\frac{dx_1}{dt} = -\frac{F}{J}x_1 + p\frac{M_{sr}}{JL_s}(x_3x_4 - x_2x_5) - \frac{T_L}{J}, \tag{13.8}$$

$$\frac{dx_2}{dt} = -\frac{1}{\tau_s}x_2 + \omega_s x_3 + \frac{M_{sr}}{\tau_s}x_4 + V_s, \tag{13.9}$$

$$\frac{dx_3}{dt} = -\frac{1}{\tau_s}x_3 - \omega_s x_2 + \frac{M_{sr}}{\tau_s}x_5, \tag{13.10}$$

$$\frac{dx_4}{dt} = -\gamma_1 x_4 + (\omega_s - px_1)x_5 + \frac{\gamma_2}{\tau_s}x_2 - p\gamma_2 x_1 x_3 - \gamma_2 V_s + \gamma_3 x_6 u_1, \tag{13.11}$$

$$\frac{dx_5}{dt} = -\gamma_1 x_5 - (\omega_s - px_1)x_4 + \frac{\gamma_2}{\tau_s}x_3 + p\gamma_2 x_1 x_2 + \gamma_3 x_6 u_2. \tag{13.12}$$

13.2.3 AC/DC Rectifier Modeling

The AC/DC rectifier, connected to the triphase power grid, is depicted in Figure 13.4. It consists of six (semiconductor) insulated gate bipolar transistors (IGBTs) and antiparallel diodes, allowing for bidirectional current flow mode, arranged in three legs denoted 1, 2, and 3. The six semiconductors are considered as ideal switches. On a given leg, only one switch is conducting at a time.

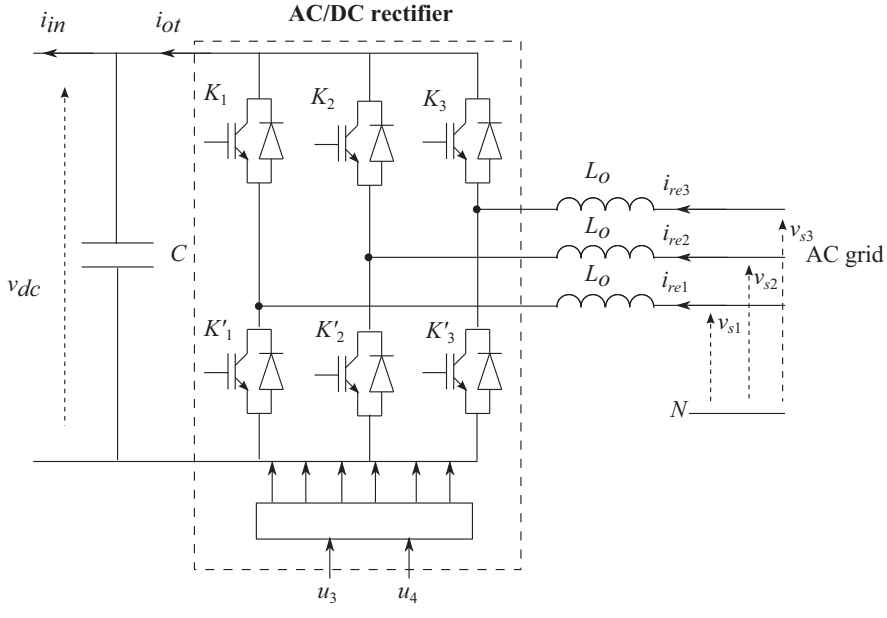

Figure 13.4 AC/DC converter power with triphase input

It is readily checked, applying Kirchhoff's laws, that the rectifier is described by the following set of differential equations:

$$L_o \frac{d[i_{re}]_{123}}{dt} = [v_s]_{123} - v_{dc}[k]_{123}, \tag{13.13}$$

$$\frac{dv_{dc}}{dt} = \frac{1}{C}(i_{ot} - i_{in}), \tag{13.14}$$

$$i_{in} = [k]^T_{123}[i_{re}]_{123}, \tag{13.15}$$

where

$$[i_{re}]_{123} = \begin{bmatrix} i_{re1} & i_{re2} & i_{re3} \end{bmatrix}^T$$

is the power grid current (rectifier side),

$$[v_s]_{123} = \begin{bmatrix} v_{s1} & v_{s2} & v_{s3} \end{bmatrix}^T$$

is the sinusoidal triphase grid voltage (with known constant frequency ω_s), i_{ot} is the rectifier output current, and k_i is a binary function, representing the position of the switch K_i.

Specifically, one has

$$k_i = \begin{cases} 1, & \text{if } K_i \text{ On } and \ K_i^{'} \text{ Off;} \\ 0, & \text{if } K_i \text{ Off } and \ K_i^{'} \text{ On;} \end{cases} \quad i = 1, 2, 3 \ldots \tag{13.16}$$

For control synthesis purpose, the Park transformation is applied to the triphase representation (13.13) and (13.14), with the d-axis being linked to the stator voltage. Doing so, one obtains the following equations, expressed in the dq-coordinates:

$$\frac{di_{red}}{dt} = \omega_s i_{req} + \frac{V_s}{L_o} - \frac{v_{dc}u_3}{L_o}, \tag{13.17}$$

$$\frac{di_{req}}{dt} = -\omega_s i_{red} - \frac{v_{dc}u_4}{L_o}, \tag{13.18}$$

$$\frac{dv_{dc}}{dt} = \frac{1}{C}(i_{ot} - i_{in}), \tag{13.19}$$

where i_{red} and i_{req} denotes the rectifier-side grid current dq-coordinates; and u_3 and u_4 represent the averaged d- and q-axis components of the triphase duty ratio system (k_1, k_2, k_3).

Introducing the state variables $x_7 = \bar{i}_{red}$ and $x_8 = \bar{i}_{req}$, and replacing i_{ot} by $i_{ot} = u_3x_7 + u_4x_8$, the above rectifier model rewrites as follows:

$$\frac{dx_6}{dt} = \frac{1}{C}(u_3x_7 + u_4x_8 - \bar{i}_{in}), \tag{13.20}$$

$$\frac{dx_7}{dt} = \omega_s x_8 + \frac{V_s}{L_o} - \frac{x_6u_3}{L_o}, \tag{13.21}$$

$$\frac{dx_8}{dt} = -\omega_s x_7 - \frac{x_6u_4}{L_o}. \tag{13.22}$$

For convenience, the state-space equations obtained so far are cast together within a single global state space model representing the whole system including the DFIM combined with the associated AC/DC/AC converters. For future referencing, the complete model is rewritten as

$$\frac{dx_1}{dt} = -\frac{F}{J}x_1 + p\frac{M_{sr}}{JL_s}(x_3x_4 - x_2x_5) - \frac{T_L}{J}, \tag{13.23}$$

$$\frac{dx_2}{dt} = -\frac{1}{\tau_s}x_2 + \omega_s x_3 + \frac{M_{sr}}{\tau_s}x_4 + V_s, \tag{13.24}$$

$$\frac{dx_3}{dt} = -\frac{1}{\tau_s}x_3 - \omega_s x_2 + \frac{M_{sr}}{\tau_s}x_5, \tag{13.25}$$

$$\frac{dx_4}{dt} = -\gamma_1 x_4 + (\omega_s - px_1)x_5 + \frac{\gamma_2}{\tau_s}x_2 - p\gamma_2 x_1x_3 - \gamma_2 V_s + \gamma_3 x_6u_1, \tag{13.26}$$

$$\frac{dx_5}{dt} = -\gamma_1 x_5 - (\omega_s - px_1)x_4 + \frac{\gamma_2}{\tau_s}x_3 + p\gamma_2 x_1x_2 + \gamma_3 x_6u_2, \tag{13.27}$$

$$\frac{dx_6}{dt} = \frac{1}{C}(x_7 u_3 + x_8 u_4 - \bar{i}_{in}), \tag{13.28}$$

$$\frac{dx_7}{dt} = \omega_s x_8 + \frac{V_s}{L_o} - \frac{x_6 u_3}{L_o}, \tag{13.29}$$

$$\frac{dx_8}{dt} = -\omega_s x_7 - \frac{x_6 u_4}{L_o}. \tag{13.30}$$

13.3 Controller Design

13.3.1 Control Objectives

There are two operational control objectives:

1. **Speed regulation:** the machine speed ω_m must track, as closely as possible, a given reference signal x_1^*, despite the load torque T_L uncertainty.
2. **PFC requirement:** the whole system input current (i_{g1}, i_{g2}, i_{g3}) must be sinusoidal with the same frequency as the supplied power grid and the reactive power absorbed by the DFIM must be null all the time.

The flexibility offered by the available four control inputs, that is, u_1, u_2, u_3, and u_4, makes possible to add two more control objectives. The following additional objectives present a practical interest:

3. **Controlling the continuous voltage** v_{dc} making it track a given reference signal $x_6^* = v_{dc}^*$. The latter is generally set to a constant value equal to the nominal voltage powering the converter.
4. **Regulating the stator flux norm** $\Phi_s = \sqrt{x_2^2 + x_3^2}$ to a reference value Φ_s^*, preferably equal to its nominal value.

13.3.2 Motor Speed and Stator Flux Norm Regulation

The problem of controlling the rotor speed and stator flux norm is presently addressed for the DFIM described by equations (13.23), (13.24), (13.25), (13.26), and (13.27). The speed reference $x_1^* = \omega_m^*$ is any bounded and derivable function of time and its two first derivatives are available and bounded. These conditions can always be complied by filtering the (possibly nondifferentiable) original reference by unit static gain second order linear filter. The stator flux reference Φ_s^* is set to its nominal value. The controller design will now be performed in two steps, using the adaptive backstepping technique (Krstic *et al.* 1995).

Step 1: Introduce the tracking errors:

$$z_1 = x_1^* - x_1, \tag{13.31}$$

$$z_2 = \Phi_s^{*2} - ({x_2}^2 + {x_3}^2). \tag{13.32}$$

It follows from (13.23), (13.24), and (13.25) that the errors z_1 and z_2 undergo the differential equations

$$\dot{z}_1 = \dot{x}_1^* + \frac{F}{J}x_1 - p\frac{M_{sr}}{JL_s}(x_3x_4 - x_2x_5) + \frac{T_L}{J}, \tag{13.33}$$

$$\begin{aligned}\dot{z}_2 &= 2\Phi_s^*\dot{\Phi}_s^* - 2(\dot{x}_2x_2 + \dot{x}_3x_3)\\ &= 2\Phi_s^*\dot{\Phi}_s^* + \frac{2}{\tau_s}({x_2}^2 + {x_3}^2) - \frac{2M_{sr}}{\tau_s}(x_2x_4 + x_3x_5) - 2x_2V_s.\end{aligned} \tag{13.34}$$

In equations (13.33) and (13.34), the quantities $p\frac{M_{sr}}{JL_s}(x_3x_4 - x_2x_5)$ and $\frac{2M_{sr}}{\tau_s}(x_2x_4 + x_3x_5)$ stand up as virtual control signals. If these were the actual control signals, the error system (13.33) and (13.34) could be globally asymptotically stabilized letting $p\frac{M_{sr}}{JL_s}(x_3x_4 - x_2x_5) = \mu_1$ and $\frac{2M_{sr}}{\tau_s}(x_2x_4 + x_3x_5) = \nu_1$ with

$$\mu_1 \overset{def}{=} c_1z_1 + \dot{x}_1^* + \frac{F}{J}x_1 + \frac{T_L}{J}, \tag{13.35}$$

$$\nu_1 \overset{def}{=} c_2z_2 + 2\Phi_s^*\dot{\Phi}_s^* + \frac{2}{\tau_s}(x_2^2 + x_3^2) - 2x_2V_s. \tag{13.36}$$

Presently, the load torque T_L is not assumed to be known. This suggests that one must consider the certainty equivalence form of equation (13.35). That is, one has

$$\mu_1 \overset{def}{=} c_1z_1 + \dot{x}_1^* + \frac{F}{J}x_1 + \frac{\hat{T}_L}{J}, \tag{13.37}$$

where c_1 and c_2 are any positive design parameters and $\hat{T}_L$ is the estimate of T_L (yet to be determined).

As the quantities $p\frac{M_{sr}}{JL_s}(x_3x_4 - x_2x_5) = \mu_1$ and $\frac{2M_{sr}}{\tau_s}(x_2x_4 + x_3x_5) = \nu_1$ are not the actual control signals, they cannot be let equal to μ_1 and ν_1, respectively. Nevertheless, we retain the expressions of μ_1 and ν_1 as first stabilizing functions and introduce the new errors

$$z_3 = \mu_1 - p\frac{M_{sr}}{JL_s}(x_3x_4 - x_2x_5), \tag{13.38}$$

$$z_4 = \nu_1 - \frac{2M_{sr}}{\tau_s}(x_2x_4 + x_3x_5). \tag{13.39}$$

Then, using the notations (13.37), (13.38) and (13.39), the dynamics of the errors z_1 and z_2, initially described by (13.33) and (13.34), can be rewritten as follows:

$$\dot{z}_1 = -c_1z_1 + z_3 + \frac{\tilde{T}_L}{J}, \tag{13.40}$$

$$\dot{z}_2 = -c_2z_2 + z_4, \tag{13.41}$$

where,

$$\tilde{T}_L = T_L - \hat{T}_L \tag{13.42}$$

Step 2: The second design step consists of choosing the actual control signals, u_1 and u_2, so that all errors (z_1, z_2, z_3, z_4) converge to zero. To this end, we should make clear how these errors depend on the actual control signals (u_1, u_2). Focusing first on z_3, it follows from (13.38) that

$$\dot{z}_3 = \dot{\mu}_1 - p\frac{M_{sr}}{JL_s}(\dot{x}_3 x_4 + x_3\dot{x}_4 - \dot{x}_2 x_5 - x_2\dot{x}_5). \tag{13.43}$$

Assume that the load torque T_L is constant or slowly time varying and using equations (13.23), (13.24), (13.25), (13.26), (13.27), (13.42) and (13.37), one gets from (13.43)

$$\dot{z}_3 = \mu_2 + \left(c_1 - \frac{F}{J}\right)\frac{\tilde{T}_L}{J} - \frac{\dot{\tilde{T}}_L}{J} - p\frac{M_{sr}}{JL_s}\gamma_3 x_6(x_3 u_1 - x_2 u_2), \tag{13.44}$$

with

$$\mu_2 = -c_1^2 z_1 + c_1 z_3 + \ddot{x}_1^* - \left(\frac{F}{J}\right)^2 x_1 + p\frac{M_{sr}}{JL_s}\left(\frac{F}{J} + \gamma_1 + \frac{1}{\tau_s}\right)(x_3 x_4 - x_2 x_5)$$

$$-\frac{F}{J}\frac{\hat{T}_L}{J} + p\frac{M_{sr}}{JL_s}\left[p x_1 x_3 x_5 + p\gamma_2 x_1 \Phi_s^2 + p x_1 x_2 x_4 + \gamma_2 x_3 V_s + x_5 V_s\right]. \tag{13.45}$$

Similarly, it follows from equation (13.39) that z_4 undergoes the following differential equation:

$$\dot{z}_4 = \dot{\nu}_1 - \frac{2M_{sr}}{\tau_s}(\dot{x}_2 x_4 + x_2\dot{x}_4 + \dot{x}_3 x_5 + x_3\dot{x}_5). \tag{13.46}$$

Using equation (13.23), (13.24), (13.25), (13.26), (13.27), and (13.36), it follows from (13.46) that:

$$\dot{z}_4 = \nu_2 - \frac{2M_{sr}}{\tau_s}\gamma_3 x_6(x_2 u_1 + x_3 u_2), \tag{13.47}$$

with

$$\begin{aligned}\nu_2 = {} & c_2(-c_2 z_2 + z_4) + 2(\dot{\Phi}_s^*)^2 + 2\Phi_s^* \ddot{\Phi}_s^* \\ & + 2\frac{M_{sr}}{\tau_s}\left(\frac{3}{\tau_s} + \gamma_1\right)(x_2 x_4 + x_3 x_5) + \frac{4}{\tau_s}\left(-\frac{1}{\tau_s}\Phi_s^2 + V_s x_2\right) \\ & - 2V_s\left(-\frac{1}{\tau_s}x_2 + \omega_s x_3 + \frac{M_{sr}}{\tau_s}x_4 + V_s\right) \\ & - 2\frac{M_{sr}}{\tau_s}\left(\frac{M_{sr}}{\tau_s}(x_4^2 + x_5^2) + \frac{\gamma_2}{\tau_s}\Phi_s^2 + p x_1(x_3 x_4 - x_2 x_5) + x_4 V_s - \gamma_2 x_2 V_s\right). \end{aligned} \tag{13.48}$$

To analyze the error system composed of (13.40), (13.41), (13.44), and (13.47), let us consider the following augmented Lyapunov function candidate:

$$V = \frac{1}{2}z_1^2 + \frac{1}{2}z_2^2 + \frac{1}{2}z_3^2 + \frac{1}{2}z_4^2 + \frac{1}{2}\frac{\tilde{T}_L^2}{J}. \tag{13.49}$$

Its time derivative along the trajectory of the state vector (z_1, z_2, z_3, z_4) is

$$\dot{V} = \dot{z}_1 z_1 + \dot{z}_2 z_2 + \dot{z}_3 z_3 + \dot{z}_4 z_4 + \frac{\dot{\tilde{T}}_L \tilde{T}_L}{J}. \tag{13.50}$$

Using equations (13.40), (13.41), (13.44), and (13.47), equation (13.50) develops as follows:

$$\begin{aligned}\dot{V} = {} & z_1\left(-c_1 z_1 + z_3 + \frac{\tilde{T}_L}{J}\right) + z_2(-c_2 z_2 + z_4) \\ & + z_3\left(\mu_2 + \left(c_1 - \frac{F}{J}\right)\frac{\tilde{T}_L}{J} - \frac{\dot{\tilde{T}}_L}{J} - p\frac{M_{sr}}{J L_s}\gamma_3 x_6(x_3 u_1 - x_2 u_2)\right) \\ & + z_4\left(\nu_2 - \frac{2M_{sr}}{\tau_s}\gamma_3 x_6(x_2 u_1 + x_3 u_2)\right) + \frac{\dot{\tilde{T}}_L \tilde{T}_L}{J}, \end{aligned} \tag{13.51}$$

adding $c_3 z_3^2 - c_3 z_3^2 + c_4 z_4^2 - c_4 z_4^2$ to the right-hand side of equation (13.51) and rearranging terms, yields

$$\begin{aligned}\dot{V} = {} & -c_1 z_1^2 - c_2 z_2^2 - c_3 z_3^2 - c_4 z_4^2 \\ & + z_3\left[\mu_2 + c_3 z_3 + z_1 - \frac{\dot{\tilde{T}}_L}{J} - p\frac{M_{sr}}{J L_s}\gamma_3 x_6(x_3 u_1 - x_2 u_2)\right] \\ & + z_4\left[\nu_2 + c_4 z_4 + z_2 - \frac{2M_{sr}}{\tau_s}\gamma_3 x_6(x_2 u_1 + x_3 u_2)\right] \\ & + \frac{\tilde{T}_L}{J}\left[\left(c_1 - \frac{F}{J}\right)z_3 + z_1 + \dot{\tilde{T}}_L\right]. \end{aligned} \tag{13.52}$$

Equation (13.52) immediately suggests the following parameter adaptation law:

$$\dot{\hat{T}}_L = -\left(c_1 - \frac{F}{J}\right) z_3 - z_1, \tag{13.53}$$

which, in view of (13.42), yields

$$\dot{\hat{T}}_L = \left(c_1 - \frac{F}{J}\right) z_3 + z_1. \tag{13.54}$$

Substituting the parameter adaptation law (13.53) to $\dot{\hat{T}}_L$ in the right-hand side of equation (13.52), gives

$$\begin{aligned}\dot{V} = &-c_1 z_1^2 - c_2 z_2^2 - c_3 z_3^2 - c_4 z_4^2 \\ &+ z_3 \left[\mu_2 + \left(c_3 + \frac{1}{J}\left(c_1 - \frac{F}{J}\right)\right) z_3 + \left(1 + \frac{1}{J}\right) z_1 - p \frac{M_{sr}}{J L_s} \gamma_3 x_6 (x_3 u_1 - x_2 u_2)\right] \\ &+ z_4 \left[\nu_2 + c_4 z_4 + z_2 - \frac{2 M_{sr}}{\tau_s} \gamma_3 x_6 (x_2 u_1 + x_3 u_2)\right],\end{aligned} \tag{13.55}$$

where c_3 and c_4 are new positive real design parameters. Equation (13.55) suggests that the control signals u_1 and u_2 must be chosen so that the two quantities between curly brackets (on the right-hand side of (13.55)) are set to zero. Letting these quantities equal to zero and solving the resulting second order linear equation system with respect to u_1 and u_2, gives the following control law:

$$\begin{bmatrix} u_1 \\ u_2 \end{bmatrix} = \begin{bmatrix} \lambda_0 & \lambda_1 \\ \lambda_2 & \lambda_3 \end{bmatrix}^{-1} \begin{bmatrix} \mu_2 + (c_3 + \frac{1}{J}(c_1 - \frac{F}{J}))z_3 + (1 + \frac{1}{J}) z_1 \\ \nu_2 + z_2 + c_4 z_4 \end{bmatrix}, \tag{13.56}$$

with

$$\begin{aligned} \lambda_0 &= p \frac{M_{sr}}{J L_s} \gamma_3 x_6 x_3, \qquad \lambda_1 = -p \frac{M_{sr}}{J L_s} \gamma_3 x_6 x_2, \\ \lambda_2 &= \frac{2 M_{sr}}{\tau_s} \gamma_3 x_6 x_2, \qquad \lambda_3 = \frac{2 M_{sr}}{\tau_s} \gamma_3 x_6 x_3. \end{aligned} \tag{13.57}$$

It is worth noticing that the matrix $\begin{bmatrix} \lambda_0 & \lambda_1 \\ \lambda_2 & \lambda_3 \end{bmatrix}$ is nonsingular as its determinant, $D = \lambda_0 \lambda_3 - \lambda_2 \lambda_4 = 2p \frac{M_{sr}^2}{J L_s \tau_s} \gamma_3^2 x_6^2 (x_2^2 + x_3^2)$, stay away from zero because the flux $\Phi_s = \sqrt{x_2^2 + x_3^2}$ never vanishes in practice due to the presence of the remnant flux.

Substituting the control law (13.56) to u_1 and u_2 on the right-hand side of (13.55) yields

$$\dot{V} = -c_1 z_1^2 - c_2 z_2^2 - c_3 z_3^2 - c_4 z_4^2. \tag{13.58}$$

As the right-hand side of equation (13.58) is a negative definite function of the state vector (z_1, z_2, z_3, z_4), the latter are globally asymptotically vanishing (Khalil 2003). The result thus established is more precisely formulated in the following proposition:

Proposition 13.3.1 *(Speed regulation). Consider the closed-loop system composed of:*

1. *the DFIM-DC/AC inverter association, described by model (13.23), (13.24), (13.25), (13.26), and (13.27),*
2. *the nonlinear controller defined by the control law (13.56), and*
3. *the parameter update law (13.54).*

Then, one has the following properties:

1. *The closed-loop error system undergoes, in the $(z_1, z_2, z_3, z_4, \tilde{T}_L)$ coordinates, the following equations:*

$$\dot{z}_1 = -c_1 z_1 + z_3 + \frac{\tilde{T}_L}{J}, \tag{13.59}$$

$$\dot{z}_2 = -c_2 z_2 + z_4, \tag{13.60}$$

$$\dot{z}_3 = -c_3 z_3 - z_1 + \left(c_1 - \frac{F}{J}\right)\frac{\tilde{T}_L}{J}, \tag{13.61}$$

$$\dot{z}_4 = -c_4 z_4 - z_2, \tag{13.62}$$

$$\dot{\tilde{T}}_L = -\left(c_1 - \frac{F}{J}\right) z_3 - z_1. \tag{13.63}$$

2. *The above linear system is stable with respect to the Lyapunov function $V = \frac{1}{2}z_1^2 + \frac{1}{2}z_2^2 + \frac{1}{2}z_3^2 + \frac{1}{2}z_4^2 + \frac{1}{2}\frac{\tilde{T}_L^2}{J}$ and the errors (z_1, z_2, z_3, z_4) are exponentially vanishing, whatever their initial values.*

Proof: Equations (13.59) and (13.60) are immediately obtained from (13.40) and (13.41). Equation (13.61) is obtained by substituting the control law (13.56) and the parameter update law (13.54) to (u_1 and u_2) on the right-hand side of (13.44). Equation (13.62) is obtained by substituting the control law (13.56) to u_1 and u_2 on the right-hand side of (13.47). Equation (13.63) is a copy of (13.53). Part 1 is proved. On the other hand, it is readily seen from (13.49) and (13.53) that $V = \frac{1}{2}z_1^2 + \frac{1}{2}z_2^2 + \frac{1}{2}z_3^2 + \frac{1}{2}z_4^2 + \frac{1}{2}\frac{\tilde{T}_L^2}{J}$ is a (radially unbounded) Lyapunov function of the error system (13.59), (13.60), (13.61), and (13.62). As $\dot{V}$ is a semi-negative definite function of the state vector $(z_1, z_2, z_3, z_4,)$, the whole error system is stable (by Lyapunov's equilibrium point theorem) and the above errors converge to zero (by Lasalle's invariant principle), whatever are their initial values. Besides, asymptotic stability implies exponential stability due to system linearity (Khalil 2003). Proposition 13.3.1 is established. □

Remark 13.3.2 *Note that the exponential nature of stability guarantees stability robustness with respect to modeling and measurements errors (Khalil 2003).*

13.3.3 Power Factor Correction and DC Voltage Controller

Controlling Rectifier Input Current to Meet PFC Requirement

The PFC objective means that the grid current, powering the overall system, should be sinusoidal and in phase or in opposite phase with the AC supply voltage. Accordingly, one seeks a regulator that makes the q-components of the input current, that is, $\bar{i}_{gq} = \bar{i}_{sq} + \bar{i}_{req}$, track a null reference signal i_{gq}. Doing so, one ensures that the grid current i_g will be in phase with the voltage supply v_s.

As the reference signal $i^*_{gq} = 0$, it follows that the tracking error $z_5 = i^*_{gq} - i_{gq}$ undergoes the following equation:

$$z_5 = -\bar{i}_{sq} - x_8. \tag{13.64}$$

Using the fact that

$$x_3 = L_s i_{sq} + M_{sr} x_5, \tag{13.65}$$

equation (13.64) becomes

$$z_5 = -\frac{x_3}{L_s} + \frac{M_{sr}}{L_s} x_5 - x_8. \tag{13.66}$$

In view of equations (13.25), (13.27), and (13.30), the above error variable undergoes the following equations:

$$\begin{aligned}
\dot{z}_5 &= -\frac{\dot{x}_3}{L_s} + \frac{M_{sr}}{L_s}\dot{x}_5 - \dot{x}_8 \\
&= -\frac{1}{L_s}\left(-\frac{1}{\tau_s}x_3 - \omega_s x_2 + \frac{M_{sr}}{\tau_s}x_5\right) + \left(\omega_s x_7 + \frac{x_6 u_4}{L_o}\right) \\
&\quad + \frac{M_{sr}}{L_s}\left(-\gamma_1 x_5 - (\omega_s - p x_1)x_4 + \frac{\gamma_2}{\tau_s}x_3 + p\gamma_2 x_1 x_2 + \gamma_3 x_6 u_2\right).
\end{aligned} \tag{13.67}$$

To get a stabilizing control law for this first order system, consider the quadratic Lyapunov function $V_5 = 0.5 z_5^2$. It can be easily checked that the time derivative $\dot{V}_5$ is a negative definite function of z_5 if the control input $u_4 x_6$ is chosen as follows:

$$u_4 x_6 = -c_5 L_o z_5 - L_o \omega_s x_7 + h_1(x), \tag{13.68}$$

with $c_5 > 0$ is a design parameter and

$$h_1(x) = \frac{L_o}{L_s}\left(-\frac{1}{\tau_s}x_3 - \omega_s x_2 + \frac{M_{sr}}{\tau_s}x_5\right)$$
$$+\frac{L_o M_{sr}}{L_s}\left(\gamma_1 x_5 + (\omega_s - p x_1)x_4 - \frac{\gamma_2}{\tau_s}x_3 - p\gamma_2 x_1 x_2 - \gamma_3 x_6 u_2\right). \tag{13.69}$$

DC Link Voltage Regulation

The aim is now to design a control law u_3 so that the rectifier output voltage $x_6 = \overline{v}_{dc}$ is steered to a given reference value $x_6^* = v_{dc}^*$. As mentioned above, v_{dc}^* is generally (not mandatory) set to the nominal value of the rotor voltage amplitude. The point is that u_3 acts also on the current x_7. A suitable control strategy is one that simultaneously regulates well the DC voltage x_6 and allows the control of the current transient. This double requirement is to be met using only one control input, namely u_3. This suggests the use of a cascade control strategy. Accordingly, an inner loop is first designed so that the current x_7 is enforced to track a reference signal x_7^*, by acting on the only available control signal u_3. Then, an outer loop is designed that generates the current reference x_7^* so that the DC voltage x_6 is regulated well to its a priori known set point.

Inner Loop Design for Current x_7

Introduce the current tracking error z_7:

$$z_7 = x_7^* - x_7. \tag{13.70}$$

The z_7-dynamics are described by the following equation:

$$\dot{z}_7 = \dot{x}_7^* - \omega_s x_8 - \frac{V_s}{L_o} + \frac{x_6 u_3}{L_o}. \tag{13.71}$$

To get a stabilizing control signal for this first order system, consider the following quadratic Lyapunov function:

$$V_7 = \frac{1}{2}z_7^2. \tag{13.72}$$

It is easily checked that the time derivative $\dot{V}_7$ can be made negative definite in the state z_7 by letting the quantity $x_6 u_3$ be chosen as follows:

$$x_6 u_3 = -c_7 L_o x_7^* + c_7 L_o x_7 - L_o \dot{x}_7^* + L_o \omega_s x_8 + V_s, \tag{13.73}$$

with $c_7 > 0$ is a design parameter.

Outer Loop Design for DC-Voltage x_6

Now, let us introduce the squared voltage variable $y = x_6^2$. Using equation (13.28), it follows that that y undergoes the following equations:

$$\begin{aligned}\dot{y} &= \frac{2}{C}(x_7 x_6 u_3 + x_8 x_6 u_4 - x_6 \bar{i}_{in}) \\ &= -\frac{2}{C}(c_7 L_o x_7 x_7^* + L_o x_7 \dot{x}_7^* + c_5 L_o x_8 z_5) + h_2(x),\end{aligned} \tag{13.74}$$

with

$$h_2(x) = \frac{2}{C}(c_7 L_o x_7^2 + V_s x_7 + x_8 h_1(x) - x_6 \bar{i}_{in}) \tag{13.75}$$

where the second line in (13.74) is obtained using (13.73). As previously mentioned, the reference signal $y^* = {v_{dc}^*}^2$ (of the squared DC-link voltage $x_6 = v_{dc}$) is chosen to be constant (i.e., $\dot{y}^* = 0$). It is given the nominal value of the rotor voltage amplitude. Then, it follows from (13.74) that the tracking error $z_6 = y^* - y$ undergoes the following equation:

$$\dot{z}_6 = \dot{y}^* + \frac{2}{C}(c_7 L_o x_7 x_7^* + L_o x_7 \dot{x}_7^* + c_5 L_o x_8 z_5) - h_2(x). \tag{13.76}$$

To get a stabilizing control law for the system (13.76), consider the following quadratic Lyapunov function:

$$V_6 = \frac{1}{2} z_6^2. \tag{13.77}$$

Deriving V_6 along the trajectory of (13.76) yields

$$\dot{V}_6 = \dot{z}_6 z_6. \tag{13.78}$$

This suggests for x_7^* the following control law:

$$\dot{x}_7^* = -c_7 x_7^* - c_5 z_5 \frac{x_8}{x_7} + \frac{C}{2L_o x_7}\left(-c_6 z_6 - \dot{y}^* + h_2(x)\right), \tag{13.79}$$

with $c_6 > 0$ a design parameter. Indeed, substituting x_7^* to (13.78) gives $\dot{V}_6 = -c_6 z_6^2$, which is clearly negative definite in z_6.

Proposition 13.3.3 *Consider the control system consisting of the subsystem (13.28), (13.29), and (13.30) in closed-loop with the control laws (13.68), (13.73), and (13.79). The resulting closed-loop system is described, in the (z_5, z_6, z_7, x_7^*) coordinates, by the following equation:*

$$\begin{aligned}&\dot{Z} = AZ + g(x), \\ &\begin{bmatrix} \dot{z}_5 \\ \dot{z}_6 \\ \dot{z}_7 \\ \dot{x}_7^* \end{bmatrix} = \begin{bmatrix} -c_5 & 0 & 0 & 0 \\ 0 & -c_6 & 0 & 0 \\ 0 & 0 & -c_7 & 0 \\ -c_5 \frac{x_8}{x_7} & -\frac{c_6 C}{2L_o x_7} & 0 & -c_7 \end{bmatrix} \begin{bmatrix} z_5 \\ z_6 \\ z_7 \\ x_7^* \end{bmatrix} + \begin{bmatrix} 0 \\ 0 \\ 0 \\ \frac{C}{2L_o x_7}(h_2(x) - \dot{y}^*) \end{bmatrix}.\end{aligned} \tag{13.80}$$

This equation defines a stable system and the vector (z_5, z_6, z_7, x_7^*) *converges exponentially fast to* $(0, 0, 0, \frac{C}{2c_7 L_o x_7} h_2(x))$*, whatever their initial values.*

Proof: Equation (13.80) is obtained by substituting the control law (13.68), (13.73), and (13.79) to $x_6 u_3$, $x_6 u_4$, and x_7^* on the right-hand side of equations (13.67) and (13.78). It is clear that the matrix A is Hurwitz implying that the closed-loop system (13.80) is globally exponentially stable. This completes the proof of Proposition 13.3.3. □

13.4 Simulation Results

The nonlinear adaptive controller, developed in Section 13.3, including the control laws (13.54), (13.68), (13.73), and (13.79) and the parameter adaptive law (13.53), will now be evaluated by simulation, considering the experimental setup described by Figure 13.5. The simulated system is given the following characteristics:

- *Supply network*: Triphase 220 V/50 Hz
- *AC/DC/AC converters*: $L_o = 15$ mH; $C = 1.5$ mF; modulation frequency 10 KHz.
- *DFIM*: 1.5 kW power, the remaining characteristics are summarized in Table 13.1.

The simulation protocol is described by Figures 13.6 and 13.7, which show that, the reference signals and the machine load are profiled so that the machine is enforced to operate, successively, both at high and low speeds. Specifically, the machine operates in high speed ($\omega_m^* = 150$ rad/s) over the interval [0, 6 s] and at low speed ($\omega_m^* = 10$ rad/s) over [6, 8 s].

The DC-link voltage reference is set to the constant value $v_{dc}^* = 220$ V. The reference value Φ_s^* for the stator flux norm is set to its nominal value (0.7 wb).

Table 13.1 Numerical values of the considered doubly-fed induction motor characteristics

Characteristic	Symbol	Value	Unity
Nominal power	P_N	1.5	kW
Nominal stator voltage	U_{sn}	380	V
Nominal stator current	I_{sn}	4.3	A
Nominal flux	Φ_{sn}	0.56	Wb
Stator resistance	R_s	1.75	Ω
Stator inductance	L_s	0.295	H
Nominal rotor voltage	U_{rn}	225	V
Nominal rotor current	I_{rn}	4.5	A
Rotor resistance	R_r	1.68	Ω
Leakage inductance	Msr	0.195	H
Rotor inductance	L_r	0.165	H
Inertia moment	J	0.35	Kgm^2
Friction coefficient	F	0.026	$\mathrm{Nm\,s\,rad}^{-1}$
Number of pole pairs	p	2	

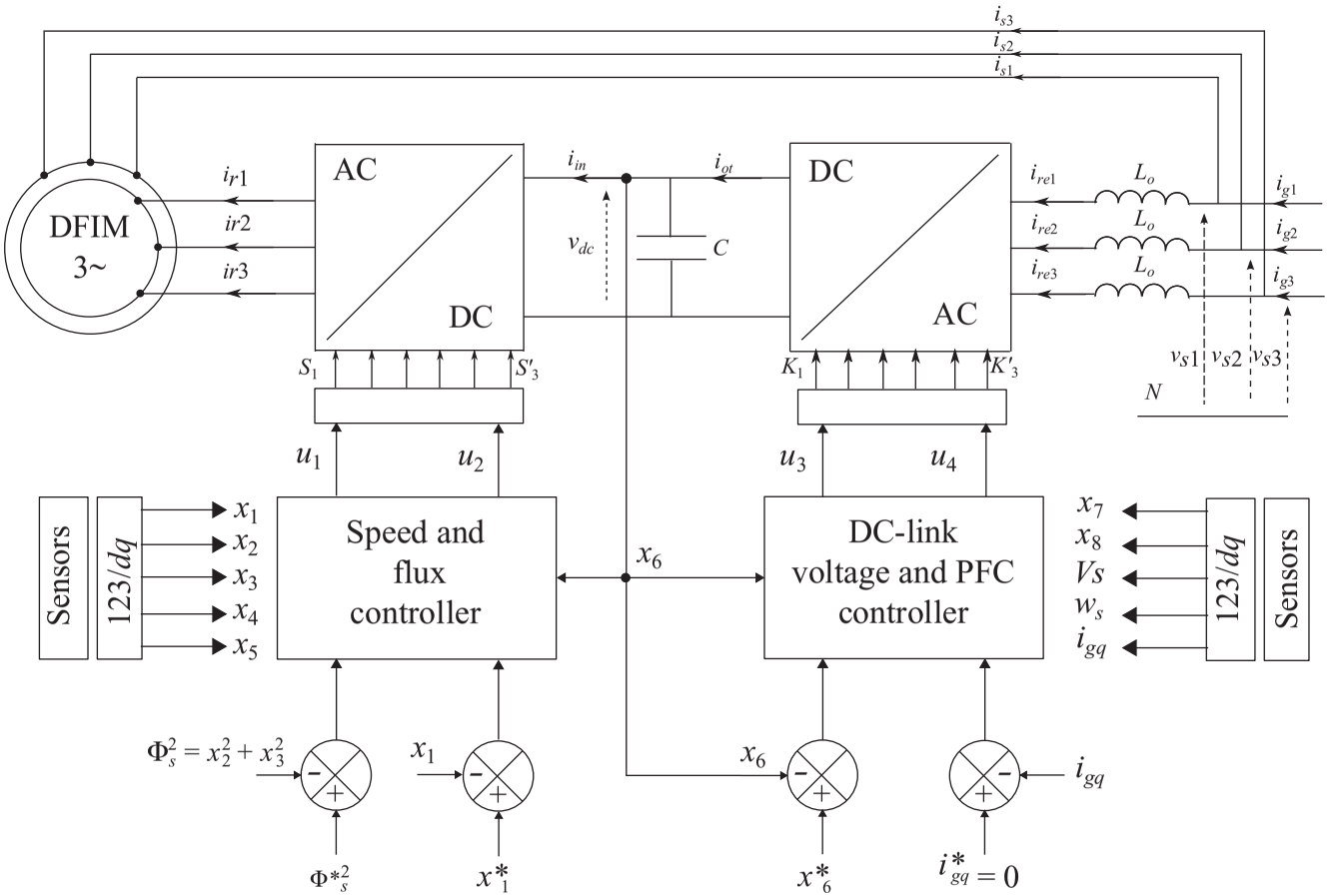

Figure 13.5 Control system including AC/DC/AC converters and a doubly-fed induction motor

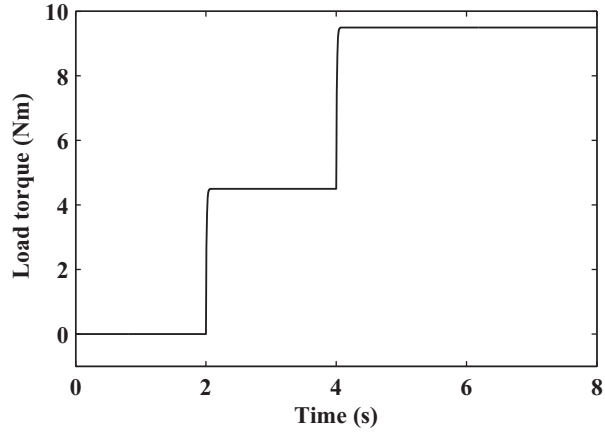

Figure 13.6 Load torque T_L(Nm)

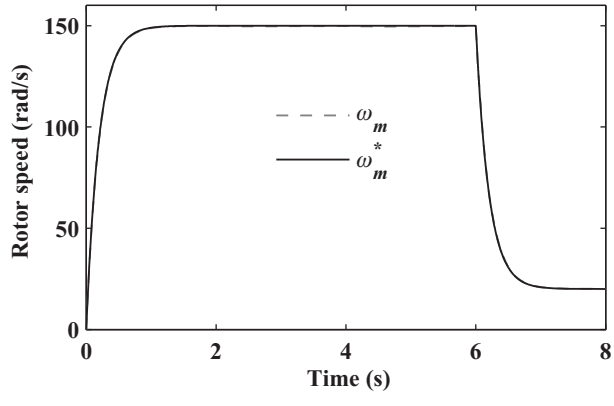

Figure 13.7 Speed ω_m (rad/s)

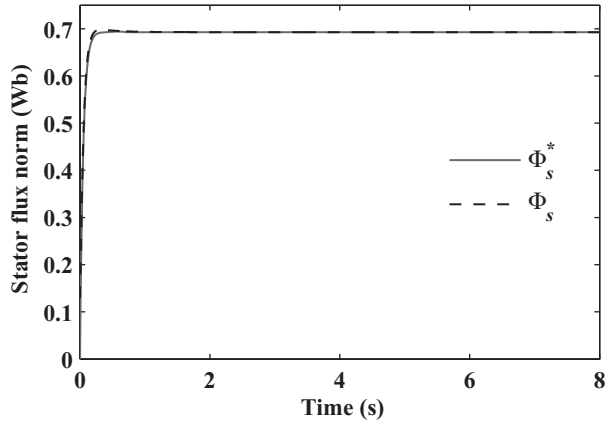

Figure 13.8 Stator flux norm (Wb)

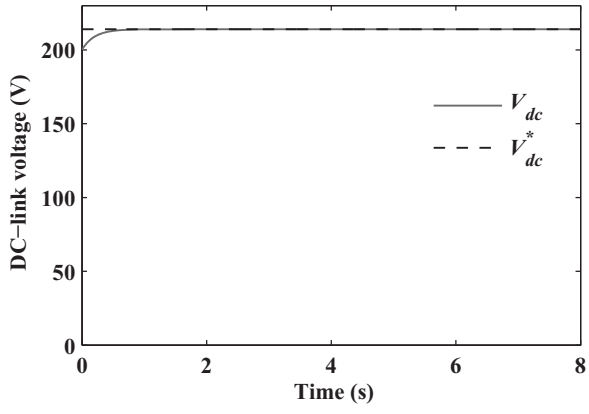

Figure 13.9 DC-link voltage v_{dc} (V)

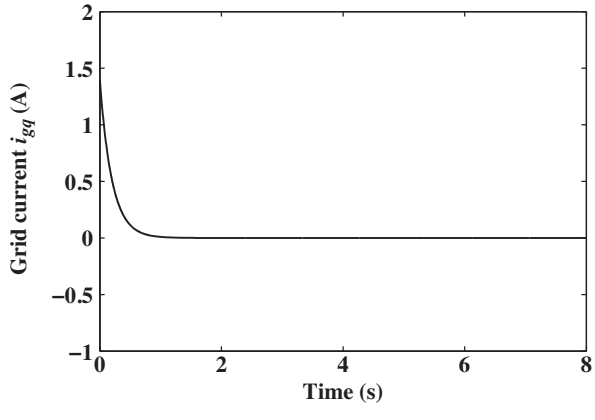

Figure 13.10 Grid current i_{gq} (A)

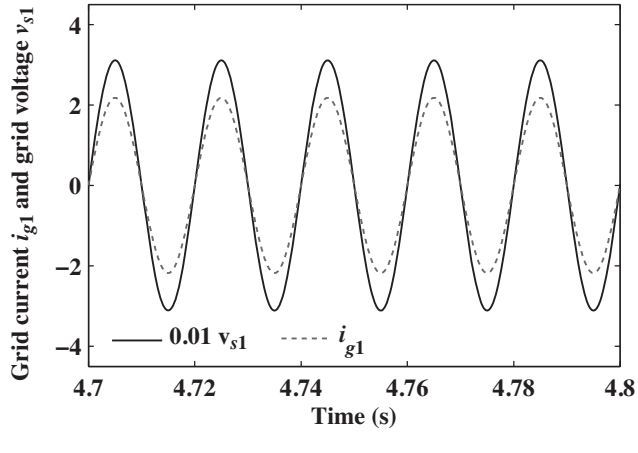

Figure 13.11 Unitary power factor checking in presence of a varying speed reference and load torque

The design parameters (c_1, c_2, c_3, c_4, c_5, c_6, c_7) have been selected using a *trial-error* search procedure. The experimental setup is simulated in the Matlab/Simulink environment with a computation step of 5 μs. This value is motivated by the fact that the inverter frequency commutation is 10 kHz. In the light of the closed-loop responses (see Figures 13.8, 13.9, 13.10, and 13.11), it is seen that the multiloop nonlinear adaptive controller meets all its objectives and enjoys quite satisfactory transient performances.

13.5 Conclusions

In this chapter, the problem of controlling systems including DFIMs and the associated AC/DC rectifier and DC/AC inverter, has been addressed. The system dynamics are described by the averaged eighth order nonlinear state space model (13.23), (13.24), (13.25), (13.26), (13.27), (13.28), (13.29), and (13.30). Based on such a model, the nonlinear controller, defined by (13.54), (13.68), (13.73), (13.79), and (13.53) has been progressively developed using the backstepping design technique. The controller, depicted by (Figure 13.5), is adaptive and multiloop. It is formally shown that this controller makes the motor velocity track well is reference trajectory and ensures a unity power factor, despite the external load torque uncertainty and variations. Furthermore, the DC link voltage is tightly regulated to its reference value. The control system performances are formally analyzed and numerically confirmed using simulation. The whole control problem is dealt with in the rotating synchronous reference frame with the *d*-axis oriented as the space voltage vector of the main AC supply.

References

Abo-Khalil AG (2012) Synchronization of DFIG output voltage to utility grid in wind power system. *Renewable Energy*, **44**, 193–198.

Bonnet F, Vidal PE, and Pietrzak-David M (2007) Dual direct torque control of doubly fed induction machine. *IEEE Transactions on Industrial Electronics*, **54**, 2482–2490.

Boukhezzar B and Siguerdidjane H (2009) Nonlinear control with wind estimation of a DFIG variable speed wind turbine for power capture optimization. *Energy Conversion and Management*, **50**, 885–892.

Gritli Y, Stefanib A, Rossib C, *et al.* (2011) Experimental validation of doubly fed induction machine electrical faults diagnosis under time-varying conditions. *Electric Power Systems Research*, **81**,7 51–766.

Hopfensperger B, Atkinson DJ, and Lakin RA (2000) Stator-flux-oriented control of a doubly-fed induction machine with and without position encoder. *IEEE Proceeding-Electrical Power Application*, **147**, 241–250.

Khalil H (2003) *Nonlinear Systems*. Prentice Hall, Upper Saddle River, NJ.

Khojet El Khil S, Slama-Belkhodja I, Pietrzak-David M, and De Fornel B (2006) Power distribution law in a doubly fed induction machine. *Mathematics and Computers in Simulation*, **71**, 360–368.

Krstic M, Kanellakopoulos I, and Kokotovic P (1995) *Nonlinear and Adaptive Control Design*. John Wiley & Sons.

Metwally HBM, Abdel-kader FE, El-Shewy HM, and El-Kholy MM (2002) Optimum performance characteristics of doubly fed inductions motors oriented control. *Energy Conversion and Management*, **43**, 3–13.

Michael J, Ryan D, and Rik W (1998) Modeling of sinewave inverters: a geometric approach. *IEEE Conference on Industrial Electronic Conference*, pp. 396–401.

Ourici A (2012) Double flux orientation control for a doubly fed induction machine. *International Journal of Electrical Power and Energy Systems*, **43**, 617–620.

Peresadaa S, Tillib A and Toniellib A (2004) Power control of a doubly fed induction machine via output feedback. *Control Engineering Practice*, **12**, 41–57.

Poitiers F, Bouaouiche T, and Machmoum M (2009) Advanced control of a doubly-fed induction generator for wind energy conversion. *Electric Power Systems Research*, **79**, 1085–1096.

Salloum G, Mbayed R, Pietrzak-David M, and De Fornel B (2007) Loop shaping H_∞ control for doubly fed induction motor. *European Conference on Power Electronics and Applications EPE*. pp. 1–9.

Song Z, Shi T, Xia C, and Chen W (2012) A novel adaptive control scheme for dynamic performance improvement of DFIG-Based wind turbines. *Energy*, **38**, 104–117.

Verma V, Maiti S and Chakraborty C (2010) Grid-connected vector-controlled slip-ring induction machine drive with out speed sensor. *Simulation Modeling Practice and Theory*, **18**, 984–997.

Vidal P.E, Pietrzak-David M, and Bonnet F (2008) Mixed control strategy of doubly fed induction machine. *Electrical Engineering, Archiv fur Electrotechnik*, Elsevier-Verlag. **90**, 337–346.

Xiying D and Jian W (2010) A new control strategy of doubly fed induction machine for hybrid electric vehicle. *International Conference on Computer, Mechatronics, Control and Electronic Engineering (CMCE)*, pp 60–63.

14

Fault Detection in Induction Motors

Alessandro Pilloni,[1] Alessandro Pisano,[1] Martin Riera-Guasp,[2]
Ruben Puche-Panadero,[2] and Manuel Pineda-Sanchez[2]
[1]*Department of Electrical and Electronic Engineering (DIEE), University of Cagliari, Italy*
[2]*Department of Electrical Engineering (DIE), Universidad Politécnica de Valencia, Spain*

14.1 Introduction

This chapter introduces recent developments in fault diagnostics of induction motors (IMs), by providing theoretical, simulative, and experimental results along with a number of implementation-related practical considerations and guidelines. Remarkably, methods for IM fault detection in both steady-state and transient operating conditions will be outlined. The chapter is structured as follows: Section 14.2 is a short introduction in which the more common faults of IM are concisely described as well as their causes, consequences, and symptoms. Section 14.3 introduces an example of model-based approach for fault detection and isolation (FDI) in IMs based on dynamical observers. Sections 14.4, 14.5, 14.6, 14.7, 14.8, and 14.9 deal with diagnostic techniques based on signal analysis approaches; in all of these approaches the stator current is used as diagnostic signal; stator current is the most used diagnostic signal in the industrial applications, since it enables for noninvasive diagnostic and does not require the use of additional probes. Sections 14.4 and 14.5 are dedicated to signal analysis techniques valid for steady-state operation; these methods, commonly designated as motor current signature analysis (MCSA) include the conventional Fourier transform (FT) approaches, and the more recently developed Hilbert-transform (HT)-based approaches. Today, the steady-state-based techniques are the most spread in the industrial environment; nevertheless, they cannot be used in some important applications—for example, wind generators or electrical vehicles—in which the functioning conditions continuously vary. Thus, in Sections 14.6, 14.7, 14.8, and 14.9,

AC Electric Motors Control: Advanced Design Techniques and Applications, First Edition. Edited by Fouad Giri.

Table 14.1 Main faults in electrical machines

Failure	Percentage
Bearings damaged	41%
Stator faults	37%
Rotor faults	10%
Other faults	12%

Source: Durocher and Feldmeier 2004.

state-of-the-art approaches based on time-frequency analysis tools, which enable for diagnostic in transient conditions are introduced. In these sections, the basis and practical remarks for the application to IM diagnostic of time-frequency analysis tools are given; the discrete wavelet transform (DWT), in Section 14.6, the continuous wavelet transform (CWT), in Section 14.7, the Wigner-Ville distribution (WVD), in Section 14.8, and the instantaneous frequency (IF) approach, in Section 14.9, will be described along with their experimental verification.

14.2 Description and Classification of IMs Faults

Electrical machines are the main generators of mechanical power. Although its design takes into account the possibility of the most typical faults, such as overvoltage and overcurrent, it is impossible to warrant that the electrical machine hold out the normal status during all its life. During the last decades there have been several technical studies with regard to the faults in the electrical machines, attending to its origin. A fault in the machine causes a nonprogrammed stop in the process, with serious economic consequences. Table 14.1 summarizes the percentage of fault occurrences in the electrical machines.

Other studies detail the failure occurrences in each part of the machine, such as Singh *et al*. (2003). Nowadays, there is not any standardized or unified failure classification in the electrical machine, and it can be done by different criteria, such as the origin of the failure (mechanical, electrical, hydraulic, etc.), the element of the machine (stator or rotor) where the failure occurs, and so on.

14.2.1 Electrical Faults

Most commonly, electrical faults are classified according to the element in which they occur. Their origin, causes, and possible methods of detection are outlined in this chapter.

Stator Part Winding Failures

These failures occur inside the stator or in the supply system. The most common types of failures are related to failures in the windings insulation, and the different possible failures, along with the corresponding effects on the machine's operation, are listed as follows:

- Short-circuits between adjacent turns. The machine can run for an uncertain time.
- Short-circuits between coils of the same phase. The machine can run for an uncertain time.

- Short-circuits between phases. The machine stops instantly.
- Short-circuits between one phase and earth. The machine stops instantly.
- Open circuit of a given phase. The machine can run depending on the load and its protection.

These faults can cause high temperatures in the coils or stator core, stator core degradation, deterioration of clamp short-circuit end-rings, oil, moisture and dirt contamination, imbalances in supply or electric shocks, and leaks in refrigeration systems.

For example, the detection of the shorted coils is based on detecting frequency components f_{sc} given by the following equation (Nandi *et al.* 2005):

$$f_{sc} = \left(k \pm n \cdot \frac{(1-s)}{p}\right) f_1 \quad k = 1, 3, 5, \ldots \quad n = 1, 2, 3, \ldots \tag{14.1}$$

where f_1 is the frequency supply, p is the pole pair numbers, and s is the slip.

Rotor Part Broken Bar Damages

The most common electrical rotor failures, in the case of squirrel-cage IMs, are breakages in the rotor-cage winding. These failures introduce abnormalities in the magnetic air-gap field that produce sideband harmonic components of frequency f_{brb} in the line current spectrum around the fundamental component, and also near other harmonics caused by nonideal winding distribution (Kliman *et al.* 1988; El Hachemi Benbouzid 2000; Puche-Panadero *et al.* 2009). The characteristics frequencies of these fault-related harmonic components f_{brb} are given by

$$f_{brb} = ((1-s)\, k/p \pm s))\, f_1 \qquad k/p = 1, 3, 5 \ldots \tag{14.2}$$

The left sideband harmonic (LSH) is obtained by substituting $k/p = 1$ in (14.2); this component produces oscillations in the rotor speed, originating a new family of fault-related components (Bellini *et al.* 2001), with frequencies given by

$$f_{brb} = (1 \pm 2\, k\, s)\ f_1 \qquad k = 1, 2, 3, \ldots \tag{14.3}$$

Although broken rotor bars do not immediately cause the motor to fail, they can be a serious problem with several secondary effects (i.e., overheating, bar hitting, damaging of motor insulation and consequent winding failure, etc.).

External Source

These failures are related to the source supplying the machine, normally electronic equipment, or related to the load of the system.

14.2.2 Mechanical Faults

Almost always, mechanical failures occur in the rotor, as it is the moving part, and are identified as rotor's imbalances, misalignment, bearing failures, gear failures, and eccentricities in all their variants.

Imbalances

A rotating mechanical system is balanced when the resultant forces (internal and external) are constant. Because of this there are two types of imbalances:

1. **Static imbalance**, which is produced by a nonhomogeneous distribution of mass in the rotor. This failure is detectable with the rotor stopped.
2. **Dynamic imbalance**, which is produced by a nonhomogeneous longitudinal distribution of weights in the rotor.

Misalignment Failures

It is very hard to obtain a perfect coupling between the electrical machine and its mechanical load, so that the resultant forces are zero. When the coupling is not perfect, fault-related components appear in the motor current at frequencies given in Cabanas and Melero (1998).

Eccentricity Failures

Rotor eccentricity can result from a variety of sources such as design features, manufacturing tolerances, and operating conditions. The rotor may be positioned slightly off-center in the stator bore. Eccentric rotor running of IMs can result sufficient to increase in the unbalanced magnetic pull (UMP) to cause stator-rotor contact (Kral *et al.* 2004). Four types of Eccentricities can be identified via MCSA:

1. **Static eccentricity** can be produced by a stator ovality, or by a misalignment of the mounted bearings or the bearing plates. As a consequence, there is an angular position with the minimum radial air-gap length, which is fixed in space. It is characterized by a displacement of the axis of rotation, which can be caused. Since the rotor is not centered within the stator bore, the field distribution the air gap is no longer symmetrical. The nonuniform air gap gives rise to a radial force of electromagnetic origin, called UMP. This produces distortion frequencies given by

$$f_{\text{ecc\_static}} = \left[\left((k\ N)\ \left(\frac{1-s}{p}\right) \pm \upsilon\right)\right]\ f_1, \tag{14.4}$$

   where k is a positive constant, N is the number of the rotor slots, and υ is the harmonic order.
2. **Dynamic eccentricity** corresponds to the case where the rotation axis of the rotor does not coincide with its geometric center. This kind of eccentricity may be caused by a bent shaft, mechanical resonances, bearing wear on movement. For each air gap position, the radial length of the air gap varies with time, sinusoidally modulated, and this results in an asymmetric magnetic field. This causes distortion frequencies given by (n_d is a positive integer)

$$f_{\text{ecc\_dynamic}} = \left[\left((k\ N \pm n_d)\ \left(\frac{1-s}{p}\right) \pm \upsilon\right)\right]\ f_1. \tag{14.5}$$

3. **Mixed eccentricity** is the combination of static and dynamic eccentricity. It causes characteristic sideband components in the currents spectrum given by El Hachemi Benbouzid (2000), Antonino-Daviu *et al*. (2009), and Puche-Panadero *et al*. (2009):

$$f_{\text{ecc\_mixed}} = f_s \pm k\ f_r, \qquad k = 1, 2, 3 \ldots \tag{14.6}$$

   The overall (static plus dynamic) air-gap eccentricity specified by manufacturers is called the *radial air-gap eccentricity* and is normally given as a percentage of the nominal air-gap length. Levels of air-gap eccentricity should not exceed a maximum of 10% in three-phase IMs to avoid catastrophic damage.
4. **Axial eccentricity** appears when the eccentricity varies along the axis of the rotor. Therefore, the axis of rotor is not parallel to the stator axis and has different eccentricity in each section of the machine.

Gear Failures

The use of the gears in the electrical machines is due to the use of different speed and torque reference in different industrial applications. Because of this, trains are used, which are composed by different elements such as pinions, gear set, complex structure, and so on. Of course, these external elements of the machine have influence in the electrical machine behaviour. Different characteristic frequencies appear depending on the gear configuration.

Damaged Bearings

Electrical machines have two bearings where the rotor shaft end is held. These bearings allow the rotational movement of the rotor, and they wear due to the continuous friction that they undergo. A bearing is a rolling element with extremely small tolerances to avoid any internal displacement, except the rotational one.

If the bearing has been damaged, then characteristic frequencies appear as a function of the type of damage. The following equation shows the characteristic frequency if there is a fault in the inner or outer raceway (Blödt *et al.* 2010):

$$f_{\text{outer\_raceway}} = \left(\frac{N_b}{2}\right) f_r \left[1 - \frac{D_d \cos(\beta)}{D_c}\right], \tag{14.7}$$

$$f_{\text{inner\_raceway}} = \left(\frac{N_b}{2}\right) f_r \left[1 + \frac{D_d \cos(\beta)}{D_c}\right], \tag{14.8}$$

where the number of balls is denoted N_b, their diameter is D_b, the pitch or cage diameter is D_c, and the contact angle is β (see Figure 14.1). If the fault appears in the balls then

$$f_{\text{balls}} = \left(\frac{D_c\ f_r}{2D_b}\right) \left[1 - \left(\frac{D_b \cos(\beta)}{D_c}\right)^2\right]. \tag{14.9}$$

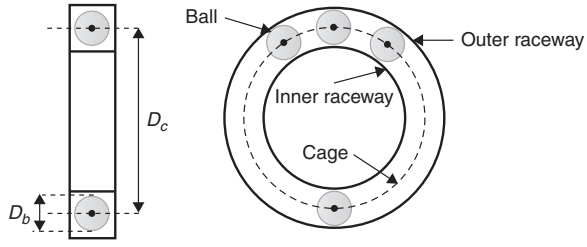

Figure 14.1 Geometry of a rolling-bearing

14.3 Model-Based FDI in IMs

14.3.1 Introduction

The model-based approach to FDI in automated processes has received considerable attention during the last two decades (Simani *et al.* 2003). The kernel of a model-based FDI algorithm is the generation of residual signals, which are indicators (symptoms) of the specific faults of interest. Ideally, each residual should selectively react to a specific fault only to allow fault isolation. Observer-based schemes were widely considered as residual generators, constructing the residual by a properly weighted output estimate error (Simani *et al.* 2003). In particular, when the system model admits significant degree of uncertainty, a particular class of nonlinear observer, the so-called *sliding-mode observers* (SMOs), appears to be an appropriate choice (Edwards *et al.* 2000; Simani *et al.* 2003; Pisano *et al.* 2008).

In this paper an observer-based FDI methodology is presented, which can detect the occurrence of broken bar fault (BBF) or eccentricity fault (EF) conditions. The method is based on a mathematical model of the motor under the considered faulty conditions, which represents the faults by means of suitably located fault injection signals. Its implementation requires the measurement of stator currents, shaft speed, and supply voltages, and the knowledge of the nominal motor electromechanical parameters. Noticeably, to overcome the uncertainty in the load torque, and to cope with, at the same time, the unknown fault injection signals, an unknown-input observation approach, robust to the presence of certain unmeasurable exogenous input terms, is taken. The framework of design relies on the so-called high-order SMO (Floquet *et al.* 2004; Fridman *et al.* 2007) and the suggested scheme is able to reconstruct at the same time both the fault injection signals and the load torque as well. The convergence property of the proposed algorithm will be supported by a Lyapunov-based stability proof.

A suitable residual is computed on the basis of the estimated fault injection signals, which can be processed by a threshold-based logic enabling a quick and computationally simple detection of the occurrence of the faulty conditions. The standard model describing the nominal (i.e., healthy) dynamics of the three-phase induction (wound-rotor or squirrel-cage) machine in the fixed (α, β) stator reference frame is expressed by the next fifth order nonlinear system (Krause and Thomas 1965; Marino *et al.* 1993):

$$\begin{cases} \dot{x}_1 = a_1 (x_3 x_4 - x_2 x_5) - a_2 x_1 + a_3 T_L, \\ \dot{x}_2 = b_1 x_4 - b_2 x_2 + b_3 x_1 x_3 + b_4 u_{s_\alpha}, \\ \dot{x}_3 = b_1 x_5 - b_2 x_3 - b_3 x_1 x_2 + b_4 u_{s_\beta}, \\ \dot{x}_4 = c_1 x_2 - c_2 x_4 - n_p x_1 x_5, \\ \dot{x}_5 = c_1 x_3 - c_2 x_5 + n_p x_1 x_4, \end{cases} \tag{14.10}$$

Table 14.2 Parameters of IM model

Model parameters		
Pole pairs number	n_p	–
Rotor and stator resistance	$R_{r,s}$	Ω
Rotor, stator, and mutual inductance	$L_{r,s,m}$	H
Viscous friction coefficient	f_v	Kg m^2/s
Rotor inertia	J	Kg m^2

where x_1 denotes the shaft speed, x_2 and x_3 denote the α and β components of the stator current in the fixed reference frame, x_4 and x_5 denote the α and β components of the rotor flux, u_α and u_β denote the α and β components of the stator supply voltage, T_L denotes the load torque, and parameters a_i, b_i and c_i take the form

$$\begin{aligned}
a_1 &= \frac{n_p L_m}{J L_r}, & a_2 &= \frac{f_v}{J}, \\
a_3 &= -\frac{1}{J}, & \sigma &= 1 - \frac{L_m^2}{L_r L_s}, \\
b_1 &= \frac{L_m R_r}{\sigma L_s L_r^2}, & b_2 &= \frac{L_m^2 R_r + L_r^2 R_s}{\sigma L_s L_r^2}, \\
b_3 &= \frac{n_p L_m}{\sigma L_s L_r}, & b_4 &= \frac{1}{\sigma L_s}, \\
c_1 &= \frac{R_r}{L_r} L_m, & c_2 &= \frac{R_r}{L_r}.
\end{aligned} \tag{14.11}$$

The electromechanical parameters of the presented model (14.10) and (14.11) are described in Table 14.2.

14.3.2 Modeling of IMs with Faults

Due to the considerations presented in Section 14.2, regarding fault patterns in the considered fault scenarios, we can devise that inserting additional exogenous voltages f_{s_α} and f_{s_β} in the stator current equation of (14.10) might be a reasonable approach to model a faulty IM drive. Therefore, a mathematical model representing a *faulty IM* can take the following form:

$$\begin{cases}
\dot{x}_1 = a_1 (x_3 x_4 - x_2 x_5) - a_2 x_1 + a_3 T_L, \\
\dot{x}_2 = b_1 x_4 - b_2 x_2 + b_3 x_1 x_3 + b_4 (u_{s_\alpha} + f_{s_\alpha}), \\
\dot{x}_3 = b_1 x_5 - b_2 x_3 - b_3 x_1 x_2 + b_4 (u_{s_\beta} + f_{s_\beta}), \\
\dot{x}_4 = c_1 x_2 - c_2 x_4 - n_p x_1 x_5, \\
\dot{x}_5 = c_1 x_3 - c_2 x_5 + n_p x_1 x_4,
\end{cases} \tag{14.12}$$

where in absence of faults the additional entries f_{s_α} and f_{s_β} are identically zero, whereas when fault conditions arise they becomes nonzero and inject in the model the appropriate characteristic frequencies.

The load torque T_L being generally not available for measurements in applications, it is treated as an "unknown input" within the observer design problem using the model (14.12).

It is concluded from the inspection of (14.2) and (14.6) that an accurate estimation of the speed x_1 is a prerequisite for making a reliable diagnosis by spectral methods.

14.3.3 Fault Detection Observer Design for IMs

An algorithm for fault detection in IMs, supported by the theory of model-based FDI (Simani *et al.* 2003), shall be presented hereinafter.

Model-based FDI is built upon a number of idealized assumptions, one of which is that the mathematical model used for constructing the observer is a faithful replica of the plant dynamics. This is, of course, not possible in practice, as an accurate and complete mathematical description of a process is never available. For these reasons a major objective of model-based FDI is to maximize the delectability of faults while minimizing at the same time the effect of modeling errors and disturbances (Simani *et al.* 2003).

The approach taken in this paper relies upon the use of robust observer based on the sliding-mode theory. Particularly, we exploit the desirable feature of SMOs of providing, under certain conditions, the capability of reconstructing the unknown inputs acting on the observed system. It is clear that the fault signals f_{s_α} and f_{s_β} contain useful information (symptoms) about the faults, and their estimation would be extremely useful for diagnosis purposes.

We will then devise a scheme that can reconstruct both the unknown exogenous faults signals f_{s_α} and f_{s_β} in (14.12) while mitigating the effect modeling errors by relying on the inherent robustness properties of SMOs.

The detection of faults will be achieved by a nonconventional, threshold-based residual evaluation procedure applied to the reconstructed fault signals.

Hereinafter, we shall describe the two main stages of the scheme for the considered case of study, respectively, *residual generation* and *residual evaluation* units.

14.3.4 Residual Generation and Evaluation

The aim of *residual generation* is to reconstruct fault symptoms using available inputs and outputs from the monitored system in order to obtain information about the occurrence of fault. The structure of the suggested *unknown-input observers* (UIO) is

$$\begin{cases} \dot{\hat{x}}_1 = a_1 (x_3 \hat{x}_4 - x_2 \hat{x}_5) - a_2 x_1 + a_3 \nu_1, \\ \dot{\hat{x}}_2 = b_1 \hat{x}_4 - b_2 x_2 + b_3 x_1 \hat{x}_5 + b_4 (u_{s\alpha} + \nu_2), \\ \dot{\hat{x}}_3 = b_1 \hat{x}_5 - b_2 x_3 - b_3 x_1 \hat{x}_4 + b_4 (u_{s\beta} + \nu_3), \\ \dot{\hat{x}}_4 = c_1 x_2 - c_2 \hat{x}_4 - n_p x_1 \hat{x}_5, \\ \dot{\hat{x}}_5 = c_1 x_3 - c_2 \hat{x}_5 + n_p x_1 \hat{x}_4. \end{cases} \tag{14.13}$$

Note that the observer equation (14.13) is a replica of the faulty motor model (14.12) with suitable injection terms ν_1, ν_2, and ν_3 replacing the unknown inputs f_{s_α}, f_{s_β}, and T_L. Shaft speed x_1 and stator currents x_2 and x_3 are supposed to be available for measurements, whereas $\hat{x}_i$ $(i = 1, \ldots, 5)$ represent the estimated state variables.

Denote the observation error variables as

$$e_i(t) = \hat{x}_i(t) - x_i(t) \qquad i = 1, \ldots, 5, \tag{14.14}$$

and note that the error variables e_1, e_2, and e_3 are accessible for measurements, while the flux errors e_4 and e_5 are unknown.

The restrictions assumed on the considered exogenous fault signals are specified as follows.

Assumption 14.3.1 *There exist a priori known constant F_s and F_L such that, at any $t \geq 0$, the time derivatives of the unknown inputs f_{s_α}, f_{s_β}, and T_L satisfy the next inequalities*

$$\left| \frac{d}{dt} f_{s_i}(t) \right|_{i=\alpha,\beta} \leq F_s, \qquad \left| \frac{d}{dt} T_L(t) \right| \leq F_L. \tag{14.15}$$

The observer injection terms are built according to the next relations

$$v_i(t) = v_{i_1}(t) + v_{i_2}(t), \qquad i = 1, 2, 3, \tag{14.16}$$

with

$$\begin{cases} v_{i_1}(t) = -k_i \sqrt{\mid e_i(t) \mid}\, \text{sign}\,(e_i(t))\,; \\ \dot{v}_{i_2}(t) = -w_i\, \text{sign}\,(e_i(t))\,, \, v_{i_2}\,(0) = 0; \end{cases} \tag{14.17}$$

where (k_i, w_i), $i = 1, 2, 3$, are proper tuning constants.

The next theorem sets the underlying tuning rules of the considered observer and establishes the associated convergence properties.

Theorem 14.3.2 *Consider the faulty IM model (14.12) and let Assumption 14.3.1 be satisfied. Then, the observer (14.13), (14.16), and (14.17) with the tuning parameters chosen according to*

$$w_i > F_i, \quad k_i^2 > 4F_i \, \frac{w_i + F_i}{w_i - F_i}, \quad i = 1, 2, 3, \tag{14.18}$$

$$F_1 = F_L, \quad F_2 = F_3 = F_s \tag{14.19}$$

guarantees the achievement of the next condition starting from a finite moment T^*

$$v_1(t) = T_L(t) + \xi_1(t), \tag{14.20}$$

$$v_2(t) = f_{s_\alpha}(t) + \xi_2(t), \qquad t \geq T^*, \tag{14.21}$$

$$v_3(t) = f_{s_\beta}(t) + \xi_3(t), \tag{14.22}$$

where $\xi_1(t)$, $\xi_2(t)$, and $\xi_3(t)$ are exponentially vanishing signals.

Proof: See Pilloni *et al*. (2012). □

The injection signals ν_2 and ν_3, which satisfy (14.21) and (14.22), will be used as residuals in the next analysis, as they provide asymptotically converging estimates of the fault signals $(f_{s_\alpha}, f_{s_\beta})$. Signal ν_1 represent an asymptotically exact estimation of the unknown load torque T_L, which may be useful in *direct torque control* (DTC) applications (see La *et al.* 2000; Youb and Craciunescu 2007). The suggested observer also provides an exponentially converging estimate of the rotor flux components, as well as a consequence of the fact that e_4 and e_5 are exponentially vanishing.

Residual evaluation exploits the relations (14.21) and (14.22). The instantaneous power of the two residuals are summed up to build a scalar measure of fault occurrence

$$r(t) = \nu_2^2(t) + \nu_3^2(t). \tag{14.23}$$

The two considered faults will be referred to as BBF (broken bar fault) and EF (eccentricity fault), respectively.

The simplest fault detection strategy could be sought as follows (Simani *et al.* 2003):

$$\begin{cases} \text{if} \quad r(t) \leq \epsilon, & \text{then} \quad \text{machine is healthy;} \\ \text{if} \quad r(t) > \epsilon, & \text{then} \quad \text{BBF or EF is active;} \end{cases} \tag{14.24}$$

with a suitably chosen constant threshold ϵ. However, the above fault detection logic suffers of the oscillating nature of $\nu_2(t)$ and $\nu_3(t)$, and it may be highly sensitive to the errors in the reconstruction of the fault injection signals due to the instantaneous dependence on $\nu_2(t)$ and $\nu_3(t)$.

For these reasons we propose to consider the average power of the residuals in a receding horizon temporal window of analysis. Then the next signal is constructed

$$E(t) = \sqrt{\int_{t-\Delta T}^{t} r(\tau) d\tau}, \qquad t \geq \Delta T, \tag{14.25}$$

where ΔT is the width of the receding horizon time window, and the fault detection logic correspondingly becoming:

$$\begin{cases} \text{if} \quad E(t) \leq \epsilon & \text{then} \quad \text{machine is healthy;} \\ \text{if} \quad E(t) > \epsilon & \text{then} \quad \text{BBF or EF is active.} \end{cases} \tag{14.26}$$

Once the occurrence of the faulty condition is detected, spectral methods can be employed to identify the types of fault occurred.

14.3.5 Experimental Results

In order to support the treatment presented in the previous sections we are going to present some experimental result validating the suggested procedure. The presented methodology has been tested offline by using real measurement acquired from several healthy and faulty

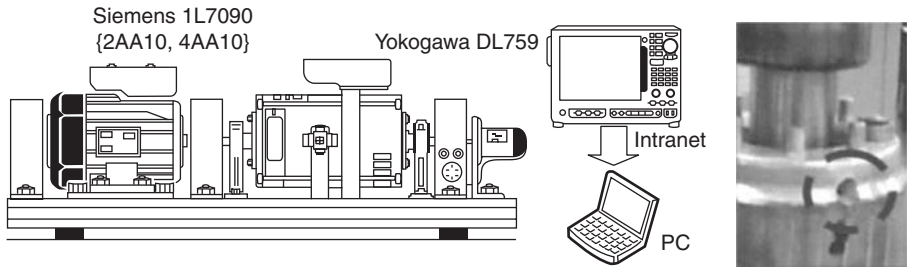

Figure 14.2 Experimental setup (left) and a drilled rotor-cage bar (right)

commercial drives intentionally damaged in order to reproduce a BBF and the two considered types of eccentricity.

Figure 14.2 (left plot) depicts the structure of the experimental setup, where a DC motor is mechanically coupled to the rotating shaft of the IMs under test in order to apply a constant load torque. Figure 14.3 shows a picture of the two motors. The three-phase supply voltages, phase currents, and speed are acquired using a digital oscilloscope. Several commercial squirrel-cage IM drives, manufactured by Siemens, in healthy and (intentionally induced) faulty condition have been tested. Two 4-pole Siemens IMs 1LA7090 4AA10 drives for the broken bar tests, and three 2-pole Siemens IMs 1LA7090 2AA10 for the eccentricity tests, fed, respectively, at 400 V $-$ Y, 50 Hz and 230 V $-$ Δ, 50 Hz were considered.

BBF has been realized by drilling a single rotor bar (see right plot of Figure 14.2), whereas EFs have been reproduced by suitable hardware modification. We have tested respectively a machine with 0.2 mm of static eccentricity, and a second one with, in addition, 0.07 mm of dynamic eccentricity.

Table 14.3 summarizes the experimental condition tests carried on the load conditions in terms of slip's percentage, the measured speeds, and the theoretical sideband frequencies associated with (see equations (14.2) and (14.6)). The electromechanical motor parameters needed for the observer implementation are derived from the motor's data sheet's. After few trial and error tests, devoted to guarantee an accurate convergence to zero of the measurable

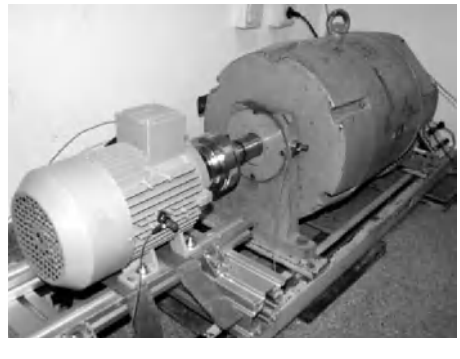

Figure 14.3 Laboratory test rig with IM and DC motor load

Table 14.3 Experimental working condition for the broken bar and eccentricity tests and fundamental fault sideband frequencies

Test	Speed (rpm)	Slip (%)	2 Slip f_s (Hz)	f_r (Hz)	f_{brb} (Hz)	f_{ecc} (Hz)
Broken bar	1452	3.2	3.21	–	46.78 53.21	–
Static eccentricity	2908	3.07	–	48.46	–	98.46
Mixed eccentricity	2906	3.15	–	48.43	–	98.43

estimation errors e_1, e_2, and e_3 in healthy operating condition, the observer gains in all tests have been set as follow

$$\begin{array}{lll} w_1 = 14 & w_2 = 22 & w_3 = 22 \\ k_1 = 80\text{'} & k_2 = 200\text{'} & k_3 = 200\text{'} \end{array} \tag{14.27}$$

Offline computations are done in the MATLAB environment. The observer scheme is digitally implemented by means of Euler discretization with sampling time $T_s = 10^{-4}$ s. Spectral analysis are made using a time window of 7 s.

Hereafter the effectiveness of proposed UIO (14.13), and the validity of the faulty IM model (14.12), will be investigated by experiments with real data.

Figure 14.4 (left) refers to data from a motor undergoing the BBF, and compares the spectra of the measured machine α current and that of the corresponding injection signal v_2. It shows that the spectra are almost analogous in shape, and differ by a scaling factor only. Figure 14.4 (right) shows the same plots during a different test with measurements data taken from a motor undergoing the EF. The conclusion is, however, the same as before.

Taking into account the proposed *residual evaluation algorithm* (14.25) and (14.26), Figure 14.5 shows the $E(t)$ residual profiles obtained using measurements from an healthy and a faulty motor in the two cases of BBFs and EFs.

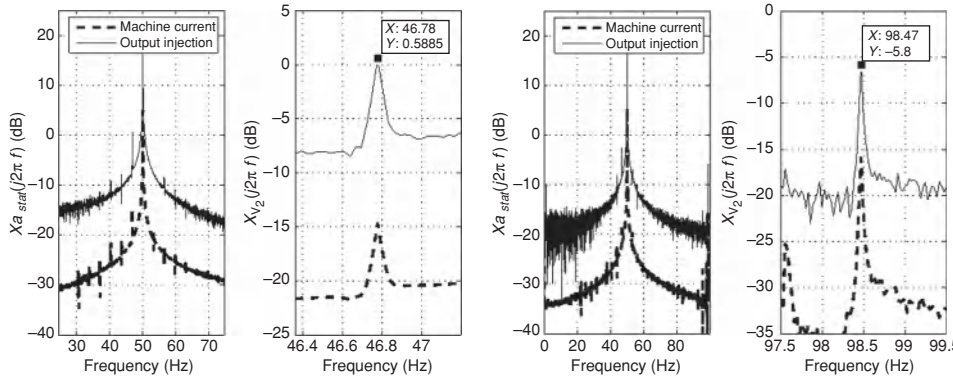

Figure 14.4 Comparison between the normalized spectra of the faulty motor stator currents and that of the observer injection signal v_2 for the broken bar test (left) and for the eccentricity test (right)

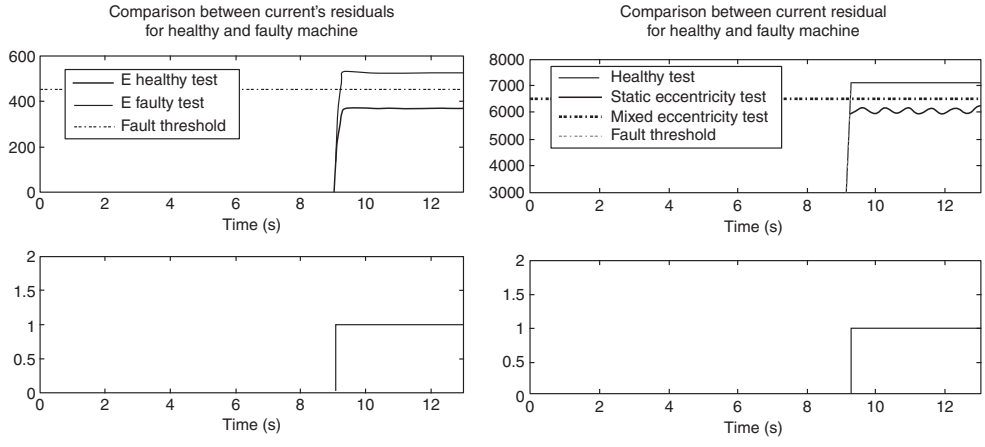

Figure 14.5 Residuals and chosen threshold (upper plot) and diagnosis signal (lower plot) for the broken bar tests (left) and for the eccentricity tests (right)

Note that the residual evaluation logic (14.25) is activated after 9 s, to let the machine reach the sinusoidal steady state during which the the receding horizon mean (14.25) has a near constant value that facilitate the detection of abnormal conditions by the simple threshold-based algorithm (14.26). These figures show that the healthy and faulty residuals are appreciably different in both the faulty scenarios investigated, and a suitable threshold value ϵ, to be used in order to obtain an accurate detection the fault occurrence, can be found. It is apparent that the faulty conditions are diagnosed almost instantaneously after that the algorithm (14.25) and (14.26) is activated.

The time window size ΔT in (14.25) has been chosen as 0.3 s. The choice of ΔT turned out to be not critical, provided it is not chosen too short to avoid permanently unsteady profiles of $E(t)$. Satisfactory performance has been obtained with different values as well.

14.4 Classical MCSA Based on the Fast Fourier Transform

The fast Fourier transform (FFT) has been the first signal analysis tool used for fault diagnostic of IMs. This technology was developed in the 1980s (Kliman *et al.* 1988), taking profit of the availability of digital oscilloscopes and computers, which enabled to sample and process the signals. Initially, the signals chosen for carrying out the diagnosis were mainly vibration-related mechanical ones, but quickly the interest turned on the stator currents, originating a family of methodologies designated as MCSA methods, which has been continuously improved since then. The use of the stator currents as diagnosis signal enable for noninvasive and cheap diagnostic techniques, since in industrial applications the IMs are usually provided with current clamps and no additional sensors are required. The basis of the MCSA approaches based on FFT is very simple. First a stator current is sampled using a sampling frequency f_s, during a time T, thus obtaining a discrete signal $I(t) = I_1, I_2, \ldots, I_N$ in the discrete time domain, were $N = f_s\ T$ is the number of samples. Once the FFT algorithm is applied to the sampled signal, a new signal in the discrete frequency domain is obtained—the signal spectrum—in

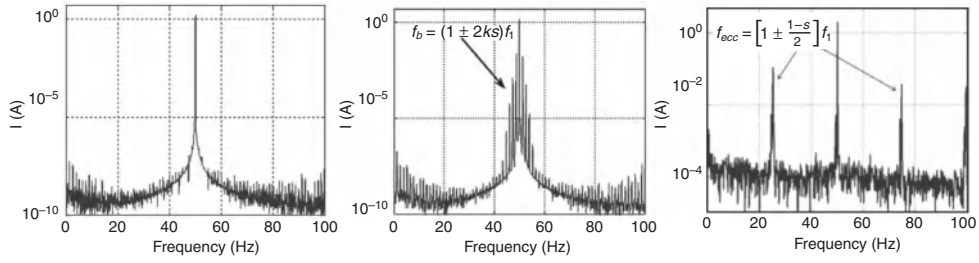

Figure 14.6 FFT spectrum of a simulated IM in healthy condition (left), with a broken rotor bar (center) and with a mixed eccentricity fault (right)

which the signal is decomposed into $N/2$ sinusoidal components with frequencies below half the sampling frequency and a frequency resolution $\Delta f = 1/T$. As it was explained in Section 14.2, different faults originate or substantially increase specific components of the signal, whose frequencies depend on the speed s, as it is shown in equations (14.1), (14.2), (14.3), (14.4), (14.5) (14.6), (14.7), (14.8), and (14.9). Diagnostic is based on the identification into the current spectrum of these fault-related components. As an example, Figure 14.6 shows three spectra corresponding to a simulated IM under different fault conditions: in healthy state (left), with a broken bar (center), and with a forced mixed eccentricity (right). The characteristic components in which diagnostic is based on are pointed out.

MCSA is based on FFT, which is the most used diagnostic approach in the industrial environment. Nevertheless, despite being a very easy and convenient method in a wide amount of applications, the industrial application of MCSA has practical limitations, mainly due to the following reasons:

- **Spectral leakage:** This is the result of sampling the signal using a finite-time window. The energy of the main frequency spreads over the other frequencies and can hide the sideband components. This problem has been reported by Eltabach *et al.* (2004), Douglas *et al.* (2005), Didier *et al.* (2006), and Jung *et al.* (2006). Solutions such as the use of a Hanning window and the Barlett periodogram have been proposed in Didier *et al.* (2006), as well as the filtering of the main frequency (Douglas *et al.* 2005).
- **Need of a high-frequency resolution:** Frequency resolution (Δf) is the frequency separation between two adjacent bins in the spectrum. It is inversely proportional to the time of measurement T. This is a theoretical limit that indicates the ability of the spectrum analysis to resolve two different tones with neighboring frequencies in the signal. Diverse techniques that can improve frequency resolution without increasing the measurement time have been presented in (Aiello *et al.* (2005), Yazidi *et al.* (2005), Bellini *et al.* (2006), and Kia *et al.* 2007).
- **Varying load conditions:** If the load varies during the sampling time, then the frequencies of the fault components, which depend on the motor slip, change with the speed. These changing frequencies can invalidate an MCSA-based diagnosed process, because they produce a typical smearing effect on the current spectrum (Thomson and Fenger 2001), which make it difficult to identify the fault components (Ian and Wendell 2007).

- **Confusing mechanical frequencies:** Speed-reducing devices such as gearboxes (Ian and Wendell 2007), or oscillating load can generate sideband frequencies that will behave identically to those caused by actual faults.

Some of the proposed solutions to the aforementioned problems are conflicting: long time periods are needed to achieve sufficient spectral resolution, but load conditions are likely to vary during this time, thus generating distorted data. All these drawbacks inherent to the FFT-based analysis have made it advisable to develop new diagnostic methods based on advanced signal analysis tools, such as Hilbert transform, or mixed time-frequency approaches.

14.5 Hilbert Transform

14.5.1 Bases of the Application of the Hilbert Transform of a Phase Current to the Diagnosis of Electrical Machines

This section introduces the HT and discusses its application to the current analysis of healthy and faulty machines. The HT of a real signal $x(t)$, as the phase current, is used to emphasize its local properties. Mathematically, it is defined as the convolution with the function $1/t$, as follows (Cizek 1970):

$$HT(x(t)) = y(t) = \frac{1}{\pi t} * x(t) = \frac{1}{\pi} \int_{-\infty}^{+\infty} \frac{x(\tau)}{t-\tau} \mathrm{d}\tau. \tag{14.28}$$

Coupling the $x(t)$ and its HT, the so-called analytic signal (AS) is created:

$$\vec{x}(t) = x(t) + j\, y(t) = a(t) e^{j\theta(t)}, \tag{14.29}$$

where

$$a(t) = \left[x^2(t) + y^2(t)\right]^{1/2}, \qquad \theta(t) = \arctan\left(x(t)/y(t)\right), \tag{14.30}$$

$a(t)$ is the instantaneous amplitude of $\vec{x}(t)$, which can reflect how the energy of $x(t)$ varies with time, and $\theta(t)$ is the instantaneous phase of $\vec{x}(t)$. Three key properties of the HT and the AS that give a more physical insight about it are:

- The HT of a trigonometric function $x(t)$ is a version of itself with a $\pi/2$ phase shift: sins are transformed to cosines and vice versa. The spectrum of a Hilbert transformed series has the same amplitude and frequencies contents as the original data, but the phase of each frequency component is shifted by $\pi/2$.
- The AS has a one-sided FT, that is, its components at negative frequencies are 0. It retains the positive frequency content of the original signal, suppressing negative frequencies and doubling the DC component.
- All the low frequencies of the original signal are in the amplitude , and the high frequencies in the phase of the AS.

The application of the HT to the analysis of faulty IMs has been considered, for example, in Liu *et al*. (2004) and Puche-Panadero *et al*. (2009).

Analytic Signal of the Current in a Healthy Machine

The steady-state phase current in an ideal machine, running at constant speed, is purely sinusoidal:

$$i(t) = I_m \cos(\omega t) = I_m \left(\frac{e^{j\omega t} + e^{-j\omega t}}{2} \right). \tag{14.31}$$

The FT of $i(t)$ shows two distinct components, at frequencies $f = \omega/2\pi$ and $f = -\omega/2\pi$, with an amplitude of $I_m/2$.

The AS corresponding to $i(t)$ is

$$\vec{i}(t) = i(t) + jHT(i(t)) = I_m(\cos(\omega t) + j\sin(\omega t)) = I_m e^{j\omega t}. \tag{14.32}$$

The FT of equation (14.32) will show a single spike corresponding to the positive frequency $f = \omega/2\pi$, with an amplitude double respect to the original signal spectrum component (14.31). The modulus of the AS reflects how the energy of $i(t)$ varies with time, and contains its low-frequency components. In the case of a healthy machine (14.32), it has a constant value of I_m, indicating that the energy of the phase current does not vary with time.

Analytic Signal of the Current in a Faulty Machine

In the case of periodic disturbances, like those produced by a broken bar in a motor that rotates at constant speed, the amplitude of the current in each phase is modulated with the principal frequency f_0 characteristic of the fault

$$i_b(t) = i(t)\left[1 + \beta \cos(\omega_0 t)\right], \tag{14.33}$$

where β denotes the modulation depth (modulation index) and $\omega_0 = 2\pi f_0$. By substituting (14.31) in (14.33)

$$i_b(t) = I_m \cos(\omega t)\left[1 + \beta \cos(\omega_0 t)\right]. \tag{14.34}$$

After performing the cosines multiplications, we get

$$i_b(t) = I_m \cos(\omega t) + \frac{\beta I_m}{2}\left[\cos\left((\omega - \omega_0)t\right) + \cos\left((\omega + \omega_0)t\right)\right], \tag{14.35}$$

which shows the presence of the two sideband frequencies characteristic of the fault. The HT of this current is constructed by changing the cosines functions by sine ones

$$HT(i_b(t)) = I_m \sin(\omega t) + \frac{\beta I_m}{2}\left[\sin\left((\omega - \omega_0)t\right) + \sin\left((\omega + \omega_0)t\right)\right], \tag{14.36}$$

which can be expressed as

$$HT(i_b(t)) = I_m \sin(\omega t)\left[1 + \beta \cos(\omega_0 t)\right]. \tag{14.37}$$

The AS is constructed by combining (14.34) (real part) and (14.37) (imaginary part):

$$\vec{i}_b(t) = \left[1 + \beta \cos(\omega_0 t)\right] I_m \left(\cos(\omega t) + j \sin(\omega t)\right) = \left[1 + \beta \cos(\omega_0 t)\right] I_m e^{j\omega t}. \tag{14.38}$$

In this case, and in contrast to the case of a healthy machine (14.31), the modulus of the AS shows a pulsation with the characteristic frequency of the machine fault.

14.5.2 Experimental Results

The proposed method has been applied to the analysis of a commercial 1.1 kW IM. Tests were carried out in two different conditions: healthy state and faulty condition in which a single bar was broken by drilling. In both cases, the test was performed at absolute no-load conditions, keeping free the motor shaft, to test the feasibility of the proposed method at very low slips. Additional test were performed with the faulty machine under three different loads (low, medium, and full) to assess the performance of the proposed method over the full range of motor load. In each tests a phase current was sampled for 100 seconds at 100 kHz, and six consecutive measurements were averaged to reduce the average noise level. Table 14.4 summarizes the load conditions of these five experimental tests, the measured speeds, and the theoretical sidebands components associated to the fault.

Two types of spectra are presented for the sake of comparison, the FFT of the phase current (classical method), and the FFT of I_{Hilbert}, the alternating component of the modulus of I_{Hilbert}.

Figure 14.7 (left) presents the spectrum of the line current. The sidebands components characteristic of the broken bar condition are distinguishable only in the tests performed under full load ($s = 6.16\%$) and medium load ($s = 2.96\%$). In the low-load test ($s = 0.61\%$) these

Table 14.4 Experimental tests of the healthy and faulty motor and theoretical fault sidebands

Motor	Load	Speed (rpm)	Slip (%)	$2sf_1$ (Hz)	Fault sidebands $f_1 \pm 2sf_1$ (Hz)
Healthy	a) No	1497.9	0.19	0.19	–
					49.86
	b) No	1498.8	0.20	0.20	50.26
Faulty					49.44
(one broken bar)	c) Low	1492.5	0.61	0.61	50.66
					47.04
	d) Medium	1456.2	2.96	2.96	52.98
					43.84
	e) Full	1407.6	6.16	6.16	56.16

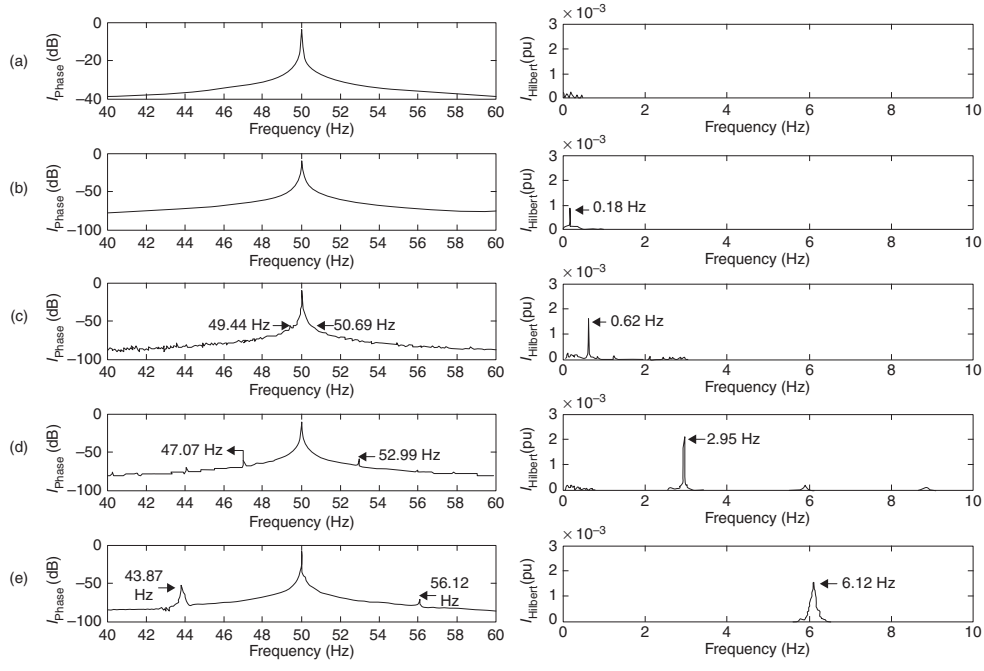

Figure 14.7 Spectrum of the phase current $i(t)$ (left) and spectrum of the modulus of I_{Hilbert} (right) in five experimental tests. Unloaded healthy machine (a), and machine with a broken bar under four different load conditions: unloaded (b), low load (c), medium load (d), and full load (e).

components are hardly detected, and in the case of absolute no-load ($s = 0.20\%$) they are completely buried under the main frequency component spectral leakage. In this last case the classical MCSA method is unable to correctly diagnose the fault.

The proposed method relies on the analysis of the variation of I_{Hilbert}. Its spectrums, in the five cases presented in Table 14.4, are shown in Figure 14.7 (right). In this case, linear scale instead of logarithmic one has been used for the vertical axis, greatly improving the legibility of the graph.

14.6 Discrete Wavelet Transform Approach

14.6.1 Basis for the Application of the DWT to Diagnostic of Electrical Machines

The DWT performs the decomposition of a sampled signal $s(t)(s_1, s_2, \ldots, s_N)$ onto $n + 1$ wavelet signals: an approximation signal $a_n(t)$ and n detail signals $d_j(t)$ with j varying from 1 to n:

$$s(t) = a_n + d_n + \cdots + d_1. \tag{14.39}$$

The parameter n is an integer known as number of decomposition levels and can be set freely. As it will be shown later, for specific diagnostic applications, n is set by considering the sampling rate f_s used for capturing $s(t)$, and the interval of frequencies covered by the fault-related component that is searched for. Conceptually, the detail signal d_1 is calculated as

$$d_1(t) = \sum_i \beta_i^1 \cdot \psi_i^1(t), \tag{14.40}$$

where β_i^1 are the wavelet coefficients (real numbers), ψ_1^1 is the mother wavelet (the base function used for the decomposition); the functions ψ_i^1 are identical to the mother wavelet but shifted in time by $\delta t = i/T$, being T the sampling period of $s(t)$. The detail signal d_j is calculated in a similar way, but using as a base the wavelet with level j, which is a scaled and time-expanded version of the mother wavelet

$$d_j(t) = \sum_i \beta_i^j \cdot \psi_i^j(t). \tag{14.41}$$

The approximation signal a_n is obtained similarly, but using the scaling function ϕ_j^n and scaling coefficients α_j^n, instead of the wavelet function and coefficients

$$a_n(t) = \sum_i \alpha_j^n \cdot \phi_j^n(t). \tag{14.42}$$

Each mother wavelet is associated with a family of scaling functions, which are perfectly determined once the mother wavelet is selected. The practical procedure for the application of DWT is known as Mallat's algorithm (Burrus *et al.* 1998) or sub-band coding algorithm; the approximation signal behaves as a low-pass filter, whereas each wavelet signal behaves as a passband filter, extracting the time evolution of the components of the original signal included within its corresponding frequency band. Figure 14.8 shows the sub-band coding algorithm regarding the coefficients of the transform at the different levels according to the description by Polikar *et al.* (1998). In this figure the length of those coefficients and frequency content at each level is shown considering an original signal with $n = 1024$ samples and sampling rate of f_s samples/s.

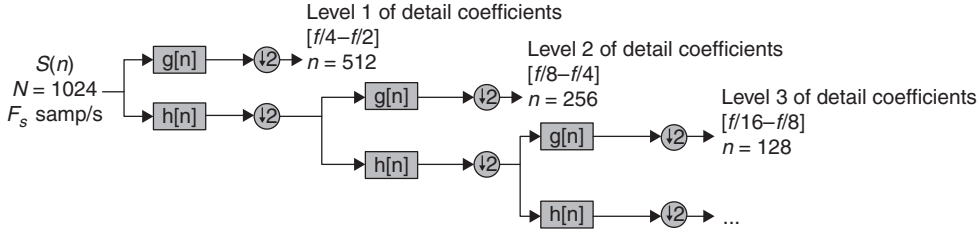

Figure 14.8 Sub-band coding algorithm scheme used for the practical application of DWT

Table 14.5 Frequency bands for the wavelet signals

Level	Frequency band $f_s = 5000$ samp/s	Frequency band $f_s = 2000$ samp/s
d_1	1250–2500 Hz	500–1000 Hz
d_2	625–1250 Hz	250–500 Hz
d_3	312.5–625 Hz	125–250 Hz
d_4	156.25–312.5 Hz	62.5–125 Hz
d_5	78.12–156.25 Hz	31.25–62.5 Hz
d_6	39.06–78.12 Hz	15.625–31.25 Hz
a_6	0–39.6 Hz	0–15.625 Hz

Source: Riera *et al*. (2008a).

The main idea that underlies the application of the DWT is the dyadic band-pass filtering process carried out by this transformation. Each one of the signals a_n, d_j generated by the wavelet filtering of the original signal $s(t)$ is associated with a specific frequency band (see Table 14.5). The analysis of these signals reveals the time evolution of the components of the signal $s(t)$ which are contained within its corresponding frequency band. More concretely, if f_s (samp/s) is the sampling rate used for capturing $s(t)$, then the detail d_j contains the information concerning the signal components with frequencies included in the interval:

$$f(d_j) \in \left[2^{-(j+1)} f_s, 2^{-j} f_s\right] \text{ Hz} \tag{14.43}$$

The approximation signal a_n includes the low-frequency components of the signal, belonging to the interval

$$f(a_n) \in \left[0, 2^{-(n-1)} f_s\right] \text{ Hz} \tag{14.44}$$

For instance, Table 14.5 (Riera-Guasp *et al.* 2008b) gives the frequency bands obtained for two different sampling frequencies ($f_s = 5000$ and 2000 samp/s) and $n = 6$ levels of decomposition.

Therefore, the DWT carries out the filtering process shown in Figure 14.9. Note that the filtering is not ideal, a fact leading to a certain overlap between adjacent frequency bands (Antonino-Daviu *et al.* 2006). This causes some distortion if a certain frequency component of

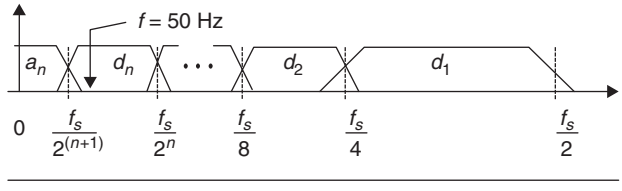

Figure 14.9 Filtering process performed by the DWT

the signal is close to the limit of a band. This undesirable effect can be minimized if high-order mother wavelet (e.g., Daubechies-40) are used.

Due to the automatic filtering performed by the wavelet transform, the tool provides a very attractive flexibility for the simultaneous analysis of the transient evolution of rather different frequency components present in the same signal. At the same time, in comparison with other tools, the computational requirements are low. In addition, the DWT is available in standard commercial software packages, so no special or complex algorithm is required for its application.

14.6.2 Application of the DWT to the Analysis of the Start-up Current of a Healthy Motor

Figure 14.10 shows the sampled start-up current (signal s, at the top) and the signals resulting from the DWT with $n = 6$ (a_6, d_6, ..., d_1), corresponding to an experimental healthy cage motor. This current was sampled at $f_s = 5000$ samp/s. These graphs can be explained as follows:

- The detail d_6 practically reproduces the analyzed start-up current. This is because, for the sampling frequency used, the frequency band corresponding to this signal is 39.06–78.12 Hz (see Table 14.5) and thus includes the fundamental component of the current, which is more than 30 times greater than the rest of the components.
- The approximation a_6 does not show any relevant pattern, once the initial oscillations due to electromagnetic transient and border effects are extinguished. This means that there are no significant low-frequency components (below 39.06 Hz) within the signal.
- Regarding the details d_5, d_4, and d_3, a clear pattern can be observed; this pattern is produced by a component with frequency increasing with time; at the beginning of the start-up, this component is included within the detail d_6; consequently it is masked by the fundamental component. At $t \approx 1.3$ s, its frequency becomes higher than 78.012 Hz and the component penetrates within the detail d_5. As time (or rotor speed) increases, so does the frequency, moving to d_4 at $t \approx 2.2$ s, crossing successively the frequency bands of d_4 ([156.25–312.5 Hz), and d_3 (312.5–625 Hz), and finally, remaining within d_2 when the steady state is reached. The pattern described above fits well the evolution during the start-up of the current principal slot harmonic (IPSH) of the machine, the frequency of which, as function of slip (Nandi *et al.* 2001), is given by

$$f_{\mathrm{PSH}} = [14\,(1 - s) - 1]\, f_1 \tag{14.45}$$

  At the beginning of start-up $s \approx 1$ and $f_{\mathrm{PSH}} \approx 50$ Hz. As slip decreases f_{PSH} increases, reaching a constant value $f_{\mathrm{PSH}} \approx 650$ Hz in steady state ($s \approx 0$). Fourier analysis of the stationary portion of d_2 confirms the previous interpretation, showing a predominant component of 640 Hz. So, this pattern, which can be almost always found in the DWT of start-up current, is not caused by the presence of any fault.
- The detail d_1 includes the high-frequency components of the signal with frequencies in the interval (1250–2500 Hz); nothing relevant is observed in this detail signal.

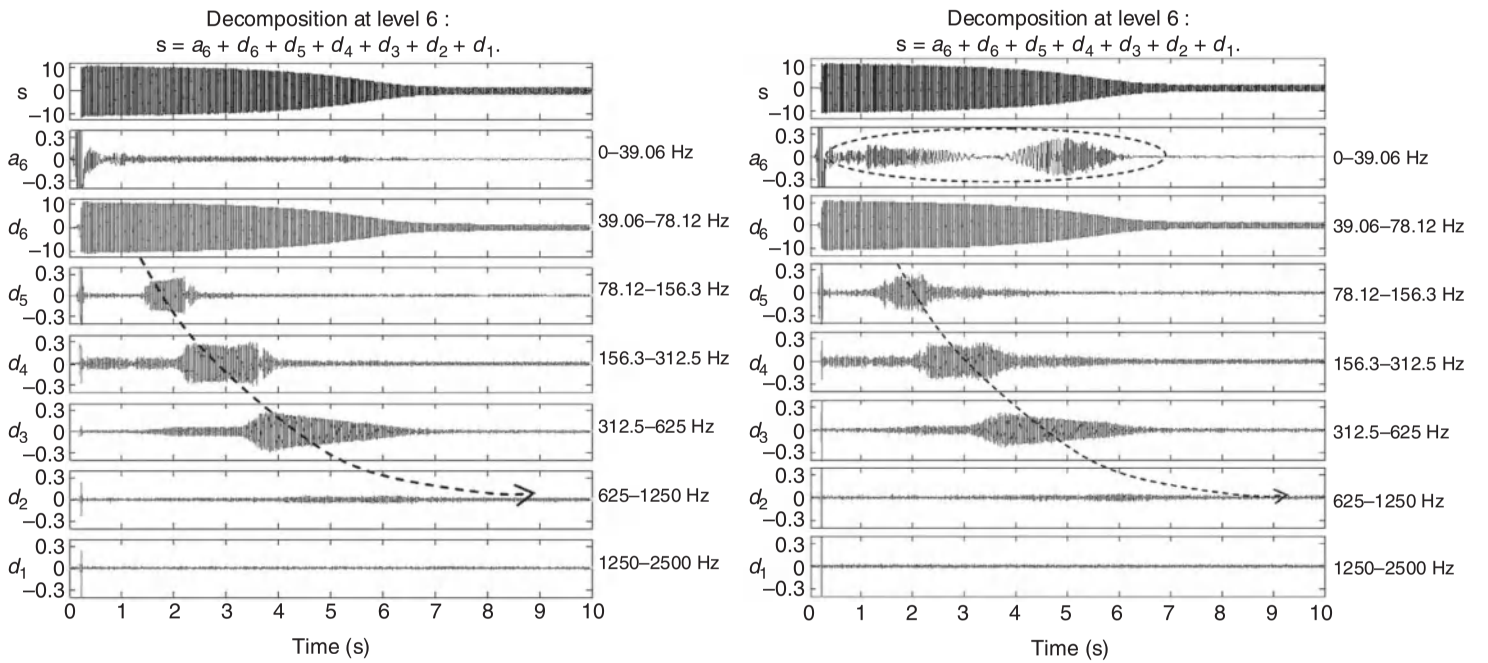

Figure 14.10 DWT of the experimental start-up current of a healthy machine (left), and a machine with a broken bar. Diagnostic based on left sideband extraction

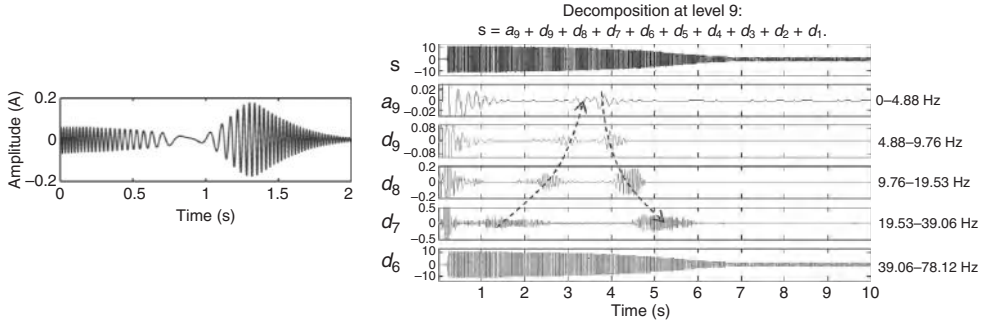

Figure 14.11 Theoretical evolution of the LSH component of the start-up current of a cage motor with one broken bar (left) and DWT of the start-up current of a machine with a broken bar (right), showing the characteristic pattern of low-frequency wavelets signals

14.6.3 Application of the DWT to the Analysis of the Start-up Current of a Motor with a Broken Bar in the Rotor

The previous test was repeated, but using a machine in which a rotor bar was artificially broken. Figure 14.10 (left) shows the DWT of the start-up current for this case. Comparison between Figures 14.10 (left) and 14.10 (right) shows that the bar breakage is clearly detected through the alteration of the approximation a_6 (or in general, the approximation of the same level as that of the detail containing the fundamental component); the change in this signal, as justified in Riera-Guasp *et al*. (2008a), is caused by the left sideband component; its amplitude increases substantially when a rotor asymmetry is present and its frequency evolves during almost the whole start-up within the frequency band of a_6; the similitude between the waveform of the approximation a_6 and the theoretical evolution of the left sideband component during the start-up, deduced in Riera-Guasp *et al*. (2008b), which is shown in Figure 14.11 (left), should be highlighted. This fact makes the diagnosis based on the approximation signal very reliable, since it is very unlikely that the pattern in a_6 could be caused by a fault or perturbation different from a rotor asymmetry. An alternative way for detecting a rotor asymmetry is shown in Figure 14.11 (right); in this approach the number of DWT decomposition levels is increased up to 9 (3 more than the level of the detail signal containing the fundamental component). In this way, the evolution of the sideband along the start-up is spread across four consecutive wavelet signals (d_7, d_8, d_9, and a_9), with frequency bands covering from near the main frequency to zero Hz. A clear pattern can be observed in these signals, which, according to the precedents sections, corresponds to a component with decreasing frequency in the time interval $1 < t < 3$ s and then, increasing frequency between $t = 3$ and $t = 6$. This also constitutes a reliable signature for the left sideband identification.

14.6.4 Diagnosis of a Machine with Mixed Eccentricity through the Start-up Current

Before carrying out this experimental investigation, it was necessary to prepare a motor introducing a certain degree of eccentricity in it. This was achieved by sanding down the inner and

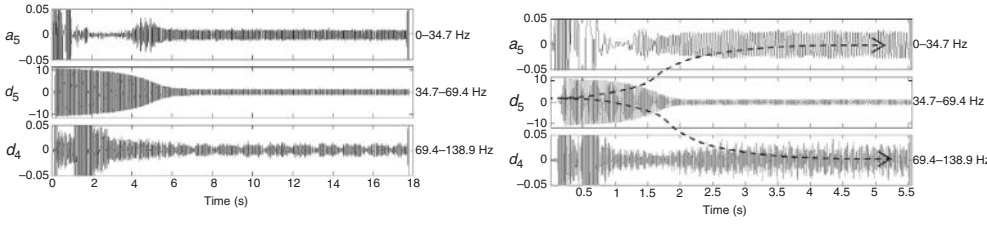

Figure 14.12 DWT of the start-up current of a healthy machine (left) and a machine with eccentricity (right)

outer rings of the bearings, so that a slight play was achieved between the bearing and the shaft (for dynamic eccentricity) and between the bearing and its housing (for static eccentricity). Conventional Fourier analysis shows steady-state mixed eccentricity-related components $f_1 \pm f_r$ increased by a factor of 3 after this process, growing their amplitude from 0.5% of the fundamental amplitude to 1.6%. Figure 14.12 shows respectively the DWT of the start-up current before (left) and after modifying the bearings (right); only the significant wavelet signals for this diagnosis are shown, that is, the signals containing the related eccentricity components ($f_1 \pm f_r$) during the start-up. Comparing both figures, clear changes in the waveforms of d_4 and a_5 can be observed. These changes are produced by the components $f_1 \pm f_r$, which eccentricity introduces into the current of the faulty machine, that are included within the detail d_5 at the beginning of start-up; as the rotor speed increases their frequencies change, reaching the limits of the band of d_5 when the start-up is almost finished. From this point, the decreasing component ($f_1 - f_r$) moves into a_5 and the increasing component ($f_1 + f_r$) moves into d_4. Subsequently, the diagnosis based on the DWT not only detects the fault through the increase of the amplitudes of the signals, like the steady-state-based analyses, but also through the characteristic pattern due to the progressive increment in this amplitudes during the transient. This fact enables a more reliable diagnosis of the fault.

14.7 Continuous Wavelet Transform Approach

14.7.1 Application of the CWT to Diagnostic of Electrical Machines

While the figures generated by the DWT clearly show the time-frequency pattern of the LSH component of the start-up current of a cage motor with one broken bar during a start-up transient (LSHst) (see Figure 14.11 (left), or the EF pattern (see Figure 14.12), they are not very suitable for being processed by automatic pattern recognition systems: there are many different images that must be simultaneously analyzed to detect the target pattern. A solution to this problem is to assemble a unique matrix, with each row containing the time evolution of the signal in a single frequency band. This matrix can be plotted as a single two-dimensional time-frequency image, by displaying the amplitude information as a color coding schema, as shown in Figure 14.13 for the case of the simulated LSHst presented in Figure 14.11 (left).

The image displayed in Figure 14.13 has two main drawbacks: it has a poor frequency resolution, due to the fixed frequency bands imposed by the dyadic character or the DWT, and the sinusoidal time variation of the signal appears as alternating color bands that obscure its

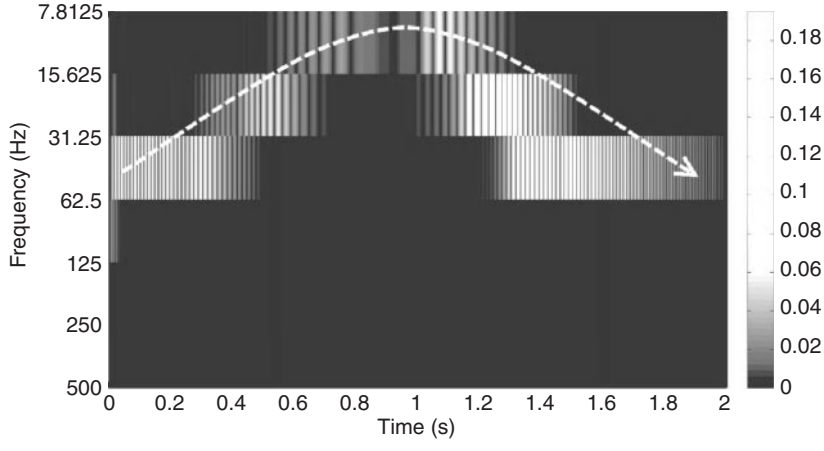

Figure 14.13 Two-dimensional image representing the time-frequency evolution of the LSH component of the start-up current of a cage motor with one broken bar, with its absolute amplitude displayed with a color coding schema. The frequency pattern is superimposed in dashed line

amplitude variation. In fact, DWT is a nonredundant representation of the signal, associated with an orthonormal basis, that can be useful for compression purposes, but not for an accurate representation of the signal in the time-frequency domain. All these drawbacks can be overcome with the use of the CWT.

The CWT is a time-scale decomposition that links a time domain function to its time-scale wavelet domain representation. The most natural way to obtain this representation (Cohen 1989) is to define a family of scaled and translated functions

$$\psi_{a,b}(t) = \frac{1}{\sqrt{a}}\,\psi\left(\frac{t-b}{a}\right), \qquad a > 0, b \in \mathbb{R}, \tag{14.46}$$

where ψ is a fixed function, called the mother wavelet, that is, an oscillatory signal, well localized both in time and frequency. The CWT of a function $f \in L_2(\mathbb{R})$ is defined as

$$CWT_f(a,b) = \langle f, \psi_{a,b}\rangle = \frac{1}{\sqrt{a}}\int f(t)\,\overline{\psi\left(\frac{t-b}{a}\right)}dt. \tag{14.47}$$

From a practical point of view, the CWT can only be computed on a discrete grid of points $(a_n, b_n)_{n\in\mathbb{Z}}$. In MCSA, the current signal $i(t)$ is sampled at instants $t_n = n\ \Delta t = n/f_s,\ n = 0 \ldots N-1$, where f_s is the sampling frequency and N is the total number of sampled values. In this case, and performing the analysis up to a maximum scale $m_{\max}$ (14.47) becomes

$$CWT_i(m,n) = \frac{1}{\sqrt{m}}\sum_{k=0}^{N-1}\int_k^{k+1} i(k\Delta t)\cdot\overline{\psi\left(\frac{t-n\Delta t}{m}\right)}dt\,, \qquad \text{with} \quad \begin{cases} m = 1...m_{\max}; \\ n = 0...N-1. \end{cases} \tag{14.48}$$

The analyzing mother wavelet used in this paper is the nth derivative of a Gaussian (DOG) function, given by (14.49). A value $n = 8$ has been selected in this work (gaus8 wavelet): it is a symmetric wavelet, it is infinitely differentiable in the time domain, and has eight vanishing moments, the minimum value proposed by Douglas *et al*. (2005).

$$\psi_n(t) = \frac{(-1)^n}{\sqrt{2^{(n-1/2)} \cdot \Gamma(n+1/2)}} \cdot \frac{d^n(e^{-t^2})}{dt^n} \tag{14.49}$$

The LSHst has been processed with the CWT, and the absolute value of the resultant coefficients are shown in Figure 14.14 (left), which offers a clear visual insight of the time-frequency evolution of the LSHst. Nevertheless, the alternating nature of this signal leads to a succession of clear and dark vertical bands, which represents an obstacle for its classification by an automatic pattern recognition system. The use of the complex CWT (CCWT) solves this problem, as it is shown in the next section.

14.7.2 Application of the Complex CWT to Diagnostic of Electrical Machines

The CCWT is defined as in equation (14.49) but using complex valued wavelets, instead of real ones, so that the modulus of the coefficients can be computed:

$$\psi_n(t) = \frac{(-1)^n}{\sqrt{2^{(n-1/2)} \cdot \Gamma(n+1/2)}} \frac{d^n(e^{-jt} \cdot e^{-t^2})}{dt^n}. \tag{14.50}$$

The CCWT has been applied to the LSHst, and the absolute value of the resultant coefficients is shown in Figure 14.14 (right). The advantage of using the CCWT to represent the time-frequency evolution of the LSHst is that the modulus of the CCWT tracks the evolution of its envelope, instead of its instantaneous value. This fact eliminates the vertical, alternating bands of Figure 14.14 (right), which facilitates the work of automatic recognition systems.

14.7.3 Experimental Results

The line current signal during the start-up transient of motor with a broken bar has been processed using the proposed method (modulus of the CCWT of the line current) to obtain a high-resolution representation of the current in the time-frequency plane, where the LSHst appears clearly defined (see Figure 14.15).

14.8 Wigner-Ville Distribution Approach

14.8.1 Basis for the Application of the WVD to Diagnostic of Electrical Machines

The distribution of the energy of a signal $x(t)$ over the two description variables time and frequency, that is, its energy density function, $P_x(t, \nu)$, can be obtained with the use of a

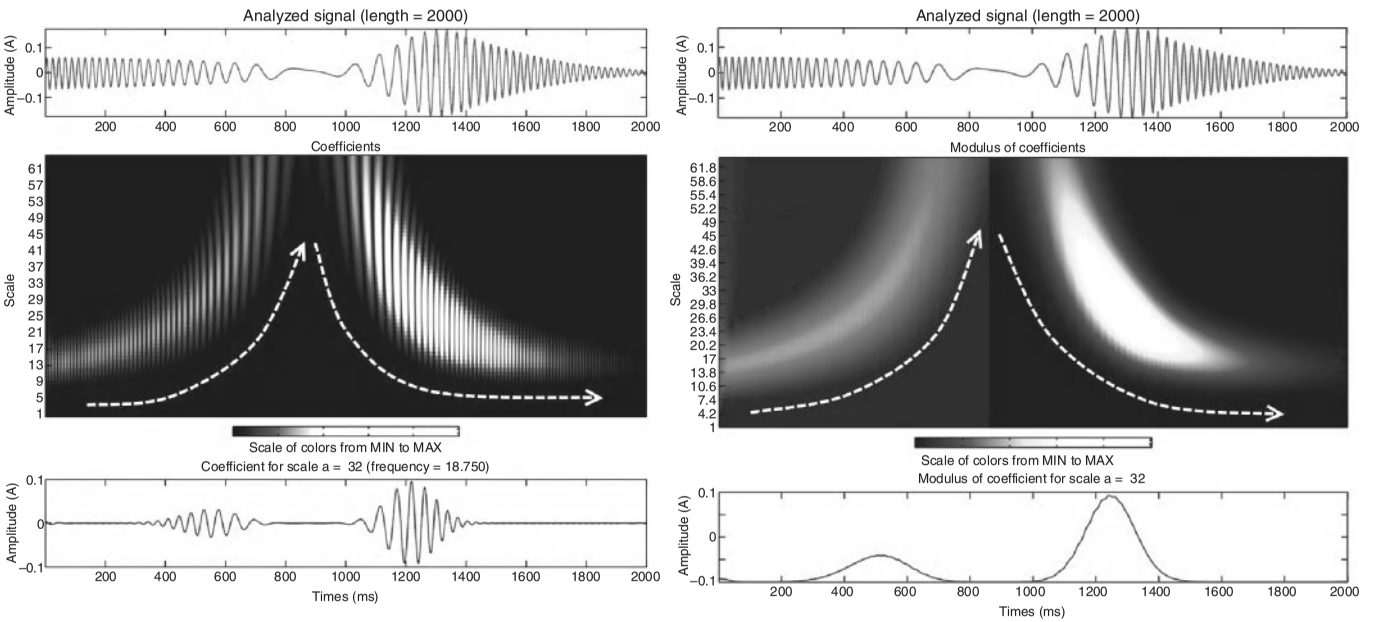

Figure 14.14 CWT (left) and complex CWT (right) of the LSH component of the start-up current of a cage motor with one broken bar. Top, analyzed signal; middle, absolute value of the CWT coefficients, with the LSHst pattern superimposed in dashed line; bottom, single transform obtained for a scale value $a = 32$

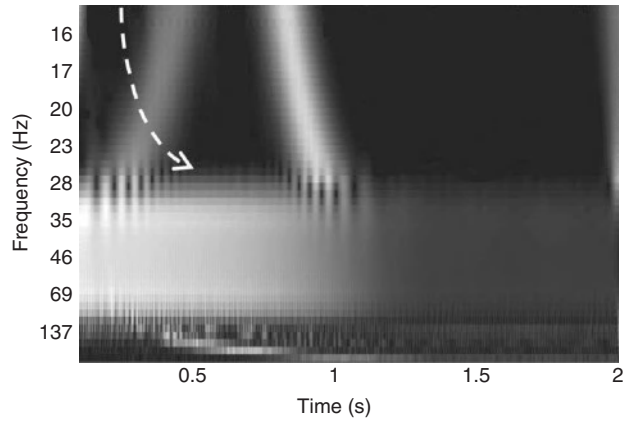

Figure 14.15 Experimental modulus of the complex CWT of the faulty motor line current during the start-up transient, with the amplitude displayed as a color intensity map (computed separately for each frequency band). The broken bar faults pattern has been superimposed in dashed line

time-frequency distribution (Hlawatsch and Boudreaux-Bartels 1992), as proposed recently for motor fault detection in Blödt *et al*. (2010) and Rajagopalan *et al*. (2008). A desirable property of such a distribution is the time and frequency covariance; that is, if the signal is delayed in time and modulated, its time-frequency distribution must be translated of the same quantity in the time-frequency plane. The class of energy time-frequency distributions verifying this property, the Cohens class, has the following general expression (Cohen 1989):

$$P_x(t,\nu) = \iint_{-\infty}^{+\infty} e^{j2\pi\xi(s-t)} f(\xi,\tau) x^*\left(s-\frac{\tau}{2}\right) x\left(s+\frac{\tau}{2}\right) e^{-j2\pi\nu\tau} d\xi ds d\tau. \quad (14.51)$$

Individual distributions (Spectrogram, Wigner-Ville, Choi-Williams, etc.) are obtained using different kernels $f(\xi,\tau)$ in equation (14.51). The WVD is the simplest one in the group of the Cohens class, with a kernel function equal to unity.

$$WV_x(t,\nu) = \int_{-\infty}^{+\infty} x^*\left(t-\frac{\tau}{2}\right) x\left(t+\frac{\tau}{2}\right) e^{-j2\pi\nu\tau} d\tau. \quad (14.52)$$

This expression shows that the WVD of a function is obtained as the FFT with respect the variable τ (delay) of the convolution of the signal with a translations in time and frequency of itself.

14.8.2 Application of the WVD to Monocomponent Signals

Figure 14.16 shows the result of applying the WVD to a monocomponent signal such as the simulated LSH of Figure 14.11. In this spectrogram a clear "V" pattern is shown. The

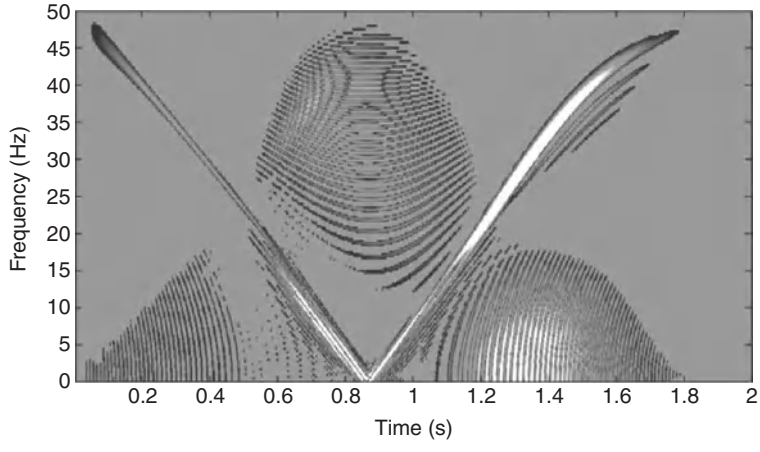

Figure 14.16 Wigner-Ville distribution of the LSH during a start-up

interpretation of this pattern is that the frequency of the analyzed signal first decreases with time, from 50 to 0 Hz (at $t \approx 0.85$ s), and then increases again, reaching a value near to 50 at the end of the signal ($t \approx 0.85$ s). Moreover, from the colored scale of the spectrogram, it is seen that the amplitude of the signal is decreasing in the descending branch, whereas in the upward branch, it first increases, reaches a maximum, and finally decreases. This behavior matches perfectly the evolution of the frequency and amplitude of the LSH during a start-up (see Figure 14.11) described in Riera-guasp *et al.* (2008b); therefore, the detection of this "V" pattern into a start-up current enables diagnostic of a rotor breakage.

One drawback of the WVD is the presence of interference cross-terms, as can be noticed in Figure 14.16. The cross-terms are artifacts resulting from the interaction between the searched components of the signal and other components or noises, which produce high-amplitude patterns in regions that actually have no energy. In real multicomponent signals, these artifacts can completely hide the searched patterns. To minimize them, other distributions belonging to the Cohens class using different kernels have been proposed, as the smoothed pseudo Wigner-Ville and the Choi-Williams distributions; nevertheless, using kernels deteriorates certain desirable properties of WVD and also increases the computational requirements.

14.8.3 Application of the WVD to Multicomponent Signals

Another alternative for minimizing the undesirable effects of the cross-terms consists of applying some kind of pretreatment to the signal before computing the WVD, in order to isolate the component of interest into a frequency band in which it is predominant. For instance, the DWT can be used as an efficient technique for isolating the LSH in a start-up current since—as it is well known—if the LSH exists, during start-up its frequency evolves below the main frequency. This technique is applied to analyze the startup current of Figure 14.11 (signal s, on the top, machine with a broken bar). The WVD is applied to the approximation a_6 , which contains the components of the current belonging the interval [0, 39.06] Hz. The resulting

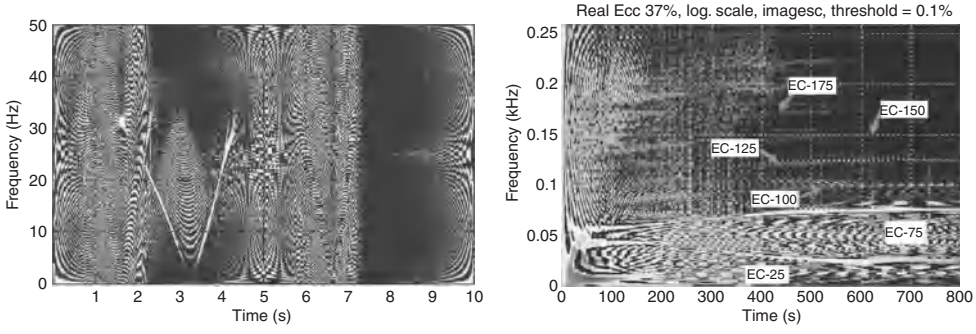

Figure 14.17 Wigner-Ville distribution of the start-up current of a machine with a broken bar (left) and of a machine with 37% eccentricity (right)

energy distribution is shown in Figure 14.17 (left); the characteristic "V" pattern associated to the LSH during start-up is clearly visible, leading to a diagnostic of faulty machine.

A more general and systematic methodology for the pretreatment of the signal before applying the WVD is proposed in Climente-Alarcon *et al*. (2011): In a first stage, the start-up current undergoes a filtering process; in this stage a series of constant frequency components not related with the fault (fundamental component and winding harmonics) are filtered using optimized notch filters. Then the HT is applied to the filtered signal to obtain an AS, whose spectrum does not contain negative frequencies. Finally high- and low-pass filters are used for keeping only the range of frequencies of interest. In this way, the WVD is applied to a signal in which the more important components not related with the fault have been suppressed, and thus, the cross-terms are strongly reduced; as a result, the computed energy distribution enables appreciation of simultaneously several fault components evolving through a wide frequency band. As an example, Figure 14.17 (right) (Climente-Alarcon *et al.* 2011) shows the result of applying this methodology to the start-up current of a cage motor having a mixed eccentricity. The spectrogram shows the evolution of the couple of main eccentricity components ($f_1 \pm f_r$) designed as EC-25 clearly and EC-75 in Figure 14.17 (right). The trajectory in the $t-f$ plane of these components can be followed during the full start-up transient, reproducing the same conceptual pattern appearing in Figure 14.12 (right), but in this case in a more explicit way. Also, the evolution of other second order eccentricity-related components (designed as EC-100, EC-125, EC-50, EC-175 in Figure 14.17 (right)) can be followed, improving the reliability of the diagnostic of faulty machine.

14.9 Instantaneous Frequency Approach

14.9.1 Basis for the Application of the IF Approach to Diagnostic of Electrical Machines

As it was explained in the previous section, the diagnostic based on conventional MCSA relies on the fact that different kind of fault produces specific families of harmonics to appear (or greatly increase their amplitude) in the currents circulating in the windings of the machine.

For instance, and considering only the most important components, it has been demonstrated that:

- Rotor asymmetry produces a substantial increase in the amplitude of the lower and upper sideband component of stator currents, whose frequencies are given by

$$f_{bS}(s) = |(1 \pm 2 \cdot s)\ f_1|\,, \tag{14.53}$$

  where f_{bS} is the frequency of the main rotor asymmetry fault-related components in the stator current, f_1 is the supply frequency, and s is the slip.
- A mixed eccentricity induces stator current harmonics at specific frequencies. The main harmonic produced by the mixed eccentricity can be found by substituting $k = 1$ in equation (14.6), at the frequency given by

$$f_{ecc}(s) = \left| f_1 - \frac{f_1}{p}(1 - s) \right|, \tag{14.54}$$

  where f_{ecc} is the frequency of the main fault component produced by a mixed eccentricity in the stator current, and p is the pole pair number.

Conventional MCSA uses equations (14.53) and (14.54) as formulas that give the frequencies at the current spectrum where the fault components appear when a fault happens. On the contrary, in the IF approach, these formulas are understood as functions that describe the trajectory of the fault components in the slip-frequency plane when a faulty machine undergoes a transient that involves any speed variation. It is remarkable that these trajectories are straight lines, with a specific slope and offset, different for every fault, irrespective of the way in which speed varies (increasing, decreasing, oscillating) and the machine characteristics (rated power, rated voltage), thus, constituting very reliable patterns for diagnostic purposes. For a direct online start-up, Figure 14.18 gives the theoretical evolution of the IF of the fault components related to a rotor asymmetry (left) and a mixed eccentricity (right). These graphs have been obtained making s vary from 1 to 0 in equations (14.53) and (14.54).

14.9.2 Calculating the IF of a Monocomponent Signal

The IF of a monocomponent signal $s_m(t)$ can be calculated using different mathematical tools, as for instance the HT and the WVD, among other.

- If x_a is the AS obtained from the HT of $s_m(t)$, the IF of this signal is defined as the derivative of the phase of the AS (Ville 1948):

$$\nu_i(t) = \frac{1}{2\pi}\frac{d\,(\arg(x_a))}{dt} = \frac{1}{2\pi}\frac{d\phi}{dt}, \tag{14.55}$$

  where $\phi(t)$ is the phase of x_a.

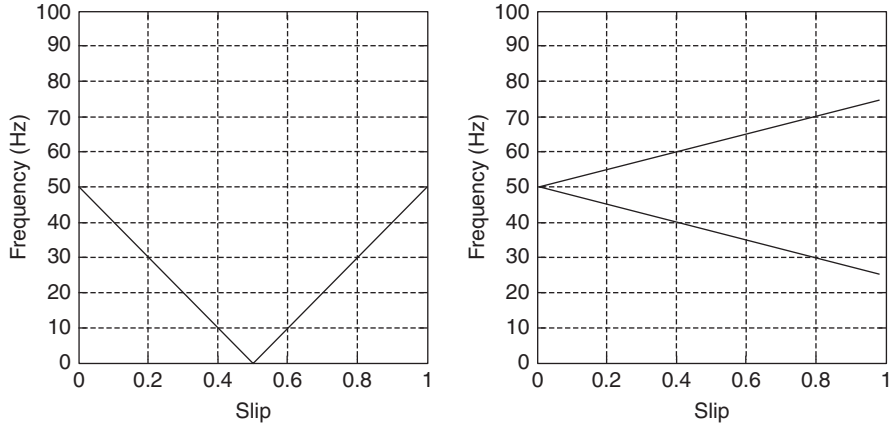

Figure 14.18 Characteristic slip-frequency pattern of the IF of the LSH of a machine with broken bars (left) and with eccentricity (right) during a start-up transient

- From the WVD, the IF of $s_m(t)$ can also be calculated as the first conditional moment of frequency for a given time of the WVD of the signal; that is, as the average of the frequencies existing in the time-frequency plane for a given time (Cohen 1989):

$$< \nu >_t = \frac{\int \nu P_x(t, \nu) d\nu}{\int P_x(t, \nu) d\nu} = \frac{1}{2\pi} \frac{d\phi_a}{dt} = \nu_i(t). \tag{14.56}$$

  It can be demonstrated that both definitions are equivalent.

14.9.3 Practical Application of the IF Approach

An important remark is that the concept of IF lacks a simple physical meaning when is applied to real multicomponent signals, as the stator current of a cage motor. This problem has been reported extensively in the technical literature: the IF of a multicomponent signal can exhibit large fluctuations, and it can extend beyond the band defined by any of the individual components (Nho and Loughlin 1999). Thus, as in the application of the WVD, the diagnosis based on the IF implies a pretreatment of the tested signal, with the aim of extracting the frequency bands from it in which the searched fault-related component, if it exists, is the most prominent. Figure 14.19 plots the calculated IF versus slip of the LSH of the tested start-up current (signal *s*) of Figure 14.10 (right). This current corresponds to a cage motor with a rotor broken bar. Also, in this case, the DWT has been used for isolating the LSH; actually this graph shows the calculated IF (blue dots) of the approximation a_6 of the tested current, since this wavelet signal contains the components of the start-up current below the fundamental frequency; therefore, if the LSH is present in the start-up current, it will be prominent in this approximation. As the calculated IF matches the theoretical pattern (red lines) perfectly, a reliable diagnostic of faulty machine is deduced.

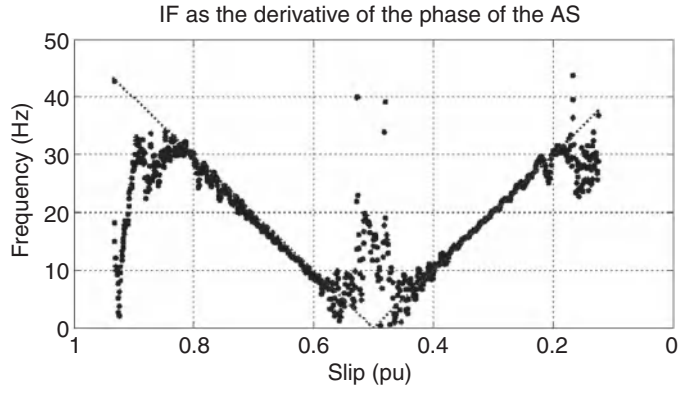

Figure 14.19 Experimental IF of the LSH extracted from the start-up stator current of a gage motor with one broken bar, computed using Hilbert transform

References

Aiello M, Cataliotti A, and Nuccio S (2005) An Induction motor speed measurement method based on current harmonic analysis with the Chirp-Z transform. *IEEE Transactions on Instrumentation and Measurement*, **54** (5), 1811–1819.

Antonino-Daviu J, Riera-Guasp M, Folch J, and Palomares M (2006) Validation of a new method for the diagnosis of rotor bar failures via wavelet transform in industrial induction machines. *IEEE Transactions on Industry Applications*, **42** (4), 990–996.

Antonino-Daviu J, Rodriguez P, Riera-Guasp M, *et al*. (2009) Transient detection of eccentricity-related components in induction motors through the hilbert-huang transform. *Energy Conversion and Management*, **50** (7), 1810–1820.

Bellini A, Filippetti F, Franceschini G, *et al*. (2001) Quantitative evaluation of induction motor broken bars by means of electrical signature analysis. *IEEE Transactions on Industry Applications*, **37** (5), 1248–1255.

Bellini A, Franceschini G, and Tassoni C (2006) Monitoring of induction machines by maximum covariance method for frequency tracking. *IEEE Transactions on Industry Applications*, **42** (1), 69–78.

Blödt M, Granjon P, Raison B, and Regnier J (2010) Mechanical fault detection in induction motor drives through stator current monitoring - theory and application examples, in *Fault Detection* (ed. W Zhang), InTech, pp. 451–487.

Burrus C, Gopinath R, and Guo H (1998) Introduction to wavelets and wavelet transforms: a primer. *Recherche*, **67**, 02.

Cabanas M and Melero M (1998) *Técnicas para el mantenimiento y diagnóstico de máquinas eléctricas rotativas*. Marcombo.

Cizek V (1970) Discrete Hilbert transform. *IEEE Transactions on Audio and Electroacoustics*, **18** (4), 340–343.

Climente-Alarcon V, Antonino-Daviu J, Riera-Guasp M, *et al.* (2011) Transient tracking of low and high-order eccentricity-related components in induction motors via TFD tools. *Mechanical Systems and Signal Processing*, **25** (2), 667–679.

Cohen L (1989) Time-frequency distributions-a review. *Proceedings of the IEEE*, **77** (7), 941–981.

Didier G, Ternisien E, Caspary O, and Razik H (2006) Fault detection of broken rotor bars in induction motor using a global fault index. *IEEE Transactions on Industry Applications*, **42** (1), 79–88.

Douglas H, Pillay P, and Ziarani AK (2005) Broken rotor bar detection in induction machines with transient operating speeds. *IEEE Transactions on Energy Conversion*, **20** (1), 135–141.

Durocher D and Feldmeier G (2004) Predictive versus preventive maintenance. *Industry Applications Magazine, IEEE*, **10** (5), 12–21.

Edwards C, Spurgeon S, and Patton R (2000) Sliding mode observers for fault detection and isolation. *Automatica*, **36** (4), 541–553.

El Hachemi Benbouzid M (2000) A review of induction motors signature analysis as a medium for faults detection. *IEEE Transactions on Industrial Electronics*, **47** (5), 984–993.

Eltabach M, Charara A, and Zein I (2004) A comparison of external and internal methods of signal spectral analysis for broken rotor bars detection in induction motors. *IEEE Transactions on Industrial Electronics*, **51** (1), 107–121.

Floquet T, Barbot J, Perruquetti W, and Djemai M (2004) On the robust fault detection via a sliding mode disturbance observer. *International Journal of control*, **77** (7), 622–629.

Fridman L, Davila J, and Levant A (2007) High-order sliding-mode observation and fault detection. *46th IEEE Conference on Decision and Control, 2007*, pp. 4317–4322.

Hlawatsch F and Boudreaux-Bartels G (1992) Linear and quadratic time-frequency signal representations. *IEEE Signal Processing Magazine*, **9** (2), 21–67.

Ian MC and Wendell R (2007) Using current signature analysis technology to reliably detect cage winding defects in *Transaction on Industry Application* squirrel-cage induction motors. *IEEE*, **43** (2), 422–428.

Jung JH, Lee JJ, and Kwon BH (2006) Online diagnosis of induction motors using MCSA. *IEEE Transactions on Industrial Electronics*, **53** (6), 1842–1852.

Kia S, Henao H, and Capolino GA (2007) A high-resolution frequency estimation method for three-phase induction machine fault detection. *IEEE Transactions on Industrial Electronics*, **54** (4), 2305–2314.

Kliman G, Koegl R, Stein J, *et al.* (1988) Noninvasive detection of broken rotor bars in operating induction motors. *IEEE Transactions on Energy Conversion*, **3** (4), 873–879.

Kral C, Habetler T, and Harley R (2004) Detection of mechanical imbalances of induction machines without spectral analysis of time-domain signals. *IEEE Transactions on Industry Applications*, **40** (4), 1101–1106.

Krause P and Thomas C (1965) Simulation of symmetrical induction machinery. *Power Apparatus and Systems, IEEE Transactions on*, **84** (11), 1038–1053.

La K, Shin M, and Hyun D (2000) Direct torque control of induction motor with reduction of torque ripple *Industrial Electronics Society, 2000. IECON 2000. 26th Annual Conference of the IEEE*, Vol. 2, pp. 1087–1092.

Liu Z, Zhang X, Yin X, and Zhang Z (2004) Rotor cage fault diagnosis in induction motors based on spectral analysis of current hilbert modulus. *Power Engineering Society General Meeting, 2004. IEEE*, pp. 1500–1503.

Marino R, Peresada S, and Valigi P (1993) Adaptive input-output linearizing control of induction motors. *IEEE Transactions on Automatic Control*, **38** (2), 208–221.

Nandi S, Ahmed S, and Toliyat H (2001) Detection of rotor slot and other eccentricity related harmonics in a three phase induction motor with different rotor cages. *IEEE Transactions on Energy Conversion*, **16** (3), 253–260.

Nandi S, Toliyat H, and Li X (2005) Condition monitoring and fault diagnosis of electrical motors—a review. *IEEE Transactions on Energy Conversion*, **20** (4), 719–729.

Nho W, and Loughlin P (1999) When is instantaneous frequency the average frequency at each time? *Signal Processing Letters, IEEE*, **6** (4), 78–80.

Pilloni A, Pisano A, and Usai E (2012) Robust FDI in induction motors via second order sliding mode technique. *12th International Workshop on Variable Structure Systems (VSS)*, pp. 467–472.

Pisano A, Davila A, Fridman L, and Usai E (2008) Cascade control of PM DC drives via second-order sliding-mode technique. *IEEE Transactions on Industrial Electronics*, **55** (11), 3846–3854.

Polikar R, Udpa L, Udpa S, and Taylor T (1998) Frequency invariant classification of ultrasonic weld inspection signals. *IEEE Transactions on Ultrasonics, Ferroelectrics and Frequency Control*, **45** (3), 614–625.

Puche-Panadero R, Pineda-Sanchez M, Riera-Guasp M, *et al*. (2009) Improved resolution of the MCSA method via hilbert transform, enabling the diagnosis of rotor asymmetries at very low slip. *IEEE Transactions on Energy Conversion*, **24** (1), 52–59.

Rajagopalan S, Restrepo JA, Aller JM, *et al*. (2008) Nonstationary motor fault detection using recent quadratic time frequency representations. *IEEE Transactions on Industry Applications*, **44** (3), 735–744.

Riera-Guasp M, Antonino-Daviu JA, Pineda-Sanchez M, *et al.* (2008a) A general approach for the transient detection of slip-dependent fault components based on the discrete wavelet transform. *IEEE Transactions on Industrial Electronics*, **55** (12), 4167–4180.

Riera-Guasp M, Antonino-Daviu JA, Roger-Folch J, and Molina Palomares MP (2008b) The use of the wavelet approximation signal as a tool for the diagnosis of rotor bar failures. *IEEE Transactions on Industry Applications*, **44** (3), 716–726.

Simani S, Fantuzzi C, and Patton R (2003) Model-based fault diagnosis in dynamic systems using identification techniques. *Recherche*, **67**, 02.

Singh GK, Saleh A, and Kazzaz A (2003) Induction machine drive condition monitoring and diagnostic research * a survey. *Electric Power Systems Research*.

Thomson W and Fenger M (2001) Current signature analysis to detect induction motor faults. *Industry Applications Magazine, IEEE*, **7** (4), 26–34.

Ville J (1948) Theorie et applications de la notion de signal analytique. *Cables et transmission*, **2** (1), 61–74.

Yazidi A, Henao H, Capolino GA, *et al*. (2005) Improvement of frequency resolution for three-phase induction machine fault diagnosis. *Proceedings of IAS Annual Meeting Conference Record*, Hong Kong, pp. 20–25.

Youb L and Craciunescu A (2007) A comparison of various strategies for direct torque control of induction motors. *International Aegean Conference on Electrical Machines and Power Electronics, 2007. ACEMP'07*, pp. 403–408.

Part Four

Control Design Techniques for Synchronous Motors

AC Electric Motors Control: Advanced Design Techniques and Applications, First Edition. Edited by Fouad Giri.

15

Sensorless Speed Control of PMSM

Dhruv Shah[1], Gerardo Espinosa–Pérez[2], Romeo Ortega[1], and Michaël Hilairet[3]
[1]*LSS, SUPELEC, CNRS, France*
[2]*Facultad de Ingeniería, UNAM, México*
[3]*LGEP, SUPELEC, CNRS, France*

15.1 Introduction

Sensorless control of electrical machines is a topic that imposes the challenging problem of eliminating the use of sensors for mechanical variables (position and speed) for controller design purposes (Rajashekara *et al.* 1996). Its solution is both important from the applications perspective (due to its economic impact) and quite attractive from the control theory approach (for the mathematical complexity that it exhibits). In spite of the maturity level achieved for understanding the usual strategies implemented in industrial applications as well as in the proposition of novel control schemes (Dawson *et al.* 1998; Ortega *et al.* 1998; Khorrami *et al.* 2003; Nam 2010), the sensorless control problem is currently recognized as a longstanding essentially open problem.

In this paper we are interested in the sensorless control for nonsalient permanent-magnet synchronous motors (PMSM). For solving it, three variables must be estimated out of the measurement of the electrical coordinates: (1) rotor position, (2) rotor speed, and (3) load torque—the latter assumed constant. Heuristically conceived solutions for this problem abound in the literature (see, e.g., Ichikawa *et al.* (2006) and Fabio *et al.* (2010) for recent surveys). Many results are also available for the (practically unrealistic) cases of known initial position (Tomei and Verrelli 2008; Ezzat *et al.* 2010b) or zero-load torque (Ezzat *et al.* 2010a), or the (theoretically unjustifiable) assumption of bounded trajectories (Ezzat *et al.* 2010b). An approximate stability analysis of the scheme proposed in Matsui (1996) is carried out in Nahid *et al.* (2001). In Marino *et al.* (2008) a probably stable sensorless scheme for wound-rotor

AC Electric Motors Control: Advanced Design Techniques and Applications, First Edition. Edited by Fouad Giri.

synchronous motors is proposed. A key difference of the latter machine from the PMSM is the availability of flux measurements that considerably simplifies the observation problem. The observability properties of PMSMs have been recently studied in Zaltni *et al.* 2008, Ezzat *et al.* (2010), Ortega *et al.* (2011).

Among other techniques, like the use of high-frequency electric variables or the implementation of extended Kalman filters, for nonsalient pole PMSMs (also known as "surface mounted" PMSMs) the simplest and most common rotor position estimation strategy considers the estimation of the back-EMF induced by the permanent magnets (Ichikawa *et al.* 2006), hence it is adopted in this paper. However, instead of using standard methods, that are difficult to tune for standstill and low-speed regimes, the globally (under some conditions, even exponentially) stable position observer reported in Ortega *et al.* (2011) is considered, which has been successfully evaluated in an experimental setting, combining it with an ad hoc linear speed estimator and a standard field-oriented controller (Lee *et al.* 2010), but without a theoretical justification.

The main objective of this paper is to prove that direct application of two well-established design methodologies—immersion and invariance (I&I) (Astolfi *et al.* 2007) for the observer, and interconnection and damping assignment passivity-based control (IDA-PBC) (Ortega and Garcia-Canseco 2004) for the control—can be combined with the observer of Ortega *et al.* (2011) to design an asymptotically stable sensorless controller. The result builds upon some preliminary work reported in Ortega *et al.* (2011) and Shah *et al.* (2009), where, assuming *position is known*, I&I techniques are used to design a speed and load torque observer, and in Akrad *et al.* (2007) and Petrovic *et al.* (2001) where *full state-feedback*, globally convergent, IDA-PBCs for the PMSM are proposed. To the best of our knowledge, this is the first time a complete theoretical analysis of a sensorless controller is done—under reasonable practical and theoretical assumptions.

The remaining of the paper is organized as follows. The models of the PMSM and the problem formulation are given in Section 15.2. The controller structure and the main result are presented in Section 15.3. In Section 15.4 the limitations of a linearization-based design are highlighted. A full information IDA-PBC is given in Section 15.5. Section 15.6 recalls the position observer of Ortega *et al.* (2011), while in Section 15.7 a new I&I speed and load torque observer is proposed. The proof of the main result is given in Section 15.8. Some simulation and experimental results are given in Section 15.9, including a comparison with the heuristic controller of Lee *et al.* (2010). Finally, we wrap-up the paper with concluding remarks in Section 15.10.

15.2 PMSM Models and Problem Formulation

The classical fixed-frame $\alpha\beta$ model of the unsaturated nonsalient PMSM is given by Chiasson (2005) and Krause (1986):

$$\begin{aligned} L\frac{di_{\alpha\beta}}{dt} &= -Ri_{\alpha\beta} - n_p\omega\Phi\mathcal{J}\begin{bmatrix}\cos(\theta)\\ \sin(\theta)\end{bmatrix} + v_{\alpha\beta},\\ J\dot{\omega} &= n_p\Phi i_{\alpha\beta}^{\top}\mathcal{J}\begin{bmatrix}\cos(\theta)\\ \sin(\theta)\end{bmatrix} - \tau_L,\\ \dot{\theta} &= n_p\omega, \end{aligned} \tag{15.1}$$

where $\mathcal{J} := \begin{bmatrix} 0 & -1 \\ 1 & 0 \end{bmatrix}$, $i_{\alpha\beta} = \begin{bmatrix} i_\alpha \\ i_\beta \end{bmatrix}$ and $v_{\alpha\beta} = \begin{bmatrix} v_\alpha \\ v_\beta \end{bmatrix}$ are the stator currents and motor terminal voltages, respectively, ω is the rotor angular velocity, with $\frac{1}{n_p}\theta$ the corresponding position, L is the stator inductance, R is the stator resistance, n_p is the number of pole pairs, J is the moment of inertia (normalized with n_p), Φ is the magnetic flux, and τ_L is the load torque, which is assumed *constant*, but unknown.

To design the observer it is convenient to embed the dynamics (15.1) into the higher dimensional system

$$L\frac{di_{\alpha\beta}}{dt} = -Ri_{\alpha\beta} - n_p\omega\Phi\mathcal{J}\rho_{\alpha\beta} + v_{\alpha\beta}, \tag{15.2}$$

$$J\dot{\omega} = n_p\Phi i_{\alpha\beta}^\top\mathcal{J}\rho_{\alpha\beta} - \tau_L, \tag{15.3}$$

$$\dot{\rho}_{\alpha\beta} = n_p\omega\mathcal{J}\rho_{\alpha\beta}, \tag{15.4}$$

where the vector

$$\rho_{\alpha\beta} := \begin{bmatrix} \rho_\alpha \\ \rho_\beta \end{bmatrix} = \begin{bmatrix} \cos(\theta) \\ \sin(\theta) \end{bmatrix} \tag{15.5}$$

is defined. Notice that, if $\rho_{\alpha\beta}$ is known, θ can be easily reconstructed inverting the trigonometric functions.

The model (15.1) can be written in rotating dq-coordinates by means of the transformation

$$e^{\mathcal{J}\theta} = \begin{bmatrix} \cos(\theta) & -\sin(\theta) \\ \sin(\theta) & \cos(\theta) \end{bmatrix} = \rho_\alpha I_2 + \rho_\beta\mathcal{J}, \tag{15.6}$$

with I_2 as the 2×2 identity matrix, to obtain

$$\begin{aligned} L\frac{di}{dt} &= -(RI_2 + n_p\omega L\mathcal{J})i - n_p\omega\Phi\mathcal{J}e_1 + v, \\ J\dot{\omega} &= n_p\Phi i_2 - \tau_L, \\ \dot{\theta} &= n_p\omega, \end{aligned} \tag{15.7}$$

where the rotated signals

$$i = \begin{bmatrix} i_1 \\ i_2 \end{bmatrix} := e^{-\mathcal{J}\theta}i_{\alpha\beta}, \quad v = \begin{bmatrix} v_1 \\ v_2 \end{bmatrix} := e^{-\mathcal{J}\theta}v_{\alpha\beta}, \quad e_1 = \begin{bmatrix} 1 \\ 0 \end{bmatrix} := e^{-\mathcal{J}\theta}\rho_{\alpha\beta}, \tag{15.8}$$

are defined.

Remark 15.2.1 *The main advantage of the dq model is that it transforms the periodic orbits associated to the constant speed operation of the αβ model of the PMSM into equilibrium points. See Section 15.5.2.*

Remark 15.2.2 *The industry standard field oriented control (Nam 2010) is designed for this model, hence the need to reconstruct θ. Indeed, it must be recalled that the input is $v_{\alpha\beta}$, while the measurable output is $i_{\alpha\beta}$, but θ is an* unmeasurable *variable.*

15.2.1 Problem Formulation

The main contribution of the paper is the solution of the following *Sensorless control problem. Consider the PMSM model* (15.2), (15.3), and (15.4) *with some desired constant speed $\omega^* \neq 0$, under the following conditions:*

A1 *The only variables available for measurement are $i_{\alpha\beta}$.*

A2 *The load torque τ_L is constant but* unknown.

A3 *The parameters R, L, Φ and J are known.*

Design an output-feedback controller that ensures the existence of a set of initial conditions, which guarantees that all signals are bounded and that $\omega(t)$ converges, exponentially fast, to ω^*.

Remark 15.2.3 *Even though we have restricted ourselves to the case of constant desired speed and constant load torque, it is clear that the controller, being exponentially stable hence robust, will be able to track (slowly) time-varying references and reject changes in the load torque. Interestingly, the simulations and experimental results of Section 15.9 show that the proposed controller yields a good performance even in the face of fast changes in the speed reference and the load torque. The constraint $\omega^* \neq 0$ is necessary in the present (sensorless) context, because it is easy to show (see, e.g., Zaltni et al. 2008; Ezzat et al. 2010a; Ortega et al. 2011), that the rank condition for observability is violated when the motor is at standstill. Practically, this assumption is not restrictive because, once again, the intrinsic robustness of the controller accommodates sign changes in the desired speed.*

15.3 Controller Structure and Main Result

To simplify the presentation of the main result it is convenient to explain the controller structure and define the notation. The proposed controller is a fourth order certainty equivalent version of a full-information globally asymptotically stabilizing controller, which is a static state-feedback IDA-PBC of the form $v_{\alpha\beta} = q(\rho_{\alpha\beta}, \omega, \tau_L, i_{\alpha\beta})$.

The certainty equivalent version is obtained by replacing $\rho_{\alpha\beta}$, ω, and τ_L by their estimates. The dynamics of the controller is, then, due to the I&I observer, which generates the estimates that we denote $\hat{\rho}_{\alpha\beta}$, $\hat{\omega}$, and $\hat{\tau}_L$, respectively. The controller, combined with the third order PMSM dynamics (15.7) yields a seventh order closed loop system.

As usual, the analysis is carried out in error coordinates, which is a mixture of regulation errors, $(\cdot) - (\cdot)^*$, and estimation errors, $\widehat{(\cdot)} - (\cdot)$. To simplify the notation, all these errors are lumped into a seventh dimensional vector denoted χ, and defined as[1]

$$\chi = \begin{bmatrix} \chi_1 \\ \chi_2 \\ \chi_3 \\ \chi_4 \\ \chi_5 \\ \chi_6 \\ \chi_7 \end{bmatrix} := \begin{bmatrix} L(i - i^*) \\ J(\omega - \omega^*) \\ e^{-\mathcal{J}\theta}\left(\hat{\rho}_{\alpha\beta} - \rho_{\alpha\beta}\right) \\ \hat{\omega} - \omega \\ \hat{\tau}_L - \tau_L \end{bmatrix}. \tag{15.9}$$

Notice that the errors in both, the currents and the vector $\rho_{\alpha\beta}$, are defined in the dq coordinates.

Our main result is the following proposition, whose proof is given in Section 15.8.4.

Proposition 15.3.1 *There exists a fourth order observer-based speed regulator of the form*

$$\begin{aligned} \dot{\psi} &= g(\psi, i_{\alpha\beta}, v_{\alpha\beta}), \\ \begin{bmatrix} \hat{\rho}_{\alpha\beta} \\ \hat{\omega} \\ \hat{\tau}_L \end{bmatrix} &= h(\psi, i_{\alpha\beta}, v_{\alpha\beta}), \\ v_{\alpha\beta} &= q(\hat{\rho}_{\alpha\beta}, \hat{\omega}, \hat{\tau}_L, i_{\alpha\beta}), \end{aligned}$$

where $\psi \in \mathbf{R}^4$ and g, h, q are suitably defined functions that solve the sensorless control problem[2]*. More precisely, the closed-loop error dynamics are described by a differential equation of the form*

$$\dot{\chi} = f(\chi), \tag{15.10}$$

with zero (locally) exponentially stable equilibrium. Consequently, there exist constants $m, \epsilon, \alpha > 0$ such that the following implication holds:

$$\left(|\chi(0)| \leq \epsilon \;\Rightarrow\; |\chi(t)| \leq m e^{-\alpha t}|\chi(0)|\right),$$

for all $t \geq 0$, where $|\cdot|$ is the Euclidean norm.

[1]The constants L and J are introduced because—consistent with the Hamiltonian formulation—the IDA-PBC is derived with the motor dynamics represented using the energy variables, flux, and momenta.

[2]The output-feedback controller consists of (15.18), the position observer (15.23) and (15.25), and the speed-load torque observer (15.30).

15.4 Unavailability of a Linearization-Based Design

Before proceeding with the design of a controller for the nonlinear model it is natural to explore the possibility of basing the design on the PMSMs linearization. This question is particularly relevant in our case since, as explained below, the stability analysis of the proposed controller relies on the linearization of the closed loop.

To answer this question, it is convenient to work with the dq model (15.7), with measurable output signals the currents $i_{\alpha\beta}$. Fixing a constant desired speed ω^*, and its corresponding constant equilibrium current i^*, define the error signals

$$\delta_x(t) = \begin{bmatrix} i(t) - i^* \\ \omega(t) - \omega^* \\ \theta(t) - \theta^*(t) \end{bmatrix}, \qquad \delta_v := v - v^*,$$

where $\theta^*(t) = \theta(0) + \omega^* t$, and v^* is the constant control signal that assigns the equilibrium (i^*, ω^*). Now, as the measurable signal is $i_{\alpha\beta}$, invoking (15.8) we define the "output" error

$$\delta_y(t) := e^{\mathcal{J}\theta(t)} i(t) - e^{\mathcal{J}\theta^*(t)} i^*.$$

The linearization of (15.7) and the output map above, along the equilibrium trajectory, yields the linear time-varying system

$$\begin{aligned} \dot{\delta}_x &= A_\ell \delta_x + B\delta_v, \\ \delta_y &= C(t)\delta_x, \end{aligned}$$

where

$$A_\ell := \begin{bmatrix} -\left(\frac{R}{L} I_2 + n_p \omega^* \mathcal{J}\right) & -n_p \mathcal{J}\left(\frac{\Phi}{L} e_1 + i^*\right) & 0 \\ \frac{n_p}{J} \Phi e_1^\top \mathcal{J}^\top & 0 & 0 \\ 0 & n_p & 0 \end{bmatrix}, \quad B := \begin{bmatrix} \frac{1}{L} I_2 \\ 0 \\ 0 \end{bmatrix},$$

$$C(t) := \begin{bmatrix} e^{\mathcal{J}\theta^*(t)} & 0 & e^{\mathcal{J}\theta^*(t)} \mathcal{J} i^* \end{bmatrix}.$$

Although, apparently, this is an innocuous linear time-varying system for which an observer-based controller could be designed, there are several aspects that stymies this task. First of all, the *equilibrium is unknown* because, on one hand, i^* depends on the unknown load torque τ_L. On the other hand, the position $\theta^*(t)$ is also unknown, due to its dependence on $\theta(0)$—see the remark below. Consequently, the system coefficients are unknown. On top of that, the "output" δ_y is known up to the bias term $e^{\mathcal{J}\theta^*(t)} i^*$. In summary, since there exist products of unknown parameters and the unmeasurable state ω, designing an output-feedback controller implies that the solution of a nonlinearly parameterized adaptive observer problem—to the best of our knowledge—is not possible with existing techniques.

Remark 15.4.1 *It is sometimes argued that the motor operation often starts at a known rotor position, hence $\theta^*(t)$ can be computed. It is obvious that this "trajectory-dependent" controller suffers, in the face of disturbances, from serious robustness problems—that, as is well known, is the main drawback of schemes based on open-loop integration.*

15.5 Full Information Control

In this section, a full-information IDA-PBC, assuming known state and load torque, similar to the one reported in Akrad *et al.* (2007) and Petrovic *et al.* (2001), is presented. This scheme serves as a basis for our certainty equivalent design.

15.5.1 Port-Hamiltonian Model

Following the IDA-PBC methodology (Ortega *et al.* 2002; Ortega and Garcia–Canseco 2004) it is convenient to write the system dynamics in port-Hamiltonian form (van der Schaft 2000), thus we define the state vector as

$$x = \begin{bmatrix} x_{12} \\ x_3 \end{bmatrix} = \begin{bmatrix} Li \\ J\omega \end{bmatrix}, \tag{15.11}$$

and the energy function $H(x) = \frac{1}{2}x^\top Qx$, with

$$Q = \begin{bmatrix} \frac{1}{L}I_2 & 0 \\ 0 & \frac{1}{J} \end{bmatrix}. \tag{15.12}$$

Then, the dq system (15.7) can be written in the form

$$\dot{x} = F(x)\nabla H(x) + \begin{bmatrix} v \\ -\tau_L \end{bmatrix}, \tag{15.13}$$

where $\nabla = (\frac{\partial}{\partial x})^\top$ and the interconnection and damping matrices are lumped into

$$F(x) = \begin{bmatrix} -RI_2 & -n_p\mathcal{J}(x_{12} + \Phi e_1) \\ n_p(x_{12} + \Phi e_1)^\top \mathcal{J}^\top & 0 \end{bmatrix}.$$

Notice that $\dot{H} = -R|i|^2 + v^\top i - \tau_L\omega$, which is the power balance equation for the motor.

The assignable equilibrium set for (15.13) is given by

$$\left\{x^* \in \mathbf{R}^3 \mid x_2^* = \frac{L}{n_p\Phi}\tau_L\right\},$$

with arbitrary x_1^* and x_3^*. Consistent with engineering practice, and without loss of generality, we will fix $x_1^* = 0$ in the sequel. See the remark below.

The objective of IDA-PBC is to find a state-feedback control law $v = v(x)$ that assigns to the closed loop a desired energy function, say $H_d(x)$, which satisfies $x^* = \arg\min H_d(x)$. This is achieved by modifying the interconnection and damping matrices, endowing the closed loop with the port-Hamiltonian form

$$\dot{x} = F_d(x)\nabla H_d(x), \tag{15.14}$$

where $F_d(x) + F_d^\top(x) \leq 0$. This ensures stability of the equilibrium x^* with Lyapunov function $H_d(x)$. Under some standard detectability assumptions (e.g., Lemma 3.8, van der Schaft 2000), the equilibrium is shown to be asymptotically stable.

15.5.2 A Full-Information IDA-PBC

Proposition 15.5.1 *Consider the PMSM dq model (15.13) with a desired equilibrium point*

$$x^* = \begin{bmatrix} 0 \\ \frac{L}{n_p \Phi}\tau_L \\ J\omega^* \end{bmatrix}. \tag{15.15}$$

The full-information control

$$v^{FI} = dx_{12} + \begin{bmatrix} -\frac{L}{J\Phi}\tau_L x_3 \\ n_p \Phi \omega^* + \frac{r}{n_p \Phi}\tau_L \end{bmatrix}, \tag{15.16}$$

where $d := \frac{R-r}{L}$, with $r > 0$ a damping injection term, renders x^* globally asymptotically stable.

Proof: Define the desired closed-loop energy function as the quadratic in the errors form

$$H_d(\chi_{13}) = \frac{1}{2}\chi_{13}^\top Q \chi_{13},$$

with

$$\chi_{13} = \begin{bmatrix} \chi_{12} \\ \chi_3 \end{bmatrix} = \begin{bmatrix} x_{12} - x_{12}^* \\ x_3 - x_3^* \end{bmatrix},$$

where Q is as in (15.12).

In order to achieve the required matching between the right-hand sides of equations (15.13) and (15.14), it is considered that matrix $F_d(x)$ is partitioned in an appropriate way, with

elements given by $F_{ij}(x)$, that $x_1^* = 0$, and the definition of x_2^* in (15.15). Thus, the third row of this marching equation, which actually states the only constraint to be solved since the first and second components can be easily satisfied with a suitable selection of the control inputs v_1 and v_2, can be written in an equivalent way as

$$\frac{n_p\Phi}{L}\chi_2 = \frac{1}{L}F_{31}\chi_1 + \frac{1}{L}F_{32}\chi_2 + \frac{1}{J}F_{33}\chi_3.$$

Then it is recognized, that a solution is given by

$$F_{31} = F_{33} = 0; \qquad F_{32} = n_p\Phi.$$

The nonpositivity condition on the symmetric part of $F_d(x)$ suggests to define $F_{23} = -F_{32} = -n_p\Phi$. Replacing this choice in the second row of the matching equation yields

$$-\frac{R}{L}x_2 - \frac{n_p}{J}x_1x_3 + v_2 = \frac{1}{L}F_{21}x_1 + \frac{1}{L}F_{22}(x_2 - x_2^*) + \frac{n_p\Phi}{J}x_3^*,$$

where the term $\frac{n_p}{J}\Phi x_3$ has been canceled. A solution to this equation is obtained by selecting $F_{21} = -\frac{Ln_p}{J}x_3$, $F_{22} = -r$ and

$$v_2 = dx_2 + \frac{r}{L}x_2^* + \frac{n_p\Phi}{J}x_3^*,$$

which, upon replacement of the definitions of x_2^* and x_3^*, yields the expression given in the proposition. With the definitions given up to this point, the third component of the matching equation can be satisfied by taking $F_{11} = -r$, $F_{12} = \frac{Ln_p}{J}x_3$, $F_{13} = 0$, and

$$v_1 = dx_1 - \frac{n_p}{J}x_2^*x_3.$$

Finally, the closed-loop system takes the desired port-Hamiltonian form (15.14) with

$$F_d(x) = \begin{bmatrix} -r & \frac{Ln_p}{J}x_3 & 0 \\ -\frac{Ln_p}{J}x_3 & -r & -n_p\Phi \\ 0 & n_p\Phi & 0 \end{bmatrix}, \tag{15.17}$$

hence, the equilibrium x^* is stable. Asymptotic stability follows, verifying that

$$\dot{H}_d = -\frac{r}{L^2}|\chi_{12}|^2$$

and that $|\chi_{12}|^2$ is a detectable output for the closed-loop system (15.14). □

15.5.3 Certainty Equivalent Sensorless Controller

If the states are measurable, the control law to be practically implemented is obtained by combining (15.16) with

$$v_{\alpha\beta}^{FI} = e^{\mathcal{J}\theta} v^{FI} = (\rho_\alpha I_2 + \rho_\beta \mathcal{J}) v^{FI}.$$

However, under the impossibility for measuring the states $\rho_{\alpha\beta}$, ω, and the unknown nature of the perturbation τ_L the proposed *implementable* sensorless controller takes the form

$$\begin{aligned} v_{\alpha\beta} &= (\hat{\rho}_\alpha I_2 + \hat{\rho}_\beta \mathcal{J})\hat{v}, \\ \dot{\hat{v}} &:= dx_{12} + \begin{bmatrix} -\frac{L}{\Phi}\hat{\tau}_L \hat{\omega} \\ n_p \Phi \omega^* + \frac{r}{n_p \Phi}\hat{\tau}_L \end{bmatrix}. \end{aligned} \tag{15.18}$$

Notice that since the controller in dq coordinates requires the currents x_{12}, its implementable structure is given in terms of the estimated currents in the $\alpha\beta$ reference frame given by $(\hat{\rho}_\alpha I_2 + \hat{\rho}_\beta \mathcal{J})x_{12}$.

15.6 Position Observer of Ortega *et al.* (2011)

In this section, the observer presented in Ortega *et al.* (2011), which estimates the rotor position θ via the observation of the flux, is briefly revisited. Also, an alternative representation of the observer, which is instrumental for the speed-load torque observer given in the next section, is presented. Before presenting the results, a word on notation is in order. To facilitate the reference to Ortega *et al.* (2011), the notation used in this paper is kept here. In particular, we define the observation error $\tilde{\lambda} := \hat{\lambda} - \lambda$, with λ the stator flux and $\hat{\lambda}$ its estimate.

15.6.1 Flux Observer and Stability Properties

In PMSMs, the stator flux, λ, is related with the currents and voltages via (Krause 1986)

$$\lambda = L i_{\alpha\beta} + \Phi \rho_{\alpha\beta}. \tag{15.19}$$

Therefore, (15.2) can be equivalently written as

$$\dot{\lambda} = -R i_{\alpha\beta} + v_{\alpha\beta}. \tag{15.20}$$

This representation of the electrical dynamics of the PMSM is used in Ortega *et al.* (2011) to develop a position observer. To explain this observer, we make the important observations that $\dot{\lambda}$ is measurable, and that the vector function

$$\eta(\lambda) := \lambda - L i_{\alpha\beta} \tag{15.21}$$

satisfies

$$|\eta(\lambda)| = \Phi. \tag{15.22}$$

In Ortega *et al.* (2011) it is shown that

$$\dot{\hat{\lambda}} = -Ri_{\alpha\beta} + v_{\alpha\beta} + \gamma\eta(\hat{\lambda})[\Phi^2 - |\eta(\hat{\lambda})|^2], \tag{15.23}$$

where $\gamma > 0$ is an observer gain, is a gradient descent observer for the flux. It is also proven that the dynamics of the observation error $\tilde{\lambda}$ is described by the second order nonautonomous equation

$$\dot{\tilde{\lambda}} = -\gamma[|\tilde{\lambda}|^2 + 2\Phi\tilde{\lambda}^\top\rho_{\alpha\beta}(t)][\tilde{\lambda} + \Phi\rho_{\alpha\beta}(t)], \tag{15.24}$$

which enjoys the following remarkable stability properties:

P1: Global stability: For arbitrary speeds, the disk

$$\{\tilde{\lambda} \in \mathbf{R}^2 | \, |\tilde{\lambda}| \leq 2\Phi\}$$

is globally attractive. This means, that all trajectories of (15.24) will converge to this disk.

P2: Exponential stability under persistent excitation: The zero equilibrium of equation (15.24) is exponentially stable if there exists constants T, and $\Delta > 0$ such that

$$\frac{1}{T}\int_t^{t+T} \omega^2(s)ds \geq \Delta,$$

for all $t \geq 0$.

P3: Constant non-zero speed: If the speed is constant and satisfies

$$|\omega| > \frac{1}{4}\gamma\Phi^2,$$

then the origin is the unique equilibrium of (15.24) and it is globally asymptotically stable[3].

15.6.2 Description of the Observer in Terms of $\rho_{\alpha\beta}$

Instrumental for the development of the position and load-torque observer, as well as for the analysis of the closed-loop system, is the representation of the previous flux observer, and its estimation error, in terms of $\rho_{\alpha\beta}$.

[3]Notice the presence of the free adaptation gain γ on the lower bound.

Proposition 15.6.1 *From equation (15.19) and the observer (15.23) define the estimate*

$$\hat{\rho}_{\alpha\beta} = \frac{1}{\Phi}\left(\hat{\lambda} - Li_{\alpha\beta}\right) \tag{15.25}$$

and the error $\tilde{\rho}_{\alpha\beta} := \hat{\rho}_{\alpha\beta} - \rho_{\alpha\beta}$. *The observer (15.23) may be written as*

$$\dot{\hat{\rho}}_{\alpha\beta} = -\gamma\Phi^2\left(|\hat{\rho}_{\alpha\beta}|^2 - 1\right)\hat{\rho}_{\alpha\beta} + n_p\omega\mathcal{J}\rho_{\alpha\beta}, \tag{15.26}$$

while the estimation error $\tilde{\rho}_{\alpha\beta}$ *satisfies*

$$\dot{\tilde{\rho}}_{\alpha\beta} = -\gamma\Phi^2\left(|\tilde{\rho}_{\alpha\beta}|^2 + 2\tilde{\rho}_{\alpha\beta}^\top\rho_{\alpha\beta}\right)\left(\tilde{\rho}_{\alpha\beta} + \rho_{\alpha\beta}\right). \tag{15.27}$$

Proof: First, notice that $\tilde{\lambda} = \Phi\tilde{\rho}_{\alpha\beta}$, which replaced in equation (15.24) yields

$$\dot{\tilde{l}} = -\gamma\Phi^3\left(|\tilde{\rho}_{\alpha\beta}|^2 + 2\tilde{\rho}_{\alpha\beta}^\top\rho_{\alpha\beta}\right)\left(\tilde{\rho}_{\alpha\beta} + \rho_{\alpha\beta}\right)$$

leading directly to (15.27). Now, notice that $|\tilde{\rho}_{\alpha\beta}|^2 + 2\tilde{\rho}_{\alpha\beta}^\top\rho_{\alpha\beta} = |\hat{\rho}_{\alpha\beta}|^2 - 1$, while $\dot{\tilde{\rho}}_{\alpha\beta} = \dot{\hat{\rho}}_{\alpha\beta} - n_p\omega\mathcal{J}\rho_{\alpha\beta}$, which replaced in (15.27) yields (15.26). □

15.7 An I&I Speed and Load Torque Observer

In this section an observer for the unmeasurable variables ω and τ_L is designed following the I&I methodology (Astolfi *et al.* 2007). The construction proceeds along the following steps:

S1: The parametrization of the mechanical dynamics—in terms of $\rho_{\alpha\beta}$—given in equation (15.3), as well as the representation of the flux observer (15.23) given in equation (15.26), are used.

S2: The term $\rho_{\alpha\beta}$ in both equations is decomposed as the sum of its estimate $\hat{\rho}_{\alpha\beta}$ and the error $\tilde{\rho}_{\alpha\beta}$, and we treat the latter as a perturbation.

S3: A globally exponentially convergent I&I observer of ω and τ_L is designed neglecting the perturbation in the system[4].

The mechanical equation (15.3) and the position observer (15.26) can be written in the "perturbed" form

$$\begin{aligned} J\dot{\omega} &= n_p\Phi i_{\alpha\beta}^\top\mathcal{J}\hat{\rho}_{\alpha\beta} - \tau_L - \left(n_p\Phi i_{\alpha\beta}^\top\mathcal{J}\tilde{\rho}_{\alpha\beta}\right), \\ \dot{\hat{\rho}}_{\alpha\beta} &= -\gamma\Phi^2\left(|\hat{\rho}_{\alpha\beta}|^2 - 1\right)\hat{\rho}_{\alpha\beta} + n_p\omega\mathcal{J}\hat{\rho}_{\alpha\beta} - (n_p\omega\mathcal{J}\tilde{\rho}_{\alpha\beta}). \end{aligned} \tag{15.28}$$

[4]The perturbation term that is neglected in this section is lumped into the overall error dynamics, whose stability is analyzed in Section 15.8.

Their corresponding unperturbed forms, that is, with $\tilde{\rho}_{\alpha\beta} = 0$, are given by

$$\begin{aligned} J\dot{\omega} &= n_p \Phi i_{\alpha\beta}^{\top} \mathcal{J} \hat{\rho}_{\alpha\beta} - \tau_L, \\ \dot{\hat{\rho}}_{\alpha\beta} &= -\gamma \Phi^2 \left(|\hat{\rho}_{\alpha\beta}|^2 - 1 \right) \hat{\rho}_{\alpha\beta} + n_p \omega \mathcal{J} \hat{\rho}_{\alpha\beta}, \\ \dot{\tau}_L &= 0, \end{aligned} \tag{15.29}$$

where, for completeness, the last (trivial) equation has been added.

Proposition 15.7.1 *Consider the system (15.29) and the speed and load torque observer*

$$\begin{aligned} \dot{\xi} &= A_{33}\xi + \begin{bmatrix} \frac{a_2}{J} - n_p a_1^2 \\ n_p a_1 a_2 \end{bmatrix} \mathcal{A}\left(\frac{\hat{\rho}_\beta}{\hat{\rho}_\alpha} \right) + \begin{bmatrix} \frac{n_p \Phi}{J} i_{\alpha\beta}^{\top} \mathcal{J} \hat{\rho}_{\alpha\beta} \\ 0 \end{bmatrix}, \\ \begin{bmatrix} \hat{\omega} \\ \hat{\tau}_L \end{bmatrix} &= \xi + \begin{bmatrix} a_1 \\ -a_2 \end{bmatrix} \mathcal{A}\left(\frac{\hat{\rho}_\beta}{\hat{\rho}_\alpha} \right), \end{aligned} \tag{15.30}$$

where $\mathcal{A}(\cdot)$ is an operator defined in Appendix A[5]*, and A_{33} is the Hurwitz matrix*

$$A_{33} := \begin{bmatrix} -n_p a_1 & -\frac{1}{J} \\ n_p a_2 & 0 \end{bmatrix}, \qquad a_1, a_2 > 0. \tag{15.31}$$

For some $\alpha > 0$ and for all initial conditions $(\omega(0), \xi(0)) \in \mathbf{R} \times \mathbf{R}^2$,

$$\lim_{t\to\infty} e^{\alpha t} \left\| \begin{bmatrix} \hat{\omega}(t) - \omega(t) \\ \hat{\tau}_L(t) - \tau_L \end{bmatrix} \right\| = 0. \tag{15.32}$$

That is, equation (15.30) is a globally exponentially convergent speed and load torque observer for the unperturbed system (15.29).

Proof: Following the I&I procedure (Astolfi *et al.* 2007), we define a manifold (in the extended state space of the plant and the observer) that should be rendered attractive and invariant. As is well known, to achieve the latter objective a partial differential equation (PDE) should be solved.

For the system (15.29), we propose the manifold

$$\mathcal{M} := \{(\xi, \omega, \hat{\rho}_{\alpha\beta}) : \xi - \begin{bmatrix} \omega \\ \tau_L \end{bmatrix} + \zeta(\hat{\rho}_{\alpha\beta}) = 0\} \subset \mathbf{R}^5, \tag{15.33}$$

where $\xi \in \mathbf{R}^2$ is the observer state, the dynamics of which are defined below, and the mapping $\zeta(\hat{\rho}_{\alpha\beta})$ is also to be defined.

[5] As explained below, the operator $\mathcal{A}(z)$, which is widely used in the drives community, is "essentially" equal to $\arctan(z)$, and is introduced to avoid singularities and jumps.

To prove that the manifold $\mathcal{M}$ is attractive and invariant it is shown that the off-the-manifold coordinate

$$\chi_{67} := \xi - \begin{bmatrix} \omega \\ \tau_L \end{bmatrix} + \zeta(\hat{\rho}_{\alpha\beta}), \tag{15.34}$$

the norm of which determines the distance of the state to the manifold $\mathcal{M}$, is such that:

- $\chi_{67}(0) = 0 \Rightarrow \chi_{67}(t) = 0$, for all $t \geq 0$ (invariance);
- $\chi_{67}(t)$ asymptotically (*exponentially*) converges to zero (attractivity).

Notice that, if $\chi_{67}(t) \to 0$, an asymptotic estimate of $\begin{bmatrix} \omega \\ \tau_L \end{bmatrix}$ is given by $\xi + \zeta(\hat{\rho}_{\alpha\beta})$.

To obtain the dynamics of χ_{67}, differentiate (15.34) along the trajectories of (15.29), yielding

$$\dot{\chi}_{67} = \dot{\xi} - \nabla\zeta[\gamma\Phi^2\left(|\hat{\rho}_{\alpha\beta}|^2 - 1\right)\hat{\rho}_{\alpha\beta} - n_p\omega\mathcal{J}\hat{\rho}_{\alpha\beta}] + \begin{bmatrix} \frac{\tau_L}{J} - \frac{n_p\Phi}{J} i_{\alpha\beta}^\top \mathcal{J}\hat{\rho}_{\alpha\beta} \\ 0 \end{bmatrix}.$$

Our objective is to find $\dot{\xi}$ and a mapping ζ to obtain an asymptotically stable linear dynamics for χ_{67}. Towards this end, notice that selecting $\dot{\xi}$ as

$$\dot{\xi} = A_{33}(\xi + \zeta) + \gamma\Phi^2\left(|\hat{\rho}_{\alpha\beta}|^2 - 1\right)\nabla\zeta\,\hat{\rho}_{\alpha\beta} + \begin{bmatrix} \frac{n_p\Phi}{J} i_{\alpha\beta}^\top \mathcal{J}\hat{\rho}_{\alpha\beta} \\ 0 \end{bmatrix} \tag{15.35}$$

yields

$$\dot{\chi}_{67} = A_{33}(\xi + \zeta) + \begin{bmatrix} \frac{\tau_L}{J} \\ 0 \end{bmatrix} + n_p\omega\nabla\zeta\,\mathcal{J}\hat{\rho}_{\alpha\beta}.$$

Consequently, if we can solve the PDE

$$\nabla\zeta\,\mathcal{J}\hat{\rho}_{\alpha\beta} = \begin{bmatrix} a_1 \\ -a_2 \end{bmatrix}, \tag{15.36}$$

recalling equation (15.34), one gets

$$\dot{\chi}_{67} = A_{33}\chi_{67}, \tag{15.37}$$

as desired. The PDE (15.36), indeed, has a solution:

$$\zeta(\hat{\rho}_{\alpha\beta}) = \begin{bmatrix} a_1 \\ -a_2 \end{bmatrix} \arctan\left(\frac{\hat{\rho}_\beta}{\hat{\rho}_\alpha}\right). \tag{15.38}$$

Now, with the definition above,

$$\nabla\zeta = \frac{-1}{|\hat{\rho}_{\alpha\beta}|^2}\begin{bmatrix} a_1 \\ -a_2 \end{bmatrix}\hat{\rho}_{\alpha\beta}^{\top}\mathcal{J}.$$

Consequently, $\nabla\zeta\,\hat{\rho}_{\alpha\beta} = 0$, and the second right-hand term in (15.35) vanishes. The proof is completed noting that

$$A_{33}\begin{bmatrix} a_1 \\ -a_2 \end{bmatrix} = \begin{bmatrix} \frac{a_2}{J} - n_p a_1^2 \\ n_p a_1 a_2 \end{bmatrix},$$

replacing the function arctan by the operator $\mathcal{A}$ in equation (15.30), and noting that the derivations above remain valid after this substitution. □

Remark 15.7.2 *If the* arctan *function is used instead of the operator $\mathcal{A}$ in order to recover the estimate $\hat{\rho}_{\alpha\beta}$, some Dirac delta functions might appear in the speed estimation and the error dynamics. To explain this phenomenon consider the case of (constant) regulation of the motor speed and assume that $\hat{\rho}_{\alpha\beta}(t) \equiv \rho_{\alpha\beta}(t)$. Then, in view of (15.38), we have that $\zeta(\hat{\rho}_{\alpha\beta}(t)) \equiv \theta(t) = \omega^* t (\mathtt{mod}\,\pi)$, which is a periodic function defined on the set $(-\pi, \pi)$. In this scenario, the* arctan *jumps instantaneously from the value $\frac{\pi}{2}$ to the value $\frac{-\pi}{2}$ inducing a train of Dirac delta functions, $\delta_T(t)$, in the derivative of* arctan*. This term propagates, through $\dot{\zeta}(\rho_{\alpha\beta})$, into the error dynamics that now reads as*[6]

$$\dot{\chi}_{67} = \begin{bmatrix} -n_p a_1 & -\frac{1}{J} \\ n_p a_2 & 0 \end{bmatrix}\chi_{67} + \begin{bmatrix} a_1 \\ -a_2 \end{bmatrix}\delta_T.$$

As illustrated in the simulations of Section 15.9 this undesirable effect is removed by using instead the operator $\mathcal{A}$ defined in Appendix A.

Remark 15.7.3 *Proposition 15.7.1 refers to the unperturbed dynamics (15.29), for which it was assumed that $\tilde{\rho}_{\alpha\beta} = 0$. Some simple calculations show that if this term is not zero the error dynamic of χ_{67} takes the form*

$$\dot{\chi}_{67} = \begin{bmatrix} -n_p a_1 & -\frac{1}{J} \\ n_p a_2 & 0 \end{bmatrix}\chi_{67} - \frac{n_p\omega}{|\hat{\rho}_{\alpha\beta}|^2}\begin{bmatrix} a_1 \\ -a_2 \end{bmatrix}\hat{\rho}_{\alpha\beta}^{\top}\tilde{\rho}_{\alpha\beta} + \begin{bmatrix} \frac{n_p\Phi}{J} i_{\alpha\beta}^{\top}\mathcal{J}\tilde{\rho}_{\alpha\beta} \\ 0 \end{bmatrix}. \tag{15.39}$$

In the next section, the effect of the additional terms on the overall dynamics is analyzed.

[6]The expression above shows that, away from the isolated points where the δ–functions appear, the observer error exponentially converges to zero.

15.8 Proof of the Main Result

In this section, the stability properties of the closed-loop system, composed by the motor (15.7), the output-feedback controller (15.18), the position observers (15.23) and (15.25), and the speed-load torque observer (15.30) are studied.

The dynamics are described using the error coordinates (15.9), which yields a set of nonlinear differential equations of the form (15.10). For ease of reference, these equations are sequentially derived for χ_{13}, χ_{45}, and χ_{67}. The stability properties of the system are established by invoking Lyapunov's indirect method. Towards this end, the equations are written in the form

$$\dot{\chi} = A\chi + \Gamma(\chi), \tag{15.40}$$

where A is the system matrix of the linearized system, that is, $A := \nabla f(0)$, where $f(\chi)$ is defined in (15.9) and (15.10), and the elements of the vector $\Gamma(\chi)$ contain (second or higher order) products of the components of χ. The proof of the claim of asymptotic stability of Proposition 15.3.1, follows showing that A is a Hurwitz matrix.

15.8.1 Currents and Speed Tracking Errors

Lemma 15.8.1 *Consider the PMSM model (15.7) in closed loop with the output-feedback controller (15.18). The first three components, χ_{13}, of the error vector χ—defined in (15.9)—evolve according to the following dynamics:*

$$\dot{\chi}_{13} = A_{11}\chi_{13} + A_{12}\chi_{45} + A_{13}\chi_{67} + \Gamma_{13}(\chi), \tag{15.41}$$

where

$$\begin{aligned}
A_{11} &= F_d(x^*)Q,\\
A_{12} &= \begin{bmatrix} -\frac{L}{J\Phi}\tau_L x_3^* & -dx_2^* - \frac{n_p\Phi}{J}x_3^* - \frac{r}{n_p\Phi}\tau_L \\ dx_2^* + \frac{n_p\Phi}{J}x_3^* + \frac{r}{n_p\Phi}\tau_L & -\frac{L}{J\Phi}\tau_L x_3^* \\ 0 & 0 \end{bmatrix},\\
A_{13} &= \begin{bmatrix} -\frac{L}{\Phi}\tau_L & -\frac{L}{J\Phi}x_3^* \\ 0 & \dfrac{r}{n_p\Phi} \\ 0 & 0 \end{bmatrix},
\end{aligned} \tag{15.42}$$

where $d = \frac{R-r}{L}$, while $F_d(x)$ and Q are defined in equations (15.17) and (15.12), respectively, and $\Gamma_{13}(\chi)$ is such that $\nabla\Gamma_{13}(0) = 0$. Moreover, the matrix A_{11} is Hurwitz.

Proof: The output-feedback controller (15.18) can be written as

$$v_{\alpha\beta} = \left[\tilde{\rho}_\alpha I_2 + \tilde{\rho}_\beta \mathcal{J}\right] \hat{v} + e^{\mathcal{J}\theta}\hat{v},$$

which, in dq coordinates, that is, considering $v = e^{-\mathcal{J}\theta} v_{\alpha\beta}$, takes the form

$$v = \hat{v} + \left[\hat{v}_1 I_2 + \hat{v}_2 \mathcal{J}\right] \chi_{45}, \tag{15.43}$$

where we have used the errors $\chi_{45} = e^{-\mathcal{J}\theta}\tilde{\rho}_{\alpha\beta}$, and $\hat{v}_1$ and $\hat{v}_2$ are the components of $\hat{v}$.

On the other hand, some simple calculations show that

$$\hat{v} = v^{FI} + \begin{bmatrix} -\frac{L}{\Phi}\tau_L & -\frac{L}{J\Phi}x_3^* \\ 0 & \frac{r}{n_p\Phi} \end{bmatrix} \chi_{67} - \begin{bmatrix} \frac{L\chi_7}{\Phi}\left(\frac{1}{J}\chi_3 + \chi_6\right) \\ 0 \end{bmatrix},$$

with the full-information control v^{FI} given by (15.16). Using the definition of χ_3, the latter can be decomposed as

$$v^{FI} = dx_{12} + \begin{bmatrix} -\frac{L}{J\Phi}\tau_L x_3^* \\ \frac{n_p\Phi}{J}x_3^* + \frac{r}{n_p\Phi}\tau_L \end{bmatrix} + \begin{bmatrix} -\frac{L}{J\Phi}\tau_L\chi_3 \\ 0 \end{bmatrix}.$$

Finally, the second term of the control law v can be expanded as

$$\left[\hat{v}_1 I_2 + \hat{v}_2\mathcal{J}\right]\chi_{45} = \begin{bmatrix} -\frac{L}{J\Phi}\tau_L x_3^* & -dx_2^* - \frac{n_p\Phi}{J}x_3^* - \frac{r}{n_p\Phi}\tau_L \\ dx_2^* + \frac{n_p\Phi}{J}x_3^* + \frac{r}{n_p\Phi}\tau_L & -\frac{L}{J\Phi}\tau_L x_3^* \end{bmatrix}\chi_{45} + \Gamma_{13}(\chi),$$

for some $\Gamma_{13}(\chi)$ verifying the conditions of the lemma. Using all the expressions above to define v, and replacing in equation (15.13), yields (15.41) and (15.42), allowing to complete the first part of the proof.

To prove that the matrix A_{11} is Hurwitz we use equations (15.17) and (15.12) to evaluate

$$F_d(x^*)Q = \begin{bmatrix} -\frac{r}{L} & \frac{n_p}{J}x_3^* & 0 \\ -\frac{n_p}{J}x_3^* & -\frac{r}{L} & -\frac{n_p\Phi}{J} \\ 0 & \frac{n_p\Phi}{L} & 0 \end{bmatrix}.$$

Some simple calculations show that the characteristic polynomial is of the form $s^3 + c_1 s^2 + c_2 s + c_3$, with the coefficients $c_i > 0$ and verifying $c_1 c_2 > c_3$ that, a simple Routh–Hurwitz test proves is the necessary and sufficient condition for stability. □

15.8.2 Estimation Error for $\rho_{\alpha\beta}$

Lemma 15.8.2 *Consider the mechanical equation of the PMSM model (15.4) together with the flux observer (15.23). The fourth and fifth components, χ_{45}, of the error vector χ—defined in equation (15.9)—satisfy the following differential equation:*

$$\dot{\chi}_{45} = A_{22}\chi_{45} + \Gamma_{45}(\chi), \tag{15.44}$$

with

$$A_{22} = \begin{bmatrix} -2\gamma\Phi^2 & \frac{n_p}{J}x_3^* \\ -\frac{n_p}{J}x_3^* & 0 \end{bmatrix}, \tag{15.45}$$

and $\Gamma_{45}(\chi)$ is such that $\nabla\Gamma_{45}(0) = 0$. Moreover, the matrix A_{22} is Hurwitz for all $x_3^* \neq 0$.

Proof: Computing the time derivative of $\chi_{45} = e^{-\mathcal{J}\theta}\tilde{\rho}_{\alpha\beta}$ yields

$$\dot{\chi}_{45} = -\frac{n_p}{J}x_3\mathcal{J}\chi_{45} + e^{-\mathcal{J}\theta}\dot{\tilde{\rho}}_{\alpha\beta}.$$

Now, from equation (15.27), and using the facts that $|\tilde{\rho}_{\alpha\beta}| = |\chi_{45}|$ and that $e^{-\mathcal{J}\theta}\rho_{\alpha\beta} = e_1$, it is possible to write

$$\dot{\tilde{\rho}}_{\alpha\beta} = -\gamma\Phi^2\left(|\chi_{45}|^2 + 2\chi_{45}^\top e_1\right)e^{\mathcal{J}\theta}\left(\chi_{45} + e_1\right).$$

Replacing the latter in the expression above yields

$$\dot{\chi}_{45} = -\left[\frac{n_p}{J}(x_3^* + \chi_3)\mathcal{J} + \gamma\Phi^2\left(|\chi_{45}|^2 + 2\chi_4\right)\right]\chi_{45} - \gamma\Phi^2\left(|\chi_{45}|^2 + 2\chi_4\right)e_1,$$

which concludes the first part of the proof.

The proof that, for all $x_3^* \neq 0$, A_{22} is Hurwitz follows trivially computing the characteristic polynomial. □

15.8.3 Speed and Load Torque Estimation Errors

Lemma 15.8.3 *Consider the mechanical equations of the PMSM model equation (15.3) and (15.4), together with the flux observer (15.23). The sixth and seventh components, χ_{67}, of the error vector χ—defined in (15.9)—satisfy the following differential equation:*

$$\dot{\chi}_{67} = A_{32}\chi_{45} + A_{33}\chi_{67} + \Gamma_{67}(\chi), \tag{15.46}$$

where

$$A_{32} = \begin{bmatrix} -\frac{n_p}{J}\left(a_1 x_3^* - \frac{\Phi x_2^*}{L}\right) & 0 \\ \frac{n_p}{J} a_2 x_3^* & 0 \end{bmatrix},$$

A_{33} is the Hurwitz matrix defined in (15.31), and $\Gamma_{67}(\chi)$ is such that $\nabla\Gamma_{67}(0) = 0$.

Proof: As indicated in Remark 15.7.3, the dynamics of χ_{67} is given by equation (15.39). For the last right-hand term we have the identity

$$i_{\alpha\beta}^\top \mathcal{J}\tilde{\rho}_{\alpha\beta} = \frac{1}{L}\chi_{12}^\top \mathcal{J}\chi_{45} + \frac{1}{L}(x_{12}^*)^\top \mathcal{J}\chi_{45}, \tag{15.47}$$

where x_{12}, defined in (15.11), is the stator current in the dq reference frame. On the other hand, after some lengthy but straightforward computations, the second right-hand term of equation (15.39) can be written as

$$\frac{n_p\omega}{|\hat{\rho}_{\alpha\beta}|^2}\hat{\rho}_{\alpha\beta}^\top\tilde{\rho}_{\alpha\beta} = \frac{n_p}{J}\left(x_3^* + \chi_3\right)\chi_4 + \Omega(|\chi|^2), \tag{15.48}$$

where $\Omega(|\chi|^2)$ contains term of order higher or equal to $|\chi|^2$. Thus, the proof follows immediately by considering that $x_1^* = 0$ and replacing equations (15.47) and (15.48) in equation (15.39). □

15.8.4 Proof of Proposition 15.3.1

Combining the results of Lemmata 15.8.1, 15.8.2, and 15.8.3 we obtain that the error vector χ satisfies a differential equation of the form (15.40) where

$$A = \begin{bmatrix} A_{11} & A_{12} & A_{13} \\ 0 & A_{22} & 0 \\ 0 & A_{32} & A_{33} \end{bmatrix}, \qquad \Gamma(\chi) = \begin{bmatrix} \Gamma_{13}(\chi) \\ \Gamma_{45}(\chi) \\ \Gamma_{67}(\chi) \end{bmatrix}.$$

Recalling that $\nabla\Gamma(0) = 0$, it only remains to prove that A is Hurwitz. For, we notice that A is similar to a block triangular Hurwitz matrix. More precisely, with

$$T = \begin{bmatrix} I_3 & 0 & 0 \\ 0 & 0 & I_2 \\ 0 & I_2 & 0 \end{bmatrix},$$

we get

$$TAT^{-1} = \begin{bmatrix} A_{11} & A_{12} & A_{13} \\ 0 & A_{33} & A_{32} \\ 0 & 0 & A_{22} \end{bmatrix},$$

which is Hurwitz due to the fact that A_{11}, A_{22}, and A_{33} are Hurwitz matrices, completing the proof.

15.9 Simulation and Experimental Results

The usefulness of the proposed control scheme was evaluated through numerical simulations and experiments. For the simulations, the considered motor parameters were $L = 0.0038$ H, $R = 0.225\ \Omega$, $\Phi = 0.17$ Wb, $n_p = 3$, and $J = 0.012$ kgm^2, which correspond to an experimental setup located in the *Laboratoire de Genie Electrique de Paris*, where the experiments were carried out.

15.9.1 Simulation Results

Three types of simulations were developed, the first was devoted to illustrate the performance under nominal (ideal) conditions, where the motor parameters are known, while the second was intended to exhibit the operation under several cases of parametric uncertainty. Finally, we carried out a third set of simulations to compare the performance of the proposed scheme with one proposed in the drives community, namely the one reported in Nam (2010). The signal profiles and the parameter variations were taken from the benchmark proposed by the French Working Group *Commande des Entraînements Electriques*[7].

In order to evaluate the scheme under stringent conditions, the motor was at standstill at the beginning of the simulations. Hence, the initial conditions for both currents and speed, as well as, the initial values for the estimated speed and load torque were set to zero. To avoid singularities, the initial conditions of the position observer were set as $\hat{\rho}_\alpha(0) = \Phi$ and $\hat{\rho}_\beta(0) = 0$. On the other hand, from $t = 1$ s to $t = 2.5$ s and from $t = 5$ s to the end of the experiment, a 1 Nm load torque was applied.

The tuning parameters of the control scheme were chosen as $\gamma = 5000$, for the $\rho_{\alpha\beta}$ observer, and $a_1 = 20$, $a_2 = 6$, for the speed-load torque observer. In both cases, the selection was taken to obtain a better response of the closed–loop system under parametric uncertainty operation. The high value assigned to the gain γ is due to the high sensitivity exhibited by the position observer with respect to the stator resistance R.

In Figure 15.1, the behavior of the motor speed and the load torque are included under nominal operation. At the top of this figure, both the actual and the desired speeds are shown. Here it can be noticed that, as predicted by the theory, when the desired speed is constant, the achieved performance is remarkable. Moreover, when the speed reference is time varying

[7]The complete evaluation procedure can be consulted in `http://www2.irccyn.ec-nantes.fr/CE2/` (accessed December 10, 2012).

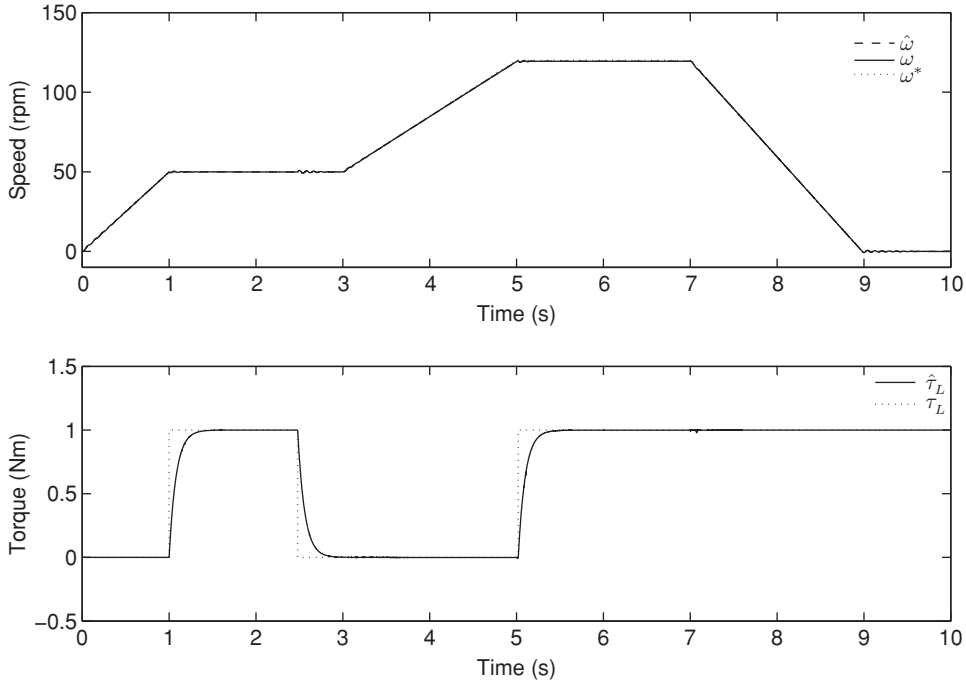

Figure 15.1 Reference and actual speed (top) and load torque and its estimate (bottom) in nominal operation

the speed error still remains within reasonable values. At the bottom of the same figure the actual load torque and its estimate are presented. In Figure 15.2, the corresponding observation errors for the position and the speed-load toque observers are presented. In both cases their magnitudes are negligible, even in the presence of changes in the load torque perturbation and under time-varying speed references. This picture is complemented with the tracking speed error. In Figure 15.3, the stator currents and voltages are presented.

To illustrate the controller robustness against parametric uncertainty, in Figure 15.4, the observer and speed tracking errors corresponding to a 50% positive variation of the stator resistance value are depicted, while the behavior of the same variables for a 50% increase of the stator inductance and a 15% positive change of the field flux are included in Figure 15.5 and Figure 15.6, respectively. It is important to mention that these parameter variations correspond to the maximum uncertainty that the controller can manage without going to instability.

In Nam (2010) (also see Lee *et al.* 2010), the observer of Ortega *et al.* (2011) is used together with a phase-locked-loop-like speed and load torque observer to implement an output-feedback version of the classical field-oriented controller Krause (1986). To compare the performance of our new speed and load torque observer and the proposed IDA-PBC, we show in Figure 15.7 the response of both schemes to the previous benchmark references. It is clear from the figure that our scheme outperforms the one in Nam (2010), both in speed regulation as well as load torque estimation.

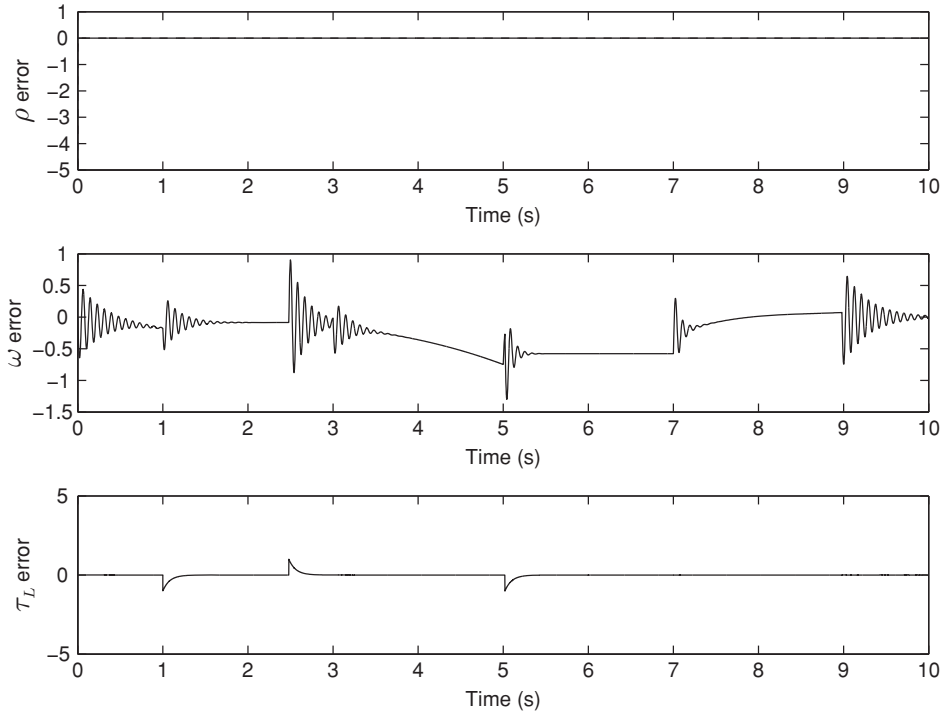

Figure 15.2 Observer and speed tracking errors in nominal operation

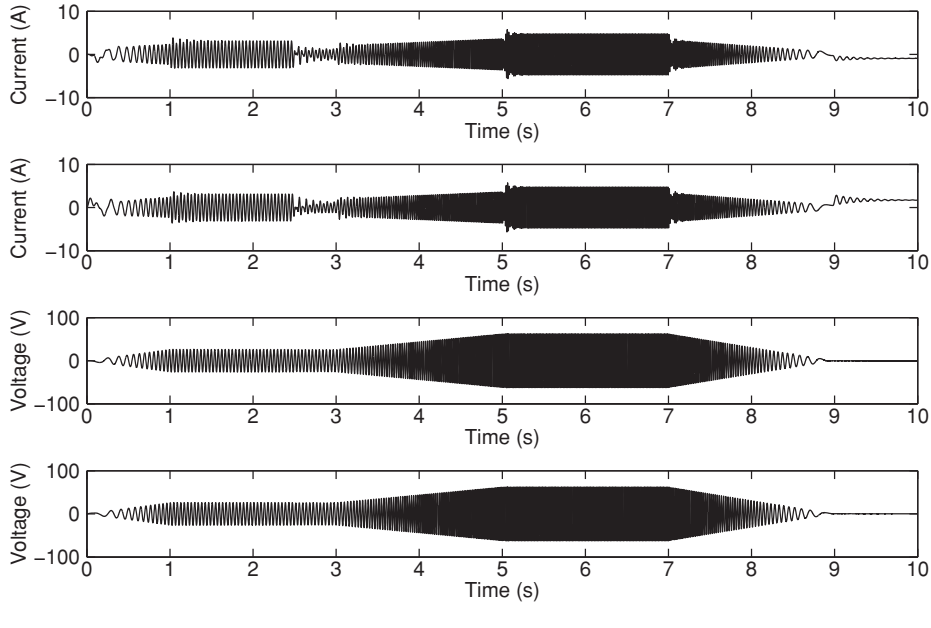

Figure 15.3 Stator currents and voltages in nominal operation

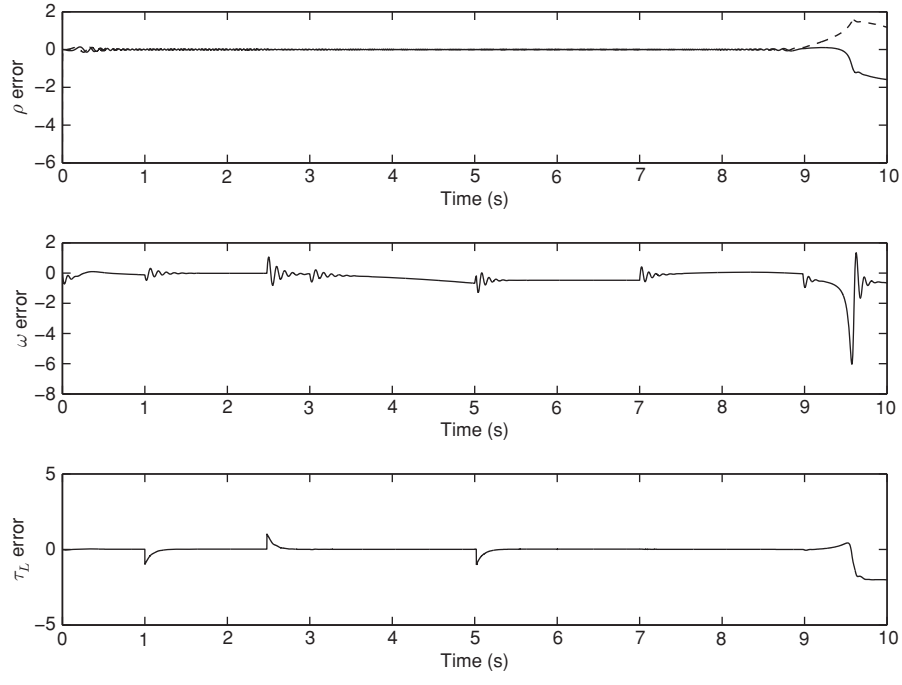

Figure 15.4 Observer and speed tracking errors with a 50% error of the stator resistance

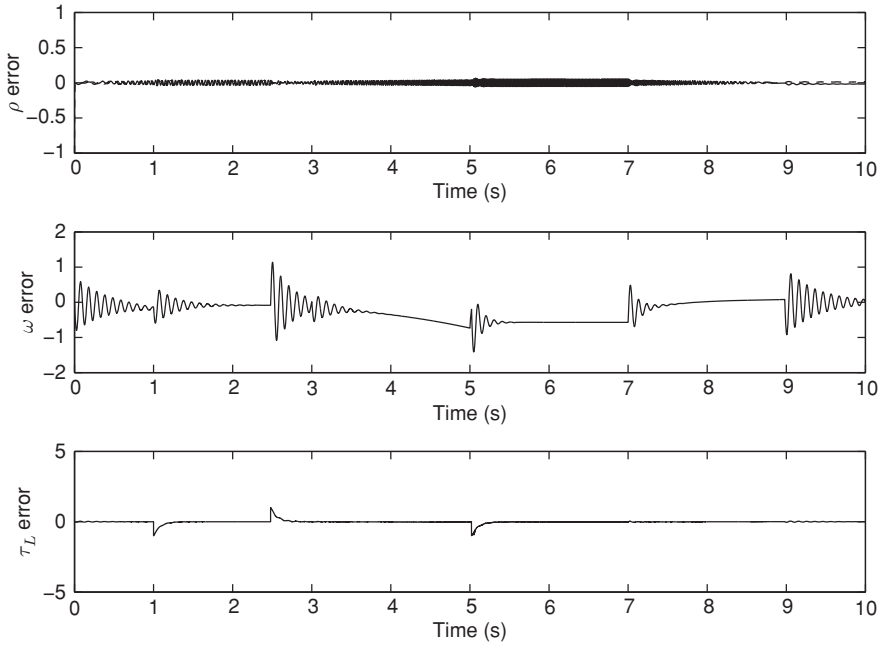

Figure 15.5 Observer and speed tracking errors with a 50% increase of the stator inductance

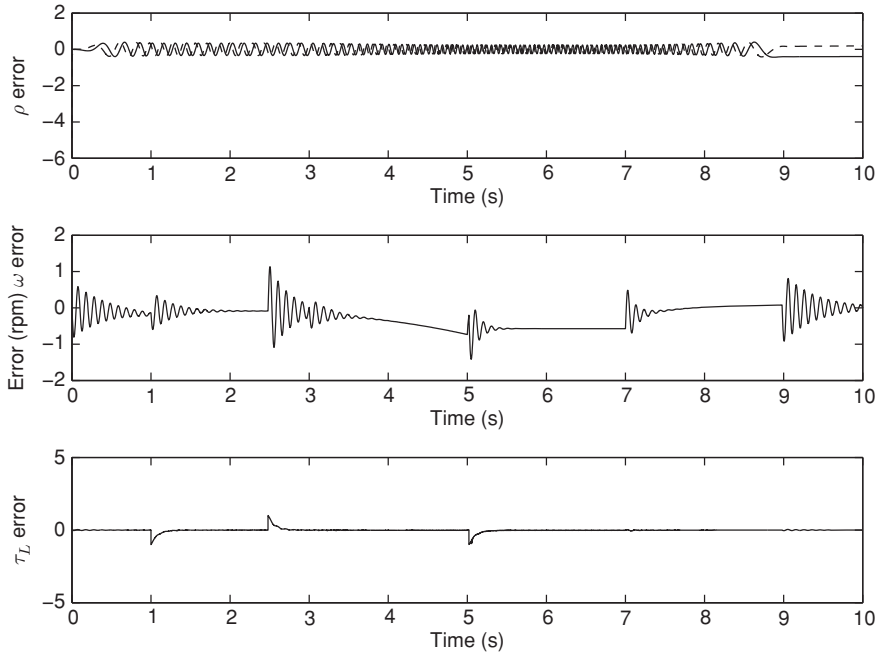

Figure 15.6 Observer and speed tracking errors with a 15% positive increase of the field flux

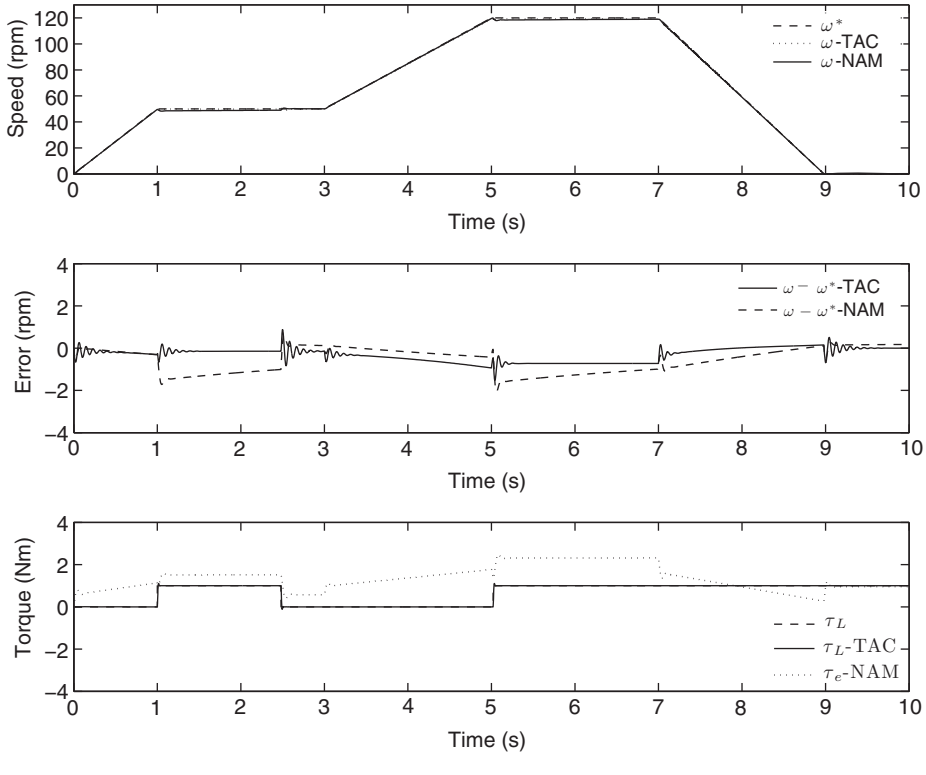

Figure 15.7 Comparative behavior of the proposed scheme (denoted TAC) with the one reported in Nam (2010) (denoted NAM)

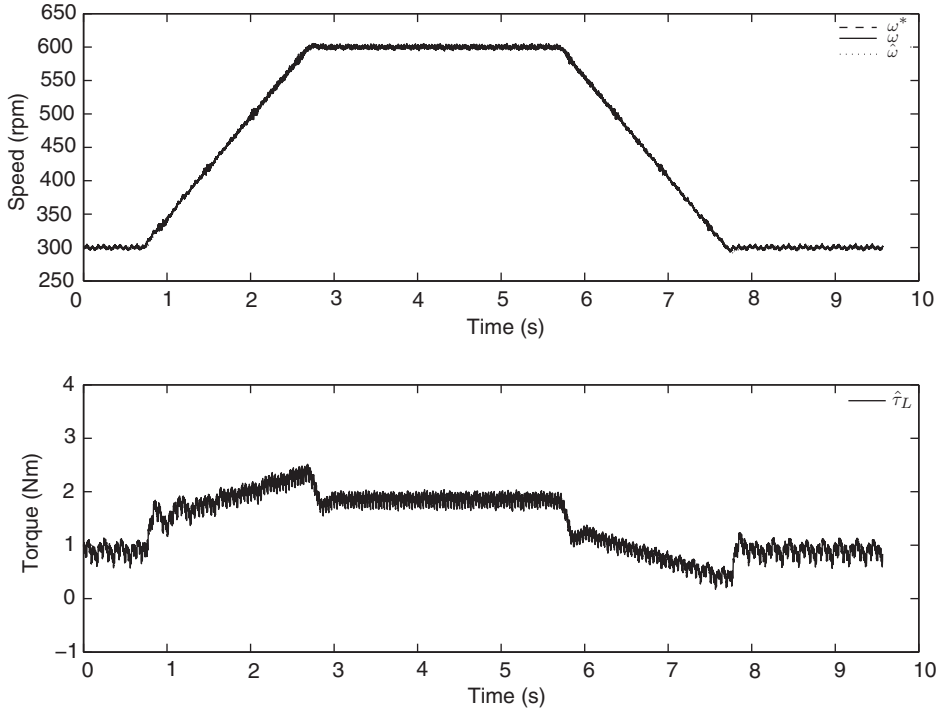

Figure 15.8 Reference, measured, and actual speeds (top) and observed load torque (bottom) in the experimental rig

15.9.2 Experimental Results

Experiments were carried out to test the performance of the proposed controller. Unfortunately, at the moment of writing this paper the evaluation of the *full-information* IDA-PBC and the observers was carried out in a separated way, that is, it was not possible to present the output-feedback operation. The behavior of the several components is depicted in Figure 15.8 for a positive speed reference, while in Figures 15.9 and 15.10, the operation for a speed reference that crosses through zero is shown.

15.10 Future Research

From a theoretical viewpoint the need to include the operator $\mathcal{A}\left(\frac{\hat{\rho}_\beta}{\hat{\rho}_\alpha}\right)$ to avoid the presence of spikes may seem unsatisfactory. However, in practice this kind of modifications are systematically applied and widely accepted. Given the theoretical complexity of the problem, we tend to believe that the problem does not admit a "smooth" solution. The result is presented without a detailed analysis of the effect of this operator—that is currently under investigation.

Another research line that we are currently pursuing is the establishment of a nonconservative estimate of the region of attraction of the equilibrium point. It has been observed in

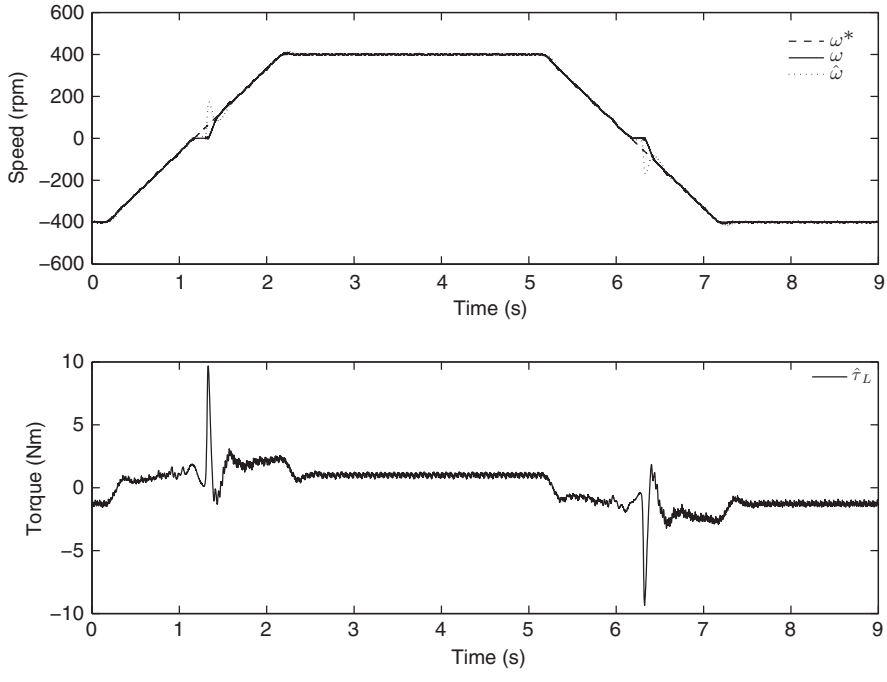

Figure 15.9 Measured and observed speed (top) and estimated load torque (bottom) in the experimental rig

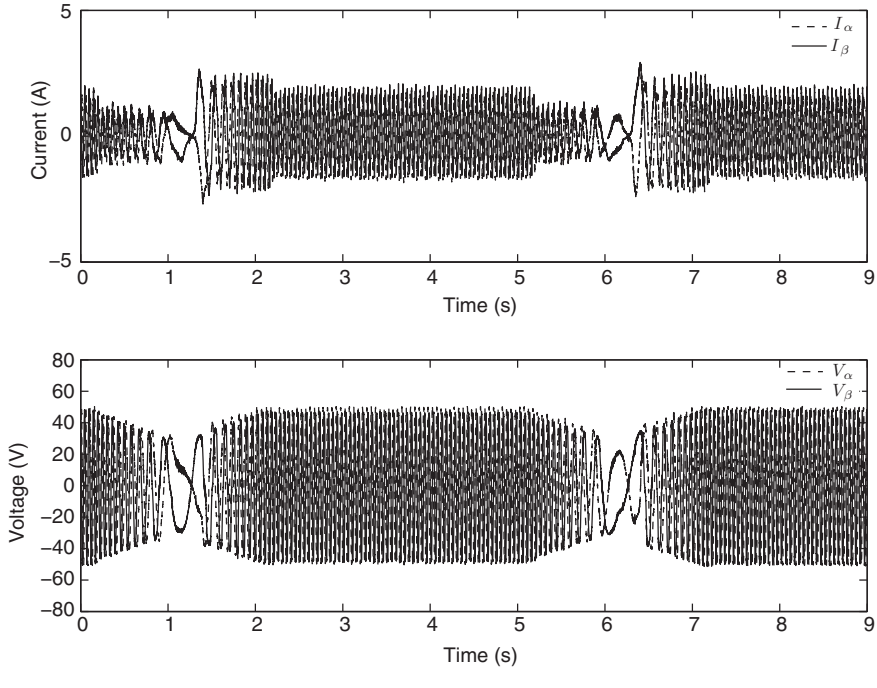

Figure 15.10 Current (top) and voltage (bottom) in the experimental rig

simulations that the estimates that are obtained with the standard Lyapunov tools are extremely conservative and provide little insight on the choice of the free parameters γ, a_1, and a_2. This research is, obviously, related with the analysis of the full-fledged nonlinear dynamics, that seems a formidable task.

Simulations have shown that performance is sensitive to parameter uncertainty, particularly in the field flux. To enhance robustness it would be interesting to incorporate an adaptation algorithm, but this task is far from trivial given the nonlinearly parameterized nature of the problem. Robustness can also be enhanced trying alternative solutions for the PDEs that appear in the IDA-PBC and the I&I design methodologies.

Some preliminary experimental results, which have confirmed the remarkable properties of the observers, have been reported here. Current research is under way to experimentally try the output-feedback controller proposed in the paper.

Part of the work of Gerardo Espinosa–Pérez was developed during a sabbatical leave at LSS–SUPELEC supported by SUPELEC Foundation. Currently, his work is supported by DGAPA–UNAM (IN111211). The work of Dhruv Shah was supported by the Indo-French project No. 3602-1, under the aegis of IFCPAR. The authors want to thank Alain Glumineau and Robert Boisliveau (IRCCyN, France) for the computational code to generate the operator $\mathcal{A}$.

15.A Appendix

In computer programming languages the single argument arctan(u) function is computed in such a way that its output value e is wrapped in the set $(-\pi, \pi]$. This situation results in the existence of discontinuities since each time the output of the function e takes a value higher (lower) than π (resp.,$-\pi$) then it is assigned the value $-\pi$ (resp.,π). With the aim of avoiding these discontinuities it is usual practice to modify the arctan (u) function by including at its output an additional block whose input is e, the output of the arctan function, and its output is given by

$$y = e + 2n\pi,$$

where n is a counter, initialized at zero, that is increased by 1 each time the $e > \pi$ or decreased by 1 if $e < -\pi$. From a mathematical perspective, the result is an operator, denoted as $\mathcal{A}(u)$, that has as input the argument of the arctan function and as output a continuous variable that corresponds to the unwrapped version of the original output of the arctan function.

It is clear that $\mathcal{A}(u)$ can be easily implemented in any programming language, like *C* or *Matlab*. The code for doing this considers two consecutive values of e at two consecutive sampling times, kT and $(k+1)T$, and compute its difference $dif = e[kT] - e[(k+1)T]$ in order to know if there has been a jump from π to $-\pi$ or viceversa. According to this, three different possibilities can appear:

1. if $dif < -2\pi$ then $n = n + 1$;
2. if $dif > 2\pi$ then $n = n - 1$;
3. otherwise the value of n is not changed.

The computational loop is closed by updating the value of y and assigning $k = k + 1$.

References

Akrad A, Hilairet M, Ortega R, and Diallo D (2007) Interconnection and damping assignment approach for reliable pm synchronous motor control. *Colloquium On Reliability in Electromagnetic Systems*, Paris, France.

Astolfi A, Karagiannis D, and Ortega R (2007) *Nonlinear and Adaptive Control with Applications*. Communications and Control Engineering. Springer-Verlag, Berlin.

Chiasson J (2005) *Modeling and High Performance Control of Electric Machines.* John Wiley & Sons.

Dawson D, Hu J, and Burg T (1998) *Nonlinear Control of Electric Machinery*, Marcel Dekker.

Ezzat M, de Leon J, Gonzalez N, and Glumineau A (2010a) Observer–controller scheme using high order sliding mode techniques for sensorless speed control of permanent magnet synchronous motor. *49th IEEE Conference on Decision and Control*, Atlanta, GA.

Ezzat M, Glumineau A, and Plestan F (2010b) Sensorless speed control of a permanent magnet synchronous motor: high order sliding mode controller and sliding mode control observer. *8th IFAC Symposium on Nonlinear Control Systems*, Bologne, Italy.

Fabio G, Miceli R, Rando C, and Ricco–Galluzzo G (2010) Back EMF sensorless-control algorithm for high-dynamic performance PMSM. *IEEE Transactions on Industrial Electronics*, **57–6**, 2092–2100.

Ichikawa S, Tomita M, Doki S, and Okuma S (2006) Sensorless control of PMSM using on-line parameter identification based on system's identification theory. *IEEE Trans Industrial Electronics*, **53–2**, 363–373.

Khorrami F, Krishnamurthy P, and Melkote H (2003) *Modeling and Adaptive Nonlinear Control of Electric Motors*. Springer, Heidelberg.

Krause PC (1986) *Analysis of Electric Machinery*. McGraw Hill, New York.

Lee J, Hong J, Nam K (2010) Sensorless control of surface-mount permanent magnet synchronous motors based on a nonlinear observer. *IEEE Transactions on Power Electronics*, **25–2**, 290–297.

Marino R, Tomei P, and Verrelli CM (2008) Adaptive field-oriented control of synchronous motors with damping windings. *European Journal of Control*, **14–3**, 177–196.

Matsui N (1996) Sensorless PM brushless DC motor drives. *IEEE Trans Industrial Electronics*, **43–2**, 300–308.

Nahid Mobarakeh B, Meibody–Tabar F, and Sargos F (2001) Robustness study of a model–based technique for mechanical sensorless control of PMSM. *Power Electronics Specialist Conference (PESC'2001)*, Vancouver, Canada.

Nam K (2010) *AC Motor Control and Electric Vehicle Applications*. CRC Press.

Ortega R, van der Schaft AJ, Maschke BM, and Escobar G (2002) Interconnection and damping assignment passivity-based control of port-controlled Hamiltonian systems. *Automatica*, **38–4**, 585–596.

Ortega R and Garcia-Canseco E (2004) Interconnection and damping assignment passivity-based control: a survey. *European Journal of Control*, **10**, 432–450.

Ortega R, Loria A, Nicklasson PJ, and Sira-Ramírez H (1998) *Passivity–based Control of Euler–Lagrange Systems*. Springer-Verlag, Berlin.

Ortega R, Praly L, Astolfi A, *et al.* (2011) Estimation of rotor position and speed of permanent magnet synchronous motors with guaranteed stability. *IEEE Transaction on Control Systems Technology*, **19–2**, 284–296.

Petrovic V, Ortega R, and Stankovic A (2001) Interconnection and damping assignment approach to control of PM synchronous motor. *IEEE Transaction of Control System Technology*, **9–6**, 811–820.

Rajashekara K, Kawamura A, and Matsuse K (1996) *Sensorless Control of AC Motor Drives*. IEEE Press.

Shah D, Ortega R, and Astolfi A (2009) Speed and load torque observer for rotating machines. *48th IEEE Conference on Decision and Control*, Shangai, China.

Tomei P, and Verrelli CM (2008) A nonlinear adaptive speed tracking control for sensorless permanent magnet step motors with unknown load torque. *International Journal of Adaptive Control and Signal Processing*, **22–3**, 266–288.

van der Schaft AJ (2000) *$\mathcal{L}_2$-Gain and Passivity Techniques in Nonlinear Control*. Springer-Verlag, Berlin.

Zaltni D, Naceur M, Ghanes M, and Barbot JP (2008) Observability analysis of PMSM. *2009 International Conference on Signals, Circuits and Systems*, Jerba, Tunisia.

16

Adaptive Output-Feedback Control of Permanent-Magnet Synchronous Motors

Patrizio Tomei and Cristiano Maria Verrelli
Dipartimento di Ingegneria Elettronica, Universitá di Roma "Tor Vergata," Italy

16.1 Introduction

Two major classes of permanent-magnet AC machines exist: (1) the trapezoidally excited machines (typically known as brushless DC motors), which are specifically designed to develop nearly constant output torque when they are excited with six-step switched current trapezoidal waveforms; (2) the sinusoidally excited machines in which the windings are typically distributed over multiple slots in order to approximate a sinusoidal distribution. While trapezoidally excited machine drives are distinguished by their control simplicity and minimal sensor requirements, sinusoidally excited machines drives offer opportunities for extended high-speed operating ranges and extremely smooth torque production. Due to their excellent serviceability and durability, high efficiency and power density, as well as high torque to inertia ratio and absence of external rotor excitation and rotor windings, the (sinusoidally excited) permanent-magnet motors are used in practical applications such as printers, tape drives, hard drives in PCs, process control systems, home appliances, and have been gradually replacing DC motors in a wide range of drive applications such as machine tools and industrial robots. The high complexity in the control of these motors is the price to pay for the above advantages.

When the motor mechanical variables (rotor position or speed) are available from measurements, high closed-loop performances can be achieved in rotor position or speed tracking applications for permanent-magnet synchronous motors (PMSMs) even in the presence of uncertain model parameters (see, for instance, Zribi and Chiasson 1991; Bodson *et al.* 1993;

AC Electric Motors Control: Advanced Design Techniques and Applications, First Edition. Edited by Fouad Giri.

Marino *et al.* 1995, 2012; Dawson *et al.* 1998; Di Gennaro 2000; Khorrami *et al.* 2003; Chiasson 2005; Bifaretti *et al.* 2011a, 2011b; Verrelli 2011a, 2011b; Verrelli 2012). The speed or the position tracking control of PMSMs requires the knowledge of rotor shaft position and speed signals in order to control the stator current vector suitably and then achieve high performance (Zribi and Chiasson 1991; Marino *et al.* 1995). When all machine parameters (in addition to load torque) are exactly known, the classical control is a nonlinear state-feedback algorithm which is designed after performing the direct-quadrature dq coordinate transformation for the two-phases currents and voltages: it may be viewed as a feedback linearizing control law (Zribi and Chiasson 1991); experimental results reported in Bodson *et al.* (1993) show that this control achieves good tracking performances even in the presence of current sensor noise and not very accurate position measurements. A full state-feedback nonlinear adaptive control is presented in Marino *et al.* (1995), which guarantees global asymptotic tracking of a desired angle reference signal when all motor parameters are unknown. The extension to the case in which the rotor speed measurement is not required can be found in Di Gennaro (2000).

Since shaft sensors induce several drawbacks such as high drive cost, large machine size, low reliability and noise immunity, as well as performance degradation owing to vibration or humidity[1], the attention of the electric drives community has been recently paid to the "sensorless" control problem of (nonsalient pole surface) PMSMs in which only stator current and voltage measurements are available for feedback. Even though relevant contributions concerning this problem have been presented and experimentally validated in the literature (see De Angelo *et al.* 2006; Nahid-Mobarakeh *et al.* 2007; Rashed *et al.* 2007; Chan *et al.* 2008; Bisheimer *et al.* 2010; Hinkkanen *et al.* 2012), a rigorous solution to such a problem (i.e., a solution guaranteed by a closed loop stability proof) turned to be rather difficult to be derived since: motor dynamics are nonlinear and multivariable; measured outputs (stator currents) do not coincide with one of the controlled outputs (rotor speed) that are required to track smooth bounded reference signals; and the load torque depends on applications and is typically an uncertain model parameter.

This chapter collects the most recent results (with stability proof) by the authors who appeared in Tomei and Verrelli (2008, 2011), and Bifaretti *et al.* (2012). The preliminary result in Tomei and Verrelli (2008) is first revisited with the well-known "*s-alignment*" and "*c-alignment*" procedures being theoretically analyzed in detail. The control algorithm in Tomei and Verrelli (2011) is then reported. It is based on stator current and voltage measurements only and incorporates two closed-loop observers: (1) the second order observer analyzed in Ortega *et al.* (2011) and experimentally validated in Lee *et al.* (2010), which constitutes an improvement of the open-loop estimators used in Tomei and Verrelli (2008) for the sine and cosine functions of the rotor position; (2) the closed-loop fourth order adaptive observer designed in Tomei and Verrelli (2008) for the rotor speed and the load torque. The overall closed-loop stability analysis shows that local exponential speed tracking is guaranteed under a persistency of excitation condition that only restricts the family of speed reference signals

[1]For instance, the installation of position (and speed) sensors in applications involving vacuum pumps is troublesome due to the difficulties of extending the motor shaft out of the motor housing, while in some crane and elevator applications the large distance between the motor and the inverter causes high sensor signal attenuation and noise interference. On the other hand, even when the motor is equipped with a motion sensor, sensorless controls are beneficial in the case of sensor failures to increase reliability.

and admits a clear physical interpretation in terms of motor observability. Simulation and experimental results (see Bifaretti *et al.* (2012) illustrate how the reported theoretical analysis provides actually effective tools for identifying conditions in which satisfactory performances can be obtained in practice.

16.2 Dynamic Model and Problem Statement

Assuming linear magnetic materials, nonlinear flux density distribution due to the air-gap geometry only, and negligible magnetic hysteresis and Foucault currents, the dynamics of a PMSM with no saliency and a sinusoidal flux density distribution in a fixed reference frame attached to the stator are given by the well-known fourth order model[2] (see, for instance, Marino *et al.* (1995); Dawson *et al.* (1998); Khorrami *et al.* (2003), Chiasson (2005) for its derivation and modeling assumptions):

$$\begin{aligned}
\dot{\theta}_r &= \omega_m, \\
\dot{\omega}_m &= -\frac{F}{J}\omega_m + \frac{K_{\mathrm{M}}}{J}\Big[-i_{sa}\sin(p\theta_r) + i_{sb}\cos(p\theta_r)\Big] - \frac{T_L}{J}, \\
\frac{\mathrm{d}i_{sa}}{\mathrm{d}t} &= -\frac{R_s}{L_s}i_{sa} + \frac{K_{\mathrm{M}}}{L_s}\omega_m\sin(p\theta_r) + \frac{v_{sa}}{L_s}, \\
\frac{\mathrm{d}i_{sb}}{\mathrm{d}t} &= -\frac{R_s}{L_s}i_{sb} - \frac{K_{\mathrm{M}}}{L_s}\omega_m\cos(p\theta_r) + \frac{v_{sb}}{L_s},
\end{aligned} \tag{16.1}$$

in which θ_r is the rotor angle, ω_m is the rotor speed, i_{sa} and i_{sb} are the stator currents $\theta_r, \omega_m, i_{sa}$ and i_{sb} constitute the state variables, v_{sa} and v_{sb} are the stator voltages (which constitute the control inputs); the output to be controlled is the rotor speed ω_m. The control problem is called "sensorless" when only stator currents and voltages are measured. The load torque T_L, which depends on applications, is assumed to be an unknown constant model parameter. The (known) motor parameters are viscous friction coefficient F, number of pole pairs p, rotor moment of inertia J, stator windings resistance R_s and inductance L_s, and motor torque constant K_{M}. While J, R_s, L_s, and K_{M} are positive parameters, F is assumed to be nonnegative, so that the main stability result of this paper is not based on the positiveness of F, which gives some advantage for the design in the speed-sensorless scenario. If we introduce, as in Park (1929); Zribi and Chiasson (1991); Tomei and Verrelli (2008), the Park's transformation, that is, the transformation of the vectors $v = [v_{sa}, v_{sb}]^T$ and $i = [i_{sa}, i_{sb}]^T$ expressed in the fixed stator frame (a, b), into vectors expressed in a frame (d, q), which rotates along the fictitious excitation vector i_f directed as the d axis:

$$\begin{bmatrix} w_d \\ w_q \end{bmatrix} = \begin{bmatrix} \cos(p\theta_r) & \sin(p\theta_r) \\ -\sin(p\theta_r) & \cos(p\theta_r) \end{bmatrix} \begin{bmatrix} w_a \\ w_b \end{bmatrix} \doteq \mathcal{R}(\theta_r) \begin{bmatrix} w_a \\ w_b \end{bmatrix},$$

[2] Model (16.1) also describes the dynamics of a permanent-magnet step motor under the above assumptions, provided that the number of rotor teeth N_r replaces the number of pole pairs p.

then the dynamics (16.1) expressed in terms of currents and voltages in rotating dq coordinates, become

$$\begin{aligned}
\dot{\theta}_r &= \omega_m, \\
\dot{\omega}_m &= -\frac{F}{J}\omega_m + \frac{K_{\mathrm{M}}}{J} i_{sq} - \frac{T_L}{J}, \\
\frac{\mathrm{d}i_{sd}}{\mathrm{d}t} &= -\frac{R_s}{L_s} i_{sd} + p\omega_m i_{sq} + \frac{v_{sd}}{L_s}, \\
\frac{\mathrm{d}i_{sq}}{\mathrm{d}t} &= -\frac{R_s}{L_s} i_{sq} - p\omega_m i_{sd} - \frac{K_{\mathrm{M}}}{L_s}\omega_m + \frac{v_{sq}}{L_s}.
\end{aligned} \tag{16.2}$$

Model (16.2) is suitable for control design since the rotor speed dynamics are influenced by the stator current vector q-component i_{sq} only: adaptive backstepping techniques may be successfully applied provided that $\cos(p\theta_r)$, $\sin(p\theta_r)$ are available for feedback along with the rotor speed ω_m. In particular, the (previously introduced) sensorless control problem, whose main technical difficulty is constituted by the lack of position and speed measurements, can be solved by resorting to a suitable closed-loop observer-based controller.

In the following, we denote by $\omega_m^*(t)$ the known smooth bounded reference signal with known bounded time derivatives $\dot{\omega}_m^*(t)$ and $\ddot{\omega}_m^*(t)$ for the rotor speed $\omega_m(t)$, and by $i_{sd}^*(t)$ the known smooth bounded reference signal with known bounded time derivative $\frac{\mathrm{d}i_{sd}^*(t)}{\mathrm{d}t}$ for the current $i_{sd}(t)$, which may be simply chosen as $i_{sd}^* = 0$ (see Marino *et al.* (2008) for the field orientation) or may be related to the reference speed $\omega_m^*(t)$ to comply with voltage saturation at high speeds (see Chiasson (2005) for the field weakening).

Remark 16.2.1 *There are cases, as in the* master–slave *synchronization problems, in which the reference signals foreknowledge is typically not available so that reference signal time derivatives cannot be directly compensated by feed-forward actions. Output tracking can be still obtained by resorting to (state-feedback) learning control algorithms (see Verrelli 2011a, 2012).*

16.3 Nonlinear Adaptive Control

The sixth order nonlinear adaptive output-feedback control of Tomei and Verrelli (2011) is reported here:

$$\begin{aligned}
\begin{bmatrix} v_{sa} \\ v_{sb} \end{bmatrix} &= \begin{bmatrix} \psi_{\theta c} & -\psi_{\theta s} \\ \psi_{\theta s} & \psi_{\theta c} \end{bmatrix} \begin{bmatrix} v_{sd} \\ v_{sq} \end{bmatrix}, \\
v_{sd} &= L_s\Big[-\phi_d - k_i(i_{sd} - i_{sd}^*)\Big], \\
v_{sq} &= L_s\Big[-\phi_q - k_i(i_{sq} - i_{sq}^*)\Big], \\
\begin{bmatrix} i_{sd} \\ i_{sq} \end{bmatrix} &= \begin{bmatrix} \psi_{\theta c} & \psi_{\theta s} \\ -\psi_{\theta s} & \psi_{\theta c} \end{bmatrix} \begin{bmatrix} i_{sa} \\ i_{sb} \end{bmatrix},
\end{aligned}$$

$$
\begin{aligned}
\phi_d &= -\frac{R_s}{L_s} i_{sd}^* + p\hat{\omega}_m i_{sq} - \frac{\mathrm{d}i_{sd}^*}{\mathrm{d}t},\\
\phi_q &= -\frac{R_s}{L_s} i_{sq}^* - p\hat{\omega}_m i_{sd} - \frac{K_\mathrm{M}}{L_s}\hat{\omega}_m - \frac{J}{K_\mathrm{M}}\left[\frac{F}{J}\dot{\omega}_m^* \right.\\
&\quad \left. -k_\omega \frac{\mathrm{d}\mathrm{sat}_\kappa(\hat{\omega}_m - \omega_m^*)}{\mathrm{d}\,(\hat{\omega}_m - \omega_m^*)}(\dot{\hat{\omega}}_m - \dot{\omega}_m^*) + \frac{\dot{\hat{T}}_L}{J} + \ddot{\omega}_m^*\right],\\
i_{sq}^* &= \frac{J}{K_\mathrm{M}}\left[\frac{F}{J}\omega_m^* - k_\omega \mathrm{sat}_\kappa(\hat{\omega}_m - \omega_m^*) + \frac{\hat{T}_L}{J} + \dot{\omega}_m^*\right],\\
\dot{\hat{i}}_{sa} &= -\frac{R_s}{L_s}\hat{i}_{sa} + \frac{K_\mathrm{M}}{L_s}\hat{\omega}_m\psi_{\theta s} + \frac{\nu_{sa}}{L_s} + k_e(i_{sa} - \hat{i}_{sa}) + p\hat{\omega}_m(i_{sb} - \hat{i}_{sb}),\\
\dot{\hat{i}}_{sb} &= -\frac{R_s}{L_s}\hat{i}_{sb} - \frac{K_\mathrm{M}}{L_s}\hat{\omega}_m\psi_{\theta c} + \frac{\nu_{sb}}{L_s} + k_e(i_{sb} - \hat{i}_{sb}) - p\hat{\omega}_m(i_{sa} - \hat{i}_{sa}),\\
\dot{\hat{\omega}}_m &= -\frac{F}{J}\hat{\omega}_m + \frac{K_\mathrm{M}}{J}[-i_{sa}\psi_{\theta s} + i_{sb}\psi_{\theta c}] - \frac{\hat{T}_L}{J}\\
&\quad + \frac{2\gamma^2 + rF\lambda J^2}{\gamma^2\lambda + rF\lambda^2 J^2}\left[\frac{K_\mathrm{M}}{L_s}\psi_{\theta s}(i_{sa} - \hat{i}_{sa}) - \frac{K_\mathrm{M}}{L_s}\psi_{\theta c}(i_{sb} - \hat{i}_{sb})\right],\\
&\doteq -\frac{F}{J}\hat{\omega}_m + \frac{K_\mathrm{M}}{J}\Big[-i_{sa}\psi_{\theta s} + i_{sb}\psi_{\theta c}\Big] - \frac{\hat{T}_L}{J}\\
&\quad + \gamma_\omega\left[\frac{K_\mathrm{M}}{L_s}\psi_{\theta s}(i_{sa} - \hat{i}_{sa}) - \frac{K_\mathrm{M}}{L_s}\psi_{\theta c}(i_{sb} - \hat{i}_{sb})\right],\\
\dot{\hat{T}}_L &= \frac{2\gamma^2 F + \lambda J\gamma + \lambda J^2 r F^2}{\gamma^2\lambda + rF\lambda^2 J^2}\left[-\frac{K_\mathrm{M}}{L_s}\psi_{\theta s}(i_{sa} - \hat{i}_{sa}) + \frac{K_\mathrm{M}}{L_s}\psi_{\theta c}(i_{sb} - \hat{i}_{sb})\right],\\
&\doteq \gamma_T\left[-\frac{K_\mathrm{M}}{L_s}\psi_{\theta s}(i_{sa} - \hat{i}_{sa}) + \frac{K_\mathrm{M}}{L_s}\psi_{\theta c}(i_{sb} - \hat{i}_{sb})\right],
\end{aligned}
\tag{16.3}
$$

$$
\begin{aligned}
\psi_{\theta c} &= \widehat{\cos(p\theta_r)} = \frac{p}{K_\mathrm{M}}\left(\hat{\xi}_a - L_s i_{sa}\right),\\
\dot{\hat{\xi}}_a &= -R_s i_{sa} + \nu_{sa} + \gamma_\theta\left(\hat{\xi}_a - L_s i_{sa}\right)\left[\frac{K_\mathrm{M}^2}{p^2} - \left(\hat{\xi}_a - L_s i_{sa}\right)^2 - \left(\hat{\xi}_b - L_s i_{sb}\right)^2\right],\\
\psi_{\theta s} &= \widehat{\sin(p\theta_r)} = \frac{p}{K_\mathrm{M}}\left(\hat{\xi}_b - L_s i_{sb}\right),\\
\dot{\hat{\xi}}_b &= -R_s i_{sb} + \nu_{sb} + \gamma_\theta\left(\hat{\xi}_b - L_s i_{sb}\right)\left[\frac{K_\mathrm{M}^2}{p^2} - \left(\hat{\xi}_a - L_s i_{sa}\right)^2 - \left(\hat{\xi}_b - L_s i_{sb}\right)^2\right].
\end{aligned}
\tag{16.4}
$$

It consists of: (1) a stator current-control loop (containing feedforward actions and suitable stabilizing terms) asymptotically forcing (i_{sd}, i_{sq}) to (i_{sd}^*, i_{sq}^*), where i_{sq}^*, designed according to the field-oriented control strategy, is responsible for the rotor speed tracking; (2) a sixth order closed-loop observer (which includes the auxiliary variables $\hat{i}_{sa}$, $\hat{i}_{sb}$, $\hat{\xi}_a$, $\hat{\xi}_b$) providing estimates for the unmeasured $\cos(p\theta_r)$, $\sin(p\theta_r)$, ω_m, and the unknown T_L. The overall control algorithm (16.3) and (16.4) depends on:

- the available signals i_{sa}, i_{sb};
- the reference signals ω_m^*, i_{sd}^*;
- the saturation function $\mathrm{sat}_\kappa(x)$ (a C^∞ odd function whose derivative is always positive and has a positive finite limit κ as x goes to $+\infty$);
- the known positive machine parameters J, K_M, p, R_s, L_s, and the known nonnegative machine parameter F;
- the positive control parameters k_i, k_ω, κ, k_e, γ_θ;
- the positive control parameters γ, λ, r satisfying the conditions

$$\begin{aligned}
\gamma &> \frac{\lambda^2 e^{4T_p} L_s^4}{p_e {K_\mathrm{M}}^4 T_p^2} + 8 p_e \frac{{K_\mathrm{M}}^4}{L_s^4}, \\
p_e &< \frac{\frac{R_s}{L_s} + k_e}{12\left(\frac{4{K_\mathrm{M}}^6}{\lambda^2 {L_s}^6} + \frac{{K_\mathrm{M}}^2 (R_s + L_s k_e)^2}{{L_s}^4} + \frac{{K_\mathrm{M}}^2}{{L_s}^2}\right) + \frac{{K_\mathrm{M}}^2}{{L_s}^2}}, \\
r &\geq (J^3 {K_\mathrm{M}}^4 T_p^2 e^{-4T_p} p_e)^{-1} (2\gamma^2 L_s^4),
\end{aligned} \tag{16.5}$$

in terms of a positive scalar $T_p \in \mathbb{R}^+$.

Remark 16.3.1 *As we shall see, the advantage of introducing the variables*

$$\begin{aligned}
\xi_a &= \frac{K_\mathrm{M}}{p}\left[\cos(p\theta_r) + \frac{pL_s}{K_\mathrm{M}} i_{sa}\right], \\
\xi_b &= \frac{K_\mathrm{M}}{p}\left[\sin(p\theta_r) + \frac{pL_s}{K_\mathrm{M}} i_{sb}\right],
\end{aligned}$$

relies on the fact that their dynamics

$$\begin{aligned}
\dot{\xi}_a &= -R_s i_{sa} + v_{sa}, \\
\dot{\xi}_b &= -R_s i_{sb} + v_{sb},
\end{aligned}$$

depend on neither the unmeasured variables (θ_r, ω_m) *nor the unknown load torque* T_L*: thus* ξ_a and ξ_b *are good candidates to be estimated in order to recover* $\cos(p\theta_r)$ and $\sin(p\theta_r)$ *through*

$$\begin{aligned}
\widehat{\cos(p\theta_r)} &= \frac{p}{K_\mathrm{M}}\left(\hat{\xi}_a - L_s i_{sa}\right), \\
\widehat{\sin(p\theta_r)} &= \frac{p}{K_\mathrm{M}}\left(\hat{\xi}_b - L_s i_{sb}\right).
\end{aligned}$$

Remark 16.3.2 *The algorithm (16.3) and (16.4) is constituted by: (1) the second order observer (16.4) analyzed in Ortega et al. (2011) and experimentally validated in Lee et al. (2010), which constitutes an improvement of the open-loop estimators used in Tomei and Verrelli (2008) for the sine and cosine functions of the rotor position; (2) the fourth order observer-based adaptive control (16.3) designed in Tomei and Verrelli (2008) which relies on the estimates of rotor speed and load torque. Note that when $\gamma_\theta = 0$, the controller (16.3) and (16.4), properly initialized, exactly reduces to the one designed in Tomei and Verrelli (2008), which, for the sake of exhaustivity, is revisited in the following section.*

16.4 Preliminary Result (Tomei and Verrelli 2008)

In this section we assume that the motor is initially (at $t = t_0$) aligned (i.e., $\cos(p\theta_r(t_0)) = 1$) so that $\sin(p\theta_r)(t)$ and $\cos(p\theta_r)(t)$ can be obtained by open-loop integration (see equation (16.4)) of known dynamics from known initial conditions. In other terms, the following theorem establishes that the adaptive control (16.3) and (16.4), properly initialized ($\widehat{\cos(p\theta_r)}(t_0) = 1$, $\widehat{\sin(p\theta_r)}(t_0) = 0$) and with $\gamma_\theta = 0$, guarantees asymptotic speed tracking.

Theorem 16.4.1 *Assume that* $\cos(p\theta_r(t_0)) = 1$ *and that* $\widehat{\cos(p\theta_r)}(t_0) = 1$, $\widehat{\sin(p\theta_r)}(t_0) = 0$. *Then, the sixth order nonlinear adaptive output-feedback control algorithm (16.3) and (16.4) with* $\gamma_\theta = 0$ *substituted in model (16.1), guarantees boundedness of* ω_m, i_{sa}, i_{sb}, $\hat{\omega}_m$, $\hat{i}_{sa}$, $\hat{i}_{sb}$, *and* $\hat{T}_L$ *and uniform local asymptotic stability of the closed-loop system equilibrium point* $(\omega_m - \omega_m^*,\ i_{sd} - i_{sd}^*,\ i_{sq} - i_{sq}^*,\ i_{sa} - \hat{i}_{sa},\ i_{sb} - \hat{i}_{sb},\ \hat{\omega}_m - \omega_m,\ T_L - \hat{T}_L) = 0$ *with domain of attraction*

$$\mathcal{B} = \left\{ [\xi_1, \xi_2, ..., \xi_7]^T \in \mathbb{R}^7 : \|[\xi_4, \xi_5, \xi_6, \xi_7]^T\| < C_r \right\},$$

where

$$C_r = \frac{L_s}{2K_{\mathrm{M}}p}\sqrt{\frac{\min\{s_1,\ p_e\}q}{p_e\left(s_2 + 2p_e\left(\frac{K_{\mathrm{M}}}{L_s}\right)^2 \max\left\{1, \left(\frac{K_{\mathrm{M}}}{L_s}\right)^2\right\}\right)}},$$

$$q = \frac{R_s}{L_s} + k_e - p_e\left[12\left(\frac{4{K_{\mathrm{M}}}^6}{\lambda^2 {L_s}^6} + \frac{{K_{\mathrm{M}}}^2(R_s + L_s k_e)^2}{{L_s}^4} + \frac{{K_{\mathrm{M}}}^2}{{L_s}^2}\right) + \frac{{K_{\mathrm{M}}}^2}{{L_s}^2}\right],$$

and $(s_1, s_2) \in \mathbb{R}^+$ *are the minimum and the maximum eigenvalues of the symmetric matrix* $P = [p_{ij}]_{1\le i,j\le 4}$, $p_{11} = p_{22} = \frac{1}{2}$, $p_{33} = \frac{\lambda}{2}$, $p_{44} = (\frac{\gamma^2}{\lambda J^2} + \frac{rF}{2})$, $p_{34} = -\frac{\gamma}{2J}$, $p_{12} = p_{13} = p_{14} = p_{23} = p_{24} = 0$.

Proof: Assume that $\cos(p\theta_r(t_0)) = 1$. Then, according to the stator currents dynamics in (16.1),

$$\cos[p\theta_r(t)] = \psi_{\theta c}(t),$$

$$\sin[p\theta_r(t)] = \psi_{\theta s}(t).$$

Introducing the tracking and the estimation errors

$$\begin{aligned}
&\tilde{\omega}_m(t) = \omega_m(t) - \omega_m^*(t), \quad e_\omega(t) = \hat{\omega}_m(t) - \omega_m(t),\\
&\tilde{i}_{sd}(t) = i_{sd}(t) - i_{sd}^*(t), \quad \tilde{i}_{sq}(t) = i_{sq}(t) - i_{sq}^*(t),\\
&\tilde{i}_{sa}(t) = i_{sa}(t) - \hat{i}_{sa}(t), \quad \tilde{i}_{sb}(t) = i_{sb}(t) - \hat{i}_{sb}(t),\\
&\tilde{T}_L(t) = T_L - \hat{T}_L(t) - F[\hat{\omega}_m(t) - \omega_m(t)],
\end{aligned}$$

we obtain the error system

$$\begin{aligned}
\dot{\tilde{\omega}}_m &= -\frac{F}{J}(\tilde{\omega}_m + e_\omega) - k_\omega \mathrm{sat}_\kappa(\tilde{\omega}_m + e_\omega) + \frac{K_\mathrm{M}}{J}\tilde{i}_{sq} - \frac{\tilde{T}_L}{J},\\
\dot{\tilde{i}}_{sd} &= -\left(\frac{R_s}{L_s} + k_i\right)\tilde{i}_{sd} - p e_\omega i_{sq},\\
\dot{\tilde{i}}_{sq} &= -\left(\frac{R_s}{L_s} + k_i\right)\tilde{i}_{sq} + p e_\omega i_{sd} + \frac{K_\mathrm{M}}{L_s} e_\omega,\\
\dot{\tilde{i}}_{sa} &= -\left(\frac{R_s}{L_s} + k_e\right)\tilde{i}_{sa} - \frac{K_\mathrm{M}}{L_s} e_\omega \sin(p\theta_r) - p\hat{\omega}_m \tilde{i}_{sb},\\
\dot{\tilde{i}}_{sb} &= -\left(\frac{R_s}{L_s} + k_e\right)\tilde{i}_{sb} + \frac{K_\mathrm{M}}{L_s} e_\omega \cos(p\theta_r) + p\hat{\omega}_m \tilde{i}_{sa},\\
\dot{e}_\omega &= \frac{2\gamma^2 + rF\lambda J^2}{\gamma^2\lambda + rF\lambda^2 J^2}\left[\frac{K_\mathrm{M}}{L_s}\sin(p\theta_r)\tilde{i}_{sa} - \frac{K_\mathrm{M}}{L_s}\cos(p\theta_r)\tilde{i}_{sb}\right] + \frac{\tilde{T}_L}{J},\\
\dot{\tilde{T}}_L &= -\frac{F}{J}\tilde{T}_L + \frac{J\gamma}{\gamma^2 + rF\lambda J^2}\left[\frac{K_\mathrm{M}}{L_s}\sin(p\theta_r)\tilde{i}_{sa} - \frac{K_\mathrm{M}}{L_s}\cos(p\theta_r)\tilde{i}_{sb}\right].
\end{aligned} \tag{16.6}$$

Consider the function

$$V = \frac{1}{2}\left(\tilde{i}_{sa}^2 + \tilde{i}_{sb}^2\right) + \frac{1}{2}\lambda e_\omega^2 + \frac{\gamma^2}{\lambda J^2}\tilde{T}_L^2 - \frac{\gamma}{J} e_\omega \tilde{T}_L + \frac{rF}{2}\tilde{T}_L^2,$$

whose time derivative satisfies

$$\dot{V} \le -\left(\frac{R_s}{L_s} + k_e\right)\left(\tilde{i}_{sa}^2 + \tilde{i}_{sb}^2\right) + \frac{\lambda}{J} e_\omega \tilde{T}_L - \frac{\gamma}{J^2}\tilde{T}_L^2 + \frac{\gamma^2}{4J^3 r} e_\omega{}^2.$$

The last four equations in (16.6) may be rewritten as

$$\begin{aligned}
\dot{x} &= Ax + B(t)z + H(t)x,\\
\dot{z} &= D(t)x + \frac{1}{J}w,\\
\dot{w} &= -\frac{F}{J}w + \frac{\lambda J\gamma}{2\gamma^2 + rF\lambda J^2} D(t)x,
\end{aligned} \tag{16.7}$$

with $x = [\tilde{i}_{sa}, \tilde{i}_{sb}]^T$, $z = e_\omega$, $w = \tilde{T}_L$, and

$$A = \begin{bmatrix} -\frac{R_s}{L_s} - k_e & 0 \\ 0 & -\frac{R_s}{L_s} - k_e \end{bmatrix},$$

$$B(t) = \begin{bmatrix} -\frac{K_M}{L_s}\sin(p\theta_r(t)) \\ \frac{K_M}{L_s}\cos(p\theta_r(t)) \end{bmatrix},$$

$$D(t) = \frac{2\gamma^2 + rF\lambda J^2}{\gamma^2\lambda + rF\lambda^2 J^2}\left[\frac{K_M}{L_s}\sin(p\theta_r(t)),\ -\frac{K_M}{L_s}\cos(p\theta_r(t))\right],$$

$$H(t) = \begin{bmatrix} 0 & -p\hat{\omega}_m(t) \\ p\hat{\omega}_m(t) & 0 \end{bmatrix}.$$

Since for all $t \geq t_0$ ($T_p > 0$)

$$\|A\| = \frac{R_s}{L_s} + k_e, \quad \|B(t)\| = \frac{K_M}{L_s}, \quad \|D(t)\| \leq \frac{2K_M}{\lambda L_s},$$

$$\|\dot{B}^T(t) + B^T(t)H(t)\| \leq \frac{K_M p}{L_s}|z|, \quad \int_t^{t+T_p} B^T(\tau)B(\tau)d\tau = \frac{{K_M}^2 T_p}{L_s^2},$$

we choose the positive control parameters γ and r in order to satisfy the inequalities in (16.5) so that system (16.7) complies with the hypotheses of Lemma 1 in Tomei and Verrelli (2008) by setting $T = T_p$ and, consequently, the point $(\tilde{i}_{sa}, \tilde{i}_{sb}, e_\omega, \tilde{T}_L) = 0$ is locally exponentially stable with domain of attraction

$$\mathcal{A} = \{\zeta \in \mathbb{R}^4 : \|\zeta\| < C_r\}.$$

The second and third equations in (16.6), may be rewritten as

$$\dot{\mu} = \begin{pmatrix} -\frac{R_s}{L_s} - k_i & -pe_\omega \\ pe_\omega & -\frac{R_s}{L_s} - k_i \end{pmatrix}\mu + \begin{pmatrix} -pi_{sq}^* \\ pi_{sd}^* + \frac{K_M}{L_s} \end{pmatrix} e_\omega,$$

with $\mu = [\tilde{i}_{sd}, \tilde{i}_{sq}]^T$. Since $(i_{sd}^*(t), i_{sq}^*(t))$ are bounded on $[t_0, +\infty)$ and, for any initial condition $[\tilde{i}_{sa}(t_0), \tilde{i}_{sb}(t_0), e_\omega(t_0), \ \tilde{T}_L(t_0)]^T$ in $\mathcal{A}$, $e_\omega(t)$ tends exponentially to zero, the system above complies with the hypotheses of Lemma III.1 in Marino and Tomei (1995) and $(\tilde{i}_{sd}, \tilde{i}_{sq})$ tend exponentially to zero for any initial condition $[\tilde{i}_{sa}(t_0), \tilde{i}_{sb}(t_0), e_\omega(t_0), \tilde{T}_L(t_0)]^T$ in $\mathcal{A}$. Recalling the first equation in (16.6), we can establish that, since, for any initial condition $[\tilde{i}_{sa}(t_0), \tilde{i}_{sb}(t_0), e_\omega(t_0), \tilde{T}_L(t_0)]^T$ in $\mathcal{A}$, $(\tilde{i}_{sq}, e_\omega, \tilde{T}_L)$ tend exponentially to zero, $\tilde{\omega}_m$ is bounded and tends uniformly asymptotically to zero for any initial condition $[\tilde{i}_{sa}(t_0), \tilde{i}_{sb}(t_0), e_\omega(t_0), \tilde{T}_L(t_0)]^T$ in $\mathcal{A}$ and for any saturation value κ: in particular, the origin is a uniformly asymptotically stable equilibrium point for system (16.6) with domain of attraction $\mathcal{B}$. □

Remark 16.4.2 *If (γ, r) are chosen so that the inequalities in (16.5) are satisfied, then, for any initial condition $[\tilde{i}_{sa}(t_0), \tilde{i}_{sb}(t_0), e_\omega(t_0), \tilde{T}_L(t_0)]^T$ in $\mathcal{A}$: (1) since $\tilde{\omega}_m$ tends uniformly asymptotically to zero, uniform asymptotic speed tracking is achieved; (2) since $(\tilde{i}_{sd}, \tilde{i}_{sq})$ tend exponentially to zero, stator currents tend exponentially to the corresponding reference signals; (3) since e_ω tends exponentially to zero, rotor speed is exponentially estimated; (4) since $\tilde{T}_L$ and e_ω tend exponentially to zero, load torque T_L is exponentially estimated.*

In the remainder of this section, the well-known "*s-alignment*" and "*c-alignment*" procedures, in which the motor is preliminarily forced to reach certain known equilibrium points, are theoretically analyzed: they can be used to comply with the conditions of Theorem 16.4.1 and to preliminarily obtain $\cos(p\theta_r(t_0)) = 1$.

Proposition 16.4.3 *"s-alignment" procedure: Let $u_{cs} \in \mathbb{R}^+$ be a positive real scalar and suppose that no-load torque T_L is applied to the motor. Then, the static controller*

$$\begin{aligned} v_{sa}(t) &= 0, \\ v_{sb}(t) &= u_{cs}, \end{aligned} \tag{16.8}$$

substituted in model (16.1), guarantees boundedness of $(\omega_m, i_{sa}, i_{sb})$ and

$$\begin{aligned} \lim_{t\to+\infty} \cos(p\theta_r(t)) &= 0, \\ \lim_{t\to+\infty} \omega_m(t) &= 0, \\ \lim_{t\to+\infty} i_{sa}(t) &= 0, \\ \lim_{t\to+\infty} i_{sb}(t) &= \frac{u_{cs}}{R_s}. \end{aligned}$$

Proof: Denoting by $\tilde{i}_{sb} = i_{sb} - \frac{u_{cs}}{R_s}$ the stator current vector b-component regulation error, the closed-loop system is

$$\begin{aligned} \dot{\theta}_r &= \omega_m, \\ \dot{\omega}_m &= -\frac{F}{J}\omega_m + \frac{K_\mathrm{M}}{J}\Big[- i_{sa}\sin(p\theta_r) + \tilde{i}_{sb}\cos(p\theta_r) + \frac{u_{cs}}{R_s}\cos(p\theta_r)\Big], \\ \frac{\mathrm{d}i_{sa}}{\mathrm{d}t} &= -\frac{R_s}{L_s} i_{sa} + \frac{K_\mathrm{M}}{L_s}\omega_m \sin(p\theta_r), \\ \dot{\tilde{i}}_{sb} &= -\frac{R_s}{L_s}\tilde{i}_{sb} - \frac{K_\mathrm{M}}{L_s}\omega_m \cos(p\theta_r), \end{aligned}$$

whose equilibrium points are

$$(\theta_r, \omega_m, i_{sa}, \tilde{i}_{sb}) = (\theta_{es}, 0, 0, 0),$$

with $\theta_{es} = \frac{\pi}{2p}, \frac{3\pi}{2p}, \ldots, \left(2p - \frac{1}{2}\right)\frac{\pi}{p}$. Consider the function

$$U_s = \frac{1}{2}\left(\frac{J}{L_s}{\omega_m}^2 + {i_{sa}}^2 + \tilde{i}_{sb}^2\right) - \frac{K_{\mathrm{M}} u_{cs}}{p L_s R_s}\left(\sin(p\theta_r) - 2\right),$$

which is always positive. Its time derivative along the trajectories of the closed loop system is

$$\dot{U}_s = -\frac{F}{L_s}\omega_m^2 - \frac{R_s}{L_s}\left({i_{sa}}^2 + \tilde{i}_{sb}^2\right).$$

Since $\dot{U}_s(t) \leq 0$ [recall that $F \geq 0$], by virtue of LaSalle theorem (see Khalil 2002), we can establish that every solution is attracted into the largest invariant subset $\mathcal{M}_s$ of the set $\dot{U}_s = 0$, consisting of the equilibrium points $(\theta_r, \omega_m, i_{sa}, \tilde{i}_{sb}) = (\theta_{es}, 0, 0, 0)$. □

Proposition 16.4.4 ("c-alignment" procedure). *Let $u_{cs} \in \mathbb{R}^+$ and $u_{cc} \in \mathbb{R}^+$ be positive real scalars. Assume that no-load torque T_L is applied to the motor and that the positive real scalars $u_{cs} \in \mathbb{R}^+$ and $u_{cc} \in \mathbb{R}^+$ satisfy the condition*

$$\frac{K_{\mathrm{M}} u_{cc}}{p L_s R_s}(1 - \delta_s) - \frac{\left(u_{cs}^2 + u_{cc}^2\right)}{2R_s^2} > 0,$$

with $\delta_s \in \mathbb{R}^+$. Then, for sufficiently small initial conditions $\|z_s(t_0)\| \doteq \left\|\left[\cos(p\theta_r(t_0)),\ \omega_m(t_0),\ i_{sa}(t_0),\ \left(i_{sb}(t_0) - \frac{u_{cs}}{R_s}\right)\right]\right\|$, the static controller

$$\begin{aligned} v_{sa}(t) &= u_{cc}, \\ v_{sb}(t) &= 0, \end{aligned} \tag{16.9}$$

substituted in model (16.1), guarantees boundedness of $(\omega_m,\ i_{sa},\ i_{sb})$ and

$$\lim_{t \to +\infty} \cos(p\theta_r(t)) = 1,$$

$$\lim_{t \to +\infty} \omega_m(t) = 0,$$

$$\lim_{t \to +\infty} i_{sb}(t) = 0,$$

$$\lim_{t \to +\infty} i_{sa}(t) = \frac{u_{cc}}{R_s}.$$

Proof: Denoting by $\tilde{i}_{sa} = i_{sa} - \frac{u_{cc}}{R_s}$ the stator current vector a-component regulation error, the closed-loop system is

$$\begin{aligned}
\dot{\theta}_r &= \omega_m,\\
\dot{\omega}_m &= -\frac{F}{J}\omega_m + \frac{K_{\mathrm{M}}}{J}\Big[-\tilde{i}_{sa}\sin(p\theta_r) - \frac{u_{cc}}{R_s}\sin(p\theta_r) + i_{sb}\cos(p\theta_r)\Big],\\
\dot{\tilde{i}}_{sa} &= -\frac{R_s}{L_s}\tilde{i}_{sa} + \frac{K_{\mathrm{M}}}{L_s}\omega_m \sin(p\theta_r),\\
\frac{\mathrm{d}i_{sb}}{\mathrm{d}t} &= -\frac{R_s}{L_s}i_{sb} - \frac{K_{\mathrm{M}}}{L_s}\omega_m\cos(p\theta_r),
\end{aligned}$$

whose equilibrium points are

$$(\theta_r, \omega_m, \tilde{i}_{sa}, i_{sb}) = (\theta_{ec}, 0, 0, 0),$$

with $\theta_{ec} = 0, \frac{\pi}{p}, \frac{2\pi}{p}, \ldots, (2p-1)\frac{\pi}{p}$. Consider the function

$$U_c = \frac{1}{2}\Big(\frac{J}{L_s}{\omega_m}^2 + \tilde{i}_{sa}^2 + {i_{sb}}^2\Big) - \frac{K_{\mathrm{M}}u_{cc}}{pL_sR_s}\Big(\cos(p\theta_r) - 2\Big),$$

which is always positive. Its time derivative along the trajectories of the closed loop system is

$$\dot{U}_c = -\frac{F}{L_s}\omega_m^2 - \frac{R_s}{L_s}\Big(\tilde{i}_{sa}^2 + {i_{sb}}^2\Big).$$

Since $\dot{U}_c(t) \leq 0$ [recall that $F \geq 0$], by virtue of LaSalle theorem (see Khalil 2002), we can establish that every solution is attracted into the largest invariant subset $\mathcal{M}_c$ of the set $\dot{U}_c = 0$, consisting of the equilibrium points $(\theta_r, \omega_m, \tilde{i}_{sa}, i_{sb}) = (\theta_{ec}, 0, 0, 0)$. Since $\dot{U}_c(t) \leq 0$, we have for all $t \geq t_0$

$$U_c(t) \leq U_c(t_0),$$

and in particular

$$\begin{aligned}
\lim_{t\to+\infty} U_c(t) &= \lim_{t\to+\infty}\Big[-\frac{K_{\mathrm{M}}u_{cc}}{pL_sR_s}\Big(\cos(p\theta_r(t)) - 2\Big)\Big],\\
&\leq U_c(t_0) = \frac{\big(u_{cs}^2 + u_{cc}^2\big)}{2R_s^2} + \frac{2K_{\mathrm{M}}u_{cc}}{pL_sR_s} + \vartheta_s(z_s(t_0)),
\end{aligned}$$

where the continuous function $\vartheta_s(\cdot) : \mathbb{R}^4 \to \mathcal{R}(\vartheta_s)$ satisfies

$$\lim_{\|z_s(t_0)\|\to 0} \vartheta_s(z_s(t_0)) = 0.$$

Choosing a sufficiently small $\|z_s(t_0)\|$ such that

$$\frac{pL_sR_s}{K_M u_{cc}}|\vartheta_s(z_s(t_0))| \leq \delta_s,$$

suffices to guarantee

$$\lim_{t\to+\infty} \cos(p\theta_r(t)) = 1.$$

□

Remark 16.4.5 *The proof of Theorem 16.5.1 clarifies that (16.9) does not guarantee*

$$\lim_{t\to+\infty} \cos(p\theta_r(t)) = 1$$

for any initial condition, since for instance

$$\left[\theta_{ec}^u = \frac{\pi}{p}, \frac{3\pi}{p}, \ldots, (2p-1)\frac{\pi}{p}\right],$$

$$\theta_r(t) \equiv \theta_{ec}^u,$$

$$\omega_m(t) = i_{sb}(t) \equiv 0,$$

$$\tilde{i}_{sa}(t) = \tilde{i}_{sa}(t_0)e^{-\frac{R_s}{L_s}(t-t_0)},$$

are solutions of the closed-loop system.

16.5 Main Result (Tomei and Verrelli 2011)

In this section, we present the main result of this chapter: the assumption that the motor that is initially aligned is definitely removed while a nonzero γ_θ will be used. For the sake of simplicity, we set $t_0 = 0$. Let $\Pi_e(t)$ be the vector whose components are the tracking and estimation errors: $\cos(p\theta_r(t)) - \widehat{\cos(p\theta_r)}(t)$, $\sin(p\theta_r(t)) - \widehat{\sin(p\theta_r)}(t)$, $\omega_m(t) - \omega_m^*(t)$, $i_{sd}(t) - i_{sd}^*(t)$, $i_{sq}(t) - i_{sq}^*(t)$, $i_{sa}(t) - \hat{i}_{sa}(t)$, $i_{sb}(t) - \hat{i}_{sb}(t)$, $\hat{\omega}_m(t) - \omega_m(t)$, $T_L - \hat{T}_L(t)$.

Theorem 16.5.1 *Assume that the rotor speed reference signal $\omega_m^*(t)$ is persistently exciting, that is, there exist positive reals T and c_p such that the persistency of excitation condition*

$$\mathcal{P}: \quad \int_t^{t+T} \omega_m^*(\tau)^2 \mathrm{d}\tau \geq c_p, \qquad \forall\, t \geq 0$$

is satisfied. Then, for the closed-loop system (16.1), (16.3), and (16.4), boundedness of $(\omega_m(t), i_{sa}(t), i_{sb}(t), \widehat{\cos(p\theta_r)}(t), \widehat{\sin(p\theta_r)}(t), \hat{\omega}_m(t), \hat{i}_{sa}(t), \hat{i}_{sb}(t), \hat{T}_L(t))$ on $[0, +\infty)$ is guaranteed along with exponential convergence to zero of $\|\Pi_e(t)\|$, provided that $\|\Pi_e(0)\|$ is sufficiently small.

Proof: Recall the expressions for the variables ξ_a and ξ_b and define the estimation error (see Lee *et al.* 2010)

$$\begin{aligned}\mathcal{F} &= \frac{K_{\mathrm{M}}^2}{p^2}\left[\cos(p\theta_r)^2 + \sin(p\theta_r)^2 - \widehat{\cos(p\theta_r)}^2 - \widehat{\sin(p\theta_r)}^2\right] \\ &= \left[\frac{K_{\mathrm{M}}^2}{p^2} - \left(\hat{\xi}_a - L_s i_{sa}\right)^2 - \left(\hat{\xi}_b - L_s i_{sb}\right)^2\right],\end{aligned}$$

which is available for feedback[3]. Design the estimation laws for $(\hat{\xi}_a, \hat{\xi}_b)$ as

$$\begin{aligned}\dot{\hat{\xi}}_a &= -R_s i_{sa} + v_{sa} - \varphi_a \mathcal{F}, \\ \dot{\hat{\xi}}_b &= -R_s i_{sb} + v_{sb} - \varphi_b \mathcal{F},\end{aligned}$$

with (φ_a, φ_b) being yet to be designed. Let us introduce the tracking and estimation errors the same, excepting for $\tilde{\xi}_a, \tilde{\xi}_b$, of the previous section with z and w directly in place of e_ω and $\tilde{T}_L$:

$$\begin{aligned}\tilde{\omega}_m &= \omega_m - \omega_m^*, \quad z = \hat{\omega}_m - \omega_m, \\ \tilde{i}_{sd} &= i_{sd} - i_{sd}^*, \quad \tilde{i}_{sq} = i_{sq} - i_{sq}^*, \\ \tilde{i}_{sa} &= i_{sa} - \hat{i}_{sa}, \quad \tilde{i}_{sb} = i_{sb} - \hat{i}_{sb}, \\ w &= T_L - \hat{T}_L - F[\hat{\omega}_m - \omega_m], \\ \tilde{\xi}_a &= \xi_a - \hat{\xi}_a, \quad \tilde{\xi}_b = \xi_b - \hat{\xi}_b,\end{aligned}$$

and the vector

$$q = [\tilde{\omega}_m, \tilde{i}_{sd}, \tilde{i}_{sq}, \tilde{i}_{sa}, \tilde{i}_{sb}, z, w, \tilde{\xi}_a, \tilde{\xi}_b]^T,$$

so that the error system can be written as

$$\begin{aligned}\dot{\tilde{\omega}}_m &= -\frac{F}{J}(\tilde{\omega}_m + z) - k_\omega \mathrm{sat}_\kappa(\tilde{\omega}_m + z) + \left[0, \frac{K_{\mathrm{M}}}{J}\right]\mu - \frac{w}{J}, \\ \dot{\mu} &= \begin{bmatrix} -\frac{R_s}{L_s} - k_i & 0, \\ 0 & -\frac{R_s}{L_s} - k_i \end{bmatrix}\mu + h_i(q,t), \\ \dot{x} &= Ax + B(t)z + H(t)x + h_x(q,t), \\ \dot{z} &= D(t)x + \frac{w}{J} + h_z(q,t), \\ \dot{w} &= -\frac{F}{J}w + \frac{\lambda J \gamma}{2\gamma^2 + rF\lambda J^2} D(t)x + h_w(q,t),\end{aligned} \tag{16.10}$$

$$\dot{\tilde{\xi}} = \frac{2K_{\mathrm{M}}}{p}\begin{bmatrix}\varphi_a(t) & -\varphi_b(t) \\ \varphi_b(t) & \varphi_a(t)\end{bmatrix}\begin{bmatrix}\cos(p\theta_r(t)) & \sin(p\theta_r(t)) \\ 0 & 0\end{bmatrix}\tilde{\xi} - \begin{bmatrix}\varphi_a(t) \\ \varphi_b(t)\end{bmatrix}\|\tilde{\xi}\|^2, \tag{16.11}$$

[3]Recall that $\sin(p\theta_r)^2 + \cos(p\theta_r)^2 = 1$.

where $\mu = [\tilde{i}_{sd}, \tilde{i}_{sq}]^T$, $x = [\tilde{i}_{sa}, \tilde{i}_{sb}]^T$ (the same as the previous section), $\tilde{\xi} = [\tilde{\xi}_a, \tilde{\xi}_b]^T$,

$$A = \begin{bmatrix} -\frac{R_s}{L_s} - k_e & 0 \\ 0 & -\frac{R_s}{L_s} - k_e \end{bmatrix},$$

$$B(t) = \frac{K_{\mathrm{M}}}{L_s} \begin{bmatrix} -\sin(p\theta_r(t)) \\ \cos(p\theta_r(t)) \end{bmatrix},$$

$$D(t) = \frac{(2\gamma^2 + rF\lambda J^2)K_{\mathrm{M}}}{(\gamma^2\lambda + rF\lambda^2 J^2)L_s} [\sin(p\theta_r(t)), -\cos(p\theta_r(t))],$$

$$H(t) = \begin{bmatrix} 0 & -p\hat{\omega}_m(t) \\ p\hat{\omega}_m(t) & 0 \end{bmatrix},$$

and h_i, h_x, h_z, and h_w are suitable functions satisfying (a_{hj} are positive reals, $j = i, x, z, w$)

$$\begin{aligned} \|h_i(q,t)\| &\le a_{hi}\left(|z| + \|\tilde{\xi}\|\right) + h_{i*}(q), \\ \|h_x(q,t)\| &\le a_{hx}\|\tilde{\xi}\| + h_{x*}(q), \\ |h_z(q,t)| &\le a_{hz}\|\tilde{\xi}\| + h_{z*}(q), \\ |h_w(q,t)| &\le a_{hw}\|\tilde{\xi}\| + h_{w*}(q), \end{aligned}$$

with

$$\lim_{\|q\|\to 0} \frac{|h_{j*}(q)|}{\|q\|} = 0, \qquad j = i, x, z, w.$$

If we choose the yet to be designed functions φ_a and φ_b as

$$\begin{aligned} \varphi_a &= -\frac{\gamma_\theta K_{\mathrm{M}}}{p}\widehat{\cos(p\theta_r)} = -\frac{\gamma_\theta K_{\mathrm{M}}}{p}\cos(p\theta_r) + \gamma_\theta\tilde{\xi}_a, \\ \varphi_b &= -\frac{\gamma_\theta K_{\mathrm{M}}}{p}\widehat{\sin(p\theta_r)} = -\frac{\gamma_\theta K_{\mathrm{M}}}{p}\sin(p\theta_r) + \gamma_\theta\tilde{\xi}_b, \end{aligned}$$

then the $\tilde{\xi}$-subsystem (16.5) becomes

$$\dot{\tilde{\xi}} = -\frac{2\gamma_\theta K_{\mathrm{M}}^2}{p^2}\mathcal{R}(\theta_r)^{-1}\begin{bmatrix} \cos(p\theta_r)\tilde{\xi}_a + \sin(p\theta_r)\tilde{\xi}_b, \\ 0 \end{bmatrix} + h_{\tilde{\xi}}(\tilde{\xi}, t), \tag{16.12}$$

with

$$\lim_{\|\tilde{\xi}\|\to 0} \sup_{t\ge 0} \frac{\|h_{\tilde{\xi}}(\tilde{\xi}, t)\|}{\|\tilde{\xi}\|} = 0,$$

so that, by introducing the nonsingular change of variables

$$\eta = \left[\eta_d, \eta_q\right]^T = \mathcal{R}(\theta_r)\tilde{\xi},$$

the dynamics (16.12), expressed in the new variables, become

$$\dot{\eta} = \begin{bmatrix} -\frac{2\gamma_\theta K_M^2}{p^2} & p\omega_m^* \\ -p\omega_m^* & 0 \end{bmatrix} \eta + p\tilde{\omega}_m \begin{bmatrix} \eta_q \\ -\eta_d \end{bmatrix} + \mathcal{R}(\theta_r) h_\xi(\mathcal{R}(\theta_r)^{-1}\eta, t). \tag{16.13}$$

The closed-loop error system, when higher order terms are neglected, exhibits a useful triangular structure (characterized by the positive reals a_{hj}, $j = i, x, z, w$)[4]: a composite Lyapunov function can be thus successfully found on the basis of the proof of Theorem 16.4.1 to guarantee, under persistency of excitation $\mathcal{P}$, the local exponential stability of the origin of the system with a computable domain of attraction depending on a_{hj}, $j = i, x, z, w$. □

Remark 16.5.2 *The exponential stability of the origin of the closed-loop error system allows for establishing certain robustness properties: ultimate boundedness of the solutions of the closed-loop error system when perturbed by modeling errors, aging, uncertainties, and disturbances, which exist in any realistic application, is guaranteed, according to Lemma 9.2 in Khalil (2002), for sufficiently small initial conditions and sufficiently small uniformly bounded perturbations that do not change the system dynamic order.*

Remark 16.5.3 *Since $\tilde{\omega}_m$ exponentially tends to zero, exponential rotor speed tracking is achieved; since $(\tilde{i}_{sd}, \tilde{i}_{sq})$ exponentially tend to zero, stator currents exponentially tend to the corresponding reference signals; since z exponentially tends to zero, rotor speed is exponentially estimated; since w and z exponentially tend to zero, the load torque T_L is exponentially estimated; since η_d and η_q exponentially tend to zero,* $\cos(p\theta_r)$ *and* $\sin(p\theta_r)$ *are exponentially estimated.*

Remark 16.5.4 *The persistency of excitation condition $\mathcal{P}$, which is to be satisfied by the rotor speed reference signal $\omega_m^*(t)$, is a sufficient condition for guaranteeing rotor speed tracking. It is related to motor observability (see Basic et al. 2010): in the case of constant admissible inputs (v_{sa}, v_{sb}), all the equilibrium points for system (16.1)*

$$(\theta_r, \omega_m, i_{sa}, i_{sb}) = \left(\theta_*, 0, \frac{v_{sa}}{R_s}, \frac{v_{sb}}{R_s}\right),$$

with θ_* satisfying

$$\frac{K_M}{R_s}\left[-v_{sa}\sin(p\theta_*) + v_{sb}\cos(p\theta_*)\right] = T_L,$$

[4]Recall that $\|\eta\| = \|\tilde{\xi}\|$.

which are indistinguishable from input-output measurements. In particular, when $\omega_m(t) \equiv 0$ *for all* $t \geq 0$ *(so that* $\theta_r(t) \equiv \theta_c$ *for all* $t \geq 0$ *with* θ_c *a constant value), all the points*

$$(\tilde{\xi}_a, \tilde{\xi}_b) = \frac{2K_{\mathrm{M}}}{p}(\cos(p\theta_c), \sin(p\theta_c))$$

for which $\widehat{\cos(p\theta_r)}^2 + \widehat{\sin(p\theta_r)}^2 = 1$*, are equilibrium points for the* $\tilde{\xi}$*-subsystem (16.5).*

Remark 16.5.5 *Note that the origin* $\tilde{\xi} = 0$ *is an equilibrium point for the* $\tilde{\xi}$*-subsystem so that if* $\cos(p\theta_r(0)) - \widehat{\cos(p\theta_r)}(0) = 0$ *and* $\sin(p\theta_r(0)) - \widehat{\sin(p\theta_r)}(0) = 0$*, then* $\cos(p\theta_r(t)) - \widehat{\cos(p\theta_r)}(t) \equiv 0$ *and* $\sin(p\theta_r(t)) - \widehat{\sin(p\theta_r)}(t) \equiv 0$ *for all* $t \geq 0$*. In this case, the persistency of excitation condition* $\mathcal{P}$ *is no longer required to obtain a result that is similar to the one stated by Theorem 16.4.1.*

16.6 Simulation Results (Bifaretti *et al.* 2012)

The proposed control algorithms (16.3) and (16.4) have been tested by simulations with control parameters (the values are in SI units) $k_i = 20$, $k_\omega = 100$, $\kappa = 9$, $k_e = 12000$, $\gamma_\theta = 180$, $\gamma_\omega = 10$, and $\gamma_T = 9$ for the (nonsalient pole surface) PMSM with sinusoidal flux distribution in Marino, Peresada, & Tomei (1995), whose parameters are:

$$\begin{aligned}
\text{viscous friction coefficient } F &= 0 \text{ kg m}^2 \text{ s}^{-1} \\
\text{number of pole pairs } p &= 6 \\
\text{total rotor-load inertia } J &= 0.01 \text{ kg m}^2 \\
\text{stator resistance } R_s &= 3\ \Omega \\
\text{stator self inductance } L_s &= 0.006 \text{ H} \\
\text{torque constant } K_{\mathrm{M}} &= 2 \text{ N m A}^{-1}.
\end{aligned}$$

The reference i_{sd}^* for $i_{sd}(t)$ has been set to zero (field orientation), while the reference $\omega_m^*(t)$ for the rotor speed $\omega_m(t)$ has been generated by using ramp functions and the third order linear filter $\mathcal{H}(s) = (\frac{s}{\varpi_0} + 1)^{-3}$ with $\varpi_0 = 45$ rad/s. The necessary first and second order derivatives have been obtained from the state space realization of the filter. All initial conditions of the motor have been set to zero excepting for $\theta_r(0) = \pi/6$ rad.

16.6.1 Response to Time-Varying Load Torque

A time-varying load torque (whose profile includes regenerating mode and ramp-wise variations) has been applied at $t = 0.05$ s. The rotor speed reference and the applied torque are reported in Figure 16.1. The initial conditions for the controller have been set to zero excepting for $\hat{\xi}_a(0) = \frac{K_{\mathrm{M}}}{p}\cos(p\theta_u)$, $\hat{\xi}_b(0) = \frac{K_{\mathrm{M}}}{p}\sin(p\theta_u)$ with $\theta_u = \theta_r(0) + \pi/576$ (obtained by using the previously described finite-time alignment procedures). Figures 16.2, 16.3, 16.4

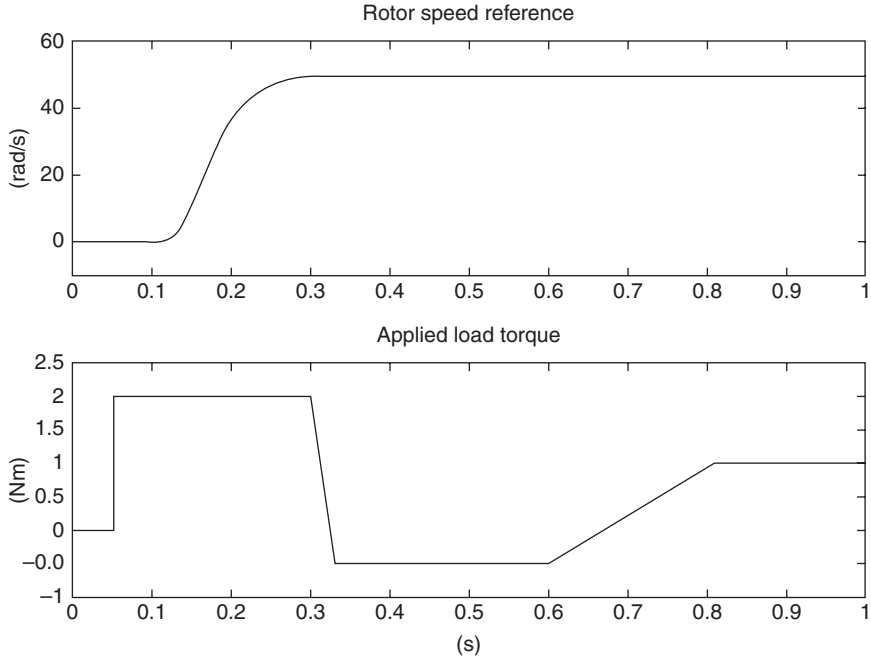

Figure 16.1 Rotor speed reference signal and applied load torque

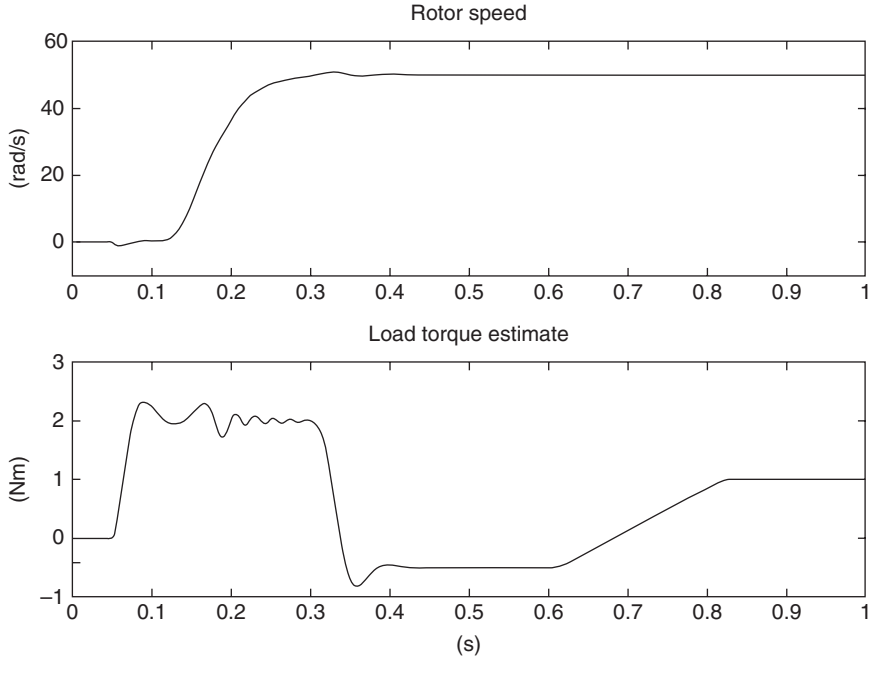

Figure 16.2 Rotor speed and load torque estimate

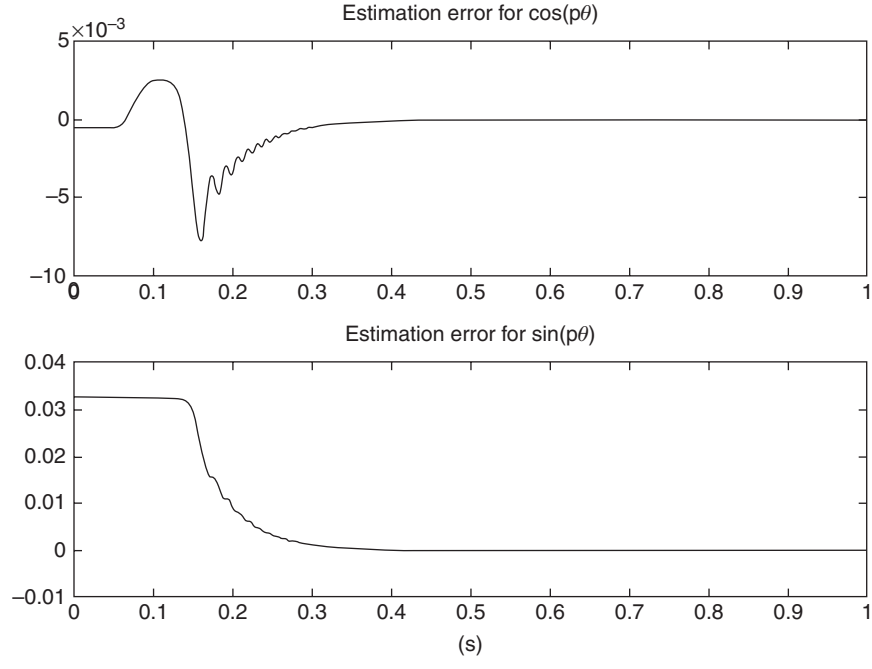

Figure 16.3 Estimation errors: $\cos(p\theta_r(t)) - \widehat{\cos(p\theta_r)}(t)$; $\sin(p\theta_r(t)) - \widehat{\sin(p\theta_r)}(t)$

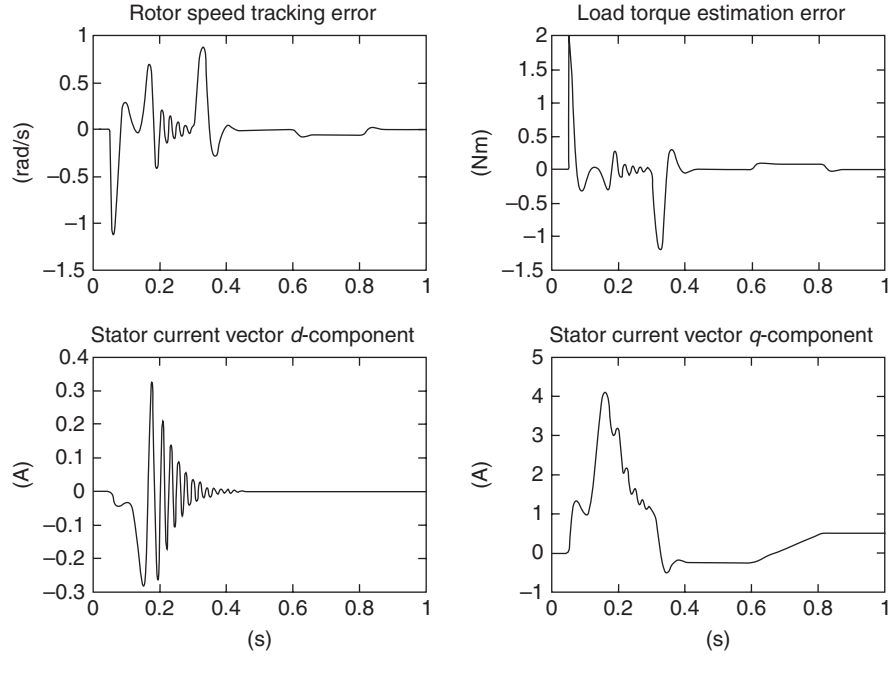

Figure 16.4 Rotor speed tracking error; load torque estimation error; stator current vector (d, q)-components

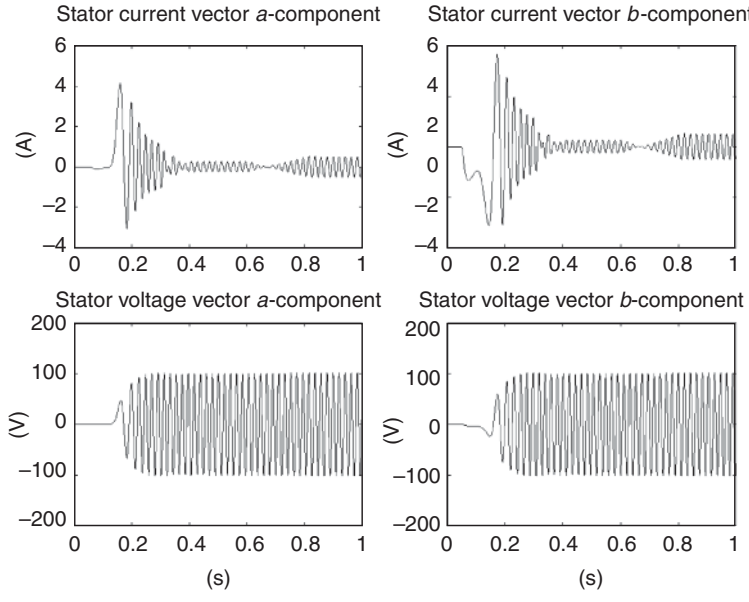

Figure 16.5 (a, b)-components of stator current and voltage vectors

and 16.5 demonstrate the effectiveness of the proposed nonlinear adaptive control algorithm even in the presence of time-varying variations of the load torque: exponential rotor speed tracking is achieved while exponential convergence of i_{sd} to $i_{sd}^* = 0$ is obtained along with exponential estimation of the unmeasured $\cos(p\theta_r)$, $\sin(p\theta_r)$ and of the unknown T_L. Similar results (see Figures 16.6 and 16.7) can be achieved for different controller initial conditions leading to larger initial estimation errors in $\sin(p\theta_r)$ and $\cos(p\theta_r)$ ($\hat{\xi}_a(0) = \frac{K_M}{p}\cos(p\theta_u)$, $\hat{\xi}_b(0) = \frac{K_M}{p}\sin(p\theta_u)$ with $\theta_u = \theta_r(0) + \pi/414$ and $\theta_u = \theta_r(0) + \pi/306$, respectively) larger transient output tracking/regulation errors are accordingly obtained.

16.6.2 Response to Parameter Uncertainties

The aim of this subsection is to illustrate the robustness of the proposed controller with respect to: (1) stator current sensor bias errors (0.05 A); (2) variations in stator resistance R_s (a 3% increase at $t = 0.3$ s); (3) uncertainties in the motor moment of inertia J (the actual value 0.018 kg m^2 is different from the nominal value 0.01 kg m^2 used by the controller). The load torque (2 Nm, the rated value) has been applied at $t = 0.05$ s. The rotor speed reference (including low speed operation) and the applied torque are reported in Figure 16.8. The controller initial conditions are the same of the previous subsection. The results are reported in Figures 16.9, 16.10, 16.11, and 16.12: a steady-state residual rotor speed tracking error appears which, as expected (recall the proof of Theorem 16.5.1 for the influence of T, c_p in $\mathcal{P}$ on the exponential rate of convergence of the overall closed-loop error system), is larger when smaller rotor speed reference signals are involved.

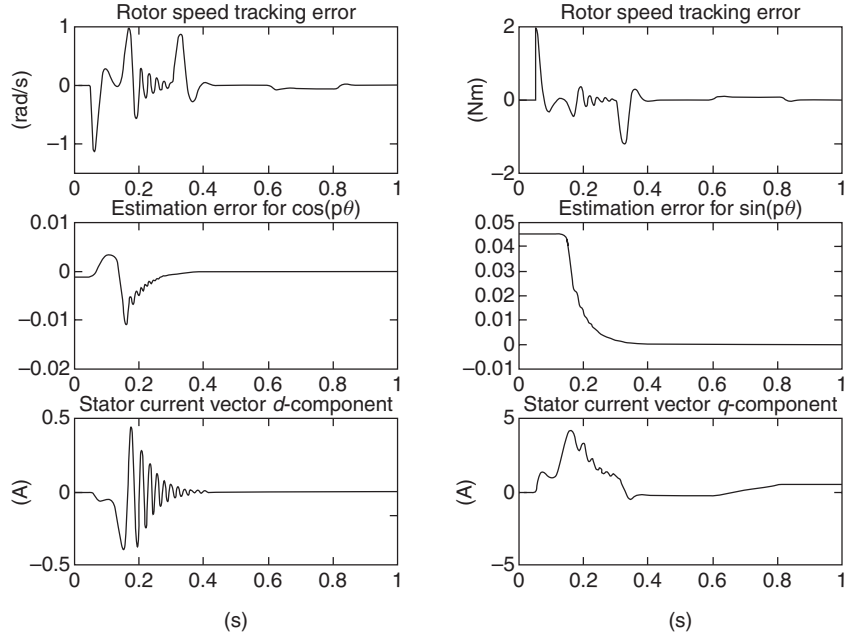

Figure 16.6 A $(\theta_u = \theta_r(0) + \pi/414)$. Rotor speed tracking error; load torque estimation error; $\cos(p\theta_r(t)) - \widehat{\cos(p\theta_r)}(t)$; $\sin(p\theta_r(t)) - \widehat{\sin(p\theta_r)}(t)$; stator current vector (d, q)-components

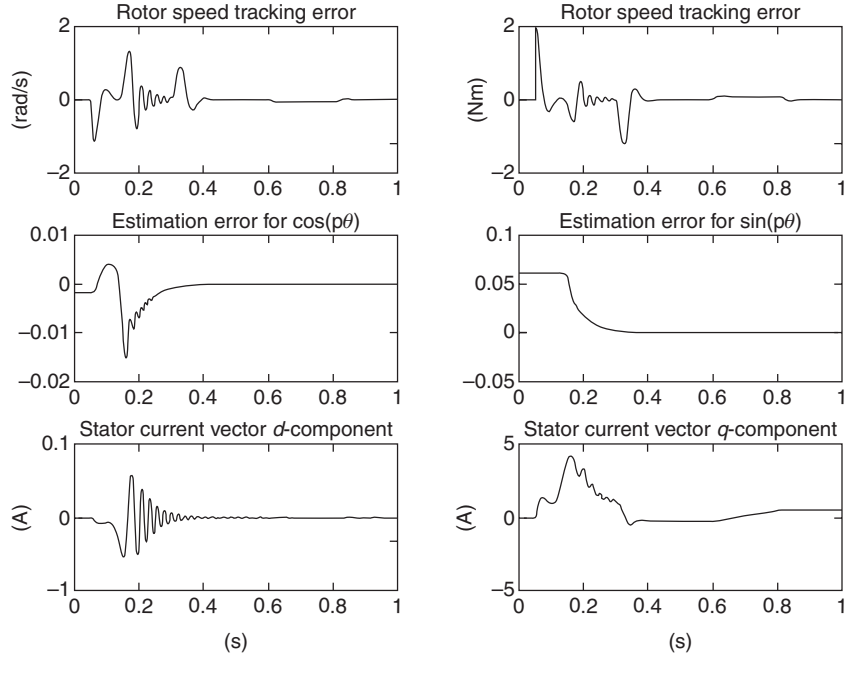

Figure 16.7 A $(\theta_u = \theta_r(0) + \pi/306)$. Rotor speed tracking error; load torque estimation error; $\cos(p\theta_r(t)) - \widehat{\cos(p\theta_r)}(t)$; $\sin(p\theta_r(t)) - \widehat{\sin(p\theta_r)}(t)$; stator current vector (d, q)-components

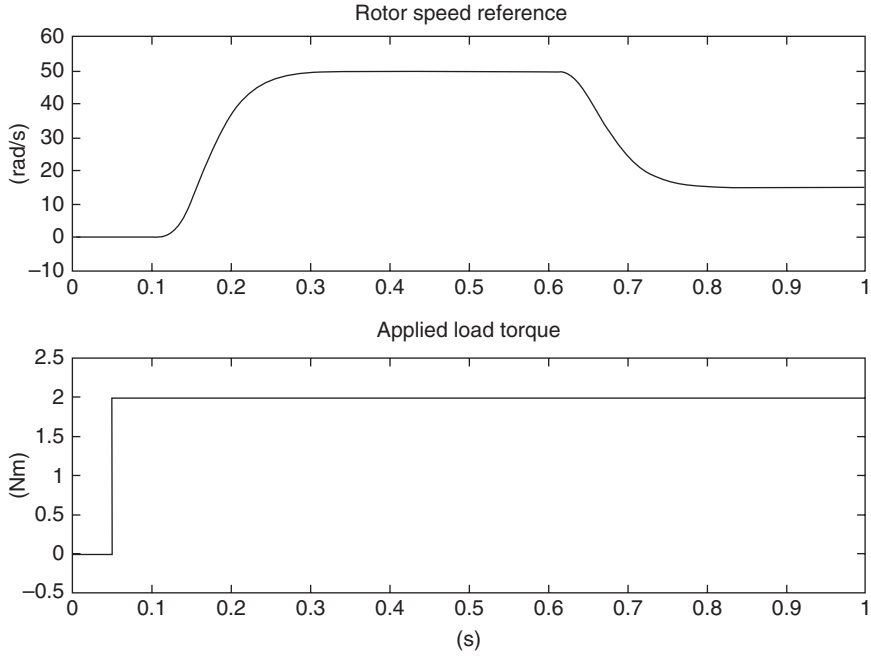

Figure 16.8 Rotor speed reference signal and applied load torque

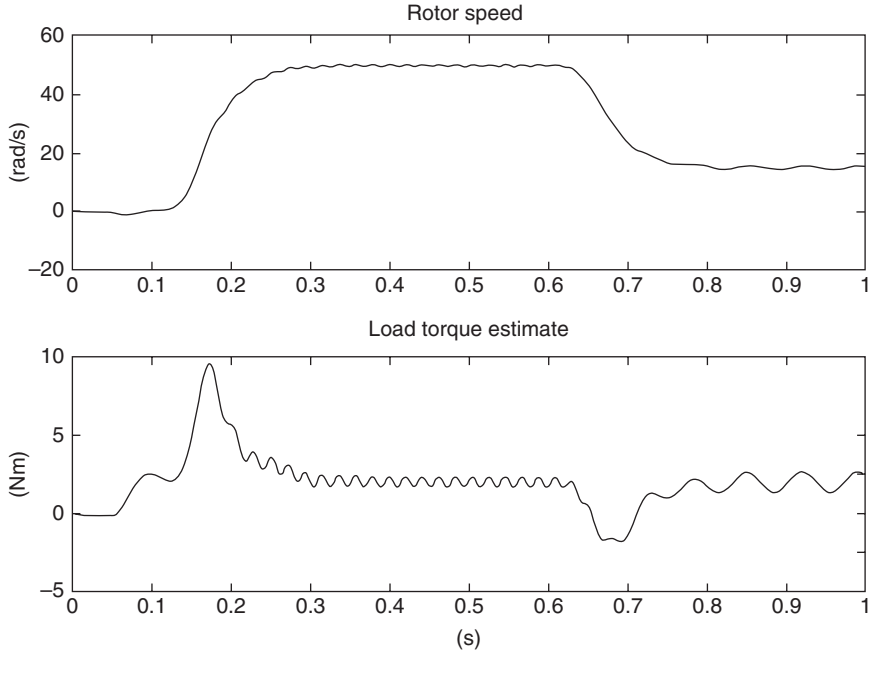

Figure 16.9 Rotor speed and load torque estimate

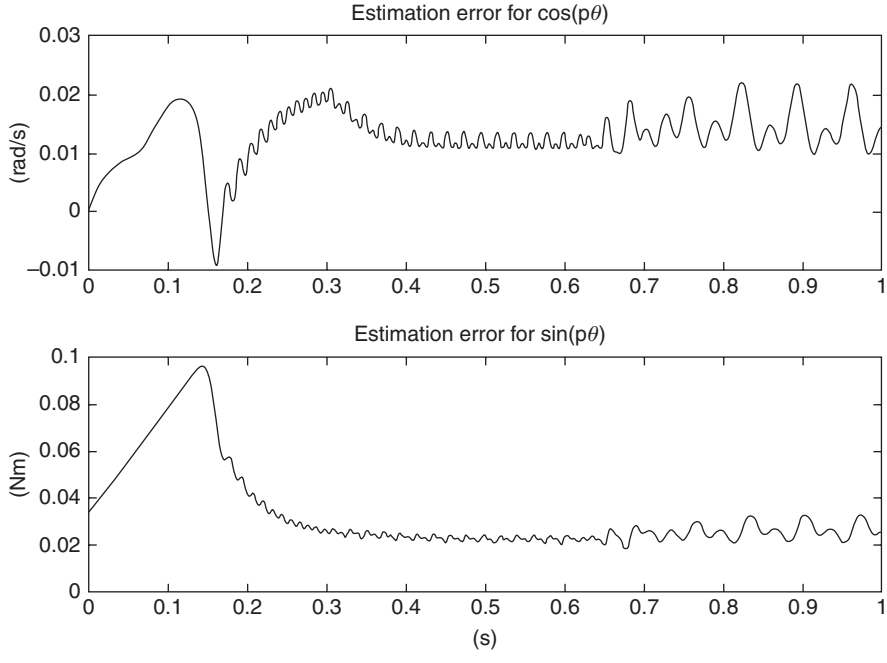

Figure 16.10 Estimation errors: $\cos(p\theta_r(t)) - \widehat{\cos(p\theta_r)}(t)$; $\sin(p\theta_r(t)) - \widehat{\sin(p\theta_r)}(t)$

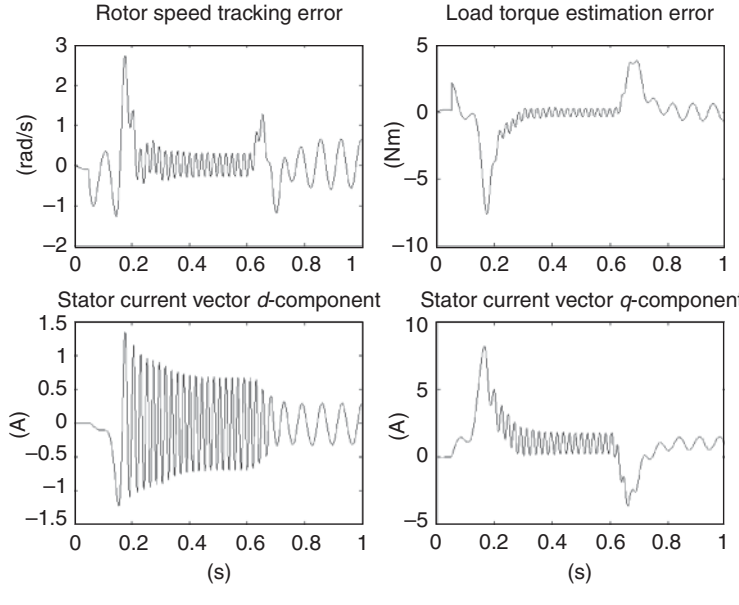

Figure 16.11 Rotor speed tracking error; load torque estimation error; stator current vector (d, q)-components

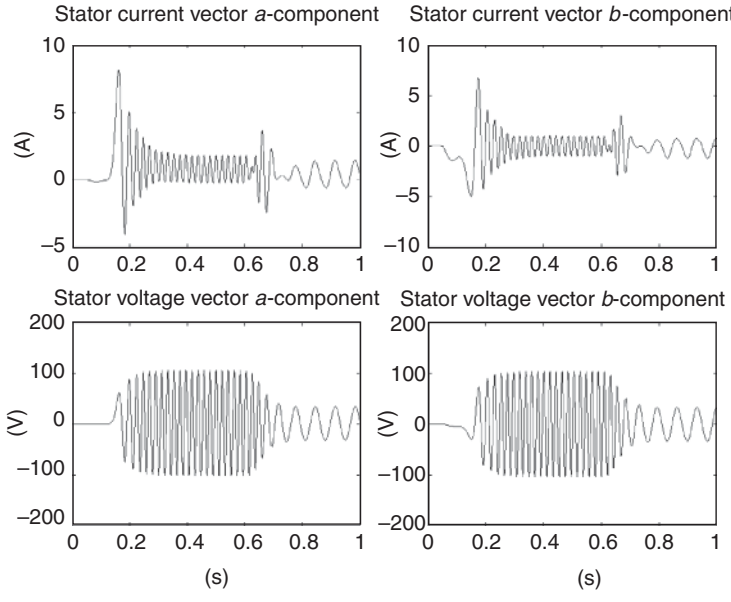

Figure 16.12 (a, b)-components of stator current and voltage vectors

16.7 Experimental Setup and Results (Bifaretti *et al.* 2012)

A Tetra 56SR1.35 three-phase PMSM, manufactured by Motor Power Company, has been used in the experiments. Its main specifications are: stall torque of 1.35 Nm, rated phase-to-phase voltage of 95 V AC, maximum phase current of 11.9 A_{rms}. A current-controlled DC motor (RS 263-6005 with rated voltage 24 V DC and motor torque constant of 9 N cm A^{-1}) provides the load torque to the PMSM. The PMSM is fed by a three-phase bridge using 70 V DC bus, while the DC motor is fed by a H-bridge using 25 V DC. The DC bus voltage is generated by single-phase grid voltage whose amplitude is, at first, reduced by a variac and then rectified. The experimental tests have been performed applying a 16 kHz switching frequency for the power MOSFET (IXYS FMM50-025TF) used for both the three-phase and the H-bridges. A Texas Instruments controller board, based on DSP TMS320F28335, is employed to implement the proposed control algorithm and to generate the logic driving signals for the power switches (see Figures 16.13 and 16.14). The sensorless control algorithms (16.3) and (16.4) are executed with a sampling interval $T_s = 62.5$ μs imposed by a suitable interrupt service. At the beginning of each sampling interval, the phase currents values, provided by two Hall effect current sensors, are acquired. The experimental prototype is shown in Figure 16.14 in which the main mechanical and electronic subsystems are highlighted by dashed boxes. A 2000 pulse per revolution encoder, interfaced to a dedicated hardware unit on the DSP that counts the rising and falling edges of the two quadrature encoder signals, provides, in conjunction with the discrete-time Kalman filter proposed in Bellini *et al.* (2003) (with a 20 Hz cut-off frequency), the rotor speed measurements required to evaluate the rotor speed tracking performance. All the initial conditions of the motor (16.1) are zero (the motor is aligned and at rest); a zero

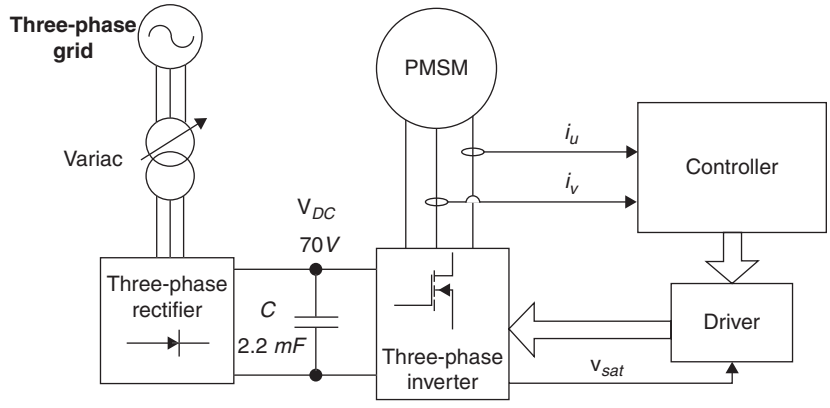

Figure 16.13 Functional block diagram

reference signal i_{sd}^* for the stator current vector d-component i_{sd} is chosen (field orientation); all the initial conditions for the sensorless controls (16.3) and (16.4) are set to zero except $\widehat{\cos(p\theta_r)}(0) = 1$; the control parameters (all values are in SI units) are: $k_i = 700$, $k_\omega = 1800$, $k_e = 3000$, $\gamma_\theta = 1000$, $\gamma_\omega = 100$, $\gamma_T = 0.08$, and $\kappa = 30$. The nominal parameter values directly provided by the manufacturer, that is. $J = 5.8 \cdot 10^{-5}$ kg m^2, $K_M = 0.4$ N m A$_{\text{rms}}^{-1}$, $p = 2$, $R_s = 1.48\ \Omega$, $L_s = 1.1 \cdot 10^{-3}$ H (the effect of F is neglected) (which can naturally

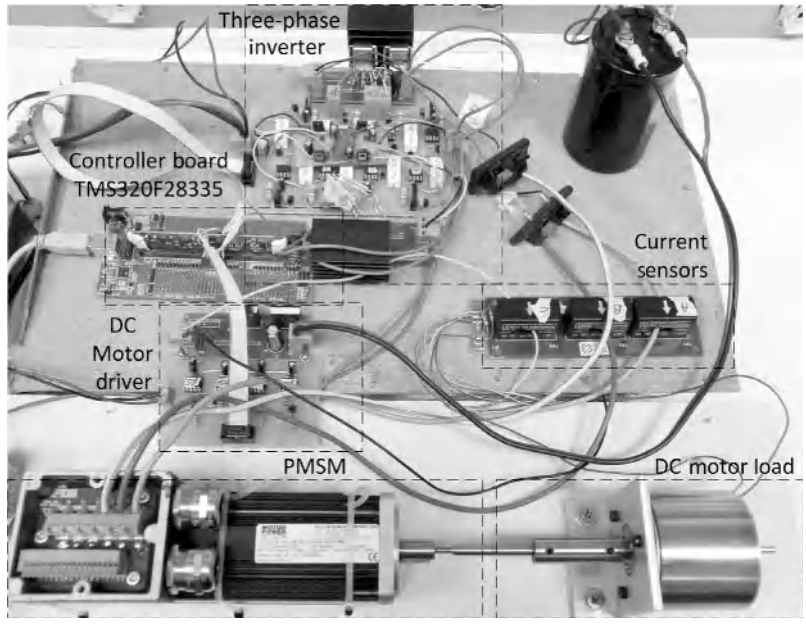

Figure 16.14 Experimental prototype

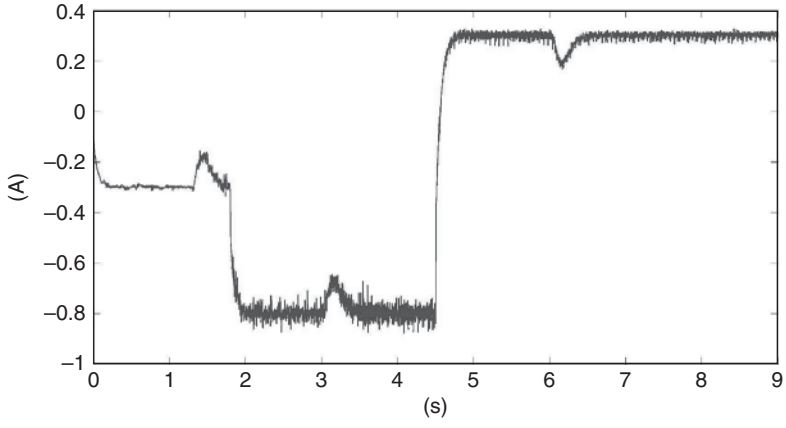

Figure 16.15 DC motor phase current i_{dc}

slightly differ from the actual motor parameter values), are used by the controller. A time-varying load torque (negative for $t \leq 4.5$ s and positive for $t \geq 4.5$ s) is provided by the DC motor and applied even when the rotor speed reference is zero (see Figure 16.15, which shows the DC motor phase current i_{dc}). Figure 16.16 shows how the rotor speed tracks its reference signal ω_m^*, while Figures 16.17 and 16.18 show the reasonable behaviors of the stator currents and voltages (i_{sa}, i_{sb}), (v_{sa}, v_{sb}). According to Figure 16.16, satisfactory rotor speed tracking is achieved (though with relatively small nonzero steady-state errors due to system uncertainties and model inaccuracies): the motor is able to start the operation with a nonzero applied load torque; only 2.5% and 2% maximum speed tracking errors are obtained when the rotor speed reference is imposed to 52 rad/s and 105 rad/s, respectively (better performance are reasonably achieved at higher speeds according to $\mathcal{P}$); even in the case of a negative load torque (braking

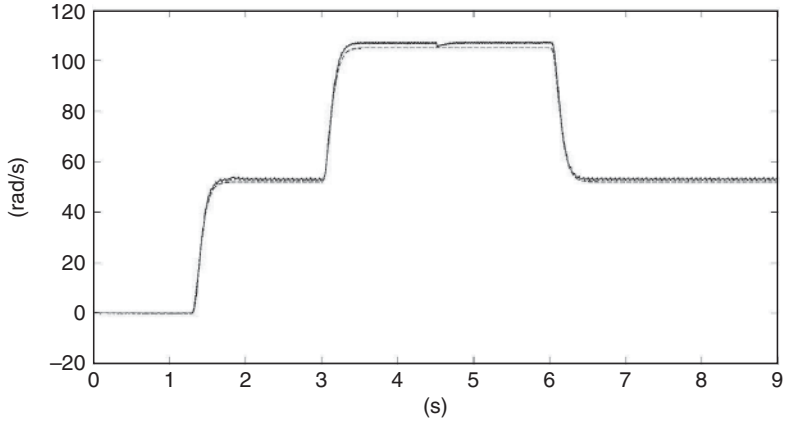

Figure 16.16 Rotor speed reference signal ω_m^* (dash) and rotor speed ω_m (solid)

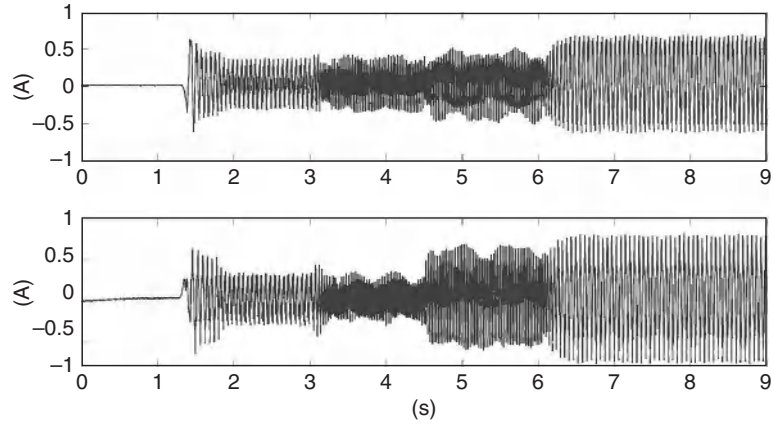

Figure 16.17 Stator current vector (a, b)-components

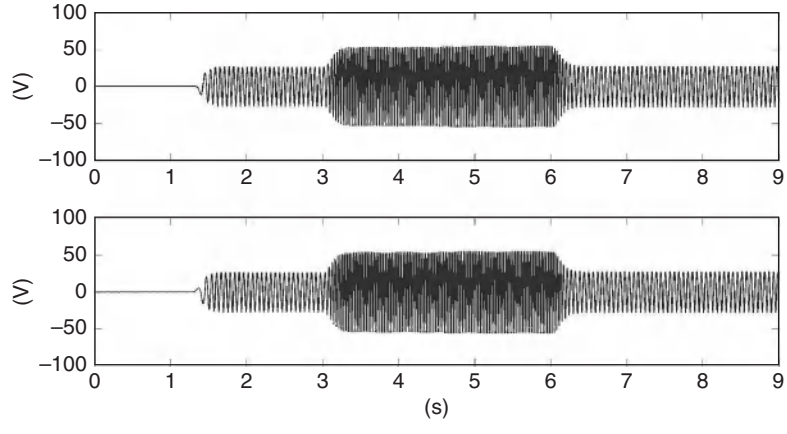

Figure 16.18 Stator voltage vector (a, b)-components

actions are to be performed by the PMSM motor in this case) only a 2.5% maximum speed tracking error is obtained.

16.8 Conclusions

According to the recent advances in Tomei and Verrelli (2008, 2011), and Bifaretti *et al.* (2012), the nonlinear adaptive speed tracking control algorithm (16.3) and (16.4) has been presented in this chapter for a (nonsalient pole surface) PMSM (16.1): it relies on the theoretical result (not based on motor friction) stated in Theorem 16.5.1. Simulation and experimental results are presented. Satisfactory performances are obtained in practice in conditions (persistently exciting rotor speed reference signals, relatively small initial tracking and estimation errors, relatively accurate knowledge of motor parameters, relatively accurate measurements

of available variables, relatively fast algorithm execution), which can be inferred by deeply analyzing the reported theoretical analysis. To this purpose, this chapter clarifies that the use of the closed-loop second order observer (16.4)—instead of the nonrobust open-loop estimators introduced in Tomei and Verrelli (2008) for theoretical purposes (see Theorem 16.4.1)-turns to be crucial: it is theoretically related to the exponential stability of the origin of the closed-loop error system, which allows for establishing certain robustness properties.

References

Basic D, Malrait F, and Rouchon P (2010) Euler-Lagrange models with complex currents of three-phase electrical machines and observability issues. *IEEE Transactions on Automatic Control*, **55**(1), 212–217.

Bellini A, Bifaretti S, and Costantini S (2003) A digital speed filter for motion control drives with a low resolution position encode. *Automatika*, **1-2**, 67–74.

Bifaretti S, Iacovone V, Rocchi A, Tomei P, and Verrelli CM (2011a) Global learning position controls for permanent magnet step motors. *IEEE Transactions on Industrial Electronics*, **58**(10), 4654–4663.

Bifaretti S, Iacovone V, Rocchi A, Tomei P, and Verrelli CM (2012) Nonlinear speed tracking control for sensorless PMSMs with unknown load torque: from theory to practice. *Control Engineering Practice*, **20**(7), 714–724.

Bifaretti S, Tomei P, and Verrelli CM (2011b) A global robust iterative learning position control for current-fed permanent magnet step motors. *Automatica*, **47**(1), 227–234.

Bisheimer G, Sonnaillon MO, De Angelo CH, *et al.* (2010) Full speed range permanent magnet synchronous motor control without mechanical sensors. *IET Electric Power Applications*, **4**(1), 35–44.

Bodson M, Chiasson JN, Novotnak RT, and Rekowski RB (1993) High-performance nonlinear feedback control of a permanent magnet stepper motor. *IEEE Transactions on Control Systems Technology*, **1**(1), 5–14.

Chan TF, Wang W, Borsje P, *et al.* (2008) Sensorless permanent-magnet synchronous motor drive using a reduced-order rotor flux observer. *IET Electric Power Applications*, **2**(2), 88–98.

Chiasson J (2005) *Modeling and High-Performance Control of Electric Machines*. Wiley-IEEE Press, Hoboken, NJ.

Dawson DM, Hu J, and Burg TC (1998) *Nonlinear Control of Electric Machinery*. Marcel Dekker, New York.

De Angelo C, Bossio G, Solsona J, *et al.* (2006) Mechanical sensorless speed control of permanent-magnet AC motors driving an unknwon load. *IEEE Transactions on Industrial Electronics*, **53**(2), 406-414.

Di Gennaro S (2000) Adaptive output feedback control of synchronous motors. *International Journal of Control*, **73**(16), 1475–1490.

Hinkkanen M, Tuovinen T, Harnefors L, and Luomi J (2012) A combined position and stator-resistance observer for salient PMSM drives: design and stability analysis. *IEEE Transactions on Power Electronics*, **27**, 601–609.

Khalil H (2002) *Nonlinear Systems*, Prentice Hall, Upper Saddle River, NJ.

Khorrami F, Krishnamurthy P, and Melkote H (2003) *Modeling and Adaptive Nonlinear Control of Electric Motors*, Springer-Verlag, Berlin.

Lee J, Hong J, Nam K, *et al.* (2010) Sensorless control of surface-mount permanent magnet synchronous motors based on a nonlinear observer. *IEEE Transactions on Power Electronics*, **25**(2), 290–297.

Marino R, Peresada S, and Tomei P (1995) Nonlinear adaptive control of permanent magnet step motors. *Automatica*, **31**(11), 1595–1604.

Marino R, and Tomei P (1995) Adaptive observers with arbitrary exponential rate of convergence for nonlinear systems. *IEEE Transactions on Automatic Control*, **40**(7), 1300–1304.

Marino R, Tomei P, and Verrelli CM (2008) Adaptive field-oriented control of synchronous motors with damping windings. *European Journal of Control*, **14**(3), 177–195.

Marino R, Tomei P, and Verrelli CM (2012) Robust adaptive learning control for nonlinear systems with extended matching unstructured uncertainties. *International Journal of Robust and Nonlinear Control*, **22**, 645–675.

Nahid-Mobarakeh B, Meibody-Tabar F, and Sargos FM (2007) Back EMF estimation-based sensorless control of PMSM: robustness with respect to measurement errors and inverter irregularities. *IEEE Transactions on Industrial Electronics*, **43**(2), 485–494.

Ortega R, Praly L, Astolfi A, *et al.* (2011) Estimation of rotor position and speed of permanent magnet synchronous motors with guaranteed stability. *IEEE Transactions on Control Systems Technology*, **19**(3), 601–614.

Park RH (1929) Two-reaction theory of synchronous machines – generalized method of analysis – part I. *AIEE Transactions*, **48**, 716–727.

Rashed M, MacConnell PF.A, Stronach AF, and Acarnley P (2007) Sensorless indirect-rotor-field-orientation speed control of a permanent-magnet synchronous motor with stator-resistance estimation. *IEEE Transactions on Industrial Electronics*, **54**(3), 1664–1675.

Tomei P and Verrelli CM (2008) A nonlinear adaptive speed tracking control for sensorless permanent magnet step motors with unknown load torque. *International Journal of Adaptive Control and Signal Processing*, **22**(3), 266–288.

Tomei P and Verrelli CM (2011) Observer-based speed tracking control for sensorless permanent magnet synchronous motors with unknown load torque. *IEEE Transactions on Automatic Control*, **56**(6), 1484–1488.

Verrelli CM (2011a) Fourier series expansion for synchronization of permanent magnet electric motors. *Applied Mathematics and Computation*, **217**(9), 4502–4515.

Verrelli CM (2011b) Adaptive learning control for robotic manipulators driven by permanent magnet synchronous motors. *International Journal of Control*, **84**, 1024–1030.

Verrelli CM (2012) Synchronization of permanent magnet electric motors: new nonlinear advanced results. *Nonlinear Analysis: Real World Applications*, **13**(1), 395–409.

Zribi M and Chiasson JN (1991) Position control of a PM stepper motor by exact linearization. *IEEE Transactions on Automatic Control*, **36**(5), 620–625.

17

Robust Fault Detection for a Permanent-Magnet Synchronous Motor Using a Nonlinear Observer

Maria Letizia Corradini[1], Gianluca Ippoliti[2], and Giuseppe Orlando[2]
[1]*Scuola di Scienze e Tecnologie, Università di Camerino, Italy*
[2]*Dipartimento di Ingegneria dell'Informazione, Università Politecnica delle Marche, Italy*

17.1 Introduction

Permanent-magnet synchronous motor (PMSM) drives are currently extensively used in many industrial applications, where continuity of operation and reliability are major features to be pursued. Indeed, a fault arising in an industrial process may produce not only safety problems but results in increased costs due to lost production. As a consequence, fast and accurate diagnosis of failures in the drive system is important for preventing major damages to the motor and, mostly, to guarantee continuity of operation and minimize eventual machine downtime for maintenance.

Common faults of electrical machines are broadly classified as (Rosero *et al.* 2006; Kim *et al.* 2010):

- Mechanical faults, like static and/or dynamic air-gap irregularities, eccentricity, bearing and gearbox failures;
- Electrical faults, like stator faults resulting in the opening and shorting of one or more stator phase winding, abnormal connections, and demagnetization of the permanent magnet.

The most common electrical faults, however, are known as stator winding fault, and are caused by the breakdown of insulation as a result of the voltage, current, and thermal stress

AC Electric Motors Control: Advanced Design Techniques and Applications, First Edition. Edited by Fouad Giri.

acted on the stator winding (Kim *et al.* 2010). In this case, the early detection of the fault is important to avoid the propagation to more stator turns, in order to reduce repair costs and maintenance time. A number of papers are available in the literature addressing fault detection in the stator winding, and the most used approaches are based on wavelet transform (Cusido *et al.* 2008), negative sequence current (Quiroga *et al.* 2008), frequency analysis of line current (Rosero *et al.* 2006), experimental methods using current monitoring (Kim *et al.* 2010), artificial neural networks (Awadallah *et al.* 2005), and AI tools (Awadallah and Morcos 2003). None of these methods use the so-called model-based diagnosis, which is nonetheless one the most common techniques used in fault detection. According to this approach, a model is needed of the unsupervised process, in order to build a residual function able to signal any difference between nominal and faulty status. Unfortunately, real processes are characterized by model uncertainties, known as structured uncertainties, associated to parameter variations. It follows that any model-based fault detection technique should be made robust with respect to structured uncertainties, to avoid generation of false alarms. Furthermore, in the case of PMSM drives, the nonlinear character of the model hinders the use of well-known observers available for linear systems (Patton *et al.* 2000) for the generation of residuals, a nonlinear control technique being claimed for. In this context, it is worth mentioning the paper (Huangfu *et al.* 2008) where second order sliding modes are used for control and observation, under the assumption of stable zero dynamics for ensuring the existence of a standard sliding surface, and assuming the availability of the whole state vector. Note that parameter variations cannot be accounted for, albeit the recognized robustness of sliding modes, because standard feedback linearization is applied. A further paper deserving attention because model-based fault detection is considered is Liu and Carter (2005), but the quasi-dynamic approach is adopted there and nonlinearity and coupling affects are basically neglected.

The present paper proposes the adoption of a robust nonlinear observer of the rotor angular position and velocity, which can be used for fault detection purposes. Convergence of such observer is ensured by the enforcement of a sliding motion on given surfaces, based on motor currents, which are of course affected by all faults influencing stator currents and can easily detect them. Simulations with additive faults have been reported, proving the reliability of the proposed solution. Note that observer and control design are not performed in the $(d,\ q)$ reference frame but in the $(\alpha,\ \beta)$ frame, since any fault affecting the angular position measurement could invalidate the whole model and the consequent design.

17.2 Preliminaries

17.2.1 PMSM Modeling

In the (α, β) reference frame, the electrical equations of motion of a PMSM can be written as

$$\begin{cases} \dfrac{di_\alpha}{dt} &= -\dfrac{R}{L} i_\alpha + \omega_e \dfrac{\lambda_0}{L} \sin(\theta_e) + \dfrac{1}{L} v_\alpha, \\ \dfrac{di_\beta}{dt} &= -\dfrac{R}{L} i_\beta - \omega_e \dfrac{\lambda_0}{L} \cos(\theta_e) + \dfrac{1}{L} v_\beta, \end{cases} \tag{17.1}$$

where i_α and i_β are the respective stator currents; v_α and v_β are the respective stator voltages; R is the winding resistance and L is the winding inductance, λ_0 is the flux linkage of the

permanent magnet, θ_e and ω_e are the electrical angular position and speed, respectively, of the motor rotor.

The electrical torque T_e is given by

$$T_e = K_t(i_\beta \cos(\theta_e) - i_\alpha \sin(\theta_e)), \tag{17.2}$$

in which $K_t = \frac{3}{2}\lambda_0 N_r$ is the torque constant with N_r as the number of pole pairs.

For the electrical angular position/speed and the mechanical angular position/speed, the following relations hold:

$$N_r = \frac{\omega_e}{\omega_r} = \frac{\theta_e}{\theta_r}, \tag{17.3}$$

with θ_r denoting the mechanical angular position of the motor rotor. In the following it will be assumed that $N_r = 1$, therefore $\omega_e = \omega_r$.

17.3 Control Design

17.3.1 A Robust Observer of Rotor Angular Position and Velocity for the Tracking Problem

In standard drives, rotor position is given by encoder measurements, and rotor speed is usually estimated as the incremental ratio of encoder positions over one sampling period. In the following, a position and speed observer will be proposed ensuring the asymptotical vanishing of the observation error and of the tracking error, in the presence of bounded uncertainties affecting the coefficients of the dynamical model, usually largely inaccurate.

The mechanical motion equation is described by

$$J\dot{\omega}_r + B\omega_r = T_e - \tau, \tag{17.4}$$

$$\dot{\theta}_r = \omega_r, \tag{17.5}$$

where J is the total mechanical inertia of the the PMSM. The torque τ summarizes the effect of the external torque (generally known with large inaccuracy) and T_e is the electromagnetic torque. It is likely to introduce the following assumption.

Assumption 17.3.1 *The model parameters appearing in (17.4) are uncertain, with bounded uncertainty:*

$$J = \bar{J} + \Delta J; \quad B = \bar{B} + \Delta B; \quad \frac{\tau}{J} = \frac{\bar{\tau}}{\bar{J}} + \Delta\tau; \tag{17.6}$$

$$|\Delta J| \leq \rho_J; \quad |\Delta B| \leq \rho_B; \quad |\Delta\tau| \leq \rho_\tau; \tag{17.7}$$

The tracking problem is considered here, that is, the variable ω_e is required to track a known reference ω^*. Consider the following copy of the plant:

$$\begin{cases} \dfrac{d\hat{i}_\alpha}{dt} = -\dfrac{R}{L}\hat{i}_\alpha + \hat{\omega}_e \dfrac{\lambda_0}{L}\sin(\hat{\theta}_e) + \dfrac{1}{L}(v_\alpha + \nu_\alpha), \\ \dfrac{d\hat{i}_\beta}{dt} = -\dfrac{R}{L}\hat{i}_\beta - \hat{\omega}_e \dfrac{\lambda_0}{L}\cos(\hat{\theta}_e) + \dfrac{1}{L}(v_\beta + \nu_\beta), \\ \bar{J}\dot{\hat{\omega}}_e = -\bar{B}\hat{\omega}_e + K_t(\hat{i}_\beta \cos(\hat{\theta}_e) - \hat{i}_\alpha \sin(\hat{\theta}_e)) - \bar{\tau}, \\ \dot{\hat{\theta}}_e = \hat{\omega}_e. \end{cases} \tag{17.8}$$

The following result can be proved.

Theorem 17.3.2 *With reference to the plant (17.1), (17.4), (17.5), the observer (17.8) is able to robustly guarantee the asymptotic vanishing of the observation error and of the tracking error for a suitable choice of the control variables v_α, v_β and of the auxiliary inputs ν_α, ν_β.*

Proof: Consider the following sliding surfaces:

$$s_\alpha = i_\alpha - \hat{i}_\alpha = 0, \tag{17.9}$$

$$s_\beta = i_\beta - \hat{i}_\beta = 0. \tag{17.10}$$

It is straightforward to verify that a sliding motion can be enforced on each surface by the following auxiliary inputs:

$$\nu_\alpha = -R(i_\alpha - \hat{i}_\alpha) + \left(\omega_e^M + |\hat{\omega}_e|\right)\lambda_0 sign(s_\alpha), \tag{17.11}$$

$$\nu_\beta = -R(i_\beta - \hat{i}_\beta) + \left(\omega_e^M + |\hat{\omega}_e|\right)\lambda_0 sign(s_\beta), \tag{17.12}$$

where it has been taken into account that physical constraints of the device are such that a maximum achievable velocity ω_e^M and a maximum admissible nominal torque τ^M exist. Once sliding motions on surfaces (17.9) and (17.10) have been established (this can be forced within a finite time t_s), one has the obvious consequence that it holds

$$\frac{di_\alpha}{dt} - \frac{d\hat{i}_\alpha}{dt} = -\frac{\lambda_0}{L}(\hat{\omega}_e \sin(\hat{\theta}_e) - \omega_e \sin(\theta_e)) = 0, \tag{17.13}$$

$$\frac{di_\beta}{dt} - \frac{d\hat{i}_\beta}{dt} = -\frac{\lambda_0}{L}(\hat{\omega}_e \cos(\hat{\theta}_e) - \omega_e \cos(\theta_e)) = 0. \tag{17.14}$$

This implying that

$$\omega_e = \hat{\omega}_e,$$

that is, that the observation error vanishes.

To guarantee the robust tracking of the assigned reference, consider the following sliding surface:

$$s_\omega = \omega^* - \hat{\omega}_e + \lambda_1(\theta^* - \hat{\theta}_e) = 0 \quad \lambda_1 \geq 0, \tag{17.15}$$

whose derivative is

$$\dot{s}_\omega = \dot{\omega}^* + \frac{\bar{B}}{\bar{J}}\hat{\omega}_e - \frac{K_t}{\bar{J}}(i_\beta \cos(\hat{\theta}_e) - i_\alpha \sin(\hat{\theta}_e)) + \frac{\bar{\tau}}{\bar{J}} + \lambda_1(\omega^* - \hat{\omega}_e). \tag{17.16}$$

According to the previous expression, one can consider two reference currents: $i_\beta^* = I^*(t)\cos(\hat{\theta}_e)$ and $i_\alpha^* = -I^*(t)\sin(\hat{\theta}_e)$, whose tracking will be ensured later and where $I^*(t)$ is to be determined. When $i_\alpha = i_\alpha^* = -I^*(t)\sin(\hat{\theta}_e)$ and $i_\beta = i_\beta^* = I^*(t)\cos(\hat{\theta}_e)$, one has

$$\dot{s}_\omega = \dot{\omega}^* + \frac{\bar{B}}{\bar{J}}\hat{\omega}_e - \frac{K_t}{\bar{J}}I^*(t) + \frac{\bar{\tau}}{\bar{J}} + \lambda_1(\omega^* - \hat{\omega}_e), \tag{17.17}$$

and choosing $I^*(t)$ as follows:

$$\frac{K_t}{\bar{J}}I^*(t) = \dot{\omega}^* + \frac{\bar{B}}{\bar{J}}\hat{\omega}_e + \frac{\bar{\tau}}{\bar{J}} + \lambda_1(\omega^* - \hat{\omega}_e), \tag{17.18}$$

the condition $\dot{s}_\omega = 0$ is guaranteed.

The imposition of the conditions $i_\alpha = i_\alpha^*$ and $i_\beta = i_\beta^*$ can be easily carried out by considering the following Lyapunov function:

$$W = \frac{1}{2}(i_\alpha - i_\alpha^*)^2 + \frac{1}{2}(i_\beta - i_\beta^*)^2, \tag{17.19}$$

and imposing that $\dot{W} < 0$, that is,

$$\begin{aligned}\dot{W} = {} & (i_\alpha + I(t)\sin(\hat{\theta}_e))\left[-\frac{R}{L}i_\alpha + \omega_e\frac{\lambda_0}{L}\sin(\theta_e) + \frac{1}{L}v_\alpha + \dot{I}(t)\sin(\hat{\theta}_e) + I(t)\hat{\omega}_e\cos(\hat{\theta}_e)\right] \\ & + (i_\beta - I(t)\cos(\hat{\theta}_e))\left[-\frac{R}{L}i_\beta - \omega_e\frac{\lambda_0}{L}\cos(\theta_e) + \frac{1}{L}v_\beta - \dot{I}(t)\cos(\hat{\theta}_e) + I(t)\hat{\omega}_e\sin(\hat{\theta}_e)\right] < 0.\end{aligned}$$

Splitting the previous inequality into the following ones:

$$(i_\alpha + I(t)\sin(\hat{\theta}_e))\left[-\frac{R}{L}i_\alpha + \omega_e\frac{\lambda_0}{L}\sin(\theta_e) + \frac{1}{L}v_\alpha + \dot{I}(t)\sin(\hat{\theta}_e) + I(t)\hat{\omega}_e\cos(\hat{\theta}_e)\right] < 0, \tag{17.20}$$

$$(i_\beta - I(t)\cos(\hat{\theta}_e))\left[-\frac{R}{L}i_\beta - \omega_e\frac{\lambda_0}{L}\cos(\theta_e) + \frac{1}{L}v_\beta - \dot{I}(t)\cos(\hat{\theta}_e) + I(t)\hat{\omega}_e\sin(\hat{\theta}_e)\right] < 0, \tag{17.21}$$

and using the fact that both $\hat{\theta}_e$ and $\hat{\omega}_e$ tend to θ_e and ω_e, respectively, possibly within a finite time (as previously proved), it turns out immediately that a possible solution is the following:

$$\frac{1}{L}v_\alpha = -\dot{I}(t)\sin(\hat{\theta}_e) - I(t)\hat{\omega}_e\cos(\hat{\theta}_e) + \frac{R}{L}i_\alpha - \zeta\left(\omega_e^M\frac{\lambda_0}{L} + \eta\right)sign(i_\alpha + I(t)\sin(\hat{\theta}_e)), \tag{17.22}$$

$$\frac{1}{L}v_\beta = \dot{I}(t)\cos(\hat{\theta}_e) - I(t)\hat{\omega}_e\sin(\hat{\theta}_e) + \frac{R}{L}i_\beta - \zeta\left(\omega_e^M\frac{\lambda_0}{L} + \eta\right)sign(i_\beta - I(t)\cos(\hat{\theta}_e)), \tag{17.23}$$

with $\zeta > 1$, $\eta > 0$. □

17.4 The Faulty Case

Variations of stator currents with respect to the healthy behavior may arise due to several reasons, such as interturn short-circuit, inherent motor instrumentation asymmetries, load variations, and unbalanced supply voltages (Quiroga *et al.* 2008). Such conditions can be reflected in negative sequence components, whose spectral behavior at high frequency has been largely studied in order to discriminate, not always easily, between fault occurrence and load fluctuation (Quiroga *et al.* 2008). This section is devoted to show that the introduction of the previously described observer allows to easily detect variations of stator currents with respect to the healthy behavior, regardless of the presence of load variations within a prescribed range.

Consider the case of additive faults affecting currents, that is, such that the faulty currents $\bar{i}_\alpha$ and $\bar{i}_\beta$ have the form

$$\begin{cases}\bar{i}_\alpha = i_\alpha + f_\alpha(t),\\ \bar{i}_\beta = i_\beta + f_\beta(t),\end{cases} \tag{17.24}$$

where $f_\alpha(t)$ and $f_\beta(t)$ represent (possibly time-dependent) perturbations affecting the stator currents acting from a given time on

$$f_\alpha(t) = f_1(t)\delta_{-1}(t - T_{f\alpha}); \qquad |f_\alpha(t)| \le \rho_{f\alpha};$$
$$f_\beta(t) = f_2(t)\delta_{-1}(t - T_{f\beta}); \qquad |f_\beta(t)| \le \rho_{f\beta};$$

$f_1(t)$ and $f_2(t)$ being unknown but bounded functions, and $T_{f\alpha}$ and $T_{f\beta}$ representing the times of occurrence of the faults. It is straightforward that in the perturbed case, the auxiliary inputs (17.11) and (17.12) are unable to *necessarily* enforce sliding motions on surfaces (17.9) and (17.10), since the measure of variable i_α is not reliable, due to the fault. Therefore $\hat{\omega}_e$ deviates from the actual ω_e. Consequently, with reference to the variable $I(t)$, it is verified that the variable $I^*(t)$ (17.18) deviates from the variable corresponding to the vanishing of the surface s_ω (17.15), and the vanishing of W given by (17.19) is no longer ensured.

Corollary 17.4.1 *With reference to the plant (17.1) fed by the controllers (17.22) and (17.23), whenever it holds $W(\tau) \neq 0$ for any time $\tau \geq \bar{t}$ then a fault has occurred at a time $t \leq \tau$, $\bar{t}$ being the reaching time for the surface $W = 0$, W being given by (17.19).*

Proof: Recalling the proof of the previous result, it is verified that, whenever the auxiliary inputs (17.11) and (17.12) are unable to enforce sliding motions on surfaces (17.9) and (17.10), then $\hat{\omega}_e$ deviates from the actual ω_e and the described control policy cannot ensure the vanishing of W. In this case one can deduce that an extra term, not accounted for, has perturbed the sliding mode. Note that load variations can be excluded since they are allowed as long as they are below the admissible threshold τ^M. □

17.5 Simulation Tests

Simulations have been performed using technical data of the Technosoft MBE.300.E500 PMSM, as a preliminary step before experimental implementation. The motor catalog electric and mechanical parameters are given in Table 17.1.

Some of the performed speed-tracking tests are shown in Figures 17.1, 17.2, 17.3, 17.4, and 17.5. The following conditions have been used for simulations:

- A reference speed trajectory of the form $\omega^*(t) = 150 * \sin(\frac{2\pi}{0.1}t)$.
- A nominal load torque of 0.01 Kg, with a 20% variation.
- 20% parameter variations applied to nominal values of parameters B, J.
- Boundary layers have been used to avoid chattering.

Table 17.1 Technosoft MBE.300.E500 PMSM parameters

Coil-dependent parameters		
Phase-phase resistance	Ω	8.61
Phase-phase inductance	mH	07.13
Back-EMF constant	V/1000 rpm	3.86
Torque constant	mNm/A	36.8
Pole pairs	–	1
Dynamic parameters		
Rated voltage	V	36
Maximum voltage	V	58
No-load current	mA	73.2
No-load speed	rpm	9170
Maximum continuous current (at 5000 rpm)	mA	913
Maximum continuous torque (at 5000 rpm)	mNm	30
Maximum permissible speed	rpm	15000
Peak torque (stall)	mNm	154
Mechanical parameters		
Rotor inertia	$Kgm^2\ 10^{-7}$	11
Mechanical time constant	ms	7

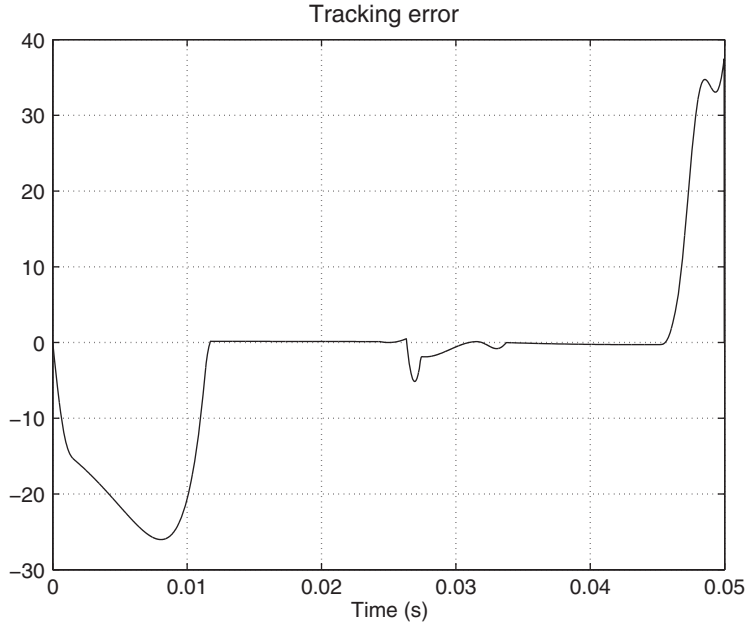

Figure 17.1 Tracking error

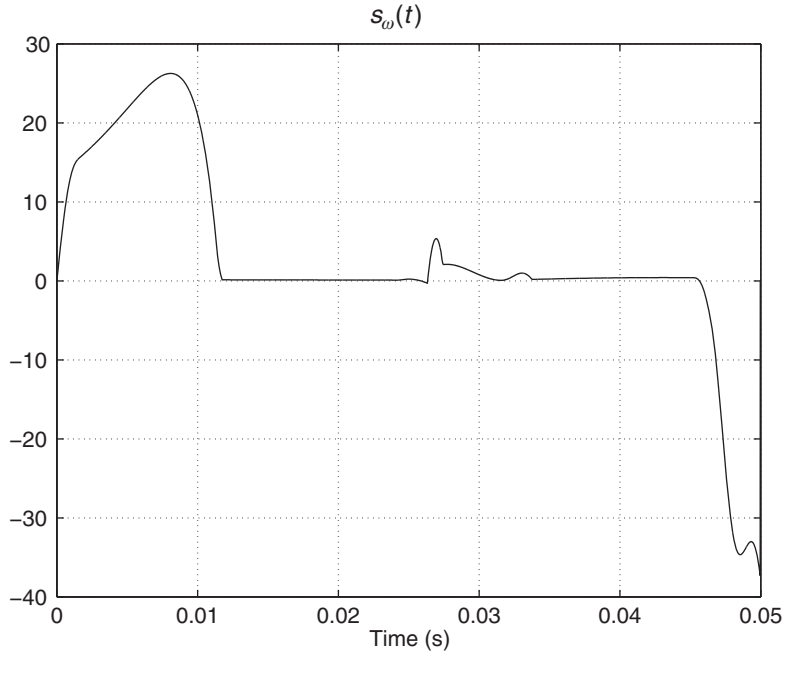

Figure 17.2 Sliding surface s_ω (17.15)

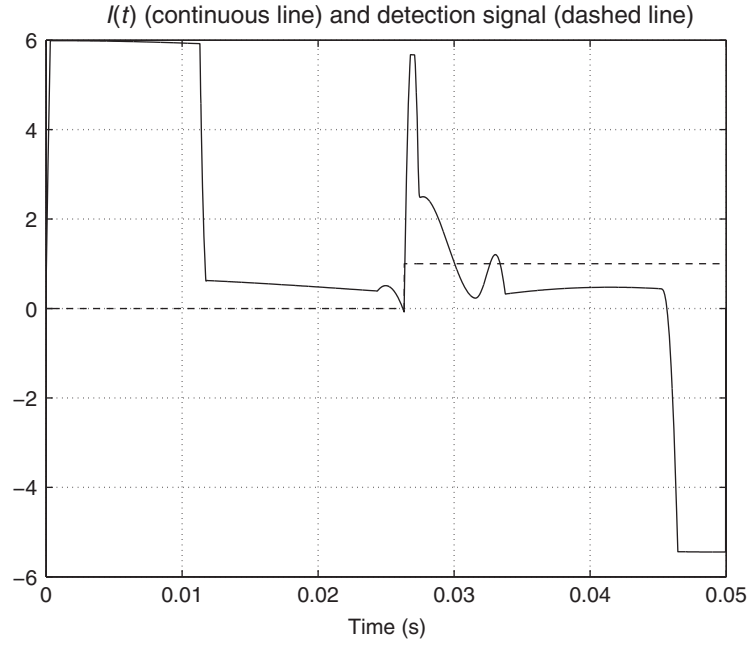

Figure 17.3 Variable $I(t)$ (17.18) along with the output of the detection device (dashed line)

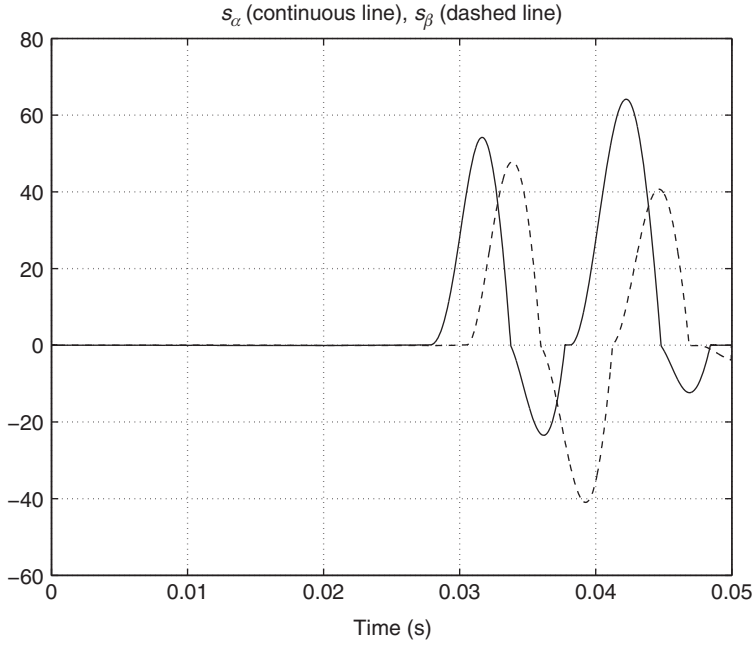

Figure 17.4 Sliding surfaces s_α (continuous line), s_β (dashed line)

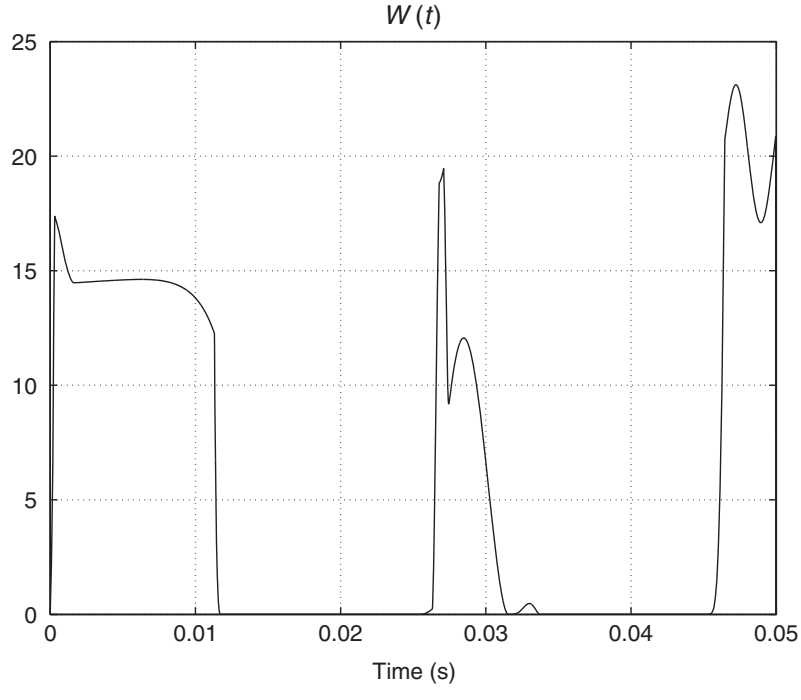

Figure 17.5 Lyapunov function $W(t)$ (17.19)

Moreover, a time-varying fault has been considered to affect current i_α additively as follows:

$$\bar{i}_\alpha = i_\alpha + f_\alpha(t) = i_\alpha + \frac{1}{2}\left[1 - e^{-\left(\frac{t-0.025}{0.001}\right)}\right] \qquad \text{for } t > 0.025 \text{ s}$$

in order to simulate a progressive reduction of effectiveness.

Figure 17.1 shows the tracking performance obtained considering the sinusoidal velocity profile. Notice the presence of an initial transient of duration of nearly $t_s = 0.012$ s due to the reaching phase of the sliding motion. This fact is also particularly evident in Figure 17.2 showing the sliding surface s_ω (17.15).

Figure 17.3 reports the variable $I(t)$ (17.18), showing a peak at time $t_f = 0.0263$ s, which signals the detection of the time-varying fault. To emphasize detection, a dotted variable has been reported in the picture when detection is made. Finally, Figure 17.4 depicts the sliding surfaces s_α and s_β, showing a relevant activity far from zero after the fault occurrence, and Figure 17.5 shows the Lyapunov function (17.19).

References

Awadallah M and Morcos M (2003) Application of AI tools in fault diagnosis of electrical machines and drives-an overview. *IEEE Transactions on Energy Conversion*, **18**(2), 245–251.

Awadallah M, Morcos M, Gopalakrishnan S, and Nehl T (2005) A neuro-fuzzy approach to automatic diagnosis and location of stator inter-turn faults in CSI-fed PM brushless DC motors. *IEEE Transactions on Energy Conversion*, **20**(2), 253–259.

Cusido J, Romeral L, Ortega J, *et al.* (2008) Fault detection in induction machines using power spectral density in wavelet decomposition. *IEEE Transactions on Industrial Electronics*, **55**(2), 633–643.

Huangfu Y, Liu W, and Ma R (2008) Permanent magnet synchronous motor fault detection and isolation using second order sliding mode observer. *3rd IEEE Conference on Industrial Electronics and Applications*, pp. 639–644.

Kim KH, Choi DU, Gu BG, and Jung IS (2010) Fault model and performance evaluation of an inverter fed permanent magnet synchronous motor under winding shorted turn and inverter switch open. *IET Electric Power Applications*, **4**(4), 214–225.

Liu L and Carter DA (2005) On-line identification and robust fault diagnosis for nonlinear pmsm drives. *2005 American Control Conference*, pp. 2023–2027.

Patton RJ, Frank PM, and Clark RN (ed.) (2000) *Issues of Fault Diagnosis for Dynamic Systems*. Springer-Verlag, New York.

Quiroga J, Liu L, and Carter DA (2008) Fuzzy logic based fault detection of PMSM stator winding short and long fluctuations using negative sequence analysis. *2008 American Control Conference*, pp. 4262–4267.

Rosero J, Cusido J, Garcia A, *et al.* (2006) Broken bearings and eccentricity fault detection for a permanent magnet synchronous motor. *32nd Annual Conference on IEEE Industrial Electronics, IECON 2006*, pp. 964–969.

18

On Digitization of Variable Structure Control for Permanent Magnet Synchronous Motors

Yong Feng[1,2], Xinghuo Yu[2], and Fengling Han[3]
[1]*Department of Electrical Engineering, Harbin Institute of Technology, China*
[2]*School of Electrical and Computer Engineering, RMIT University, Australia*
[3]*School of Computer Science and Information Technology, RMIT University, Australia*

18.1 Introduction

AC Motors have been widely used in various applications, such as factory automation, household electrical appliances, computers, CNC (Computer Numerical Control) machine tools, industrial robots, high-speed aerospace drives and high-technology tools used for outer space in the past decades (Jang *et al.* 2003; Zhang *et al*. 2006; Feng *et al.* 2011). There are two main types of AC motors depending on the principle of operation, the induction motor (IM) and the permanent magnet synchronous motor (PMSM). The rotor of IM includes a winding, while the rotor of a PMSM is a permanent magnet and has no winding. The rotor of PMSMs turns at the same speed as the rotating synchronous magnetic field of the stator which is generated by the stator currents. Unlike PMSMs, an IM always turns slightly slower than the rotating stator magnetic field generated by the stator currents. The difference is called the slip, which generates the torque of the motor (Trzynadlowski 2001).

IMs are generally used for fans, pumps, compressors, elevators, hydraulics, machinery, and actuation systems as well as industrial, aerospace, and medical applications because of their simple design, no brushes, rugged construction, load-bearing capacity, flexibility, relatively low cost, and characteristically long operating life.

AC Electric Motors Control: Advanced Design Techniques and Applications, First Edition. Edited by Fouad Giri.

PMSMs, on the other hand, can be used in specialized high-performance applications requiring smooth and fast operation, and demanding low torque ripple because PMSMs offer the advantages of relatively high power density, high efficiency, low rotor inertia, fast dynamics, good compatibility, reduced rotor losses, efficient heat dissipation structure, reduced motor size, the elimination of brushes, ease of control, and minimal maintenance requirements. The most important application of PMSMs is servo systems commonly used in a positioning application that requires high instantaneous torque response, lower torque ripple, a wide adjustable speed range, and excellent speed regulation. Since PMSMs are mainly used in specialized high-performance applications, this chapter focuses on the control of PMSM servo systems, which play an important role in achieving the objective of high precision, high speed, high efficiency, and high reliability in many practical applications. PMSMs are multivariable, time-variant, strong coupling, and uncertain nonlinear systems. The control of PMSM servo systems aims at the goal of good performances of servo systems subjected to parameter variations and external load disturbances. Many control methods have been proposed to improve the robustness and dynamic performance of PMSM servo systems, such as the adaptive control, fuzzy control, artificial neural networks, and the active disturbance rejection control (Rahman and Hoque 1998; Baik *et al.* 2000). Among them, sliding mode control method does not request a high accurate mathematical model, and is strongly robust with respect to the system parameter perturbation and external disturbances (Edwards and Spurgeon 1998; Utkin *et al.* 1999).

18.2 Control System of PMSM

Vector control is an important technique used for the control of AC motors. It makes possible the application of AC servo systems in high-performance tasks where traditionally only DC servo systems were applied. A PMSM employing vector control can be used for high-performance servo applications. A typical structure of the vector control system of the PMSM is shown in Figure 18.1. There are three feedback loops in the PMSM servo system: position control loop, velocity control loop, and current control loop. An encoder, a tachometer, or a resolver can be used to measure the speed of the rotor. An encoder can be used to measure the position of the rotor. Generally, the measurement of both the position and speed of the rotor can be done using an encoder in practical applications.

The design task of a PMSM servo system is to design three controllers, position controller, speed controller and current controller, and a filter in speed loop. The design process of the three controllers is from the inner loop (current loop) to outer loop (position loop). Compared to the velocity controller, the design of the current controller and the position controller are usually easy. The parameters of the current controller mainly depend on the measureable parameters of the motor stator, such as the inductance and resistor. Firstly, the current controller is designed. Secondly, the speed controller is designed based on the current closed-loop control system. Finally, the position controller is designed, which is easy because the speed closed-loop control system has been regulated well according to some classical model, such as a second-order system. Compared to the current controller and the position controller, the design of the velocity controller is more challenging, since mechanical resonances, backlash, and friction in servo systems mainly influence the performance and stability of the velocity loop. In order to suppress the mechanical resonance in servo systems, a notch filter is generally utilized in

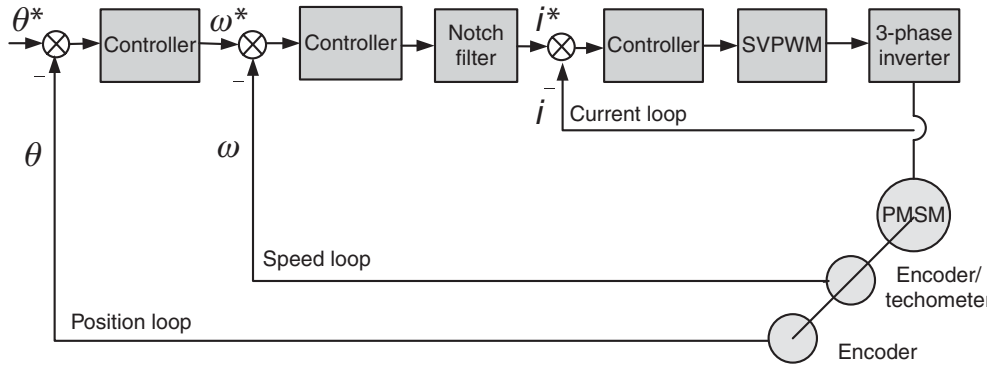

Figure 18.1 A typical structure of PMSM servo systems

the velocity loop to eliminate a single frequency or narrow band of frequencies, as shown in Figure 18.1.

18.3 Dynamic Model of PMSM

In order to derive the dynamic model of PMSMs, the following assumptions are made:

(a) The induced EMF is sinusoidal.
(b) The eddy current and magnetic hysteresis loss are negligible.
(c) The magnetic saturation is neglected.

With the above assumptions and taking the rotor coordinates (d–q axes) of the motor as the reference coordinates, the dynamic model for the PMSM can be expressed in the state-space by both an electrical model (Su *et al.* 2005; Feng *et al.* 2011):

$$\begin{cases} \dot{i}_d = -\frac{R_s}{L} i_d + p\omega i_q + \frac{u_d}{L}, \\ \dot{i}_q = -p\omega i_d - \frac{R_s}{L} i_q - \frac{p\psi_f}{L}\omega + \frac{u_q}{L}, \end{cases} \tag{18.1}$$

and a mechanical model (Su *et al.* 2005; Feng *et al.* 2011):

$$\begin{cases} \frac{d\theta}{dt} = \omega, \\ J\frac{d\omega}{dt} + B\omega + T_L = T_M, \end{cases} \tag{18.2}$$

where u_d and u_q are the d–q axes stator voltages, i_d and i_q the d–q axes stator currents, L the d–q axes inductance, R_s the stator winding resistance, ψ_f the rotor flux, p the number of pole pairs, T_M the driving torque of the motor (Nm), T_L the load torque of the motor (Nm), J the moment of inertia of the motor rotor and the load (kgm^2), B the viscous damping coefficient, ω the angular speed of the motor (rad/s), and θ the angular position of the motor (rad). The

driving torque T_M in equation (18.2) can be expressed by the following equation (Zhu *et al.* 2000):

$$T_M = \frac{3p}{2}\left(\psi_f i_q + (L_d - L_q) i_d i_q\right), \tag{18.3}$$

where L_d and L_q denote the d- and q-axis inductances, respectively. According to the principle of the vector control of PMSMs, the d-axis current i_d in equations (18.1) and (18.3) should be controlled to be zero in the current loop of the motor system. Therefore, equation (18.3) can be rewritten as

$$T_M = \frac{3p}{2}\psi_f i_q = k_q i_q, \tag{18.4}$$

where $k_q = (3p/2)\psi_f$ denotes an electrical-mechanical energy conversion constant, or simply a torque constant, which can be determined by using the experimental data. It can be seen from equation (18.4) that the driving torque T_M is only proportional to i_q and k_q is a constant, which means that T_M can be controlled only by the q-axis current i_q.

18.4 PI Control of PMSM Servo System

PMSM servo systems generally utilize PI controllers in industrial applications. The typical structure of PI control-based PMSM servo system is shown in Figure 18.2. The vector control technique is applied in the current control loop. Three phase currents of the motor stator (i_a, i_b, i_c) are transformed into the direct and quadrature components i_d and i_q in two rotor coordinates (d–q axes). In order to realize the maximization of the driving torque of a PMSM, the stator magnetic field should be orientated perpendicularly to the rotor field, which can be implemented by forcing i_d to zero. On the other hand, i_q is the component of the stator flux that is producing the driving torque. In order to overcome the integral saturation of PI controller in

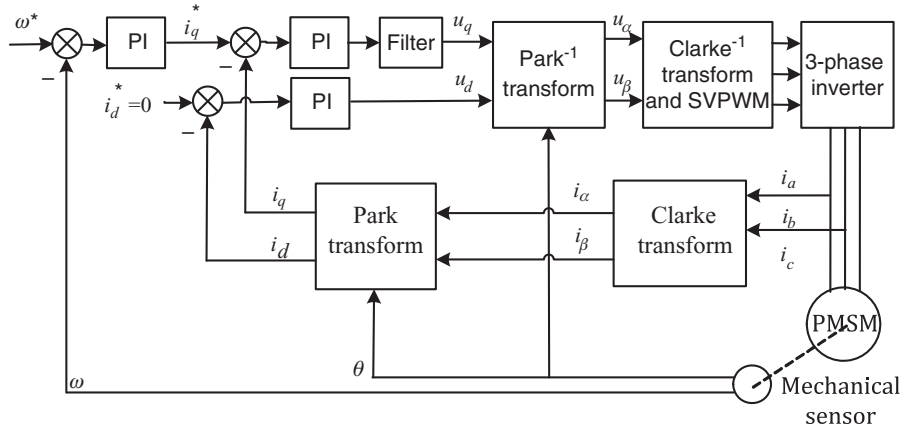

Figure 18.2 PID control of PMSM servo system

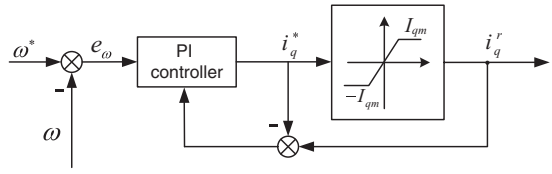

Figure 18.3 PI controller with anti-reset windup structure

Figure 18.2, the anti-reset windup method (Shin 1998) can be used. The PI speed controller with anti-reset windup structure is shown in Figure 18.3. The algorithm of the controller can be expressed by the following equation:

$$i_q^* = k_p e_\omega + \left[e_\omega \frac{k_p}{\tau_i} - \frac{1}{k_c}(i_q^* - i_q^r) \right] \frac{1}{s}, \tag{18.5}$$

where, $k_c > 0$ is the compensation coefficient, both i_q^* and i_q^r are depicted in Figure 18.3.

Equation (18.5) can be rewritten as follows:

$$i_q^* = \frac{k_c k_p}{\tau_i} \frac{\tau_i s + 1}{k_c s + 1} e_\omega + \frac{1}{k_c s + 1} i_q^r. \tag{18.6}$$

18.5 High-Order Terminal Sliding-Mode Control of PMSM Servo System

In order to improve the performances of PMSM servo systems, such as the precision, response speed, and robustness, high-order terminal sliding-mode (TSM) control strategy is employed to control PMSM servo systems (Feng *et al.* 2002, 2004, 2007, 2009). The structure of the system is shown in Figure 18.4 (Zheng *et al.* 2008).

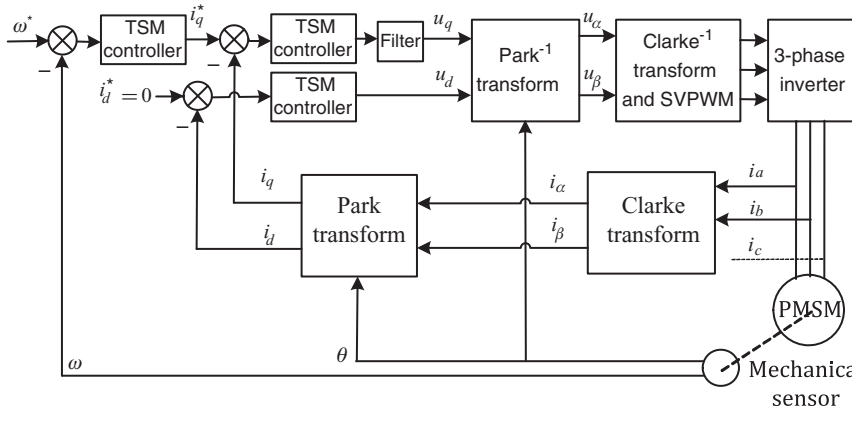

Figure 18.4 High-order TSM control of PMSM servo system

18.5.1 Velocity Controller Design

The design of the velocity controller can be described step by step as follows:

1. A TSM manifold is chosen as follows:

$$l_\omega = \dot{e}_\omega + \gamma_\omega e_\omega^{q_\omega/p_\omega}, \tag{18.7}$$

   where $e_\omega = \omega^* - \omega$ denotes the motor speed error, ω^* the desired motor speed.
2. The TSM control strategies are designed as follows:

$$i_q^* = i_{qeq} + i_{qn}, \tag{18.8}$$

$$i_{qeq} = \frac{J}{k_q}\left(\dot{\omega}^* + \gamma_\omega e_\omega q_\omega / p_\omega + \frac{B}{k_q}\right), \tag{18.9}$$

$$\dot{i}_{qn} + T_\omega i_{qn} = v_\omega, \tag{18.10}$$

$$v_\omega = (k_{T\omega} + k_{dL} + \eta_\omega) sgn(l_\omega), \tag{18.11}$$

   where $k_{T\omega}$, T_ω, and k_{dL} are constants, which satisfy the following condition:

$$\left|i_{qn}^*\right| < \frac{k_{T\omega}}{T_\omega}, \tag{18.12}$$

$$\left|\dot{T}_L^*\right| < k_{dL} k_q. \tag{18.13}$$

   $\eta_\omega > 0$ is a design parameter. The error speed of the motor $e_\omega = \omega^* - \omega$ will converge to zero in finite time.

The high-order sliding-mode technique is employed in the control strategies in equations (18.8)–(18.11). Although a switching function exists in equation (18.11), the actual output signal of the speed controller in equation (18.8) is softened to be smooth, hence there is no chattering phenomenon in the TSM controller.

18.5.2 q-Axis Current Controller Design

1. A TSM manifold is chosen as follows:

$$s_q = \dot{e}_q + \gamma_q e_q^{q_q/p_q}, \tag{18.14}$$

   where, $\gamma_q > 0$, p_q and q_q are odds, $1 < p_q/q_q < 2$; $e_q = i_q^* - i_q$ is the q-axis current error; i_q^* is the desired q-axis current.
2. The control law is designed as follows:

$$u_q = u_{qeq} + u_{qn}, \tag{18.15}$$

$$u_{qeq} = L\dot{i}_q^* + Lp\omega i_d + R_s i_q + p\psi_f \omega + L\gamma_q e_q^{q_q/p_q}, \tag{18.16}$$

$$\dot{u}_{qn} + T_q u_{qn} = v_{qn}, \tag{18.17}$$

$$v_{qn} = (k_{T_q} + \eta_q) sgn(s_q), \tag{18.18}$$

where $\eta_q > 0$ is a design parameter; k_{Tq} and T_q are constants, which satisfy the following condition:

$$\left|u_{qn}\right| < \frac{k_{T_q}}{T_q}. \tag{18.19}$$

The q-axis current controller can guarantee the q-axis current converge to its desired reference in finite time.

18.5.3 d-Axis Current Controller Design

1. A nonsingular TSM (NTSM) manifold is chosen as follows:

$$s_d = \dot{e}_d + \gamma_d e_d^{q_d/p_d}, \tag{18.20}$$

where, $\gamma_d > 0$, p_d and q_d are odds, $1 < p_d/q_d < 2$; $e_d = i_d^* - i_d = -i_d$ is the current error; $i_d^* = 0$ is the desired current;

2. The control law is designed as follows:

$$u_d = u_{deq} + u_{dn}, \tag{18.21}$$

$$u_{deq} = R_s i_d - Lp\omega i_q + L\gamma_d e_d^{q_d/p_d}, \tag{18.22}$$

$$\dot{u}_{dn} + T_d u_{dn} = v_{dn}, \tag{18.23}$$

$$v_{dn} = (k_{T_d} + \eta_d) sgn(s_d), \tag{18.24}$$

where $\eta_d > 0$ is a design parameter; k_{Td} and T_d are constants, which satisfy the following condition:

$$|u_{dn}| < \frac{k_{T_d}}{T_d}. \tag{18.25}$$

The d-axis current controller can guarantee the d-axis current converge to its desired reference in finite time.

18.5.4 Simulations

Some simulations are carried out for evaluating the TSM control strategies of PMSM servo systems. The parameters of the PMSM are $P_N = 1.5$ kW, $n_N = 1000$ rpm, $I_N = 3.5$ A, $U_N = 380$ V, $p = 3$, $R_s = 2.875\ \Omega$, $L = 33$ mH, $J = 0.011$ kgm^2, $B = 0.002$, $\psi_f = 0.8$ Wb. The q-axis current limit is $I_{q\max} = 4$ A. The simulation results of PI controllers and TSM controllers are shown in Figures 18.5 and 18.6. The motor speed responses for the different perturbation of the inertia, $\Delta J = \pm 0.5J$, are depicted in Figure 18.5. The motor speed responses for the different perturbation of the stator flux, $\Delta\psi_f = \pm 0.2\psi_f$, are displayed in Figure 18.6. It can be seen from these simulation results that the robustness of the TSM controller is better than that of the PI controllers.

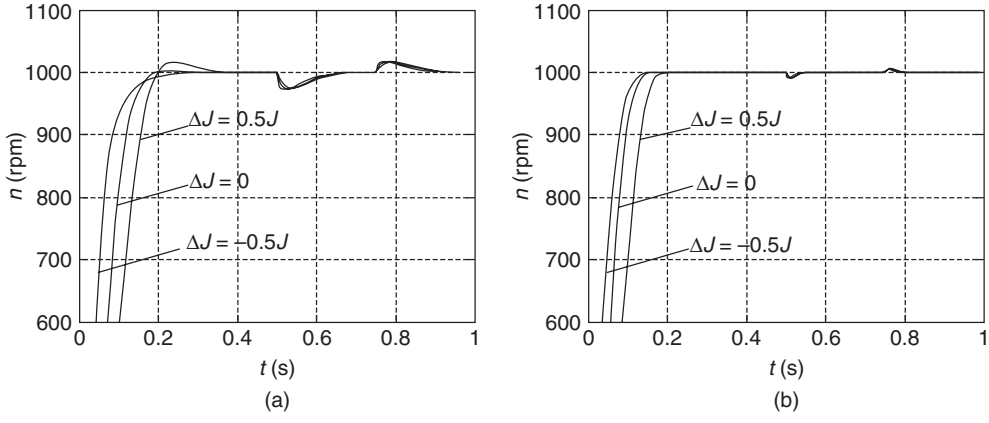

Figure 18.5 Motor speed response when J has a perturbation: (a) PI control; (b) high-order TSM control

18.6 Sliding-Mode-Based Mechanical Resonance Suppressing Method

Mechanical resonance is one of the most common problems when trying to improve the dynamic response speed and accuracy of servo systems. It is usually caused by a combination of high servo gains and a flexible coupling between the motor and load, such as drive shafts, belts, gears, harmonic speed changer, and so on. These transmission mechanisms have a finite stiffness, and a pair of conjugate complex poles is introduced in the transfer function of the system. The phenomenon of mechanical resonance can deteriorate the system stability, damage motors and transmission mechanisms, and reduce the system reliability. However, in practical applications, the phenomenon is often neglected or considered to be unmodeled dynamics, so the bandwidth of the system is limited by the resonant frequency (Zheng *et al.*

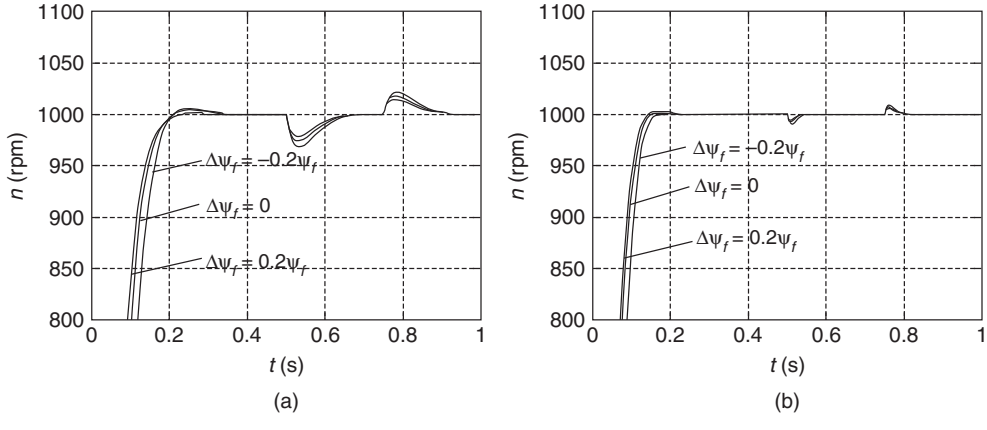

Figure 18.6 Motor speed response when ψ_f has a perturbation: (a) PI control; (b) high-order TSM control

2007; Zheng and Feng 2008). Three kinds of methods have been proposed to suppress the phenomenon of mechanical resonance. The first method is to use filter, as shown in Figure 18.1. The low-pass filter is easy to use, but inefficient for the commonly found case of low-frequency resonances, and it introduces the phase lag (Ellis and Lorenz 2000). The notch filter is utilized to reduce the effects of resonance in Schmidt and Rehm (1999). However, the system is sensitive to parameter changes. If the mechanical parameters such as load inertia or spring constant changes, the notch filter may be ineffective. The second method is to use the motor acceleration feedback (Schmidt and Lorenz 1992; Lee *et al.* 1995). Acceleration feedback can reduce the sensitivity to mechanical resonance, since it can increase the motor inertia equivalently. This method is robust, but the system response becomes slow to the input signal. On the other hand, the method is limited by the cost of the acceleration transducer and the application conditions. The third method is to use the observer of the motor acceleration or load torque (Ji and Sul 1995; Valenzuela *et al.* 2005). However, they still have disadvantages such as high dependency on system models. This chapter describes a TSM based mechanical resonance suppressing method (Zheng *et al.* 2007; Zheng and Feng 2008). TSM manifolds are designed for stator currents and the load speed, respectively, to realize convergence in finite time and obtain better tracking precision. A full-order state observer is applied to estimate the load speed and the shaft torsion angle which cannot be measured directly in applications. And a high-order sliding-mode control is designed to guarantee the stability of the system. Compared to the acceleration feedback and the notch filter method, the TSM controller can suppress mechanical resonance more effectively, increase convergence speed of the system, and reduce the overshoot. In addition, it is robust and does not need to use the acceleration transducer. Based on the vector control principle, high-order TSM controllers are designed for two stator currents i_d, i_q, and the load speed ω_L, respectively, as shown in Figure 18.7. $\Delta\hat{\theta}$ is the estimate of the shaft torsion angle $\Delta\theta = \theta_M - \theta_L$, and $\hat{\omega}_L$ is the estimate of ω_L. A

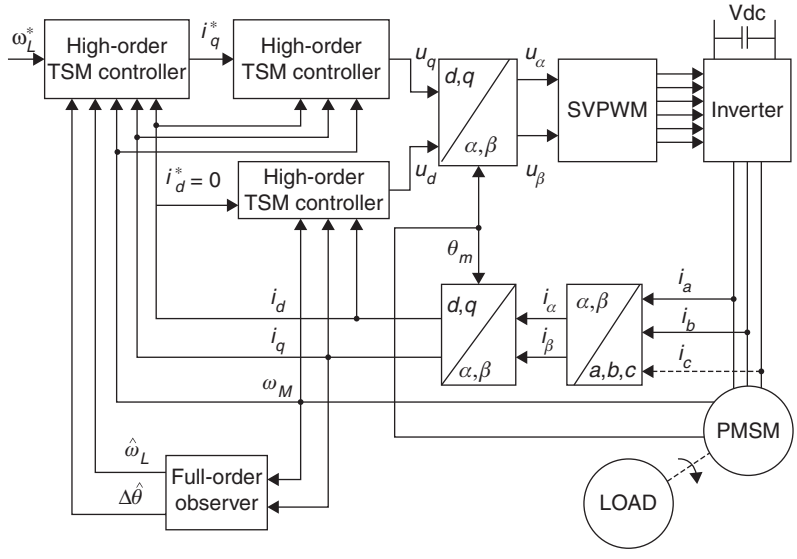

Figure 18.7 PMSM servo system with mechanical resonance suppressing

full-order state observer is utilized to obtain the two variables, for they are difficult to measure directly in applications but the stator currents, the angular position and angular velocity of the motor are measurable.

18.6.1 Load Speed Controller Design

Suppose that e_ω is the error between the given value and the actual value of the load speed i.e.

$$e_\omega = \omega_L^* - \omega_L. \tag{18.26}$$

Then, the error system is:

$$\dot{e}_\omega = \dot{\omega}_L^* - [K_s \Delta\theta + b_s(\omega_M - \omega_L) - T_L]\frac{1}{J_L}. \tag{18.27}$$

A linear sliding mode (LSM) manifold and a TSM manifold are designed as follows:

$$s_\omega = e_\omega + \beta_\omega \dot{e}_\omega, \tag{18.28}$$

$$l_\omega = s_\omega + \gamma_\omega \dot{s}_\omega^{p_\omega/q_\omega}, \tag{18.29}$$

where, $\beta_\omega > 0$, $\gamma_\omega > 0$, $p_\omega > 0$, and $q_\omega > 0$ are odds, $1 < p_\omega/q_\omega < 2$. In order to eliminate chattering, a third-order sliding mode controller is designed step by step as followings (Zheng *et al.* 2007; Zheng and Feng 2008):

1. The LSM manifold and the TSM manifold are chosen as equations (18.28) and (18.29), respectively;
2. The control law is designed as follows:

$$i_q^* = i_{qeq} + i_{qn}, \tag{18.30}$$

where

$$i_{qeq} = \frac{J_M J_L}{b_s p \phi_f}\left[\ddot{\omega}_L^* + \left(\frac{b_s^2}{J_p J_L} - \frac{K_s}{J_L}\right)(\omega_M - \omega_L) + \frac{K_s b_s}{J_p J_L}\Delta\theta\right] \tag{18.31}$$

and i_{qn} is obtained by the following low-pass filter:

$$i_{qn} + \beta_\omega \dot{i}_{qn} = \frac{J_M J_L}{b_s p \psi_f}\left[(k_\omega + \eta_\omega) sgn(l_\omega) + \frac{q_\omega}{\gamma_\omega p_\omega}\dot{s}_\omega^{2-p_\omega/q_\omega}\right], \tag{18.32}$$

where $k_\omega > \left|-\frac{b_s}{J_L^2}T_L + (-\beta_\omega \frac{b_s}{J_L^2} + \frac{1}{J_L})\dot{T}_L + \frac{\beta_\omega}{J_L}\ddot{T}_L\right|$, $\eta_\omega > 0$, $1/J_p = 1/J_M + 1/J_L$. The load speed of the system can converge to the equilibrium point asymptotically.

18.6.2 d-Axis Current Controller Design

Suppose that e_d is the error between the given value and the actual value of the d-axis current i.e.

$$e_d = i_d^* - i_d. \tag{18.33}$$

Then, the d-axis current error system is

$$\dot{e}_d = -p\omega_M i_q + \frac{R_s}{L} i_d - \frac{u_d}{L}. \tag{18.34}$$

In order to realize fast convergence and better tracking precision, a nonsingular terminal sliding mode manifold is designed as follows:

$$s_d = e_d + \gamma_d \dot{e}_d^{p_d/q_d}, \tag{18.35}$$

where, $\gamma_d > 0$, p_d, q_d are all odds, $1 < p_d/q_d < 2$. The d-axis current controller can be designed as following steps:

(a) An NTSM manifold is chosen as equation (18.35).
(b) The control law is designed as follows:

$$u_d = u_{deq} + u_{qn}, \tag{18.36}$$

$$u_{deq} = R_s i_d - Lp\omega i_q, \tag{18.37}$$

$$u_{dn} = L \int_0^t [q_d/(\gamma_d p_d)\dot{e}_d^{2-p_d \cdot q_d} + k_d sgn(s_d)]d\tau, \tag{18.38}$$

where, $k_d > 0$. The d-axis current of the error system (18.34) can converge to zero in finite time.

18.6.3 q-Axis Current Controller Design

Suppose that e_q is the error between the given value and the actual value of the q-axis current i.e.

$$e_q = i_q^* - i_q. \tag{18.39}$$

Then, the q-axis current error system is

$$\dot{e}_q = \dot{i}_q^* + p\omega_M i_d + \frac{R_s}{L} i_q + \frac{p\psi_f}{L}\omega_M - \frac{u_q}{L}. \tag{18.40}$$

The NTSM manifold is designed as follows:

$$s_q = \dot{e}_q + \gamma_q e_q^{p_q/q_q}, \tag{18.41}$$

where, $\gamma_q > 0$, p_q , q_q are all odds, $1 < p_q/q_q < 2$. The q-axis current controller can be designed as following steps:

(a) The TSM manifold is chosen as equation (18.41);
(b) The control law is designed as follows:

$$u_q = u_{qeq} + u_{qn}, \tag{18.42}$$

$$u_{qeq} = Lp\omega_M i_d + R_s i_q + p\psi_f \omega_M + L\dot{i}_q^*, \tag{18.43}$$

$$u_{qn} = L\int_0^t [q_q/(\gamma_q p_q)\dot{e}_q^{2-p_q.q_q} + k_q sgn(s_q)]d\tau, \tag{18.44}$$

where $k_q > 0$. The q-axis current of the error system (18.40) can converge to zero in finite time.

18.6.4 Simulations

Some simulations are carried out for evaluating the sliding-mode based mechanical resonance suppressing method. The parameters of the controllers are designed as $\beta_\omega = 0.01, \gamma_\omega = 0.008$, $p_\omega = 7, q_\omega = 5, k_\omega + \eta_\omega = 500$ and $k'_\omega = 200$. The step responses of the motor speed for three different methods, namely, notch filter, acceleration feedback, and TSM control, are shown in Figure 18.8a. The step responses of the load speed are depicted in Figure 18.8b. It can be seen that the speeds of both the motor and the load using notch filter are fastest compared to other two methods. The effect of suppressing mechanical resonance using the acceleration feedback is better than the notch filter. Compared to other two methods, effect of suppressing mechanical resonance in both the motor speed and the load speed using the TSM control is best. The speed response time of the TSM control is similar to the notch filter.

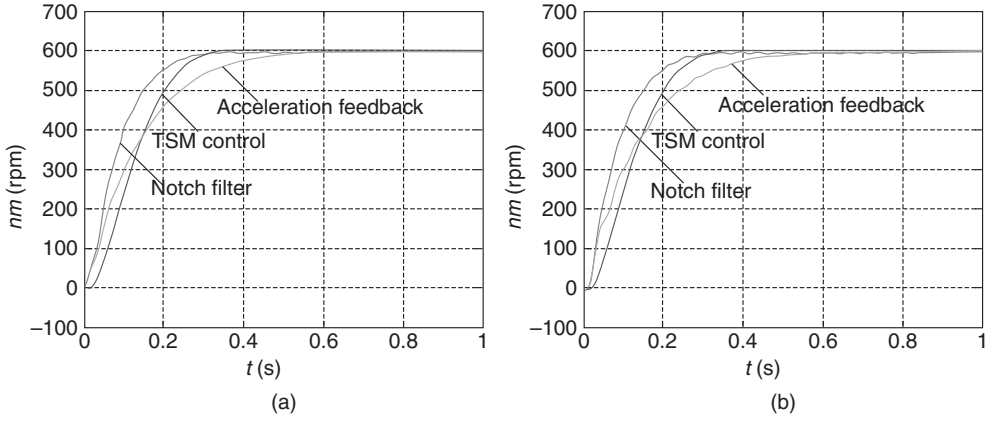

Figure 18.8 Step responses of the motor speed and load speed: (a) motor speed response; (b) load speed response

18.7 Digitization of TSM Controllers of PMSM Servo System

In industrial applications, the PMSM servo systems are generally implemented by DSP or microcontroller. It means that all controllers for a PMSM servo system are executed by a program. Therefore, all the designed controllers must be transformed into their discrete versions. There are many existing numerical approximation methods to transform continuous-time system representations to discrete-time and vice versa, such as standard z-transform, backward difference, forward difference, bilinear transform, pole-zero mapping, impulse invariance, Simpson's rule, and matched z-transform, (Phillips and Nagle 1995). In particular, backward difference and bilinear transform are regarded as two of the most practical numerical approximations in all aspects of digital control applications (Lin and Tsai 2009). Here, we use backward difference and bilinear transform discretization method to digitize the continuous TSM controllers in previous sections.

The TSM control strategies can be rewritten as the following form:

$$u(t) = u_{eq}(t) + u_n(t) = u_l(t) + \int_0^t u_i(t)dt, \tag{18.45}$$

where $u_l(t)$ and $u_i(t)$ are two parts of the TSM control law.

18.7.1 Backward Difference Discretization Method

Let $t = kT, k = 0, 1, 2, \cdots$, where T is denoted as the sampling time. From equations (18.45), $u(k)$ and $u(k-1)$ can be obtained as follows:

$$u(k) = u_l(k) + \int_0^{kT} u_i(t)dt, \tag{18.46}$$

$$u(k-1) = u_l(k-1) + \int_0^{(k-1)T} u_i(t)dt. \tag{18.47}$$

Subtracting equation (18.47) from equation (18.46) gives

$$u(k) = u(k-1) + u_l(k) - u_l(k-1) + \int_{(k-1)T}^{kT} u_i(t)dt. \tag{18.48}$$

Therefore, the digitization of TSM controllers of PMSM servo system can be obtained using the backward difference method as follows from equation (18.48):

$$u(k) = u(k-1) + u_l(k) - u_l(k-1) + Tu_i(k). \tag{18.49}$$

18.7.2 Bilinear Transformation

The bilinear transform is a technique of transforming continuous-time system representations to the discrete-time counterpart. It is the most commonly used method for converting controllers from the continuous-time domain into the discrete time domain. The digitization of TSM

controllers of PMSM servo system using the bilinear transform can be obtained as follows from equation (18.48):

$$u(k) = u(k-1) + u_l(k) - u_l(k-1) + \frac{T}{2}(u_i(k) + u_i(k-1)). \tag{18.50}$$

It should be mentioned that discretization of sliding mode control may result in periodic, near-periodic, and irregular orbits. It was found (Yu *et al.* 2012) that the reason of emergence of these behaviors is due to the fact that the sampling period must satisfy certain boundary conditions between the system parameters and the sampling period. Here only the motor speed controller is analyzed. For the purpose of the simplicity, the following two assumptions are made:

(a) The LSM manifold is utilized to replace the TSM manifold in (18.7):

$$g(x) = \dot{e}_\omega + \gamma_\omega e_\omega^{p_\omega/q_\omega} = c^T x, \tag{18.51}$$

where $e_\omega = \omega^* - \omega$ denotes the speed error, ω^* the desired speed, $x = [e_\omega \ \dot{e}_\omega]^T$.

(b) The load torque T_L in (18.2) is time invariant, that is,

$$\dot{T}_L = 0. \tag{18.52}$$

From equations (18.2) and (18.4), it can be obtained:

$$\dot{e}_\omega = \dot{\omega}^* - \dot{\omega} = \dot{\omega}^* - \frac{p_n \psi_f}{J} i_q^* + \frac{B}{J}\omega + \frac{T_L}{J} \tag{18.53}$$

or

$$\dot{e}_\omega = -\frac{k_q}{J} i_q^* + \frac{B}{J}\omega + \frac{T_L}{J} \tag{18.54}$$

the control i_q^* is designed as follows:

$$i_q^* = -\frac{B}{k_q}\omega + v. \tag{18.55}$$

Then equation (18.54) can be rewritten as

$$\dot{e}_\omega = -\frac{k_q}{J} v + \frac{T_L}{J}. \tag{18.56}$$

Taking the derivative of equation (18.56) with the time gives

$$\ddot{e}_\omega = -\frac{k_q}{J}\dot{v} + \frac{\dot{T}_L}{J} = -\frac{k_q}{J}\dot{v}. \tag{18.57}$$

The system (18.57) can be rewritten as the following state space representation:

$$\dot{x} = Ax + bu, \tag{18.58}$$

where $x = [\, e_\omega \quad \dot{e}_\omega \,]^T$, $u = -k_q / J\dot{v}$, A and b are as follows:

$$A = \begin{bmatrix} 0 & 1 \\ 0 & 0 \end{bmatrix}, \qquad b = \begin{bmatrix} 0 \\ 1 \end{bmatrix}.$$

In (18.51), it can be assumed $c = [\, c_1 \quad 1 \,]^T$. Therefore, $c^T b = 1$. The control signal u in system (18.58) can be designed as follows:

$$u = u_{eq} + u_n, \tag{18.59}$$

where $u_{eq} = -(c^T b)^{-1} c^T Ax = -c^T Ax$ and $u_n = -\alpha (c^T b)^{-1} sgn(g(x)) = -\alpha sgn(g(x))$.

To study the discretization behaviors, the continuous-time system (18.58) is converted into the discrete form firstly:

$$x(k+1) = e^{Ah} x(k) + \int_0^h e^{Ah} d\tau b u_k, \tag{18.60}$$

where h is the sampling time, $u_k = u_{eq}(k) + u_n(k) = -c^T Ax(k) - \alpha sgn(g(x(k)))$, $k = 0, 1, \ldots$. System (18.60) can be rewritten as:

$$x(k+1) = \Phi x(k) - \alpha \Gamma s_k, \tag{18.61}$$

where $\Phi = e^{Ah} - \int_0^h e^{A\tau} d\tau c^T A$, $\Gamma = \int_0^h e^{A\tau} d\tau b$, $s_k = sgn(g(x(k)))$. System (18.61) can be further rewritten as the following form:

$$x_1(k+1) = x_1(k) + \upsilon x_2(k) - \gamma_1 \alpha s_k, \tag{18.62}$$

$$x_2(k+1) = d x_2(k) - \gamma_2 \alpha s_k. \tag{18.63}$$

Equations (18.62) and (18.63) can be considered as a dynamical system switching between two discrete-time invariant linear systems with two different equilibriums. The behaviors of the system can be described using the following theorem:

Theorem 18.7.1 *(Yu and Chen 2003): The system (18.62) and (18.63) is stable in the sense of Lyapunov if*

$$-1 < d < 1, \qquad \left| \frac{\upsilon \gamma_2}{1 - |d|} \right| < |\gamma_1. \tag{18.64}$$

Furthermore, the system state is bounded by

$$|x_1(\infty)| \le \gamma_1 \alpha + \frac{(c_1 - 1 - \upsilon)|\gamma_2|\alpha}{1 - |d|}, \qquad |x_2(\infty)| \le \frac{|\gamma_2|\alpha}{1 - |d|}. \tag{18.65}$$

For analyzing the discretization behaviors, some strict assumptions have been made and the linearized models of the PMSM systems have been obtained. The PMSM systems are actually nonlinear systems and include internal parameter uncertainties and time-varying disturbances. But at least near the desirable operation points, the linearized models would help obtain approximate boundary conditions for the sampling period. This area of research is to be further explored.

18.8 Conclusions

This chapter has described the sliding-mode control of PMSM servo systems. The typical structure of the systems consists of the position, velocity, and current control loops. The design of three controllers, position controller, speed controller, and current controller, and a filter in speed loop has been described respectively, aimed at reaching high-performances of PMSM servo systems, such as fast response, strong robustness, and high precision. The digitization of TSM controllers of PMSM servo system has been discussed for the purpose of practical implementation.

This work was supported in part by the National Natural Science Foundation of China (61074015), and also in part by the Linkage Project (LP100200538) and the Discovery Project (DP0986376) of the Australian Research Council.

References

Baik C, Kim KH, and Youn MJ (2000) Robust nonlinear speed control of PM synchronous motor using boundary layer integral sliding mode control technique. *IEEE Transactions on Control Systems Technology*, **8**, 47–54.

Edwards C and Spurgeon SK (1998) *Sliding Mode Control Theory and Applications*. London: Taylor & Francis Ltd.

Ellis G and Lorenz RD (2000) Resonant load control methods for industrial servo drives. *Proceedings of World Congress Industrial Application Electrical Energy and 35th IEEE-IAS, Rome*, pp. 1438–1445.

Feng Y, Yu XH, and Man ZH (2002) Non-singular terminal sliding mode control of rigid manipulators. *Automatica*, **38**, 2159–2167.

Feng Y, Bao S, and Yu X (2004) Inverse dynamics nonsingular terminal sliding mode control of two-link flexible manipulators. *International Journal of Robotic and Automation*, **19**, 91–102.

Feng Y, Han X, Wang Y, and Yu X (2007) Second-order terminal sliding mode control of uncertain multivariable systems. *International Journal of Control*, **80**, 856–862.

Feng Y, Zheng J, Yu X, and Truong NV (2009) Hybrid terminal sliding mode observer design method for a permanent magnet synchronous motor control system. *IEEE Transactions on Industrial Electronics*, **56**, 3424–3431.

Feng Y, Yu X, and Wang L (2011) *Chapter 18 AC Servo Systems* (in Industrial Electronics Handbook 2nd editions, BM Wilamovski, and JD Irvin (eds)), CRC Press Taylor and Francis Group, London.

Jang JH, Sul SK, Ha JI *et al*. (2003) Sensorless drive of surface-mounted permanent-magnet motor by high-frequency signal injection based on magnetic saliency. *IEEE Transactions on Industrial Applications*, **39**, 1031–1039.

Ji JK and Sul SK (1995) Kalman Filter and LQ based Speed controller for torsional vibration suppression in a 2-mass motor drive system. *IEEE Transactions on Industrial Electronics*, **42**, 564–571.

Lee YM, Kang JK, and Sul SK. (1999) Acceleration feedback control strategy for improving riding quality of elevator system. *Proceedings of 34th Annual Meeting of the IEEE Industry Applications Society, Phoenix, AZ*, pp. 1375–1379.

Lin S-C and Tsai C-C (2009) Development of a self-balancing human transportation vehicle for the teaching of feedback control. *IEEE Transactions on Education*, **52**, 157–168.

Phillips CL, and Nagle HT (1995) Digital Control System Analysis and Design, 3rd edn, Prentice-Hall, Englewood Cliffs, NJ.

Rahman MA and Hoque MA (1998) Online adaptive artificial neural network based vector control of permanent magnet synchronous motors. *IEEE Transactions on Energy Conversion*, **13**, 311–518.

Shin HB (1998) New antiwindup PI controller for variable-speed motor drives. *IEEE Transactions on Industrial Electronics*, **45**, 445–450.

Schmidt PB and Lorenz RD (1992) Design principles and implementation of acceleration feedback to improve performance of DC drives. *IEEE Transactions on Industrial Applications*, **28**, 594–599.

Schmidt P and Rehm T (1999) Notch filter tuning for resonant frequency reduction in dual inertia systems. *Proceedings of 34th Annual Meeting of the IEEE Industry Applications, Phoenix, AZ*, pp. 1730–1734.

Su YX, Zheng CH, and Duan BY (2005) Automatic disturbances rejection controller for precise motion control of permanent-magnet synchronous motors. *IEEE Transactions on Industrial Electronics*, **52**, 814–823.

Trzynadlowski M A (2001) Control of Induction Motors, London: Academic Press.

Utkin V, Guldner J, and Shi J (1999) Sliding Mode Control in Electromechanical Systems, (1st edn), Taylor & Francis, London.

Valenzuela MA, Bentley JM, Villablanca A, and Lorenz RD (2005) Dynamic compensation of torsional oscillation in paper machine section. *IEEE Transactions on Industrial Applications*, **41**, 1458–1466.

Yu X and Chen G (2003) Discretization behaviors of equivalent control based sliding-mode control systems. *IEEE Transactions on Automatic Control*, **48**, 1642–1664,

Yu X, Wang B and LX (2012) Computer-controlled variable structure systems: the state of the art. *IEEE Transactions on Industrial Informatics* **8**, 197–205.

Zhang Y, Akujuobi CM, Ali WH *et al.* (2006) Load disturbance resistance speed controller design for PMSM. *IEEE Transactions on Industrial Electronics*, **53**, 1198–1208.

Zheng J, Feng Y, and Yu X (2007) Mechanical resonance suppressing method for PMSM system based on high-order sliding modes. *Proceedings of the 33rd Annual Conference of IEEE Industrial Electronics Society*, pp. 704–709.

Zheng J and Feng Y (2008) High-order terminal sliding mode based mechanical resonance suppressing method in servo system. *Proceedings of International Symposium of Systems and Control in Aeronautics and Astronautics (ISSCAA)*, pp. 1–6.

Zheng J, Feng Y, and Yu X (2008) Hybrid terminal sliding mode observer design method for permanent magnet synchronous motor control system. *Proceedings IEEE International Workshop on Variable Structure Systems (VSS)*, Antalya, Turkey, pp. 106–111.

Zhu G, Dessaint L-A, Akhrif O, and Kaddouri A (2000) Speed tracking control of a permanent-magnet synchronous motor with state and load torque observer. *IEEE Transactions on Industrial Electronics*, **47**, 346–355.

19

Control of Interior Permanent Magnet Synchronous Machines

Faz Rahman and Rukmi Dutta
School of Electrical Engineering and Telecommunications, University of New South Wales, Australia

19.1 Introduction

Synchronous machines with permanent magnet excitation in the rotor became viable since commercialization of the Neodymium Iron Boron (NdFeB) magnet material from 1984 by GE and Sumitomo Metals. The availability of Neodymium in the earth's crust is as plentiful as lead (though quite localized, such as in China, as of now). The much lower price of this material in sintered and bonded varieties with energy product ($BH_{\max}$) higher than Samarium Cobalt thus offered commercial viability for such machines. The Sumitomo (later Hitachi) production process offers the sintered variety with remanent flux density (B_r) as high as 1.4 T, while the GE process offers the cheaper more easily shaped and manufactured bonded variety with B_r around 0.8. The sintered material is prone to corrosion, thus requiring special coating to seal the magnet surfaces and it has higher conductivity than the bonded variety leading to high eddy current losses at high speed operation. Both versions also suffer from high temperature dependence of its flux density, becoming more prone to demagnetization as the temperature of the magnet rises towards 100°C. By alloying the material with Dysprosium, the maximum withstand capability is now 175°C that is adequate for most applications. The world market for the sintered variety is now 10 times larger than the bonded variety, largely because of the more compact machines that become possible with the sintered material.

The remanent flux density (B_r) and coercivity (H_c) of NdFeB and two other low-cost PM materials are shown in the second quadrant of the BH plane in Figure 19.1. Because the magnets are subject to the demagnetizing MMF of the stator, this is the quadrant which is of

AC Electric Motors Control: Advanced Design Techniques and Applications, First Edition. Edited by Fouad Giri.

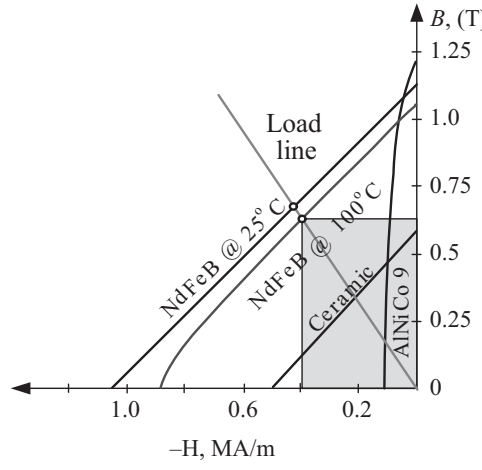

Figure 19.1 Demagnetization characteristics of several PM materials

interest to machine designers and users. The NdFeB material characteristic is also indicated at 100°C in Figure 19.1, showing the knee of the BH characteristic encroaching into the second quadrant at this temperature. This implies that at this temperature, the magnet B is unable to recoil along its characteristic line to its designed value if the stator MMF H exceeds about 750 kA/m in operation after the high temperature and the applied MMF are removed. This implies some permanent demagnetization of the magnets, which must be avoided.

The design of the interior permanent magnet synchronous machine (IPMSM) with the desired air gap and the best utilization of the iron in the stator and rotor circuits, places the operating point down the left-hand side of the BH characteristic, to a point where the load line of the magnetic circuit intersects this characteristic. A sufficient margin at the operating point for preventing demagnetization at the maximum working MMF of the stator and at the highest operating temperature and also achieving high energy product $BH_{\max}$, given by the shaded area in Figure 19.1b, are also the considerations at the design stage (Miller 1989). Proper consideration of these issues leads to an IPMSM that yield high power density, high efficiency and wide field weakening/constant-power speed range (CPSR).

A number of designs of the IPMSMs have emerged in recent years that incorporate some of the above design goals. The IPMSM, as opposed to the surface magnet SM, has the magnets buried inside the rotor iron in slots. This offers the magnets additional protection against demagnetization and also offers the mechanical housing to withstand the centrifugal force when the operating speed is high. This also allows the q-axis inductance (L_q) of the machine to be larger than the d-axis inductance (L_d), resulting in the exploitation of the inherent reluctance torque capability of such a machine, while simultaneously weakening the magnet flux by armature reaction, allowing operation of the machine above the base speed with constant power. This is particularly desirable in electric traction applications. Figures 19.2a–e depicts a few cross-sections of rotor magnetic circuits of IPMSMs, indicating the d- and q-axes for each design. The stators of these machines all have sine distributed winding, as with other conventional AC machines.

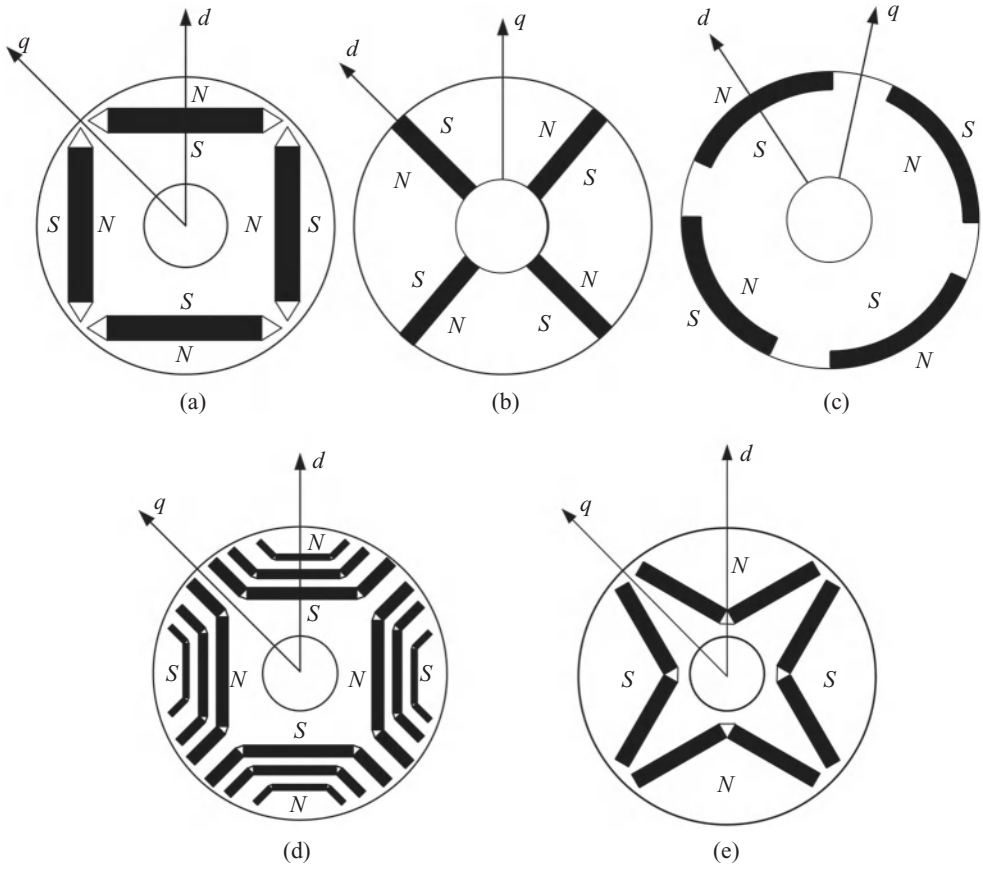

Figure 19.2 Cross-sections of some well-known IPM rotor structures: (a) Radially magnetized; (b) tangentially magnetized; (c) inset magnet; (d) multi-layer magnets; and (e) V-shaped magnet

Cross-sections of some well-known IPM rotor structures are indicated in Figure 19.2. Depending on the direction of flux crossing in the air gap, the IPM rotors can be broadly categorized as axially laminated, transversally magnetized, and radially magnetized. The axially laminated design (Soong *et al.* 1995) can produce very large ratio of L_q to L_d, but mechanical construction is expensive and complex. Because of this, the axially laminated IPM rotor has limited applications. In the tangentially magnetized IPM rotor, the magnet poles are in the form of spokes. In this machine, the d-axis inductance (L_d) is higher than the q-axis inductance (L_q). Because of this reversal of inductance values, the reluctance torque does not enhance the torque contributed by the magnets, as it does in a conventional IPM machine (Bianchi and Bolognani 1999). There are also problems of high cogging torque and nonsinusoidal back EMF associated with the tangentially magnetized design of the IPM machines. However, some recent studies are showing its potential in wind power generation (Haraguchi *et al.* 2009).

Table 19.1 Typical machine parameter of a radially magnetized IPM machine

Number of pole pairs	2
Stator resistance	5.8 (Ω)
Magnet flux linkage	0.377 (Weber)
d-axis inductance	0.0448 (Henry)
q-axis inductance	0.1024 (Henry)
Rated phase voltage	132 (V rms)
Rated phase current	3 (A rms)
Rated base speed	1260 (rpm)
Maximum speed	1460 (rpm)
Rated torque	3.7 (Nm)
Rated power	1 (kW)

Since the IPM machine is a new emerging technology, none of the configurations yet has been standardized. Nevertheless, the most common construction is the radially magnetized type rotor (Wang *et al.* 2011). In the radially magnetized design, there exist narrow iron bridges at the interpolar regions that are usually deeply saturated by the magnet leakage fluxes. The flux barriers/guards made of nonmagnetic material at the either sides of a magnet pole prevent magnetic short circuit of the adjacent opposite poles. The flux barriers also aid in the flux concentration at the individual pole shoe. The conventional radial flux design has modest $\frac{L_q}{L_d}$ ratio and a narrow constant power speed range. Some new IPM rotor structures have emerged in recent years such as the inset magnet, multilayered and *V*-shaped magnet (Kamiya 2006; Wang *et al.* 2011).

The inset magnet IPM machine can operate in an extended torque-speed range and has some field-weakening capability (Satoh *et al.* 2004). It has been used as a traction motor in Honda's first-generation mild hybrid electric vehicles. The required magnet volume in this type of IPM rotor is larger than for other types. The multilayered IPM rotor of Figure 19.2d can produce relatively large $\frac{L_q}{L_d}$ ratio, hence larger reluctance torque than any other types (Honda *et al.* 1998). However, the design is relatively complex and mechanically less robust. Recently *V*-shaped magnet design has gained popularity because of its successful use in Toyota's hybrid electric vehicle (Kamiya 2006). With this design very good flux-concentration is possible by optimizing the magnet pole pitch angle (Dutta and Rahman 2008). A wider constant power speed range is also achievable with this design.

The typical machine parameters of a radially magnetized IPM machine is shown in Table 19.1.

A typical torque-speed characteristic of a radially magnetized IPM machine is shown in Figure 19.3a. Figure 19.3b shows a torque speed characteristic of a *V*-shaped magnet IPM machine used in Toyota hybrid electric vehicle (Kamiya 2006).

19.2 IPM Synchronous Machine Model

For dynamic control of the developed torque, the IPMSM is represented in the rotor reference frame, via Park's dq-transformation. Equations (19.1) and (19.3) are for d- and q-axes voltages,

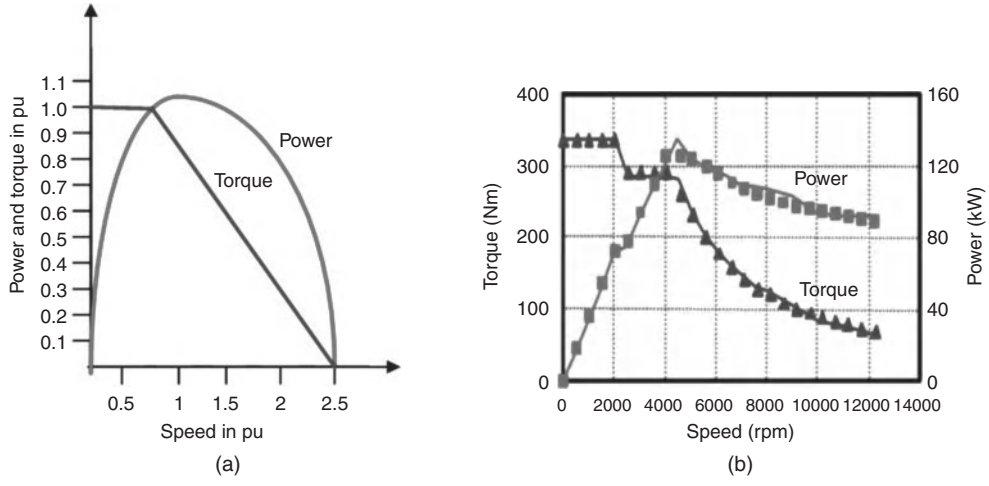

Figure 19.3 (a) Typical torque-speed characteristic of a radially magnetized IPM machine and (b) torque speed characteristic of a IPM machine with *V*-shaped magnet used in Toyota hybrid electric vehicle (Toyota Company)

respectively, Equation (19.3) for d- and q-axes flux linkages and equation (19.4) for the developed torque. The circuit representation of the machine in the rotor dq frame, as indicated in Figure 19.4, follows from equation (19.1):

$$v_d = R_d + \frac{d\lambda_d}{dt} - \lambda_q \frac{d\theta}{dt} = R_d + L_d \frac{di_d}{dt} - \omega\, L_q i_q, \tag{19.1}$$

$$v_q = R_q + \frac{d\lambda_q}{dt} + \lambda_d \frac{d\theta}{dt} = R_q + L_q \frac{di_q}{dt} + \omega\,(L_d i_d + \lambda_f), \tag{19.2}$$

$$\lambda_d = L_d\, i_d + \lambda_f \quad \lambda_d = L_q\, i_q, \tag{19.3}$$

$$T = \frac{3p}{2}(\lambda_d i_q - \lambda_q i_d) = \frac{3p}{2}\left[\lambda_f i_q + \left(L_d - L_q\right) i_q\, i_d\right]. \tag{19.4}$$

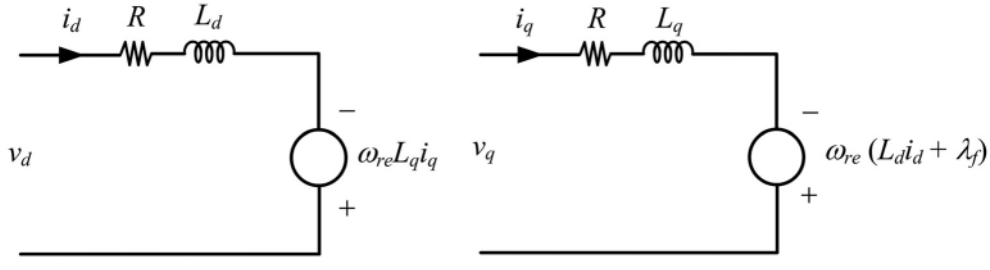

Figure 19.4 Circuit representation of an IPMSM in rotor d- and q-axes

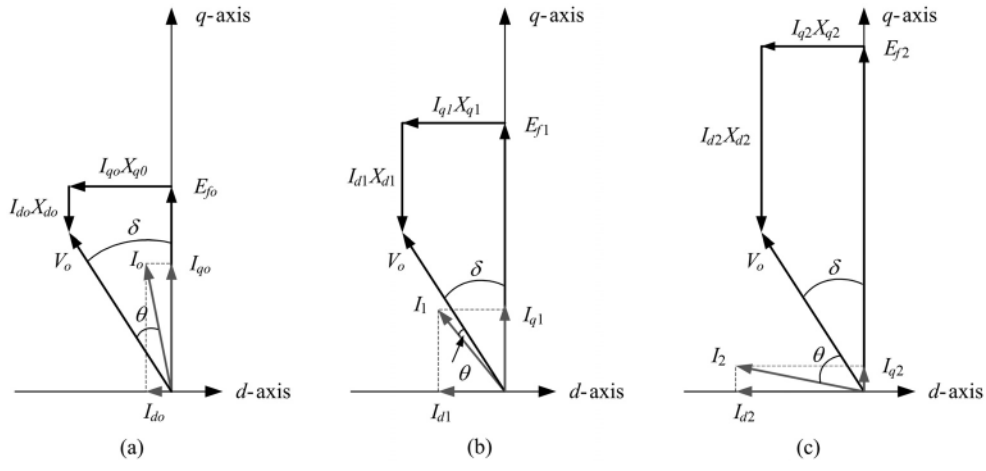

Figure 19.5 Phasor diagram of an IPMSM at base and higher speeds: (a) at base speed, ω_o, (b) at speed $\omega_1 > \omega_o$, (c) at speed $\omega_2 > \omega_o$

Control of flux linkage and torque can be approached based on equations (19.3) and (19.4), respectively, when the machine is driven from a current source inverter with independent and decoupled control of i_d and i_d. In order to understand the torque-speed envelope of the machine and some of its control restrictions, it is useful to represent the machine in terms of its steady-state equivalent circuit, in which the dq stator windings are stationary, but produces their MMFs along the rotor dq axes. In this representation, the dq stator windings have AC voltages, currents and flux linkages at the frequency corresponding to the speed of rotation. Figure 19.5 shows the phasor diagrams of the IPMSM at the base and two other speeds that are higher than the base speed, assuming that the voltage drops in the stator resistances are negligible at these speeds. V_0 is the rated phase voltage. E_{fo} is the PM excited phase voltage at base speed. θ and δ are the power factor and load angles, respectively.

19.2.1 Torque-Speed Characteristics in the Steady State

The torque-speed characteristic of the IPMSM near and above the base speed where the stator resistance voltage drop is negligible, is given by equation (19.5), in which the first term, the so-called reluctance torque, is due to the PM excitation and the second term is because of the difference in the d- and q-axes inductances of the machine. Typical proportions of these two torque components are indicated in Figure 19.6:

$$T = \frac{3p}{\omega_s}\left[\frac{E_f V}{X_d}\sin\,\delta + \frac{V^2}{2}\left(\frac{X_d - X_q}{X_d X_q}\right)\sin\,2\delta\right]. \tag{19.5}$$

It is clear from equation (19.5) that the inverter RMS output voltage V should increase proportionately with speed up to the rated voltage at base speed if the machine is to be capable of developing its maximum torque. For operation at higher speeds, the inverter output voltage

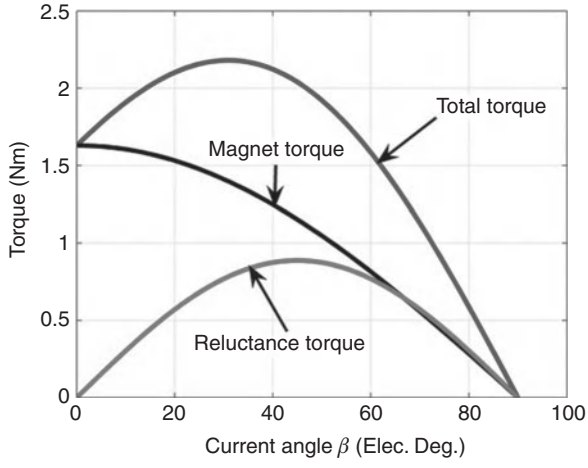

Figure 19.6 Developed torque components of an IPMSM

remains fixed at this value corresponding to the DC link voltage, while the speed is increased by increasing the supply frequency ω_s $(= 2\pi f_s)$. The excitation voltage E_f and the d- and q-axes reactances also increase proportionately with ω_s. The phasor diagrams of Figure 19.5 show the V, E_f and the input current I phasors at three speeds above the base speed. These figures also indicate that operation at higher than base speed can be arranged by controlling the phase angle of the input current phasor from the excitation voltage E_f, when a current source inverter drive is used. This type of control increases the $-$ve d-axis current as speed is increased beyond base speed, thereby reducing the air-gap field by armature reaction. Equation (19.4) implies that the $-$ve d-axis current increases the reluctance torque component of an IPM machine, which is beneficial because the total current $I = \sqrt{I_d^2 + I_q^2}$ of the machine must also be subject to a maximum limit, where I_d and I_q are the RMS values of i_d and i_q. It other words, the increased reluctance torque afforded by increased $-I_d$ may allow reduction in I_q, helping the drive to operate within its maximum current limit while at the same time maximizing the total developing torque.

In a servo type drive, the machine is required to develop the maximum possible torque from zero speed up to the rated speed. Operation above this speed may not be required. It may be noted from Equation (19.4) that for an IPM machine, a given torque can be obtained by many combinations of i_d and i_q. For such applications, the emphasis in machine and controller design is on covering the required speed range with minimum current, the so-called maximum torque per ampere (MTPA) trajectory in the (i_d, i_q) plane, in order to achieve high efficiency (Jahns *et al.* 1986). Traction and spindle type applications require diminishing torque as the operating speed increases beyond the base speed. In other words, such applications require constant-power operation over an extended speed range. For traction drives, a constant maximum torque over a low speed range and a wide CPSR is also required. The CPSR is covered by weakening the total air-gap field by armature reaction. Field weakening by $-$ve i_d current allows the machine air-gap field to be reduced, leading to increase of speed beyond the base speed that is achieved when the machine is supplied with its rated voltage. The $-$ve i_d helps the machine to maintain torque so that a wide speed range is covered at constant power, by exploiting its

reluctance torque capability. In general, a saliency difference, $L_q - L_d$, or more appropriately the saliency ratio, $\xi = \frac{L_q}{L_d}$, is good for a wide constant power range, however, the ratio $\frac{\lambda_f}{L_d}$ also plays a more significant role in this, as will be explained later.

19.2.2 Optimum Control Trajectories for IPM Synchronous Machines in the Rotor Reference Frame

The torque reference, T^*, which is determined by an outer speed loop, must be translated into i_q^* and i_d^* references, so as to achieve the maximum efficiency and minimum inverter capacity for both constant torque and constant power (field-weakening) speed ranges. This is because the developed torque of the IPMSM is determined by both i_q and i_d (see equation (19.4)).

The Maximum Torque per Ampere Trajectory

To obtain fast transient response and high torque, the current phase angle β must be controlled to achieve the maximum torque/current characteristic. In equation (19.4), i_d and i_q can be replaced by the d- and q-axes intercepts of the stator current vector $\bar{i}_s = \hat{i}_s \angle\beta = I_s \cos\beta + I_s \sin\beta$, as indicated in Figure 19.7. In order to determine the β angle that produces the maximum torque for a given amplitude I_s,

$$\frac{dT}{d\beta} = -\frac{3}{2}\lambda_f \, I_s \sin\beta + \frac{3p}{2}(L_d - L_q) I_s^2 \, \cos 2\beta = 0. \tag{19.6}$$

From this, the relationship between i_d and i_q for the MTPA trajectory can be derived as

$$i_d = \frac{\lambda_f}{2(L_d - L_d)} - \sqrt{\frac{\lambda_f^2}{4(L_d - L_d)^2} + i_q^2}. \tag{19.7}$$

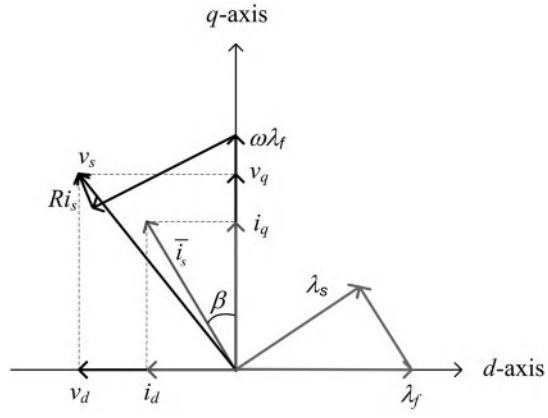

Figure 19.7 Voltage and currents phasors in the stator frame

Equation (19.7) implies that the MTPA can be achieved if i_d is determined by this equation for any i_q. i_q can be determined by the outer speed loop (Sebastiangordon and Slemon 1987). It should be noted that torque is not proportional to i_q, which is why torque control via only i_q current control is sometimes referred to as indirect torque control.

MTPA control was initially proposed by Jahns *et al.* (Jahns *et al.* 1986) in order to achieve high-efficiency operation of IPM motors by improving torque production in the constant torque region. As a result, the required power rating of the inverter was reduced. It was shown that the MTPA trajectory is tangent to the q-axis at the origin of the rotor flux reference frame axes and asymptotes to a 45° trajectory on a normalized i_{dn}, i_{qn} plane. As torque increases, the reluctance torque term, which is proportional to the product of d- and q-axes currents, increases compared with the field-alignment torque term, which is only linearly proportional to the i_q current. This reflects the hybrid nature of the torque production. Morimoto revealed further that with MTPA control, higher torque is produced also with higher power factor (Morimoto *et al.* 1994).

Constraints Imposed by Machine/Inverter Current and Voltage Limits

When an IPM synchronous motor is supplied from an inverter, the maximum stator current and voltage must be limited by the inverter/motor current and dc-link voltage ratings, respectively (Morimoto *et al.* 1990, Morimoto *et al.* 1994). These constraints can be expressed as

$$I_s = \sqrt{i_d^2 + i_q^2} \leq I_{sm}, \tag{19.8}$$

$$V_s = \sqrt{v_d^2 + v_q^2} \leq V_{sm}, \tag{19.9}$$

where I_{sm} and V_{sm} are the available maximum current and voltage of the inverter/motor.

Equation (19.9) may be expressed in terms of i_d and i_q instead of v_d and v_q. For simplicity, the analysis of the voltage constraint is based on the steady-state voltage equations which are obtained from equation (19.1) as follows:

$$\begin{bmatrix} v_d \\ v_q \end{bmatrix} = \begin{bmatrix} R & -\omega L_q \\ \omega L_d & R \end{bmatrix} \begin{bmatrix} i_d \\ i_q \end{bmatrix} + \begin{bmatrix} 0 \\ \omega \lambda_f \end{bmatrix}. \tag{19.10}$$

From equation (19.10) into equation (19.9),

$$V_s = \sqrt{(R\, i_d - \omega L_q i_q)^2 + (R\, i_q + \omega L_d i_d + \omega \lambda_f)^2} \leq V_{sm}. \tag{19.11}$$

Equation (19.11) can be simplified as equation (19.12) if the stator resistance is neglected:

$$\left(L_q\, i_q\right)^2 + \left(L_d\, i_d + \lambda_f\right)^2 \leq \left(\frac{V_{sm}}{\omega}\right)^2. \tag{19.12}$$

Equation (19.8) defines a circle of radius I_{sm} centred at the origin of the $i_d - i_q$ plane, while equation (19.12) gives ellipses located at $(0, -\frac{\lambda_f}{L_d})$ that become smaller as speed ω increases,

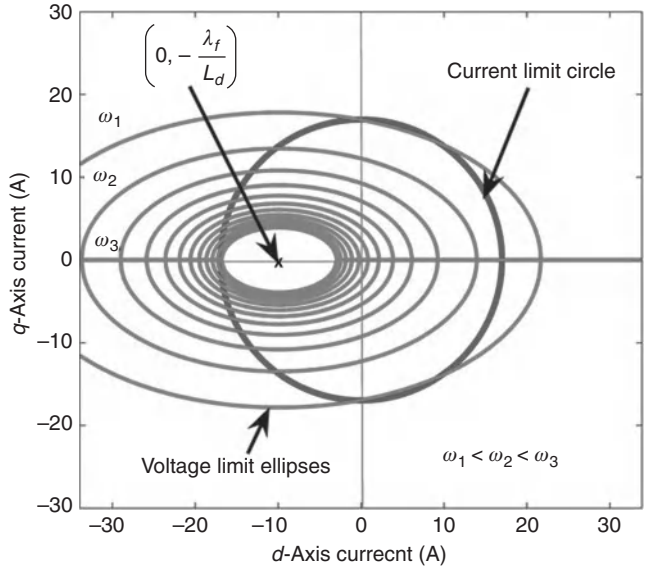

Figure 19.8 Current and voltage limit trajectories in the $i_d - i_q$ frame

as indicated in Figure 19.8. The trajectories of i_d and i_q satisfying the MTPA characteristic and current and voltage limit constraints are represented by equations (19.7), (19.8), and (19.12), respectively. These are drawn for an IPMSM in the $i_d - i_q$ plane of Figure 19.8. If the current vector is controlled inside the circle, the current limit constraint is always satisfied. Otherwise, if the current vector lies outside the circle, the motor current will exceed its limitation. The MTPA and current limit trajectories are independent of the rotor speed and are only determined by the motor parameters and inverter current rating.

It is seen that the voltage limit trajectory is an ellipse which contracts when the rotor speed increases. When the rotor speed increases infinitely, the voltage limit ellipse becomes a point on the −ve axis. The d-axis current represented by this point is the so-called characteristic current, I_{ch}, of the machine.

$$\text{Characteristic current, } I_{ch} = -\left(\frac{\lambda_f}{L_d}\right). \tag{19.13}$$

If the IPM machine is so designed that its I_{ch} falls inside the current limit circle, the machine field can be weakened by −ve i_d so that the field weakening speed range extends to infinity producing zero torque at the infinite speed. If it is outside, the maximum −ve i_d satisfying the current limit of Equation (19.8) applies and the machine has finite field weakening speed range. A special case applies when $|I_{ch}| = I_{sm}$, in which case the machine produces high torque as it approaches infinite speed by exploiting the reluctance torque to the fullest extent (the optimum field weakening condition) (Jahns 1987). The control trajectories at any speed are selected by satisfying MTPA, maximum current and voltage limits given by equations

(19.7), (19.8), and (19.12), respectively. After selecting i_q, normally by the speed controller, i_d is selected as described below.

19.3 Optimum Control Trajectories

19.3.1 The MTPA Trajectory

This trajectory is indicated by line OA on the $i_d - i_q$ plane in Figure 19.9. The i_d and i_q references (or load) and speed are such that I_{sm} will not be exceeded. The i_d reference is obtained from equation (19.7). The intersection of the trajectory at point A with the current limit circle is found from

$$i_{dA} = \frac{\lambda_f}{2(L_q - L_d)} - \sqrt{\frac{\lambda_f^2}{4(L_q - L_d)^2} + I_{sm}^2 - i_{dA}^2}$$

$$= \frac{\lambda_f}{4(L_q - L_d)} - \sqrt{\frac{\lambda_f^2}{16(L_q - L_d)^2} + \frac{I_{sm}^2}{2}},$$

$$i_{qA} = \sqrt{I_{sm}^2 - i_{dA}^2}. \tag{19.14}$$

The intersection point A of the MTPA and the current limit trajectory occurs for a speed ω_b at which the machine develops its maximum torque. This speed, referred to as the base speed (ω_b) of the machine, is given by

$$\omega_b = \frac{V_{sm}}{\sqrt{\left(\lambda_f + L_d i_{dA}\right)^2 + \left(L_q i_{qA}\right)^2}}. \tag{19.15}$$

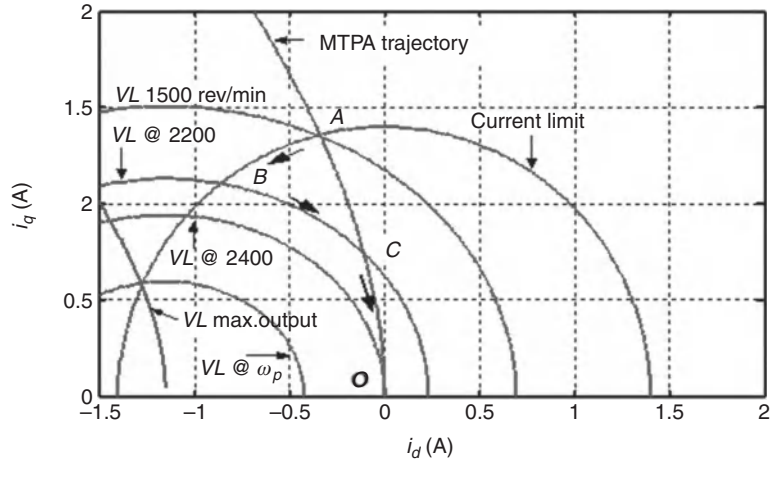

Figure 19.9 Current limit, voltage limit, and MTPA trajectories of an IPMSM

This trajectory should be followed when operation is below the base speed. i_{dA} and i_{qA} are the current limits that must be placed on the d- and q-axes current controllers when operation is along this trajectory during transient operation.

19.3.2 The Field-Weakening (Constant-Power) Trajectory

When operation is above the base speed ω_b, field weakening has to be employed so that the stator voltage is kept within the rated limit given by equation (19.11). In Figure 19.9, the voltage limit trajectory for the base speed of 1500 rpm is indicated. As the speed increases, the i_d and i_q current limits must follow the values given by equation (19.14), along the intersections of current and voltage limit trajectories for each speed. The d- and q-axes currents are controlled in order to satisfy the machine voltage limit V_{om} given by

$$v_o = \sqrt{v_{do}^2 + v_{qo}^2} \leq V_{om}, \tag{19.16}$$

where, $v_{do} = -\omega L_q i_q$, $v_{qo} = \omega\lambda_f + \omega L_d i_d$, and $V_{om} = V_{sm} - RI_{sm}$. The relationship between the i_d and i_q in the field weakening range is given from equation (19.12) with V_{sm} replaced by V_{om} in order to include the effect of stator resistance drop. Thus,

$$i_d = -\frac{\lambda_f}{L_d} + \frac{1}{L_d}\sqrt{\frac{v_{om}^2}{\omega^2} - (L_q\, i_q)^2}. \tag{19.17}$$

By controlling the current vector according to equation (19.17), the terminal voltage is always kept within V_{sm} in the steady state. The intersection between the current limit and voltage limit trajectories at each speed provides the respective current limits for producing maximum torque at each operating speed. These limit values are given by

$$i_{dv} = -\frac{\lambda_f L_d}{a} + \frac{1}{a}\sqrt{\lambda_f^2 L_d^2 - ab}, \tag{19.18}$$

$$i_{qv} = \sqrt{I_{sm}^2 - i_{dv}^2}, \tag{19.19}$$

where $a = L_d^2 - L_q^2$, $b = I_{sm}^2 L_q^2 + \lambda_f^2 - \frac{V_{sm}^2}{\omega^2}$.

The voltage limit trajectory is also indicated in Figure 19.9 for the crossover speed (ω_c) of 2400 rpm when the load is zero (or $i_d = i_q = 0$). When the machine is operated between the base and crossover speeds, the operating mode is determined by the load. For example, when the motor runs at 2200 rpm, the corresponding voltage limit trajectory is BCO in Figure 19.9.

If the machine is heavily loaded, the $i_d - i_q$ trajectory is along BC. When lightly loaded, the trajectory is along CO which is on the MPTA trajectory.

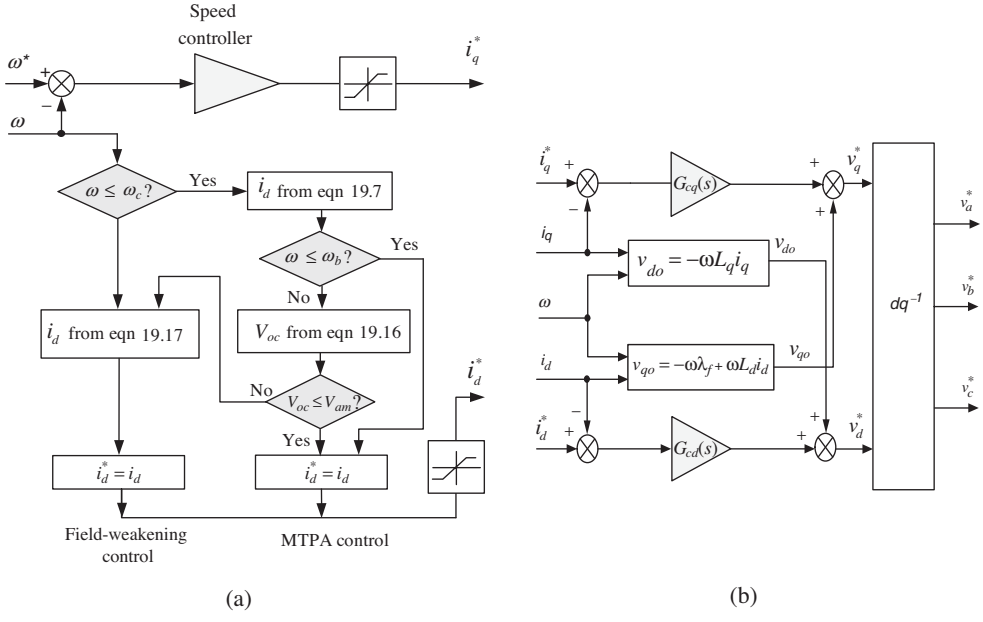

Figure 19.10 Trajectory selection and control: (a) Trajectory calculation, (b) dq current control with decoupling

19.3.3 Implementation Issues of Current Vector Controlled IPMSM Drive

As mentioned earlier, the speed controller output determines the q-axis current reference i_d^*. The i_d^* reference is obtained from considerations explained above and further described by Figure 19.10a and b. The compensated current controller outputs in Figure 19.10b can be further decoupled using the back-emf and voltage drops in the dq axes as indicated in this figure. Full decoupling has some stability implications because of the positive feedback indicated in Figure 19.10b.

The analysis of the stator voltage constraint in the previous sections was based on the steady-state equations. In the flux-weakening operation, the stator voltage is kept equal to the maximum stator voltage V_{sm}. The voltage resulting from commanded i_d^* and i_q^* may exceed V_{sm} in transient operations when i_d or i_q are required to change abruptly, when the drive is also in the field weakening speed range. As a result, the dq current controllers can become saturated and the current control performance may become poor. As is revealed by Jahns *et al.* (1986), and suggested by Morimoto (Morimoto *et al.* 1994) the i_d current should be controlled prior to i_q current in the case of current controller saturation. The voltage compensation in which v_{qo} is determined from equation (19.19), as shown in Figure 19.11, can be used to prevent the current controls from saturating.

Separate closed-loop controllers are normally employed to regulate machine dq currents to their reference values, as indicated in Figure 19.12. This entails measuring motor currents $i_a - i_c$ and transforming into i_d and i_q currents in the rotor reference frame using the rotor

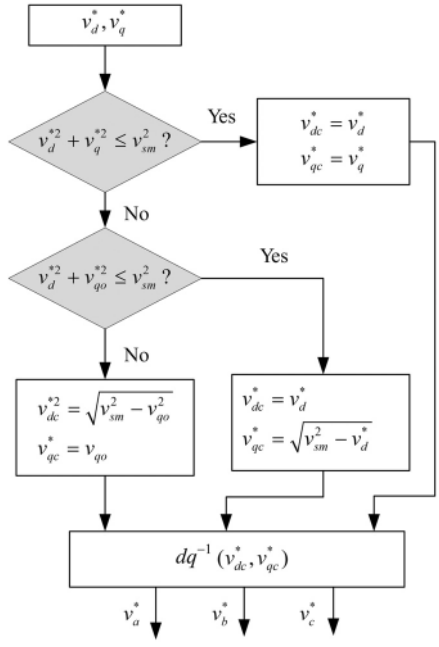

Figure 19.11 Voltage compensation scheme to prevent current controller saturation

position feedback obtained from a high-resolution mechanical sensor. The compensated i_d^* and i_q^* values are then decoupled according to the voltage equations of equations (19.1) and (19.3), followed by inverse dq transformation, producing the voltage references for the PWM inverter. The limit values for the i_d and i_q current references are determined by equations (19.14) and (19.19), respectively, according to the trajectory selected. Figures 19.13a–d illustrate a few

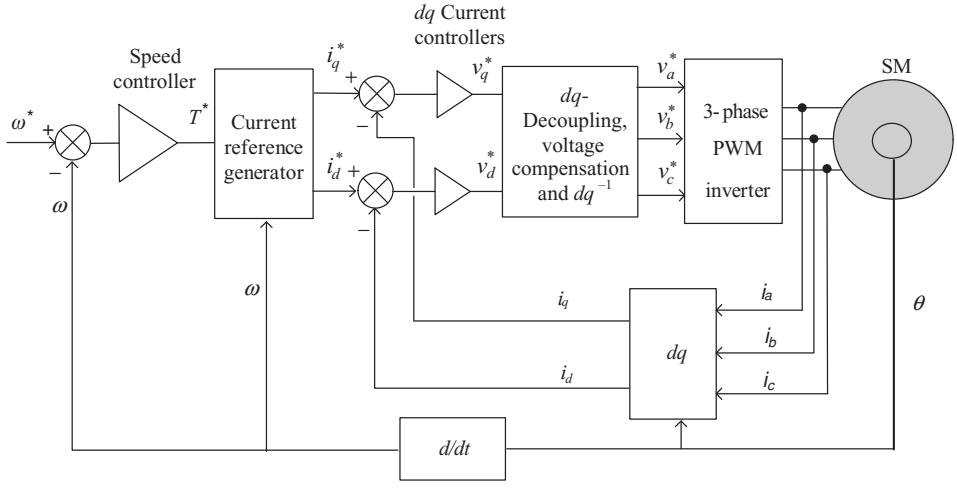

Figure 19.12 dq current vector control scheme for an IPMSM

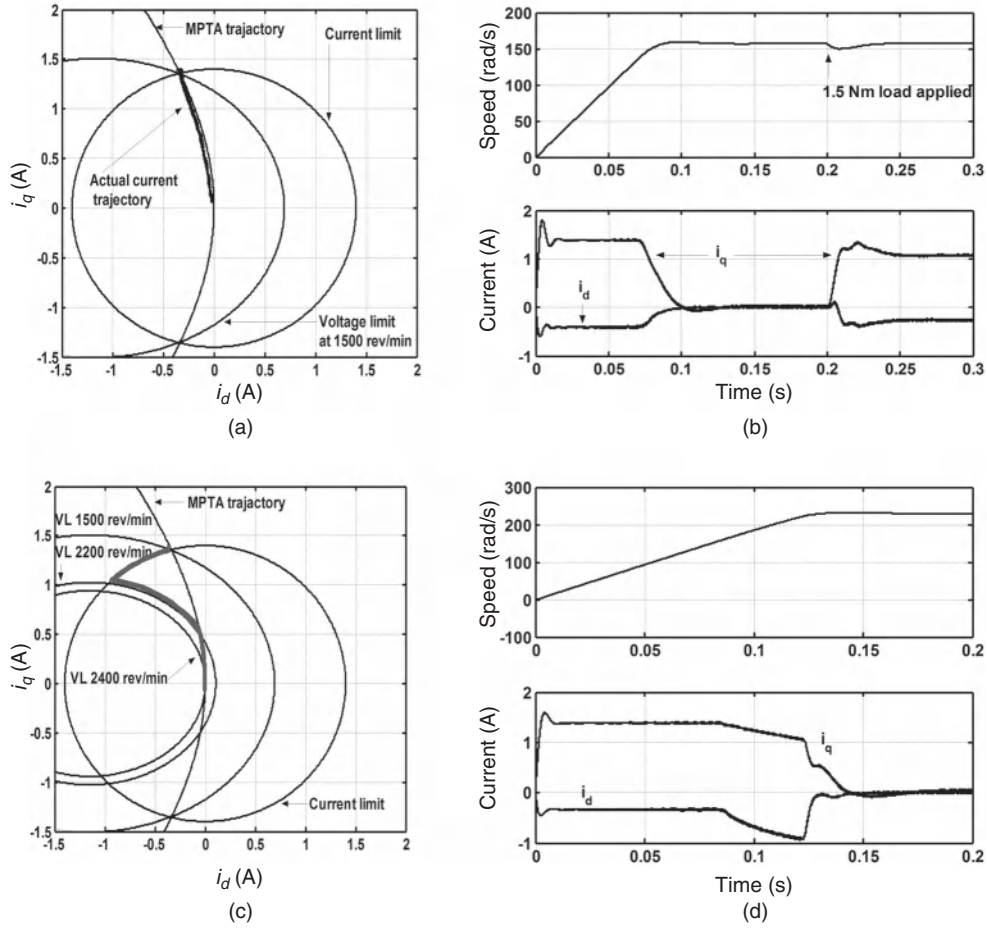

Figure 19.13 Trajectory following of a current vector controlled IPMSM drive. (a) i_d, i_q currents along the MTPA, (b) i_d, i_q currents during acceleration and on load application, (c) MTPA and FW trajectory following, (d) i_d, i_q during MTPA and FW following (experimental results)

cases of optimum trajectory followings when an IPMSM is operated with MTPA below (base speed), and with flux–weakening at higher speeds. Precise trajectory following with smooth transition between the two trajectories, using the controls indicated in Figures 19.10, 19.11, and 19.12), is clearly demonstrated.

19.4 Sensorless Direct Torque Control of IPM Synchronous Machines

The above-mentioned control techniques are based on i_d and i_q current vector controls in the rotor dq-reference frame. The demanded torque reference from the outer speed control loop primarily defines the i_q current reference. The d-axis current is also controlled simultaneously

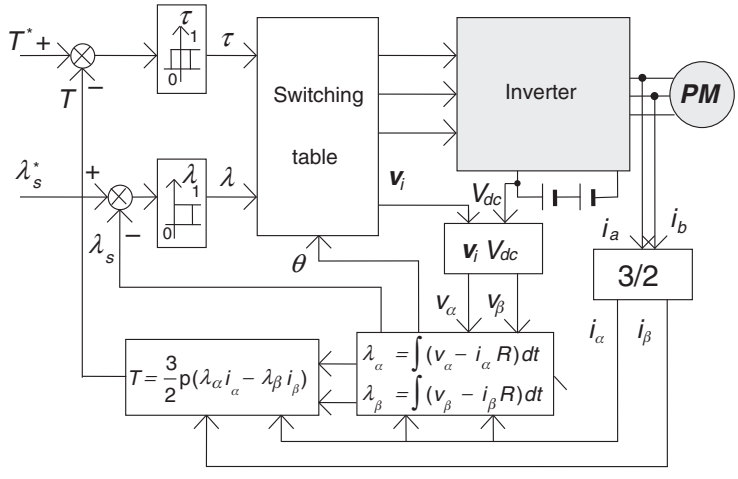

Figure 19.14 Block diagram of a DTC drive in the stator reference frame

in order to exploit the machine's reluctance torque and field-weakening capabilities. A shaft-mounted mechanical sensor is mandatory for this type of control.

Mechanical sensorless drive systems have drawn industrial interest for a variety of reasons (Corley and Lorenz 1998). The IPMSM, because of its inductance variation with angular position, lends easily to sensorless control, as will be described further in latter sections. A more direct torque and flux control approach than the current vector control of the previous section is the so-called direct torque control (DTC), in which the developed torque T and the stator flux linkage λ_s are controlled using estimations of these quantities from the machine model. In this approach, the torque T and λ are the control inputs directly, rather than current references for i_d and i_q in the indirect schemes of the previous sections. This approach is also inherently mechanical sensorless. The method only requires the initial rotor position at start, which can be obtained in a variety of ways, without requiring a mechanical sensor (Haque and Rahman 1994; Kim *et al.* 2004). The feedback signals for T and λ_s can be obtained in the stator flux reference frame in a number of ways. The control of torque T and λ_s is via application of stator voltage vectors relative to the estimated rotor angular position or load angle δ of the machine (Zhong *et al.* 1997; Rahman *et al.* 1998; Sayeef and Rahman 2009). The control scheme in its simple form is indicated in Figure 19.14 in which subscripts α and β refer to the quantities in the stator α and β axes (α-axis being the magnetic axis of the stator winding A). The stator flux linkages λ_α and λ_β are computed from simple integration of the stator voltages minus the respective resistance voltage drops. This figure also indicates the hysteresis torque and flux comparators, the discrete outputs of which, in conjunction of the six sectoral information (θ) of the rotor flux λ_f, selects the required machine voltage vectors for optimum torque and flux linkage response. Such direct torque control method has been shown to deliver as fast responses of torque and flux as with the dq current vector control strategy of Sections 19.2 and 19.3, if not faster (Zhong *et al.* 1997; Rahman *et al.* 1998).

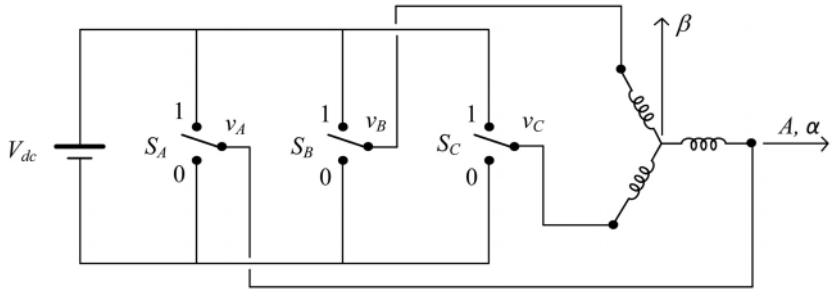

Figure 19.15 Voltage vectors in a two-level inverter

19.4.1 Control of the Amplitude and Rotation of the Stator Flux Linkage Vector

The DTC scheme, using the two-level inverter of Figure 19.15, is based on applying the six to eight voltage vectors available from the inverter and according to the errors in torque T and stator flux linkage λ_s to the machine. When hysteresis comparators of Figure 19.14 are used, full voltage vectors indicated in Figure 19.16 that must be applied for regulating the torque and the stator flux linkage in an optimal way can be deduced from simple logic. Additionally, the current and voltage limits described in Section 19.3 must not be crossed. The stator flux linkage in the stator reference is obtained from a simple integration of the back EMF, as given by equation (19.20):

$$\lambda_s = v_s\, t - R \int i_s dt + \lambda_s|_{t=0}, \quad \text{where} \quad \lambda_s = \sqrt{\lambda_d^2 + \lambda_Q^2} \angle \tan^{-1}\left(\frac{\lambda_Q}{\lambda_D}\right). \tag{19.20}$$

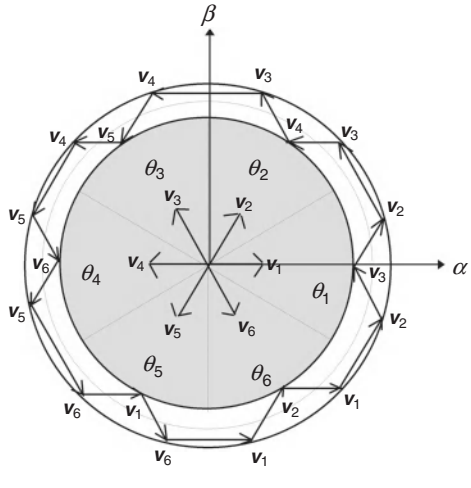

v_1	V(100)
v_2	V(110)
v_3	V(010)
v_4	V(011)
v_5	V(001)
v_6	V(101)
v_7	V(000)
v_8	V(111)

Figure 19.16 Stator flux trajectory with voltage of a two-level inverter

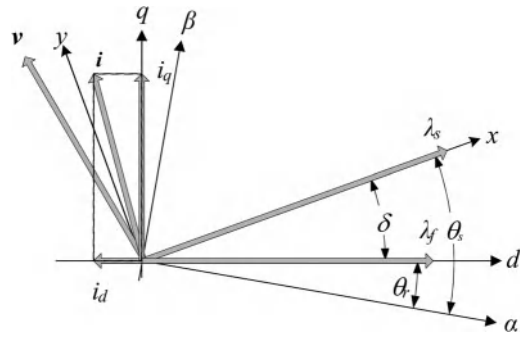

Figure 19.17 Angular relationships between stator flux and dq reference frames

If the applied voltage vectors remain constant during a switching interval and if the resistance voltage drops are neglected, the tip of the stator flux linkage vector moves in the direction of the applied voltage vectors as indicated in Figure 19.16 (left).

The angular relationships of the moving rotor and stator flux vectors with the stator $\alpha\beta$ and rotor dq axes are indicated in Figure 19.17. By resolving the d- and q-axes fluxes and currents into the stator flux axes xy, it can be shown that the developed torque can be expressed as in equation (19.21), when the stator flux linkage is held constant:

$$T = \frac{3p}{2}\lambda_s i_y, \tag{19.21}$$

where $i_y = \frac{1}{2L_d L_q}\left[2\lambda_f L_q \sin\delta - \lambda_s(L_q - L_d)\sin 2\delta\right]$ and

$$T = \frac{3p\lambda_s}{4L_d L_q}\left[2\lambda_f L_q \sin\delta - \lambda_s(L_q - L_d)\sin 2\delta\right]. \tag{19.22}$$

When torque is controlled by placing the stator flux linkage vector ahead or behind of the rotor flux linkage vector by a suitable angle δ, two requirements must be fulfilled, namely, that $\lambda_s < \frac{L_q}{L_q - L_d}\lambda_f$ so that $|T|$ increases with increase of $|\delta|$, and

$$\delta_m = \cos^{-1}\left[\frac{1}{4}\left(\frac{a}{\lambda_s} - \sqrt{\left(\frac{a}{\lambda_s}\right)^2 + 8}\right)\right], \tag{19.23}$$

where $a = \frac{\lambda_s L_q}{L_q - L_d}$, so that the limiting load angle δ_m is not exceeded. The variation of δ and the limiting δ_m, with variation in λ_s are indicated in Figure 19.18.

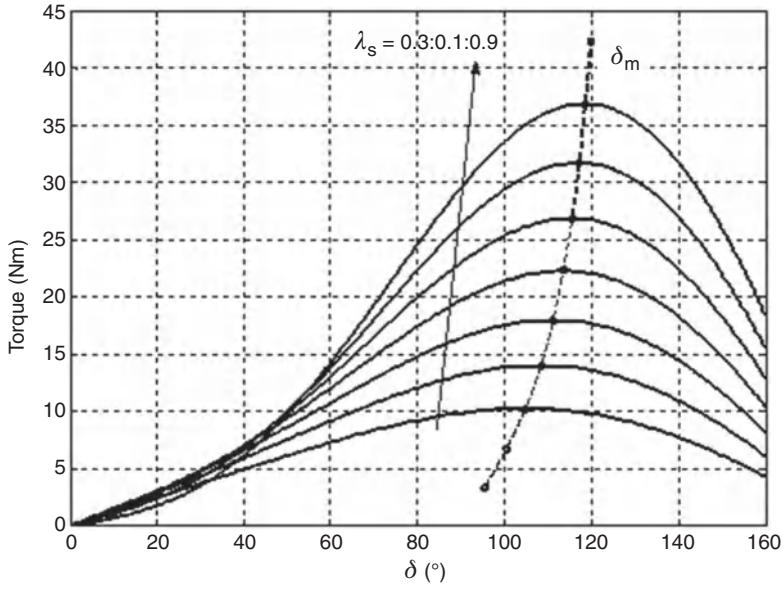

Figure 19.18 Torque characteristics of an IPMSM with load angle δ and stator flux linkage

19.4.2 Optimum Control Trajectories with DTC

For each i_d, i_q pair, there exist corresponding T, λ_s, and δ values, any two of which will be related to the other one:

$$T = \frac{3p}{2}\left[\lambda_f i_q + \left(L_d - L_q\right) i_q i_d\right], \tag{19.24}$$

$$\lambda_s = \sqrt{\left(\lambda_f + L_d i_d\right)^2 + \left(L_q i_q\right)^2}, \tag{19.25}$$

$$\delta = \tan^{-1}\left(\frac{L_q i_q}{\lambda_f + L_d i_d}\right). \tag{19.26}$$

Maximum Torque per Ampere Trajectory

For the MTPA trajectory, using equation (19.7), the flux linkage and load angle trajectories are given by

$$\lambda_s = \sqrt{\lambda_f^2 - \left(\frac{L_d^2}{L_q - L_d} + L_q - L_d\right)\lambda_f i_d + \left(L_d^2 + L_q^2\right) i_d^2}, \tag{19.27}$$

$$\delta = \tan^{-1}\left(\frac{L_q}{\lambda_f} + L_d i_d \sqrt{i_d^2 - \frac{\lambda_f}{L_d - L_q} i_d}\right). \tag{19.28}$$

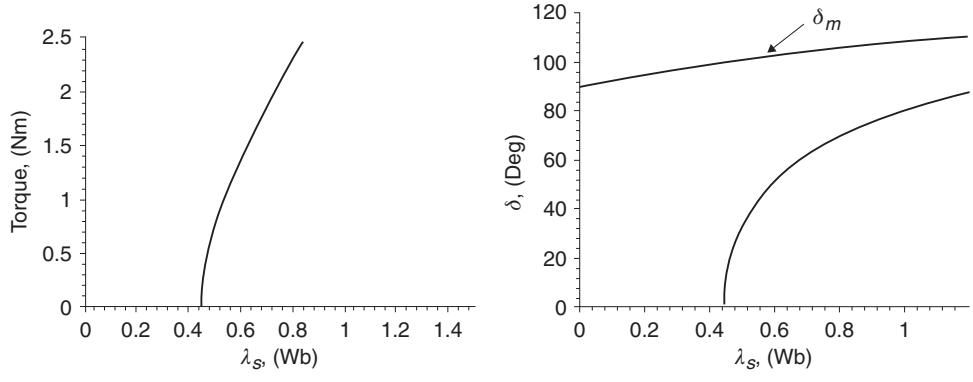

Figure 19.19 Torque and δ as a function of the amplitude of stator flux linkage for the MTPA trajectory

The relationships among λ_s, δ and positive T for the prototype motor are shown in Figure 19.19. For negative torque, λ_s remains the same and δ becomes negative. It is seen from Figure 19.19 that both the amplitude and angle increase with the increase of torque. As is also seen from this figure, the load angle δ will not exceed δ_m with the MTPA control when the torque is limited below the maximum torque the motor can produce.

Also, according to equations (19.24)–(19.26), if two of the three variables, namely, T, λ_s, and δ, are known, the third one is uniquely determined. Provided the torque is known, maximum torque per ampere (MTPA) control is achieved if the amplitude or the angle of the stator flux is determined from the MTPA trajectory of Figure 19.19a, which can be stored in a lookup table. For direct torque control, it is obvious that the torque and the amplitude of the stator flux linkage, rather than its angle, should be controlled (Zhong *et al.* 1997). When the torque and λ_s are controlled in this way, the angle δ will be automatically controlled and for the prototype motor it will not exceed δ_m.

Current and Voltage Constraints in $T-\lambda_s$ Plane

Similar to the trajectory control described in Sections 2 and 3, the maximum current and voltage constraints of the motor/inverter have to be also taken into account under DTC when the motor operates in the constant-torque (i.e., below base speed) and field-weakening regions. The current and voltage constraints are rewritten below in equations (19.29) and (19.30):

$$|i_d| = \sqrt{I_{sm}^2 - i_q^2}, \tag{19.29}$$

$$|v_d| = \sqrt{V_{sm}^2 - v_q^2}. \tag{19.30}$$

From equations (19.24), (19.25), and (19.29), the current limit trajectory in the T–λ_s plane can be plotted as shown in Figure 19.20a. Because the stator voltage is proportional to the product

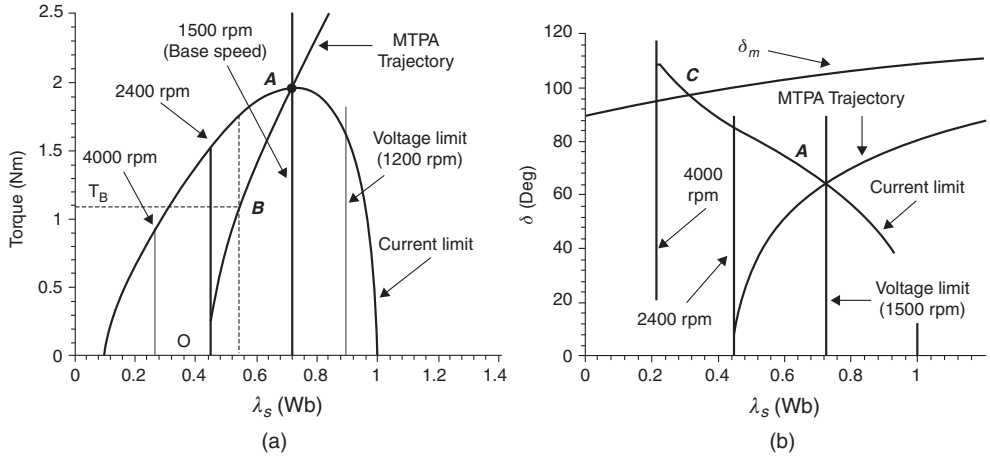

Figure 19.20 (a) MTPA, current limit and voltage limit trajectories with DTC; (b) requirement for limiting the minimum λ_s

of the rotational speed and the amplitude of the stator flux linkage, if the stator resistance is neglected,

$$V_s = \omega_r \lambda_s, \tag{19.31}$$

where ω_r is the rotational speed of the stator flux linkage. In the steady state, the rotational speeds of the stator flux linkage and the rotor magnet flux linkage are the same and equation (19.30) can be rewritten as

$$V_s = \omega_r \lambda_s = \omega_b \lambda_{sr} = \omega_c \lambda_f, \tag{19.32}$$

where ω_r, ω_b, and ω_c are the rotor speed, base speed, and crossover speed, respectively. λ_{sr} is the rated stator flux linkage. ω_c is the crossover speed for which the unloaded motor develops the rated phase voltage V_{sm}. Maximum voltage trajectories for a motor can be determined by each (i_d, i_q) pair and speed, and by using the voltage equations (19.1) and (19.3). From equation (19.31), the maximum voltage limit for each speed is a vertical line (if voltage drop in stator resistance is neglected), as indicated in Figure 19.20a. As speed increases, these lines move to the left as also indicated. The current and voltage limit trajectories in the T–λ_s plane are as shown in Figure 19.20a. If these trajectories are plotted in the δ–λ_s plane, it is revealed that with very low λ_s (deep flux weakening), the limiting δ_m angle may be exceeded when an IPMSM is operated at its current and voltage limits, as indicated in Figure 19.20b, indicating a limit to the maximum field weakening.

The current limit is satisfied if T and λ_s are controlled below the current limit trajectory. The intersection of the current limit and maximum torque-per-ampere trajectories is at point *A* in Figure 19.20a, which corresponds to the operating point with the maximum torque and current. The current limit is always satisfied if the torque is limited below the value at the operating point *A* for the maximum torque-per-ampere control. Below base speed, the voltage

limit trajectories are to the right of the MTPA *OA* in Figure 19.20a. Therefore, there is no requirement here to control the amplitude of the stator flux linkage λ_s to satisfy the voltage limit.

When the rotor speed increases, the voltage limit trajectories move to the left of the intersection point *A* and the stator flux will have to be reduced in order to satisfy the voltage limit requirement. For operation below the base speed, the MTPA should be selected. For the operation above the crossover speed, field-weakening control is selected since the voltage limit will no longer be satisfied if the torque and λ_s are controlled along the MTPA trajectory. However, for the operation between the base and crossover speeds, the control mode is determined by load torque. With the MTPA control, for instance, if the vertical dashed line in Figure 19.20a represents the voltage limit corresponding to the operation with the rotor speed between ω_b and ω_c, there is an intersection of this line and the maximum torque-per-ampere trajectory, and at this point the torque is T_B. If the actual torque is greater than T_B, field-weakening control is selected. Otherwise, if the actual torque is smaller than T_B, MTPA is selected even though the rotor speed is above the base speed.

19.4.3 Implementation of Trajectory Control for DTC

The block diagram of the outer speed loop for implementation of the trajectory control in DTC is show in Figure 19.21a. A lookup table is used to determine the amplitude of the stator flux linkage according to the MTPA trajectory for constant torque control. For field-weakening operation, the amplitude of the stator flux linkage is simply determined by the inverse of the speed. The control flow-chart for the control mode selection is shown in Figure 19.21b.

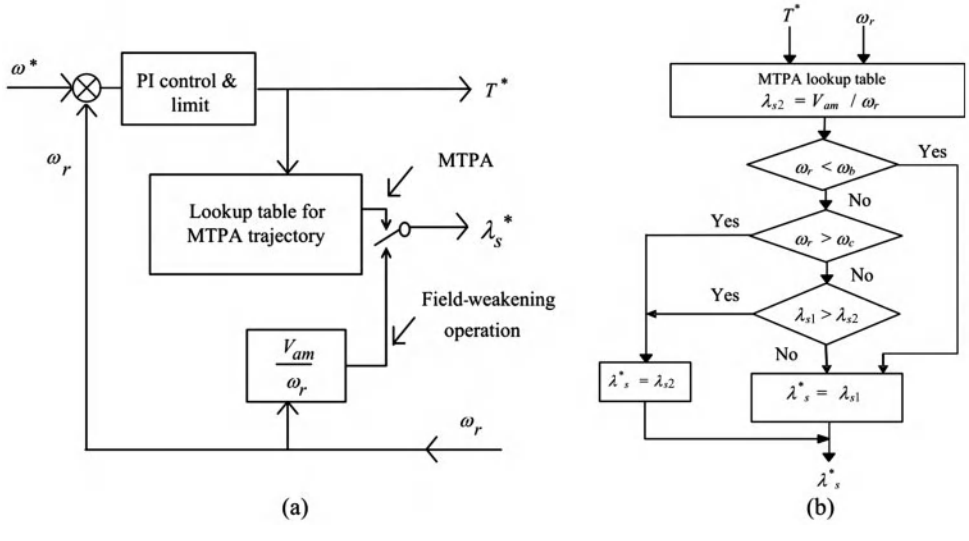

Figure 19.21 (a) Block diagram of the speed loop for trajectory control in DTC; (b) flow chart for the control mode selection

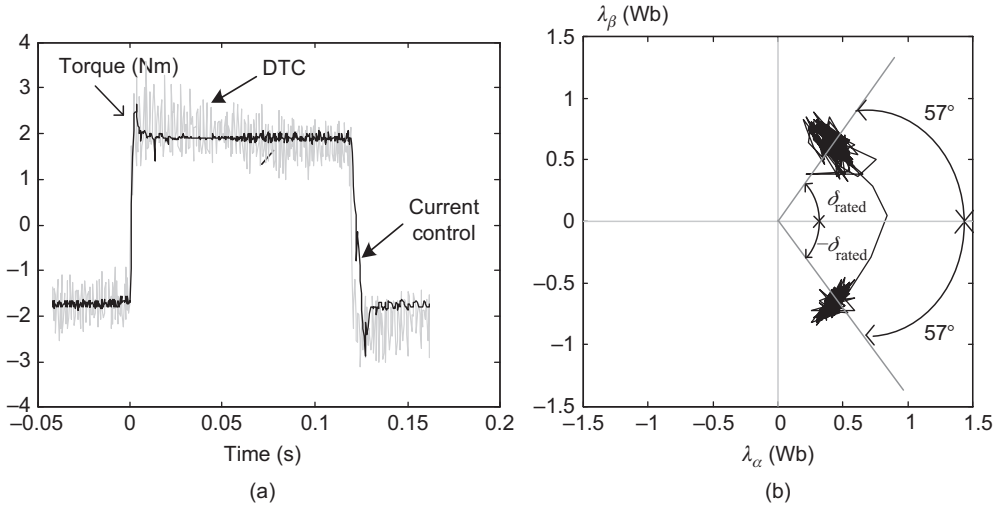

Figure 19.22 (a) Torque control dynamics under DTC and current control; (b) δ angle limitation during operation with MTPA

For applying DTC with trajectory control, it is necessary to check, if δ is smaller than δ_m. As mentioned earlier, with MTPA control, δ is always smaller than δ_m for the prototype motor. The field-weakening operation starts from point A in Figure 19.20a, and shifts to the current limit trajectory when the speed controller is still in saturation as shown in Figure 19.20b. Correspondingly, δ increases as the rotor speed increases. After point C, at which δ is equal to δ_m, δ should be limited at the value of δ_m. In this case, the torque limit value should be calculated from Figure 19.22, in which the amplitude of the stator flux linkage is already known, with δ_m obtained from Figure 19.23.

Figure 19.22a shows experimental data on torque responses of the test machine under a square-wave torque reference, with closed-loop $i_d - i_q$ current control and DTC during the MTPA mode operation. The dark trace represents torque response in the current controlled system, while the faint trace indicates the torque response under DTC. The variation of the load angle δ in the case of DTC is indicated in Figure 19.22b, clearly showing the limit values of δ during acceleration and deceleration along the MTPA trajectory. Figures 19.23a–e show a few more dynamic responses for torque, fluxes and trajectory following, with MTPA and field weakening controls. Smooth trajectory following with MTPA and field-weakening are demonstrated, similar to responses under current vector control shown in Figure 19.13.

19.5 Sensorless DTC with Closed-Loop Flux Estimation

It is be noted from Figure 19.15 and equation 19.20 that the stator flux linkage, which is used also to produce the feedback signal for torque, may be obtained from a simple, open-loop integration of the machine back EMF. The errors of such a flux estimator becomes unacceptably large at low speed when the back EMF amplitude becomes too low compared to the voltage drops in the stator resistance, the inverter switches, and distortions due to the inverter dead

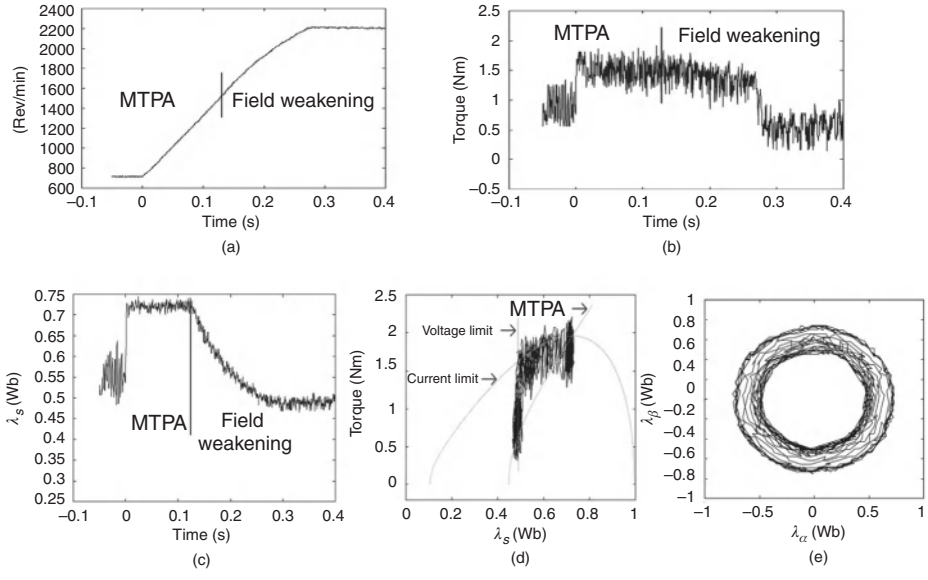

Figure 19.23 DTC drive over MTPA and FW speed range: (a) speed response; (b) torque response; (c) stator flux linkage response; (d) trajectory following; and (e) stator flux locus. Experimental results

time. Integration of signals that may have offset in measurements also causes unacceptable errors at low speed. The minimum sampling time restriction of cost-effective realization of the hysteresis controllers for torque and flux also causes unacceptable ripples. The errors in flux estimation at low speed also causes unacceptable error in the estimation of speed that is required for closing the speed loop in a speed control system. The results of Figure 19.23 also show the high torque and flux ripples when DTC is realized with cost-effective controllers of limited sampling speed (about 75 μs). The dynamic performance of the DTC scheme of Figure 19.14 for drives covering full rated torque cannot generally be guaranteed below 10% of the base speed.

The problem of high the torque and flux ripples has been overcome with the IPMSM DTC drive by the replacement of hysteresis comparators with SVM (Tang *et al.* 2004). Torque and flux references of Figure 19.14 are used to produce the stator voltage references v_α and v_β or the space vector modulation (SVM) in several ways (Xu and Rahman 2007; Boldea *et al.* 2008). A sliding-mode (SM; variable-structure) controller is suitable for the nonlinear IPMSM. It restricts the error trajectories of the controller to specified boundaries as it regulates the system. Design of such a controller and the proof of its stability have been fully described in references (Xu and Rahman 2007; Sayeef and Rahman 2009). It produces the voltage references v_α and v_β for the SVM.

SM closed-loop flux observers based on forcing the errors in estimated currents from the actual measured currents have delivered more accurate flux linkage estimation than is possible with integrating the bemf for flux estimation. Use of SM flux observers using the concept of extended back EMF and extended rotor flux (Chen *et al.* 2003; Boldea *et al.* 2006; Piippo *et al.* 2008) with online compensations for switch voltage drops, inverter dead-time and stator

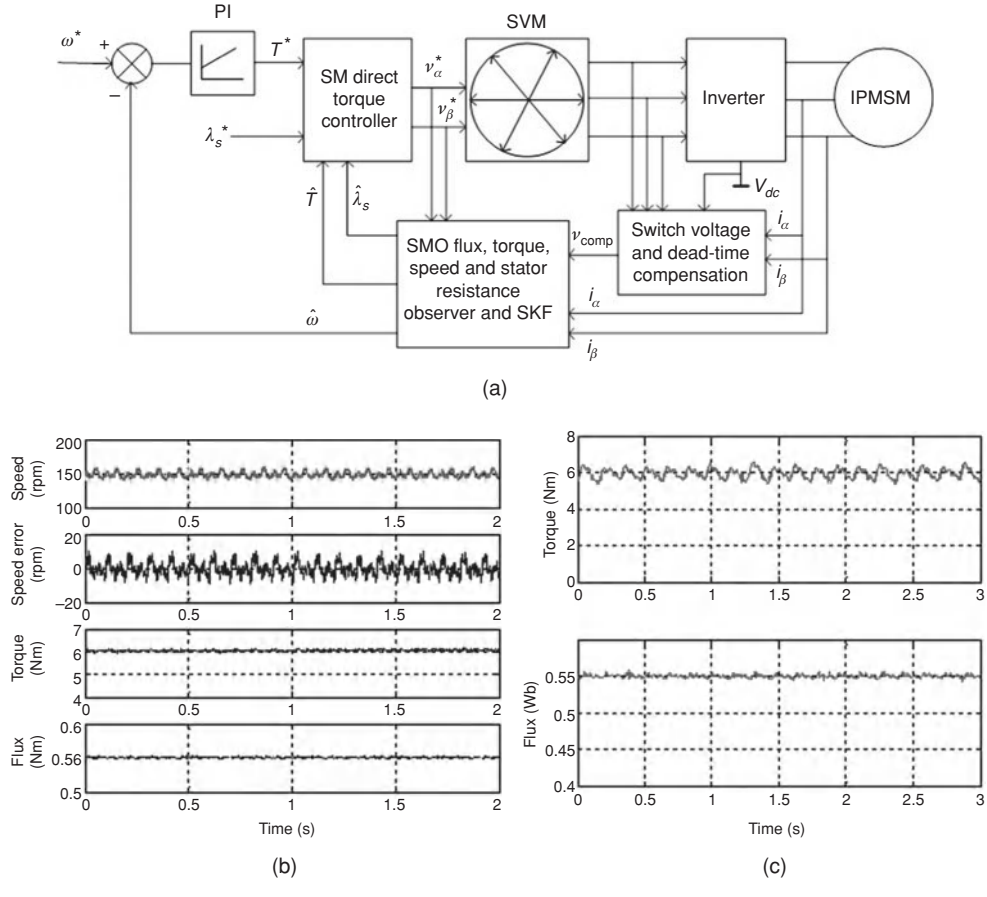

Figure 19.24 (a) Sliding-mode DTC drive with closed-loop estimators for λ_s and speed; (b) steady-state performance with full load torque 150 rev/min and (c) at 95 rev/min. SMO, slide-mode observer

resistance variation and a simplified Kalman filter for speed estimation, have demonstrated significant extension of the low speed operating speed range (Sayeef and Rahman 2009). Full analysis and design of these SM controllers and flux observers are included in Xu and Rahman (2007) and Sayeef and Rahman (2009) and will not be covered here. Figure 19.24a shows the block diagram of the SM DTC drive with closed-loop SM observer for flux for a 4-pole IPMSM with rated load torque applied. Nearly ripple-free steady-state torque and flux at 150 rev/min and the slightly deteriorated results at 95 rev/min are evident from these results. It may be noted that persistent operation at very low speeds and at zero speed, with variation of load torque from no load to full rated torque, is still not achievable with these methods. The dynamic response of such a drive retains the fast response characteristic of DTC, and furthermore, the scheme can be applied reliably as the speed becomes higher than about 100 rev/min for a 4-pole IPMSM.

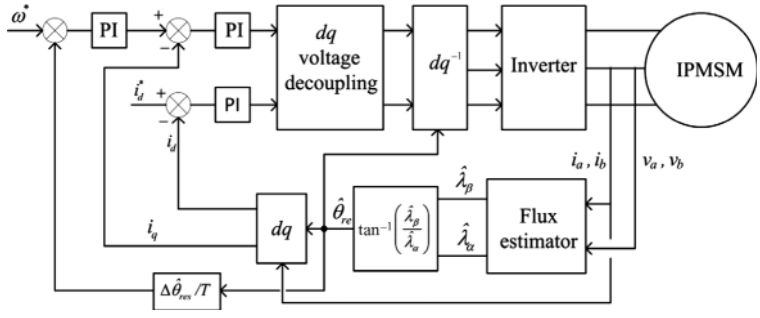

Figure 19.25 A sensorless control scheme in the estimated dq reference frame

Another scheme of sensorless control employs the indirect torque and flux control scheme of Sections 19.2 and 19.3, via i_d and i_q controls, as indicated in Figure 19.25. In this scheme, the rotor velocity/position is estimated from a closed-loop flux and current observers and the position information is then used for transforming the stator currents into i_d and i_q. Current vector control of Section 19.2 and 19.3 is then used for indirect torque and flux control (Corley and Lorenz 1998; Bolognani *et al.* 1999; Kim *et al.* 2002). Various refinements of this method have been available, however, reliable operation at very low speed has not been guaranteed.

19.6 Sensorless Operation at Very Low Speed with High-Frequency Injection

The desirability to operate mechanical sensorless at very low speed and standstill has led to the recent development of another sensorless approach where the saliency of the machine is used to modulate a high frequency signal injected into the stator in order to extract flux or rotor position information. Several high frequency signal injection techniques for current vector controlled IPMSM drives have been reported in recent literature (Jung-Ik and Seung-Ki 1999; Spiteri *et al.* 2002; Caruana *et al.* 2003). While some of these methods require additional hardware, the DTC scheme is favorably disposed to the dq frame rotating injection, because the voltage vectors applied in the DTC scheme can readily be adapted for the HF injection without requiring additional hardware. The following section will describe the dq frame rotating injection that has been adopted industrially.

The rotating HF injection, being at a reasonably high frequency compared to the fundamental AC current in the machine, removes the influence of stator resistance on the machine model. We assume that a carrier frequency voltage given by equation (19.33) is injected into the estimated d-axis.

$$\begin{bmatrix} v_{dc} \\ v_{qc} \end{bmatrix} = V_c \cos(\omega_c t) \begin{bmatrix} 1 \\ 0 \end{bmatrix}. \tag{19.33}$$

The model of the machine to the carrier frequency voltage is then given by

$$\begin{bmatrix} v_{\alpha c} \\ v_{\beta c} \end{bmatrix} \approx \frac{d}{dt} \begin{bmatrix} L_0 + L_1 \cos(2\theta_{re}) & -L_1 \sin(2\theta_{re}) \\ -L_1 \sin(2\theta_{re}) & L_0 - L_1 \cos(2\theta_{re}) \end{bmatrix} \begin{bmatrix} i_{\alpha c} \\ i_{\beta c} \end{bmatrix}, \tag{19.34}$$

resulting in

$$\begin{bmatrix} i_{\alpha c} \\ i_{\beta c} \end{bmatrix} = \cos(\omega_c t) \begin{bmatrix} I_{c0} \cos(\hat{\theta}_{re}) - I_{c1} \cos(2\theta_{re} - \hat{\theta}_{re}) \\ -I_{c0} \sin(\hat{\theta}_{re}) + I_{c1} \sin(2\theta_{re} - \hat{\theta}_{re}) \end{bmatrix}, \tag{19.35}$$

where $L_0 = \frac{L_q + L_d}{2}$ and $L_1 = \frac{L_q - L_d}{2}$ are the average inductance and the amplitude of the spatial modulation of the inductance, respectively, and $I_{c0} = \frac{V_c}{\omega_c} \frac{L_0}{L_0^2 - L_1^2}$ and $I_{c1} = \frac{V_c}{\omega_c} \frac{L_1}{L_0^2 - L_1^2}$. By transforming equation (19.35) into the estimated dq axes, the HF component in the estimated q-axis is

$$\hat{i}_{qc} = I_{c1} \cos(\omega_c t) \sin\left(2(\theta_{re} - \hat{\theta}_{re})\right). \tag{19.36}$$

By using a band-pass, demodulation, and low-pass filters as indicated in Figure 19.26a and a phase-locked loop with a PI controller and integrator, the estimated rotor position can be extracted as indicated in Figure 19.26b. While the HF injection described above delivers reliable operation at very low and zero speeds in the face of change of full load, temperature and machine parameters (Foo *et al.* 2010), the HF injection scheme loses its merit when the drive is operated at high speeds where the separation between the fundamental AC frequency

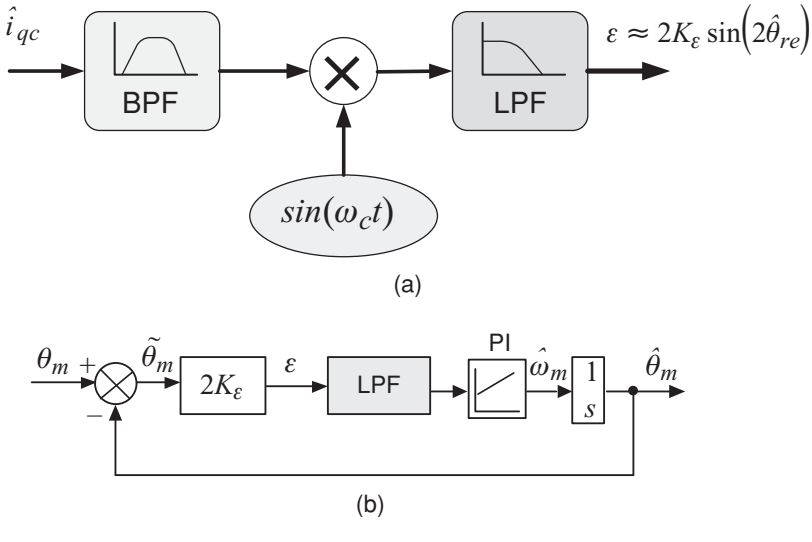

Figure 19.26 (a) Filtering and demodulation of HF q-axis current for rotor position estimation; (b) extraction of rotor position with PLL. LPF, low-pass filtering

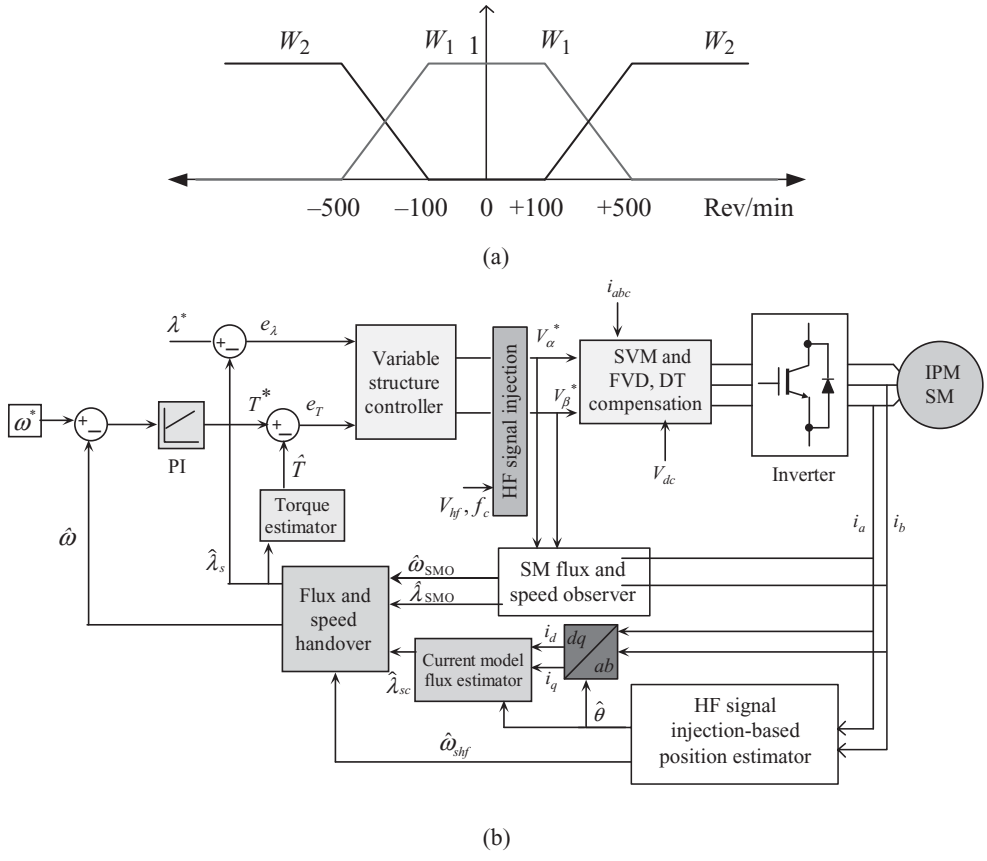

Figure 19.27 (a) Flux and speed handover scheme (b) Combined HF and SM flux observers with SM DTC

in the stator and the HF signal is not high. Clearly, the HF injection is best applied at very low speed and it should be removed when the drive reaches a reasonable speed. A handover mechanism is therefore needed that allows this transfer to take place smoothly. The transfer algorithm may consist of a linear transition weighting of $0 - 1$ between speeds of ± 100 and ± 500 rev/min, as indicated in Figure 19.27a (Foo and Rahman 2010). The flux and speed estimations are mainly supplied by the HF injection scheme (i.e., $W_1 = 1$) from 0 to ± 100 rev/min, linearly reducing to zero at ± 500 rev/min while these are mainly supplied by the SM observer (i.e., $W_2 = 1$) from and ± 500 rev/min to top speed, linearly reducing to zero at ± 100 rev/min. Figure 19.27b shows the combined HF and SM flux observers with SM DTC. Figure 19.28 shows the steady-state (at zero speed) and dynamic performance of the controller of Figure 19.27b. Figure 19.28a indicates the zero-speed performance in terms of actual and estimated speeds, estimated torque, estimated flux and the speed error, when rated torque is applied and removed abruptly. The HF injection scheme fully supplies the position, speed, flux linkage and torque feedback signals during this test. Figure 19.28b shows these signals

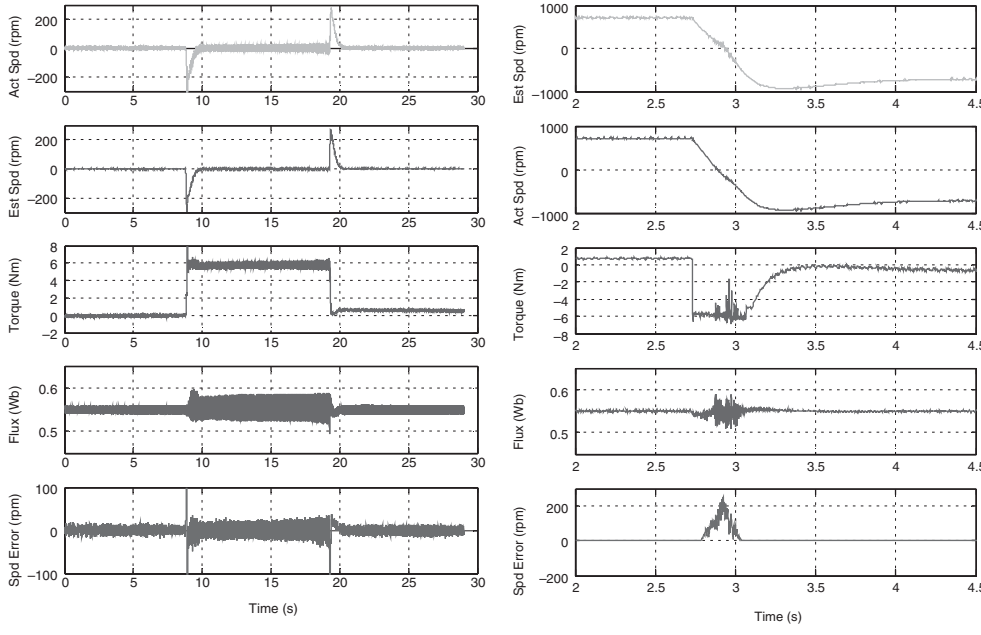

Figure 19.28 Performance of the combined SM DTC and HF injection scheme of Figure 19.27 (a) zero-speed performance with full rated torque applied abruptly; (b) speed reversal between ± 1000 rev/min. [experimental results]

when the machine is driven with speed reference reversing between ± 1000 rev/min. Smooth transition of these estimated signals between the SMO and HF injection schemes is clearly observed.

19.7 Conclusions

This chapter has described the control characteristics and techniques for the interior permanent magnet synchronous machine, which has been adopted in traction and a host of other industrial applications lately. It starts with some description of the magnetic circuits of the machine followed by a description of its steady-state torque-speed characteristics in a stator quadrature frame and its dynamic model. The exploitation of the inverse saliency for reluctance torque in order to achieve a high field-weakening (constant-power) speed range is highlighted. The above models are used in determining the references for its inner torque control. The control of the machine in the rotor dq reference frame with mechanical position feedback for transforming the measured stator currents into the rotor dq reference is then described. There are no issues with operating this machine under such control to cover a wide speed range from zero to full field weakening speed range. The mechanical sensor, which is a weak link in drive systems such as in vehicle traction, is eliminated in sensorless operation. Sensorless control techniques, which employ the direct torque control and high-frequency injection approaches, are described in detail. Open-loop and closed-loop stator flux estimators, which are at the heart

of any sensorless scheme, are then illustrated and their problems and applicability at very low speed are highlighted. The high-frequency signal injection scheme which estimates the stator flux with adequate accuracy by exploiting the saliency of such machines for operation at very low and zero speed is then described. In conclusion, it can be stated that the IPM machine drive technology now offers very attractive solutions for industrial drives covering speed from zero to a wide constant-power speed range.

References

Bianchi N and Bolognani S (1999) Performance analysis of An IPM Motor with segmented rotor for flux-weakening application. *International Conference on Electrical Machine and Drives*, 49–53.

Boldea I, Pitic CI, Lascu C, *et al.* (2006) DTFC-SVM motion sensorless control of a PM-assisted reluctance synchronous machine as starter-alternator for hybrid vehicles. *IEEE Transactions on Power Electronics*, **21**(3), 711–719.

Boldea I, Paicu MC, and Andreescu GD (2008) Active flux concept for motion sensorless unified AC drives. *IEEE Transactions on Power Electronics*, **23**, 2612–2618.

Bolognani S, Oboe R, and Zigliotto M (1999) Sensorless full-digital PMSM drive with EKF estimation of speed and rotor position. *IEEE Transactions on Industrial Electronics*, **46**, 184–191.

Caruana C, Asher GM, Bradley KJ, and Woolfson MS (2003) Flux position estimation in cage induction machines using synchronous injection and kalman filtering. *IEEE Transactions on Industry Applications*, **39**(5), 1372–1378.

Chen Z, Tomita M, Doki S, and Okuma S (2003) An extended electromotive force model for sensorless control of interior permanent-magnet synchronous motors. *IEEE Transactions on Industrial Electronics*, **50**, 288–295.

Corley M and Lorenz RD (1998) Rotor position and velocity estimation for a salient-pole permanent magnet synchronous machine at standstill and high speeds. *IEEE Transactions on Industry Applications*, **43**(4), 784–789.

Dutta R and Rahman MF (2008) Design and analysis of an interior permanent magnet (IPM) machine with very wide constant power operation range. *IEEE Trans on Energy Conversion*, **23**(1), 25–33.

Foo G and Rahman MF (2010) Sensorless sliding mode MTPA control of an IPM synchronous motor drive using a sliding mode observer and HF signal injection. *IEEE Transactions on Industrial Electronics*, **57**(4), 1270–1278.

Foo G, Sayeef S, and Rahman MF (2010) Low speed and standstill operation of a sensorless direct torque and flux controlled IPM synchronous motor drive. *IEEE Transactions on Energy Conversion*, **25**(1), 25–33.

Haque ME and Rahman MF (1994) A Sensorless initial rotor position estimation scheme for a direct torque controlled interior permanent magnet synchronous motor drive. *IEEE Transactions on Power Electronics*, **18**(6), 1376–1383.

Haraguchi H, Morimoto S, and Sanada M (2009) Suitable design of a PMSG for a small-scale wind power generator. In *Electrical Machines and Systems ICEMS 2009*, 1–6.

Honda Y, Higaki T, Morimoto S, and Takeda Y (1998) Rotor design optimisation of a multi-layer interior permanent-magnet synchronous motor. *Electric Power Applications, IEE Proceedings*, vol. **145**, 119–124.

Honda Y, Higaki T, Morimoto S, and Takeda Y (1986) Interior permanent-magnet synchronous motors for adjustable-speed drives. *IEEE Transaction on Industry Applications*, **22**, 738–747.

Jahns TM (1987) Flux-weakening regime operation of an interior permanent magnet synchronous motor drive. *IEEE Trans. on Industry Applications*, **23**, 398–407.

Jahns TM, Kaliman GB, and Neumann TW (1986) Interior permanent-magnet synchronous motors for adjustable speed drives. *IEEE Transactions on Industry Applications*, **22**, 738–747.

Jung-Ik Ha and Seung-Ki Sul (1999) Sensorless field-orientation control of an induction machine by high-frequency signal injection. *IEEE Transaction on Industry Applications*, **35**(1).

Kamiya M (2006) Development of traction drive motors for the toyota hybrid system. *Transactions of the Institute of Electrical Engineers of Japan*, **126**, 473–479.

Kim H, Harke MC, and Lorenz RD (2002) Sensorless control of interior permanent magnet drives with zero-phase lag position estimation. *Conference REC IEEE-IAS Annual Meeting*, 86–91.

Kim H, Huh KK, Lorenz RD, and Jahns TM (2004) A novel method for initial rotor position estimation for IPM synchronous motor drives. *IEEE Transactions on Industry Applications*, **40**(5), 1369–1378.

Miller TJE (1989) *Brushless Permanent-Magnet and Reluctance Machines*. University Press, Oxford.

Morimoto S, Takeda Y, Hirasa T, and Taniguchi K (1990) Expansion of operating limits for permanent magnet motor by current vector control considering inverter capacity. *IEEE Transaction on Industry Applications*, **26**, 866–871.

Morimoto S, Sanada M, and Takeda Y (1994) Wide-speed operation of interior permanent magnet synchronous motors with high-performance current regulator. *IEEE Transactions on Industry Applications*, **30**, 920–926.

Piippo A, Hinkkanen M, and Luomi J (2008) Analysis of adaptive observer for sensorless control of interior permanent magnet synchronous motors. *IEEE Transactions on Industrial Electronics*, **55**, 570–576.

Rahman MF, Zhong L, and Lim KW (1998) A Direct torque controlled interior magnet synchronous motor drive incorporating field weakening. *IEEE Transactions on Industry Applications*, **34**(6), 1246–1253.

Satoh H, Akutsu S, Miyamura T, and Shinoki H (2004) Development of traction motor for fuel cell vehicle. In *SAE World Congress*, Detroit, Michigan.

Sayeef S and Rahman MF (2009) Improved flux and torque estimators of a direct torque controlled interior pm machine with compensations of dead-time effects and forward voltage drops. *Journal of Power Electronics (JPE)*, **9**(3), 438–446.

Sebastiangordon T and Slemon GR (1987) Operating limits of inverter-driven permanent magnet motor drives. *IEEE Transactions on Industry Applications*, **IA-23**, 327–333.

Soong WL, Staton DA, and Miller TJE (1995) Design of a new axially-laminated interior permanent magnet motor. *IEEE Transaction on Industry Applications*, **31**, 358–367.

Spiteri, Cilia C, Michallef J, and Apap M (2002) Sensorless vector control of surface mount pmsm using high frequency injection. *Power Electronics Machines and Drives Conference Publication (487) IEE2002*.

Tang L, Zhong L, Rahman MF, and Hu Y (2004) A novel direct torque controlled interior permanent magnet synchronous machine drive with low ripple in flux and torque and fixed switching frequency. *IEEE Transactions on Power Electronics*, **19**(2), 346–354.

Wang A, Jia Y, and Soong WL (2011) Comparison of five topologies for an interior permanent magnet machine for a hybrid electric vehicle. *IEEE Transactions on Magnetics*, **47**(10), 3606–3609.

Xu Z and Rahman MF (2007) An adaptive sliding stator flux observer for a direct torque controlled IPM synchronous motor drive. *IEEE Transactions on Industrial Electronics*, **54**(5), 2398–2406.

Zhong L, Rahman MF, and Hu WY (1997) Analysis of direct torque control in permanent magnet synchronous motor drives. *IEEE Transactions on Power Electronics*, **12**(3), 528–536.

20

Nonlinear State-Feedback Control of Three-Phase Wound Rotor Synchronous Motors

Abdelmounime El Magri, Vincent Van Assche, Abderrahim El Fadili, Fatima-Zahra Chaoui, and Fouad Giri
GREYC Lab, University of Caen Basse-Normandie, France

20.1 Introduction

Compared to others, synchronous motors present several benefits. As already pointed out, for exanple, in Chapter 3, they feature a remarkable speed reversion flexibility, they exist in a variety of characteristics (ranging from a few kilowatts to several megawatts), and they enjoy three control inputs (this is the case of wound rotor synchronous machines (WRSMs)) making possible to achieve energetic optimization, in addition to speed control.

It is well known that for WRSMs (and generally for all AC machines), the speed variation can only be performed by changing the stator frequency. Therefore, three-phase DC/AC inverters are resorted, due to their high capability, to ensuring flexible voltage and frequency variation. In the case of AC supply, the (three-phase) net is connected to the three-phase DC/AC inverter through a transformer and an AC/DC rectifier. The connection line between the rectifier and the inverter is called DC link.

The control problem at hand is to design controllers able to ensure speed regulation for the system including the AC/DC converter, the DC/AC inverter and the WRSM (Figure 20.1). As the rotor is wound, a variable DC voltage source is needed. This is realized by inserting a DC/DC converter as shown by Figure 20.1. The point is that such system behaves as a nonlinear load with respect to the AC supply line. Then, undesirable current harmonics are likely to be generated in the AC line. These harmonics reduce the rectifier efficiency, induce

AC Electric Motors Control: Advanced Design Techniques and Applications, First Edition. Edited by Fouad Giri.

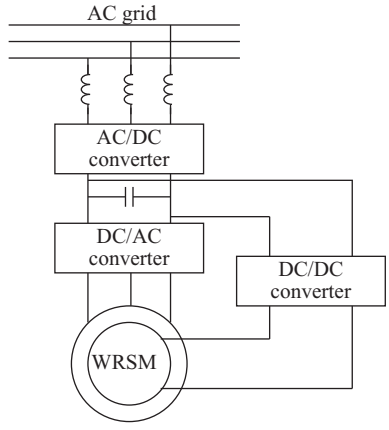

Figure 20.1 Structure of the AC/DC/AC-WRSM system

voltage distortion in the AC supply line and cause electromagnetic compatibility problems. To overcome this drawback, the control objective must not be limited to speed regulation, it should also include the compensation of current harmonics. The last objective is referred to power factor correction (PFC) (Singh *et al.* 2006).

In most works dealing with WRSM control, the control design is simplified by only focusing on the subsystem "DC/AC inverter—Machine." That is, the the dynamics of the AC/DC rectifier are neglected and, consequently, the interaction with the power supply grid is ignored. The simpler problem has been dealt with using several control strategies ranging from simple techniques, for example, field-oriented control (Saleh *et al.* 2004), to more sophisticated nonlinear approaches, for example, feedback linearization (Kuroe *et al.* 1998), direct torque control (Pyrhonen *et al.* 1998) or backstepping design technique (El Magri *et al.* 2006), or nonlinear adaptive control (Tomei and Vorelli 2008). A control strategy that ignores the presence of the AC/DC rectifier suffers at least from two drawbacks. First, the controller design relies on the assumption that the DC voltage (provided by the AC/DC rectifier) is perfectly regulated. The point is that perfect regulation of the rectifier output voltage cannot be ensured ignoring the rectifier load which is nothing other than the set "DC/AC inverter-Motor." The second drawback lies in the entire negligence of the PFC requirement.

The problem of controlling the whole association "AC/DC/AC-PMSM," connected to a mono-phase AC grid hase been addressed in El Magri *et al.* (2010a) and El Magri *et al.* (2012). A nonlinear multiloop control strategy has been developed and shown to meet speed regulation and PFC. This control strategy is presently revisited in two directions by considering WRSMs (instead of PMSMs) and three-phase AC/DC rectifiers (instead of monophase rectifier). It turns out that the controlled "AC/DC/AC-WRSM" system is directly supplied by a three-phase power grid.

The nonlinear multiloop control system is progressively developed in several steps. First, a three-variable loop is designed that (i) makes the speed motor track its varying reference value; (ii) regulates the d-component of stator current to zero optimizing thus the absorbed stator current; and (iii) enforces the excitation current (and consequently the flux in the excitation

winding) to track a given reference signal. Then, the voltage at the DC link between the AC/DC rectifier and inverter is regulated to a constant reference value despite changes of the motor operation conditions. Finally, a reactive power loop is designed that controls the reactive power delivered to the supply grid. All control loops are designed using the Lyapunov and the backstepping technique (Krstic *et al.* 1995). Furthermore, the load torque T_L, the rotor inertia J, the friction coefficient F, and the rotor resistor R_f are considered to be unknown parameters. This parameter uncertainty is coped with by equipping the controller with a parameter adaptation capability. It will be formally proved that the proposed multiloop adaptive controller actually stabilizes (globally and asymptotically) the global controlled system and meets its tracking objectives with a good accuracy. These theoretical results are obtained making judicious use of adequate control theory tools (Khalil 2003).

The chapter is organized as follows: the system under study (i.e., the AC/DC/AC-PMSM association) is modeled and given a state space representation in Section 20.2; the controller design and the closed-loop system analysis are presented in Section 20.3; the controller performances are illustrated through numerical simulations in Section 20.4.

20.2 System Modeling

The controlled system is illustrated by Figure 20.1. It consists of three subsystems: an AC/DC boost rectifier, a combination "inverter-synchronous motor," and a DC/DC converter (excitation circuit). All converters are operating according to the pulse wide modulation (PWM) principle.

20.2.1 Three-Phases AC/DC Rectifier Modeling

The considered rectifier is a three-phase DC/AC converter of boost type (Figure 20.2). It involves six semiconductors (insulated gate bipolar transistors (IGBTs) with antiparallel diodes for bidirectional current flow mode) displayed in three legs a, b, and c. To avoid the short-circuit of the three-phase voltage source, only one switch on the same leg can be conducting at a time. Applying Kirchhoff's laws, this subsystem is shown to be described by the following

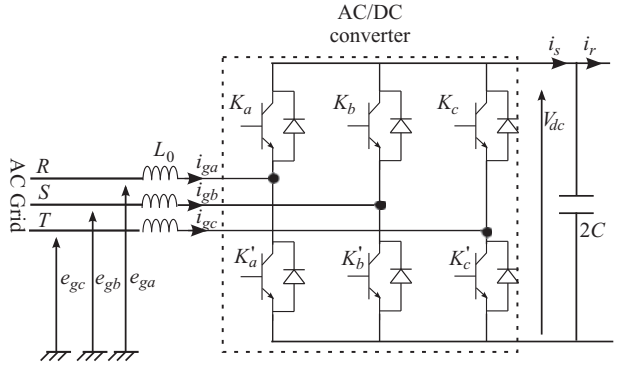

Figure 20.2 AC/DC rectifier power circuit for three-phase inputs

set of differential equations:

$$L_0 \frac{d[i_{gabc}]}{dt} = [e_{gabc}] - v_{dc}[k_{abc}] \tag{20.1a}$$

$$2C \frac{dv_{dc}}{dt} = i_s - i_r \tag{20.1b}$$

$$i_s = [k_{abc}]^T [i_{gabc}], \tag{20.1c}$$

where $[i_{gabc}] = [\, i_{ga} \; i_{gb} \; i_{gc} \,]^T$ is the three-phase input currents in the electric grid, $[e_{gabc}] = [\, e_{ga} \; e_{gb} \; e_{gc} \,]^T$ is the sinusoidal three-phase net voltages (with known constant frequency ω_g), v_{dc} denotes the voltage in capacitor 2C, i_r designates the output current converter and $k_i \;\; (i = a, \; b, \; c)$ is a binary control input determining the switch position. Specifically, one has

$$k_i = \begin{cases} 1 \;\; \text{if} \;\; K_i \;\; \text{is} \;\; \text{ON} \;\; \text{and} \;\; K_i' \;\; \text{is} \;\; \text{OFF} \\ 0 \;\; \text{if} \;\; K_i \;\; \text{is} \;\; \text{OFF} \;\; \text{and} \;\; K_i' \;\; \text{is} \;\; \text{ON} \end{cases} \qquad (i = a, \; b, \; c). \tag{20.2}$$

To simplify the three-phase representation (20.1a) for the synthesis of control laws, the Park transformation is resorted to project the triphase electrical quantities onto the two-coordinate dq-frame. Doing so, one gets the following two-phase model:

$$\frac{di_{gd}}{dt} = \frac{1}{L_0} E_{gd} + \omega_g i_{gq} - \frac{1}{L_0} u_{gd} v_{dc}, \tag{20.3a}$$

$$\frac{di_{gq}}{dt} = \frac{1}{L_0} E_{gq} - \omega_g i_{gd} - \frac{1}{L_0} u_{gq} v_{dc}, \tag{20.3b}$$

$$2C \frac{dv_{dc}}{dt} = i_s - i_r, \tag{20.3c}$$

where (E_{gd}, E_{gq}), (i_{gd}, i_{gq}), and (u_{gd}, u_{gq}) denote, respectively, the network voltage and current and input control of the rectifier in dq-coordinate. Averaging is performed (over the PWM cutting ratio) to get around the difficulty associated to the binary nature of the physical three-phase control input (k_a, k_b, k_c).

The instantaneous power absorbed by the AC/DC converter is given by the well-known expression $P_{\text{Load}} = [e_{gabc}]^T [i_{gabc}] = E_{gd} i_{gd} + E_{gq} i_{gq}$. On the other hand, the power released by the network is given by $P_{\text{Out}} = i_s v_{dc}$. Using the power conservation principle, that is, $P_{\text{Out}} \approx P_{\text{Load}}$, one gets $i_r v_{dc} = E_{gd} i_{gd} + E_{gq} i_{gq}$. Then, multiplying by v_{dc} the first equation of the system (20.3a-c), this rewrites:

$$2v_{dc} \frac{dv_{dc}}{dt} = \frac{1}{C} E_{gd} i_{gd} + \frac{1}{C} \left(E_{gq} i_{gq} - v_{dc} i_r \right), \tag{20.4a}$$

$$\frac{di_{gd}}{dt} = \frac{1}{L_0} E_{gd} + \omega_g i_{gq} - \frac{1}{L_0} u_{gd} v_{dc}, \tag{20.4b}$$

$$\frac{di_{gq}}{dt} = \frac{1}{L_0} E_{gq} - \omega_g i_{gd} - \frac{1}{L_0} u_{gq} v_{dc}. \tag{20.4c}$$

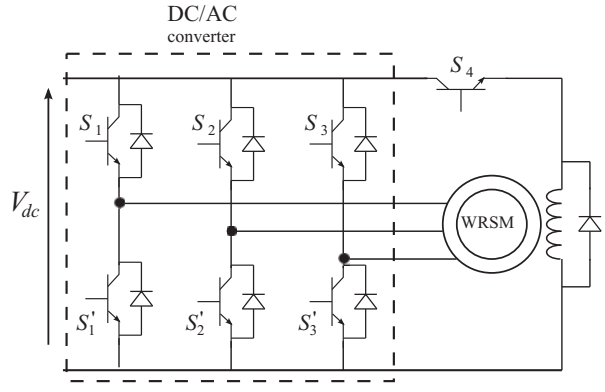

Figure 20.3 The association of the three-phase inverter, DC/DC power circuits, and WRSM

20.2.2 Inverter-Motor Subsystem Modeling

The considered inverter is depicted by Figure 20.3. It contains of six IGBTs, with antiparallel diodes for bidirectional power flow purpose, connected in bridge mode. The whole system modeling is generally accomplished in the rotating dq-coordinate frame. Accordingly, all sinusoidal signals are transformed into continuous quantities along the d- or the q-axis. It is shown in El Magri *et al.* (2006) and El Magri *et al.* (2010b) that the WRSM model, expressed in the dq-coordinates, can be given the following state space form:

$$\frac{d\omega}{dt} = -\frac{F}{J}\omega + \frac{a_1}{J} i_{sd} i_{sq} + \frac{a_2}{J} i_f i_{sq} - \frac{1}{J} T_L, \tag{20.5a}$$

$$\frac{di_{sq}}{dt} = -b_1 i_{sq} - b_2 i_{sd}\omega - b_3 i_f \omega + b_4 v_{sq}, \tag{20.5b}$$

$$\frac{di_{sd}}{dt} = -c_1 i_{sd} + c_2 R_f i_f + c_3 i_{sq}\omega + c_4 v_{sd} - c_5 v_f, \tag{20.5c}$$

$$\frac{di_f}{dt} = -d_1 R_f i_f + d_2 i_{sd} - d_3 i_{sq}\omega - d_4 v_{sd} + d_5 v_f, \tag{20.5d}$$

where (v_{sd},v_{sq}) denotes the averaged stator voltage in dq-coordinates, v_f denotes the averaged rotor excitation voltage. The involved coefficients are described in Table 20.1.

The inverter features the fact that the d- and q-components of the stator voltage can be controlled independently. To this end, these voltages are expressed in function of the corresponding control action (Michael *et al.* 1998):

$v_{sq} = u_1 v_{dc}$, $v_{sd} = u_2 v_{dc}$, $v_f = u_3 v_{dc}$.
In turn, the averaged current writes:

$$\bar{i}_r = u_1 \bar{i}_{sq} + u_2 \bar{i}_{sd} + u_3 \bar{i}_f,$$

where $u_1 = \overline{u}_{sq}$; $u_2 = \overline{u}_{sd}$ represent the averaged d- and q-axis components of the three-phase duty ratio system (s_1, s_2, s_3); $u_3 = \overline{u}_f$ is the averaged duty ratio of s_4. The binary control

Table 20.1 Notations used in the WRSM model (20.5)

$a_1 = p(L_d - L_q)$	$a_2 = pM$			
$b_1 = \frac{R_s}{L_q}$	$b_2 = p\frac{L_d}{L_q}$	$b_3 = p\frac{M}{L_q}$	$b_4 = \frac{1}{L_q}$	
$c_1 = \frac{R_s L_f}{L_d L_f - M^2}$	$c_2 = \frac{M}{L_d L_f - M^2}$	$c_3 = \frac{pL_f L_q}{L_d L_f - M^2}$	$c_4 = \frac{L_f}{L_d L_f - M^2}$	$c_5 = \frac{M}{L_d L_f - M^2}$
$d_1 = \frac{L_d}{L_d L_f - M^2}$	$d_2 = \frac{R_s M}{L_d L_f - M^2}$	$d_3 = \frac{pML_q}{L_d L_f - M^2}$	$d_4 = \frac{M}{L_d L_f - M^2}$	$d_5 = \frac{L_d}{L_d L_f - M^2}$

R_s, stator resistor; R_f, rotor resistor; (L_d, L_q), d- and q-axis stator inductances; L_f, rotor inductance; M, rotor and stator mutual inductance; p, number of pole pairs; F, combined rotor and load viscous friction; J, combined rotor and load inertia; T_L, motor load torque.

inputs $s_i (i = 1 \ldots 4)$, representing the switch positions, are defined as follows:

$$s_i = \begin{cases} 1 \text{ if } S_i \text{ is ON and } S_i^{'} \text{ is OFF} \\ 0 \text{ if } S_i \text{ is OFF and } S_i^{'} \text{ is ON} \end{cases} \qquad (i = 1, 2, 3) \tag{20.6a}$$

$$s_4 = \begin{cases} 1 \text{ if } S_4 \text{ is ON} \\ 0 \text{ if } S_4 \text{ is OFF.} \end{cases} \tag{20.6b}$$

Now, let us introduce the state variables,

$x_1 = \overline{\omega}$, $x_2 = \overline{i}_{sq}$, $x_3 = \overline{i}_{sd}$, $x_4 = \overline{i}_f$, $x_5 = \overline{v}_{dc}^2$, $x_6 = \overline{i}_{gd}$, and $x_7 = \overline{i}_{gq}$, and the inputs,

$u_4 = \overline{u}_{gd}$, $u_5 = \overline{u}_{gq}$.

The latter represent the average d- and q-axis components of the three-phase duty ratio system (k_a, k_b, k_c). Wherever it comes in, the averaging is intended over the PWM cutting periods.

The state space equations established so far form a state-space model of the whole system including the AC/DC/AC converters combined with the wound rotor synchronous motor. For convenience, the whole model is rewritten here for future referencing:

$$\frac{dx_1}{dt} = -\frac{F}{J}x_1 + \frac{a_1}{J}x_2 x_3 + \frac{a_2}{J}x_2 x_4 - \frac{1}{J}T_L, \tag{20.7a}$$

$$\frac{dx_2}{dt} = -b_1 x_2 - b_2 x_1 x_3 - b_3 x_1 x_4 + b_4 u_1 v_{dc}, \tag{20.7b}$$

$$\frac{dx_3}{dt} = -c_1 x_3 + c_2 R_f x_4 + c_3 x_1 x_2 + c_4 u_2 v_{dc} - c_5 u_3 v_{dc}, \tag{20.7c}$$

$$\frac{dx_4}{dt} = -d_1 R_f x_4 + d_2 x_3 - d_3 x_1 x_2 - d_4 u_2 v_{dc} + d_5 u_3 v_{dc}, \tag{20.7d}$$

$$\frac{dx_5}{dt} = \frac{1}{C}E_{gd}x_6 + \frac{1}{C}\left(E_{gq}x_7 - v_{dc}\overline{i}_r\right), \tag{20.7e}$$

$$\frac{dx_6}{dt} = \frac{1}{L_0}E_{gd} + \omega_g x_7 - \frac{1}{L_0}u_4 v_{dc}, \tag{20.7f}$$

$$\frac{dx_7}{dt} = \frac{1}{L_0}E_{gq} - \omega_g x_6 - \frac{1}{L_0}u_5 v_{dc}. \tag{20.7g}$$

20.3 Nonlinear Adaptive Controller Design

20.3.1 Control Objectives

Based on the system model (20.7a–d), a controller has to be developed in order to achieve the following control objectives:

> CO 1: The machine speed ω must track, as closely as possible, a given reference signal ω_{ref}.
>
> CO 2: The inverter output currents ($i_{ga},\ i_{gb},\ i_{gc}$) must be sinusoidal with the same frequency as the supplied power grid, the reactive power in the AC grid must be well regulated.

As there are five control inputs at hand, namely, u_1, u_2, u_3, u_4, and u_5, we seek three additional control objectives, namely:

> CO 3: Regulate the current i_{sd} to a reference value i_{sdref}, preferably equal to zero in order to guarantee the absence of d-axis stator current, implying thus no reluctance torque. Doing so, only the q-axis reactance impacts the final voltage. In particular, no direct magnetization/demagnetization along the d-axis is needed, that is, only the field winding contributes to producing the flux along this direction (Muhammad and Rashid 2001).
>
> CO 4: Control the excitation current i_f (and so the flux in the excitation winding) making it track as closely as possible a given reference signal i_{fref} (generally equal to the constant nominal excitation current).
>
> CO 5: Control the continuous voltage v_{dc} making it track a given reference signal v_{dcref}. Generally, this is set equal to the constant nominal voltage applied at the inverter input.

The above control objectives must be achieved despite the fact that the load torque T_L, the inertia J, the viscous friction F, and the rotor resistor R_f are presently allowed to be unknown and changing. This parameter uncertainty is coped with by providing the controller with an adaptation capability. The adaptive controller design will be performed using the backstepping technique (Krstic *et al.* 1995). This technique has already used in previous chapters (e.g., 10 and 13). It involves a progressive construction of Lyapunov functions, virtual control signals, and stabilizing control functions. Given the system complexity and the control objective multiplicity, the resulting adaptive controller will consist of several loops the design of which will be organized in two major stages. The control design for the inverter-motor subsystem is dealt with in the first stage; the rectifier control design will be is investigated in the second stage.

20.3.2 Inverter-Motor Subsystem Control Design

The control inputs that act on the inverter-motor subsystem are (u_1, u_2, u_3). The corresponding control laws must be designed in order to meet the three control objectives concerning the inverter-motor, namely, CO 1, CO 3, and CO 4. These objectives will be separately investigated in three separate subsections, where the control law of each input (u_1, u_2, u_3) is established.

Speed Regulator Design for WRSM

Presently, the focus is made on the control objective CO 1. Based on equations (20.7a–b), a first equation involving the control inputs (u_1, u_2, u_3) will now be designed, using the backstepping technique (Krstic *et al.* 1995), so that the motor speed ω tracks well any reference ω_{ref}. As the subsystem (20.7a–b) is of relative degree 2, the design towards that equation is performed in two steps.

Step 1: Let z_1 denotes the speed tracking error:

$$z_1 = x_1 - x_1^* \underset{=}{\text{def}} \omega - \omega_{ref}. \tag{20.8}$$

In view of (20.7a), this error undergoes the following equation:

$$\dot{z}_1 = -\frac{F}{J} x_1 + \frac{1}{J} (a_1 x_3 + a_2 x_4)\, x_2 - \frac{T_L}{J} - \dot{x}_1^*. \tag{20.9}$$

In (20.9), the quantity $\alpha = (a_1 x_3 + a_2 x_4)\, x_2$ stands up as a (virtual) control input for the z_1-dynamics because the actual control inputs (presently u_1, u_2, and u_3) act on z_1 indirectly through α. Following the backstepping design technique, the following Lyapunov function candidate is considered:

$$V_1 = 0.5\, z_1^2. \tag{20.10}$$

Deriving V_1 along the trajectory of (20.9) yields

$$\dot{V}_1 = z_1\, \dot{z}_1 = z_1 \left(-\frac{F}{J} x_1 + \frac{1}{J} \alpha - \frac{T_L}{J} - \dot{x}_1^* \right). \tag{20.11}$$

This suggests the following control law for the (virtual control) α:

$$\alpha^* = -k_1 J\, z_1 + F\, x_1 + T_L + J\, \dot{x}_1^* \tag{20.12}$$

with $k_1 > 0$ a design parameter. Indeed, substituting α^* to α gives $\dot{V}_1 = -k_1\, z_1^2$ that is negative definite in z_1. The point is that J, F, and T_L are unknown. Then, these must be replaced in equation (20.12) by their estimates (denoted $\hat{J}$, $\hat{F}$, and $\hat{T}_L$ that have yet to be determined). Doing so, one gets the following stabilizing function:

$$\hat{\alpha}^* = -k_1 \hat{J}\, z_1 + \hat{F}\, x_1 + \hat{T}_L + \hat{J}\, \dot{x}_1^*. \tag{20.13}$$

As $\alpha = (a_1 x_3 + a_2 x_4)\, x_2$ is just a virtual control input, one cannot set $\alpha = \hat{\alpha}^*$. Nevertheless, the above expression of $\hat{\alpha}^*$ is retained and a new error is introduced:

$$z_2 = \alpha - \hat{\alpha}^*. \tag{20.14}$$

Using equations (20.13)–(20.14), it follows from (20.9) that the z_1-dynamics undergo the following equation:

$$\dot{z}_1 = -k_1\, z_1 + \frac{z_2}{J} + \frac{\tilde{J}}{J}\, \left(k_1\, z_1 - \dot{x}_1^*\right) - \frac{\tilde{T}_L}{J} - \frac{\tilde{F}}{J}\, x_1, \tag{20.15}$$

where $\tilde{J} = J - \hat{J}$, $\tilde{F} = F - \hat{F}$, and $\tilde{T}_L = T_L - \hat{T}_L$.

Step 2: Now, the aim is to make the couple of errors (z_1, z_2) vanish asymptotically. The trajectory of the error z_2 is obtained by time-derivation of the equation (20.14):

$$\dot{z}_2 = (a_1 \dot{x}_3 + a_2 \dot{x}_4)\, x_2 + (a_1 x_3 + a_2 x_4)\, \dot{x}_2 - \dot{\hat{\alpha}}^*. \tag{20.16}$$

Using equations (20.13)–(20.15) and the subsystem (20.7a–b) in (20.16) yields the following z_2-dynamics:

$$\begin{aligned}
\dot{z}_2 = {} & \alpha_1\, u_1 v_{dc} + \alpha_2\, u_2 v_{dc} + \alpha_3\, u_3 v_{dc} \\
& + \beta\,(x_{1\ldots4}) - \hat{J}\, \left(k_1^2\, z_1 + \ddot{x}_1^*\right) + k_1\, z_2 + \hat{F}\, \left(k_1\, z_1 - \dot{x}_1^*\right) \\
& - \tfrac{\hat{J}}{J}\, \left(k_1\, z_2 - \hat{J}\, k_1\, \left(k_1\, z_1 - \dot{x}_1^*\right)\right) - \tfrac{\hat{F}}{J}\, \hat{J}\, k_1\, x_1 - \tfrac{\tilde{T}_L}{J}\, (\hat{J}\, k_1 + \hat{F}) \\
& + \left(k_1\, z_1 - \dot{x}_1^*\right)\, \dot{\hat{J}} - \dot{\hat{T}}_L - \dot{\hat{F}}\, x_1 \\
& - \tfrac{\hat{F}}{J}\, \left(z_2 + \tilde{J}\, \left(k_1\, z_1 - \dot{x}_1^*\right) - \tilde{T}_L - \tilde{F}\, x_1\right) + x_2 x_4\, (a_1 c_2 - a_2 d_1)\, \tilde{R}_f
\end{aligned} \tag{20.17}$$

with

$$\begin{aligned}
\beta\, (x_{i=1\ldots4}) = {} & (a_1\, x_3 + a_2\, x_4)\, (-b_1\, x_2 - b_2\, x_1\, x_3 - b_3\, x_1\, x_4) \\
& + a_1\, x_2\, \left(-c_1\, x_3 + \hat{R}_f c_2\, x_4 + c_3\, x_1 x_2\right) \\
& + a_2\, x_2\, \left(-\hat{R}_f d_1\, x_4 + d_2\, x_3 - d_3\, x_1 x_2\right) \\
\alpha_1 = {} & b_4\, (a_1\, x_3 + a_2\, x_4) \\
\alpha_2 = {} & x_2\, (a_1\, c_4 - a_2\, d_4) \\
\alpha_3 = {} & x_2\, (-a_1\, c_5 + a_2\, d_5)\,,
\end{aligned}$$

where $\tilde{R}_f$ denotes an estimate (yet to be determined) of R_f and $\tilde{R}_f = R_f - \hat{R}_f$. For convenience, the error equations (20.15) and (20.17) are put together:

$$\dot{z}_1 = -k_1\, z_1 + \frac{z_2}{J} + \frac{\tilde{J}}{J}\, \left(k_1\, z_1 - \dot{x}_1^*\right) - \frac{\tilde{T}_L}{J} - \frac{\tilde{F}}{J}\, x_1, \tag{20.18a}$$

$$\begin{aligned}\dot{z}_2 = \gamma &- \tfrac{F}{J}\, z_2 + x_2 x_4\ (a_1 c_2 - a_2\, d_1)\, \tilde{R}_f \\ &- \tfrac{\tilde{J}}{J}\ \left(k_1\, z_2 - (\hat{J}\, k_1 - \hat{F})\left(k_1\, z_1 - \dot{x}_1^*\right)\right) \\ &- \tfrac{\tilde{F}}{J}\ \left((\hat{J}\, k_1 - \hat{F}) x_1 + z_2\right) - \tfrac{\tilde{T}_L}{J}\ \left(\hat{J}\, k_1 - \hat{F}\right),\end{aligned} \tag{20.18b}$$

with

$$\begin{aligned}\gamma = \beta\,(x_{1\ldots4}) + k_1\, z_2 + \alpha_1\, u_1 v_{dc} + \alpha_2\, u_2 v_{dc} + \alpha_3\, u_3 v_{dc} \\ - \hat{J}\ \left(k_1^2\, z_1 + \ddot{x}_1^*\right) + \hat{F}\ \left(k_1\, z_1 - \dot{x}_1^*\right) + \dot{\hat{J}}\left(k_1\, z_1 - \dot{x}_1^*\right) - \dot{\hat{T}}_L - \dot{\hat{F}}\, x_1,\end{aligned} \tag{20.19}$$

Note that the actual control inputs (u_1, u_2, u_3) have come out for the first time in the second differential equation (20.18a), through the quantity γ which acts there as a control variable. To determine a stabilizing control law for (20.18a), let us consider the following quadratic Lyapunov function candidate:

$$V_2 = \frac{1}{2}\, z_1^2 + \frac{1}{2}\, z_2^2 + \frac{1}{2J}\ \tilde{J}^2 + \frac{1}{2J}\ \tilde{F}^2 + \frac{1}{2J}\ \tilde{T}_L^2. \tag{20.20}$$

Using (20.18a), one gets from (20.20):

$$\begin{aligned}\dot{V}_2 &= z_1 \dot{z}_1 + z_2 \dot{z}_2 + \tfrac{\tilde{J}}{J}\ \dot{\tilde{J}} + \tfrac{\tilde{F}}{J}\ \dot{\tilde{F}} + \tfrac{\tilde{T}_L}{J}\ \dot{\tilde{T}}_L \\ &= -k_1\, z_1^2 + \gamma\, z_2 + \tfrac{1}{J} z_1 z_2 - \tfrac{F}{J}\, z_2^2 + (a_1 c_2 - a_2 d_1)\, x_2 x_4 z_2\ \tilde{R}_f \\ &\quad + \tfrac{\tilde{J}}{J}\left(z_1\,(k_1\, z_1 - \dot{x}_1^*) - k_1\, z_1^2 + (\hat{J} k_1 - \hat{F})(k_1\, z_1 - \dot{x}_1^*) z_2 - \dot{\hat{J}}\right) \\ &\quad + \tfrac{\tilde{F}}{J}\left(-\, x_1 z_1 - z_2^2 - (\hat{J}\, k_1 - \hat{F}) x_1 z_2 - \dot{\hat{F}}\right) \\ &\quad + \tfrac{\tilde{T}_L}{J}\left(-\, z_1 - (\hat{J}\, k_1 - \hat{F}) z_2 - \dot{\hat{T}}_L\right).\end{aligned} \tag{20.21}$$

The three last terms in the second equality (20.21) can be canceled by using the following adaptive laws:

$$\dot{\hat{J}} = z_1\ \left(k_1\, z_1 - \dot{x}_1^*\right) - k_1\, z_1^2 + (\hat{J} k_1 - \hat{F})\left(k_1\, z_1 - \dot{x}_1^*\right) z_2, \tag{20.22a}$$

$$\dot{\hat{F}} = -x_1 z_1 - z_2^2 - (\hat{J}\, k_1 - \hat{F}) x_1 z_2, \tag{20.22b}$$

$$\dot{\hat{T}}_L = -z_1 - (\hat{J}\, k_1 - \hat{F}) z_2. \tag{20.22c}$$

Substituting (20.22a–c) in (20.21), one gets

$$\dot{V}_2 = -k_1\, z_1^2 + \gamma\, z_2 + \frac{1}{J} z_1 z_2 - \frac{F}{J}\, z_2^2 + (a_1 c_2 - a_2 d_1)\, x_2 x_4 z_2\ \tilde{R}_f. \tag{20.23}$$

This suggests for the control variable γ the following choice:

$$\gamma = -k_2\, z_2, \tag{20.24}$$

where $k_2 > 2$ is a new design parameter. Indeed, substituting equation (20.24) in (20.23) yields (20.25):

$$\dot{V}_2 = -k_1\, z_1^2 - \left(k_2 + \frac{F}{J}\right)\, z_2^2 + \frac{1}{J} z_1 z_2 + a_1(c_2 - d_1)\, x_2 x_4 z_2\, \tilde{R}_f. \tag{20.25}$$

Now, substituting (20.24) in (20.18a), one obtains the following speed closed-loop control system:

$$\dot{z}_1 = -k_1\, z_1 + \frac{z_2}{J} + \frac{\tilde{J}}{J}\, \left(k_1\, z_1 - \dot{x}_1^*\right) - \frac{\tilde{T}_L}{J} - \frac{\tilde{F}}{J}\, x_1 \tag{20.26}$$

$$\begin{aligned} \dot{z}_2 = &-k_2\, z_2 - \tfrac{F}{J}\, z_2 + (a_1 c_2 - a_2 d_1)\, x_2 x_4 z_2\, \tilde{R}_f \\ &-\tfrac{\tilde{J}}{J}\, \left(k_1\, z_2 - (\hat{J}\, k_1 - \hat{F})(k_1\, z_1 - \dot{x}_1^*)\right) \\ &-\tfrac{\tilde{F}}{J}\, \left((\hat{J}\, k_1 - \hat{F}) x_1 + z_2\right) - \tfrac{\tilde{T}_L}{J}\, (\hat{J}\, k_1 - \hat{F}). \end{aligned} \tag{20.27}$$

Finally, combining (20.24) and (20.19) gives a first equation involving the three actual control inputs (u_1, u_2, u_3):

$$\begin{aligned} (\alpha_1\, u_1 + \alpha_2\, u_2 + \alpha_2\, u_2) v_{dc} = &-k_2\, z_2 - \beta(x_{1\ldots 4}) - \hat{F}\left(k_1\, z_1 - \dot{x}_1^*\right) \\ &+\hat{J}\left(k_1^2\, z_1 + \ddot{x}_1^*\right) - k_1\, z_2 - \dot{\hat{J}}\, \left(k_1\, z_1 - \dot{x}_1^*\right) + \dot{\hat{T}}_L + \dot{\hat{F}}\, x_1. \end{aligned} \tag{20.28}$$

Control Design for the Stator *d*-axis Current

Here, the focus is put on the control objective CO 3 that involves the d-axis current $x_3 = \bar{i}_{sd}$ that is required to track its reference $x_3^* \stackrel{\text{def}}{=} i_{sdref} = 0$. To harmonize notation throughout this section, the corresponding tracking error is denoted $z_3 = x_3 - x_3^* = x_3$. It follows from equation (20.7c) that z_3 undergoes the differential equation $\dot{z}_3 = -c_1\, z_3 + v$ with,

$$v = c_2 R_f\, x_4 + c_3\, x_1 x_2 + c_4\, u_2 v_{dc} - c_5\, u_3 v_{dc}. \tag{20.29}$$

Clearly, v acts as a virtual input in the differential equation $\dot{z}_3 = -c_1\, z_3 + v$. As the latter is a first order, it can be (globally asymptotically) stabilized using a simple proportional control law, that is, $v = c_1\, z_3 + k_3\, z_3$ with k_3 any positive real parameter. The point is that the parameter R_f is unknown making this resistor not accessible to measurements. Therefore, we consider as virtual input the following equivalence form of v:

$$\hat{v} = c_2 \hat{R}_f\, x_4 + c_3\, x_1 x_2 + c_4\, u_2 v_{dc} - c_5\, u_3 v_{dc}, \tag{20.30}$$

where $\hat{R}_f$ is an estimate (yet to be found) of R_f. Then, equation $\dot{z}_3 = -c_1\, z_3 + v$ can be expressed in term of $\hat{v}$ as follows:

$$\dot{z}_3 = c_1\, z_3 + \hat{v} + \tilde{R}_f c_2\, x_4, \tag{20.31}$$

where $\tilde{R}_f = R_f - \hat{R}_f$. To asymptotically stabilize this first-order system, we consider the following (adaptive) proportional control law:

$$\hat{v} = c_1\, z_3 - k_3\, z_3. \tag{20.32}$$

Substituting the right side of equation (20.30) to $\hat{v}$ in (20.31), one gets the following representation of the d-axis current control loop:

$$\dot{z}_3 = -k_3\, z_3 + \tilde{R}_f c_2\, x_4. \tag{20.33}$$

The asymptotic stability of the error equation (20.33) cannot be performed before a variation law is associated to $\tilde{R}_f = R_f - \hat{R}_f$ (or, equivalently, to R_f). This will be done in a next subsection because the parameter R_f influences also the excitation current i_f. In other words, the update law for R_f must selected bearing in mind both control objectives CO 3 and CO 4, which concern the currents i_{sd} and i_f, respectively. Nevertheless, one major result of the present subsection is the couple of equations (20.30) and (20.32). Combining these, one gets a second equation in the three control inputs (u_1, u_2, u_3), that is,

$$-c_4\, u_2 v_{dc} + c_5\, u_3 v_{dc} = \hat{R}_f c_2\, x_4 + c_3\, x_1 x_2 - c_1\, z_3 + k_3\, z_3. \tag{20.34}$$

Excitation Current Control Design

According to the control objective CO 4, the excitation current $x_4 = \bar{i}_f$ must track its reference signal $x_4^* = i_{fref}$, generally equal to the nominal value of that current. Introducing the tracking error $z_4 = x_4 - x_4^*$, it follows from (20.7d) that this error undergoes the following equation:

$$\dot{z}_4 = -d_1 R_f\, x_4 + w - \dot{x}_4^*, \tag{20.35}$$

where

$$w = d_2\, x_3 - d_3\, x_1 x_2 - d_4\, u_2 v_{dc} + d_5\, u_3 v_{dc}. \tag{20.36}$$

The signal w acts in (20.35) as a virtual control input. As the equation (20.35) is a first-order system, it can be asymptotically stabilized using a simple proportional control law, that is, $w = d_1 R_f\, x_4 + \dot{x}_4^* - k_4\, z_4$, with k_4 is any positive real parameter. Indeed, combining this control law with (20.35) gives $\dot{z}_4 = -k_4\, z_4$ which clearly is globally asymptotically stable because k_4 is positive. The point is that the rotor resistor R_f is unknown. Then, the above control law is replaced by its equivalence form, simply obtained by substituting $\hat{R}_f$ to R_f:

$$w = \hat{R}_f d_1\, x_4 + \dot{x}_4^* - k_4\, z_4. \tag{20.37}$$

Combining (20.37) and (20.35), one obtains the following differential equation describing the closed-loop for the current $\bar{i}_f$:

$$\dot{z}_4 = -k_4\, z_4 - d_1 \tilde{R}_f\, x_4. \tag{20.38}$$

Combining equations (20.36) and (20.37), one gets a third equation in the control inputs (u_1, u_2, u_3):

$$d_4\, u_2 v_{dc} - d_5\, u_3 v_{dc} = -\hat{R}_f d_1\, x_4 - d_3\, x_1 x_2 + d_2\, x_3 + k_4\, z_4 - \dot{x}_4^*. \tag{20.39}$$

Control Laws and Rotor Resistor Update Law

Solving equations (20.34) and (20.39) with respect to (u_2, u_3), one gets

$$\begin{bmatrix} u_2 \\ u_3 \end{bmatrix} = \frac{1}{v_{dc}} \begin{bmatrix} c_4 & -c_5 \\ -d_4 & d_5 \end{bmatrix}^{-1} \begin{bmatrix} c_1\, z_3 - k_3\, z_3 - \hat{R}_f c_2\, x_4 - c_3\, x_1 x_2 \\ \hat{R}_f d_1\, x_4 - k_4\, z_4 - d_2\, x_3 + d_3\, x_1 x_2 + \dot{x}_4^* \end{bmatrix}. \tag{20.40}$$

Now that (u_2, u_3) are available, one can obtain u_1 from (20.28), that is,

$$\begin{aligned} u_1 = \tfrac{1}{\alpha_1\, v_{dc}} \{ & -\alpha_2\, u_2 v_{dc} - \alpha_3\, u_3 v_{dc} - k_2\, z_2 - \beta(x_{1\ldots4}) - \hat{F}(k_1\, z_1 - \dot{x}_1^*) \\ & + \hat{J}\left(k_1^2\, z_1 + \ddot{x}_1^*\right) - k_1\, z_2 - \dot{\hat{J}}\,(k_1\, z_1 - \dot{x}_1^*) + \dot{\hat{T}}_L + \dot{\hat{F}}\, x_1 \}. \end{aligned} \tag{20.41}$$

The above control laws involve the parameter estimates $\hat{J}$, $\hat{T}_L$, $\hat{F}$, and $\hat{R}_f$. The first three parameters are updated by the adaptive laws (20.22a–c). The update law of the fourth parameter has yet to be determined. To this end, consider the following augmented Lyapunov function:

$$V = V_2 + \frac{1}{2}\left(z_3^2 + z_4^2 + \tilde{R}_f^2\right). \tag{20.42}$$

Using equations (20.25), (20.33), and (20.38), the time-derivation of (20.42) gives

$$\begin{aligned} \dot{V} &= \dot{V}_2 + z_3 \dot{z}_3 + z_4 \dot{z}_4 + \tilde{R}_f \dot{\tilde{R}}_f \\ &= -k_1\, z_1^2 - \left(k_2 + \tfrac{F}{J}\right) z_2^2 + \tfrac{1}{J}\, z_1 z_2 - k_3\, z_3^2 - k_4\, z_4^2 \\ &\quad + \tilde{R}_f\left(c_2\, x_4 z_3 - d_1\, x_4 z_4 + (a_1 c_2 - a_2 d_1)\, x_2 x_4 z_2 - \dot{\tilde{R}}_f\right). \end{aligned} \tag{20.43}$$

The last line on the right side of equation (20.43) suggests the following update law for $\tilde{R}_f$:

$$\dot{\tilde{R}}_f = -\dot{\hat{R}}_f = -c_2\, x_4 z_3 + d_1\, x_4 z_4 - (a_1 c_2 - a_2 d_1)\, x_2 x_4 z_2. \tag{20.44}$$

Remark 20.3.1 *The inversed matrix in (20.40) is actually invertible because its determinant $c_4 d_5 - c_5 d_4$, equal to $\frac{1}{L_{sd} L_f - M^2}$, is nonzero. Also, the division by the DC-link voltage v_{dc} implies no singularity risk in practice. In this regard, recall that v_{dc} is the DC voltage at the output of the AC/DC rectifier. This will be regulated to track a nonzero constant reference value, generally equal to the amplitude of the nominal inverter input voltage. That is, the (theoretical) singularity risk may only occur in transient periods. Also, note that a null voltage v_{dc} means that the motor is no longer powered and so it stops rotating. Practically, this situation is mainly faced at start-up stages. This issue is usually coped with by resorting to open-loop control at start-up stages which last a short time, just the necessary time to make the motor*

start rotating. In practice, it is also usual to substitute in (20.40), $\max(v_{dc}, \epsilon)$ *to* v_{dc} *with* ϵ *a sufficiently small threshold.*

Theorem 20.3.2 *(inverter-motor control performances). Consider the closed-loop system composed of the inverter-motor subsystem, described by equations (20.7a-d), and the adaptive regulator (20.40)–(20.41). Then, one has the following properties.*

(1) The error vector $Z_1 = [z_1 \;\; z_2 \;\; z_3 \;\; z_4]^T$ *undergoes the following equation:*

$$\dot{Z}_1(t) = B_1 Z_1(t) + \eta(Z_1(t),\ \tilde{\Theta}), \tag{20.45}$$

with

$$\tilde{\Theta} = \left[\tilde{J} \;\; \tilde{F} \;\; \tilde{T}_L \;\; \tilde{R}_f\right]^T; \qquad B_1 = \begin{pmatrix} -k_1 & \frac{1}{J} & 0 & 0 \\ 0 & -\left(k_2 + \frac{F}{J}\right) & 0 & 0 \\ 0 & 0 & -k_3 & 0 \\ 0 & 0 & 0 & -k_4 \end{pmatrix}$$

$$\eta(Z_1,\ \tilde{\Theta}) = \begin{pmatrix} \frac{\tilde{J}}{J}(k_1\, z_1 - \dot{x}_1^*) - \frac{\tilde{T}_L}{J} - \frac{\tilde{F}}{J}\, x_1 \\ \\ \frac{\tilde{J}}{J}\left(k_1\, z_2 - (\hat{J}k_1 - \hat{F})(k_1\, z_1 - \dot{x}_1^* + \frac{\tilde{F}}{J}\, x_1 + \frac{\tilde{T}_L}{J})\right) \\ +\frac{\tilde{F}}{J} z_2 + (a_1 c_2 - a_2 d_1)\tilde{R}_f\, x_2 x_4 z_2 \\ \\ c_2 \tilde{R}_f\, x_4 \\ \\ -d_1 \tilde{R}_f\, x_4 \end{pmatrix}.$$

(2) Let the design parameters $(k_1,\ k_2,\ k_3,\ k_4)$ *be any positive real numbers such that* $\delta > 0$*, with* $\delta \stackrel{\text{def}}{=} min(k_1,\ (k_2 + \dfrac{F}{J})) - \dfrac{J}{2}$*. Then, the vectors* Z_1 *and* $\tilde{\Theta}$ *remain bounded and* $Z_1 = [z_1 \;\; z_2 \;\; z_3 \;\; z_4]^T$ *vanishes asymptotically, whatever their initial conditions.*

Proof: The system with the augmented state vector $\left[Z_1^T \;\; \tilde{\Theta}^T\right]^T$ is defined by equations (20.22a–c), (20.44), and (20.45) that actually can be given the compact form:

$$\dot{Z}_1(t) = B_1 Z_1(t) + \eta(Z_1(t),\ \tilde{\Theta}) \tag{20.46}$$

$$\dot{\tilde{\Theta}} = \xi(Z_1,\ \tilde{\Theta}), \tag{20.47}$$

where the four components of $\xi(Z_1,\ \tilde{\Theta})$ are nothing other than the right sides of (20.22a–c) and (20.44). To analyze the nonautonomous system (20.46), consider again the Lypunov function (20.42) and its time-derivative (20.43). Substituting the right side of (20.44) to $\dot{\tilde{R}}_f$ in (20.42), one obtains the time derivative of Lyapunov function V:

$$\dot{V} = -k_1\, z_1^2 - \left(k_2 + \frac{F}{J}\right) z_2^2 + \frac{1}{J}\, z_1 z_2 - k_3\, z_3^2 - k_4\, z_4^2. \tag{20.48}$$

Using the well known inequality $z_1 z_2 \leq \frac{1}{2}(z_1^2 + z_2^2)$ in (20.48), one gets

$$\dot{V} \leq -\delta\left(z_1^2 + z_2^2\right) - k_3\, z_3^2 - k_4\, z_4^2 \text{ with } \delta \stackrel{\text{def}}{=} \min\left(k_1,\ \left(k_2 + \frac{F}{J}\right)\right) - \frac{J}{2}. \quad (20.49)$$

As $\delta > 0$, the derivative $\dot{V}$ turns out to be a negative definite function of $(z_1,\ z_2,\ z_3,\ z_4)$. This immediately implies that V, and so $z_i (i = 1 \ldots 4)$ and $\tilde{\Theta}$, remain bounded. Furthermore, applying Lasalle's invariant principle, it follows from equation (20.49) that the vector $Z_1 = [z_1 \quad z_2 \quad z_3 \quad z_4]^T$ converges to the origin, whatever the initial conditions. □

20.3.3 Reactive Power and DC Voltage Controller

In this subsection, we seek the realization of the control objectives (CO 2) and (CO 5). The former consisting in making sure that the input current is sinusoidal and in phase or opposite-phase (if the references of the reactive power is regulated equal to zero) with the supply grid voltage. The objective (CO 5) entails the regulation of the continuous voltage v_{dc} making it track a given reference signal v_{dcref}. These objectives will be achieved by designing two additional control loops. The DC voltage regulation loop is designed first. and the second ensures the injection of the desired reactive power.

DC voltage Loop

Based on equations (20.7e–g), a first equation involving the control input u_4 will now be designed so that the squared DC-link voltage $x_5 = \overline{v}_{dc}^2 > 0$ tracks well any reference signal $x_5^* = v_{dcref}^2$. As the subsystem (20.7e–f) is of relative degree 2, the design towards that equation is performed in two steps.

Step 1: Let z_5 denote the squared DC-link voltage tracking error:

$$z_5 = x_5 - x_5^*. \quad (20.50)$$

In view of (20.7e), the above error undergoes the following equation:

$$\dot{z}_5 = \frac{1}{C} E_{gd}\, x_6 + \beta_1(x_{1\ldots7}, z_{1\ldots4}) - \dot{x}_5^*, \quad (20.51)$$

where

$$\beta_1 = \frac{1}{C} E_{gq}\, x_7 - \frac{v_{dc}}{C}\left(u_1 x_2 + u_2 x_3 + u_3 x_4\right).$$

In equation (20.51), the quantity $\rho = \frac{1}{C} E_{gd}\, x_6$ stands up as a (virtual) control input for the z_5-dynamics because the actual control input u_4 acts on z_5 indirectly through ρ. Following the backstepping design technique, the Lyapunov function candidate $V_5 = \frac{1}{2} z_5^2$ is considered. Deriving V_5 along the trajectory of (20.7e) yields

$$\dot{V}_5 = z_5 \dot{z}_5 = -z_5 \left(-\frac{E_{gd}}{C}\, x_6 - \beta_1(x, z) + \dot{x}_5^*\right). \quad (20.52)$$

This suggests for the (virtual control) ρ the following control law:

$$\rho^* = k_5\, z_5 + \beta_1(x, z) - \dot{x}_5^*. \tag{20.53}$$

with $k_5 > 0$ a design parameter. Indeed, substituting ρ^* to $\rho = \frac{1}{C} E_{gd}\, x_6$ gives $\dot{V}_5 = -k_5\, z_5^2$ which clearly is negative definite in z_5. As ρ is just a virtual control input, one can not set $\rho = \rho^*$. Nevertheless, the above expression of ρ^* is retained and a new error is introduced:

$$z_6 = \rho - \rho^*. \tag{20.54}$$

Using (20.53), it follows from (20.51) that the z_5-dynamics undergoes the following equation:

$$\dot{z}_5 = -k_5\, z_5 + z_6. \tag{20.55}$$

Step 2: Now, the aim is to make the couple of errors (z_5,z_6) vanish asymptotically. The trajectory of the error z_6 is obtained by time-derivation of (20.54), that is,

$$\dot{z}_6 = \frac{E_{gd}}{C}\, \dot{x}_6 + k_5\, \dot{z}_5 + \dot{\beta}_1(x, z) - \ddot{z}_5^*. \tag{20.56}$$

Using equations (20.55) and (20.7e–f) in (20.56) yields

$$\dot{z}_6 = \beta_2(x_i,\ z_i) - \frac{E_{gd}}{CL_0}\, u_4 v_{dc}, \tag{20.57}$$

with

$$\beta_2(x_i,\ z_i) = k_5\, \dot{z}_5 + \dot{\beta}_1(x, z) - \ddot{x}_5^* + \frac{E_{gd}^2}{CL_0} - \frac{E_{gd}}{C}\omega_g x_7. \tag{20.58}$$

To determine a stabilizing control law for (20.7e–f), let us consider the quadratic Lyapunov function candidate $V_6 = \frac{1}{2}\, z_5^2 + \frac{1}{2}\, z_6^2$. Using (20.38)–(20.55), one gets from the expression of V_6 that

$$\dot{V}_6 = -k_5\, z_5^2 + z_6 \left(z_5 + \beta_2(x, z) + \frac{E_{gd}}{CL_0}\, u_4 v_{dc} \right). \tag{20.59}$$

This suggests for the control variable u_4 the following choice:

$$u_4 = -\frac{CL_0}{E_{gd} v_{dc}} \left(k_6\, z_6 + z_5 + \beta_2(x, z) \right), \tag{20.60}$$

where $k_6 > 0$ is a new design parameter. Indeed, substituting (20.60) in (20.59) yields

$$\dot{V}_6 = -k_5\, z_5^2 - k_6\, z_6^2 < 0. \tag{20.61}$$

Now, substituting (20.60) in (20.57) one obtains the DC voltage closed-loop control system:

$$\dot{z}_5 = -k_5\, z_5 + z_6, \tag{20.62a}$$

$$\dot{z}_6 = -k_6\, z_6 - z_5. \tag{20.62b}$$

Reactive Power Loop

To meet the control objective (CO 2), the reactive power Q_g must be enforced to track its reference Q_g^*. In this respect, note that the electrical reactive power injected in the grid is given by $Q_g = E_{gd}\, x_7 - E_{gq}\, x_6$. To harmonize notation throughout this section, the corresponding tracking error is denoted $z_7 = Q_g - Q_g^*$. It follows from (20.7f–g) that z_7 undergoes the following differential equation:

$$\dot{z}_7 = \beta_3(x_6,\ v_{dc}) - \frac{v_{dc}}{L_0}\left(E_{gd}\, u_5 - E_{gq}\, u_4\right), \tag{20.63}$$

with

$$\beta_3(x_6,\ v_{dc}) = -\omega_g\left(E_{gd}\, x_6 + E_{gq}\, x_7\right) - \dot{Q}_g^*.$$

As the equation (20.63) is a first order, it can be (globally asymptotically) stabilized using a simple proportional control law:

$$\left(E_{gq}\, u_4 - E_{gd}\, u_5\right)\, \frac{v_{dc}}{L_0} = -k_7\, z_7 - \beta_3(x_6,\ v_{dc}) \qquad \text{with} \quad k_7 > 0. \tag{20.64}$$

Then the control law u_5 is given by

$$u_5 = \left(\frac{L_0}{E_{gd} v_{dc}}\ (k_7\, z_7 + \beta_3(x_6,\ v_{dc})) + \frac{E_{gq}}{E_{gd}}\, u_4\right). \tag{20.65}$$

It can be easily checked that the dynamic of z_7 undergoes the following equation:

$$\dot{z}_7 = -k_7\, z_7. \tag{20.66}$$

The DC voltage and reactive power regulators, defined by (20.60) and (20.65), are analyzed in the following theorem.

Theorem 20.3.3 *Consider the control system consisting of the subsystem (20.7e–g) and the control laws (20.60) and (20.65). The resulting closed-loop system undergoes, in the* $Z_2 = [z_5 \quad z_6 \quad z_7]^T$ *coordinates, the following equation:*

$$\dot{Z}_2 = B_2\, Z_2, \tag{20.67}$$

with,

$$B_2 = \begin{pmatrix} -k_5 & 1 & 0 \\ -1 & -k_6 & 0 \\ 0 & 0 & -k_7 \end{pmatrix}.$$

This equation defines a stable system and the error vector $Z_2 = [z_5 \quad z_6 \quad z_7]^T$ *converges exponentially fast to zero, whatever their initial values.*

Proof: Equation (20.67) is directly obtained from equations (20.62) and (20.66). It is clear that the matrix B_2 is Hurwitz, implying that the closed loop system (20.67) is globally exponentially stable. This completes the proof of theorem 20.3.3. □

Remark 20.3.4 ***(i)*** *The motor speed, the d-component of its stator current and the excitation current all converge to their respective references because the errors* (z_1, z_3, z_4) *converge to zero. This is a direct result of Theorem 20.3.2.*

(ii) *Theorem 20.3.3 also demonstrates that the tracking objectives concerning the DC-link squared voltage* $x_5 = v_{dc}^2$ *and the reactive power* $Q_g = E_{gd}\, x_7 - E_{gq}\, x_6$ *are actually achieved.*

20.4 Simulation

20.4.1 Simulation and Implementation Considerations

The global control system described by Figure 20.4 is simulated using the Matlab/Simulink (V. R2010a), operating under Windows Vista. The ODE14x (extrapolation) solver is selected

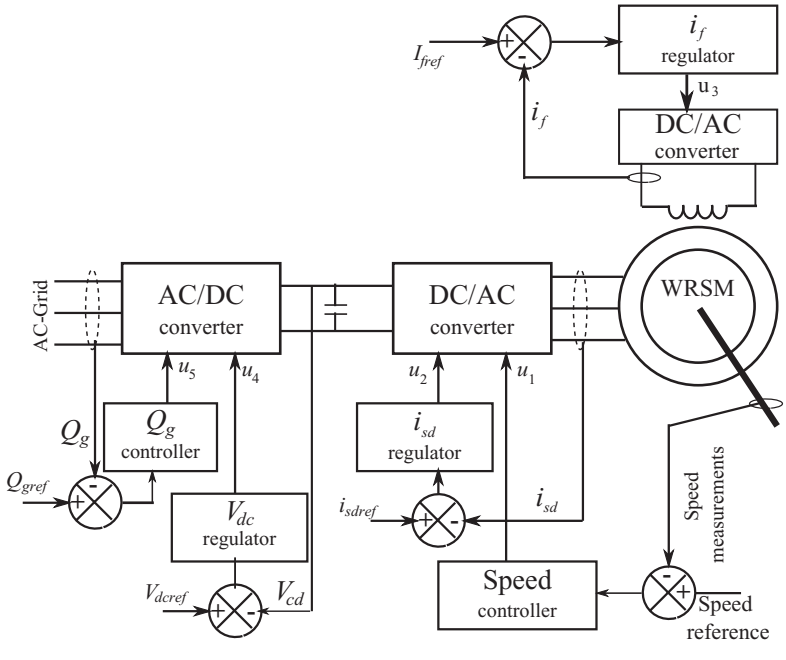

Figure 20.4 Adaptive control system developed for the association including AC/DC/AC converters and a wound rotor synchronous motor

Table 20.2 System characteristics

Characteristics	Symbol	Value	Unity
Supply network			
Three-phase voltages		380–220	V
Network frequency	f_g	50	Hz
AC/DC/AC converters			
Inductor	L_0	10.00	mH
Capacitor	C	47.00	mF
Modulation frequency		10.00	KHz
Synchronous motor			
Nominal power	P_n	7.00	KW
Stator resistor	R_s	1.11	Ω
d-axis stator inductance	L_d	45.40	mH
q-axis stator inductance	L_q	37.48	mH
Number of pole pairs	p	2	
Combined rotor and load inertia	J	0.22	Nm/rad/s^2
Combined rotor and load viscous friction	F	0.0064	Nm/rad/s

with fixed step time $10\mu s$. The controlled part is a system including the associated three-phases AC/DC/AC power converters and the wound rotor synchronous motor with the numerical values of Table 20.2. The adaptive nonlinear feedback controller, including the control laws (20.40), (20.41), (20.65), and (20.65), is also implemented using Matlab/Simulink resources. The same equation solver as previously is selected.

For convenience, let us recapitulate the underlying control and update laws generating the five control actions $(u_1, u_2, u_3, u_4, u_{5)}$:

$$
\begin{aligned}
u_1 &= \tfrac{1}{\alpha_1\ v_{dc}}\{-\alpha_2\ u_2 v_{dc} - \alpha_3\ u_3 v_{dc} - k_2\ z_2 - \beta(x_{1\ldots4}) - \hat{F}(k_1\ z_1 - \dot{x}_1^*) \\
&\quad + \hat{J}\left(k_1^2\ z_1 + \ddot{x}_1^*\right) - k_1\ z_2 - \dot{\hat{J}}\ (k_1\ z_1 - \dot{x}_1^*) + \dot{\hat{T}}_L + \dot{\hat{F}}\ x_1\}, \\
\begin{bmatrix} u_2 \\ u_3 \end{bmatrix} &= \tfrac{1}{v_{dc}} \begin{bmatrix} c_4 & -c_5 \\ -d_4 & d_5 \end{bmatrix}^{-1} \begin{bmatrix} c_1\ z_3 - k_3\ z_3 - \hat{R}_f c_2\ x_4 - c_3\ x_1 x_2 \\ \hat{R}_f d_1\ x_4 - k_4\ z_4 - d_2\ x_3 + d_3\ x_1 x_2 + \dot{x}_4^* \end{bmatrix}, \\
u_4 &= -\tfrac{C L_0}{E_{gd} v_{dc}}\ (k_6\ z_6 + z_5 + \beta_2(x, z))\,, \\
u_5 &= \left(\tfrac{L_0}{E_{gd} v_{dc}}\ (k_7\ z_7 + \beta_3(x_6,\ v_{dc})) + \tfrac{E_{gg}}{E_{gd}}\ u_4\right), \\
\dot{\hat{J}} &= z_1\ (k_1\ z_1 - \dot{x}_1^*) - k_1\ z_1^2 + (\hat{J} k_1 - \hat{F})(k_1\ z_1 - \dot{x}_1^*) z_2, \\
\dot{\hat{F}} &= -x_1 z_1 - z_2^2 - (\hat{J}\ k_1 - \hat{F}) x_1 z_2, \\
\dot{\hat{T}}_L &= -z_1 - (\hat{J}\ k_1 - \hat{F}) z_2, \\
\dot{\hat{R}}_f &= c_2\ x_4 z_3 - d_1\ x_4 z_4 + (a_1 c_2 - a_2 d_1)\ x_2 x_4 z_2.
\end{aligned}
$$

As a matter of fact, the control performances depend, among others, on the numerical values given to the controller parameters, that is, $k_i (i = 1 \ldots 7)$. The point is that there is no systematic way, especially in nonlinear control, to make suitable choices for these values. Therefore, the

usual practice consists in proceeding with a try-and-error search. Doing so, the following (nonunique) suitable numerical values are obtained:

$$k_1 = 9; \quad k_2 = 100; \quad k_3 = 20; \quad k_4 = 20; \quad k_5 = 10; \quad k_6 = 900; \quad k_7 = 9.$$

The controller performances will be evaluated in presence of (time-varying) rotor speed reference $x_1^* = \omega_{ref}$ and load torque T_L. According to the control design (Section 20.3), the remaining closed loop inputs are kept constant, namely, $x_3^* = i_{sdref} = 0$, $x_4^* = i_{fref} = 3.5$ A, $v_{dcref} = 600$ V and $Q_{gref} = 0$ VAR. The system unknown parameters (i.e., the combined rotor/load inertia J(Nm/rd/s^2), the viscous friction F(Nm/rd/s) and the rotor resistor (R_f) will also be subject to variations.

20.4.2 Simulation Results

Presently, both the rotor speed reference ω_{ref} and load torque T_L are filtered step-like signals (Figure 20.5a). First, Figure 20.5a shows that the speed signal reference takes a low, a

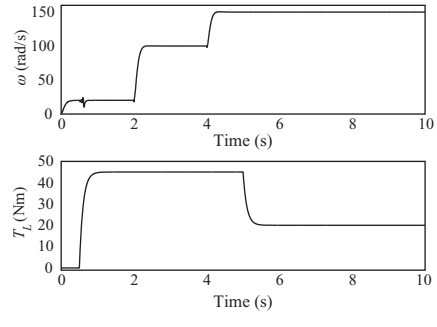

(a) Rotor speed ω(rad/s) and Load torque T_L(Nm)

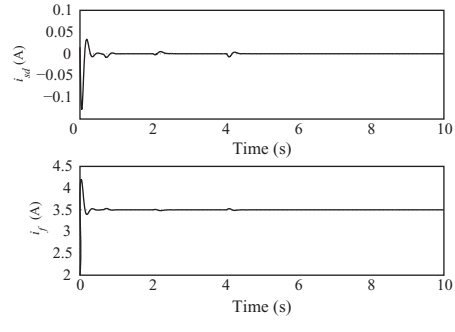

(b) *d*-axis stator current i_{sd} (A) and Excitation current i_f (A)

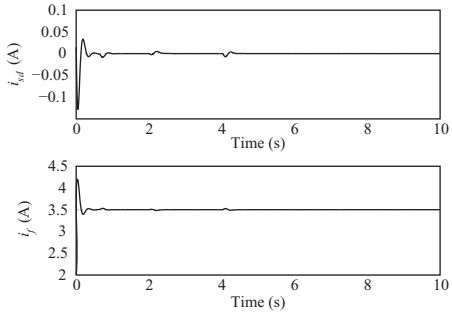

(c) Control signals u_1, u_2 , u_3

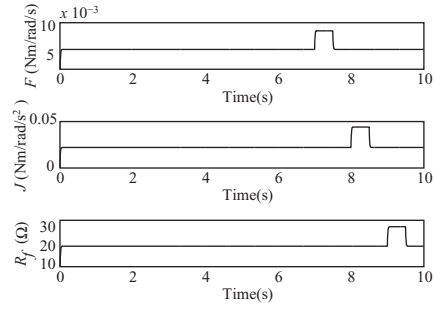

(d) inertia J (Nm/rad/s^2), viscous friction F (Nm/rad/s) and rotor resistor R_f (Ω) variations

Figure 20.5 Tracking performances of the controller defined by equations (20.41) and (20.40) in response to the varying speed reference and load torque and variations of the machine parameters.

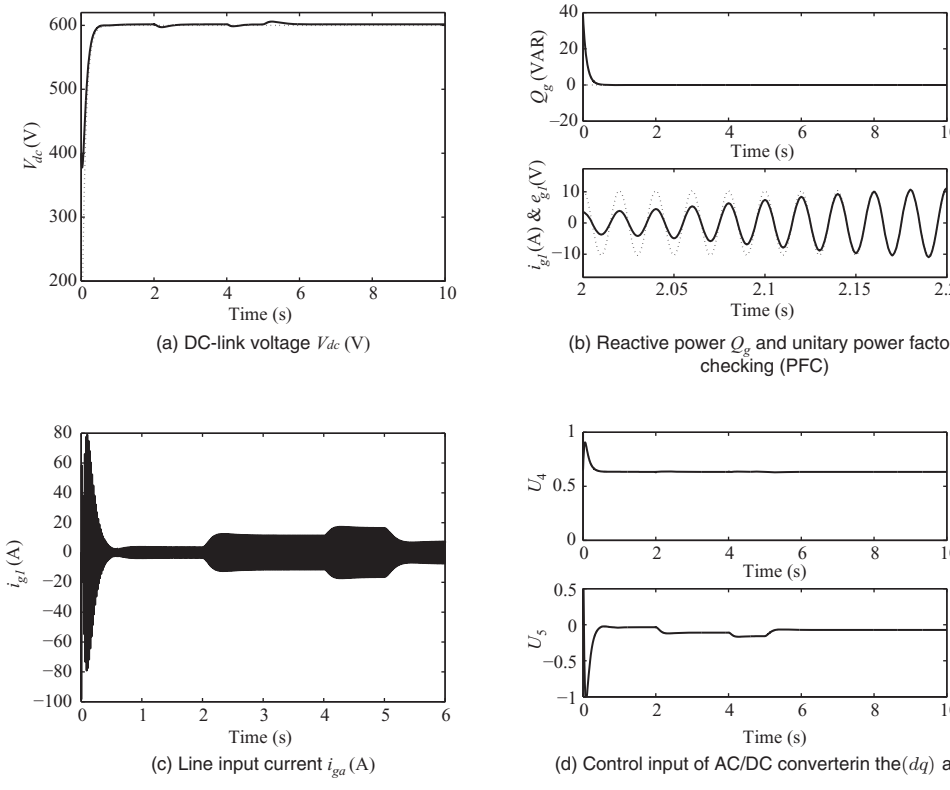

Figure 20.6 Tracking performances of the controller defined by (20.60) and (20.65) in response to the varying speed reference and load torque.

medium and a high value (respectively, equal to 20, 100, and 150). Filtering is resorted to make these references derivable and their derivatives available because these are needed in the controller. The unknown system parameters are varying as shown by Figure 20.5d. Accordingly, the viscous friction coefficient is subject to a step variation of 50% of its nominal value, 0.0096Nm/rd/s, between $t = 9$ s and $t = 9.5$ s. Similarly, a variation of 100% (resp. 50%) of the inertia (resp. the rotor resistor) between $t = 8$ s and $t = 8.5$ s (resp. $t = 7$ s and 7.5 s) is considered. All parameter variations are entirely ignored in the controller which solely relies on the nominal values.

The adaptive controller performances are illustrated by the curves in Figures 20.5 and 20.6.

Curves (a) and (b) show that the machine speed, $x_1 = \omega$, the d-component of the stator current, $x_3 = i_{sd}$ and the excitation current $x_4 = i_f$, all perfectly converge to their respective references; confirming thus theorem (20.3.2). The tracking quality, of these variables, is quite satisfactory as the response time (after each change in the speed reference, load torque and/or the unknown variations of the parameters values) is less than $0.3s$ for all variables. The resulting control actions ($u_1,\ u_2,\ u_3$) are illustrated by Figure 20.5c. It is seen, from this figure, that

all the control inputs of the DC/AC converter are bounded and belong to the interval $[-1\ \ 1]$. Figure 20.6a shows that DC-link voltage v_{dc} is tightly regulated: it quickly settles down after each change in the speed reference and/or load torque.

Figures 20.6b and 20.6c show respectively the reactive power (Q_g) extracted at the three-phases AC-grid and the corresponding current in phase a (i_{ga}). It is seen that the reactive power is perfectly converging to its reference trajectory. Figure 20.6c shows that the current amplitude changes whenever the speed reference and/or the load torque vary (compare with Figure 20.5a). But, the current frequency is insensitive to these changes (second figure in Figure 20.6b). Furthermore, the current remains (almost) all time in phase with the supply net voltages complying with the PFC requirement. This is particularly demonstrated by Figure 20.6d which shows that the control inputs ($u_4,\ u_5$), of the three phase AC/DC converter, converge to constant values, after transient periods following the changes in rotor speed reference, and/or load torque.

20.5 Conclusion

We have addressed the problem of adaptively controlling associations including an AC/DC rectifier, a DC/AC inverter and a wound rotor synchronous motor. The controlled system is connected with a three-phase supply grid. Parameter adaptation is resorted to cope with the uncertainty on the rotor inertia J, the viscous friction F, the load torque T_L, and rotor resistor R_f . The system dynamics have been described by the averaged seventh order nonlinear state-space model (20.7). Based on this model, the multiloop nonlinear controller defined by the control laws (20.41), (20.40), (20.60), and (20.65) is developed using the backstepping design technique. It is formally shown that the multiloop nonlinear adaptive controller meets all control objectives (CO 1, CO 2, CO 3, CO 4, and CO 5). This theoretical result is confirmed by simulation.

References

El Magri A, Giri F, Abouloifa A, and Chaoui FZ (2010) Robust control of synchronous motor through AC/DC/AC converters. *Control Engineering Practice*, **18**, 540–553.

El Magri A, Giri F, Abouloifa A, and El Fadili A (2010) Wound rotor synchronous motor control through AC/DC/AC converters. *IFAC Symposium on Nonlinear Control Systems*, pp. 1344–1349.

El Magri A, Giri F, Abouloifa A, and Haloua M (2006) Nonlinear control of wound-rotor synchronous-motor. *IEEE International Conference on Control Applications*, pp. 3110–3115.

El Magri A, Giri F, Abouloifa A, *et al.* (2009) Nonlinear control of association including synchronous motors and AC/DC/AC converters: a formal analysis of speed regulation and power factor correction. In *American Control Conference*, pp. 3470–3475.

El Magri A, Giri F, El Fadili A, and Chaoui FZ (2012 An adaptive control strategy for wound rotor synchronous machines. *International Journal of Adaptive Control and Signal Processing*, **26**, 10.1002/acs.2271.

Khalil H (2003) *Nonlinear Systems*. Prentice Hall.

Krstic M, Kanellakopoulos I, and Kokotovic P (1995) *Nonlinear and Adaptive Control Design*. John Wiley & Sons, Inc.

Kuroe Y, Okamura K, Nishidai H, and Maruhashi T (1998) Optimal speed control of synchronous motors based on feedback linearization. *International Conference on Power Electronics and Variable-Speed Drives*, pp. 328–331.

Michael J, Ryan D, and Rik W (1998) Modeling of sinewave inverters: A geometric approach. *IEEE Conference Industrial Electronics*, **1**, 396–401.

Muhammad H and Rashid (2001) *Power electronics handbook*. Academic Press.

Pyrhonen O, Niemela M, Pyrhonen J, and Kaukonen J (1998) Excitation control of DTC controlled salient pole synchronous motor in field weakening range. *International Workshop on Advanced Motion Control*, Coimbra, pp. 294–298.

Saleh KI, Mohammed OA, and Badr MA (2004) Field oriented vector control of synchronous motors with additional field winding. *IEEE Transactions on Energy Conversion*, **19**, 95–101.

Singh B, Bhuvaneswari G, and Garg V (2006) Improved power quality AC-DC converter for electric multiple units in electric traction. *Power India Conference*, p. 6.

Tomei P and Verrelli CM (2008) A nonlinear adaptive speed tracking control for sensorless permanent magnet step motors with unknown load torque. *International Journal of Adaptive Control and Signal Processing*, **22**, 266–288.

Part Five

Industrial Applications of AC Motors Control

AC Electric Motors Control: Advanced Design Techniques and Applications, First Edition. Edited by Fouad Giri.

21

AC Motor Control Applications in Vehicle Traction

Faz Rahman and Rukmi Dutta
School of Electrical Engineering & Telecommunications, University of New South Wales, Australia

21.1 Introduction

The application of electric machines in electric and hybrid electric vehicles, in which an electric motor is used for providing the traction either fully (for EVs) or partially (for HEVs), has been gathering pace after many decades of sporadic developments (Rajashekara 1994; Dutta *et al.* 2011). Currently, there exist many variants of HEVs in which one or two electric motors combine with an internal combustion engine (ICE) in delivering traction to the wheels. The impetus for the current trend towards HEVs and EVs stems not only from considerations of environmental issues and fuel saving but also from adding enhanced functionalities and features that can be derived from electric traction (Hori *et al.* 1998). At the heart of a modern EV or HEV is an electric motor that can deliver bidirectional torque quickly and precisely over a wide speed range on demand set by a driver or the vehicle control system. An electric motor, which does this job better than an ICE, will have the following attributes:

1. Ability to produce high torque at low speed, including zero speed, for operation without a clutch. This torque must be produced with high dynamics.
2. Operation with a high field-weakening (constant-power) speed range (CPSR), up to about five times the base speed. The base speed is the speed up to which the motor is capable of producing its maximum or rated torque.
3. Operation of the motor and its drive circuits over the whole speed range with high efficiency, high reliability and low maintenance.
4. Four-quadrant operation with regenerative braking, returning the overhauling energy into a storage device.

AC Electric Motors Control: Advanced Design Techniques and Applications, First Edition. Edited by Fouad Giri.

These attributes can be met by well-designed AC machines, such as the AC induction and interior permanent magnet (IPM) synchronous machines. Recently developed switched reluctance motors are also showing signs of comparable performance, notwithstanding the poorer volt-ampere capacity of its power converter, compared to the other AC machines.

The dynamic response of an electric machine to a torque demand is considered to be at least an order of magnitude faster than an ICE, and not subject to driving conditions such as air temperature, fuel type, and the regular maintenance requirements of the ICE as much. These make possible many new functionalities to be included in EVs (Hori *et al.* 1998). Although various configurations of HEVs and EVs have been tried over more than a century, HEVs became commercially viable since 1997 when Toyota introduced the Prius model. Honda introduced its Insight HEV in 1999. Toyota has now sold more than 2.5 million HEVs and the worldwide sale of this type of vehicles appears to be rising exponentially. Almost all major vehicle makers now have an HEV product line. Pure electric vehicles, which do not use an ICE for traction directly but may use the ICE for charging the batteries for extending the drive range. GM Volt, introduced in 2011, uses this strategy. Other than these, various HEV and EV structures are now finding use in electric bicycles, motor cycles, scooters, trucks, buses and military vehicles, not to mention the electric propulsion in railway locomotives and ships. Even Boeing has declared its intention of using electric propulsion in subsonic aircraft in order to shorten the take-off distance and to reduce noise.

During the past 15 years, several generations of hybrid electric vehicles have evolved. These combine an ICE with an electric motor for traction, and for regenerative braking in which some of the energy of the overhauling vehicle are returned to a battery for later use in traction and start-stop duty. The start-stop duty may eliminate the idling mode of operation that is routine for vehicles with ICE only. The latter two modes of operation immediately improve the fuel efficiency of the vehicle. Sharing of the traction load with both the ICE and the electric machine and the faster response of the electric machine allows additional features to be incorporated. The development and adoption of commercial electric and plug-in electric vehicles have lagged behind HEVs mainly owing to lack of cost- and space-effective battery capacity.

The major equipment for electric traction in vehicles consist of bidirectional power conversion units, electric machines for traction and generation, and battery charging circuits that may be shared with inverter used for driving the traction motor. Figure 21.1a depicts a parallel hybrid system popularized by Toyota in which the shaft torque from an ICE and a traction motor are coupled through a planetary gearbox indicated in Figure 21.1b. The power range of

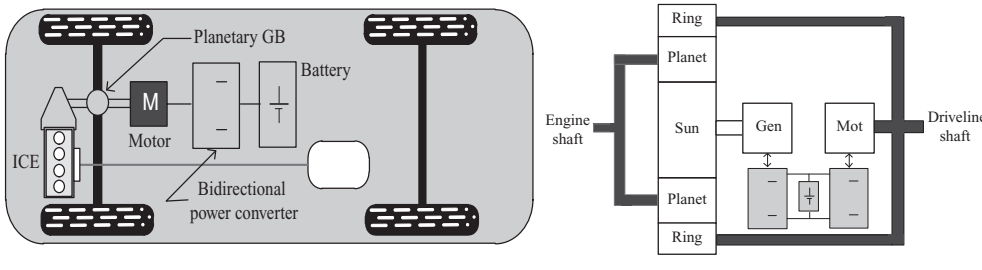

Figure 21.1 (a) Configuration Toyota parallel HEV and (b) its planetary gear system

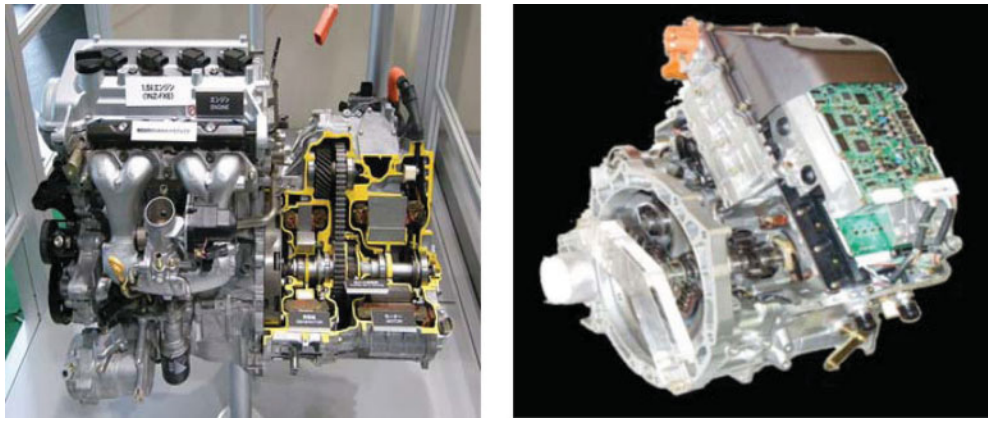

(a) (b)

Figure 21.2 (a) Toyota THS parallel hybrid drivetrain and (b) Ford parallel hybrid drivetrain. (For a color version of this figure, please see color plates.)

the traction motor is normally in the range of 30–100 kW. A separate smaller capacity electric machine, operating as generator, may also be used for charging the battery when the ICE drives the traction load. The traction motor typically operates, in conjunction with the ICE and the smaller machine, to accelerate the vehicle from start. Once the acceleration is completed, that is, during steady-speed running, the ICE drives the vehicle. The battery capacity for this structure is small, sufficient enough for recuperating the regenerative energy and for driving the vehicle over a short acceleration period. Re-use of the regenerative braking energy and use of the ICE for nearly constant speed operation are primarily responsible for the fuel saving, while faster vehicle dynamics are afforded by a combination of electric traction, ICE and the additional battery charging machine, if used. Figures 21.2a–b depict the Toyota and Ford HEVs. Honda Insight vehicles use a somewhat less complex parallel system, as depicted in Figure 21.3, in which an electric motor of lower capacity than the Toyota system is located on the driveshaft between the ICE and the transmission. This allows the electric machine to assist traction, provide recuperation of regenerative braking energy, and act as an integrated starter-alternator.

Figure 21.4 depicts a series hybrid system, such as in the GM Volt. In this scheme, an ICE/generator charges a battery that supplies the traction motor. The ICE is not normally used for traction duty directly. This scheme is easily amenable to plug-in EV with drive range extension via the ICE.

Figure 21.5 depicts an Audi retro-fit approach to HEVs in which the front-wheel ICE drive is kept unchanged except for some reduction of the ICE capacity, while adding an independent electric traction to rear wheels. The integration of the two independent traction systems is done via a controller.

The advent of pure electric vehicles of configuration indicated in Figure 21.6, that is, without any ICE support, is already taking place. Some of the drive power electronics in this scheme may be shared between plug-in charging and traction, as indicated in this figure. A few automotive manufacturers have already marketed low capacity pure electric vehicles

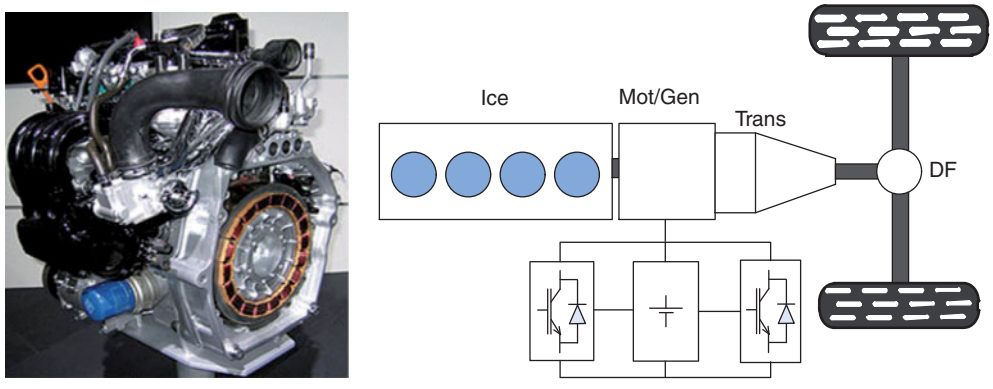

(a) (b)

Figure 21.3 (a) Configuration of Honda Insight parallel hybrid and (b) schematic of Honda Insight drivetrain. (For a color version of this figure, please see color plates.)

in this category. Although driving range is an issue because of the limited storage capacity and density of existing batteries/ultra-capacitors, nevertheless, this trend is expected to gain significant momentum in coming years.

This chapter primarily aims to describe machine and control techniques that are applied in control of traction of modern automotive vehicles. This application employ machines typically in the power range from about 10–100 kW. The focus is on the control of the traction motor

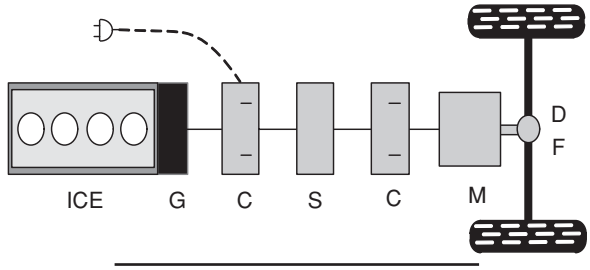

Legend	Signification
ICE	Internal combustion engine
G	Generator
C	Charger
S	Electricity storage devices
C	Converter
M	Electric motor
DF	Differential

Figure 21.4 Configuration of GM Volt series HEV

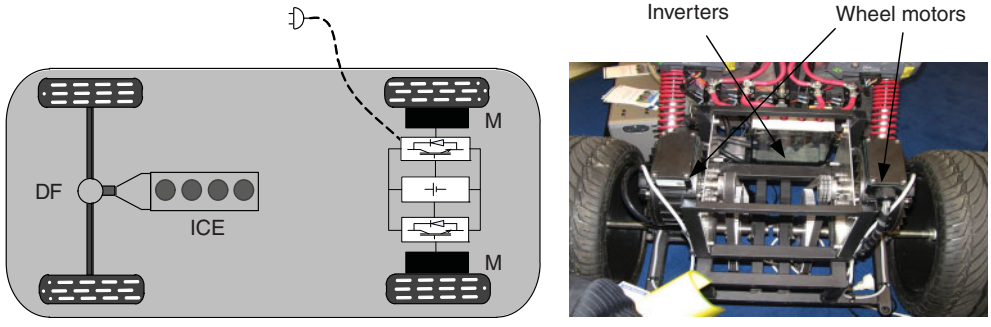

Figure 21.5 (a) Schematic of an Audi experimental HEV, and (b) photo of rear electric drivetrain from PCIM2010, Nuremberg. (For a color version of this figure, please see color plates.)

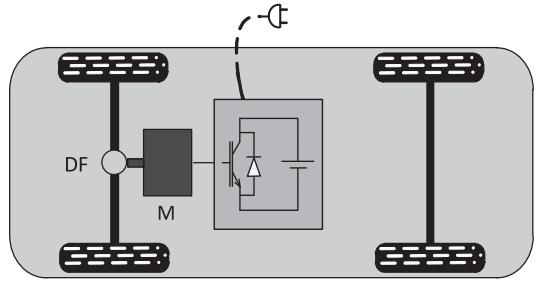

Figure 21.6 Configuration of pure EV drive with plug-in charging

drive, which can be for a single or more than one machines in HEV or EVs with plug-in charging of its battery as indicated in Figure 21.7. The major components of electric traction part of these vehicles are indicated in this figure. Elaborate descriptions of the power converters and the energy management of the storage devices such as batteries, ultra-caps and fuel cells are excluded.

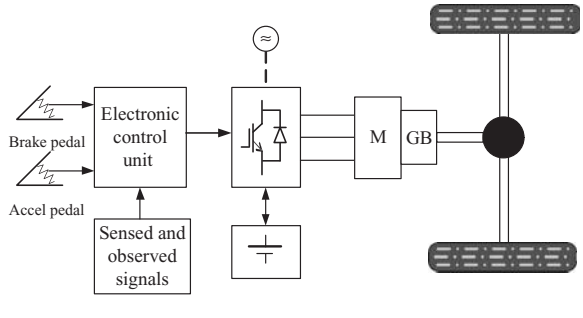

Figure 21.7 Schematic of a plug-in EV system

21.1.1 Electromechanical Requirements for Traction Drives in the Steady-State

Torque-speed Requirements for Vehicle and Motor

Before an electric motor can be contemplated for electric traction, the short-time and steady-state torque-speed requirements for the vehicle which the traction motor must match needs to be considered. The total tractive effort which must be provided for propulsion of a vehicle is given by

$$F_{\text{trac}} = m_{eq}\frac{\mathrm{d}x^2}{\mathrm{d}t^2} + F_{\text{aero}} + F_{rf} + F_{rr} + F_{\text{grade}}\, N. \tag{21.1}$$

In this equation, m_{eq} = the equivalent mass of the vehicle, passenger and other payload referred to the traction motor shaft position in terms of the vehicle's longitudinal displacement in metres:

$$F_{\text{aero}} = \text{the aerodynamic force} = \text{sgn}(V - V_{\text{air}})\frac{1}{2}\rho_{\text{air}} C_d A (V - V_{\text{air}})^2\, N, \tag{21.2}$$

where V and V_{air} are the vehicle and tail wind velocities, A is the frontal area of the vehicle, ρ is the density of air and C_d is it's drag coefficient.

$$F_{rf} = \text{front wheel rolling resistance force} = R_{of}\, m_{vf}\, g \cos\alpha\, N, \tag{21.3}$$

where R_{of} is the rolling resistance coefficient in kg/kg and m_{vf} is the vehicle kerb mass (kg) referred to the front wheel, g is the acceleration due to gravity and α is the road gradient:

$$F_{rr} = \text{rear wheel rolling resistance force} = R_{or} m_{vr} g \cos\alpha\, N, \tag{21.4}$$

where R_{or} is the rolling resistance coefficient in kg/kg and m_{vr} is the vehicle kerb mass (kg) referred to the rear wheel:

$$F_{\text{grade}} = \text{tractive force to overcome the road grade} = m_{eq} g \sin\alpha\, N, \tag{21.5}$$

where the grade angle α should be taken as negative when the vehicle is moving down grade.

The vehicle speed V is different from the crankshaft speed because of wheel slip. This difference in speeds is normally expressed as a ratio, called the slip-speed ratio λ, which is the ratio of the slip speed to vehicle speed. It should be noted that the maximum longitudinal traction force F_{trac} that can be applied to the wheels is limited by the coefficient of friction μ of tyres with the road surface. The longitudinal aerodynamic friction coefficient indicated in equation (21.2) as a function of slip is indicated in Figure 21.8 (Miller 2003).

If an electric motor takes a fraction of the entire traction load, the masses and velocities of equation (21.1) must take into account the effective gear ratios and their transfer efficiencies, so that the reflected traction force on the motor and ICE shaft can be determined. This involves knowing the gear ratios, the vehicle dimensions in terms of the wheel base, the centre of gravity of the vehicle in terms of its location, and the distance along the wheel base. Assuming

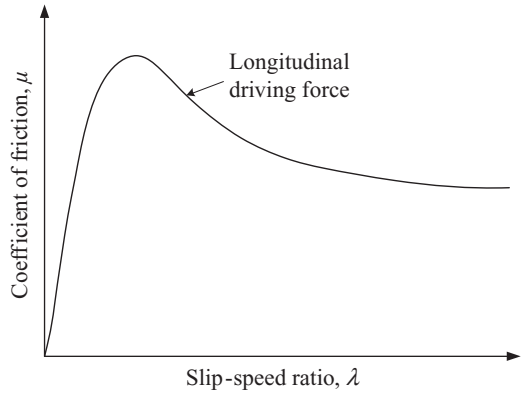

Figure 21.8 Friction coefficients versus slip-speed ratio

that the load on the traction motor for the HEV or EV is known, the following observation can be made:

1. The tractive force F_{trac} in equation (21.1) is in the longitudinal (x) direction in which the vehicle is required to travel providing for acceleration, regenerative braking and fuel economy over the full speed range. Tractive forces along the pitch (lateral) and yaw (vertical, along gravity) axes, which also govern the dynamics of the vehicle along these axes are in general of secondary consideration (Miller 2003). Motions along these axes are modified with inputs from the steering wheel and other sensors. The speed and acceleration of the vehicle along the longitudinal direction is governed by input signals from the acceleration and brake pedals indicated in Figure 21.8. Signals from both pedals stand for the desired torque, accelerating or braking.
2. The maximum traction force is required at low speed, from start of motion, when the acceleration $\left(\frac{dx^2}{dt^2}\right)$ is the highest. Vehicles are frequently characterized in terms of a certain number of seconds to achieve 0–100 km/h of speed and this defines the maximum torque that the traction motor must deliver, in conjunction with the other terms in equation (21.1). This force or torque demand is desired to be maintained until a predetermined longitudinal speed, the so-called base speed ω_b, is reached, beyond which the fast acceleration will not in general be required. Over this speed range, the first term in equation (21.1) dominates. Because production of maximum torque is desired in this mode, the air-gap flux should be maintained constant; that is, the machine should be driven with its maximum torque per ampere (MTPA) characteristic. This translates to a roughly V/f operation of the AC machine. The maintenance of flux to a constant level during this period of operation usually requires decoupled vector control of the machine. The base speed is also the speed at which the machine develops its maximum back EMF, which is consistent with the inverter DC voltage rating.
3. The continuous power rating of the motor, which largely determines it size, is found from the product of the desired maximum steady torque and the base speed specifications. It may be noted that the maximum short time torque/current rating of an electric motor is about twice its continuously rated torque/current limit from power loss and heat dissipation

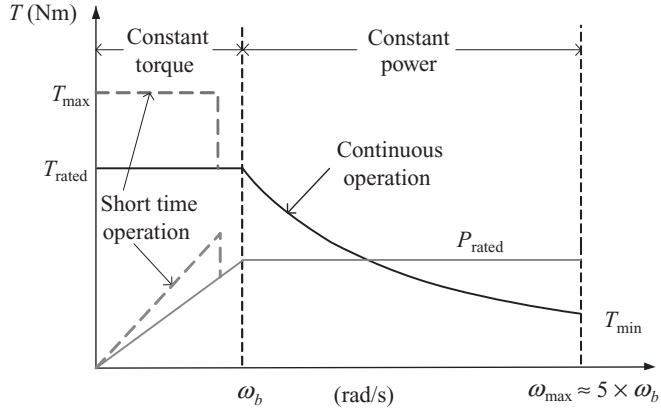

Figure 21.9 Limiting torque-speed characteristics of traction motors

considerations. The torque-speed envelops of machines for traction loads generally have a large constant-power speed range as indicated in Figure 21.9. Most electrical machines generally have a CPSR, except machines with permanent magnets at the surface of the air gap. The black trace in Figure 21.9 indicates the rated toque-speed envelope in the steady state, indicating constant torque and constant power speed ranges. The low-speed torque also indicates an intermittent (short-time) maximum torque rating (the red trace) which is required for the fastest acceleration/deceleration (braking) of the vehicle. The base speed ω_b is also defined as the speed at which the machine develops its continuous rated torque and power with rated inverter output voltage, the available DC link supply voltage and rated magnetic field in the air gap. This speed is approximately matched to the average vehicle speed at which acceleration from start is completed and the torque demand begins to fall as higher speed is attained.

4. Once the vehicle reaches the desired speed after start, the demand for acceleration falls to a low value. In order to maintain steady speed beyond the base speed, the torque demand is much lower than the maximum torque mentioned above. Fast acceleration above the base speed requires higher power than the product of the rated torque and the base speed, so that a compromise is struck between the required maximum acceleration at high speed and motor power rating.
5. At high speed, the aerodynamic force begins to prevail because it is proportional to speed squared. Thus a maximum speed, ω_{max}, is defined beyond which the motor cannot meet the torque demand. The ratio, ω_{max}/ω_b, is the speed range over which the motor can deliver some acceleration subject to the limitation of its power rating. Note that in the speed range of w_b to w_{max}, the maximum power which the machine can develop remains fixed because of the voltage and current rating limitations of the machine and the inverter. The speed range is thus aptly called the constant-power speed range (CPSR, $= \omega_{max}/\omega_b$). It has been found that for clutch less (i.e., without variable gearbox) operation over the desired vehicle speed range, the required CPSR ≈ 5. The CPSR has a profound impact on the efficiency, weight, volume and cost of the drive. Such constant power operation above the base speed is normally achieved by weakening the air-gap field of the machine linearly with speed,

so that operation along the full CPSR may take place without exceeding the voltage and current limits of the machine. In other words, the machine in a vehicle should be controlled by a torque controller (with appropriate limits) while the speed is lower than the base speed, and by a field controller also with an overriding voltage limiter in addition to maximum torque or current limit as a function of the speed when the operating speed is higher than the base speed. It should be noted here that machines with such wide CPSR have to be carefully designed in order to cover this speed range.

6. In order to have adequate dynamic performance for longitudinal traction, and for pitch and yaw motion controls, the motor drive system needs to employ high-performance controllers. Decoupled field oriented (vector) control incorporating a mechanical position and velocity sensor of high resolution is routinely applied in HEVs and EVs. Sensorless control techniques, such as direct torque control (DTC), are also capable of achieving the required response requirements, with the advantage of not requiring the delicate electromechanical position and speed sensor. It should be noted here that highly dynamic control over the developed torque is also required at very low speed, in fact down to zero speed. For mechanical sensorless drives, this is still a significant challenge.

21.1.2 The Impact of CPSR on Motor Power Rating and Acceleration Time of a Vehicle

Under the idealized conditions that the traction motor drives the vehicle via a fixed gear ratio, the friction torque is negligible, and the vehicle reaches a certain speed ω_{rv} in T_F seconds, the following can be written:

$$J \int_0^{\omega_b} \frac{d\omega}{T_m} = T_F, \tag{21.6}$$

where J is the total equivalent rotating moment of inertia, ω_b is the base speed and T_m is the rated maximum torque which the motor develops. From equation (21.6),

$$J \left(\int_0^{\omega_b} \frac{d\omega}{P_R/\omega} + \int_{\omega_b}^{\omega_{rv}} \frac{d\omega}{P_R/\omega} \right) = T_F. \tag{21.7}$$

From equation (21.7), the motor power rating P_R is given by

$$P_R = \frac{J}{2T_F} \left(\omega_b^2 + \omega_{rv}^2 \right). \tag{21.8}$$

Using the expression, $CPSR = \dfrac{\omega_{\max}}{\omega_b}$, equation (21.8) becomes

$$P_R = \frac{J\omega_b^2}{2T_F} \left(1 + \frac{\omega_{\max}}{CPSR^2\, \omega_{rv}^2} \right) = \frac{J\omega_b^2}{2T_F} \left(1 + \frac{\omega_b^2}{\omega_{rv}^2} \right). \tag{21.9}$$

If $\omega_b = 0$, so that the entire speed range is covered with constant power and $CPSR = \infty$, the required power rating of the machine is minimum, with a value

$$P_R = \frac{J\omega_b^2}{2T_F} \text{ Watts.} \tag{21.10}$$

If $\omega_b = \omega_{\max}$, so that the entire speed range is covered with constant torque and $CPSR = 1$, the required power rating of the machine is given by

$$P_R = \frac{J\omega_b^2}{T_F} \text{ Watts,} \tag{21.11}$$

which is twice the minimum rated power of (21.10). For $CPSR = 5$, say, and $\omega_b = \omega_{rv}$,

$$P_R = \frac{J\omega_b^2}{2T_F}\left(1 + \frac{\omega_b^2}{5\omega_{rv}^2}\right) \approx 1.25 P_{R\min}. \tag{21.12}$$

Thus, a high *CPSR* reduces the required power rating of the traction motor, based on the assumptions taken for this simple analysis. It also tends to reduce the total loss in the drive. $CPSR > 5$ may lead to diminishing returns because of the increase of F_{aero} with vehicle speed.

21.2 Machines and Associated Control for Traction Applications

Traction machines which have been adopted for automotive vehicles in recent years include induction machines (IMs), interior permanent magnet synchronous machines (IPMSM), and switched reluctance machines (SRM). The IMs have been used in the Tesla Roadstar and Audi HEVs; IPMSMs tend to have been preferred by most other HEV and EV manufacturers. Table (21.1) shows some typical data of traction motors used in present day EVs and HEVs. The present scarcity of permanent magnet materials like Neodymium and associated materials to enhance its temperature withstand capability has led to renewed development efforts in SRMs that require no PM material (Rahman and Schultz 2002; Takano *et al.* 2010). Promising developments in enhancing the torque density and efficiency of SRMs were reported by Rahman and Schultz (2002). The SRM reported by Takano *et al.* (2010) compares very favourably with a similar sized Toyota IPMSM machine used in its current Prius HEVs. Noise and Volt-Ampere data for this machine, which are drawbacks of SRM, are not available yet. It may be noted that an SRM based HEV was used in a showcase GM Commodore vehicle in Australia as far back as in 2000 (Lovatt and Dunlop 2002).

One of the important issues of traction machines, apart from the CPSR, is the efficiency, because of the limited power source available in a vehicle. Also because of this MTPA rather than rated flux operation is preferred in the low-speed region. As a result, some magnetic saturation of the machine's iron is inevitable (Jeong and Lee 2011).

The IPMSMs typically offer efficiencies higher than 92% over the full CPSR (Dutta and Rahman 2008; Olszewski 2008; Reddy *et al.* 2011). The IMs offer lower efficiencies and larger volume because of the extra electric loading in the stator in order to establish the rotor flux (Gosden *et al.* 1994). Figures 21.10a–c indicate a few typical efficiency maps of

Table 21.1 Traction motor, ICE and battery data of a few recent HEV and EVs

Vehicle	Traction machines used	ECE data	Battery
Honda Insight hybrid, 2010	Brushless PMDC, 9.7 kW, @ 1500 rev/min	1.3 L petrol	100.8 V, 5.75 Ah
Ford Fusion hybrid	PMSM, 79 kW @ 6500 rev/min	2.5 L petrol	275 V, NiMH
Toyota Prius hybrid, 2011	PMSM 1, 30 kW @ 1800 rev/min	1.8 L petrol, 73 kW @ 5200 rev/min	201.6 V, NiMH
	PMSM 2, 50 kW @ 1200 rev/min		Inverter DC link voltage = 600 V
Toyota Lexus 450h hybrid, 2010	PMSM, 123 kW on front wheel; 50 kW on rear wheels	3.5 L V6 petrol	37 kW, NiMH
GM Volt hybrid, 2011	PMSM, one 55 kW MG, & one 111 kW motor	1.4 L petrol	16 kWh, 45 Ah, Li-Ion
Hyundai Sonata hybrid, 2011	PMSM, 30 kW,	2.4 L Petrol	Li-Polymer
Tesla Roadstar, 2009, EV	Induction machine, 215 kW	–	Li-Ion, 375 V, 53 kW; range: 365 km
Mistubishi iMiEV	PMSM, 47 kW	–	16 kWh, Li-ion, range: 160 km
Renault Fluence EV	PMSM, 7 kW	–	22 kWh Li-ion, range: 185 km
BMW Active EV	PMSM, 125 kW	–	32 kWh, Li-ion, range: 151 km
Ford Focus BEV	PMSM, 107 kW	–	23 kWh, Li-ion, range: 122 km

traction motors superimposed on their limiting $T - \omega$ characteristics. In the following three subsections, the above three types of machines and their controls are briefly discussed.

21.2.1 Induction Machines

This machine has the advantage of being low-cost and simple construction and wide availability. A 215 kW 4-pole IM has been adopted notably in the Tesla Roadstar and by a few other automakers. Unlike PM machines, the position of the rotor flux vector (or phasor) cannot be directly measured for an IM. For fast dynamical control of IMs, as is required for modern vehicles, two control strategies have evolved, namely, the rotor flux oriented control (RFOC) and the DTC (Nash 1997; Casadei *et al.* 2008).

Indirect Rotor Flux Oriented Control

In RFOC, the desired stator flux angle is obtained by adding the slip speed, $\omega_{sl} = \omega_e - \omega_r$, to the rotor speed. By fully decoupling the d- and q-axes equations of the machine, the slip

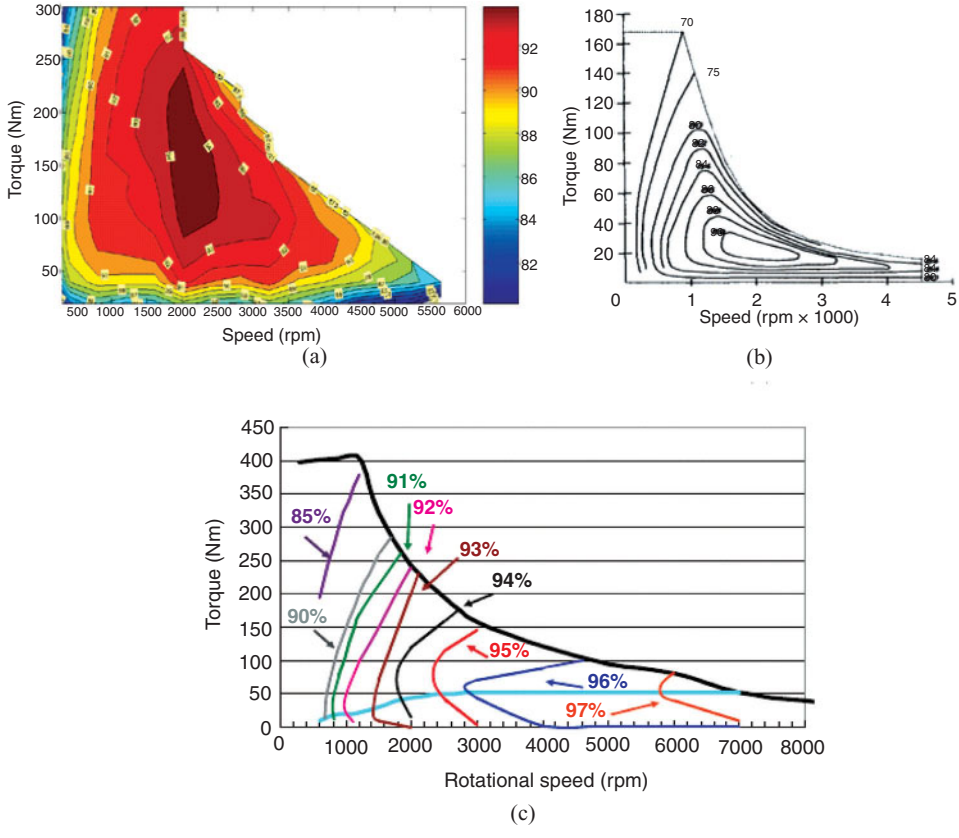

Figure 21.10 Torque-speed characteristics and efficiency maps of (a) the IMPMSM in Toyota Camri Hybrid (Olszewski 2008), (b) an induction machine (Gosden *et al.* 1994), and (c) an SRM (Takano *et al.* 2010). (For a color version of this figure, please see color plates.)

speed can be made proportional to torque and the q-axis current i_{qs} in the synchronously rotating frame, subject to magnetic saturation and change of rotor resistance. The IM machine dynamics in this reference frame, the slip speed, rotor flux and torque equations are given as

$$\begin{bmatrix} v_{ds} \\ v_{qs} \\ v_{dr} \\ v_{qr} \end{bmatrix} = \begin{bmatrix} R_s + pL_s & -\omega_e L_s & pL_m & -\omega_e L_m \\ \omega_e L_s & R_s + pL_s & \omega_e L_m & pL_m \\ pL_m & -(\omega_e - \omega_r) & R_r + pL_r & -(\omega_e - \omega_r)L_r \\ (\omega_e - \omega_r)L_m & pL_m & (\omega_e - \omega_r)L_r & R_r + pL_r \end{bmatrix} \begin{bmatrix} i_{ds} \\ i_{qs} \\ i_{dr} \\ i_{qr} \end{bmatrix}, \tag{21.13}$$

$$\omega_e - \omega_r = \omega_{sl} = \frac{L_m}{\lambda_r} \frac{R_r}{L_r} i_{qs}, \tag{21.14}$$

$$\frac{L_r}{R_r}\frac{d\lambda_r}{dt} + \lambda_r = L_m i_{ds}, \tag{21.15}$$

$$T = \frac{3P}{2}\frac{L_m}{L_r}\lambda_r i_{qs}. \tag{21.16}$$

The control structure for torque and rotor flux is depicted in Figure 21.11.

The torque reference for the traction motor, received either from the acceleration pedal or the braking pedal, with the braking pedal input overriding, defines the q-axis current reference i_q^* from equation (21.16), and in turn defines the slip reference from equation (21.14). Below the base speed ω_b, the rotor flux remains at the rated value defined by equation (21.15) for achieving MTPA characteristic. At higher speed, the rotor flux reference, λ_r^*, is reduced in order to maintain the motor/inverter voltage at the rated value. The reduction in λ_r must be matched by corresponding increase in ω_{sl}, so that the integrity of rotor flux and torque controllers remain fixed. The slip speed ω_{sl} cannot increase beyond a certain limit from power loss consideration, and in any case, the limited slip mode of operation in the high-field weakening range is not useful for traction applications. The torque-speed envelope of an IM with slip-speed limits for operations below and above the base speed are indicated in Figure 21.12.

The significant parameter dependence of the RFOC, in particular to changes in T_r and L_m, is one of the problem of tuning high-performance torque and flux controllers of this drive. These can be overcome in a number of ways. Look up tables with inputs of i_{ds} and temperature has some merit. Neural and observer methods that do not require a temperature sensor are also effective (Telford *et al.* 2003; Karanayil *et al.* 2005).

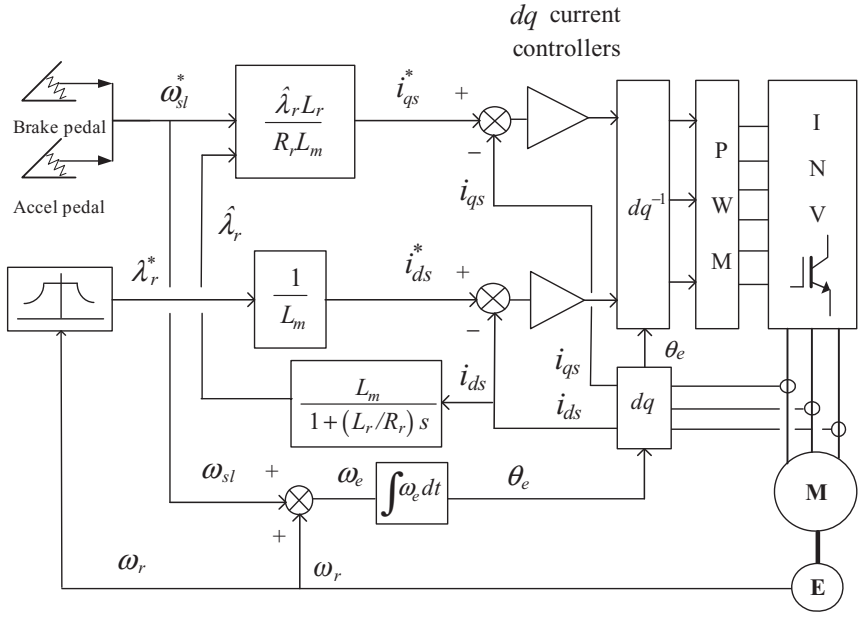

Figure 21.11 The RFOC control structure for induction machines

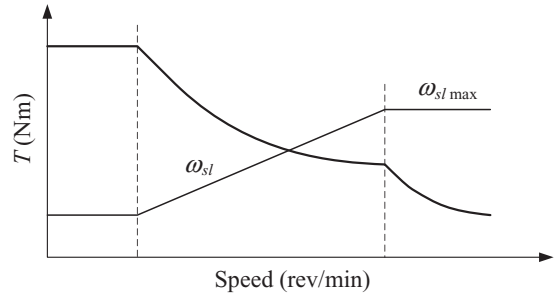

Figure 21.12 IM limiting torque-speed characteristic with slip limit and flux weakening

Direct Torque Control

In DTC, the machine torque, and stator and rotor flux linkages are estimated from the machine model using machine voltages and currents that are sensed at the machine/inverter terminals, without requiring the mandatory mechanical position sensor which is indicated in the RFOC scheme of Figure 21.11 (West and Lorenz 2009). According to the errors in torque and flux, hysteresis controllers with optimum switching states for the inverter are determined which apply one of the eight voltage vectors to the motor. Space vector modulators, replacing the hysteresis controller that introduces variable switching frequency, have also been used. The DTC has been applied successfully in railway traction applications for some time (Kondou and Matsuoka 1997). The torque and flux control responses of the DTC scheme of Figure 21.13 can

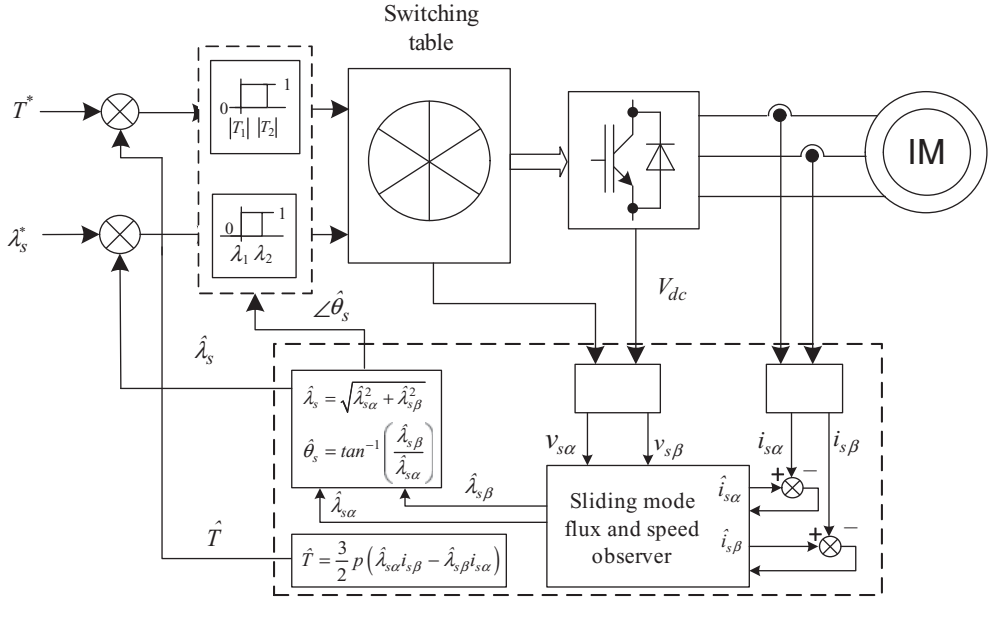

Figure 21.13 DTC scheme for an induction motor drive

be just as fast as, if not higher, than the RFOC scheme of Figure 21.11, because of the absence of delays suffered through linear controllers and pulse-width modulators. The elimination of the position sensor, considering the harsh environment in which a traction drive is expected to operate in, combined with the fast torque and flux responses of the DTC drive, makes this scheme a strong contender for traction drives. Simple, open-loop torque and stator flux estimators can be obtained from the integrator equation (21.17), in the stator orthogonal *xy* reference frame:

$$\bar{\lambda}_s = \int_0^t \left(\bar{v}_s - R_s \bar{i}_s\right) dt + \bar{\lambda}_{so}, \tag{21.17}$$

$$T = \frac{3P}{2} \frac{L_m}{\sigma L_s L_r} \bar{\lambda}_s \bar{\lambda}_r = \frac{3p}{2} \frac{L_m}{\sigma L_s L_r} |\bar{\lambda}_s| |\bar{\lambda}_r| \sin(\theta_s - \theta_r), \tag{21.18}$$

where

$$\sigma = 1 - \frac{L_m^2}{L_s L_r}. \tag{21.19}$$

Also,

$$\bar{\lambda}_s = L_s \bar{i}_s + L_m \bar{i}_r, \tag{21.20}$$

$$\bar{\lambda}_r = L_m \bar{i}_s + L_r \bar{i}_r, \tag{21.21}$$

$$\bar{\lambda}_r = \frac{L_r}{L_m} \left(\bar{\lambda}_s - \sigma L_s \bar{i}_s\right) = \lambda_{rx} + j\lambda_{ry}, \tag{21.22}$$

$$\theta_r = \tan^{-1}\left(\frac{\lambda_{ry}}{\lambda rx}\right). \tag{21.23}$$

The dynamics of the rotor flux is given by

$$R_r \bar{i}_r + \frac{d\bar{\lambda}_r}{dt} - j\omega_r \bar{\lambda}_r = 0. \tag{21.24}$$

The dynamics of the rotor flux vector is much slower compared to the rate at which the stator flux vector can be rotated. This implies, from equation (21.18), that torque and flux responses under the DTC is determined mainly by the speed with which the stator flux linkage can be rotated. When the inverter applies full voltage vectors to the motor without significant delay, and the delays in the controllers are also negligible, the torque and flux responses under DTC can be as fast as, or even faster than, RFOC. This also implies that the switching table applied to the motor must have a high sampling frequency. Typically, sampling frequency of the order of about 25 kHz is called for. Figures 21.14a and b compare the dynamic torque responses of an IM under RFOC and DTC.

The estimated stator and rotor fluxes and the estimated torque from equations (21.17) and (21.18) suffer from errors due to offsets in measurements and stator resistance variation. The parameters used in the computation of torque and rotor flux using equation (21.18) and

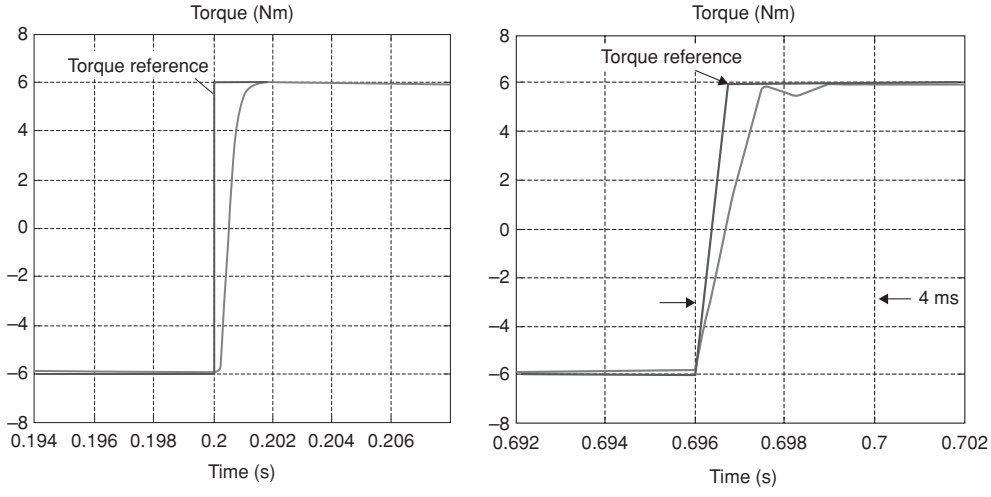

Figure 21.14 Torque response of an IM under RFOC and DTC

(21.22) also have to be compensated. Various improvements in computing the stator flux using closed-loop techniques, notably the sliding-mode and variable-structure observers that depend on eliminating the errors in the estimated and measured stator d- and q-axes currents, have led to high performance DTC schemes down to quite low speed (West and Lorenz 2009). Furthermore, the inductances L_m amd L_r may both suffer from magnetic saturation when the applied voltage and load are high, so these must also be adjusted with the help of look-up tables using $\bar{i}_s$ and $\bar{i}_r$ or by using some observer techniques.

The simple integrator of equation (21.17) for estimating the stator flux is not very accurate at low speed. A better approach is to use some closed-loop observer, such as the sliding-mode observer (SMO) that delivers more accurate estimations down to a much lower speed. Figure 21.15 compares the performance of pure integrator versus SMO observers on the control of torque in an IM.

The DTC scheme for vehicles also entails operation of the machine with the rated rotor flux up to the base speed ω_b, followed by linear reduction in rotor flux with speed, up to the maximum speed $\omega_{\max}$. It should be mentioned here that the sensorless DTC scheme for induction machines do not have the advantage of saliency to exploit at very low speed, as with the IPMSM, in order to, guarantee operation down to very low and zero speeds.

When operation at very low speed is required, for instance, when the vehicle is operated at crawling speed for parking, other means of improving the very-low speed performance with stability is required. High-frequency injection of voltage superimposed on the estimated d-axis stator voltage and adaptive (closed-loop) flux observers have proved to be effective (Holtz 2006) as a means of mechanical sensorless control. Traction control for vehicles must have full zero-speed performance with guaranteed stability. Operation of an IM down to very low speed that rely on high-frequency injection (explained in Chapter 19 for the DTC IPMSM drive) with full torque capability have been reported in literature (Holtz 2006). Industrial adoption this HF injection technique is still awaited.

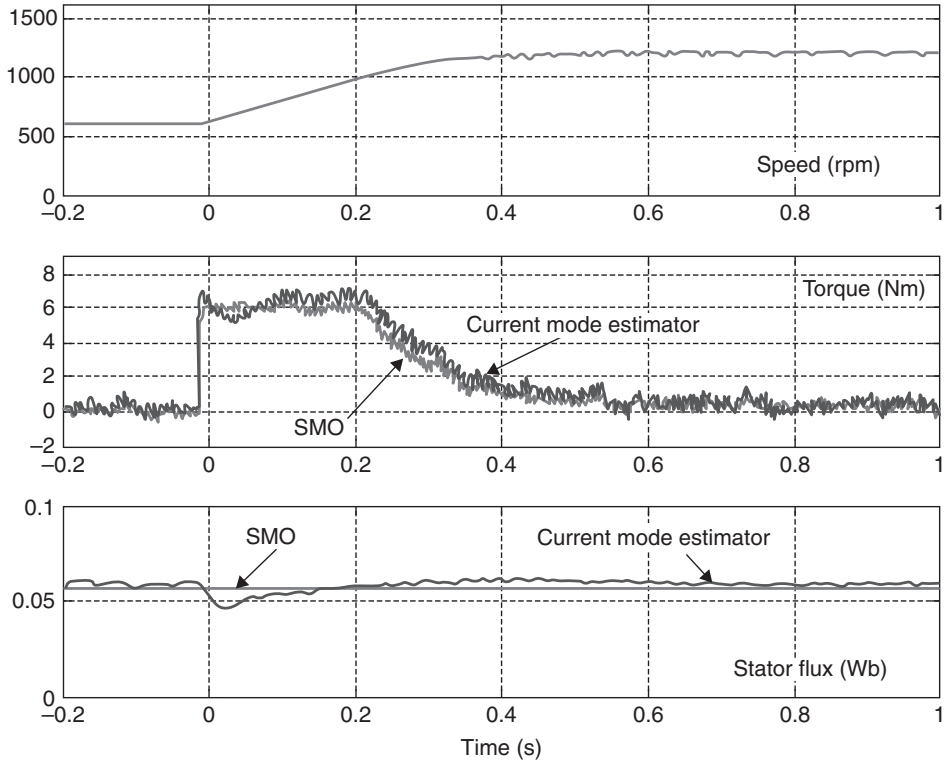

Figure 21.15 Comparison of integrator and SMO flux observers for a DTC IM drive

21.2.2 Interior Permanent Magnet Synchronous Machines

The overwhelming majority of HEVs and EVs in production today have adopted this type of machine for vehicle traction, as indicated in Table 21.1. The main advantages are the high torque and power to volume ratio achievable because of high energy-density permanent magnets, and the high efficiency which this machine can deliver because of the PM excitation. Although the IPM synchronous machines in early HEVs did not deliver a sufficiently high CPSR (it was not perhaps needed because the motor was required only to operate below the base speed for acceleration duty only), however, traction machines for EVs must have a CPSR close to five or higher. The desired CPSR (or field weakening range) of recently developed interior permanent machines with distributed and fractional-slot windings have reached values greater than 5. PM machine structures are still evolving vigorously. The IPMSM with distributed winding in the stator and *V*-shaped magnets in the rotor, as indicated in Figure 21.16, has been adopted in the HEVs from Toyota and a number of other vehicle manufactures and in a few recently commercialised EVs. The drive towards PM machines with higher torque and power densities than the IPMSM has recently led to developments of the fractional-slot SPM and IPM machines, examples of which are indicated in Figures 21.17 and 21.18, respectively.

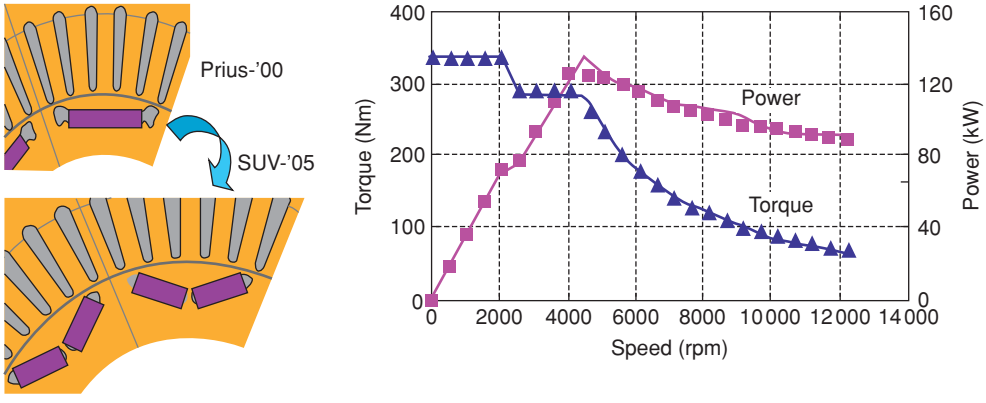

Figure 21.16 The electromagnetic design of the IPMSM in Toyota Prius HEV and its torque-speed and CPSR characteristics. (For a color version of this figure, please see color plates.)

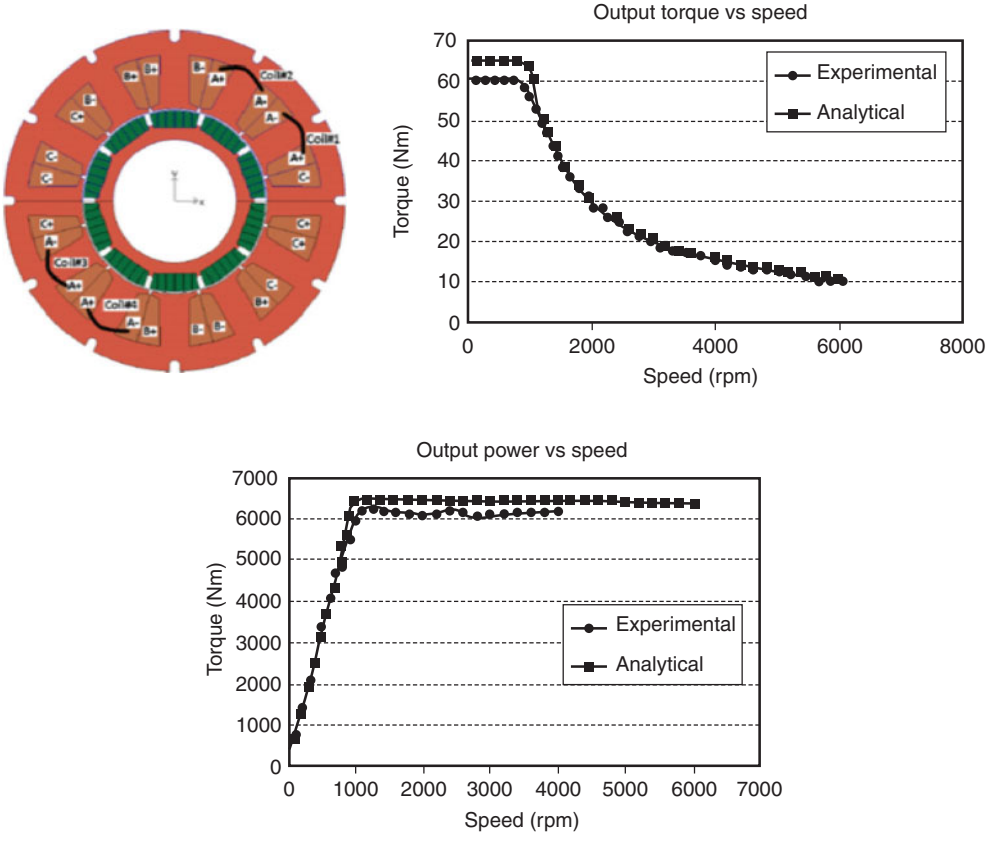

Figure 21.17 The electromagnetic design of the SPM machine with fractional-slot winding developed at the University of Wisconsin-Madison (Reddy *et al.* 2011). (For a color version of this figure, please see color plates.)

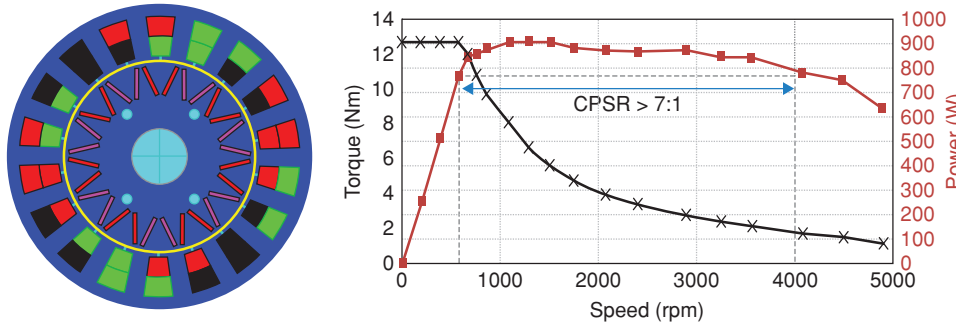

Figure 21.18 The electromagnetic design of the SPM machine with fractional-slot winding developed at the University of New South Wales (Dutta *et al.* 2011). (For a color version of this figure, please see color plates.)

Descriptions of the IPM machine and its control techniques, both sensor-based RFOC and sensorless DTC controls have been included in Chapter 19 of this book and in Rahman *et al.* (1998). Sensorless control of such machines using high frequency injection in the estimated rotor *d*-axis has also been described in Chapter 19. These techniques have been reported further in Foo *et al.* (2010) and Sayeef *et al.* (2010). These will not be repeated here.

21.2.3 Switched Reluctance Machines

The SRM, having no PM excitation in the rotor and a doubly salient structure as indicated in Figure 21.19, are very rugged and of low cost. These qualities have provided the incentive for using this type of machine for vehicle traction, leading to recent developments of SRMs which are claimed to have power densities and efficiencies comparable to IPMSMs (Rahman and Schultz 2002; Takano *et al.* 2010).

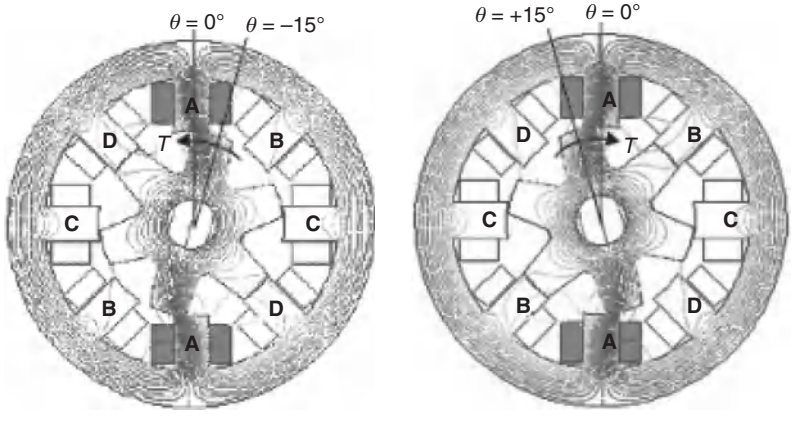

Figure 21.19 Cross-section of an 8/6 SRM. (For a color version of this figure, please see color plates.)

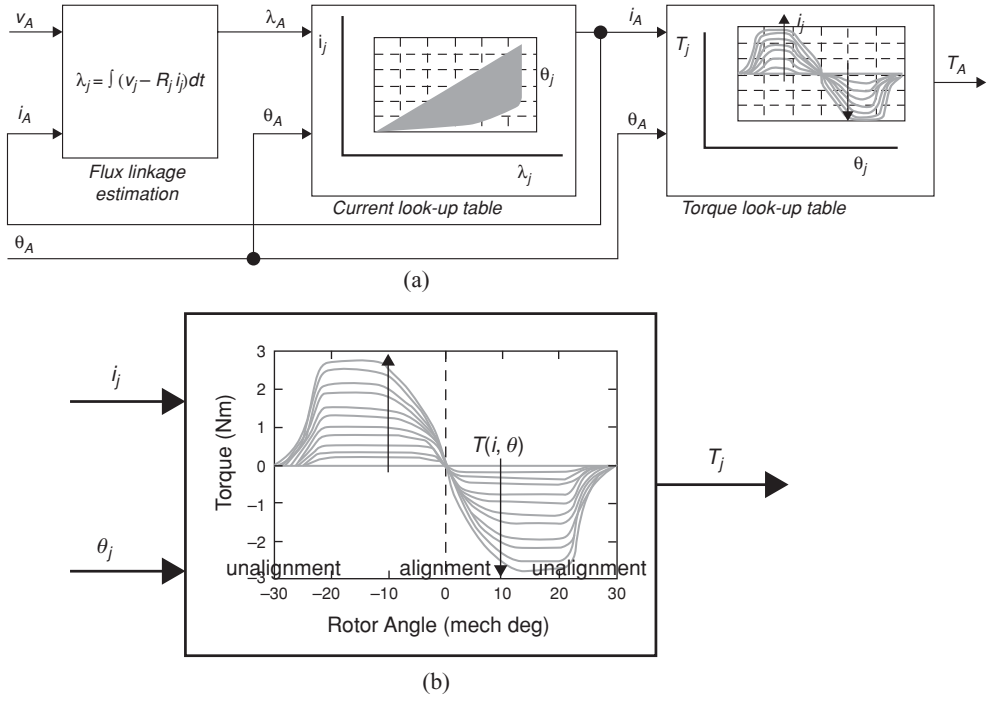

Figure 21.20 (a) Torque production mechanism of phase A of an SRM; (b) Torque versus current versus displacement characteristic of an SRM

The control of torque of an SRM is via control of amplitude, duration and angular position of rectangular phase current pulses relative to the rotor position. Placement of a phase current pulse over the displacement angle $\theta_{on} - \theta_{off}$, where the rate of change of co-energy of the winding with respect to the rotor angular position is the most positive than for all other windings maximizes the positive developed torque (MTPA). Placement of a phase current pulse over the displacement angle where the rate of change of co-energy of the winding with respect to the rotor angular position is the most negative than for all other windings maximizes the reverse (regenerative) developed torque, as indicated in Figure 21.20. Each phase of the machine contributes to the developed torque according to the representation of Figure 21.20, in which the nonlinear relationships of current, flux linkage and torque versus current versus angular position characteristics are also indicated. A fast response torque controller based on the flux-linkage versus current versus angular position characteristics of Figure 21.20 is indicated in Figure 21.21. The control parameters are the turn-on angle (θ_{on}), turn-off angle (θ_{off}) and the amplitude for phase currents. The reference and estimated torque of each phase of four-phase SRM is indicated in Figure 21.22a, while Figure 21.22b shows the actual torque response when the machine accelerated and decelerated.

The torque control scheme of Figure 21.21 requires a high-resolution position sensor. Another control scheme is one which does not require a high-resolution encoder and does not control the phase currents in closed loops explicitly. In this scheme, direct control of torque via

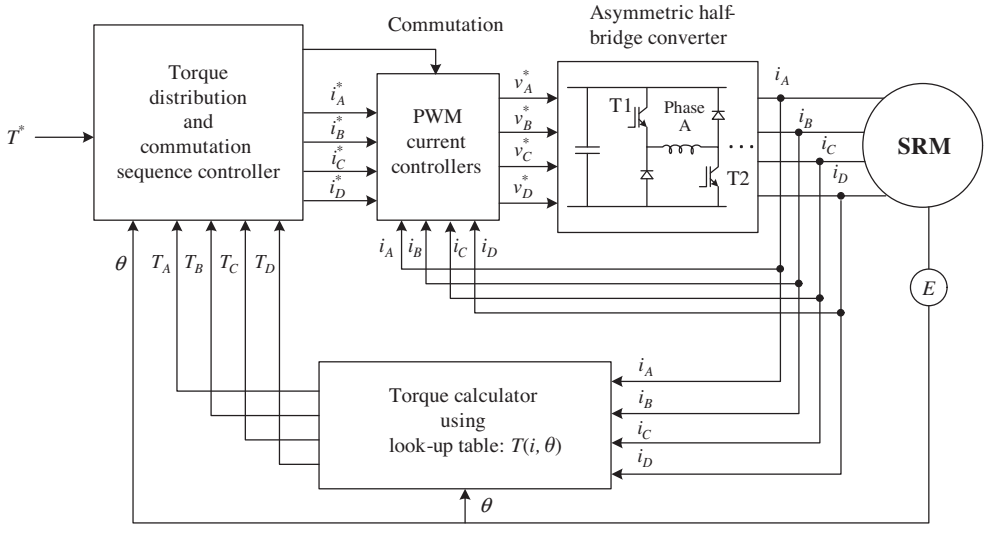

Figure 21.21 Torque controller structure for an SRM with asymmetric half-bridge converter for each phase

flux estimation and PWM control of voltage to the phases, albeit with commutation arranged via a low-resolution position sensor. This approach is similar to the DTC schemes that have been used with induction and IPM synchronous machines, except that phase commutation signals must be derived from a position sensor. The method is based on relating the developed torque to phase current and flus linkage of a phase winding, as indicated in Figure 21.23. The DTC based on Figures 21.23 is depicted in Figure 21.24. The dynamic response of torque obtained from this scheme is indicated in Figure 21.25.

21.3 Power Converters for AC Electric Traction Drives

With AC traction drives, there often are two stages of power conversions, as indicated in Figures 21.26a–b, in order to optimize the selection of motor and DC supply voltage levels. Often the battery voltage is around 300 V DC; it is normally boosted to a higher level of about 600 V. The reverse arrangement is also possible. The bidirectional boost or buck input converters of Figures 21.26a and b respectively, and the three-phase inverter for the traction motor allow some flexibility when ultra-capacitors are used for rapid acceleration and deceleration. The inverter input DC voltage in this case is supplied by ultra-capacitors that allow faster discharging (during motor operation) and charging (during regenerative operation) than it is possible with a battery. Transfer of energy between the two storage devices is arranged through outer voltage and inner current controls of each converter. The dynamics of the controllers for the ultra-capacitor is about an order of magnitude higher than the controllers for the battery, in order to decouple the operation of the two storage devices. Control system designs for these two storage systems will not be discussed here.

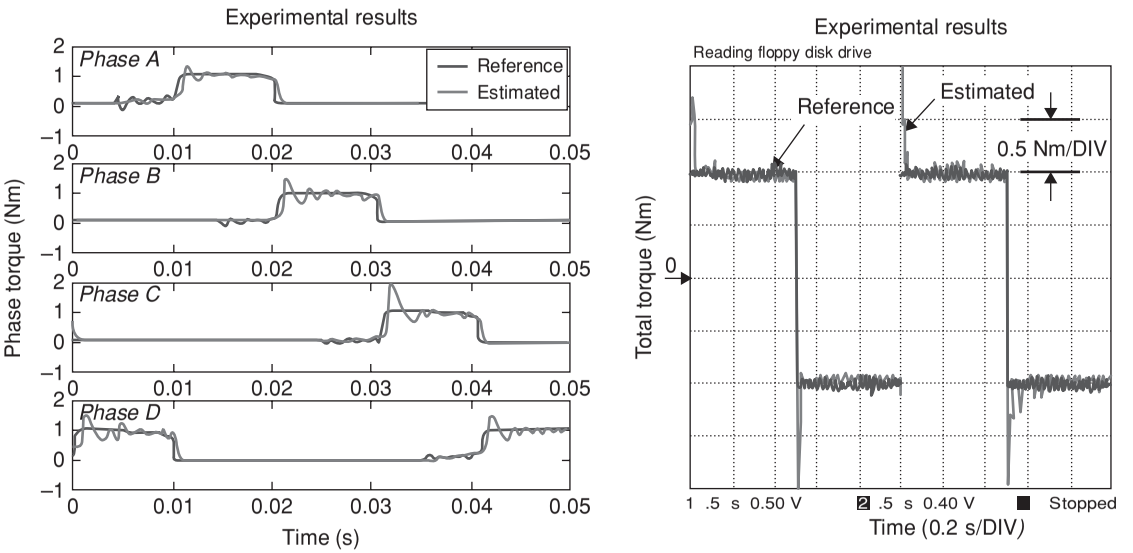

Figure 21.22 Reference and estimated torque for each phase of an SRM and total estimated torque during acceleration and deceleration

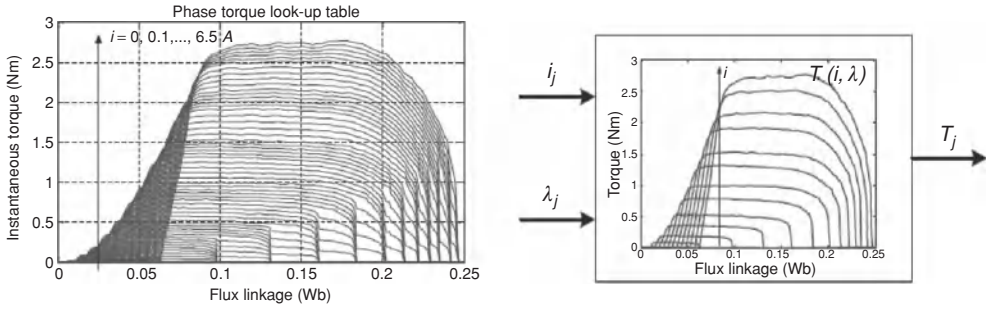

Figure 21.23 Torque versus current versus flux linkage of an SRM

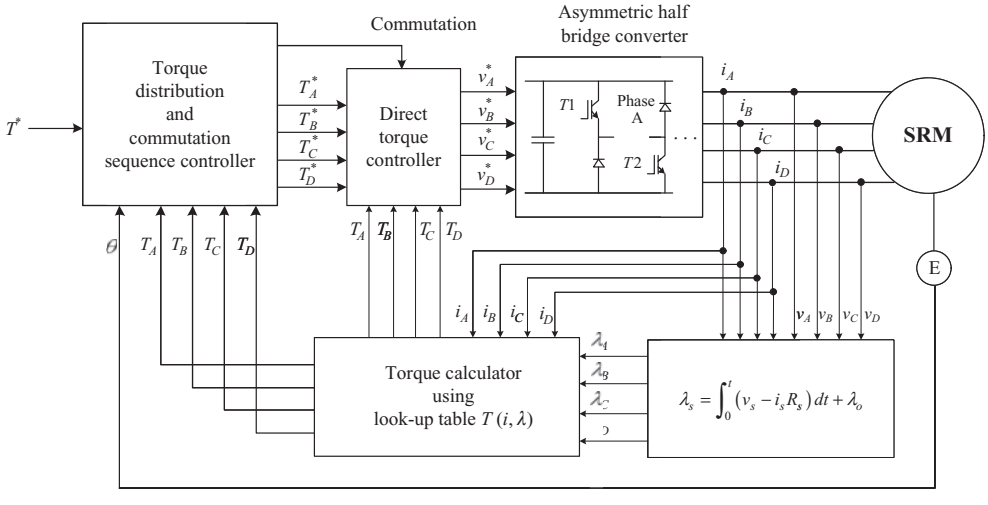

Figure 21.24 Direct torque control structure for an SRM

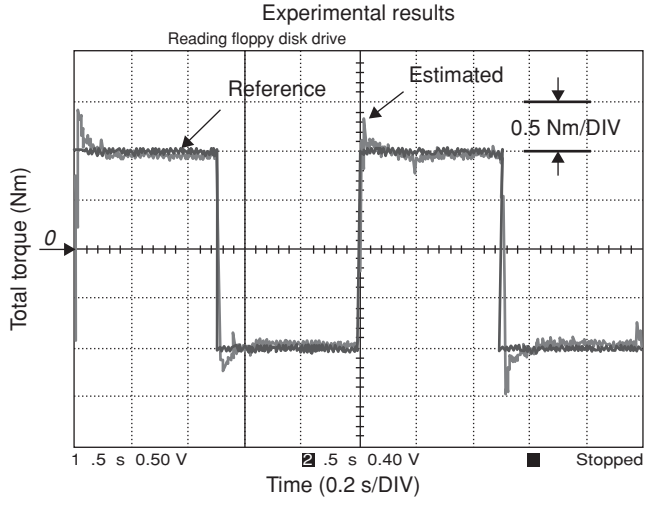

Figure 21.25 Dynamic torque response of an 8/6 SRM with direct torque control

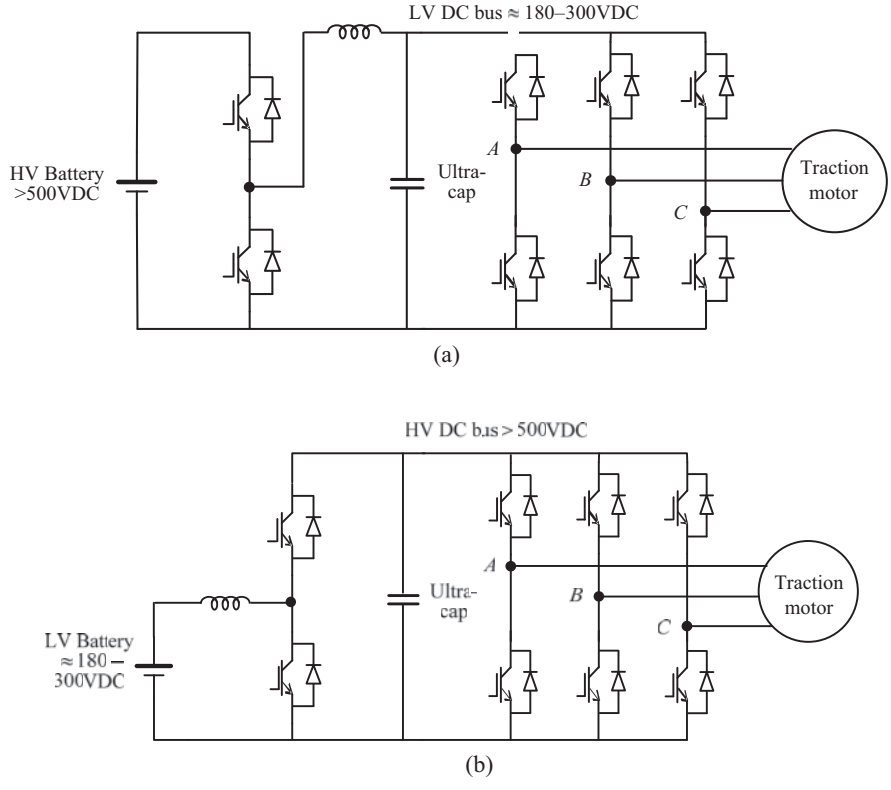

Figure 21.26 Bidirectional (a) buck converter/inverter and (b) boost converter/inverter, with ultra-capacitor for traction drives

21.4 Control Issues for Traction Drives

Apart from fast torque and flux control, the three other important elements of control in an electric traction drive are as follows:

1. Slip-speed ratio and torque control for the desired longitudinal and lateral motion.
2. Control of regenerative braking.
3. Sensorless control.

21.4.1 Torque and Slip-Speed Ratio Control

It is well known that electric traction affords torque response 100–500 times faster than ICE driven vehicles, in both forward traction and regenerative braking modes of operation (Fujii and Fujimoto 2007). The slow response of an ICE-driven vehicle stems from the requirements for adjustment of air valve, fuel and oil pressure. The delay associated with these adjustments

is often more than 200 ms. In contrast, the AC electric motors when driven with RFOC and DTC have delays less than 10 ms. The fast response implies more accurate regulation of the optimum slip-speed ratio, and hence better delivery of torque from the motor to the wheels. This has significant impact on the control of vehicle dynamics and stability, as well as longer driving range per battery charge because low-drag tyres can be used (Fujii and Fujimoto 2007).

With electric traction, the actuator motor applies two forces on the vehicle body, namely, the longitudinal and lateral (yaw) forces. These forces depend significantly on the slip-speed ratio, λ, as defined in terms of the difference between the wheel and vehicle speeds, v_w and v, respectively, as defined in equation (21.25):

$$\lambda = \frac{(v_w - v)}{v}. \tag{21.25}$$

The wheel speed v_w can be obtained from the effective radius of the driving wheel; however, the vehicle speed is normally estimated from the wheel speed(s) and vehicle accelerometer sensor (Hori *et al.* 1998). The relationship between coefficients of friction and the slip-speed for longitudinal and lateral motions are as indicated in Figure 21.27, for a certain road surface condition.

The friction or driving force f_d between the road and the wheel is given by

$$f_d = F_v \mu(\lambda) \text{where } F_v \text{ is the vertical force } m_{eq} g \text{ of the vehicle.} \tag{21.26}$$

The traction motor delivers the total torque rf_d via the fixed gear ratio that may exist between the motor and the driven wheel. It may be noted that the lateral force diminishes rapidly with increase in the slip-speed ratio. It is also ameliorated by steering control, so that motor torque is mainly used for longitudinal control. The torque control system for the vehicle primarily receives its torque reference from the angle of the acceleration and brake pedals (with brake pedal over-riding the two references); however, a slip-speed controller, as indicated in Figure 21.28, precedes input to the torque reference so that the slip-speed is

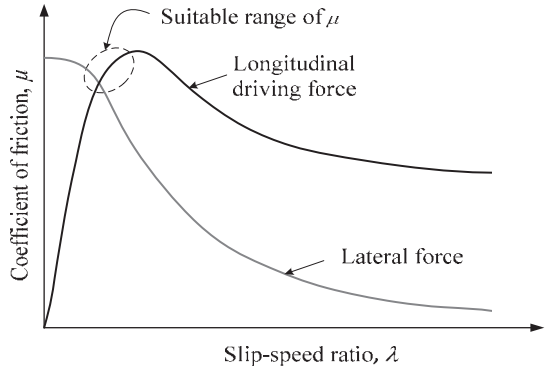

Figure 21.27 Longitudinal and lateral force coefficients versus slip-speed ratio

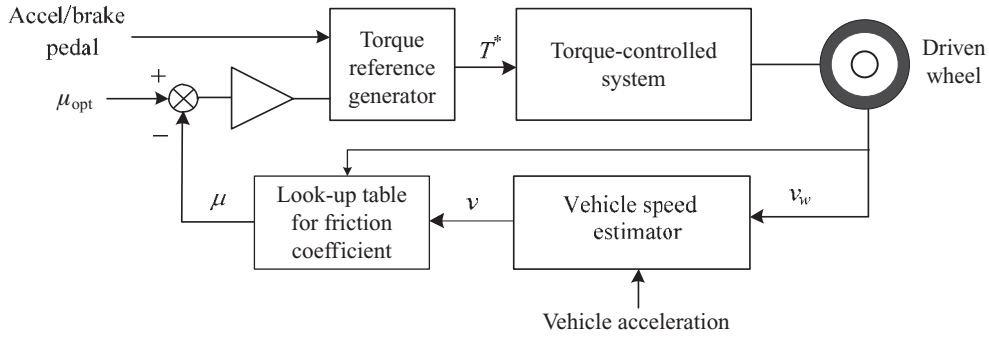

Figure 21.28 Slip-speed ratio controller

maintained close to the optimum value for achieving maximum adhesion of the wheel with the road surface. With estimated vehicle speed, the slip-speed is also estimated and controlled in a closed loop for the maximum adhesion to be achieved.

Several methods of reducing the slip-speed to the optimum value, as the tyre slips on application of motor torque to the wheel, have been described in the literature (Hori *et al.* 1998; Fujii and Fujimoto 2007). These are based on the mechanical system model of the vehicle and will not be covered here. It suffices to mention here that with very fast control of torque developed by an electric motor, the requirement for optimum slip speed control becomes much more important than with an ICE driven vehicle. Fast torque response from the motor also allows the optimum slip speed, and hence optimum adhesion of the driven wheel with road surface, to be achieved easily, as indicated in Figure 21.29

21.4.2 Control of Regenerative Braking

In a vehicle, the reference for braking torque is derived from the brake pedal angle. Initially this signal produces a negative torque or $-i_q$ reference in the reference frame used for controlling the AC machine. When the brake pedal is depressed hard, mechanical friction braking may also be applied simultaneously. The braking effort may be distributed among the front, rear or individual wheels depending on the driving condition. When regenerative braking is employed, the braking current charges the ultra-capacitor across the DC link and the battery system taking into account the voltage rise of the storage systems, state of charge, current limits and battery temperature. The battery and ultra-capacitor voltage must be placed under closed-loop control, followed by an inner current loop. The d-axis current must also be appropriately adjusted with speed as the machine slows down, in order to ensure that the machine operates with rated back EMF and MTPA characteristic when slowing down in the constant power speed range.

Dynamic Model of DC-Link Voltage Control for IM and PMSM

Dynamics of the inverter and machine during regenerative braking can be represented as shown in Figure 21.30. The leakage resistance of the ultra-capacitor C is represented by R_{DC}. The

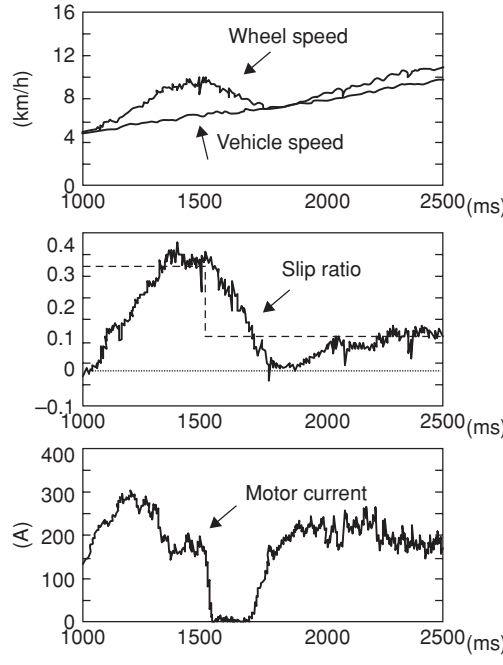

Figure 21.29 Experimental results of optimum slip-speed ratio control (Fujii and Fujimoto 2007)

dynamics of the ultra-cap is assumed to be much faster than the battery, so the battery model is ignored.

By balancing the DC and AC sides,

$$v_{DC} i_1 = \frac{3}{2} \left(v_{qs} i_{qs} + v_{ds} i_{ds} \right). \tag{21.27}$$

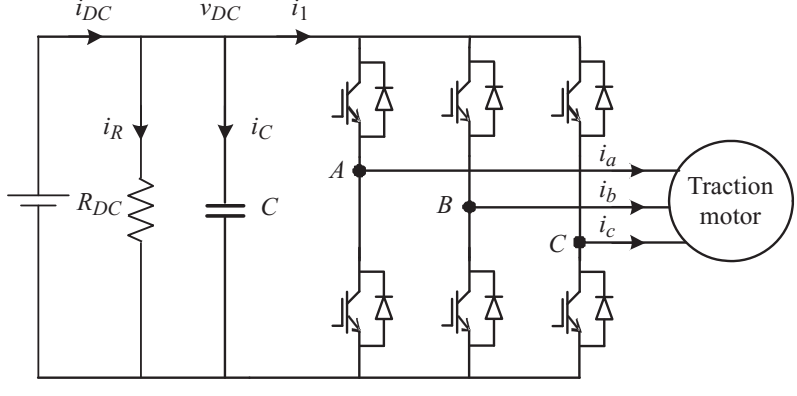

Figure 21.30 Representation of the DC link capacitor charging circuit

For the DC side of the inverter,

$$i_1 = i_{DC} - i_C - i_R = i_{DC} - C\frac{dv_{DC}}{dt} - \frac{v_{DC}}{R_{DC}}. \tag{21.28}$$

From (21.27) and (21.28),

$$v_{DC}\frac{dv_{DC}}{dt} + \frac{v_{DC}^2}{R_{DC}C} = \frac{P_{DC}}{C} - \frac{3}{2C}\left(v_{qs}i_{qs} + v_{ds}i_{ds}\right). \tag{21.29}$$

By ignoring the small power loss in the stator resistance, compared to the power from the machine back EMF,

$$v_{DC}\frac{dv_{DC}}{dt} + \frac{v_{DC}^2}{R_{DC}C} = \frac{P_{DC}}{C} - \frac{3}{2C}\omega_e\frac{L_m}{L_r}\lambda_{dr}i_{qs} \text{ for an IM,} \tag{21.30}$$

$$v_{DC}\frac{dv_{DC}}{dt} + \frac{v_{DC}^2}{R_{DC}C} = \frac{P_{DC}}{C} - \frac{3}{2C}\left(\omega_e\{\lambda_f i_q + \left(L_d - L_q\right)i_d i_q\}\right) \text{ for an IPMSM.} \tag{21.31}$$

Equations (21.30) and (21.31) can be rewritten by multiplying both sides by $2R_{DC}C$ and expressing the left-hand side as

$$R_{DC}C\frac{dv_{DC}^2}{dt} + 2v_{DC}^2 = 2R_{DC}\left(P_{DC} - \frac{3}{2}\omega_e\frac{L_m}{L_r}\lambda_{dr}i_{qs}\right) \text{ for an IM.} \tag{21.32}$$

If the variable v_{DC}^2, instead of v_{DC}, is regarded as the control variable, and if the control bandwidths of i_{ds} and i_{qs} are much faster than the control bandwidth of the capacitor voltage v_{DC}, equation (21.32) can be drawn as in Figure 21.31a. With the fast current control and complete decoupling of RFOC, the above control block diagram simplifies to Figure 21.31b.

It may be noted that with a large input capacitor C and fast current controls in the d–q axes, the DC bus voltage control is independent of machine dynamics (IM and IPMSM). Figure 21.32 shows experimental data of the DC bus voltage dynamics when an IM is operated with fast acceleration and deceleration into and out of field weakening range. The DC bus voltage is tightly regulated under this highly dynamic situation.

Dynamic Model of DC-Link Voltage Control for SRM

Regenerative control of the switched reluctance generator entails control of the switches for each phase winding while the flux linkage is *decreasing*, as opposed to *increasing* that is required for motoring. From the phase voltage equation,

$$v = Ri + \frac{\partial\lambda}{\partial i}\frac{\partial i}{\partial t} + \frac{\partial\lambda}{\partial\theta}\frac{\partial\theta}{\partial t}. \tag{21.33}$$

The back EMF of each phase reverses its sign when $\frac{\partial\lambda}{\partial\theta}$ is negative. During this period, switches T1 and T2 in the asymmetric half-bridge converter indicated in Figure 21.24 conducts,

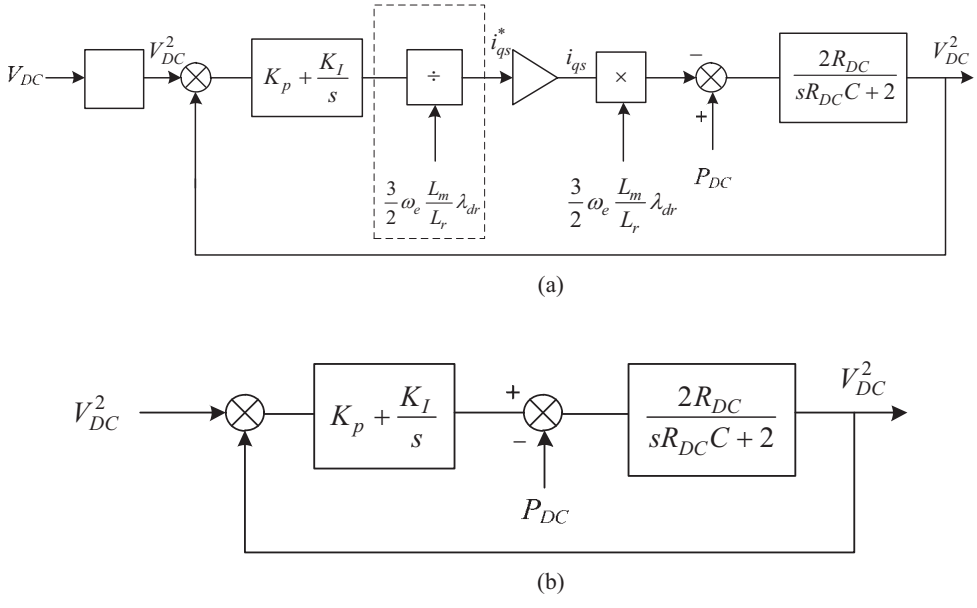

Figure 21.31 Block diagram representation DC link capacitor voltage controller

increasing the flux in the winding. When the switches are turned off, the diodes D1 and D2 charges the DC link capacitor. Figures 21.33a–c show the control structure for regenerative braking when the DC link capacitor is charged. The duty cycle of the switches is adjusted in order to control the regenerative current, and hence, the charging rate of the DC capacitor. It should be noted here that the switching interval for each winding must be appropriately advanced with increasing speed to ensure that current has time to build up to the desired value

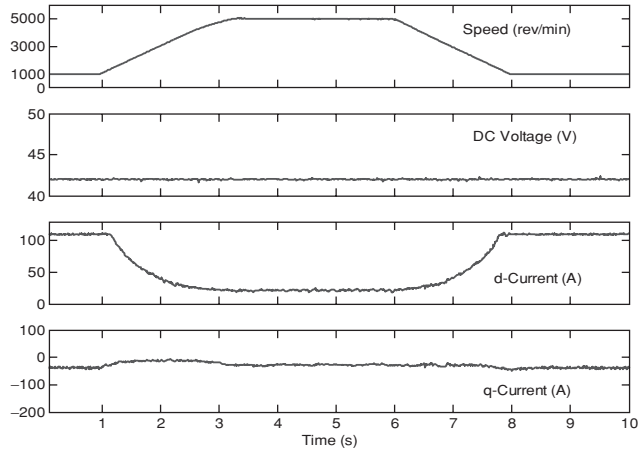

Figure 21.32 Capacitor voltage during acceleration and regenerative braking of an IM

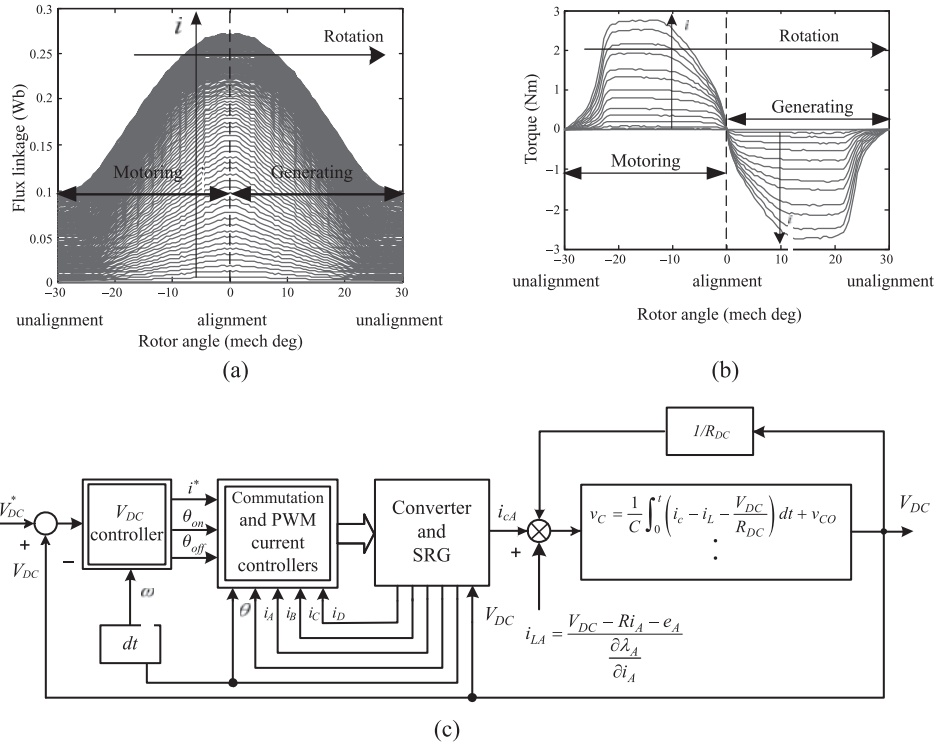

Figure 21.33 Regenerative control and DC link capacitor charging of an SRM

during the conduction period of the switches, as in motoring. As with IM and IPMSM drives, it can be shown that when phase current control is much faster than the capacitor voltage dynamics, the capacitor voltage control with regenerative braking is essentially decoupled from the current controls. Figure 21.34 shows the dynamic response of DC link voltage change when an SRM is operated as a generator charging the DC link capacitor and supplying a DC load that changes abruptly to zero.

Sensorless Control

Shaft-mounted mechanical sensor based RFOC techniques guarantee robust dynamic performance of a vehicle down to very low speed, including zero speed. This is regarded as an essential requirement for vehicles. Mechanical sensorless control techniques such as DTC of AC traction drives cannot at present guarantee this requirement without additional techniques such as position sensing using high-frequency injection into the estimated *d*-axis. The latter technique relies on some saliency in the rotor magnetic circuit that is conveniently offered by IPMSMs. The hostile conditions such as high mechanical shock, temperature and fluid ingestion are not conducive for maintaining the reliability of a mechanical sensor mounted on the drive motor shaft. Mechanical sensorless methods are currently regarded as possible

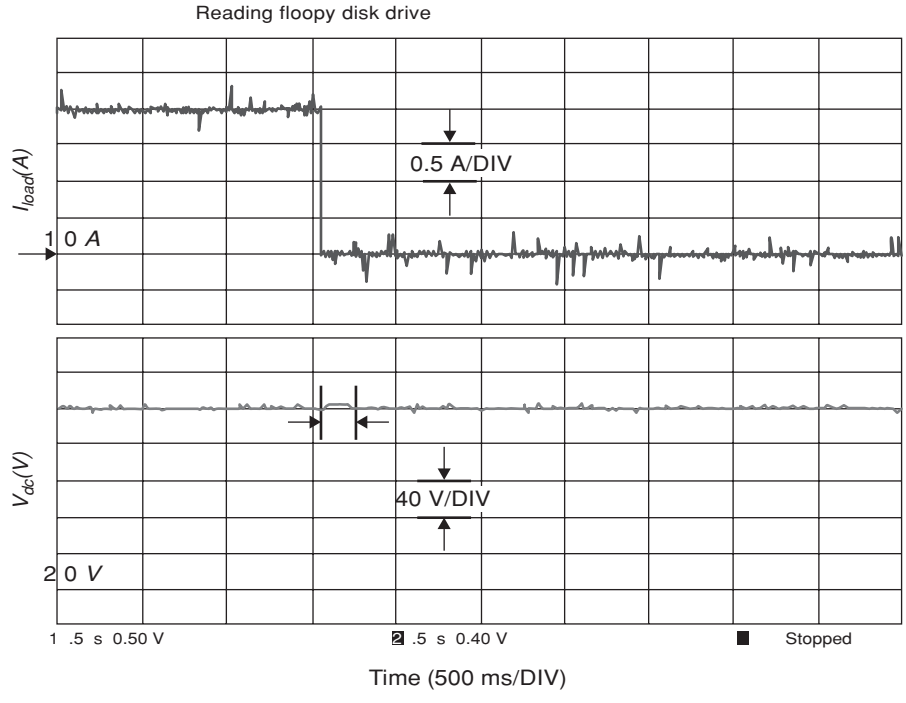

Figure 21.34 DC link capacitor voltage during abrupt change of regenerative braking

standby technique of controlling a vehicle when signals from the shaft-mounted mechanical sensor become unavailable. Sensorless control of IPMSMs suitable for zero speed operation has been described in Chapter 19 (Rahman *et al.* 1998; Foo *et al.* 2010). Methods for IMs are available in reference by Holtz (2006).

21.5 Conclusions

This chapter has brought out the characteristics required for electric machines for traction applications. The focus was on machines and their control issues for HEVs and EVs. Together with Chapter 19, the coverage of induction, permanent magnet synchronous and SRM, which are the three types of machines currently used in vehicles, has described the high-performance control, both mechanical sensor based and sensorless. It is stressed that high-performance dynamic control requirements of vehicles are met by these decoupled control techniques, such as the RFOC and DTC, which have evolved in recent years. Apart from the control of torque, stator and rotor flux linkages in the stator or rotor reference frames, the tractive forces on tyres can be controlled more effectively with electric traction, leading to enhanced energy efficiency and stability. Some of power conversion and control issues related to regenerative braking have also been described.

References

Casadei D, Milanesi F, Serra G *et al.* (2008) Control of induction motors for wide speed range for electric vehicle drives. *Proceedings of the 18 ICEM*, pp. 1–6.

Dutta R and Rahman MF (2008) Design and analysis of an interior permanent magnet (IPM) machine with very wide constant power operation range. *IEEE Trans on Energy Conversion*, **23**(1), 25–33.

Dutta R, Chong L, Rahman M-F (2011) Analysis of CPSR in motoring and generating modes of an IPM motor. *International Electrical Machines and Drives Conference (IEMDC)*, Canada.

Foo G, Sayeef SM and Rahman MF (2010) Low speed and standstill operation of a sensorless direct torque and flux controlled IPM synchronous motor drive. *IEEE Transactions on Energy Conversion*, **25**(1), 25–33.

Fujii K and Fujimoto H (2007) Traction control based on slip ratio estimation without detecting vehicle speed for electric vehicle. *Proceedings of Power Conversion Conference*, Nagoya, Japan, pp. 688–693.

Gosden DF, Chalmers BJ, and Musaba L (1994) Drive system design for an electric vehicle based on alternative motor types. *Proceedings of IEE Power Electronics and Variable Speed Drives*, No. 399, pp. 710–715.

Holtz J (2006) Sensorless control of induction machines – with or without signal injection. *IEEE Transactions on Industrial Electronics*, **53**, 7–30.

Hori Y, Toyoda Y, and Tsuruoka Y (1998) Traction control of electric vehicle: basic experimental results using the test EV, UOT electric march. *IEEE Transaction on Industry Applications*, **34**(5), 1131–1998.

Jeong Y-S and Lee J-Y (2011) Parameter identification of an induction motor drive with magnetic saturation for electric vehicle. *Journal on Power Electronics*, **11**(4), 418–423.

Kondou K and Matsuoka K (1997) Permanent magnet synchonous motor control system for railway vehicle traction and its advantages, *Proceedings of the Power Conversion Conference, Nagaoka, Japan*, **1**, pp. 63–68.

Karanayil B, Rahman MF, and Grantham C (2005) Stator and rotor resistance observers for induction motor drive using fuzzy logic and artificial neural networks. *IEEE Transactions on Energy Conversion*, **20**(4), 771–777.

Lovatt WH and Dunlop JB (2002) Optimization of switched reluctance motors for hybrid electric vehicles. *International Conference on Power Electronics, Machines and Drives, Bath UK*, pp. 177–182.

Miller J (2003) *Propulsion Systems for Hybrid Electric Vehicles*. Book in IET Power Engineering Series 45, Chapter 1, p. 31.

Nash JN (1997) Direct torque control, induction motor vector control without an encoder. *IEEE Transactions on Industry Applications*, **33**(2), 333–341.

Olszewski M (2008) Evaluation of the 2007 toyota camry hybrid synergy drive system. *Oak Ridge National Laboratory* Report FY 2008, US DOE, FreedomCAR and Vehicle Technologies, April 2008.

Rahman KM and Schultz SE (2002) Design of high efficiency and high torque density switched reluctance motor for vehicle propulsion. *IEEE Transaction on Industry Application* **38**(6), 1500–1507.

Rahman MF, Zhong L, and Lim KW (1998) A direct torque controlled interior magnet synchronous motor drive incorporating field weakening. *IEEE Transactions on Industry Applications*, **34**(6), 1246–1253.

Rajashekara K (1994) History of electric vehicles in general motors. *IEEE Transactions on Industry Applications*, **30**(4), 897–904.

Reddy PB, El-Refaie A, Huh K-K, *et al.* (2011) Comparison of interior and surface permanent magnet machines equipped with fractional-slot windings for hybrid vehicles. *IEEE ECCE 2011*, pp. 2252–2259.

Takano Y, Takeno M, Imakawa T, *et al.* (2010) Torque density and Efficiency Improvements of a Switched Reluctance Motor without Rare-Earth Material for Hybrid Vehicles. *Proceedings of IEEE ECCE*, pp. 2653–2659.

Telford D, Dunnigan MW, and Williams BW (2003) On-line identification of induction machine electrical parameters for vector control tuning. *IEEE Transactions on Industrial Electronics*, **50**, 253–261.

West NT and Lorenz RD (2009) Digital implementation of stator and rotor flux linkage observer for deadbeat direct torque control of induction machines. *IEEE Transactions on Industry Applications*, **45**(2), 729–736.

Sayeef S, Foo G, and Rahman MF (2010) Rotor position and speed estimation of a variable structure direct-torque-controlled IPM synchronous motor drive at very low speeds including standstill. *IEEE Transactions on Industrial Electronics*, **57**(11), 3715–3723.

22

Induction Motor Control Application in High-Speed Train Electric Drive

Jarosław Guziński,[1] Zbigniew Krzeminski,[1] Arkadiusz Lewicki,[1] Haitham Abu-Rub,[2] and Marc Diguet[3]

[1] *Faculty of Electrical and Control Engineering, Gdansk University of Technology, Poland*
[2] *Department of Electrical & Computer Engineering, Texas A&M University at Qatar, Qatar*
[3] *Alstom Transport, France*

22.1 Introduction

In the modern electric traction drive systems particular attention is being paid to improve their reliability by numerous diagnostic systems (Ohnishi *et al.* 1996; Kowalski 2005; Jung *et al.* 2006; Kia *et al.* 2007). Such solutions of the faults detection, which are utilized, for example, in high speed railway systems (Madej 2000; Kadowaki *et al.* 2007) can predict the inception of faults. If the failure mode is detected, then presence of the serious faults is possible. Having the knowledge of faults' symptoms, possible failures can be predicted and thus effective mitigation techniques may be developed.

Mostly, diagnostic systems of the mechanical parts are based on analysis of the signals of the measured torque. In the measurement system, different sensors are used, for example, strain gauge, accelerometers or microphones (Kucharski 2002). Unfortunately, all torque oscillation sensors are sensitive to disturbances and troublesome in practical use. Additionally, with an increase of sensors numbers, the traction system becomes more complicated, which makes a train service and its repair more complicated and expensive.

The use of the advanced microprocessor techniques makes it possible to realize sensorless diagnostic systems in such applications. In modern calculation-based diagnostic systems, only already existing sensors are used. The existing sensors are being used for other purposes, for

AC Electric Motors Control: Advanced Design Techniques and Applications, First Edition. Edited by Fouad Giri.

example, motor control. However, such solution requires complicated computational algorithms (Tondos 1993; Krzeminski 2000; Vedmar and Andersson 2003; Hedayati *et al.* 2009).

An important part of traction drive is a system that is responsible for torque transmission from motor shaft to vehicle drive axis. Previously, the diagnosis of such system was based on motor and gear vibration measurement (Kowalski 2005). Now the modern calculation-based solutions are reported (Hedayati *et al.* 2009; Guzinski *et al.* 2009a).

In the transmission diagnostic, an analysis of mutual shaft positions of the gear or of drive mechanical oscillations makes it possible for early fault detection, for example, gear damages (Hedayati *et al.* 2009; Guzinski *et al.* 2009a). The problems with torque transmission system are complicated. After an initial period of operation, the problems with the transmission can appear as a result of wearing and material consumption. The wear of gears causes growing amplitudes of the frequencies related to the gear meshing. In case of transmission faults, the train might be stopped or may work with some mechanical oscillations and noises. Some faults of the torque transmission system have also serious influence on the safety of the train and the passengers. This is the reason of the necessity to introduce the proposed diagnostic system.

Motor mechanical speed sensor is also the important part of the whole transmission system. Numerous traction drives are equipped with different speed sensors used for traction motor control. In case of motor speed sensor fault, the drive cannot work properly and is probably switched off immediately. If there is only one drive in the train, the whole vehicle is stopped, which blocks the track. If several drives used in the vehicle, the shutdown of one drive has an influence on the train speed, thus causing delay and traffic choking problem.

To solve this problem, the motor speed calculations or estimation instead of speed measurement could be implemented. Nowadays, for an increasing number of industrial drive state observers are being utilized instead of speed sensors. A lot of speed observer systems are presented in the literature (Luenberger 1971; Rajashekara *et al.* 1996; Magureanu *et al.* 2000; Orlowska 2003; Depenbrock and Evers 2006; Holtz 2006; Orlowska and Szabat 2007; Krzeminski *et al.* 2008). Most popular observers are based on Luenberger theory (Luenberger 1971), Kalman filters (Magureanu *et al.* 2000) and Neural Networks (Orlowska 2003; Orlowska and Szabat 2007), or disturbance-based algorithms (Zawirski and Urbanski 2000; Krzeminski 2008). The differences between such algorithms depend on speed calculation accuracy in steady state and in transients and on algorithms implementation and tuning complication as well.

In this chapter, a traction system is presented, in which speed and load torque observers are implemented for diagnostic purposes. The presented solution is small part of developed bigger high-speed train (HST) predictive maintenance system. In the whole diagnostic system, several problems are under consideration, for example, speed sensor faults, mechanical transmission faults, and motor stator and rotor faults.

22.2 Description of the High-Speed Train Traction System

The proposed solution is designed for the application of HST—electric traction multiple unit. The analyzed multiple unit, presented in Figure 22.1, consists of two driving cars and few passenger wagons.

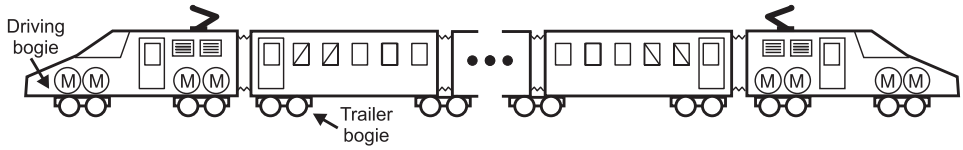

Figure 22.1 Multiple unit of the high speed train

Previously, in traction vehicles wagons (Guzinski *et al.* 2008; Guzinski *et al.* 2009a), DC motors and wounded rotor synchronous motors were popular. Nowadays, these motor are replaced by more reliable and cheaper induction motors or permanent magnet synchronous motors.

In HST, one motor propels one axle in every motorized bogie. In each bogie, one or two motors may exist. A motorized car typically has two bogies with motors. In the presented HST solution, each of the driving cars is propelled by four 1.2 MW induction motors, which are fed by separate voltage source inverters. Each of these traction motors is coupled with individual driving axles through complex torque transmission system—Figure 22.2.

The torque transmission unit consists of two-toothed gears and coupling systems to ensure a compensation of the position change between motor shaft and drive axle. The motor and the one gear are fixed with the car body; however, the next gear is fixed to bogie frame. Therefore, a sliding axle and some cardans are installed between gears shafts. The motor speed sensor is mounted directly on the motor shaft. This sensor is for motor control. Additional speed sensors, mounted on each gears output are for the wheels antislip control.

The whole model of the HST drive contains four main parts: traction motor, transmission, converter, and controller. For initial investigation of the presented system, the simulation method was used. The dedicated simulation programs in C language and in Matlab were prepared. With the simulation software different conceptions of the diagnostic procedures were verified.

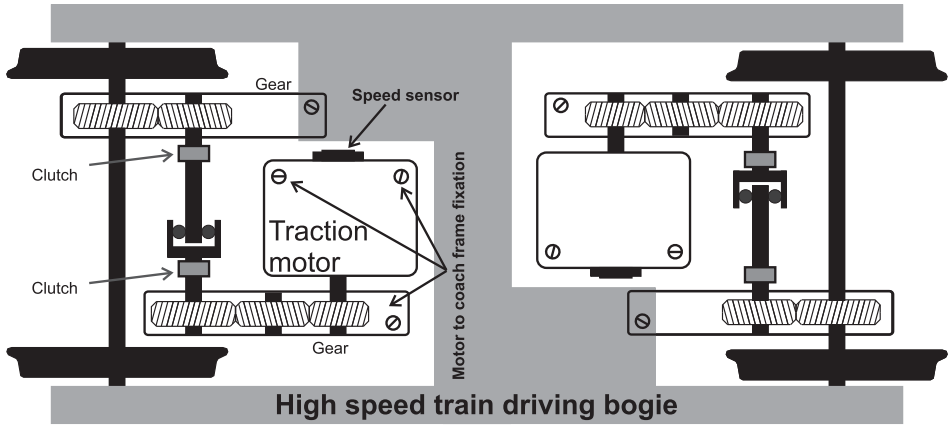

Figure 22.2 Structure of the HST driving bogie

Table 22.1 Per unit system definitions

Base value	Meaning
$V_b = \sqrt{3}U_n$	Voltage
$I_b = \sqrt{3}I_n$	Current
$Z_b = \frac{U_n}{I_n}$	Impedance
$\omega_0 = 2\pi f_n$	Electrical speed
$T_b = \frac{U_b I_b p}{\omega_0}$	Torque
$\Psi_b = \frac{U_b}{\omega_0}$	Flux
$\omega_b = \frac{\omega_0}{p}$	Mechanical speed
$L_b = \frac{\Psi_b}{I_b}$	Inductance
$J_b = \frac{T_b}{\omega_b \omega_0}$	Inertia
$\tau = \omega_0 t$	Time

22.2.1 Induction Motor

For train propulsion, high-power induction motor is used. The data of the HST motor are $P_{\max} = 1.2$[MW], $U_n = 810$[V], $n_n = 269$[rpm], $I_n = 586$[A], $f_n = 133$[Hz], $\eta_n = 96$[%], $\cos\varphi_n = 0.88$, 3 poles pairs. When used in HST gear and wheels, the motor nominal and maximum speeds are related to the train speeds of the values about 225 km/h and 320 km/h, respectively—depending on train wheels wear.

Motor model is described in the rectangular coordinates noted as xy. The xy coordinates me rotating with arbitrary speed ω_a. Next state variables were chosen: stator current i_{sx}, i_{sy} and rotor flux ϕ_{rx}, ϕ_{ry} components, and motor mechanical speed ω_m. Whole system variables were recalculated into per unit system as shown in Table 22.1 (Krzeminski 2001).

Equations of the used motor model are as follows

$$\frac{di_{sx}}{d\tau} = -\frac{R_s L_r^2 + R_r L_m^2}{L_r w_\sigma} i_{sx} + \frac{R_r L_m}{L_r w_\sigma}\phi_{rx} + \omega_a i_{sy} + \omega_m \frac{L_m}{w_\sigma}\phi_{ry} + \frac{L_r}{w_\sigma} v_{sx}, \tag{22.1}$$

$$\frac{di_{sy}}{d\tau} = -\frac{R_s L_r^2 + R_r L_m^2}{L_r w_\sigma} i_{sy} + \frac{R_r L_m}{L_r w_\sigma}\phi_{ry} - \omega_a i_{sx} + \omega_m \frac{L_m}{w_\sigma}\phi_{rx} + \frac{L_r}{w_\sigma} v_{sy}, \tag{22.2}$$

$$\frac{d\phi_{rx}}{d\tau} = -\frac{R_r}{L_r}\phi_{rx} + (\omega_a - \omega_m)\phi_{ry} + R_r \frac{L_m}{L_r} i_{sx}, \tag{22.3}$$

$$\frac{d\phi_{ry}}{d\tau} = -\frac{R_r}{L_r}\phi_{ry} - (\omega_a - \omega_m)\phi_{rx} + R_r \frac{L_m}{L_r} i_{sy}, \tag{22.4}$$

$$\frac{d\omega_m}{d\tau} = -\frac{1}{J_M}\left(\frac{L_m}{L_r}(\phi_{rx} i_{sy} - \phi_{ry} i_{sx}) - T_{S1}\right), \tag{22.5}$$

Table 22.2 Parameters of the motor equivalent circuit

Parameter	Value	Description
R_s	0.01226 p.u	Stator resistance
R_r	0.01085 p.u.	Rotor resistance
L_m	4.56150 p.u.	Mutual inductance
L_s	4.73790 p.u.	Stator inductance
L_r	4.68320 p.u.	Rotor inductance

where R_r, R_s, L_r, L_s, L_m are motor equivalent circuit parameters presented in Table 22.2, T_{S1} is the motor load torque, J_M is the motor inertia (6.1 kg m^2), and w_σ is the coefficient defined as $w_\sigma = L_r L_s - L_m^2$.

For simulation purposes, the stationary $\alpha\beta$ coordinates were used and the motor model (22.1)–(22.5) have been rewritten using motor stator currents and rotor flux $\alpha\beta$ components: $i_{s\alpha}$, $i_{s\beta}$, $\phi_{r\alpha}$, $\phi_{r\beta}$ (Krzeminski 2001).

22.2.2 Torque Transmission System

For simulation purposes HST transmission system was reduced to a two-mass system which is presented in Figure 22.3 (Tondos 1993; Orlowska and Szabat 2007).

The integral property of the traction vehicle is a macroslip / microslip effect. The rolling stock of the coach moves by the adhesion force between rail and driving wheel. Approximated relation between the adhesion force and the slip velocity is presented in Figure 22.4 (Kadowaki *et al.* 2007).

In the slip velocity two areas are distinguished: stable (microslip) and unstable (macroslip). In the investigated HST the stable area is limited to the slip up to 2%. In the coach each driven axle has different slip phenomena mainly depending on current axle load. In the investigated HST each driving axle is propelled by one electric motor which is connected to the separate inverter. Such trend simplifies the torque control of the motor to prevent macroslip. Adhesion limit for HSTs imposed by European Technical Specification Interoperability is 0.15 for speed up to 200 km/h and decreases for higher speeds.

In the considered two-mass model, the macroslip phenomena was omitted according to assumption that superior adhesion control is implemented in the system. Small microslip phenomenon was included in the elastic model of the shaft and gear.

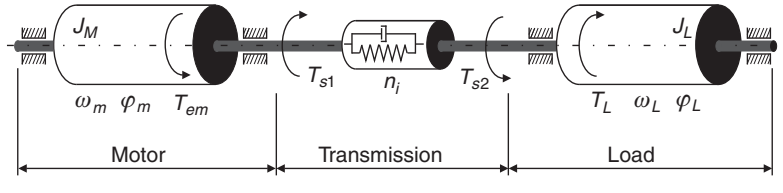

Figure 22.3 Reduced, two-mass model of the torque transmission system

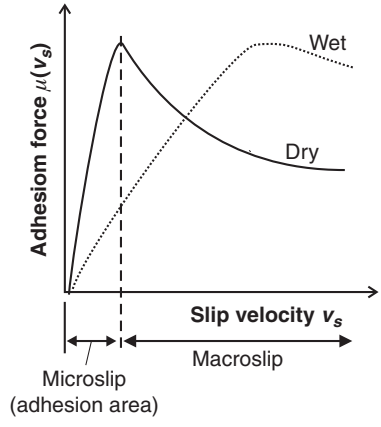

Figure 22.4 Relation between adhesion force $\mu(v_s)$ and slip velocity v_s of the coach

The two-mass model of the mechanical system is as follows:

$$J_M \frac{d\omega_m}{dt} = T_{\text{em}} - T_{S1}, \tag{22.6}$$

$$J_L \frac{d\omega_L}{dt} = n_i T_{S2} - T_L, \tag{22.7}$$

$$\frac{d\varphi_r}{dt} = \omega_m, \tag{22.8}$$

$$\frac{d\varphi_L}{dt} = \omega_L, \tag{22.9}$$

$$T_{S1} = K_2 (\theta_m - n_i \theta_L) + H_2 (\omega_m - n_i \omega_L), \tag{22.10}$$

$$T_{S2} = n_i |T_{S1}|, \tag{22.11}$$

where ω_L is the mechanical speed of the load, θ_m is the angle position of the motor rotor, θ_L is the angle position of the load, T_e is the motor electromagnetic torque, T_L is the traction load torque, T_{S1} is the transmitted torque on gear input = motor load torque, T_{S2} is the transmitted torque on gear output, K_2 is the stiffness function, H_2 is the damping coefficient (170 Ns/m), J_L is the load inertia (3000 kgm^2), and n_i is the gear ratio (1.97).

Function K_2 depends on gear wheel tooth stiffness (Muller 1979):

$$K_2 = K_S + K_D \sin(z\varphi_m), \tag{22.12}$$

where K_S is the stiffness average value (3.5×10^5 N/m), K_D is the stiffness maximum value (5.7×10^5 N/m), and z is the number of the gear driving wheel teeth (25 teeth).

In (22.7), the meshing frequency higher harmonics were omitted. It is a result of skew teeth in the modeled gear. For such gear the meshing amplitudes in healthy condition are very small.

The misalignment in the transmission system was modeled as an additional load torque component T_w:

$$J_M \frac{d\omega_m}{dt} = T_{\text{em}} - T_{S1} - T_w. \tag{22.13}$$

The additional torque component T_w is sinusoidal value with frequency equal to the motor shaft rotation:

$$T_w = T_{wav} \left(1 + \sin(\varphi_m)\right), \tag{22.14}$$

where T_{wav} is the average value of the misalignment load torque component (720 Nm).

In (22.6), a viscous friction was considered:

$$J_M \frac{d\omega_m}{dt} = T_{\text{em}} - T_{S1} - T_w + T_f, \tag{22.15}$$

where T_f is the viscous friction load torque component.

The torque component T_f is

$$T_f = F\omega_m, \tag{22.16}$$

where F is the viscous friction coefficient (0.8 Ns/m).

22.2.3 High-Power Electronic Converter

The HST traction system has double way supply: ac supply 25 kV 50 Hz and dc supply 1.5 kV. The train high-speed range is obtained only with the ac high-voltage traction mode. In case of using an ac train supply, one-phase transformer is utilized (Wilk 2009). The transformer output ac supply is converted into dc by full controlled transistorized rectifier, filtered in the intermediate dc link and converted to ac motor supply by a three-phase voltage inverter with insulated gate bipolar transistor (IGBT) transistors (Figure 22.5). In the simulation program, the voltage inverter was modeled with ideal switches controlled with a pulse width modulation method. Regarding the high power of the drive transistor, a switching frequency of the IGBT in the traction drive is variable within the range from 450 Hz for low speeds of the motor to square wave for highest motor speeds.

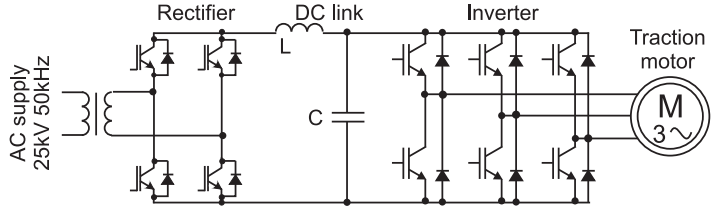

Figure 22.5 Supply system of the HST traction motor

22.2.4 Motor Control Principle

The most popular in industrial applications, field-oriented control (FOC) scheme is used for precise and fast dynamics and response of traction motor (Blaschke 1971). The control structure used in the presented work is illustrated in Figure 22.6. In the traction application of the field-oriented method, torque mode of operation is used and thus as such the speed controller was not used. The operator commanded value is the motor torque that is changed using stator current component i_{sq}. The traction system of the HST is working also in the field weakening region that is used to obtain high speed of the train.

22.3 Estimation Methods

22.3.1 Speed Observer

Speed computation in real time is presented in many publications (Luenberger 1971; Rajashekara *et al.* 1996; Krzeminski 2000; Magureanu *et al.* 2000; Krzeminski 2001; Orlowska 2003; Depenbrock and Evers 2006; Holtz 2006; Krzeminski *et al.* 2008). Most popular solutions are based on motor models using the concept of Luenberger state observer (Luenberger 1971). One of these methods, characterized by high precision and fast dynamics, was used in the diagnostic system in Krzeminski (2000), Krzeminski (2008), and Krzeminski (2001). The use of state observer makes it possible to simultaneously compute the angular speed and magnetic flux (Krzeminski 2001).

Each of the observers has limited bandwidth depending on observer internal structure. For diagnostic purposes, the observer bandwidth should satisfy the interesting diagnostic bandwidth. For that reason, the observer solution presented in Krzeminski (2001) was applied into presented HST system. The bandwidth of the chosen observer is significantly higher than other comparable observers (Bogalecka and Kolodziejek 2008).

In this application, the speed observer needs only four input signals, which are usually accessible in the control. These signals are signals of inverter output currents and signals of

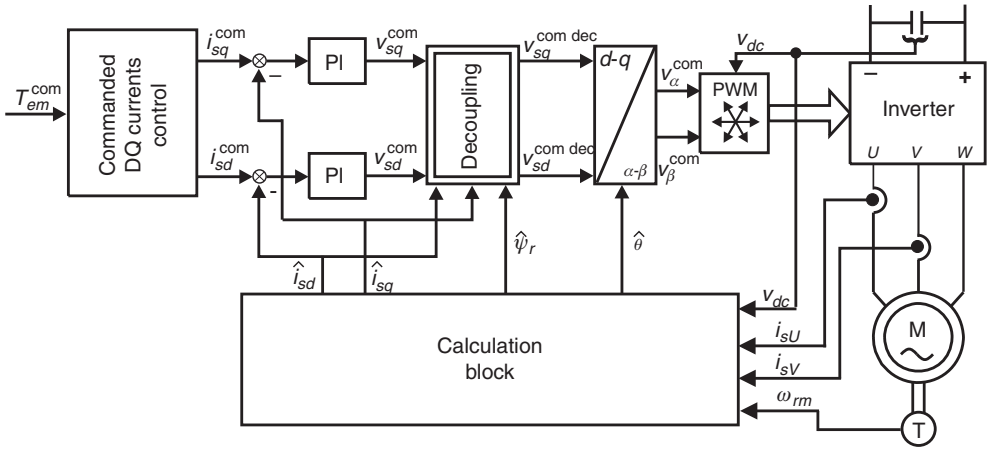

Figure 22.6 Base structure of the HST motor control algorithm

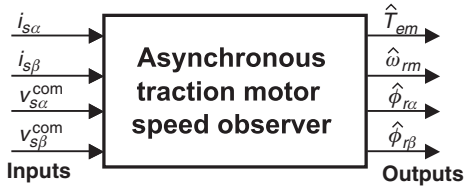

Figure 22.7 Input/output block of the induction motor observer

the PWM commanded voltages (Figure 22.7). The equations of the speed observer in stationary $\alpha\beta$ coordinates are as follows (Guzinski *et al.* 2009b):

$$\frac{d\hat{i}_{s\alpha}}{d\tau} = a_1\hat{i}_{s\alpha} + a_2\hat{\phi}_{r\alpha} + a_3\hat{\xi}_\beta + a_4 v_{s\alpha}^{com} + k_1(i_{s\alpha} - \hat{i}_{s\alpha}), \tag{22.17}$$

$$\frac{d\hat{i}_{s\beta}}{d\tau} = a_1\hat{i}_{s\beta} + a_2\hat{\phi}_{r\beta} - a_3\hat{\xi}_\alpha + a_4 v_{s\beta}^{com} + k_1(i_{s\beta} - \hat{i}_{s\beta}), \tag{22.18}$$

$$\frac{d\hat{\phi}_{r\alpha}}{d\tau} = a_5\hat{\phi}_{r\alpha} + a_6\hat{i}_{s\alpha} - \xi_\beta - k_2 S_b\hat{\phi}_{r\alpha} + k_3\hat{\phi}_{r\beta}(S_b - S_{bF}), \tag{22.19}$$

$$\frac{d\hat{\phi}_{r\beta}}{d\tau} = a_5\hat{\phi}_{r\beta} + a_6\hat{i}_{s\beta} + \xi_\alpha - k_2 S_b\hat{\phi}_{r\beta} - k_3\hat{\phi}_{r\alpha}(S_b - S_{bF}), \tag{22.20}$$

$$\frac{d\hat{\xi}_\alpha}{d\tau} = a_5\hat{\xi}_\alpha + a_6\hat{\omega}_m\hat{i}_{s\alpha} - \hat{\omega}_m\hat{\xi}_\beta - k_1(i_{s\beta} - \hat{i}_{s\beta}), \tag{22.21}$$

$$\frac{d\hat{\xi}_\beta}{d\tau} = a_5\hat{\xi}_\beta + a_6\hat{\omega}_m\hat{i}_{s\beta} - \hat{\omega}_m\hat{\xi}_\alpha + k_1(i_{s\alpha} - \hat{i}_{s\alpha}), \tag{22.22}$$

$$\frac{dS_{bF}}{d\tau} = k_{fo}(S_b - Si_{bF}), \tag{22.23}$$

$$\hat{\omega}_m = \frac{\hat{\phi}_{r\alpha}\hat{\xi}_\alpha + \hat{\phi}_{r\beta}\hat{\xi}_\beta}{\phi_{r\alpha}^2 + \phi_{r\beta}^2}, \tag{22.24}$$

where $\wedge$ denotes calculated value in the observer, S_b, S_{bF} are internal observer variables, $a_1 \cdots a_6$ are constants depending on motor parameters $a_1 = -(R_s L_r^2 + R_r L_m^2)/(L_r w_\sigma)$, $a_2 = R_r L_m/(L_r w_\sigma)$, $a_3 = L_m/(L_r w_\sigma)$, $a_4 = L_r/w_\sigma$, and $k_1, k_2, k_3, k_4, k_{fo}$ are observer gains.

With observer calculation, the motor electromagnetic torque could be also identified:

$$\hat{T}_{\text{em}} = \hat{\phi}_{r\alpha}\hat{i}_{s\beta} - \hat{\phi}_{r\beta}\hat{i}_{s\alpha}. \tag{22.25}$$

The block structure of the observer is presented in Figure 22.8. The speed observer (22.17)–(22.24) is based on the Luenberger observer theory (Luenberger 1971) in addition using motor electromotive forces as additional state variables. The mechanical equation of the system was omitted and the motor mechanical speed is treated as a variable parameter of the motor. Such approach was also successfully implemented for the synchronous permanent magnet motor (Zawirski and Urbanski 2000).

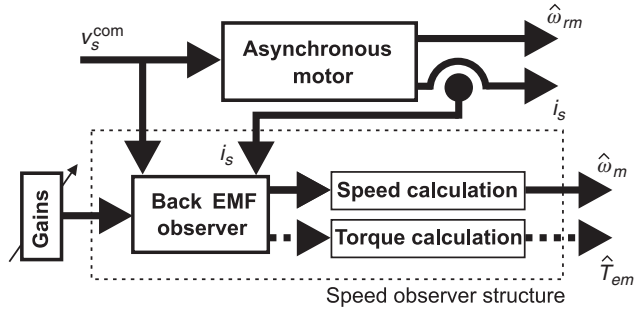

Figure 22.8 Speed observer structure

In the observers equations (22.17)–(22.24), in contrary to Krzeminski (2008), the component related to motor speed derivative was omitted assuming that for small step of the observer calculation this component is close to zero for high-inertia train system.

Observer gains require appropriate tuning to assure fast estimation and to guarantee stable work of the observer. Practically that process is based mainly on the experience of the designer. It is a result of high complexity of the whole system. With the modern simulation tools and high-speed computers, this approach seems to be more precisely performed than using formal mathematical computation. For that reason sometimes the neural network-based algorithms are employed; for example, the numerous observer's gains and time constants could be tuned using algorithm random weight change (RWC) (Burton *et al.* 1997). In each step of the RWC algorithm, the transient state of the observer were simulated and quality coefficient were calculated. At the beginning, the observer gains were tuned randomly in wide range of the field of research. After that the field of research was reduced and observer gains were precisely found (Pajchrowski and Urbanski 2001). That way is very close to the designer experimental tuning.

22.3.2 Motor Torque Estimation

In the industry, instead of the mechanical vibrations measurements, calculation methods are much more interesting. For the diagnostic of traction torque transmission system using calculation-based methods the analysis of the motor supply current or motor load toque signals is used (Tondos 1993; Begg *et al.* 1999; Kucharski 2002; Vedmar and Andersson 2003; Kowalski 2005). Especially, an analysis of the motor load torque looks promising (Hedayati *et al.* 2009).

The simplest method for load torque calculation is to use the mechanical equations:

$$\hat{T}_{S1} = \hat{T}_{\text{em}} - J_M \frac{d\omega_m}{d\tau}, \tag{22.26}$$

where $\hat{T}_{S1}$ is the estimated motor load torque.

The load torque calculation method (22.26) is very simple; however, it is not precise. This results from its sensitivity to any inaccuracy and the simplifications in the mechanical equations. Because of that it is rather not viable tool for diagnostic system.

Instead of simple estimation (22.26), the observer methods seems to be more precise. Some of the load torque observers are presented in the literature, for example, the concept of the observers for systems with unknown and inaccessible inputs or the concept of full order Luenberger-based systems (Brdys and Du 1991). Unfortunately, some of the observers have strongly limited bandwidth or are not applicable to the FOC control algorithm.

In the presented application, different methods for the load torque calculations were previously tested (Guzinski *et al.* 2009a). The best results were obtained with an observer based on the Gopinanth's method (Ohnishi *et al.* 1996) that was previously used in the traction application as part of train wheels slip detection system (Kadowaki *et al.* 2007).

The load torque observer is described as the next:

$$\frac{d}{d\tau}\begin{bmatrix} z_1 \\ z_2 \end{bmatrix} = \begin{bmatrix} 0 & -k_{1L} \\ 1 & -k_{2L} \end{bmatrix}\begin{bmatrix} z_1 \\ z_2 \end{bmatrix} + \begin{bmatrix} k_{1L}k_{2L}J_M & (k_{2L}^2 - k_{1L})J_M \end{bmatrix}\hat{\omega}_m + \begin{bmatrix} k_{1L} \\ k_{2L} \end{bmatrix}\hat{T}_{\text{em}}, \quad (22.27)$$

$$\hat{T}_{S1} = z_2 - k_{2L}J_M\hat{\omega}_m, \quad (22.28)$$

where k_{1L}, k_{2L} are observer gains, z_1, z_2 are internal observer variables, $\hat{T}_{\text{em}}$ are motor torque computed by equation (22.25).

Presented load torque observer (22.27)–(22.28) does not require speed sensor because the motor speed is computed in the speed observer procedure.

22.4 Simulation Investigations

Simulation was realized using Matlab software. An example of the results obtained using speed observer operation are depicted in Figure 22.9. In Figure 22.9, the desired motor torque is used as the commanded value.

For improving simulation time a smaller inertia of the whole train was assumed. Motor speed is changed to the next values referring to train speed $30 \cdots 160 \cdots 210 \cdots 150$ km/h. The error between the measured and estimated speeds is also shown, and it is observed that this error is significantly small and it is less than 2%.

In the next simulation test, the load torque T_L is applied at the start of the drive transmission with simultaneous changes of motor speed. Also in this case, the operation of the proposed observer is correct as illustrated in Figure 22.10.

In Figure 22.10, a comparison of he real motor load torque T_{S1} with the computed one in the observer $\hat{T}_{S1}$ is presented. The results show correct performance except at initial time, in which load observer started computation.

22.5 Experimental Test Bench

In the second step of verification of the speed and load torque observers the experiments were done. The experiments were provided in the HST factory, where the HST test bench were

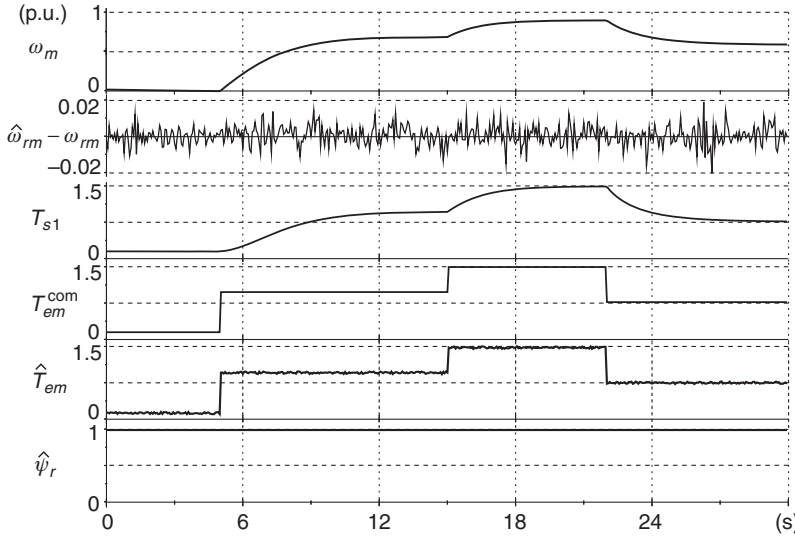

Figure 22.9 Speed observer simulation results

accessible. In the test, bench singular train drive with 1.2 MW is installed. The traction motor, power converter, and control system are the same as in real train. The HST control system is based on digital signal processors (DSP). The differences are in the gear, which has different gear ratio and different gear wheels' teeth number. That gear ratio fits the speed of the load machine. The simplified structure of the test bench is presented in Figure 22.11. On the test bench, series of tests were performed to investigate observer action at different motor speeds and load torque levels in steady states and in transient conditions.

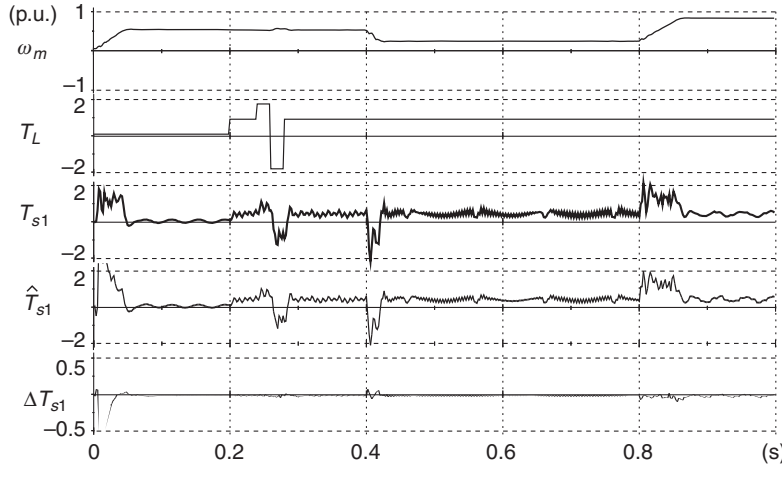

Figure 22.10 Load torque observer simulation results

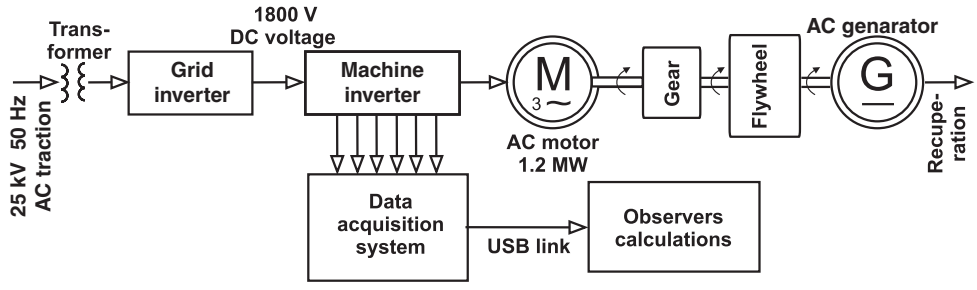

Figure 22.11 Simplified structures of the experimental test bench

The test bench has efficient data acquisition structure. The DSP control board has several programmable analog outputs where some internal control variables are sent. These variables are the measured signals, for example, motor currents or internal DSP variables of the control algorithm. The chosen signals in analog form are sent through wiring system to the general purpose data acquisition board (DAB) connected to PC computer through USB interface. The PC software collects data in graphic waveforms and in binary files, which are used for data processing. The block structure of the data acquisition system is presented in Figure 22.12. Due to limited time access to the test bench, a two-step, procedure was used in the experiments. In the first step a list of desired tests was prepared and next required DSP variables and measurements were collected: input inverter voltage, motor speed, PWM modulation index, angle position of PWM commanded voltage vector, and motor two-phase currents.

The next tests were done: starting of the train and work with constant speed with different load levels and motor speed, breaking of the train with different load levels and work with different constant motor speed for 0%, 25%, 50%, 75%, 100% load, and so on. An example of recorded experimental waveform is presented in Figure 22.13. For the obtained data analysis, the observer calculation were done off-line in PC with the help of the Matlab software. The experimental data were used as inputs for observers *S*-function.

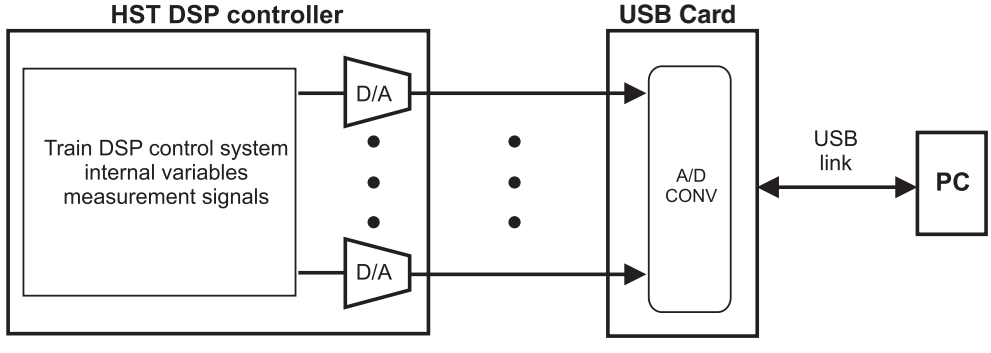

Figure 22.12 Structure of the test bench, data acquisition system

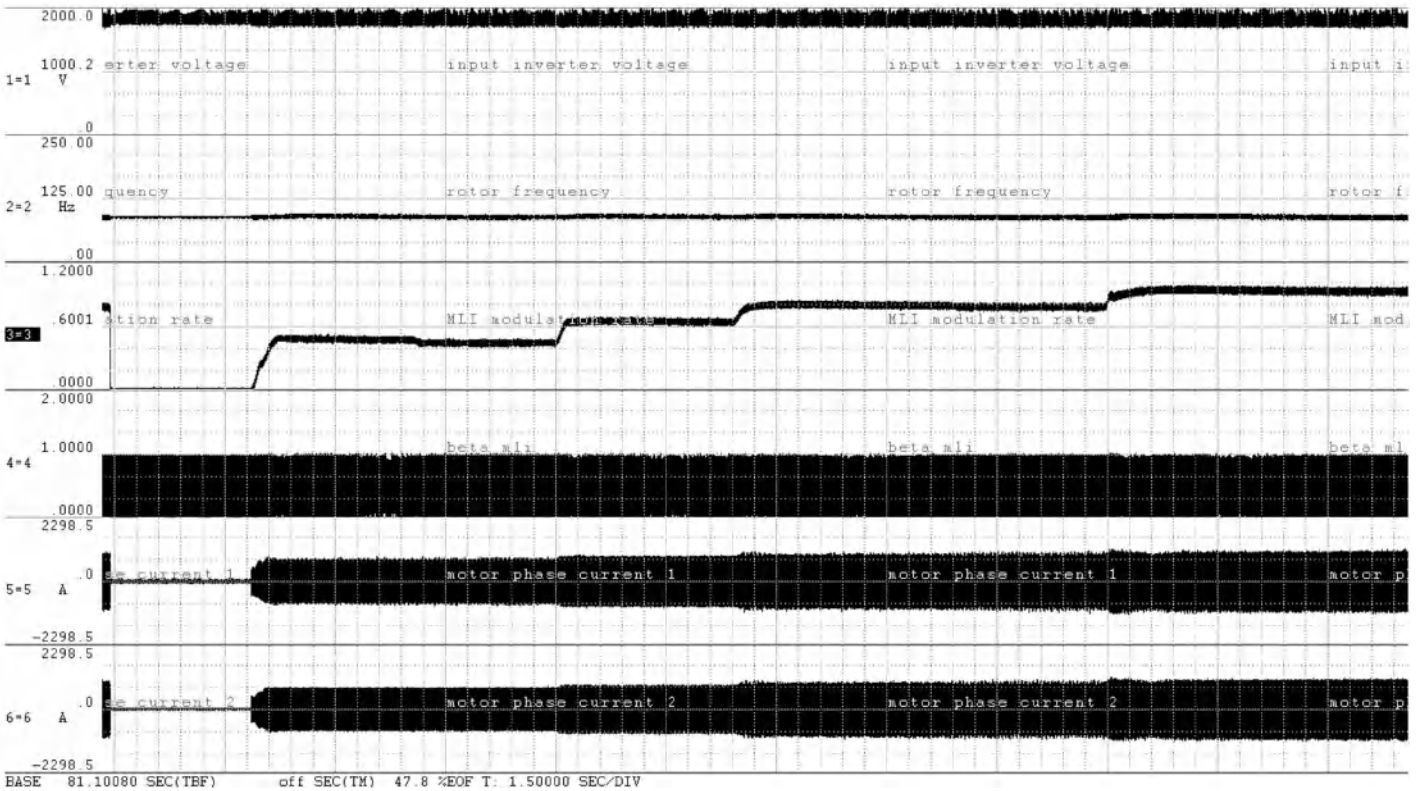

Figure 22.13 Experiment: the example of the recorded waveforms during system with different load levels (1-inverter supply voltage, 2-motor speed, 3-PWM modulation index, 4-motor supply voltage vector position, 5-stator currents)

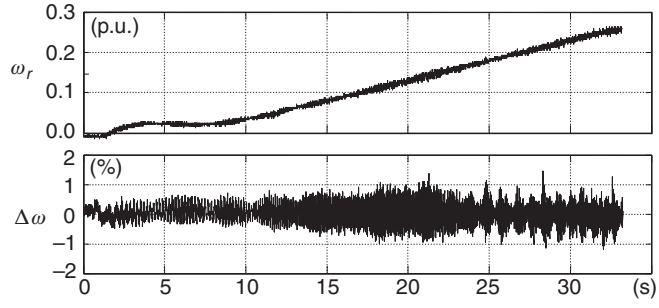

Figure 22.14 Speed observer experimental results—the train start to 50 km/h

22.6 Experimental Investigations

The examples of the experimental speed observer calculations are illustrated in Figures 22.14 and 22.15. In the test of Figure 22.14, speed observer error is low and does not exceed 1.5%. In Figure 22.15, an increase in computation error with train speed is noticed. At speed 320 km/h (the train full speed), this error reached 5%. This error is caused by a distortion in motor stator current. With an increase in motor speed, inverter switching frequency was decreased from 450 Hz until an operation without PWM for full train speed. The changes in PWM are done to fully utilize the inverter dc supply voltage in the motor high-speed range. The distortion of the motor current in the high-speed range are presented in Figure 22.16.

The proposed load torque observer is supposed to be used for fault detection in the torque transmission system. Comparable experimental investigation should be realized for correctly working torque transmission system and for faulty system for different fault types. However, because of limited access to faulty real system and because of high cost of faulty transmission system, experimental investigations were up to now limited to the existing in the HST factory

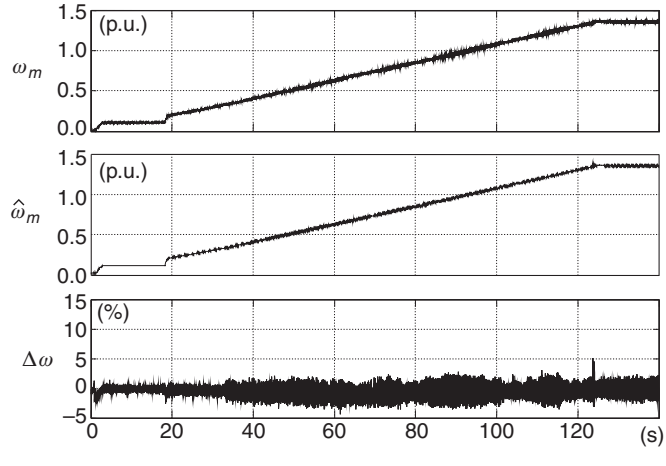

Figure 22.15 Experimental results—the train start up to 320 km/h

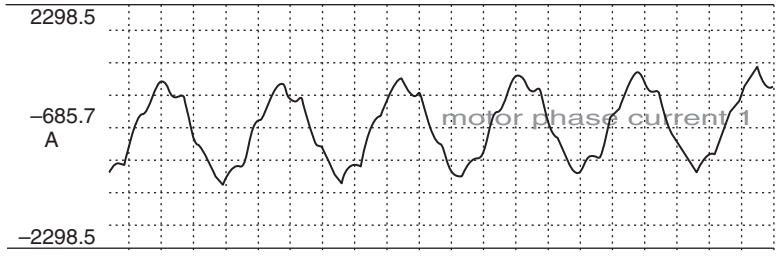

Figure 22.16 Motor supply phase current at motor speed related to train speed of 320 km/h

healthy system only. The realized tests of the torque observer for the healthy system aims to know if the suggested observer is able to develop the same motor shaft torque as the one measured using installed torque sensor.

The realized tests have shown torque observer's acceptable precision. In the test bench, it was possible to identify meshing frequency of transmission driving wheel. The vibration amplitudes that result from such frequency were out of measurement bandwidth of the existing instrumentation system of the torque sensor. Nevertheless, the proposed observer identifies these signals correctly.

The examples of the experimental results of the load torque observer are presented in Figures 22.17 and 22.18. In Figures 22.17 and 22.18 tests, the motor operates at constant

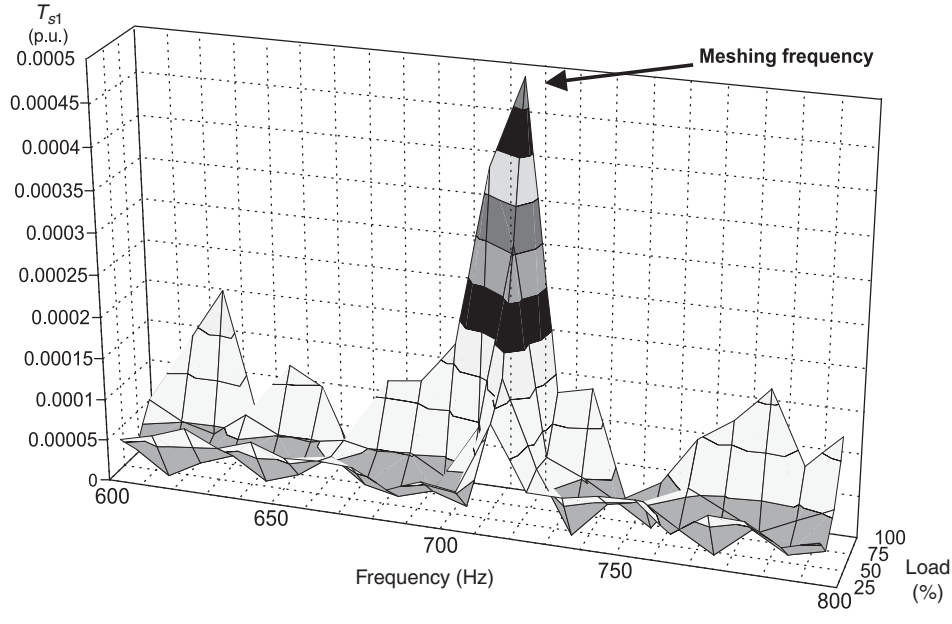

Figure 22.17 Identification of the gear meshing frequency for motor speed related to 50 km/h train velocity. (For a color version of this figure, please see color plates.)

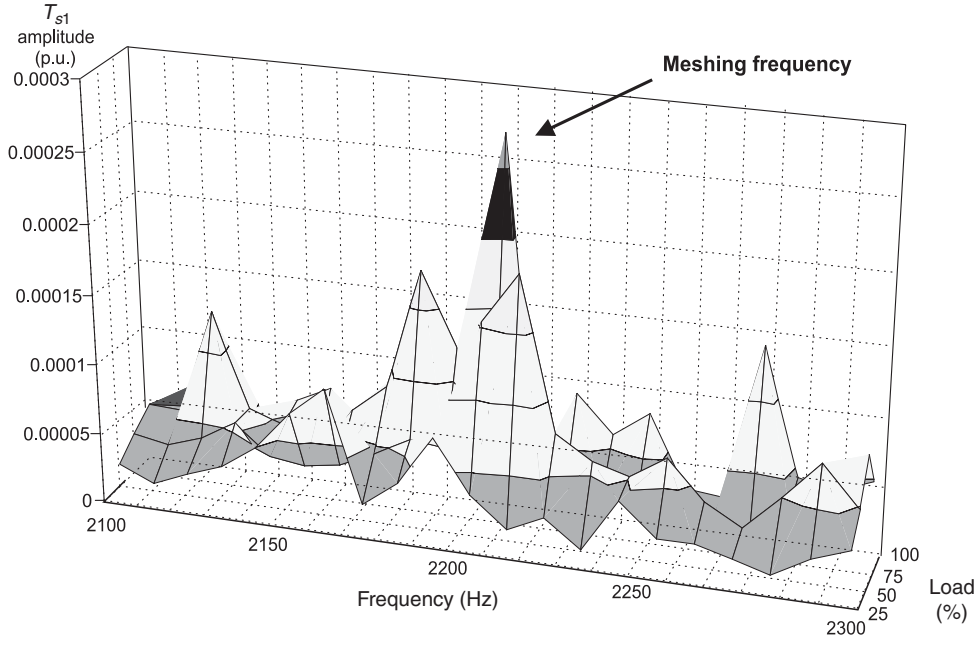

Figure 22.18 Identification of the gear meshing frequency for motor speed related to ca. 150 km/h train velocity. (For a color version of this figure, please see color plates.)

speeds—related to next train speeds: 50 km/h and 150 km/h. For each speed, the load was changed to the levels 25%, 50%, 75%, 100%. Fast Fourier transform (FFT) harmonic analysis was then realized for the load torque and next the amplitudes levels related to meshing frequencies were plotted. According to the transmission theory, an increase of amplitudes with load increment is noticed (Muller 1979).

Higher precision of computation was observed for lower speed 50km/h which is, similarly to the case of speed observer, caused by distorting current waveform with decreasing inverter transistors switching frequency at higher speeds.

Above 150 km/h torque observer was not able to identify meshing frequency, which makes it possible to assume that its practical use could be limited for speed range up to 150 km/h. Nevertheless, torque observer is applicable for diagnosis purposes, because it is not required that it works all the time but, for example, at lower speeds only. This is supposed to ensure a detection of transmission system faults. Assembly defects of transmission system are characterized by violent failures, which could be detected during initial test for train travels at lower speeds.

22.7 Diagnosis System Principles

Diagnosis system is currently intended to evaluate diagnostic criterion. It is assumed that a diagnostic system will not utilize any additional sensor except the sensors that are currently used in existing HST. The main parts of our diagnostic system are speed and load torque

observers. For condition detection of speed sensor and drive transmission system, specific values computation is going to be realized and analyzed according to the defined criterions. This aims for proper fault detection appearing and to the prediction of future faults before their occurring.

22.7.1 Diagnosis of Speed Sensor

The base speed sensor diagnosis depends on real-time inspection of the next diagnostic criterion:

$$|\hat{\omega}_m - \omega_m| > E_{mlimit} \tag{22.29}$$

where E_{mlimit} is the error limit between the measured and the computed speed.

On the base of the simulation and experimental tests, it was assumed that this error level E_{mlimit} is limited to 3%. This value was selected to be higher than the maximum observed speed observer computational error, a 2% value.

If the diagnostic system identifies crossing of this limit level, then the system should give an appropriate fault alarm and then HST control system could be switched to sensorless mode of operation (Figure 22.19). In Figure 22.19, the speed sensor fault appeared at instant 5 s. At this instant, the measured speed was equated to zero. The control system detected fault and a diagnostic indicator d_{ω_m} has been changed from 0 to 1. This was done immediately—in one step of the control calculation algorithm. Simultaneously, the whole system was switched to the speed sensorless operation mode without any noticeable disturbances. After fault detection, the commanded motor torque was changed and the system has reacted correctly.

The other fault of the speed sensor is also possible—in the speed scanning buffer the last proper value of the measured speed could be memorized. If this happens during a steady state, the diagnostic system does not react immediately. In such case, the whole system still works

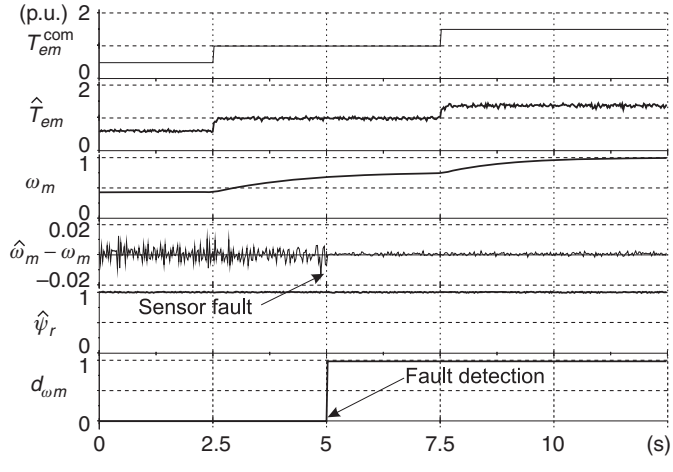

Figure 22.19 Speed sensor fault identification and switch to speed sensorless control

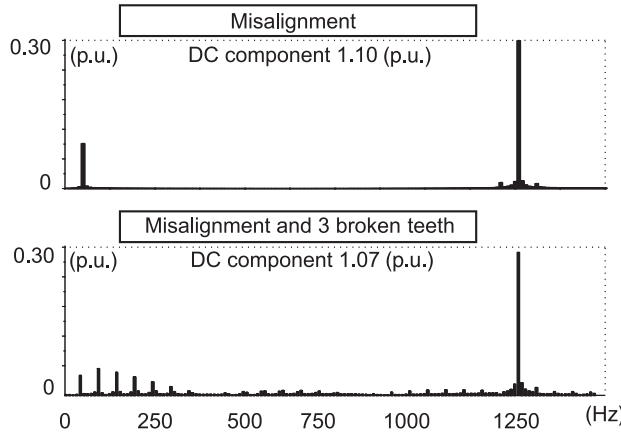

Figure 22.20 Load torque harmonics analysis

properly until the moment when the torque commanded signal is set or when the system starts losing its operating point. In that case, after the time when the diagnostic indicator reaches a 3% level, the fault is also identified with some delay.

It is assumed that to differentiate between the sensor failure and motor failure a different motor stator and rotor diagnostic system has to be used. The HST motor failure is going to be monitored by separate algorithm based on analysis of the control signals in the closed loop (Cruz and Cardoso 2006).

22.7.2 Diagnosis of Traction Torque Transmission

Vibrations of the torque transmission unit are caused by, for example nonexact meshing in the gear, eccentricity of toothed wheel, and variable teeth stiffness (Guzinski *et al.* 2009c). Such vibration causes a creation of harmonics with frequencies of torque transmission elements rotation and of meshing frequencies.

Diagnostic system of torque transmission system uses harmonic analysis of the computed load torque (Figure 22.20). The proposed structure of the transmission diagnostic system is shown in Figure 22.21.

This structure presented in Figure 22.21 is divided into two parts: "online" and "off-line." An "online" part is used for detection of serious faults, which are characterized by violent increase in the selected harmonics. An "off-line" subsystem is used to predict slowly increasing faults.

For an analysis of computed load torque, initially a classic power spectral concentration is used. More advanced signal spectrum computation or wavelet analysis could be also employed in future development.

22.8 Summary and Perspectives

The provided simulation and experimental investigations have proved an applicability of presented observers for diagnostic purposes. Because of that the proposed diagnostic solution is currently under implementation in a real railway system of HST.

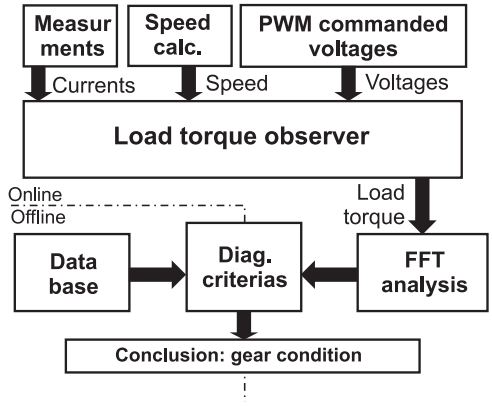

Figure 22.21 Conception of the transmission diagnostic system

According to the requirements of the train manufacturer, in the first step of the practical implementation a specialized additional microprocessor DSP system will be installed in the trains. The designed DSP system will first operate in an open-loop mode to collect speed and load torque values calculated online by observer systems. The collected information is to be used for the further analysis, simultaneously with the information obtained from the HST maintenance center. On the basis of that data, the diagnostic criteria will be elaborated and verified. A DSP system will communicate with the existing HST control system through communication interface using an industrial network link. By this way, DSP system will obtain the essential information needed to analyze the measured values and command values for the control system.

Regularly, all data about the condition of transmission system are registered by train operator. Thus, in this way it is possible to prepare essential data base of the system faults. With verified diagnostic criteria, the additional DSP diagnostic system will be included into HST control system and will work in closed loop mode.

The presented diagnostic system concept is general in nature and is not limited to only HST induction motor drives. The implementation to other traction systems is also possible. Nowadays diagnostic systems are also under implementation for tramway vehicles and also for the newest traction drives with permanent magnet synchronous motors.

References

Begg CD, Merdes T, Byington C, and Maynard K (1999) Dynamics modeling for mechanical fault diagnostics and prognostics. *Mechanical System Modeling for Failure Diagnosis and Prognosis, Maintenance and Reliability Conference (MARCON'99)* Gatlinburg, Tennessee, USA, pp. 1–13.

Blaschke F (1971) Das Prinzip der feldorientierung, die grundlage fur transvector-regelung von drehfeld-maschine. *Siemens Zeitschrift*, **45**, 757–760.

Bogalecka E and Kolodziejek P (2008) Frequency characteristics of induction machine speed observers. *XX Symposium Electromagnetic Phenomena in Nonlinear Circuits (EPNC 2008)*, Lille, France, pp. 125–126.

Brdys M. A and Du T (1991) Algorithms for joint state and parameter estimation in induction motor drive systems. *Proceedings of IEE International Conference on Control (Control'91)*, Edinburgh, UK, vol. II, pp. 915–920.

Burton B, Kamran F, Harley RG, *et al*. (1997) Identification and control of induction motor stator currents using fast on-line random training of a neural network. *Transaction on Industry Applications*, **33**, 697–704.

Cruz SMA and Cardoso AJM (2006) Diagnosis of rotor faults in closed-loop induction motor drives. *Proceedings of IEEE/ IAS Annual Meeting, Conference*, Tampa, Florida, USA, pp. 2346–2353.

Depenbrock M and Evers C (2006) Model-based speed identification for induction machines in the whole operating range. *Transaction on Industrial Electronics*, **53**, 31–40.

Guzinski J, Diguet M, Krzeminski Z, *et al*. (2008) Application of speed and load torque observers in high speed train. *13th International Power Electronics and Motion Control Conference (EPE-PEMC 2008)*, Poznań, Poland, pp. 1405–1412.

Guzinski J, Diguet M, Krzeminski Z, *et al*. (2009a) Application of speed and load torque observers in high speed train drive for diagnostic purposes. *IEEE Transaction on Industrial Electronics*, **56**, 248–256.

Guzinski J, Krzeminski Z, and Lewicki A (2009b) Diagnostics of traction motor torque transmission system by the use of state observers. *9th International Scientific Conference Modern Electric Traction (MET'2009)*, Gdańsk – Krynica Morska, Poland, pp. 19–24.

Guzinski J, Krzeminski Z, Lewicki A, and Abu-Rub H (2009c) *State observers for diagnostic applications in modern electric traction*. Chapter 7 in monograph *Modern Electric Traction—Vehicles*. Gdansk University of Technology, Faculty of Electrical and Control Engineering, Gdansk.

Hedayati Kia Sh, Henao H, and Capolino GA (2009) Torsional vibration assessment in railway traction system mechanical transmission, in *7th IEEE International Symposium on Diagnostics for Electric Machines, Power Electronics and Drives (SDEMPED 2009)*, Cargese, France, pp. 1-8.

Holtz J (2006) Sensorless control of induction machines—with or without signal injection. *IEEE Transaction on Industrial Electronics*, **53**, 7–30.

Jung JH, Lee JJ, and Kwon BH (2006) Online Diagnosis of induction motors using MCSA. *Transaction on Industrial Electronics*, **53**, 1842–1852.

Kia SH, Henao H, and Capolino GA (2007) A high-resolution frequency estimation method for three-phase induction machine fault detection. *Transacton on Industrial Electronics*, **54**, 2295–2304.

Kadowaki S, Ohishi K, Hata T, *et al*. (2007) Antislip readhesion control based on speed-sensorless vector control and disturbance observer for electric commuter train—series 205-5000 of the East Japan Railway Company. *IEEE Transactions on Industrial Electronics*, **24**, 2001–2007.

Kowalski CT (2005) Monitoring and diagnostic of the induction motor faults using neural networks (in polish—Monitorowanie i diagnostyka uszkodzen silników indukcyjnych z wykorzystaniem sieci neuronowych). Wroclaw University of Technology Publishing House, Wroclaw, Poland.

Krzeminski Z (2000) Sensorless control of the induction motor based on new observer. *International Conference on Power Electronics, Intelligent Motions and Power Quality (PCIM 2000)*, Nuremberg, Germany.

Krzeminski Z (2001) Digital control of the asynchronous machines (in polish—Cyfrowe sterowania maszynami asynchronicznymi). Gdansk University of Technology Publishing House, Gdansk, Poland.

Krzeminski Z (2008) Observer of induction motor speed based on exact disturbance model, in *International Conference (EPE-PEMC 2008)*, Poznan, Poland, pp. 2294–2299.

Kucharski T (2002) Mechanical vibration measuring system (in polish—System pomiaru drgan mechanicznych). Scientific-Technical Publishing House, Warsaw, Poland.

Luenberger DG (1971) An introduction to observers. *IEEE Transactions on Automatic Control*, **AC-16**, 596–602.

Madej J (2000) Traction torque transmission mechanics (in polish—Teoria ruchu pojazdow szynowych). Warsaw University of Technology Publishing House, Warsaw, Poland.

Magureanu R, Ilas C, Bostan V, Cuibus M, and Radut V (2000) Luenberger, Kalman, neural observers and fuzzy controllers for speed induction motor control. in *Buletinul Institutului Politehnica, University of Bucharest, Romania*, vol. XLVI (L), pp. 191–198.

Muller L (1979) Toothed gears—design (in polish—Przekładnie zebate projektowanie). Scientific-Technical Publishing House, Warsaw, Poland.

Ohnishi K, Shibata M, and Murakami T (1996) Motion control for advanced mechatronics. *IEEE/ASME Transactions on Mechatronics*, **1**, 56–67.

Orlowska-Kowalska T (2003) Sensorleess drives with induction motors, sensorless control of the induction motor based on new observer. (in polish—Bezczujnikowe ukÁady napedowe z silnikami indukcyjnymi), Wroclaw University of Technology Publishing House, Wroclaw, Poland.

Orlowska-Kowalska T and Szabat K (2007) Neural-network application for mechanical variables estimation of a two-mass drive system. *Transaction on Industrial Electronics*, **54**, 1352–1364.

Pajchrowski T and Urbanski K (2001) DSP application to robust speed control of PMSM by means of artificial neural network (in Polish—Zastosowanie DSP do odpornej regulacji predkosci SSMT z wykorzystaniem sztucznych sieci neuronowych). *Proceedings of Scientific Conference (SENE'2001) Lodz-Arturowek, Poland*, vol. II, pp. 647–652.

Rajashekara K, Kawamura A, and Matsuse K (1996) Sensorless control of ac motor drives. *IEEE Industrial Electronics Society*. IEEE Press.

Tondos MS (1993) Minimizing electromechanical oscillations in the drives with resilient couplings by means of state and disturbance observers. *European Power Electronics Conference (EPE1993)*, Brighton, United Kingdom, pp. 360–365.

Vedmar L and Andersson A (2003) A method to determine dynamic loads on spur gear teeth and on bearings. *Journal of Sound and Vibration*, **267**, 1065–1084.

Wilk (2009) Winding internal faults diagnosis of the traction transformer based on analysis of energy dissipated per period. *9th International Scientific Conference Modern Electric Traction (MET'2009)*, Gdansk—Krynica Morska, Poland, pp. 72–78.

Zawirski K and Urbanski K (2000) Rotor speed and position detection for PMSM Control System. *9th International Conference on Power Electronics and Motion Control (EPE-PEMC 2000)*, Koszyce, Slovakia, vol. VI, pp. 239–243.

23

AC Motor Control Applications in High-Power Industrial Drives

Ajit K. Chattopadhyay
Electrical Engineering Department, Bengal Engineering & Science University, India

23.1 Introduction

The power ratings of large medium voltage (2.2–13.8 kV) industrial drives range between few hundred kilowatts to a few tens of megawatts and even 100 MW. The upper limit is decided by the requirements of the applications rather than by the technology of the converters and machines (Stemmler 1994). The available speed range lies from 10 rpm for low-speed machines (e.g. Cement mills), 1500/3000 rpm for normal-speed drives to even 18 000 rpm for very high power high speed drives (e.g., compressors). The limits for the dc motors such as cost, size, commutator problems and inability to operate satisfactorily in a dirty and explosive environment have called for ac motor drives for high power applications. Major technical breakthroughs have occurred both in the power conversion and in control areas of variable voltage variable frequency (VVVF) ac drives to meet the exacting requirements of ac drives using direct ac/ac cycloconverters or ac/dc/ac link inverters that feed either induction motors (IM) or synchronous motors (SM). The machine may be excited by a voltage source inverter (VSI) or a current source inverter (CSI). Synchronous motor drives have the advantages over the induction motor drives in that, with separate field excitation, these can be operated at any power factor-leading, lagging and unity. The operation near unity power factor reduces armature copper loss and permits inverter size reduction with simplicity of commutation (load commutation) with thyristors as switches. Further, a synchronous motor runs at a precisely set speed independent of load and voltage fluctuations unlike an induction motor.

The recent trends in high-power ac drives are to use pulse width modulated (PWM) VSI or CSI with self-commutated devices like insulated gate bipolar transistors (IGBTs), gate turn

AC Electric Motors Control: Advanced Design Techniques and Applications, First Edition. Edited by Fouad Giri.

off thyristors (GTOs), integrated gate commutated thyristors (IGCTs) and injection enhanced gate transistors (IEGTs) for efficient VVVF control with harmonic reduction. The development of new high-power semiconductors such as 3.3/4.5 kV, 1.7/1.2 kA IGBTs, 6 kV, 6 kA IGCTs and 4.5 kV, 5.5 kA IEGTs capable of snubberless operation and the introduction of three level topologies in contrast to earlier two level ones have led to an increased application of PWM controlled Voltage Source Converters (VSC) ranging from 0.5 MVA to about 30 MVA (Chattopadhyay 2010). CSI-fed drives with simplified regeneration control and microcomputer-controlled drives implementing evolutionary concepts like *field orientation* or *vector control (VC)*, with either inverter or cycloconverter-fed induction or SM by which dc machine-like performance can be obtained and *direct torque control* (DTC) are now finding increasing acceptance in *high-performance* industrial ac drives for applications such as steel mills, ore-grinding mills, cement kilns, ship drives, mine winders, and electric traction (Chattopadhyay 1997a). The converters for such drives meeting the *high performance* requirements must:

- generate smoothly variable frequency and voltage;
- produce nearly sinusoidal current waveforms throughout the operating range to avoid undesirable torque oscillations;
- permit highly dynamic control both in forward and reverse motoring and braking applications;
- provide as nearly as possible or even better performance than that of the dual converter-fed dc drives as regards cost, service reliability and harmonic effects on the system.

Besides the application of field-oriented control (FOC) in PWM inverter-fed motor drives with various PWM schemes like carrier-based, hysteresis-band control and space vector modulation (SVM), the recent application of DTC to ac drives (Chattopadhyay 2010) has been claimed to achieve the highest torque and speed performance ever achieved with variable speed drives, making it possible to control the full torque within a few milliseconds, reducing the impacts of load shocks.

Thus, rapid and remarkable progress has been made over the years in the ac drive technology used in the high-power drives and their control. Figure 23.1 shows a block diagram of a typical high power ac drive system for a mill with its various components. The technology is vast and the objective of this chapter is to present a brief but comprehensive state-of-the-art overview of the development of each of the components such as high-power semiconductor devices, converter topologies, motors used and the control strategies employed together with their various application examples in the industry. The brief features of the industrial ac drives developed by the leading manufacturers worldwide are also provided as well as new developments and possible future trends.

23.2 High-Power Semiconductor Devices

Rapid advances in industrial ac drives and power conversion systems have been possible due to continuous and astonishing development of the rating and performance of the power semiconductor devices over the last 50 years. Two major types of high-power semiconductor devices are used in high power converters in the industry: the thyristor-based (*current switched*)

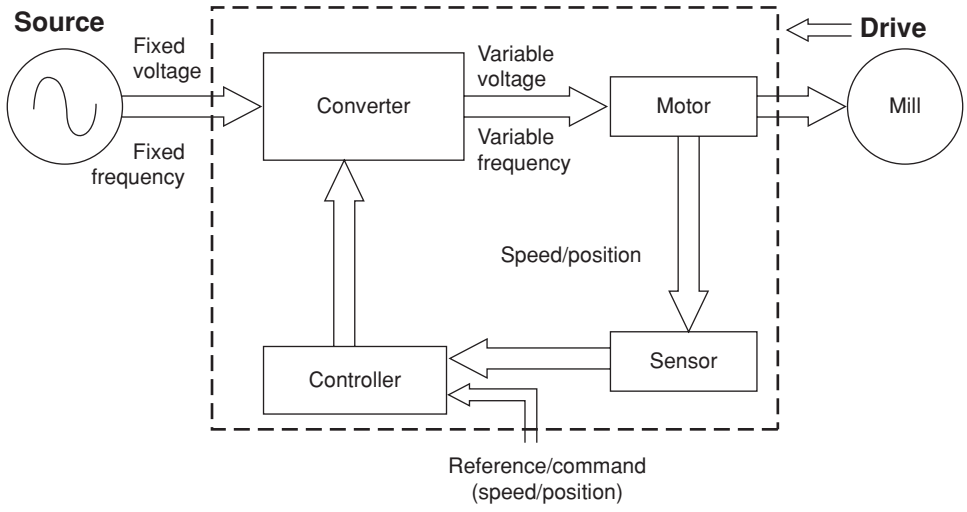

Figure 23.1 Block diagram of a typical drive system. Reprinted with permission from IEEE (Chattopadhyay 2010)

devices that include SCR (silicon-controlled rectifier), GTO, IGCT (or GCT), and the transistor based (*voltage switched*) devices that comprise IGBT and IEGT. The voltage and current ratings of these devices as commercially available today for high power converters are shown in Figure 23.2 (Wu 2006). Some typical high-power devices are shown in Figures 23.3 and 23.4 (Sato and Yamamoto 2001; Ichikawa *et al.* 2004).

23.2.1 High-Power SCR

Figure 23.3a shows a 12 kV /1.5 kA SCR that is a high-power press-pack thyristor-based device with three terminals: gate, anode, and cathode. Its turn-on process is initiated by applying a pulse of positive gate current and it turns off when anode current becomes negative. The turn-on time is 14 μs and turn-off time is 1200 μs. The on-state voltage drop is about 4 V. This device blocks voltage in both forward and reverse directions. Originally, developed and marketed by GE, USA in 1958, it is the highest rated power device so far (specially with the light-triggered ones) for use with cycloconverter—and load-commutated inverter (LCI) fed motor drives besides High Voltage DC (HVDC) systems and Static VAR Compensators (SVC).

23.2.2 High-Power GTO

The GTO is a self-commutated thyristor-based device that can be turned off by a negative gate current. Figure 23.3b shows a 6 kV, 6 kA press-pack GTO (high-power GTOs being developed by Japanese since 1980s), which is turned on by a pulse of positive gate current and turned off by a negative gate current pulse. However, the turn-off current gain is typically 4–5 which means that a GTO with a 6000 A anode current rating may require −1500 A gate current pulse

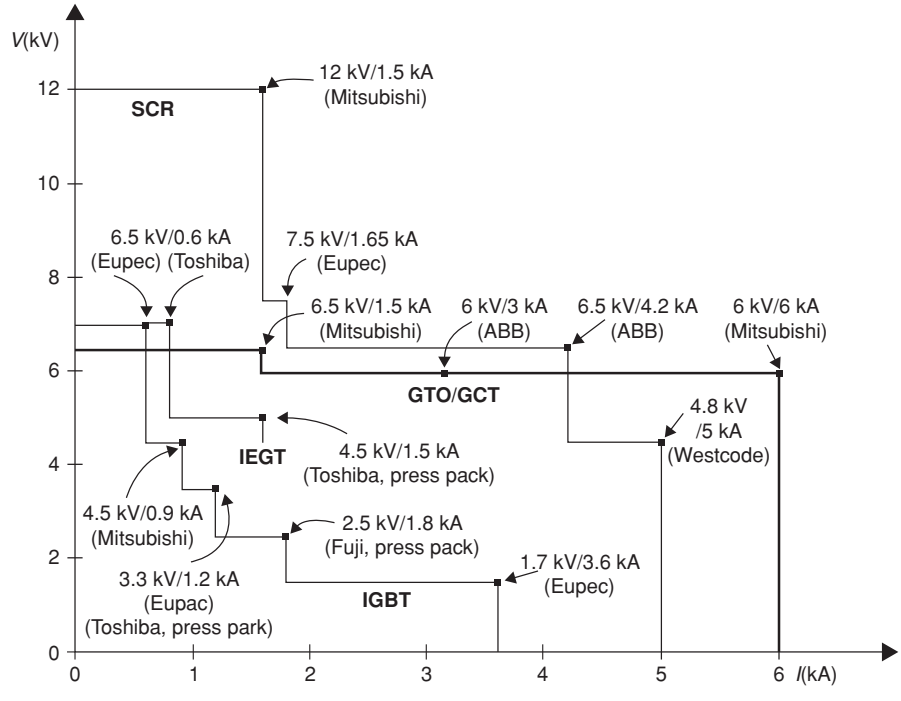

Figure 23.2 Voltage and current ratings of high-power semiconductor devices. Reprinted with permission from IEEE (Chattopadhyay 2010)

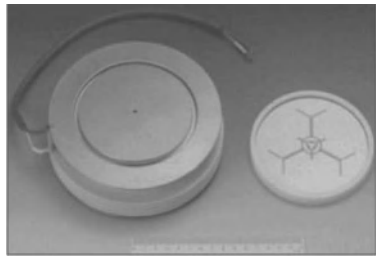

(a) 12-kV, 1.5-kA SCR

(b) 6-kV, 6-kA GTO

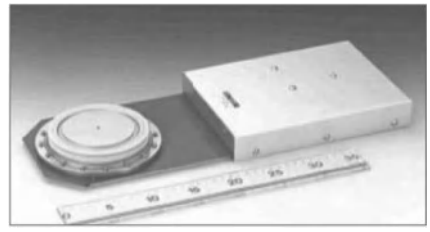

(c) 6-kV, 6-kA IGCT/GCT

Figure 23.3 Thyristor-based (current switched) high-power semiconductor devices. Reprinted with permission from IEEE (Chattopadhyay 2010)

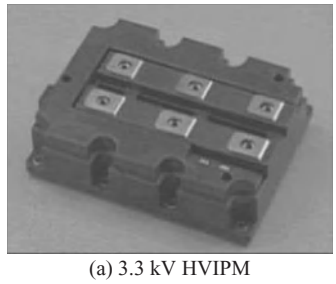

(a) 3.3 kV HVIPM

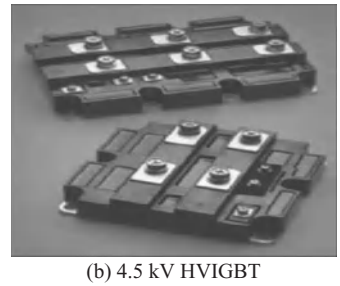

(b) 4.5 kV HVIGBT

(c) IEGT with gate driver

Figure 23.4 Transistor-based (voltage-switched) high-power semiconductor devices. Reprinted with permission from IEEE (Chattopadhyay 2010)

to turn off. GTOs need bulky and expensive turn-off snubbers and complex gate driver. The typical turn on time is 2.5 μs and turn-off time is 25 μs. The on-state voltage drop is typically 4.4 V. The GTO switching frequency is lower than that of IGBTs and IGCTs (to be described later). So, the GTO converters operating in PWM (high-frequency) mode use energy recovery snubbers consisting of a capacitor, a diode and a resistor across each device in addition to a turn-on snubber consisting of an anode inductor in series with each device to reduce di/dt of the anode current. The GTO can be fabricated with asymmetrical structures suitable for VSIs or symmetrical structures suitable for CSIs.

23.2.3 IGCT/GCT

IGCT (also known as GCT) is a hard-driven GTO (developed by ABB in 1996) with unity current gain that means that a 6000 A (anode current) device is turned off by a -6000 A gate current (Sato and Yamamoto 2001). However, the current pulse should be very narrow with low energy for fast turn off. Figure 23.3c shows an ABB press-pack type 6.5 kV, 6 kA IGCT with a built-in integrated gate drive circuit (consisting of several MOSFETs in parallel) on the same module. The IGCTs have replaced the GTOs for the medium-voltage drives over the past few years due to their special features like snubberless operation and low switching loss. The snubberless operation is possible because of extremely low gate inductance (typically < 3 nH compared to < 30 nH for GTOs) by special construction. The rate of the gate current change at turn-off is normally greater than 3000 A/μs compared to around 40 A/μs for GTO. The turn-on and turn-off times are much faster than those of the GTO. Though the IGCT does not

require a turn-off snubber, it requires a simple turn-on snubber or a clamping circuit since the di/dt capability of the device at turn-on is around 1000 A/μs only. The on-state voltage of IGCT at 6000 A is only 4 V compared to 4.4 V for a GTO at 4000 A. As the storage time of IGCT is reduced to 1/10th compared to GTO, a high switching speed is obtained. IGCTs have a higher switching frequency (typically 1.0 kHz) than GTOs (typically 0.5 kHz). Besides the asymmetrical IGCT (suitable for VSI as shown in the Figure 23.3c, marketed by ABB), symmetrical SGCTs (suitable for CSI) are available from Mitsubishi for smaller ratings. IGCTs are simple to use, easily available and have demonstrated their reliability in many applications that include rolling mill drives (e.g., ACS 6000 by ABB and SIMOVERT-ML2 by Siemens).

23.2.4 IGBT

After completely dominating the low-voltage converters, IGBTs are increasingly used for medium-voltage converters. It is a voltage controlled hybrid device (developed by Baliga of GE in 1983) combining the advantages of MOSFET's high-gate circuit resistance and BJT's small collector-emitter drop at saturated condition. The ratings of these devices have reached as high as 6.5 kV/0.6 kA or 3.3 kV or 4.5 kV/1.2 kA. It can be turned on with a 15 V gate voltage and turned off when the gate voltage *is* zero or negative. The majority of high-power IGBTs are of modular design as shown in Figure 23.4a and b. It can be turned on within 1 μs and turned off within 2 μs. The main advantages of IGBT are simple gate driver, snubberless operation, high-switching speed, modular design, and controllability of switching behavior providing reliable short-circuit protection. Presspack devices are also available which are suitable for series operation. The device has only forward blocking capability and can be used in a VSI with a feedback diode. However, very recently, reverse-blocking IGBTs are also available. High-voltage IGBTs have a higher voltage drop (e.g., 4.3 V for a 3.3 kV/1.2 kA device) during conduction compared to thyristors or GTOs. IGBT devices can be available in intelligent power module (IPM or HVIPM in Figure 23.4a) form with gate drivers and built-in protection features to provide lower size and cost, improved reliability and fewer EMI problems.

23.2.5 IEGT

IEGT is basically an advanced high-voltage high-power IGBT with special gate construction commercially developed by Toshiba in 1999 (Ichikawa *et al.* 2004). It is designed in such a way that large numbers of electrons accumulate at its electrodes and it exhibits low on-state voltage (compared to IGBTs and GTOs of the same rating). Figure 23.4c shows a 4.5 kV/2.1 kA (turn-off current 5.5 kA) IEGT and its gate driver that is less than 1/200 in gate power compared with that of GTO/IGCT and more reliable. It can be turned on by the gate voltage of $+15$ V and turned off by that of -15 V. The transistor-based IEGT has the potential to achieve higher output frequencies than the IGCT/GCT. Another advantage over the IGCT is the power required to turn the device on and off. Figure 23.5 (Tessendorf and Hosoda 2004) shows the comparison of typical gate trigger pulses required for equivalent power devices. As a transistor-based device, the gating power of IEGT is low and approximately equal for both turn-on and turn-off. The on-state voltage drop across this device is of the order of 3.0 V (much less than that of IGBT or GTO of similar rating). In the IEGT-based system, neither turn-on nor turn-off snubber is required for each IEGT as in the case of GTO. However, each IEGT

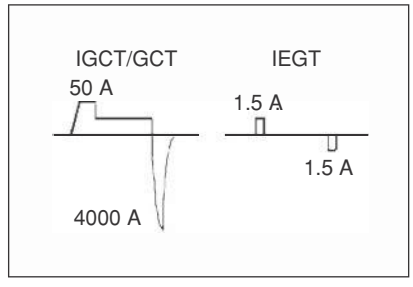

Figure 23.5 Typical gate trigger pulses for IGCT/GCT and IEGT. Reprinted with permission from IEEE (Chattopadhyay 2010)

leg needs simple and efficient clamp circuits to eliminate the snubbers. As discussed later, Toshiba has supplied 8 MVA IEGT-based three-level inverter systems for rolling mill drives in 2000 with an efficiency of 98.5%, which is 2% more than that of an equivalent GTO-based system thus saving a lot of energy.

23.3 High-Power Converters for AC Drives and Control Methods

Figure 23.6 shows a classification of converters as used for the high-power drive applications. The *direct* topology connects the load directly to the source through power semiconductors and a suitable control logic, while the *indirect* topology transfers the power in two stages, rectification and inversion. For direct connection, the cycloconverter is the most used topology

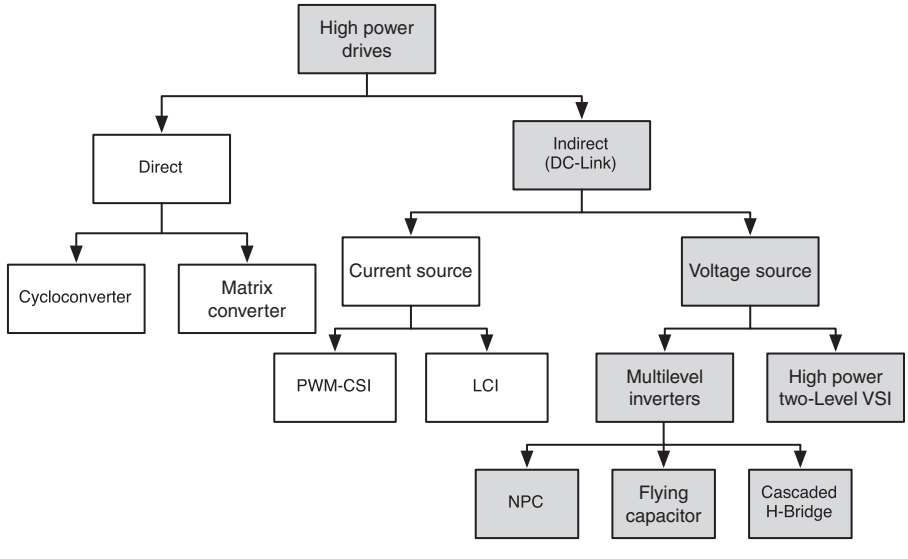

Figure 23.6 Classification of converters for high-power drives

in high-power applications that uses an array of naturally commutated power semiconductor devices such as thyristors, to connect directly the power supply to the machine, converting a three-phase ac voltage with fixed magnitude and frequency to a three-phase ac voltage with variable magnitude and variable frequency (VVVF). Matrix converters (MC), belonging to this category using self-commutated bilateral devices have a limited application. Only very recently they have been used for medium-voltage, high-power drives with multilevel operation (Yamamoto *et al.* 2011). Indirect dc-link inverters may be current source (CSI) or voltage source (VSI) type depending on the dc-link energy-storage component which can be a capacitor that provides a stiff dc voltage in voltage source drives or an inductor that smoothes the dc current in current source drives. While the CSIs for high-power applications may be either PWM-CSI or LCI, the VSIs may be two-level PWM with switches in series or multi-level PWM. Inverter originally developed as the neutral-point clamped (NPC) three-level inverter in 1981 (Nabae *et al.* 1981). Other topologies of the multilevel inverters that have been commercialised are flying capacitor (Rodriguez *et al.* 2007) and cascaded H-Bridge (Rodriguez *et al.* 2007) for medium-voltage drives up to about 40 MVA.

23.3.1 Pulse Width Modulation for Converters

Pulse width modulation techniques to control the voltage output and improve the waveform of the converters may be carrier-based sinusoidal pulse width modulation (SPWM), PWM with selected harmonic elimination, hysteresis band current control PWM and SVM. These modulation techniques have become mature technology and implemented in power converters for high-performance drives as commercial products (Rodriguez *et al.* 2007). Out of these schemes, SVM is an advanced digital modulation technique preferred over the SPWM technique as it provides better utilisation of the dc bus voltage and lower harmonics. This method deals with the interactions among all the phases in contrast to the case of SPWM, where each phase is treated independently. The concept of rotating space vectors are involved here and it needs a microcomputer or digital signal processor (DSP) (Bose 2002) for its implementation.

23.3.2 Control Methods of High-Power Converter-Fed Drives

Converter-fed AC drives with, either induction or SM, are controlled with control of frequency and voltage (or current). To obtain high performance, closed loop control is preferred, while the open-loop control is popular for pump, fan- and compressor-type drives, because this control is simple and does not involve any complex feedback signal measurement or estimation as needed for closed loop control. In general, the control methods for converter-fed drives may be classified as scalar (volts/hertz or V/f) control, VC or FOC and DTC. DTC is an advanced scalar control with performance comparable with the VC method. The VC inherently provides high performance and permits to control the ac machine like a dc machine and most of the advanced control techniques like adaptive control, optimal control, intelligent control (with AI techniques) and fault-tolerant control can be applied to ac drives with the VC (Bose 2011a). Scalar control, unlike VC, means control of the magnitude of a variable, whereas in the latter, both magnitude as well as phase of the space vector variables are controlled.

23.4 Control of Induction Motor Drives

23.4.1 Induction Motor Drives with Scalar or Volts/Hz Control

The simplest type of scalar control is open-loop Volts/Hz (V/f) control with low performance compared to closed-loop VC. Machines are normally operated at rated flux so that the developed torque/Amp of stator current is high and transient response is fast.

PWM Two-Level VSI Induction Motor Drive

The well-known two-level VSI as shown in Figure 23.7a with a line side PWM rectifier using either IGBTs or GTOs feeding a well-regulated dc voltage with little ripple and at a high-power factor to a load side PWM inverter also using IGBTs or GTOs is applied for medium- and high-power industrial drives. To increase the converter voltage, a series connection of these switches is applied. The capacitor used as a dc-link filter provides the voltage source. A simple and most common SPWM method of *2-level* voltage control is shown in Figure 23.7b. An isosceles triangle carrier is compared with the sine wave reference signal and the crossover points determine the points of switching. Except at low-frequency range, the carrier

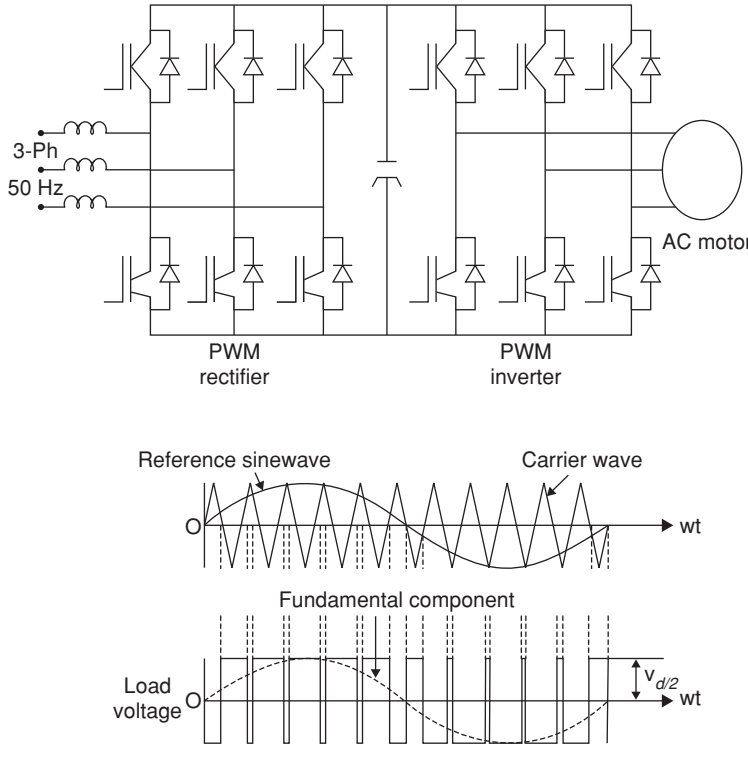

Figure 23.7 (a) Two-level PWM Rectifier-PWM-VSI Inverter, (b) Two-level carrier-based sinusoidal PWM. Reprinted with permission from IEEE (Chattopadhyay 2010)

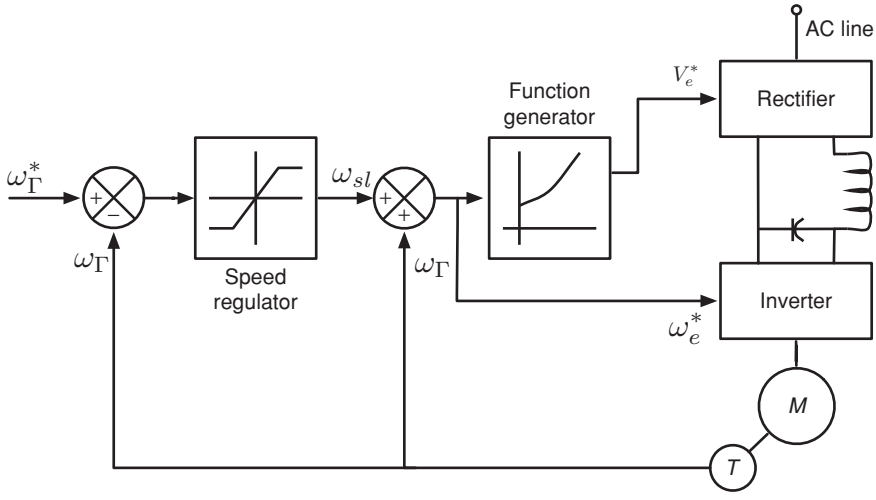

Figure 23.8 Constant V/f or scalar control of a rectifier-inverter induction motor drive with slip regulation

is synchronised with the signal and an integral ratio (multiple of 3) is maintained to improve harmonic content. The fundamental output voltage can be varied by variation of the modulation index (the ratio A_r/A_c, where A_r and A_c are the amplitudes of reference and carrier waves, respectively).

The classical flux regulation control scheme for an SCR-rectifier-inverter fed drive with simple *constant V/f ratio or scalar control* for the constant torque region with slip regulation is shown in Figure 23.8 (Bose 1982). The slip frequency ω_{sl} which is proportional to torque is regulated by the speed loop error. The ω_{sl} signal is added to ω_r to generate the inverter frequency ω_e. The voltage control signal V_e is generated from ω_e through a function generator so as to maintain the airgap flux nearly constant. A small boost voltage is added with the estimated voltage to overcome the machine resistance drop that becomes dominant at very low frequency. The drive accelerates with the clamped value of slip corresponding to the maximum torque and then settles down to a value as dictated by the load torque. If the commanded speed ω_r^* is reduced at steady state, the slip becomes negative and the drive system goes into the dynamic or regenerative braking mode. Instead of regulating the slip, it can be maintained constant and the speed loop error may control the dc-link voltage. The variation of V/f ratio causes the variation of air-gap flux and correspondingly the developed torque is regulated. The open-loop scalar control is popular in the industry when a small drift in speed and air-gap flux due to fluctuation are of no significance. Commercial drives with V/f control are also available with efficiency optimisation control (Bose 2011a).

PWM Three-Level VSI-Induction Motor Drive

Figure 23.9 shows a three-phase three-level PWM inverter (also known as neutral-clamped converter (NPC) using IGBTs / GTOs). In two-level inverters, the output voltages consist of

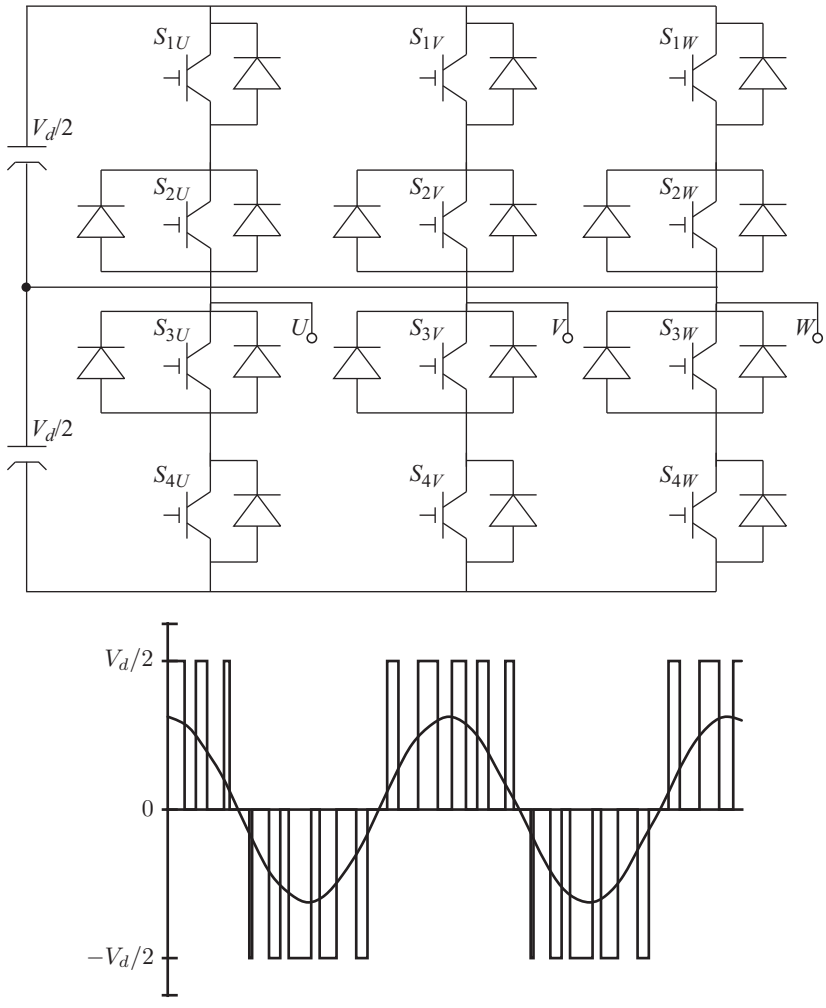

Figure 23.9 Three-level PWM inverter circuit diagram with output voltage waveform

pulses of either $+V_d/2$ or $-V_d/2$, whereas with a three-level inverter, these may be $+V_d/2$, 0, and $-V_d/2$. For high-power high-speed drives, three-level inverters have been preferred as they can be operated with twice the rated voltage without any series connection and therefore with twice the rated power with significantly improved output voltage waveform when compared to a two-level inverter. However, a three-level inverter consists of 12 IGBTs/GTOs—4 IGBTs/GTOs per phase. Here, the connection in each phase may be represented by a three-point changeover switch, the output of which can be connected to the positive pole, zero or the negative pole of the dc supply. One three-level inverter can be regarded as an inverter that can be operated with two independent pulse patterns. Till 1993, the rated power and frequency of GTO-VSIs were limited to about 2 MW/60 Hz for two-level VSIs and 4 MW/130 Hz for three-level VSIs but now with IGCTs (developed by ABB in 1996) and IEGTs (developed by

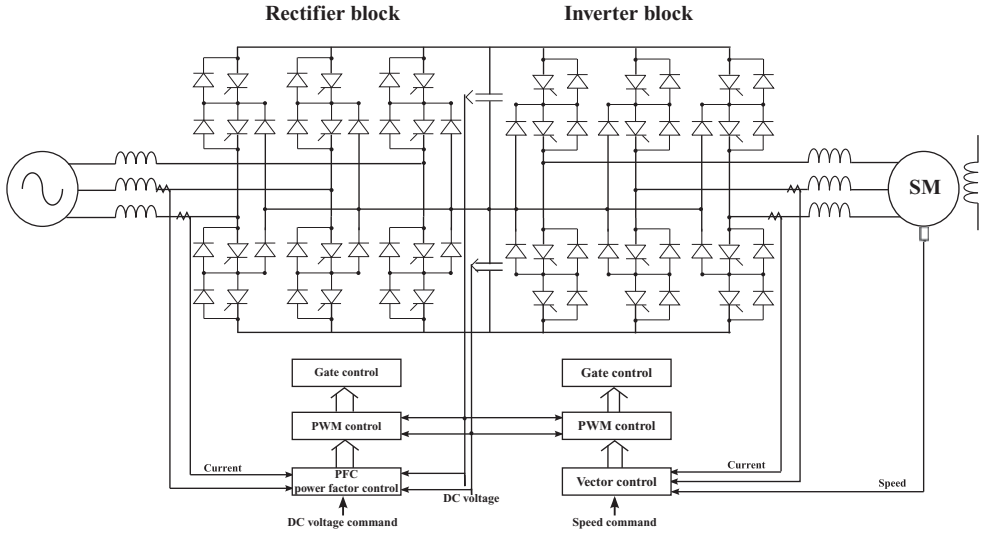

Figure 23.10 Three-level GTO converter-inverter system for steel rolling mills

Toshiba in 1999) and breakthrough in series connection, the rating of the converters has gone above 10 MVA. Siemens has introduced SIMOVERT-ML drive with three-level converters of MW range with VC for application to synchronous or induction motor drives.

Hitachi Ltd., Japan, also developed three-level GTO-based 6.4 MW inverter induction motor drive for steel rolling mills in 1996. The synchronous motor is often the most cost-effective solution for applications with a wide field weakening range and for high surge load requirements. Several recent applications of three-level inverters for large drives with regenerative front end includes a 20 MW downhill conveyer system with GTOs. Figure 23.10 (Okayama *et al.* 1996) shows a three-level GTO converter-inverter system used for steel rolling mills with VC (to be discussed later). The same configuration has been used with IGBTs, IGCTs or IEGTs as switches replacing GTOs with improvement in efficiency and reduced volume and weight.

Current Source Inverter-Induction Motor (CSI-IM) Drive

A schematic diagram of a *dual PWM* CSI-fed drive using GTOs is shown in Figure 23.11 (Chattopadhyay 2002). The system is a dual of the PWM-VSI rectifier-inverter system in Figure 23.7a. The PWM rectifier provides sinusoidal input current at unity power factor. This scheme has replaced the earlier phase-controlled rectifier-fed auto-sequentially commutated inverter (ASCI) using SCRs with capacitors and series diodes as commutation elements, Figure 23.12 (Chattopadhyay 2002). The variable dc voltage is converted to a current source by connecting a large inductor in series eliminating the filter capacitor of the VSI. The freewheeling diodes, typical of VSI, are absent in CSI as when supplied by a current source, current in any half-leg of the inverter cannot change in polarity and can only flow through the power switches. A method of speed control with CSI in which the slip ω_{sl} is varied as a function of the I_d

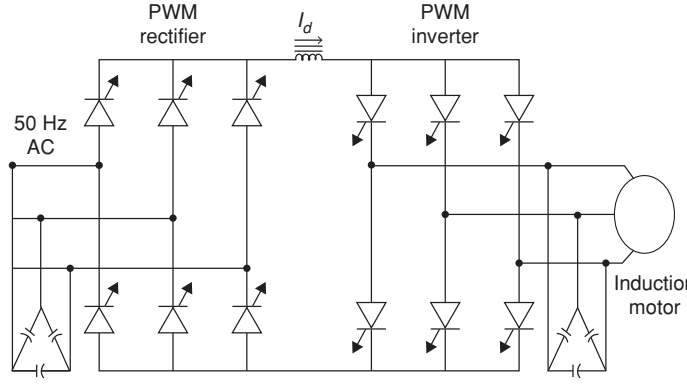

Figure 23.11 CSI-PWM rectifier PWM-inverter fed induction motor drive

(pre-computed for given parameters of the machine) to maintain constant air-gap flux (as in the V/f control of the VSI-fed drive) is shown in Figure 23.13 (Chattopadhyay 2002). The full four-quadrant capability of the drive can be obtained.

Cycloconverter-AC Motor Drive

A cycloconverter converts ac line power from one frequency to that in another directly (AC/AC) in contrast to the dc link inverter (AC/DC/AC). For large drives, 6 or 12 pulse converter

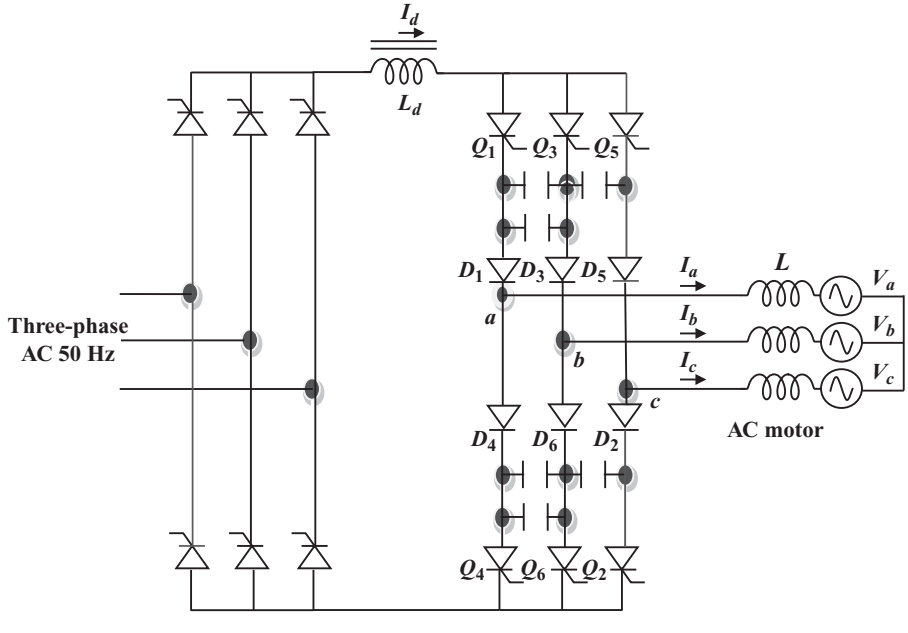

Figure 23.12 ASCI-fed induction motor drive

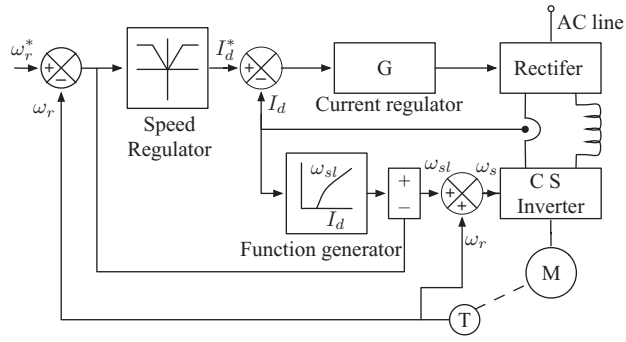

Figure 23.13 CSI-drive with slip-frequency control

bridges are used requiring 36 or 72 thyristors in total, respectively. Like dual converters, the cycloconverters can be operated in the circulating current-free mode where no circulating current is permitted between the *P*- and *N*-groups by appropriate logic control. The circuit operates in phase control line commutation mode and the firing angles are modulated to synthesise a mean sine wave voltage. Basic cycloconverter configurations (both for non-circulating and circulating current type) are shown in Figure 23.14 (Chattopadhyay 2010) with voltage and current waveforms for the non-circulating current one. The bridge that

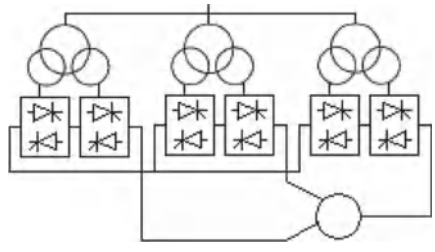

(a)

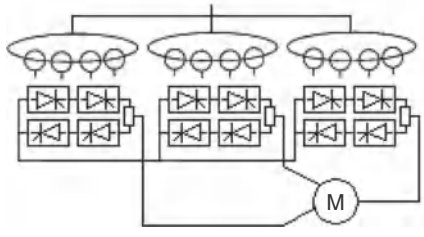

(b)

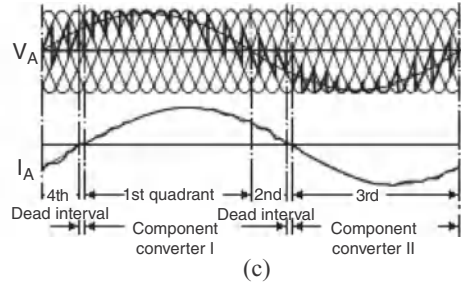

(c)

Figure 23.14 (a) Non-circulating current-type cycloconverter, (b) circulating current-type cycloconverter, (c) voltage and current waveforms for (a). Reprinted with permission from IEEE (Chattopadhyay 2010)

conducts the current generates the voltage. Due to line commutation, its output frequency is limited to, typically, 1/3 to 1/2 of the line frequency and is suitable for low-speed high-power drives, with easy four quadrant operation. The circulating current type, though expensive, is commonly employed for its simplicity, less torque ripple, higher maximum output frequency compared to the noncirulating current type, which though more efficient has a dead time of 1 to 3 ns for switching between forward and reverse current resulting in a higher torque ripple.

The output voltage of a cycloconverter contains a complex harmonic pattern given by $k_1 n f_i \pm k_2 f_0$, where f_i is the input frequency, f_o is the output frequency, n is the pulse number and k_1, k_2 are integers. A cycloconverter output may contain sub-harmonics of lower frequency than the output frequency that may be reduced by modifying the cosine firing control technique and feedback method to improve power quality and operating output frequency range. Because of the phase control principle, the cycloconverter presents lagging reactive power at the input irrespective of the power factor of the load and various schemes to improve this power factor have been developed including fast current control loop or trapezoidal modulation. The control method concepts discussed with VSI and CSI can be extended to cycloconverter drives. The cycloconverter-fed induction/synchronous motor drives have been used with scalar control for low-speed multi-motor-driven steel mill roller tables and with *VC*, in cement mills and rolling mill drives as discussed later.

Matrix Converter-Fed AC Motor Drive

The MC is a development of the force-commutated cycloconverter (Gyugi and Pelly 1976) based on bi-directional fully controlled switches, incorporating PWM voltage control, as mentioned earlier. With the initial progress made by Venturini (1980), it has received considerable attention in recent years as it provides a good alternative to the double-sided PWM voltage source rectifier-inverters having the advantages of being a single-stage converter with only nine switches for three-phase to three phase conversion and inherent bi-directional power flow, sinusoidal input/output waveforms with moderate switching frequency, possibility of a compact design due to absence of dc link reactive components and controllable input power factor independent of the output load current. The main disadvantages of the MCs developed so far are the inherent restriction of the *voltage transfer ratio* (0.866), complex control, commutation and protection strategy and above all the non-availability of a fully controlled bi-directional high-frequency switch integrated in a silicon chip. The power circuit diagram of the most practical three-phase to three-phase MC is shown in Figure 23.15a that uses nine bi-directional switches so arranged that any of three input phases can be connected to any output phase as shown in the switching matrix in Figure 23.15b. Thus, the voltage at any input terminal may be made to appear at any output terminal or terminals while the current in any phase of the load may be drawn from any phase or phases of the input supply. For the switches, the inverse-parallel combination of reverse-blocking self-controlled devices like Power MOSFETs or IGBTs or transistor embedded diode bridge as shown have been used so far. New perspective configuration of the bi-directional switch is to use two RB-IGBTs with reverse blocking capability in anti-parallel eliminating the diodes reducing the conducting losses in the converter significantly. The circuit is called a MC as it provides exactly one switch for each of the possible connections between the input and the output. The switches should be controlled in such a way that, at any time, one and only one of the three switches

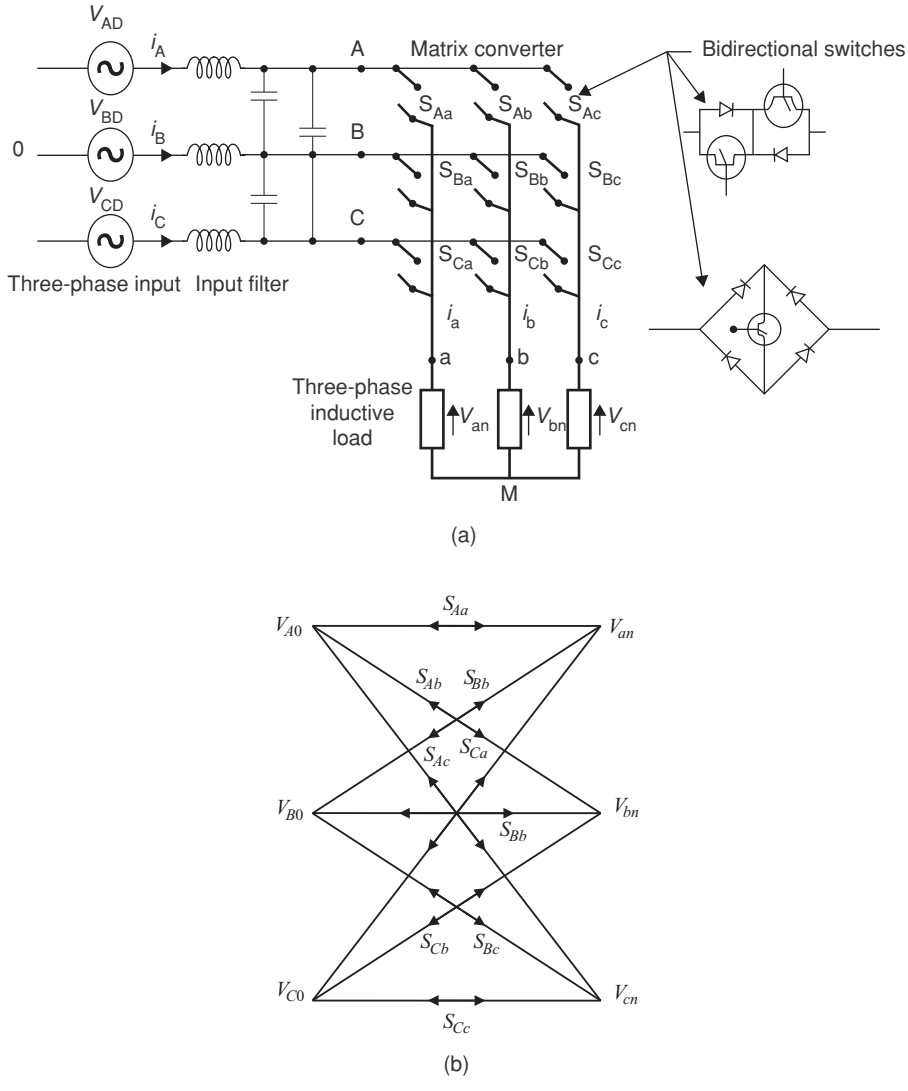

Figure 23.15 Three-phase to three-phase MC circuit with input filter, (b) Switching matrix for (a)

connected to an output phase must be closed to prevent "short circuiting" of the supply lines or interrupting the load.

The control methods adopted so far for the MC are quite complex and are subjects of continuing research (Zhang *et al.* 1998). Out of the several methods proposed for independent control of the output voltages and input currents, two methods are of wide use: (i) the *Venturini* method based on a mathematical approach of transfer function analysis and (ii) the SVM approach (as has been standardised now in the case of PWM control of the dc link inverter). These are discussed in Zhang *et al.* (1998).

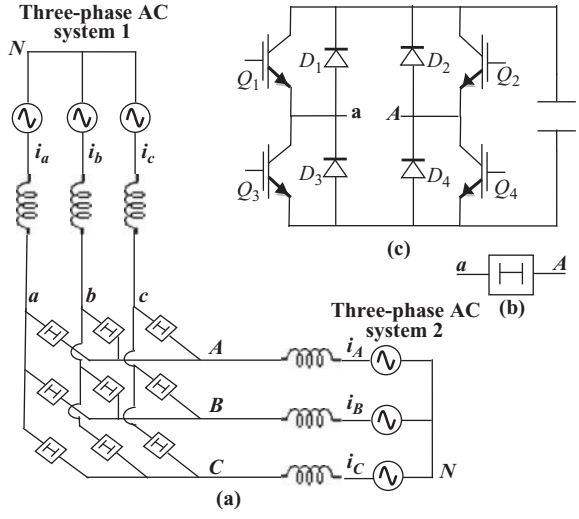

Figure 23.16 Multi-level MC: (a) configuration, (b) switch symbol, (c) switch realisation (Erickson and Al-Naseem 2001)

A vector controlled high-performance MC-induction motor is described in Ishii *et al.* (2000). A multilevel MC with four-quadrant dc link *H*-bridge switching cells suitable as shown in Figure 23.16 for medium or high voltage ac-to-ac power conversion was introduced in 2001 (Erickson and Al-Naseem 2001). The use of four transistors in the switch cell of Figure 23.16c allows the average current to be doubled relative to the conventional MC whose four-quadrant switches are realized using two transistors and two diodes. With dc capacitor, the switch cell is capable of producing instantaneous voltages $+V$, 0, $-V$.

The Yaskawa medium voltage MC (Yamamoto *et al.* 2011) utilises a series connected multi-level topology shown in Figure 23.17, where a three-phase input/single phase output MC is a basic component called the cell. Connecting three cells in series, each designed for 635V yields a line-neutral voltage of 1905 V, corresponding to a line-line voltage of 3300 V. These multi-cell medium voltage MCs (FS Drive-MXIS) of rating 3 kV, 200–3000 kVA or 6 kV, 400–6000 kVA have been built by Yaskawa and applied to 200 V, 22 kW wind turbine generator system, 400 V, 16 kW elevator system and 3.3 kV, 3 MVA skin-pass mills (Yamamoto *et al.* 2011). Compared to PWM converter-inverter system, the MC scheme has higher reliability, improved efficiency from 92.7% to 96.9% and weight about 62% (Yamamoto *et al.* 2011).

Slip-Power Controlled Induction Motor Drive

With wound rotor IM, while the stator is connected to the ac system, the rotor side slip power can be controlled by a converter cascade, either a rectifier-inverter or a cycloconverter, via slip rings as described in (Akagi 1998). New applications for high power ratings of some hundred megawatts involving cycloconverters or GTO inverters are in the fixed-frequency variable speed motor generators in pumped-storage plants in Japan. Figure 23.18 shows the

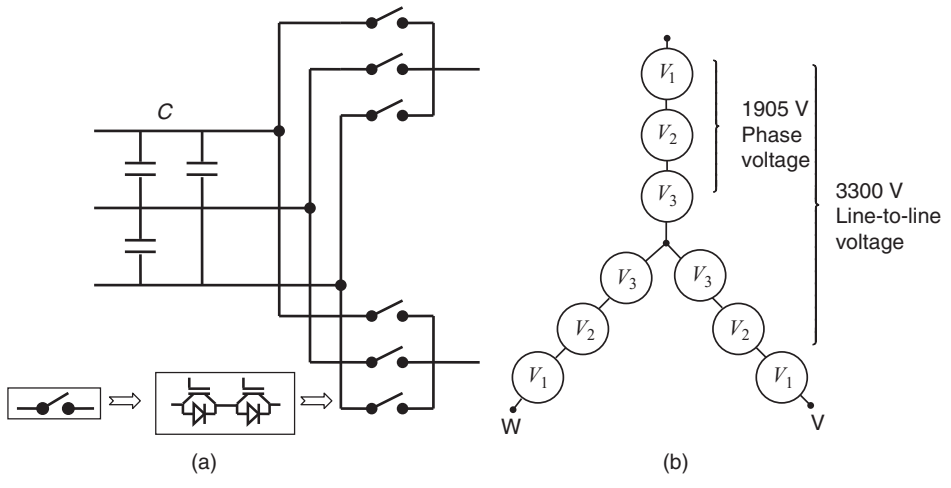

Figure 23.17 Schematic of multicell MC with three cells in series in each phase (Yamamoto *et al.* 2011). (a) One cell, (b) Single-phase and line-to-line voltage

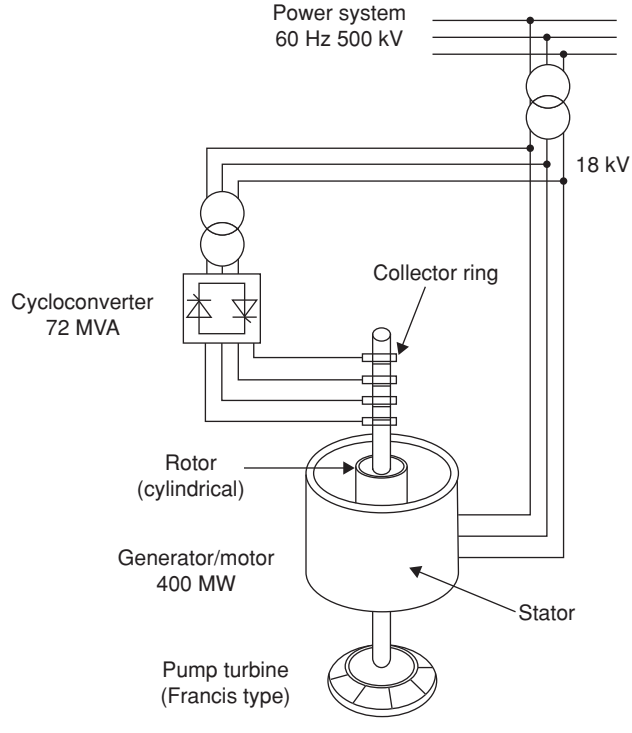

Figure 23.18 400 MW Adjustable speed pumped storage system (Akagi 1998)

arrangement of a 400 MW adjustable-speed pumped-storage system in Japan where a 72 MVA, 3-phase, 12-pulse line-commutated cycloconverter feeds the slip rings of the Scherbius drive. The armature terminals, rated at 18 kV, of the 20-pole induction machine are connected to a 500 kV utility grid through a step-up transformer. The output frequency of the circulating current-free cycloconverter is controlled within ±5 Hz, and the line frequency is 60 Hz. With a synchronous speed of 360 rpm the speed can be controlled from 330 rpm to 390 rpm. The total operational efficiency of the system increases by 3% when compared to the conventional constant-speed version of the system.

23.4.2 Induction Motor Drives with Vector Control

The vector or FOC, introduced in the beginning of 1970s (Blaschke 1972), has revolutionised the control of high-performance ac drives when, with this control, an induction motor drive can be operated like a separately excited dc motor drive. The stability and sluggish response problems of the higher order and complex coupling model of ac machine under scalar control vanishes with VC. In a separately excited dc machine, use of power electronic converters with current feedback provides a direct control of the magnitude of the armature current and in proportion, the torque. For ac machine, however, this control is to be achieved in terms of both *amplitude* and *phase* that has led to the generic term *VC*. In addition, unlike the dc machine, where the orientation of the field flux and the armature MMF is fixed by commutator and brushes, ac machine requires external control to fix this orientation without which the space angle between various fields vary with load (and during transients), giving rise to oscillatory dynamic response. *Field orientation control* (FOC) directly controls this space angle and, in particular, attempts to make it 90° between the specifically chosen field components so as to emulate a dc machine and provide *de-coupling control*. The technique can be applied to either induction or synchronous motor fed from either CSI/ CRPWM (current regulated PWM VSI) / VSI or cycloconverter (Chattopadhyay 1997a). Early conceptual works on VC were developed in Germany in the beginning of seventies and its implementation progressed with the development of microprocessors in early eighties. In *VC*, the currents i_{ds}^e and i_{qs}^e, the d-axis and q-axis components, respectively, of the stator current in synchronously rotating reference frame are analogous to the field current I_f and to the armature current I_a of the dc machine and therefore the torque can be expressed as $T_e = K_t \Psi_m i_{qs} = K_t' I_f I_a = K_t'' i_{qs}^e i_{ds}^e$. These two components can be independently controlled. For normal operation as in the dc machine, the current i_{ds}^e remains constant and the torque is varied by varying the i_{qs}^e component. There are two basic methods of VC based on the acquisition of the flux vector angle θ_e $(= \omega_e t)$ that assures the alignment of i_{ds}^e with Ψ_m and i_{qs}^e with the airgap voltage (Bose 2002). The *direct method* is based on the measurement or computation of the magnitude as well as the position of the flux vector and the *indirect method* uses a *slip relation* to compute θ_e as a sum of θ_r and θ_{sl} (corresponds to ω_r and ω_{sl}, respectively).

Direct Vector Control (Flux Feedback)

Figure 23.19 shows the block diagram of a direct VC scheme for a Current-regulated PWM (CRPWM) inverter-fed induction motor drive (Chattopadhyay 1997a). The reference control signals i_{ds}^{e*} and i_{qs}^{e*}, which are dc quantities, are converted to a stationary reference frame by

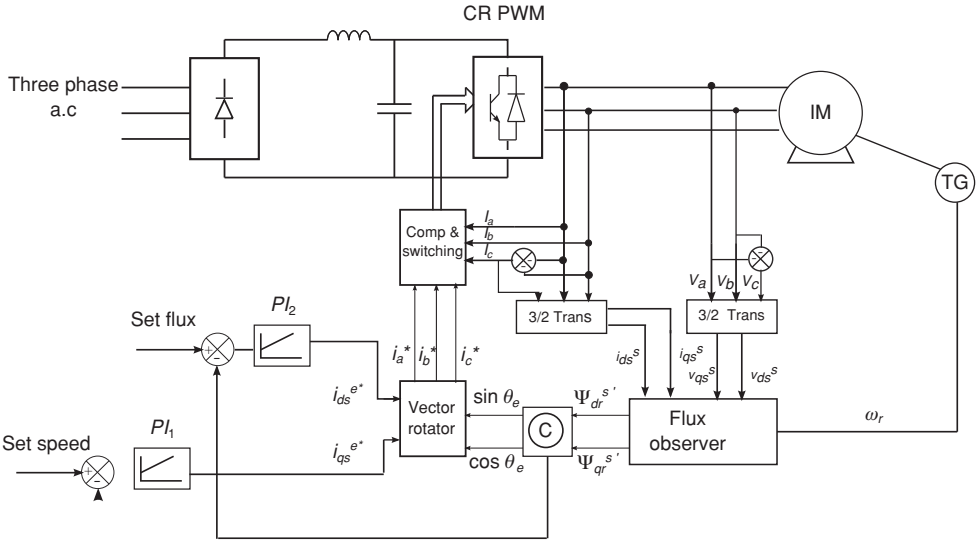

$$\left|\widehat{\psi}_r\right| = \sqrt{\left(\widehat{\psi}_{dr}^{s\prime}\right)^2 + \left(\widehat{\psi}_{qr\prime}\right)^2}$$

$$\cos\theta_e = \frac{\widehat{\psi}_{dr}^{s\prime}}{\left|\widehat{\psi}_r\right|}, \quad \sin\theta_e = \frac{\widehat{\psi}_{qr}^{s\prime}}{\left|\widehat{\psi}_r\right|}$$

Figure 23.19 Direct vector control scheme for a CRPWM-fed induction motor with a rotor flux observer (Chattopadhyay 1997a)

a *vector rotator* with the $\cos\theta_e$ and $\sin\theta_e$ signals generated from the flux signals followed by 2/3 phase transformation as shown. A flux feedback loop provides precision flux control. The speed control loop provides the torque command that generates the current reference. The air-gap fluxes Ψ_{dm}^s and Ψ_{qm}^s can be measured directly by search coils /Hall probes or estimated (observed) from stator voltage and current signals. Though the air-gap or the *stator flux orientation* is attractive due to ease of flux measurement or computation, it has been shown that they lead to instability and not a perfect de-coupling and the *orientation to rotor flux* is resorted to by synthesising the rotor flux Ψ_r from the directly sensed air-gap flux.

Indirect Vector Control (Flux Feed-Forward)

An alternative to direct measurement or estimation of the flux position for application of VC is to employ a slip relation derived from rotor voltage equations in a synchronously rotating reference system with rotor flux entirely in the *d*-axis (Bose 2002),

$$\omega_{sl} = \frac{L_m}{\Psi_r'^e}\left(\frac{R_r'}{L_r'}\right) i_{qs}^e \tag{23.1}$$

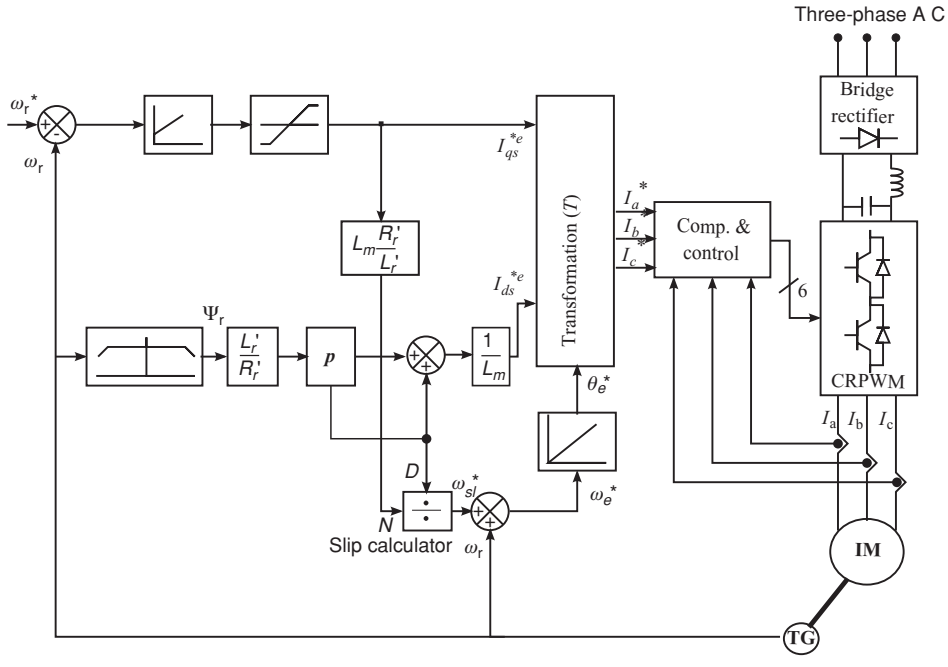

Figure 23.20 Rotor flux oriented indirect vector control for an induction motor with a CRPWM inverter (Chattopadhyay 1997a)

to compute the flux position relative to the rotor by summing a sensed rotor position signal with a commanded slip position signal

$$\theta_e^* = \theta_{sl}^* + \theta_r. \tag{23.2}$$

Figure 23.20 shows the block diagram of the *indirect* vector-controlled induction motor drive (Chattopadhyay 1997a). The commanded currents i_{qs}^{e*} and i_{ds}^{e*} are converted to stator referred reference currents by transformation as in the case of the direct field orientation. i_{qs}^{e*} is controlled according to the desired torque and constant rotor flux. i_{ds}^{e*} is obtained as Ψ'_{dr}/L_m at the steady state. Indirect VC, also known as *flux feedforward control*, has the limitation in the slip calculation that depends on the commanded machine parameters that may differ from the actual values during the running condition of the drive. Several methods of parameter adaptation have been attempted as discussed in Bose (2002). A *universal field oriented controller* applicable to both direct and indirect field orientation was reported in DeDoncker and Novotny (1994).

Few typical simulation results as obtained and experimentally verified (Chattopadhyay 1997a) are shown in Figure 23.21 for both indirect and direct VC.

Sensorless Vector Control of Induction Motors

Sensorless VC essentially means VC without any speed and flux sensor (Figure 23.22). A mechanical speed encoder is undesirable in a drive as it adds to the cost and reliability

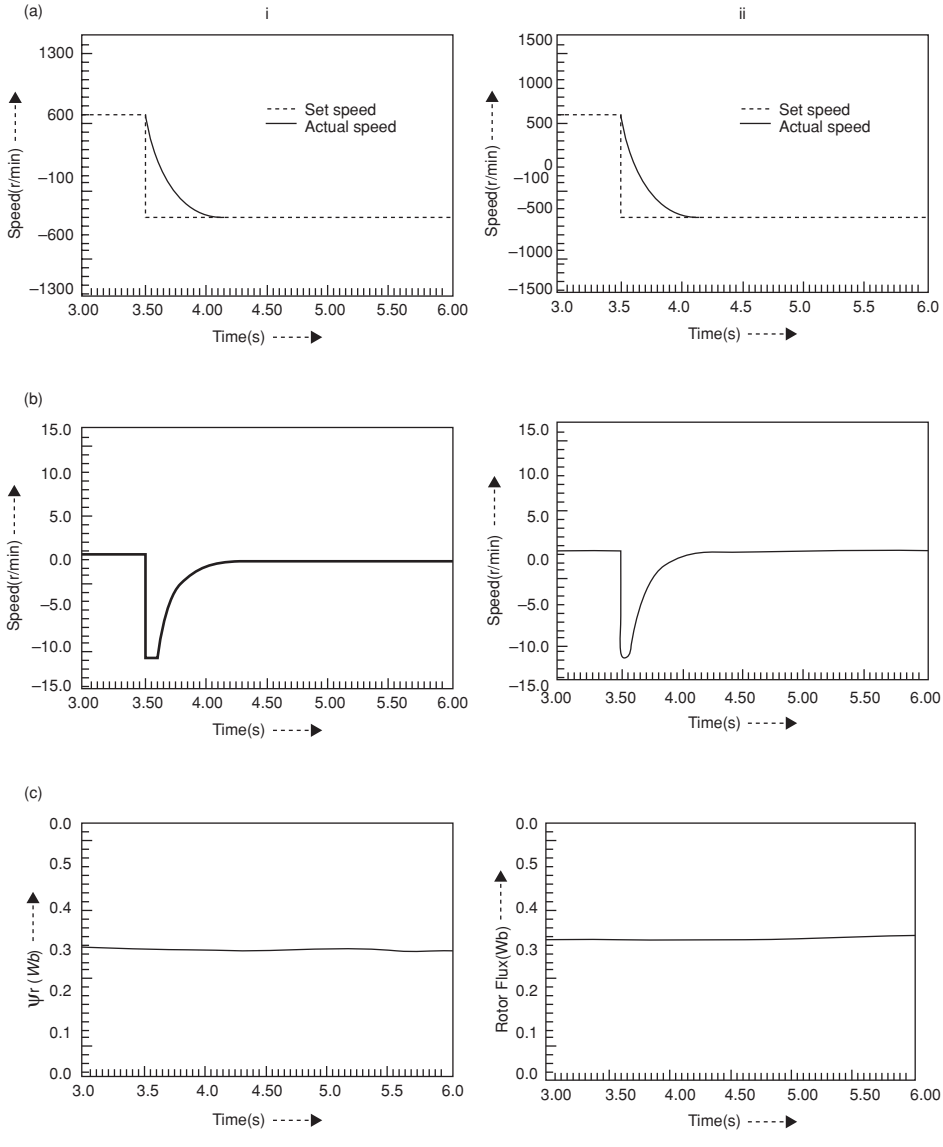

Figure 23.21 Simulation results showing (a) speed, (b) torque and (c) rotor flux of a vector-controlled induction motor drive for speed reversal (+600 to −600 rpm) (i) direct VC and (ii) indirect VC (Chattopadhyay 1997a)

problems, besides the need for shaft extension and mounting arrangement. The speed signal can be estimated from machine terminal voltages and currents by a number of methods (Rajashekara *et al.* 1996; Bose 2002) such as slip calculation, direct synthesis from machine state equations, model referencing adaptive systems, speed adaptive flux observer, extended Kalman filter and slot harmonics. These estimation methods are complex and dependent on

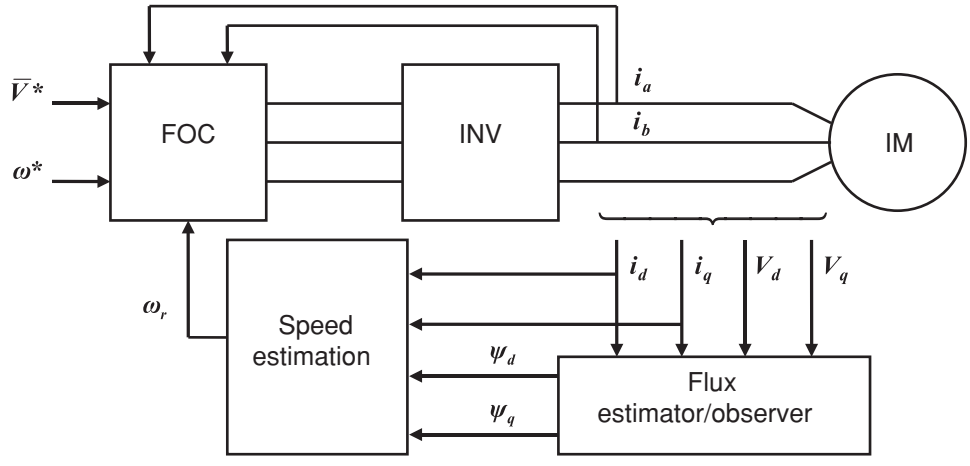

Figure 23.22 Block diagram of a sensor-less VC system

machine parameters. Further the estimation near zero speed imposes a challenge. Attempts have been made to inject auxiliary signal at a carrier frequency from the stator side for a machine designed with saliency and processing the response but with limited success (Holtz 2002). Several *speed-sensorless* vector-controlled induction motor drives have been implemented by Toyo Electric Company of Japan in newspaper printing machines, coating machine, textile machines and so on. with a wide range of speed control with speed control accuracy of $\pm 0.5\%$ and speed response of 90 rad/s (Akagi 1998).

Two commonly used methods for flux estimation by sensing the machine terminal voltages and currents are the *voltage model* and *current model* as described in Bose (2002). Voltage model flux estimation is better at higher speed ranges, whereas the current model estimation can be made at any speed. A hybrid model (Jansen and Lorenz 1992) is possible where the voltage model is effective at higher speed ranges but transitions smoothly to the current model at lower speed ranges.

Speed-sensorless vector-controlled system requires information on motor parameters to realise high performance. A speed-sensorless vector-controlled inverter equipped with auto-measuring of the parameters is reported in Ohmori *et al.* 1995). A DSP-based speed adaptive flux observer is described in Kubota *et al.* (1993).

23.4.3 Induction Motor Drives with Direct Torque Control (DTC)

A new concept to control the torque and flux in induction motor drives, popularly known as DTC, which is basically a performance-enhanced *scalar* control was developed in the late eighties and commercialised in the late nineties by the ABB with IGCT inverters. It can be shown that the developed torque of the machine is proportional to the product of synchronously rotating stator flux Ψ_s, rotor flux Ψ_r and the angle θ_s between them. The main variable to be controlled in the DTC scheme is Ψ_s that can be directly controlled by the stator voltage v_s (neglecting stator resistance). With this scheme it is possible to obtain a good dynamic control

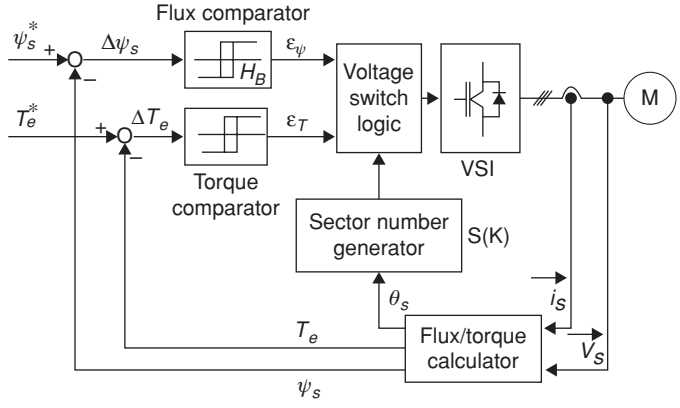

Figure 23.23 DTC control of induction motor (Wu 2006). Reprinted with permission from IEEE (Chattopadhyay 2010)

of the torque without any mechanical sensor on the shaft (*sensorless*). The scheme is shown in Figure 23.23 (Wu 2006), where both the flux Ψ_s and the torque T_e are controlled by the hysteresis controllers in the outer loops as indicated. The machine voltages and currents are sensed to estimate the torque and the flux vector that gives information about the angle θ_s in one of the 60° sectors as shown in Figure 23.24 (Bose 2006). The vector Ψ_s rotates in a circular orbit within a hysteresis band covering six sectors as shown. Figure 23.24 (Bose 2006) shows the six active voltage vectors and two zero vectors of the two-level inverter (relevant to the Space Vector PWM control) controlled by the voltage switch logic unit (SLU) of Figure 23.23. If a voltage vector is applied for time Δt, the corresponding flux vector increment is given by the relation $\Delta\overline{\psi}_s = \overline{V}_s \Delta t$. The flux increment vector contributed by each voltage vector is indicated in the same figure. The flux is initially established at zero frequency in the radial

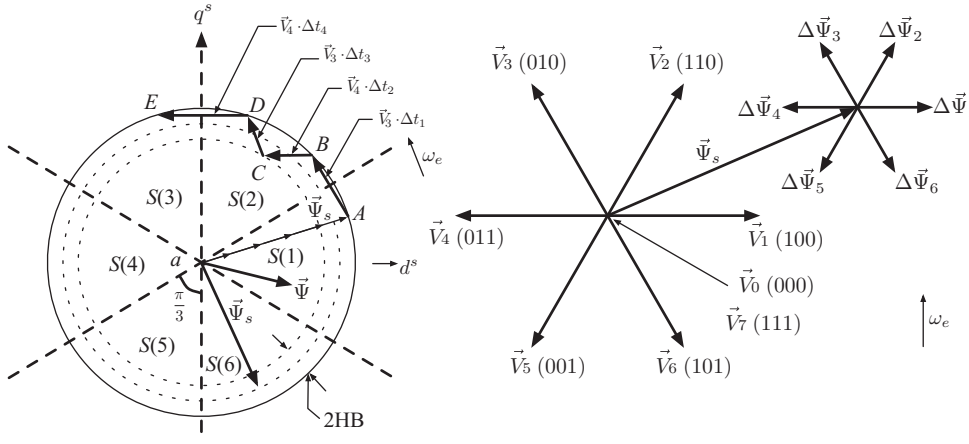

Figure 23.24 Stator flux trajectory and voltage vectors (Bose 2006) for a two-level VSI

direction aA, as shown in Figure 23.24a. With the rated flux, the command torque is applied and the flux vector starts rotating in the usual counterclockwise direction within the hysteresis band depending on the selected voltage vector. The motor state calculations are updated in each sampling period Δt (e.g. 25 μs) in the software model by a DSP. The control loop errors generate the digital signals ε_Ψ and ε_T through the respective hysteresis-band comparators. The delays associated with the PWM stage are replaced by an optimal switching flux vector selection table SLU (can be realised by an ASIC hardware or through a DSP software) or a look-up table which selects the most appropriate voltage vector to satisfy the flux and the torque demands. The drive has a faster response than the field oriented/VC and the absence of the closed loop current control, PI regulators, vector transformation and conventional PWM algorithm simplifies the scheme. However, as the feedback signals are estimated from the machine terminals, the low speed limitation and the parameter variation problems are similar to those of the stator flux oriented direct VC. In contrast to FOC, which is a linear control where the PWM and the static converter are modeled as a linear actuator, DTC is nonlinear, which in turn exploits the discrete nature of the static converter for the sake of robustness and dynamics. Recently, a number of solutions of the inherent problems have been developed with the use of improved switching logic, discrete SVM techniques, three-level inverters, adaptive hysteresis-band control (Okumas and Aktas 2007) and introduction of fuzzy and neuro-fuzzy techniques involving more computer power. Figure 23.25 (Malik and Khage 1998) shows a circuit configuration of a compact 5 MW three-level IGCT converter motor system ACS 1000 with front-end rectifier and DTC control where the static speed control error is in the range of 0.1%. Typical torque response of a DTC drive is $<$10 ms compared with 10–20 ms for a vector-controlled drive and $>$100 ms for an open-loop PWM drive. This has been used for pumps, compressors, conveyors and other auxiliary processes in a steel or process industry. ABB has supplied IGCT-based ACS 6000 (3–27 MVA) with front-end controlled rectifier (Active Rectifier Unit) designed to meet specific challenges faced by plate mills and reversing cold mills-one in the new 5 m wide plate mill in China in 2005 where 10 MW synchronous motors are used.

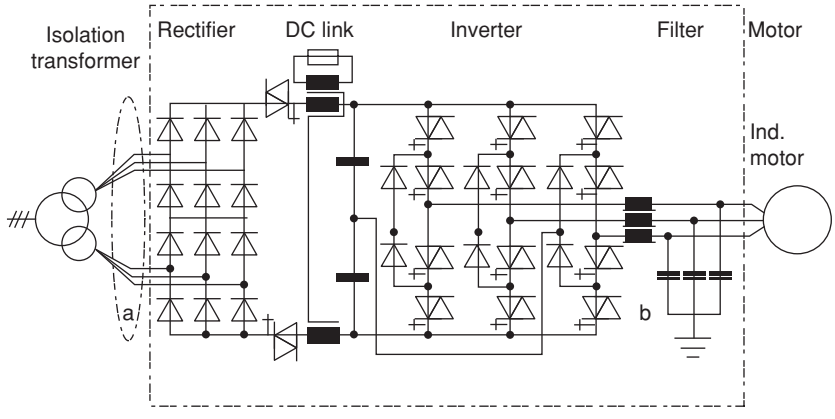

Figure 23.25 Three-level IGCT Inverter topology for ACS1000 (ABB) (Malik and Khage 1998). Reprinted with permission from IEEE (Chattopadhyay 2010)

23.5 Control of Synchronous Motor Drives

23.5.1 Synchronous Motor Drives with Scalar Control

Self-Synchronous or Commutator-Less Motor

The synchronous motor drives have essentially two different modes of operation. One is the true synchronous mode in which the machine is controlled by inverter or cycloconverter through an independent oscillator just like the V/f control of an induction motor drive. The other mode is the self-synchronous mode which is known as commutator-less motor (CLM) mode (Figure 23.26) where the inverter or cycloconverter firing signals are derived from a rotor shaft position sensor; dc-CLM, when supplied from an inverter and ac-CLM when supplied from a cycloconverter. In the self-synchronous mode, the synchronous motor acts exactly like a dc motor-the mechanical brush system being replaced by the shaft position sensitive converter. Here, the frequency is slaved to the speed and not vice versa. Therefore, there is no risk of pull out. Any slow down of the motor, no matter sudden, causes a corresponding drop in frequency. The magnitude of the dc current supplied to the static commutator (for dc CLM) determines the torque and the speed.

LCI Synchronous Motor Drive

An important feature of the synchronous machine is that it can be operated at leading power factor and when supplied by a CSI, load commutation can be used. Figure 23.27 shows the power circuit for such a drive. With a normal synchronous motor, the inverter is not capable of load commutation below a certain speed (typically 10%) because of inadequate counter EMF. Special starting arrangements with forced commutation through fourth leg or 'current pulsing' are to be made at starting /low speed running. In 1997, an SCR-based inverter based load-commutated commutator-less *series* motor (CLSM) (SenGupta *et al.* 2000) with unaided *start-up* capability, having the field winding in the dc link (Figure 23.28), suitable for a vehicle drive as developed at IIT Kharagpur, India, has been reported. LCI-fed drives in CLM mode are widely used in high-power drives such as pumps, compressors, pumped storage hydro- and gas turbine start-up applications besides continuous rolling mills and traction drives. The

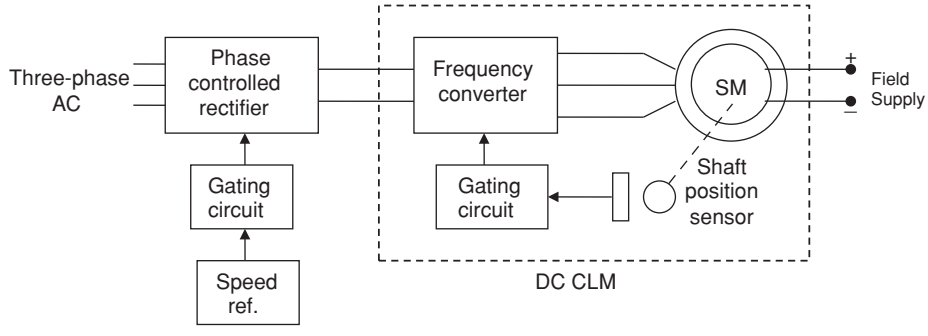

Figure 23.26 Commutator-less dc motor

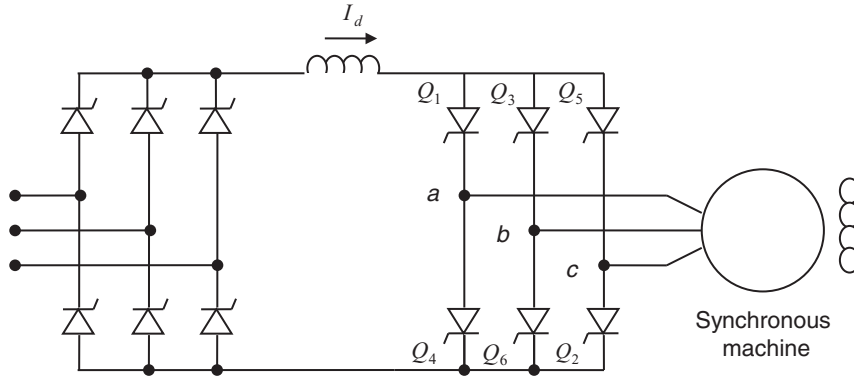

Figure 23.27 LCI-fed synchronous motor drive

power rating for this drives has gone up to 100 MW for a NASA wind tunnel drive with a single synchronous motor as discussed later.

Cycloconverter-Synchronous Motor (ac-CLM) Drive

Four quadrant torque-speed operation at a high power level with high torque at low speed is the drive requirement for which the cycloconverter-fed synchronous motor as ac-commutatorless (ac-CLM) drive (Figure 23.29) is best suited (Das and Chattopadhyay 1996). Some of the applications are:

- Gear-less cement mill drives; the mill tube is driven from a low-speed wrap-around motor with higher number of poles (Richlen 1971; Salzmann 1978);
- Reversing rolling mill drives with high dynamic requirements for torque and speed reversal employing VC (Timpe 1982; Sugi *et al.* 1983; Nakano *et al.* 1984; Ichihara *et al.* 1986);

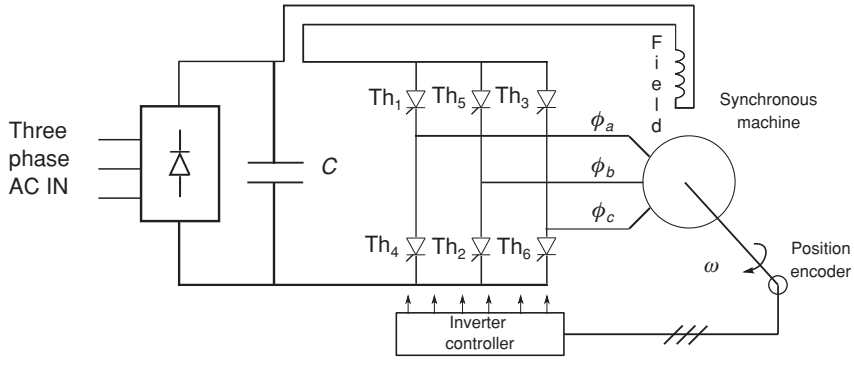

Figure 23.28 Power circuit diagram of an SCR-based CLSM (SenGupta *et al.* 2000)

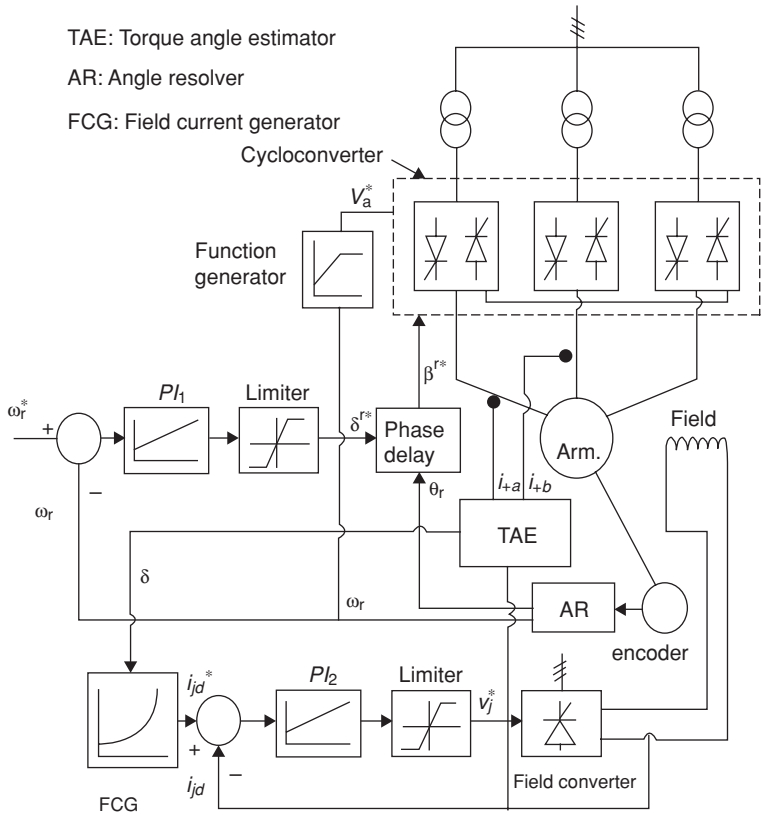

Figure 23.29 Cycloconverter synchronous motor drive with scalar control (ac-CLM) (Das and Chattopadhyay 1996)

- Drives for mine hoists with high power ratings (Madiseti and Ramlu 1986);
- Icebreakers and other ships equipped with diesel generator-fed cycloconverter-fed SM with power rating up to about 20 MW rating per unit (Hill *et al.* 1987).

The cycloconverter is normally operated with line commutation but can have load commutation if the output frequency approaches or exceeds the line frequency. The firing pulses are derived from shaft position sensors and the machine terminal power factor is maintained at unity by field excitation control. The method of driving the motor from a cycloconverter with the *transvector* control principle involving FOC was patented and used by Siemens in Germany, for years, in very high capacity cement Mills (>8 MW) and also for rolling mills rated above 3 MW since 1978. A 4 MW (peak loading 10 MW) blooming mill with a cycloconverter-synchronous motor drive having a speed of 60–120 rpm was commissioned in 1981 together with a 4 MW roughing stand of a strip mill (Timpe 1982). The control concept and relevant vector diagrams for field oriented operation is detailed in Salzmann (1978) and Sugi *et al.* (1983) and discussed briefly in the next sub-section.

23.5.2 Synchronous Motor Drives with Vector Control

The VC of SM is different from that of induction motors primarily due to the fact that, in the latter, the magnetising current can be supplied from the field side independently of the armature current and the space position of the field is located by the position of the rotor. Additionally, the steady-state slip between the rotor (field winding) and the controlled flux vector vanishes in the steady state. Therefore, the indirect or feed-forward type of VC as used extensively for the induction motor does not seem obvious for a synchronous machine. For a self-synchronous or CLM with rotor position feedback and VC, the implementation calls for control of the magnitude and the phase of the stator current with respect to the location of the field winding axis. The response of the field current is sluggish because of the large time constant and as a result, the response of a self-controlled synchronous machine is slow. The response can be improved considerably by using *VC*, where the transient magnetising current demand to maintain the rated flux can be temporarily supplied from the stator side.

Vector Control of a Cycloconverter-Fed Synchronous Motor Drive

Figure 23.30 (Trantner and Wick 1988; Rodriguez *et al.* 2005) shows the vector diagram of the synchronous machine (as preferred for a high-capacity steel mill), used to develop FOC required to adjust speed and torque, where e_s is the air-gap emf, i_q (torque-producing component) is the quadrature axis component of the current i_s, i_d (flux-producing component) is the direct axis component of current i_s, Ψ the magnetic flux, i_μ is the magnetizing current, φ_L is the load angle, φ_s is the flux axis angle and λ is the rotor axis angle. The currents i_d and i_q of the stator current in synchronously rotating reference frame are analogous to the field current I_f and to the armature current I_a of the dc machine and the toque can be expressed as $T_e = K_t i_q = K_t' I_f I_a = K_t'' i_d i_q$. These two components can be independently controlled with VC. Figure 23.31 shows the simplified block diagram (Rodriguez *et al.* 2005) of the speed and torque control system adopted by Siemens (Trantner and Wick 1988) that includes a PI controller for the speed n and another PI controller for the flux Ψ. The speed controller delivers the reference value of the torque-producing current i_q^*, while the flux controller delivers the reference value of the field-controlling current i_d^*. The stator currents i_{L1}, i_{L2} and i_{L3} and the

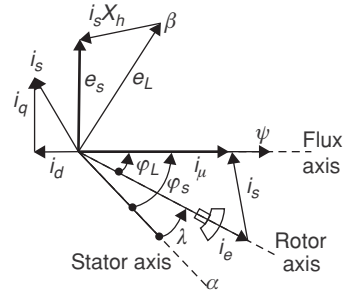

Figure 23.30 Vector diagram of the synchronous machine. Reprinted with permission from IEEE (Chattopadhyay 2010)

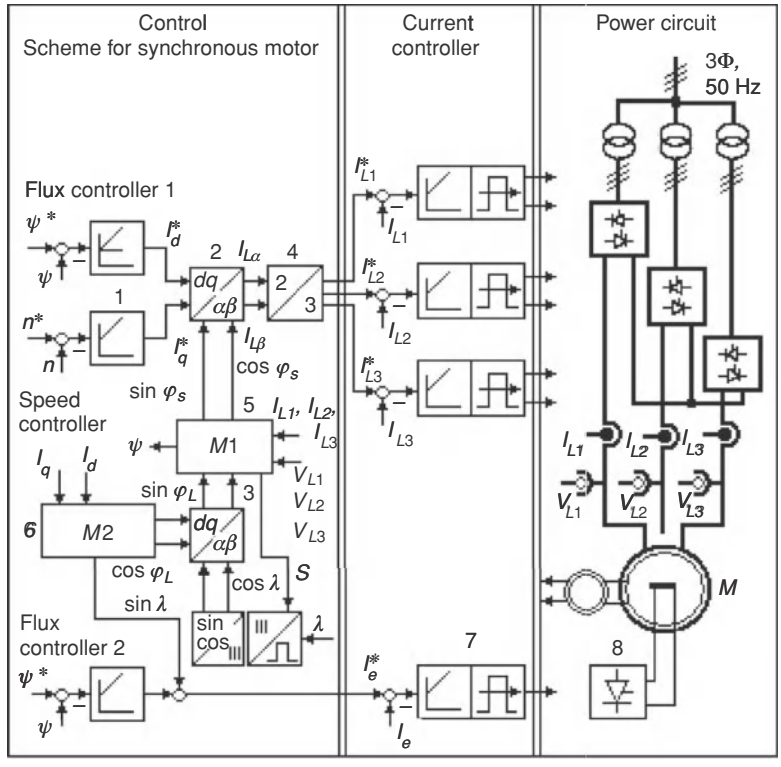

Figure 23.31 Block Diagram of the speed and torque control for the the mill with cycloconverter (Siemens). Reprinted with permission from IEEE (Chattopadhyay 2010)

voltages v_{L1}, v_{L2} and v_{L3} are measured and used in voltage model block M1 to calculate the magnitude $|\Psi|$ and the position ($\sin\varphi_S$, $\cos\varphi_S$) of the flux. The position of the flux is used to transform from $d-q$ to $\alpha-\beta$ reference axis in block 2. Block 4 transforms the two-phase currents $i_{L\alpha}$ and $i_{L\beta}$ into three-phase reference currents i^*_{L1}, i^*_{L2} and i^*_{L3} which are delivered to the current controllers of the cycloconverter. M2 in block 6 is the current model that uses the current components in field coordinates (i_d, i_q) to determine the flux position with respect to the rotor axis. Then, the field position with respect to the stator axis is obtained by adding φ_L to the rotor position λ. The current model is useful during low-operating speeds as needed at starting and positioning of the mill when the machine voltage terminals are very noisy for using voltage model. Block 2 is the field flux controller used to generate the reference value of the rotor current i^*_e fed to the controlled rectifier of block 8. Nakano *et al.* (1984) reported the development of a high-performance synchronous motor drive for a rolling mill by Fuji in Japan, with an open-loop flux estimator and PI current controller. Here, the flux linkage was kept constant by feeding part of the field current to the armature windings transiently and the power factor could be controlled to unity. An improved PC (personal computer)-based VC scheme for a 6-pulse non-circulating current cycloconverter-fed synchronous motor with a closed-loop flux observer and operating with unity power factor for a rolling mill drive as

developed in IIT Kharagpur, India, in 1996 and a prototype made by C-DAC, Trivundrum, India, is reported in Das and Chattopadhyay (1997) and Chattopadhyay (1997b). It is briefly described in the following sub-section.

Observer-Based Vector Control of a Cycloconverter-Fed Synchronous Motor Drive

Figure 23.32 shows the block diagram of an observer-based stator flux oriented vector controlled six-pulse cycloconverter drive as applicable to rolling mills (Das and Chattopadhyay 1997) and the corresponding phasor diagram. This is an improvement on the Siemens' drives (Bayer *et al.* 1972; Trantner and Wick 1988) as well as the Japanese one (Nakano *et al.* 1984). The implementation aims at a control that maintains a spatial orthogonality between the flux vector Ψ_s and the armature current vector i_a as shown in the space phasor diagram. The reference speed and reference flux commands are given to the vector rotator that generates the reference analog voltages for the cyclocoverter (through the current controller) and the field converter. The stator flux is estimated by a closed loop reduced order observer. $C1$ is the speed controller (PI) that generates the torque command that is divided by the stator flux to generate the torque component of current i_{sT}. The magnetisation current along the flux axis i'_m is obtained from a flux controller (PI) $C2$. The transient stator flux component of current i_{sm} is obtained from the relationship, $I^*_{sm} = i'_m - i_{fd} \cos\delta$, which decays down to zero in the steady-state. The steady state displacement angle is decided by the displacement angle controller and the power factor can be maintained at unity. The set value of the field current is obtained from the relation, $i_{fd} = i'_m / \cos\delta$. $C3$ is the field current controller (PI) that generates the control voltage for triggering the field converter. The vector rotator (VR) transforms the vector from two-axes flux-torque reference frame to abc stationary reference frame. The observer and the control circuit design aspects together with the PC-based implementation are detailed in (Das and Chattopadhyay 1997). The observer is closed loop in nature, having constant gain matrix, and is robust to speed variation. It is easier for digital computer implementation as it does not contain any derivative term. The synchronous motor model with state variables comprising stator fluxes and stator as well as field currents is utilised to estimate the stator fluxes using the current measurements (Das and Chattopadhyay 1997).

Figure 23.33 shows the simulated and experimental current waveform of a phase following a speed reversal from $+200$ to -200 rpm, a range appropriate for reversing rolling mill applications.

23.6 Application Examples of Control of High-Power AC Drives

23.6.1 Steel Mills

While motors used in the primary area of steel making like Coke Oven, Blast Furnace, Steel Melting Shop do not need very accurate speed or torque regulation, the motors used in Roughing mills, Finishing mills, Plate mills, Tube mills, Run-out Tables, Coilers/Un-Coilers, Pinch roles and so on need speed and torque regulation of higher accuracy. Since 1970s, AC motor drives having either IM or SM fed from either direct ac/ac cycloconverters or ac/dc/ac link inverters have replaced the earlier Thyristor-Leonard DC motor drives. The AC Drive realises higher efficiency, less maintenance and a smaller motor. Synchronous motor drives

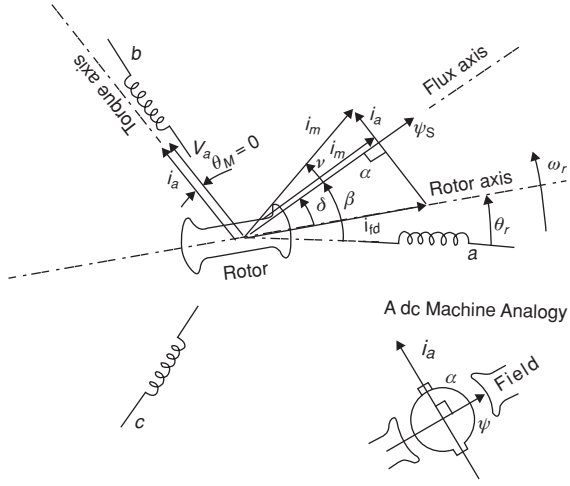

(a) Phasor diagram

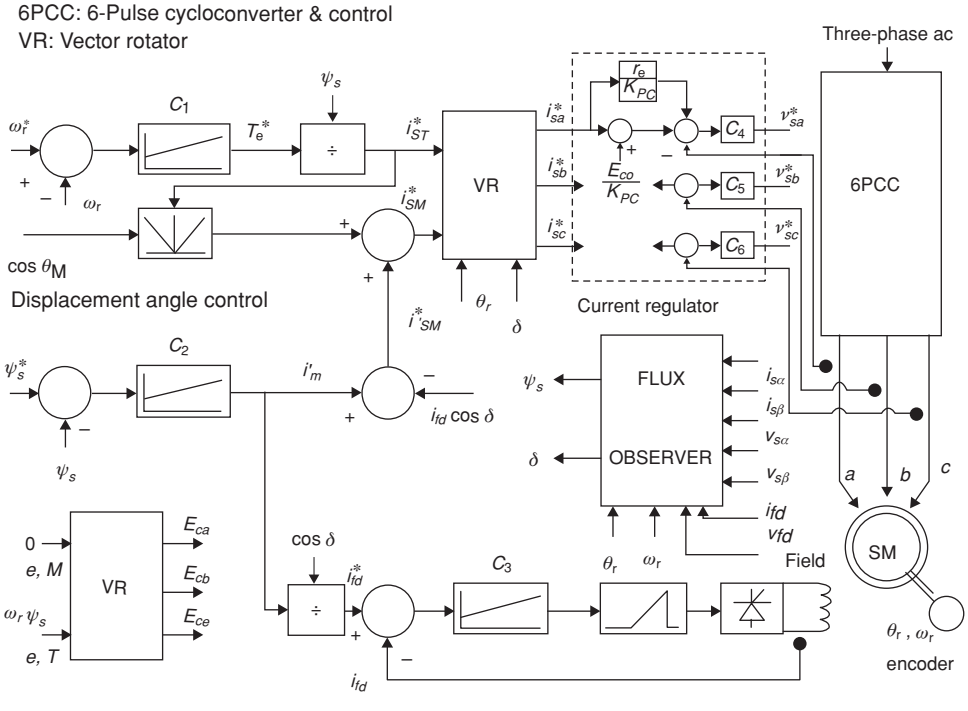

(b) Block diagram

Figure 23.32 Stator-flux oriented flux-observer based vector-controlled cycloconverter synchronous motor drive. Reprinted with permission from IEEE (Das and Chattopadhyay 1997)

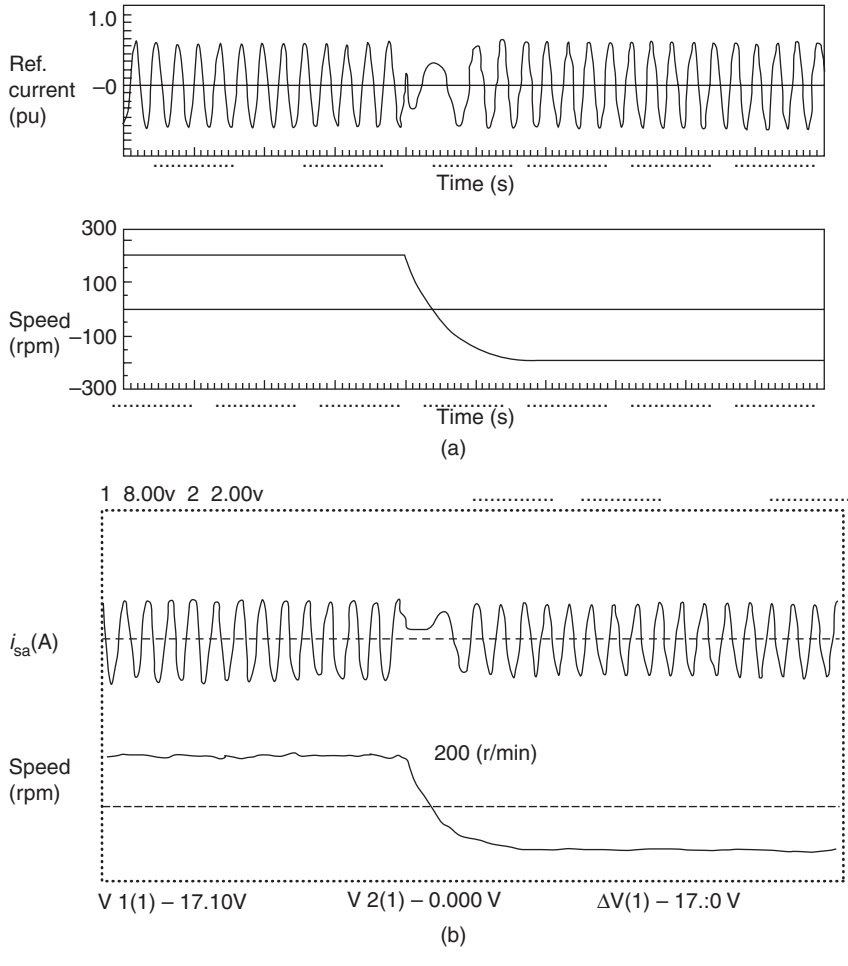

Figure 23.33 Speed and current response to step speed reversal: (a) simulation results, (b) experimental results. The entire experiment lasts 5 seconds. Reprinted with permission from IEEE (Das and Chattopadhyay 1997).

have the advantages over the induction motor drives in that these can be operated in near unity or even leading power factor with excitation control, reducing armature copper loss and permitting simplicity of commutation with thyristors or SCRs (silicon-controlled rectifiers) as switches (as in a LCI-fed drive) and it runs at a precisely set speed independent of load and voltage fluctuations. Thyristor or SCR-based cycloconverter-fed with FOC or VC (Chattopadhyay 1997b) have been extensively used in main rolling mill drives and cycloconverter-fed induction motor drives with scalar V/Hz control have been utilised in roller / run-out table drives.

With the introduction of FOC, a high performance 4 MW Blooming Mill with a cycloconverter-synchronous motor drive having a speed of 60–120 rpm was commissioned by Siemens in 1981 together with a 4 MW roughing stand of a strip mill (Chattopadhyay

2010). Major manufacturers of cycloconverter drives above 10 MVA are Siemens (Simovert D), Toshiba (Tosvert-μ /S850), ABB (ACS6000C) and Alstom (ALSPA CL9000). Cold rolling mills such as tandem mills require high dynamic response, accurate speed and torque control of main and auxiliary drives while hot rolling mills, such as roughers, and hot strip mills require good torque control and momentary overloadability; all such performance criteria are met by these drives.

Because of the limitations of cycloconverters such as low-power factor, presence of low-frequency inter-harmonics, less maximum output frequency, advances in IGBT and GTO technology cleared the way for their application to the steel mill drives with PWM two-level and later three-level NPC-inverters with high switching frequency, since 1990s. Hitachi and Mitsubishi of Japan reported the development of high-performance three-level GTO-based 6.4 MW and 10 MVA inverters for induction and synchronous motors, respectively, for steel main rolling mill drives in 1996. One such configuration developed by Mitsubishi is shown earlier (Figure 23.10). Regenerative snubber circuit developed to have high efficiency and a SVM method to minimise harmonic distortion are discussed in Okayama *et al.* (1996). Hitachi (Tobise *et al.* 1996) developed similar GTO-based three-level inverters 5–6.4 MW and 2 MW IGBT-based three-level inverters for steel rolling mills at the same time. Siemens introduced SIMOVERT-ML drive with three-level GTO converters of MW range with VC for application to synchronous and induction motors. These converters compete with cyclo-coverters in the capacity region of 10 MVA or less. Three-level IGBT inverters with the same configuration as the three-level GTO inverters in Figure 23.10 were introduced in many steel plants up to 3 MW of medium capacity, for example 1.5 MVA IGBT inverter as in Tobise *et al.* (1996), where three inverters were driven by a common converter. Group-drive applications like Approach Tables, Run-Out Tables are configured with one inverter supplying several motors in a simple V/f mode. Mitsubishi MELVEC 2000 N three-level IGBT inverter (1.5–3 MVA) is claimed to be 40% smaller than the conventional equipment (Masuda and Toyoda 2000).

Figure 23.34 (Yullang *et al.* 2008) shows the application of DTC controlled IGCT-based ACS 6000 as supplied by ABB to a cold reversing mill and plate mill, respectively. These schemes result in higher switching frequency (1 kHz) compared with GTO-based schemes (0.5 kHz), higher efficiency (98%) and higher input power factor (0.97) and less space because of snubberless operation. The DTC method employed allows accurate control of both rotor speed and torque without pulse encoder feedback from the motor shaft.

High-performance three-level IEGT inverters have been introduced by Toshiba for main drives in the steel industry since 2000 (Ichikawa *et al.* 2000, 2004; Suzuki *et al.* 2001), replacing the GTOs in the same converter-inverter configuration as shown in Figure 23.10, resulting in higher efficiency and less size of the equipments. 4.5 kV, 5.5 kA press-packaged IEGTs have been used in an 8 MVA converter-inverter with 99% efficiency, 50% reduction in converter volume and weight (Ichikawa *et al.* 2000). The 8 MVA IEGT inverter supplied by TMEIC, Japan (Hosada *et al.* 2005), for a hot strip mill of Hunan Valin Liangang Steel Co. of China is working since 2003. A new method of PWM control named as *fixed pulse pattern PWM* to reduce the harmonics in the source input currents without increasing the switching frequency for use with these inverters has been reported in Tsukakoshi *et al.* (2005). GE-Toshiba has developed 6–26 MVA Dura-bilt5 MV drives with IEGT-based NPC inverters (GE Toshiba 2003). Figure 23.35 shows one phase leg of a three-level 10 MVA IEGT Inverter with its packaging unit (Tessendorf *et al.* 2008) for rolling mills.

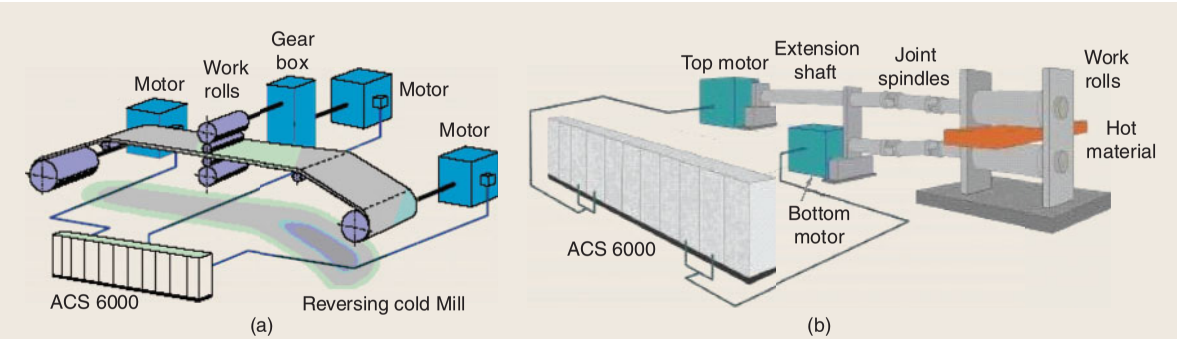

Figure 23.34 (a) Cold reversing mill with ACS6000 and (b) plate mill with ACS 6000 ABB Reprinted with permission from IEEE (Chattopadhyay 2010). (For a color version of this figure, please see color plates.)

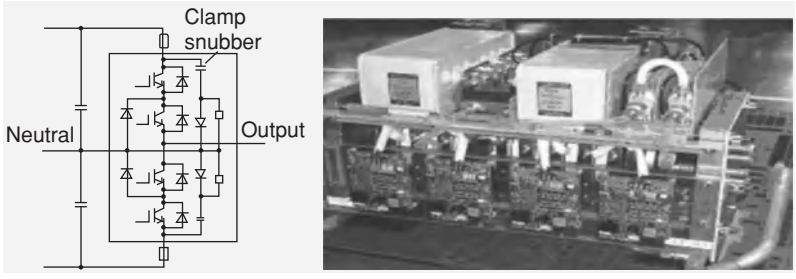

Figure 23.35 One phase leg of a three-level 10 MVA IEGT inverter with packaging unit for a rolling mill (Tessendorf *et al.* 2008). Reprinted with permission from IEEE (Chattopadhyay 2010) (For a color version of this figure, please see color plates.)

23.6.2 Cement and Ore Grinding Mills

By the end of 1960s, the advent of thyristors and control equipment made it possible to design gearless drives via a cycloconverter and a synchronous motor for cement and ore-grinding mills. The world's first gearless Tube/Ball mill drive with motor rating of 8700 hp (6400 kW) at 15 rpm (44 poles, 5.5 Hz) in Le Havre, France, was reported in 1970 (Wurgler 1970). The electrical aspects of the first large gearless ball mill installed at St. Lawrence Cement company in Ontario, Canada, were reported in Allan *et al.* (1975) with a motor rating 8750 hp (6500 kW) at 14.5 rpm (4.84 Hz). The motor is in the self-controlled mode with the stator frequency directly controlled by rotor speed (ac-commutatorless motor) with a rotor position sensor. The motor thus cannot fall out of step and the characteristics are similar to dc machine. However, control of these cycloconverter-fed drives was scalar. First gearless drive with the ring motor (rotor of the synchronous machine wrapped directly round the mill cylinder) and FOC is reported by Siemens in 1978 (Salzmann 1978) and later an improved version in Trantner and Wick (1988). The VC system of the cycloconverter-fed synchronous motor used is described under Section 23.5.2. ABB developed world's largest gearless ball mill drive in cement rated 15 000 hp (11 200 kW) installed in the United States for a mineral grinding process (Errath 1996). A view of the the "wrap-around" gearless ring motor without shaft and bearings is shown in Figure 23.36. The rotor is divided into a number of segments equaling the number of poles that are mounted directly on the mill tube flange. The flange is bolted on to the mill drum. A typical gearless ore grinding mill for mining applications looks the same (Rodriguez *et al.* 2005). The grinding circuit of a typical variable speed SAG mill of 12 MW with two fixed ball mills with SM of 5.5 MW for a copper mine is reported in (Pontt *et al.* 2003; Rodriguez *et al.* 2005; Bose 2011b). Cycloconverters were preferred instead of LCIs to improve the quality and global performance of the grinding process.

23.6.3 Ship Drive and Marine Electric Propulsion

Electric propulsion is now well-established in large ship drives and in the merchant marine, particularly, in cruise liners, icebreakers, shuttle tankers, and so on, as well as in warships. The schemes include power electronic converters located between the generators and the propulsion

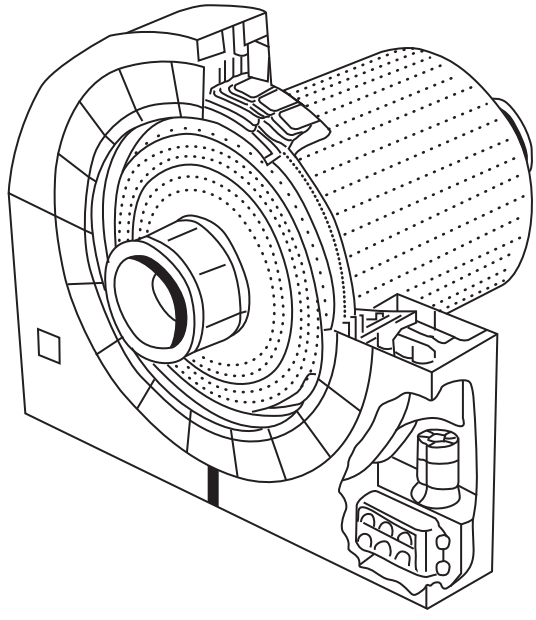

Figure 23.36 View of a wrap-around or ring motor for cement or ore grinding mill

motors to facilitate variable motor speed and thrust from fixed or controllable pitch propellers. The power electronic converters mostly used in modern marine electrical propulsion are ac cycloconverter, LCI and the PWM VSI. The feasibility of a practical marine MC for electrical propulsion system has been studied recently (Bucknall and Ciaramella 2010).

Cycloconverter drive technology is ideally suited to the extreme requirements (large powers at low speeds and high dynamic performance) of the icebreaker. For example, US Coast Guard Icebreaker Healy is equipped with 2 × 11.2 MW, 0–130/160 rpm dual wound motors driving twin shafts, each motor being powered by two 5.6 MW 12-pulse ALSTOM Alspa CL9000 Cycloconverters capable of providing 175% full load trorque for 30 s at zero speed (English 2001; Radan 2004). A shuttle tanker equipped with ABB made cycloconverter propeller drives is also mentioned in Radan (2004). A vector-controlled cycloconverter-fed drive designed for icebreaker to deliver 16 000 hp to the twin propeller shafts of a Canadian Coast Guard icebreaker is reported in (Hill *et al.* 1987).

LCI-fed synchronous motor drives (also known as Synchroconverter-CSI drives) are ideally suited to normal high-power ship propulsion applications such as the cruise liners, for example, RCI Cruise Liner INFINITY with two 19 MW Mermaid podded propulsers which use 2 × 7 MW, 0–118/135 rpm motors with 2 × 12-pulse synchroconverters (English 2001; Radan 2004). Another interesting application of LCIs is in a container ship (Clegg *et al.* 1999), where a 24-pulse SCR-rectifier-inverter system serves as a frequency converter to convert a voltage of 14–25.7 Hz generated by the shaft generator to a bus voltage of 6.6 kV, 60 Hz for the ship's main distribution system.

Medium voltage source two-level inverters with water-cooled series IGBTs with ratings typically up to 20 MW, 2000 rpm, 6.6 kV have been used in drill ships. The ship *Pride*

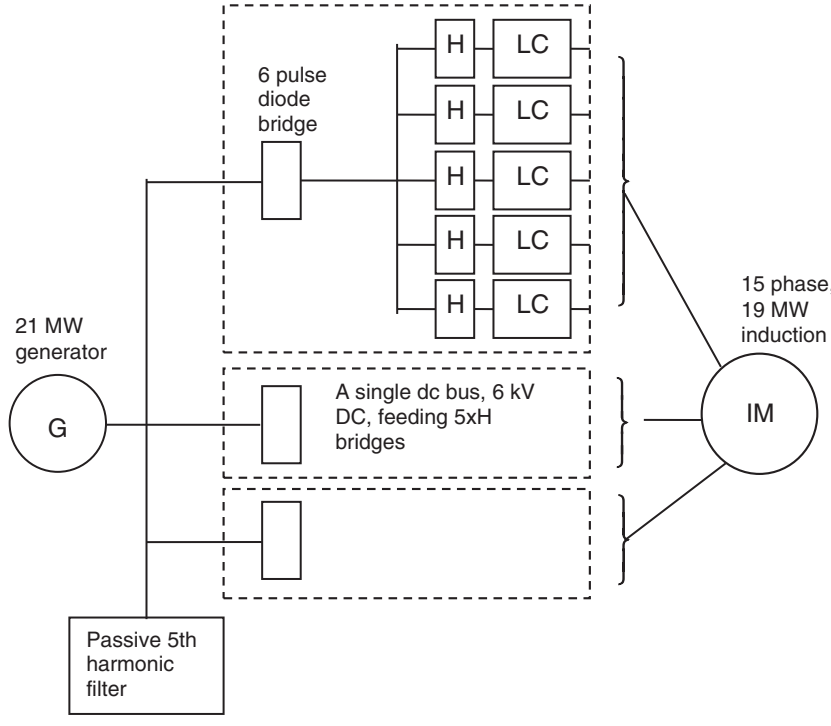

Figure 23.37 Schematic diagram of a IPS drive system of a ship (Crane and McCoy 1999)

Africa is fitted with 7 medium voltage ALSTOM VDM5000 IGBT variable speed thrustor drives up to 4.5 MW (English 2001). World's first electric warship-UK's "daring class" *Type-45 Destroyer*, in service from 2007 is fitted with two 15-phase 20 MW, 4.16 kV ALSTOM VDM25000 PWM drives with advanced induction motors for main propulsion. An integrated power system for all electric ship in a full-scale main propulsion drive for US navy (Crane and McCoy 1999) consists of a main propulsion 19 MW induction motor drive system. The PWM converter (Figure 23.37) consists of three 6-pulse rectifier bridges, three 6 kV dc links and 15 IGBT-based H bridges feeding a 15-phase induction motor.

23.6.4 Mine Hoists, Winders, and Draglines

The trends in the electronic control of mine hoists and winders in the 1970s and 1980s were reviewed in Madiseti and Ramlu, (1986), where it was mentioned that SM supplied by cycloconverter control are ideally suited for hoisting applications that are directly coupled. Torques of about six times the rated torque at low speed are possible and with digital monitoring the winding cycle can be optimised, smooth and accurate. Advanced hoist technologies in coal mines in China and zinc and copper mines in Finland with high-power SM (e.g 2.5 MW, 3 $\times$ 3050 V, 8.7 Hz, 65.8 rpm by ABB in *Pyhasalmi* mine in Finland with shaft depths of 1450 m) are enumerated in Chadwick (2010). The *Pyhasalmi* mine hoist is the first in the world to

use ABB's state-of-the-art ACS6000SD with DTC control using IGCTs to power the16-pole 2.5 MW synchronous motor of the mine hoist. This technology offers several advantages over the alternative systems like cycloconverter and PWM converter in terms of footprint, high reliability, high torque control over the entire speed range, unity power factor and lower energy consumption. The Siemens has supplied two winders for a 537.5-m-deep Majaling coal mine in China equipped with one 3 500 kW synchronous motor and another 435 kW, having Simatic programmable logic controllers for the automation system. Gearless AC drive system-Simine DRAG has been developed by Siemens and Bucyrus with 13 000 hp drive with a performance of 9.7 MW for hoist and dragline for use in *Zhungeer* coal line in China. The drive with ring motor is controlled by IGBT inverters supplied by Siemens Energy & Automation and is in operation since 2007 (Siemens 2011)

23.6.5 Pumps, Fans and Compressors in the Industry

Pumps, compressors and fans are used in the widest range of industry: oil and gas sector, water supply and waste water, chemical and pharmaceutical, cement plants, textile and paper, mining, food and beverage, power plants, climate control and refrigeration systems. AC drive applications in this market, sometimes referred as HVAC (Heating, Ventilation and Air Conditioning) have been developing over the last 35 years. An adjustable speed 10 000 hp ac drive utilising a doubly-fed wound rotor ac motor and a cycloconverter in the rotor circuit was proposed in 1974 (Weiss 1974) for driving a pump or compressor for transportation of gas or liquid through a pipe line. Later in 1980s, adjustable-speed LCI-fed synchronous motor drive system with constant V/Hz control for pump and compressors were discussed in Weiss (1983). LCIs with typical power range of 10–75 MW have emerged for these applications (Hiller *et al.* 2010). Learning experiences encountered on a large variable frequency induction motor drive installation for retrofit of 22 pipeline pumping stations with 3000 HP motors are reported in (Rossman and Ellis 3000). Largest variable-speed synchronous motor fan drive is for the NASA 100 MW wind tunnel consisting of a converter with two independent channels, resulting in a total of four identical six-pulse thyristor bridges and a six-phase synchronous motor having two sets of stator windings with 30° electrical phase shift between them (Bhatia *et al.* 1999). The efficiency of the LCI drive is very high (99%) and is very important in high-power drives in energy saving.

Oil & Gas utilities and LNG (liquefied natural gas) plants requiring large compressors make use of large-scale variable speed drive systems such as VSI and high-power ac motor drive. TMEIC (Toshiba-Mitsubishi Electric Industrial Systems Co) has developed a 30 MVA IGCT controlled five-level VSI-fed synchronous motor (25 MW, 7.2 kV, 3600 rev min) drive system applicable to oil and gas industry (Tsukakoshi *et al.* 2009). The five-level inverter is configured with two NPC legs per phase, connected in a single phase and these phases are combined with a star connection for three-phase output. The five-level inverter output voltage and current are much more sinusoidal and of higher magnitude compared to three-level inverter. The 7.2 kV 30 MVA converter can be applied in parallel up to four sets for a maximum capacity of 120 MVA using balancing reactors. Recently, TMEIC has developed a 20 MVA 6.0 kV five-level IEGT Inverter for the LNG Industry with efficiency more than 99% (Tsukakoshi *et al.* 2010). Commercial drives developed by Siemens (e.g. Siemens *Sinamics* GM150 converter with IGBTs) and ABB (e.g. ACS 1000, ACS 5000 & ACS 6000 with IGCTs and DTC) are widely used for high-power pump and compressor applications.

23.7 New Developments and Future Trends

With the continued development of power semiconductor devices, multi-level inverters, control and estimation technologies, variable speed high power ac drives have gone through a dynamic evolution and poised for new developments in future. Few among various promising fields are as follows:

- The application of silicon carbide (SiC) power semiconductor devices (Singh and Pecht 2008) replacing the present silicon power devices (as described) in high power drives is expected to improve the system performance, reduce system size, reduce power loss, process high power for a given temperature and thus potentially lowering the overall cost. However, the challenges are the SiC device fabrication processes which are expected to advance in the next few years.
- FPGAs (field programmable gate array) are being progressively used in high-performance industrial control systems (Monmassom and Christea 2007) including rotor flux oriented control (Sinard *et al.* 2009) and direct torque control of IM (Kowalski *et al.* 2007). The extremely fast FPGA computation time allows higher throughput and parallel architecture to overcome the typical bottlenecks of DSP sequential algorithms
- Adaptive, optimal and intelligent control based on fuzzy logic (FL) and neural network are emerging technologies (Bose 2012) that, when commercialised, will have dominant impact on high power drives in future. Adaptive controls can be *self-tuning control*, *model reference adaptive control* and *sliding mode or variable structure control*. Optimal control may be *model-based predictive control* where a performance parameter like response time, efficiency, or energy consumption is optimised. It has shown lot of promise recently in the high-performance drives (Kouro *et al.* 2009). Intelligent control is based on artificial intelligence (AI) techniques like expert system, FL, artificial neural network and genetic algorithm. Fuzzy logic has been used in online search-based flux programming efficiency optimisation control of indirect vector-controlled induction motor drive (Sousa *et al.* 1995). Neural network applications have been proposed in motor drives and power electronics as discussed in Bose (2007). Various *fault tolerant control* systems of ac motor drives have been researched (Wechko *et al.* 2004; Delgado *et al.* 2008) to improve reliability in their operation. The concept here is that the drive will continue to operate at a minimum level of performance as per system requirements after sustaining a fault.

23.8 Conclusions

A comprehensive but brief state-of-the-art review of the development of AC motor control in industrial high-power drives involving high-power semiconductor devices, power converter topologies, induction and SM, advanced control strategies used and their implementation, along with their application examples is presented in this chapter. Scalar and VC of induction and synchronous motor drives using VSI, CSI, LCI and cycloconverter are discussed. Scalar control includes V/Hz control and DTC control as used extensively in high power industrial drives. Vector-controlled IM and SM drives including sensorless control have been elaborated. Recent improvement in MC, for medium-voltage highpower drives is also reported. Application

examples of AC motor control in high-power drives such as steel mills, cement and ore-grinding mills, ship drives, mining winders and hoists, pumps, compressors and fans as developed for these industries by the leading drive manufacturers worldwide are highlighted. At the end, new technology developments and future trends in this field have been indicated. It is hoped that this chapter will serve as a useful reference for the academic researchers as well as the practicing engineers working in the field of high power converters and control of adjustable-speed drives.

References

Akagi H (1998) The state-of-the-art of power electronics in Japan. *IEEE Transactions on Power Electronics*, **13**(2), 345–356.

Allan JA, Weyth WA, Hwerzog GW, and Young JAL (1975) Electrical aspects of the 8750 hp gearless ball mill drive at st. lawrence cement company. *IEEE Transactions on Industry Applications*, **IA-11**(6), 681–686.

Bayer KH, Waldmann H, and Weibelzahl M (1972) Field oriented close loop control of synchronous machine with new transvector control system. *Siemens Review*, **39**, 220–223.

Bhatia R, Krattiger H, Bonanini A *et al.* (1999) Adjustable speed drive using a single 135,000 hp synchronous motor. *IEEE Transactions on Energy Conversion*, **14**(3), 571–576.

Blaschke F (1972) The principle of field orientation as applied to the new transvector closed loop control system for rotating field machines. *Siemens Review*, **34**, 217–220.

Bose BK (1982) Adjustable speed ac drives-a technology status review. *Proceedings of IEEE*, **70**(2), 116–135.

Bose BK (2002) *Modern Power Electronics and AC Drives*. Pearson Education Inc. (Asia).

Bose BK (2006) *Power Electronics and Motor Drives–Advances and Trends*. Academic, Burlington, MA.

Bose BK (2007) Neural network applications in power electronics and motor drives – an introduction and perspective. *IEEE Transactions on Industrial Electronics*, 14–33.

Bose BK (2011a) Control and estimation techniques of high power variable speed ac drives-part1 of 3). *IEEE Power Electronics Society Newsletter*, 26–30.

Bose BK (2011b) Ore grinding cycloconverter drive operation and fault-my experience with an australian grid. *IEEE Industrial Electronics Magazine*, 12–22.

Bose BK (2012) Control and estimation techniques of high power variable speed ac drives-(part 3 of 3). *IEEE Power Electronics Newsletter*, 35–38.

Bucknall RWG and Ciaramella K (2010) On the conceptual design and performance of a matrix converter for marine electric propulsion. *IEEE Trans on Power Electron*, **25**(6), 1497–1508.

Chadwick J (2010) Hoist by technology. *International Mining*, 38–44.

Chattopadhyay AK (1997a) Advances in vector control of ac motor drives-a review. *Sadhana (Journ. of Ind, Acad. of Science)*, **22**(6), 797–820.

Chattopadhyay AK (1997b) Cycloconverters and cycloconverter-fed ac motor drives. *Special Issue of Journal of Indian Institute of Science*, **77**(5), 397–419.

Chattopadhyay AK (2002) High power high performance industrial ac drives – a review. *Proceedings of Indian International Conference on Power Electronics (IICPE)*, 1–12.

Chattopadhyay AK (2010) Alternating current drives in the steel industry. *IEEE Industrial Electronics Magazine*, **4**(4), 30–42.

Clegg B, Griffiths HR, Hall DJ, and Tavner PJ (1999) The application of drives and generator technology to a modern container ship. *Proceedings of 9th International Conference on Electro Machanical Drives*, 312–316.

Crane A and McCoy TL (1999) EMC design for a 19 MW PWM motor drive. *Proceedings of IEEE Industry Applications Society Conference*, vol. 3, 1590–1595.

Das SP and Chattopadhyay AK (1996) Comparison of simulation and test results for an ac commutatorless motor drive. *Proceedings of PEVD'96 (IEE)*, 294–299.

Das SP and Chattopadhyay AK (1997) Observer-based stator flux oriented vector control of a cycloconverter-fed synchronous motor drive. *IEEE Transactions on Industry Applications*, **IA-33**, 943–955.

DeDoncker RW and Novotny DW (1994) The universal field oriented controller. *IEEE Transactions on Industrial Applications*, **30**(1), 92–100.

Delgado DVC, Trejo DRE, and Palacious E (2008) Fault tolerant control in variable speed drives: A survey. *IET Electrical Power Applications*, **2**(2), 121–134.

English P (2001) The evolution of marine and drilling drives in today's market. *Dynamic Positioning Conference* September, 2001 ALSTOM Power Conversion Ltd (Rugby, UK).

Erickson EW and Al-Naseem OA (2001) A new family of matrix converters. *Proceedings of IEEE-IECON'01*, vol. 2, 1515–1520.

Errath RA (1996) 15000-hp gearless ball mill drive in cement-why not? *IEEE Transactions on Industrial Applications*, **32**(1), 663–669.

GE Toshiba (2003) *A new family of MV drives for a new converter DURABUILT-5i MV* Product Brochure, March.

Gyugi L and Pelly BR (1976) *Static Power Frequency Changers: Theory, Design and Applications*. Wiley-Interscience, New York.

Hill WA, Turton RA, Dungan RJ, and Schwalm CL (1987) A vector-controlled cycloconverter drive for an icebreaker. *IEEE Transactions on Industry Applications*, **IA-23**(6), 1030–1041.

Hiller M, Sommer R, and Beuermann M (2010) Medium voltage drives-an overview of the common converter topologies and power semiconductor devices. *IEEE Industry Applications Magazine*, **16**(2), 22–30.

Hosada H, Wada S, Kodama S, and Junfeng I (2005) Recent hot strip mill in China. *IEEE-PEDS 2005 Conference REC*, pp. 1078–1083.

Ichihara K, Katayama S, Kokubu T, *et al.* (1986) Application of new drive systems for plate mill drives. *IEEE Transactions on Industry Applications*, **IA-22**(2), 345–351.

Ichikawa K, Shimoura T, Kawakami K, *et al.* (2000) New advanced high voltage inverter employing IEGTs. *Proceedings on International Power Electronics Conference (IPEC)*, pp. 994–999.

Ichikawa K, Tsukakoshi M, and Nakajima R (2004) Higher efficiency three level inverters employing IEGTs. *Proceedings of 19th Annual IEEE Applied Power Electronics Conference (IEEE-APEC)*, 1663–1668.

Ishii S, Yamamoto E, Hara H, *et al.* (2000) A vector-controlled high performance matrix converter induction motor drive. *Proceedings of IPEC*, 235–240.

Jansen P and Lorenz RD (1992) A physically insightful approach to the design and accuracy assessment of the flux observers for field oriented induction machine drives. *IEEE IAS Annual Meet Conference Record*, 570–577.

J. Holtz (2002) Sensorless control of induction motor drives. *Proceedings of IEEE*, **90**(6), 1359–1394.

Kouro S, Cortes P, Vargas R, *et al.* (2009) Model predictive control – a simple and powerful method to control power converters. *IEEE Transactions on Industrial Electronics*, **56**(6), 1826–1838.

Kowalski CT, Lis J, and Kowalski TO (2007) FPGA implementation of dtc control method for the induction motor drive. *IEEE-EUROCON*, 1916–1921.

Kubota H, Matsuse K, and Nakano T (1993) DSP-based speed adaptive flux observer of induction motor. *IEEE Transactions on Industry Applications*, **29**, 344–348.

Madiseti MK and Ramlu MA (1986) Trends in electronic control of mine hoists. *IEEE Transactions on Industry Applications*, **IA-22**(6), 1105–1112.

Malik S and Khage D (1998) ACS 1000–world's first standard ac drive for medium voltage applications. *ABB Review*, **2**, 4–11.

Masuda H and Toyoda M (2000) Variable speed drive systems for steel plants. *Mitsubashi Electric ADVANCE*, 17–29.

Monmassom E and Christea M (2007) FPGA design methodology for industrial control systems-a review. *IEEE Transactions on Industrial Electronics*, **54**(4), 1824–1842.

Nabae A, Takahasi T, and Akagi H (1981) A new neutral point clamped pwm inverter. *IEEE Transactions Industry Applications*, **IA-17**(5), 518–523.

Nakano T, Oswawa H, and Endoh K (1984) A high performance cycloconverter-fed synchronous motor drive system. *IEEE Transactions Industry Applications*, **IA-20**(5), 1278–1284.

Ohmori Y, Nakanishi T, and Kobayashi H (1995) A speed sensorless spatial vector controlled inverter adding an auto-measuring function. *Proceedings of 1995 European Power Electronics Conference*, vol. 3, 452–457.

Okayama H, Koyama M, Tamai S, *et al.* (1996) Large capacity high performance 3-level gto inverter system for steel main rolling mill drives. *IEEE IAS Conference Record*, 174–179.

Okumas HI and Aktas M (2007) Direct torque control of induction machine drives using adaptive hysteresis band for constant switching frequency. *IEMDC Conference Record*, 1762–1767.

Pontt J, Rodriguez J, Valderrama W, *et al.* (2003) Current issues on high power cycloconverter-fed gearless motor drives for grinding mills. *Proceedings of ISIE*, 369–374.

Radan D (2004) Power electronic converters for ship propulsion electric motors, NTNU project All Electric Ship Norway, 2004-11-11.

Rajashekara K, Kawamura A, and Matsuse K (1996) *Sensorless Control of AC Motor Drives: Speed and Position Sensorless Operation*. IEEE Press.

Richlen D (1971) Gearless drive for a cement mill. *Siemens Review*, **38**(9), 398–401.

Rodriguez J, Benett S, Wu B, *et al.* (2007) Multilevel voltage-source converter topologies for industrial medium -voltage drives. *IEEE Transactions on Industry Electronics*, **54**(6), 2930–2943.

Rodriguez JR, Pontt J, Newman P, *et al.* (2005) Technical evaluation and practical experience of high power grinding mill drives in mining applications. *IEEE Transactions on Industrial Applications*, **41**(3), 866–873.

Rossman WC and Ellis RG (1998) Retrofit of 22 pipeline pumping stations with (3000) hp motors and variable frequency drives. *IEEE Transactions on Industry Applications*, **34**(I), 178–186.

Salzmann T (1978) Cycloconverter and automatic control of ring motors driving tube mill. *Siemens Review*, **XLV**(1), 3–8.

Sato K and Yamamoto M (2001) The present state-of-the-art in high power semiconductor devices. *Proceedings of IEEE*, **89**(6), 813–821.

Sengupta S, Mukherjee K, Bhattacharya TK, and Chattopadhyay AK (2000) Performance of an SCR-inverter based commutatorless series motor with load commutation and un-aided start-up capability. *IEEE Transactions on Industry Applications*, **36**(4), 1151–1159.

Siemens (2011) *Gearlessly Into the Mine Gearless drives, July, 26–27.* http://www.industry.siemens.com/ . . . / mining . . . /26_MM0711_GearlessMM0711_technology.pdf.

Sinard S, Begunenane R, and Maillox JG (2009) Performance evaluation of rotor flux oriented control on FPGA for advanced ac drives. *Journal of Robot Mechatronics*, **21**(1), 113–120.

Singh R and Pecht M (2008) Commercial impact of silicon carbide-opportunities and challenges in realizing the full potential of sic power devices. *IEEE Industrial Electronics Magazine*, **2**(3), 19–31.

Sousa GCD, Bose BK, and Cleland JG (1995) Fuzzy logic based on-line efficiency optimization control of an indirect vector controlled induction motor drive. *IEEE Transactions Industrial Electronics*, **42**(2), 192–198.

Stemmler H (1994) High power industrial drives. *Proceedings of IEEE*, **82**(8), 1266–1286.

Sugi K, Naito Y, Kurusowa R, *et al.* (1983) A microcomputer-based high capacity cycloconverter drive for main rolling mill. *Proceedings of IPEC*, 744–755.

Suzuki K, Hosada H, Tsukakoshi M, and Fickier R (2001) IEGT inverter for main drives in the steel industry. *Proceedings of Association of Iron and Steel Engineers (AISE)*, 1–7.

Tessendorf R and Hosoda H (2004) Ac drive technology – 5 year trends. *Proceedings of AISTechnology*, pp. 1–15.

Tessendorf R, Kodama S, and Hosada H (2008) Large PWM inverters for rolling mills. *Iron and Steel Industry*, **5**(1), 65–74.

Timpe W (1982) Cycloconverter drives for rolling mills. *IEEE Transactions on Industry Applications*, **IA-18**(4), 401–404.

Tobise M, Onda K, Sugiyama S, and Yamashina M (1996) Inverter-fed ac drive system for steel rolling mills. *Hitachi Review*, **45**(6), 299–304.

Trantner J and Wick A (1988) Dc link converter and cycloconverter-fed ac motors: The concept and properties of large variable speed drives. *Siemens Rev. (Energy and Automation Special Issue on Large Electric Motor AC Variable Speed Drives)*, **1**, 16–31.

Tsukakoshi M, Mammun MA, Hashimara K, and Hosada H (2009) Performance evaluation of a large capacity vsd system for oil and gas industry. *IEEE Energy Conversion Congress and Exposition (ECCE2009)*, 3485–3492.

Tsukakoshi M, Mammun MA, Hashimara K, *et al.* (2010) Introduction of a large scale high efficiency 5-level iegt inverter for oil and gas industry. *IEEE Energy Conversion Congress and Exposition (ECCE2010)*, 4313–4320.

Tsukakoshi M, Mukunoki M, and Nakamura R (2005) High performance IEGT inverter for main drives in the steel industry. *Proceedings on International Power Electronics Conf (IPEC)*, vol. S15-2, 724–729.

Venturini M (1980) A new sine-wave in sine-wave out converter technique eliminates reactor elements. *Proceedings of POWERCON'80*, vol. E3-1, E3.1–E3.5.

Wechko BA, Lipo TA, Jahns TM, and Schulz SE (2004) Fault tolerant three phase ac motor drive topologies: A comparison of features, cost and limitations. *IEEE Transactions on Power Electronic*, **19**(4), 1108–1116.

Weiss HW (1974) Adjustable speed ac drive systems for pump and compressor applications. *IEEE Transactions on Industry Applications*, **IA-10**(1), 162–167.

Weiss HW (1983) Power transmission to synchronous machines for adjustable-speed pump and compressor drive systems. *IEEE Transactions Industry Applications*, **IA-19**(6), 996–1002.

Wu B (2006) *High Power Converters and AC Drives*, IEEE Press/Wiley-Inter-science 18.

Wurgler HU (1970) The world's first gearless mill drive. *IEEE Transactions on Industril and Gen Appl.*, **IGA-6**(5), 524–527.

Yamamoto E, Hara H, Uchino T, *et al.* (2011) Development of MCs and its applications in industry. *IEEE Industrial Electronics Magazine*, 4–12.

Yullang Z, Frimanand A, and Modig L (2008) Advanced single and multi drive systems for plate rolling mills. *Millenium Steel*, 168–170.

Zhang L, Wathanasarn C, and Shepherd W (1998) Analysis and comparison of control strategies for ac-ac matrix converters. *IEE Proceedings of Elecric Power Applications*, **145**(4), 284–294.

Index

AC Electric Motors Control: Advanced Design Techniques and Applications, First Edition. Edited by Fouad Giri.

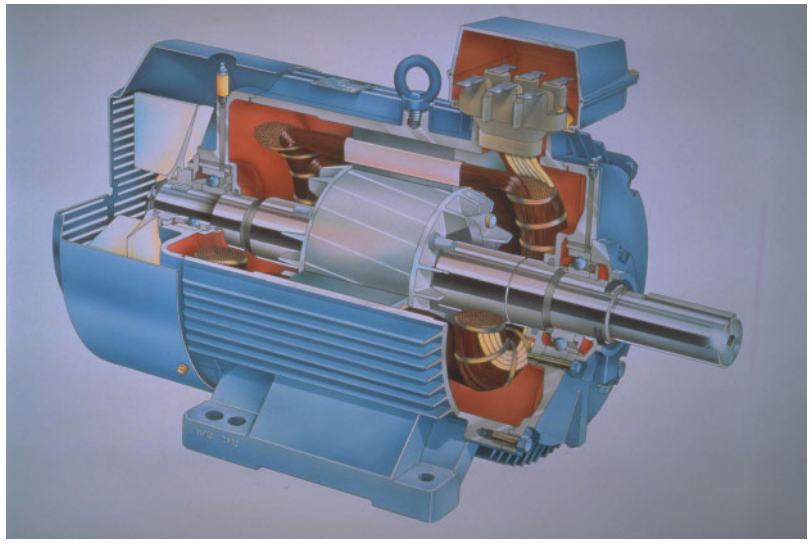

Figure 2.1 Squirrel-cage induction motor. Copyright granted, 2012, ABB; all rights reserved. (See page 18).

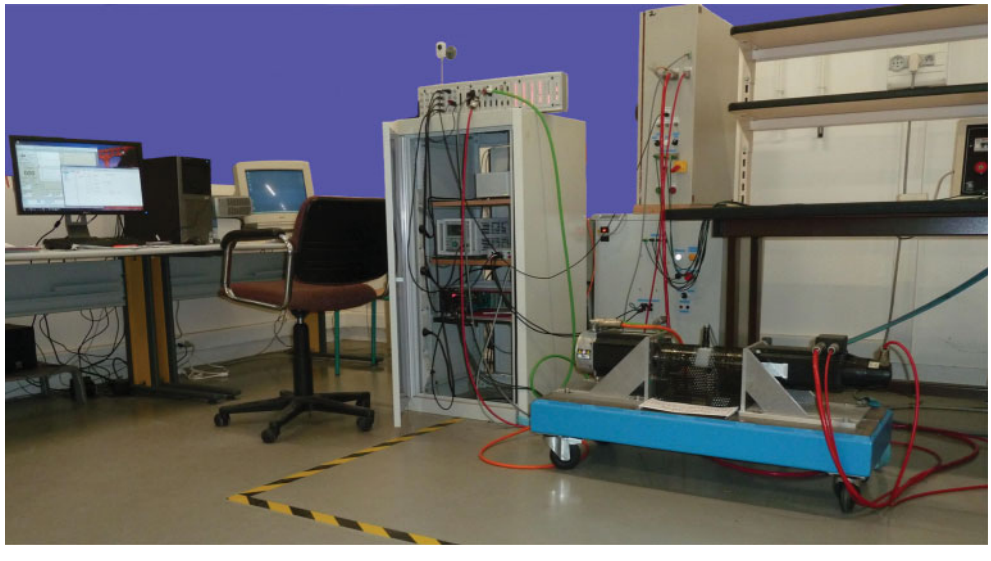

Figure 11.1 Experimental setup. (See page 219).

AC Electric Motors Control: Advanced Design Techniques and Applications, First Edition. Edited by Fouad Giri.

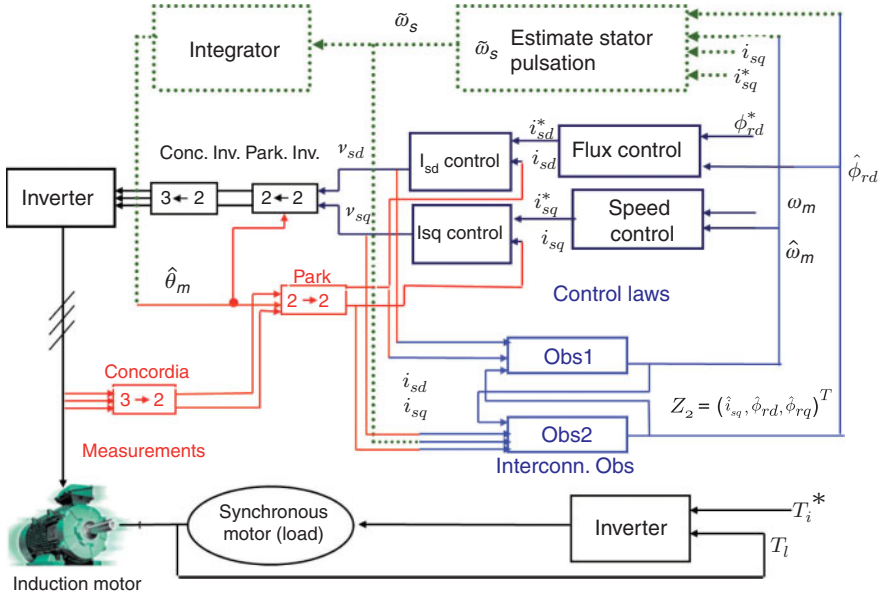

Figure 11.2 Experimental setup and observer-control scheme. (See page 219).

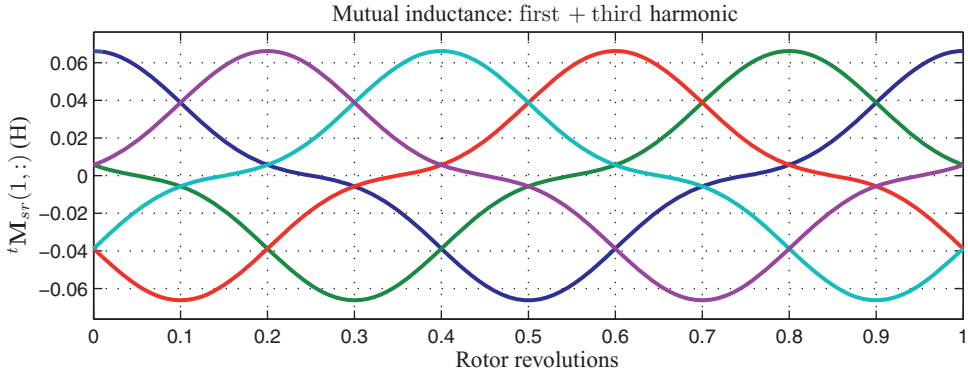

Figure 12.8 Mutual inductance between the first stator phase and the rotor phases. (See page 248).

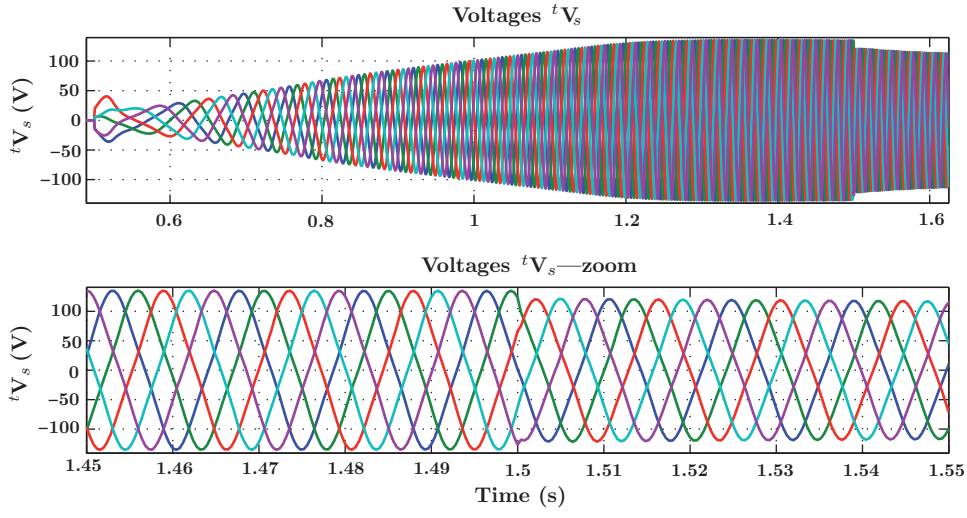

Figure 12.12 Stator voltages in the original reference frame Σ_t during the velocity rising ramp. (See page 250).

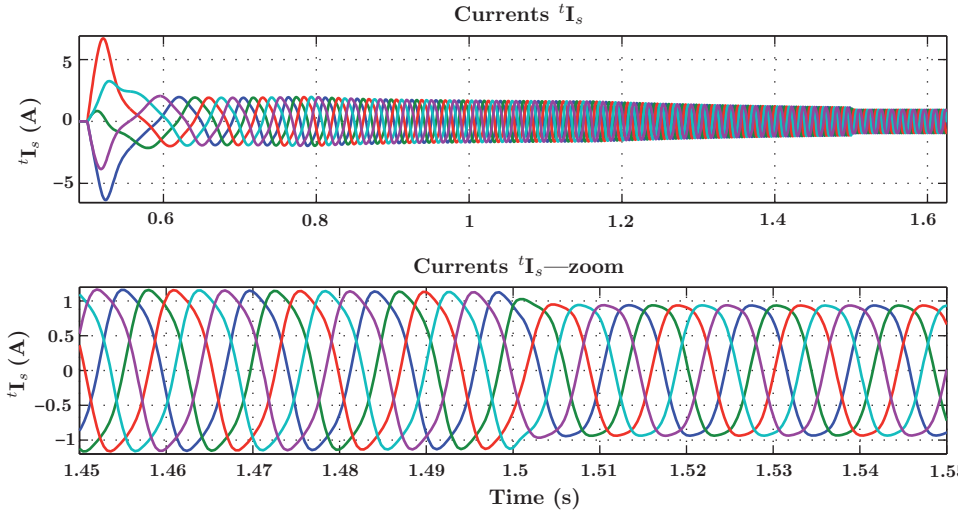

Figure 12.13 Stator currents in the original reference frame Σ_t during the velocity rising ramp. (See page 250).

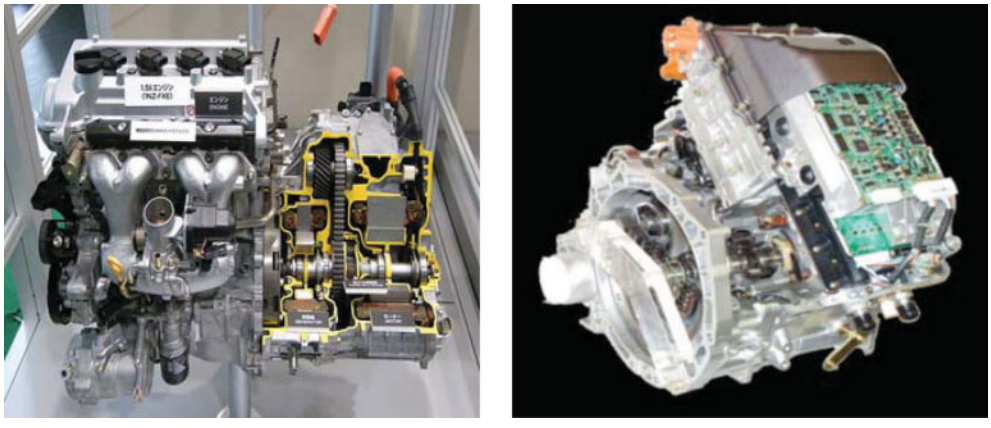

(a) (b)

Figure 21.2 (a) Toyota THS parallel hybrid drivetrain and (b) Ford parallel hybrid drivetrain. (See page 457).

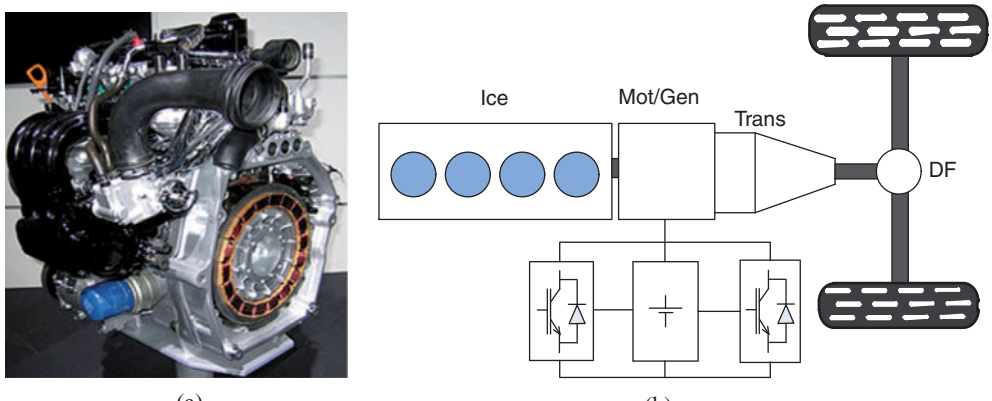

(a) (b)

Figure 21.3 (a) Configuration of Honda Insight parallel hybrid and (b) schematic of Honda Insight drivetrain. (See page 458).

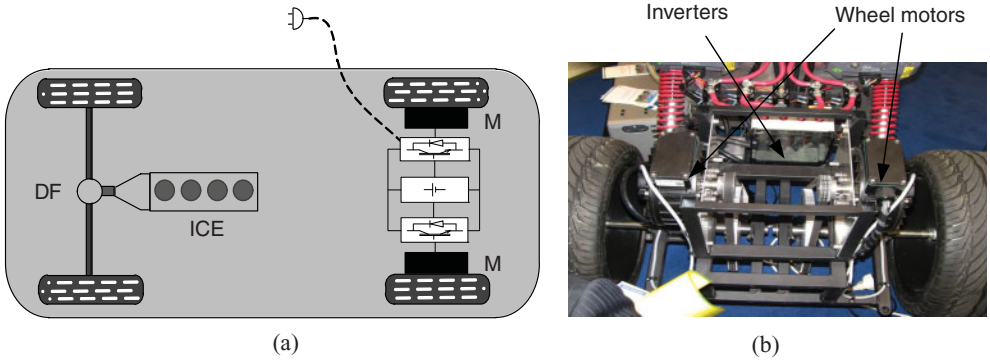

(a) (b)

Figure 21.5 (a) Schematic of an Audi experimental HEV, and (b) photo of rear electric drivetrain from PCIM2010, Nuremberg. (See page 459).

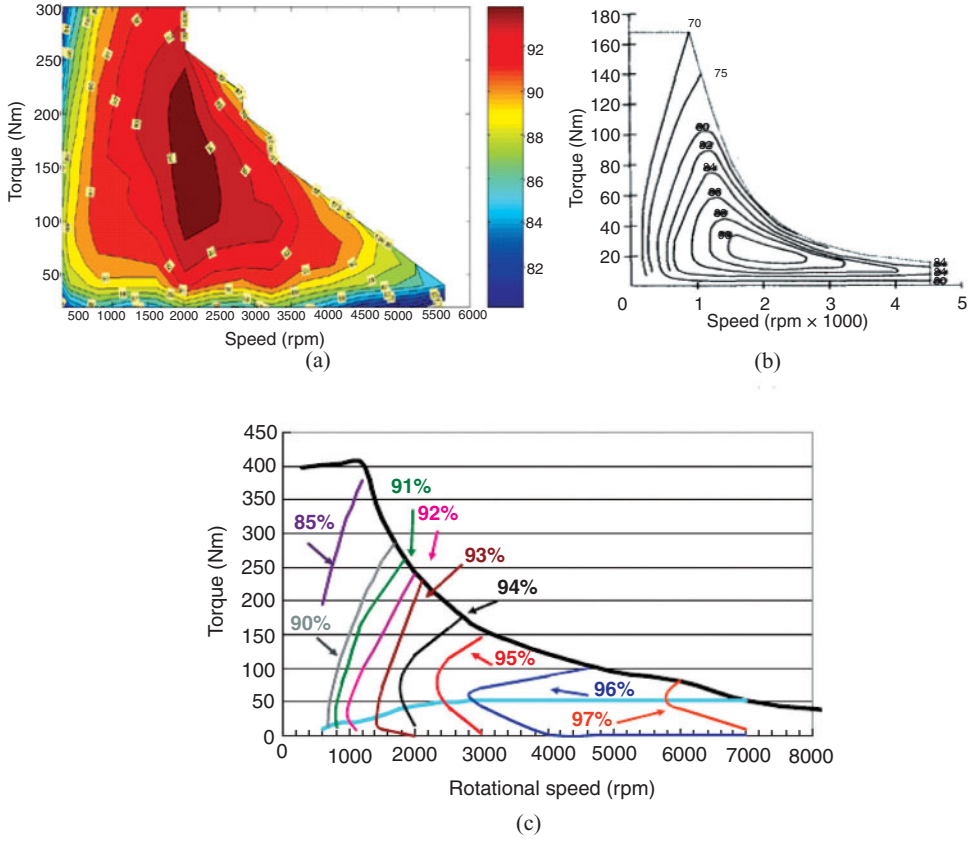

Figure 21.10 Torque-speed characteristics and efficiency maps of (a) the IMPMSM in Toyota Camri Hybrid (Olszewski 2008), (b) an induction machine (Gosden *et al.* 1994) and (c) an SRM (Takano *et al.* 2010). (See page 466).

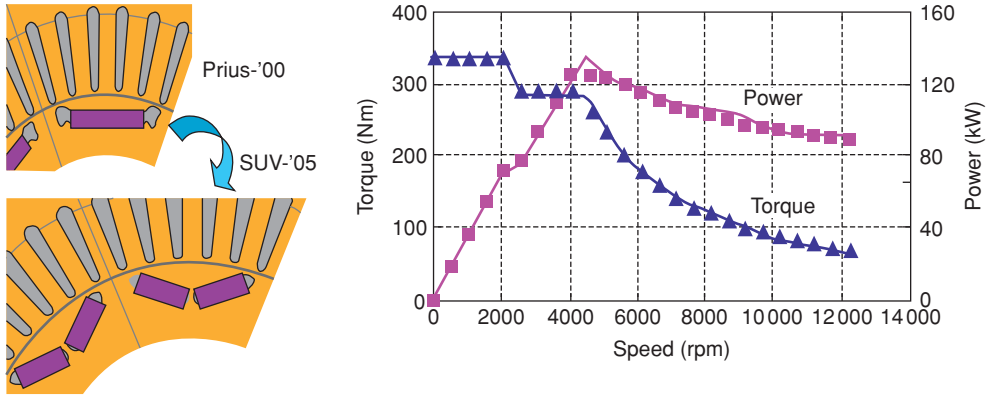

Figure 21.16 The electromagnetic design of the IPMSM in Toyota Prius HEV and its torque-speed and CPSR characteristics. (See page 472).

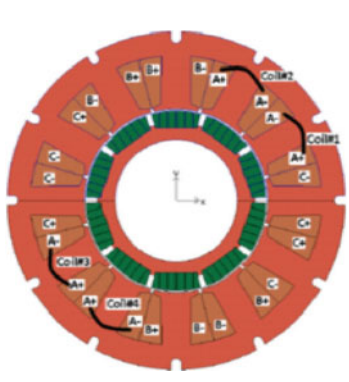

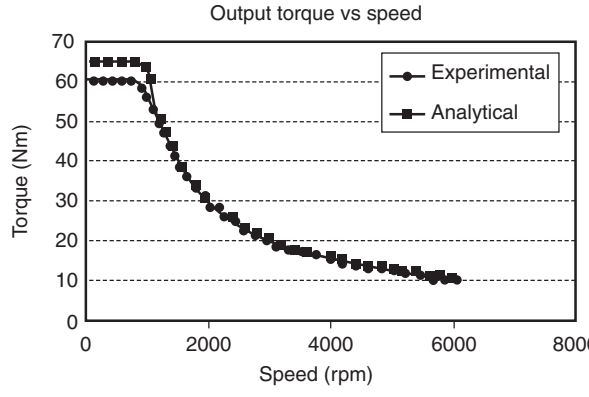

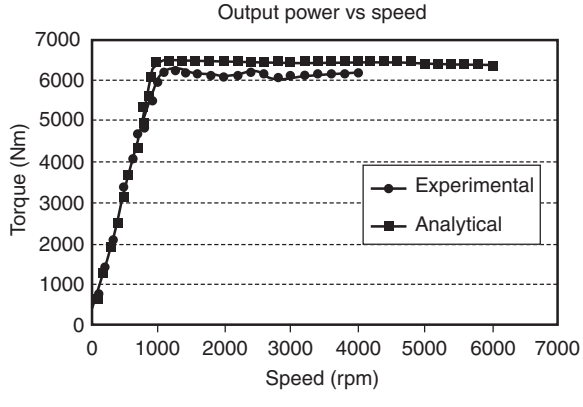

Figure 21.17 The electromagnetic design of the SPM machine with fractional-slot winding developed at the University of Wisconsin-Madison (Reddy *et al.* 2011). (See page 472).

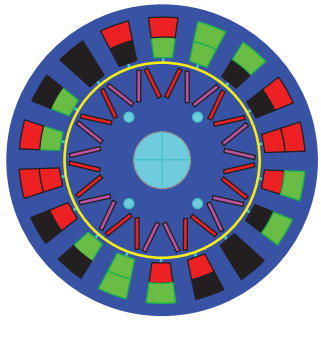

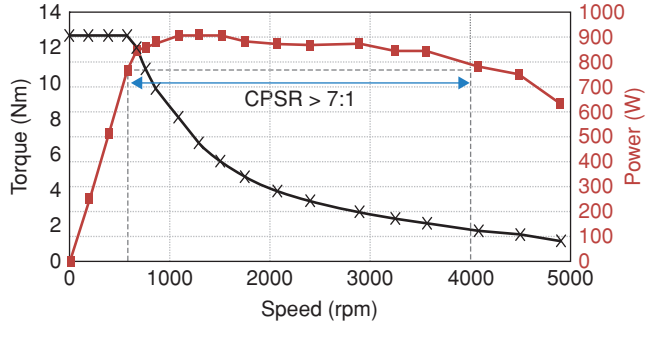

Figure 21.18 The electromagnetic design of the SPM machine with fractional-slot winding developed at the University of New South Wales (Dutta *et al.* 2011). (See page 473).

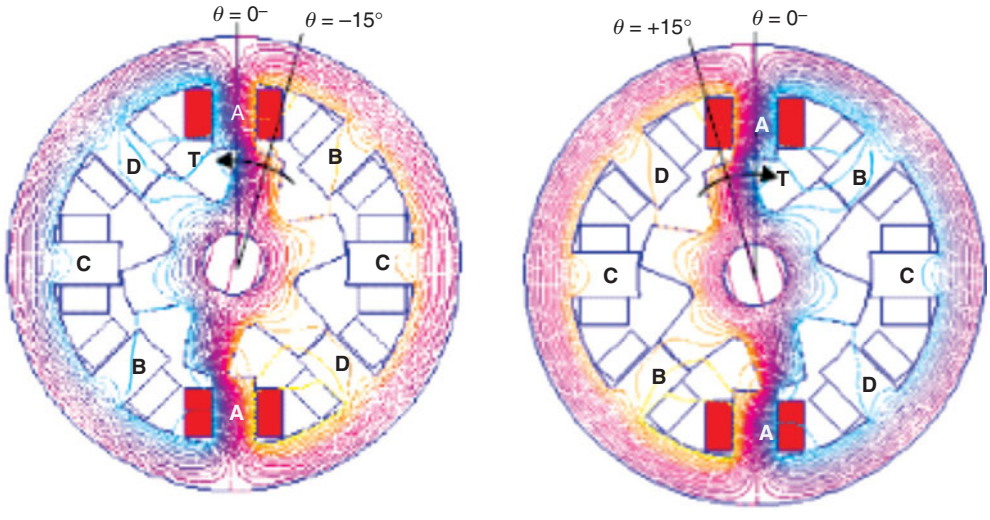

Figure 21.19 Cross section of an 8/6 SRM. (See page 473).

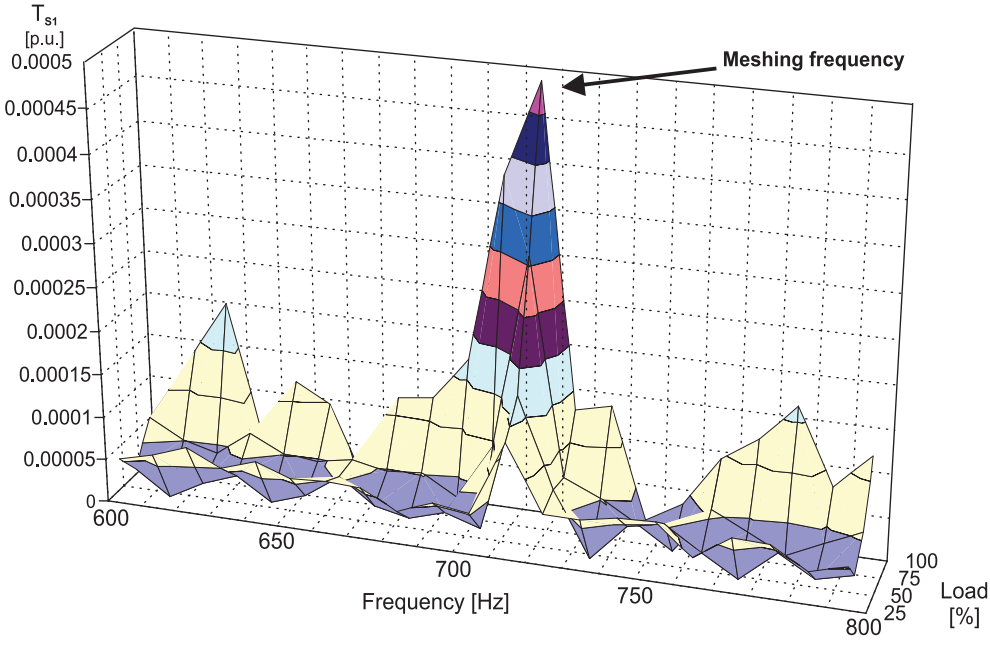

Figure 22.17 Identification of the gear meshing frequency for motor speed related to 50 km/h train velocity. (See page 502).

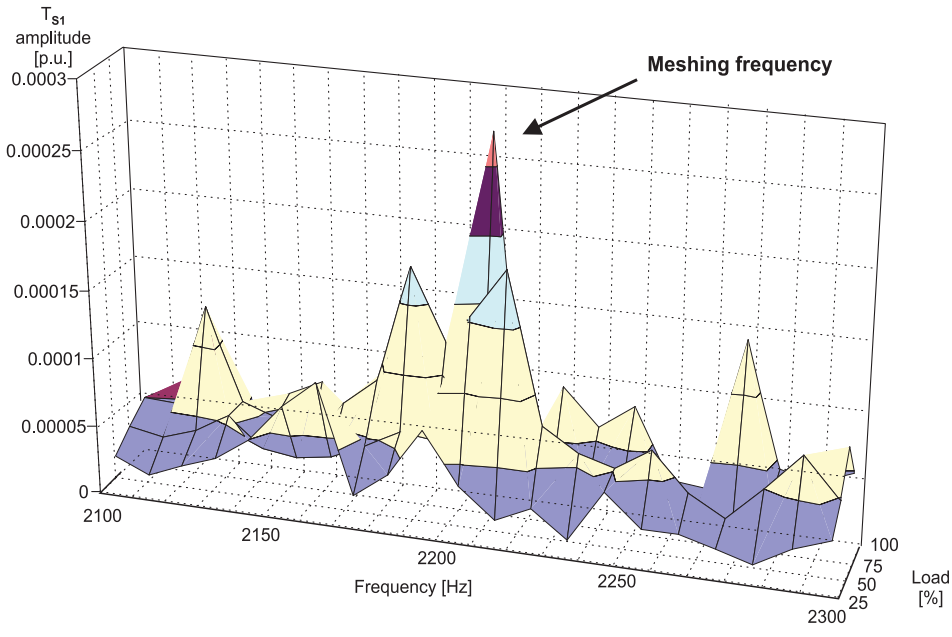

Figure 22.18 Identification of the gear meshing frequency for motor speed related to ca. 150 km/h train velocity. (See page 503).

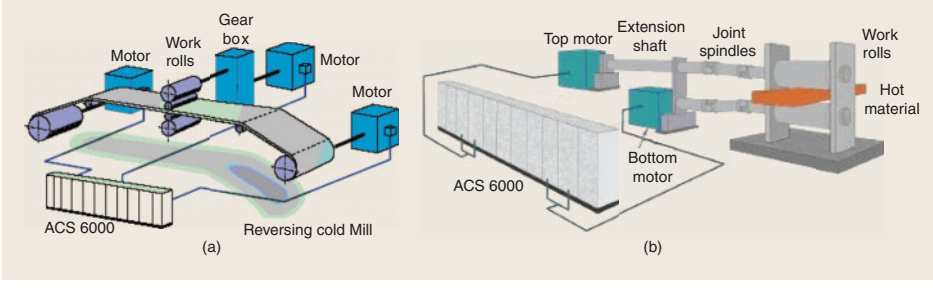

Figure 23.34 (a) Cold reversing mill with ACS6000 and (b) plate mill with ACS 6000 ABB Reprinted with permission from IEEE (Chattopadhyay 2010). (See page 543).

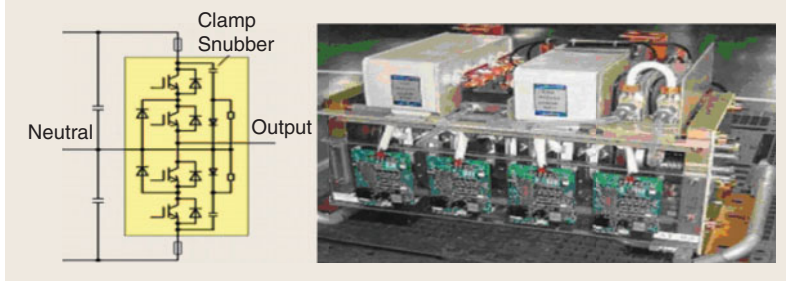

Figure 23.35 One phase leg of a three-level 10 MVA IEGT inverter with packaging unit for a rolling mill (Tessendorf *et al.* 2008) Reprinted with permission from IEEE (Chattopadhyay 2010). (See page 544).